Challa S.S.R. Kumar   *Editor*

X-ray and Neutron Techniques for Nanomaterials Characterization

Springer

X-ray and Neutron Techniques for Nanomaterials Characterization

Challa S. S. R. Kumar

Editor

X-ray and Neutron Techniques for Nanomaterials Characterization

With 328 Figures and 19 Tables

Springer

Editor
Challa S. S. R. Kumar
Integrated Mesoscale Architectures for
Sustainable Catalysis (IMASC)
Rowland Institute of Science
Harvard University
Cambridge, MA, USA

Printed on acid-free paper

Contents

v

Contributors

Kiyotaka Asakura Catalysis Research Center, Hokkaido University, Sapporo, Hokkaido, Japan

Kyoko Bando Nanosystem Research Institute, National Institute of Advanced Industrial Science and Technology (AIST), Tsukuba, Japan

Loïc Barré IFP Energies Nouvelles, Rueil Malmaison, France

Oier Bikondoa Department of Physics, University of Warwick, Coventry, UK
XMaS, The UK-CRG Beamline, ESRF – The European Synchrotron, Grenoble, France

Lisa Bovenkamp-Langlois CAMD (Center for Advanced Microstructures and Devices), Louisiana State University, Baton Rouge, LA, USA
Center for Atomic-Level Catalyst Design, Cain Department of Chemical Engineering, Louisiana State University, Baton Rouge, LA, USA

Antonio Cervellino Swiss Light Source, Paul Scherrer Institut, Villigen, Switzerland

Suresh M. Chathoth Department of Physics and Materials Science, City University of Hong Kong, Kowloon Tong, Hong Kong

Wang-Jae Chun Graduate School of Arts and Sciences, International Christian University, Mitaka, Tokyo, Japan

Ruggero Frison Istituto di Cristallografia and To.sca.Lab., Consiglio Nazionale delle Ricerche, Como, Italy
Department of Chemistry, University of Zurich, Zurich, Switzerland

Alexandre Giuliani Synchrotron SOLEIL, L'Orme des Merisiers, Gif-sur-Yvette, France
UAR1008, CEPIA, INRA, Nantes, France

Antonietta Guagliardi Istituto di Cristallografia and To.sca.Lab., Consiglio Nazionale delle Ricerche, Como, Italy

Yuriy Halahovets Institute of Physics, Slovak Academy of Sciences, Bratislava, Slovakia

Bernhard Hesse ESRF – The European Synchrotron, Grenoble, France

Adam Hitchcock Department of Chemistry and Chemical Biology, McMaster University, Hamilton, ON, Canada

Martin Hodas Institute of Physics, Slovak Academy of Sciences, Bratislava, Slovakia

Matej Jergel Institute of Physics, Slovak Academy of Sciences, Bratislava, Slovakia

Maria Katsikini School of Physics, Department of Solid State Physics, Aristotle University of Thessaloniki, Thessaloniki, Greece

Toshihiro Kondo Global Research Center for Environment and Energy based on Nanomaterials Science (GREEN), National Institute for Materials Science (NIMS), Tsukuba, Japan
Graduate School of Humanities and Sciences, Ochanomizu University, Bunkyo-ku, Tokyo, Japan

Dusan Korytar Institute of Electrical Engineering, Slovak Academy of Sciences, Bratislava, Slovakia

Max Langer CREATIS, CNRS UMR5220, Inserm U1206, Université de Lyon, INSA-Lyon, Université Claude Bernard Lyon 1, Villeurbanne, France
ESRF – The European Synchrotron, Grenoble, France

Eva Majkova Institute of Physics, Slovak Academy of Sciences, Bratislava, Slovakia

Nebojsa Marinkovic Department of Chemical Engineering, Columbia University, New York, NY, USA

Norberto Masciocchi Dipartimento di Scienza e Alta Tecnologia and To.sca.Lab., Università dell'Insubria, Como, Italy

Takuya Masuda Global Research Center for Environment and Energy based on Nanomaterials Science (GREEN), National Institute for Materials Science (NIMS), Tsukuba, Japan
Advanced Key Technologies Division, National Institute for Materials Science (NIMS), Tsukuba, Japan
Precursory Research for Embryonic Science and Technology (PRESTO), Japan Science and Technology Agency (JST), Kawaguchi, Japan

Aleksandar R. Milosavljević Institute of Physics Belgrade, University of Belgrade, Belgrade, Serbia

Christophe Nicolas Synchrotron SOLEIL, L'Orme des Merisiers, Gif-sur-Yvette, France

Martin Obst Bayreuth Center of Ecology and Environmental Research (BayCEER), University of Bayreuth, Bayreuth, Germany

Eleni C. Paloura School of Physics, Department of Solid State Physics, Aristotle University of Thessaloniki, Thessaloniki, Greece

Marco Pelletta Institute of Physics, Slovak Academy of Sciences, Bratislava, Slovakia

Kotaro Sasaki Chemistry Department, Brookhaven National Laboratory, Upton, NY, USA

Martha W. Schaefer CAMD (Center for Advanced Microstructures and Devices), Louisiana State University, Baton Rouge, LA, USA

Department of Geology and Geophysics, Louisiana State University, Baton Rouge, LA, USA

Department of Physics and Astronomy, Louisiana State University, Baton Rouge, LA, USA

Gregor Schmid Center for Applied Geoscience, Eberhard Karls University Tuebingen, Tuebingen, Germany

Peter Siffalovic Institute of Physics, Slovak Academy of Sciences, Bratislava, Slovakia

Satoru Takakusagi Catalysis Research Center, Hokkaido University, Sapporo, Hokkaido, Japan

Hiroyuki Takeno Department of Chemistry and Chemical Biology, School of Science and Technology, Gunma University, Kiryu, Gunma, Japan

Madhusudan Tyagi NIST Center for Neutron Research, Gaithersburg, MD, USA

Department of Materials Science and Engineering, University of Maryland, College Park, MD, USA

Yohei Uemura Division of Electronic Structure, Department of Materials Science, Institute for Molecular Science, Okazai, Aichi, Japan

Kohei Uosaki Global Research Center for Environment and Energy based on Nanomaterials Science (GREEN), National Institute for Materials Science (NIMS), Tsukuba, Japan

International Center for Materials Nanoarchitectonics (MANA), National Institute for Materials Science (NIMS), Tsukuba, Japan

Peter Varga Julius-Wolff-Institute & Berlin Brandenburg School for Regenerative Therapies, Charité-Universitätsmedizin Berlin, Berlin, Germany

AO Research Institute Davos, Davos, Switzerland

Karol Vegso Institute of Physics, Slovak Academy of Sciences, Bratislava, Slovakia

Loriane Weber CREATIS, CNRS UMR5220, Inserm U1206, Université de Lyon, INSA-Lyon, Université Claude Bernard Lyon 1, Villeurbanne, France

ESRF – The European Synchrotron, Grenoble, France

Juan Wu Department of Chemistry and Chemical Biology, McMaster University, Hamilton, ON, Canada

Zdeno Zaprazny Institute of Electrical Engineering, Slovak Academy of Sciences, Bratislava, Slovakia

Synchrotron X-Ray Phase Nanotomography for Bone Tissue Characterization

Peter Varga, Loriane Weber, Bernhard Hesse, and Max Langer

Contents

P. Varga (✉)
Julius-Wolff-Institute & Berlin Brandenburg School for Regenerative Therapies,
Charité-Universitätsmedizin Berlin, Berlin, Germany

AO Research Institute Davos, Davos, Switzerland
e-mail: peter.varga@aofoundation.org

L. Weber • M. Langer
CREATIS, CNRS UMR5220, Inserm U1206, Université de Lyon, INSA-Lyon, Université Claude
Bernard Lyon 1, Villeurbanne, France

ESRF – The European Synchrotron, Grenoble, France
e-mail: loriane.weber@esrf.fr; max.langer@esrf.fr

B. Hesse
ESRF – The European Synchrotron, Grenoble, France
e-mail: bernhard.hesse@esrf.fr

1   Definition of the Topic

X-ray phase nano-tomography allows the characterisation of bone ultrastructure: the lacuno-canalicular network, nanoscale mineralisation and the collagen orientation. In this chapter, we review the different X-ray imaging techniques capable of imaging the bone ultrastructure and then describe the work that has been done so far in nanoscale bone tissue characterisation using X-ray phase nano-tomography.

2   Overview

X-ray computed tomography at the micrometric scale is more and more considered as the reference technique in imaging of bone microstructure. The trend has been to push towards higher and higher resolution. Due to the difficulty of realising optics in the hard X-ray regime, the magnification has mainly been due to the use of visible light optics and indirect detection of the X-rays, which limits the attainable resolution with respect to the wavelength of the visible light used in detection. Recent developments in X-ray optics and instrumentation have allowed the implementation of several types of methods that achieve imaging limited in resolution by the X-ray wavelength, thus enabling computed tomography at the nanoscale. We review here the X-ray techniques with 3D imaging capability at the nanoscale: transmission X-ray microscopy, ptychography and in-line holography. Then, we present the experimental methodology for the in-line phase tomography, both at the instrumentation level and the physics behind this imaging technique. Further, we review the different ultrastructural features of bone that have so far been resolved and the applications that have been reported: imaging of the lacuno-canalicular network, direct analysis of collagen orientation, analysis of mineralisation on the nanoscale and the use of 3D images at the nanoscale as the basis of mechanical analyses. Finally, we discuss the issue of going beyond qualitative description to quantification of ultrastructural features.

3   Introduction

X-ray imaging and assessment of bone have been intimately linked already since the discovery of X-rays. Actually, the first application of X-rays was visualisation of bone on the organ level [1]. This consisted in simple projection images, usually known as radiographs. X-ray computed tomography (CT) [2, 3], that is, cross-sectional imaging, enables three-dimensional (3D) imaging by combining the acquisition of radiographs at several angles of rotation around the targeted object and a tomographic reconstruction algorithm. This modality has gained wide use in medical imaging. X-ray CT at the micron scale (μCT) combines CT imaging with the use of high-resolution detectors. X-ray μCT has recently assumed the place as the reference method for bone microstructure imaging, among other applications [4]. This is, apart from the excellent contrast in hard materials, sufficient penetration in bone and 3D

nature of the images, due to compact μCT systems being increasingly available [5–7]. Synchrotron sources in combination with insertion devices are powerful X-ray sources enabling highly monochromatic X-rays. If such a source is used, the resulting modality is called synchrotron radiation μCT (SR-μCT) [8] that allows functional imaging, i.e. direct 3D quantification of the degree of mineralisation of bone (DMB) at the micro-scale [9].

The trend in μCT and other X-ray microscopy techniques has been to go towards higher and higher resolution [10], since the properties of X-rays are very appealing: short wavelength (so a lower diffraction limit than with visible light) combined with high penetration power yielding good contrast in bone. This goes hand in hand with the increasing demand of quantitative 3D images of bone at the micro- and nano-scale, due to the links between ultrastructure and failure [11, 12]. The high penetration power makes it difficult to implement X-ray focusing optics, however, which has kept the magnification factor due to the X-ray beam fairly low. High-resolution imaging has instead been achieved by indirect detection: a fluorescent screen, a scintillator with a high efficiency in converting X-rays to visible light, imaged by standard visible light microscope optics onto a CCD camera [13]. This kind of system is diffraction limited in resolution by the wavelength of the visible light emitted by the scintillator, however. In this case, imaging of the ultrastructure cannot be considered, since this is usually reserved for features that are smaller than those resolvable with a standard bright field visible light microscope operating in transmission mode.

Osteoporosis and other bone fragility-related diseases are not yet fully understood and are thus the subject of active research. While previously the main focus was the characterisation, description and diagnosis of these diseases, currently the main aim is to uncover the mechanisms behind bone loss and those involved in bone failure. Bone mass is the most important determinant of bone strength, but it is known not to be the only factor. For example, collagen cross-linking is thought to be important for the integrity of the bone tissue [14]. Bone fragility is thought to result from failed material or structural adaptations to mechanical stress [15]. Since bone adapts to externally imposed mechanical stresses through a process of remodelling, the bone tissue changes its macro-, micro- and ultrastructure during its lifetime.

Bone remodelling is achieved via the processes of mechanosensation and mechanotransduction, which are thought to be performed by the osteocyte system. Osteocytes are the most abundant bone cells dispersed throughout the bone system. They differentiate from osteoblasts, which are the cells responsible for bone formation, by getting trapped in the pre-bone matrix during tissue formation. The osteocytes interconnect and communicate through dendritic processes [16–19]. The imprint of osteocytes and their processes are called the lacunae and the canaliculi, respectively, and form the lacuno-canicular network (LCN) [20]. The sensitivity of osteocytes to external strain could be due to sensing substrate deformation directly or by strains induced by the flow of interstitial fluid circulating in the LCN [21–23]. Moreover, microcracks are also thought to trigger remodelling by interrupting osteocyte dendrites [24–27]. The interest in studying osteocytes and their pore network has been on the rise the last few years, which can be witnessed by

published statements such that the LCN is "the unrecognized side of bone tissue" or that osteocytes "can't hide forever" [28–32]. Apart from their presumed role in the bone remodelling, these cells are also thought to contribute to the maintenance of mineral homeostasis. In relation to this, they secrete a number of biochemical factors, of which some are seen as potential therapeutic targets [33]. It should be mentioned however that the complete role of the osteocyte, and other possible processes for bone remodelling, is not yet fully elucidated but is rather the topic of active research [34].

Osteocytes and the LCN are not the only aspects of bone ultrastructure that are interesting to study, however. At the ultrastructural level, bone tissue is a natural nanocomposite consisting of mineralised collagen fibres. These fibres are organised in a regular fashion around the vessel canals: the Haversian canals forming the centre in units of bone remodelling called osteons and Volkmann canals interconnecting the Haversian canals and the periosteum. During the lifetime of bone tissue, mineralised matrix is being resorbed by osteoclasts and replaced by osteoblasts with new osteons. Between these secondary osteons, there remain rests of older tissue called interstitial tissue. At the boundary of each osteon, there is a layer of mineralised tissue called the cement line, which is thought to have an important role in limiting crack propagation and to affect the overall stiffness of bone [35, 36]. The cement line has previously been characterised mainly using quantitative backscatter electron imaging (qBEI). It has been disputed whether the cement line is hypo-mineralised [35, 36] or hyper-mineralised [37, 38]. It may also act as a boundary of the interconnected porosity within an osteon. At least one study has reported canalicular tunnelling through the cement line, however [39].

The organisation of the collagen fibrils is thought to directly influence bone strength and toughness. The analysis of collagen orientation has so far been performed mainly in 2D using scanning electron microscopy [40–43], transmission electron microscopy [44] and atomic force microscopy [45] or indirectly analysed by polarised light microscopy [46] and Raman spectral mapping [47, 48]. So far very little data is available on the 3D fine structure of the LCN and the bone matrix on the nanoscale. X-ray µCT has been used extensively to study bone tissue microstructure. There has been some work performed on imaging the LCN using µCT [49–55]. Since the diameter of the canaliculi can be as small as ~100 nm, µCT cannot by definition be used to image ultrastructure however, as mentioned above.

The techniques used to image bone ultrastructure in 3D have so far been transmission electron microscopy, scanning electron microscopy and confocal laser scanning microscopy (CLSM). CLSM is however limited by the depth of penetration in mineralised tissue, and its spatial resolution is anisotropic, depending on the depth into the sample where the focus is placed. It is also a scanning technique, which implies that data acquisition is relatively slow. Finally, advanced staining and sample preparation is necessary [56].

Another technique which has recently been progressing towards chemical imaging of bone ultrastructure is infrared nanoscopy. Even though this technique gives only access to the chemical properties in 2D, it might be of increasing interest due to

the increasing number of available instruments, relatively simple sample preparation and high spatial resolution up to tens of nm at a field of view in the order of 100 × 100 μm [57, 58].

Serial sectioning using a focused ion beam followed by imaging with scanning electron microscopy (FIB-SEM) to image the lacuno-canalicular network has been reported [42, 43, 59, 60]. While this technique offers excellent spatial resolution, it is a destructive technique, and it requires advanced sample preparation. The repeated sectioning and imaging also lead to long acquisition times. Finally, transmission electron tomography has been used to image osteocyte ultrastructure in situ [61]. However, this kind of imaging is limited to very thin sections, 3 μm in the cited work. Thus, the 3D information is quite limited and only provides a very local visualisation of the osteocyte.

We review here the work that has been done in imaging of the ultrastructure of bone in 3D using X-rays. We give a brief introduction to high-resolution X-ray imaging physics. We then continue to describe the different imaging methods that have been used for ultrastructural imaging in bone, along with the results that were obtained. We give particular attention to the propagation-based technique, where we outline more in detail the image formation and reconstruction. We then describe the type of analyses that have so far been possible at shorter length scales than can be seen by visible light. Finally, we briefly discuss what we consider the next step of 3D ultrastructure imaging in bone: the possibility of in situ cell imaging in bone using X-ray phase nano-tomography.

4   Experimental and Instrumental Methodology

4.1   Instrumentation

4.1.1   X-Ray Source

The work described in Sects. 5.1.3, 5.2, 5.3 and 5.4 was performed on beamline ID22 at the European Synchrotron Radiation Facility (ESRF), Grenoble, France. ID22 is located on a high-β straight section and was equipped with two insertion devices: an in-vacuum U23 and a revolver U35/U19. The electron beam in the synchrotron had a current of ~200 mA, an energy of 6 GeV and a relative energy spread of 0.001. The vertical (horizontal) emittance, β values and dispersion were 39 pm (3.9 nm), 3 m (37.2 m) and 0 m (0.137 m), respectively. The revolver device was chosen to give maximum photon output in a moderately narrow energy range centred on 17.5 keV, which is the principal working energy for imaging at ID22 [62].

4.1.2   X-Ray Optics

The X-ray focusing optics consisted of two graded multilayer coated mirrors mounted in a crossed Kirkpatrick-Baez (KB) configuration [63]. The vertical mirror was 112 mm long and had a focusing distance of 180 mm, and the horizontal mirror was 76 mm long and had a focusing distance of 83 mm. The mirrors were

dynamically bendable to create the appropriate elliptical shape required to focus the X-ray beam. The resulting reflectivity at 17 keV was 73 % and yielded a spot size of approximately 50 nm × 50 nm. The vertical mirror images directly the undulator source (~25 μm FWHM), whereas in the horizontal direction, a virtual source is created by the use of high heat-load slits. The multilayer mirrors both focus and monochromatise the beam, resulting in a very high flux of about 5×10^{12} photons/s and a moderate degree of monochromaticity of $\Delta E/E \approx 10^{-2}$ [64–68].

4.2   Image Formation

The refractive index n of an object can be described as [69]:

$$n(x, y, z) = 1 - \delta(x, y, z) + i\beta(x, y, z), \tag{1.1}$$

where δ is the refractive index decrement, related to the phase shift of the incident wave after passing through the sample, and β is the absorption index, related to the attenuation of the incident beam induced by the sample.

The refractive index decrement δ and the absorption index β can be respectively expressed as [69]

$$\delta = \frac{r_c \lambda^2}{2\pi} \rho_e \tag{1.2}$$

and

$$\beta = \frac{r_c \lambda^3 \rho_e}{4\pi^2 c} \sum_j \frac{f_j \gamma_j}{Z}, \tag{1.3}$$

where r_c denotes the classical electron radius, λ the wavelength of the X-ray beam, ρ_e the electron density, c the light velocity, f_j the number of electrons per atom with damping constant γ_j and Z the atomic number that corresponds to the total number of electrons per atom. Here, j corresponds to an electron in the atom.

The absorption index β is related to the attenuation coefficient μ by the following relationship [70]:

$$\mu(x, y) = \frac{4\pi}{\lambda} \int \beta(x, y, z) dz. \tag{1.4}$$

The attenuation B and phase shift φ induced by the object can be described as projections parallel to the propagation direction (here, the z-axis). Note that **x** represents the vector (x, y).

$$B(\mathbf{x}) = \frac{2\pi}{\lambda} \int \beta(\mathbf{x}, z)\, dz \tag{1.5}$$

and

$$\varphi(\mathbf{x}) = -\frac{2\pi}{\lambda} \int \delta(\mathbf{x},\ z)\, dz. \tag{1.6}$$

At each angle θ, the interaction between the object and the X-ray wave can be described as a transmittance function:

$$T_\theta(\mathbf{x}) = \exp(-B_\theta(\mathbf{x}) + i\varphi_\theta(\mathbf{x})). \tag{1.7}$$

Thus, if $u_{inc}(\mathbf{x})$ denotes the incident wave front and $u_0(\mathbf{x})$ the wave front right after the sample (i.e. for a null propagation distance), we obtain

$$u_0(\mathbf{x}) = T_\theta(\mathbf{x}) u_{inc}(\mathbf{x}). \tag{1.8}$$

The corresponding intensity recorded by the detector, without any propagation, is

$$I_0(\mathbf{x}) = |u_0(\mathbf{x})|^2 \tag{1.9}$$

$$I_0(\mathbf{x}) = |T_\theta(\mathbf{x}) u_{inc}(\mathbf{x})|^2 \tag{1.10}$$

$$I_0(\mathbf{x}) = \left|e^{-B_\theta(\mathbf{x})} e^{i\,\varphi_\theta(\mathbf{x})} u_{inc}(\mathbf{x})\right|^2 = \left|e^{-B_\theta(\mathbf{x})}\right|^2 \left|e^{i\,\varphi_\theta(\mathbf{x})}\right|^2 |u_{inc}(\mathbf{x})|^2 \tag{1.11}$$

$$I_0(\mathbf{x}) = e^{-2.B_\theta(\mathbf{x})} |u_{inc}(\mathbf{x})|^2 = e^{-2B_\theta(\mathbf{x})} I_{inc}(\mathbf{x}). \tag{1.12}$$

The free-space propagation over a distance D can be modelled by the Fresnel transform involving the propagator P_D [71]:

$$P_D(\mathbf{x}) = \frac{1}{i\lambda D} \exp\left(i\frac{\pi}{\lambda D} |\mathbf{x}|^2\right) \tag{1.13}$$

and its Fourier transform:

$$\tilde{P}_D(\mathbf{f}) = \exp\left(-i\pi\lambda D |\mathbf{f}|^2\right), \tag{1.14}$$

where $\mathbf{f} = (f, g)$ are the conjugate variables corresponding to $\mathbf{x}$.

Usually, in computer implementations, the propagator is applied in the Fourier domain, since there it becomes a multiplication instead of a convolution in the spatial domain. Mathematically, if $u_0(\mathbf{x})$ and $u_D(\mathbf{x})$ respectively denote the wave fronts right after the sample and at a distance D from the sample, we obtain

$$u_D(\mathbf{x}) = P_D(\mathbf{x}) * u_0(\mathbf{x}), \tag{1.15}$$

in the spatial domain, which corresponds to

$$\tilde{u}_D(\mathbf{f}) = \tilde{P}_D(\mathbf{f})\tilde{u}_0(\mathbf{f}) \tag{1.16}$$

in the Fourier domain.

Since u_D usually stays in the real domain, and the propagator is applied in the Fourier domain, we get

$$u_D(\mathbf{x}) = \mathcal{F}^{-1}\tilde{P}_D\mathcal{F}[u_0](\mathbf{x}). \tag{1.17}$$

The operator

$$\mathcal{F}r_D = \mathcal{F}^{-1}\tilde{P}_D\mathcal{F} \tag{1.18}$$

is called the Fresnel transform. If we assume flat illumination, the interaction between the incident wave front and the sample followed by free-space propagation over a distance D can be modelled by

$$T_{\theta, D}(\mathbf{x}) = (T_\theta * P_D)(\mathbf{x}). \tag{1.19}$$

The intensity recorded by the detector at a distance D is

$$I_{\theta, D}(\mathbf{x}) = \left|T_{\theta, D}(\mathbf{x})\right|^2. \tag{1.20}$$

In the Fourier domain, the intensity can be expressed as

$$\tilde{I}_D(\mathbf{f}) = \int T\left(\mathbf{x} - \frac{\lambda D\mathbf{f}}{2}\right)T^*\left(\mathbf{x} + \frac{\lambda D\mathbf{f}}{2}\right)\exp(-i2\pi\mathbf{x}\cdot\mathbf{f})d\mathbf{x}. \tag{1.21}$$

Thus, images recorded by the detector are quantitatively related to the phase shift of the wave induced by the object.

Holotomography consists in acquiring projections for a complete rotation of the sample, at different sample-to-detector distances. This enables to cover well the Fourier domain (the Fresnel transform can have zero crossing at certain distances).

4.2.1 Magnified Images Formation

Since the beam is divergent, recording an image at sample-to-detector distance D also induces, apart from phase contrast, magnification of the projections and creates a spherical wave front (Fig. 1.1). The magnification M is expressed using the well-known Thales' theorem:

Fig. 1.1 The incoming parallel X-ray beam (X) is focused onto a focal spot (F) using Kirkpatrick-Baez mirrors, curved reflective optics that will horizontally and vertically focus the beam. D_1 represents the distance between the spot (F) and the sample (S). D_2 denotes the propagation distance, i.e. the distance between the sample and the detector [72]
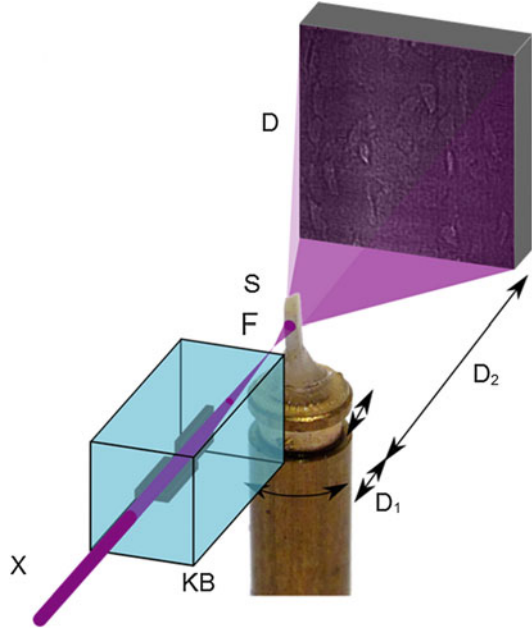
$$M = \frac{D_1 + D_2}{D_1}.$$ (1.22)

We obtain projections with different magnification by modifying the propagation distance. In practice, the detector and the focus point are fixed, i.e. $D_1 + D_2$ is constant. It means that it is the sample that moves along a translation stage to get images with different magnifications.

Note that the spherical wave Fresnel diffraction phenomenon can be seen as a plane-wave illumination problem at the defocusing distance D defined by

$$\frac{1}{D} = \frac{1}{D_1} + \frac{1}{D_2}$$

$$\leftrightarrow D = \frac{D_1 D_2}{D_1 + D_2}$$

$$\leftrightarrow D = \frac{D_2}{M}.$$ (1.23)

In the following, D denotes the defocusing distance and can be seen as an equivalent of the propagation distance that takes into account the magnification.

Since the position of the focus and the detector are kept fixed, $[D_1, D_2, D_n, \ldots, D_N]$ represents the equivalent propagation distance indexed by n, with N the total number of distances used.

4.3   Phase Retrieval

4.3.1   Contrast Transfer Function

To retrieve the phase information from the image recorded by the detector (which is a non-linear problem), and since we are in the Fresnel diffraction regime, we can use the contrast transfer function (CTF) model. This linear model, which expresses the intensity as a linear function of the absorption and the refractive index decrement, is valid for slowly varying phase and weakly absorbing objects. These two conditions can be mathematically written as

$$|\varphi(\mathbf{x}) - \varphi(\mathbf{x} + \lambda D\mathbf{f})| \ll 1 \qquad (1.24)$$

for slowly varying phase and

$$B(\mathbf{x}) \ll 1 \qquad (1.25)$$

for weak absorption.

The CTF is based on the linearisation of the transmittance function to the first order:

$$T(\mathbf{x}) \approx 1 - B(\mathbf{x}) + i\varphi(\mathbf{x}). \qquad (1.26)$$

By substituting the linearisation of the transmittance function in Eq. 1.21 and keeping only the first-order terms, we get the CTF:

$$\tilde{I}_D(\mathbf{f}) = \delta_{\text{Dirac}}(\mathbf{f}) - 2\cos\left(\pi\lambda D|\mathbf{f}|^2\right)\tilde{B}(\mathbf{f}) + 2\sin\left(\pi\lambda D|\mathbf{f}|^2\right)\widetilde{\varphi}(\mathbf{f}), \qquad (1.27)$$

Where ~ denotes the Fourier transform and δ_{Delta} the Dirac delta function.

Nevertheless, for nano-tomography, the propagation distances are relatively long compared to the pixel size and wavelength. This means the condition in Eq. 1.24 and thus the linearisation in Eq. 1.26 are no longer valid, so that the non-linear contribution of the phase cannot be neglected [73].

The CTF can be rewritten to take this into account:

$$\tilde{I}_D(\mathbf{f}) = \delta_{\text{Dirac}}(\mathbf{f}) - 2\cos\left(\pi\lambda D|\mathbf{f}|^2\right)\tilde{B}(\mathbf{f}) + 2\sin\left(\pi\lambda D|\mathbf{f}|^2\right)\widetilde{\varphi}(\mathbf{f}) + \tilde{I}_{\text{NL, D}}(\mathbf{f}),$$
$$(1.28)$$

where $\tilde{I}_{\text{NL,D}}(\mathbf{f})$ represents the non-linear contribution.

Phase retrieval is thus performed in two stages. An initial guess of the phase is determined using a classical linear least square minimisation using the CTF, described in Sect. 4.3.2. This first guess corresponds to the linear part of the retrieved phase, but is not sufficient to provide good image quality at such high resolution. After, the non-linear term is determined using a non-linear iterative method, for example, a non-linear conjugate gradient algorithm [72].

4.3.2 Phase Retrieval with the CTF

To retrieve the phase using the CTF, linear least square optimisation is used. This method is usually used to solve an overdetermined problem, for example, a problem containing one unknown and N equations, as it is the case here, since we recorded images at N distances (that constitute our N equations) and want to determine one unknown, the phase.

Consider the following overdetermined problem:

$$y_n = A_n x + \varepsilon_n, \tag{1.29}$$

where n is an integer so that $n \in [1 : N]$, x is the unknown, y_n denotes one of the N measurements and A_n is the linear transformation applied to x to get y_n. The linear least square method determines an estimate of x, $\hat{x}$, so that

$$\frac{1}{N} \sum_{n=1}^{N} A_n^2 \hat{x} = \frac{1}{N} \sum_{n=1}^{N} A_n y_n. \tag{1.30}$$

Solving CTF (Eq. 1.27) is equivalent to minimise

$$\sum_{n=1}^{N} \left| 2 \sin \left(\pi \lambda D_n |\mathbf{f}|^2 \right) \widetilde{\varphi}(\mathbf{f}) - 2 \cos \left(\pi \lambda D_n |\mathbf{f}|^2 \right) \tilde{B}(\mathbf{f}) - \tilde{I}_{D_n}(\mathbf{f}) \right|^2. \tag{1.31}$$

Here, Tikhonov regularisation is used to solve this minimisation problem [74]:

$$\hat{\widetilde{\varphi}}(\mathbf{f}) = \frac{\left[K_{aa} \sum_{n=1}^{N} 2 \sin \left(\pi \lambda D_n |\mathbf{f}|^2 \right) \tilde{I}_{D_n}(\mathbf{f}) - K_{ap} \sum_{n=1}^{N} 2 \cos \left(\pi \lambda D_n |\mathbf{f}|^2 \right) \tilde{I}_{D_n}(\mathbf{f}) \right]}{K_{aa} K_{pp} - K_{ap}^2} \tag{1.32}$$

with

$$K_{aa} = \sum_{n=1}^{N} \left(2 \cos \left(\pi \lambda D_n |\mathbf{f}|^2 \right) \right)^2 \tag{1.33}$$

$$K_{ap} = \sum_{n=1}^{N} 2 \cos \left(\pi \lambda D_n |\mathbf{f}|^2 \right) 2 \sin \left(\pi \lambda D_n |\mathbf{f}|^2 \right) \tag{1.34}$$

$$K_{pp} = \sum_{n=1}^{N} \left(2 \sin \left(\pi \lambda D_n |\mathbf{f}|^2 \right) \right)^2. \tag{1.35}$$

Once the projections are well conditioned, phase retrieval is performed according to the scheme presented above. A linear least square method is performed to assess roughly the phase and a non-linear conjugate gradient method to refine it. The obtained phase projections are eventually used as an input of a tomographic reconstruction algorithm (here, the filtered back projection method) to get a volume of the refractive index decrement.

5   Key Research Findings

5.1   Literature Review: X-Ray Nano-tomography of Bone

We review here the imaging methods that have so far been used to image bone ultrastructure at higher than 400 nm spatial resolution and the results that were obtained. To achieve such resolutions, advanced X-ray microscopy methods have to be used, where some magnification has to be implemented on the X-ray beam. This is not straightforward, however, as mentioned above, since the very small deviation from unity of the refractive index for X-rays makes it difficult to implement X-ray optics. The methods are surprisingly heterogeneous in their design, relying on attenuation and far-field and near-field diffraction, respectively.

5.1.1   Ptychographic Tomography

One way to achieve high-resolution imaging with X-rays is to exploit diffraction. This requires the use of a pencil beam, either by using a pinhole or X-ray focusing optics. An image is then recorded at a relatively long distance downstream of the object, which corresponds to far-field or Fraunhofer diffraction. Images recorded in this way will contain information closely related to the squared modulus of the Fourier transform of the imaged object, convolved with the Fourier transform of the incident beam. It is in certain cases possible to reconstruct the object transmission function by the use of iterative phase retrieval algorithms based on projections onto sets [75–78]. This approach is usually known as coherent diffraction imaging (CDI) [79, 80]. Since the recorded image is in the frequency domain, the attainable resolution is limited by how far from the centre of the detector signal can be measured (and, of course, the wavelength of the probe). In practice, this means that the resolution limit is related to the signal-to-noise ratio in the recorded images. Therefore, very high resolution can be achieved with this technique. CDI is limited to imaging of isolated particles with a support smaller than the used X-ray beam, however, such as isolated nanoparticles [82] or single cells [83].

The small support requirement can be obviated by scanning the probe across an extended sample while letting the probe position overlap at each image position (in practice the sample is scanned through the beam). By using an iterative reconstruction scheme, a complete phase projection can be reconstructed [84–86]. This is known as ptychographic imaging [87].

Since the phase shift introduced by the object in the X-ray beam can be considered as a straight-line projection, if we have access to the phase shift, we can use it to reconstruct the 3D refractive index decrement distribution in the sample, in analogy to the classical attenuation case. What is particularly attractive with this is that for hard X-rays, the refractive index decrement is proportional to the local mass density in the sample [88]. This means that, for example, the use of X-ray phase tomography images to drive mechanical simulations avoids the need to infer the mass density from measurements of the degree of mineralisation of bone (DMB), which has to be done if density is to be related to the attenuation index [9]. In practice, phase tomography is implemented by a two-step process: first, the phase is retrieved at

each projection angle, and then the refractive index decrement is reconstructed by feeding the resulting phase maps into a tomographic reconstruction algorithm such as filtered back projection (FBP) [89–91].

Ptychographic tomography has been used to image bone ultrastructure [81]. A human cortical bone sample cut to an approximately cylindrical shape with a diameter of ~25 μm was imaged using a 2.3 μm pinhole (Fig. 1.2a). The sample was scanned through the resulting pencil beam so that the X-ray spots lie on concentric circles, covering a rectangular area of 40 μm × 32 μm (Fig. 1.2b) for a total of 704 diffraction patterns per projection. Such projections were recorded over a 180° turn of the sample, at increments of 1° for a total of 180 projections.

Figure 1.2c, d shows virtual sections through the reconstructed electron density map. The bright shell on the surface of the sample is due to the sample preparation; the sample was cut using a focused ion beam, which deposits a residue of heavy ions on the surface (in this case gallium ions). We can easily see the lacunae and the canaliculi. Note that the reported electron densities are truly quantitative due to the sample being completely covered by the projections. 3D renderings (Fig. 1.2e, f) show that the imaged volume contains three partial lacunae. The canaliculi are fairly well resolved, but some spurious structures remain.

The major strength of ptychographic tomography is that it is capable of attaining very high resolutions without the use of X-ray optics. Isotropic 3D resolutions up to 16 nm have been reported [92], however, in energy ranges that are probably too low to be practical for bone imaging (~6 keV). A major drawback of ptychographic tomography is its scanning nature. This makes the acquisition time for a single projection relatively long; in practice, it limits the number of projections that can be acquired and the field of view that can be covered. In the work of Dierolf et al. [81], only 180 angular positions were acquired, normally far too few to achieve correct angular resolution, and a relatively small sample was imaged, comprising only parts of three lacunae. The duration of the complete acquisition was reported to be ~40 h. Another disadvantage, shared with the in-line phase imaging (Sect. 5.1.3), is that reconstruction is not always straightforward. Considerable expertise seems to be needed to perform correct reconstructions. These two drawbacks taken together seem to limit the applicability of ptychographic tomography for quantitative studies. Additionally, ptychography can only reconstruct phase shifts in the range 0–2π. This means that if the true phase shift is larger than 2π, the reconstruction has to be unwrapped, which is a problem unto itself [93].

5.1.2 Transmission X-Ray Microscopy (TXM)

Magnification on the X-ray side can be achieved by the implementation of a transmission X-ray microscope, analogously to what can be done with visible light. Due to the weak refraction of X-rays, diffractive optics, so-called Fresnel zone plates, are used for this purpose. A full-field TXM implementation has been reported by Andrews et al. [94], using either a rotating anode X-ray source or a synchrotron source to image bone tissue at the nanoscale. They used a reflective capillary collimator due to its high focusing efficiency. The sample was placed in the focus. A Fresnel zone plate was used as objective lens to image the beam onto the
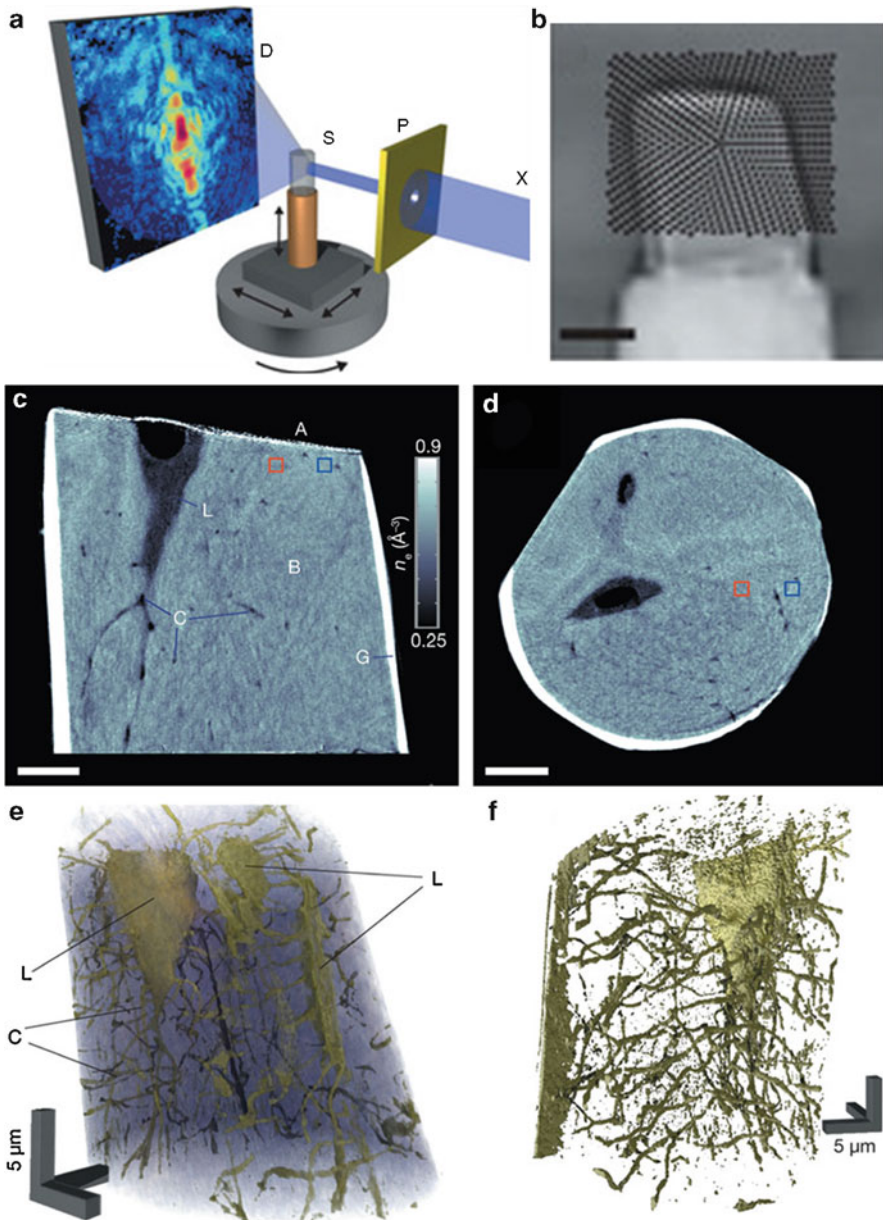
Fig. 1.2 Ptychographic X-ray tomography. (**a**) Schematic of the experimental setup. (**b**) The scanning pattern of the X-ray spot over the sample to form one projection. (**c**, **d**) Virtual cuts through the reconstructed volume showing very good contrast between bone and the LCN. The bright shell consists of gallium ions deposited by the focused ion beam cutting of the sample. (**e**) Volume rendering of the complete imaged volume. Three lacunae can be partially seen, and a fair amount of the canaliculi seem well resolved. (**f**) Zoom on one lacuna and its canaliculi. A fair amount of spurious porosity remains (Images from Dierolf et al. [81])
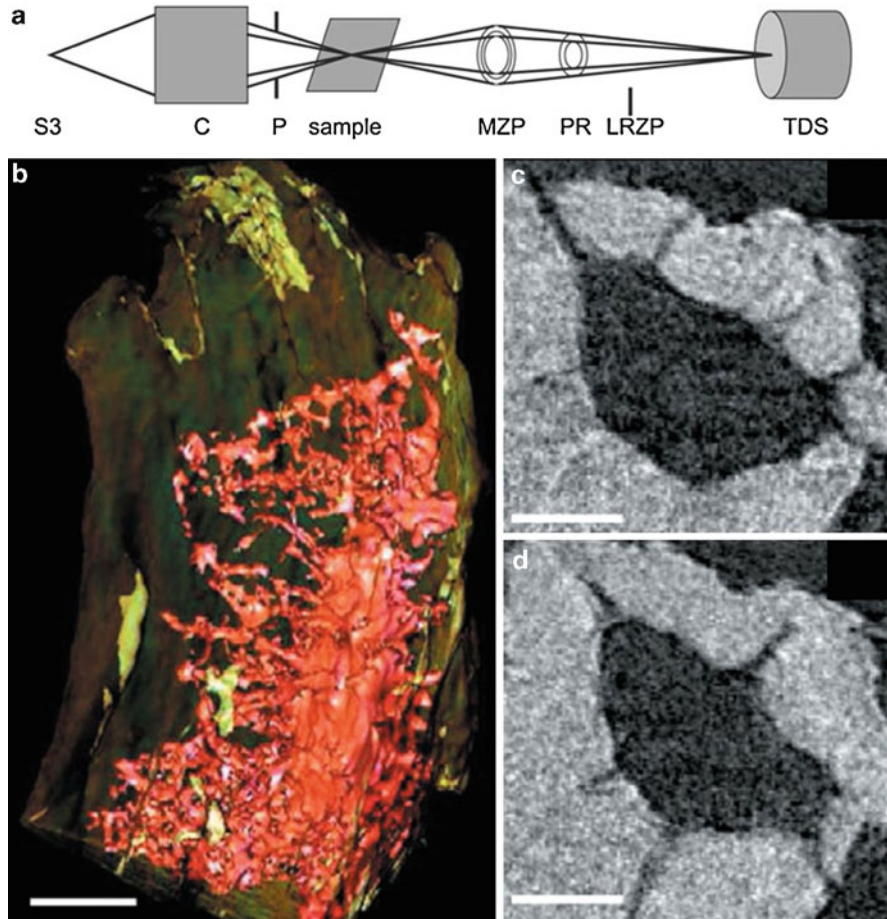
Fig. 1.3 Transmission X-ray microscopy (TXM). (**a**) Schematic of the experimental setup. (**b**) Volume rendering of an osteocyte lacuna in an isolated murine trabecula. (**c**, **d**) Virtual cuts through the reconstructed volume showing the contrast between bone, the lacuna and the canaliculi (Images from Andrews et al. [94])

detector. Detection was done using a scintillator-based high-resolution CCD camera with a physical pixel size of ~2 μm. A schematic of the instrument is shown in Fig. 1.3a. The X-ray energy used was in the range of 4–14 keV. They achieved a spatial resolution of ~50 nm, compared to the theoretical resolution limit of ~35 nm.

The reported TXM setup was used to image the LCN. Part of one lacuna and its environing canaliculi were imaged in trabecular bone. The sample was extracted from the proximal region of a mouse tibia by microtome cutting, followed by washing with a saline jet to remove marrow. It was then dried and attached to a steel cannula tip with epoxy for imaging. The resulting sample consisted of a single trabecula and was less than 50 μm thick, which is approximately the depth of focus

of the TXM. The sample was stained with 1 % uranyl acetate for 12 h to improve contrast. The lacuna and canaliculi are well resolved in the image, but are fairly weakly contrasted (Fig. 1.3c, d). Looking at a volume rendering (Fig. 1.3b), the lacuna and its canaliculi are clearly visible. The canaliculi show a surprising rate of branching, however, compared to the two other techniques reported here.

A TXM images the attenuation of the sample, i.e. the same contrast as in standard X-ray µCT. An advantage of TXM is that it can achieve high spatial resolution without the need for advanced image reconstruction. The disadvantages seem to be the demanding sample preparation and the limited sample size due to the short depth of field, approximately 50 µm. The technique also requires fairly low energies, thereby limiting the thickness of the samples that can be traversed. The lower energy also increases the X-ray dose deposited in the sample, thus increasing the risk of radiation damage.

5.1.3   In-line Phase Tomography

It is possible to implement a transmission projection microscope by the use of X-ray optics to focus the beam and placing the sample after the focus in the resulting divergent beam. This kind of microscope has been implemented using Kirkpatrick-Baez reflective optics [95]. As for the methods discussed above, the sample is placed on a translation/rotation stage to enable tomographic imaging. The camera is mounted on a translation stage to allow for different factors of geometrical magnification. The magnification is a function of the beam divergence after the focus, the focus-to-sample distance and the focus-to-detector distance. The resulting free-space propagation not only creates a magnification effect however, but due to the high degree of coherence of the beam, phase contrast is also induced. This contrast can be used to reconstruct the phase shift in the object. One particularity, however, is that the recorded images will lack information at certain spatial frequencies due to the properties of the transfer function of the Fresnel propagator. In high-resolution imaging, this makes it necessary to acquire several (at least two) images per projection angle, corresponding to different sample-to-detector distances. Another aspect is that bone samples will always introduce a considerable attenuation effect at the energies used in practice. This means that both attenuation and phase contrast will be present in the recorded images, which also imposes a minimum of two images per projection angle. Otherwise, strong assumptions have to be made on the sample composition to make phase retrieval possible.

The phase can be retrieved at each projection angle by a process known as phase retrieval. Several algorithms for phase retrieval from Fresnel diffraction patterns have been developed. Most of them are based on linearisation of the squared modulus of the Fresnel transform to achieve efficient, filtering-based solutions [89, 90, 96–99]. In the high-resolution case, there will be non-negligible non-linear contributions. This makes the use of non-linear reconstruction algorithms necessary to achieve the resolution permitted by the experimental setup (Sect. 4.3) [100–104].

In-line phase tomography has been used to image several ultrastructural features in bone [72]. The LCN can be imaged over a relatively large field of view (Fig. 1.4a–d). The LCN also seems better resolved than then in the previously
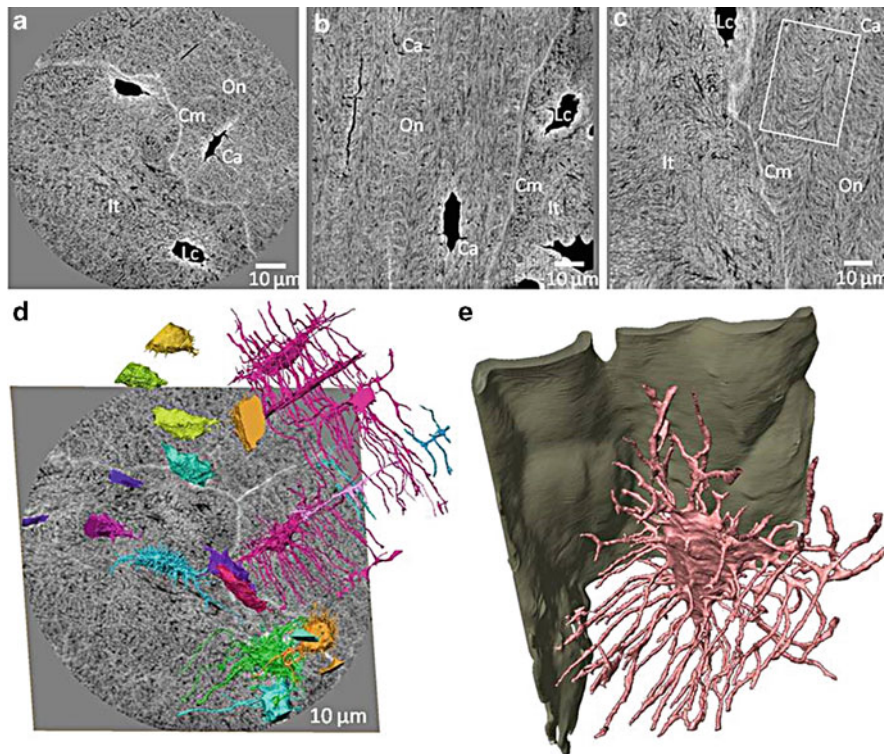
Fig. 1.4 Magnified phase tomography of bone. (**a**–**c**) Virtual cuts through the reconstructed volume. Note the high contrast between the LCN and the bone matrix and also the strong contrast in the matrix presumably due to oblique cutting of the mineralised collagen fibres, as well as the well-resolved cement line. (**d**) Volume rendering of all LCN porosity in the sample showing a relatively large number of lacunae. (**e**) Zoom on one lacuna and its canaliculi (*pink*) and the cement line (*green*). The LCN is rendered in unprecedented detail, and its relationship to the cement line can be studied [72]

reported studies (cf. Figs. 1.2f, 1.3b and 1.4e). The bone matrix appears strongly textured (Fig. 1.4a–c) compared to, e.g. images acquired with X-ray ptychographic tomography (Fig. 1.2c–d). By comparison to qBEI [40] and TEM [44] images, the arching structure can be identified to be due to the oblique cutting of the mineralised collagen fibrils. This means that the collagen fibre orientation can be studied directly in 3D using texture analysis, as we will see below. The cement lines are comparatively very well contrasted. In phase tomography, the reconstructed grey level corresponds to the mass density in non-hydrogen-rich materials. In the images, it can be seen that the cement line has a significantly higher mass density than the surrounding osteonal and interstitial tissue regions.

In-line phase tomography has some aspects that make it attractive for bone imaging. It is a full-field imaging technique, which means that the image acquisition is relatively fast. Acquisition time of ~4 h per sample has been reported [72], using

full sets of projections (i.e. 3000 projections using a 2048-element-wide detector). This means that quantitative studies on large series of samples are potentially within the capabilities of this technique. Further, due to the full-field nature, a relatively large field of view can be imaged compared to the other available techniques.

The in-line technique currently has one disadvantage in common with ptychographic tomography, however. Image reconstruction is not straightforward, since it relies on advanced reconstruction algorithms that presently require considerable expertise to operate. A disadvantage compared to ptychography is currently the achievable spatial resolution. While no measurement has been reported, by inspection of the reconstructed volumes, the spatial resolution so far achieved seems to be ~200 nm (FWHM at interfaces in the reconstructed 3D object). With these advantages and disadvantages taken together, in-line phase tomography seems to be an appropriate method for quantitative studies and study of ultrastructural features in addition to the LCN.

5.2 Collagen Orientation

Three-dimensional images acquired by means of in-line phase tomography allow to explore the details of the submicron-scale architecture of bone. In particular, the structure of bone lamellae can be analysed in unprecedented detail.

Lamellar pattern is the dominating arrangement of bone in the human skeleton and can be found most frequently in the form of osteons. Osteons are approximately 200 μm diameter cylindrical structural units constituted by concentrically arranged lamellae surrounding the central Haversian canal of 50–100 μm diameter hosting blood vessels and nerves. Lamellae are 3–7 μm thick layers that were characterised and defined originally on microscopy images of cut sections. The reason for the appearance of lamellae was already more than hundred years ago proposed to be the ultrastructure, namely, the orientation of the collagen-mineral composite [105].

One interesting question has been – and still is – if the lamellar structure is the result of a collagen self-assembly processes [44, 106] or if it is determined by the activity of the osteoblasts laying down bone tissue, driven through their mechanosensing ability, following a predefined programme or signals sent by osteocytes. However, the major driving force behind studies investigating bone microarchitecture has been the role of these structural details in determining function and vice versa. Ultimately, in-depth knowledge on structure-function relationships may complete our understating of the complex design and remarkable mechanical properties of these highly optimised skeletal elements [107]. The effect of bone diseases on the mechanical competence and the underlying alterations in the composition and architecture are also of great interest. Moreover, the underlying principles may be useful for the design of new materials for mimicking bone tissue [106] or for other bio-inspired engineering purposes.

With respect to the role of ultrastructure in mechanical properties of lamellar bone, besides numerous other studies, the works of Ascenzi and colleagues have to be mentioned. These authors extensively researched and reported the potential

relationships between the osteonal types classified based on appearance under confocal microscopy and mechanical properties of isolated osteons [108–111] and lamellae [111] assessed experimentally. However, understanding the exact architecture of lamellar bone remained a challenging task mainly due to the available tools of investigation. Inference of the three-dimensional arrangement of collagen fibrils and/or mineral particles was attempted from 2D sections acquired mainly by various microscopy techniques [109, 112–119], scattering [120–122] and diffraction based [123], i.e. mainly in reflection or transmission mode. Interpretation of these results therefore required assumptions and theoretical models. Some of these approaches lead to partially or fully misleading conclusions as it was pointed out, e.g. by Giraud-Guille et al. [112]. Using these various methods, several researchers' opinion converged towards the agreement that lamellae have a periodic plywood structure. However, various descriptive models have been proposed including orthogonal [105], twisted [112], rotated [114] and helicoidal [124] plywoods. Furthermore, a remarkably different opinion was formulated by Marotti et al. [125], proposing that the collagen matrix is rather disorganised and the lamellar pattern is the result of neighbouring regions having distinct collagen densities. A potential explanation for these different observations has been provided recently [126]. However, there was a clear need for truly three-dimensional analysis techniques to fully resolve these structural details and explain the partially or fully contradicting findings of previous 2D analyses.

In-line phase tomography provides the density contrast and spatial resolution that are sufficient to investigate and quantitatively describe this complex arrangement in three dimensions.

As pointed out in Sect. 5.1.3, the characteristic arcing pattern apparent in Fig. 1.4a–c is the result of this lamellar structure and was an important basis for previous 2D, e.g. electron microscopy-based analyses attempting to resolve the lamellar structure [112]. Having the 3D data at hand, it is possible to virtually prepare slices in arbitrary directions. Aligning these slices with the lamellar plane allows one to observe the arrangement of collagen fibrils within sub-lamellae. This principle was the basis of the image analysis protocol presented in [127]. In particular, slice-wise autocorrelation analysis was performed to quantify the local orientation of the fibrils. We assumed that the in-plane pattern of the fibrils was quasi-periodic and used the major principal axis of the autocorrelation-based orientation distribution function of periodicity to identify the dominant direction of fibrils within the given plane. Independently assessed results of consecutive parallel slices provided the evolution of the mean orientation of the bone lamellae. Several sub-volumes aligned with the local lamellar coordinate system were investigated.

Using this technique, we confirmed that mineralised collagen fibrils in lamellar bone are organised into a plywood structure that is made of parallel quasi-planes in which the fibrils have unidirectional alignment. Within the largest analysed region, having an in-lamellar-plane dimension of approximately 30×70 μm, the standard deviation of the quantified fibril orientation was as small as five degrees. The evolution of fibril orientation across lamellae was dominated by smooth transitions; discrete changes were rare. We found two major plywood pattern types. The first one

resembled the rotating plywood described earlier [112], with the orientation changing continuously. For the first time, to our knowledge, we quantified the rate of twist and found that it was fairly constant across regions and specimens, being approximately 25°/μm. The range of twist was close to either 180 or 360°. Fibrils completed a 180° twist in approximately 7 μm, which corresponds well with lamellar thickness values reported earlier [128]. In the second lamellar type, the change of fibril orientation followed a closely sinusoidal pattern, with average amplitude of approximately 30° and a relatively small offset, on average seven degrees, around the osteon axis. We called this pattern oscillating plywood and found cases resembling symmetric as well as rather asymmetric sinusoids. The average half period of these sinusoids was close to six microns, which is again close to previously reported lamellar thickness values. This pattern was close to that found earlier [123] in a single sample, however, with a much smaller offset with respect to the osteon axis.

We found twisting and oscillating plywood patterns to coexist within the same osteon in a consecutive manner. Close to the external boundary of the osteon, i.e. at the cement line, we observed in all investigated cases twisting plywood arrangement. The lamellar structure of osteons was hypothesised to have importance mechanically by acting as an efficient crack arresting boundary and thus protect the vessels and nerves within the central canal [107]. Our finding is in line with this hypothesis as twisted plywood contains all fibril orientations and, by means of collagen bridging, may therefore be a general defensive mechanism against cracks in any direction [129] and it is located directly at the external border of the osteon. Furthermore, the outermost lamella, being the firstly deposited one, may be important in the early phase of the construction of the osteon.

As a qualitative validation of our approach, in a selected analysis region, the computed orientation was used to construct a virtual 3D fibril model that compared well with the corresponding sub-volume of the original greyscale image, and, in particular, the arch pattern could be reproduced (Fig. 1.5). The figure illustrates the necessity of 3D analysis as the evaluated complex arrangement displayed in the centre panel of Fig. 1.5 cannot be retrieved from a 2D section, e.g. from the oblique cut shown in the left panel.

Apart from the plywood-type arrangements, we could observe rather disorganised regions [130]; however, these had very rare occurrence. Furthermore, we found that fibrillar orientation was independent of the local mass density values, suggesting that the known fluctuation of mechanical properties across lamellae [117, 131–133] is dominated by the orientation of the fibrils rather than the level of mineralisation.

In summary, our results not only corroborated findings of earlier studies, but provided novel insight into the lamellar microstructure in bone. Further, a unique set of quantitative results could be derived from nanoscale three-dimensional data and allowed reinterpretation of previous observations. Moreover, our findings were in line with the results of the concurrent, but independently performed, studies of Reznikov et al. investigating lamellar arrangement in various species by means of FIB-SEM [42, 60, 134]. This approach is attractive as it provides a resolution of about 10 nm. However, it is limited to a field of view of 10 μm and at the price of full destruction of the sample. Finally, the existence of the two plywood arrangements
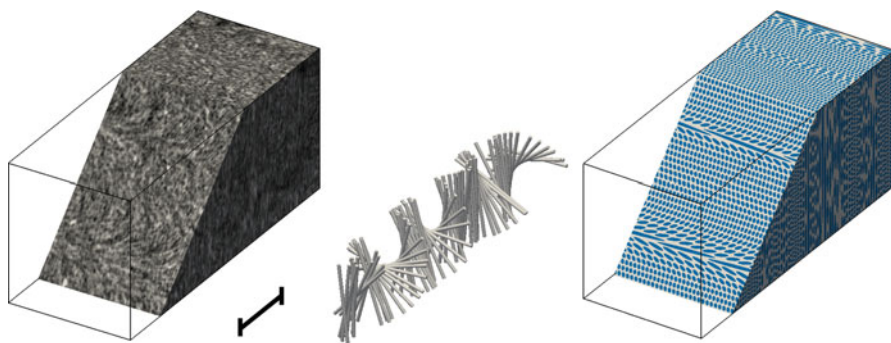
Fig. 1.5 Qualitative validation of the autocorrelation-based approach to quantify mineralised collagen fibril orientation. *Left*: rectangular analysis volume cropped from the synchrotron nano-CT image of a human femoral cortical bone sample with an oblique cut. *Grey* values represent the inverted mass density in arbitrary units. Scale bar, 10 μm. *Middle*: *cylinders* representing the quantified fibril orientation of 600 μm thick sections across the lamellae. *Right*: 3D illustration of the extracted orientations with the fibrils shown in *blue* and the matrix in *white*. The arc pattern in the oblique cut corresponds well to that in the original image (*left*) [127]

was corroborated in a later study using polarised Raman microscopy for the chemical and structural analysis of human osteonal bone [48].

Nevertheless, the analysis method developed and applied in [127] had several limitations, since:

(i) Its application was restricted to large osteons in which the curvature of lamellae was relatively small, allowing to have a rectangular ROI with slices that contained data of distinct lamellar quasi-planes and that were large enough for the extraction of the orientation.

(ii) The analysis region had to be aligned with the local lamellar planes, which required time-consuming manual preprocessing (image rotation, ROI selection).

(iii) The analysis regions had to be located sufficiently far away from osteocyte lacunae, and fibril orientation around these pores could not be assessed.

Most of these limitations can be overcome by employing a truly 3D approach. The lamellar arrangement consists of planes with unidirectional fibrils, orientation of which changes relatively rapidly across the lamellae. This direction-dependent rate of the orientation change requires the analysis method to be well tuned to this structure. The updated analysis protocol has two steps. In the first one, the rough lamellar orientation is assessed, which is used in a second step to align the rectangular analysis volume. The size of the latter, to be in accordance with the above discussed closely transversely isotropic orientation change rate, is larger in the lamellar plane than out of this plane. The capabilities of this approach are illustrated in Fig. 1.6 which shows the quantified fibril orientation around an osteocyte lacuna. In comparison to the previous method, the improved analysis protocol requires much
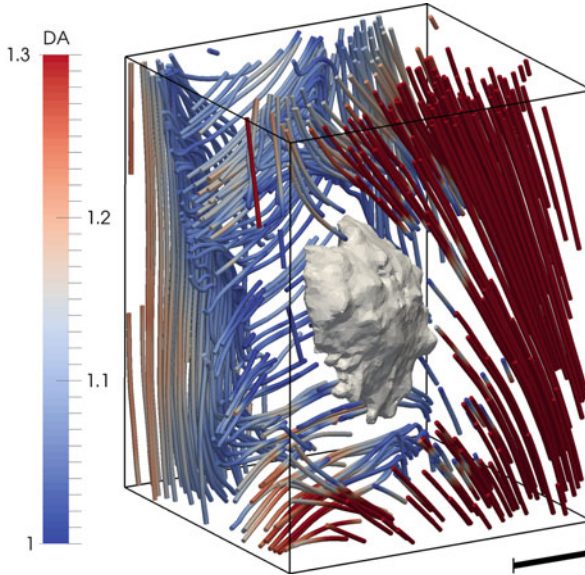
Fig. 1.6 Illustration of the mineralised collagen fibril orientation around an osteocyte lacuna, as estimated by the updated 3D autocorrelation-based approach. The lacuna is shown as *white* surface in the *middle* of the rectangular volume. Colour of the cylinders represents the degree of anisotropy (*DA*) of the autocorrelation-based measure, i.e. the fidelity of the orientation estimation. On the *left side* of the lacuna, the orientation may have abrupt changes from closely vertical to horizontal. However, the low DA values suggest that fibrils are rather disorganised in this region. Scale bar, 5 μm

less user interaction, essentially limited to the selection of the volume of interest. Moreover, as shown in the figure, the region does not have to be aligned with the lamellar plane and can include larger voids such as lacunae. Therefore, the new approach is expected to allow for high-throughput analyses, which is a strong requirement in, e.g. comparative studies with several groups and larger sample sizes.

A rather general limitation of all high-resolution methods is the strong sampling effect due to the available field of view. This effect can be compensated by scanning multiple regions of the same sample and/or increasing the number of specimens to strengthen statistical power. The expected improvements in imaging technology should provide the basis for larger, even clinically relevant studies. However, the relatively low accessibility of the infrastructure remains a challenge. In this respect, the role of coarser-scale methods that are sensitive to the alteration of the lamellar structure or the fluctuations of its mechanical properties has to be emphasised. More easily accessible laboratory techniques such as scanning acoustic microscopy [117], Raman microscopy [48] or second harmonic imaging [135, 136] have been demonstrated for this purpose. Moreover, these methods allow for the investigation of larger domains, however, only in 2D. These approaches may therefore efficiently complement the higher-resolution 3D techniques, and their combination should open new possibilities towards more extensive studies in the future.

5.3   Morphology and FE Modelling of the Lacuno-Canicular Network

Porosity of bone is at least as important as the mineralised tissue matrix itself, both biologically and mechanically. On the micro-scale of cortical bone, one finds the pore network of osteocytes that consists of the lacunae hosting the cell bodies and the canaliculi, which are tiny tunnels connecting lacunae of neighbouring cells [11, 137]. Given the important role of the mechanosensitive osteocyte in the coordination of the activities of other bone cells and its active participation in remodelling [29, 138], the LCN has received increasing attention during the last years. Imaging of this pore network became an important, but not yet fully solved, challenge [11, 139].

Osteocyte lacunae are ellipsoidal-shaped voids in the bone matrix with approximate sizes of 5 μm × 10 μm × 20 μm and can therefore be resolved with laboratory devices such as confocal microscopy and desktop μCT [11, 12, 140]. Nevertheless, most studies used μCT in combination with a synchrotron source to image lacunae and quantify their morphology [49, 53, 54, 141–143]. Not only the morphology of lacunae [12, 53, 144] but also that of the entire LCN including the canaliculi has been reported to be altered in different bone diseases [145].

The connection between lacunae provided by the canalicular network is essential due to several reasons. Osteocyte dendrites can extend in these tunnels and connect to the neighbouring cell via gap junctions, allowing for direct communication [146]. Even more importantly, this network is filled with interstitial fluid which is in motion due to changes in blood pressure and to deformations caused by mechanical loading of bones [147]. Fluid flow transports nutrients, removes cell waste and distributes signalling molecules. The latter are important in the biochemical control of bone remodelling.

Nevertheless, the remodelling process is driven also by mechanical signals to which these cells are also sensitive [31]. There is increasing evidence that motion of this liquid may stimulate osteocytes by deforming the membrane of the cell body or the dendrites [148, 149] or the primary cilia [150]. However, these processes are not yet fully understood, and fluid flow may not be the source of or may not be the only mechanism of triggering osteocytes to initiate remodelling. Direct straining through the deformation of the surrounding extracellular matrix may be an alternative or additional means for mechanical stimulation of osteocytes [151].

An unresolved issue with respect to both previous theories is the order of magnitude difference between the strains available in vivo (few thousand microstrains) [152] and the one required to stimulate these cells in vitro (few tens of thousands of microstrains) [153], giving rise to a missing strain amplification mechanism. This phenomenon has received increased attention during the last years and has been researched using experimental [154], analytical [149, 153, 155, 156] and numerical [22, 23, 157–162] approaches. In-depth analysis of the potential relevance of the pore network of osteocytes in bone diseases and in remodelling in general requires appropriate description of the geometry and 3D architecture of the entire LCN including the canaliculi. This task is far more challenging than imaging

of the lacunar pores described above, mainly due to the tiny dimensions of these canals embedded in the dense mineralised tissue.

The repertoire of the available appropriate experimental tools is very restricted; the available data is limited and shows high deviations for certain quantitative descriptors of the LCN [137, 163]. Scanning electron microscopy-based studies of Marotti et al. reported canalicular diameter to be between 150 and 500 nm [164], but 3D analysis is not possible with this method. The network properties of LCN can be investigated based on confocal microscopy images [56, 165–167], but detailed description of the canal geometry is not possible since the resolution of this method is practically the same as the average canalicular diameter, i.e. approximately 300 nm. The same is true for attenuation-based synchrotron tomography [54, 55].

Higher-resolution imaging can be achieved by means of the FIB-SEM approach [59], ptychography [81] or tomographic transmission electron microscopy [61]. However, these methods are expensive in terms of time and resources and provide a relatively small field of view; and FIB-SEM is fully destructive. In-line phase tomography can overcome some of these limitations by providing very high spatial resolution in a relatively large field of view within reasonable image acquisition time (Sect. 5.1.3). We used this technique to reconstruct the geometrical details of the LCN and investigate a potential means of mechanical stimulus of osteocytes [168].

In that study, the in-line phase tomography protocol described above (Sect. 5.1.3) was used to image cylindrical samples of human femoral cortical bone. Sample preparation was challenging since cylindrical samples with diameter less than 700 μm had to be prepared from several specimens within a relatively short time and with reasonable costs. We used a precision lathe for this purpose. First, a few mm wide and deep and approximately 15–20 mm long rods were cut, by means of a diamond-coated wheel saw, from a prescribed location of the femoral cortical cross sections. These samples were then mounted on the lathe using custom-built holders, and the required sample diameter was achieved by careful turning. This protocol allowed to preserve the close to native state of the samples. However, the resulting bone cylinders had to be dried prior to scanning to avoid potential sample motion during image acquisition.

Imaging provided us with an overview image with 715 μm field of view containing the entire cross section of the cylinders with 350 nm voxel size and a high-resolution image of selected regions with 102 μm field of view and 50 nm voxel size. Rectangular volumes of interest (VOIs) were selected from the high-resolution images to analyse the LCN and deformations of osteocytes. Each VOI contained a single lacuna with its canaliculi (Fig. 1.7a).

First, the geometry of the pores was identified using specialised segmentation methods including thresholding, morphological operations and a custom-developed connectivity enhancement algorithm. The latter was required to correct the effects of ring artefacts artificially cutting some canaliculi. In each VOI, the lacuna was then separated from the canaliculi, and several morphological parameters of both pore compartments were quantified (Fig. 1.7b). These included volumes, surfaces, descriptors of shape as well as number, diameter and spacing of canaliculi.
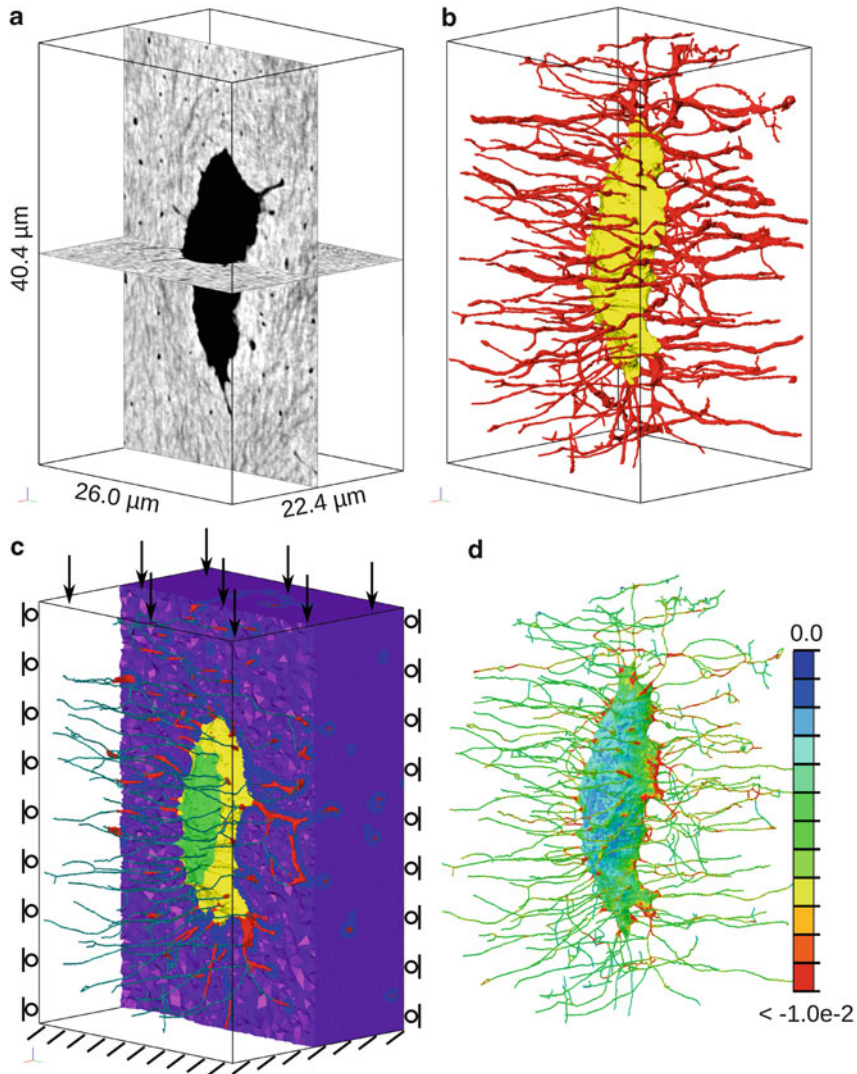
Fig. 1.7 Quantification of lacunar-canalicular morphology and prediction of osteocyte strains. (**a**) Selected VOIs from phase nano-CT images of femoral cortical bone of a 66-year-old female donor. *Grey* values represent the mass density. (**b**) Surface rendering of the segmented lacunar (*yellow*) and canalicular (*red*) pores. (**c**) Finite element mesh containing the mineralised extracellular matrix (*purple* and *blue*), the pericellular soft tissue in the lacuna (*yellow*) and in the canaliculi (*red*), as well as the cell body (*light green*) and processes (*turquoise*), with both the latter reconstructed artificially based on literature data. Parts of the model are transparent to allow visualisation of all compartments. Boundary conditions applied in the deformation analysis, i.e. constrained uniaxial compression of 1000 microstrains, are also shown. (**d**) Minimum (compressive) principal strain results of the finite element analysis in the osteocyte, showing deformation peaks (*red*, >10,000 microstrains; i.e. an at least tenfold strain amplification) at the junctions of the dendrites and cell body as well as at certain locations of the dendrites further away from the lacuna [168]

Case-specific finite element models of the VOIs were created from the same images. These models included the extracellular matrix surrounding the pores, the pericellular soft tissue matrix in the lacuna and the canaliculi as well as the osteocyte with its cell body and dendrites (Fig. 1.7c). As the cell itself was not visible on the images, assumptions based on previous literature data collected with electron microscopy imaging [160, 169] were used to artificially reconstruct its geometry from the available pore-matrix interface data. Moreover, each canaliculus was assumed to contain a cell dendrite. Material properties were modelled as linear elastic and isotropic, with parameters assigned based on literature data [22]. The models were subjected to confined uniaxial compressive deformation along the direction of the longest lacunar dimension with magnitude set to the physiologically relevant 1000 microstrains [152].

In-line phase tomography imaging provided unprecedented details of the LCN (Fig. 1.7). The most important results of the quantitative morphological analysis of the ten investigated regions of interest were as follows. The lacunar volume (min, 342 μm^3; max, 686 μm^3), surface (min, 295 μm^2; max, 503 μm^2) and aspect ratio of the approximating ellipsoid (min, 2.0; max, 4.8) varied considerably between the investigated VOIs. Lacunae located at the outer border of the osteons, i.e. in the direct vicinity of the cement lines were less elongated than others. Average canalicular diameter was comparable among different VOIs (min, 0.29 μm; max, 0.44 μm), but the number of canaliculi per lacuna (min, 53; max, 126), as well as the total volume (min, 2.4×10^{-3}; max, 9.3×10^{-3}) and surface area (min, 23×10^{-3} μm^{-1}; max, 84×10^3 μm^{-1}) of canaliculi, with both latter being normalised bone volume, showed higher variations. However, average distance between the canaliculi was found to fall into a relatively narrow range (min, 4.3 μm; max, 5.1 μm). This finding, in combination with the correlation between canalicular number and lacunar surface area (R = 0.79), suggested that the spatial distribution of canaliculi was very well regulated. Within the VOIs, the volume of canaliculi was 2–9 times smaller than that of the lacuna, but their surface area was 1.3–4.5 times larger. These results, although limited by the VOI-based analysis, underlined the potential of these pores in the interaction with the matrix.

The main outcome of the finite element analysis was that the magnitude of the strains at the junctions of the osteocyte cell body and dendrites reached up to 70 times the externally applied deformations and further local peaks were observed in the dendrites (Fig. 1.7d). Resulting strain magnitudes are in the range reported to stimulate osteocytes in vitro [153]. These findings provide a potential explanation of the sought strain amplification effect described above. The case-specific models predicted higher strain amplification factors compared not only to idealised ones [157–159] but also to previously reported case-specific simulations using either different image source [22] or less refined modelling approach [162].

However, these high strains were localised in a very small portion on the cell volume. There was no evident relation between the cell deformation and the parameters of the LCN morphology of the investigated osteocytes. One of the derived deformation-related parameters, the relative dendrite volume in which the strain amplification was higher than tenfold, was similar in the VOIs originating

from the same bone sample – and practically the same osteon – in two out of three cases. This suggests that local tissue age, even if not considering the related increase in the mineralisation and consequently in the stiffness of the extracellular matrix, may have an impact on osteocyte deformations.

Our analyses were limited by the number of investigated osteocytes. Future studies should therefore include several samples from numerous donors so that appropriate statistical analyses can be performed. The automated analysis protocol presented in [168] provides the efficiency required for such large-scale studies. Moreover, the effect of bone diseases on LCN morphology and osteocyte deformations could be investigated with the above described tools.

A further main limitation was the fact that the cells were not visible in the nano-CT images and thus had to be reconstructed artificially using literature-based data and a priori assumptions. However, recent advances in imaging technology are providing very high contrast and spatial resolution. This contrast may provide the possibility of imaging not only the mineralised matrix but also the cell itself in situ. Promising results in this respect have been achieved by means of both ptychography and in-line phase tomography. Moreover, the ultra-high resolution of these methods may allow to examine unprecedented details of osteocytes and their connection to the mineralised wall. Particularly interesting in this respect would be the focal adhesions of the cell dendrites to the canalicular wall [149, 169] as these were reported to be highly sensitive to mechanical stimuli [170]. However, conservation of the in vivo-like conditions of the cells would still remain a challenge for these imaging experiments [169].

Direct straining is just one of the potential theories for mechanical stimulation of osteocytes. Fluid flow-induced stimuli may indeed be of key importance in this respect. The potential of this theory, demonstrated analytically [149] and numerically [23], may be further refined with the aid of 3D spatial description of the pericellular space and the adhesion sites of osteocytes. Advances in imaging are expected to provide important details also to these models and ultimately the answer to the still not fully resolved phenomenon of osteocyte mechanosensation.

5.4 Mineralisation on the Nanoscale

Phase-contrast-based X-ray imaging techniques at the nanoscale allow to gain new insight into mineral exchange at the interface between the osteocyte network and the surrounding mineralised matrix for human bone tissue. The findings summarised in this section suggest that spatial distribution of bone tissue mass density is determined by the canalicular network morphology.

Bone is a biological material structured hierarchically over several length scales, from the molecular level of collagen to the organ level [107, 171]. Mechanical properties of bone depend on its composition and structure at all length scales. However, structural support is only one of the functions of bones; their role as mineral storage has been receiving attention recently. On the way towards

understanding the latter, details on the morphology of the micro(n) porosity as well as the properties of the surrounding mineralised tissue at this scale became of high interest.

In bone remodelling, maturation of the newly formed osteonal bone tissue is associated with a rapid primary increase in mineralisation followed by a slower secondary phase. This increase in mineralisation requires supply and precipitation of minerals into the bone matrix. Mineral delivery can occur only from the extra-cellular fluid via interfaces such as the Haversian system and the osteocyte pore network.

After the process of rapid initial mineralisation, a secondary mineralisation process takes place, which adds about 10 % more mineral over a period of several years [172]. In [172] it is also outlined that an average turnover of about 12 % per year at a total body calcium of 1000 g and a bone loss of about 1 % per year leads to a net calcium flux of about 30 mg out of an adult skeleton each day. However, much larger fluxes of calcium between the extracellular fluid (ECF) and the bone matrix have been reported than could be explained through osteoblast/osteoclast activity [172–174].

It is believed that the calcium concentration in the ECF is controlled mainly by the parathyroid hormone (PTH) [175], a non-collagenous protein. This study also reports that it is via PTH that the concentration of calcium in the ECF is elevated from the basic level of 35 mg/l to the required physiological level of 50 mg/l. Excess mineral ions are limited by the renal threshold for calcium which has to be coordi-nated with the processes of mineral exchange at the ECF-bone matrix interface by PTH. A large amount (~90 %) of the ECF-bone interface is made up by the lacuna-canalicular surface [176].

The role of non-collagenous proteins in regulating the mineralisation process is of great interest in literature [177]. For example, non-collagenous proteins which are found at the borders of the collagen matrix attached to the minerals in the ECF inhibit crystal growth, while crystals that are not in contact with non-collagenous protein in the collagen matrix grow normally [175]. This study further concluded that the calcium movement into and out of hydroxyapatite is due to crystal growth and crystal dissolution, respectively.

Crystal growth and crystal dissolution occur through equilibrium processes at the surfaces and potentially explain the stability of the calcium supply demanded by all kinds of physiological processes [135, 136].

The role of the osteocyte, of which there are as many as tens of thousands per cubic millimetre of bone [49, 51, 53, 142], in the metabolism of phosphate has recently been investigated [178, 179]. Moreover, it is believed that osteocytes dissolve calcium from the peri-lacunar space and replace it according to demand, in order to maintain calcium homeostasis [176]. The process of calcium removal from the peri-lacunar matrix is called osteocytic osteolysis [180], which has been demonstrated recently in mice during lactation [138], confirming that osteocytes also actively participate in calcium homeostasis. Alterations in lacunar size have also been observed in response to changes in the mechanical environment, e.g. enlarged lacunae have been reported in mice after space flights [181] or after glucocorticoid
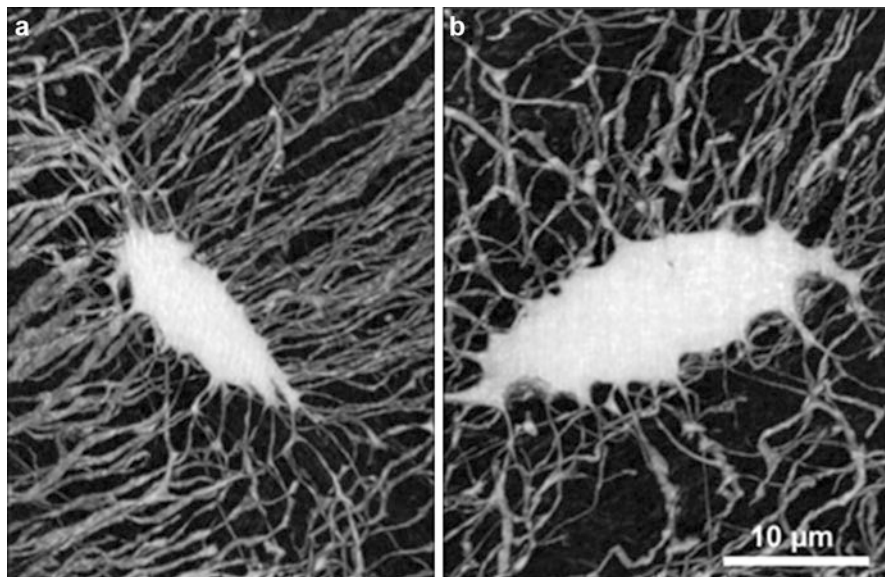
Fig. 1.8 Minimum intensity projections along z (**a**) and y (**b**) of one volume of interest containing the lacuna in the centre and the canaliculi pores connecting the lacunae to neighbouring cells. The size of the volume of interest is z = 630 pixel, x = 800 pixel and y = 600 pixel (200 pixel = 10 μm) [52]

treatment [182]. Both lacunar size and density were found to be altered in newly formed bone after anti-resorptive and anabolic pharmaceutical treatment in ovariectomised rats [183].

The distribution of osteocytes and their dendrites is thus not only crucial for proper sensing of mechanical signals across the bone matrix but also for easy access to mineral reservoirs. The distance between the extracellular tissue and the LCN is therefore of particular importance and has recently been demonstrated to be strongly related to the thickness and orientation of mineral particles and thus tissue quality [167]. The canalicular network provides a direct interface with the bone tissue which is much larger and much closer to the mineralised matrix compared to the interface formed by the lacunar walls [167] (Fig. 1.8). It has therefore been hypothesised that cell dendrites are involved in the active role of the osteocytes in tissue remodelling [138, 167, 184]. However, no measurement could support this hypothesis so far, possibly due to the lack of adequate three-dimensional quantitative imaging modalities at the length scales of the canaliculi [139].

In a recent study [52], we hypothesised that mineral exchange during mineralisation is achieved by the diffusion of minerals from the ECF in the LCN to the bone matrix, resulting in a gradual change in tissue mineralisation with respect to the distance from the pore-matrix interface. Based on this assumption, alterations in the mass density distribution with tissue age would be expected. In addition, we hypothesised that mineral exchange occurs not only at the lacunar but also at the canalicular boundaries.

We could provide evidence, by means of in-line phase nano-tomography, that the mass density in the direct vicinity of the LCN is indeed different from the mean mass density of the bone tissue, resulting in mass density gradients with respect to both the lacunar and the canalicular boundaries (Fig. 1.9).

The results indicated that mass density gradients diminished with increasing tissue age, resulting in a higher and a more homogeneously distributed extracellular matrix mass density in old tissue. These findings supported our hypothesis that extracellular matrix mineralisation is achieved through the diffusion of calcium from the extracellular fluid contained in the LCN to the bone matrix through all interfaces including the canaliculi. The smaller mass density values and gradients found in the peri-canalicular tissue compared to the peri-lacunar regions can be explained by the morphology of the LCN, indicating a higher mineral flux at the lacunar interfaces. We estimated that the amount of calcium stored in the subdomain of the bone tissue located within 0.5 μm distance from the LCN greatly exceeds the amount required for a rapidly exchangeable calcium pool to be used to compensate daily fluctuations in the serum calcium level. However, further studies are needed to confirm a mineral flux from the mineralised matrix into the LCN. Supporting the important role of this micropore network, we quantified the surface density (pore wall surface normalised to bone volume) of the LCN to be about 20 times higher than the surface density of the Haversian system. This relation holds despite the volume ratio of the lacunae being approximately one order of magnitude smaller than that of the Haversian canals.

In line with recent studies, these findings underlined the importance of the entire LCN in mineral homeostasis and the influence of its morphology on the spatial distribution of mass density in the mineralised extracellular matrix of bone. The role of the increased mass density adjacent to this pore network should therefore be taken into account in drug deposition studies and mechanical models studying the mechanosensation of osteocytes. Future studies using synchrotron radiation phase-contrast nano-computed tomography are expected to further aid the investigation of the diffusion and mineralisation processes and their coordination via osteocytes or other factors.

6   Conclusions and Future Perspective

6.1   Instrumentation

The work on in-line phase nano-CT shown here was performed on beamline ID22 at the ESRF. This beamline has now moved to the ID16 section and is run as a two two-branch nano-imaging (ID16A) and nano-analysis (ID16B) beamline. The ID16A end station is located at 185 m from the source and is mainly dedicated to problems in biology, biomedicine and nanotechnology. It is optimised for high-resolution quantitative 3D imaging techniques with a specific focus on X-ray fluorescence and projection microscopy. This branch will be optimised for ultimate hard X-ray focusing of the beam (<20 nm) at specific energies (17 and 33.6 keV,
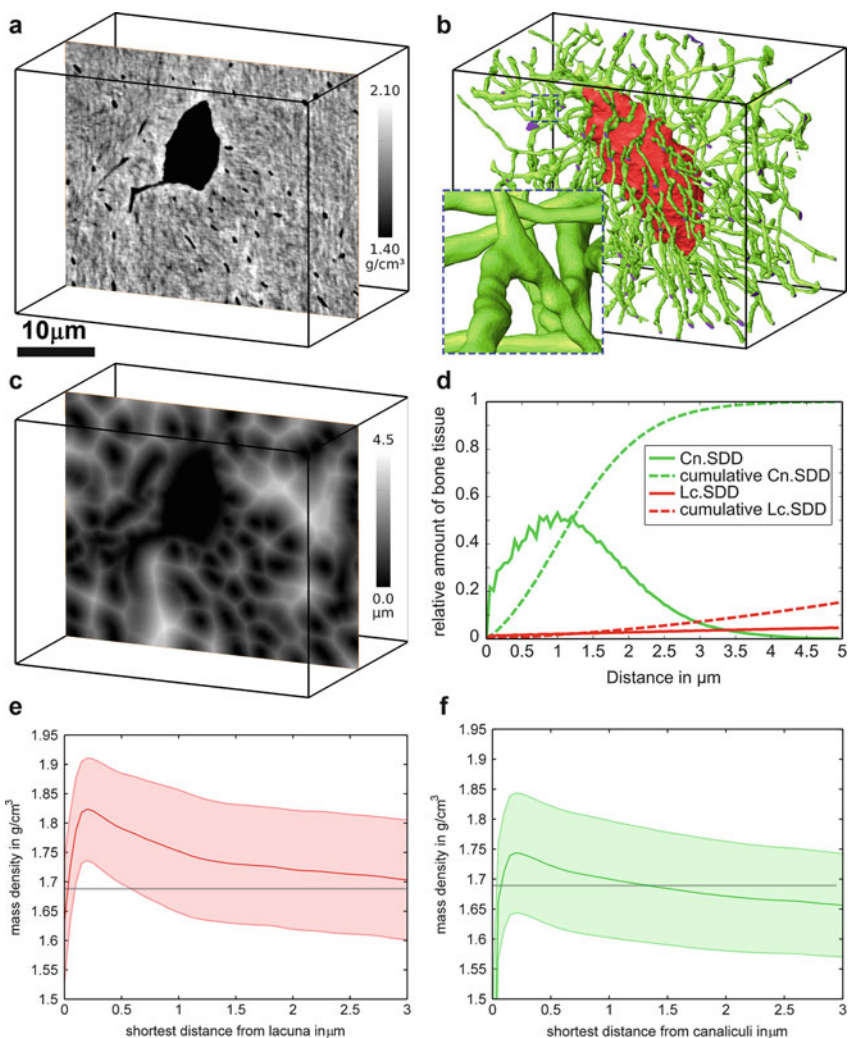
Fig. 1.9 Assessment of the peri-lacunar and peri-canalicular bone tissue mass densities based on in-line tomography images. (**a**) One slice of a volume of interest containing one osteocyte lacuna, cropped from the 3D reconstructed phase nano-CT image. The dimensions of the VOI are $800 \times 600 \times 630$ pixels. The *grey*scale corresponds to mass density. (**b**) Surface rendering of the lacunar (*red*) and canalicular (*green*) compartments segmented from the VOI. (**c**) Distance transform image showing the shortest distance from each point in the matrix to the lacunar-canalicular network. (**d**) Histogram of the 3D distance map (shortest distance distribution, SDD) of the canalicular (*green*) and the lacunar (*red*) boundaries shown together with their cumulative functions for the same VOI. From the *solid lines*, one can see that 50 % of the bone tissue is situated within about 1.2 μm distance from the canalicular boundaries, while at this distance, the cumulative function of the histogram of the distances considering the lacuna is only about ten times smaller. (**e** and **f**) Average mass density and standard error bands as a function of the shortest distance to the osteocyte lacuna (**e**) and canaliculi (**f**), shown for the same VOI. The *grey horizontal lines* represent the mean mass density within the VOI [52]

$\Delta E/E \sim 10^{-2}$). The beamline uses fixed curvature multilayer coated KB optics. 3D nano-positioning is done using a metrologic reference under control of capacitive sensors and an on-line video microscope for sample placement. One main difference to the previous imaging implementation is that samples are imaged in a vacuum environment. In the future, cryo-cooling capabilities will be added to increase the scope for imaging in life science.

The ID16B end station, in parallel operation, is located at approximately 165 m from the source and is optimised for high-resolution (50 nm to 1 μm) spectroscopic applications ($\Delta E/E \sim 10^{-4}$), including X-ray fluorescence (XRF), X-ray absorption spectroscopy (XAS) and X-ray-excited optical luminescence. It offers a multimodal approach (XAS, XRD, XRI) capable of in situ experiments. In a complementary way to the ID16A end station, ID16B will provide a monochromatic beam tuneable over a large energy range (5–70 keV). The ID16 beamlines opened for user experiments in late 2014.

6.2 Bone Nano-imaging

The above described technological advancements are expected to provide further insights into the structure and function of bone on the submicron scale. An important issue to be addressed here is the detailed morphology of canaliculi and in particular the interface of the osteocyte dendrites and the mineralised extracellular tissue. Moreover, the geometries of both the osteocytes and its pericellular space filled with interstitial fluid are of high interest. These details should provide the basis for image analysis and finite element methods aiming at unravelling the not yet fully understood mechanosensation of these cells. The interaction of osteocytes with the mineralised matrix, in the context of both remodelling and mineral homoeostasis, could be more efficiently analysed with even higher-resolution imaging. Bone tissue structure, density and composition at the direct vicinity of the cells are of highest interest in this respect. Even more accurate and detailed data on collagen orientation also around the LCN porosity would allow for better description of the mechanical properties of bone at these fine scales. Besides the topic of microcrack formation, more exact description of the deformations arriving to the cell through the heterogeneous and anisotropic bone tissue could be better analysed in possession of the higher-resolution image data.

Due to the high sensitivity of in-line phase tomography, it should also be possible to image the osteocytes directly in situ. We have some indication that there is enough contrast to do this (Fig. 1.10). Note that the cells seem severely shrunken, in a similar manner to what has earlier been observed with electron microscopy [185]. Also note that these structures are different from the mineralised ones reported in Ref. [142]; the structures shown here are very weakly contrasted, as opposed to those in Ref. [142]. No particular care was taken in the sample preparation with respect to cell preservation, however. Again, as in electron microscopy, the most important aspect for the in situ 3D observation of the osteocyte is probably the sample preparation [169]. Several options can be investigated; the future cryo-tomography capabilities
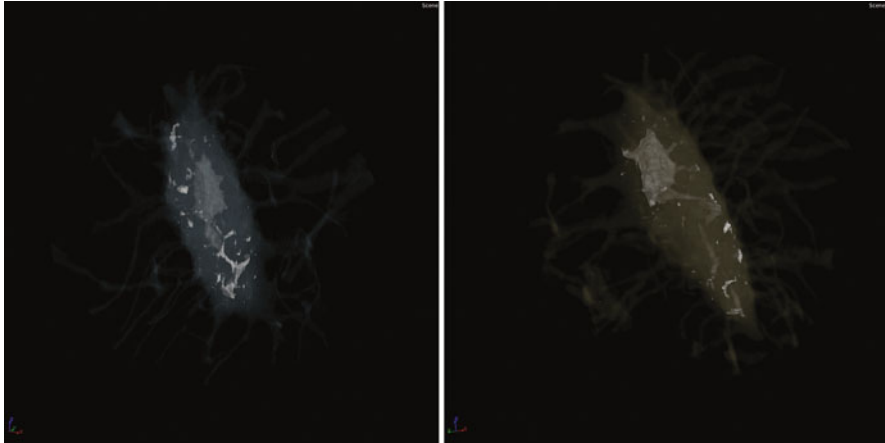
Fig. 1.10 Renderings of soft tissue preservations inside osteocyte lacunae, imaged in situ in dry bone using in-line phase nano-CT. The bone matrix is rendered as transparent, the lacuna and canaliculi are rendered in semi-transparent colour and the soft tissue preservations are rendered in *white*. Note the severely shrunken aspect of the eventual osteocytes. This indicates that contrast is probably sufficient for in situ osteocyte imaging, but that special care needs to be taken with respect to the sample preparation. The size of the box showing the renderings is approximately 40 μm × 40 μm

of ID16A will be used to this effect, for example. Preservation of cell geometry is known to require special sample preparation techniques, which will be a challenging part of future nano-CT experiments in this direction. The applicability of previously established methods towards this end has to be explored, and there may be a need for the development of new approaches.

References

1. Röntgen WC (1896) On a new kind of rays. Nature 53:274–277
2. Cormack AM (1963) Representation of a function by its line integrals, with some radiological applications. J Appl Phys 34:2722
3. Hounsfield GN (1972) A method and apparatus for examination of a body by radiation such as X-ray or gamma radiation. 1283915
4. Bonse U (2002) Developments in X-ray tomography II. In: Proceedings of the SPIE, vol. 4503
5. Bouxsein ML, Boyd SK, Christiansen BA, Guldberg RE, Jepsen KJ, Müller R (2010) Guidelines for assessment of bone microstructure in rodents using micro-computed tomography. J Bone Miner Res 25(7):1468–1486
6. Engelke K, Karolczak M, Lutz A, Seibert U, Schaller S, Kalender W (1999) Micro-CT. Technology and application for assessing bone structure. Radiologe 39(3):203–212

7. Hildebrand T, Laib A, Müller R, Dequeker J, Rüegsegger P (1999) Direct three-dimensional morphometric analysis of human cancellous bone: microstructural data from spine, femur, iliac crest, and calcaneus. J Bone Miner Res 14(7):1167–1174

8. Salomé M, Peyrin F, Cloetens P, Odet C, Laval-Jeantet A-M, Baruchel J, Spanne P (1999) A synchrotron radiation microtomography system for the analysis of trabecular bone samples. Med Phys 26(10):2194

9. Nuzzo S, Peyrin FF, Cloetens P, Baruchel JJ, Boivin G (2002) Quantification of the degree of mineralization of bone in three dimensions using synchrotron radiation microtomography. Med Phys 29(11):2672

10. Peyrin F, Salomé M, Nuzzo S, Cloetens P, Laval-Jeantet AM, Baruchel J (2000) Perspectives in three-dimensional analysis of bone samples using synchrotron radiation microtomography. Cell Mol Biol 46(6):1089–1102

11. Schneider P, Meier M, Wepf R, Müller R (2010) Towards quantitative 3D imaging of the osteocyte lacuno-canalicular network. Bone 47(5):848–858

12. van Hove RP, Nolte PA, Vatsa A, Semeins CM, Salmon PL, Smit TH, Klein-Nulend J (2009) Osteocyte morphology in human tibiae of different bone pathologies with different bone mineral density – is there a role for mechanosensing? Bone 45(2):321–329

13. Labiche J-C, Mathon O, Pascarelli S, Newton MA, Ferre GG, Curfs C, Vaughan G, Homs A, Carreiras DF (2007) Invited article: the fast readout low noise camera as a versatile x-ray detector for time resolved dispersive extended x-ray absorption fine structure and diffraction studies of dynamic problems in materials science, chemistry, and catalysis. Rev Sci Instrum 78 (9):091301

14. Paschalis EP, Mendelsohn R, Boskey AL (2011) Infrared assessment of bone quality: a review. Clin Orthop Relat Res 469(8):2170–2178

15. Seeman E, Delmas PD (2006) Bone quality – the material and structural basis of bone strength and fragility. N Engl J Med 354(21):2250–2261

16. Bonewald LF (2006) Mechanosensation and transduction in osteocytes. Bonekey Osteovision 3(10):7–15

17. Klein-Nulend J, Bacabac RG, Mullender MG (2005) Mechanobiology of bone tissue. Pathol Biol 53(10):576–580

18. Knothe Tate ML, Adamson JR, Tami AE, Bauer TW, Nijweide PJ, Burger EH, Nulend JK (2004) The osteocyte. Int J Biochem Cell Biol 36(1):1–8

19. Nijweide PJ, Burger EH, Nulend JK (2002) The osteocyte, pp 93–108

20. Burger EH, Klein-Nulend J (1999) Mechanotransduction in bone – role of the lacuno-canalicular network. FASEB J 13(Suppl):S101–S112

21. Nicolella D, Feng J (2008) Effects of nanomechanical bone tissue properties on bone tissue strain: implications for osteocyte mechanotransduction. J Musculoskelet 8(4):330–331

22. Verbruggen SW, Vaughan TJ, McNamara LM (2012) Strain amplification in bone mechanobiology: a computational investigation of the in vivo mechanics of osteocytes. J R Soc Interface 9(75):2735–2744

23. Verbruggen SW, Vaughan TJ, McNamara LM (2013) Fluid flow in the osteocyte mechanical environment: a fluid–structure interaction approach. Biomech Model Mechanobiol, epub, Apr 2013

24. Hazenberg JG, Freeley M, Foran E, Lee TC, Taylor D (2006) Microdamage: a cell transducing mechanism based on ruptured osteocyte processes. J Biomech 39(11):2096–2103

25. Taylor D, Hazenberg JG, Lee TC (2007) Living with cracks: damage and repair in human bone. Nat Mater 6(4):263–268

26. Qiu S, Rao DS, Fyhrie DP, Palnitkar S, Parfitt AM (2005) The morphological association between microcracks and osteocyte lacunae in human cortical bone. Bone 37(1):10–15

27. Dooley C, Tisbo P, Lee TC, Taylor D (2012) Rupture of osteocyte processes across microcracks: the effect of crack length and stress. Biomech Model Mechanobiol 11(6):759–766

28. Bonewald LF, Kneissel M, Johnson M (2013) Preface: the osteocyte. Bone 54(2):181
29. Bonewald LF (2011) The amazing osteocyte. J Bone Miner Res 26(2):229–238
30. Kalajzic I, Matthews BG, Torreggiani E, Harris MA, Divieti Pajevic P, Harris SE (2013) In vitro and in vivo approaches to study osteocyte biology. Bone 54(2):296–306
31. Klein-Nulend J, Bakker AD, Bacabac RG, Vatsa A, Weinbaum S (2013) Mechanosensation and transduction in osteocytes. Bone 54(2):182 (in press)
32. Rochefort GY, Pallu S, Benhamou CL (2010) Osteocyte : the unrecognized side of bone tissue. Osteoporos Int 21(9):1457–1469
33. Seeman E (2006) Osteocytes – martyrs for integrity of bone strength. Osteoporos Int 17(10):1443–1448
34. Atkins A, Dean MN, Habegger ML, Motta PJ, Ofer L, Repp F, Shipov A, Weiner S, Currey JD, Shahar R (2014) Remodeling in bone without osteocytes: billfish challenge bone structure-function paradigms. Proc Natl Acad Sci U S A 111(45):16047–16052
35. Burr DB, Schaffler MB, Frederickson RG (1988) Composition of the cement line and its possible mechanical role as a local interface in human compact bone. J Biomech 21(11):939–945
36. Schaffler MB, Burr DB, Frederickson RG (1987) Morphology of the osteonal cement line in human bone. Anat Rec 217(3):223–228
37. Davies JE (2007) Bone bonding at natural and biomaterial surfaces. Biomaterials 28(34):5058–5067
38. Skedros JG, Holmes JL, Vajda EG, Bloebaum RD (2005) Cement lines of secondary osteons in human bone are not mineral-deficient: new data in a historical perspective. Anat Rec A: Discov Mol Cell Evol Biol 286(1):781–803
39. Milovanovic P, Zimmermann EAE, Hahn M, Djonic D, Püschel K, Djuric M, Amling M, Busse B (2013) Osteocytic canalicular networks: morphological implications for altered mechanosensitivity. ACS 7(9):7542–7551
40. Kingsmill VJ, Boyde A (1998) Mineralisation density of human mandibular bone: quantitative backscattered electron image analysis. J Anat 192(Pt 2):245–256
41. Pannarale L, Braidotti P, d'Alba L, Gaudio E (1994) Scanning electron microscopy of collagen fiber orientation in the bone lamellar system in non-decalcified human samples. Acta Anat (Basel) 151(1):36–42
42. Reznikov N, Almany-Magal R, Shahar R, Weiner S (2013) Three-dimensional imaging of collagen fibril organization in rat circumferential lamellar bone using a dual beam electron microscope reveals ordered and disordered. Bone 52(2):676–683
43. Reznikov N, Shahar R, Weiner S (2014) Three-dimensional structure of human lamellar bone: the presence of two different materials and new insights into the hierarchical organization. Bone 59(2012):93–104
44. Giraud-Guille M-M, Besseau L, Martin R (2003) Liquid crystalline assemblies of collagen in bone and in vitro systems. J Biomech 36(10):1571–1579
45. Hassenkam T, Fantner GE, Cutroni JA, Weaver JC, Morse DE, Hansma PK (2004) High-resolution AFM imaging of intact and fractured trabecular bone. Bone 35(1):4–10
46. Bromage TG, Goldman HM, McFarlin SC, Warshaw J, Boyde A, Riggs CM (2003) Circularly polarized light standards for investigations of collagen fiber orientation in bone. Anat Rec B New Anat 274(1):157–168
47. Kazanci M, Roschger P, Paschalis EP, Klaushofer K, Fratzl P (2006) Bone osteonal tissues by Raman spectral mapping: orientation-composition. J Struct Biol 156(3):489–496
48. Schrof S, Varga P, Galvis L, Raum K, Masic A (2014) 3D Raman mapping of the collagen fibril orientation in human osteonal lamellae. J Struct Biol 187(3):266–275
49. Carter Y, Thomas CDL, Clement JG, Peele AG, Hannah K, Cooper DMLL (2013) Variation in osteocyte lacunar morphology and density in the human femur – a synchrotron radiation micro-CT study. Bone 52(1):126–132
50. Carter Y, Thomas CDL, Clement JG, Cooper DML (2013) Femoral osteocyte lacunar density, volume and morphology in women across the lifespan. J Struct Biol 183(3):519–526

51. Dong P, Haupert S, Hesse B, Langer M, Gouttenoire P-J, Bousson V, Peyrin F (2014) 3D osteocyte lacunar morphometric properties and distributions in human femoral cortical bone using synchrotron radiation micro-CT images. Bone 60:172–185

52. Hesse B, Varga P, Langer M, Pacureanu A, Schrof S, Männicke N, Suhonen H, Maurer P, Cloetens P, Peyrin F, Raum K (2014) Canalicular network morphology is the major determinant of the spatial distribution of mass density in human bone tissue – evidence by means of synchrotron radiation phase-contrast nano-CT. J Bone Miner Res 30(2):346–356

53. Hesse B, Langer M, Varga P, Pacureanu A, Dong P, Schrof S, Männicke N, Suhonen H, Olivier C, Maurer P, Kazakia GJ, Raum K, Peyrin F (2014) Alterations of mass density and 3D osteocyte lacunar properties in bisphosphonate-related osteonecrotic human jaw Bone, a synchrotron μCT study. PLoS One 9(2), e88481

54. Pacureanu A, Langer M, Boller E, Tafforeau P, Peyrin FF (2012) Nanoscale imaging of the bone cell network with synchrotron x-ray tomography: optimization of acquisition setup. Med Phys 39(4):2229–2238

55. Pacureanu A, Larrue A, Langer M, Olivier C, Muller C, Lafage-Proust M-H, Peyrin F (2013) Adaptive filtering for enhancement of the osteocyte cell network in 3D microtomography images. IRBM 34(1):48–52

56. Sugawara Y, Kamioka H, Honjo T, Tezuka K, Takano-Yamamoto T (2005) Three-dimensional reconstruction of chick calvarial osteocytes and their cell processes using confocal microscopy. Bone 36(5):877–883

57. Gourion-Arsiquaud S, Marcott C, Hu Q, Boskey AL (2014) Studying variations in bone composition at nano-scale resolution: a preliminary report. Calcif Tissue Int 95(5):413–418

58. Geith T, Amarie S, Milz S, Bamberg F, Keilmann F (2014) Visualisation of methacrylate-embedded human bone sections by infrared nanoscopy. J Biophotonics 7(6):418–424

59. Schneider P, Meier M, Wepf R, Müller R (2011) Serial FIB/SEM imaging for quantitative 3D assessment of the osteocyte lacuno-canalicular network. Bone 49(2):304–311

60. Magal RA, Reznikov N (2014) Three-dimensional structure of minipig fibrolamellar bone: adaptation to axial loading. J Struct 186(2):253–264

61. Kamioka H, Murshid SA, Ishihara Y, Kajimura N, Hasegawa T, Ando R, Sugawara Y, Yamashiro T, Takaoka A, Takano-Yamamoto T (2009) A method for observing silver-stained osteocytes in situ in 3-microm sections using ultra-high voltage electron microscopy tomography. Microsc Microanal 15(5):377–383

62. Martínez-Criado G, Tucoulou R, Cloetens P, Bleuet P, Bohic S, Cauzid J, Kieffer I, Kosior E, Labouré S, Petitgirard S, Rack A, Sans JA, Segura-Ruiz J, Suhonen H, Susini J, Villanova J (2012) Status of the hard x-ray microprobe beamline ID22 of the European Synchrotron Radiation Facility. J Synchrotron Radiat 19(Pt 1):10–18

63. Morawe C, Hignette O, Cloetens P, Ludwig W, Borel C, Bernard P, Rommeveaux A (2006) Graded multilayers for focusing hard x-rays below 50 nm. In: SPIE optics + photonics, pp 63170F–63170F-11

64. Barrett R, Baker R, Cloetens P, Dabin Y, Morawe C, Suhonen H, Tucoulou R, Vivo A, Zhang L (2011) Dynamically-figured mirror system for high-energy nanofocusing at the ESRF. In: SPIE optical engineering + applications. pp 813904–813904-12

65. Hignette O, Cloetens P, Morawe C, Borel C, Ludwig W, Bernard P, Rommeveaux A, Bohic S (2007) Nanofocusing at ESRF using graded multilayer mirrors. AIP Conf Proc 879(1):792–795

66. Zhang L, Baker R, Barrett R, Cloetens P, Dabin Y, Garrett R, Gentle I, Nugent K, Wilkins S (2010) Mirror profile optimization for nano-focusing KB mirror. In: SRI 2009, 10th international conference on radiation instrumentation, vol 1234(1), pp 801–804

67. Cloetens P, Suhonen H, Bay A, Bohic S, Fleck C, Langer M, Pacureanu A, Peyrin F, Rack A, Vigneron JP, Zaslansky P (2012) Non-destructive and multi-modal 3D imaging of biological materials. In: 2012 MRS spring meeting and exhibit

68. Tucoulou R, Martinez-Criado G, Bleuet P, Kieffer I, Cloetens P, Labouré S, Martin T, Guilloud C, Susini J (2008) High-resolution angular beam stability monitoring at a nanofocusing beamline. J Synchrotron Radiat 15(Pt 4):392–398

69. Jackson JD (1975) Classical electrodynamics
70. Snigirev A, Snigireva I, Kohn V, Kuznetsov S, Schelokov I (1995) On the possibilities of x-ray phase contrast microimaging by coherent high-energy synchrotron radiation. Rev Sci Instrum 66(12):5486
71. Goodman JW (2005) Introduction to fourier optics
72. Langer M, Pacureanu A, Suhonen H, Grimal Q, Cloetens P, Peyrin F (2012) X-ray phase nanotomography resolves the 3D human bone ultrastructure. PLoS One 7(8), e35691
73. Cloetens P, Ludwig W, Baruchel J, Van Dyck D, Van Landuyt J, Guigay JP, Schlenker M (1999) Holotomography: quantitative phase tomography with micrometer resolution using hard synchrotron radiation x rays. Appl Phys Lett 75(19):2912
74. Langer M, Cloetens P, Guigay J-P, Peyrin F (2008) Quantitative comparison of direct phase retrieval algorithms in in-line phase tomography. Med Phys 35(10):4556–4566
75. Elser V (2003) Solution of the crystallographic phase problem by iterated projections. Acta Crystallogr Sect A: Found Crystallogr 59(3):201–209
76. Fienup JR (1982) Phase retrieval algorithms: a comparison. Appl Opt 21(15):2758–2769
77. Gerchberg RW, Saxton WO (1972) A practical algorithm for the determination of phase from image and diffraction plane pictures. Optik (Stuttg) 35:237–246
78. Bauschke HH, Combettes PL, Luke DR (2002) Phase retrieval, error reduction algorithm, and Fienup variants: a view from convex optimization. J Opt Soc Am A 19(7):1334
79. Thibault P, Elser V (2010) X-ray diffraction microscopy. Annu Rev Condens Matter Phys 1 (1):237–255
80. Elser V, Rankenburg I, Thibault P (2007) Searching with iterated maps. Proc Natl Acad Sci U S A 104(2):418–423
81. Dierolf M, Menzel A, Thibault P, Schneider P, Kewish CM, Wepf R, Bunk O, Pfeiffer F (2010) Ptychographic x-ray computed tomography at the nanoscale. Nature 467(7314):436–439
82. Schroer C, Boye P, Feldkamp J, Patommel J, Schropp A, Schwab A, Stephan S, Burghammer M, Schöder S, Riekel C (2008) Coherent X-ray diffraction imaging with nanofocused illumination. Phys Rev Lett 101(9):090801
83. Huang X, Nelson J, Kirz J, Lima E, Marchesini S, Miao H, Neiman A, Shapiro D, Steinbrener J, Stewart A, Turner J, Jacobsen C (2009) Soft X-ray diffraction microscopy of a frozen hydrated yeast cell. Phys Rev Lett 103(19):198101
84. Maiden AM, Rodenburg JM (2009) An improved ptychographical phase retrieval algorithm for diffractive imaging. Ultramicroscopy 109(10):1256–1262
85. Thibault P, Dierolf M, Menzel A, Bunk O, David C, Pfeiffer F (2008) High-resolution scanning x-ray diffraction microscopy. Science 321(5887):379–382
86. Thibault P, Dierolf M, Bunk O, Menzel A, Pfeiffer F (2009) Probe retrieval in ptychographic coherent diffractive imaging. Ultramicroscopy 109(4):338–343
87. Hoppe W (1969) Beugung im inhomogenen Primärstrahlwellenfeld. I. Prinzip einer Phasenmessung von Elektronenbeugungsinterferenzen. Acta Crystallogr Sect A 25(4):495–501
88. Guinier A (1994) X-ray diffraction in crystals, imperfect crystals, and amorphous bodies. Courier Dover Publications
89. Langer M, Cloetens P, Peyrin F (2010) Regularization of phase retrieval with phase-attenuation duality prior for 3-D holotomography. IEEE Trans Image Process 19(9):2428–2436
90. Paganin D, Mayo SC, Gureyev TE, Miller PR, Wilkins SW (2002) Simultaneous phase and amplitude extraction from a single defocused image of a homogeneous object. J Microsc 206 (1):33–40
91. Wilkins SW, Gureyev TE, Gao D, Pogany A, Stevenson AW (1996) Phase-contrast imaging using polychromatic hard x-rays. Nature 384(6607):335–338
92. Holler M, Diaz A, Guizar-Sicairos M, Karvinen P, Färm E, Härkönen E, Ritala M, Menzel A, Raabe J, Bunk O (2014) X-ray ptychographic computed tomography at 16 nm isotropic 3D resolution. Sci Rep 4:3857

93. Dennis MDP, Ghiglia C (1998) Two-dimensional phase unwrapping: theory, algorithms, and software. Wiley, New York
94. Andrews JC, Almeida E, van der Meulen MCH, Alwood JS, Lee C, Liu Y, Chen J, Meirer F, Feser M, Gelb J, Rudati J, Tkachuk A, Yun W, Pianetta P (2010) Nanoscale x-ray microscopic imaging of mammalian mineralized tissue. Microsc Microanal 16(3):327–336
95. Mokso R, Cloetens P, Maire E, Ludwig W, Buffière J-Y (2007) Nanoscale zoom tomography with hard x rays using Kirkpatrick-Baez optics. Appl Phys Lett 90(14):144104
96. Guigay JP, Langer M, Boistel R, Cloetens P (2007) Mixed contrast transfer and transport of intensity approach for phase retrieval in the Fresnel region. Opt Lett 32:1617–1619
97. Langer M, Hesse B, Pacureanu A, Suhonen H, Cloetens P, Raum K, Peyrin F (2013) Priors for x-ray in-line phase tomography of heterogeneous objects. Phil Trans R Soc A 372: 20130129
98. Langer M, Cloetens P, Hesse B, Pacureanu A, Raum K, Lafage-Proust M-H, Peyrin F (2012) X-ray in-line phase micro-CT for simultaneous bone and soft tissue visualisation. In: Nouvelles m{é}thodologies en imagerie du vivant, p 9581
99. Langer M, Cloetens P, Peyrin F (2009) Fourier-wavelet regularization of phase retrieval in x-ray in-line phase tomography. J Opt Soc Am A Opt Image Sci Vis 26(8):1876–1881
100. Davidoiu V, Sixou B, Langer M, Peyrin F (2011) Non-linear iterative phase retrieval based on Frechet derivative and projection operators. Opt Express 19(23):106–109
101. Davidoiu V, Sixou B, Langer M, Peyrin F (2013) Nonlinear approaches for the single-distance phase retrieval problem involving regularizations with sparsity constraints. Appl Opt 52(17):3977–3986
102. Davidoiu V, Sixou B, Langer M, Peyrin F (2013) In-line phase tomography using nonlinear phase retrieval. Ann Univ Bucharest Math Ser 4(LXII):115–122
103. Moosmann J, Hofmann R, Baumbach T (2011) Single-distance phase retrieval at large phase shifts. Opt Express 19:12066–12073
104. Moosmann J, Hofmann R, Bronnikov A, Baumbach T (2010) Nonlinear phase retrieval from single-distance radiograph. Opt Express 18:25771–25785
105. Gebhardt W (1906) Ueber funktionell wichtige Anordnungsweisen der groberen und feineren Bauelemente des Wirbeltierknochens. Arch Entw Mech 20:187–322
106. Wang Y, Azaïs T, Robin M, Vallée A, Catania C, Legriel P, Pehau-Arnaudet G, Babonneau F, Giraud-Guille M-M, Nassif N (2012) The predominant role of collagen in the nucleation, growth, structure and orientation of bone apatite. Nat Mater 11(8):724–733
107. Fratzl P, Weinkamer R (2007) Nature's hierarchical materials. Prog Mater Sci 52(8):1263–1334
108. Ascenzi A, Bonucci E (1967) The tensile properties of single osteons. Anat Rec 158(4):375–386
109. Ascenzi A, Bonucci E (1968) The compressive properties of single osteons. Anat Rec 161(3):377–391
110. Ascenzi A, Bonucci E (1972) The shearing properties of single osteons. Anat Rec 172(3):499–510
111. Ascenzi A, Benvenuti A, Bonucci E (1982) The tensile properties of single osteonic lamellae: technical problems and preliminary results. J Biomech 15(1):29–37
112. Giraud-Guille MM (1988) Twisted plywood architecture of collagen fibrils in human compact bone osteons. Calcif Tissue Int 42(3):167–180
113. Marotti G, Muglia MA, Palumbo C (1994) Structure and function of lamellar bone. Clin Rheumatol 13(Suppl 1):63–68
114. Weiner S, Arad T, Sabanay I, Traub W (1997) Rotated plywood structure of primary lamellar bone in the rat: orientations of the collagen fibril arrays. Bone 20(6):509–514
115. Ascenzi MG, Ascenzi A, Benvenuti A, Burghammer M, Panzavolta S, Bigi A (2003) Structural differences between 'dark' and 'bright' isolated human osteonic lamellae. J Struct Biol 141(1):22–33

116. Ascenzi M-G, Lomovtsev A (2006) Collagen orientation patterns in human secondary osteons, quantified in the radial direction by confocal microscopy. J Struct Biol 153(1):14–30
117. Hofmann T, Heyroth F, Meinhard H, Fränzel W, Raum K (2006) Assessment of composition and anisotropic elastic properties of secondary osteon lamellae. J Biomech 39(12): 2282–2294
118. Kazanci M, Wagner HD, Manjubala NI, Gupta HS, Paschalis E, Roschger P, Fratzl P (2007) Raman imaging of two orthogonal planes within cortical bone. Bone 41(3):456–461
119. Spiesz EM, Kaminsky W, Zysset PK (2011) A quantitative collagen fibers orientation assessment using birefringence measurements: calibration and application to human osteons. J Struct Biol 176(3):302–306
120. Gourrier A, Wagermaier W, Burghammer M, Lammie D, Gupta HS, Fratzl P, Riekel C, Wess TJ, Paris O (2007) Scanning x-ray imaging with small-angle scattering contrast. J Appl Crystallogr 40(s1):s78–s82
121. Seidel R, Gourrier A, Kerschnitzki M, Burghammer M, Fratzl P, Gupta HS, Wagermaier W (2011) Synchrotron 3D SAXS analysis of bone nanostructure. Bioinspired Biomim Nanobiomaterials 1:123–131
122. Granke M, Gourrier A, Rupin F, Raum K, Peyrin F, Burghammer M, Saïed A, Laugier P (2013) Microfibril orientation dominates the microelastic properties of human bone tissue at the lamellar length scale. PLoS One 8(3), e58043
123. Wagermaier W, Gupta HS, Gourrier A, Paris O, Roschger P, Burghammer M, Riekel C, Fratzl P (2007) Scanning texture analysis of lamellar bone using microbeam synchrotron x-ray radiation. J Appl Crystallogr 40(1):115–120
124. Wagermaier W, Gupta HS, Gourrier A, Burghammer M, Roschger P, Fratzl P (2006) Spiral twisting of fiber orientation inside bone lamellae. Biointerphases 1(1):1
125. Marotti G (1993) A new theory of bone lamellation. Calcif Tissue Int 53(Suppl 1):S47–S55; discussion S56
126. Marotti G, Ferretti M, Palumbo C (2013) The problem of bone lamellation: an attempt to explain different proposed models. J Morphol 274(5):543–550
127. Varga P, Pacureanu A, Langer M, Suhonen H, Hesse B, Grimal Q, Cloetens P, Raum K, Peyrin F (2013) Investigation of the 3D orientation of mineralized collagen fibrils in human lamellar bone using synchrotron x-ray phase nano-tomography. Acta Biomater 9:8118–8127
128. Rho JY, Kuhn-Spearing L, Zioupos P (1998) Mechanical properties and the hierarchical structure of bone. Med Eng Phys 20(2):92–102
129. Ritchie RO (2011) The conflicts between strength and toughness. Nat Mater 10(11):817–822
130. Marotti G (1993) Calcified tissue a new theory of bone lamellation, vol 53
131. Gupta HS, Stachewicz U, Wagermaier W, Roschger P, Wagner HD, Fratzl P (2006) Mechanical modulation at the lamellar level in osteonal bone. J Mater Res 21:1913–1921
132. Reisinger AG, Pahr DH, Zysset PK (2011) Elastic anisotropy of bone lamellae as a function of fibril orientation pattern. Biomech Model Mechanobiol 10(1):67–77
133. Carnelli D, Vena P, Dao M, Ortiz C, Contro R (2013) Orientation and size-dependent mechanical modulation within individual secondary osteons in cortical bone tissue. J R Soc Interface 10(81):20120953
134. Faingold A, Cohen SR, Reznikov N, Wagner HD (2013) Osteonal lamellae elementary units: lamellar microstructure, curvature and mechanical properties. Acta Biomater 9(4):5956–5962
135. Chen X, Nadiarynkh O, Plotnikov S, Campagnola PJ (2012) Second harmonic generation microscopy for quantitative analysis of collagen fibrillar structure. Nat Protoc 7(4):654–669
136. Williams RM, Zipfel WR, Webb WW (2005) Interpreting second-harmonic generation images of collagen I fibrils. Biophys J 88(2):1377–1386
137. Currey JD, Shahar R (2013) Cavities in the compact bone in tetrapods and fish and their effect on mechanical properties. J Struct Biol 183(2):107–122
138. Qing H, Ardeshirpour L, Pajevic PD, Dusevich V, Jähn K, Kato S, Wysolmerski J, Bonewald LF (2012) Demonstration of osteocytic perilacunar/canalicular remodeling in mice during lactation. J Bone Miner Res 27(5):1018–1029

139. Webster DJ, Schneider P, Dallas SL, Müller R (2013) Studying osteocytes within their environment. Bone (in press)
140. Vatsa A, Breuls RG, Semeins CM, Salmon PL, Smit TH, Klein-Nulend J (2008) Osteocyte morphology in fibula and calvaria – is there a role for mechanosensing? Bone 43(3):452–458
141. Hannah KM, Thomas CDL, Clement JG, De Carlo F, Peele AG (2010) Bimodal distribution of osteocyte lacunar size in the human femoral cortex as revealed by micro-CT. Bone 47 (5):866–871
142. Hesse B, Männicke N, Pacureanu A, Varga P, Langer M, Maurer P, Peyrin F, Raum K (2014) Accessing osteocyte lacunar geometrical properties in human jaw bone on the submicron length scale using synchrotron radiation μCT. J Microsc 255(3):158–168
143. Dong P, Pacureanu A, Zuluaga MA, Olivier C, Grimal Q, Peyrin F (2014) Quantification of the 3D morphology of the bone cell network from synchrotron micro-ct images. Image Anal Stereol 33(2):157
144. Mullender MG, Tan SD, Vico L, Alexandre C, Klein-Nulend J (2005) Differences in osteocyte density and bone histomorphometry between men and women and between healthy and osteoporotic subjects. Calcif Tissue Int 77(5):291–296
145. Knothe Tate ML, Tami A, Bauer TW, Knothe U (2002) Micropathoanatomy of osteoporosis – indications for a cellular basis of bone disease. Adv Osteoporotic Fract Manag 2(1):9–14
146. Loiselle AE, Jiang JX, Donahue HJ (2013) Gap junction and hemichannel functions in osteocytes. Bone 54(2):205–212
147. Price C, Zhou X, Li W, Wang L (2011) Real-time measurement of solute transport within the lacunar-canalicular system of mechanically loaded bone: direct evidence for load-induced fluid flow. J Bone Miner Res 26(2):277–285
148. You L-D, Weinbaum S, Cowin SC, Schaffler MB (2004) Ultrastructure of the osteocyte process and its pericellular matrix. Anat Rec A: Discov Mol Cell Evol Biol 278 (2):505–513
149. Wang Y, McNamara LM, Schaffler MB, Weinbaum S (2007) A model for the role of integrins in flow induced mechanotransduction in osteocytes. Proc Natl Acad Sci U S A 104 (40):15941–15946
150. Nguyen AM, Jacobs CR (2013) Emerging role of primary cilia as mechanosensors in osteocytes. Bone 54(2):196–204
151. Stern AR, Nicolella DP (2013) Measurement and estimation of osteocyte mechanical strain. Bone 54(2):191–195
152. Group M, Hero S, Burr DB (1996) In vivo measurement of human tibial strains during vigorous activity 18(5)
153. You L, Cowin SC, Schaffler MB, Weinbaum S (2001) A model for strain amplification in the actin cytoskeleton of osteocytes due to fluid drag on pericellular matrix. J Biomech 34 (11):1375–1386
154. Nicolella DP, Moravits DE, Gale AM, Bonewald LF, Lankford J (2006) Osteocyte lacunae tissue strain in cortical bone. J Biomech 39(9):1735–1743
155. Weinbaum S, Cowin SC, Zeng Y (1994) A model for the excitation of osteocytes by mechanical loading-induced bone fluid shear stresses. J Biomech 27(3):339–360
156. Han Y, Cowin SC, Schaffler MB, Weinbaum S (2004) Mechanotransduction and strain amplification in osteocyte cell processes. Proc Natl Acad Sci U S A 101(47): 16689–16694
157. McCreadie BR, Hollister SJ, Schaffler MB, Goldstein SA (2004) Osteocyte lacuna size and shape in women with and without osteoporotic fracture. J Biomech 37(4):563–572
158. Bonivtch AR, Bonewald LF, Nicolella DP (2007) Tissue strain amplification at the osteocyte lacuna: a microstructural finite element analysis. J Biomech 40(10):2199–2206
159. Deligianni DD, Apostolopoulos CA (2008) Multilevel finite element modeling for the prediction of local cellular deformation in bone. Biomech Model Mechanobiol 7(2): 151–159

160. Anderson EJ, Knothe Tate ML (2008) Idealization of pericellular fluid space geometry and dimension results in a profound underprediction of nano-microscale stresses imparted by fluid drag on osteocytes. J Biomech 41(8):1736–1746
161. Rath AL, Bonewald LF, Ling J, Jiang JX, Van Dyke ME, Nicolella DP (2010) Correlation of cell strain in single osteocytes with intracellular calcium, but not intracellular nitric oxide, in response to fluid flow. J Biomech 43(8):1560–1564
162. Schneider P, Ruffoni D, Larsson D, Chiapparini I, Müller R (2012) Image-based finite element models for the investigation of osteocyte mechanotransduction. J Biomech 45(1): S436
163. Cardoso L, Fritton SP, Gailani G, Benalla M, Cowin SC (2013) Advances in assessment of bone porosity, permeability and interstitial fluid flow. J Biomech 46(2):253–265
164. Marotti G (1990) The original contributions of the scanning electron microscope to the knowledge of bone structure. In: Bonucci E, Motta PM (eds) Ultrastructure of skeletal tissues SE – 2, vol 7. Springer, pp 19–39
165. Kerschnitzki M, Wagermaier W, Liu Y, Roschger P, Duda GN, Fratzl P (2011) Poorly ordered bone as an endogenous scaffold for the deposition of highly oriented lamellar tissue in rapidly growing ovine bone. Cells Tissues Organs 194(2–4):119–123
166. Sharma D, Ciani C, Marin PAR, Levy JD, Doty SB, Fritton SP (2012) Alterations in the osteocyte lacunar-canalicular microenvironment due to estrogen deficiency. Bone 51(3):488–497
167. Kerschnitzki M, Kollmannsberger P, Burghammer M, Duda GN, Weinkamer R, Wagermaier W, Fratzl P (2013) Architecture of the osteocyte network correlates with bone material quality. J Bone Miner Res 28(8):1837–1845
168. Varga P, Hesse B, Langer M, Schrof S, Männicke N, Suhonen H, Pacureanu A, Pahr D, Peyrin F, Raum K (2015) Synchrotron x-ray phase nano-tomography-based analysis of the lacunar-canalicular network morphology and its relation to the strains experienced by osteocytes in situ as predicted by case-specific finite element analysis. Biomech Model Mechanobiol 14(2):267–282
169. McNamara LM, Majeska RJ, Weinbaum S, Friedrich V, Schaffler MB (2009) Attachment of osteocyte cell processes to the bone matrix. Anat Rec 292(3):355–363
170. Wu D, Ganatos P, Spray DC, Weinbaum S (2011) On the electrophysiological response of bone cells using a Stokesian fluid stimulus probe for delivery of quantifiable localized picoNewton level forces. J Biomech 44(9):1702–1708
171. Weiner S, Traub W (1992) Bone structure: from angstroms to microns. FASEB J 6(3):879–885
172. Parfitt AM (2003) Misconceptions (3): calcium leaves bone only by resorption and enters only by formation. Bone 33(3):259–263
173. Marenzana M, Shipley AM, Squitiero P, Kunkel JG, Rubinacci A (2005) Bone as an ion exchange organ: evidence for instantaneous cell-dependent calcium efflux from bone not due to resorption. Bone 37(4):545–554
174. Pirklbauer M, Mayer G (2011) The exchangeable calcium pool: physiology and pathophysiology in chronic kidney disease. Nephrol Dial Transplant 26(8):2438–2444
175. Talmage RV, Mobley HT (2008) Calcium homeostasis: reassessment of the actions of parathyroid hormone. Gen Comp Endocrinol 156(1):1–8
176. Atkins GJ, Findlay DM (2012) Osteocyte regulation of bone mineral: a little give and take. Osteoporos Int 23(8):2067–2079
177. Hunter GK, Hauschka PV, Poole AR, Rosenberg LC, Goldberg HA (1996) Nucleation and inhibition of hydroxyapatite formation by mineralized tissue proteins. Biochem J 317 (Pt 1):59–64
178. Nakashima T, Hayashi M, Fukunaga T, Kurata K, Oh-Hora M, Feng JQ, Bonewald LF, Kodama T, Wutz A, Wagner EF, Penninger JM, Takayanagi H (2011) Evidence for osteocyte regulation of bone homeostasis through RANKL expression. Nat Med 17(10): 1231–1234

179. Feng JQ, Clinkenbeard EL, Yuan B, White KE, Drezner MK (2013) Osteocyte regulation of phosphate homeostasis and bone mineralization underlies the pathophysiology of the heritable disorders of rickets and osteomalacia. Bone 54(2):213–221
180. Bélanger LF, Bélanger C, Semba T (1967) Technical approaches leading to the concept of osteocytic osteolysis. Clin Orthop Relat Res 54:187–196
181. Blaber EA, Dvorochkin N, Lee C, Alwood JS, Yousuf R, Pianetta P, Globus RK, Burns BP, Almeida EAC (2013) Microgravity induces pelvic bone loss through osteoclastic activity, osteocytic osteolysis, and osteoblastic cell cycle inhibition by CDKN1a/p21. PLoS One 8(4), e61372
182. Lane NE, Yao W, Balooch M, Nalla RK, Balooch G, Habelitz S, Kinney JH, Bonewald LF (2006) Glucocorticoid-treated mice have localized changes in trabecular bone material properties and osteocyte lacunar size that are not observed in placebo-treated or estrogen-deficient mice. J Bone Miner Res 21(3):466–476
183. Tommasini SM, Trinward A, Acerbo AS, De Carlo F, Miller LM, Judex S (2012) Changes in intracortical microporosities induced by pharmaceutical treatment of osteoporosis as detected by high resolution micro-CT. Bone 50(3):596–604
184. Qing H, Bonewald LF (2009) Osteocyte remodeling of the perilacunar and pericanalicular matrix. Int J Oral Sci 1(2):59–65
185. Rubin MA, Rubin J, Jasiuk I (2004) SEM and TEM study of the hierarchical structure of C57BL/6J and C3H/HeJ mice trabecular bone. Bone 35(1):11–20

3D Chemical Imaging of Nanoscale Biological, Environmental, and Synthetic Materials by Soft X-Ray STXM Spectrotomography

2

Gregor Schmid, Martin Obst, Juan Wu, and Adam Hitchcock

Contents

G. Schmid
Center for Applied Geoscience, Eberhard Karls University Tuebingen, Tuebingen, Germany
e-mail: gregor.schmid@uni-tuebingen.de

M. Obst (✉)
Bayreuth Center of Ecology and Environmental Research (BayCEER), University of Bayreuth, Bayreuth, Germany
e-mail: martin.obst@uni-bayreuth.de

J. Wu • A. Hitchcock
Department of Chemistry and Chemical Biology, McMaster University, Hamilton, ON, Canada
e-mail: wuj77@mcmaster.ca; aph@mcmaster.ca

43

Definition of the Topic

Synchrotron-based soft X-ray scanning transmission X-ray microscopy is applied to 3D chemical imaging using tilt-series tomography at multiple photon energies. Instrumentation, methodology and examples from a range of nanoscale biological, environmental and materials science are presented.

Overview

Synchrotron-based soft X-ray scanning transmission X-ray microscopy is applied to 3D chemical imaging using tilt-series tomography at multiple photon energies (STXM spectro-tomography). Instrumentation, methodology and examples from a range of nanoscale biological, environmental and materials science are presented. Dry and wet samples dealing with biomineralization and the interface of bacteria and minerals are shown. 3D chemical maps are generated from a model system for the perfluorosulfonic acid ionomer in the electrodes of polymer electrode membrane fuel cells. Results for 3D imaging of wet biofilms and wet latex microspheres are presented. Future improvements in the forms of soft X-ray spectro-ptychography, cryo-spectro-tomography, laminography and improved instrumentation for wet samples are discussed.

1   Introduction

Characterization tools for nanoscience and nanotechnology must provide information on structure and chemical composition of samples on the nanoscale. The development of high-brightness X-ray sources and high-resolution optics has led to the development of powerful X-ray microscopies that are very complementary to electron microscopy in terms of the information that these techniques can provide. Recently a relatively new approach has been developed that combines synchrotron-based scanning transmission X-ray microscopy (STXM) [1, 2] with tilt-series tomography. Since it provides near edge X-ray absorption fine structure (NEXAFS) spectroscopy with high spatial resolution imaging ($<$30 nm) in three dimensions (3D), STXM spectro-tomography is capable not only of elemental mapping but also of chemical mapping (speciation) in 3D. Using soft X-rays for this spectro-tomography approach allows for the analysis of both soft organic matter that contains light elements such as carbon, nitrogen, and oxygen and hard matter, such as minerals or metals. Similar to electron tomography, the major limitation is the restriction to thin (hundreds of nm) samples, although use of higher photon energy ($>$1 keV) or low-density samples means that multi-micron thick samples can be studied in some cases.

Over the last two decades third-generation synchrotrons were built worldwide, providing access for scientists from various scientific fields. Modern, third-generation synchrotron light sources generate X-rays with high intensity that, depending on the technique, can be monochromated and focused to narrow spot

sizes. Synchrotron radiation stretches across the electromagnetic spectrum from infrared light to hard X-rays. It is generated by deflecting the beam path of relativistic electrons in the storage ring of a synchrotron either by bending magnets or by insertion devices such as wigglers or undulators. Bending magnets are strong dipole magnets in arced sections in the storage ring, deflecting and changing the direction of the electron beam in the storage ring. Synchrotron radiation is produced in a fan tangentially to each bending magnet (BM). In contrast, wigglers and undulators (ID) are located in straight sections of a storage ring. Their physical properties – gap, phase, and magnetic field strength – are tunable to produce synchrotron radiation with higher flux, higher brilliance and smaller divergence angles as compared to bending magnet radiation [3, 4]. Furthermore, so-called elliptically polarizing undulators (EPUs) allow for controlling the polarization of the light, both the direction of linearly polarized light and fully circular (in 1st harmonic) or highly elliptical (3rd and higher harmonics) polarized light [5]. Currently two of the most common 3D X-ray microscopy approaches that make use of the high brilliance of soft X-ray synchrotron radiation are scanning transmission X-ray microscopy (STXM), a technique that focuses mainly on the combination of spectroscopy with microscopy, and full field transmission X-ray microscopy (TXM) that has strength mostly in the field of efficient imaging and tomography at a single photon energy (see Fig. 2.1). In this chapter we focus on chemically specific STXM spectro-tomography. However, soft X-ray TXM tomography, hard X-ray tomographies, and their major advantages and disadvantages as compared to soft X-ray STXM are discussed briefly.

1.1 STXM

STXM is a spectromicroscopy approach that combines NEXAFS spectroscopy in the X-ray energy range between 100 and 2500 eV with imaging capabilities at 10–40 nm spatial resolution [2, 6]. Monochromatic soft X-rays are focused by a Fresnel zone plate (ZP) onto the sample that is raster scanned perpendicular to the beam axis while transmitted photons are detected (see Sect. 2.1 for instrumentation). Data can be acquired as single images, as spectra at particular points or transects of interest or as a sequence of images with tens to hundreds of photon energies across an absorption edge, so-called stacks. These can be analyzed by linear spectral decomposition or by statistical approaches such as principal component and other types of multivariate statistical analysis, but all methods have in common that they result in quantitative chemical maps (see Sect. 2.4 for data analysis). Thus, STXM is one particularly powerful approach amongst various other focusing and coherent diffraction X-ray microscopy techniques. Schematics of the STXM and TXM methods are shown in Fig. 2.1. Recent developments that combine STXM with tilt-series tomography now allow for chemical mapping in 3D.

Scanning Transmission X-ray
Microscopy STXM

**Monochromatic
X Rays**

Zone Plate
Focusing Lens

Scanning
Sample Stage

X-Ray
Detector

Transmission X-ray Microscopy
TXM

**Polychromatic
X Rays**

Condensor
Zone Plate

Monochromator
Pinhole −20μm

Sample

Micro
Zone Plate

CCD
Camera
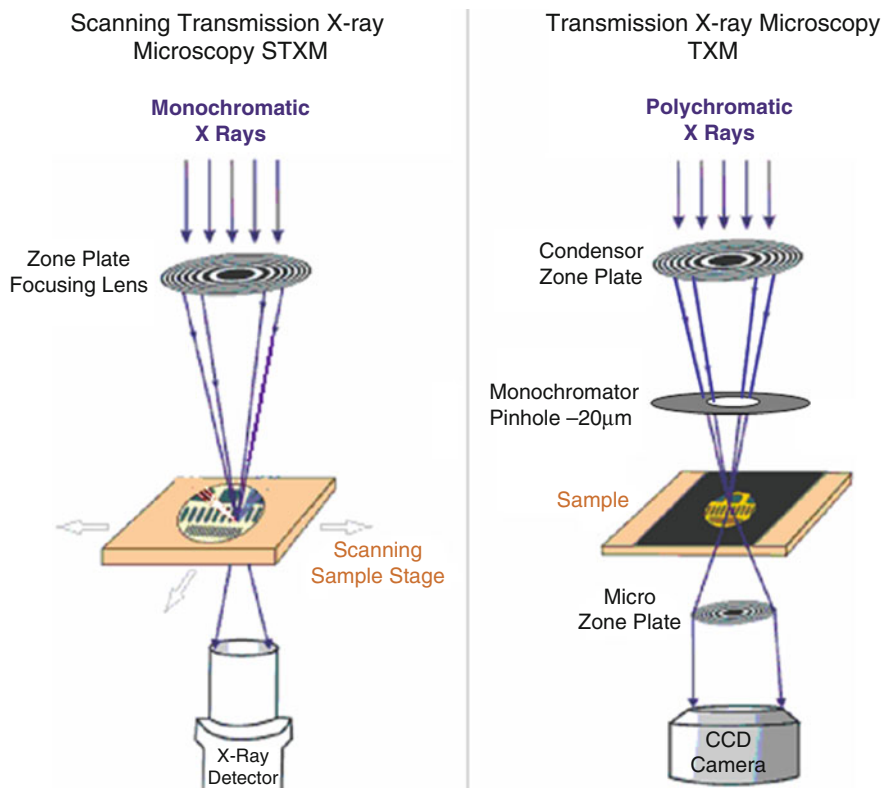
Fig. 2.1 Schematics of (**a**) scanning transmission X-ray microscope (STXM) and (**b**) full field, transmission X-ray microscope (Adapted from [3])

Pioneer STXM development was achieved by Kirz and Rarback back in the 1980s [7] and further developed by Kirz, Jacobsen and colleagues [8] at the National Synchrotron Light Source (NSLS) in Brookhaven (USA). In the last decade, in large part stimulated by the success of the Advanced Light Source (ALS, Berkeley, USA) BM 5.3.2.1 interferometer equipped design [9] and its commercialization by Accel (now Bruker), soft X-ray STXMs have been installed at various synchrotron facilities (Table 2.1). STXM spectro-tomography is available to users at some of these facilities (see Table 2.1). STXM is a particularly powerful technique for analyzing chemical (polymer), biological, environmental, geoscientific and material science samples, and the number of publications is increasing rapidly. STXM is now well established as an important tool in geomicro-biological and environmental studies, an area that requires both high spatial resolution and redox-sensitive analytics which can study both organic and inorganic

Table 2.1 Full field (TXM) and scanning (STXM) transmission X-ray microscope equipped beamlines on bending magnet (BM), elliptically polarizing (EPU) or undulator (Und-L) based synchrotron radiation sources (as of December 2014)

Facility	Name/ beamline	City	Country	Source	E-range (eV)	Tomography ?
TXM – operating						
Alba	Mistral	Barcelona	Spain	BM	270–2600	Y
ALS	XM1	Berkeley	USA	BM	250–900	Y
ALS	NCXT	Berkeley	USA	BM	520	Y
Astrid	XRM	Aarhus	Denmark	BM	520	??
Bessy	U41-TXM	Berlin	Germany	Und-L	250–600	Y
Diamond	B24 cryo-TXM	Didcot	UK	BM	250–2500	Y
Elettra	Twin-mic	Trieste	Italy	Und-L	250–2000	Y
NSRL	TXM	Hefei	China	BM	520	??
Ritsumeikan	BL12	Kyoto	Japan	BM	520	N
STXM – operating						
ALS	5.3.2.2	Berkeley	USA	BM	250–750	Y
ALS	5.3.2.1	Berkeley	USA	BM	250–2500	Y
ALS	11.0.2	Berkeley	USA	EPU	100–2000	Y
Australian SR	SXR	Melbourne	Australia	Und-L	100–2000	Y
Bessy	old-STXM	Berlin	Germany	BM	250–600	N
Bessy	MAXYMUS	Berlin	Germany	EPU	250–1500	N
CLS	10ID1 a-STXM	Saskatoon	Canada	EPU	130–2500	Y
Diamond	I08	Didcot	UK	EPU	250–2500	??
Elettra	Twin-mic	Trieste	Italy	Und-L	250–2000	N
UVSOR	BL4U	Okazaki	Japan	Und-L	50–800	??
PLS	Nanoscopy	Pohang	Korea	EPU	100–2000	??
Photon factory	Various BL	Tsukuba	Japan	BM	100–8000	N
SLS	PolLux	Villigen	Switzerland	BM	250–750	??
SLS	NanoXAS	Villigen	Switzerland	BM	270–1800	N
SSRF	SXS	Shanghai	China	EPU	200–2000	??
SSRL	13-1	Stanford	USA	EPU	250–1000	N
STXM – construction or commissioning						
CLS	10ID1 cryo-STXM	Saskatoon	Canada	EPU	130–2500	Y
NSRRC – TPS	BL09A1	Hinschu	Taiwan	Und	60–1500	(planning)
Max IV	SoftiMax	Lund	Sweden	EPU	250–2100	??
Soleil	Hermes	Saint-Aubin	France	EPU	250–1500	Y

components. For example, early STXM studies of environmental river biofilms focused on the structure and chemical composition, and mapped the distribution of biomacromolecules such as proteins and polysaccharides [10]. Soon, these studies on biofilm structure were linked to functional aspects, such as the influence of biofilms on the formation of chemical microenvironments and biofilm influence on the sorption of Fe [11], the sorption properties for heavy metals [12, 13],

the sorption and transformation of nanoparticles [14, 15] or the fate of antimicrobial agents in biofilms [16]. The excellent capabilities of STXM for mapping organic species were also used to understand microbially mediated redox reactions [17–30], Cd^{2+} release during microbial Fe(III) reduction [31], influence of humic acids on microbial Fe(III) reduction [32], goethite sorption to bacterially produced EPS [33], microbial Ca carbonate precipitation [34, 35], the formation of magnetosomes in magnetotactic bacteria [36, 37], chemical speciation of Fe particles [38], microbial nitrogen residues in soils [39, 40] and microbial sulfur oxidation and reduction in an acid mine drainage [41]. After implementing low-energy X-ray fluorescence detection it was also possible to study the sorption of arsenic to cell-(iron)mineral aggregates formed by Fe(II)-oxidizing bacteria [42] and unusual oxidation states of trace Ni in river biofilms [43].

STXM is used extensively to study structure and processes in material science, such as metal-insulator transitions in tunnel bronzes [44], graphene electronic corrugations and doping [45], nanostructured thin film electrodes for fuel cells [46], domain orientation in organic electronic films [47], magnetic dynamics of spin injection devices [48], synthetic organic materials [1, 49], etc. A full, annotated bibliography of the soft X-ray spectromicroscopy literature, originally published as a supplement to a review article [1], is available at http://unicorn.mcmaster.ca/xrm-biblio/xrm_bib.html.

1.2 STXM Spectro-tomography

STXM in combination with tilt-series tomography allows for analyzing the chemical composition of samples in three dimensions (3D). Two-dimensional (2D) STXM spectromicroscopy is sometimes limited in its ability to associate structural features and compositional information due to lack of information about the distribution in the 3rd dimension along the X-ray beam axis. This ambiguity can be circumvented by analyzing the sample in 3D. This can be done in a variety of ways, including serial sectioning [50], laminography [51] and tilt-series tomography. The latter has much in common with medical [52], materials science [53] and environmental [54] X-ray computed tomography imaging, as well as electron tomography in materials [55] and biological sciences [56]. A tomography data set is a set of projection images of a sample from various directions, ideally fully covering the range of $\pm 90°$, with the rotation axis perpendicular to the X-ray beam axis. Ideally the angle range is sampled at $1°$ intervals, but radiation damage and limited beamtime availability mean that typically 3–5° steps are used. The data acquisition is followed by a tomographic reconstruction of the volume. Similar to electron tomography, for certain types of sample mounting, the angle range might be restricted to smaller ranges such as $\pm 72°$ in a typical transmission electron microscopy (TEM) grid-based setup. Additionally, there are geometric restrictions for the maximum size of the sample mounting as the order sorting aperture is located upstream of the sample at a typical distance of only a few hundred μm in soft X-ray STXMs (Fig. 2.3b).

Soft X-ray STXM tomography was implemented for the first time by Haddad and colleagues [57, 58], who acquired images of a gold pattern on Si_3N_4 windows in a tilt-series of rotation angles from $-50°$ to $+55°$ and were able to reconstruct in 3D the written pattern. The technique was developed further by using a cryo-STXM to acquire a 3D tomogram of a mouse fibroblast cell at a single photon energy and employing the intrinsic absorption contrast of the sample without adding any contrasting agents such as heavy metal stains [59].

The first real 3D chemical mapping (i.e. with multiple photon energies) with STXM was implemented using serial sectioning instead of tilt-series tomography. Imaging of serial sections of toner particles at multiple energies across the C 1s absorption edge allowed for a full 3D reconstruction of the chemical composition of these particles [50]. While this technique is quite effective it requires a lot of skill in sample preparation. In the following decade the tilt-series approach was developed further by implementing various types of sample mounting that were optimized both for environmental and material science applications. The first STXM spectro-tomography using tilt-series was a study of polyacrylate-filled polystyrene micro-spheres in solution inside a pulled glass capillary [60, 61]. Dry samples such as bacteria or mineral particles can be mounted on formvar-coated TEM grids that are subsequently cut into single grid strips for tilt-series tomography. This approach was used for the first time to study carbonate biomineralization by cyanobacteria [62]. The quantitative 3D analysis of the correlation between calcium and organic carbon in this study provided insight into mechanisms of Ca sorption and calcite ($CaCO_3$) biomineral nucleation of the cyanobacterial strain *S. leopoliensis* PCC 7942.

Whereas analysis of biological or environmental samples was one of the driving forces for STXM spectro-tomography development, the technique has also established itself as a powerful tool in materials science. For example, STXM spectro-tomography was used to identify the internal structure of colloidal photonic (silicate) crystals at the S 1s absorption edge [63]. Silicate crystals were grown directly onto platinum- or palladium-coated TEM grids and a single grid-strip prepared and mounted similar to the previously mentioned study. The chemical 3D reconstruction revealed a crystal with a thickness of eight particle layers with one disordered particle layer at the boundary between crystal and TEM grid. Additionally, the crystal stacking configuration and defects of the colloidal photonic crystal were identified. Furthermore, 3D chemical mapping by STXM spectro-tomography was applied to polymer electrolyte membrane fuel cell (PEM-FC) cathodes that were prepared either by focused ion beam (FIB) milling or by ultramicrotomy after resin-embedding. 3D analysis at the C 1s and F 1s absorption edges resulted in the reconstruction of the 3D distribution of catalyst nanoparticles, and a fluorine-rich ionomer in the PEM-FC cathode [64]. Various questions from both environmental and materials science required development of alternative sample mounting to circumvent artefacts from sample drying that affect the structure and composition of samples. Hydrated tomography samples were prepared using glass micro-capillaries. With these capillaries it was possible to immobilize environmental biofilms for 3D chemical mapping of their

organochemical composition at the O 1s absorption edge [65]. The same approach was used to study the 3D chemical composition of a polymer composite of polyacrylate-filled polystyrene microspheres in aqueous suspensions, allowing for separating between polystyrene (PS) and polyacrylate [60]. A major advantage of using glass micro-capillaries is the possibility of rotating the sample by ±90° such that subsequent reconstructions are not affected by a missing wedge of tilt angles. However, the major drawback of glass capillaries is the limited transparency of the glass walls for soft X-rays. For example, this type of sample mounting does not allow for measurements at the C 1s absorption edge. This problem was overcome by using carbon nanopipettes [66] instead of glass, which enabled spectro-tomographic determination of the spatial distribution of polyacrylate in polystyrene microspheres at the C 1s absorption edge [61].

A novel wet cell for the analysis of fully hydrated samples was developed in collaboration with Luxel (Luxel, Friday Harbor, USA). This wet cell was used for the first time to map intracellular sulfur globules and to identify their association with polysaccharides in a cell of the sulphur-metabolizing bacteria *Allochromatium vinosum*. Individual components were mapped in 3D at the C 1s and Ca 2p absorption edges, and complemented by a 2D analysis at the S 2p absorption edge [67]. The same authors showed – also in 3D – the close association and enrichment of Cu(I) species at the cell walls of *Saccharomyces cerevisiae* that were treated with dissolved Cu^{2+}, indicating the reduction of Cu(II) to Cu(I) at the cell walls. Another study that analyzed microbial samples in their natural, hydrated state focused on the mechanisms of Fe(II) oxidation and iron biomineral precipitation by the nitrate-reducing anaerobic Fe(II)-oxidizing *Acidovorax* sp. strain BoFeN1. The distributions of protein and of iron minerals were analyzed in 3D at the O 1s and Fe 2p absorption edges [68]. This type of sample was also used in a study that applied a variety of different tomography approaches such as focused ion beam (FIB)/scanning electron microscopy (SEM) tomography, TEM tomography and confocal laser scanning microscopy (CLSM) to systematically compare the information content that could be derived from the individual approaches and to merge the complementary information to gain comprehensive insights into the mechanism of iron biomineral precipitation [69].

A hydrated sample from this study is used in Sect. 2.2 to illustrate methods for preparing wet cells for STXM spectro-tomography; the results of the study are discussed in Sect. 3.3. In addition to the dataset for the hydrated sample, the preparation of dry samples of another, photoautotrophic Fe(II)-oxidizing *Rhodobacter* ferrooxidans strain SW2 are shown in Sect. 2.2 and major findings are discussed in Sect. 3.1.

1.3 TXM

TXM is also a synchrotron-based X-ray microscopy that employs soft (and hard) X-rays. There are two fundamental differences between TXM and STXM. Firstly, STXM is a point probe, raster-scanning technique that acquires data in a

pixel-by-pixel mode, whereas TXM is a full-field technique that acquires images simultaneously, but usually with a rather restricted field of view in the range of $10 \times 10 \ \mu m^2$. Secondly, TXM requires imaging optics in addition to the condenser optics – in both cases zone plates can be used. Full-field TXM was first developed by Schmahl and Rudolf in the 1960s [70, 71]. The basic principle of a full-field TXM is similar to a conventional light microscope (see Fig. 2.1). A zone plate (ZP) acting as a condenser and concomitantly as a monochromator focuses the monochromatic (soft) X-ray beam onto the sample. A second ZP, located downstream of the sample, is acting as an objective and projects the transmitted X-rays onto a CCD camera. Magnification and spatial resolution are determined by the outermost zone width of the ZP, by the diffraction order, and by the position of the ZP. Exposure times for an entire image typically vary between 0.1 and 10 seconds, and the field of view is normally limited to <30 μm. TXM is a powerful approach for efficiently acquiring images and also tomography data. However on most beamlines lines, including the recent ones at Bessy II (Berlin, Germany) and ALBA (Barcelona, Spain) which are equipped with a full monochromator, there are significant drawbacks with respect to spectral resolution, illumination uniformity, ability to maintain focus and the stability of the imaging position with changes in photon energy. Perhaps the factor that most strongly limits TXM for spectro-tomography is that it has a much higher radiation damage rate per useful information than STXM because there is an inefficient focusing optic after the sample, which means that the flux the sample receives is 5–10 times larger in TXM than in STXM. All of these factors mean that speciation capabilities are much more limited in TXM than in STXM. That being said, the rapid acquisition and development of eucentric mounting for cryo-tomography [72] have led to a number of single photon energy tomography studies which are summarized below. In comparison, both TXM and STXM have individual advantages and drawbacks, which are discussed briefly. Relative to TXM there are two major advantages of STXM spectro-tomography – excellent chemical speciation capabilities and a high detection efficiency [73]. TXM requires an additional imaging ZP in the beam path that, depending on the X-ray energy, has an efficiency of typically a few % to approximately 10 %. Thus, in comparison to STXM, TXM requires an order of magnitude higher X-ray dose on the sample to extract the same type of chemical information. For questions that require solely structural information but do not require detailed chemical information (and thus imaging at multiple energies and multiple absorption edges) TXM benefits from the more efficient image acquisition as the entire image is acquired simultaneously. If knowledge of the 3D distribution of elements or chemical species is required to answer a certain scientific question, typically images at multiple energies and multiple absorption edges are acquired; the higher dose and the associated beam damage limit the capabilities of TXM significantly relative to STXM spectro-tomography. Although radiation damage involving breaking of chemical bonds and the associated changes in the chemical (speciation) composition cannot be reduced significantly by analyzing samples in the frozen state [74], the structural integrity can benefit significantly from performing tomography with frozen samples. Therefore, biological samples are often plunge-frozen

and measured on a cryo-stage in TXM tomography. Similarly, and with the same general restrictions, samples for TXM tomography can be either loaded into glass capillaries or mounted on TEM grids. At present there is no STXM capable of cryo-tomography available for general user access, despite one being operational at NSLS-I for ~5 years about a decade ago [59]. A new STXM focused on cryo-tomography is under development at the Canadian Light Source (CLS, Saskatoon, Canada) [Adam Leontowich, private communication] and should be available to general users some time in 2017.

Although extensive discussion of TXM would be out of the scope of this chapter, a few special setups are mentioned here. A soft X-ray TXM spectro-tomography beamline with an outstanding energy resolution that allows for acquiring NEXAFS spectra with a spatial resolution down to 25 nm is installed at BESSY II (Berlin; Germany) [75]. The BESSY II TXM uses partially coherent light with an energy resolving power $E/\Delta E$ of up to 10^4 and a capillary condenser instead of a condenser-ZP. Another TXM working with a capillary condenser that also allows acquisition of NEXAFS spectra is the BL09 (Mistral) beamline at ALBA (Barcelona, Spain) [76]. In contrast both of the soft X-ray TXMs at the ALS (Berkeley, USA) (BL 6.3.1 (XM1) and Beamline 2.1 (XM-2, NCXT)) use a condenser-ZP that simultaneously acts as a monochromator with an energy resolving power $E/\Delta E$ of 3×10^2. The ALS TXM provides the choice of various objective micro-zone plates for different spatial resolution [77]. A combination of a scanning and full-field (soft) X-ray microscope (TwinMic) is installed at the Elettra (Trieste, Italy) [78]. TwinMic has been constructed for a relatively fast conversion from a full-field imaging microscope to a scanning microscope, and X-rays can be switched between partially coherent illumination (full-field mode) and coherent light (scanning mode). The instrument is optimized for soft X-ray fluorescence detection in scanning mode. Currently, a new TXM beamline (B24) is in construction on a conventional monochromated beamline at Diamond (Didcot, UK) and started operation in 2015.

TXM was developed with a strong focus on biological applications particularly by using the intrinsic X-ray absorption contrast of the samples and thus does not require any staining (e.g. using heavy metals) as is necessary for transmission electron microscopy and tomography. Early work on TXM tomography was performed at BESSY I (Berlin, Germany) on the green algae *Chlamydomonas reinhardtii* [79]. The acquired tilt-series of images allowed for identification of the internal structure and organelles of the algae [79, 80]. Subsequent TXM tomography studies were done on yeast cells such as *Saccharomyces cerevisiae* [81, 82] and *Schizosaccharomyces pombe* [83, 84] to reveal cell organelles. As an example, different stages of the cell cycles of haploid and diploid yeast cells *Saccharomyces cerevisiae* were studied with TXM tomography [82]. Other studies focused on the internal structure of the vaccinia virus [85], the malaria parasite *P. falciparum* [86, 87] and several mammalian cells [88–91]. TXM tomography is well established in the biological community for various kinds of studies that deal with the internal structure of biological cells. Recently, it was possible to correlate TXM tomography with fluorescence tomography [92].

1.4   Hard X-ray Tomography

In contrast to soft X-ray spectro-microscopy, hard X-ray tomographic microscopy (XTM) is used to record 3D data of thicker samples, accompanied by chemical mapping of heavier elements. XTM cannot provide analytical information on soft matter consisting of light elements, but phase contrast imaging is used to visualize soft matter components. Different optical setups for XTM are available, such as reflective, refractive or diffractive optics, making XTM suitable for various applications for solid bulk samples, mostly in material science but also for addressing biological and environmental questions [4]. Similar to soft XTM, hard XTM allows tomography allows non-destructive measurements, with a low detection limit and low beam damage with quite fast acquisition times per rotation angle, in the range of minutes and seconds, down to sub-seconds for synchrotron-based XTM [93]. Fresnel ZPs for XTM provide a spatial resolution down to 40 nm [94]. Full-field imaging with Fresnel ZP-based XTM in combination with multiple detectors allows for fluorescence element mapping, transmission imaging or nanodiffraction [93]. Hard X-ray XTM is an established analysis tool for a variety of different scientific applications such as Ca mapping within fly ash particles [93] or the analysis of diameter variations of nanofibers [95]. An extensive and excellent overview of the huge variety of different applications of hard X-ray computed tomography was presented in a current review by Maire and Withers [53].

1.5   Ptychography

Ptychography is a coherent diffraction imaging (CDI) technique that uses an X-ray point probe created by KirkPatrick-Baez optics or Fresnel ZPs [96] to generate an array of diffraction images from a series of overlapping points on a sample. The requirement that the solution of the amplitude, phase and illumination components of the reconstruction for each CDI must match in the overlapping regions of the four adjacent CDI images provides a powerful constraint which leads to rapid and reliable convergence of the analysis compared to all other CDI methods. Spatial resolutions down to 10 nm in the hard X-ray [97] and below 3 nm in the soft X-ray [98] have been achieved. Ptycho-tomography is also implemented with angle scanning of samples, to produce quantitative 3D density maps with a 3D isotropic spatial resolution of 16 nm [99]. Hard X-ray pytcho-tomography has been used to study cortical bone and to reconstruct structures down to the 100 nm scale [100]. At present hard X-ray ptychography and ptycho-tomography is well established, with instrumentation accessible to general users through peer review access at a number of facilities, including SLS (Villingen, Switzerland) and PETRA-III (Hamburg, Germany). In the soft X-ray region the COSMIC beamline at the ALS is expected to be completed some time in 2016 and to be open to general users one or two cycles after that. Exploratory and developmental soft X-ray ptychography and ptycho-tomography is being carried on other beamlines at the ALS (5.3.2.1, 11.0.2) [98, 101], as well as at the CLS (10ID1). Spectro-ptychography has only just

begun [98, 101, 102]. Multi-energy ptychography promises to have additional sensitivity beyond that of regular STXM because of the knowledge of the illumination function, the spectral sensitivity of the phase as well as the amplitude signals and the higher spatial resolution. Given the 5- to 10-fold spatial resolution improvement that ptychography provides relative to the focused spot size, as well as the ever-increasing brightness of third-generation and diffraction-limited light sources [96] it is likely that most of the existing STXMs and all new STXMs (such as the softi-MAX combined STXM CDI beamline at Max IV (Lund, Sweden)) will be equipped with appropriate high dynamic-range cameras, high-performance computing and other instrumentation to enable ptychography as a relatively routine, high-resolution extension of conventional STXM imaging.

2 Instrumental and Experimental Methodology of STXM Spectro-tomography

2.1 Instrumentation

STXM requires a synchrotron as soft X-ray source. A schematic of the spectromicroscopy beamline 10ID1 at the CLS is shown in Fig. 2.2. Soft X-rays are generated by an elliptically polarized undulator (EPU) that allows for changing the gap to tune the maximum intensity of the X-rays of a given energy and changing the phase (relative position of lower right, lower left, upper right and upper left magnet arrays) to change the polarization of the light, both linear, horizontal or inclined (over $\pm 90°$) and left and right circular/elliptical. No entrance slits are used in this infinity corrected plane grating monochromator (PGM) so the effective entrance slit is the vertical size and position of the electron beam in the storage ring. The X-rays are deflected and collimated by a first mirror (M1) before they enter the monochromator, which consists of a mirror (M2) and grating with correlated incidence and exit angles that selects the desired X-ray photon energy (130–2800 eV) and directs it to the end stations on a path parallel to the floor. Downstream of the monochromator, the M3-STXM mirror focuses the X-ray beam onto a set of exit slits, one in the dispersive direction, the other perpendicular to it. With these slits the flux, coherence and energy resolution can be controlled. The CLS 10ID1 beamline design [103] is similar to that of beamline 11.0.2 at the ALS in Berkeley, USA [104], beamline UE46 (MAXYMUS) at Bessy II in Berlin, Germany [105], and beamline I08 at the Diamond Light Source in Didcot, UK. A simpler beamline design using a bend-magnet and a spherical grating monochromator is implemented at beamlines 5.3.2.1 [9] and 5.3.2.2 [106] at the ALS and at beamline X07DA PolLux at the Swiss Light Source (SLS) in Villigen, Switzerland [107]. The STXM microscopes of the previously mentioned beamlines are very similar. A Fresnel zone plate (ZP) acts as X-ray lens, focusing the X-ray photon beam onto the sample. Fresnel ZPs are radially symmetric diffractive optics with a central stop. The diameter and the width of the outermost zone of the ZP control the focal length at a given photon energy and spatial resolution (1.22 times the outermost zone width
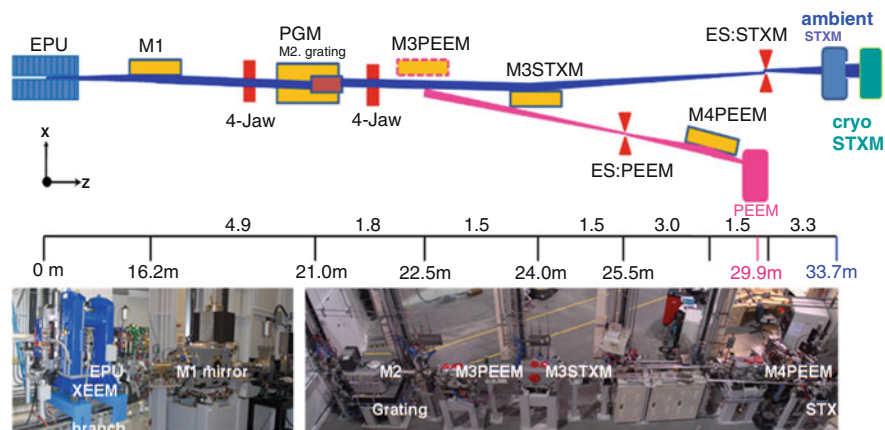
Fig. 2.2 Schematic of the CLS spectromicroscopy beamline. The ambient STXM on the STXM branch line has operated since 2006. A cryo-STXM is being constructed and was installed downstream of the ambient STXM in 2015

under diffraction limited illumination). STXM in standard operation achieves 20–30 nm spatial resolution, but advanced ZPs have achieved spatial resolutions down to 10 nm [108]. The focal length and the depth of field depend on the details of the zone plate and the X-ray energy. For the range of photon energies and zone plates available at the CLS, the focal length ranges from 0.6 to 21 mm and the depth of field ranges from 0.13 to 15 μm. An Excel-based calculator, which provides details of the X-ray optical performance, is available as supplemental material at http://exshare.lightsource.ca/sm/Pages/SM-Home.aspx. Since the depth of field is very important in STXM spectro-tomography it is helpful to use the ZP calculator to help guide choice of zone plate and other parameters for a given study. An order-sorting aperture (OSA) is located between the Fresnel ZP and the sample to block non-focused zeroth- and higher-order photon light, in combination with the central stop of the ZP that is aligned with the OSA pinhole and the beam axis. In the conventional STXM setup, a stepping-motor stage raster scans the sample in x- and y-directions for larger-scale overview images (typically 0.1–2 mm). Fine and fast scans of the sample are performed by a piezoelectric stage with a range from 0.1 to 60 μm, and a positioning precision of a few nm. The position of the sample relative to the zone plate, and thus the precision of imaging, is actively controlled in both coarse and fine scans by a 2D differential interferometer [9]. When modern, interferometer-controlled STXM instruments are properly tuned, spatial registry of images over a single edge (e.g. 40 eV) can be accurate to less than 100 nm, while image displacement over larger energy ranges (e.g. C 1s (280 eV) to Si 1s (1840 eV) at the CLS) can be less than 500 nm. Typical dwell times (acquisition times per pixel) are in the range of fractions of, to several milliseconds. Increasing the scan speeds in future STXM instruments would greatly enhance STXM, particularly for radiation-sensitive samples and spectro-tomography.
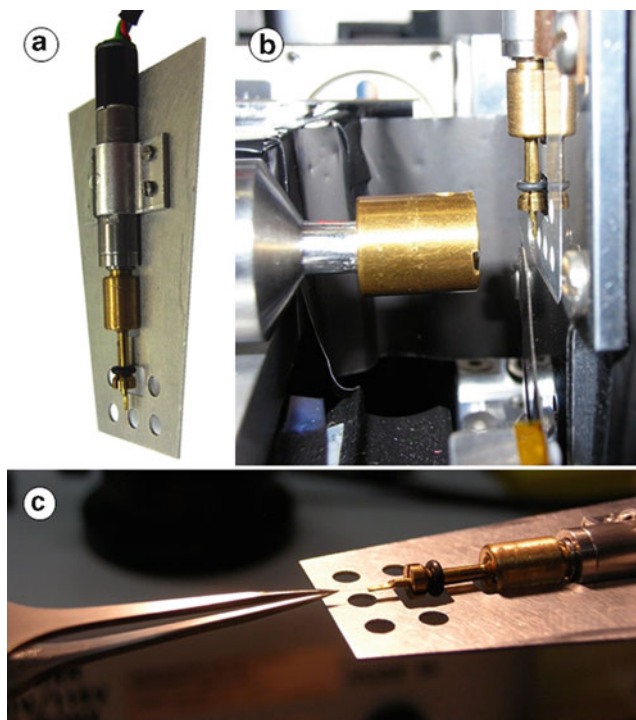
Fig. 2.3 (**a**) Photo of the tilt-series rotation apparatus mounted on a standard sample plate. (**b**) The rotation system mounted in the STXM kinematic mount. The ZP – OSA and sample-OSA distances have been increased for clarity. (**c**) Photograph of the process of mounting a grid strip on the tip of the tomo pin using the micrometer driven locking tweezer system described in the text

Tilt-series tomography requires rotating the sample perpendicular to the beam axis for acquiring 2D projection images at various rotation angles. To achieve this, a tomography stage is installed on a support plate, which is attached to the piezo-driven stage of the STXM using a standardized 3-pin kinematic mount (Fig. 2.3). The tomography stage (available to general users at the ALS and CLS STXMs, along with appropriate drive interfacing and software) consists of a stepper motor, a planetary gearhead and a mounting mechanism that allows for mounting glass capillaries or sample rods to which one can attach TEM grid strips, or wet cells. The motor is controlled by a stepper motor controller (in our case TIMS0201, Jova Solutions, San Francisco, CA), and the angle is software controlled (in our case via a LabView-based program).

Soft X-ray photons are converted by a phosphor scintillator to visible light pulses, which are then detected by high-performance photomultiplier tubes (Hamamatsu R647P), or by various types of silicon or avalanche photodiodes in the different instruments. STXM can be operated under low (10^{-3} torr) or high (10^{-8} torr) vacuum, under atmospheric pressure or under He atmosphere. A partial atmosphere (1/6th to 1/3rd) of He is preferred since He is transparent for soft X-rays and is a good

thermal conductor, which allows rapid thermalization of the sample environment and cooling for stages and motors. However, vacuum is used for STXM applications where sample cooling or heating is required. The spectral resolving power of most STXM beamlines is $E/\Delta E > 3000$ with a photon flux of 10^7–10^9 s^{-1}.

NEXAFS spectra are acquired by repeatedly scanning a sample with X-ray photon energies that are successively increased across an X-ray absorption edge. X-rays of certain energies are preferentially absorbed by the sample, resulting in excitation of core electrons to a higher unoccupied energy state [109, 110]. The fine structure of the resulting NEXAFS spectra contains information about the elemental composition and the local chemical bonding environment of the elements in the sample. It can also provide information about molecular orientation, particularly if multiple polarizations are used [111]. Spectral information can be extracted from image sequences (also called stacks [112]) that contain images at tens to hundreds of photon energies, thus providing detailed spectra at each spatial pixel. Quantitative chemical maps can be generated by a variety of techniques including forward fitting to pre-defined reference spectra, placed on absolute optical density scales [2] (*unicorn.mcmaster.ca/aXis2000.html*), or by multivariate statistical analysis using principal component analysis followed by a cluster-based co-ordinate rotation to identify end-member NEXAFS reference spectra from the image stack without assumptions of the chemical species present [113] (http://spectromicroscopy.com/).

Beam-induced sample heating in STXM was measured to be <1 °C [114], but radiation damage such as breakage of chemical bonds by ionization and radical formation can be observed after acquiring a NEXAFS stack of a sample or acquiring multiple photon energies and angles for spectro-tomography [62]. Systematic, quantitative studies of critical doses for various damage processes in polymers and biological materials [115–117] have been reported. STXM spectro-tomography users are strongly advised to evaluate the radiation stability of the critical spectral features needed for 3D speciation and to plan an appropriate acquisition strategy to enable acquisition of scientifically meaningful data.

2.2 Sample Preparation

2.2.1 Cell Cultivation

Studies of two kinds of Fe(II)-oxidizing bacteria and cyanobacteria will be shown as examples of biological applications of STXM spectro-tomography. The first Fe(II)-oxidizing bacterium is the photoferrotrophic, anaerobic *Rhodobacter* ferrooxidans strain SW2 that was isolated from a freshwater pond [118]. Cells of SW2 were grown in the presence of 4 mM FeCl$_2$ in anoxic freshwater medium under light conditions (>600 lux) for 7 days [119]. The second Fe(II)-oxidizing bacterium is the nitrate-reducing, anaerobic *Acidovorax* sp. strain BoFeN1, isolated from sediments of Lake Constance [120]. BoFeN1 cells were grown for 7 days in the presence of 8–10 mM FeCl$_2$, 10 mM nitrate and 5 mM acetate in anoxic freshwater medium [69]. The cyanobacteria of the strain *Synechococcus leopoliensis* PCC 7492 were

grown for 25 days in nutrient-poor freshwater medium Z/10 as described elsewhere [35].

2.2.2 Geomicrobiological Samples

Samples for STXM spectro-tomography can be prepared in various ways. For specimens that are not much affected by drying artefacts, STXM spectro-tomography samples can be prepared by wet deposition on a formvar-coated 300-mesh or 200-mesh copper TEM grid (Fig. 2.4). In such cases a few droplets of the sample – in our case a cell-mineral suspension – are transferred on to the TEM grid using a pipette. The advantage of formvar is that it has a characteristic and simple C 1s NEXAFS spectrum which can be accounted for during data analysis by measuring the I_0 (incident flux) spectrum through an adjacent area of formvar not covered by sample. To prevent artificial formation of precipitates, excess water can be withdrawn from the side of the grid using a piece of filter paper. After air-drying, the TEM grid is previewed under an optical microscope and an area of interest selected. The area of interest should be far away from grid bars and other sample material that could obscure the view upon rotation during STXM spectro-tomography. Cutting the TEM grid is done under a stereomicroscope using a fresh, curved scalpel blade in a rolling motion to prevent shear stress on the formvar coating. The strip is carefully picked up with reverse (self-closing) tweezers. For easier alignment and mounting of the strip on the flattened brass rod, a custom-made tool was used that allows for remotely opening the tweezers with a linear stepper motor (currently available at both ALS and CLS). The reverse tweezers with the strip are loaded into the tool. The grid strip is then precisely aligned parallel to and centred on the rod using a XYZ micromanipulator. Nail polish turns out to be an ideal glue to mount the strip onto the rod as it remains flexible for some time and thus allows for correcting the alignment as necessary. With care, a range of non-eucentric motion less than 50 microns can be achieved. After gluing, the strip is released remotely, and upon settling of the glue, the rod with the mounted strip or the Luxel wet cell can be clamped onto the tomography rotation stage.

This type of sample mounting on a formvar-coated 300-mesh copper TEM grid was used for the cell-mineral suspensions of the Fe(II)-oxidizing bacterial strain SW2 that is presented in Sect. 3.1. SW2 cell-mineral complexes were cultivated for 7 days as described in Sect. 2.2.1. Cell-mineral suspensions were sampled anoxically in a glove box (N_2 atmosphere) and washed twice with anoxic, sterile deionized (DI) water upon centrifugation to remove residual salts from the freshwater medium. A few droplets of the cell-mineral suspension were transferred onto a formvar-coated 300-mesh copper TEM grid, blotted and air dried under N_2 atmosphere (Fig. 2.4). For the cyanobacteria dataset, shown in Sect. 3.1, cyanobacteria were harvested by filtration and resuspended in 1.4 mM $NaHCO_3$ solution. $CaCl_2$ was added to a final concentration of 2.9 mM (six times saturated with respect to calcite). After the onset of $CaCO_3$ precipitation detected by a drop in pH, the cell suspension was sampled, centrifuged and washed with deionized water. Lacey carbon-coated 300-mesh copper grids were dipped into the cell
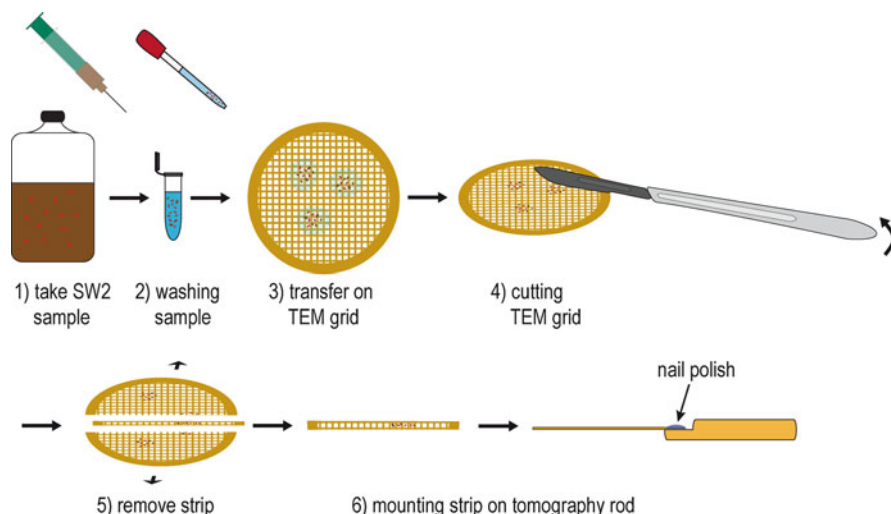
Fig. 2.4 Outline of the preparation procedure used to make samples of air-dried SW2 cells for STXM tomography

suspension. Excess water was removed completely from beneath using a filter paper to prevent precipitation upon drying. The samples were then prepared as described above.

If hydrated samples are required, aqueous samples can be loaded into glass micro-capillaries of 150–200 nm wall thickness and a diameter of 3–5 μm [60] using a syringe. Alternatively, carbon nanopipettes with a diameter of 2–3 μm and 45 nm wall thickness can be used [61]. The capillaries must be sealed at both ends after sample loading, e.g. with silicone grease. The capillaries are then attached to the tomography rotation stage. Data from several of this type of sample – a wet natural river biofilm inside a pulled glass capillary, and microspheres inside a carbon nanopipette – are shown in Sects. 3.3 and 3.4.

This type of sample mounting is relatively simple but has two major disadvantages. Firstly, the glass capillaries are not transparent throughout the entire energy range of soft X-rays so that, e.g. the C 1s absorption edge is not accessible for such samples. Secondly, in some cases the biofilms were not well attached to the glass capillary walls so that the spatial resolution was limited by sample movement during scanning.

Both of these problems can be circumvented using wet cells for tomography produced by Luxel (Friday Harbor, USA). These consist of a 15 μm thick and 250 μm wide metal frame that is covered by 30 nm LUXFilm® polyimide membranes on both sides [67, 68]. The Luxel wet cell is first mounted on a flattened brass rod using glue or nail polish. The wet cells are filled with an aqueous sample (e.g. bacterial cell suspension) using a glass micro-capillary. Upon sucking the sample into the capillary, the suspension is injected into the wet cell using an injector system such as the Eppendorf CellTram or a similar nano-injector.

Our portable nano-injector, for example, was built from a modified micrometer gauge that allows for gentle handling and injection of the aqueous sample [68]. A few nL of the sample are injected carefully into the gap between LUXFilm® polyimide membranes after punching the glass micro-capillary into a channel of the Luxel wet cell. Upon injection of the sample, the membranes collapse around the sample (in our case cell-mineral aggregates) and both keep them hydrated and immobilize the particles. The injection hole can be sealed with nail polish. For an easier injection of the aqueous sample, a second hole can be punched in the filling channel on the opposite site of the cell for pressure compensation. An improved wet cell tomography system has been fabricated recently by Luxel. This includes open entry and exit ports at the top and bottom of the Luxel wet cell. These can easily be used to fill the cell with an aqueous sample, after which the device is sealed at each end using nail polish. A bacterial cell-mineral aggregate of Fe(II)-oxidizing BoFeN1 cells (shown in Sect. 3.3) was prepared as described previously. In brief, BoFeN1 cells were cultivated as described in Sect. 2.2.1, then cell-mineral suspensions were sampled anoxically in a glove box (N_2 atmosphere) after 7 days with a syringe, centrifuged and resuspended in Fe(II)-, nitrate- and acetate-free anoxic freshwater medium. After transfer into an oxic environment a few µL of cell-mineral suspension were taken up with a glass micro-capillary and injected into the wet cell via the portable nano-injector. More detailed information about STXM sample preparation and 3D reconstruction is given elsewhere [121].

2.2.3 Material Samples

As an example of a materials science application of STXM spectro-tomography we present results from a "standard" sample used to develop a variety of quantitative 3D mapping methods for applications to optimization of automotive hydrogen-based fuel cell electrode materials. The "standard" sample consists of the overlay of two thin polymer films with Pt-coated carbon fibres embedded in resin as one layer and Teflon™ fibres embedded in resin as the second layer. The bilayer sample was microtomed and mounted on a formvar-coated grid. A strip from this grid was then excised and mounted on the tomography stage, using methods described above. This approach provides a model system with appropriate spatial scales and relevant spatial correlations of the chemical components present in the electrodes of a polymer electrolyte membrane fuel cell (PEM-FC). The second materials science example is taken from the first STXM spectro-tomography experiments [60]. In this case the sample is an aqueous suspension of core-shell polymer latex microspheres with a ∼100 nm thick polystyrene (PS) shell and a very low-density aqueous solution of linear polyacrylic acid (PAA) as the core. An aqueous colloidal dispersion of the microspheres was injected into a pulled glass capillary and the ends sealed with silicone grease. An alternative sample of the PS/PAA colloidal microspheres was prepared in a carbon nanopipette [66] which enabled studies at the C 1s edge since the X-ray absorbance of the ∼45 nm thin-walled nanotube container was much less than that of the ∼200 nm walls of the glass capillary at the C 1s edge.

2.3   Data Acquisition

The sample (either glass micro-capillary, carbon nanopipette, or Luxel wet cell / TEM grid strip mounted onto brass rod) is clamped to the rotation stage for STXM spectro-tomography measurements. The tomography stage is then mounted onto the piezo stage of the STXM. The rotation is software controlled. The maximum rotation angle above which the grid bars obscure the view is typically around $\pm 72°$ for grid samples (Sect. 3.1); the Luxel wet cell samples (Sect. 3.3) allowed for $\pm 80°$ rotation, whereas capillaries (Sect. 3.4) can be rotated by $\pm 90°$. The sample is rotated stepwise, typically in $4°$ steps, which is a compromise that allows for good-quality reconstruction and efficient data acquisition. Thus, an entire STXM spectro-tomography dataset consists of measurements at ≈ 37 different rotation angles. A time-efficient data collection approach that also limits radiation damage is to acquire datasets with a small number of selected photon energies that are specific for certain chemical species. For example, 288.2 eV, the peak of the C $1s \rightarrow \pi^*_{peptide}$ transition [122], is the photon energy specific for proteins. In our examples this photon energy is denoted as the characteristic protein absorption peak, but it also has some minor contributions of other carbon-containing compounds, including polysaccharides or lipids. One or multiple additional energies can be selected that are more or less specific for certain compounds. For example, lipids display a characteristic C $1s \rightarrow \pi^*_{COOR}$ transition at 288.5 eV. For chemical tomography it is necessary to record an additional image in the respective pre-edge, e.g. at 280 eV for C, and thus prior to the onset of C specific absorption. Figure 2.5 provides reference spectra and indicates the selected energies that were used for acquiring NEXAFS images of SW2 and cyanobacteria. Energies at the C 1s absorption edge were 280 eV for the pre-edge and 288.2 eV for the dominant protein peak (Fig. 2.5a). At the O 1s absorption edge, images were acquired at 5 energies for SW2 that are specific for the pre-edge, protein, goethite (an Fe(III)-(oxyhydr)oxide) (Fig. 2.5b) and polysaccharides. Equivalent to the previously described peak at 288.2 eV at the C 1s edge, the absorption at an energy of 532.2 eV at the O 1s edge is dominated by the O $1s \rightarrow \pi^*_{C=O}$ transition of proteins [122] with minor contributions of other organic macromolecules that contain oxygen. The BoFeN1 wet cell sample was mapped at the O 1s absorption edge with three specific energies (528, 532.2 and 538 eV, Fig. 2.5b) [68]. X-ray energies at the Fe 2p absorption edge were 704 eV for the pre-edge and 723.3 eV (Fig. 2.5c), characteristic for iron in the Fe(III) oxidation state at the Fe L_2 edge [17, 123]. Calcium images of the cyanobacteria were acquired at 352.6 eV, a characteristic energy for the Ca $2p_{1/2} \rightarrow$ Ca 3d resonance peak, and at 350.3 eV, an energy between the Ca $2p_{3/2}$ and Ca $2p_{1/2}$ resonance peaks [62]. Pixel spacings of 20 nm for the air-dried SW2 sample and the cyanobacteria sample and 25 nm for the BoFeN1 wet cell sample were chosen. The optimal effective thickness of (dry) biological samples for studies at the C 1s absorption edge should be <300 nm with an optical density (OD) <2; most bacteria, cell-mineral aggregates and thin biofilms lie within this range. STXM tomography data sets of the SW2 and BoFeN1 samples were acquired at CLS 10ID1, the cyanobacteria sample was measured at ALS 5.3.2.2 and 11.0.2, the core-shell microspheres at ALS 5.3.2.2 and the PEM-FC standard sample at both ALS 5.3.2.2 and CLS 10ID1.
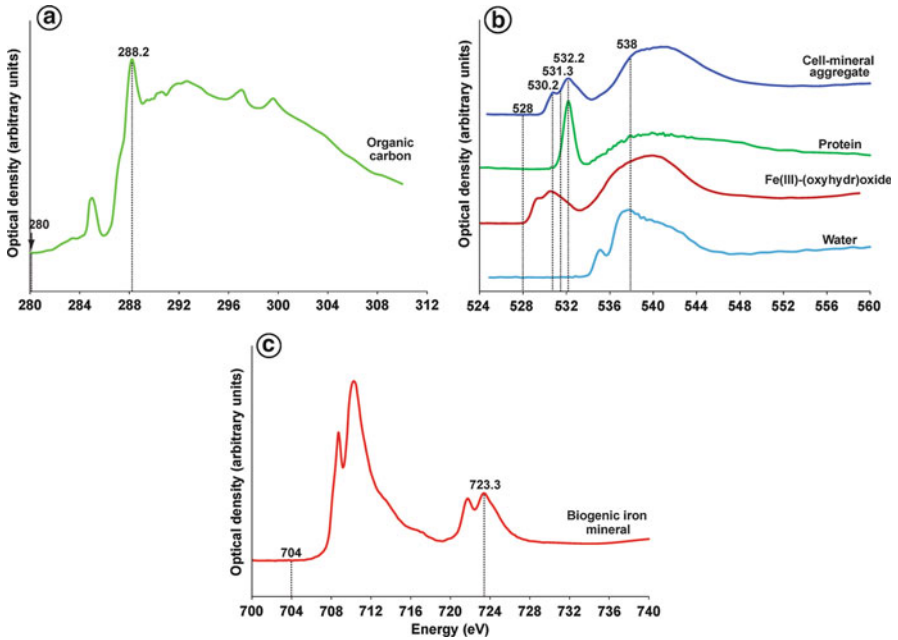
Fig. 2.5 Specific energies used for stack maps in study of SW2 and the BoFeN1 wet cell sample (**a**) SW2 organic carbon spectrum at the C 1s absorption edge, (**b**) SW2 cell-mineral aggregate spectrum at the O 1s absorption edge with reference spectra of protein, Fe(III)-(oxyhydr)oxide and water, (**c**) SW2 biogenic iron mineral spectrum at the Fe 2p absorption edge

2.3.1 Spatial Resolution and Quantitative Aspects of STXM Spectro-tomography

As for other tilt-series tomography approaches, the spatial resolution in STXM spectro-tomography is anisotropic. The resolution in the direction parallel to the tilt axis is defined by the chosen pixel spacing [124]. The resolution orthogonal to the tilt axis is dependent on the sample thickness D and the number of tilt steps N: $d_y = \pi D/N$ [125]. For example, for the biological samples presented in Sect. 3, we used $N \approx 37$ and a thickness of ≈ 500 nm, resulting in a theoretical resolution d_y of ≈ 43 nm. For samples that cannot be rotated $\pm 90°$ against the x-, y-plane perpendicular to the beam axis, the resolution along the beam axis is decreased compared to x- and y-direction and defined by the missing wedge. In this case the resolution is related to the maximum tilt range angle α by [126]:

$$d_z = ((\alpha + \sin\alpha\cos\alpha)/(\alpha - \sin\alpha\cos\alpha))^{\frac{1}{2}}d_y$$

Since rotation angles α of up to $\pm 72°$ ($\approx \pm 1.26$ rad) were measured, the theoretical resolution d_z is ≈ 54 nm. Furthermore, the resolution will depend on the zone plate used, and on the X-ray energy of the measurements since the depth of field

increases with increasing energy. A precise evaluation of the achieved resolution would require measurements on a three-dimensional test pattern, which have not yet been performed. However, based on the separation of small features in actual samples, spatial resolutions of at least 80 nm [62] and <50 nm [68] in the z-direction have been demonstrated.

For quantitative analysis of the 3D distribution of the individual chemical species, for example, by 3D correlation analysis [127], the intensities in the reconstructed 3D volume dataset can be calibrated based on the quantitative transmission measurement at one angle (usually at $0°$). Quantification in a transmission STXM setup is based on Beer's law [$I = I_0 \exp(-\Sigma \chi_i \rho_i t_i)$, where χ_i is the absorbance, ρ_i is the density and t_i is the thickness of the ith component]. There is a linear relationship between absorbance (optical density, OD) and the amount of the absorbing component in the X-ray beam path. Calibration of the 3D dataset then allocates the sum $OD_{x,y}$ for each individual pixel of a 2D transmission measurement to the $OD_{x,y,z}$ of the 3D voxels in the volume according to their individual contribution to the sum absorbance along the beam path when the sample is at pixel (x,y). The sum of the OD values of all voxels along the beam axis z is equal to the OD of the pixel with the same x and y coordinate in the two-dimensional transmission image according to the following formula:

$$\Sigma_z\big(OD\big(voxel_{x,y,z}\big)\big) = OD\big(pixel_{x,y}\big)$$

where $OD(voxel_{x,y,z})$ is the optical density of an individual voxel in the reconstructed 3D tomography dataset and $OD(pixel_{x,y})$ is the optical density of an individual pixel of the respective 2D species map at the rotation angle of $0°$ (Fig. 2.6). Quantification is limited by the specificity of the spectral analysis procedure with a limited number of X-ray energies. For thicker samples, potential problems with absorption saturation should be considered in the selection of the X-ray energies [128]. Furthermore, the anisotropic spatial resolution, in particular the elongation of features perpendicular to the beam and rotation axes as a result of the missing wedge problem, might result in a slight underestimation of concentrations. Obst and colleagues [62] estimated this error to be in the range of 5–10 % and discussed quantification and its limitations in STXM spectro-tomography in more detail.

2.4 Data Analysis

2.4.1 Pre-processing

The transmission images acquired at a single rotation angle are aligned and converted to linear absorbance in optical density units $OD = -\ln(I/I_0)$, where I is the measured intensity of a pixel and I_0 is the incident flux measured in an empty area adjacent to the sample. Several software packages are available that provide tools for image alignment and conversion into OD units, such as *aXis2000*
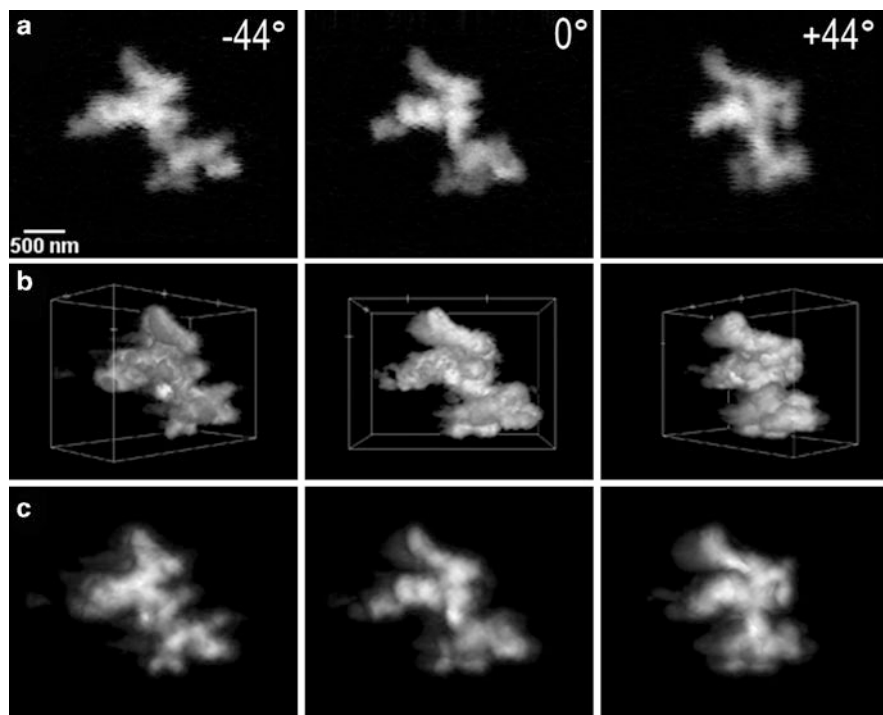
Fig. 2.6 (a) Acquired 2D iron stack maps ($OD_{723.3eV} - OD_{704eV}$) of SW2 (see Fig. 2.8) at $-44°$, $0°$ and $+44°$, (b) rendered reconstructed 3D volumes (with *VolumeJ*), respectively, (c) projections of the reconstructed 3D volumes (with *VolumeViewer*) at the same angles. The sum of $OD_{x,y}$ for each pixel in the acquired 2D image is set equal to sum of the $OD_{x,y,z}$ for each voxel in the 3D volume. The distribution in the projections of the 3D reconstruction is almost but not exactly the same as the measured 2D projections. The main reasons for differences are (i) noise that is present in the single angle measurement (**a**) but gets averaged out in the reconstructions (**b**), and (ii) artifacts due to the missing wedge of rotation angles that are visible as a slight blurring of the edges in panel (**c**)

(http://unicorn.mcmaster.ca/aXis2000.html) or *Mantis* [129] (http://www. spectromicroscopy.com). In general, several different approaches of data analysis can be used to obtain quantitative chemical maps from sets of OD images (Fig. 2.7).

1. The first approach is to subtract an image acquired in the pre-edge region from an image acquired at a specific characteristic energy (described in Sect. 2.3). This approach is the quickest method, but its precision is limited by the specificity of the selected energies. Typically it works well for elemental maps or for chemical maps of compounds that have strong resonance absorption peaks such as the C 1s $\rightarrow$ $\pi^*_{C=O}$ transition of protein.
2. If more than two images were recorded across an absorption edge, the second approach, linear decomposition, can be used in combination with the spectra of known reference compounds [12, 130].
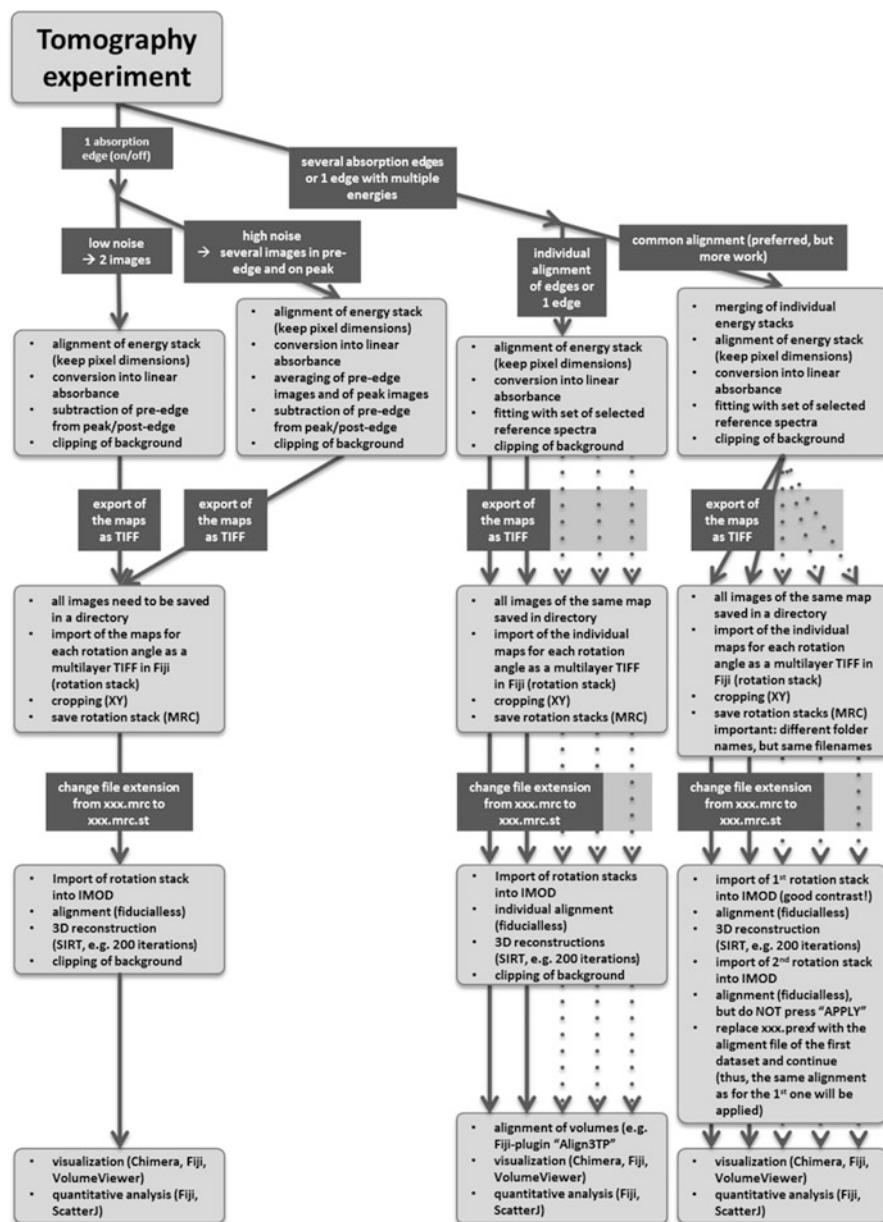
Fig. 2.7 Flow chart of the data acquisition, analysis and 3D reconstruction procedures for STXM spectro-tomography

3. The third approach, principle component analysis (PCA) in combination with cluster analysis [113, 129], can be used if the sample is spectroscopically completely unknown, which is rarely the case in STXM spectro-tomography but often possible with environmental samples that are analyzed by STXM in 2D.

All three approaches result in quantitative elemental/species maps that in some cases can be normalized to an effective thickness of the respective compound in nm. The chemical maps (on a relative or absolute thickness scale) at all rotation angles are then merged into a rotation stack for correct angle-to-angle alignment and subsequent 3D reconstruction (Fig. 2.7).

For the examples presented in Sect. 3.1, quantitative maps were obtained for organic carbon at the C 1s absorption edge by using OD image difference, $OD_{288.2eV} - OD_{280eV}$ for the SW2 and cyanobacteria examples. The same procedure was applied to obtain quantitative iron maps at the Fe 2p absorption edge for both the SW2 and the BoFeN1 examples, $OD_{723.3eV} - OD_{704eV}$. In this case, linear decomposition of the datasets was not possible at the C 1s and Fe 2p absorption edges for SW2 and at the Fe 2p absorption edge for BoFeN1 due to the high sample thickness and the associated spectral distortions due to absorption saturation $(OD > 2)$ [128]. Quantitative maps of calcium of the cyanobacteria were obtained in the same manner, $OD_{352.6eV} - OD_{350.3eV}$. In contrast, OD images of SW2 and BoFeN1 recorded at the O 1s absorption edge were not affected by absorption saturation. In this case, linear decomposition was used to obtain quantitative maps on effective thickness scale.

Quantitative maps of SW2 at the O 1s absorption edge were obtained by fitting the image stacks across the O 1s edge with reference spectra of protein [122], goethite and a calculated, non-specific background spectrum based on the atomic scattering factors [131]. For the example of BoFeN1, O 1s reference spectra of protein, ferrihydrite (an Fe(III)-(oxyhydr)oxide), water and a non-specific background were used (Fig. 2.5b).

In the previously mentioned examples, the data of all absorption edges were handled individually, and thus, an alignment of the volume files resulting from the reconstruction is necessary (see Sect. 2.4.2). This can be circumvented by merging the images at all X-ray energies and edges per rotation angle into the same stack file for a first alignment (Fig. 2.7). This approach was applied to the examples in Sect. 3.2 and the river biofilm example in Sects. 3.3 and 3.4.

2.4.2 3D Reconstruction

A number of software tools for 3D tomographic reconstruction were developed by various groups around the world in the last decade, mostly for transmission electron tomography. Several of them turned out to be useful and compatible with the image quality provided by STXM tilt-series spectro-tomography. Two very powerful packages are *IMOD* [132, 133] (http://bio3d.colorado.edu/imod/) and *TomoJ*

[134] (http://u759.curie.fr/en/download/softwares/EFTEM-TomoJ). The latter was implemented as a plug-in for *ImageJ/Fiji* [135] (http://fiji.sc/Fiji). Both programs offer comfortable-to-use and powerful tools for aligning the rotation series to obtain rotation stacks free of lateral shifts. This is essential for a good 3D reconstruction, in particular when considering that the measurements are most often done without fiducials such as gold beads that are often used for TEM tomography [56, 125]. The alignment tools of both programmes are based on cross-correlation between individual images but also provide the possibility of manual alignment corrections. *TomoJ* offers various reconstruction algorithms such as the conventional weighted back projection (WBP) and more modern iterative approaches that reduce the effect of missing wedges during data acquisition such as the algebraic iterative technique (ART) [136] and simultaneous iterative reconstruction (SIRT) [137]. The cyanobacteria cell (Sect. 3.1) was reconstructed with *TomoJ*, using SIRT with 200 iterations, and a relaxation coefficient of 0.5. *IMOD* also provides filtered back projection and SIRT as reconstruction algorithms. The STXM spectro-tomography datasets of SW2 (Sect. 3.1) and BoFeN1 (Sect. 3.3) were reconstructed with *IMOD*, employing the SIRT algorithm with 400 iterations (filter settings: radial filter cut-off = 0.4; falloff = 0.05). The SIRT reconstructed volumes of the different compounds that were acquired at different absorption edges were afterwards aligned using the *Fiji* plug-in *Align3TP* (http://www.med.harvard.edu/JPNM/ij/plugins/Align3TP.html). As mentioned previously, this step is not required if a common stack through all X-ray energies and absorption edges per rotation angle was created and aligned before OD conversion (see Sect. 2.4.1, Fig. 2.7). In those cases, the alignment of the rotation stack is done once on the component that provides the best contrast, and the same file of alignment shifts is subsequently applied to all other components. This approach was used for the reconstructions of the polymer-electrolyte membrane fuel cells (Sect. 3.2), the river wet cell sample (Sect. 3.3) and the polymer wet samples (Sect. 3.4).

Various types of noise affect the quality of the reconstructed 3D volumes. Two main sources are real background (non-specific) absorption signal and streaking artefacts that are caused by the rather coarse angle step-size that we use as a compromise for efficiency and to reduce beam damage, and by the missing wedge effect [124]. The missing wedge effect is an artefact due to limited angle range of rotation for some types of STXM spectro-tomography samples. A powerful tool to remove such background noise in reconstructed 3D volumes is the segmentation software *ilastik* [138] (http://ilastik.org/) that can be used to efficiently create a binary mask of the noise and of the region of interest. This binary mask can then be multiplied with the original volume dataset to separate the region of interest (ROI) from the noise. A binary mask was applied to the reconstructed 3D volumes of SW2. For rendering and visualization of the reconstructed 3D volumes for SW2, BoFeN1 and the cyanobacteria cell, the software package *Chimera* was used [139] (http://www.cgl.ucsf.edu/chimera/). Various *Fiji* plugins (e.g. *3D Viewer*, *Volume Viewer*, *VolumeJ*) are also available for 3D rendering and visualization and were used in the examples shown in this chapter.

3   Key Research Findings

Here we present recent key research findings of biogeochemical and material science studies that are based on 3D chemical analysis of samples using STXM spectro-tomography.

3.1   Biological: Dry Chemical Mapping

Fe-(oxyhydr)oxides represent some of the most important scavengers for other metal ions such as heavy metals in polluted environments. Often these minerals are of biogenic origin and associated with organic matter. Thus, understanding the influence of microbial Fe(II)-oxidation and subsequent precipitation of Fe(III) minerals is essential to comprehend the fate of heavy metals or pollutants in the environment. The photoferrotrophic, anaerobic *Rhodobacter* ferrooxidans strain SW2 was used as a model organism to study bacterial Fe(II)-oxidation and subsequent cell-(iron)mineral aggregate formation. SW2 cells are loosely associated with biogenic iron minerals that are not subject to cellular modification, in contrast to the nitrate-reducing, anaerobic *Acidovorax* sp. strain BoFeN1 (see Sect. 3.3) that precipitates dense shells of organic-associated iron minerals around the cells. STXM spectro-tomography studies of SW2 revealed evidence for several mechanisms of Fe-sorption and precipitation. SW2 cells were air dried onto formvar-coated TEM grids. Grid strips were sliced, mounted onto a tomography stage and analyzed by chemical tomography at the C 1s, O 1s and Fe 2p absorption edges, as described previously. Figure 2.8 shows the reconstructed 3D volumes of several chemical species of a SW2 cell-(iron)mineral aggregate, including organic carbon ($OD_{288.2eV}-OD_{280eV}$), iron ($OD_{723.3eV}-OD_{704eV}$), protein and goethite (both derived from spectral fits). The 3D volumes of the chemical components revealed an SW2 cell mainly free of any iron minerals but associated with extracellular organic carbon and extracellularly precipitated iron minerals. This confirmed results from previous 2D studies [22, 140] that Fe(II)-oxidation of SW2 takes place at the cell surface and is accompanied by the production of extracellular polymeric substances (EPS), consisting of polysaccharides, lipids and protein to localize and control iron mineral precipitation in the vicinity of the cell, but to prevent the cell from encrustation. The wealth of information hidden in the multi-species 3D datasets motivated the development of new software tools such as *ScatterJ*. This tool, implemented as a plug-in for *ImageJ/Fiji,* allows for a more automated analysis of such complicated multi-species 3D datasets [127]. In particular the generation of 2D histograms or so-called scatterplots allows for the identification of correlations between chemical species that are present in the analyzed volume. Analysis using *ScatterJ* is very efficient. A back-mapping function allows for an efficient segmentation in real space of clusters that become apparent in the scatterplot. Additionally, *ScatterJ* can create an angular distance map that highlights regions in the 3D volumes that differ in the association of chemical species. In this case, the scatterplot of iron and organic carbon (Fig. 2.8b)
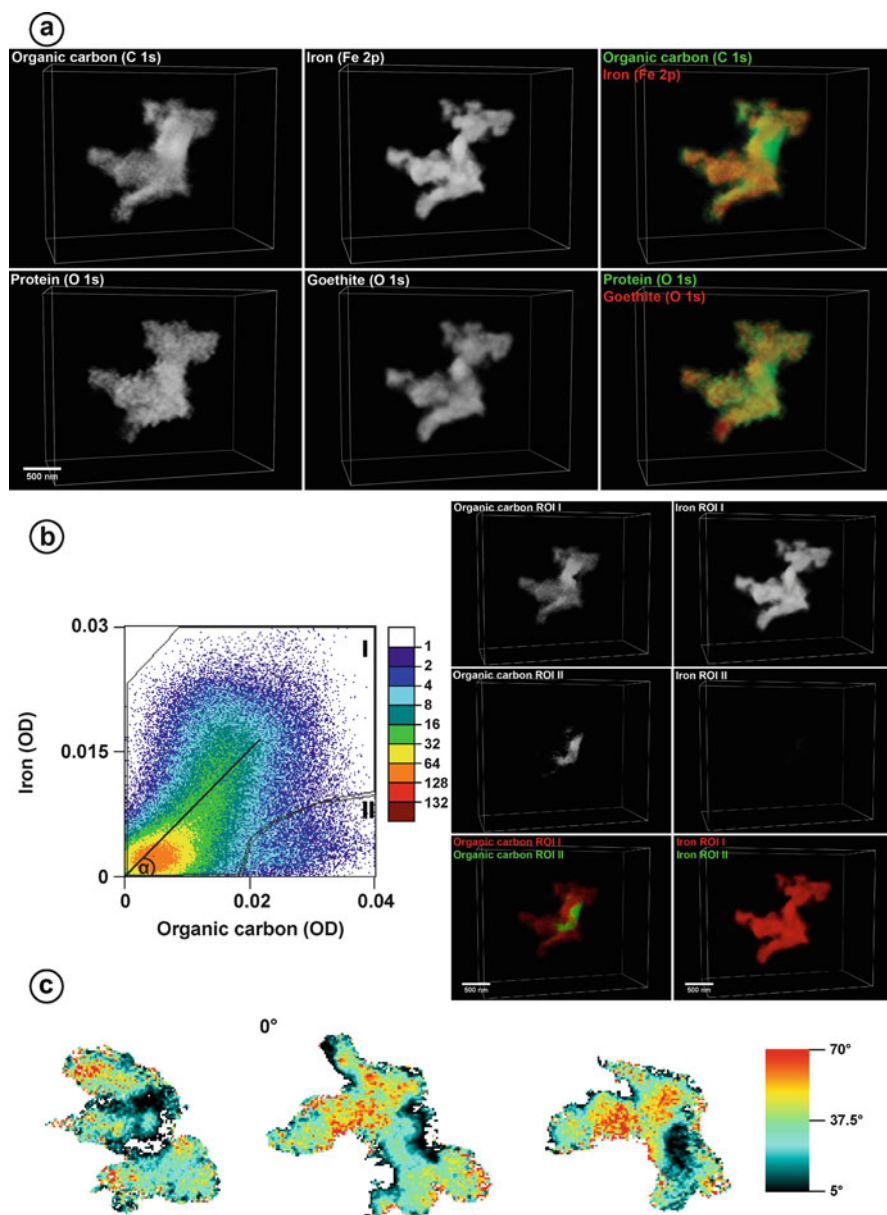
Fig. 2.8 (**a**) 3D component maps for organic carbon, protein, goethite and iron, derived from reconstruction of a STXM spectro-tomography data set for air-dried SW2, visualized with Chimera. 3D color-coded composites to visualize spatial correlations, (**b**) (*left*) Scatterplot from *ScatterJ* of iron and organic carbon 3D maps with ROI I and ROII. (*right*) 3D component maps obtained by back-mapping of ROI I and ROI II (visualized with *Chimera)*, (**c**) Angular distance maps of the scatterplot, at two different rotation projections and at 0°. *Color* scale shows the angular distance (α) from the organic carbon axis. Saturated values were normalized to 5° and 70°. See text for details

indicated two correlation centres, which were manually selected and denoted as ROI I (region of interest) and ROI II, respectively. ROI I revealed a positive correlation, describing iron and organic carbon are associated with each other. In contrast, ROI II shows no correlation, characterized by organic carbon that is not associated with any iron. Figure 2.8a also reveals that some iron is attached to the cell surface, resulting in overlapping correlation centres in the scatterplot. Back-mapping of both ROIs into real 3D space (Fig. 2.8b) and a 3D colour representation of an angular distance map based not on the manual selection of ROIs but on the angular distance (α) from the organic carbon axis (Fig. 2.8c) verified these hypotheses. Two different perspectives of the angular distance map in 3D and a projection along the beam axis show high variability of iron independent of carbon (red) as well as high variability of carbon concentrations independent of iron (dark blue) (Fig. 2.8c). STXM spectro-tomography also allowed us to calculate quantitative amounts of specific chemical species for individual voxels or for the whole reconstructed volume. Quantitative amounts for the complete reconstructed 3D volumes were calculated. About ≈ 0.53 pg goethite was deduced from the Fe 2p absorption signal, and ≈ 0.20 pg of organic carbon was deduced from the C 1s absorption edge (the calculations assume densities of 4.13 g/cm^3 for goethite and of 1 g/cm^3 for organic carbon). This type of 3D quantitation can be helpful to follow Fe(II)-oxidation of cells over time or to determine sorption of heavy metals to cell-(iron)mineral aggregates. In particular the quantitative correlation analysis of the 3D dataset, combined with consideration of the spatial distribution of the chemical components, helped to unambiguously elucidate Fe(II)-oxidation mechanisms of SW2. As proposed previously, SW2 regulates Fe(II)-oxidation and in particular the subsequent precipitation of iron minerals by producing extracellular organic carbon, likely with negatively charged functional groups that adsorb positively charged iron minerals to prevent cell encrustation [22]. Similar mechanisms to prevent cell encrustation are assumed to exist for microaerophilic Fe(II)-oxidizing bacteria [23–25]. Cell-(iron)mineral aggregates formed by SW2 can act as sink for heavy metals such as Ni in the environment [119].

In another study, the quantitative analysis of chemical tomography datasets at the C 1s and the Ca 2p absorption edges resulted in a detailed understanding of the mechanisms of calcium carbonate precipitation by planktonic cyanobacteria [62]. The combination of the STXM tilt-series spectro-tomography with a detailed spectro-microscopic characterization of the sample in 2D was used to develop a model of the entire process from Ca^{2+} sorption to the cell surfaces and the associated extracellular polymeric substances, to the subsequent step of mineral nucleation. Cyanobacteria are photoautotrophic organisms that can use either CO_2 or HCO_3^- as carbon source. The latter process results in a significant pH increase. In aqueous systems where Ca^{2+} ions are present this can result in a significant supersaturation with respect to the calcium carbonates calcite, aragonite and vaterite, where calcite is the thermodynamically most stable form. Cyanobacteria are known to cause massive precipitation events in lakes, so-called whitings. However, the precipitation of stable mineral phases attached to the cell would not be beneficial for planktonic cyanobacteria as the cells would lose their buoyancy and precipitate out

of the photic zone. Therefore the cells developed a protection mechanism that prevents the formation of stable mineral phases that are attached to the cells. The quantitative 3D analysis of the correlation between the concentrations of calcium and organic carbon in this sample revealed the presence of two different types of EPS with different sorption capacities for the Ca^{2+}-cation. At the time of the study, manual segmentation of the 3D dataset showed the spatial distribution of the two EPS layers around a single cyanobacterium and the presence of two critical nuclei of calcite on the cell surface (Fig. 2.9a). *ScatterJ* was used for analysis of the 3D datasets [127] of calcium and organic carbon (Fig. 2.9b). In this study, tilt-series STXM spectro-tomography was performed at two absorption edges at four different X-ray energies in total. The 3D study [62] was combined with a very detailed spectro-microscopic study [35] that included spectral mapping at 100 meV energy resolution at the C 1s and 80 meV spectral resolution at the Ca 2p edges. The combination of these two complementary approaches turned out to be extremely powerful for the identification, mapping and quantification of the different organo-chemical constituents and mineral phases in this sample, which facilitated the interpretation of the tomography data so that a model of the biogenic formation of calcium carbonates could be established. Ca^{2+} ions sorb to a layered structure of EPS consisting of EPS closely bound to the cyanobacterial cell surface and loosely bound EPS. Additionally, a metastable amorphous $CaCO_3$ with aragonite-like short-range order is precipitated within the EPS. This efficiently lowers the super-saturation with respect to calcium carbonates and might allow the cyanobacteria to overcome short periods of elevated pH and thus high carbonate concentrations in the daily cycle without nucleating thermodynamically stable calcite minerals on their cell surface [35, 62].

3.2 Polymer: Dry Chemical Mapping

Polymer-electrolyte membrane fuel cells (PEM-FC) operating at low temperature (50–80 °C) with pure H_2 as fuel are being developed by many car manufacturers for near-term implementation in mass-produced automobiles, as a means of reducing carbon emissions. While the automotive performance of present devices is similar to that of gasoline-powered cars, there is a cost premium and some concerns about reliability. Research is focused on reducing the amount of Pt catalyst in the electrodes and making the systems less susceptible to known degradation processes such as carbon corrosion, Pt migration and modifications at low temperature. Over the past 5 years the Hitchcock group has collaborated with researchers at the Automotive Fuel Cell Cooperation (AFCC) Corporation and Ballard Power systems to develop STXM as a means to provide unique analytical information which can assist with materials and process optimization. Studies have been performed on the role of N-containing ligands of Pt catalyst precursors in Pt migration [141], effect of different carbon support types on rates of carbon corrosion [142] and alternative catalysts [46]. A particular value-added aspect of STXM in PEM-FC research is its ability to quantitatively map the perfluorosulfonic acid (PFSA)
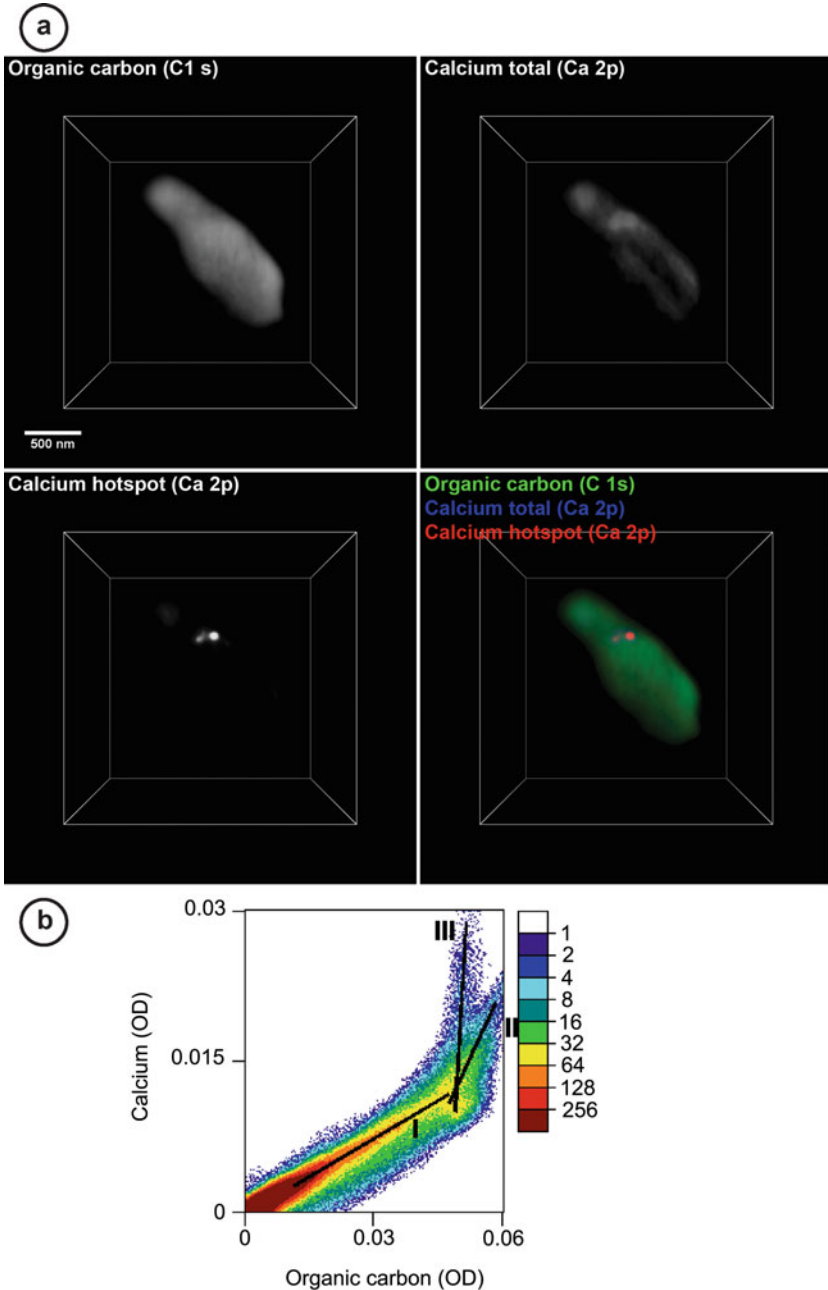
Fig. 2.9 (**a**) *S. leopoliensis* PCC 7942; 3D tomographic reconstruction of the organic carbon and calcium distributions in/around the cyanobacterial cell (visualized with *Chimera*), (**b**) scatterplot (from *ScatterJ*) of organic carbon and calcium. The distributions are rather broad but can be split into three distinct subgroups of voxels. (I) for low ODs (i.e. concentrations), there is a linear

ionomer component of the cathode and anode. The ionomer is critical to optimization of Pt usage since a proton transport path to each active catalyst particle is needed for that particle to contribute to the overall cell activity. PFSA is extremely radiation sensitive. Prior attempts to provide quantitative analysis by electron microscopies have been hampered by radiation damage and loss of the fluorine signal. By using a simple, accurate four-energy approach, we have shown that STXM can provide quantitative 2D projection mapping of ionomer in cathodes [143, 144]. While this has provided many valuable insights into the dependence of the ionomer spatial distributions on materials choices, fabrication and processing, the 2D projection results contain ambiguities with respect to the 3D distributions. In addition PFSA is extremely radiation sensitive so it is critical to develop and use dose-efficient methods. Thus, we are developing a range of 3D chemical imaging approaches to visualize PFSA ionomer in 3D. Initially we used angle-scan STXM spectro-tomography to study cathode samples prepared with focused ion beam (FIB) milling [64]. FIB was chosen to avoid penetration of the embedding medium (needed for ultramicrotomy) into the porous cathode structure, which might cause swelling and distortion of the porosity or ionomer distributions. While 3D pore mapping was possible for the FIB sample, we found that almost all of the fluorine of the PFSA ionomer was removed by the ion beam during the FIB milling step [145]. Thus we made subsequent 3D mapping measurements using cathode samples which were embedded, microtomed and mounted on TEM grids and then cut with a scalpel to make a grid strip suitable for STXM spectro-tomography (see Fig. 2.3).

In order to develop confidence in 3D ionomer mapping and to have a means of evaluating the spatial resolution and quantitative accuracy of competing 3D chemical mapping techniques, we developed in parallel a standard test sample, which could be prepared in a simple reproducible manner, with known properties, which contained all of the chemical components of the PEM-FC cathode system but with a much simpler spatial organization. Figure 2.10 presents 3D chemical mapping results for such a test sample. The sample (Fig. 2.10a, b) consists of a two-layer structure with Pt-coated carbon fibres embedded in resin in one layer and Teflon fibres embedded in resin in the second layer. Figure 2.10c is a projection of the carbon fibre, Pt and Teflon^{TM} fibre extracted from a reconstruction of a tomographic data set consisting of measurements at 40 angles ($-80°$ to $+80°$, every $4°$) with images at 4 photon energies (278.0, 285.1, 684.0, 693.3 eV) measured at each angle. The transmission images at each angle were aligned and converted to quantitative Pt (from the OD_{278} eV image, corrected for F-absorption [143]), carbon ($OD_{285.2}$ eV$-OD_{278}$ eV) and fluorine ($OD_{693.3}$ eV$-OD_{684}$ eV) maps using *aXis2000*. The maps at the full set of angles were then aligned and

---

Fig. 2.9 (continued) correlation between organic carbon and calcium with a rather shallow slope. For higher concentrations, there are two subgroups (II) and (III), both with a linear relationship but rather steep slopes of calcium/organic carbon, the latter interpreted as calcium adsorbed to EPS. One is almost vertical (III), which indicates that the amount of calcium is almost independent of the organic carbon content. This is interpreted as precipitation of $CaCO_3$ [62]
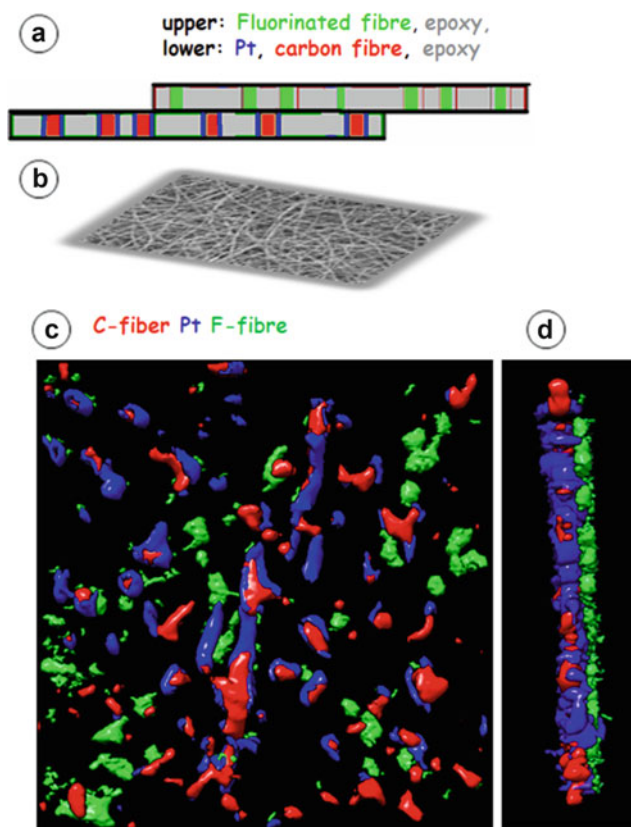
Fig. 2.10 (**a**) Schematic of the standard bilayer thin film sample used to explore application of 3D chemical imaging methods to characterization of the chemical structure of electrodes in polymer electrolyte membrane fuel cells (PEM-FC). (**b**) cartoon of the fibre sample. (**c**) *Amira* rendering of the 3D chemical mapping viewed from the normal to the film. (**d**) *Amira* rendering of the 3D chemical mapping viewed edge-on to the bilayer film

reconstructed using SIRT with 200 iterations using *IMODJ* (http://www.snv.jussieu.fr/~wboudier/softs/imodj.html). The rendering was performed using *Amira*. In the rendering shown in Fig. 2.10c all of the black regions are in fact filled with embedding resin. Close associations of the Pt and carbon fibre are clearly seen, while the 3D imaging reveals that the F-containing Teflon^{TM} fibre is in a different plane (Fig. 2.10d).

3.3 Biological: Wet Chemical Mapping

Biological or biogeochemical samples are often not compatible with sample preparation methods that involve sample dehydration and solvents that alter sample

composition and thus would affect the chemical analysis. At the cost of ultrastructural details, air or vacuum drying is often used for samples that are compatible and not subject to cell lysis. However, some samples need to be analyzed in their natural hydrated state to avoid drying artefacts and to evaluate possible artefacts from the drying procedure. There are several mounting approaches that allow for STXM spectro-tomography of natural, hydrated samples. STXM spectro-tomography has been performed on wet biological samples in pulled glass capillaries and in wet cells developed in collaboration with Luxel (Friday Harbor, USA) that are based on a metal frame coated with polyimide membranes on both sides [67]. Here we show exemplary results that were obtained on Fe(II)-oxidizing bacteria. In contrast to the Fe(II)-oxidizing strain SW2 (Sect. 3.1) that is loosely associated with iron minerals, bacterial mediated Fe(II)-oxidation by BoFeN1 results in the encrustation and ultimately entombing of the cells within iron minerals. To study the mechanism of bacterial Fe(II)-oxidation, BoFeN1 were analyzed spectro-tomographically in pristine hydrated conditions to avoid artefacts such as dehydration and shrinkage of cells and EPS. BoFeN1 cell-(iron)mineral suspensions were injected into Luxel wet cells and imaged at selected photon energies and from various angles at the O 1s and Fe 2p absorption edges. 3D reconstruction of this data lead to 3D chemical imaging [68]. Figure 2.11 shows the 3D volumes of the individual chemical components, iron ($OD_{723.3eV} - OD_{704eV}$) (Fig. 2.11d), Fe(III)-(oxyhydr)oxide, protein and water (Fig. 2.11a–c). Figure 2.5b shows the O 1s reference spectra that were used for spectral fitting at the O 1s absorption edge. The X-ray energies selected for chemically specific mapping are also indicated (Fig. 2.5b). The transmitted signal intensities were converted into linear absorbance scale using I_0 measured through the water layer adjacent to the bacterial cell-(iron)mineral aggregate, so that the homogeneous water layer was normalized out during the conversion. Thus, the thickness of the water layer was systematically underestimated by ~120 nm; this has been compensated for in the data processing. Clearly indicated in Fig. 2.11 is that the periplasm (the space between the inner and outer cell membrane) of one cell is homogeneously filled with iron minerals and EPS is associated with iron minerals in the hydrated state and thus not just dried onto the cells. However, a second cell free of any iron minerals is revealed in the protein map only (Fig. 2.11b). A profile through the iron distribution in the periplasm (Fig. 2.11f) shows a rim-like structure with a full-width half-maximum (FWHM) of ~35–50 nm, which is consistent with previously published TEM-based work on this strain [19]. The thickness measured by STXM spectro-tomography lies in the range of the spatial resolution and illustrates the capabilities of the technique. Based on the distributions of the iron minerals, the cells and the EPS we conclude that, similar to SW2, bacterially produced EPS influences the precipitation of Fe(III)-minerals around the BoFeN1 cells but, in the case of BoFeN1, without success in preventing the cell from encrustation. That is likely due to an abiotic pathway of Fe(II) oxidation by the nitrate-reducing bacteria via nitrite [146]. In a more extensive study, different cellular encrustation patterns of BoFeN1 were identified for BoFeN1 by several complementary tomography approaches including STXM spectro-tomography [69].
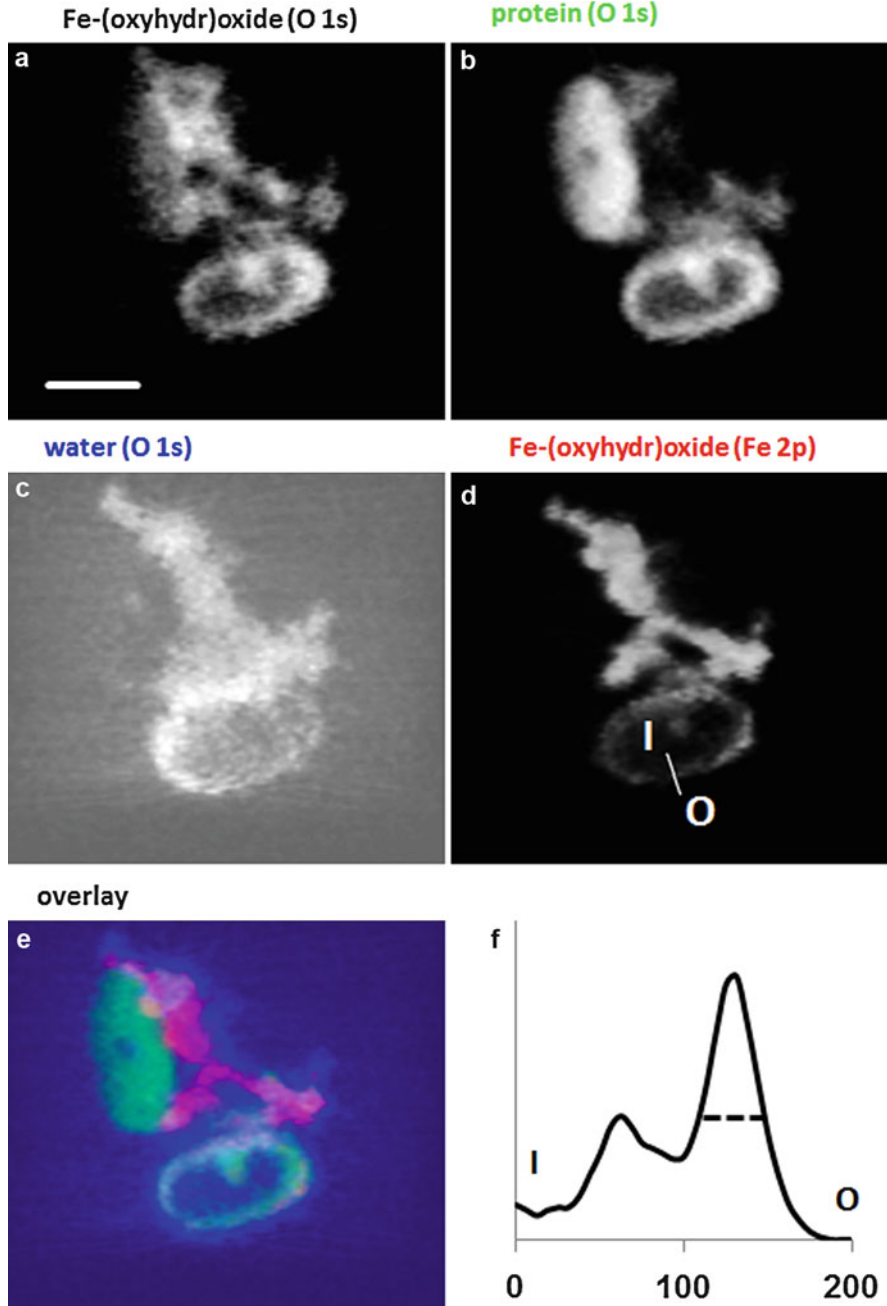
Fig. 2.11 Hydrated prepared BoFeN1 "wet cell" 3D reconstruction, (**a–c**) 3D components maps of Fe(III)-(oxyhydr)oxide, protein and water obtained by spectral fits at the O 1s absorption edge, (**d**) iron (denoted as Fe(III)-(oxyhydr)oxide) acquired at the Fe 2p absorption edge and (**e**) an

In contrast to the pure cultures of Fe(II)-oxidizing bacteria, natural river biofilms are more complex multi-species systems in which extensive synergy and competition among different species results in an extra-cellular matrix with many different chemical components. STXM has been used in a number of studies of river biofilms taken from the South Saskatchewan River in Saskatoon, where CLS is located. These studies have addressed correlative microscopy themes (confocal laser, TEM and STXM) [10] as well as biofilm adaptation to toxic metals [12, 13], antimicrobials [16] and nanomaterials [14]. All of these studies used only 2D projection spectro-microscopy and thus the third dimension was masked. STXM spectro-tomography provides a means to achieve 3D chemical mapping in natural biofilms. Figure 2.12 presents results for an O 1s edge study of a wet river biofilm in a pulled glass capillary. Due to the strong absorption by the glass walls and the water it was only possible to get adequate transmission in a 4 eV region just below the onset of the strong O 1s absorption by water and SiO_2. Even so the three common classes of bio-molecules (proteins, polysaccharides and lipids) have chemically distinct signals in this energy range (Fig. 2.12a) leading to strong changes in STXM images which can be analyzed with confidence to produce five distinct chemical maps, as shown by the 2D analysis at one angle in Fig. 2.12b. Figure 2.12c, d and e are renderings of the 3D chemical maps of the protein, the glass wall and the water. The cell, seen clearly in the protein map of one projection (Fig. 2.12b), is most easily seen in the 3D view from the top of the capillary.

3.4   Polymer: Wet Chemical Mapping

Pulled glass capillaries [60] and carbon nanopipettes [61] have been used to mount fully hydrated polymer core-shell microspheres for STXM spectro-tomography. Figures 2.13, 2.14 and 2.15 show results from both preparations. For the pulled-glass capillary approach, the substantial X-ray absorption by the glass and the relatively thick water layer meant that the C 1s regions could not be used. Instead the polyacrylate fill was differentiated from the polystyrene shell by the difference in tomograms measured below the O 1s edge at 530.0 eV and at the O 1s → π* transition in the acrylate at 532.2 eV. In this case, a combination of careful segmentation of the OD_{530} eV 3D signal and the chemically specific difference signal allowed a clean separation of the glass capillary, the water and the PS shell (Fig. 2.13). The 3D distribution of the polyacrylate was quantified using the difference OD signal, the known OD/nm response of polyacrylate, and the

---

Fig. 2.11 (continued) overlay (visualized with *Chimera*). (**f**) shows the thickness of the iron crust of ∼40 nm (full-width at half-maximum of the line profile indicated in **d**). *I* inside cell, *O* outside cell. Scale bar is 500 nm (Permission to reproduce figure from [68] under Rights Link license 3591541244472)
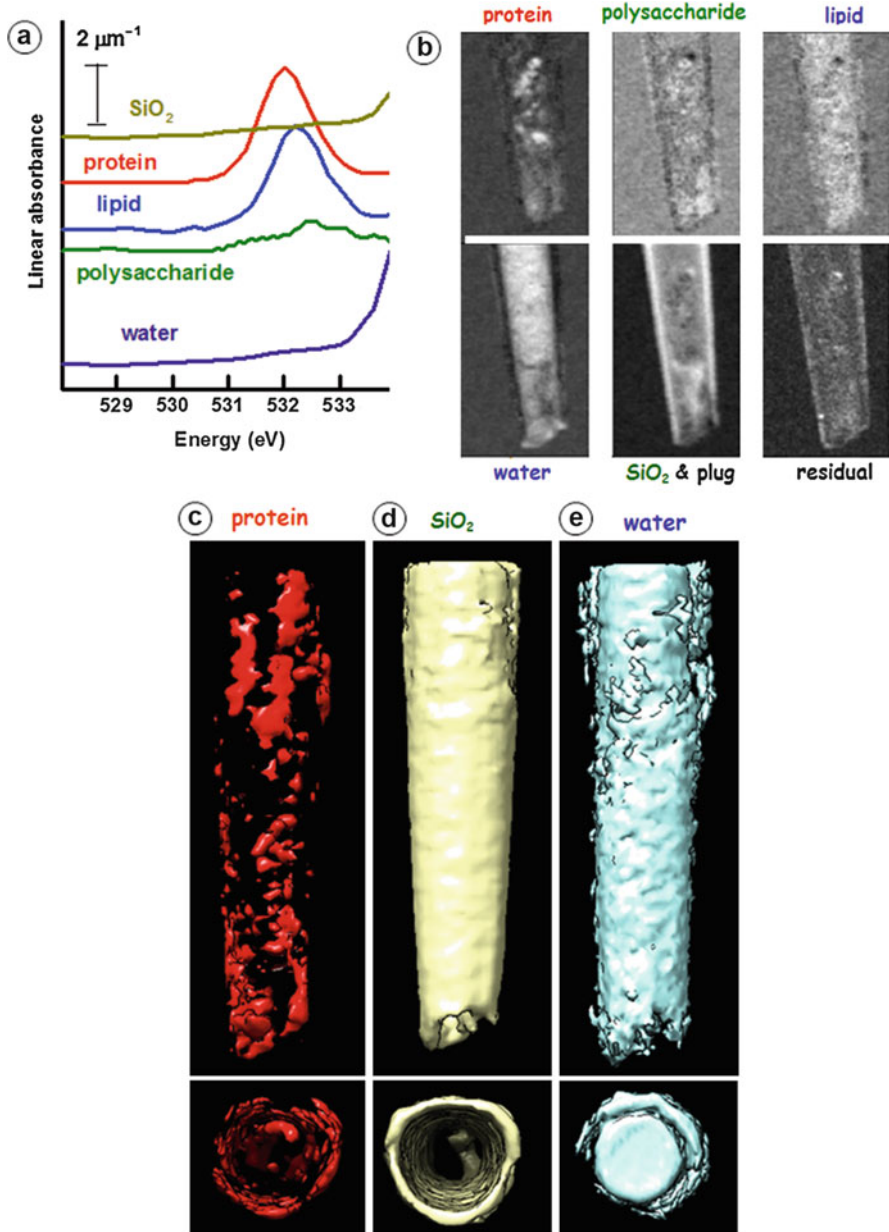
Fig. 2.12 Results of 3D chemical mapping of a natural river biofilm in a pulled glass capillary. (a) O 1s spectra of the chemical components in the region below the onset of strong absorption by water. (**b**) component maps derived by fitting spectra in (**a**) to a set of 13 energy stacks, at one angular orientation. (**c**) *Chimera* rendering of the 3D map of the protein. (**d**) *Chimera* rendering of the 3D map of the glass wall. (**e**) *Chimera* rendering of the 3D map of the water
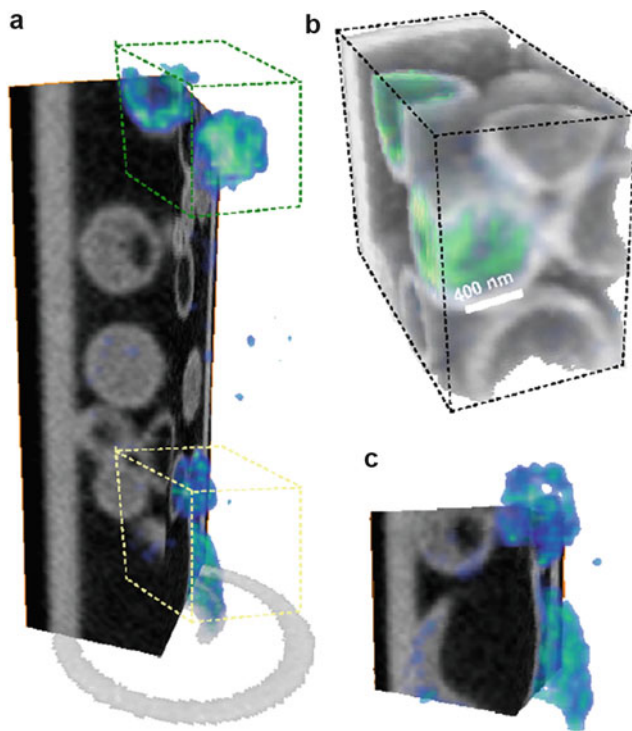
Fig. 2.13 3D visualization of a wet colloid consisting of hollow polystyrene microspheres (∼120 nm wall thickness) containing a low density linear polyacrylate fill, rendered by *Amira* from a reconstruction of a two-energy O 1s spectro-tomography data set. (**a**) A cut through the whole volume, with the gray scale indicating both the PS and glass components, and the *blue/green* colorization indicating two density levels of the polyacrylate. (**b**) Expanded area of the upper box, using a different view and rendering. (**c**) Expanded view of the lower box (Permission to reproduce figure from [61] under Rights Link license 3570490606168)

3D reconstruction [60, 147]. In order to explore use of the more chemically sensitive C 1s edge for 3D mapping of these wet core-shell microspheres, they were also measured in carbon nanopipettes [66]. The much thinner walls (30 nm instead of 150 nm) meant there was sufficient transmission in the C 1s region to allow meaningful measurements despite the presence of the C 1s spectrum of the carbon nanotube walls (Fig. 2.14a). However the total thickness of the PS shell was such that there was significant spectral distortion from absorption saturation. Despite that, it was possible to generate 3D maps of the polyacrylate fill and the PS shells by using absorption saturated spectra extracted from the data set, and matched outside of the distorted region to the correct quantitative reference spectra (Fig. 2.14b, c). Figure 2.15a–c are component maps of the carbon tube, polyacrylate fill and the polystyrene shell, derived from the C 1s stack which consisted of images at 26 energies between 283 and 299 eV. Figure 2.15d is a
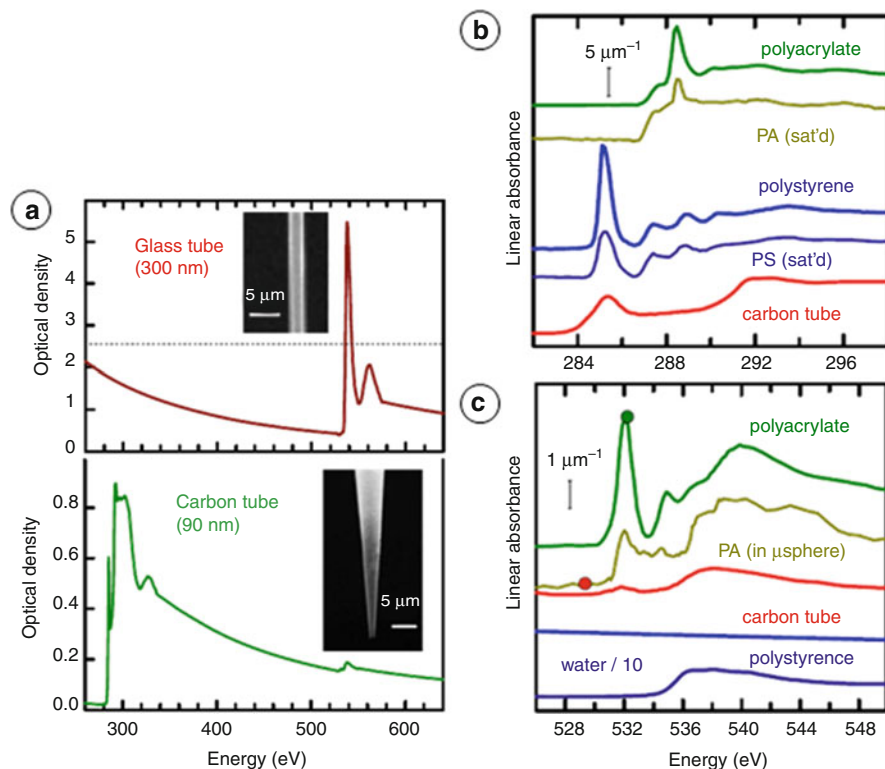
Fig. 2.14 (**a**) Optical density spectrum in the 260–640 eV range of a thin walled (∼150 nm) pulled glass capillary (*upper*) and a thin walled (∼45 nm) carbon nanopipette (*lower*). The *insets* are STXM images. The *dashed horizontal line* indicates the OD at which spectral distortions from absorption saturation effects typically appear in STXM. (**b**) Comparison of the C 1s spectra of polyacrylate (PA), polystyrene (PS) and the carbon tube on a linear absorbance scale (optical density per nm thickness). Two sets of data for PA and PS are indicated, unsaturated, and that with partial absorption saturation which was extracted from spectra measured from the sample in the carbon tube. (**c**) Comparison of the O 1s spectra of PA, PS, carbon tube, and water (Adapted from [61]. Permission to reproduce under Rights Link license 3570490606168)

colour-coded composite of these 2D chemical component maps. Similar C 1s stacks were measured at 50 angles, and 3D chemical images were derived from the angle dependence of the component maps. Figure 2.15e is a 3D rendering of the combined polyacrylate and polystyrene 3D maps derived from a SIRT reconstruction of the angle sets of these component maps, which were merged and rendered with *Amira*. In the thinner volumes at the bottom of the tube the 3D chemical imaging is similar to that obtained at the O 1s edge in the glass capillary, but the result is less clear in the upper regions of the nanopipette where there is much more material and thus greater distortions and mixing/blurring of component signals due to the absorption saturation.
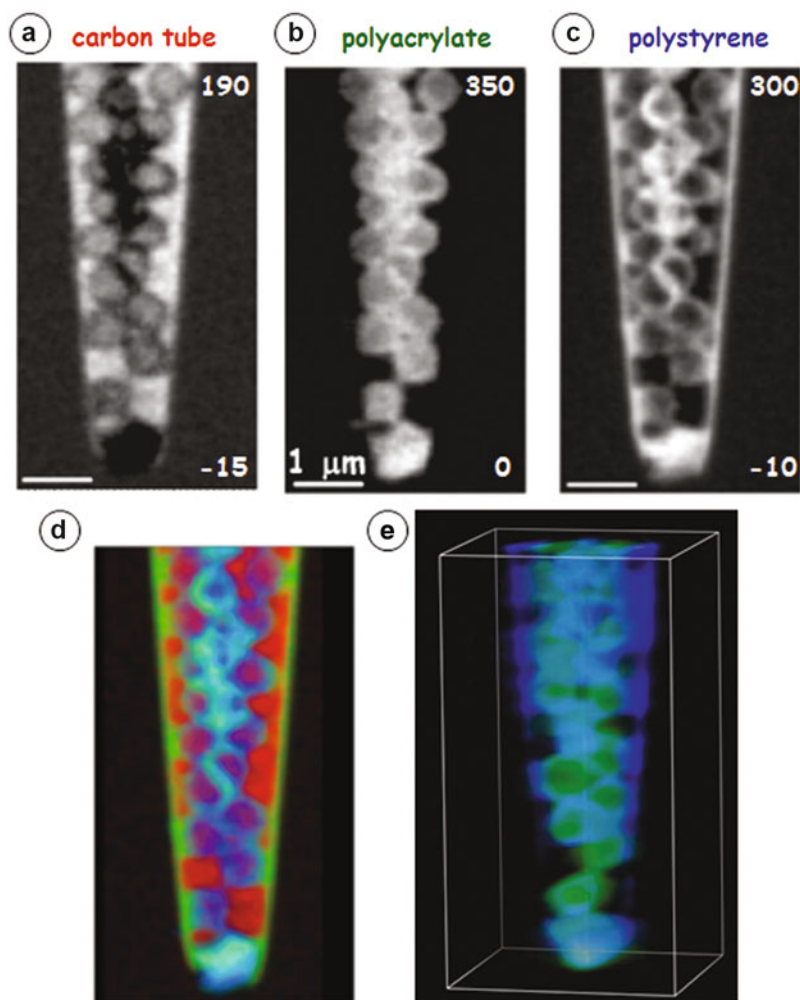
Fig. 2.15 Component maps for (**a**) the carbon tube, (**b**) polyacrylate and (**c**) polystyrene derived from a fit to a C 1s image sequence (282–306 eV, 23 energies) at one angle, using the PA (sat'd), PS (sat'd) and carbon tube reference spectra plotted in Fig. 2.14b. The gray scales are thickness in nm. (**d**) Color-coded composite where the red maps the carbon tube, green maps the polyacrylate fill, and blue maps the polystyrene shell. The intensity of each color at any pixel is proportional to the amount of that component in the column traversed by the X-ray beam. Each color is rescaled independently of the other two. (**e**) *Amira* rendering of the 3D distributions of polyacrylate (*green*) and polystyrene (*blue*) from a merging of the SIRT reconstructions of the PA and PS component maps at 50 angles (Adapted from [61]. Permission to reproduce under Rights Link license 3570490606168)

4   Conclusions and Future Perspective

4.1   Strengths and Limitations of STXM Spectro-tomography

As shown in the previous sections, STXM spectro-tomography allows for quantitative 3D mapping not only of elements but also of chemical species. In particular the statistical (correlation) analysis of chemical datasets in 3D turns out to be powerful for gaining insights into reaction mechanisms and for efficiently analyzing the spatial distribution of chemical species with different affinities for each other such as EPS that sorbs metal ions and the precipitation of a mineral phase. This approach relies significantly on speciation capabilities and on spatial resolution in 3D. Most soft X-ray STXM-beamlines are optimized for spectro-microscopy and, with energy resolving power $E/\Delta E > 3000$, provide excellent chemical speciation capabilities making them ideally suited for chemical nano-tomography.

One of the major advantages of STXM spectro-tomography with soft X-rays in comparison to hard X-ray techniques is the accessibility of absorption edges of light elements such as C, N and O. In particular for biological, biogeochemical and for polymer science, this allows for employing the chemically specific, intrinsic absorption contrast of the sample to map the distribution of organic molecules in 3D, which is not accessible using higher-energy photons of hard X-rays. Simultaneously, the energy range of soft X-rays is a major limiting factor of STXM spectro-tomography as the high absorption of these low-energy photons requires the sample thickness to be restricted to the sub-µm up to few µm ranges, depending on sample composition and density.

Another disadvantage of the approach is the limited accessibility of synchrotron beamtime via proposal-based, peer-reviewed access and by the so far limited efficiency due to long acquisition times and a poor duty cycle. The situation regarding the latter problem can be expected to improve in the next years with installation of next-generation STXM instruments that will allow for a more automated acquisition and thus better duty cycle, as explained in the next sections.

4.2   Future Instrument and Technique Developments

STXM spectro-tomography provides the most value added when applied to systems that are difficult or impossible to study by analytical TEM tomography, which typically means highly radiation-sensitive materials (such as the PFSA ionomer in PEM-FC) or when one wishes to perform 3D chemical analysis of wet samples (e.g. to avoid drying artefacts of sensitive structures such as microbial extracellular biopolymers). Recently there have been dramatic improvements in the ability of modern TEMs to handle wet samples and in situ modifications of samples by, e.g. electrochemistry [148]. However core-level electron energy loss is nearly impossible in wet samples due to plural scattering [149], fluorescence tomography analysis is very challenging and, to our knowledge, no one has applied either TEM-based analytical method to 3D chemical imaging of wet samples. Thus a

logical place to advance STXM spectro-tomography is in the area of 3D character-
ization of wet, radiation-sensitive materials, such as ionomer in PEM-FC cathodes
under actual working conditions (80 °C and 50–70 % relative humidity). At present
there is a major effort in several directions to achieve this capability in STXM, for
both 2D and 3D analysis. An environmental cell to achieve relevant conditions in a
STXM has been constructed [150]; in situ spectro-electrochemistry in STXM has
been demonstrated [151] and is being further developed [152]. While neither of
those devices are set up for tomography, an ultramicrotomed section can be loaded
into the latest-generation Luxel wet tomography device. Spectro-tomography of
humidified and wet PEM-FC MEA samples in the wet tomo cells is underway.

Another major advance in STXM spectro-tomography is the development of a
near-ultra-high vacuum (UHV) STXM at the CLS optimized for cryo-tomography.
This novel instrument will enable studies of frozen hydrated samples, thereby
reducing mass-loss radiation damage distortions and ultimately allowing 3D chem-
ical imaging studies of plunge-frozen biological samples, similar to those
performed with the first cryo-tomo-STXM [59]. By adapting a TEM system for
eucentric mounting of cryo samples it is expected that, in addition to reducing
mass-loss damage, the rate of analysis will be significantly improved through
automated data collection, resulting in higher throughput compared to our present,
manual-intensive procedures. Soft X-ray TXM systems for cryo-tomography are
very well developed and even commercially available (Zeiss – Xradia, Pleasanton,
California). While these instruments excel at 3D morphological studies and have in
a number of cases provided functional segmentation based on characteristic optical
densities at 510 eV [76–88], in general the present-generation soft X-ray TXMs on
beamlines with a conventional monochromator and thus high-quality spectroscopy,
still do not provide the same quality of chemical imaging as STXM spectro-
tomography. Improvements in the illumination and ability to preserve beam-sample
alignment and focus while changing the photon energy will produce an instrument
in many ways superior to STXM spectro-tomography, although there will continue
to be advantages to using STXM for radiation-sensitive samples.

Alternatives to tilt-series tomography scanning include stereo-imaging, which is
being developed in the hard X-ray region [153], and laminography, again already
developed using hard X-rays [154, 155]. The latter appears particularly promising
for flat samples where 3D chemical imaging can be measured over a much wider
area, as compared to tilt-series tomography. Instrumentation for STXM spectro-
laminography exists, and soft X-ray spectro-laminography is under development.

Finally, perhaps the most exciting near-future instrumentation development is
soft X-ray spectro-ptycho-tomography. The Nanosurveyor instrument at ALS
(presently on BL 5.3.2.1, and soon to move to the COSMIC beamline) is fully
equipped for 3D chemical imaging by ptycho-tomography, and the first data sets
already exist. In addition to improved instrumentation, there are continual improve-
ments in the data analysis and extraction of value-added information from post-3D
reconstruction methods. For example, a recent development particularly well suited
(but not yet applied) to STXM spectro-tomography is 3D reconstruction using
compressed sensing (CS), a method known from other fields which is now being

applied to TEM tomography [156, 157]. CS algorithms are able to generate high-quality 3D reconstructions from a much sparser data set than is usually assumed to be needed for tilt-series tomography [158]. This approach can be expected to improve the quality of reconstructions in particular for setups that are affected by a missing wedge of rotation angles due to sample mounting, and for the analysis of radiation-sensitive samples for which the number scans and thus tilt angles have to be limited to reduce the total dose. Advances in simultaneous, quantitative analysis of full spectro-tomography data sets (images over a set of energies and tilt angles) – so-called 4D tomography [159, 160] – are also in the works, that will allow for analyzing quantitatively and in detail spatial correlations in 3D of chemically distinct clusters and sub-volumes in the sample. Finally another active area of research is correlative methods whereby STXM spectro-tomography is combined with 3D imaging and 3D chemical imaging using other methods such as TEM and Fourier transform infrared spectroscopy (FTIR) spectro-tomography [161].

4.3 Improvements in Sample Mounting and Acquisition

With the possibility of analyzing samples in their pristine, hydrated state, STXM spectro-tomography has significantly reduced one of the major limitations, in particular in the field of biological and biogeochemical sciences, but also for material sciences, namely, artefacts from sample drying. First experiment using glass micro-capillaries as sample mounts on the one hand had the advantage of a rotation range of $\pm 90°$ so that this approach was not affected by the missing wedge problem. On the other hand, the strong absorption of the glass walls did not allow for accessing the C 1s absorption edge and significantly limited the energy range accessible at the O 1s absorption edge. Furthermore, the capillaries were quite flexible and thus subject to vibrations when scanned on the piezo-driven sample stage, which limits spatial resolution. With the development of wet cells in collaboration with Luxel (Friday Harbor, USA) that are based on metal frames coated with polyimide membranes on both sides, the limited energy range was overcome. In the meantime, the second, improved version of the wet tomo cells further reduced vibrations by optimizing the geometric design and facilitated the filling procedure by providing filling channels in the metal frame structure.

The most modern, next-generation STXMs will allow for scanning the ZP in the plane perpendicular to the beam axis instead of scanning the sample. Current instruments move the sample using a fast piezo-driven scanner. As the rotation stage for tomography is mounted onto the piezo scanner, the rotation stage and sample mounting needs to be optimized for a weight of a few 10s of grams. This is the main reason why until today there have not been any successful attempts of using a eucentric rotation stage that is mounted on the piezo scanner. The capabilities of scanning the ZP instead of the sample will allow for using more bulky and stable, eucentric rotation stages that can be adapted from TEM tomography. With a eucentric stage the sample will not go out of focus or move laterally out of the field of view during rotation, which will allow for more efficient and eventually

automated data acquisition similar to scanning transmission electron microscopy (STEM) tomography. At the same time, this will allow for using the previously mentioned cryo-stage for sample mounting, so that frozen hydrated samples can be analyzed in 3D by STXM spectro-tomography. The analysis of samples in the frozen state has advantages for sample preparation and reduced beam-induced damage due to radical formation that can become a problem in particular when analyzing hydrated samples in wet cells.

References

1. Ade H, Hitchcock AP (2008) NEXAFS microscopy and resonant scattering: composition and orientation probed in real and reciprocal space. Polymer 49(3):643–675
2. Hitchcock AP (2012) Soft X-ray imaging and spectromicroscopy. In: van Tendeloo G, van Dyck D, Pennycook SJ (eds) Handbook of nanoscopy. Wiley-VCH Verlag GmbH & Co. KGaA, Weinheim, pp 745–791
3. Attwood D (1999) Soft X-rays and extreme ultraviolet radiation: principles and applications. Cambridge University Press, Cambridge
4. Willmott PR (2011) An introduction to synchrotron radiation: techniques and applications. 1. publ. ed. Wiley, Chichester
5. Sasaki S (1994) Analyses for a planar variably-polarizing undulator. Nucl Instrum Methods Phys Res A 347(1–3):83–86
6. Bluhm H, Andersson K, Araki T, Benzerara K, Brown GE, Dynes JJ, Ghosal S, Gilles MK, Hansen HC, Hemminger JC, Hitchcock AP, Ketteler G, Kilcoyne ALD, Kneedler E, Lawrence JR, Leppard GG, Majzlan J, Mun BS, Myneni SCB, Nilsson A, Ogasawara H, Ogletree DF, Pecher K, Salmeron M, Shuh DK, Tonner B, Tyliszczak T, Warwick T, Yoon TH (2006) Soft X-ray microscopy and spectroscopy at the molecular environmental science beamline at the Advanced Light Source. J Electron Spectrosc Relat Phenom 150(2–3):86–104
7. Kirz J, Rarback H (1985) Soft-X-ray microscopes. Rev Sci Instrum 56:1–13
8. Kirz J, Ade H, Jacobsen C, Ko CH, Lindaas S, McNulty I, Sayre D, Williams S, Zhang X, Howells M (1992) Soft x-ray microscopy with coherent x rays. Rev Sci Instrum 63(1): 557–563

9. Kilcoyne ALD, Tyliszczak T, Steele WF, Fakra S, Hitchcock P, Franck K, Anderson E, Harteneck B, Rightor EG, Mitchell GE, Hitchcock AP, Yang L, Warwick T, Ade H (2003) Interferometer-controlled scanning transmission X-ray microscopes at the Advanced Light Source. J Synchrotron Radiat 10:125–136

10. Lawrence JR, Swerhone GDW, Leppard GG, Araki T, Zhang X, West MM, Hitchcock AP (2003) Scanning transmission X-ray, laser scanning, and transmission electron microscopy mapping of the exopolymeric matrix of microbial biofilms. Appl Environ Microbiol 69 (9):5543–5554

11. Hunter RC, Hitchcock AP, Dynes JJ, Obst M, Beveridge TJ (2008) Mapping the speciation of iron in *Pseudomonas aeruginosa* biofilms using scanning transmission X-ray microscopy. Environ Sci Technol 42(23):8766–8772

12. Dynes JJ, Tyliszczak T, Araki T, Lawrence JR, Swerhone GDW, Leppard GG, Hitchcock AP (2006) Speciation and quantitative mapping of metal species in microbial biofilms using scanning transmission X-ray microscopy. Environ Sci Technol 40(5):1556–1565

13. Hitchcock AP, Dynes JJ, Lawrence JR, Obst M, Swerhone GDW, Korber DR, Leppard GG (2009) Soft X-ray spectromicroscopy of nickel sorption in a natural river biofilm. Geobiology 7(4):432–453

14. Lawrence JR, Dynes JJ, Korber DR, Swerhone GDW, Leppard GG, Hitchcock AP (2012) Monitoring the fate of copper nanoparticles in river biofilms using scanning transmission X-ray microscopy (STXM). Chem Geol 329:18–25

15. Lawrence JR, Swerhone GD, Dynes JJ, Korber DR, Hitchcock AP (2014) Soft X-ray spectromicroscopy for speciation, quantitation and nano-eco-toxicology of nanomaterials. J Microsc. doi:10.1111/jmi.12156

16. Dynes JJ, Lawrence JR, Korber DR, Swerhone GDW, Leppard GG, Hitchcock AP (2006) Quantitative mapping of chlorhexidine in natural river biofilms. Sci Total Environ 369 (1–3):369–383

17. Miot J, Benzerara K, Morin G, Kappler A, Bernard S, Obst M, Ferard C, Skouri-Panet F, Guigner JM, Posth N, Galvez M, Brown GE, Guyot F (2009) Iron biomineralization by anaerobic neutrophilic iron-oxidizing bacteria. Geochim Cosmochim Acta 73(3):696–711

18. Miot J, Benzerara K, Morin G, Bernard S, Beyssac O, Larquet E, Kappler A, Guyot F (2009) Transformation of vivianite by anaerobic nitrate-reducing iron-oxidizing bacteria. Geobiology 7(3):373–384

19. Miot J, Maclellan K, Benzerara K, Boisset N (2011) Preservation of protein globules and peptidoglycan in the mineralized cell wall of nitrate-reducing, iron(II)-oxidizing bacteria: a cryo-electron microscopy study. Geobiology 9(6):459–470

20. Pantke C, Obst M, Benzerara K, Morin G, Ona-Nguema G, Dippon U, Kappler A (2012) Green rust formation during Fe(II) oxidation by the nitrate-reducing *Acidovorax* sp. strain BoFeN1. Environ Sci Technol 46(3):1439–1446

21. Miot J, Li JH, Benzerara K, Sougrati MT, Ona-Nguema G, Bernard S, Jumas JC, Guyot F (2014) Formation of single domain magnetite by green rust oxidation promoted by microbial anaerobic nitrate-dependent iron oxidation. Geochim Cosmochim Acta 139:327–343

22. Miot J, Benzerara K, Obst M, Kappler A, Hegler F, Schadler S, Bouchez C, Guyot F, Morin G (2009) Extracellular iron biomineralization by photoautotrophic iron-oxidizing bacteria. Appl Environ Microbiol 75(17):5586–5591

23. Chan CS, De Stasio G, Welch SA, Girasole M, Frazer BH, Nesterova MV, Fakra S, Banfield JF (2004) Microbial polysaccharides template assembly of nanocrystal fibers. Science 303 (5664):1656–1658

24. Chan CS, Fakra SC, Edwards DC, Emerson D, Banfield JF (2009) Iron oxyhydroxide mineralization on microbial extracellular polysaccharides. Geochim Cosmochim Acta 73 (13):3807–3818

25. Chan CS, Fakra SC, Emerson D, Fleming EJ, Edwards KJ (2011) Lithotrophic iron-oxidizing bacteria produce organic stalks to control mineral growth: implications for biosignature formation. ISME J 5(4):717–727

26. Bennett SA, Toner BM, Barco R, Edwards KJ (2014) Carbon adsorption onto Fe oxyhydroxide stalks produced by a lithotrophic iron-oxidizing bacteria. Geobiology 12(2):146–156

27. Coker VS, Byrne JM, Telling ND, van der Laan G, Lloyd JR, Hitchcock AP, Wang J, Pattrick RA (2012) Characterisation of the dissimilatory reduction of Fe(III)-oxyhydroxide at the microbe-mineral interface: the application of STXM-XMCD. Geobiology 10 (4):347–354

28. Rothe J, Kneedler EM, Pecher K, Tonner BP, Nealson KH, Grundl T, Meyer-Ilse W, Warwick T (1999) Spectromicroscopy of Mn distributions in micronodules produced by biomineralization. J Synchrotron Radiat 6(Pt 3):359–361

29. Pecher K, Kneedler E, Rothe J, Meigs G, Warwick T, Nealson K, Tonner B (2000) Charge state mapping of mixed valent iron and manganese mineral particles using scanning transmission X-ray microscopy (STXM). AIP Conf Proc 507(1):291–300

30. Toner B, Fakra S, Villalobos M, Warwick T, Sposito G (2005) Spatially resolved characterization of biogenic manganese oxide production within a bacterial biofilm. Appl Environ Microbiol 71(3):1300–1310

31. Muehe EM, Obst M, Hitchcock A, Tyliszczak T, Behrens S, Schroder C, Byrne JM, Michel FM, Kramer U, Kappler A (2013) Fate of Cd during microbial Fe(III) mineral reduction by a novel and Cd-tolerant *Geobacter* species. Environ Sci Technol 47(24):14099–14109

32. Shimizu M, Zhou J, Schroder C, Obst M, Kappler A, Borch T (2013) Dissimilatory reduction and transformation of ferrihydrite-humic acid coprecipitates. Environ Sci Technol 47 (23):13375–13384

33. Liu X, Eusterhues K, Thieme J, Ciobota V, Hoschen C, Mueller CW, Kusel K, Kogel-Knabner I, Rosch P, Popp J, Totsche KU (2013) STXM and NanoSIMS investigations on EPS fractions before and after adsorption to goethite. Environ Sci Technol 47(7):3158–3166

34. Benzerara K, Menguy N, Obst M, Stolarski J, Mazur M, Tyliszczak T, Brown GE Jr, Meibom A (2011) Study of the crystallographic architecture of corals at the nanoscale by scanning transmission X-ray microscopy and transmission electron microscopy. Ultramicroscopy 111 (8):1268–1275

35. Obst M, Dynes JJ, Lawrence JR, Swerhone GDW, Benzerara K, Karunakaran C, Kaznatcheev K, Tyliszczak T, Hitchcock AP (2009) Precipitation of amorphous CaCO (3) (aragonite-like) by cyanobacteria: a STXM study of the influence of EPS on the nucleation process. Geochim Cosmochim Acta 73(14):4180–4198

36. Lam KP, Hitchcock AP, Obst M, Lawrence JR, Swerhone GDW, Leppard GG, Tyliszczak T, Karunakaran C, Wang J, Kaznatcheev K, Bazylinski DA, Lins U (2010) Characterizing magnetism of individual magnetosomes by X-ray magnetic circular dichroism in a scanning transmission X-ray microscope. Chem Geol 270(1–4):110–116

37. Kalirai SS, Lam KP, Bazylinski DA, Lins U, Hitchcock AP (2012) Examining the chemistry and magnetism of magnetotactic bacterium Candidatus Magnetovibrio blakemorei strain MV-1 using scanning transmission X-ray microscopy. Chem Geol 300:14–23

38. von der Heyden BP, Roychoudhury AN, Mtshali TN, Tyliszczak T, Myneni SCB (2012) Chemically and geographically distinct solid-phase iron pools in the Southern Ocean. Science 338(6111):1199–1201

39. Nico P, Keiluweit M, Kleber M, Hatton PJ, Zeller B, Derrien D (2010) The speciation of organic matter in soil mineral organic associations – inference from STXM and N, C and Fe NEXAFS. Geochim Cosmochim Acta 74(12, Supplement):A758–A758

40. Keiluweit M, Bougoure JJ, Zeglin LH, Myrold DD, Weber PK, Pett-Ridge J, Kleber M, Nico PS (2012) Nano-scale investigation of the association of microbial nitrogen residues with iron (hydr)oxides in a forest soil O-horizon. Geochim Cosmochim Acta 95:213–226

41. Norlund KLI, Southam G, Tyliszczak T, Hu YF, Karunakaran C, Obst M, Hitchcock AP, Warren LA (2009) Microbial architecture of environmental sulfur processes: a novel syntrophic sulfur-metabolizing consortia. Environ Sci Technol 43(23):8781–8786

42. Hitchcock AP, Obst M, Wang J, Lu YS, Tyliszczak T (2012) Advances in the detection of as in environmental samples using low energy X-ray fluorescence in a scanning transmission

X-ray microscope: arsenic immobilization by an Fe(II)-oxidizing freshwater bacteria. Environ Sci Technol 46(5):2821–2829

43. Hitchcock AP, Toney MF (2014) Spectromicroscopy and coherent diffraction imaging: focus on energy materials applications. J Synchrotron Radiat 21(Pt 5):1019–1030

44. Patridge CJ, Wu TL, Sambandamurthy G, Banerjee S (2011) Colossal above-room-temperature metal-insulator switching of a Wadsley-type tunnel bronze. Chem Commun 47 (15):4484–4486

45. Schultz BJ, Patridge CJ, Lee V, Jaye C, Lysaght PS, Smith C, Barnett J, Fischer DA, Prendergast D, Banerjee S (2011) Imaging local electronic corrugations and doped regions in graphene. Nat Commun 2:372

46. Lee V, Berejnov V, West M, Kundu S, Susac D, Stumper J, Atanasoski RT, Debe M, Hitchcock AP (2014) Scanning transmission X-ray microscopy of nano structured thin film catalysts for proton-exchange-membrane fuel cells. J Power Sources 263:163–174

47. Watts B, Schuettfort T, McNeill CR (2011) Mapping of domain orientation and molecular order in polycrystalline semiconducting polymer films with soft X-ray microscopy. Adv Funct Mater 21(6):1122–1131

48. Yu XW, Pribiag VS, Acremann Y, Tulapurkar AA, Tyliszczak T, Chou KW, Brauer B, Li ZP, Lee OJ, Gowtham PG, Ralph DC, Buhrman RA, Stohr J (2011) Images of a spin-torque-driven magnetic nano-oscillator. Phys Rev Lett 106(16):167202

49. Watts B, Ade H (2012) NEXAFS imaging of synthetic organic materials. Mater Today 15 (4):148–157

50. Hitchcock AP, Araki T, Ikeura-Sekiguchi H, Iwata N, Tani K (2003) 3D chemical mapping of toners by serial section scanning transmission X-ray microscopy. J Phys IV France 104:509–512

51. Xu F, Helfen L, Suhonen H, Elgrabli D, Bayat S, Reischig P, Baumbach T, Cloetens P (2012) Correlative nanoscale 3D imaging of structure and composition in extended objects. PLoS One 7(11), e50124

52. Ginat DT, Gupta R (2014) Advances in computed tomography imaging technology. Annu Rev Biomed Eng 16(1):431–453

53. Maire E, Withers PJ (2014) Quantitative X-ray tomography. Int Mater Rev 59(1):1–43

54. de Jonge MD, Ryan CG, Jacobsen CJ (2014) X-ray nanoprobes and diffraction-limited storage rings: opportunities and challenges of fluorescence tomography of biological specimens. J Synchrotron Radiat 21(Pt 5):1031–1047

55. Midgley PA, Dunin-Borkowski RE (2009) Electron tomography and holography in materials science. Nat Mater 8(4):271–280

56. Frank J (2006) Electron tomography. In: Methods for three-dimensional visualization of structures in the cell, 2nd edn. Springer, New York

57. Haddad WS, McNulty I, Trebes JE, Anderson EH, Levesque RA, Yang L (1994) Ultrahigh-resolution X-ray tomography. Science 266(5188):1213–1215

58. McNulty I, Haddad WS, Trebes JE, Anderson EH (1995) Soft x-ray scanning microtomography with submicrometer resolution. Rev Sci Instrum 66(2):1431

59. Wang Y, Jacobsen C, Maser J, Osanna A (2000) Soft X-ray microscopy with a cryo scanning transmission X-ray microscope: II. Tomography. J Microsc 197(Pt 1):80–93

60. Johansson GA, Tyliszczak T, Mitchell GE, Keefe MH, Hitchcock AP (2007) Three-dimensional chemical mapping by scanning transmission X-ray spectromicroscopy. J Synchrotron Radiat 14(Pt 5):395–402

61. Hitchcock AP, Johansson GA, Mitchell GE, Keefe MH, Tyliszcak T (2008) 3-D chemical imaging using angle-scan nanotomography in a soft X-ray scanning transmission X-ray microscope. Appl Phys Mater Sci Process 92(3):447–452

62. Obst M, Wang J, Hitchcock AP (2009) Soft X-ray spectro-tomography study of cyanobacterial biomineral nucleation. Geobiology 7(5):577–591

63. Hilhorst J, van Schooneveld MM, Wang J, de Smit E, Tyliszczak T, Raabe J, Hitchcock AP, Obst M, de Groot FM, Petukhov AV (2012) Three-dimensional structure and defects in

colloidal photonic crystals revealed by tomographic scanning transmission X-ray microscopy. Langmuir 28(7):3614–3620

64. Berejnov V, Susac D, Stumper J, Hitchcock AP (2013) 3D chemical mapping of PEM fuel cell cathodes by scanning transmission soft X-ray spectrotomography. ECS Trans 50 (2):361–368

65. Johansson GA, Dynes JJ, Hitchcock AP, Tyliszczak T, Swerhone GDW, Lawrence JR (2006) Chemically sensitive 3D imaging at sub 100 nm spatial resolution using tomography in a scanning transmission x-ray microscope. Proc SPIE 6318. doi:10.1117/12.681217

66. Schrlau MG, Falls EM, Ziober BL, Bau HH (2008) Carbon nanopipettes for cell probes and intracellular injection. Nanotechnology 19:015101. doi:10.1088/0957-4484/19/01/015101

67. Wang J, Hitchcock AP, Karunakaran C, Prange A, Franz B, Harkness T, Lu Y, Obst M, Hormes J (2011) 3D chemical and elemental Imaging by STXM spectrotomography. AIP Conf Proc 1365(1):215–218

68. Schmid G, Zeitvogel F, Hao L, Ingino P, Kuerner W, Dynes JJ, Karunakaran C, Wang J, Lu Y, Ayers T, Schietinger C, Hitchcock AP, Obst M (2014) Synchrotron-based chemical nano-tomography of microbial cell-mineral aggregates in their natural, hydrated state. Microsc Microanal 20(2):531–536

69. Schmid G, Zeitvogel F, Hao L, Ingino P, Floetenmeyer M, Stierhof YD, Schroeppel B, Burkhardt CJ, Kappler A, Obst M (2014) 3-D analysis of bacterial cell-(iron)mineral aggregates formed during Fe(II) oxidation by the nitrate-reducing *Acidovorax* sp. strain BoFeN1 using complementary microscopy tomography approaches. Geobiology 12(4):340–361

70. Schmahl G, Rudolph D (1969) Lichtstarke Zoneplatten als abbildende Systeme für weiche Röntgenstrahlung (High power zone plates a image forming systems for soft X-rays). Optik 29:577–585

71. Schmahl G, Rudolph D, Guttmann P, Christ O (1980) Zone-plate X-ray microscopy. Q Rev Biophys 13:297–315

72. McDermott G, Le Gros MA, Knoechel CG, Uchida M, Larabell CA (2009) Soft X-ray tomography and cryogenic light microscopy: the cool combination in cellular imaging. Trends Cell Biol 19(11):587–595

73. Leontowich AF, Hitchcock AP, Tyliszczak T, Weigand M, Wang J, Karunakaran C (2012) Accurate dosimetry in scanning transmission X-ray microscopes via the cross-linking threshold dose of poly(methyl methacrylate). J Synchrotron Radiat 19(Pt 6):976–987

74. Beetz T, Jacobsen C (2003) Soft X-ray radiation-damage studies in PMMA using a cryo-STXM. J Synchrotron Radiat 10(3):280–283

75. Guttmann P, Bittencourt C, Rehbein S, Umek P, Ke XX, Van Tendeloo G, Ewels CP, Schneider G (2012) Nanoscale spectroscopy with polarized X-rays by NEXAFS-TXM. Nat Photonics 6(1):25–29

76. Pereiro E, Nicolas J, Ferrer S, Howells MR (2009) A soft X-ray beamline for transmission X-ray microscopy at ALBA. J Synchrotron Radiat 16(4):505–512

77. Le Gros MA, McDermott G, Cinquin BP, Smith EA, Do M, Chao WL, Naulleau PP, Larabell CA (2014) Biological soft X-ray tomography on beamline 2.1 at the Advanced Light Source. J Synchrotron Radiat 21(6):1370–1377

78. Kaulich B, Bacescu D, Susini J, David C, di Fabrizio E, Morrison GR, Charalambous P, Thieme J, Wilhein T, Kovac J, Cocco D, Salom M, Dhez O, Weitkamp T, Cabrini S, Cojoc D, Gianoncelli A, Vogt U, Podnar M, Zangrando M, Zacchigna M, Kiskinova M (2006) TwinMic – a European twin X-ray microscopy station commissioned at ELETTRA. In: IPAP conference series 7, Himeji

79. Weiss D, Schneider G, Niemann B, Guttmann P, Rudolph D, Schmahl G (2000) Computed tomography of cryogenic biological specimens based on X-ray microscopic images. Ultramicroscopy 84(3–4):185–197

80. Hummel E, Guttmann P, Werner S, Tarek B, Schneider G, Kunz M, Frangakis AS, Westermann B (2012) 3D ultrastructural organization of whole *Chlamydomonas reinhardtii* cells studied by nanoscale soft x-ray tomography. PLoS One 7(12):e53293

81. Larabell CA, Le Gros MA (2004) X-ray tomography generates 3-D reconstructions of the yeast, *Saccharomyces cerevisiae*, at 60-nm resolution. Mol Biol Cell 15(3):957–962

82. Uchida M, Sun Y, McDermott G, Knoechel C, Le Gros MA, Parkinson D, Drubin DG, Larabell CA (2011) Quantitative analysis of yeast internal architecture using soft X-ray tomography. Yeast 28(3):227–236

83. Gu WW, Etkin LD, Le Gros MA, Larabell CA (2007) X-ray tomography of *Schizosaccharomyces pombe*. Differentiation 75(6):529–535

84. Parkinson DY, McDermott G, Etkin LD, Le Gros MA, Larabell CA (2008) Quantitative 3-D imaging of eukaryotic cells using soft X-ray tomography. J Struct Biol 162(3):380–386

85. Carrascosa JL, Chichon FJ, Pereiro E, Rodriguez MJ, Fernandez JJ, Esteban M, Heim S, Guttmann P, Schneider G (2009) Cryo-X-ray tomography of vaccinia virus membranes and inner compartments. J Struct Biol 168(2):234–239

86. Hanssen E, Knoechel C, Klonis N, Abu-Bakar N, Deed S, LeGros M, Larabell C, Tilley L (2011) Cryo transmission X-ray imaging of the malaria parasite, *P. falciparum*. J Struct Biol 173(1):161–168

87. Kapishnikov S, Weiner A, Shimoni E, Guttmann P, Schneider G, Dahan-Pasternak N, Dzikowski R, Leiserowitz L, Elbaum M (2012) Oriented nucleation of hemozoin at the digestive vacuole membrane in *Plasmodium falciparum*. Proc Natl Acad Sci U S A 109(28):11188–11193

88. Hagen C, Guttmann P, Klupp B, Werner S, Rehbein S, Mettenleiter TC, Schneider G, Grunewald K (2012) Correlative VIS-fluorescence and soft X-ray cryo-microscopy/tomography of adherent cells. J Struct Biol 177(2):193–201

89. Clowney EJ, LeGros MA, Mosley CP, Clowney FG, Markenskoff-Papadimitriou EC, Myllys M, Barnea G, Larabell CA, Lomvardas S (2012) Nuclear aggregation of olfactory receptor genes governs their monogenic expression. Cell 151(4):724–737

90. Duke EM, Razi M, Weston A, Guttmann P, Werner S, Henzler K, Schneider G, Tooze SA, Collinson LM (2014) Imaging endosomes and autophagosomes in whole mammalian cells using correlative cryo-fluorescence and cryo-soft X-ray microscopy (cryo-CLXM). Ultramicroscopy 143:77–87

91. Cruz-Adalia A, Ramirez-Santiago G, Calabia-Linares C, Torres-Torresano M, Feo L, Galan-Diez M, Fernandez-Ruiz E, Pereiro E, Guttmann P, Chiappi M, Schneider G, Carrascosa JL, Chichon FJ, Martinez Del Hoyo G, Sanchez-Madrid F, Veiga E (2014) T cells kill bacteria captured by transinfection from dendritic cells and confer protection in mice. Cell Host Microbe 15(5):611–622

92. Cinquin BP, Do M, McDermott G, Walters AD, Myllys M, Smith EA, Cohen-Fix O, Le Gros MA, Larabell CA (2014) Putting molecules in their place. J Cell Biochem 115(2):209–216

93. Holt M, Harder R, Winarski R, Rose V (2013) Nanoscale hard X-ray microscopy methods for materials studies. Annu Rev Mater Res 43(1):183–211

94. Chu YS, Yi JM, De Carlo F, Shen Q, Lee W-K, Wu HJ, Wang CL, Wang JY, Liu CJ, Wang CH, Wu SR, Chien CC, Hwu Y, Tkachuk A, Yun W, Feser M, Liang KS, Yang CS, Je JH, Margaritondo G (2008) Hard-x-ray microscopy with Fresnel zone plates reaches 40nm Rayleigh resolution. Appl Phys Lett 92(10):103119

95. Allahkarami M, Bandla S, Winarski RP, Hanan JC (2014) X-ray nanotomography of a nanofiber: quantitative measurement of diameter fluctuations. Appl Surf Sci 297:9–15

96. Thibault P, Guizar-Sicairos M, Menzel A (2014) Coherent imaging at the diffraction limit. J Synchrotron Radiat 21(Pt 5):1011–1018

97. Takahashi Y, Suzuki A, Zettsu N, Kohmura Y, Senba Y, Ohashi H, Yamauchi K, Ishikawa T (2011) Towards high-resolution ptychographic x-ray diffraction microscopy. Phys Rev B 83 (21):214109

98. Shapiro DA, Yu YS, Tyliszczak T, Cabana J, Celestre R, Chao WL, Kaznatcheev K, Kilcoyne ALD, Maia F, Marchesini S, Meng YS, Warwick T, Yang LL, Padmore HA (2014) Chemical composition mapping with nanometre resolution by soft X-ray microscopy. Nat Photonics 8(10):765–769

99. Holler M, Diaz A, Guizar-Sicairos M, Karvinen P, Färm E, Härkönen E, Ritala M, Menzel A, Raabe J, Bunk O (2014) X-ray ptychographic computed tomography at 16 nm isotropic 3D resolution. Sci Rep 4:1–5

100. Dierolf M, Menzel A, Thibault P, Schneider P, Kewish CM, Wepf R, Bunk O, Pfeiffer F (2010) Ptychographic X-ray computed tomography at the nanoscale. Nature 467 (7314):436–440

101. Zhu ZH, Tyliszczak T, Shiu HW, Shapiro D, Bazylinski DA, Lins U, Hitchcock AP (2015) Magnetic studies of magnetotactic bacteria by soft X-ray STXM and ptychography. J Phys Conf Ser (in review)

102. Beckers M, Senkbeil T, Gorniak T, Reese M, Giewekemeyer K, Gleber SC, Salditt T, Rosenhahn A (2011) Chemical contrast in soft x-ray ptychography. Phys Rev Lett 107 (20):208101

103. Kaznatcheev KV, Karunakaran C, Lanke UD, Urquhart SG, Obst M, Hitchcock AP (2007) Soft X-ray spectromicroscopy beamline at the CLS: commissioning results. Nucl Instrum Methods Phys Res A 582(1):96–99

104. Warwick T, Ade H, Fakra S, Gilles M, Hitchcock A, Kilcoyne D, Shuh D, Tyliszczak T (2003) Further development of soft X-ray scanning microscopy with an elliptical undulator at the Advanced Light Source. Synchrotron Radiat News 16(3):22–27

105. Follath R, Schmidt JS, Weigand M, Fauth K (2010) The X-ray microscopy beamline UE46-PGM2 at BESSY. AIP Conf Proc 1234(1):323–326

106. Kilcoyne D, Ade H, Attwood D, Hitchcock AP, McKean P, Mitchell GE, Monteiro P, Tyliszczak T, Warwick T (2010) A new scanning transmission X-ray microscope at the ALS for operation up to 2500eV. AIP Conf Proc 1234(1):465–468

107. Raabe J, Tzvetkov G, Flechsig U, Boge M, Jaggi A, Sarafimov B, Vernooij MGC, Huthwelker T, Ade H, Kilcoyne D, Tyliszczak T, Fink RH, Quitmann C (2008) PolLux: a new facility for soft x-ray spectromicroscopy at the Swiss Light Source. Rev Sci Instrum 79:113704. doi:10.1063/1.3021472

108. Chao W, Fischer P, Tyliszczak T, Rekawa S, Anderson E, Naulleau P (2012) Real space soft x-ray imaging at 10 nm spatial resolution. Opt Express 20(9):9777–9783

109. Stöhr J (1992) NEXAFS spectroscopy. Springer, Berlin/New York

110. Hahner G (2006) Near edge X-ray absorption fine structure spectroscopy as a tool to probe electronic and structural properties of thin organic films and liquids. Chem Soc Rev 35 (12):1244–1255

111. Najafi E, Cruz DH, Obst M, Hitchcock AP, Douhard B, Pireaux JJ, Felten A (2008) Polarization dependence of the C 1s X-ray absorption spectra of individual multi-walled carbon nanotubes. Small 4(12):2279–2285

112. Jacobsen C, Wirick S, Flynn G, Zimba C (2000) Soft X-ray spectroscopy from image sequences with sub-100 nm spatial resolution. J Microsc 197:173–184

113. Lerotic M, Jacobsen C, Schäfer T, Vogt S (2004) Cluster analysis of soft X-ray spectromicroscopy data. Ultramicroscopy 100(1–2):35–57

114. Leontowich AFG, Hitchcock AP (2012) Experimental investigation of beam heating in a soft X-ray scanning transmission X-ray microscope. Analyst 137(2):370–375

115. Coffey T, Urquhart SG, Ade H (2002) Characterization of the effects of soft X-ray irradiation on polymers. J Electron Spectrosc Relat Phenom 122(1):65–78

116. Howells MR, Beetz T, Chapman HN, Cui C, Holton JM, Jacobsen CJ, Kirz J, Lima E, Marchesini S, Miao H, Sayre D, Shapiro DA, Spence JC, Starodub D (2009) An assessment of the resolution limitation due to radiation-damage in x-ray diffraction microscopy. J Electron Spectrosc Relat Phenom 170(1–3):4–12

117. Wang J, Morin C, Li L, Hitchcock AP, Scholl A, Doran A (2009) Radiation damage in soft X-ray microscopy. J Electron Spectrosc Relat Phenom 170(1–3):25–36

118. Ehrenreich A, Widdel F (1994) Anaerobic oxidation of ferrous iron by purple bacteria, a new type of phototrophic metabolism. Appl Environ Microbiol 60(12):4517–4526

119. Eickhoff M, Obst M, Schroder C, Hitchcock AP, Tyliszczak T, Martinez RE, Robbins LJ, Konhauser KO, Kappler A (2014) Nickel partitioning in biogenic and abiogenic ferrihydrite: the influence of silica and implications for ancient environments. Geochim Cosmochim Acta 140:65–79

120. Kappler A, Schink B, Newman DK (2005) Fe(III) mineral formation and cell encrustation by the nitrate-dependent Fe(II)-oxidizer strain BoFeN1. Geobiology 3(4):235–245

121. Obst M, Schmid G (2014) 3D chemical mapping: application of scanning transmission (soft) X-ray microscopy (STXM) in combination with angle-scan tomography in bio-, geo-, and environmental sciences. In: Kuo J (ed) Electron microscopy. Humana Press, New York, pp 757–781

122. Stewart-Ornstein J, Hitchcock AP, Cruz DH, Henklein P, Overhage J, Hilpert K, Hale JD, Hancock REW (2007) Using intrinsic X-ray absorption spectral differences to identify and map peptides and proteins. J Phys Chem B 111(26):7691–7699

123. Bourdelle F, Benzerara K, Beyssac O, Cosmidis J, Neuville D, Brown GJ, Paineau E (2013) Quantification of the ferric/ferrous iron ratio in silicates by scanning transmission X-ray microscopy at the Fe $L_{2,3}$ edges. Contrib Mineral Petrol 166(2):423–434

124. Midgley PA, Weyland M (2003) 3D electron microscopy in the physical sciences: the development of Z-contrast and EFTEM tomography. Ultramicroscopy 96(3–4):413–431

125. Crowther RA, DeRosier DJ, Klug A (1970) The reconstruction of a three-dimensional structure from projections and its application to electron microscopy. Proc Roy Soc London A 317(1530):319–340

126. Radermacher M (1988) Three-dimensional reconstruction of single particles from random and nonrandom tilt series. J Electron Microsc Tech 9(4):359–394

127. Zeitvogel F, Schmid G, Hao L, Ingino P, Obst M (2014) ScatterJ: an ImageJ plugin for the evaluation of analytical microscopy datasets. J Microsc. doi:10.1111/jmi.12187

128. Hanhan S, Smith AM, Obst M, Hitchcock AP (2009) Optimization of analysis of soft X-ray spectromicroscopy at the Ca 2p edge. J Electron Spectrosc Relat Phenom 173(1):44–49

129. Lerotic M, Mak R, Wirick S, Meirer F, Jacobsen C (2014) MANTiS: a program for the analysis of X-ray spectromicroscopy data. J Synchrotron Radiat 21(5):1206–1212

130. Koprinarov IN, Hitchcock AP, McCrory CT, Childs RF (2002) Quantitative mapping of structured polymeric systems using singular value decomposition analysis of soft X-ray images. J Phys Chem B 106(21):5358–5364

131. Henke BL, Gullikson EM, Davis JC (1993) X-ray interactions – photoabsorption, scattering, transmission, and reflection at E=50–30,000 eV, Z=1–92. At Data Nucl Data Tables 54(2): 181–342

132. Kremer JR, Mastronarde DN, McIntosh JR (1996) Computer visualization of three-dimensional image data using IMOD. J Struct Biol 116(1):71–76

133. Mastronarde DN (1997) Dual-axis tomography: an approach with alignment methods that preserve resolution. J Struct Biol 120(3):343–352

134. Messaoudii C, Boudier T, Sanchez Sorzano CO, Marco S (2007) TomoJ: tomography software for three-dimensional reconstruction in transmission electron microscopy. BMC Bioinf 8:288. doi:10.1186/1471-2105-8-288

135. Schindelin J, Arganda-Carreras I, Frise E, Kaynig V, Longair M, Pietzsch T, Preibisch S, Rueden C, Saalfeld S, Schmid B, Tinevez J-Y, White DJ, Hartenstein V, Eliceiri K, Tomancak P, Cardona A (2012) Fiji: an open-source platform for biological-image analysis. Nat Methods 9(7):676–682

136. Herman GT, Lent A, Rowland SW (1973) ART: mathematics and applications: a report on the mathematical foundations and on the applicability to real data of the algebraic reconstruction techniques. J Theor Biol 42(1):1–32

137. Gilbert P (1972) Iterative methods for the three-dimensional reconstruction of an object from projections. J Theor Biol 36(1):105–117

138. Sommer C, Straehle C, Kothe U, Hamprecht FA (2011) Ilastik: interactive learning and segmentation toolkit. In: Proceedings/IEEE international symposium biomedical imaging. IEEE, Chicago
139. Pettersen EF, Goddard TD, Huang CC, Couch GS, Greenblatt DM, Meng EC, Ferrin TE (2004) UCSF Chimera: a visualization system for exploratory research and analysis. J Comput Chem 25(13):1605–1612
140. Schaedler S, Burkhardt C, Hegler F, Straub KL, Miot J, Benzerara K, Kappler A (2009) Formation of cell-iron-mineral aggregates by phototrophic and nitrate-reducing anaerobic Fe (II)-oxidizing bacteria. Geomicrobiol J 26(2):93–103
141. Berejnov V, Martin Z, West M, Kundu S, Bessarabov D, Stumper J, Susac D, Hitchcock AP (2012) Probing platinum degradation in polymer electrolyte membrane fuel cells by synchrotron X-ray microscopy. Phys Chem Chem Phys 14(14):4835–4843
142. Hitchcock AP, Berejnov V, Lee V, West M, Colbow V, Dutta M, Wessel S (2014) Carbon corrosion of proton exchange membrane fuel cell catalyst layers studied by scanning transmission X-ray microscopy. J Power Sources 266:66–78
143. Susac D, Berejnov V, Hitchcock AP, Stumper J (2011) STXM study of the ionomer distribution in the PEM fuel cell catalyst layers. ECS Trans 41(1):629–635
144. Susac D, Berejnov V, Hitchcock AP, Stumper J (2013) STXM characterization of PEM fuel cell catalyst layers. ECS Trans 50(2):405–413
145. de A Melo LG, Lee V, Susac D, Berejnov V, Stumper J, Botton GA, Hitchcock AP (2014) Effects of sample preparation technique on quantitative analysis of automotive fuel cell catalyst layers. Microsc Microanal 20(S3):472–473
146. Klueglein N, Zeitvogel F, Stierhof YD, Floetenmeyer M, Konhauser KO, Kappler A, Obst M (2014) Potential role of nitrite for abiotic Fe(II) oxidation and cell encrustation during nitrate reduction by denitrifying bacteria. Appl Environ Microbiol 80(3):1051–1061
147. Hitchcock AP, Dynes JJ, Johansson G, Wang J, Botton G (2008) Comparison of NEXAFS microscopy and TEM-EELS for studies of soft matter. Micron 39(6):741–748
148. de Jonge N, Ross FM (2011) Electron microscopy of specimens in liquid. Nat Nanotechnol 6(11):695–704
149. Holtz ME, Yu Y, Gao J, Abruna HD, Muller DA (2013) In situ electron energy-loss spectroscopy in liquids. Microsc Microanal 19(4):1027–1035
150. Hitchcock AP, Berejnov V, Lee V, Susac D, Stumper J (2014) In situ methods for analysis of polymer electrolyte membrane fuel cell materials by soft X-ray scanning transmission x-ray microscopy. Microsc Microanal 20(S3):1532–1533
151. Guay D, Stewart-Ornstein J, Zhang X, Hitchcock AP (2005) In situ spatial and time-resolved studies of electrochemical reactions by scanning transmission X-ray microscopy. Anal Chem 77(11):3479–3487
152. Hitchcock AP, Qin Z, Rosendahl SM, Lee V, Hosseinkhannazer H (2015) In situ electrochemical deposition of Cu studied with scanning transmission x-ray microscopy. J Phys Conf Ser (in press)
153. Hoshino M, Uesugi K, Pearson J, Sonobe T, Shirai M, Yagi N (2011) Development of an X-ray real-time stereo imaging technique using synchrotron radiation. J Synchrotron Radiat 18(Pt 4):569–574
154. Helfen L, Baumbach T, Mikulík P, Kiel D, Pernot P, Cloetens P, Baruchel J (2005) High-resolution three-dimensional imaging of flat objects by synchrotron-radiation computed laminography. Appl Phys Lett 86(7):071915
155. Helfen L, Xu F, Suhonen H, Cloetens P, Baumbach T (2013) Laminographic imaging using synchrotron radiation – challenges and opportunities. J Phys Conf Ser 425(19):192025
156. Saghi Z, Holland DJ, Leary R, Falqui A, Bertoni G, Sederman AJ, Gladden LF, Midgley PA (2011) Three-dimensional morphology of iron oxide nanoparticles with reactive concave surfaces. A compressed sensing-electron tomography (CS-ET) approach. Nano Lett 11(11):4666–4673

157. Goris B, Van den Broek W, Batenburg KJ, Mezerji HH, Bals S (2012) Electron tomography based on a total variation minimization reconstruction technique. Ultramicroscopy 113:120–130
158. Midgley P (2014) Electron tomography for nanoscale materials science. In: Plenary presentation at the 2014 international microscopy conference, Prague
159. Reader AJ, Verhaeghe J (2014) 4D image reconstruction for emission tomography. Phys Med Biol 59(22):R371–R418
160. Haberfehlner G, Orthacker A, Albu M, Li J, Kothleitner G (2014) Nanoscale voxel spectroscopy by simultaneous EELS and EDS tomography. Nanoscale 6(23):14563–14569
161. Quaroni L, Obst M, Nowak M, Zobi F (2015) Three-dimensional mid-infrared tomographic imaging of endogenous and exogenous molecules in a single intact cell with subcellular resolution. Angew Chem Int Ed 54(1):318–322

X-Ray Photon Correlation Spectroscopy for the Characterization of Soft and Hard Condensed Matter

3

Oier Bikondoa

Contents

1   Definition of the Topic

X-ray photon correlation spectroscopy (XPCS) allows to access a wide variety of dynamic phenomena at the nanoscale by studying the temporal correlations among photons that are scattered by a material when it is illuminated using a coherent X-ray beam. Here, we describe how XPCS is used to study the dynamics of soft and hard condensed matter, review the recent literature and briefly discuss the future of the

O. Bikondoa (✉)
Department of Physics, University of Warwick, Coventry, UK

XMaS, The UK-CRG Beamline, ESRF – The European Synchrotron, Grenoble, France
e-mail: oier.bikondoa@esrf.fr

technique, especially in the context of the emerging diffraction-limited storage rings and X-ray free electron laser sources.

2 Overview

When a disordered system is illuminated with coherent light, the interference between the scattered waves gives rise to a speckle pattern. The speckle pattern depends on the exact arrangement of the scatterers. Information about the dynamics of the system can be obtained by analysing the temporal correlations of the speckle intensities. This is the basis of the X-ray photon correlation spectroscopy (XPCS) technique, which is the counterpart of photon correlation spectroscopy (PCS) using coherent X-rays instead of laser light. XPCS is one of the main techniques to probe the slow nanoscale fluctuations and dynamics of soft and hard condensed matter systems. If a coherent X-ray beam from a third-generation synchrotron source is used as the illumination probe, then, depending on the sample and the scattering geometry, the dynamics of materials on timescales ranging from microseconds to thousands of seconds and length scales from microns down to nanometres can be accessed. At present, the main limitations of XPCS are the relatively low coherent flux of existing X-ray sources and the limited speed of X-ray area detectors. The upcoming new X-ray sources (diffraction-limited storage rings and X-ray free electron lasers) will enable to measure dynamics at large momentum transfer values with tenths of picoseconds time resolution.

The principles, experimental methodology and recent application of XPCS are reviewed here, followed by a brief discussion about the possibilities that the new X-ray sources will create for future XPCS experiments.

3 Introduction

Scattering experiments based on coherent X-ray beams have opened new possibilities for the investigation of soft and hard condensed matter (reviews and relevant bibliography can be found in [130, 134, 161, 188, 189, 240]). When a rough surface or an inhomogeneous medium is illuminated using coherent light, the pattern in the far field generated by the scattered light shows a grainy intensity distribution called speckle [47]. The speckle pattern consists of distinct bright and dark zones of irregular shapes. This characteristic pattern arises from the interference between the light that is scattered from different parts of the illuminated area; strong intensities are observed at those points in the far field where the interference is constructive, while weak intensities occur when the interference is destructive. The speckle pattern depends on the characteristics of the illuminating light and the length scale of the inhomogeneities: for example, speckle does not occur if the illuminating probe is incoherent or the scattering medium is homogeneous or smooth at the scale of the wavelength of the illuminating light. The speckle pattern also depends on the exact morphology of the illuminated area, and if the scattering medium evolves with time,
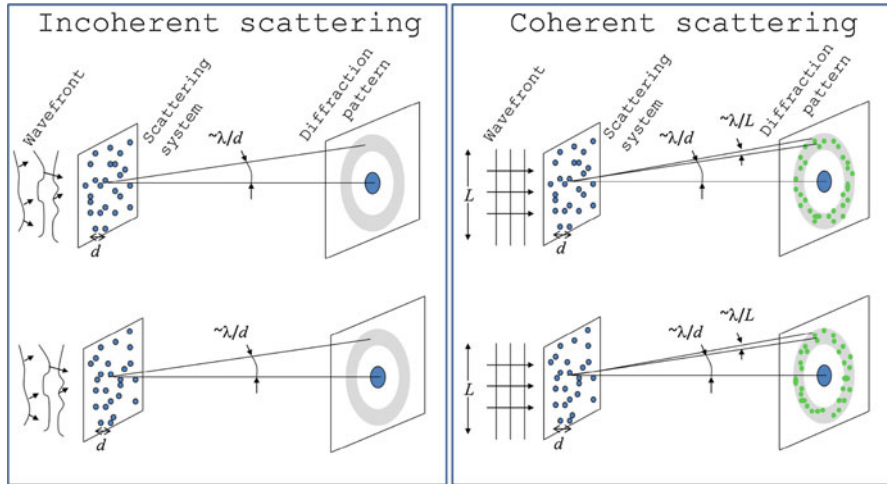
Fig. 3.1 Schematic representation of the difference between the scattering of incoherent or coherent radiation by a disordered medium. When using incoherent radiation, the diffracted pattern gives rise to a continuous diffraction ring. If the arrangement of the scatterers changes but their ensemble-averaged properties are not modified, the diffraction pattern is alike. However, with a coherent beam, the diffraction ring is composed of speckles. The envelope of the speckles corresponds to the diffraction ring obtained with incoherent radiation. If the arrangement of the scatterers changes, the speckle pattern will be modified, even if the ensemble-averaged properties do not change

the speckle pattern will also change and the intensity of the speckles will fluctuate (see Fig. 3.1). Information about the underlying dynamics of the evolving medium can be obtained from the study of the speckle intensity fluctuations. This is the basis of the X-ray photon correlation spectroscopy (XPCS) technique, also known as X-ray intensity fluctuation spectroscopy (XIFS) [26, 53, 78, 80, 126, 215, 220, 233, 234]. XPCS is the counterpart of dynamic light scattering (DLS) or photon correlation spectroscopy (PCS) [17, 37, 180] in the X-ray region. Although the basic aspects of XPCS and DLS are the same, there are several significant differences. With X-rays, shorter distances than with visible light can be probed. Furthermore, multiple scattering effects are not as important as with visible light and can usually be neglected. However, X-ray sources are much weaker than lasers and XPCS is a signal-limited technique.

We shall analyse these aspects separately. In this introduction, we describe the origin of static speckle (Sect. 3.1), its statistical properties, the influence of the illuminating probe on the speckle and its size and shape (Sect. 3.2). The relationship between the dynamics of an evolving medium and the speckle intensity fluctuations, which is the basis of the XPCS technique, is described in Sect. 3.3 and illustrated with an example (Sect. 3.3.1). The functional shape of the autocorrelation function is considered in Sect. 3.3.2, and the case of XPCS for non-equilibrium systems is treated in Sect. 3.3.3.

3.1   Static Speckle

Speckles are easily observed with highly coherent illumination. When a laser pointer impinges on a surface that is rough at the scale of the wavelength—such as a piece of paper or a wall—the illuminated spot is not uniform and has areas with very high and very low (or zero) intensities, randomly arranged. A simulated speckle pattern is shown in Fig. 3.2. This characteristic effect arises from the interference between the random contributions from many scattering points. The same effect is observed if coherent light traverses a medium with refractive index fluctuations at the scale of the wavelength, yet speckles are not observed if the illumination is incoherent. The origin and statistical properties of speckle patterns can be understood analytically studying the scattering by a disordered system of particles.

We consider a system of N particles that is illuminated by a coherent monochromatic wave with amplitude E_0 and wave vector $\vec{k}_i$. The total scattered field measured at a point $\vec{R}$ far from the system is obtained by summing up all the wavelets scattered by the individual particles and taking into account the phase shifts between them. In a quantum mechanics formalism, this procedure is equivalent to a superposition of the scattering probability amplitudes. In the case of individual scatterers, the instantaneous total scattered field at momentum transfer $\vec{q} = \vec{k}_f - \vec{k}_i$ is given by:

$$E\left(\vec{q},t\right) = -E_0 \frac{\exp\left[i\left(\vec{k}_i \cdot \vec{R} - wt\right)\right]}{\left|\vec{R}\right|} \sum_{j=1}^{N} b_j\left(\vec{q},t\right)\exp\left[-i\,\vec{q}\cdot\vec{R}_j(t)\right] \quad (3.1)$$

Fig. 3.2 Simulated speckle pattern. The simulation is done by summing up many phasors with random phases (Image taken from Wikimedia Commons)
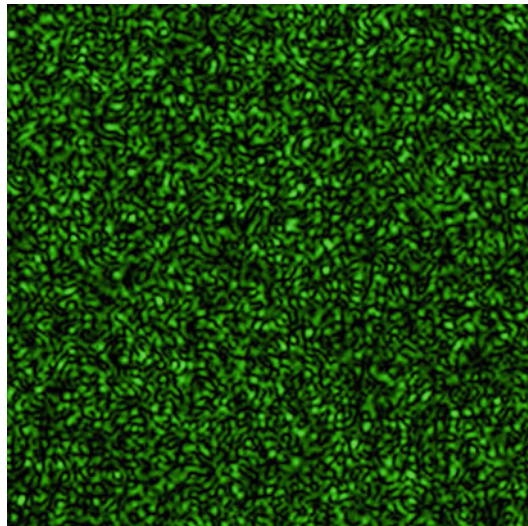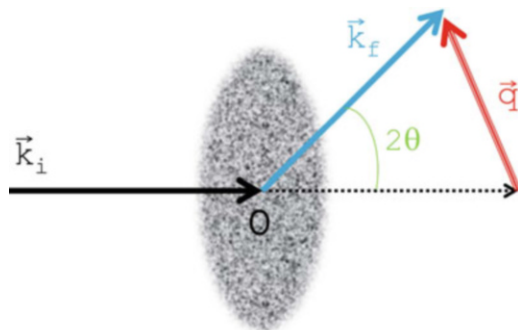
Fig. 3.3 Scattering geometry. A sample composed of N independent scatterers is illuminated by electromagnetic radiation of wavelength λ and propagation vector $\vec{k}_i$. The radiation is scattered at an angle 2θ and has a propagation vector $\vec{k}_f$. The scattering is assumed to be elastic (i.e. $|\vec{k}_i| = |\vec{k}_f| = 2\pi/\lambda$). The scattering vector $\vec{q}$ is defined as $\vec{q} \equiv \vec{k}_f - \vec{k}_i$. With this definition, $\left|\vec{q}\right| = \frac{4\pi}{\lambda}\sin\theta$

The prefactor $E_0 \dfrac{\exp\left[i\left(\vec{k}_i \cdot \vec{R} - wt\right)\right]}{\left|\vec{R}\right|}$ corresponds to the amplitude scattered by a free electron (other prefactors have been omitted and polarisation is not considered). The negative sign accounts for the π phase shift. $\vec{q} = \vec{k}_f - \vec{k}_i$ is the scattering vector, $\vec{k}_f$ being the wave vector of the scattered wave (Fig. 3.3). w is the angular frequency of the incoming wave. $b_j(\vec{q}, t)$ is the amplitude of the field scattered by particle j, which in general can be time dependent. $\vec{R}_j(t)$ is the position of the centre of mass of particle j at time t. For clarity, in the following we omit the prefactors in Eq. (3.1). The instantaneous total scattered field at point $\vec{q}$ in the reciprocal space can be expressed as:

$$E\left(\vec{q}, t\right) = \sum_{j=1}^{N} b_j\left(\vec{q}, t\right) \exp\left[-i\,\vec{q} \cdot \vec{R}_j(t)\right] \tag{3.2}$$

Equation (3.2) represents the resultant of the sum of N phasors of the form Ae^{ϕ}, A and ϕ being the (time and momentum transfer dependent) amplitude and phase, respectively.[1] If $b_j(q, t)$ or the position of the scatterers, $\vec{R}_j(t)$, changes with time,

---

[1] The derivation of Eqs. (3.2) and (3.3) from the scattering of a set of N particles is very adequate to describe, for example, the scattering by a colloidal system. For other systems, such as surfaces, it may be more adequate to consider a continuous electron density and replace the summation in Eq. (3.2) by an integral. In that case, the instantaneous total electric field is

$$E\left(\vec{q}, t\right) = \int \rho\left(\vec{r}', t\right) \exp\left[-i\,\vec{q} \cdot \vec{r}'(t)\right] d\vec{r}'$$

then the total scattered field at $\vec{q}$ (Eq. (3.2)) fluctuates. The electric fields $E(\vec{q}, t)$ and $E(\vec{q}, t + \Delta t)$ will still be correlated if the time difference Δt is small. However, for long time differences, the fluctuations of the electric field become completely uncorrelated. Information about the dynamics of the scatterers is encoded in these fluctuations and can be extracted using correlation functions (see Sect. 3.3). The square of the instantaneous electric field yields the instantaneous intensity:

$$I\left(\vec{q}, t\right) = \left|E\left(\vec{q}, t\right)\right|^2 = \left|\sum_{j=1}^{N} \exp\left[-i\,\vec{q}\cdot\vec{R}_j(t)\right]\right|^2 \tag{3.3}$$

Both the instantaneous intensity and the instantaneous electric field are extremely sensitive to any slight changes in position. That is why the speckle pattern depends on the exact arrangement of the scatterers. However, it has to be taken into account that in an experiment the measurement of the intensity is done over an acquisition time T. Thus, the measured intensity does not exactly correspond to that of Eq. (3.3) but to a time average of the instantaneous intensity (I_{inst}) over the acquisition time T: $I_{exp}(\vec{q}, t) = \langle I_{inst}(\vec{q}, t)\rangle_T$. If the system is static or it fluctuates at timescales much larger than the acquisition time, then $I_{exp} \sim I_{inst}$. However, if the system fluctuations are much faster than the acquisition time, the intensity fluctuations will be averaged during the measurement and I_{exp} will be featureless (in time).

A last remark: when the intensity is measured, information about the phase is lost. This is the so-called phase problem of crystallography. Phase retrieval techniques could be applied to retrieve the positions of the scatterers from the speckle pattern. This problem is beyond the scope of this chapter. An extensive set of references can be found in [161].

3.2   Statistical Properties of Static Speckle Patterns

The speckle pattern not only contains information about the arrangement of the scatterers but also provides information about the light that produced it, namely, the degree of coherence and the illuminated area. The degree of coherence can be estimated studying the first-order statistical properties (i.e. at a single point in space) of the intensities.[2] For fully coherent illumination, if the number of phasors that contribute to the speckle pattern is very large, their phases are uniformly distributed over $(-\pi, \pi)$ and their amplitudes and phases are statistically independent, then the speckle pattern follows negative exponential statistics and the probability density function of the intensity is given by [74]:

$$p(I) = \left(1/\bar{I}\right)\mathrm{e}^{\left(-I/\bar{I}\right)} \tag{3.4}$$

---

[2]This is also referred to as 'second-order statistical properties of the fields' in the literature.

The overline denotes a statistical average. $\overline{I}$ is the mean of the intensity and the standard deviation is[3] $\sigma = \sqrt{\left(\overline{I^2} - \overline{I}^2\right)} = \overline{I}$. Equation (3.4) indicates that in a speckle pattern obtained using fully coherent illumination, the most probable value for the intensity at any point in the speckle pattern is zero. To quantify how strong the speckles are compared with the average intensity, the contrast β is defined:

$$\beta = \frac{\sigma_I}{\overline{I}} \tag{3.5}$$

For partially coherent illumination, either because the illumination volume is larger than the coherence volume or because the illumination is not fully coherent, the speckle pattern can be thought as arising from the sum of N independent speckle patterns. The probability distribution for a speckle pattern resulting from the intensity sum of N independent speckle patterns, all with identical average intensity I_0, is described by a *gamma* density function of order N [47, 74, 151]:

$$p_N(I) = \frac{N^N I^{N-1}}{\Gamma(N)\overline{I}} e^{\left(-N\frac{I}{\overline{I}}\right)} \tag{3.6}$$

N is the number of coherence volumes. $\overline{I} = N\,I_0$ is the total mean intensity. The standard deviation is $\sigma = \frac{\langle I \rangle}{\sqrt{N}}$, and the contrast is $\beta = \left(\frac{1}{N}\right)$. Equation (3.4) is the limiting case of (3.6) when $N \rightarrow 1$. Equations (3.4) and (3.6) show that for fully coherent illumination, the contrast is equal to unity, and for incoherent illumination, $N \rightarrow \infty$ and the contrast is zero. The contrast gives an estimation of the sharpness of the speckles.

The probability density functions (3.4) and (3.6) correspond to two ideal cases. In general, the illumination will not be fully coherent, and the speckle pattern will not be the sum of many patterns with the same average intensity either. For example, in some cases, the speckle pattern can be superimposed to a constant intensity background. Abernathy et al. showed experimentally that by subtracting the contribution of this background, it is possible to obtain a good quantitative estimation of the contrast value [1]. Comprehensive calculations about the statistics of speckle patterns in different situations can be found in [74]. For most of the practical cases in XPCS, the contrast can be estimated employing Eq. (3.6) and combining it, if necessary, with the methods introduced in [1].

3.2.1   Size and Shape of Speckles

The angular width of the speckles produced by an object illuminated with a fully coherent beam of size L is [240]:

---

[3]The qth moments of the distribution (3.4) are given by $\overline{I^q} = \overline{I}^q q!$. Thus, the second moment is $\overline{I^2} = 2\overline{I}^2$. For more details, see [74].

$$\theta_s \sim \frac{\lambda}{L} \tag{3.7}$$

where L is the size of the aperture delimiting the beam (Fig. 3.1). In general, the structure (size and shape) of the speckle pattern depends on the scattering medium and the bandwidth of the light [47]. To obtain information about the size and shape of the speckles, the higher-order statistical properties of speckles (i.e. at two or more points in space) must be studied. One method is by using correlation functions in terms of two points (x, y) or radial and azimuthal scattering angles [47]. An example of this procedure for X-ray-generated speckle patterns can be found in [1]. Abernathy and coworkers used a normalised two-point correlation function of the intensities at two different points $\vec{r}_1$ and $\vec{r}_2$ in the small-angle scattering approximation $|\vec{q}| = k|r|z$ ($k = 2\pi/\lambda$ being the magnitude of the wave vector and z the sample-to-detector distance) [1]:

$$C\left(\vec{r}_1, \vec{r}_2\right) = \frac{\overline{I\left(\vec{r}_1\right)I\left(\vec{r}_2\right)}}{\overline{I\left(\vec{r}_1\right)}\,\overline{I\left(\vec{r}_2\right)}} - 1 \tag{3.8}$$

where the ensemble averages were done over a set of samples. The contrast of the speckle pattern is obtained from the value of the equal point correlation $\beta(\vec{r}) = C(\vec{r}, \vec{r})$. $C(\vec{r}_1, \vec{r}_2)$ is a function that has a maximum when $\vec{r}_1 = \vec{r}_2$ and decays with increasing $|\vec{r}_1 - \vec{r}_2|$ distance. The sizes of the speckles were obtained from the width of $C(\vec{r}_1, \vec{r}_2)$ and were found to be q-dependent. If the bandwidth of the illumination is non-zero, the magnitude of the wave vector has a certain width $\Delta k = 2\pi/(\Delta\lambda)$ and the speckles are elongated in the radial direction.

Sinha, Tolan and Gibaud [221] have developed a general formalism to describe the scattering of partially coherent X-rays by matter in the kinematical approximation. They calculate how the mutual coherence function is propagated via the scattering from an aperture before the sample to an exit aperture. This formalism has been used to calculate speckle patterns from rough surfaces and analyse the effects of the beam coherence [237].

3.3 X-Ray Photon Correlation Spectroscopy

If the sample structure varies with time, the corresponding speckle pattern will also reflect this time dependent variation. The speckle intensity fluctuations provide information about the dynamics of the system. Such information can be accessed by measuring the temporal intensity autocorrelation function $g^{(2)}(\vec{q}, \Delta t)$ defined by:

$$g^{(2)}\left(\vec{q}, \Delta t\right) \equiv \frac{\overline{\langle I_t I_{t+\Delta t}\rangle}}{\overline{\langle I_t\rangle}^2} = \frac{\overline{\langle E_t^* E_{t+\Delta t}^* E_t E_{t+\Delta t}\rangle}}{\overline{\left\langle |E_t|^2\right\rangle}^2} \tag{3.9}$$

The superscript $^{(2)}$ indicates that $g^{(2)}$ is a temporal correlation function of order two on the electric fields, i.e. four field variables are correlated at two different times. I_t is

the intensity at time t and at momentum transfer $\vec{q}$, $I(\vec{q}, t)$ (Eq. (3.3)). For clarity, the quantities between brackets have been removed. Δt is the time delay. The brackets $\langle\rangle$ denote a time average. The bar $\overline{\langle\rangle}$ indicates the ensemble average over wave vectors with equivalent $|\vec{q}|$ momentum transfer value and for which it is expected that the correlations are statistically equivalent.

For short time delays, the value of Eq. (3.9) is high because the structure will still be similar to its initial configuration. As the structure evolves, the correlation will decrease, and at long delay times (compared with the period of the fluctuations), the correlation with respect to the initial state will be lost. For a non-periodic function, the time correlation function will decay from its initial value $\langle I^2 \rangle$ to $\langle I \rangle^2$ [17]. How the correlation decays is determined by the dynamics of the system. To fit this decay and obtain information about the dynamics and the equations of motion, models based on assumptions about the system under study are used.

A very important case occurs when the total scattered field can be considered to arise from the sum of a large number of statistically independent subregions. In that case, the central limit theorem of statistics (see, e.g. Ref. [73]) implies that the total scattered field, which is the sum of many independent scatterers, is a random variable with a Gaussian probability distribution, and the time correlation function of the intensity $g^{(2)}(\vec{q}, \Delta t)$ can be expressed in terms of the normalised time correlation of the electric field $g^{(1)}(\vec{q}, \Delta t)$ [17, 180]:

$$g^{(2)}\left(\vec{q}, \Delta t\right) = 1 + \beta\left(\vec{q}\right)\left|g^{(1)}\left(\vec{q}, \Delta t\right)\right|^2 \tag{3.10}$$

with

$$g^{(1)}\left(\vec{q}, \Delta t\right) \equiv \frac{\overline{\langle E_t E_{t+\Delta t}\rangle}}{\overline{\langle E_t\rangle}^2} \tag{3.11}$$

The optical contrast $\beta\left(\vec{q}\right) = \frac{\sigma^2}{\langle I \rangle}$ in Eq. (3.10) is a factor that is used to account for the degree of coherence of the incident radiation, depends also on the experimental set-up[4] and is given by the variance of the intensity (σ^2) divided by its mean value [73]. It varies between 0 (completely incoherent radiation) and 1 (completely coherent radiation), and it corresponds, roughly, to one over the number of coherence volumes in the scattering volume [234] (see also Sect. 3.2). Equation (3.10) is often called the 'Siegert relation' in the literature. Using Eqs. (3.2), (3.10) and (3.11), the

---

[4]This separation of the sample properties and the coherence properties of the beam is only valid under certain conditions: the coherence length of the light must be larger than the correlation length of the sample, and the scattering volume has to be larger than the correlation length of the sample fluctuations too. Especially in grazing incidence geometry, these conditions may not be fulfilled and a more elaborate treatment is needed. Gutt et al. have developed a rigorous treatment of the effects of partial coherence and detector resolution on the intensity autocorrelation function measured by XPCS [86].

Siegert relation can be rewritten in terms of the intermediate scattering function of the sample, $S(\vec{q}, \Delta t)$:

$$g^{(2)}\left(\vec{q}, \Delta t\right) = \frac{\overline{\langle I_t I_{t+\Delta t}\rangle}}{\overline{\langle I_t\rangle^2}} = 1 + \beta\left(\vec{q}\right)\left|\frac{S\left(\vec{q}, \Delta t\right)}{S\left(\vec{q}\right)}\right|^2 \qquad (3.12)$$

where

$$S\left(\vec{q}, \Delta t\right) = \sum_{J}^{N}\sum_{k}^{N}\left\langle b_j\left(\vec{q}, 0\right)b_k^*\left(\vec{q}, \Delta t\right)\exp\left\{-i\ \vec{q}\cdot\left[\vec{R}_j(0) - \vec{R}_j(\Delta t)\right]\right\}\right\rangle \qquad (3.13)$$

or alternatively,

$$S\left(\vec{q}, \Delta t\right) = \frac{1}{N}\left\langle \rho\left(\vec{q}, 0\right)\rho\left(-\vec{q}, \Delta t\right)\right\rangle \qquad (3.14)$$

if a continuous electron density is considered. N is the number of scatterers and $S(\vec{q}, \Delta t)|_{\Delta t=0} = S(\vec{q})$ is the static structure factor. $S(\vec{q}, \Delta t)$, the intermediate scattering function, is the spatial Fourier transform of the Van Hove correlation function [239], and its power spectrum (i.e. the temporal Fourier transform of $S(\vec{q}, \Delta t)$) yields the dynamic structure factor $S(\vec{q}, w)$. The dynamic structure factor contains information about the interparticle correlations and their time evolution [180]. $F(\vec{q}, \Delta t) = S(\vec{q}, \Delta t)/S(\vec{q})$ is called the normalised intermediate scattering function. The Siegert relation (3.10) yields only the modulus of $F(\vec{q}, \Delta t)$ so its phase is undetermined. The real and complex part of $F(\vec{q}, \Delta t)$ can, in principle, be obtained in a heterodyne XPCS experiment, in which the scattered beam is mixed with a static reference signal. For details, see [135, 136].

We remark that the Siegert relation is not always valid: it is obtained under the assumption that the electron density follows Gaussian statistics and that using the central limit theorem is justified. For example, for very diluted systems, the number of scatterers may be too small to apply the central limit theorem. However, the conditions to use Eq. (3.10) are met in most of the practical cases [17].

3.3.1 Example: System of Noninteracting Monodisperse Particles Undergoing Brownian Motion

Let's illustrate the use of XPCS with an example and determine which kind of information can be derived from it. Let's consider a dynamic system of identical particles undergoing Brownian motion in a dilute suspension. Using Eqs. (3.2) and (3.11), $g^{(1)}(\vec{q}, \Delta t)$ can be expressed as:

$$g^{(1)}\left(\vec{q},\Delta t\right) = \frac{\sum_j^N \sum_k^N \left\langle b_j\left(\vec{q},0\right) b_k^*\left(\vec{q},\Delta t\right) \exp\left\{-i\vec{q}\cdot\left[\vec{R}_j(0)-\vec{R}_j(\Delta t)\right]\right\}\right\rangle}{\sum_j^N \sum_k^N \left\langle b_j\left(\vec{q},0\right) b_k^*\left(\vec{q},0\right) \exp\left\{-i\vec{q}\cdot\left[\vec{R}_j(0)-\vec{R}_k(0)\right]\right\}\right\rangle}$$

$$(3.15)$$

Considering identical, particles that do not change shape Eq. (3.15) simplifies to:

$$g^{(1)}\left(\vec{q},\Delta t\right) = \frac{\sum_j^N \sum_k^N \left\langle \exp\left\{-i\vec{q}\cdot\left[\vec{R}_j(0)-\vec{R}_j(\Delta t)\right]\right\}\right\rangle}{\sum_j^N \sum_k^N \left\langle \exp\left\{-i\vec{q}\cdot\left[\vec{R}_j(0)-\vec{R}_k(0)\right]\right\}\right\rangle}$$

$$(3.16)$$

For noninteracting particles, the cross terms $j \neq k$ in Eq. (3.16) average to zero because their positions are uncorrelated. Using Eqs. (3.10) and (3.12), the intermediate scattering function is:

$$S\left(\vec{q},\Delta t\right) = \left\langle e^{i\vec{q}\cdot\Delta\vec{R}(\Delta t)}\right\rangle$$

$$(3.17)$$

with $\Delta\vec{R}(\Delta t) \equiv \vec{R}(\Delta t) - \vec{R}(0)$. Thus, for this particular case, an XPCS experiment in which $S(\vec{q},\Delta t)$ is obtained would yield information about the average motion of a single particle. For particles in Brownian motion, the probability that a particle is found between $\vec{R}$ and $\vec{R} + d\vec{R}$ after a certain time t is a Gaussian probability distribution [17, 180]:

$$P\left[\Delta\vec{R}(\Delta t)\right] = \left[\frac{3}{2\pi\langle\Delta R^2(\Delta t)\rangle}\right]^{3/2} \exp\left[-\frac{3\Delta R^2(\Delta t)}{2\langle\Delta R^2(\Delta t)\rangle}\right]$$

$$(3.18)$$

Then, using Eq. (3.18) to evaluate Eq. (3.16), one obtains:

$$g^{(1)}\left(\vec{q},\Delta t\right) = \exp\left[-\frac{q^2}{6}\langle\Delta R^2(\Delta t)\rangle\right] = \exp(-q^2 D_0 \Delta t)$$

$$(3.19)$$

D_0, the diffusion constant for a sphere of radius a moving in a medium of viscosity η, is given by the Stokes-Einstein equation:

$$D_0 = \frac{k_B T}{6\pi\eta a}$$

$$(3.20)$$

k_B and T are Boltzmann's constant and the temperature, respectively. Thus, by measuring the intensity-intensity autocorrelation (3.9) (see also Fig. 3.4) and using
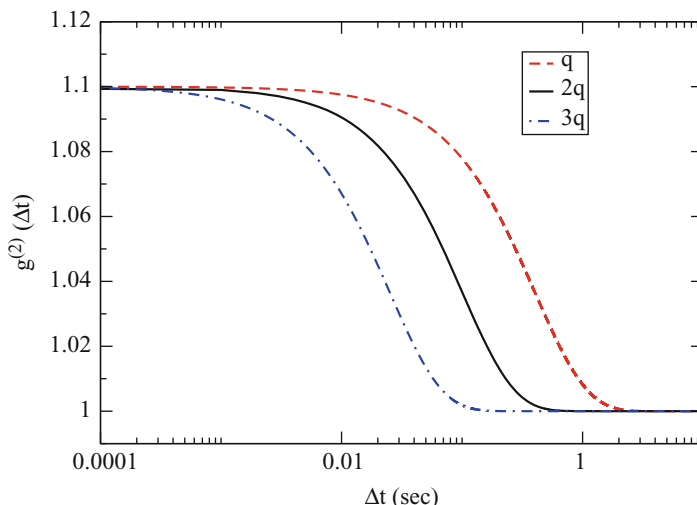
Fig. 3.4 Simulated correlation function of a diffusive system at three different $|\vec{q}|$ momentum transfer values

the Siegert relation (3.10) and (3.19), one can determine any of the parameters in Eq. (3.20), if all the other parameters are known. These relations are often used to determine either the radii of unknown colloidal particles or the viscosity of the fluid.

When the interparticle interaction cannot be neglected or when the system is polydisperse, the two approximations that were made to simplify Eq. (3.15) and obtain Eq. (3.19) are no longer valid. For a polydisperse system of spherical particles, the particles of different sizes will behave differently; the intermediate scattering function becomes a sum of exponentials corresponding to the different particles and weighted by the intensities scattered by each of them [180]. This sum may in general deviate from a perfect single exponential decay.

In concentrated systems, the interactions between the particles cannot be neglected and the motions of the different particles can be strongly correlated. In such systems, the diffusion coefficient can have a very marked dependence on $\vec{q}$, and the behaviour of the intermediate scattering function may differ from a single exponential decay. To describe such systems, the diffusion coefficient D_0 is often replaced by a coefficient $D(\vec{q}, t)$ that depends on the scattering vector and the time [78].

3.3.2 Functional Shape of the Correlation Function

In the example of Sect. 3.3.1 where we have studied the Brownian motion of free particles, the autocorrelation function decays exponentially, Eq. (3.19). However, this is not a general behaviour. The functional shape of the autocorrelation function can deviate from a pure decaying exponential. Stretched or compressed exponential behaviours of the autocorrelation function are observed in complex dynamics of

condensed matter like capillary waves or glass-forming liquids [148]. Often, the decay is described by an empirical equation, the Kohlrausch-Williams-Watts function:

$$c(t) \propto e^{-(t/\Delta t_{cor})^{\gamma}} \tag{3.21}$$

Δt_{cor} is the correlation time. γ is the Kohlrausch-Williams-Watts exponent in the decaying function. $\gamma > 1$ ($\gamma < 1$) implies that the decay is faster (slower) than purely exponential [148]. Other forms of time correlation functions also occur. For example, Gaussian-type correlation functions of the form:

$$c(t) \propto e^{(-t^2/\tau^2)} \tag{3.22}$$

arise in the study for perfect gas dynamics [171] or sums of exponentials:

$$c(t) = \sum_i a_i e^{(-t/\tau_i)} \tag{3.23}$$

are observed in processes where many different timescales are involved [183]. A discussion about correlation functions and scattering experiments, which is especially relevant for measurements of dynamic properties, can be found in [171].

3.3.3 XPCS of Non-equilibrium Systems

For non-equilibrium systems (i.e. for systems with average properties changing with time), the time average in Eq. (3.9) cannot be performed because the dynamics are evolving and may strongly depend on the sample age. For those systems the evolution of the correlation function can still be captured by using a more general expression than Eq. (3.9), namely, a two-time correlation function (TTCF) [28]:

$$\Gamma\left(\vec{Q}, t_1, t_2\right) = \frac{\overline{I_{t_1} I_{t_2}} - \overline{I}_{t_1} \overline{I}_{t_2}}{\sqrt{\overline{I_{t_1}^2} - \overline{I}_{t_1}^2} \sqrt{\overline{I_{t_2}^2} - \overline{I}_{t_2}^2}} \tag{3.24}$$

Γ is the autocovariance of the intensity normalised by its standard deviation. Different correlation functions are also used [235]:

$$G\left(\vec{Q}, t_1, t_2\right) = \frac{\overline{I_{t_1} I_{t_2}}}{\overline{I}_{t_1} \overline{I}_{t_2}} \tag{3.25}$$

or

$$C\left(\vec{Q}, t_1, t_2\right) = \overline{D\left(\vec{Q}, t_t\right) D\left(\vec{Q}, t_2\right)} \tag{3.26}$$

where

$$D\left(\vec{Q},t\right) = \frac{I_t - \bar{I}_t}{\bar{I}_t} \tag{3.27}$$

For random Gaussian fluctuations the standard deviation equals the average intensity [28, 139]. Therefore, $C(\vec{q}, t_1, t_2) = \Gamma(\vec{q}, t_1, t_2) - 1$ and the different correlation functions (Eqs. (3.24), (3.25) and (3.26)) are equivalent.

The TTCF of non-equilibrium systems are usually analysed using an alternative coordinate system that was introduced in [28]. The sample age is taken along the $t_1 = t_2$ diagonal and defined as $t_{\text{age}} := \frac{t_2 + t_1}{2}$. The delay time Δt is taken along lines perpendicular to the $t_1 = t_2$ diagonal and is given by $\Delta t := |t_2 - t_1|$ (see Fig. 3.5). A cut of the TTCF along these perpendicular lines corresponds to values with constant sample age and is symmetric by construction around the $\Delta t = 0$ value. One-time correlation functions (OTCF) are extracted from the TTCFs for a given sample age or for limited age intervals where the dynamics are quasi-stationary by averaging the terms along the age diagonal [65]. For a series of intensities $I_0, I_1 \ldots$ measured at times $t_0, t_1, \ldots, t_N$, the terms in the OTCF at age t_a have the form $I_{t_a - \Delta t} I_{t_a + \Delta t}$. Except for the delay $\Delta t = 0$, the terms in the OTCF have no direction relationship with the intensity measured at age t_a.
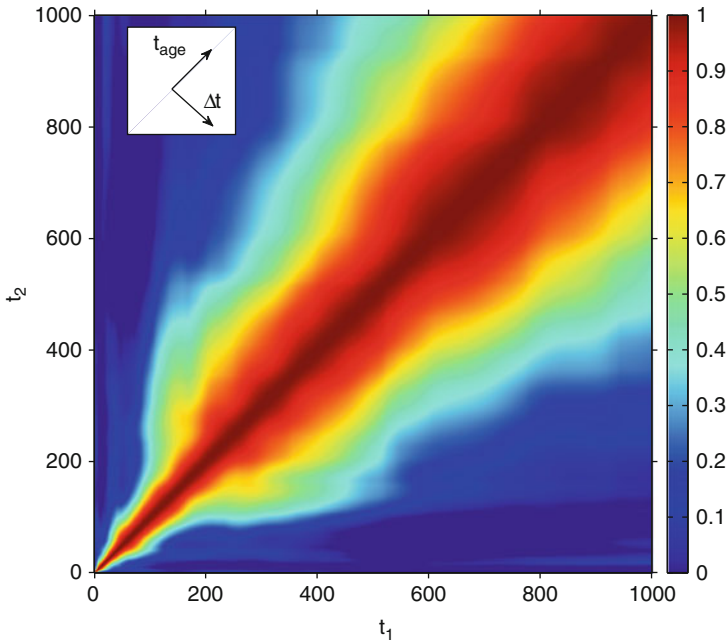
Fig. 3.5 Example of a two-time correlation function (TTCF) of a non-equilibrium system. The *inset* shows the axes of the coordinate system that is generally used to analyse the TTCFs: $t_{\text{age}} \equiv \frac{t_1 + t_2}{2}$ and $\Delta t \equiv |t_2 - t_1|$ (see text for details). The colour scale gives the value of the TTCF

The TTCFs can also be analysed using another coordinate system which is more in line with the definition of the autocorrelation function [20]. One-time correlations are obtained cutting the TTCF along lines where t_1 (or equivalently t_2) is constant. In this coordinate system, one-time correlation functions for systems in equilibrium are symmetric upon time inversion, while for non-equilibrium systems they are asymmetric. The terms in the OTCF at age t_a have the form $I_{t_a}I_{t_a+\Delta t}$. Thus, all the terms have a direct relationship with the intensity measured at time t_a. It has to be taken into account that the decay times obtained with one coordinate system or the other will be, in general, different. With both coordinate systems, the autocorrelation function (3.9) is obtained by averaging the terms at different lag times.

4   Experimental and Instrumental Methodology

XPCS experiments require a coherent source, an extremely stable set-up and a detector with very high angular resolution and sufficient speed. These requirements pose some limitations or boundaries to the technique. The absence of lasers in the X-ray regime has limited the use of XPCS to synchrotrons, although with the development of the new free electron lasers, the panorama is already changing (see Sect. 6). The principal factor that limits the timescales that can be probed with XPCS is the flux of coherent photons that impinge on the sample. An approximate criterion is that at least one scattered photon per speckle over the timescale probed is needed [78]. Figure 3.6 shows the time and length scales accessible with XPCS. Highly efficient detectors with adequate resolution to observe speckles and measure their intensity fluctuations are mandatory, but they have also limitations in terms of speed and pixel size. A 2D detector can be used to increase the measured signal, but the readout speed of current area detectors may then become the limiting factor. Another issue to consider is that designing and operating stable set-ups that preserve the coherence properties can also be problematic. We discuss these points in the following sections.

4.1   Coherent X-Ray Source

In XPCS experiments the samples must be illuminated with a coherent X-ray beam. For a chaotic X-ray source such as third-generation synchrotron radiation storage rings [130, 152], the coherence volume is determined by three parameters: ξ_l, the longitudinal (or temporal) and $\xi_t^{h,v}$, the two transverse (or spatial) coherence lengths [73]. For coherence experiments, the maximum path length difference on the sample must lie within the coherence volume $V_c \sim \xi_l \times \xi_t^h \times \xi_t^v$.[5] For a scattering geometry with incident wave

---

[5]In general, the specific prerequisites for the degree of coherence and wavefront curvature depend on the application. For example, other techniques such as phase contrast imaging typically require a planar wavefront [161], whereas curved wavefronts can even be advantageous in some cases for coherent diffraction imaging [249], and focused beams have been used to study nanoparticles [52, 204].
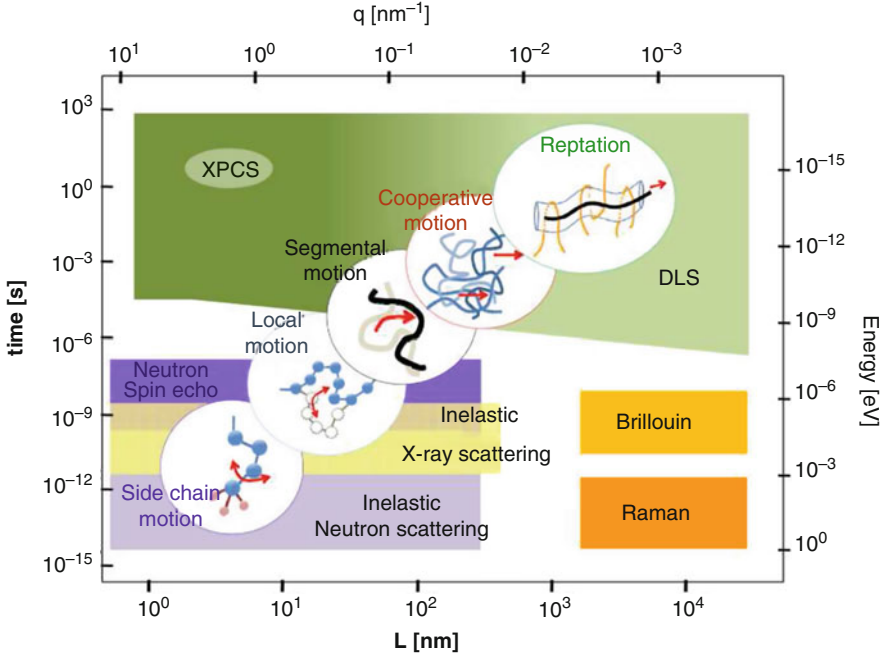
Fig. 3.6 Map showing the time and length regions that are covered by various techniques that can access the dynamic structure factor: inelastic neutron scattering (*INS*), Raman and Brillouin scattering, inelastic X-ray scattering (*IXS*), neutron spin echo, nuclear forward scattering (*NFS*), dynamic light scattering or photon correlation spectroscopy (*PCS*) and X-ray photon correlation spectroscopy (*XPCS*). The *insets* represent the time and length scale of a hierarchical dynamic structure in polymers. XPCS typically gives access to the segmental and cooperative motion on such systems (Figure reproduced from [99] with permission from the Physical Society of Japan)

vector $\vec{k}_i = k(0, 1, 0)$ and scattered wave vector $\vec{k}_f = k(\sin 2\theta \cos \phi, \cos 2\theta, \sin 2\theta \sin \phi)$, the path length difference (δ) for two points $\vec{r}_1 = (x_1, y_1, z_1)$ and $\vec{r}_2 = (x_2, y_2, z_2)$ is [199]

$$\delta = 2(x_2 - x_1) \sin \theta \cos \theta \cos \phi + 2(y_2 - y_1) \sin \theta^2 \\ + 2(z_2 - z_1) \sin \theta \cos \theta \sin \phi \qquad (3.28)$$

Equation (3.28) can be specified for Bragg geometry (reflection) and transmission geometries [80]:

$$\delta \sim \begin{cases} \dfrac{2}{\mu} \sin^2\theta & \text{Bragg} \\ 2W \sin^2\theta + d \sin \theta & \text{transmission} \end{cases} \qquad (3.29)$$

μ is the linear absorption coefficient, d the beam diameter, θ the scattering angle and W the sample thickness. The combination of Eq. (3.29) and the lengths that define

the coherence volume $V_c \sim \xi_l \times \xi_t^h \times \xi_t^v$ determine the maximum momentum transfer measurable in an experiment. ξ_l is directly related to the monochromaticity of the radiation by:

$$\xi_l \simeq \lambda^2/\Delta\lambda \tag{3.30}$$

where λ is the X-ray wavelength and $\Delta\lambda$ is the spectral width. For synchrotron sources, with a Gaussian intensity distribution of the form $I(x, y) \propto e^{-\left(x^2/2\sigma_h + y^2/2\sigma_v\right)}$, the transverse coherence length in the vertical (horizontal) direction is given by [199]:

$$\xi_t^{v,h} = \lambda L/\left(2\pi\sigma_{v,h}\right) \tag{3.31}$$

$\sigma_{v,h}$ being the vertical (horizontal) source size (rms) and L the distance between the source and the observation point. $\xi_t^{v,h}$ can also be considered as a measure of the degree of collimation of the radiation in the vertical (horizontal) plane. These lengths are generally much smaller than the cross-section of the full beam.[6] For an X-ray beam, a practical requirement to obtain good coherence properties is that the beam size ϕ at the sample position fulfils [134]:

$$\phi\epsilon \leq \lambda \tag{3.32}$$

where ϵ is the divergence (full width at half maximum) of the beam. The beam size is generally determined by slit apertures or pinholes, while the divergence can be intrinsic from the source or further modified by optical elements. By tuning the beam size and divergence, the spatial coherence properties can be adjusted. However, satisfying condition (3.32) always results in an important reduction of intensity with respect to the full beam. The coherent flux in XPCS experiments at the ESRF is typically of the order of 10^{10}–11^{11} ph/s. An intensity increase can be achieved by using focusing elements. Yet, focusing elements modify the coherence length and alter the shape of the wavefront [227]. In the case of XPCS, the conditions are not too stringent: the exact shape of the wavefront is not relevant and a rather low degree of coherence is enough to observe speckles [73, 134]. Therefore, using focusing elements can be highly beneficial for XPCS, in particular when beam damage is not an issue. However, because the transverse coherence length is reduced as the beam divergence is increased, it is important to be able to characterise the coherence properties, performing, for example, a statistical analysis of a static speckle pattern, as shown in Sect. 3.2. Knowing the degree of coherence, that is, β in Eq. (3.10), may be needed to determine if there are two decays on the correlation function (see Fig. 3.7). If the first decay is too fast and cannot be detected, then the contrast value

---

[6]The number of photons that passes through an aperture with dimensions $\xi_t^{v,h}$ per unit time is related to the brightness B of the source as $I_{coh} \propto \lambda^2 B/4$. The units of B are $ph/photons/s/mrad2/mm2/0.1\%$ bandwidth [78].
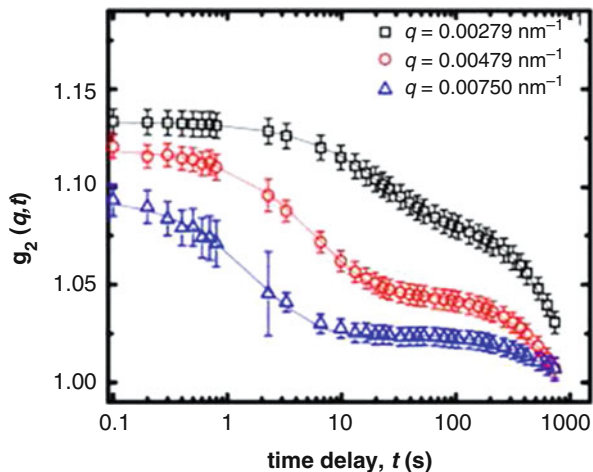
of the second correlation function will be smaller than expected from the degree of coherence. Sometimes, one can trade off between intensity and coherence. For example, in small-angle scattering experiments, the monochromaticity condition—that is, the longitudinal coherence length, Eq. (3.30)—can be relaxed and optics such as multilayer mirrors that allow for a wider bandpass than crystal monochromators can be used [78].

The time structure and the lifetime of the synchrotron beam need also special consideration. Synchrotron beams are composed of bunches that circulate along the storage ring. The time structure of the synchrotron beam will come up in the correlation function measured by XPCS. The actual time structure depends on the filling mode. As an example, the ESRF storage ring has a circumference of 844 m, and it takes ~2.8 μ*s* for an electron to make a complete turn; in the uniform filling mode, there are 992 bunches of electrons equally distributed around the storage ring, which gives a characteristic time of 2.8 ns that would be detected by XPCS. In the 4×10 mA filling mode (four equidistant bunches with 10 mA/bunch), a characteristic time of 0.7 μ*s* would be detected. Thus, the frequencies due to the synchrotron beam time structure may be an issue when studying very fast dynamics if the dynamics under study have very similar frequencies. In addition, the beam decay has also to be taken into account, especially when analysing slow dynamics. In a synchrotron, the beam intensity decays exponentially as $I_{SR} \propto e^{-t/t_0}$, where t_0 is the lifetime (of the order of ~60 h for the uniform filling mode at the European Synchrotron Radiation Facility – ESRF). The autocorrelation of this decaying intensity is:

$$g_{SR}^{(2)} = \frac{\langle I_{SR}(t) I_{SR}(t + \tau) \rangle_T}{\langle I_{SR} \rangle^2} = \frac{T}{2t_0} \left\{ \frac{1 - e^{-2T/t_0}}{1 + e^{-2T/t_0 - 2e^{-T/t_0}}} \right\} e^{-\tau/t_0} \qquad (3.33)$$

The autocorrelation of a dynamic system illuminated with a decaying beam will have contributions from the dynamics due to the sample and to the beam decay: $g^{(2)} = g_{SR}^{(2)} \times g_{\text{sample}}^{(2)}$. Normalising the data to the incoming intensity may therefore be necessary to circumvent the contribution from the beam decay. When using a 2D detector, if the static structure factor does not change with time, the integrated intensity of the images can also be used for normalisation.

4.2   Set-Up: Stability and Coherence Preserving Elements

Any movement of the set-up, vibration, drift or instability may cause spurious dynamics that would be reflected on the autocorrelation function; hence, the complete set-up (i.e. optical elements, sample environment and detection system) must be extremely stable. Small changes in the optical path or the illuminated area on the optical elements due to beam movements can alter the coherence properties at the sample position. This is especially relevant when using elements operated at glancing incidence, such as mirrors, because in this geometry the aberrations become particularly important [21, 121]. Moreover, mirrors are not perfect and may present surface waviness, slope errors and roughness that yield non-uniform wavefronts with intensity stripes along the sagittal plane. A discussion about the physical reasons behind the loss of coherence due to imperfect optics can be found in [161]. For coherence experiments very high-quality X-ray optics elements are required, not only with good surface quality but also with a uniform shape. The quality of the slits and pinholes is also of concern, as is discussed by LeBolloc'h et al.: good-quality polished blades are needed to reduce stray scattering [125].

Fraunhofer diffraction patterns from slits can be used to assess qualitatively the suitability of optical elements or beamline components for coherence experiments. We placed a 4 mm thick unpolished 360° beryllium window of a vacuum chamber for in-situ X-ray scattering experiments [33] in the beam at the sample position, and we measured the slit diffraction pattern after propagation through the beryllium window (Fig. 3.8). This test was particularly relevant, as this chamber is a fundamental element of set-up for XPCS experiments on ion beam-induced self-organised surfaces [23]. Superimposed on the Fraunhofer fringes, spurious speckles appear due to grain boundaries, surface roughness and other imperfections of the beryllium window. On the other hand, a 125 µm thick kapton (polyimide) window does not give rise to speckles, and it is thus better adapted for coherence experiments. As a consequence, for coherent beam experiments with samples placed in a vacuum environment, the chamber was modified to replace the beryllium window by kapton viewports [33].

4.3   Detectors

In the same way as it is done in DLS, XPCS experiments can be realised using a point detector coupled with a correlator electronics that works out the intensity

Fig. 3.8 Fraunhofer
diffraction pattern from a pair
of slits after transmission
through 125 μm kapton
(*black*) and 4 mm beryllium
(*red*)
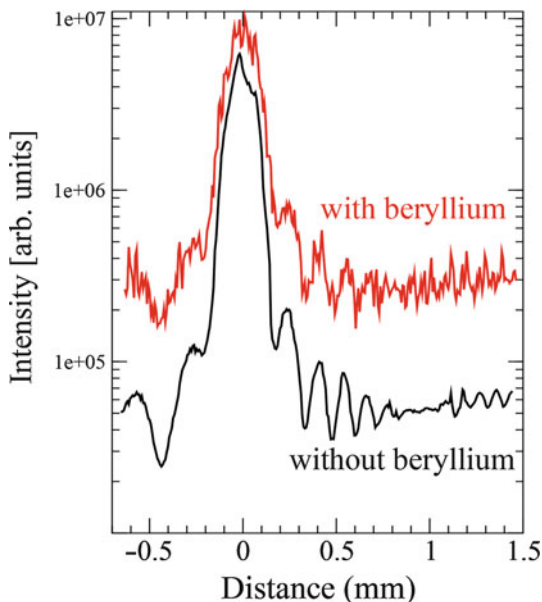
autocorrelation function. Besides the limit set by the correlator electronics, X-ray
detectors also set a limit to the fastest accessible timescales. The fastest point
detectors at present are the avalanche photodiodes, which have a dead time of ~1 ns
or lower. Scintillation detectors can only be used up to few hundred kHz [78].

2D detectors (area detectors) have smaller counting rate (frame rate) than point
detectors but are very well suited to study slow dynamics. With 2D detectors, a range
of q-values is recorded simultaneously, and the signal-to-noise ratio is increased by
the square root of the number of pixels [61]. Thus, using 2D detectors, the limitations
due to low flux can be partially overcome. Charge-coupled devices (CCDs), due to
their low readout noise and dark current, large area and small pixel size (~20 μm),
have been extensively used in XPCS in direct illumination mode, with no additional
optics. In CCDs, each detected photon generates a distribution of charge in several
neighbouring pixels. The electronic noise can be suppressed, and the charge distri-
butions can be converted into number of detected photons using special algorithms
[137]. CCDs with integrated magnification optics can also be used, but only if the
signal is strong enough that the attenuation due to the magnification optics is sill
tolerable. The low-flux photon-counting CCD camera PI-LCX:1300 from Princeton
Instruments (pixel size 20 μm) is well suited for XPCS experiments [202]. Hybrid
photon-counting (HPC) 2D pixel detectors are used more and more. The MAXIPIX
[176], due to its small pixel size (~55 μm) and speed (maximum framing rate
1.4 kHz), is an excellent option, although it has a rather small area [202]. When
using 2D detectors (CCDs and HPCs alike), the images are stored, and the analysis is
done subsequently calculating the autocorrelation function pixel by pixel and aver-
aging those pixels corresponding to an equivalent momentum transfer value. In some

cases, it is necessary to perform the usual corrections to the detector images, namely, the subtraction of the zero level (dark image correction), the normalisation of the quantum efficiency of each pixel (flat-field correction) and the spatial distortion correction [24].

In the case of point detectors, slits are placed in front of the detector to define the resolution. If the slits are too large, several speckles will be integrated on the detector, and the signal-to-noise ratio may be improved at the expense of optical contrast. This aspect is very important in XPCS, because in many cases XPCS is a signal-limited technique. For 2D detectors, the resolution is determined by the pixel size. By choosing the right detector distance, which depends on the angular pixel size and the angular source size, the signal-to-noise ratio can be optimised. The best signal-to noise ratio is achieved when the detector is at a position where the angular pixel size matches the angular source size [61].

5   Key Research Findings

The number and type of XPCS studies is continuously increasing. The recent literature since 2009 is reviewed here although some older works have also been included. An important amount of work is related to technical developments, be it beamlines, sources or detectors (Sect. 5.1). Soft matter studies are presented in Sect. 5.2. Hard condensed matter studies are summarised in Sect. 5.3.

There are other recent XPCS reviews in the literature. X-ray coherent scattering and XPCS are described in [138, 161]. The principles, applications and novel approaches are treated in [215, 234]. A more detailed and extended review is in [78]. Surfaces and thin film studies have been surveyed with great detail in [220]. Studies of the structure and dynamics in interfacial systems with synchrotron radiation techniques are discussed in [42], and more specifically, surface and inter-face studies on polymer brushes are surveyed in [99]. Nanoscale motion and rheology are the focus of [126]. XPCS for non-equilibrium dynamics and non-exponential correlation functions is well illustrated in [148].

5.1   Technical Developments

5.1.1   Detectors

XPCS experiments are an excellent benchmark test for detectors. The ideal detector for XPCS should have a large area to probe large regions of reciprocal space simultaneously; a very small pixel size and, hence, an excellent resolution to be able to resolve the speckles; a uniform and linear response to radiation to prevent artefacts on the time correlations; and a very high framing rate with minimal dead time to access fast dynamics. A criterion that is not usually crucial when using synchrotron sources is the dynamic range because often the measured signals are weak. However, high detection efficiency is required. For X-ray free electron lasers, high dynamic range and radiation hardness are also imperative.

At present, the fastest detectors are point detectors (0D) such as avalanche photodiodes, which can have a time resolution better than 1 ns [9]. There is a very significant activity to develop 1D and 2D pixel array detectors. The Mythen 1D, developed by the Paul Scherrer Institute (PSI), can be operated at a frame rate of 2000 Hz, when it is used at its lowest dynamic range mode (4 bits). The Mythen 1D detector has been tested in an XPCS experiment on a model colloidal systems of spherical particles in solution [248]. Similar tests have been done with the 2D MAXIPIX detector by the same group [202]. The MAXIPIX, designed at the ESRF, is based on the MEDIPIX-2 chip and can operate up to a 1.4 kHz frame rate [176]. XPCS results obtained using an APD, the Mythen 1D and the MAXIPIX detectors are comparable [202, 248]. The new MEDIPIX-3 chip, which is still under development, will have improved capabilities [71, 72]. Good results have also been achieved with a 2D multiwire gas detector with ~ μs time resolution in test studies with disordered aerogels and polymer blends [208]. The PILATUS detector has a rather large pixel size (172 μm) but used with long sample-to-detector distances can yield satisfactory intensity autocorrelation functions of model colloidal systems [246]. Grid masks have been employed to enhance the angular resolution of the PILATUS. In this way, XPCS experiments can be performed with grid hole sizes customised for the experimental conditions [95]. The next generation of the PILA-TUS, the EIGER detector, has a smaller pixel size (75 μm). This detector already allows to measure autocorrelation functions with relaxation times below a millisecond [112].

The readout time is often what restricts the time resolution of 2D detectors and what limits their use for studying fast dynamics. A variation of XPCS, X-ray speckle visibility spectroscopy (XSVS), can overcome this limitation [49, 104]. In XSVS, instead of measuring many frames with the same acquisition time and then correlate the frame-to-frame intensity fluctuations as is done in XPCS, frames with different exposure times are acquired to obtain information about the dynamics. For a dynamic system, the visibility of the speckles will depend on the exposure time: for longer exposure times, the speckle patterns will be more blurred. The dependence of the speckle visibility with the exposure time is related to the sample dynamics. The time resolution of XSVS is limited by the minimum exposure time and not by the frame rate of the detector. Evidently, the minimum exposure time is also limited by the intensity of the incoming X-ray beam and the strength of the scattered signal. Experiments on model colloidal systems have been employed to demonstrate the capabilities of the XSVS technique [49, 104] and show that submillisecond measurements are possible with the intensity levels of current undulator sources [49]. XSVS measures a time integral (the integration range is given by the exposure time) over the intermediate scattering function. If the form of the intermediate scattering function (Eq. 3.14) is not known, then the XSVS data interpretation can be difficult [49]. For non-equilibrium systems, since the intermediate scattering function evolves in time, the problem is even more complicated. The XSVS analysis can be eased if the expected photon statistics on the speckle pattern obtained with partial coherent illumination is taken into account: this approach has successfully been proven in the study of the Brownian motion of spherical particles on a colloidal suspension [131].

New detector developments are under way, especially foreseeing the future operation of the European XFEL and other free electron laser sources. The Adaptive Gain Integrating Pixel Detector (AGIPD), which will be able to operate at 4.5 MHz, is one example of the projects that are being carried out [177]. The HORUS software toolkit [13] has been employed to simulate the performance in XPCS experiments of different configurations of the AGIPD [10–12]. Another project, the XNAP, seeks to build a 2D detector with nanosecond time resolution. The work done with prototypes of the XNAP is indeed very promising [60]. A Geiger-mode avalanche photodiode array has already been applied on a test colloidal sample, and time correlations of few milliseconds could be acquired [113]. The Vertically Integrated Photon Imaging Chip (VIPIC) has been especially designed for XPCS [51] and the trials have been positive [50]. The charge pump detector has also been conceived for XPCS [206]. Indirectly illuminated area detectors have been proven useful for slow dynamics with correlation times of the order of several seconds [209].

A pixel array detector prototype based on field-programmable gate arrays (FPGAs) has been proposed in [100, 101]. With this type of detector, it will be possible to acquire an autocorrelation function with 100 ns time resolution, in real time, that is, on the fly, without having to analyse the recorded images. A scheme for processing multi-speckle XPCS data using the multi-tau algorithm is presented in [236]. A user-friendly graphical user interface for real-time XPCS data analysis that uses high-performance cluster units is introduced in [218]. Event correlation techniques can provide time correlation functions equivalent to those obtained with standard methods but with reduced computing time [39]. Continuous processing and compression of XPCS data with FPGAs has been demonstrated in [145–147]. In this compression scheme only the pixel signals that are above a low threshold are stored and the rest is thrown away; the compression can be very efficient [146]. How to store data in a convenient and easy-to-share way is a long-standing issue. A data exchange model based on the Hierarchical Data Format 5 (HDF5) is described in [48]. A solution based on GridFTP (an extension of the standard file transfer protocol (FTP)) is proposed in [159]. In addition to data compression applications in XPCS, FPGAs have also been developed to give additional functionalities to the VIPIC detector [150]. Another design based on FPGAs is reported in [251]. A pixelated detector that uses an event-driven address time-stamp method to determine where and when the X-rays impinge on the detector, capable of counting at 100 MHz rate, has been recently built and tested. This detector does not have dead time and can be used to investigate dynamics from 10^{-6} s to 10^4 s [250]. The achievable efficiency of a low-noise high-speed camera with non-linear gain has been discussed in [90].

The interest of having detectors with small pixel size was already highlighted in [61]. Small pixel size can also be advantageous to investigate systems without long-range order in a configuration that is intermediate between the far-field (Fraunhofer) and near-field (Fresnel) regimes. Working in this intermediate regime allows using larger beam sizes, and the ensemble averaged correlation functions are equivalent to those measured in the far field [143]. Working in the near field demands very small pixel sizes to achieve the required resolution, but longer length scales than with traditional (far-field) XPCS can be studied. The capabilities and limitations of X-ray

near-field speckle are analysed in [142]. A further advantage of using 2D detectors is that it can reduce the collection time as many speckles are measured simultaneously. This aspect is crucial in systems prone to degradation by X-ray irradiation. For example, it has been observed that X-ray irradiation induces the rearrangement of silica particles in rubber [214].

5.1.2 Beamlines and Set-Ups

Sources with low emittance (i.e. the product of the source size and the divergence) are essential for coherent X-ray techniques. XPCS does not require a high degree of coherence, and often a trade-off between coherence and intensity is sought (see Sect. 4.1). The design of the coherent hard X-ray (CHX) scattering beamline of NSLS-II has been optimised for XPCS experiments. CHX is designed to obtain a partially coherent beam at the sample with a degree of coherence within 0.1–0.5 and a maximised intensity on the sample, which will allow to study timescales two orders of magnitude faster than currently existing beamlines [62]. The focusing elements at CHX are cylindrical compound refractive lenses [223] for the vertical focusing and parabolic lenses with kinoform profiles [200] for the horizontal. The use of kinoform lenses in XPCS experiments is examined in [200]. The coherent X-ray scattering beamline at the upgraded Pohang Light Source (PLS-II), devised for coherent X-ray diffraction imaging and XPCS, is presented in [253] and it is already open to users. The 8-ID-E beamline at the Advanced Photon Source for high resolution and coherent grazing incidence X-ray scattering experiments is introduced in [110].

Soft X-ray pulsed lasers, combined with a time-delayed beam splitting system, have been used to study ferroelectric materials with XPCS (see also Sect. 5.3.1). The time delay is achieved with a Michelson-type system composed of a beam splitter and two multilayer mirrors [115]. With this system, dynamics of materials on the picosecond timescale can be studied [158]. The principle of a time-delay system was discussed in [79] and its practical viability demonstrated in [88], where 2D speckle patterns are analysed in terms of photon statistics and speckle contrast (see also Sect. 6). The XSVS technique discussed above and the beam splitting approach give complementary information [104]. Another time-delayed beam splitting method, based on energy separation, is described in [229]. For sources with short temporal coherence, inclined beams with respect to the propagation direction can be used to produce speckles and do heterodyne measurements, as explained in [27].

Many XPCS soft matter experiments are done in SAXS geometry (see Sect. 5.2). A compact chamber for low temperature (110–330 K) and low magnetic field (up to 0.12 T) SAXS studies has been developed recently and can be applied to study, for example, supercooled liquids and ferrofluids [228]. By performing XPCS measurements at ultra-small angles, it is possible to study systems at momentum transfers that cannot be accessed otherwise and decrease the gap in accessible values between DLS and XPCS [255, 257]. The combination of USAXS and XPCS has been applied to the study of colloidal polystyrene microspheres in glycerol and dental composites. For the dental nanocomposites, USAXS-XPCS has allowed to identify non-equilibrium dynamics that cannot be analysed with other techniques [257]. In another study, USAXS and XPCS have been complemented with three-dimensional

finite element analysis and wave propagation theory to show that stress relaxation mechanisms are at the origin of the non-equilibrium dynamics observed in a glass filler particle-based composite [144]. The USAXS-XPCS instrument at APS is presented in [103]. XPCS has been combined with diffracted X-ray tracking measurements to study the translational and rotational motion of black carbon nanoparticles embedded in a rubber matrix. Information about the translational motion is obtained from XPCS, and information on the rotational motion is retrieved from the changes in the positions of the diffracted spots. In these measurements, a 'pink' beam is used to increase the probability of capturing a Bragg reflection on the detector [213].

5.2   Soft Condensed Matter

5.2.1   Colloids

Understanding the dynamical behaviour and stability of colloidal suspensions is of interest in many areas ranging from industrial products (food, cosmetics, paints, etc.) to fundamental science and biology. The volume fraction, the strength and nature of the colloidal interactions, temperature, etc. are parameters that influence the physicochemical, transport and rheological properties of colloids. Fluid, gel and glassy states often appear in the phase diagrams of colloidal suspensions, and they can also exhibit remarkable rheological properties like shear thickening or thinning. The study of colloids in solution with XPCS is the natural extension of visible light PCS studies into the X-ray regime, where much shorter lengths can be investigated and multiple scattering is, in general, negligible. Indeed, one of the first XPCS works inquired into the Brownian motion of gold colloids in glycerol and the findings were consistent with results extrapolated from visible light PCS [54]. XPCS experiments on colloids are usually carried out in transmission geometry to probe bulk properties[7] such as the diffusion of solutes in a solvent or particles in solution.[8] Using XPCS, the short-time self-diffusion constant of charge-stabilised colloidal particles in suspension was measured. The experimental self-diffusion constant is smaller than the predicted values using theoretical models that include many-body hydrodynamic interactions. These results indicate that the charge-stabilised character of the particles needs to be included in the theoretical description [186]. The thermal gradients should also be considered, as they may affect the dynamical behaviour of suspensions [97].

The dependence of concentration and ionic strength on the collective diffusion of charge-stabilised fluorinated latex spheres in aqueous suspensions was investigated in [69]. The hydrodynamic function $H(q)$, which yields the configuration-averaged

---

[7]Recent experiments on colloids in films or at surfaces are reviewed in Sect. 5.2.1.

[8]As shown in the example of Sect. 3.3.1 for noninteracting spherical particles, the relaxation time obtained from the autocorrelation function is $1/D_0 q^2$ (see Eq. (3.19)), and from it, one can obtain the hydrodynamic radius of the particles using the Stokes-Einstein equation (Eq. (3.20)).

effect of the hydrodynamic interactions on the short-time dynamics of the colloidal suspension [156], is given by $H(q) = D(q) S(q)/D_0$, where $D(q)$, $S(q)$ and D_0 are the short-time collective diffusion coefficient, the static structure factor and the particle diffusion coefficient at infinite dilution, respectively. $D(q)$ was obtained from XPCS measurements and $S(q)$ from SAXS. The behaviour of the hydrodynamic function can be explained by the effect of many-body hydrodynamic interactions. The results presented in [187] on dense suspensions of charge-stabilised colloidal particles agree qualitatively with [69]. However, lower mobilities than the ones predicted by the hard-sphere model and which are probably influenced by strong direct particle interactions are reported in [187]. Works done on charged sphere suspension yield results in agreement with theoretical models [68, 170].

The dynamical behaviour of sterically stabilised poly(methyl methacrylate) (PMMA) colloidal suspensions was studied for different volume fractions (Φ) up to $\Phi \approx 0.49$ [166]. The system behaves like hard spheres. It was found that the short-time mobility, which is related to the random motion of individual particles hindered by neighbouring particles, is smaller than that of free particles, even for low concentrations. This reduced mobility is a consequence of indirect hydrodynamic interactions mediated by the solvent and depends on the structural properties of the system. The results for $\Phi < 0.4$ agree with the analytical many-body theory derived by Beenakker and Mazur [14, 15], but above that concentration the agreement worsens because the hydrodynamic effects are overestimated by the theory. A good agreement is found between experimental results and numerical algorithm developed by Banchio and Brady [8] for the whole concentration range studied [166]. An excellent agreement with the theory of Beenakker and Mazur was found in a study of low polydisperse charged poly-acrylate (PA) spheres for concentrations up to a volume fraction of $\Phi \approx 0.32$ and different salinities to control the interparticle interaction strength. Deviations from the theory were only observed for low salinity systems at the highest concentrations studied [247]. In another study of sterically stabilised PMMA particle suspensions with volume fractions $\Phi > 0.3$, the analysis of the two-time correlation function shows that two quasi-diffusive regimes exist in the short-time and long-time limits. These regimes are associated with the cage escape scenario. Mode-coupling theory does not describe the data adequately. At high concentrations, the systems show ageing and intermittent collective rearrangements emerge (Fig. 3.9). These rearrangements lead to the restoration of ergodicity [122]. Dynamic light scattering and XPCS were used to study a hard-sphere system as function of the volume fraction and scattering vector. A scaling behaviour is observed for several decades in time. However, in the long-time regime, no scaling is detected, and moreover, suspensions with high volume fractions show a strong dependence in q. These findings put into question the existence of a collective long-time diffusive regime [153].

The equilibrium dynamics of concentrated suspensions of polystyrene micro-spherical particles dispersed in glycerol for volume fractions in the 10–20 % range have been studied combining USAXS and XPCS. It has been found that the effective diffusion coefficient shows a peak when represented against the momentum transfer q, the relaxation time is inversely proportional to q and the autocorrelation functions
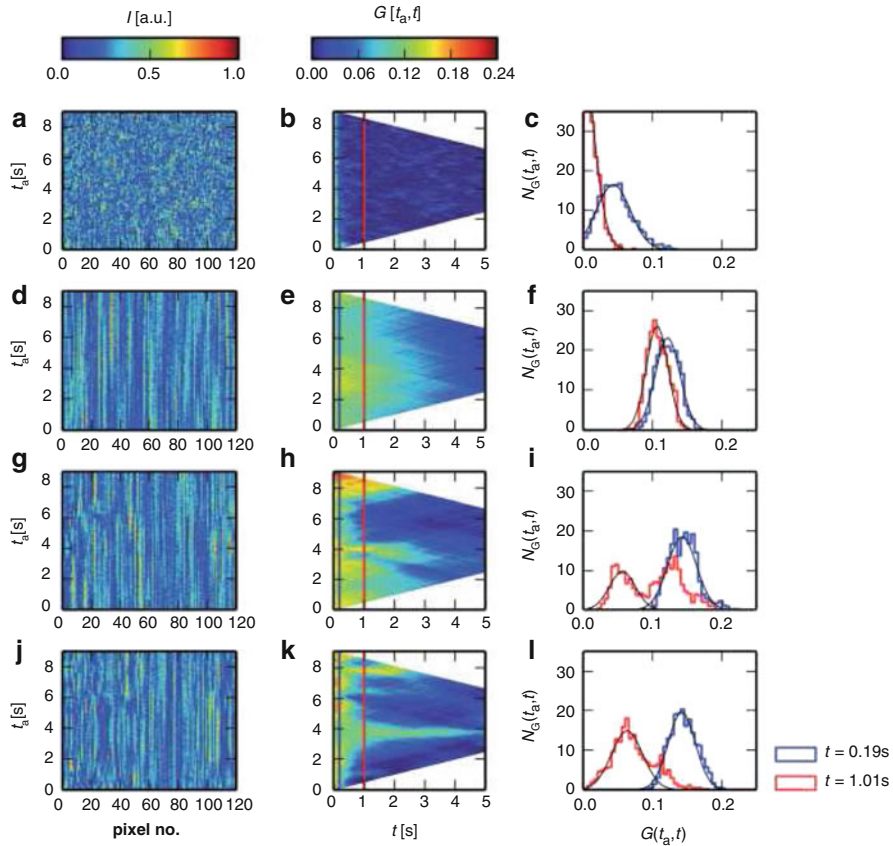
Fig. 3.9 Development of intermittent, heterogeneous dynamics in concentrated hard-sphere suspensions. *Left column*: pixel intensities vs. time ('waterfall plot') for pixels at wave vectors near the hard-sphere structure factor peak at $q \cdot R \sim 3.42$. *Middle column*: time-resolved correlation function $G(q, t_{age}, t)$. *Right column*: histograms of G for two delay times t. The delay times are indicated with a *blue* and a *red vertical line* in the middle column graphs. Panels (**a**–**c**): data for sample with volume fraction $\Phi \approx 0.57$. Panels (**d**–**f**), (**g**–**i**) and (**j**–**l**): samples with $\Phi \approx 0.61$ after 30 min, 2.5 h and 9 h, respectively (Reproduced from [122] with permission from The Royal Society of Chemistry)

are better described by stretched exponential shapes. These three findings suggest that the microspheres move collectively [256].

The dynamics as a function of the volume fraction of dilute suspensions of stiff, platelet-shaped phosphoantimonate particles was investigated in [41]. These platelets arrange into a lamellar phase. The collective diffusion coefficient along the director of the phase—that is, the direction parallel to the average alignment of the platelets—was measured. At low concentrations (i.e. $\Phi \approx 0.8$ %) there is no hydrodynamic coupling between nearest neighbours. Already at $\Phi \approx 1.1$ % the coupling has to be taken into account to explain the data. The high q-value of the diffusion

coefficient in the lamellar phase decreases with concentration and remains constant across the liquid to gel transition. This implies that longer length and timescales than those probed in the experiment are involved in the transition [41]. In the case of the fluid nematic phase of goethite (α-FeOOH) nanorods, the collective diffusion coefficient in the plane perpendicular to the director varies strongly with the momentum transfer. For momentum transfers smaller than a value q_{max} for which the structure factor is maximum, the dynamics of the system slow down. This behaviour differs from that of isotropic suspensions of thin rods and is related to the particle anisotropy and the nematic order [178]. Indeed, the asymmetry shape of particles may generate additional modes that contribute to the dynamics. This is demonstrated by comparing the relaxation spectra obtained with platelet-shaped gibbsite particles to the one expected from spherical particles [94]. Rod-shaped hematite particles in suspension can be aligned with an external magnetic field. The principal components of the translational diffusion tensor, that is, the diffusion constants along the parallel ($D_{\parallel}$) and perpendicular ($D_{\perp}$) directions to an external magnetic field, have been obtained. The $D_{\parallel}/D_{\perp}$ ratio increases with increasing aspect ratio of the rods [241].

A transition from Brownian to hyperdiffusive motion was observed in the dynamics of sterically stabilised silica colloidal particles used as tracers in a supercooled solvent (1,2-propanediol). At temperatures far from the glass transition temperature, the particles follow Brownian motion (free diffusive behaviour) and the relaxation time scales as $\tau \propto 1/D_0 q^2$. As the transition temperature is approached, the dynamics change gradually to ballistic type, with $\tau \propto q^{-1}$. Moreover, the correlation function decay changes from a pure exponential to a compressed exponential form (Fig. 3.10). The change is induced by the modifications of the solvent properties as the glass transition temperature is approached and may be related to relaxations of elastic-like stress in the supercooled liquid [35]. In a very detailed study of the collective dynamics of silica particles in a binary mixture near its consolute point, it has been shown that the binary mixture goes through a glass transition upon heating and cooling [140, 141]. Dynamics that evolve from diffusive to hyperdiffusive have been observed for cadmium sulphide nanoparticles suspended in low molecular weight polystyrene homopolymers in the 120–180 °C temperature range, when decreasing the temperature. However, for higher molecular weight polystyrene, the dynamics are always hyperdiffusive [105]. A crossover from hyperdiffusion to subdiffusion was observed on the dynamics of polystyrene-grafted silica nanoparticles dispersed in a polystyrene matrix, upon temperature increase, at 1.25 T_g of the glass transition temperature (T_g) of polystyrene [96, 98].

The porosity of a material can also influence its dynamics. In porous materials (aerogels and nanocomposite aerogels with iron oxide particles), hyperdiffusive dynamics have been detected at room temperature. On the other hand, in non-porous polymer xerogels, no significant dynamics have been observed. Thus, the dynamics seem to arise from the porous structure and not from the presence of nanoparticles [91]. The temporal evolution of the entangled high molecular weight polystyrene polymer mesh is at the origin of the subdiffusive motion observed in embedded gold nanoparticles [82]. This subdiffusive motion is in agreement with the predictions made using scaling theory [31]. According to theory, particles that are
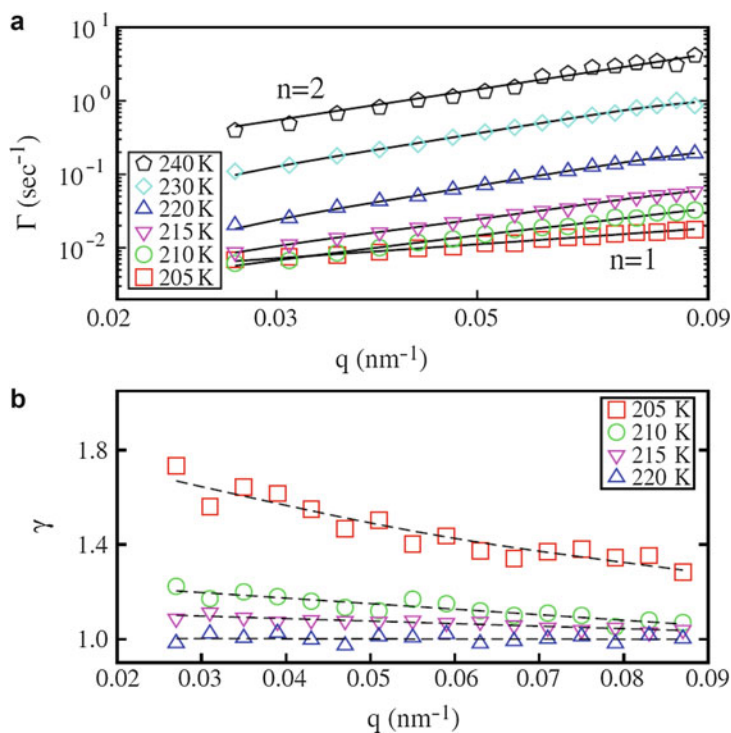
Fig. 3.10 (a) Relaxation rate $\Gamma(q)$ and (b) Kohlrausch-Williams-Watts factor $\gamma(q)$ obtained from fits of the $g^2(\tau) \propto exp[-2(\Gamma\tau)^\gamma] + 1$ to the data. Solid lines are fits with a simple power law $\Gamma \propto q^n$; dashed lines are guides for the eye (Reprinted with permission from [35]. Copyright (2008) by the American Physical Society)

smaller than the mesh should undergo diffusive motion [31], and such behaviour is observed for the motion of gold nanoparticles in diluted solutions of low molecular weight polystyrene melts at high temperature and follows the empirical Vogel-Fulcher temperature dependence, but close to the glass transition temperature, the dynamics become hyperdiffusive [81] (Fig. 3.10).

5.2.2 Ageing Phenomena

Ageing, that is, changes in dynamics that occur as time goes by, is a very interesting phenomenon that arises in a wide variety of systems. Ageing behaviour is characterised by a slowing down of the relaxation times with sample age, although ageing does not necessarily imply a change in the type of dynamics.

As shown in [85], the slow dynamics of silicone oil droplets in water nanoemulsions are determined by a nondiffusive motion; an intermediate scattering function with a compressed exponential form and an inverse relationship between the relaxation time and the momentum transfer vector is found. The line shape of the compressed exponential function does not depend systematically on the waiting time
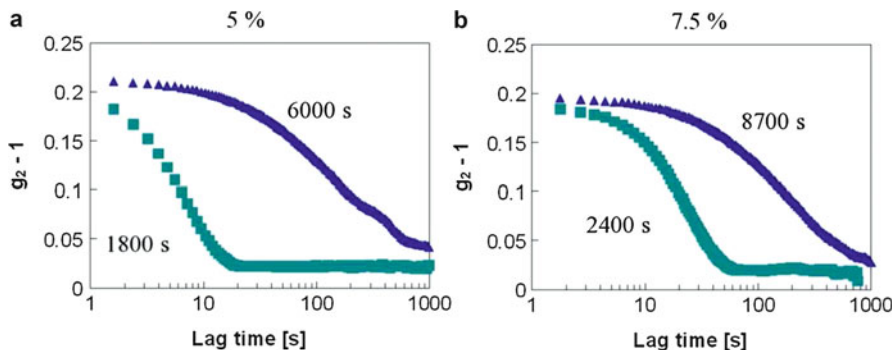
Fig. 3.11 Intensity autocorrelation functions at q = 0.033 nm^{-1} for two different ages: early (light squares) and late (dark triangles). Colloid volume fractions: (**a**) $\Phi = 5$ %; (**b**) $\Phi = 7.5$ % (Reprinted figure with permission from [92]. Copyright (2009) by the American Physical Society)

(sample age) or the effective droplet volume fraction. Its shape is indicative of an extremely slow ballistic motion with a broad distribution of velocities, and these dynamics are related to heterogeneous local stress [85]. Ballistic-like dynamics have also been reported to occur on young samples of colloid-stabilised emulsions as they become a thick cream (Fig. 3.11). These ballistic-like dynamics are related to local rearrangements of the droplets and are characterised by a compressed exponential with a KWW exponent equal to 1.5. The KWW exponent decreases to less than 1 as the emulsions age and large regions of the sample start to become strongly correlated [92].

In a glassy colloidal suspension of laponite, in spontaneously aged samples, the correlation functions are stretched with a decay slower than a pure exponential (i.e. $\beta < 1$). However, if the system is sheared, the correlation function is compressed and the decay is faster than exponential (i.e. $\beta > 1$). In both cases, the relaxation time scales as $\tau \propto q^{-1}$ (Fig. 3.12). The rejuvenation process by applying shear may have induced internal stresses that may generate ballistic-type motions. Rejuvenation by shear would play a similar role to temperature quenching in structural glasses [7]. The range of the localised colloidal motion, which has been determined by analysing the Debye-Waller factors of the intermediate scattering functions obtained with XPCS, does not change for the rejuvenated suspensions, but it decreases steadily with age in the spontaneously aged ones [5]. These results show laponite suspensions depend on sample preparation and history, and that comparison between samples prepared using different protocols may be delicate [5]. A spontaneous glass-glass transition can occur in laponite suspensions. Generally, glass-glass transitions are brought about by modifications of the effective interparticle interactions induced by changing an external parameter. Notwithstanding, by combining dilution experiments, XPCS, SAXS, rheological measurements and Monte Carlo simulations, it has been proven that without modifying the external parameters, and at fixed ionic strength and concentration ($C_w = 3$ %), a spontaneous glass-glass transition arises: after a waiting time of several hours, the laponite suspension
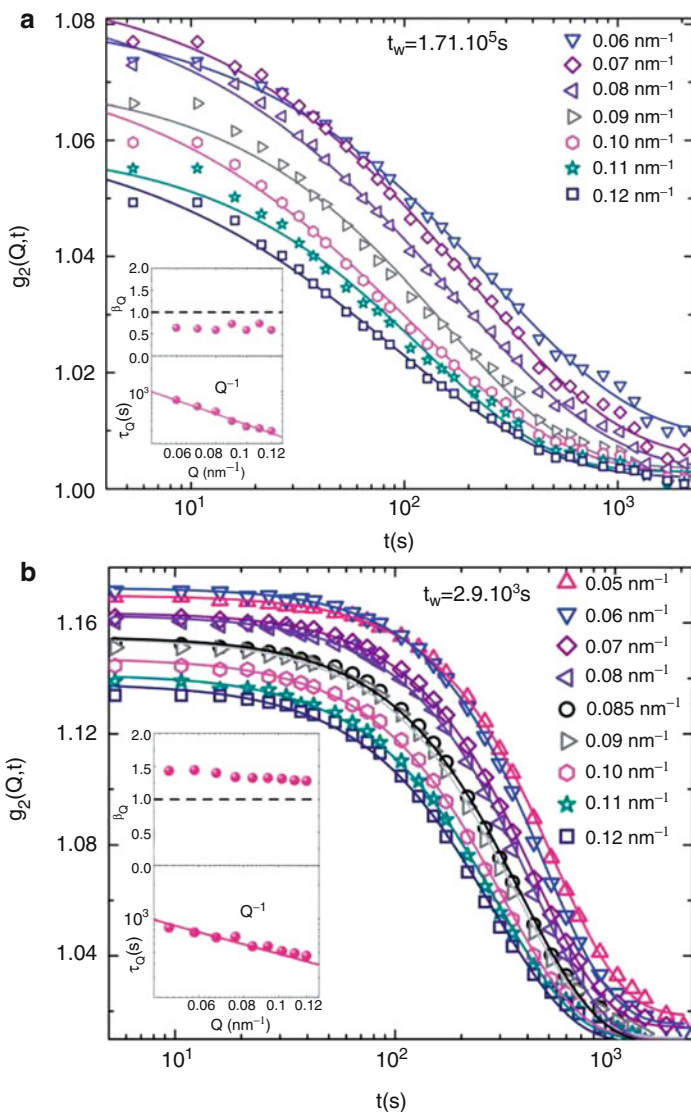
Fig. 3.12 (**a**) Intensity autocorrelation functions at different q-values of (**a**) an aqueous laponite suspension at concentration of 3.0 %, at waiting time $t_w = 1.71 \times 10^5$ s, and (**b**) a rejuvenated aqueous laponite suspension ($t_R \sim 3.5$ days) at concentration of 3.0 %, at waiting time $t_w = 2.9 \times 10^3$ s. The solid lines represent the best ts using a Kohlrausch-Williams-Watts decaying function. Insets: KWW exponent β_Q and relaxation times τ_Q obtained from the fits. The full line in the inset of τ_Q represents a t with a power law (Reproduced from [7] with permission from The Royal Society of Chemistry)

evolves into a Wigner glass in which a long-range screened coulombic repulsion dominates; after much longer waiting times, of the order of days, a second glass state, stabilised by orientational attractions between clay platelets, appears (disconnected house of cards). This glass-glass transition that takes place as a result of the competition between electrostatic repulsion and orientation-dependent attraction is probably a generic feature of heterogeneously charged systems when driven out of equilibrium [6].

The dynamics of filler particles in stretched-filled elastomers were studied by homodyne and heterodyne XPCS combined with tensile stress. The dynamics show ageing. The measurements yield compressed correlation functions and indicate that motion of filler particles is ballistic and also show that stretching induces a shear effect [57, 58]. Ageing is also observed in the dynamics of silica particles in unvulcanised rubber. The size of the aggregates does not change with time, and the ageing depends on the type of silane coupling agent and the volume fraction of silica particles. The silane coupling material is used to modify the adhesion of the nanoparticles to the rubber polymers, and thus, changes in dynamics are to be expected. Increasing the volume fraction alters the dynamics in a complex way [210–212]. Silica particles were used as tracers to investigate the gelation dynamics of a biopolymer physical gel, methylcellulose, using XPCS, electrophoresis and rheological measurements. Electrophoresis was used to check for possible interactions between the silica nanoparticles and the methylcellulose network. For the values used for dynamical experiments, no interaction was found and it was determined that the silica particles do not aggregate. Rheological measurements were used to determine the gelation temperature ($T_{gel} \sim 60\ °C$), and XPCS measurements were performed as a function of temperature around T_{gel}. The structural relaxation process slows down rapidly with increasing temperature. Moreover, ageing is observed. These findings support the idea that a common mechanism is responsible for the relaxation dynamics of complex systems out of equilibrium and that undergo physical ageing [197]. Flocculation and oscillatory shear experiments were conducted on two filled polymer systems, a polycarbonate melt filled with multiwalled carbon nanotubes and a silica-filled ethylene propylene diene monomer elastomer, and the flocculation data of both systems could be modelled using a 'power saturation' equation. XPCS was used to determine that the relaxation time scales as $\tau \sim q^{-1}$ and that the functional shape of the correlation functions is described by the KWW function with a KWW exponent equal to 1.5, as has been found in other jammed systems [184, 185].

Nanocomposites formed by a liquid crystal—4′-pentyl-4-biphenylcarbonitrile (5CB)—and dispersed silica nanoparticles show intriguing ageing dynamics with an anisotropic relaxation rate (Fig. 3.13). Slowing down and speeding up are observed on the two-time correlation functions, and the ageing is due to the slow relaxation of the composite. The anisotropy in the dynamics depends on the sample preparation and is assigned to the local arrangement of nematic domains, although it is not clear how an anisotropic arrangement of domains is maintained across lengths that exceed greatly the nematic correlation length, which is of the order of 10 μm [254]. A study about the dependence on temperature and volume fraction of a
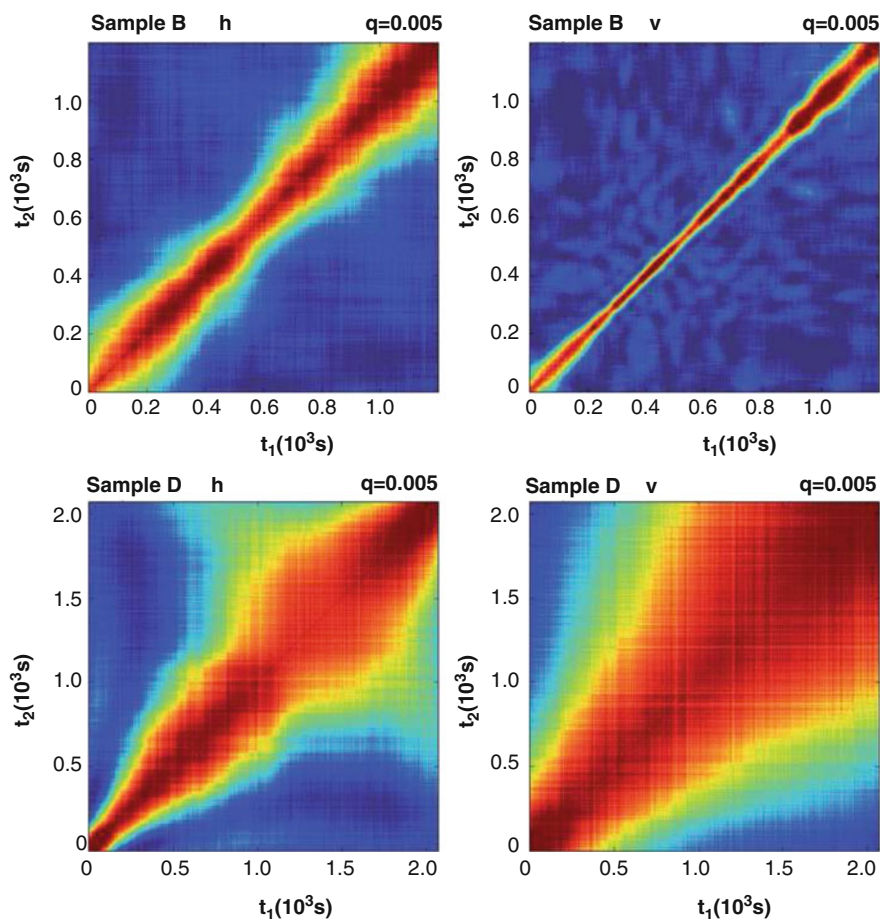
Fig. 3.13 Two-time correlation functions for horizontal (left) and vertical (right) directions with respect to the alignment of the capillary, for $q = 0.005\,\text{Å}^{-1}$. (top) Sample B: the systems have faster dynamics in the vertical direction than in the horizontal. For both directions, there is unusual behaviour: the system speeds up (i.e. narrowing of the two-time correlation) and later it slows down again. (bottom) Sample D: the dynamics are faster in the horizontal direction and slow down with age, after which they speed up again (Figure reproduced from [254] with permission from The Royal Society of Chemistry)

nanocomposite of polymethyl methacrylate (PMMA)-capped gold particles on a PMMA matrix shows the possible existence of an intrinsic length scale that is associated with the dynamical heterogeneities. Stretched and compressed relaxations are observed, dependent of the temperature [225].

A transition from stretched to compressed exponential decay with increasing scattering vector is observed on the dynamics of spherical silica colloids in ice. The samples are prepared by diluting the silica particles in water and subsequent freezing. Ice has a dentritic morphology, and during freezing, regions with high
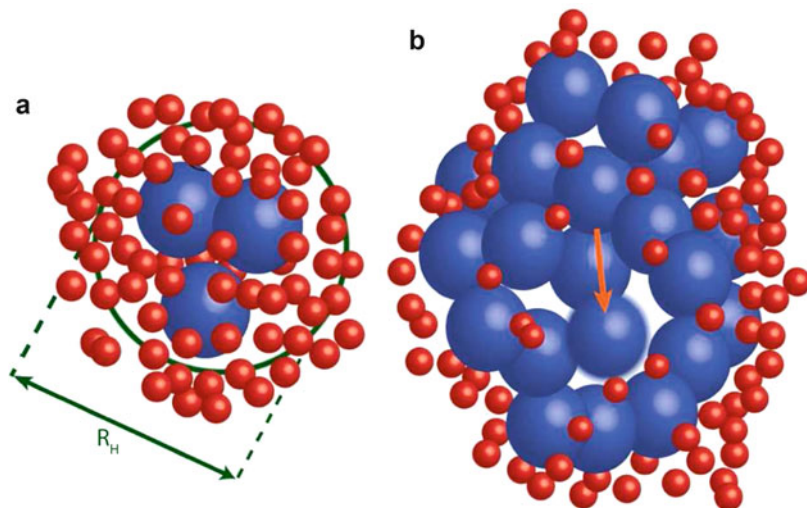
Fig. 3.14 Schematic model of the large-sphere-rich aggregates for: (**a**) low and (**b**) high concentration of large spheres. The circle in (**a**) represents the hydrodynamic radius of an aggregate. The arrow in (**b**) indicates a possible rearrangement within the domain (Reprinted figure with permission from [219]. Copyright (2011) by the American Physical Society)

density of silica particles are created. In these regions, the silica particles move ballistically and their velocity increases with temperature. The transition of the KWW exponent from <1 to >1 may be related to ice grain boundary migration induce by the coarsening of the ice crystal [224]. Depletion-induced demixing of bimodal hard-sphere colloidal suspensions causes heterogeneities that result on a dynamics characterised by two distinct timescales. Mixtures of latex spheres of radii $R_{large} = 54$ nm and $R_{small} = 11$ nm dispersed in glycerol, with a constant combined volume fraction kept at $\Phi = 0.4$ and for different relative contents of large and small spheres, were studied with SAXS and XPCS. The motion of the small particles is independent of the composition, but the motion of the large spheres depends on the size of the domains rich in large particles. This results in two timescales that are associated with the dynamics within the domains rich in large or small particles (Fig. 3.14) [219].

Temporally heterogeneous dynamics were observed on colloidal gels made with moderately attractive carbon particles. The dynamical fluctuations are quantified using a q-dependent dynamical susceptibility that is obtained from the variance of the instantaneous intensity correlation function. The q-dependence of the susceptibility is very different to previous findings on strongly attractive gels, and the behaviour of the average dynamics and its fluctuations can be explained using scaling arguments [238]. In strongly repulsive dispersions of $\gamma - Fe_2O_3$ (maghemite) nanoparticles, if the volume fraction of magnetic material is above a threshold value Φ^*, a freezing of the translational and rotational degrees of freedom can be achieved. XPCS has been used to study the translational dynamics of such

systems at volume fraction $\Phi/\Phi^* \approx 1.2$. SAXS results show a correlation peak due to a mean interparticle distance of ~14 nm. From a series of speckle patterns recorded over a period of 10 to 12 h, the two-time correlation function is calculated. The dynamics show a compressed exponential relaxation, characteristic of ballistic-like dynamical behaviour, with a relaxation time that scales as $\tau \sim q^{-1}$ and is age dependent. The dynamical susceptibility, calculated from the degree of correlation between patterns distant by a lag time Δt, shows that these dynamics have an intermittent nature and are associated with a series of rearrangement events [243]. The dynamics of similar systems under an applied magnetic field have also been studied by the same group [242]. In the study of a composite-type material consisting of polyurethane gel and carbonyl iron micrometric spheres under three magnetic fields (0, 300 and 600 mT), it was found that the polyurethane matrix is the main source for the observed dynamics. For fields below 300 mT, there is a clear dependence of the dynamics and the direction of the magnetic field. At 600 mT, this dependence disappears but the relaxation rates decrease, suggesting that the magnetic field may reinforce the material and increase its stiffness [75, 76]. Magnetic repulsion can induce the arrest of diffusive motion, as has been shown for an inverse ferrofluid consisting of diamagnetic silica particles suspended in a paramagnetic ionic liquid (bis(1-ethyl-3-methylimidazolium)-tetrakis(isothicyanato)cobalt (II)) [168].

The dynamics of a laponite colloidal suspension across the glass transition has been studied over a wide range of momentum transfer and timescales in [154], using XPCS, neutron spin echo, dynamic light scattering and molecular dynamics simulations. The dynamics of such system is characterised by a two-step decay as a result of two main relaxation processes: a fast relaxation due to the motion of a particle within the cage formed by its neighbour particles (β-relaxation), followed by a slower process that is associated with the escape of the particle from the cage and the structural rearrangements of the particles (α-relaxation) [18, 40]. In particular, the dependence on q and age of the fast and slow relaxation times of the glass has been explored. The two relaxations have a different behaviour across the glass transition. The fast relaxation time scales as q^{-2}, which is indicative of diffusive single particle dynamics, and this behaviour does not change across the glass transition. The slow relaxation evolves from a q^{-2} to q^{-1} dependence, and the correlation functions have a stretched exponential shape, indicating that the dynamics change from diffusive to discontinuous hopping of caged particles [154]. These results are in full agreement with recent theoretical predictions [19]. The disaggregation and reformation of fibres determine the dynamics of fibrous gels made of solutions of fluorenylmethoxycarbonyl (Fmoc-FF) in dimethyl sulfoxide mixed with water. Gradually the network becomes more uniform and the elastic modulus increases and saturates at long times [55].

5.2.3   Rheology

One advantage of studying samples under flow is that beam-induced damage is limited. But more importantly, effects in the diffusion due to confinement, the influence of strain on the flowing properties, etc. can be studied. As a model

example, the dynamics of a hard-sphere (PMMA) suspension was investigated in transverse and longitudinal laminar flow. Although the static properties are found to be isotropic in the range of parameter values studied—average flow velocities between 0 and 200 mm s^{-1} and q-values between 3 and 10 in q $\cdot$ a units, a being the particle radius—the dynamic properties are not isotropic: while in transverse flow (i.e. $\vec{q} \perp \vec{v}$), the correlation functions are unaffected by the flow (Fig. 3.15, left), for longitudinal flow ($\vec{q} \parallel \vec{v}$), they are strongly affected (Fig. 3.15, right). The method and its capabilities are described in detail in [30, 63, 64].

Similar findings have been reported in a study of the dynamics due to advection and diffusion under homogeneous shear flow of charge-stabilised 100 nm radius polystyrene particles suspended in glycerol [29]. The applied shear deformation dominates the decay of the autocorrelation function: the autocorrelation functions show a dependence on the flow rate when they are measured at a scattering vector $\vec{q}$ that has a component parallel to the flow direction. Information unique to the diffusive dynamics can be obtained by measuring at scattering vectors
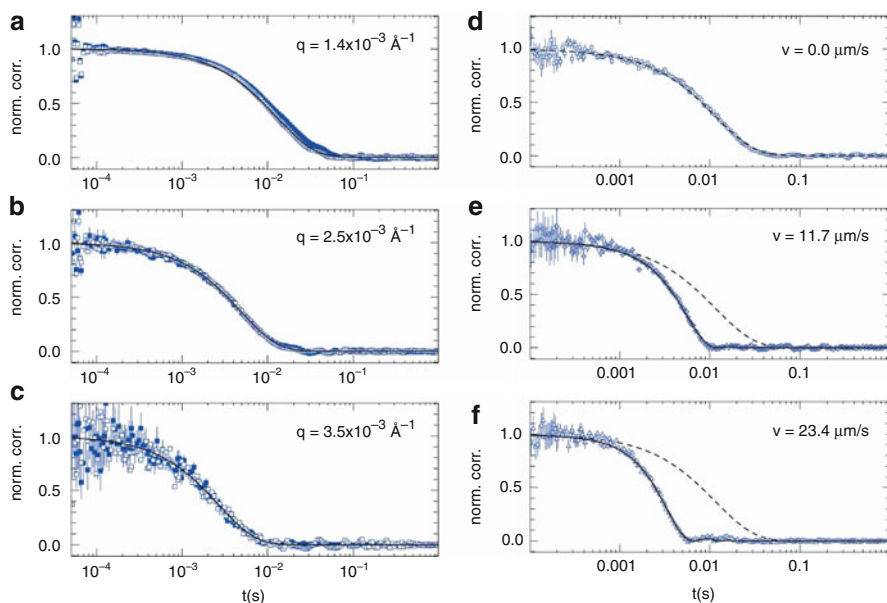
Fig. 3.15 Normalised autocorrelation functions $[g^{(2)}(\vec{q}, t) - 1]/\beta$ obtained in (**a**), (**b**) and (**c**): transverse flow geometry ($\vec{q} \perp \vec{v}$), for three different $|\vec{q}|$ values, at zero flow (full symbols) and at $|\vec{v}| \simeq 58.5$ µm (open symbols). The solid lines correspond to fits of open symbol data to the function f(t) = e$^{-2\Gamma t}$; (**d**),(**e**) and (**f**): longitudinal flow geometry ($\vec{q} \parallel \vec{v}$), at $|\vec{q}| = 1.3 \times 10^{-3}$ Å^{-1} for three different flow velocities. The lines represent the fit to the function $f(t) = e^{-2\Gamma t}\left[\frac{\sin(\Gamma_s t)}{\Gamma_s t}\right]^2$ for the corresponding flow rates (solid) or zero flow (dashed) (Adapted from [64]. Copyright (2008) International Union of Crystallography (IUCr). Link http://dx.doi.org/10.1107/S0909049508006420)

perpendicular to the flow direction. However, above a certain shear rate, the data measured at $\vec{q}$ ($\vec{v}_{\parallel} = 0$) may have also contributions due to shear effects or to decorrelation induced as particles enter and leave the scattering volume (transit effects). Shear effects will usually dominate over particle transit effects [29].

Long-range properties like the connectivity of the gel structure or the bond percolation seem to play a minor role in the local dynamics and rheological properties of a gel formed on cooling moderately concentrated suspensions of silica colloids [83]. The results of this study are well explained by a simplified mode-coupling theory [205]. This theory considers only local properties, and thus, the good agreement between theory and the combination of rheological and XPCS results implies that it is principally the local structure that determines the mechanical and dynamical properties of such gels [83].

Deviations from the simplified mode-coupling theory predictions are observed in the temporal evolution of gel formation and ageing in suspensions of silica nanocolloids for a volume fraction of $\Phi = 0.43$ and close to the gel transition. By reducing the temperature below the theta point, a short-range attractive interaction is suddenly introduced. The suspensions maintain their fluid nature for a very long latency period longer than usual before acquiring a measurable elastic shear modulus. The length of the latency period depends on the strength of the interparticle attraction [84].

When oscillatory shear strain is applied to a concentrated nanocolloidal gel of silica spheres, periodic peaks appear on the intensity autocorrelation function. If the applied strain is above a threshold, the amplitude of the peaks decays exponentially with the number of shear cycles, which indicates that the particles undergo irreversible rearrangements. The decay rate of the amplitude of the peaks depends on the momentum transfer value, and a power law distribution in the sizes of the regions that rearrange due to shear is determined. Below a threshold, the microscopic rearrangements are reversible [190].

5.2.4 Polymers

Polymers are a large class of soft matter systems that display a very rich variety of structural and dynamical properties. As a result of the long, string-like, flexible configurations of polymers, many of their properties have universal attributes such as scaling laws and characteristic exponents [70]. XPCS is an excellent tool to investigate the slow dynamics and related phenomena like reptation, entanglement, etc. that occur in polymers and composite materials (see Fig. 3.6 and Ref. [99]).

The gelation of a cross-linked polymer composed of resorcinol and formaldehyde was studied by XPCS and SAXS. Two relaxations are observed: a fast, non-ergodic relaxation related to the stiffening of the polymer network and a slow relaxation due to the stress relaxation dynamics of the network that restores ergodicity to the system. No dynamical heterogeneity is observed [45]. Adding molybdenum to the system induces a change in the gelation process and larger clusters are formed [46]. The relaxation behaviour of poly (N-isopropylacrylamide) hydrogels is hyperdiffusive due to a uniform shrinkage of the polymer matrix [123, 124].

Diblock copolymer melts have been investigated in several works. Stretched exponential relaxations have been measured for a styrene-isoprene diblock copolymer above the microphase separation transition, and it has been found that the corresponding relaxation times change exponentially with temperature [106]. In a highly asymmetric styrene-isoprene, the structural dynamics due to micelle diffusion have been characterised. The order formation leads to an increase of the microscopic relaxation time [169]. The development of concentration fluctuations in styrene and ethyl methacrylate block copolymer in its disordered phase below the disorder to order transition temperature and in the ordered lamellar system has been investigated. In the disordered phase, nondiffusive dynamics associated with compositional fluctuations are observed. In the lamellar phase, the dynamics become diffusive and the relaxation times depend on q^{-2} [201]. The binary glass former system methyltetrahydrofuran and oligomeric methyl methacrylate, close to the glass transition temperature, yields compressed relaxation functions and shows non-equilibrium dynamics [203].

Mechanical reinforcement in polymer nanocomposites seems to be controlled by interparticle interactions, as has been suggested from XPCS, electron microscopy and rheology experiments on polystyrene homopolymers mixed with polystyrene-grafted silica nanoparticles [2].

5.2.5   Surfaces, Films and Systems Under Confinement

Research on the dynamic fluctuations on surfaces, thin films or systems in confinement is one of the principal areas where XPCS is applied [220]. The intrinsic dynamics of polymers or colloidal solutions is modified at, or close to, surfaces and interfaces. The movement of polymeric chains or colloidal particles is also hindered in confinement or in thin films when the film thickness is comparable to the radius of gyration or the size of the colloidal particles [108, 109]. Many applications and uses of polymers or colloidal solutions, ranging from drug delivery to lubrication, imply a confined environment in which surface or interfacial properties play a crucial role and may affect the stability, properties and dynamical behaviour of the different structural phases. One example is the glass transition temperature: large deviations are observed between the bulk T_g and that of confined systems or films [59]. Surface or thin film XPCS studies are generally conducted in reflectivity or grazing incidence SAXS (GISAXS) geometry. In GISAXS geometry, due to the shallow incidence angle used, the penetration depth of the X-rays into the material is restricted to only few nanometres, and thus, a high surface sensitivity is achieved.[9] The penetration depth can be tuned by changing the incidence angle.

Monitoring the surface height fluctuations due to thermally induced capillary waves in polystyrene top layers (thickness in the 27–127 nm range) in bilayer films, for underlaying films with very different elastic moduli, it has been determined that the capillary wave relaxation, close to the glass transition temperature, depends on

---

[9]Hexemer and Müller-Buschbaum [93] reviews in detail the application of neutron and X-ray grazing incidence techniques to the study of soft matter systems.
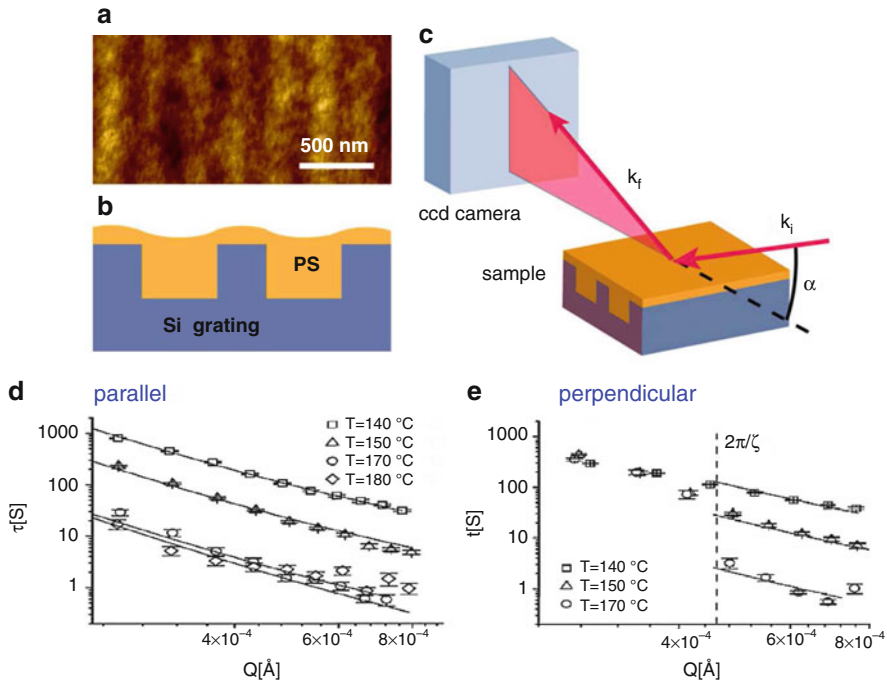
Fig. 3.16 (**a**) Atomic force microscopy image of a polystyrene film on a silicon grating. The dark and bright lines correspond to the grooves and lines, respectively. (**b**) Cross-sectional illustration of the sample. (**c**) Experimental geometry, for measurements along the perpendicular direction of the grooves. (**d**) and (**e**) Capillary relaxation time constants as a function of wave vector q for different temperatures, in the parallel and perpendicular configuration, respectively. Solid lines are the t curves from the parallel data. The vertical dashed line indicates the cut-off wave vector (Figure adapted with permission from [4]. Copyright (2012) by the American Physical Society)

two factors: the substrate modulus and the film thickness. Faster relaxations are observed on the polystyrene film if the substrate modulus is lower, and capillary waves relax faster for thinner films. Far from the glass transition temperature, confinement and substrate-induced effects disappear [59]. The influence of the substrate on the surface dynamics of thin films is clearly evinced on thin molten polystyrene films on nanoscale periodic silicon line-space gratings. The patterning of the substrate introduces a lateral anisotropy in the films and the capillary wave dynamics reflect this anisotropy: along the grooves, the behaviour is similar to thick polystyrene films while perpendicular to the grating channels, there is a cut-off length scale that marks a transition from non-suppressed to suppressed surface fluctuations (Fig. 3.16). The transition arises from an interplay between surface tension and van der Waals' interactions between film and substrate [4]. Temperature is also a determinant factor of the surface dynamics. A transition from a single to a stretched exponential, followed by another transition to another single exponential regime, was found on the surface capillary wave dynamics on silicon-

supported liquid polystyrene films of different molecular weights. Moreover, a universal scaling of the dynamics was recognised over a wide range of film thickness and temperatures in the single exponential regimes. The results agree with hydro-dynamic theory predictions [111]. The influence of the branching architecture on the surface dynamics of branched comb polystyrene films has been studied in [133, 245]. For some architectures, the discrepancy between the viscosity as determined from (surface) XPCS data and by bulk rheometry is larger than for others. The differences may be due to the degree of interpenetration of the side chains, which depends on the architecture [133, 245]. For cyclic polystyrene films, similar effects related to the architecture have been reported [244]. The formation of an ordered monolayer on the surface of a side chain comb poly(n-alkyl acrylate) (PA) polymer induces a sharp slowdown of the liquid meniscus below the surface ordering transition temperature [179]. The dynamics of covalently tethered polystyrene chains do not show relaxations in the 0.1–1000 s time window, showing that tethering can be used to adapt the properties of polymer surfaces [3]. Recent surface and interface studies on polymer brushes using synchrotron radiation techniques, XPCS included, are comprehensively reviewed in [99].

In polymer blends, a thin layer with a composition that differs from the bulk may form at the free surface due to preferential segregation of one of the components to the surface. The surface chain dynamics can also be different from those of the bulk, as has been shown for poly(vinyl methyl ether) (PVME) chains at the free surface of a polystyrene and PVME blend. Two relaxations are observed. From the analysis of the dependence of the relaxation times with respect to momentum transfer and film thickness, the two relaxations are ascribed to two separate populations of chains in two environments. One of the populations undergoes translational motion and the other, ballistic and caged behaviour [66]. These results demonstrate that the rheology depends strongly on the local composition of the blends. With the addition of polystyrene-coated gold nanoparticles, the surface dynamics of chain segments are faster than the pure mixture (i.e. without gold nanoparticles), and the surface viscosity is reduced by one order of magnitude [67]. The dynamics of gold nanoparticles moving on the surface of a polystyrene film show KWW-type relaxations, with KWW exponents in the 0.7–1.5 range, depending on sample age and temperature. As the relaxation rates scale linearly with q, simple diffusive Brownian motion can be discarded. The observed behaviour is explained by ballistic-type dynamics with a power law distribution of nanoparticle velocities [231]. The slow particle dynamics in gold and polystyrene nanocomposite thin films was analysed in [160] and indicates that the dynamics are non-Brownian. Thiol-functionalised gold nanoparticles embedded in polystyrene films on substrates were used as markers to determine how the local viscosity changes with the distance from the polymer-substrate interface. The surface viscosity above the glass transition temperature is lower than that at the centre of the film [116–118]. The 'marker' grazing incidence XPCS technique has been recently reviewed in [107].

The influence that a low concentration (below 0.1 % in weight) of gold nanoparticles has on the dynamics of photosensitive azopolymer Langmuir-Schaefer films deposited on silicon was studied in [164, 165]. The nanoparticles show

non-Brownian hyperdiffusive behaviour. Illuminating the system with ultraviolet light, the dynamics become faster due to a reduced viscosity of the film, but the functional shape of the correlation function is not modified [164]. In a Langmuir film formed by stabilised gold nanoparticles at the water-air interface, anisotropic and heterogeneous dynamics have been identified. Information about the lifetime of the dynamical heterogeneities upon approaching dynamical arrest is obtained from the fourth-order correlation function of the intensity [163]. The relation of the fluctuations on the Langmuir film to its structure and mechanical response is analysed in [167]. It has been reported that the evanescent wave light scattering method can provide information on the air-water interface comparable to that obtained with XPCS. The method takes advantage of the enhancement of scattering that occurs when the system is illuminated at the critical angle. The method is discussed in [230].

The surface dynamics of the [bmim][BF$_4$] ionic liquid has been investigated at the transition from propagating to overdamped thermal capillary waves. [bmim][BF$_4$] has a dense layer, 0.6 nm thick, at the free surface which may affect the dynamics. However, the XPCS results can be explained using linear response theory, and the influence of the dense surface layer in the dynamics can be ruled out [222]. In a supercooled liquid of polypropylene glycol, to explain the observed surface dynamics in the supercooled liquid state, low-frequency elasticity showing a non-Arrhenius temperature behaviour and a frequency-dependent viscosity must be considered [38]. In another supercooled organic glass-forming system, dibutyl phthalate, evidence of surface-induced elasticity and a liquid-liquid surface layer of high mobility were found [217]. The dynamics parallel and perpendicular to the surface of a colloidal suspension of stabilised silica particles are very different. Parallel to the surface, the particle dynamics are ballistic and heterogeneous, whereas they are non-ballistic and much slower in the perpendicular direction [56].

5.3   Hard Condensed Matter

5.3.1   Magnetism and Related Phenomena

Antiferromagnetic domain fluctuations in bulk chromium were examined with XPCS for temperatures below and above the Néel temperature, by measuring the time variation of the speckle pattern at the region of the (200) Bragg reflection. In this way, the short wavelength structure associated with the spin and charge density waves can be accessed. The domain walls move back and forth by distances of the order of 1 μm and the dynamics are temperature dependent. Upon cooling, the fluctuations become slower. The intensity autocorrelation functions are compressed exponentials, which suggests that the dynamics are elastically coupled between blocks of spins. Even at temperatures well below the Néel temperature, the antiferromagnetic domains can be unstable on timescales of fractions of an hour [216]. On the USb antiferromagnet, the intensity autocorrelation function at the pure magnetic (003) reflection, measured at the uranium M_4 edge, is essentially static over 1000 s, although a small change (~0.4 %) is noticed. Thus, the magnetic domains on USb

seem to be static [132]. Jammed domains have been observed in epitaxially grown yttrium/dysprosium/yttrium, which forms a spiral antiferromagnet ($T_{Néel} = 180$ K). The active layer is 500 nm thick dysprosium (Fig. 3.17). The autocorrelations decay as stretched exponentials with a KWW exponent equal to 1.5, as it has been found in many jammed systems (see above). This behaviour is explained in terms of stress release. Domain wall fluctuations get frozen at a temperature T ~ 177 K and the time constant of the fluctuations becomes extremely large. The dependence of the relaxation times with temperature is described by a Vogel-Fulcher law, as it has also been found in other jammed systems [36]. In helical antiferromagnetic domains on ultra-
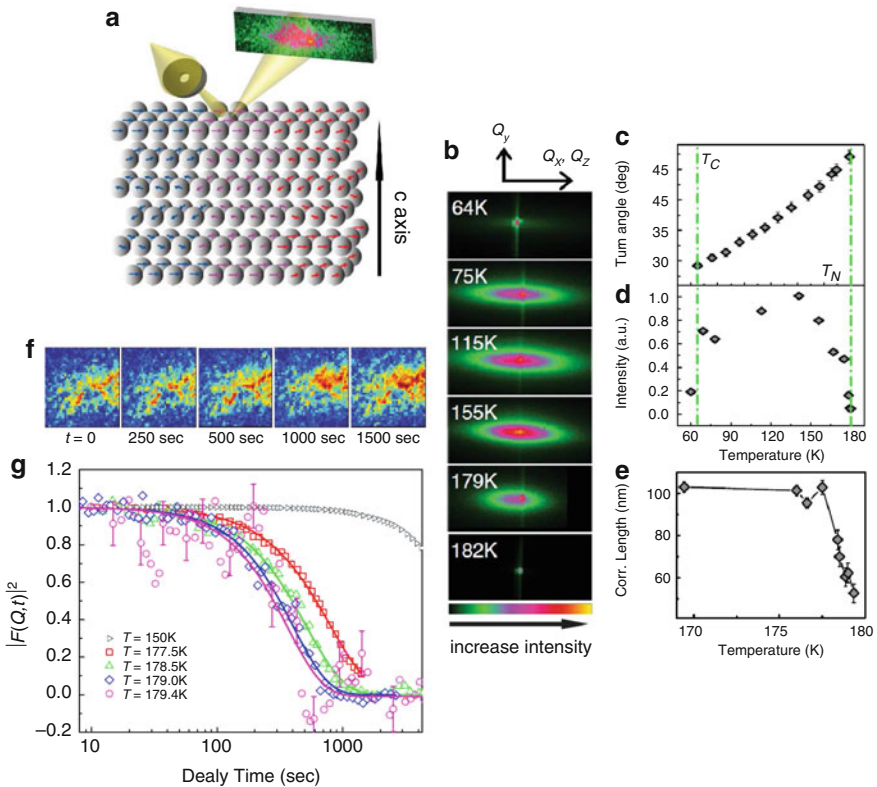
Fig. 3.17 (**a**) Schematic diagram of the spiral spin structure along the c axis. Three types of spin structure are shown that give rise to domains in the Bragg plane. (**b**) $(0,0,Q_m)$ antiferromagnetic Bragg reflection measured with an incoherent beam, for different temperatures. At T = 182 K, the system is paramagnetic and the magnetic reflection disappears. At T = 64 K the system is ferromagnetic and the reflection also disappears. (**c**), (**d**) and (**e**) Evolution of the spiral turn angle, integrated intensity and lateral correlation, respectively, as a function of the temperature. The green vertical lines denote the transition temperatures. (**f**) Time snapshots of the speckles at 178.50 K. (**g**) Normalised autocorrelation functions for different temperatures. Solid lines are fit to the data using stretched exponentials (Reprinted figure with permission from [36]. Copyright (2013) by the American Physical Society)

thin holmium films (11 monolayers thick, nominal $T_{Néel} = 76$ K) grown pseudomor-phically on yttrium, the fluctuations increase with the temperature. The system is non-ergodic and parts of the sample fluctuate while the other are static, which could be due to variations of the holmium thickness, because the Néel temperature depends critically on the thickness [120].

The charge density wave dynamics of nominally pure and Ti-doped TaS_2 have been investigated in [232]. Collective pinning stabilises the charge density wave phase structures against spontaneous fluctuations. By quenching the samples, meta-stable states can be prepared for the pure and doped samples. The fluctuations in these metastable states are similar to those found in jammed soft matter [232]. It has been proposed that combining resonant X-ray scattering and XPCS, new insights into the charge density wave dynamics of systems like $La_{1.72}Sr_{0.28}NiO_4$ could be gained [182].

Near a thermally driven spin-reorientation phase transition, the Au/Co/Au heterostructure presents slow magnetic fluctuations that yield stretched exponential autocorrelations. Sensitivity to magnetism is achieved tuning the X-ray energy to the L_3 edge of cobalt (778 eV). In that study, it is assumed that the charge scattering does not change in time. The stretched shape of the autocorrelation suggests that there is cooperative motion through the phase transition. The local magnetisation of the system changes continuously from a perpendicular to an in-plane orientation [207].

Extremely fast relaxation times could be accessed using a pulsed soft X-ray laser. The nanoscale dipole moments in polarisation clusters in $BaTiO_3$ fluctuate at timescales in the picosecond range. These timescales are not accessible using synchrotron radiation, but using a Michelson-type delay pulse generator and acquir-ing data for single laser shots at different delay times, the intensity autocorrelation function can be obtained. The relaxation times are of the order of tens of picosec-onds. The longest relaxation time (~90 ps) is found at 4.5 K degrees above the Curie temperature and coincides with the temperature at which the polarisation is maximum [158].

The dynamics near the charge ordering temperature in the valence fluctuation compound Eu_3S_4 were studied in [157], and a slow fluctuation with a relaxation time of the order of 10 s was found. In the relaxor ferroelectric material PZN-9 %PT, near the transition temperature at which the system changes from ferroelectric to relaxor ($T_c = 455$ K), the relaxation times are also of the order of 10 s [162].

5.3.2   Surface Dynamics

A quasihexagonal reconstruction of the Au(001) surface can be obtained by high-temperature annealing (T ~ 1200 K) in vacuum. This quasihexagonal reconstruction has been studied by XPCS analysing the intensity fluctuations near the (1.2 1.2 0.3) reflection of the quasihexagonal phase and the (001) anti-Bragg reflection of the substrate. The data could be fitted with pure exponentials and relaxation times in the range of 10–10^6 were obtained. The speckle fluctuations at the bulk (002) Bragg reflection are much slower than at the (001) [173]. When in contact with an electrolyte solution (0.1 M $HClO_4$), the step edges and islands on the Au(001) surface are highly mobile, and their evolution and speed are also dependent on the

applied potential [175]. Flow of steps in Pt(001) causes persistent oscillations of speckle intensities that last for tens of minutes [174]. The Pt(001) surface has decorrelation times faster than the Au(001) one [172]. Island growth by iron deposition on MgO and Au(001) has been investigated with XPCS in [181]. The surface dynamics of electrodes and of Au(001) in different experimental conditions are discussed in [252].

5.3.3 Atomic Diffusion

Atomic diffusion can be studied with XPCS by measuring along several reciprocal space directions the intensity fluctuations in the diffuse scattering, away from Bragg peaks. The diffusion of single atoms in the intermetallic alloy $Cu_{90}Au_{10}$ has been studied in this way, and the experimental correlation times can be explained using a model with nearest-neighbour exchanges, while a model that considers jumps between the second-nearest neighbours is inconsistent with the data [128]. For more details on the model, see also [129]. The atomic motion of platinum and their interaction with vacancies have been investigated in $Ni_{97}Pt_3$ by XPCS and Monte Carlo simulations. High sensitivity to short-range order is achieved, and from the data, an activation energy (i.e. the sum of a vacancy formation and migration energy) of $E_{act} = 2.93$ eV and diffusion coefficients of the order of $D_{T\,=\,830K} \sim 10^{-23}$ m^2/s are obtained [226].

The diffusive dynamics of a martensitic shape memory alloy ($Au_{50.5}Cd_{49.5}$) are unusual. Slow non-equilibrium dynamics occur only in a narrow temperature interval close to the athermal martensitic phase transition. The speckle diffraction pattern on the (001) Bragg reflection changes abruptly at $T_c = 305.35$ K within a temperature interval of less than 0.05 K. Above T_c, the (one-time) autocorrelation functions have a compressed exponential shape with KWW exponent values up to 2. This has been explained as originating from strain dominated dynamics, as the martensitic transition induces strain fields due to the change in lattice symmetry. Below the transition temperature they are almost exponential. At a temperature close to T_c, the behaviour is better characterised by a two-time correlation function, and it shows that the dynamics slow down gradually and present avalanche-like features, which are ascribed to sudden progressions of the phase transition [155]. Microstructural avalanches have also been detected using coherent X-ray scattering in the martensitic phase transition of cobalt [198].

5.3.4 Metallic Glasses

The dynamics of the metallic glass former $Mg_{65}Cu_{25}Y_{10}$ below and above the glass transition temperature ($T_g \sim 405$ K) have been studied to determine what is the physical mechanism underlying structural relaxations and how these depend on the thermal history and waiting time. A dynamical crossover takes place between the supercooled liquid phase and the metastable glass state: the shape of the correlation function changes abruptly across the transition. In the supercooled state, the dynamics are diffusive and the correlation functions are stretched exponentials. The dynamics in the glass state are driven by internal stress relaxation and the correlation functions are compressed exponentials. The relaxation of stress depends on the

thermal history of the samples and different ageing regimes are found [195–197]. Compressed correlation functions and different ageing regimes have also been found in the $Zr_{67}Ni_{33}$ metallic glass well below the glass transition temperature [194]. Thus, the dynamics of metallic glasses resemble those of soft matter gels and other soft materials out of equilibrium, which suggests that there may be some universal microscopic dynamics for all these systems.

The crystallisation of the metallic glass $Zr_{65}Ni_{10}Cu_{17.5}Al_{7.5}$ and the influence of temperature on the dynamics have been investigated with XPCS. The pristine samples were prepared in the glassy state by melt spinning followed by cold rolling of ribbons and were studied in transmission geometry. The correlations have a compressed exponential decay and the dynamics slow down progressively. The data are explained with a phenomenological model. According to the results, crystallisation and atomic mobility are manifestations of the same process [127].

5.3.5   Self-Organised Systems

Diverse non-equilibrium systems can form similar self-organised patterns, and often, their evolution is described by using equivalent models [43]. Ion beam sputtered surfaces and patterns formed by erosion of sand are a compelling example: ripples and dunes are observed at the macroscale on sandy soils due to the action of wind on the sand bed, and analogous structures can also be formed at the nanoscale by eroding surfaces with ion beams.[10] Normal incidence sputtering of semiconductor surfaces can lead to the formation of very well-ordered nanodot patterns. At off-normal incidence, typically ripples are obtained. Ion beam eroded surfaces have dynamics governed by the complex interplay between the mechanisms that tend to roughen and smoothen the surface. Long-term evolution of pattern formation on sputtered surfaces is well characterised by continuum models developed in close analogy to the hydrodynamic models used to describe the dynamics of granular matter. One interesting phenomenon that has been observed on several surfaces upon normal ion beam sputtering is pattern coarsening and stabilisation. Various continuum models (phenomenological and based on first principles) can account for coarsening and stabilisation and predict similar asymptotic behaviours for variables such as the surface roughness. Even if their predictions about ensemble-averaged quantities can be comparable, the dynamical behaviour that they forecast is very different. Using XPCS and two-time correlation functions, the correctness of the different models can be verified [22].

The dynamics of GaSb(001) during sputtering at normal incidence with 500 eV argon ions have been studied experimentally with XPCS [23], using a special chamber designed for in situ surface X-ray scattering experiments [33]. The sputtering process induces a progressive change to the surface morphology: the formation of ordered surface nanostructures (Fig. 3.18a) with pattern wavelength (or lateral periodicity) λ is manifested in the GISAXS pattern by the development of

---

[10]A recent review on erosion can be found in [119]. Ion beam sputtering is the focus of a special review issue [44].
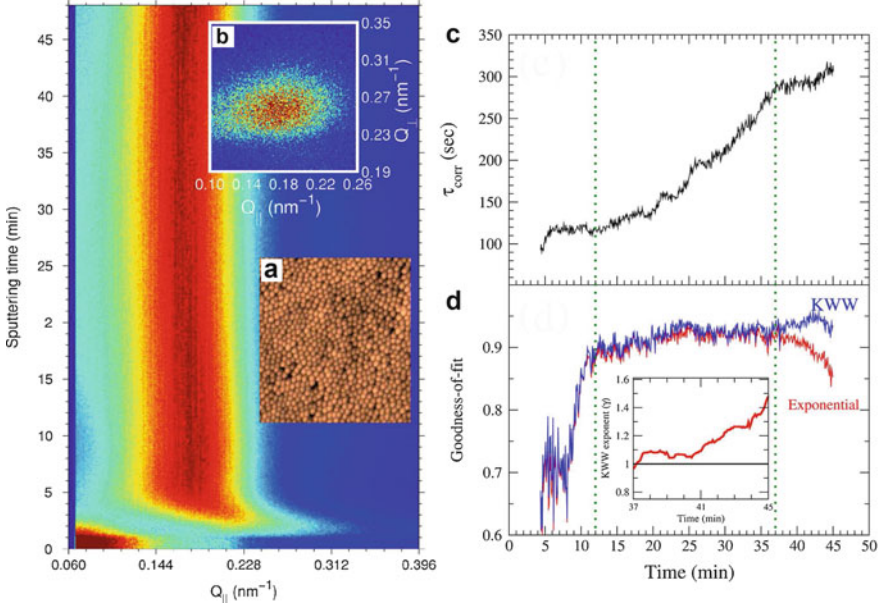
Fig. 3.18 (Left) GISAXS sputtering time map for a GaSb surface eroded at 500 eV. The onset of a self-organised pattern is evidenced by the appearance of the correlation peak at $t_{sputt} \sim 1$ min. Inset images: (**a**) atomic force microscopy image ($1 \times 1\ \mu^2$ area) of a GaSb sample sputtered at normal incidence, (**b**) the speckled correlation peak at $t = 47$ min, (Right) (**c**) evolution of the correlation time as a function of the sputtering time, and (**d**) R-square goodness of fit using a single decaying exponential (red full line) and Kohlrausch-Williams-Watts function (blue full line) to fit the correlation data. Inset: evolution of the KWW exponent for the late time regime. The vertical (green) dotted lines mark the separation between the early, intermediate and late regimes of the dynamics (Figure adapted from [23])

order-induced peaks at a specific Fourier component $q_{\parallel} = \frac{2\pi}{\lambda}$ (Fig. 3.18, left). At $t_{sputt} \sim 5$ min, the pattern wavelength reaches a saturation value of $\lambda \sim 36$ nm which is maintained during the whole sputtering time. The ordering of the pattern, characterised by the lateral correlation length $\xi \sim \frac{2\pi}{\Delta q}$, Δq being the FWHM of the GISAXS peak [32], also stabilises at a value of $\xi \sim 100$ nm. The two-time correlation function shows that the dynamics are nonstationary and that they slow down with sputtering time. By extracting one-time correlations at different sputtering times, three regimes are identified (Fig. 3.18c). In the early period ($t_{sputt} = 5$–12 min), the correlation time is approximately constant, with $\tau_{corr} \sim 119$ s. The decay of the correlation function is poorly described by a pure exponential or the KWW function (Eq. (3.21)). In the intermediate stage, between 12 and 37 min, ageing occurs, τ_{corr} increases gradually with sputtering time, and the correlation function decays as a pure exponential. At the late stage ($t > 37$ min), the correlation time

stabilises at $\tau_{corr} \sim 295$ s for 6 min and starts to increase again. In this late regime, the functional shape of the correlation function is better described by the KWW function than by a pure exponential, as shown by the goodness of fit (Fig. 3.18d). The KWW exponent evolves from 1 to 1.5. At the early stage, the transition between the pattern wavelength coarsening and saturation regimes is not fully complete yet. The ageing in the intermediate stage is ascribed to the gradual increase of the nanodot height, which hampers mass redistribution. The ageing and the evolution from a purely exponential correlation function to a compressed exponential may be related to stress build-up at the surface due to sputtering [23], in analogy with soft matter systems and also with the dynamics observed in granular systems [114].

6   Conclusions and Future Perspective

The use of XPCS to study the dynamics of slow processes ($t > 1$ μs) of soft and hard condensed matter systems is continuously increasing. New detectors and dedicated synchrotron beamlines will undoubtedly contribute to further develop such studies. But the developments from which XPCS will benefit most are the 'ultimate' or diffraction-limited storage rings (DLSRs) [16, 25] and X-ray free electron lasers (XFELs) that will start their operation in the near future.

At DLSRs, the brightness and coherent flux will be increased considerably. As an example, the upgrade plans of the ESRF and APS envisage a 100-fold increase in coherent flux, and this will allow to access timescales 10^4 times faster [215]. The exact timescales accessible will depend on the particular system and the experimental conditions (energy, q-range, detectors, etc.). For many systems, which currently can be probed up to ~10 ms timescale fluctuations, fluctuations of ~1 μs will be accessible. These timescales can be comparable with the time structure of the storage rings (see Sect. 4.1), and therefore, this aspect has to be taken into account when normalising the XPCS data. The temporal resolution can also be increased using time-delayed beam splitting methods (see, e.g. [115]) or with the X-ray speckle visibility spectroscopy approach [49, 104]. A detailed discussion about the benefits of DLSR sources for XPCS can be found in [215].

XFELs will be a completely new playground. A survey of the requirements and challenges of XPCS experiments at XFEL sources is presented in [77, 79, 87, 149, 220]. The flux of a single lasing pulse, which can last from few to hundreds of femtoseconds, is comparable to the flux obtained in a third-generation synchrotron storage ring integrated over 1 s. XFELs will enable to study fast processes at large q momentum transfer values and to cover the frequency gap between the ranges accessible by inelastic neutron scattering and XPCS (see Fig. 3.19). Speckle patterns with almost 100 % contrast can be obtained with a single pulse, as has been demonstrated at the Linac Coherent Light Source at SLAC [89, 102]. Moving samples, if their dynamics are within the timescales of the pulse length, should
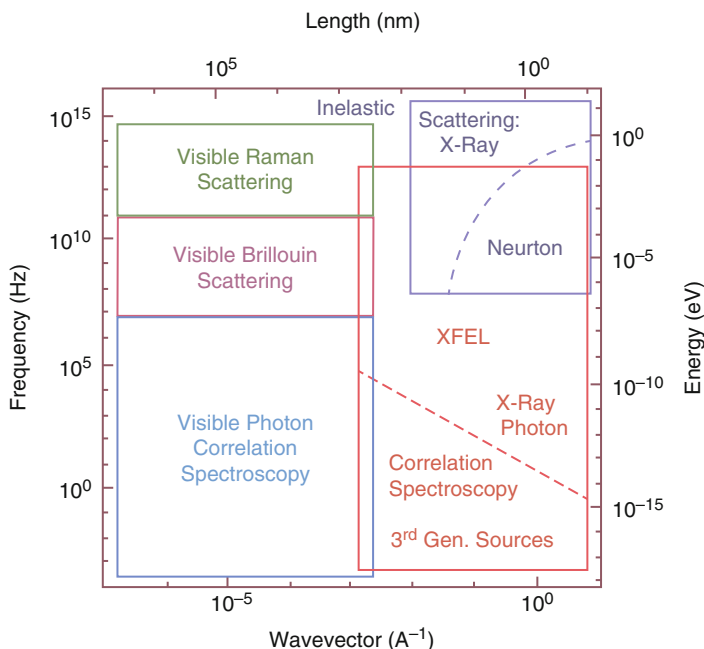
Fig. 3.19 Frequency-wave vector space covered by different experimental techniques. X-ray photon correlation spectroscopy can operate at large momentum transfer values and cover slow dynamics at third-generation sources and fast dynamics at XFEL sources (Reproduced from [78]. Copyright (2008) Elsevier Masson SAS. All rights reserved)

reduce the contrast, and this reduction could be used to probe the dynamics, in a similar way as is done in the aforementioned X-ray speckle visibility spectroscopy technique (Sect. 5.1.1). The pulse length at the European XFEL will be ~100 fs and the pulse separation ~200 ns. The feasibility of dynamic experiments on nanoparticles embedded in polymer melts at XFELs has been addressed in [34]. Slow dynamics will be investigated using the sequential technique (i.e. the most usual XPCS is performed, that is, a sequence of speckle patterns are acquired and the correlation function is calculated). To cover the gap in between these timescales and measure time relaxations of those orders, delay lines are mandatory [79, 191–193]. Pump-probe experiments, in which speckle patterns before and after the pumping probe has excited the system are compared, will also be possible. These three techniques are schematically shown in Fig. 3.20. Other aspects such as beam damage on such intense source or jittering of the beam will also need to be considered, but if these issues can be solved, XPCS experiments at XFELs will yield direct access to the dynamic structure factor at extremely short timescales.
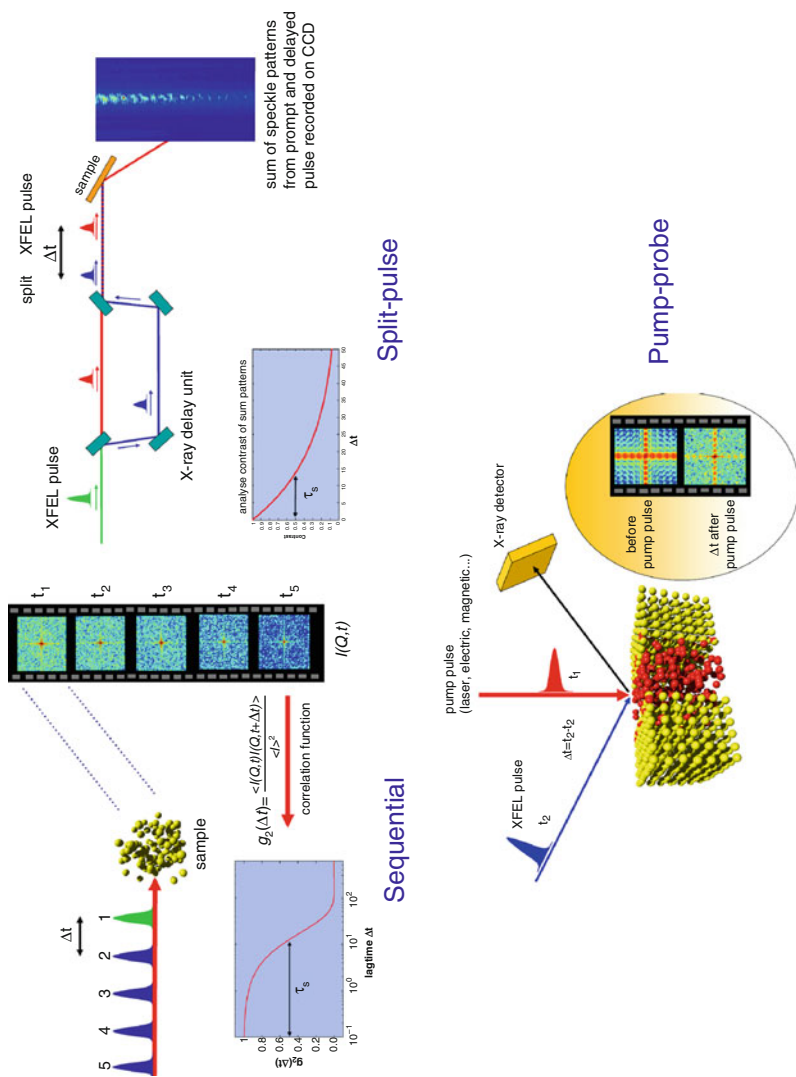
Fig. 3.20 Schematic illustrations of the sequential, split-pulse and pump-probe XPCS techniques (Reprinted from [79], Copyright (2007), with permission from Elsevier)

References

1. Abernathy DL, Grubel G, Brauer S, McNulty I, Stephenson GB, Mochrie SGJ, Sandy AR, Mulders N, Sutton M (1998) Small-angle X-ray scattering using coherent undulator radiation at the ESRF. J Synchrotron Radiat 5(1):37–47
2. Akcora P, Kumar SK, Moll J, Lewis S, Schadler LS, Li Y, Benicewicz BC, Sandy A, Narayanan S, Illavsky J, Thiyagarajan P, Colby RH, Douglas JF (2010) "Gel-like" mechanical reinforcement in polymer nanocomposite melts. Macromolecules 43(2):1003–1010
3. Akgun B, Ugur G, Jiang Z, Narayanan S, Song S, Lee H, Brittain WJ, Kim H, Sinha SK, Foster MD (2009) Surface dynamics of "Dry" homopolymer brushes. Macromolecules 42(3):737–741
4. Alvine KJ, Dai Y, Ro HW, Narayanan S, Sandy AR, Soles CL, Shpyrko OG (2012) Capillary wave dynamics of thin polymer films over submerged nanostructures. Phys Rev Lett 109 (20):207801
5. Angelini R, Madsen A, Fluerasu A, Ruocco G, Ruzicka B (2014) Aging behavior of the localization length in a colloidal glass. Colloids Surf A Physicochem Eng Asp 460:118–122
6. Angelini R, Zaccarelli E, Marques FAM, Sztucki M, Fluerasu A, Ruocco G, Ruzicka B (2014) Glass-glass transition during aging of a colloidal clay. Nat Commun 5:4049
7. Angelini R, Zulian L, Fluerasu A, Madsen A, Ruocco G, Ruzicka B (2013) Dichotomic aging behaviour in a colloidal glass. Soft Matter 9(46):10955–10959
8. Banchio AJ, Brady JF (2003) Accelerated Stokesian dynamics: Brownian motion. J Chem Phys 118(22):10323
9. Baron AQR, Kishimoto S, Morse J, Rigal JM (2006) Silicon avalanche photodiodes for direct detection of X-rays. J Synchrotron Radiat 13(2):131–142
10. Becker J, Graafsma H (2012) Advantages of a logarithmic sampling scheme for XPCS experiments at the European XFEL using the AGIPD detector. J Instrum 7, P04012
11. Becker J, Graafsma H (2012) Impact of aperturing and pixel size on XPCS using AGIPD. J Instrum 7, C02064
12. Becker J, Gutt C, Graafsma H (2011) Simulation study of the impact of AGIPD design choices on x-ray photon correlation spectroscopy utilizing the intensity autocorrelation technique. J Instrum 6, P11005
13. Becker J, Pennicard D, Graafsma H (2012) The detector simulation toolkit HORUS. J Instrum 7, C10009
14. Beenakker C, Mazur P (1983) Diffusion of spheres in a concentrated suspension – resummation of many-body hydrodynamic interactions. Phys Lett A 98(1–2):22–24
15. Beenakker C, Mazur P (1983) Self-diffusion of spheres in a concentrated suspension. Phys A 120(3):388–410
16. Bei M, Borland M, Cai Y, Elleaume P, Gerig R, Harkay K, Emery L, Hutton A, Hettel R, Nagaoka R, Robin D, Steier C (2010) The potential of an ultimate storage ring for future light sources. Nucl Instrum Methods Phys Res Sect A 622(3):518–535
17. Berne B, Pecora R (2000) Dynamic light scattering: with applications to chemistry, biology, and physics. Dover Publications, Mineola (N.Y.), unabridged edn
18. Berthier L, Biroli G, Bouchaud JP, Cipelletti L, Saarloos WV (2011) Dynamical heterogeneities in glasses, colloids, and granular media. International Series of Monographs on Physics 150. Oxford University Press, Oxford
19. Bhattacharyya SM, Bagchi B, Wolynes PG (2010) Subquadratic wave number dependence of the structural relaxation of supercooled liquid in the crossover regime. J Chem Phys 132 (10):104503
20. Bikondoa O Analysis of X-ray photon correlation spectroscopy data using two-time correlation functions, (in preparation) edn
21. Bikondoa O (2001) Estudio de la focalización vertical de un haz mediante espejos con incidencia rasante. Master Thesis, Euskal Herriko Unibertsitatea

22. Bikondoa O, Carbone D, Chamard V, Metzger TH (2012) Ion beam sputtered surface dynamics investigated with two-time correlation functions: a model study. J Phys Condens Matter 24(44):445006
23. Bikondoa O, Carbone D, Chamard V, Metzger TH (2013) Ageing dynamics of ion bombardment induced self-organization processes. Sci Rep 3:1850
24. Boesecke P (2007) Reduction of two-dimensional small-and wide-angle X-ray scattering data. Appl Crystallogr 40(1):s423–s427
25. Borland M (2013) Progress toward an ultimate storage ring light source. 11th international conference on synchrotron radiation instrumentation (sri 2012), 425: UNSP 042016
26. Brock JD, Sutton M (2008) Materials science and X-ray techniques. Mater Today 11(11):52–55
27. Brogioli D, Salerno D, Croccolo F, Ziano R, Mantegazza F (2011) Speckles generated by skewed, short-coherence light beams. New J Phys 13:123007
28. Brown G, Rikvold PA, Sutton M, Grant M (1997) Speckle from phase-ordering systems. Phys Rev E 56(6):6601
29. Burghardt WR, Sikorski M, Sandy AR, Narayanan S (2012) X-ray photon correlation spectroscopy during homogenous shear flow. Phys Rev E 85(2):021402
30. Busch S, Jensen TH, Chushkin Y, Fluerasu A (2008) Dynamics in shear flow studied by X-ray photon correlation spectroscopy. Eur Phys J E 26(1–2):55–62
31. Cai LH, Panyukov S, Rubinstein M (2011) Mobility of nonsticky nanoparticles in polymer liquids. Macromolecules 44(19):7853–7863
32. Carbone D, Biermanns A, Ziberi B, Frost F, Plantevin O, Pietsch U, Metzger TH (2009) Ion-induced nanopatterns on semiconductor surfaces investigated by grazing incidence x-ray scattering techniques. J Phys Condens Matter 21(22):224007
33. Carbone D, Plantevin O, Gago R, Mocuta C, Bikondoa O, Alija A, Petit L, Djazuli H, Metzger TH (2008) Versatile vacuum chamber for in situ surface x-ray scattering studies. J Synchrotron Radiat 15(4):414–419
34. Carnis J, Cha W, Wingert J, Kang J, Jiang Z, Song S, Sikorski M, Robert A, Gutt C, Chen SW, Dai Y, Ma Y, Guo H, Lurio LB, Shpyrko O, Narayanan S, Cui M, Kosif I, Emrick T, Russell TP, Lee HC, Yu CJ, Gruebel G, Sinha SK, Kim H (2014) Demonstration of feasibility of x-ray free electron laser studies of dynamics of nanoparticles in entangled polymer melts. Sci Rep 4: 6017
35. Caronna C, Chushkin Y, Madsen A, Cupane A (2008) Dynamics of nanoparticles in a supercooled liquid. Phys Rev Lett 100(5):055702
36. Chen SW, Guo H, Seu KA, Dumesnil K, Roy S, Sinha SK (2013) Jamming behavior of domains in a spiral antiferromagnetic system. Phys Rev Lett 110(21):217201
37. Chu B (2007) Laser light scattering: basic principles and practice, secondth edn. Dover Publications, Mineola
38. Chushkin Y, Caronna C, Madsen A (2008) Low-frequency elastic behavior of a supercooled liquid. Epl 83(3):36001
39. Chushkin Y, Caronna C, Madsen A (2012) A novel event correlation scheme for x-ray photon correlation spectroscopy. J Appl Crystallogr 45:807–813
40. Cipelletti L, Ramos L (2002) Slow dynamics in glasses, gels and foams. Curr Opin Colloid Interface Sci 7(3–4):228–234
41. Constantin D, Davidson P, Freyssingeas E, Madsen A (2010) Slow dynamics of a colloidal lamellar phase. J Chem Phys 133(22):224902
42. Cristofolini L (2014) Synchrotron x-ray techniques for the investigation of structures and dynamics in interfacial systems. Curr Opin Colloid Interface Sci 19(3):228–241
43. Cross M, Greenside H (2009) Pattern formation and dynamics in nonequilibrium systems. Cambridge University Press, Cambridge, UK/New York
44. Cuerno R, Vzquez L, Gago R, Castro M (2009) Surface nanopatterns induced by ion-beam sputtering. J Phys Condens Matter 21(22):220301
45. Czakkel O, Madsen A (2011) Evolution of dynamics and structure during formation of a cross-linked polymer gel. Epl 95(2):28001

46. Czakkel O, Nagy B, Geissler E, Laszlo K (2012) Effect of molybdenum on the structure formation of resorcinol-formaldehyde hydrogel studied by coherent x-ray scattering. J Chem Phys 136(23):234907

47. Dainty JC (1975) Introduction. In: Laser speckle and related phenomena, vol 9, Topics in applied physics. Springer, Berlin Heidelberg, pp 1–7

48. De Carlo F, Guersoy D, Marone F, Rivers M, Parkinson DY, Khan F, Schwarz N, Vine DJ, Vogt S, Gleber SC, Narayanan S, Newville M, Lanzirotti T, Sun Y, Hong YP, Jacobsen C (2014) Scientific data exchange: a schema for HDF5-based storage of raw and analyzed data. J Synchrotron Radiat 21:1224–1230

49. DeCaro C, Karunaratne VN, Bera S, Lurio LB, Sandy AR, Narayanan S, Sutton M, Winans J, Duffin K, Lehuta J, Karonis N (2013) X-ray speckle visibility spectroscopy in the single-photon limit. J Synchrotron Radiat 20:332–338

50. Deptuch GW, Carini G, Grybos P, Kmon P, Maj P, Trimpl M, Siddons DP, Szczygiel R, Yarema R (2014) Design and tests of the vertically integrated photon imaging chip. Ieee Trans Nucl Sci 61(1):663–674

51. Deptuch GW, Trimpl M, Yarema R et al (2010) VIPIC IC – design and test aspects of the 3D pixel chip. 2010 I.E. nuclear science symposium conference record (NSS/MIC), pp 1540–1543

52. Diaz A, Mocuta C, Stangl J, Mandl B, David C, Vila-Comamala J, Chamard V, Metzger TH, Bauer G (2009) Coherent diffraction imaging of a single epitaxial InAs nanowire using a focused x-ray beam. Phys Rev B 79(12):125324

53. Dierker S (1997) X-ray photon correlation spectroscopy. In: Pike ER, Abbiss JB (eds) Light scattering and photon correlation spectroscopy. Springer, New York, pp 65–78

54. Dierker SB, Pindak R, Fleming RM, Robinson IK, Berman L (1995) X-ray photon correlation spectroscopy study of Brownian motion of gold colloids in glycerol. Phys Rev Lett 75(3):449–452

55. Dudukovic NA, Zukoski CF (2014) Nanoscale dynamics and aging of fibrous peptide-based gels. J Chem Phys 141(16):164905

56. Duri A, Autenrieth T, Stadler LM, Leupold O, Chushkin Y, Gruebel G, Gutt C (2009) Two-dimensional heterogeneous dynamics at the surface of a colloidal suspension. Phys Rev Lett 102(14):145701

57. Ehrburger-Dolle F, Morfin I, Bley F et al (2009) Investigation of stress relaxation in filled elastomers by XPCS with heterodyne detection. In: Paniago RM (ed) Synchrotron radiation in materials science, vol 1092, pp 29–33

58. Ehrburger-Dolle F, Morfin I, Bley F, Livet F, Heinrich G, Richter S, Piche L, Sutton M (2012) XPCS investigation of the dynamics of filler particles in stretched filled elastomers. Macromolecules 45(21):8691–8701

59. Evans CM, Narayanan S, Jiang Z, Torkelson JM (2012) Modulus, confinement, and temperature effects on surface capillary wave dynamics in bilayer polymer films near the glass transition. Phys Rev Lett 109(3):038302

60. Fajardo P, Baron AQR, Dautet H et al (2013) XNAP: a hybrid pixel detector with nanosecond resolution for time resolved synchrotron radiation studies. 11th international conference on synchrotron radiation instrumentation (sri 2012). 425: UNSP 062005

61. Falus P, Lurio LB, Mochrie SGJ (2006) Optimizing the signal-to-noise ratio for x-ray photon correlation spectroscopy. J Synchrotron Radiat 13(3):253–259

62. Fluerasu A, Chubar O, Kaznatcheev K, Baltser J, Wiegart L, Evans-Lutterodt K, Carlucci-Dayton M, Berman L (2011) Analysis of the optical design of the NSLS-II coherent hard x-ray beamline. Adv Comput Meth X-Ray Opt Ii 8141:81410J

63. Fluerasu A, Kwasniewski P, Caronna C, Destremaut F, Salmon JB, Madsen A (2010) Dynamics and rheology under continuous shear flow studied by x-ray photon correlation spectroscopy. New J Phys 12:035023

64. Fluerasu A, Moussaid A, Falus P, Gleyzolle H, Madsen A (2008) X-ray photon correlation spectroscopy under flow. J Synchrotron Radiat 15:378–384

65. Fluerasu A, Sutton M, Dufresne E (2005) X-ray intensity fluctuation spectroscopy studies on phase-ordering systems. Phys Rev Lett 94(5):055501

66. Frieberg B, Kim J, Narayanan S, Green PF (2013) Surface layer dynamics in miscible polymer blends. Acs Macro Lett 2(5):388–392

67. Frieberg B, Kim J, Narayanan S, Green PF (2014) Surface dynamics of miscible polymer blend nanocomposites. ACS Nano 8(1):607–613

68. Gapinski J, Patkowski A, Banchio AJ, Buitenhuis J, Holmqvist P, Lettinga MP, Meier G, Naegele G (2009) Structure and short-time dynamics in suspensions of charged silica spheres in the entire fluid regime. J Chem Phys 130(8):084503

69. Gapinski J, Patkowski A, Banchio AJ, Holmqvist P, Meier G, Lettinga MP, Naegele G (2007) Collective diffusion in charge-stabilized suspensions: concentration and salt effects. J Chem Phys 126(10):104905

70. Gennes PG (1979) Scaling concepts in polymer physics. Cornell University Press, Ithaca

71. Gimenez E, Ballabriga R, Campbell M, Horswell I, Llopart X, Marchal J, Sawhney KJ, Tartoni N, Turecek D (2011) Characterization of medipix3 with synchrotron radiation. IEEE Trans Nucl Sci 58(1):323–332

72. Gimenez EN, Ballabriga R, Campbell M et al (2010) Evaluation of the radiation hardness and charge summing mode of a medipix3-based detector with synchrotron radiation. 2010 I.E. nuclear science symposium conference record (NSS/MIC), pp 1976–1980

73. Goodman JW (1985) Statistical optics, Wiley series in pure and applied optics. Wiley, New York

74. Goodman JW (2007) Speckle phenomena in optics: theory and applications. Roberts & Co, Englewood, Colorado

75. Grigoriew H, Wiegart L, Boczkowska A, Mirkowska M (2010) Dynamic correlation in magnetorheological composite under magnetic field studied by XPCS. Solid State Commun 150(17–18):840–843

76. Grigoriew H, Wiegart L, Boczkowska A et al (2010) XPCS study of dynamic correlation in polyurethane gel-carbonyl iron composite under magnetic field. Xiv international conference on small-angle scattering (sas09), 247: 012048

77. Grübel G (2008) X-ray photon correlation spectroscopy at the European X-Ray Free-Electron Laser (XFEL) facility. C R Phys 9(5–6):668–680

78. Grübel G, Madsen A, Robert A (2008) X-ray photon correlation spectroscopy (XPCS). In: Borsali, Redouane, Pecora, Robert (eds) Soft matter characterization. Springer, New York, pp 953–995

79. Grübel G, Stephenson G, Gutt C, Sinn H, Tschentscher T (2007) XPCS at the European x-ray free electron laser facility. Nucl Instrum Methods Phys Res Sect B 262(2):357–367

80. Grübel G, Zontone F (2004) Correlation spectroscopy with coherent X-rays. J Alloys Compd 362(1–2):3–11

81. Guo H, Bourret G, Corbierre MK, Rucareanu S, Lennox RB, Laaziri K, Piche L, Sutton M, Harden JL, Leheny RL (2009) Nanoparticle motion within glassy polymer melts. Phys Rev Lett 102(7):075702

82. Guo H, Bourret G, Lennox RB, Sutton M, Harden JL, Leheny RL (2012) Entanglement-controlled subdiffusion of nanoparticles within concentrated polymer solutions. Phys Rev Lett 109(5):055901

83. Guo H, Ramakrishnan S, Harden JL, Leheny RL (2010) Connecting nanoscale motion and rheology of gel-forming colloidal suspensions. Phys Rev E 81(5):050401

84. Guo H, Ramakrishnan S, Harden JL, Leheny RL (2011) Gel formation and aging in weakly attractive nanocolloid suspensions at intermediate concentrations. J Chem Phys 135 (15):154903

85. Guo H, Wilking JN, Liang D, Mason TG, Harden JL, Leheny RL (2007) Slow, nondiffusive dynamics in concentrated nanoemulsions. Phys Rev E 75(4):041401

86. Gutt C, Ghaderi T, Tolan M, Sinha S, Grbel G (2008) Effects of partial coherence on correlation functions measured by x-ray photon correlation spectroscopy. Phys Rev B 77(9):094133

87. Gutt C, Leupold O, Gruebel G (2007) Surface XPCS on nanometer length scales – what can we expect from an x-ray free electron laser? Thin Solid Films 515(14):5532–5535

88. Gutt C, Stadler LM, Duri A, Autenrieth T, Leupold O, Chushkin Y, Gruebel G (2009) Measuring temporal speckle correlations at ultrafast x-ray sources. Opt Express 17(1):55–61

89. Gutt C, Wochner P, Fischer B, Conrad H, Castro-Colin M, Lee S, Lehmkuehler F, Steinke I, Sprung M, Roseker W, Zhu D, Lemke H, Bogle S, Fuoss PH, Stephenson GB, Cammarata M, Fritz DM, Robert A, Gruebel G (2012) Single shot spatial and temporal coherence properties of the SLAC Linac Coherent Light Source in the hard x-ray regime. Phys Rev Lett 108(2):024801

90. Hansen K, Randall M, Schleitzer S, Gutt C (2010) System-level simulation of a x-ray imager with nonlinear gain and per-pixel digitizer: XPCS case study. Nucl Instrum Methods Phys Res Sect A 613(2):323–333

91. Hernandez R, Nogales A, Sprung M, Mijangos C, Ezquerra TA (2014) Slow dynamics of nanocomposite polymer aerogels as revealed by x-ray photocorrelation spectroscopy (XPCS). J Chem Phys 140(2):024909

92. Herzig EM, Robert A, van't Zand DD, Cipelletti L, Pusey PN, Clegg PS (2009) Dynamics of a colloid-stabilized cream. Phys Rev E 79(1):011405

93. Hexemer A, Müller-Buschbaum P (2015) Advanced grazing-incidence techniques for modern soft-matter materials analysis. IUCrJ 2(1):106–125

94. Holmqvist P, Meester V, Westermeier F, Kleshchanok D (2013) Rotational diffusion in concentrated platelet systems measured with x-ray photon correlation spectroscopy. J Chem Phys 139(8):084905

95. Hoshino T, Kikuchi M, Murakami D, Harada Y, Mitamura K, Ito K, Tanaka Y, Sasaki S, Takata M, Jinnai H, Takahara A (2012) X-ray photon correlation spectroscopy using a fast pixel array detector with a grid mask resolution enhancer. J Synchrotron Radiat 19:988–993

96. Hoshino T, Kikuchi M, Murakami D et al (2011) X-ray photon correlation spectroscopy of silica particles grafted with polymer brush in polystyrene matrix. In: Takahara A, Sakurai K (eds) Future trends in soft materials research with advanced light sources, vol 272, p 012020

97. Hoshino T, Murakami D, Ito K, Tanaka Y, Sasaki S, Takata M, Jinnai H, Takahara A (2013) Thermal gradient effect on the dynamical behavior of nanoparticles observed using x-ray photon correlation spectroscopy. Polym J 45(1):94–99

98. Hoshino T, Murakami D, Tanaka Y, Takata M, Jinnai H, Takahara A (2013) Dynamical crossover between hyperdiffusion and subdiffusion of polymer-grafted nanoparticles in a polymer matrix. Phys Rev E 88(3):032602

99. Hoshino T, Tanaka Y, Jinnai H, Takahara A (2013) Surface and interface analyses of polymer brushes by synchrotron radiation. J Physical Soc Japan 82(2):021014

100. Hromalik MS, Green K, Philipp H et al (2012) Asynchronous and synchronous implementations of the autocorrelation function for the FPGA x-ray pixel array detector. 18th IEEE-NPSS real time conference (rt)

101. Hromalik MS, Green KS, Philipp HT, Tate MW, Gruner SM (2013) The FPGA pixel array detector. Nucl Instrum Methods Phys Res Sect A 701:7–16

102. Hruszkewycz SO, Sutton M, Fuoss PH, Adams B, Rosenkranz S, Ludwig KF, Roseker W, Fritz D, Cammarata M, Zhu D, Lee S, Lemke H, Gutt C, Robert A, Gruebel G, Stephenson GB (2012) High contrast x-ray speckle from atomic-scale order in liquids and glasses. Phys Rev Lett 109(18):185502

103. Ilavsky J, Zhang F, Allen AJ, Levine LE, Jemian PR, Long GG (2013) Ultra-small-angle x-ray scattering instrument at the advanced photon source: history, recent development, and current status. Metall Mater Trans a-Phys Metall Mater Sci 44A(1):68–76

104. Inoue I, Shinohara Y, Watanabe A, Amemiya Y (2012) Effect of shot noise on x-ray speckle visibility spectroscopy. Opt Express 20(24):26878–26887

105. Jang WS, Koo P, Bryson K, Narayanan S, Sandy A, Russell TP, Mochrie SG (2014) Dynamics of cadmium sulfide nanoparticles within polystyrene melts. Macromolecules 47(18):6483–6490

106. Jang WS, Koo P, Sykorsky M, Narayanan S, Sandy A, Mochrie SGJ (2013) The static and dynamic structure factor of a Diblock copolymer melt via small-angle x-ray scattering and x-ray photon correlation spectroscopy. Macromolecules 46(21):8628–8637

107. Jiang N, Endoh MK, Koga T (2013) 'Marker' grazing-incidence x-ray photon correlation spectroscopy: a new tool to peer into the interfaces of nanoconfined polymer thin films. Polym J 45(1):26–33

108. Jiang Z, Kim H, Jiao X, Lee H, Lee YJ, Byun Y, Song S, Eom D, Li C, Rafailovich MH, Lurio LB, Sinha SK (2007) Evidence for viscoelastic effects in surface capillary waves of molten polymer films. Phys Rev Lett 98(22):227801

109. Jiang Z, Kim H, Lee H, Lee YJ, Jiao X, Li C, Lurio LB, Hu X, Lal J, Narayanan S, Sandy A, Rafailovich M, Sinha SK (2007) Structure and dynamics of thin polymer films using synchrotron x-ray scattering. J Appl Crystallogr 40:S18–S22

110. Jiang Z, Li X, Strzalka J, Sprung M, Sun T, Sandy AR, Narayanan S, Lee DR, Wang J (2012) The dedicated high-resolution grazing-incidence x-ray scattering beamline 8-ID-E at the advanced photon source. J Synchrotron Radiat 19:627–636

111. Jiang Z, Mukhopadhyay MK, Song S, Narayanan S, Lurio LB, Kim H, Sinha SK (2008) Entanglement effects in capillary waves on liquid polymer films. Phys Rev Lett 101 (24):246104

112. Johnson I, Bergamaschi A, Buitenhuis J, Dinapoli R, Greiffenberg D, Henrich B, Ikonen T, Meier G, Menzel A, Mozzanica A, Radicci V, Satapathy DK, Schmitt B, Shi X (2012) Capturing dynamics with Eiger, a fast-framing x-ray detector. J Synchrotron Radiat 19:1001–1005

113. Johnson I, Sadygov Z, Bunk O, Menzel A, Pfeiffer F, Renker D (2009) A Geiger-mode avalanche photodiode array for x-ray photon correlation spectroscopy. J Synchrotron Radiat 16:105–109

114. Kabla A, Debrégeas G (2004) Contact dynamics in a gently vibrated granular pile. Phys Rev Lett 92(3):35501

115. Kishimoto M, Namikawa K, Sukegawa K, Yamatani H, Hasegawa N, Tanaka M (2010) Intensity correlation measurement system by picosecond single shot soft x-ray laser. Rev Sci Instrum 81(1):013905

116. Koga T, Jiang N, Gin P, Endoh MK, Narayanan S, Lurio LB, Sinha SK (2011) Impact of an irreversibly adsorbed layer on local viscosity of nanoconfined polymer melts. Phys Rev Lett 107(22):225901

117. Koga T, Li C, Endoh MK, Koo J, Rafailovich M, Narayanan S, Lee DR, Lurio LB, Sinha SK (2010) Reduced viscosity of the free surface in entangled polymer melt films. Phys Rev Lett 104(6):066101

118. Koga T, Li C, Endoh MK, Narayanan S, Lurio L, Sinha SK (2011) X-ray photon correlation spectroscopy study on dynamics of the free surface in entangled polystyrene melt films. In: Takahara A, Sakurai K (eds) Future trends in soft materials research with advanced light sources, vol 272., p 012003

119. Kok JF, Parteli EJR, Michaels TI, Karam DB (2012) The physics of wind-blown sand and dust. Rep Prog Phys 75(10):106901

120. Konings S, Schuessler-Langeheine C, Ott H, Weschke E, Schierle E, Zabel H, Goedkoop JB (2011) Magnetic domain fluctuations in an antiferromagnetic film observed with coherent resonant soft x-ray scattering. Phys Rev Lett 106(7):077402

121. Korsch D (1991) Reflective optics. Elsevier Science, Oxford

122. Kwasniewski P, Fluerasu A, Madsen A (2014) Anomalous dynamics at the hard-sphere glass transition. Soft Matter 10(43):8698–8704

123. Laszlo K, Fluerasu A, Moussaid A, Geissler E (2010) Deswelling kinetics of PNIPA gels. Soft Matter 6(18):4335–4338

124. Laszlo K, Fluerasu A, Moussaid A, Geissler E (2011) Kinetics of jammed systems: PNIPA gels. Polym Netw 306–307:27–32

125. Le Bolloc'h D, Livet F, Bley F, Schulli T, Veron M, Metzger TH (2002) X-ray diffraction from rectangular slits. J Synchrotron Radiat 9(4):258–265

126. Leheny RL (2012) XPCS: nanoscale motion and rheology. Curr Opin Colloid Interf Sci 17(1):3–12

127. Leitner M, Sepiol B, Stadler LM (2012) Time-resolved study of the crystallization dynamics in a metallic glass. Phys Rev B 86(6):064202
128. Leitner M, Sepiol B, Stadler LM, Pfau B, Vogl G (2009) Atomic diffusion studied with coherent x-rays. Nat Mater 8(9):717–720
129. Leitner M, Vogl G (2011) Quasi-elastic scattering under short-range order: the linear regime and beyond. J Phys Condens Matter 23(25):254206
130. Lengeler B (2001) Coherence in x-ray physics. Naturwissenschaften 88(6):249–260
131. Li L, Kwasniewski P, Orsi D, Wiegart L, Cristofolini L, Caronna C, Fluerasu A (2014) Photon statistics and speckle visibility spectroscopy with partially coherent x-rays. J Synchrotron Radiat 21(6):1288–1295
132. Lim JA, Blackburn E, Beutier G et al (2014) Coherent magnetic diffraction from the uranium M-4 edge in the multi-k magnet, Usb. Rexs 2013 – workshop on resonant elastic x-ray scattering in condensed matter 519:012010
133. Liu B, Narayanan S, Wu DT, Foster MD (2013) Polymer film surface fluctuation dynamics in the limit of very dense branching. Macromolecules 46(8):3190–3197
134. Livet F (2007) Diffraction with a coherent x-ray beam: dynamics and imaging. Acta Crystallogr Sect A 63(2):87–107
135. Livet F, Bley F, Ehrburger-Dolle F, Morfin I, Geissler E, Sutton M (2006) X-ray intensity fluctuation spectroscopy by heterodyne detection. J Synchrotron Radiat 13(6):453–458
136. Livet F, Bley F, Ehrburger-Dolle F, Morfin I, Geissler E, Sutton M (2007) Homodyne and heterodyne x-ray photon correlation spectroscopy: latex particles and elastomers. J Appl Crystallogr 40:S38–S42
137. Livet F, Bley F, Mainville J, Caudron R, Mochrie S, Geissler E, Dolino G, Abernathy D, Gruebel G, Sutton M (2000) Using direct illumination CCDs as high-resolution area detectors for x-ray scattering. Nucl Instrum Methods Phys Res, Sect A 451(3):596–609
138. Livet F, Sutton M (2012) X-ray coherent scattering in metal physics. C R Phys 13(3):227–236
139. Loudon R (1983) The quantum theory of light, 2nd edn. Oxford Science Publications. Clarendon Press/Oxford University Press, Oxford/New York
140. Lu X, Mochrie SGJ, Narayanan S, Sandy AR, Sprung M (2008) How a liquid becomes a glass both on cooling and on heating. Phys Rev Lett 100(4):045701
141. Lu X, Mochrie SGJ, Narayanan S, Sandy AR, Sprung M (2010) Temperature-dependent structural arrest of silica colloids in a water-lutidine binary mixture. Soft Matter 6 (24):6160–6177
142. Lu X, Mochrie SGJ, Narayanan S, Sandy AR, Sprung M (2011) X-ray near-field speckle: implementation and critical analysis. J Synchrotron Radiat 18:823–834
143. Ludwig K (2012) X-ray photon correlation spectroscopy in systems without long-range order: existence of an intermediate-field regime. J Synchrotron Radiat 19:66–73
144. Ma L, Zhang F, Allen A, Levine L (2014) Unveiling the origin of a nonequilibrium dynamic process detected by x-ray photon correlation spectroscopy via a finite element analysis approach. Acta Crystallogr Sect A 70(4):338–347
145. Madden T, Fernandez P, Jemian P, Narayanan S, Sandy AR, Sikorski M, Sprung M, Weizeorick J (2011) Firmware lower-level discrimination and compression applied to streaming x-ray photon correlation spectroscopy area-detector data. Rev Sci Instrum 82(7):075109
146. Madden T, Jemian P, Narayanan S et al (2010) FPGA-based compression of streaming x-ray photon correlation spectroscopy data. 2010 I.E. nuclear science symposium conference record (NSS/MIC), pp 730–733
147. Madden T, Jemian P, Narayanan S, Sandy AR, Sikorski M, Sprung M, Weizeorick J (2011) Real-time compression of streaming x-ray photon correlation spectroscopy area-detector data. Nucl Instrum Methods Phys Res Sect A 649(1):237–239
148. Madsen A, Leheny RL, Guo H, Sprung M, Czakkel O (2010) Beyond simple exponential correlation functions and equilibrium dynamics in x-ray photon correlation spectroscopy. New J Phys 12(5):055001

149. Madsen A (2011) Conceptual design report: scientific instrument MID. http://dx.doi.org/10.3204/XFEL.EU/TR-2011-008

150. Maj P (2013) FPGA based extension to the multichannel pixel readout ASIC. 2013 I.E. nuclear science symposium and medical imaging conference (NSS/MIC)

151. Mandel L, Wolf E (1995) Optical coherence and quantum optics. Cambridge University Press, Cambridge

152. Margaritondo G (1988) Introduction to synchrotron radiation. Oxford University Press, New York

153. Martinez VA, Thijssen JHJ, Zontone F, van Megen W, Bryant G (2011) Dynamics of hard sphere suspensions using dynamic light scattering and x-ray photon correlation spectroscopy: dynamics and scaling of the intermediate scattering function. J Chem Phys 134(5):054505

154. de Melo Marques F et al (2015) Structural and microscopic relaxations in a colloidal glass. Soft Matter 11:466–471

155. Müller L, Waldorf M, Gutt C, Gruebel G, Madsen A, Finlayson TR, Klemradt U (2011) Slow aging dynamics and avalanches in a gold-cadmium alloy investigated by x-ray photon correlation spectroscopy. Phys Rev Lett 107(10):105701

156. Nägele G (1996) On the dynamics and structure of charge-stabilized suspensions. Phys Rep 272(5–6):215–372

157. Nakao H, Ohwada K, Shimomura S et al (2010) X-ray photon correlation spectroscopy study in valence fluctuation compound Eu(3)S(4). In: Garrett R, Gentle I, Nugent K, Wilkins S (eds) Sri 2009: the 10th international conference on synchrotron radiation instrumentation, vol 1234, pp 935–938

158. Namikawa K, Kishimoto M, Nasu K, Matsushita E, Tai RZ, Sukegawa K, Yamatani H, Hasegawa H, Nishikino M, Tanaka M, Nagashima K (2009) Direct observation of the critical relaxation of polarization clusters in $BaTiO_3$ using a pulsed x-ray laser technique. Phys Rev Lett 103(19):197401

159. Narayanan S, Madden TJ, Sandy AR et al (2012) Grid FTP based real-time data movement architecture for x-ray photon correlation spectroscopy at the advanced photon source. In: 2012 I.E. 8th international conference on E-science (e-Science)

160. Narayanan S, Sandy AR, Sprung M et al (2007) Initial characterization and design of an UHV-compatible artificial channel-cut monochromator. In: Choi JY, Rah S (eds) Synchrotron radiation instrumentation, Pts 1 and 2, vol 879, pp 911–914

161. Nugent KA (2010) Coherent methods in the x-ray sciences. Adv Phys 59(1):1–99

162. Ohwada K, Shimomura S, Nakao H, Matsushita M, Namikawa K, Mizuki J (2011) X-ray photon correlation spectroscopy of structural fluctuations in relaxor ferroelectrics PZN-9%PT. Int Conf Frustration in Condens Matter (icfcm) 320:012086

163. Orsi D, Cristofolini L, Baldi G, Madsen A (2012) Heterogeneous and anisotropic dynamics of a 2D gel. Phys Rev Lett 108(10):105701

164. Orsi D, Cristofolini L, Fontana MP (2011) Equilibrium and out-of-equilibrium dynamics in a molecular layer of azopolymer floating on water studied by interfacial shear rheology. J Non Cryst Solids 357(2):580–586

165. Orsi D, Cristofolini L, Fontana MP, Pontecorvo E, Caronna C, Fluerasu A, Zontone F, Madsen A (2010) Slow dynamics in an azopolymer molecular layer studied by x-ray photon correlation spectroscopy. Phys Rev E 82(3):031804

166. Orsi D, Fluerasu A, Moussaid A, Zontone F, Cristofolini L, Madsen A (2012) Dynamics in dense hard-sphere colloidal suspensions. Phys Rev E 85(1):011402

167. Orsi D, Ruta B, Chushkin Y, Pucci A, Ruggeri G, Baldi G, Rimoldi T, Cristofolini L (2014) Controlling the dynamics of a bidimensional gel above and below its percolation transition. Phys Rev E 89(4):042308

168. Passow C, Fischer B, Sprung M, Kckerling M, Wagner J (2014) Direction-dependent freezing of diamagnetic colloidal tracers suspended in paramagnetic ionic liquids. Langmuir 30 (25):7283–7288

169. Patel AJ, Mochrie S, Narayanan S, Sandy A, Watanabe H, Balsara NP (2010) Dynamic signatures of microphase separation in a block copolymer melt determined by x-ray photon correlation spectroscopy and rheology. Macromolecules 43(3):1515–1523

170. Patkowski A, Gapinski J, Fluerasu A, Holmqvist P, Meier G, Lettinga MP, Naegele G (2008) Structure and dynamics of colloidal suspensions studied by means of XPCS. Acta Phys Pol A 114(2):339–350

171. Pecora R (2008) Basic concepts scattering and time correlation functions. In: Borsali R, Pecora R (eds) Soft matter characterization. Springer, Netherlands, pp 2–40

172. Pierce MS, Barbour A, Komanicky V, Hennessy D, You H (2012) Coherent x-ray scattering experiments of Pt(001) surface dynamics near a roughening transition. Phys Rev B 86 (18):184108

173. Pierce MS, Chang KC, Hennessy D, Komanicky V, Sprung M, Sandy A, You H (2009) Surface x-ray speckles: coherent surface diffraction from Au(001). Phys Rev Lett 103 (16):165501

174. Pierce MS, Hennessy DC, Chang KC, Komanicky V, Strzalka J, Sandy A, Barbour A, You H (2011) Persistent oscillations of x-ray speckles: Pt (001) step flow. Appl Phys Lett 99 (12):121910

175. Pierce MS, Komanicky V, Barbour A, Hennessy DC, Zhu C, Sandy A, You H (2012) Dynamics of the Au (001) surface in electrolytes: in situ coherent x-ray scattering. Phys Rev B 86(8):085410

176. Ponchut C, Rigal JM, Clment J, Papillon E, Homs A, Petitdemange S (2011) MAXIPIX, a fast readout photon-counting x-ray area detector for synchrotron applications. J Instrum 6(01), C01069

177. Potdevin G, Graafsma H (2011) Analysis of the expected AGIPD detector performance parameters for the European x-ray free electron laser. Nucl Instrum Methods Phys Res Sect A 659(1):229–236

178. Poulos AS, Constantin D, Davidson P, Pansu B, Freyssingeas E, Madsen A, Chaneac C (2010) Communications: short-range dynamics of a nematic liquid-crystalline phase. J Chem Phys 132(9):091101

179. Prasad S, Jiang Z, Sprung M, Sinha SK, Dhinojwala A (2010) Effect of surface freezing on meniscus relaxation in side chain comb polymers. Phys Rev Lett 104(13):137801

180. Pusey P (2002) Dynamic light scattering. In: Lindner PP, Zemb TT (eds) Neutrons, x-rays, and light: scattering methods applied to soft condensed matter, North-Holland delta series. Elsevier, Amsterdam; Boston, pp 203–220

181. Reitinger R, Pfau B, Stadler LM et al (2007) Surface diffusion and island growth. In: Cermak J, Stloukal I (eds) Diffusion and thermodynamics of materials, vol 263, pp 177–182

182. Ricci A (2014) Nanoscale dynamics in complex materials by resonant x-ray photon correlation spectroscopy (rXPCS). J Supercond Nov Magn 28(4):1295–1298

183. Richert R (2002) Heterogeneous dynamics in liquids: fluctuations in space and time. J Phys Condens Matter 14(23):R703

184. Richter S, Saphiannikova M, Stckelhuber KW, Heinrich G (2010) Jamming in filled polymer systems. Macromol Symp 291–292(1):193–201

185. Richter S, Saphiannikova M, Stoeckelhuber KW et al (2010).Jamming in filled polymer systems. In: Patrickios CS (ed) Polymer networks: synthesis, properties, theory and applications, vol 291–292, pp 193–201

186. Robert A (2007) Measurement of self-diffusion constant with two-dimensional x-ray photon correlation spectroscopy. J Appl Crystallogr 40:S34–S37

187. Robert A, Wagner J, Haertl W, Autenrieth T, Gruebel G (2008) Dynamics in dense suspensions of charge-stabilized colloidal particles. Eur Phys J E 25(1):77–81

188. Robinson I, Gruebel G, Mochrie S (2010) Focus on x-ray beams with high coherence. New J Phys 12(3):035,002

189. Robinson I, Harder R (2009) Coherent x-ray diffraction imaging of strain at the nanoscale. Nat Mater 8(4):291–298

190. Rogers MC, Chen K, Andrzejewski L, Narayanan S, Ramakrishnan S, Leheny RL, Harden JL (2014) Echoes in x-ray speckles track nanometer-scale plastic events in colloidal gels under shear. Phys Rev E 90(6):062310

191. Roseker W, Franz H, Schulte-Schrepping H, Ehnes A, Leupold O, Zontone F, Lee S, Robert A, Gruebel G (2011) Development of a hard x-ray delay line for x-ray photon correlation spectroscopy and jitter-free pump-probe experiments at x-ray free-electron laser sources. J Synchrotron Radiat 18:481–491

192. Roseker W, Franz H, Schulte-Schrepping H, Ehnes A, Leupold O, Zontone F, Robert A, Gruebel G (2009) Performance of a picosecond x-ray delay line unit at 8.39 keV. Opt Lett 34 (12):1768–1770

193. Roseker W, Lee S, Walther M, Schulte-Schrepping H, Franz H, Gray A, Sikorski M, Fuoss PH, Stephenson GB, Robert A, Gruebel G (2012) Hard x-ray delay line for x-ray photon correlation spectroscopy and jitter-free pump-probe experiments at LCLS. X-Ray Free-Electron Lasers 8504:85040I

194. Ruta B, Baldi G, Monaco G, Chushkin Y (2013) Compressed correlation functions and fast aging dynamics in metallic glasses. J Chem Phys 138(5):054508

195. Ruta B, Chushkin Y, Monaco G et al (2013) Relaxation dynamics and aging in structural glasses. 4th international symposium on slow dynamics in complex systems: keep going Tohoku 1518:181–188

196. Ruta B, Chushkin Y, Monaco G, Cipelletti L, Pineda E, Bruna P, Giordano VM, Gonzalez-Silveira M (2012) Atomic-scale relaxation dynamics and aging in a metallic glass probed by x-ray photon correlation spectroscopy. Phys Rev Lett 109(16):165701

197. Ruta B, Czakkel O, Chushkin Y, Pignon F, Nervo R, Zontone F, Rinaudo M (2014) Silica nanoparticles as tracers of the gelation dynamics of a natural biopolymer physical gel. Soft Matter 10(25):4547–4554

198. Sanborn C, Ludwig KF, Rogers MC, Sutton M (2011) Direct measurement of microstructural avalanches during the martensitic transition of cobalt using coherent x-ray scattering. Phys Rev Lett 107(1):015702

199. Sandy AR, Lurio LB, Mochrie SGJ, Malik A, Stephenson GB, Pelletier JF, Sutton M (1999) Design and characterization of an undulator beamline optimized for small-angle coherent x-ray scattering at the advanced photon source. J Synchrotron Radiat 6(6):1174–1184

200. Sandy AR, Narayanan S, Sprung M, Su JD, Evans-Lutterodt K, Isakovic AF, Stein A (2010) Kinoform optics applied to x-ray photon correlation spectroscopy. J Synchrotron Radiat 17:314–320

201. Sanz A, Ezquerra TA, Hernndez R, Sprung M, Nogales A (2015) Relaxation processes in a lower disorder order transition diblock copolymer. J Chem Phys 142(6):064904

202. Schavkan A, Westermeier F, Zozulya A, Bondarenko S, Grübel G, Schroer C, Sprung M (2013) Using the MAXIPIX detector for coherent x-ray scattering applications. J Phys: Conf Ser 425(20):202004

203. Schramm S, Blochowicz T, Gouirand E, Wipf R, Stuehn B, Chushkin Y (2010) Concentration fluctuations in a binary glass former investigated by x-ray photon correlation spectroscopy. J Chem Phys 132(22):224505

204. Schroer CG, Boye P, Feldkamp JM, Patommel J, Schropp A, Schwab A, Stephan S, Burghammer M, Schder S, Riekel C (2008) Coherent x-ray diffraction imaging with nanofocused illumination. Phys Rev Lett 101(9):090801

205. Schweizer KS, Yatsenko G (2007) Collisions, caging, thermodynamics, and jamming in the barrier hopping theory of glassy hard sphere fluids. J Chem Phys 127(16):164505

206. Segal JD, Kenney CJ (2012) Charge pump detector: optimization with process and device simulation. In: Yu B (ed) 2012 I.E. nuclear science symposium and medical imaging conference record (NSS/MIC), pp 507–510

207. Seu KA, Roy S, Turner JJ, Park S, Falco CM, Kevan SD (2010) Cone phase and magnetization fluctuations in Au/Co/Au thin films near the spin-reorientation transition. Phys Rev B 82(1):012404

208. Shin TJ, Dierker SB, Smith GC (2008) Two-dimensional multiwire gas proportional detector for x-ray photon correlation spectroscopy of condensed matter. Nucl Instrum Methods Phys Res Sect A 587(2–3):434–440

209. Shinohara Y, Imai R, Kishimoto H, Yagi N, Amemiya Y (2010) Indirectly illuminated x-ray area detector for x-ray photon correlation spectroscopy. J Synchrotron Radiat 17:737–742

210. Shinohara Y, Kishimoto H, Maejima T, Nishikawa H, Takata M, Amemiya Y (2011) Observation of filler dynamics in rubber with x-ray photon correlation spectroscopy. Buried Interface Sci with X-Rays and Neutrons 2010 24:012005

211. Shinohara Y, Kishimoto H, Maejima T, Nishikawa H, Yagi N, Amemiya Y (2012) Observation of microscopic dynamics of carbon black in rubber during the vulcanization process. Soft Matter 8(12):3457–3462

212. Shinohara Y, Kishimoto H, Yagi N, Amemiya Y (2010) Microscopic observation of aging of silica particles in unvulcanized rubber. Macromolecules 43(22):9480–9487

213. Shinohara Y, Watanabe A, Kishimoto H, Amemiya Y (2013) Combined measurement of x-ray photon correlation spectroscopy and diffracted x-ray tracking using pink beam x-rays. J Synchrotron Radiat 20:801–804

214. Shinohara Y, Yamamoto N, Kishimoto H, Amemiya Y (2015) X-ray irradiation induces local rearrangement of silica particles in swollen rubber. J Synchrotron Radiat 22(1):119–123

215. Shpyrko OG (2014) X-ray photon correlation spectroscopy. J Synchrotron Radiat 21 (5):1057–1064

216. Shpyrko OG, Isaacs ED, Logan JM, Feng Y, Aeppli G, Jaramillo R, Kim HC, Rosenbaum TF, Zschack P, Sprung M, Narayanan S, Sandy AR (2007) Direct measurement of antiferromagnetic domain fluctuations. Nature 447(7140):68–71

217. Sikorski M, Gutt C, Chushkin Y, Lippmann M, Franz H (2010) Dynamics at the liquid-vapor interface of a supercooled organic glass former. Phys Rev Lett 105(21):215701

218. Sikorski M, Jiang Z, Sprung M, Narayanan S, Sandy AR, Tieman B (2011) A graphical user interface for real-time analysis of XPCS using HPC. Nucl Instrum Methods Phys Res Sect A 649(1):234–236

219. Sikorski M, Sandy AR, Narayanan S (2011) Depletion-induced structure and dynamics in bimodal colloidal suspensions. Phys Rev Lett 106(18):188301

220. Sinha SK, Jiang Z, Lurio LB (2014) X-ray photon correlation spectroscopy studies of surfaces and thin films. Adv Mater 26(46):7764–7785

221. Sinha SK, Tolan M, Gibaud A (1998) Effects of partial coherence on the scattering of x rays by matter. Phys Rev B 57(5):2740

222. Sloutskin E, Huber P, Wolff M, Ocko BM, Madsen A, Sprung M, Schoen V, Baumert J, Deutsch M (2008) Dynamics and critical damping of capillary waves in an ionic liquid. Phys Rev E 77(6):060601

223. Snigirev A, Kohn V, Snigireva I, Lengeler B (1996) A compound refractive lens for focusing high-energy X-rays. Nature 384(6604):49–51

224. Spannuth M, Mochrie SGJ, Peppin SSL, Wettlaufer JS (2011) Dynamics of colloidal particles in ice. J Chem Phys 135(22):224704

225. Srivastava S, Kandar AK, Basu JK, Mukhopadhyay MK, Lurio LB, Narayanan S, Sinha SK (2009) Complex dynamics in polymer nanocomposites. Phys Rev E 79(2):021408

226. Stana M, Leitner M, Ross M, Sepiol B (2013) Studies of atomic diffusion in Ni-Pt solid solution by x-ray photon correlation spectroscopy. J Phys-Condens Matter 25(6):065401

227. Stangl J, Mocuta C, Chamard V, Carbone D (2014) Nanobeam x-ray scattering: probing matter at the nanoscale. Wiley-VCH, Weinheim

228. Steinmann R, Chushkin Y, Caronna C, Chavanne J, Madsen A (2011) A small-angle scattering chamber for x-ray photon correlation spectroscopy at low temperatures. Rev Sci Instrum 82 (2):025109

229. Stetsko YP, Shvyd'ko YV, Stephenson GB (2013) Time-delayed beam splitting with energy separation of x-ray channels. Appl Phys Lett 103(17):173508

230. Stocco A, Tauer K, Pispas S, Sigel R (2009) Dynamics at the air-water interface revealed by evanescent wave light scattering. Eur Phys J E 29(1):95–105
231. Streit S, Gutt C, Chamard V, Robert A, Sprung M, Sternemann H, Tolan M (2007) Two-dimensional dynamics of metal nanoparticles on the surface of thin polymer films studied with coherent X rays. Phys Rev Lett 98(4):047801
232. Su JD, Sandy AR, Mohanty J, Shpyrko OG, Sutton M (2012) Collective pinning dynamics of charge-density waves in 1T-TaS2. Phys Rev B 86(20):205105
233. Sutton M (2006) X-ray intensity fluctuation spectroscopy. In: Neutron and x-ray spectroscopy. Springer Netherlands, Berlin, pp 297–318
234. Sutton M (2008) A review of x-ray intensity fluctuation spectroscopy. C R Phys 9 (5–6):657–667
235. Sutton M, Laaziri K, Livet F, Bley F (2003) Using coherence to measure two-time correlation functions. Opt Express 11(19):2268–2277
236. Tieman B, Narayanan S, Sandy A, Sikorski M (2011) MPICorrelator: a parallel code for performing time correlations. Nucl Instrum Methods Phys Res Sect A 649 (1):240–242
237. Tolan M, Sinha SK (1998) X-ray scattering with partial coherent radiation: the exact relationship between "resolution" and "coherence". Phys B: Condens Matter 248 (1–4):399–404
238. Trappe V, Pitard E, Ramos L, Robert A, Bissig H, Cipelletti L (2007) Investigation of q-dependent dynamical heterogeneity in a colloidal gel by x-ray photon correlation spectroscopy. Phys Rev E 76(5):051404
239. Van Hove L (1954) Correlations in space and time and born approximation scattering in systems of interacting particles. Phys Rev 95(1):249–262
240. Veen FVD, Pfeiffer F (2004) Coherent x-ray scattering. J Phys Condens Matter 16 (28):5003–5030
241. Wagner J, Maerkert C, Fischer B, Mueller L (2013) Direction dependent diffusion of aligned magnetic rods by means of x-ray photon correlation spectroscopy. Phys Rev Lett 110 (4):048301
242. Wandersman E, Chushkin Y, Dubois E, Dupuis V, Demouchy G, Robert A, Perzynski R (2009) Repulsive and attractive ferroglasses: a SAXS and XPCS study. Braz J Phys 39 (1A):210–216
243. Wandersman E, Dubois E, Dupuis V, Duri A, Robert A, Perzynski R (2008) Heterogeneous dynamics and ageing in a dense ferro-glass. J Phys-Condens Matter 20 (20):204124
244. Wang SF, Jiang Z, Narayanan S, Foster MD (2012) Dynamics of surface fluctuations on macrocyclic melts. Macromolecules 45(15):6210–6219
245. Wang SF, Yang S, Lee J, Akgun B, Wu DT, Foster MD (2013) Anomalous surface relaxations of branched-polymer melts. Phys Rev Lett 111(6):068303
246. Westermeier F, Autenrieth T, Gutt C, Leupold O, Duri A, Menzel A, Johnson I, Broennimann C, Gruebel G (2009) Fast two-dimensional detection for x-ray photon correlation spectroscopy using the PILATUS detector. J Synchrotron Radiat 16:687–689
247. Westermeier F, Fischer B, Roseker W, Gruebel G, Naegele G, Heinen M (2012) Structure and short-time dynamics in concentrated suspensions of charged colloids. J Chem Phys 137 (11):114504
248. Westermeier F, Zozulya AV, Bondarenko S et al (2013) X-ray photon correlation spectroscopy using the Mythen 1D detector. 11th international conference on synchrotron radiation instrumentation (sri 2012) 425: UNSP 202005
249. Williams GJ, Quiney HM, Peele AG, Nugent KA (2007) Coherent diffractive imaging and partial coherence. Phys Rev B 75(10):104102
250. Williams GM, Rhee J, Lee A, Kevan SD (2014) Pixelated detector with photon address event driven time stamping and correlation. Ieee Trans Nucl Sci 61(4):2323–2332

251. Yong LZ, Misra D, Siddons DP et al (2011) A 256-channel (element) correlator design based on an FPGA for x-ray photon correlation spectroscopy. 2011 I.E. nuclear science symposium and medical imaging conference (NSS/MIC), pp 496–502
252. You H, Pierce M, Komanicky V, Barbour A, Zhu C (2012) Study of electrode surface dynamics using coherent surface x-ray scattering. Electrochim Acta 82:570–575
253. Yu CJ, Lee HC, Kim C, Cha W, Carnis J, Kim Y, Noh DY, Kim H (2014) Coherent x-ray scattering beamline at port 9C of Pohang light source II. J Synchrotron Radiat 21:264–267
254. van 't Zand DD, Chushkin Y, Belkoura L et al (2012) Anisotropic dynamics of the tenuous gel in a liquid crystal-nanoparticle composite. Soft Matter 8(15):4062–4066
255. Zhang F, Allen AJ, Levine LE, Espinal L, Antonucci JM, Skrtic D, O'Donnell JNR, Ilavsky J (2012) Ultra-small-angle x-ray scattering-x-ray photon correlation spectroscopy studies of incipient structural changes in amorphous calcium phosphate-based dental composites. J Biomed Mater Res A 100A(5):1293–1306
256. Zhang F, Allen AJ, Levine LE, Ilavsky J, Long GG (2013) Structure and dynamics studies of concentrated micrometer-sized colloidal suspensions. Langmuir 29(5):1379–1387
257. Zhang F, Allen AJ, Levine LE, Ilavsky J, Long GG, Sandy AR (2011) Development of ultra-small-angle x-ray scattering-x-ray photon correlation spectroscopy. J Appl Crystallogr 44:200–212

4

XAFS for Characterization of Nanomaterials

Maria Katsikini and Eleni C. Paloura

Contents

1 Definition of the Topic

X-ray absorption fine structure (XAFS) spectroscopy studies the modification of the X-ray absorption coefficient, above the absorption edge of a specific element, due to the presence of neighboring atoms and delivers information on materials nano- and electronic structure. The long-range translational symmetry is not a prerequisite, as in the case of diffraction-based techniques, which, along with the atom-specific character of XAFS, renders it a powerful tool for the study of nanomaterials.

M. Katsikini (✉) • E.C. Paloura
School of Physics, Department of Solid State Physics, Aristotle University of Thessaloniki, Thessaloniki, Greece
e-mail: katsiki@auth.gr; paloura@auth.gr

2   Overview

In the following the principles of XAFS spectroscopy will be discussed. A brief
introduction of the theoretical basis of the spectroscopy will be presented, the
emphasis being on the phenomena that affect the spectrum at energies below, near,
and far above the absorption edge. In addition to that, the main experimental setups
used for the acquisition of the XAFS spectra in the soft and hard X-ray regimes will
also be presented. Furthermore, the analysis procedure of the extended part of the
XAFS (called extended XAFS, acronym EXAFS) spectrum and the related param-
eters, as well as methodologies followed in the analyses of the near-edge part of the
spectrum (called X-ray absorption near-edge structure or near-edge X-ray absorption
fine structure, the corresponding acronyms being XANES and NEXAFS, respec-
tively), will be described. Finally, recently published representative applications of
XAFS spectroscopy for the study of various types of nanomaterials, for example,
nanocatalysts, carbon-based nanomaterials, semiconductor quantum dots, etc., will
be reviewed.

3   Introduction

XAFS is the acronym of X-ray absorption fine structure and refers to the fine
structure of the X-ray absorption coefficient as a function of the energy of the
impinging X-ray beam. The necessity of energy scanning during the acquisition of
the absorption spectrum makes the use of conventional X-ray sources impractical
and thus renders synchrotron radiation (SR) sources as unique candidates for the
acquisition of XAFS spectra. The most common experimental configuration is based
on the measurement of the intensity, I, of the transmitted beam, which, according to
the law of Beer–Lambert, is given by the equation:

$$I = I_0 e^{-\mu x} \tag{4.1}$$

where I_0 is the intensity of the incident beam, μ is the X-ray absorption coefficient,
and x is the sample thickness (Fig. 4.1). In general, I_0 exhibits an energy dependence
determined by the experimental configuration, whereas the energy dependence of I,
and consequently of μ, is additionally affected by the absorption properties of the
studied material. The incident beam of X-rays, either in the soft or hard X-ray
spectral region (the wavelength of 1 Å is considered as a non-strict boundary
between the two), causes excitation of atoms which eject electrons from core shells,
mainly the K and L shells. The kinetic energy of the emitted photoelectron is given
by the equation:

$$E_K = h\nu - E_B \tag{4.2}$$

where E_B is the binding energy of the photoelectron and $h\nu$ is the energy of the
impinging photon. The binding energy depends on the atomic number, Z. Detailed

Fig. 4.1 Detection modes of the X-ray absorption signal
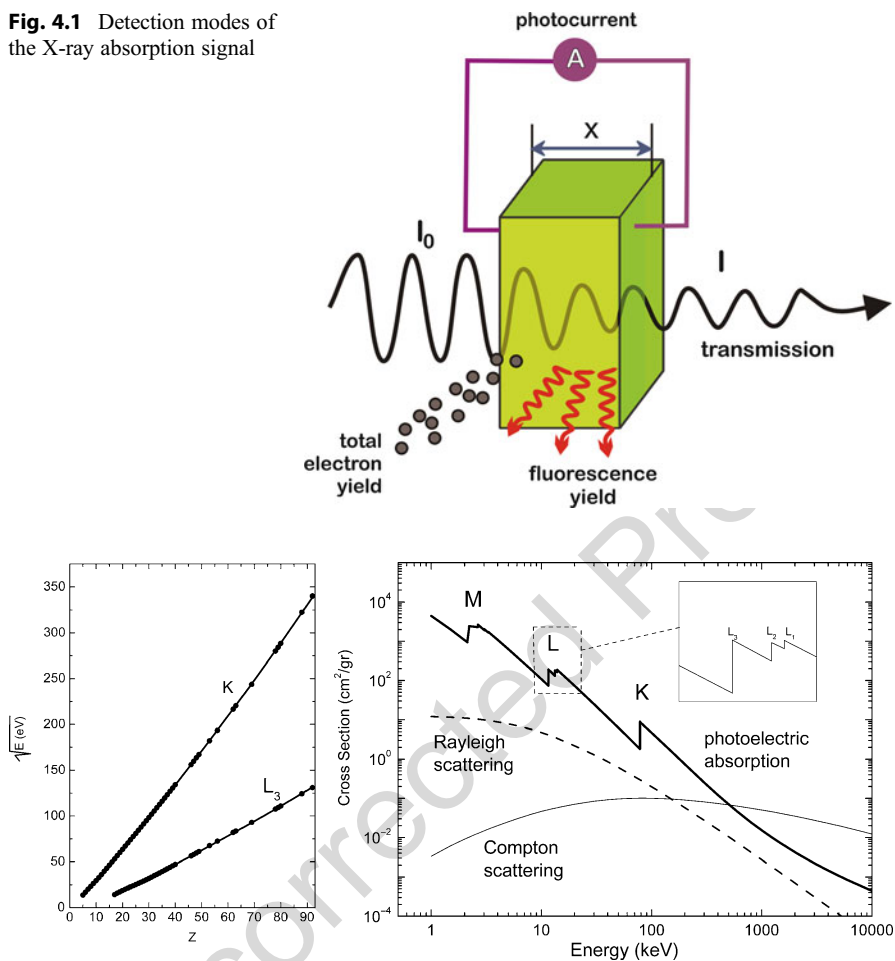
Fig. 4.2 (Left) Dependence of the square root of the energies of the K- and L_3-absorption-edges on the atomic number. The data were derived from the HEPHAESTUS software [2]. Polynomial fitting revealed the following dependence of $E^{1/2}$ on Z: $\sqrt{E_K} = -2.5 \pm 0.1 + (3.184 \pm 0.008)Z + (5.71 \pm 0.08) \times 10^{-3}Z^2$ and $\sqrt{E_{L_3}} = -9.1 \pm 0.3 + (1.32 \pm 0.01)Z + (2.3 \pm 0.1) \times 10^{-3}Z^2$ for K-and L_3-edges, respectively. (Right) Attenuation cross sections of Pt [3]

tables with the binding energies of K and L shells are listed in the X-ray Data Booklet [1] and proper databases or software like HEPHAESTUS [2]. The variation of the electron binding energies in the K and L shells as a function of Z is shown in Fig. 4.2.

The X-ray absorption coefficient μ is proportional to the photoabsorption cross section. As shown in Fig. 4.2, Rayleigh (coherent) and Compton (incoherent) scattering also contributes to the reduction of the transmitted beam intensity.
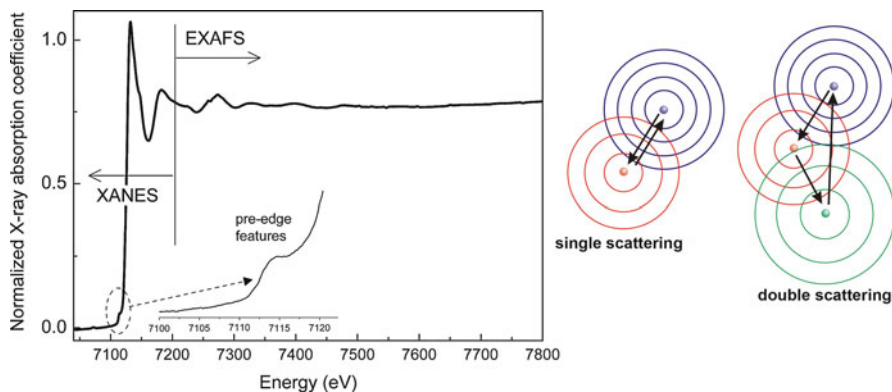
Fig. 4.3 XANES and EXAFS part of a XAFS spectrum recorded at the Fe–K-edge of a FeOOH sample. Pre-edge features which appear in the K-edge spectra of transition elements are shown in the inset. Schematic representations of single and double scattering events are shown in the right panel

However, the Rayleigh and Compton cross sections are small and their energy dependence is rather smooth. Therefore, they contribute only in the background of the XAFS spectra, which however can be easily removed. The XAFS spectra are usually recorded at the K- and L-absorption-edges which are prominent in the photoabsorption cross section as shown in Fig. 4.2.

A characteristic XAFS spectrum recorded at the Fe–K-edge is displayed in Fig. 4.3. The portion of the spectrum close to the absorption edge (and approximately up to 50 eV above the edge) is called XANES (X-ray absorption near-edge structure) or NEXAFS (near-edge X-ray absorption fine structure). The latter term is traditionally used in the soft X-ray spectral regime. The part of the XAFS spectrum that extends from 50 up to approximately 1000 eV above the absorption edge is called EXAFS (extended XAFS). Although the mechanism that modifies the X-ray absorption coefficient is the same in the whole XAFS region, the XANES (NEXAFS) and EXAFS parts of the spectrum are usually treated separately. This can be explained by the fact that the kinetic energy of the photoelectron, according to Eq. (4.2), is very low close to the absorption edge. In this case the photoelectron can be shortly trapped in empty states (e.g., antibonding molecular orbital states or states in the conduction band of semiconductors). At higher energies, i.e., above 50 eV, the electron is considered "free" and the atom becomes ionized. However, the outgoing photoelectron can be described as a quantum wave that spreads out in the solid with wavelength $\lambda = h/p$, where h is the Planck constant and p the momentum of the photoelectron. The latter is quantum mechanically defined as $p = \hbar k$, where k is the photoelectron wave number, and $\hbar = h/2\pi$. The treatment of the photoelectron as a wave results in interference effects between the outgoing wave and the backscattered to the neighboring atoms, as schematically illustrated in Fig. 4.3. However, this wave

Fig. 4.4 Structure of $CaTiO_3$. The first and the second nearest neighbor shells of Ti are the octahedron formed by the six oxygen atoms and eight Ca atoms in a cubic arrangement, respectively. Single (SS), double (DS), and triple (TS) scattering paths with two, three, and four legs, respectively, which apply when Ca is the absorbing atom, are also shown
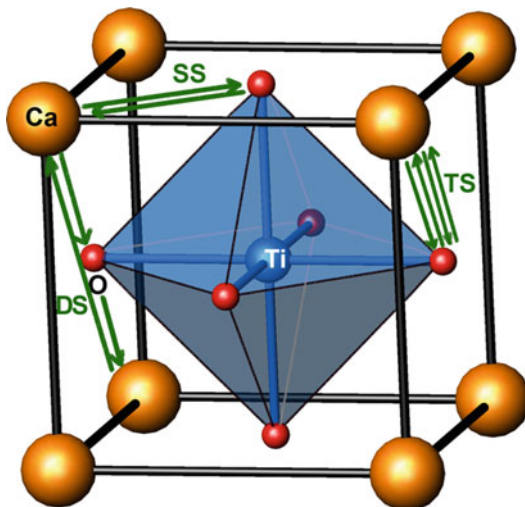
is attenuated during its propagation in the matter due to inelastic losses in the course of its interaction with and/or excitation of other electrons. Based on such a short-range-order treatment of the absorption coefficient, the XAFS signal does not depend on the translational symmetry, as in the case of diffraction-based character-ization techniques. Furthermore, it is element specific and provides information on the bonding configuration of the absorbing atom.

In order to obtain structural information from the XAFS spectra, the structure of the studied material is often treated as a number of atomic shells that surround the absorbing atom in an onion-like scheme. A shell is defined as a set of atoms of the same element which are (almost) equidistant to the absorbing atom. An example is shown in Fig. 4.4 for $CaTiO_3$ [3]. When the EXAFS spectrum is recorded at the Ti–K-edge, the first shell consists of 6 oxygen atoms in octahedral coordination, and the second of 8 Ca atoms that form a cube. Often, multiple scattering to more than one neighboring atom becomes important, and the interference characteristics depend strongly on the bonding geometry of the absorbing atom. Such multiple (double and triple) scattering paths, which can be important when the spectrum is recorded at the Ca–K-edge, are also indicated in Fig. 4.4. In the EXAFS spectra, multiple scattering is usually considered important when the atoms are positioned in a nearly linear arrangement that results in strong forward scattering. However, multiple scattering cannot be neglected and is actually determinative of the XANES structure. Therefore the analysis of XANES spectra by fitting the absorption contribution of separate neighboring shells is rather impossible.

After proper treatment of the EXAFS spectrum, which includes the subtraction of a rather smooth atomic absorption (as it will be discussed in Sect. 5), the $\chi(k)$ spectrum results. It actually provides the modification of the X-ray absorption

111 coefficient, due to the presence of neighboring atoms, as a function of the photo-
112 electron wave number. The $\chi(k)$ spectrum is a sum of sinusoidal functions of the
113 distance R_j of each neighboring shell, j, with modulated amplitude:

$$\chi(k) = S_0^2 \sum_j \frac{1}{kR_j^2} N_j |F_j(k)| e^{-2\sigma_j^2 k^2} e^{\frac{-2R_j}{\lambda_e(k)}} \left[\sin\left(2kR_j + 2\delta_i(k) + \Phi_j(k)\right)\right] \quad (4.3)$$

114 where N_j is the coordination number, σ_j^2 the Debye–Waller factor, λ_e the mean free
115 path of the photoelectron, $F_j(k)$ the backscattering function of amplitude $|F_j(k)|$, and
116 argument $\Phi_j(k)$ and $\delta_i(k)$ is the phase shift induced by the absorbing atom during the
117 emission of the photoelectron. The relatively small value of the photoelectron mean
118 free path (few tens of Å) is responsible for the fast damping of the EXAFS
119 oscillations and thus its local character. S_0^2 is an amplitude reduction factor that
120 usually takes values in the range 0.7–1 and accounts for inelastic losses. These
121 processes lead to the excitation of the remaining (passive) electrons of the absorbing
122 atom to a bound state (shake-up) and/or to a state in the continuum (shake-off). The
123 Debye–Waller factor, σ_j^2, sums contributions for the thermal (due to vibrational
124 motion of the atoms) and the static disorder. The former is strongly temperature
125 dependent and thus measurements at low temperatures reduce the fast damping of
126 the EXAFS oscillations. The Debye–Waller factor is defined as the mean square
127 relative displacement projected along the bond direction, i.e.,

$$\sigma_j = \sqrt{\left\langle \left[\hat{r}_j \cdot \left(\vec{u}_j - \vec{u}_i\right)\right]^2 \right\rangle} \quad (4.4)$$

128 where $\vec{u}_j$ and $\vec{u}_i$ are the displacements of the neighboring and absorbing atoms,
129 respectively, and $\hat{r}_j$ is the unit vector along the direction of the bond. In general, the
130 Debye–Waller factor increases for further shells since the motion of distant neigh-
131 boring atoms becomes weakly correlated to that of the absorbing atom. The
132 Debye–Waller factors are usually fitting parameters. However, in systems with
133 small structural disorder, its temperature-dependent component due to thermal
134 disorder can be related to the local vibrational structure [5]. The use of the
135 Debye–Waller factor in the exponential term of Eq. (4.3) is particularly applicable
136 in systems with small disorder which can be approximated by a Gaussian function.
137 However, the Gaussian approximation is not appropriate for highly disordered
138 systems or when the measurements are performed at high temperatures where
139 anharmonicity effects should be considered [6]. To take into account such effects,
140 Eq. (4.3) can be rewritten as

$$\chi(k) = S_0^2 |F_j(k)| \int \rho(R_j) \frac{1}{kR_j^2} e^{\frac{-2R_j}{\lambda_e(k)}} \sin\left(2kR_j + 2\delta_i(k) + \Phi_j(k)\right) dR_j \quad (4.5)$$

141 where $\rho(R_j)dR_j$ is the probability of finding an atom of the jth shell at a distance
142 between R_j and $R_j + dR_j$. The distribution function, $\rho(R_j)$, may be expanded in

a moment series. To achieve better convergence, the logarithm of the Fourier transform of the effective distribution $P(R_j, \lambda_e) = \frac{\rho(R_j)}{R_j^2} e^{\frac{-2R_j}{\lambda_e(k)}}$ is expanded, i.e.,

$$\ln[\tilde{P}(k, R_j)] = \sum_{n=0}^{\infty} \frac{(2ik)^n}{n!} C_n(R_j) \tag{4.6}$$

where $\tilde{P}(k, R_j) = \int P(R_j, \lambda_e) e^{i2k\Delta r} d(\Delta r)$, Δr is defined as $r = R_j + \Delta r$, and C_n are the cumulants [7–9]. The odd and even cumulants are decoupled and contribute separately to the phase and amplitude logarithm. Higher-order cumulants (C_n for $n > 2$) correspond to deviation of the distribution from the symmetric Gaussian. Such a parameterization is useful in the amplitude ratio method, where the Debye–Waller factor, the coordination number, and the nearest neighbor distance, as well as higher-order cumulants of an unknown sample, can be determined by direct comparison with a known reference sample without a shell-by-shell fitting [7]. Another important parameter that affects the amplitude of the EXAFS oscillations is the amplitude of the backscattering function which depends on the atomic number of the neighboring atom.

A useful parameterization of $\chi(k)$, which allows for the extraction of structural parameters from the analysis of the EXAFS spectrum, is provided by Eq. (4.3). Some of the parameters that appear in the equation, e.g., the backscattering amplitude, the phase shifts, and the mean free path of the photoelectron, are calculated using proper software. Other parameters such as the nearest neighbor distances, the coordination numbers, and the Debye–Waller factors are obtained after proper fitting of the EXAFS spectra. The EXAFS formula (Eq. 4.3) can include both single and multiple scattering paths after proper calculation of the scattering function. For a detailed presentation of the theoretical background of XAFS, readers are referred to the books of Teo [10], Bunker [8], and Koningsberger and Prins [11] as well as to the paper of Rehr and Albers [12].

As mentioned above, in the near-edge part of the XAFS spectrum, the emitted photoelectron has low kinetic energy and can thus be trapped shortly in unoccupied electron states. The initial state $|\psi_i\rangle$ is a core state of well-defined energy, whereas the final state $|\psi_f\rangle$ can be an antibonding molecular orbital state of a molecule or a state in the conduction band or even an empty defect state in a crystalline material. Even though the initial and the final states are actually multi-electron states, it is usually assumed that only one electron participates in the transition, whereas many body effects are taken into account at a later stage [9]. According to the theory of absorption, the absorption coefficient, μ, is proportional to the absorption cross section, σ_X, which can be calculated from the Fermi "golden rule" that provides the transition probability per unit time, P_{if}, between the initial and final state [12–15]:

$$P_{if} \propto |\langle\psi_f|H'|\psi_i\rangle|^2 \rho_f(E) \tag{4.7}$$

where $H' \propto \vec{A} \cdot \vec{p}$ is the operator that accounts for the interaction of the electromagnetic field of the X-ray photon with the absorbing atom. $\vec{A} = \hat{e}A_0 e^{i\vec{k}\cdot\vec{r}}$ is the spatial variation of the vector potential of the incident beam with $\hat{e}$ being the unit vector that

determines its polarization, $\vec{p}$ is the electron momentum operator, and $\rho_f(E)$ is the energy-dependent density of empty final states. Assuming the validity of the dipole approximation, the spatial dependence of the electric field can be approximated as $e^{i\vec{k}\cdot\vec{r}} \simeq 1$ because the wavelength of the X-ray beam is larger compared to the size of the atom and thus $kr << 1$. Taking also into account that the momentum of the electron can be described by the operator $\vec{p} = -i\hbar\vec{\nabla}$, after proper rearrangement of the quantum operators, the absorption coefficient can be written as [12]

$$\mu \propto \left| \langle \psi_f | \hat{e} \cdot \vec{r} | \psi_i \rangle \right|^2 \rho_f(E) \tag{4.8}$$

where $\vec{r}$ is the position operator. Taking into account that synchrotron radiation is linearly polarized (unless special experimental arrangements are used, e.g., for the study of magnetic materials with circularly polarized beams), the absorption cross section depends, according to Eq. (4.8), on the orientation of the sample. Such a dependence is not observed in materials of cubic symmetry or in powder samples. Equation (4.8) imposes useful selection rules under the dipole approximation: $\Delta\ell = \pm 1$ and $\Delta m_\ell = 0$ for linearly or $\Delta m_\ell = \pm 1$ for circularly polarized light, where ℓ and m_ℓ are the quantum numbers of angular momentum and its projection along the axis of external magnetic field, respectively. Thus, when the spectra are recorded at the K-edge, the initial state is an s-state with $\ell = 0$ and the final state should have (partial) p character ($\ell = 1$).

In crystalline materials, band structure methods apply for the calculation of the density of empty states taking into account proper projection to specific state symmetry according to the selection rules, as well as the presence of a core hole in the calculation of the energy of the final state [11, 12, 16]. An extended review on the available methods for the calculation of the density of unoccupied states can be found in Ref. [17]. However, these methods cannot be applied in nonperiodic materials where full multiple scattering theory can be successfully used [8, 12]. The XANES spectrum is very sensitive to the geometrical arrangement of the atoms in the cluster, and in general the contribution of many-leg multiple scattering paths is determinative. Effective treatment of the multiple scattering paths can be achieved in real space using the Green's function formulation [8, 12, 15, 17]. The absorption coefficient given in Eq. (4.8) can be modified as

$$\mu(E) \propto \sum_f \langle \psi_i | \hat{e} \cdot \vec{r}' | \psi_f \rangle \delta(E + E_i - E_f) \langle \psi_f | \hat{e} \cdot \vec{r} | \psi_i \rangle \tag{4.9}$$

where the sum runs over all final states and the delta function assures the conservation of energy. The sum over the final states and the delta function can be represented by a Green's function propagator $G = (H - E + i\eta)^{-1}$ that connects various scattering centers. H is the ground state Hamiltonian, and η is a lifetime that includes elastic and inelastic loses which provide a finite lifetime of the photoelectron and [8–10, 12]

$$-\frac{1}{\pi}\mathrm{Im}G = \sum_f |\psi_f\rangle\delta(E + E_i - E_f)\langle\psi_f| \qquad (4.10)$$

216 Thus, the projected photoelectron density of final states can be written as the
217 imaginary part of the one particle Green's function. Equation (4.9) can then be
218 written as $\mu(E) \propto \mathrm{Im}\langle\psi_i|\hat{e}\cdot\vec{r}'G\hat{e}\cdot\vec{r}\,|\psi_i\rangle\xi(E - E_F)$ where $\xi(E - E_F)$ is a broad step
219 function around the Fermi level, E_F [12]. G can be expressed in terms of wave

functions in position space as $G\left(\vec{r},\vec{r}';E\right) = \sum_f \dfrac{\psi_f\left(\vec{r}'\right)\psi_f^*\left(\vec{r}'\right)}{E - E_f + i\eta}$ [12, 17]. The

221 wave functions ψ_f are final states with energy E_f which are solutions of the Dyson
222 equation $\left[\frac{p^2}{2m} + V_{coul} + \Sigma(E)\right]\psi_f = E_f\psi_f$ where $\Sigma(E)$ accounts for many-body effects
223 and the presence of the core hole is included in the V_{coul} term. In multiple scattering
224 theory, the potential $V_{coul} + \Sigma(E)$ is represented by a sum of localized potential

contributions, $\upsilon_{\vec{R}}$, of each atom at position $\vec{R}$ designated as $\sum_{\vec{R}} \upsilon_{\vec{R}}\left(\vec{r} - \vec{R}\right)$, which

226 is usually approximated with "muffin-tin" potentials. The usefulness of the real-
227 space Green function propagator is that it can be expressed as a sum of two
228 contributions, G^c and G^{sca}, which stem from the absorbing atom and multiple
229 scattering from the neighboring centers, respectively [18]. Then the absorption
230 coefficient can be expressed as $\mu = \mu_0(1 + \chi)$ where μ_0 is the atomic absorption,
231 $\chi = \mathrm{Im}\left\{e^{i\delta}\left[1 - G^0T\right]^{-1}G^0e^{-i\delta}\right\}$, where G^0 is the free particle propagator, T is the
232 scattering matrix, and δ and δ' are the partial wave shifts. The term $\left[1 - G^0T\right]^{-1}G^0$
233 can be written as a sum of terms $G^0TG^0 + G^0TG^0TG^0 + \dots$ that contains contribu-
234 tions of single and multiple scattering. This formulation can be used for the simu-
235 lation of both the EXAFS and XANES parts of the spectrum. However, in the
236 XANES region, convergence is usually achieved for full multiple scattering [12, 19].
237   In Sects. 4 and 5, the experimental methodology and analysis procedure will be
238 discussed and key research findings from the literature will be reviewed in Sect. 6.

239 4   Experimental and Instrumental Methodology

240 XAFS spectra are almost exclusively recorded in synchrotron radiation
241 (SR) facilities that offer X-ray beams with unique characteristics. The SR beam is
242 emitted by light, charged particles, usually electrons, forced to move in closed orbits
243 with a speed that approaches that of light. A list of the available SR facilities all over
244 the world can be found in http://www.lightsources.org/. The main advantages of
245 synchrotron radiation include the following: (1) It is emitted in a broad, continuous
246 spectrum that can be monochromatized using suitable monochromators. (2) It has
247 high flux that is defined as the emitted power per 0.1 % bandwidth. (3) The high flux
248 in combination with the small divergence and beam size results in a beam with high

brilliance that allows the study of diluted materials (i.e., with low concentration of the element of interest) or of small sample volumes. The beam size, depending on the facility and the beamline, takes values in the range 0.3–3 mm, but can be further decreased by using proper focusing (e.g., Kirkpatrick–Baez combination of two concave mirrors that focus the beam in two orthogonal directions) or beam size reduction (e.g., capillaries that reduce the beam size by total reflection) elements. The use of such experimental setups provides X-ray beams with diameter in the range 1–5 μm. In beamlines dedicated to X-ray spectromicroscopy, the use of zone plates provides spatial resolution better than 50 nm [20] and allows the acquisition of XANES spectra on sample spots carefully selected from scanning X-ray transmission microscopy images (SXTM). Furthermore, SXTM images can be recorded with different incident beam energies that span the energy range of a NEXAFS spectrum, and proper image processing can provide spectra that correspond to each point of the sample image.

Most of the SR facilities all over the world offer beamlines for XAFS characterization. The use of a beam size at the mm or μm scale provides average information on the bonding configuration of the absorbing atom. Taking into account that nanomaterials comprise a broad family of nanosized materials (semiconductors, metal oxides, clusters of transition or noble metals, nanocomposites, carbon nanotubes, and others) which are built of elements with atomic numbers that range from 6 (C) to 78 (Pt), various experimental setups are used in suitable beamlines. The beamlines deliver the SR beam produced by an appropriate source in the storage ring, properly focused and monochromatized, to the position where the sample is located and the measurements take place. Three types of sources commonly exist in SR facilities: bending magnets, wigglers, and undulators. A bending magnet is a dipole magnet with uniform field between its poles that exerts a Lorentz force on the electron beam obliging it to move in curved trajectories, thus emitting SR tangentially in the horizontal plane. The opening angle of the beam is $\pm 1/\gamma$ in radians ($\gamma = E/mc^2$, where E, m, and c are the total energy, mass of the electrons, and speed of light, respectively). Thus, the beam opening produced by a bending magnet in a storage ring with energy of 5 GeV is approximately 10^{-4} rad. Wigglers and undulators are magnetic arrays that produce a magnetic field of alternating direction which forces the electron beam to move in sinusoidal trajectories. In the former case, the beam deflection is larger than the SR beam opening angle, whereas in the latter it is smaller. Bending magnets and wigglers generate a continuous spectrum (wigglers provide higher flux and "harder" radiation). On the other hand, undulators offer a quasi-monochromatic beam (fundamental energy and higher harmonics) of very high brilliance. Energy scanning with undulators is possible by changing the opening (gap) between the magnetic poles, thus changing the intensity of the magnetic field [21, 22]. Therefore in order to acquire XAFS spectra using an undulator as a source, simultaneous scanning of the undulator gap and the monochromator is necessary.

The SR beam before impinging on the sample is modified by the beamline optics that mainly consist of focusing elements (curved mirrors that also act as filters of the unwanted part of the emitted spectrum from the source), the monochromator, and
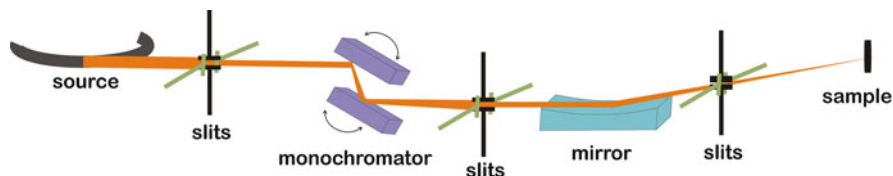
Fig. 4.5 Schematic representation of a typical beamline for the acquisition of XAFS spectra

slits that decrease the beam size. In beamlines dedicated to spectromicroscopy or micro-XAFS, additional focusing elements are used, for example, Fresnel zone plates, Kirkpatrick–Baez mirrors, or capillary optics [23]. A schematic representation of a typical beamline dedicated for XAFS measurements is shown in Fig. 4.5.

To avoid contamination of the X-ray optical elements, the beamline is kept under vacuum. However, there are some differences in the beamlines dedicated to XAFS measurements in the soft and hard X-ray region. In the hard X-ray regime, crystal monochromators [usually Si(111) or Si(311)] are used and the measurements can be performed in air. The crystal monochromators operate on the basis of Bragg's law $n\lambda = 2d\sin\theta$, where n is an integer (diffraction order), λ is the wavelength of the impinging beam, and θ is the angle of incidence. When a polychromatic beam impinges on the crystal, the diffraction condition for a specific wavelength is satisfied at a certain angle of incidence which is equal to the angle between the diffracted beam and the sample surface. To achieve the fixed-exit condition (i.e., stability of the position of the monochromatized beam irrespective of the energy), two crystals in parallel geometry are used. By slightly detuning the second crystal, the double crystal monochromators permit the suppression of higher-order harmonics (n > 1 in the Bragg law equation) [11]. The energy resolution is affected by the quality of the crystal monochromator, the divergence of the beam that enters the monochromator, and the opening of the slits located after the monochromator. Resolving power values, $E/\Delta E$, in the range of 5000–15,000 are offered in various beamlines dedicated to XAFS spectroscopy. The energy resolution, which is necessary to resolve the NEXAFS fine structure, can be improved using a narrow monochromator exit slit, of course at the expense of the flux.

In the hard X-ray spectral range, the penetration depth of the beam is large, thus permitting measurements in the transmission mode (see Fig. 4.1), which is usually applied for the determination of the bonding environment of metals (e.g., K-edge of Fe-, Cu-, Ni-, Mn-, or L_3-edge of heavier metals like Pt, Au, or rare earths, e.g., Sm). In this geometry the sample is positioned in-between two ionization chambers that record the impinging, I_0, and transmitted intensity, I, thus providing the $\ln(I_0/I)$ which is proportional to the absorption coefficient, μ, according to Beer–Lambert's law (Eq. 4.1). In powder samples the grain size should be small in order to avoid effects related to inhomogeneous thickness. The observed attenuation in the EXAFS signal depends on the energy and the sample composition [24]. A reference sample, usually a metal foil, is positioned between the second and a third ionization chamber to obtain a reference spectrum that can be used for the correction of the

monochromator-induced energy shifts. The gas mixture and partial pressure in the ionization chambers should be properly selected according to the energy range of interest. When the measurements in the transmission mode are not possible, for example, in diluted samples or thin films deposited or grown on substrates, the fluorescence yield (FLY) mode is preferred. The fluorescence detector counts the number of the fluorescence photons emitted from the sample. Since the number of emitted fluorescence photons is proportional to the number of holes in an inner shell, created proportionally to the absorbed photons, the fluorescence yield is directly analogous to the absorption coefficient. The main disadvantage of the fluorescence yield mode is the self-absorption of the emitted fluorescence photons by the sample itself, which is significant when the samples are concentrated or thick. However self-absorption corrections are possible in many occasions [25]. A strong advantage of the FLY mode is the possibility to electronically discriminate fluorescence photons emitted by a specific atom and/or to suppress the background due to preceding edges, by proper selection of regions of interest (ROIs). The definition of ROI is possible when energy dispersive fluorescence detectors are used, for example, high-purity Ge or Si-drift detectors. Si photodiode or scintillation detectors, which are also used for the acquisition of the FLY signal, do not permit energy discrimination. Due to the linear polarization of the SR beam in the horizontal plane, reduction of the background due to scattering is achieved when the fluorescence detector is positioned on the horizontal plane at right angle to the beam [26].

When the XAFS spectra are recorded with soft X-rays (200–2000 eV), for example, at the K-edge of light elements (e.g., C, B, N, O) or $L_{2,3}$-edges of transition metals, instead of crystal monochromators, plane or curved diffraction gratings are usually used [16]. To achieve the fixed-exit condition, the grating and a mirror are combined in a parallel geometry. Given that the soft X-rays are strongly absorbed by the air, the sample should be positioned in an (ultra)high-vacuum chamber which is mounted windowless on the beamline. The detectors are also mounted without the use of a window on the chamber. Measurements in the transmission mode are not possible in this configuration, and thus the spectra can be recorded in either the FLY or in the electron yield mode (see Fig. 4.1). In certain cases, the photocurrent induced in the sample can be directly measured using a cable connection to the sample (drain current). The total electron yield (TEY) refers to the total number of electrons emitted after the creation of a core hole (photoelectrons, Auger electrons, secondary electrons), and it is in general proportional to the number of the created holes. TEY is usually recorded using a channeltron. Compared to FLY that is bulk sensitive, TEY is surface sensitive due to the small electron mean free path (less than 100 Å). The surface sensitivity of TEY can be further increased by using a retarding potential on a grid positioned in front of the electron detector. In this case the partial electron yield (PEY) is recorded. It is also possible to select the energy of the detected electrons to a specific Auger decay channel, thus decreasing the information depth compared to TEY. The main difference between the Auger electron (AEY) and TEY yields is that the energy of the Auger electrons is well defined and independent of the energy of the impinging photon. However, such an energy selection requires proper electron energy analyzers. The surface sensitivity of each electron yield detection scheme is

affected by the kinetic energy of the electron that determines its mean free path
according to a "universal curve" [13, 14, 27]. Irrespective of the acquisition mode
(FLY or EY), the spectra should be normalized with I_0 to account for the transmis-
sion function of the beamline optics. In the soft X-ray region, ionization chambers
cannot be conventionally used due to the strong window absorption. Instead, a Au
grid positioned in the beam, ahead of the sample, can be used and the induced
photocurrent is proportional to I_0. It should be mentioned that emission of fluores-
cence photons is a mechanism competitive to the emission of Auger electrons during
the atom de-excitation. The fluorescence yield increases with the atomic number and
it is particularly low for low-Z elements [28]. Thus in order to improve the signal-to-
noise ratio of FLY spectra recorded using soft X-rays, it is usually necessary to
acquire and average several spectra (the noise level decreases with $1/\sqrt{r}$, where r is
the number of averaged spectra). Furthermore, the signal-to-noise ratio of the FLY
signal can be significantly improved when multielement detectors are used.

Different kinds of experiments require specific setups. For example, time-
resolved XAFS measurements require very fast data acquisition that allows, for
example, the in situ real-time study of chemical reactions. For that reason, bent
crystal polychromators, which diffract each wavelength at a specific angle, are used.
The beam passes though the sample and the transmitted beam is detected with a
position sensitive detector, thus allowing the detection of a XAFS spectrum in time
significantly shorter that 1 s [29, 30]. In situ and often real-time measurements are
usually required for the study of catalytic processes using especially constructed
cells which allow the flow of the reacting gas or fluid in a controlled atmosphere.
Liquid nitrogen cooling and resistance heating are also feasible in most of the cells
[11, 31].

5 Spectrum Treatment and Analysis Procedure

Prior to analysis, the XAFS spectra need special handling. Initially the spectra are
corrected for energy shifts induced by the monochromator. In the hard X-ray regime,
this is usually done using the energy position of the absorption edge of a reference
metal foil. The exact energy of the absorption edge is determined by the maximum of
the first derivative of the spectrum. In the soft X-ray regime, the position of the
$1s \rightarrow \pi^*$ sharp resonance of the highly oriented pyrolytic graphite (HOPG) located
at 285.35 eV is often used. Another option is the use of the energy position of
specific features due to O and C contamination in the spectrum of the Au grid (I_0),
provided that it is recorded. The procedure used to extract the oscillatory part of the
EXAFS spectrum and the NEXAFS/XANES part is shown graphically in Fig. 4.6.

First a straight line that fits the pre-edge region and simulates the background due
to absorption of preceding edges or due to scattering is subtracted. Then the smooth
atomic background, μ_0, which corresponds to the absorption of the absorbing atom
in the absence of neighboring atoms, is removed, and the resulting difference is
normalized with the post-edge line which in most cases is the same with μ_0.
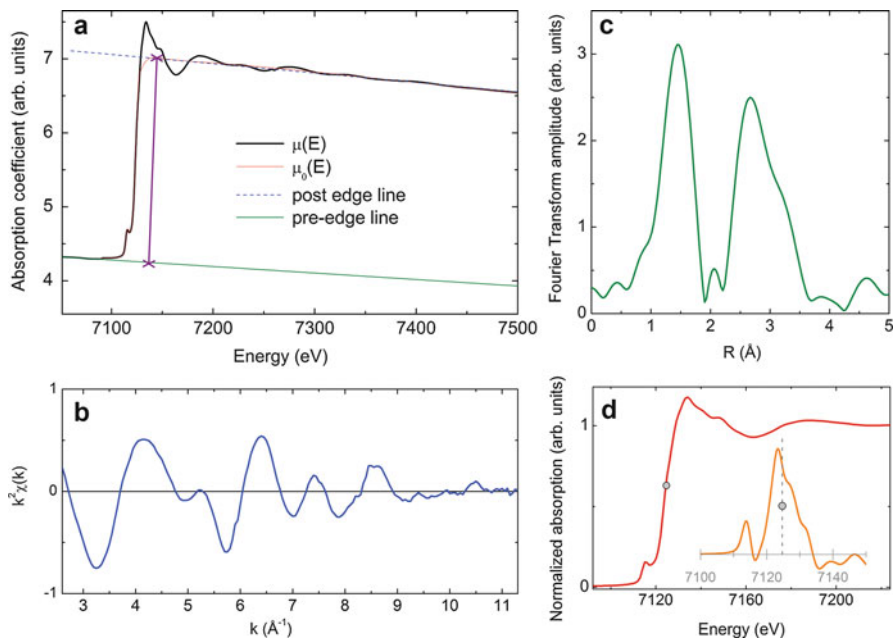
Fig. 4.6 Analysis procedure of the XAFS spectra: (**a**) subtraction of the atomic background, $\mu_0(E)$ and the pre-edge line from the XAFS spectrum, $\mu(E)$. The vertical purple line indicates the edge jump; (**b**) transformation from the energy space to the photoelectron wave number, k, space, and multiplication by k^n where n = 1, 2, or 3; (**c**) transformation from the k-space to the R-space by Fourier transforming using a proper window function; and (**d**) NEXAFS/XANES spectrum properly normalized at the edge jump. The inset shows the derivative of the spectrum that can be used for the determination of the position of the absorption edge

416   The resulting $\chi(E) = \frac{\mu(E) - \mu_0(E)}{\mu_0(E)}$ spectrum is converted from the energy space to the
417   k-space using the equation $k = \sqrt{\frac{2m}{h^2}(E - E_0)}$ where m is the electron mass and E_0
418   the binding energy of the electron or equivalently the position of the absorption edge.
419   The k(E) relation, $k = \sqrt{0.2625(E - E_0)}$, is a consequence of the energy conser-
420   vation principle in the photoelectric effect. The resulting $\chi(k)$ spectrum, multiplied
421   with k^2 to enhance the high-k contributions, is shown in Fig. 4.6b. The Fourier
422   transform (FT) of the k-weighted $\chi(k)$, using a proper window function, corresponds
423   to a pseudo-radial distribution function (Fig. 4.6c), and the resulting peaks corre-
424   spond to the nearest neighboring shell positions. The apparent distances of the peaks
425   from the absorbing atom are slightly smaller than the real distances (by 0.2–0.5 Å)
426   because of the phase shift induced due to the emission and backscattering of the
427   photoelectron.
428   The portion of the spectrum close to the absorption edge (Fig. 4.6d), i.e., the
429   NEXAFS spectrum, can be also used after the subtraction of the pre-edge
430   line and normalization with the edge jump (i.e., the intensity difference between

the post-edge and pre-edge lines), as indicated by a *purple vertical line* in Fig. 4.6a.
In order to compare NEXAFS spectra of different samples, it is necessary to have
them normalized. The procedure shown in Fig. 4.6 was done using the ATHENA
software [2]. The NEXAFS spectra can be also normalized to the intensity of the
spectrum at the atomic limit which is defined as the energy where the
EXAFS oscillations start and the NEXAFS transitions cease. At the atomic limit,
the photoelectron wavelength is roughly equal to the interatomic distance, R, i.e.,
$k \sim 2\pi/R$ [11]. Furthermore, the intensity of the spectrum at this energy is expected
to be independent of the angle of incidence of the beam. Normalization at the atomic
limit is particularly useful when it is not possible to record spectra extended to the
EXAFS regime, for example, due to the interference with other absorption edges,
due to considerable noise of the spectra, or due to the low concentration of the
absorbing atom.

To obtain structural information from the EXAFS spectra, the $\chi(k)$ spectrum (see
Fig. 4.6b) is fitted using a theoretical curve based on a proper model that consists of a
cluster of atoms up to a certain distance from the absorbing atom. In crystalline materials
such a cluster can be easily constructed when the space group, the lattice constants, and
the fractional positions of the atoms in the unit cell are known [32–36]. This cluster is
used for the construction of scattering paths which contain the backscattering amplitude,
phase shifts, and the photoelectron mean free path, λ_e. A least square fitting procedure is
then followed using the theoretical curve described by Eq. (4.3) where the coordination
numbers, nearest neighbor distances, and Debye–Waller factors are iterated for each
neighboring shell. The fitting is usually done simultaneously in both the R-space and
k-space. The main codes available for the calculation of the EXAFS parameters and/or
XANES spectra are EXCURV [37, 38], FEFF [19, 39], and GNXAS [40, 41]. For the
calculation of the L-edge XANES spectra of transition metals, the TT-Multiplets
software is available [42]. MXAN is a software for the analysis of the XANES spectra
that was initially used for the study of the bonding environment of metals in bio-
molecules [43]. It performs full multiple scattering simulations by changing geometrical
parameters of the structure around the absorbing atom.

Contrary to bulk crystalline materials, where the bonding configuration of the
element of interest is approximately the same throughout the sample, in nanosized
materials variation of the bonding environment is expected. This is due to the
considerable number of surface atoms compared to the number of atoms in the
"bulk," both contributing in the average XAFS signal. However the surface atoms
are expected to have a reduced coordination number especially in the second or
further shells. In addition to that, variations in the nearest neighbor distances are
expected to occur due to local strains or relaxation at the surface of the nanocrystal.
This effect may be reflected as an increase in the static disorder and consequent
increase in the Debye–Waller factors. This problem has been identified since the
1980s when EXAFS was applied for the study of small metal clusters. Since then
various models have been proposed which depend mainly on the shape and the
symmetry of the nanocrystal. The application of these models in the analysis of the
EXAFS spectra of nanosized materials allows for the determination of the size of the
nanoparticles by correlating the observed reduction in the coordination numbers in

comparison to the corresponding bulk values. Greegor and Lylte [44] proposed
models for face-centered-cubic (*fcc*) metal clusters in the form of spheres, cubes,
and disks. The dependence of the ratio of the observed (which is called effective)
coordination number in a specific shell j, $\overline{N}_j$, and the corresponding number in the
unperturbed crystal, N_j, on the total number of the atoms in the metal cluster is
shown in Fig. 4.7 for spherical and discoid shapes. The values were adopted from
Ref. [44] and are plotted in black. In the case of a spherical cluster, the radius R is
given by $R = \frac{\alpha}{1.82} \sqrt[3]{N_T}$, where α is the smallest interatomic distance and N_T is the
total number of atoms in the cluster. Correspondingly, for a disk with packing along
the (111) direction, the height C is given by $C = \frac{\alpha}{2.12} \sqrt{N_T} \cdot$ S. De Panfilis et al. [45]
discussed the effect of cluster size on the coordination number of nanophase Pd
considering that the *fcc* structure can be built by adding successive layers of atoms
forming a cuboctahedron. The average coordination number N(n) as a function of
the number of layers, n, and the size of the cluster, D, is given by the following
equations:

$$N(n) = \frac{40n^3 - 96n^2 + 80n - 24}{\frac{1}{3} \left(10n^3 - 15n^2 + 11n - 3 \right)} \quad \text{and} \quad D = 2R_1(n - 1) \quad (4.11)$$

where R_1 is the distance from the central atom to the first nearest neighbor. The
dependence of the average coordination number, normalized to the value 12 that
corresponds to a bulk crystal, on the size of the cluster is also plotted in Fig. 4.7 (*red*
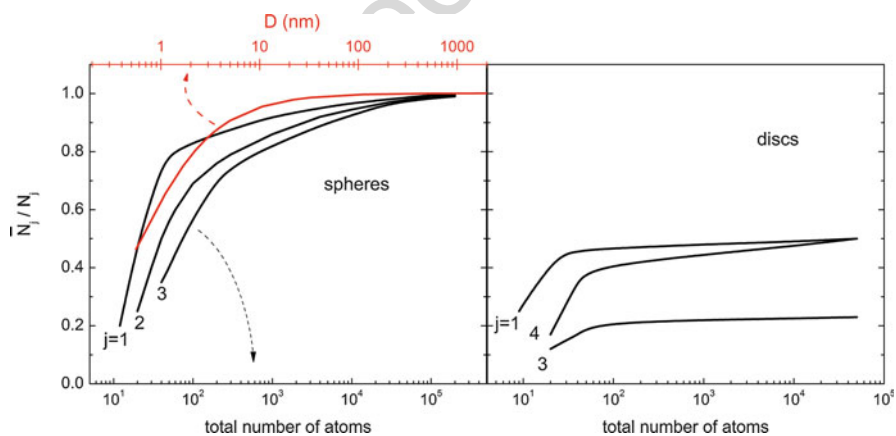
Fig. 4.7 (Black lines) Dependence of the effective coordination number over the coordination
number of an unperturbed crystal, on the total number of the atoms in the cluster, for *fcc* metal
clusters that crystallize in the form of spheres or disks. j is the order of the neighboring shell. The
data were obtained from the paper of Greegor and Lylte [44]. (Red lines) Dependence of the average
coordination number in the first nearest neighboring shell (a distance of 2.8 Å was considered)
relative to the coordination number for an unperturbed crystal as a function of the *fcc* crystal size
according to the model of de Panfilis et al. [45]

494 *line*). Borowski [46] proposed a simple equation for the determination of the size of
495 spherical Cu clusters using the average number of neighboring atoms normalized to
496 the corresponding number in the bulk, N_{red}. More specifically, $\langle N_{red}(\rho) \rangle = 1 - \frac{3}{4}\rho$
497 $+ \frac{1}{16}\rho^3$, where $\rho = 2R_i/D$, D is the diameter of the cluster and R_i is the distance of the
498 *i*th shell from the absorbing atom. Further discussion of size effects on the EXAFS
499 coordination numbers in metallic clusters can be found in Refs. [47–49].

500 Contrary to the analysis of the EXAFS spectra, which is done by properly fitting
501 the experimental spectrum in a path-by-path fashion, the analysis of NEXAFS spectra
502 is not trivial. Four approaches are generally applied: (i) direct comparison of the
503 spectra with those from reference compounds, (ii) linear combination of spectra of
504 known compounds, (iii) fitting using a number of peak functions to determine the
505 position and intensity of NEXAFS resonances, and (iv) simulation using full multiple
506 scattering procedures. In all the above cases, prior to analysis, the NEXAFS spectra
507 should be subjected to subtraction of a linear background and normalization to the
508 edge jump or the atomic limit as described in Fig. 4.6. In case (i) the spectra of the
509 studied compounds are directly compared with spectra of reference compounds, e.g.,
510 oxides, metal foils, etc. The first derivative of the spectra can be also compared, while
511 in some cases the difference spectrum is also provided. For example, the difference
512 spectrum is used in X-ray magnetic circular dichroism (XMCD) where the XANES
513 spectra of magnetic materials, usually recorded in the $L_{2,3}$ edges of a transition metal,
514 using left and right circularly polarized SR beam are subtracted from each other
515 [50]. In another application the difference spectra are obtained from the NEXAFS
516 spectra recorded at different angles of incidence [51]. An important piece of infor-
517 mation that can be derived from the NEXAFS spectra is the oxidation state of the
518 absorbing atom which is deduced from the chemical shift of the absorption edge.
519 Higher oxidation states result in a blue shift of the absorption edge, which usually
520 indicates a smaller bond length. An example of the chemical shift of the absorption
521 edge in Fe-containing compounds is shown in Fig. 4.8. The position of the absorption
522 edge can be determined from the maximum of the first derivative.

Fig. 4.8 Fe–K-edge XANES spectra of reference compounds (Fe foil, FeS, Fe_3O_4, and $FePO_4$)
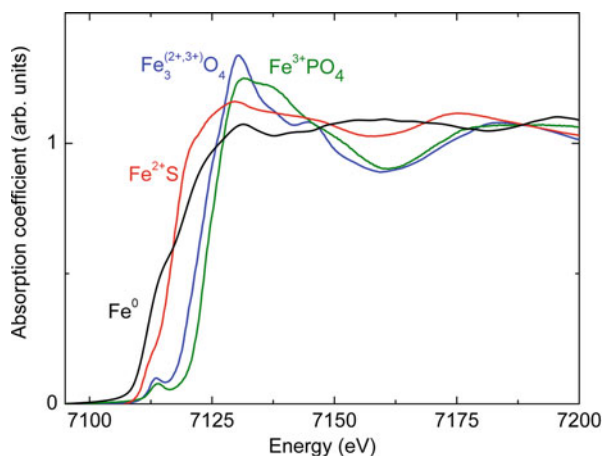
Fig. 4.9 Fitting (thick solid line) of the Pd–K-edge XANES spectrum of Pd-doped poly-o-methoxyaniline (POM) as a linear combination of XANES spectra of component Pd-containing samples (thin solid lines) (Reprinted from the Journal of Alloys and Compounds, Vol. 362, J. W. Sobczak, E. Sobczak, A. Drelinkiewicz, M. Hasik, and E. Wenda, Local structure of a Pd-doped polymer investigated using a linear combination of XANES spectra, Pages 162–166, Copyright 2004, with permission from Elsevier)
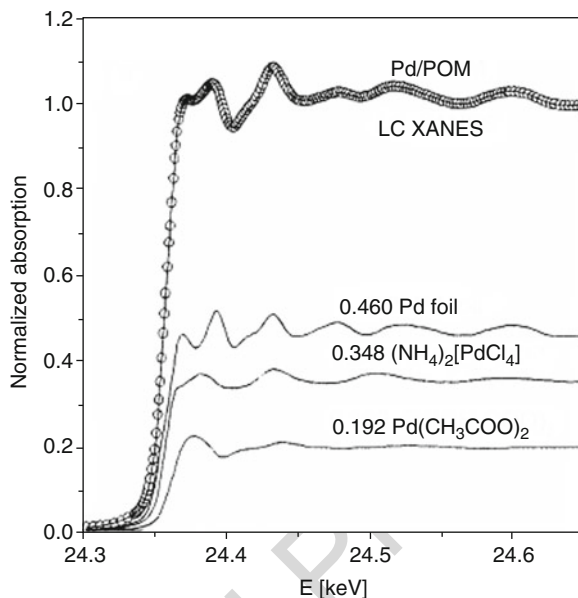
In approach (ii) the spectra of multiphase materials are simulated as a weighted average of spectra from reference compounds. This method is applicable due to the localized character of XANES which is mainly dominated from the small photo-electron mean free path. An example of the linear combination fitting (sometimes it is referred to as principal component analysis) of Pd–K-edge XANES spectra from a Pd-doped polymer adopted from [52] is shown in Fig. 4.9.

Approach (iii) is applied when the XANES spectrum is considered proportional to the density of empty states in the conduction band, or to antibonding molecular orbital states, or even when information should be extracted from pre-edge peaks that appear in the spectra recorded at the K-edge of transition metals. An example of fitting of a C–K-edge XANES spectrum of the polymer poly(2,5-bis (3-tetradecylthiophen-2-yl)thieno-[3,2-b] thiophene) [PBTTT] adopted from Ref. [53] is shown in Fig. 4.10. The NEXAFS spectrum is fitted with a step function and a number of Gaussians. The step function accounts for the transitions from the initial 1s state to final states in the continuum. In this case the C atom is ionized and the photoelectron may have any kinetic energy. Peak functions are used to account for transitions from the initial 1s state to a final bound empty state of an antibonding molecular orbital. Such states, which result from the formation of covalent bonds, are strongly directional and result in strong localization of the electron charge in the interatomic space. Gaussian functions are used when the experimental broadening, related to the energy resolution of the monochromator, is larger than the natural width of the transition, denoted with Γ. It is determined as $\Gamma \simeq \hbar/\tau$, where τ is the transition lifetime defined by $1/\tau = 1/\tau_e + 1/\tau_h$, τ_h and τ_e are the lifetimes of the initial state (core-hole lifetime) and the final state of the electron. Although the latter
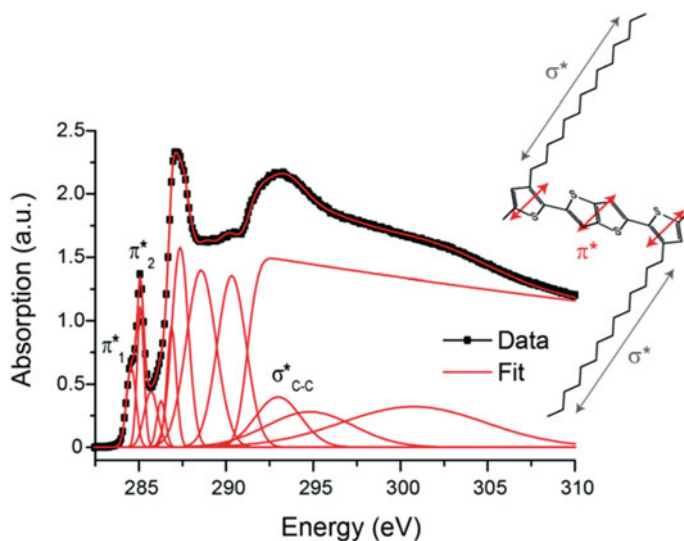
Fig. 4.10 Fitting of a C–K-edge NEXAFS spectrum of the polymer PBTT using a number of Gaussians and a step function. The orientation of the π* and σ* antibonding orbitals in the structure of PBTT is also shown (Reproduced from Ref. [53] with permission of The Royal Society of Chemistry)

is very high, the core-hole lifetime is generally much smaller and decreases with the atomic number of the absorbing atom, thus resulting in sharp NEXAFS features in the K-edge spectra of low-Z elements, e.g., B, C, N, O etc. [13, 54]. Gaussian functions are also used when the samples are highly disordered. When the natural broadening dominates the experimental one, Lorentzian functions are used, whereas when the natural and experimental broadening is comparable, Voigt functions (convolution of a Gaussian and a Lorentzian) can be used.

Additional valuable information on the geometry of the polyhedron formed around transition metal atoms (Fe, Mn, Co, V, Cr, etc.) as well as on their oxidation state can be obtained from the fitting of the pre-edge peaks that appear in their K-edge spectra. The pre-edge peak corresponds to transitions from the 1s initial state to a final (empty) d-state. Although such a transition is forbidden due to the $\Delta\ell = \pm 1$ selection rule in the dipole approximation, it gains intensity due to the p-d hybridization that is induced by the modification of the metal crystal field by its ligands. An example of a pre-edge peak fitting is shown in Fig. 4.11 [55]. The pre-edge peaks were recorded in the micro-XANES mode (with capillary optics and a beam diameter of 5 μm) at the Fe–K-edge from different spots of a sample with inhomogeneous distribution of Fe. In regions with low Fe concentration, the pre-edge peak was sharp and intense and could be fitted with one Lorentzian function. Contrary to that, the pre-edge peak recorded from Fe-rich regions is broader and with lower intensity and can be fitted with two or more Voigt functions. Furthermore, redshifts of the pre-edge peak centroid indicate reduction of the oxidation state of the absorbing atom. Extended
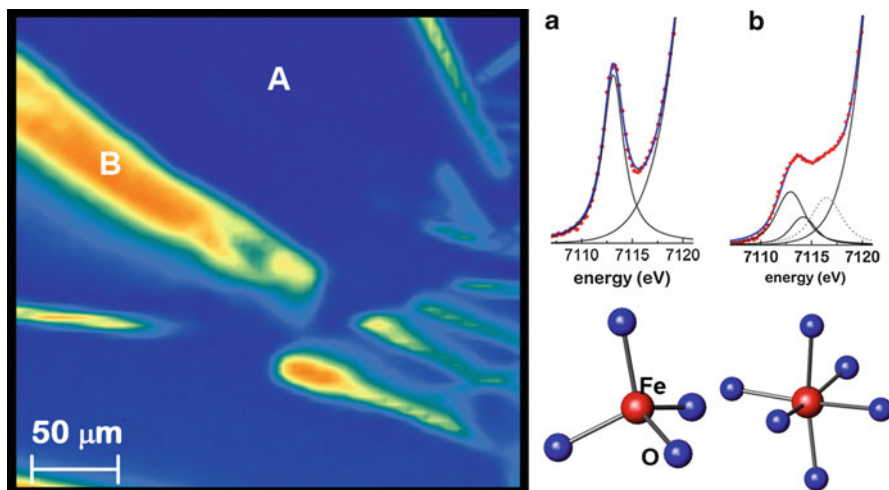
Fig. 4.11 Fitting of pre-edge peaks of Fe–K-edge micro-XANES spectra recorded in different spots from a vitroceramic sample with inhomogeneous distribution of Fe [55]. The blue regions (A) in the X-ray fluorescence image that maps the Fe K_α emission intensity correspond to low Fe concentration and the red (B) to high Fe concentration. Fe in A and B is tetrahedrally and octahedrally coordinated, respectively

discussions on the fitting process and the information that can be extracted from the pre-edge peak of Fe and Mn can be found in Refs. [56–58].

The approach (iv) in the analysis of the XANES spectra, i.e., the simulation using proper software, is generally more difficult and time-consuming. The simulations necessitate the use of a structural model, i.e., Cartesian coordinates of the atoms that comprise a cluster around the absorbing atom, which is either provided by other characterization techniques, e.g., diffraction techniques in crystalline materials or by theoretical calculations, e.g., molecular dynamics [49]. Despite the complexity of this method, the significance of multiple scattering contributions in the XANES spectra provides a sensitive tool in the local bonding geometry since the XANES spectra of structural polymorphs, which are hardly distinguishable by EXAFS, are considerably different [13, 51]. Full multiple scattering calculations prevail in the simulation of the XANES spectra due to their applicability in materials that lack long-range periodicity and take into account effects such as core hole and inelastic losses. Examples of simulations of XANES spectra using the FEFF code are shown in Fig. 4.12 (Zn–K-edge) and Fig. 4.13 (N–K-edge).

Among the abovementioned procedures, fitting of the spectrum with step function(s) and a number of peak functions permits (i) the quantification of defects from defect-related states [61], (ii) the quantification of charge transfer from the intensity of "white lines" assigned to transitions to final states strongly localized on the absorbing atom [62], (iii) the determination of the different contributions in the magnetic moments from the XMCD spectra (Sect. 6.1), and (iv) polarization studies. The latter refers to the angular dependence of the XANES or NEXAFS spectra and originates

Fig. 4.12 Simulation of the Zn–K-edge spectra of coprecipitated (cpt) and sorbed (ads) Zn on ferrihydrite (Reprinted from Geochimica et Cosmochimica Acta, Vol. 67, G. A. Waychunas, C. C. Fuller, J. A. Davis, J. J. Rehr, Surface complexation and precipitate geometry for aqueous Zn(II) sorption on ferrihydrite: II. XANES analysis and simulation, Pages 1031–1043. Copyright (2003), with permission from Elsevier [60])
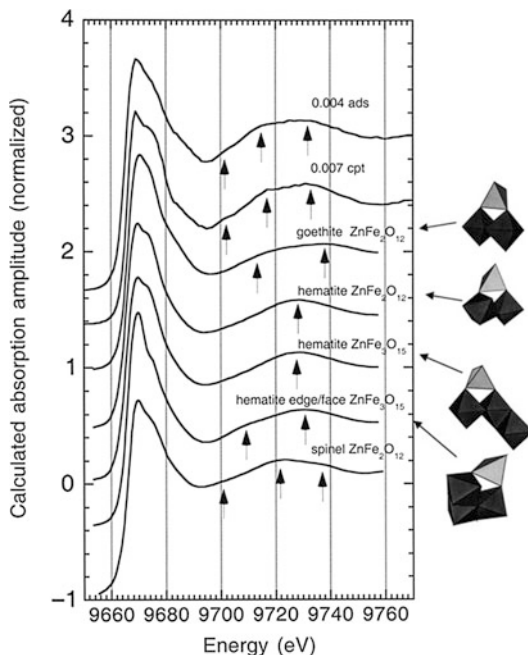
Fig. 4.13 Simulation of the N–K-edge NEXAFS spectrum of hexagonal GaN using the FEFF code and full multiple scattering in a cluster of 195 atoms [61]
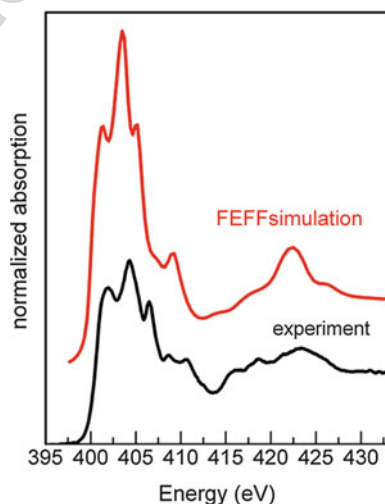
from the linear polarization of the SR beam and the directionality of the covalent bonds. A characteristic case is that of carbon-related materials (more examples can be found in Sect. 6.5), the simplest example being that of highly oriented pyrolytic graphite (HOPG).

596   The hexagonal rings formed by the C atoms lie parallel to the sample surface and
597 normal to the hexagonal axis. sp^2 hybridization of the C atomic orbitals results in the
598 formation of π* antibonding molecular orbitals (the direction of maximum electron
599 charge density is along a vector normal to the carbon ring) and σ* orbitals that can be
600 represented as planes of maximum electron charge density normal to the c-axis. The
601 C–K-edge NEXAFS spectra of HOPG recorded in the TEY mode for various angles
602 of incidence of the SR beam, θ, are shown in Fig. 4.14. The area under the
603 characteristic π* resonance that appears at 285 eV depends linearly on cos^{2}θ, as
604 shown in the inset.

6   Key Research Findings

606 In the following, representative, recently published applications of the XAFS spec-
607 troscopy in various types of nanomaterials will be discussed.

6.1   Metallic and Intermetallic Nanomaterials

609 Metal or intermetallic nanoclusters, supported, embedded, or self-standing, comprise
610 an important class of materials since they have the potential for several applications
611 including catalysis and magnetic recording media as well as due to their superior
612 tribological and optical properties.

6.1.1   Metal Nanocatalysts

614 Since the late 1970s, it was established that the catalytic activity increases signifi-
615 cantly with increasing the surface area of the catalyst, thus driving their preparation
616 in the form of tiny particles. A review on XAFS characterization of metallic and
617 nonmetallic catalysts till late 1980s can be found in ▶ Chap. 8 of Ref. [11]. A more
618 recent review can be found in Ref. [63]. The catalytic activity of nanocatalysts (e.g.,
619 Pt, Rh, Ni) can be improved further when they are deposited on supports (e.g.,
620 alumina, silica, TiO$_2$) with high surface area. In this case, the metal–oxide interface
621 plays an important role in charge transfer. In homogeneous catalysis, where cata-
622 lysts, reactants, and products are dissolved in the same phase, the catalyst is a
623 coordination complex or an organometallic compound. Homogeneous catalysts
624 comprised by a metal-ion core surrounded by ancillary ligands allow tuning of
625 their structure toward optimization of their reactivity and selectivity. Heterogeneous
626 catalysts lack such tunability, but they can be recyclable [64]. XAFS finds applica-
627 tions in the study of metallic nanocatalysts for the determination of the size of the
628 nanocrystals (see Fig. 4.7), which is an important parameter affecting their activity.
629 In addition to that, XAFS provides information on the oxidation state of the
630 nanocatalyst which is related to chemical effects and charge transfer. The latter can
631 be assessed from the position of the absorption edge and the position and intensity of
632 the white line as well as from the EXAFS spectrum that allows for the detection of
633 different kinds of neighboring atoms. Finally, time-resolved XAFS (Quick-XAFS) is
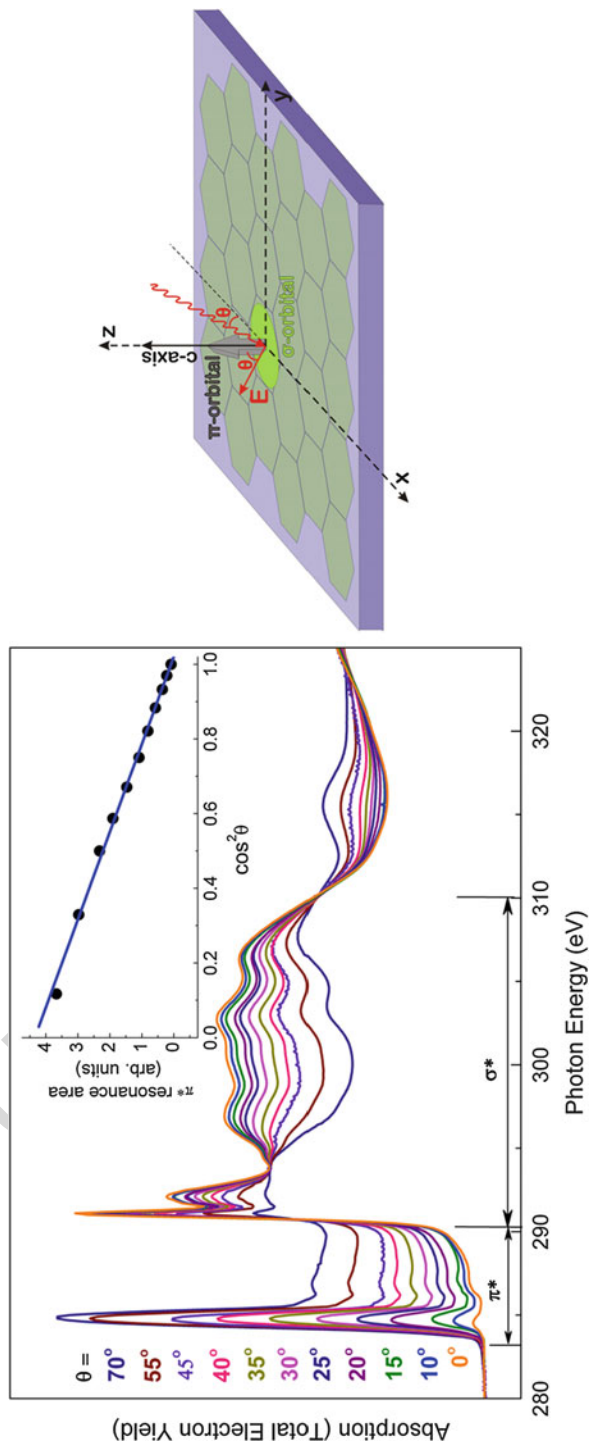
Fig. 4.14 (*Left*) C–K-edge TEY spectra of HOPG recorded at different angles of incidence. The *inset* shows the variation of the intensity of the π^* resonance at 285 eV on $\cos^2\theta$. (*Right*) σ [plane] and π [vector] orbital orientation and definition of the angle of incidence θ. E is the electric field vector of the incident beam. The spectra were kindly provided by Dr. Maria Brzhezinskaya, BESSY-II Storage Ring – Helmholtz-Zentrum Berlin
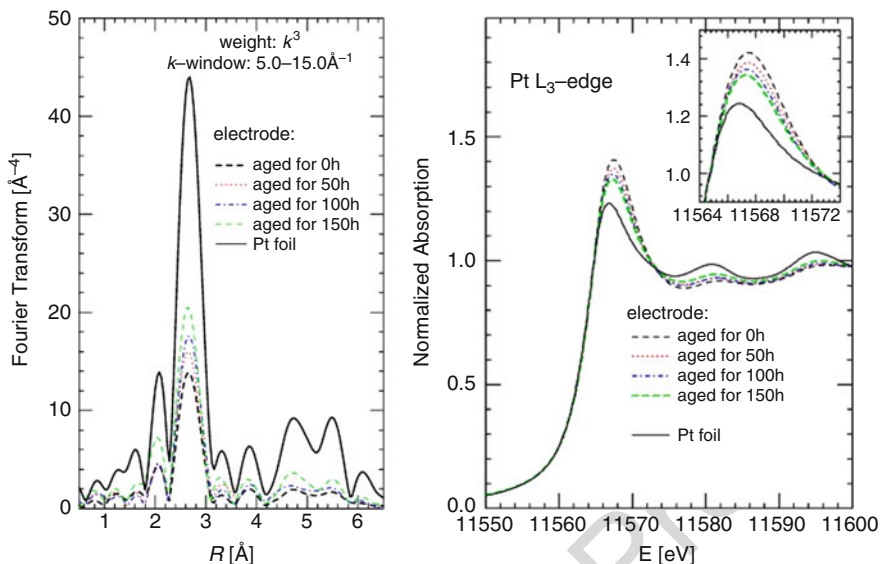
Fig. 4.15 Effect of aging on the Fourier transform of the EXAFS spectra (*left*) and XANES spectra (*right*) of Pt-nanoparticle supported catalysts recorded at the Pt–L$_3$-edge (Reprinted from Journal of Non-Crystalline Solids, Vol. 401, A. Witkowska G. Greco, S. Dsoke, R. Marassi, A. Di Cicco, Structural change of carbon supported Pt nanocatalyst subjected to a step-like potential cycling in PEM FC, Pages 169–174. Copyright (2014) with permission from Elsevier)

applied for the in situ real-time study of the formation of catalyst nanoparticles, during their synthesis or reduction processes or even during the catalytic reaction.

Polymer electrolyte membrane (PEM) fuel cells offer solutions in energy production with applications from electric vehicles to power plants. However, aging of the catalyst is an important issue. Witkowska et al. studied the effect of aging of Pt nanocatalysts supported on Vulcan (E-TEK) with XAFS measurements at the Pt–L$_3$-edge [65]. Aging for working times 0 to 150 h resulted in the variation of the size distribution of the Pt nanoparticles with the average size, as determined with XRD and TEM, increasing although remaining smaller than 3 nm. The Pt–L$_3$-EXAFS spectra were fitted using the model of metallic Pt and the GNXAS ab initio code where the absorption cross section was expanded in terms of multiple scattering contributions up to the fifth neighbor [66]. Fourier transform of EXAFS and XANES spectra of the catalysts, as a function of the working time, is shown in Fig. 4.15. The peak intensity of the Fourier transform, and consequently the coordination numbers, increased, signifying an increase of the particle size. Furthermore, phase changes, for example, formation of PtO, did not take place due to the aging-induced degradation of the catalyst. The intensity of the white line (attributed to 2p → d transitions) in the Pt–L$_3$-XANES spectra (Fig. 4.15) decreased with aging. Although changes in the white-line intensity could be attributed to the variation of the particle size that affects the surface-to-volume atom ratio, the observed increase was much higher and was attributed to the occupancy of the 5d electronic states of the Pt atoms with aging.
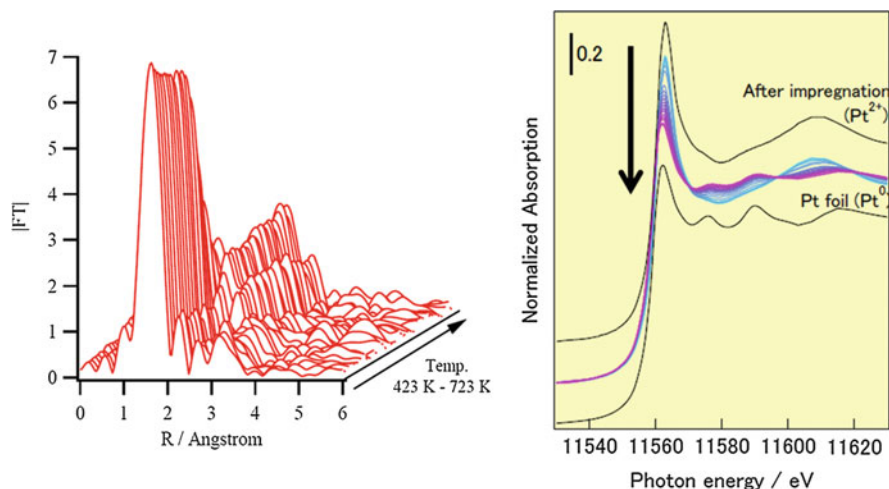
Fig. 4.16 (*Left*) Fourier transform of the time-resolved EXAFS spectra and (*right*) corresponding XANES spectra of the SiO$_2$-supported Pt-nanoparticle catalysts recorded at the Pt–L$_3$-edge (Reproduced with permission of IOP Publishing from T. Shishido, H. Nasu, L. Deng, K. Teramrua, and T. Tanaka, Study of formation process of metal nanoparticles on metal oxides by in-situ XAFS technique. Journal of Physics: Conference Series, 2013. **430**: 012060.1–012060.4)

The usual method for the preparation of supported catalysts is impregnation. A solution of a metal precursor is added to the catalyst support followed by a drying or calcination process that promotes the formation of the metal particles on the supporting material. A reduction process (heating in a H$_2$ atmosphere) follows afterward. The formation of Pt nanoparticles on SiO$_2$ by impregnation in an aqueous solution of Pt(NH$_3$)$_4$(NO$_3$)$_2$ was investigated using in situ time-resolved (Quick)-XAFS by Shishido et al. [67]. The Pt–L$_3$-edge XAFS measurements were performed in H$_2$ or He flow. The in situ time-resolved Fourier transforms of the XAFS spectra and the corresponding XANES spectra, recorded in He flow with increasing temperature, are shown in Fig. 4.16. The XANES spectra revealed variations in the white line. More specifically, the intensity increased slightly when the temperature was increased from 460 to 500 K and then at 700 K decreased to the value that corresponds to metallic Pt. This variation in the intensity of the white line, which is consistent with the change in the oxidation state of Pt from +2 in the Pt(NH$_3$)$_4$(NO$_3$)$_2$ precursor to 0 in the metallic Pt, is also verified by the shift in the absorption edge and the EXAFS spectra. At temperatures above 542 K, the Pt–Pt contribution of metallic Pt is detected in the Fourier transform (2.5–3 Å). On the other hand, the peak due to Pt–N and/or Pt–O bonding in Pt(NH$_3$)$_4$(NO$_3$)$_2$ (~1.8 Å) loses intensity indicating the formation of metallic Pt at the expense of the precursor as a function of temperature. The gradual formation of Pt nanoparticles and the invariability of their size were verified by the linear combination fit of the XANES spectra using the spectra of Pt and the precursor.

677   In situ time-resolved XAFS was applied in order to study the formation of Rh
678 nanoparticles from the reaction of $RhCl_3 \cdot H_2O$ and polyvinylpyrrolidone (PVP) in
679 ethylene glycol solution at elevated temperatures [68]. Direct comparison of the
680 Rh–K-edge XANES spectra of the reaction mixture with the spectra of $RhCl_3 \cdot H_2O$
681 and Rh metal revealed the progressive formation of metallic Rh at the expense of
682 $RhCl_3 \cdot H_2O$ within 1 h at the temperature of 408 K. Simulation of the XANES
683 spectra of the mixture as a linear combination of the spectra of $RhCl_3 \cdot H_2O$ and Rh
684 foil was applied for the quantification of the Rh^{3+} consumption rate. The analysis of
685 the EXAFS spectra disclosed similar results. The Rh–Rh distance was found slightly
686 shorter compared to the corresponding distance in bulk Rh. In addition to that, the
687 average approximate particle size was determined from the coordination numbers.
688 Comparison of the time evolution of the intensity of specific peaks in the Fourier
689 transform provided information on the kinetics of Rh nanoparticle formation. Similar
690 time-resolved XAFS studies on the formation kinetics of Cu, Rh, and Pd
691 nanoparticles have been also reported [69, 70].

692   Except from time-resolved studies applied for the investigation of the synthesis or
693 aging processes, XAFS is also applied for the study of the structure of nanocatalysts.
694 γ-Alumina-supported Pt nanoclusters with average particle size 0.8 nm were studied
695 by means of Pt–L_3-edge XAFS [71]. When the particles are so small, the cluster
696 contains less than 300 atoms resulting in a drastic increase of the ratio of corners and
697 edges relative to terrace atoms and thus affecting strongly the catalytic properties.
698 The studied catalysts were prepared by impregnation of the Pt^{2+} precursor on
699 γ-Al_2O_3 and reduction by heating for 10 min at 200 °C under H_2 flow. Direct
700 comparison of the catalyst XANES spectra with the spectra from reference Pt foil
701 and PtO_2 samples revealed the metallic state of Pt. This result was also verified by
702 the EXAFS spectra where a shell with coordination number 6.1 at a distance of
703 2.67 Å was identified. This distance is smaller compared to the corresponding
704 distance in the bulk material (2.76 Å) due to the unsaturated environment of the
705 metal atoms. This effect became less significant as the size of the cluster increased. In
706 addition to the metallic state of Pt, a weak contribution of Pt–O was also detected.

707   γ-Al_2O_3-supported Ag nanoparticles are effective catalysts for oxidant-free cat-
708 alytic dehydrogenation of alcohols to carbonyl compounds. The efficiency of the H_2
709 reduction process was studied through Ag–K-XAFS [72]. The XANES spectra
710 revealed that Ag was successfully reduced to metallic Ag, for Ag loadings
711 1–10 %, after heat treatment with H_2. The formation of small metallic Ag
712 nanoparticles was also verified by EXAFS. More specifically the number of Ag
713 neighbors increased at the expense of O neighbors, while the smaller Ag–Ag
714 distances, compared to the corresponding values in the bulk counterpart, identified
715 the formation of nanoparticles. The determined Ag–Ag coordination numbers were
716 used for the estimation of the nanoparticle size as a function of the Ag loading of the
717 heterogeneous catalyst. Zeolites comprise a family of porous aluminosilicate min-
718 erals that can be used as catalysts. The catalytic activity of a Ag-loaded zeolite
719 (ZSM-5) for the oxidation of CH_4 was studied by Kuroda et al. [73]. The changes in
720 the Ag bonding environment with the evacuation temperature of the Ag-loaded
721 zeolite were investigated using Ag–K-XAFS. It was found that above a certain

temperature, Ag metal clusters were formed. The coexistence of Ag+ ions and small Ag metal clusters leads to prominent catalytic behavior in the partial oxidation of CH_4, for the Ag-loaded zeolite evacuated at temperatures higher than of 573 K.

Miller et al. [74] studied Au nanoparticles on different oxide supports (alumina, ceria, zirconia, and others) by means of Au–L_3-edge XAFS measurements. Au exhibits catalytic activity for hydrogen–deuterium exchange, olefin hydrogenation, NO_x reduction with H_2, paraffin skeletal isomerization, and partial oxidation. Au nanoparticles are highly active for CO oxidation, with the activity increasing as the size of the Au particles decreases, especially when the particle size is less than 50 Å. The EXAFS characterization revealed that irrespective of the support oxide, both the coordination number in the first nearest neighboring shell and the interatomic distance decreased, due to the decrease in the nanoparticle size. The reactivity of Au nanoparticles with O_2 was also studied by the use of XAFS. Upon reaction with atmospheric air, the intensity of the white line in the XANES spectra increased revealing that about 10 % of the Au atoms were oxidized. Oxidation was further promoted at increased temperature. The degree of oxidation was also assessed from the Au–O peak that appeared in the Fourier transform of the EXAFS spectra at approximately 0.9 Å below the Au–Au peak.

Kroner et al. [75] considered doping of Rh nanoparticles with ceria and/or zirconia, which is expected to increase the catalytic performance and improve the catalyst lifetime. The Rh nanoparticles were supported on γ-alumina, and the structure of the catalyst was studied with Rh–K-edge XAFS. Regarding potential applications, Rh is the main component in the three-way automotive exhaust catalyst due to its superior selectivity for NO_x removal. In order to determine the oxidation state of the catalyst, its XANES spectra were compared with the spectra of Rh foil and Rh_2O_3. Both the position of the absorption edge and the intensity of the spectrum at a specific energy were taken into account. It was found that the Rh/Al_2O_3 catalyst (prepared by impregnation with $RhCl_3 \cdot H_2O$, drying in air and reduction) contained mostly oxidized Rh particles. Furthermore, the method used for the ceriation of the Rh catalyst, i.e., Rh catalyst deposition on CeO_2/γ-Al_2O_3 or decomposition of metal–organic $Ce(acac)_3$ on Rh/γ-Al_2O_3, affected the degree of Rh oxidation, with the latter providing less oxidized Rh. Similar trends were observed in the zirconia-promoted Rh catalysts that were even less oxidized. Quantification of the amount of Rh that was oxidized was achieved by fitting the Rh–K-edge EXAFS spectra where the Rh–Rh and Rh–O distances yielded well-separated peaks in the Fourier transform (at 2.68 and 2.02 Å, respectively). The results supported that ceria and zirconia can protect the Rh particles from extensive oxidation. The size of the Rh particles, as it was deduced from the coordination numbers obtained from the EXAFS analysis, was discussed as a function of the synthesis method.

A method alternative to impregnation for the preparation of supported nanocatalysts is based on colloidal deposition. For the deposition of Pt on TiO_2, the following procedure was followed: a Pt precursor was reduced to Pt nanoparticles in the presence of protecting polymers, then the nanoparticles were deposited on TiO_2, and finally the polymers were decomposed and the Pt nanoparticles were reduced. Einaga et al. [76] prepared Pt/TiO_2 nanoparticles

using DNA as a protecting polymer which stabilized the Pt colloid. The deposition of the colloid on TiO_2 was followed by annealing in O_2 atmosphere. Pt–L_3-edge XAFS spectra were recorded for the study of both the Pt colloidal and the Pt/TiO_2 particles. As expected, the intensity of the peak in the Fourier transforms of the Pt colloids and the Pt/TiO_2 nanoparticles were characterized by very low intensity. Furthermore, only Pt–O (and not Pt–Pt) contributions were detected verifying the formation of small-sized Pt oxide colloid particles. Further oxidation occurred after the deposition process. The EXAFS results were verified by the XANES spectra, where the intensity of the white line was the characteristic of the formation of Pt oxide in the colloid.

Dendrimer-encapsulated Au nanoparticles, with size ranging from 1 to 2 nm, were investigated using EXAFS in order to evaluate an analysis model that would take into account the asymmetry in the bond-length distribution. Encapsulation within a dendrimer template results in negligible interactions with the support. On the other hand, controlled disorder of the Au nanoparticle was achieved by different concentrations of thiols which are small molecules that penetrate easily the dendrimer and are strongly adsorbed on the particle surface [77]. The Au–L_3-edge EXAFS spectra of the nanoparticles were simulated taking into account the average signal of each Au atom, which was calculated using the atom sites determined by molecular dynamics. The accuracy of molecular dynamic simulations of such disordered systems was tested by its ability to reproduce accurately the experimental (EXAFS) spectra. The theoretically calculated pair distribution function for the Au–Au atom pair was compared with the experimentally determined Gaussian function used for the fitting of the Au nearest neighboring shell in the EXAFS spectra. As the coverage of the Au particle increased, the disorder increased and the pair distribution function deviated more from the symmetric distribution described by EXAFS. A similar approach was presented by Roscioni et al., where the EXAFS spectra of 2–6 nm nanoparticles were simulated using structural snapshots of the cluster obtained with molecular dynamic calculations. Averaging took place for different structural configurations and for all the photoabsorbing atoms in the cluster [78]. A similar approach was applied for modeling the EXAFS spectra of supported Pt nanoparticles [79]. A review on the methods used to model the EXAFS spectra of nanoparticles with various shapes, where issues like homogeneity, the width of the size and compositional distribution functions, were taken into account, can be found in Ref. [48]. In the same paper, multiple scattering contributions are also discussed.

Mixed noble metal nanoparticles have a higher conversion rate and thus are expected to exhibit superior catalytic properties compared to the single component counterparts resulting in lower required loadings. Therefore, optimal performance in direct methanol fuel cells has been achieved using a bimetallic catalyst. Christensen et al. [80] applied Ru–K-edge XAFS spectroscopy for the study of bimetallic Ru–Pt nanoparticles with average size of 1.2 ± 0.3 nm deposited on spherical alumina nanoparticles. The Ru–Ru distance was found smaller by 0.08 Å compared to the corresponding distance in the Ru foil. A Ru–Pt shell was also used to fit the EXAFS spectra. The results indicated that the nanoparticles were bimetallic and excluded formation of separate Pt and Ru particles. The formation of bimetallic particles was
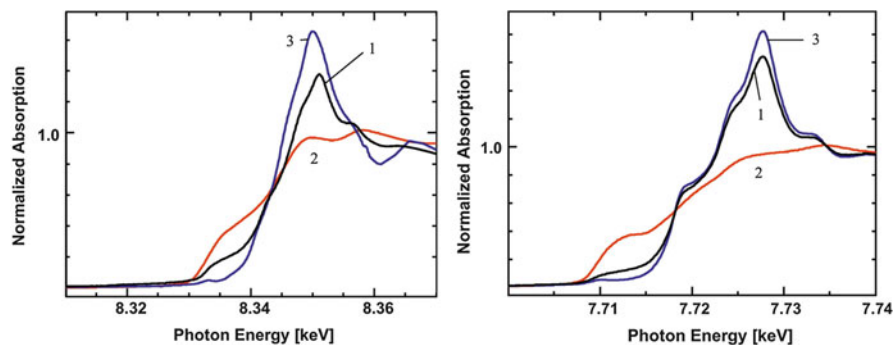
Fig. 4.17 (*Left*) Ni–K-edge and (*right*) Co–K-edge XANES spectra of a Ni–Co coprecipitated catalyst reduced at 750 °C for 4 h (*black, 1*), X metal foil (*red, 2*) and XO (*blue, 3*) where X=Ni (*left*) and Co (*right*) (Reprinted from Catalysis Today, Vol. 207, H. Wang, J. T. Miller, M. Shakouri, C. Xi, T. Wu, H. Zhao and M. Cem Akatay, XANES and EXAFS studies on metal nanoparticle growth and bimetallic interaction of Ni-based catalysts for CO_2 reforming of CH_4, Pages 3–12. Copyright (2013), with permission from Elsevier)

also supported by the redshift in the absorption edge of the Ru–K-edge XANES spectra of the studied particles compared to a pure Ru catalyst deposited on SiO_2.

Except from the application of noble metals in catalysis, other metals are attractive for catalytic reactions as well. For example, Ni can be used in the CO_2 reforming of CH_4, a reaction that finds applications in fuel cell technology as well as in the conversion of the greenhouse gases to a mixture containing H and CO. It also shows catalytic activity in reactions like hydrogenation of aromatic compounds and steam reforming reactions. Compared to noble metals, Ni has the advantage of higher abundance in nature. Higher catalytic activity is expected when the particle size is reduced to the nanoscale because the concentration of atoms with deficient coordination increases with decreasing volume-to-surface ratio. Wang et al. [81] studied, by means of Ni- and Co–K-edge XAFS spectroscopy, Ni, Co, and Ni_xCo_y nanoparticles prepared by coprecipitation or impregnation on $MgAlO_x$ supports. The spectra were recorded both from the reduced catalysts (heated at 750 °C in H_2/ He flow for 4 h) and in situ during the reduction process. Representative XANES spectra of reduced catalysts recorded at the Ni–K- and Co–K-edge are shown in Fig. 4.17. Direct comparison of the spectra from the nanoparticles with those of the reference oxides and metal foils revealed that the catalysts were not fully reduced. To quantify the degree of oxidation, the XANES spectra were fitted as linear combinations of the spectra of the reference samples using proper weighting factors. The results were discussed as a function of the catalyst preparation process (impregnation and coprecipitation). Furthermore, the extent of reduction of the Ni and Co particles was also determined as a function of the duration of the reduction process by in situ XAFS measurements. The EXAFS spectra were also analyzed taking into account the degree of reduction as estimated by the XANES analysis. The size of the Ni and Co particles was inferred using the coordination numbers determined by EXAFS, as in the case of Pt catalysts [82]. The authors also discussed the effect of the interaction

between Ni and Co as well as with the support structures on the catalyst reduction rate and stability in addition to the particle size distribution and dispersion uniformity.

Kitagawa et al. [83] applied Ni–K-edge XAFS for the study of a Ni nanocluster catalyst on alumina. Small particle size and good homogeneity were achieved using colloidal methods with Ni loading approximately equal to 3 %. Direct comparison of the XANES spectra of the catalysts with that of NiO and Ni metal foil revealed that in all the samples the dominant species was Ni^0. Linear combination fit determined that more than 80 % of Ni was reduced to Ni^0 excluding thus the formation of $NiAl_2O_4$ which is a common phase formed during the preparation of the catalyst by impregnation methods. Regarding the EXAFS analysis, fitting was performed for the first nearest neighboring shell using the model of Ni metal. The coordination numbers were found to range from 6.7 to 10.3 (12 is the coordination number in the Ni foil) depending on the synthesis conditions.

6.1.2 Magnetic Metal Nanomaterials

XAFS spectroscopy is extensively applied for the study of magnetic materials, both for the investigation of their nanostructure and for the determination of spin and orbital magnetic moments using X-ray magnetic circular dichroism (XMCD). For the acquisition of the XMCD signal, left- and right-handed circularly polarized SR light is utilized and the corresponding spectra, recorded in the presence of a magnetic field, are subtracted. The theoretical background of the XMCD and the so-called sum rules that can be used to extract information on the magnetic moments from the spectra can be found in Refs. [84–86]. It should be reminded that the atom-selectivity of XAFS spectroscopy allows the quantification of the contribution of each specific element in the average magnetic behavior.

Metallic nanoparticles exhibit a variety of magnetic phenomena, for example, super-paramagnetism, magnetoresistance, and magnetic anisotropy. Their properties depend strongly on several parameters such as their size, structure, and morphology, as well as on their chemical composition and interactions with substrates, matrices, and/or capping layers. Colloidal systems consisting of Co nanoparticles, with size of approximately 3 nm, embedded in surfactant matrices were studied by means of Co–K-edge XANES. The Co nanoparticles were prepared by Co^{2+} reduction of cobalt bis(2-ethylhexyl) sulfosuccinate $Co(AOT)_2$ and cobalt bis(2-ethylhexyl) phosphate $Co(DEHP)_2$ reverse micelle solutions [87]. In addition to XAFS, the authors used complementary characterization techniques including electron microscopy, to correlate the magnetic with the structural properties of the nanoparticles. The electron microscopy results indicated that the Co nanoparticles were oxidized. Therefore, the authors fitted the Co–K-edge XANES spectra as a linear combination of the spectra of *hcp*-Co (foil), CoO, Co_3O_4, Co^{2+} in the unreacted micellar solution, and *fcc*-Co. The *fcc*-Co, Co^{2+}, and Co^{3+} contributions were necessary and their relative content in the nanoparticles was discussed as a function of the synthesis conditions and the type of the used micelle.

Binary nanoalloys attracted a lot of interest because they allow tuning of the magnetic moments and magnetic anisotropy energy. CoPt clusters in the form of

truncated octahedrons, with a diameter of approximately 3 nm, crystallized in the *fcc* structure, were studied through Co–K and Pt–L_3-edge XAFS. Chemical ordering in the tetragonal $L1_0$ phase was achieved after proper annealing [88]. Prior to annealing, the intensity of the Fourier transform peak that corresponded to the first neighbor of Co decreased along with the diameter of the nanoparticles. Furthermore, contraction of the lattice was observed. After annealing, the Co–K- and Pt–L_3-edge spectra were fitted using the model of the $L1_0$ ordered phase using only Co–Pt atom pairs in the first nearest neighboring shell. Again the intensity of the first peak in the Fourier transform decreased with the diameter of the nanoparticles in accordance with finite size effects. Furthermore, the Co–Co distance was found smaller than the Co–Pt which in turn was shorter than the Pt–Pt due to local atomic relaxations. As a result, strong distortion in the pure Co planes occurs resulting in a "mismatch" with the underlying Pt atomic plane in chemically ordered $L1_0$-like clusters. This distortion could explain the low magnetic anisotropy energy measured on chemically ordered CoPt nanomagnet assemblies. The EXAFS analysis was discussed in combination with the Vienna ab initio simulation package (VASP).

The formation of CoPt alloys after thermal treatment of Co nanoparticles on Pt (111) and Pt(100) films was investigated using XAFS spectroscopy. The use of textured substrates provides a method for ordered deposition of the Co nanoparticles which is important for a number of applications, for example, for chemical and biological sensors, data storage, and synthesis of nanowires and nanotubes [89]. The Co–$L_{2,3}$-edge XMCD signal of the Co nanoparticles, in the as-prepared state as well as after in situ annealing in a H_2 atmosphere, was measured at the temperature of approximately 12 K. The element-specific hysteresis loops were also presented, and the differences in the coercive field for the orbital to spin moment ratios were discussed as a function of the properties of the substrate, either MgO(100) or $SrTiO_3$(100), where the textured Pt films were grown.

Fe-containing nanosized metallic systems are promising materials for magnetic recording, development of mini magnets, and biological applications. In binary metallic alloys, with low concentration of the magnetic element, scattering of conduction electrons due to magnetic impurities results in a characteristic temperature dependence of the electrical resistivity (Kondo effect). At higher concentrations of the magnetic element, coupling of the nuclear magnetic moments or the localized inner shell (d or f) electron spins through the conduction electrons occurs. At even higher concentrations, ferromagnetic-like coupling takes place resulting in superferromagnetic behavior. Nanogranular thin films of Fe_7Au_{93}, Fe_7Ag_{93}, and Fe_9Cu_{91} sputtered on Si, with granule size smaller than 10 nm, were studied by means of XMCD at the Au–$L_{2,3}$-edge (at 5 K and room temperature) and with Fe–K-edge XANES (at 77 K) [90]. Simulation of the Fe–K-edge spectra revealed that Fe partially formed nanoparticles (with *bcc* structure) and partially was diluted in the *fcc* matrix of the other metals. The XMCD signal at the Au–$L_{2,3}$-edges demonstrated a net magnetic moment of the Au atoms, indicating that the Au atoms get polarized by the Fe nanoparticles. The magnetic moment of Au was increased further by approximately 15 % after annealing at 200 °C. Furthermore, measurements at low temperatures produced an XMCD signal larger by one order of magnitude.

928   Schmitz-Antoniak [91] studied Fe_xPt_{1-x} nanoparticles by means of XAFS and
929 XMCD at the Fe–K- and Pt–L-edge. The results were compared with the bulk
930 counterparts. Fe_xPt_{1-x} alloys crystallize in the *fcc(bcc)* structure for x < 0.8
931 (>0.8). The "chemical disorder" that is related to the formation of a random alloy
932 can be estimated by taking into account the percentage of the Fe or Pt neighboring
933 atoms as a function of x. Analysis of the EXAFS spectra revealed that the environ-
934 ment of Fe (Pt) was Fe- (Pt-) rich indicating that the FePt alloys were not random.
935 However, EXAFS could not distinguish between random segregation and formation
936 of a core/shell structure. Chemically ordered nanoparticles can be grown after
937 annealing. The XMCD signal was measured at 15 K with the magnetic field pointing
938 normal and almost parallel to the sample surface. Annealing resulted in an increase
939 of the orbital magnetic moments, whereas the spin magnetic moment remained
940 almost unaffected. At the Pt sites the magnetic moments were small and did not
941 change upon annealing. XMCD was also applied for the study of Ni_xFe_{1-x}
942 nanowires. At certain compositions the magnetism of Ni_xFe_{1-x} is not equal to the
943 sum of the local moments of Ni and Fe but rather depends on the interactions
944 between the two. These interactions rely strongly on the structure of the alloy
945 because Ni and Fe adopt the *fcc* and *bcc* symmetries, respectively [92]. The
946 XMCD spectra were recorded with the photon wave parallel to the wire's long
947 axis. As the Ni concentration, x, increased, the structure changed from *bcc* (x = 0.3)
948 to *bcc* and *fcc* (x = 0.5) and *fcc* (x = 1.0). Although the Fe–$L_{2,3}$- and Ni–$L_{2,3}$-edge
949 XANES spectra did not depend strongly on the Ni concentration, strong variations were
950 observed in the XMCD spectra. As shown in Fig. 4.18, when the Ni concentration
951 increased, the Ni-edge XMCD signal decreased, whereas that of Fe increased.
952 Furthermore, less Fe oxidation was observed as the Ni concentration increased.
953 Annealing resulted in enhancement (suppression) of the Fe (Ni) XAS white-line inten-
954 sities that reflected the available 3d states. The results indicated charge transfer from
955 Ni to Fe.

956   Decreasing of the metal nanoparticle size results in variation of their magnetic
957 properties. Thus, although bulk Rh, that is, a 4d metal, is paramagnetic, Rh nano-
958 particles tend to be ferromagnetic. Furthermore, the magnetic moment is strongly
959 affected by the number of the atoms that comprise the nanoparticle. Barthem
960 et al. [93] studied Rh nanoparticles comprised of about 150 atoms by Rd–L_2-edge
961 XMCD. They applied strong magnetic fields (2–17 T) in order to investigate their
962 magnetic properties close to the onset of stable magnetism. The fact that the spin
963 moment was found about 20 times higher than in the bulk counterpart and the
964 non-expected temperature dependence of the XMCD signal were attributed to the
965 correlation between electrons. Au exhibits also changes in the magnetic behavior
966 when synthesized in the form of nanoparticles. Thus, although Au is a diamagnetic
967 metal, when prepared in the form of nanoparticles with diameter of few nm, it
968 becomes strongly paramagnetic, as it was verified by Au–$L_{2,3}$-edge XMCD [94].

969   Magnetic proximity effects are phenomena that take place in heterostructures
970 where the magnetic properties of the one layer control the properties of the other.
971 Suturin et al. [95] studied ferromagnetic Co nanostructured films grown on antifer-
972 romagnetic MnF_2 with (111) surface orientation that has uncompensated spin
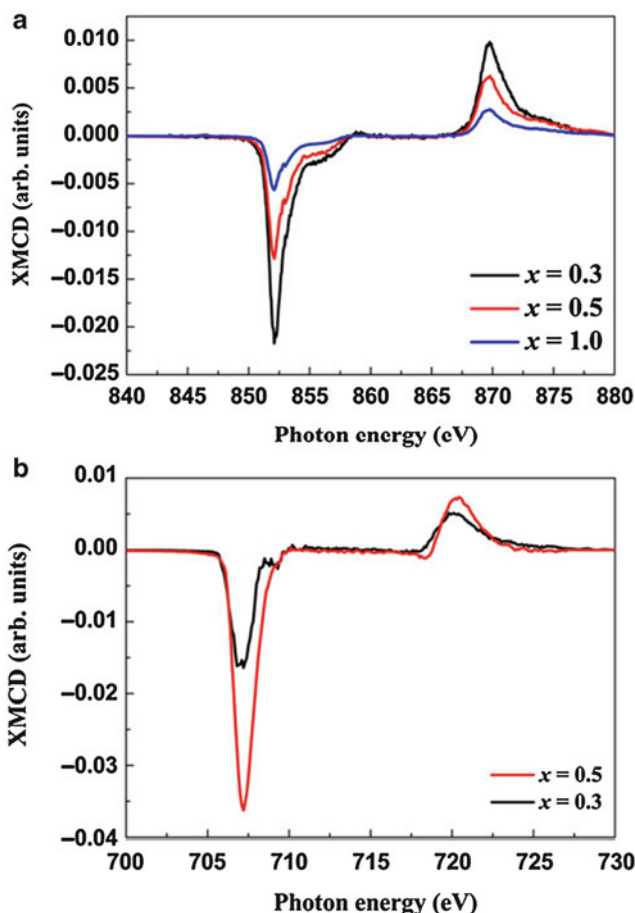
Fig. 4.18 XMCD signal of Ni_xFe_{1-x} nanowires recorded at the $L_{2,3}$ edges of (**a**) Ni and (**b**) Fe (Reprinted from Journal of Magnetism and Magnetic Materials, Vol. 332, S.-J. Chang, C.-Y. Yang, H.-C. Ma, Y.-C. Tseng, Complex magnetic interactions and charge transfer effects in highly ordered Ni_xFe_{1-x} nano-wires, Pages 21–27. Copyright (2013), with permission from Elsevier)

structure with magnetic moments ideally out of plane by 35°. XAS spectra were recorded at the Co–L- and Mn–L-edges. XMCD spectra were also recoded with the magnetic field applied in the two opposite directions. The effectiveness of a 3 nm thick CaF_2 protective layer was proved from the XAS spectra of Co where no traces of oxidation were detected. The spectrum of the MnF_2 was as expected revealing that the Co/MnF_2 system was chemically stable and intermixing between the two layers did not take place. The XMCD signals of Co and Mn were opposite indicating the antiparallel coupling between the Co film and the Mn ion spins at the antiferromagnetic interface. Spectra recorded at normal incidence did not reveal an XMCD signal indicating that the magnetic moments were parallel to the surface, taking into

account that the XMCD signal is proportional to $\vec{k} \cdot \vec{M}$ where $\vec{k}$ is the wavevector of the SR beam and $\vec{M}$ is the sample magnetization. Element selective hysteresis loops were obtained from the XMCD signals of Mn and Co at 14 and 300 K. The Mn loops were antisymmetric to those of Co, but they had the same shape and width indicating that the majority of the Mn ions were controlled by the Co magnetization. Finally, the effect of the measurement temperature on the hysteresis loops was also discussed.

Gridneva et al. [96] studied Au/Co/Au dots organized on a $Si_{0.5}Ge_{0.5}$ thin film capped with Si. These substrates have a characteristic faceted surface suitable for the evaporation of ordered structures. Taking into account that only the magnetization projected to the beam direction is probed, the sample was properly rotated in order to measure the magnetization normal and parallel to the surface. The external magnetic field was applied either parallel or perpendicular to the surface in two opposite directions. The remanence could be measured after the application of pulses of the magnetic field before the acquisition of the XAS spectrum. The authors discussed the values of the spin moments for out-of-plane and in-plane magnetization at 100 and 300 K for Au-capped Co and Au/Co films with various thicknesses of the Au and Co layers. Stable remanence of the Co/Au and Au/Co/Au magnetic nanodots grown on the nanostructured substrate was verified. The in-plane magnetic order was stable even at room temperature contrary to the out-of-plane magnetization that was stable only at low temperatures. The behavior of these nanodots is contrary to that of thin multilayers, most probably due to the interaction between the dots. EXAFS measurements at the Co–K-edge were also presented to account for relaxation phenomena.

6.1.3   Metal Nanoparticles for Optical Applications

Metal nanoparticles embedded in transparent matrices, e.g., silica glass, have attractive linear and nonlinear optical properties based mainly on surface plasmon resonance. The formation of Ag nanoparticles in aqueous ethanol solution of PVP by photoreduction of $AgClO_4$ using benzoin as photoactivator was studied means of in situ time-resolved Ag–K-edge EXAFS [97]. Prior to photoreduction, only the contribution of Ag–O could be detected in the spectra of the ionic solution of $AgClO_4$. The formation of Ag–Ag bonds could be detected after photoreduction, with their contribution increasing with the exposure time. In the absence of benzoin, reduction of Ag from the $AgClO_4$ precursor was not complete. To investigate the kinetics of the Ag nanoparticle formation, time-resolved (dispersive) EXAFS spectra were recorded. It was found that after an induction period, the Ag–O bonds started to exponentially dissociate (i.e., Ag^+ was reduced to Ag^0) and Ag–Ag bonds (i.e., Ag nanoparticles) were formed. Values of the absorption coefficient at selected energies were used to quantify the rate of Ag–Ag formation, and coordination numbers obtained from the EXAFS analysis were used as a measure of the particle size. The latter was found to increase with time. The time scale for the observation of

these changes was strongly affected by the presence of benzoin. The formation of Au nanoparticles by irradiation of the ionic liquid [BMIM] [AuCl$_4$] with synchrotron radiation was studied by means of in situ XAFS at the Au–L$_3$-edge [98]. The XANES spectrum of the liquid prior to irradiation was measured by Quick-XAFS and had a characteristic white line. As the irradiation time increased, the intensity of the white line decreased, and after about 10 h of irradiation, the XANES spectrum became similar to the spectrum of Au foil signifying the formation of Au nanoparticles. In the corresponding EXAFS spectra, two peaks were detected corresponding to Cl and Au neighboring atoms with the number of Au neighbors increasing with irradiation time at the expense of Cl atoms.

Intermixing of Au and Ag for the formation of bimetallic Au–Ag nanoparticles was verified by EXAFS measurements at the Au–L$_3$-edge since the backscattering amplitude of the Au is considerably different from this of Ag. Haug et al. [99] studied Ag–Au nanoparticles fabricated by ion implantation in glass by means of Ag–K- and Au–L$_3$-edge XAFS measurements. They found that above a certain implantation dose, bimetallic Au–Ag nanoparticles were formed. Chen et al. [100] applied XAFS to compare Ag–Au alloys and Ag–Au core/shell structures (Ag$_{core}$Au$_{shell}$) with the same Ag–Au atomic ratio. In the core/shell structure, more Au atoms were found to be bonded with Au.

The peculiar optical properties of metal nanoparticles lead to their use for decoration purposes in cultural heritage artifacts. Ag and Cu nanoparticles dispersed in a glassy matrix were used for coloring Medieval and Renaissance pottery. Padovani et al. [101] applied XAFS for the study of the metallic nanoparticles in lustered glazes of shards belonging to tenth- and thirteenth-century pottery. The luster used for the decoration – which is actually a composite material consisting of glass and metal nanoparticles – had characteristic brilliant, metallic reflections, with mainly red and gold color. The extent of oxidation of the Ag and Cu nanoparticles was studied with EXAFS and XANES. In the latter case, linear combination fit with spectra of reference compounds (Cu$_2$O, CuO, Cu, Ag, Ag$_2$O) was performed for the determination of the percentage of the metallic phase in the nanoparticles. This information was important for the EXAFS analysis, because smaller coordination numbers, compared to the bulk values in the *fcc* structure, may be attributed to small size of the metal aggregates and/or their partial oxidation. In red luster partially oxidized Ag and Cu nanoparticles were detected. In gold luster Ag was partially oxidized, whereas Cu was present only in the oxidized form (with oxidation state +1 and +2) participating in different phases with S, Cl, and/or O. Similar studies on luster decoration of the thirteenth-century pottery were applied for the determination of the percentage of oxidized Cu aggregates which were related to color variations [102]. In order to detect changes in the microscale, micro-EXAFS spectra were recorded from sample spots with different colors as well as from other spots in the same decoration. The Cu–K-edge micro-EXAFS spectra were modeled as a weighted average of the spectra of Cu$_2$O and metallic Cu. Red and green color was related to a higher content of Cu and Ag nanoparticles, respectively. However, in the green areas, higher content of Cu$^+$ compared to metallic Cu was also identified.

6.2   Semiconductor Nanostructures

Semiconducting nanostructures, for example, quantum dots (QD), nanoparticles (NP), quantum wells (QW), nanowires, nanorods, and nanoribbons, attracted a lot of interest for microelectronic, spintronic, and photonic applications. QDs are nanoparticles with dimensions of a few nanometers which are smaller than the exciton Bohr radius. This results in strong quantum confinement of the electronic states which affects the value and type (direct/indirect) of the energy gap. XAFS is extensively applied for the study of strain, size, and alloying effects in the nanostructure and the electronic structure of the nanoparticles, the extent of intermixing the QDs with the substrate or capping layers, their interaction with agents used in their synthesis, for monitoring the synthesis processes by time-resolved measurements, and for the study of the magnetic properties in transition element diluted semiconductors. Examples on the application of XAFS for the study of semiconductor nanomaterials can be found in Ref. [9].

A large number of applications of nanosemiconductors rely on their optical emission properties which in turn depend on their electronic structure. As discussed in Sect. 3, the XANES spectrum is analogous to the partial density of empty states. Thus, in the case of semiconductors, XANES is a tool for the investigation of the density of states in the conduction band with orbital character determined by the selection rules [Eq. (4.8)]. A modification of XANES spectroscopy that is often employed in semiconductors is X-ray excited optical luminescence (XEOL) spectroscopy, which is the X-ray analogue of photoluminescence. It studies the energy spectrum of the visible light emitted by the recombination of thermal electrons and holes (promoted to bottom of the conduction and top of the valence band, respectively) following the excitation with X-rays [9]. The luminescence yield in a specific energy range can be used for the acquisition of the XAFS spectra and for the discrimination of the various phases or sites in the sample that contribute to light emission.

To elucidate the origin of photoluminescence of Ge nanocrystals, Karatutlu et al. [103] used EXAFS, optically detected X-ray absorption spectroscopy (ODXAS), and XEOL spectroscopies. Depending on the synthesis routes of the nanoparticles, similarities or strong differences were found between the EXAFS and ODXAS, with the latter probing only sites in the sample that contribute to light emission. The differences between EXAFS and ODXAS were attributed to the presence of the GeO_2 phase. Ge and GaN quantum dots formed due to elastic strain on Si and AlN, respectively, were studied the use of XAFS [104]. The stacking sequence of the Ge/Si nanostructures with different number of Ge layers and different thickness of the Si barrier layer was studied at the Ge–K-edge. The total number of Si and Ge atoms in the first nearest neighboring shell was found equal to 4. The number of Ge atoms in the first shell was modified by the thickness of the Si barrier due to better nucleation of the Ge nanocrystals. The Ge–Ge distances were slightly smaller compared to those in bulk Ge. In the GaN/AlN heterostructures, the coordination number in the second nearest neighboring shell (consisting of Ga–Ga and Ga–Al bonds) was found to be affected by the thickness of the GaN layer and the

formation of QD structures. EXAFS was also used to detect mixing between the nanoparticles and the matrix. For example, Cd–Zn intermixing between the CdSe QDs and ZnSe matrix was identified by Cd–K-edge EXAFS [105].

PdS QDs have potential applications in solar cells. The band gap of PbS is very sensitive to finite size effects (it takes values in the range 0.4–2.8 eV depending on the QD size) since the exciton Bohr radius is approximately 20 nm, a value considerably larger than in other nanoparticles. Demchenko et al. [106] studied colloidal PbS nanoparticles (~50 nm) and QDs (~5 nm) with S–K-edge XANES. They found that the absorption edge of the QDs was blueshifted by about 1.67 eV compared to the bulk counterpart. This observation was attributed to the increase of the band gap and more specifically to the shift of the conduction band minimum. Simulations of the XANES spectra of bulk and QD PbS, taking into account the cluster size in the latter case, were performed in order to explain the variations observed in the experimental spectra. The conduction band minimum of the semi-conductor QDs is also affected by the doping. Cd–M$_3$-edge XANES spectra of Cu-doped CdSe QDs, with a diameter of 5 nm, were used to study the effect of Cu concentration on the energy of the conduction band minimum [107]. The onset of the absorption edge can be assigned to the lowest unoccupied states after taking into account the selection rules that determine the type of the final state [108]. The differences in the energy gap of the QDs and their bulk counterparts were attributed to various effects including confinement, electron–hole binding, doping, and hybrid-ization of the wave functions of Cu and Cd. Hybridization appeared to be important for the explanation of the experimental data at the Cd–M$_3$-edge. On the contrary the hybridization term was not important in the Se–L$_3$-edge spectra. A theoretical model that accounts for the hybridization of the dopant and host atom states, which also takes into account the size-dependent bond-length variation, was presented in Ref. [109]. This model explains very well the experimental results on the conduction band minimum as determined from the Cd–M$_3$-edge XANES spectra of Cu-doped CdSe QDs.

The use of ternary instead of binary semiconductors offers more flexibility for band gap engineering, since the gap can be controlled by either altering the size or the stoichiometry. On the other hand, the photoluminescence quantum yield of QDs is expected to increase when a thin layer with a higher band gap blankets the core, resulting in strong confinement. CdSe$_x$S$_{1-x}$ QDs with size of 5 nm and $0 < x < 1$ were studied through XAFS spectroscopy at the Cd–K- and Se–K-edge [110]. The EXAFS results indicated phase separation in the form of a core/shell structure that was held responsible for the enhancement of the photoluminescence quantum efficiency for increasing values of x. The results were substantiated by the fact that the Se–K-edge XANES spectra were not affected by the change of the Se content. Contrary to the formation of core/shell structures, in homogeneous, random alloys, variations were observed in both the Cd–K- and Se–K-edge spectra with the variation of x [111].

Another ternary alloy that was studied in the form of nanocrystals is Mg$_x$Zn$_{1-x}$O. Band gap engineering via control of the value of x results in materials with optoelectronic applications in the UV spectral region. However, in this case the

end binary compounds, ZnO and MgO, crystallize in different structures, wurtzite and rocksalt, respectively. The bonding environment of Mg and Zn in $Mg_xZn_{1-x}O$ ($0 < x < 1$) nanocrystals was studied through XANES by Limpijumnong et al. [112]. The XANES spectra recorded at the Zn–K- and Mg–K-edges were simulated using the models of MgO, where Zn substitutes for Mg in sixfold coordinated sites, and of ZnO, where Mg substitutes for Zn in fourfold coordinated sites. Using this formulation, the authors determined the fraction of the fourfold or sixfold coordinated Zn and Mg atoms as a function of x.

The emission properties of ZnO–ZnS nanoribbons were studied with XANES at the Zn–K- and $S–L_{2,3}$-edges employing the luminescence yield (emission in the visible spectrum) for the acquisition of the spectra [113]. Comparison of the S–K-edge XANES spectra recorded in the total electron yield and luminescence yield revealed similar signals in ZnS powder and nanowires, whereas luminescence yield was diminished in the spectrum of the ZnS–ZnO nanoribbons. This was an indication that S (and consequently ZnS) did not contribute in the optical decay channel. Similar results were obtained for the $S–L_{2,3}$-edge. The Zn–K-edge spectra of the nanoribbons, recorded in the luminescence yield, were similar to the spectra of ZnO nanoneedles and exhibited strong differences with the spectrum of ZnS nanowires, verifying that ZnS does not contribute to the luminescence of the nanoribbons.

SnO_2 is an n-type semiconductor that is widely used in flammable gas sensors. Rammutla et al. [114] studied doping of SnO_2 with Y^{3+} and Zr^{4+} which are expected to improve its sensing properties. The as-prepared samples had crystallite sizes of ~3 nm, whereas heating up to 1000 °C resulted in an increase of the size to ~40 nm. EXAFS analysis at the K-edge of the dopant revealed that Y was incorporated in the SnO_2 lattice when the sample was annealed at temperatures higher than 900 °C. On the contrary, Zr substituted for Sn at temperatures as low as 200 °C.

Semiconductor nanowires are promising structures for various applications including memory, sensing, logic, light emission, and waveguiding. Segura-Ruiz et al. [115] studied $In_xGa_{1-x}N$ nanowires by nano-XANES, nano-XRD, and nano-X-ray fluorescence (XRF) with a spatial resolution of 55 nm. XRF and XRD revealed the existence of strong phase separation both from the edge to the center and from the bottom to the top of the nanowire. The Ga–K-edge XANES spectra recorded with the electric field vector of the SR beam parallel and perpendicular to the c-axis, exhibited angular dependence characteristic of the wurtzite structure excluding the formation of metallic phases at both the bottom and the top of an individual wire. Cross-shaped semiconducting nanowires gained considerable attention for interconnection applications in nanodevices. Martínez-Criado et al. used X-ray nano-beam to study junctions created in Ga_2O_3/SnO_2 multiwire structures, focusing on the intersection [116]. The Ga–K-edge XANES spectra recorded in the junction and on the Ga_2O_3 nanowire (i.e., out of the junction) were the same indicating that intermixing with SnO_2 does not take place at the junction. The spectra were interpreted as having contributions of both tetrahedrally and octahedrally coordinated Ga with oxygen atoms.

Incorporation of magnetic ions in semiconductor QDs has also attracted a lot of interest, since the magnetic properties due to orbital exchange can be further tuned

by the size of the nanoparticle. Such diluted magnetic semiconductor QDs are attractive for spintronics, quantum computing, and magneto-optical applications. $Ga_{1-x}Mn_xAs$ is a ferromagnetic semiconductor with a Curie temperature of 191 K. Self-assembled $Ga_{0.92}Mn_{0.08}As$ QDs with mean diameter of 16.5 nm, grown epitaxially on Si, were investigated using Mn–K-edge XANES spectroscopy [117]. The spectrum of the QDs resembled the spectrum of the single-crystalline film, revealing that Mn was divalent, substituted for Ga, and was tetrahedrally coordinated with As. As in the case of the $Ga_{1-x}Mn_xAs$ film, ferromagnetic order in the QDs was probably mediated by the presence of holes since Mn acts as an acceptor substituting for Ga. Similar results were obtained in the case of $Ga_{1-x}Mn_xAs$ ($x \leq 0.05$) nanowires [118]. The sample with $x = 0.03$ exhibited the highest magnetic moment among the studied samples. The temperature dependence of the Mn–$L_{2,3}$-edge XMCD signal was also discussed.

Mn-doped GaN nanowires were studied by means of Mn–K-edge XAFS and Mn–$L_{2,3}$-XMCD [119]. It was found the Mn atoms substitute for Ga sites participating in the formation of the wurtzite network of host GaN. The XMCD spectra revealed that Mn had local magnetic moment and the electronic configuration of the doped Mn was mainly $3d^5$. In another study, Mn-doped GaN nanowires with ~10 at. % Mn concentration were studied by means of Mn–$L_{2,3}$-edge XANES combined with scanning transmission X-ray microscopy (STXM) [120]. The latter allowed the generation of images using a beam with diameter of 30 nm that raster-scanned the sample. The XANES spectrum at a given element edge was reconstructed from a stack of images recorded in an energy range close to the absorption edge of the element of interest. The spectra obtained at preselected positions on an individual nanowire were studied. It was found that Mn substitutes for Ga uniformly along the wire. Linear combination fit of the spectra revealed that 70 % was Mn^{2+} and 30 % Mn^{3+}, both in tetrahedral coordination. Mn–$L_{2,3}$-edge XMCD measurements demonstrated that the magnetic moment was at least one order of magnitude higher compared to Mn-doped bulk GaN crystals. This finding was attributed to the long-range order of the Mn dopants. Finally, the authors discussed the variations of the XMCD signal with the orientation of the nanowire.

The incorporation of Cr^{3+} ions in the lattice of ZnSe QDs was studied by means of Cr–$L_{2,3}$-edge XANES [121]. The energy and spectral shape of the $L_{2,3}$ edge revealed that Cr was trivalent. To achieve satisfactory simulation of the XANES spectra, a tetragonal distortion was assumed for the octahedron around Cr, where the Cr–Se bond was compressed along the z-axis. Such a distortion was explained by the removal of Zn atoms for charge balance reasons.

Fe-doped ZnO is another example of a diluted magnetic semiconductor. $Zn_{0.99}Fe_{0.01}O$ nanorods synthesized by coprecipitation were studied by means of O–K- and Fe–$L_{2,3}$-edge XANES [122]. The spectra of the nanorods recorded at the Fe–$L_{2,3}$-edge are compared with the spectra of reference Fe oxides. The strong similarity of the nanorod spectrum with that of Fe_2O_3 revealed that Fe was trivalent in $Zn_{0.99}Fe_{0.01}O$. Thus substitution of Zn by Fe atoms would result in excess of holes that could be responsible for the weak room temperature ferromagnetism. Increase of x up to 0.05 in $Zn_{1-x}Fe_xO$ nanorods resulted in a variation of the Fe^{3+}/Fe^{2+} ratio

although Fe still substituted for Zn [123]. ZnO nanowires doped with Co by means of ion implantation were studied by means of XRF and XANES spectroscopy with a 100 nm spatial resolution [124]. Such resolution allows for the study of a single nanowire. XRF imaging revealed the homogeneous distribution of Co throughout the wire. The Zn–K-edge spectra were recorded for two different sample orientations, i.e., with the electric field of the beam parallel and perpendicular to wire's axis, which is parallel to the c-axis of the crystal. In the former case $1s \rightarrow p_z$ transitions were favored, whereas in the latter case $1s \rightarrow p_{x,y}$ transitions dominated. The angular dependence of the spectra revealed that implantation and subsequent annealing did not induce structural disorder. Figure 4.19 shows the Co–K- and Zn–K-edge XANES spectra recorded at two spots on the nanowire.

For better comparison, the energy scale was shifted by an amount equal to the energy of the absorption edge of each atom. The strong similarities between the spectra revealed that Co substitutes for Zn. Furthermore, the position of the absorption edge (which is the same with that of the thin film alloy) indicates that Co is divalent. The Zn–K-edge EXAFS spectra recorded at different spots in the wire did not exhibit differences and did not show evidence of significant structural disorder.

Size reduction in semiconductor structures triggered peculiar phenomena like the observation of ferromagnetic behavior of nonmagnetic materials. This behavior has been attributed to symmetry breaking at the surfaces and the consequent modification of the electronic structure. ZnO nanoparticles with dimensions of 20 nm capped with different organic molecules (trioctylphosphine, dodecylamine, and dodecanethiol) were studied by means of XMCD [125]. The Zn–K-edge XMCD signal of ZnO nanoparticles capped with dodecanethiol, measured with magnetic fields of 2–10 T, exhibited differences compared to the other two capping molecules. The differences were attributed to the formation of a ZnS-like phase with the S atoms of dodecanethiol. To explain the dependence of the XMCD intensity on the applied magnetic field, the coexistence of two different magnetic contributions was assumed. The core of the nanoparticles contributed with a paramagnetic term, whereas a ferromagnetic-like contribution stemmed from the interface between the capping organic molecule and the ZnO nanoparticle. The ferromagnetic-like behavior was reinforced when neat interfaces were formed, as in the case of dodecanethiol capping layer.

ZnO nanorods can be grown with a hydrothermal method using Zn acetate as a precursor and surfactant which is necessary for the modulation of the crystal morphology and size of the nanoparticles [126]. A seed layer of Zn/sodium dodecyl sulfate (SDS) was used in order to grow well-oriented nanorods. Zn–$L_{2,3}$-edge spectra of the Zn/SDS seed layer and the ZnO nanorod films were recorded for different growth reaction times (5 min–4 h). The spectra of Zn/SDS and ZnO were considerably different allowing monitoring of the evolution of the ZnO nanorods. Gradual variations of the spectra were observed up to reaction times of 30 min at which time ZnO was formed. The XANES spectra did not change for longer reaction times. Zn–K-edge time-resolved XAFS was applied for the investigation of the formation mechanism of ZnO nanoparticles via sol–gel synthesis using zinc acetate
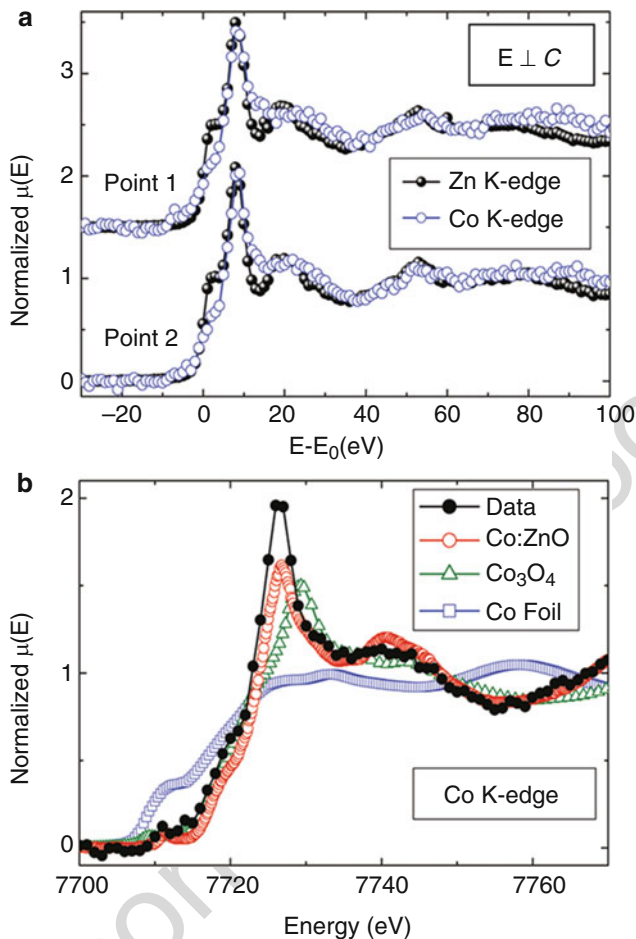
Fig. 4.19 (**a**) Zn–K (*solid circles*)- and (**b**) Co–K (*open circles*)-edge XANES spectra recorded from two different spots of a Co-doped ZnO single nanowire. (**b**) Co–K-edge average XANES spectrum of the nanowire (*solid circles*), a high-quality $Zn_{0.9}Co_{0.1}O$ epitaxial film (*open circles*), a Co_3O_4 sample (*open triangles*), and a metallic Co foil (*open squares*) (Reprinted with permission from J. Segura-Ruiz, G. Martínez-Criado, M. H. Chu, S. Geburt, and C. Ronning, Nano-X-ray Absorption Spectroscopy of Single Co-Implanted ZnO Nanowires. Nano Letters, **11**:5322–5326. Copyright (2011), American Chemical Society)

salt dissolved in alcohol media [127]. The EXAFS oscillations, i.e., the $\chi(k)$ spectra, were fitted as a linear combination of the corresponding spectra of nano-ZnO and the unreacted precursors in the solution, as a function of the aging time. The amount of ZnO formed (about 17 % of the Zn in the precursor was converted to ZnO) in the hydrolyzed solutions at 60 °C reached a plateau after 45 min. Similar results were obtained in Ref. [128]. Another in situ time-resolved XAFS study of the synthesis process of ZnSe QDs capped with glutathione was performed at the

Se–K-edge [129]. Only one peak, which corresponds to the Zn neighboring shell of Se in the zincblende structure of ZnSe, was visible in the Fourier transform of the spectra. The formation of ZnSe crystals started when the solution was heated just to 80 °C, without any time elapse, indicating that the formation of ZnSe QDs from aqueous formation undergoes a fast nucleation process. As the reaction time elapsed, the coordination number in the first nearest neighboring shell progressively increased approaching the corresponding value in the ZnSe crystal.

A promising method for the synthesis of QDs is based on microorganisms due to the low-cost and environment-friendly character of the process. Fellowes et al. [130] studied the ex situ formation of CdSe QDs using bacterially generated Se^{2-} as an alternative precursor. CdSe nanoparticles, synthesized using abiotic and biogenic Se^{2-} and $Cd(ClO_4)_2$-glutathione solution, were characterized by S–K-edge XANES in order to investigate the interaction between the glutathione capping agent and the QDs. The S–K-edge XANES spectra of the synthesized CdSe QDs were compared with the spectra of reference compounds. The CdSe QD spectrum exhibited strong similarities with the spectrum of CdS, indicating that S originating from glutathione was incorporated in the QD structure. Se–K-edge XANES was used to investigate the stability of abiotic and biogenic Se^{2-} under SR irradiation. Compared to abiotic Se^{2-} solution, which exhibited oxidation to Se^{6+} upon SR irradiation for 15 min, the biogenic Se^{2-} was not susceptible to oxidation. The behavior of the latter was explained by the presence of proteins in the biogenic Se^{2-} solution that acted as stabilizing agents. Time-resolved XANES was applied to the Se–K-edge in order to investigate the differences between the uses of abiotic and biogenic Se^{2-} precursors in the formation of ZnSe QDs. Addition of $ZnCl_2$-β-mercaptoethanol (βME) in biogenic and abiotic Se^{2-} solution resulted in rapid formation of βME-ZnSe. The Se–K-edge XANES spectra for both the biogenic and abiotic Se^{2-} solutions differed significantly from the spectra of the βME-ZnSe. Intensity differences at characteristic energies in the time-resolved XANES spectra of Se^{2-} solutions and βME-ZnSe were used to monitor the rate of formation of the ZnSe QDs.

Semiconductor QDs are used for biological imaging as well. The stability of water soluble ZnO QDs with diameters 3 nm and 4 nm was investigated in vivo in oral epidermoid carcinoma cells by Zn–K-edge XANES [131]. The absorption of the QDs with a copolymer shell in the cells was verified by proton-induced X-ray emission (PIXE) imaging. It was found that the bonding configuration of Zn was stable and did not change upon absorption in the cell.

6.3   Metal Oxide Nanomaterials

Metal oxides find numerous applications in catalysis, as electrodes for Li-ion batteries, for magnetic and biomedical applications, etc. XAFS spectroscopies are extensively applied for the determination of the oxidation state of the metal, of the coexistence of various phases in the sample, and for the site preference, e.g., tetrahedral or octahedral coordination.

6.3.1   Metal Oxides Used for Electrodes

Sn-based nanomaterials are used as anode materials for rechargeable Li-ion batteries. Monodisperse and size tunable Sn/SnO_x nanoparticles (with Sn core diameter in the range 10–20 nm and oxide shell thickness of 3 nm) were studied by means of Sn–K-edge XAFS [132]. The Sn–K-edge XANES spectra of the nanoparticles were fitted as a linear combination of the spectra of reference compounds (Sn, SnO, SnO_2). It was reported that in the smaller nanoparticles, the concentration ratio [Sn/(Sn-oxide)] was smaller compared to the value corresponding to the larger ones. This finding explained the high charge storage capacities and the improved cycling stability of nanoparticles with size smaller than 10 nm. Another anode material is CoO. Co–K-edge EXAFS spectroscopy was applied for the study of CoO nanoparticles obtained by calcination (i.e., heating in N_2 atmosphere) of $Co(OH)_2$ at 200 and 900 °C [133]. The variations in the coordination numbers in the first and second nearest neighboring shells for the two different calcination temperatures were interpreted as variations in the oxygen-to-cobalt ratio. MnO is another attractive anode material for rechargeable Li-ion batteries. Porous MnO microspheres were characterized by ex situ Mn–K-edge XAFS [134]. The XANES spectra of the pristine sample were identical to the spectra of MnO. After discharge to 0 V, the XANES spectrum changed and became similar to that of metallic Mn. After recharging, the pre-edge peak reappeared with a higher intensity (indicating larger distortion of the bonding environment of Mn), and the absorption edge returned to the position that corresponded to the pristine sample. However, the spectral features above the absorption edge were broader indicating that the crystalline quality was not fully restored. The linear dependence of the position of the absorption edge on the oxidation state was also applied [135] for the determination of the Mn oxidation state in MnO_x samples. The oxidation state of Mn changed during charge–discharge cycles of composite MnO_2-carbon nanotubes (MnO_2/CNT) which are candidates for electrochemical capacitors in energy storage devices, with applications in electric vehicles, uninterruptible power supplies (UPS), etc. [136]. The spectra of the MnO_2/CNT, in the as-prepared state, as well as after heat treatment, were recorded during charge–discharge cycles and were compared to the spectra of reference oxides (MnO, Mn_2O_3, MnO_2). Charging of the electrode resulted in a blueshift of the absorption edge, consistent with an increase of the oxidation state of Mn (between 3 + and 4+), while discharge had the opposite effect due to the reduction of the oxidation state of Mn (between 2+ and 3+). This observation indicated that the electrochemical reaction of the MnO_2/CNT nanocomposite electrode during charge–discharge was due to Faradaic redox reaction between MnO_2 and Li + accompanied by changes in the oxidation state of Mn. Electrochemical measurements of $Sn_{1-x}Co_xO_{2-x}$ nanocrystals revealed that the substitution of Sn with Co significantly enhanced the negative electrode performance [137]. Co–K- and Sn–L_3-XANES spectroscopy for various ratios of the Co and Sn precursors identified that the oxidation state of Co and Sn was +2 and +4, respectively.

Lithium manganese oxides (LMO) comprise another family of oxides used for Li-ion batteries. Although nanostructured materials have a number of advantages, for example, shorter diffusion length and faster pathway for Li-ion transport, they

also present certain disadvantages such as particle agglomeration and reduced packing density. To overcome such problems, hybrid materials with metal nanoparticles of 20–50 nm size were homogeneously dispersed in a CNT network. The samples were prepared by heating MnO_2-coated CNT composite with appropriate amounts and concentrations of an aqueous LiOH solution [138]. The position of the absorption edge and the EXAFS spectra were used for the determination of the oxidation state of Mn for different LiOH concentrations. Low LiOH concentration resulted in the spinel-type $LiMn_2O_4$ where the oxidation state of Mn, which occupies a site with Jahn-Teller distortion, is 3.5+. At higher LiOH concentrations, the layered-type Li_2MnO_3 phase was formed where Mn is tetravalent and free of Jahn-Teller distortion.

Another metal oxide that has been proposed for applications in electrodes is GeO_2. The Coulombic efficiency (defined as the amount of charge that exits the battery during the discharge cycle to the amount of charge that enters the battery during the charge cycle) of this oxide can be improved by adding metallic components. Kim et al. [139] studied $MGeO_3$ (M = Cu, Fe, and Co) where the additional metal components (M) are expected to form nanosize particles. The XAFS spectra that were recorded at the Ge–K- and Cu–K-edge at various stages of the discharge–charge process of the $CuGeO_3$/Li cell are shown in Fig. 4.20.

The Cu–K- and Ge–K-edge spectra of the $CuGeO_3$ electrode at the beginning of the process (point 1) revealed that the oxidation states of Cu and Ge were +2 and +4, respectively. As the lithiation process proceeded, Cu was reduced to its metallic state. Reduction of Ge occurred at a later stage. The XANES observations were supported by the EXAFS spectra. In the corresponding Fourier transforms, the evolution of the formation of Cu and Ge metals, at the expense of the corresponding oxides, was tracked from the intensity of the Cu–Cu (Ge–Ge) and Cu–O (Ge–O) peaks, respectively. Similar XAFS analysis revealed that during delithiation (points 6–10) Cu remained mainly in the metallic state, whereas Ge started to oxidize after point 8. It was proposed that the formation of the Cu metal nanoparticles promotes the oxidation of Ge, thus improving the Coulombic efficiency of the electrode.

Layered double hydroxides (LDH) are described with the general formula $\left[A_{1-x}^{2+}B_x^{3+}(OH)_2\right]^{x+}\left[C_{x/n}^{n-}\right]^{x-}\cdot zH_2O$ where A, B, and C denote divalent metal cations (e.g., Zn^{2+}), trivalent metal cations (e.g., Fe^{3+}), and the interlayer anions, respectively. LDH materials exhibit anion-exchange capability. The anions are introduced in the interlayer space of the LDH to compensate the positive charge of the host layers which is generated by the partial replacement of the divalent by trivalent metal ions. Woo et al. [140] studied the formation of $ZnO–ZnFe_2O_4$ nanocomposites and porously assembled $ZnFe_2O_4$ nanocrystals by proper heat treatment of Zn,Fe-LDH precursors. $ZnFe_2O_4$ is used as a negative electrode in Li-ion batteries. The nanocrystals were prepared after selective etching of the nanocomposite. The Fe–K-edge XANES spectra of the precursor, its calcined derivatives, and etched materials were compared with the $ZnFe_2O_4$, Fe_2O_3, and FeO reference compounds. From the characteristics of the pre-edge peak in the Fe–K-edge XANES spectra (see Fig. 4.8 in Sect. 5), it was deduced that Fe was
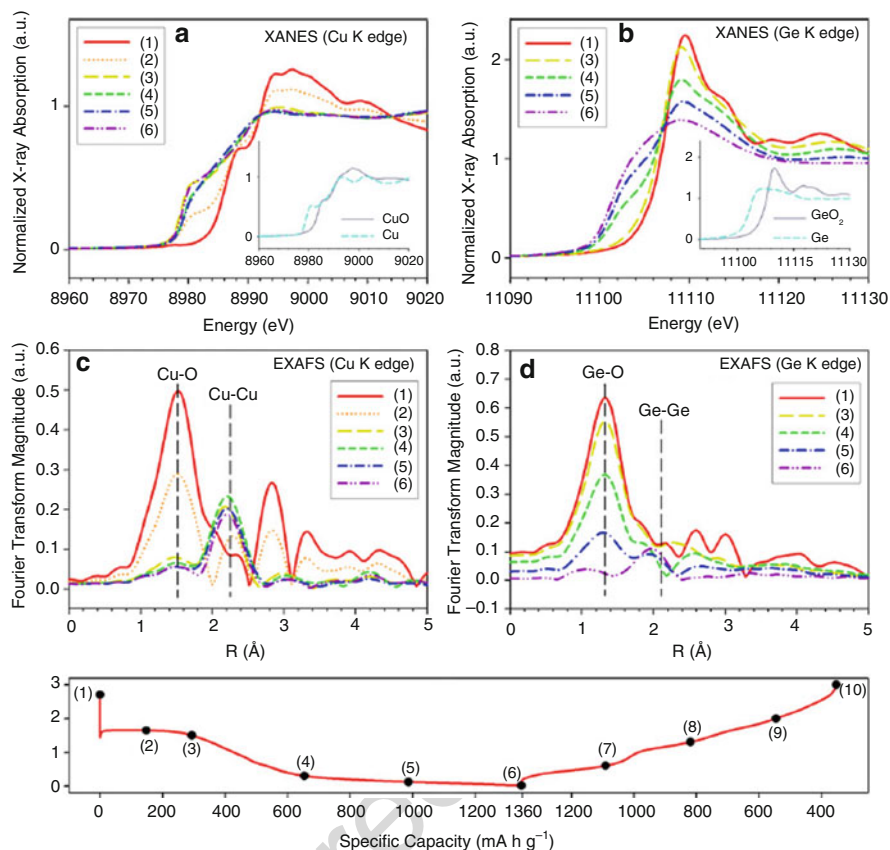
Fig. 4.20 XAFS spectra recorded at various stages of the lithiation of the CuGeO₃ electrode in the first charge–discharge cycle: (**a**) Cu–K-edge XANES, (**b**) Ge–K-edge XANES, (**c**) Fourier transform of the Cu–K-edge EXAFS signal, and (**d**) Fourier transform of the Ge–K-edge EXAFS signal. The numbers 1–10 denote the values in the voltage profile, shown in the bottom, where the spectra were recorded. Spectra of reference compounds are shown in the *insets* (Reprinted from Electrochimica Acta, Vol. 54, C. H. Kim, Y. S. Jung, K. T. Lee, J. H. Ku, and S. M. Oh, The role of in-situ generated nano-sized metal particles on the Coulombic efficiency of MGeO₃ (M=Cu, Fe, and Co) electrodes, Pages 4371–4377. Copyright (2009), with permission from Elsevier)

trivalent and octahedrally coordinated in the spinel structure. Calcination resulted in the transformation of LDH to $ZnFe_2O_4$ which was not affected by etching.

The formation mechanism of MoO_2 nanorods, which are also used as electrodes, was studied with in situ Mo–K-edge XANES spectroscopy. A linear combination fit of the spectra obtained during the synthesis reaction with the spectra of the MoO_2Cl_2 precursor and the final product yielded the ratio of the two phases. After 90 min, about 90 % of the precursor was converted to MoO_2 [141].

Metal oxides can be combined with conducting polymers for the formation of composite electrodes. NiO-polypyrrole (PPy) nanocomposites were studied at the

Ni–K-edge at various stages of the discharge/recharge cycle [142]. The EXAFS spectrum of the as-prepared NiO-PPy composite is the same with the spectrum of NiO indicating that NiO was unaffected by the PPy coating. However, strong interaction between Ni and PPy occurred in the discharged electrode, where Ni was bonded with N (the Ni–N distance was found equal to 2.18 Å). Linear combination fitting of the EXAFS spectra revealed the variation of the percentage of PPy–Ni–O, metallic Ni, and NiO during the discharge/recharge process. The structure of the PPy–Ni–O complex was modeled with density functional theory calculations.

TiO$_2$ is another oxide with applications in Li-ion batteries. Zhou et al. [143] studied TiO$_2$ nanotube arrays prepared by anodic oxidation of Ti foil before and after intercalation of Li. The XANES spectra were recorded at the Ti–L$_{2,3}$, O–K, and Li–K edges. In the Ti–L$_{2,3}$-edge spectra, the splitting due to spin–orbit coupling, which determines the L$_2$–L$_3$-edge separation, is much smaller compared to heavier transition metals. For an ideal octahedral environment of Ti, the combination of spin–orbit coupling and modification of the states by the crystal field resulted in two double peaks in the L$_3$ (at approximately 458 and 460 eV) and the L$_2$ (at approximately 463 and 465 eV) edges. In the case of the anatase and rutile polytypes of TiO$_2$, tetragonal distortion caused further splitting of the peak that appears at 460 eV with the relative intensity of the two components depending on the polytype. The spectra of the annealed TiO$_2$ nanotube arrays revealed that they adopted the anatase structure. For the as-prepared samples, splitting due to tetragonal distortion was not observed and the peaks were significantly broader indicating higher disorder. The effect of annealing on the crystalline quality of the sample was also deduced from the O–K-edge spectra. The Li–K-edge spectra of the Li-intercalated nanotubes indicated that Li was in the ionic state. The Ti–L$_{2,3}$-edge spectra recorded after Li intercalation indicated that TiO$_2$ was distorted after the intercalation with rutile being the dominant phase, most probably due to charge redistribution. Finally, crystallization of 9 nm TiO$_2$ nanoparticles synthesized by the chemical vapor synthesis in the anatase structure was also verified by Ti–K-edge XANES [144].

6.3.2 Oxide Catalysts

Pure TiO$_2$ or doped with metallic ions finds applications in photocatalysis which has many applications, for example, in water splitting, organic pollutant scavenging, and antifouling. The size of the nanoparticles, their composition, and the presence of oxygen vacancies are important parameters for their photocatalytic function. TiO$_2$ is stabilized in three phases: rutile is stable for macroscopic crystals, while brookite and anatase can be stable in nanoparticles. The photocatalytic activity of TiO$_2$ was found to be dependent on the adopted phase and/or the formation of a mixture of two phases. C.-Yu Liao et al. [145] applied XAFS for the study of mesoporous TiO$_2$ hollow spheres which have potential applications in the photoanodes of dye-sensitized solar cells where they play an important role on the loading of the sunlight sensitive dyes. The XANES spectra recorded at the Ti–K-edge are characterized by a pre-edge peak, similar to the one in the Fe–K-edge spectra discussed

previously. The pre-edge peak of the studied mesoporous TiO_2 had four contributions that were attributed to tetrahedrally coordinated (TiO_4), fivefold square pyramid [$(Ti = O)O_4$] and octahedrally coordinated Ti. The authors deconvoluted each contribution using proper fitting with Gaussian–Lorentzian peaks and determined the percentage of the square-pyramid Ti polyhedra which have high activity for photocatalytic degradation of organic pollutants. The deconvolution of the pre-edge peak by peak fitting is shown in Fig. 4.21. Analysis of the EXAFS spectra revealed that mesoporous TiO_2 is characterized by smaller coordination numbers compared to nano-TiO_2. The photo-conversion efficiency of the mesoporous material was much better compared to the nanosized one.

Kityakarn et al. [146] studied Ce-doped TiO_2 nanoparticles by means of XANES. Doping of TiO_2 with Ce improves its photocatalytic activity. The Ti–K-edge spectra of $Ti_{1-x}Ce_xO_2$ (x = 0–0.1) were fitted using linear combinations of the anatase, rutile, and brookite spectra. It was found that upon Ce doping, the anatase/rutile mixture was replaced by anatase/brookite. The Ce–L_3-edge XANES spectra revealed that the dominant oxidation state of Ce was 4+ with a small contribution of Ce^{3+} for low doping levels.

Enhancement of the photocatalytic efficiency of titanate nanotubes in dissolution of organic pollutants is improved with the addition of Cu dopants. R.-a. Doong et al. [147] studied Ti–K- and Cu–$L_{2,3}$-edge XANES titanate nanotubes that were calcined to form TiO_2-titanate nanotube nanocomposites doped with Cu^{2+}. From the relative intensity of the components of the pre-edge peak in the Ti–K-edge spectra, it was deduced that the as-prepared titanate nanotubes adopted a layered structure, whereas calcination and Cu photo-deposition led to the formation of the anatase structure. Another promising strategy to reduce the electron–hole recombination is the formation of a heterostructure. Mourão et al. [148] reported on the synthesis of TiO_2 nanostructures and TiO_2:SnO_2 heterostructures. The materials were synthesized from TiO_2 and $SnCl_2 \cdot 2H_2O$ precursors which were subjected to hydrothermal treatment using KOH solutions with various concentrations. The Ti–K-edge spectra of the TiO_2 and TiO_2/SnO_2 nanostructures with a small value of the Ti/Sn ratio, prepared at lower KOH concentrations, revealed that the samples adopted the anatase structure. On the contrary, in the spectra from the sample with a higher value of the Ti/Sn ratio, a characteristic contribution in the pre-edge peak (A2 in Fig. 4.21) was detected. This contribution, which was considerably higher, was attributed to five-coordinated Ti due to the elongated morphology of the nanostructures prepared under these conditions. The photocatalytic activity of TiO_2 is enhanced with deposition of noble metals on its surface. Ag–L_3-edge XANES spectra of Ag-modified TiO_2 with average size of approximately 7 nm showed that Ag was in the Ag^+ ionic state [149].

ZnO has a direct and wide band gap and thus finds applications in UV shielding. However, it also exhibits photocatalytic activity that hinders its applications in UV shielding. For example, it causes skin damage, deterioration of paints and plastics, and color fading in plastics and fabrics. It has been proposed that the photocatalytic activity of ZnO can be reduced by doping with Co. The bonding configuration of Co dopants in ZnO nanoparticles (with particle size 10–50 nm) and doping levels
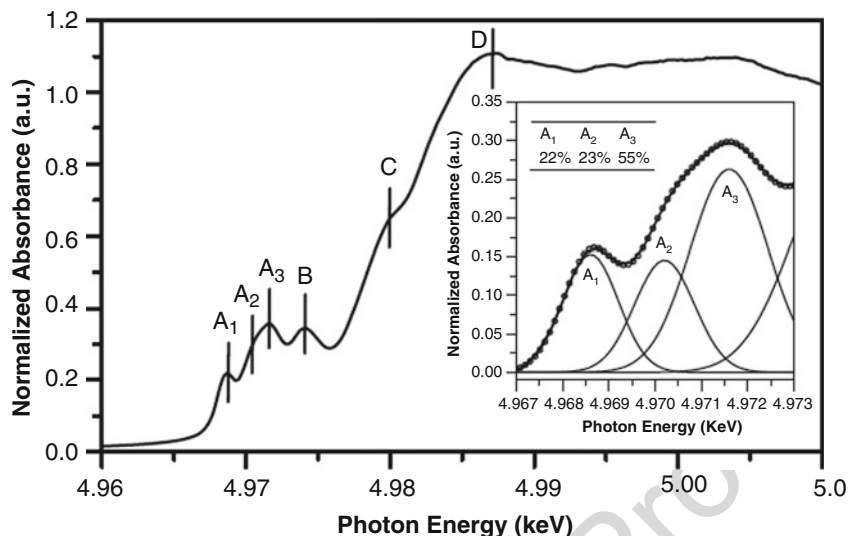
Fig. 4.21 Ti–K-edge XANES spectra of mesoporous TiO₂ hollow spheres. Fitting of the pre-edge peak using various components is shown in the *inset* (Reprinted from Journal of Physics and Chemistry of Solids, Vol, 75, C.-Yu Liao, S.-T. Wang, F.-C. Chang, H. P. Wang, and H.-P. Lin, Preparation of TiO₂ hollow spheres for DSSC photoanodes. Pages 38–41. Copyright (2014), with permission from Elsevier)

0.25–5 at.% was studied by means of XAFS [150]. The authors reported that the photocatalytic activity of the ZnO nanopowders, as determined via the decomposition of dye molecules under simulated sunlight, is indeed reduced with Co doping. The Co–K-edge XANES spectra of the Co-doped ZnO nanoparticles were compared with spectra of the reference compounds CoO, Co_2O_3, and Co-methylimidazole. In CoO, Co^{2+} is octahedrally coordinated resulting in a low-intensity broad pre-edge peak, whereas in Co-methylimidazole the tetrahedral coordination of Co gives rise to a sharp pre-edge peak. Judging from the intensity of the pre-edge peak, Co was found tetrahedrally coordinated in the Co-doped ZnO. In addition to that, from the position of the absorption edge, it was deduced that its oxidation state was +2. The EXAFS analysis revealed that Co substitutes for Zn retaining the tetrahedral coordination of Zn in ZnO. The incorporation of Co in host lattice sites, instead of interstitial positions, is held responsible for the reduction in the photocatalytic activity, most probably due to the creation of deep levels in the gap that act as electron–hole traps.

MnO₂ catalysts have potential applications for electrochemical water splitting that is a key step in the use of H₂ in energy storage. MnO₂ exists in a number of polymorphs that adopt layered or tunneled structures where the octahedra around Mn share corners and/or edges. Bergmann et al. [151] studied Mn–K-edge XAFS of MnO₂ synthesized with two different methods, symproportionation deposition–precipitation (s) and incipient wetness impregnation (i). The XANES spectra revealed that the oxidation state of Mn was around 3.5+ and 3+ and became 3.5+ in both cases

after deposition on the electrode. After the electrocatalytic process, the oxidation state of Mn in both cases increased to 4+. Analysis of the EXAFS spectra revealed that Mn was octahedrally coordinated. The nanoparticles synthesized by the s-method adopted a layered structure with edge-sharing octahedra, whereas in those synthesized by the i-method, significant contribution of corner sharing was detected.

ZrO_2–CeO_2 substitutional solid solutions attracted interest due to their applications in three-way catalysts. ZrO_2 is added to inhibit the CeO_2 deactivation. On the other hand, the catalytic activity of the ceria–zirconia catalysts is improved with the interaction of noble metal phases. Acuña et al. [152] studied pure $Zr_{0.1}Ce_{0.9}O_2$ and $Zr_{0.1}Ce_{0.9}O_2$/Pd nanotubes. The latter were studied also after reduction. Comparison of the Ce–L_3-edge XANES spectra of the samples with spectra of reference compounds, which contained Ce^{3+} and Ce^{4+}, revealed that Ce was mainly in the tetravalent state in all the samples. A small amount of Ce was found in the trivalent state with its proportion increasing as the particle size decreased. Doping of the $Zr_{0.1}Ce_{0.9}O_2$ nanotubes with Pd resulted in a considerably higher amount of Ce^{3+} that was not affected significantly by the reduction process. The spectra recorded at the Pd–L_3-edge demonstrated that Pd was in a higher oxidation state compared to metallic Pd (as deduced from the position of the absorption edge and the intensity of the white line). The results indicated that Pd was incorporated in the nanotube structure. Ce–L_3- and Pd–L_3-edge XANES recorded in situ during heating under reducing conditions revealed that as the temperature increased, the percentage of Ce^{3+} increased but at much higher amount in the presence of Pd.

The formation of PdO nanoparticles in the pores of various medium- or large-pore zeolites by Pd ion exchange and heating was reported by Park et al. [153]. These materials are effective catalysts for methane combustion. Pd–K-edge EXAFS revealed the formation of PdO and Pd particles. The size of the zeolite pores was found to control the size of the PdO particles, thus affecting their catalytic activity.

Johnston-Peck et al. [154] studied CeO_x particles (with size 5–45 nm) on TiO_2 support by Ce–$L_{2,3}$-edge XANES. The position of the L-edges was used for the determination of the oxidation state of Ce. It was found that a large fraction of Ce was trivalent. This was an indication that the incorporation of ceria on the titania surface results in charge transfer between O and Ce. Furthermore, comparison of the spectra recorded in the TEY and FLY modes, which are characterized by different information depths, revealed a different value of the Ce^{3+}/Ce^4 concentration ratio. The results indicate that Ce exists in a reduced state not at the surface but probably near the ceria−titania interface. Variations in the oxidation state of Ce in Pt–CeO_x catalysts were also observed in the Ce–L_3-edge XANES [155]. More specifically, synthesis of mixed CeO_2/Pt catalysts resulted in the formation of Ce^{3+} species although Ce in pure CeO_2 is tetravalent. After immersing the Pt–CeO_x in H_2SO_4 solution for oxygen reduction catalysis, the edge jump decreased to approximately 6 % implying the dissolution of CeO_x. The XANES spectra revealed that only Ce^{3+} remained in the sample.

1592   Cu–Al–O_x catalysts of the water–gas shift reaction in proton-exchange membrane
1593 fuel cells were studied for daily start-up/shut-down operation [156]. The Cu–Al–O_x
1594 catalysts were investigated with in situ Cu–K-edge XAFS spectroscopy. The acqui-
1595 sition time was 60 s and the spectra were recorded at 33 s intervals. Cu foil, Cu_2O,
1596 and CuO were used as reference compounds for the 0, +1, and +2 oxidation state of
1597 Cu, respectively. Cu–K-edge XANES and EXAFS spectra revealed that during the
1598 start-up/shut-down-like operation, oxidation of Cu metal to Cu_2O and then reduction
1599 to Cu take place. However, variations in the amount of Cu^+ during the first and the
1600 second cycle were observed between the coprecipitated and impregnated catalysts.
1601 The results were discussed in combination with the particle size, as deduced from the
1602 coordination numbers. In a perspective article, Rodriguez et al. [157] present
1603 applications of time-resolved in situ XAFS for the study of catalysts which combine
1604 Cu, Au, or Pt with oxides such as ZnO, CeO_2, TiO_2, CeO_x/TiO_2, and Fe_2O_3. Under
1605 reaction conditions most water–gas shift catalysts undergo chemical transformations
1606 that can be easily detected by XAFS spectroscopy.

6.3.3 Fe Oxides and Other Magnetic Nanoparticles

1608 Nanosized Fe oxides find various applications due to their magnetic, electronic,
1609 photonic, and optical properties. Magnetic nanoparticles have been a subject of
1610 intensive research because of their applications in nano-diagnosis and nanotherapy.
1611 Magnetite (Fe_3O_4) and maghemite (γ-Fe_2O_3) have attracted particular interest
1612 because they are ferromagnetic and biocompatible while they can be easily removed
1613 from the body via natural routes. The chemical formula of Fe_3O_4 is often written as
1614 (Fe_2O_3) · (FeO) in order to indicate the coexistence of Fe^{3+} (which occupies tetra-
1615 hedral and octahedral sites) and Fe^{2+} (in octahedral coordination). In maghemite
1616 (γ-Fe_2O_3), which also adopts the spinel structure, Fe^{2+} is oxidized to Fe^{3+} and the
1617 charge neutrality is maintained by the presence of vacancies in octahedral sites.
1618 α-Fe_2O_3 (hematite) is a nonmagnetic allotropic form of trivalent Fe with rhombo-
1619 hedral crystal structure. One phenomenon that is observed in nanosized Fe oxides is
1620 the apparent oxidation of the magnetite nanoparticles. Corrias et al. [158] used
1621 XAFS to study the effect of the nanoparticle size and oxidation degree
1622 (by sequential injection of an oxidizer during synthesis), on the structure of mono-
1623 disperse iron oxide nanoparticles. The characteristic pre-edge peak was quite pro-
1624 nounced in the XANES spectra of Fe_3O_4 and γ-Fe_2O_3, where Fe was both
1625 tetrahedrally and octahedrally coordinated. Its intensity was lower in structures
1626 where Fe was only octahedrally coordinated, for example, FeO and α-Fe_2O_3. XRD
1627 and TEM revealed that polycrystalline nanoparticles, consisting of FeO and a spinel
1628 phase, were formed at low oxidant amounts, whereas single-crystalline spinel
1629 nanoparticles were obtained by increasing the oxidation degree. EXAFS analysis
1630 disclosed that in nanoparticles of 10 and 14.5 nm size, the relative amount of the
1631 spinel phase was 76 % and 58 %. Single-crystalline spinel nanoparticles were
1632 obtained by increasing the degree of oxidation. In the polycrystalline colloids,
1633 spontaneous slow oxidation takes place, whereas the larger nanocrystals oxidize
1634 more readily. Finally, in the 8 nm particles, the spinel structure was a mixture of
1635 mainly Fe_3O_4 and γ-Fe_2O_3, whereas in the 13 nm crystals, the γ-Fe_2O_3 phase was
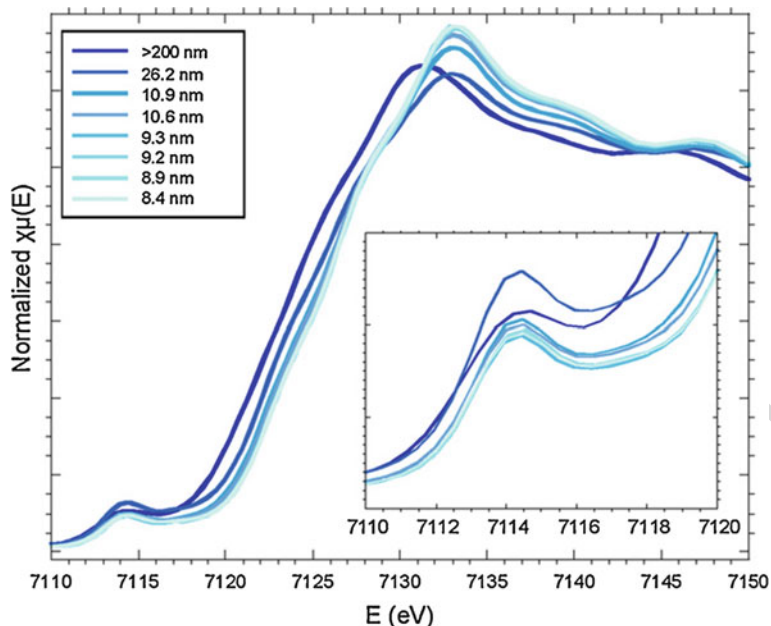
Fig. 4.22 Fe–K-edge XANES spectra of Fe_3O_4 nanoparticles as a function of the particle size (Reprinted from Electrochimica Acta, Vol. 94, M. C. Menard, A. C. Marschilok, K. J. Takeuchia, and E. S. Takeuchi, Variation in the iron oxidation states of magnetite nanocrystals as a function of crystallite size: The impact on electrochemical capacity, Pages 320–326. Copyright (2013), with permission from Elsevier)

dominant. In another investigation of Fe_3O_4 as an electrode material for Li-ion batteries, Menard et al. [159] applied Fe–K-edge XAFS spectroscopy in order to study size-related effects in magnetite nanoparticles. In the Fe–K-edge XANES spectra shown in Fig. 4.22, both the position of the absorption edge and the pre-edge peak shift toward higher energies with decreasing particle size. Using the spectra of reference Fe oxides, the position of the absorption edge and the pre-edge peak were used for the determination of the oxidation state of Fe in the magnetic nanoparticles. The results revealed that upon exposure to air, a number of Fe^{3+} surface atoms oxidized to Fe^{2+}. This oxidation was held responsible for the increase in the discharge capacity of Fe_3O_4 electrodes. Similar shifts in the position of the absorption edge of γ-Fe_2O_3 compared to Fe_3O_4 were observed by Mendoza Zélis et al. [160].

Piquer et al. [161] applied Fe–K- and $L_{2,3}$-edge XANES and XMCD in order to study iron oxide nanoparticles synthesized by various methods. The problem addressed was whether oxidation of Fe is better explained by the formation of separate Fe_3O_4 and γ-Fe_2O_3 phases that coexist in the nanoparticles, or if a single, non-stoichiometric phase is formed throughout the nanoparticles. $L_{2,3}$-edge XANES and XMCD analysis could not easily discriminate between the γ-Fe_2O_3 and Fe_3O_4 phases and could not provide accurate determination of the coexistence of the two

phases in a sample. The Fe–K-edge XANES spectra of the nanoparticles had a profile intermediate to that of bulk magnetite and maghemite. The nanoparticle size rather than the synthesis method appeared to affect the profile of the XANES spectra. However, the linear combination method for the fitting of the spectra from the nanoparticles, as a weighted average of the spectra of bulk magnetite and maghemite, did not work properly. MXAN simulations indicated that a single phase non-stoichiometric oxide was grown with crystal structure possessing a cell parameter lying in-between those of the pure stoichiometric magnetite and maghemite oxides.

Surfactant effects on the morphological, structural, and magnetic properties of iron oxide nanoparticles produced by coprecipitation were investigated by Filippousi et al. [162]. The use of the different surfactants resulted in nanoparticles with different sizes (7–12 nm), different unit cell parameters (as determined by XRD), and different Fe oxidation states that took values in-between those of γ-Fe$_2$O$_3$ and Fe$_3$O$_4$. The oxidation state was determined from the position of the absorption edge in the Fe–K-edge spectra. EXAFS analysis revealed that the nanoparticles adopt the spinel structure, while the Fe–O distance was slightly smaller compared to the corresponding value in magnetite, in consistence with the increased Fe oxidation state detected by XANES. Bora et al. [163] used Fe–K-edge XANES in order to study the effect of different heat treatment temperatures (250–900 °C) during the synthesis of Fe$_2$O$_3$ nanoparticles. From the variations in the pre-edge peak characteristics, i.e., intensity under the pre-edge peak and relative contribution of various components, they deduced that at low temperatures maghemite (γ-Fe$_2$O$_3$) was the dominant phase, whereas as the temperature increased, the oxidation state of Fe increased and hematite (α-Fe$_2$O$_3$) dominated.

γ-Fe$_2$O$_3$ nanoparticles coated with Cu were studied by means of Fe– and Cu–L$_{2,3}$-edge XANES [164]. The XANES spectra revealed that the particles consisted of γ-Fe$_2$O$_3$ coated with a mixture of Cu and Cu^{2+} consistent with the formation of CuO layer at the interface of Cu and γ-Fe$_2$O$_3$. Taking into account the XRD and TEM results, it was concluded that the thickness of this layer was very small and was consistent with the formation of bonds between O atoms of γ-Fe$_2$O$_3$ with the Cu coating. Temperature-dependent XMCD at the Fe–L$_{2,3}$- and Cu–L$_{2,3}$-edges indicated that the Cu coating altered the surface anisotropy of γ-Fe$_2$O$_3$ nanoparticles and apparently modified the Fe(octahedral)–O–Fe(tetrahedral) super-exchange. Variations observed in the nanomagnetism as a function of the Cu shell thickness were also discussed. The effect of a polypyrrole shell, which covers Fe$_3$O$_4$ nanoparticles [165], and oleic acid coating of iron oxide nanoparticles, in the oxidation state of Fe [166] was also investigated using XAFS. Porous iron oxide fabricated on a wood template were also investigated using Fe–K-edge EXAFS that verified the formation of α-Fe$_2$O$_3$ [167].

Bulk NiO is an antiferromagnetic material. However, magnetic behavior is observed when the NiO particle size is reduced down to the nanoscale. NiO nanoparticles with size 2–10 nm were studied by means of Ni–K-edge XAFS [168]. The EXAFS spectra revealed that the coordination number in the first nearest neighboring shell (Ni–O) was not affected by the particle size. Reduction of the

coordination number in the second nearest neighboring shell (Ni–Ni) from 11 to 9.6 was observed as the particle size was reduced from 9 to 2.5 nm. Size-dependent variations were not observed in the XANES spectra indicating that the oxidation state was Ni^{2+}, i.e., as in the bulk. Another approach for the analysis of the EXAFS spectra of NiO nanoparticles was presented in Refs. [169, 170]. The relaxed atomic positions in the NiO nanoparticles that were used to simulate the EXAFS spectra were calculated with molecular dynamics. Several thousands of atomic configurations were adopted in order to take into account configurational averaging in the EXAFS signal.

Another family of magnetic materials is the magnetic spinel ferrites which are described with the general chemical formula $M_xFe_{3-x}O_4$, where M=Fe, Co, Mn, Ni, or Zn. They have biological applications such as thermal activation therapy, hyperthermia, biosensing, drug delivery, and magnetic resonance imaging. Addition of other metals in the structure of Fe_3O_4 allows for the modification of the magnetic properties of the nanoparticles. The distribution of the metal ions in the tetrahedral and octahedral sites of the spinel structure depends on the radii, the oxidation state, and the electronic configuration of the ions. Another important parameter that affects the properties of the nanoparticles is the inversion parameter, i, which is defined as the number of divalent cations in octahedral sites. Co–K- and Fe–K-edge EXAFS was applied for the study of silica-coated $CoFe_2O_4$ nanoparticles [171]. The Fe–K-edge XANES spectra revealed that the $CoFe_2O_4$ nanoparticles adopt the structure of the reference $CoFe_2O_4$ material, i.e., an inverse spinel structure with the Fe^{3+} ions occupies all the tetrahedral sites and half of the octahedral sites, while Fe^{2+} occupies a fraction of the remaining octahedral sites. The Co–K-edge XANES spectra of the unleached nanoparticles disclosed that a portion of the Co ions occupied tetrahedral sites. Leaching, which took place spontaneously after dilution in water, resulted in a spectrum similar to that of the reference $CoFe_2O_4$ sample. EXAFS verified the XANES observations, i.e., variations in the Co bonding environment that occurred upon leaching. In the unleached nanoparticles, Co occupied tetrahedral sites, whereas after leaching it occupied octahedral sites. These leaching-induced variations in the inversion degree were held responsible for the changes in the magnetic behavior of the nanoparticles.

Co-substituted ferrite nanoparticles with size 5–6 nm and Co content varying from 0 to 0.94 were studied by means of XAFS [172]. XANES revealed that the oxidation state of Fe and Co was 3+ and 2+, respectively. From the characteristics of the pre-edge peak, it was deduced that a larger number of Fe than Co atoms occupy tetrahedral sites. EXAFS analysis demonstrated that although the Co content was varied considerably, the ratio of the Co ions occupying tetrahedral and octahedral sites did not vary and the inversion degree was found 0.7 for all the samples.

The size effect on the structural properties of Mn ferrites has been also investigated using XAFS [173]. The size of the nanoparticles took values in the range 3–6 nm and the Mn/Fe ratio varied from 1.65 to 1.76. The position of the absorption edge and the pre-edge peak characteristics in the XANES spectra were used for the determination of the oxidation state. It was found that Fe adopts the spinel structure

with higher occupation of tetrahedral sites by Fe atoms which were predominantly in the oxidation state 3+. A significant fraction of the Mn ions was also found in the 3+ oxidation state as it was deduced from the Mn–K-edge XANES spectra. For the EXAFS analysis, the structural formula of stoichiometric Mn ferrite can be written as $[Mn_{1-i}Fe_i]^A[Mn_iFe_{2-i}]^BO_4$ where A and B denote tetrahedral and octahedral sites, respectively. For normal and inverse spinel, i takes the values 0 and 1, respectively. For the EXAFS analysis, nearest neighbor configurations of both the tetrahedral and octahedral sites, with proper weighting factors, should be taken into account. The inversion degree in the nanoparticles was found to range between 0.57 and 0.60 and it was lower compared to the value 0.7 that was determined for the bulk sample. Stoichiometric Mn ferrites with size of approximately 8 nm were also studied by means of XAFS [174]. Fe was found trivalent, whereas the oxidation state of Mn varied between 2+ and 3+. Partial oxidation of the Mn^{2+}, which was controlled by the used Mn precursor, was detected and resulted in the reduction of the inversion degree from 0.42 to 0.22. The size effect on the inversion degree of nanosized Ni, Co, and Zn ferrites was investigated by Nordhei et al. [175] for nanoparticle size ranging from 4 to 25 nm and by Hellner Nilsen et al. [176] for nanoparticle size ranging from 39 to 105 nm.

6.3.4 Nanoceramics

ZrO_2-based ceramics exhibit excellent electrical and mechanical properties which are attributed to the small, usually in the nanoscale, grain size. Fábregas and Lamas [177] studied $ZrO_2–Y_2O_3$ and $ZrO_2–CeO_2$ powders, synthesized by gel combustion, at the Zr–K- and Y–K-edges. During the synthesis, various fuels (amino acids or citric acid) were added in the Zr and Y precursor solution to form gels. The ceramic powders were produced after combustion. Direct comparison of the Zr–K-edge spectra of the powders with reference compounds revealed that when amino acids were used as fuels, the bonding configuration was similar to the $ZrOCl_2$ precursor, whereas when citric acid was used, the XANES spectra did not have any similarities with the reference compounds. The spectra of the precursor gels, when amino acids were used as fuels, were fitted using three O paths for the first nearest neighboring shell (the total coordination number ranged from 6.9 to 7.5) and one Zr–Zr path (the coordination number ranged from 2 to 3). This model was similar to the one used for the $ZrOCl_2$ precursor. For the precursor gels that contained citric acid as fuel, the more symmetric model of cubic ZrO_2 was used. Contrary to the Zr atoms which were found chelated, Y atoms had one neighboring shell consisting of eight oxygen atoms at a distance of 2.35–2.39 Å

6.4 Nanocomposites

Nanocomposites are multiphase materials where one of the phases has one, two, or three dimensions smaller that 100 nm. The mechanical, electrical, optical, and thermal properties of the nanocomposites differ significantly from those of the constituent phases. In the following, representative applications of XAFS
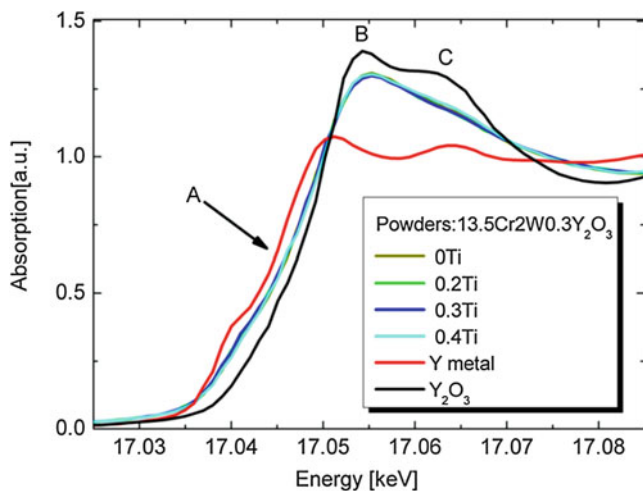
Fig. 4.23 Y–K-edge XANES spectra of the powder steel samples containing Y_2O_3, after mechanical alloying of pre-alloyed Fe-13.5Cr-2 W powders with 0.3 wt% Y_2O_3 and 0–0.4 wt% TiH_2 powders (sample names 0Ti – 0.4Ti). Metal Y and Y_2O_3 are used as reference samples. The absorption edge, the main peak, and the shoulder at the post edge are marked by A, B, and C, respectively (Reprinted from Materials Chemistry and Physics, Vol. 136, P. He, T. Liu, A. Möslang, R. Lindau, R. Ziegler, J. Hoffmann, P. Kurinskiy, L. Commin, P. Vladimirov, S. Nikitenko, and M. Silveir, XAFS and TEM studies of the structural evolution of yttrium-enriched oxides in nanostructured ferritic alloys fabricated by a powder metallurgy process, Pages 990–998. Copyright (2012), with permission from Elsevier)

spectroscopies for the study of nanocomposites with improved mechanical, wear, and irradiation resistance and tribological properties will be discussed.

Oxide dispersion-strengthened (ODS) ferritic steels, which contain high concentration of nanosized oxide particles, are characterized by enhanced resistance to irradiation and thus are promising materials for applications in nuclear technology, for example, in reactors and in the waste incineration process. They are also candidates for CO_2-free production of hydrogen and other applications such as in corrosive environments under high temperatures. ODS ferrite steel samples with 0.25–0.5 wt% Y_2O_3 were studied by He et al. [178]. The samples were prepared by mechanical alloying of Fe-13.5% Cr-2%W pre-alloyed powders with 0.3 wt% Y_2O_3 and 0–0.5 wt% TiH_2 powders. The samples were studied after mechanical alloying and consolidation with hot isostatic pressing. The synthesis conditions were expected to affect strongly the mechanical properties due to the varying degree of Y_2O_3 dissolution and incorporation of Y and O in the steel matrix. The oxidation state of Y was determined from the Y–K-edge XANES spectra using as reference samples Y foil and Y_2O_3. The XANES spectra of Y (oxidation state = 0), Y_2O_3 (oxidation state 3+), and the powders with 0.3 wt% Y_2O_3, with varying amount of Ti, are shown in Fig. 4.23. The absorption edge of the powders lies in-between the absorption edges of the Y foil and pure Y_2O_3, thus indicating that a portion of Y is in the metallic state (since Y cannot be found in oxidation states other than 0 and +3).

The structure of the spectrum above the absorption edge is smeared out denoting that the Y_2O_3 particles lack long-range order. From the linear combination fit of the XANES spectra, it was deduced that less than 15 % of Y was in the metallic form. The XANES spectra of the compacted samples revealed that the oxidation state of Y was 3+ and indicated the formation of new Y-oxide phases. The EXAFS analysis of the powder samples disclosed that Y was in the form of Y_2O_3. The fact that the calculated coordination numbers are smaller is attributed to the plastic deformation introduced by the mechanical alloying. In the compacted Ti-free samples, $YCrO_3$ and Y_2O_3 phases were found to coexist. In the compacted samples that contained Ti, mixed Y–Ti oxide phases were taken into account to fit the EXAFS spectra.

Precipitation-hardened Al alloys find applications in the aircraft industry. Staab et al. [179] applied XAFS for the study of nanoprecipitate phases in Al alloys. Such precipitates are held responsible for the hardening of Al alloys similar to the case of steel. However, in Al alloys synthesized by solution heating followed by quenching, such precipitates appeared to be formed after storage. The formation of precipitates in the alloys plays an important role in the increase of their strength even if the size of the precipitate is smaller than 1 nm. However, precipitates of such small sizes cannot be detected with HRTEM and/or XRD. Cu–K-edge XAFS was applied for the study of AlCu and AlCuMg alloys containing 1.7 and 1.87 at.% Cu, respectively. The latter also contained 1.78 at.% Mg. The Cu–K-edge measurements were conducted at -40 ° C after an increasing–decreasing temperature cycle, a process that simulates natural aging. In regard to the analysis of the XAFS spectra, FEFF simulations were performed using a cluster that contained more than 87 atoms and assuming the Debye model for the estimation of the Debye–Waller factors. The simulations of the AlCu alloy spectra revealed that in the as-quenched state, isolated Cu atoms as well as Cu atoms participating in the formation of Guinier–Preston zones (Cu precipitates in the form of monoatomic platelets) existed, whereas after heat treatment the Al_2Cu phase (Θ-phase) was formed. The Cu–K-edge XAFS spectra of the AlCuMg alloy were fitted to identify variations with aging (storage time). As the aging time increased (from 8 min to 8 h), the distance between Cu and its neighboring atoms decreased, exhibiting relaxation. FEFF simulations revealed that the S-phase was formed after heat treatment.

Transition metal carbides find applications in wear- and oxidation-resistant protective coatings and in low-friction solid lubricants. The applications are based on the nanocrystalline/amorphous-C nanocomposite structure. Furlan et al. [180] investigated $Ni_{1-x}C_x$ ($x < 0.62$) films prepared by magnetron sputtering, in order to determine the crystalline to amorphous ratio. The XANES spectra were recorded at the $Ni–L_{2,3}$- and C–K-edges. The $Ni–L_{2,3}$-edge spectra for different C content are shown in Fig. 4.24. The two peaks, characteristic of the L_3 and L_2 edges, correspond to transitions from $2p_{3/2}$ and $2p_{1/2}$ to three-dimensional states, respectively, and are representative of the formed NiC_y phases (*fcc* and *hcp*). Compared to the pure Ni metal, the peaks in the spectra of the NiC_x samples are broader and shifted toward higher energies, indicating higher structural disorder and charge transfer from Ni to C. Furthermore, as x increases, the intensity of the L_3 peak decreases indicating changes in the Ni ionicity. The splitting of the L_3 peak observed for x = 0.16 is characteristic of the *hcp* phase (contrary to the *fcc* phase where only a single peak is expected).
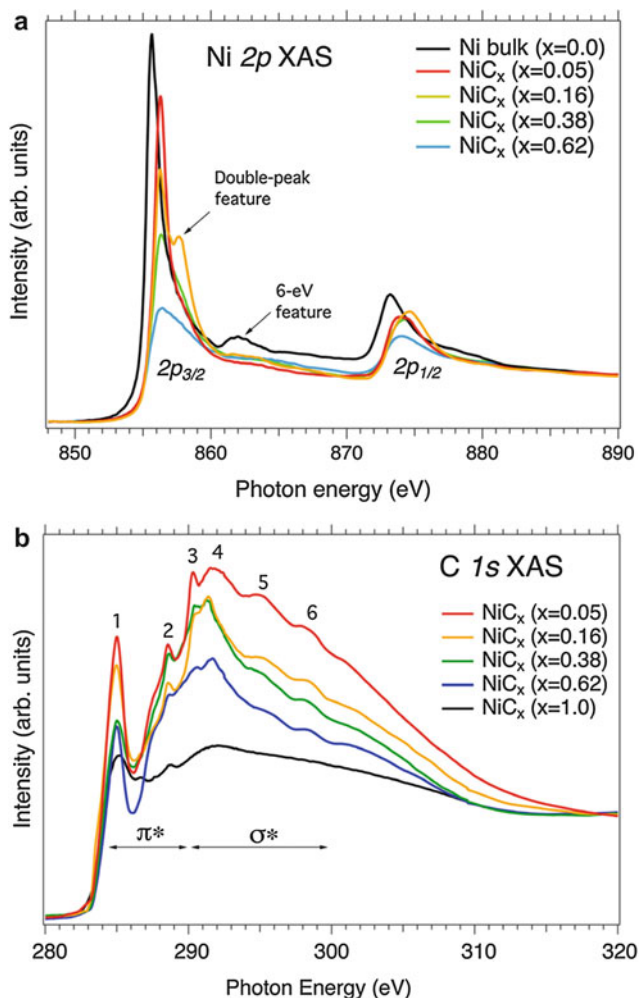
Fig. 4.24 (*Top*) Ni–$L_{2,3}$-edge and (*Bottom*) C–K-edge XANES spectra of the sputtered $Ni_{1-x}C_x$ films, as a function of x (Reprinted from Journal of Physics: Condensed Matter, Vol. 26, A. Furlan, J. Lu, L. Hultman, U. Jansson, and M. Magnuson, Crystallization characteristics and chemical bonding properties of nickel carbide thin film nanocomposites, Pages 415501:1–11. Copyright (2014), with permission from Elsevier)

The C–K-edge NEXAFS spectra are shown in the right panel of Fig. 4.24. The spectra have contributions from both the $Ni_{1-x}C_x$ (*fcc* or *hcp* phases) and the C matrix. Variations in the value of x affect the intensity of the π^* resonances (features designated 1 and 2) relative to the intensity of the σ^* region (features designated 3–6), indicating variations in the sp^2 and sp^1 bonding. In another study, nanocomposite $Fe_{1-x}C_x$ (with $0.2 < x < 0.7$) films consisting of metal carbide and amorphous C phases were investigated [181]. The Fe–$L_{2,3}$-edge XANES spectra

had similar characteristics with the Ni–$L_{2,3}$-edge spectra shown in Fig. 4.24. However, crystal field-induced splitting of the L_2 and L_3 peaks was observed in all studied samples and was attributed to the formation of an amorphous FeC_y carbide phase. Variations in the relative intensity of the L_3 and L_2 peaks revealed variations in the Fe ionicity in the FeC_y phase. The C–K-edge spectra was also found to depend on x with the relative intensity of the π^* to the total π^* and σ^* intensity decreasing with x. This variation has been attributed to the reduction of sp^2 (C=C) and sp^1 hybridization in the amorphous C-phase and the C 2p–Fe 3d hybridized states in the iron carbide phase.

TiBC/amorphous-C nanocomposite films grown by sputtering from $TiC:TiB_2$ and graphite targets, with varying B/C ratios, were studied by means of Ti–K-edge XAFS [182]. The XANES spectra had intermediate characteristics between those of hexagonal-TiB_2 and *fcc*-TiC. Incorporation of C in the TiB_2 phase was detected. As the C content increased, further peaks in the Fourier transform gained intensity, indicating that TiC and/or TiB_xC_y phases were formed.

TiN/Ni nanocomposite films were studied by Pinakidou et al. [183] with XAFS at the N–K- and Ni–K-edge. The samples consisted of TiN nanocrystals covered by an intergranular Ni phase and attracted interest due to superhardness and high chemical stability. They were prepared by sputtering and the Ni content was below 21.5 at.%. The N–K-edge NEXAFS did not reveal any differences among the samples with different Ni content indicating that the TiN structure was not affected by the Ni concentration. The EXAFS analysis at the Ni–K-edge disclosed that differences in the chemical composition affected strongly the coordination environment of Ni. More specifically, the number of Ni and Ti atoms bonded to Ni increased as the Ni content increased, and the total coordination number of Ni (with Ni and Ti atoms) increased with the [Ni]/[N] concentration ratio. The results indicated that the Ni atoms belong to a Ni matrix and also form bonds with Ti atoms in the TiN nanocrystals. TiN/Cu nanocomposites prepared by sputtering were also studied by means of Cu–K-edge EXAFS [184]. The authors reported that when the Cu content increased from 24 to 53 %, the total coordination number of Cu in the first nearest neighboring shell (comprised of Cu and Ti neighbors) increased from 6 to 11. The number of Ti neighboring atoms did not change significantly. The results demonstrated that as the Cu content increased, the Cu–Cu bonding became predominant indicating the formation of metallic Cu in-between the TiN nanocrystals.

6.5 Carbon-Based Nanomaterials

Carbon nanomaterials, for example, carbon nanotubes (CNTs), fullerene, and nanodiamond films, have tunable optical, electronic, and mechanical properties and are attractive for the fabrication of micro- and optoelectronic devices, chemical sensors, composite materials, and medical implants, as well as in renewable energy and environmental technologies. Recently, graphene, a single layer of sp^2 bonded C, attracted a lot of interests as a promising material for the fabrication of the next-generation electronic devices. C–K-edge NEXAFS spectroscopy is widely applied

for the study of carbon-based nanomaterials. Examples of such applications are discussed in the following.

6.5.1 Carbon Nanotubes

Carbon nanotubes are hexagonal arrays of carbon atoms rolled in such a way to form long, thin, hollow cylinders. They can be single-walled (SWNT) or multi-walled (MWNT) with their length and diameter varying from few hundred nanometers to several microns and from 1 to few hundred nanometers, respectively [185]. Information on their amorphous character and/or sp^3 content, the degree of alignment, the effectiveness of functionalization processes, and the presence of defects can be provided by NEXAFS, which is applied extensively. Functionalization refers to the attachment of atoms, molecules, or aggregates on the surface of the CNTs in order to reduce their chemical inertness. XAFS spectroscopy is also applied in intercalated CNTs in order to study the orientation, symmetry, and/or strain state of the intercalated compound. Due to the small binding energy of the K electrons in the carbon atom, acquisition of C–K-edge NEXAFS spectra necessitates ultrahigh vacuum conditions. Electron yield detectors (channeltrons) are mainly used for the detection of the total or partial electron yield (see also Sect. 4). For the energy calibration, due to monochromator shifts, the π^* resonance of HOPG at 285.35 eV is commonly used (see Sect. 5).

The electronic structure of the nanotubes is similar to that of graphite, and thus their C–K-edge NEXAFS spectra exhibit strong similarities (see Fig. 4.14). More specifically, the sharp resonance at 285.4 eV (i.e., before the absorption edge), which is detected in the spectra of C-nanotubes, is attributed to $1s \rightarrow \pi^*$ transitions. In addition to that, the broad band, with a prominent resonance at approximately 291.5 eV (i.e., above the absorption edge) is attributed to $1s \rightarrow \sigma^*$ transitions [13]. In the energy range between the π^* and σ^* resonances, absorption attributed to defects, i.e., bonding of C with O and/or H, is observed. Broadening of the π^* resonance in the spectra of MWNTs is attributed to the bending of the graphene layers that induces splitting of the $\pi \, 2p_z$ conduction sub-band [186]. Furthermore, variations in the width of the π^* and σ^* resonances, related to the synthesis process and the presence of defects, were observed. Fleming et al. [187] applied C–K-edge NEXAFS on SWNTs self-assembled on Si(100) in order to study the intensity variations of the π^* resonance for various sample orientations and angles of incidence. In general, the linear polarization of the SR beam is employed in C–K-edge NEXAFS in order to study the orientation of the CNTs. Aligned CNTs have potential applications as field emitters and in high strength materials. Li et al. applied angle-resolved C–K-edge NEXAFS to study the orientation of single-walled nanotubes (SWNTs), with diameter equal to 2 nm, that were vertically aligned on a Si wafer [188]. The spectra were collected at incidence angles ranging from grazing to normal to the sample surface. As discussed in Sect. 5, the intensity of the π^* resonance is proportional to $\cos^2\delta$, where δ is the angle between the electric field vector of the polarized incident beam and the direction of the maximum electron density that corresponds to the molecular orbitals. The π^* orbital is considered normal to the hexagonal honeycomb structure, i.e., to the CNT wall. For the σ^* orbital, a planar
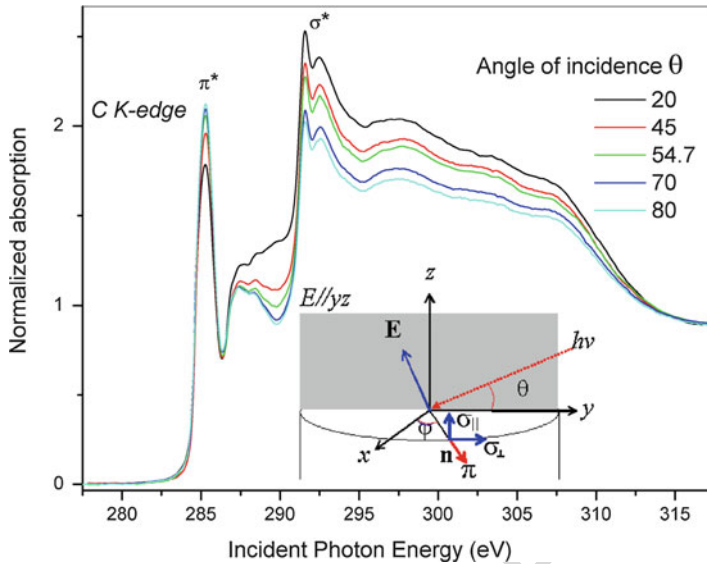
Fig. 4.25 Angle-resolved C–K-edge NEXAFS spectra of SWNT vertically aligned on a Si wafer. The orientation of the π* and σ* (decomposed to $\sigma_\perp$* and $\sigma_\parallel$*) orbitals relative to the nanotube and the incidence geometry that shows the direction of the electric field vector **E** relative to the nanotube are shown in the *inset* (Reprinted with permission from Z. Li, L. Zhang, D. E. Resasco, B. S. Mun, and F. G. Requejo, Angle-resolved x-ray absorption near edge structure study of vertically aligned single-walled carbon nanotubes. Applied Physics Letters, 2007. **90**(10): 103115.1–103115.3. Copyright [2007], AIP Publishing LLC)

distribution of electron density on the hexagonal lattice plane is taken into account. In CNTs, the σ* orbital can be modeled as having two contributions, one parallel to the tube axis, $\sigma_\parallel$, and one tangential to the tube perimeter, $\sigma_\perp$ (see inset of Fig. 4.25). The authors verified the well-oriented character of the nanotubes by the angular dependence of the π* and σ* resonances, which was in agreement with the theoretical predictions. The application of C–K-edge spectroscopy for the determination of the CNT orientation is also discussed in Ref. [189]. In order to assess the degree of order in the orientation of the CNTs, an order parameter (OP), which is also defined as dichroic ratio, is often adopted. The OP is defined as $OP = (I_\perp - I_\parallel)/(I_\perp + I_\parallel)$ where $I_\perp$ and $I_\parallel$ are the π* resonance intensities at normal and grazing incidence [190]. Absolute values close to unity indicate high order.

Another important property of the CNTs that renders them suitable for applications is functionalization, i.e., the attachment of atoms, molecules, or aggregates on the surface of the tube which is otherwise chemically inert. Functionalization of the CNTs results in improvement of their dispersion in various matrices to form composite materials and expands their applications in nanoelectronics, hydrogen storage, bioengineering, etc. Depending on the required CNT properties for specific applications, different functionalization, obtained via different processing steps, is necessary [191]. Functionalization of SWNT via oxidation (e.g., wet air oxidation of

ozone/H_2O_2-treated tubes) revealed that the intensity of the π^* resonance decreased and additional peaks due to C=O (σ^*) and C–O (π^*) appeared in the energy range 287–290 eV [190]. Functionalization is also important for the application of CNTs as heterogeneous catalyst supports, for example, in hydrogen storage in fuel cells – e.g., proton-exchange membrane fuel cells (see Sect. 6.3.2). Carbon-based materials have several unique properties as catalyst supports compared to oxides, for example, dissolution resistance in high-temperature aqueous solutions, chemical resistance, engineering of the chemical properties by different ways of functionalization, and electrical conductivity. The employment of CNTs as catalyst supports for Pt nanoparticles and improvement of their uniform dispersion necessitates oxidation of the CNTs which creates oxygen-containing surface groups that act as absorption sites for the Pt nanoparticles. Wang et al. [192] studied the effect of different oxygen-containing groups on MWNT-supported Pt catalysts. The C–K-edge NEXAFS spectra of the MWNTs after treatment with HNO_3 revealed the formation of C–O bonds. More specifically, the π^* and σ^* transitions of C–O appear at 287.6 and 288.2 eV, respectively (i.e., in-between the π^* and σ^* transitions of C–C). Annealing in He atmosphere at 1273 K resulted in partial removal of the C–O bonds. The same trend was observed in the O–K-edge spectra where the O content can be determined from the edge jump height. Comparison of the C–K-edge NEXAFS spectra recorded under different PEY retarding voltages and in the FLY mode revealed that the oxygen-containing groups were mainly located on the surface of the MWNT. The authors studied also the spectra recorded at the L_3 edge of Pt. The spectra of the Pt-loaded MWNTs (non-treated, functionalized with HNO_3, and subsequently annealed) were compared with the spectra of a Pt foil. In the spectra of the MWNTs, the white line (see Sect. 6.1.1) had lower intensity compared to that of the Pt foil and the absorption edge was shifted to lower energies indicating charge transfer between the Pt cluster and the MWNT. The Pt–L_3-edge EXAFS spectra verify that Pt was in the form of metallic nanoparticles. The authors estimated the size of the nanoclusters from the average coordination number.

Contrary to applications where functionalization is necessary, there exist a number of other applications where an increased inertness is important. For example, Brzhezinskaya et al. [193] applied N–K- and F–K-edge NEXAFS for the study of fluorination of MWNTs. The authors compared the fluorinated MWNTs with HOPG and white graphite fluoride (WGF). The C–K-edge spectra of the MWNTs that were in powder form exhibited strong similarities with the spectrum of HOPG. More specifically, upon fluorination, the π^* resonance progressively lost intensity (see Fig. 4.26) and the spectrum became gradually similar to that of the WGF. The intensity of the π^* resonance decreased as the F content increased, implying that the F atoms were attached perpendicular to the graphene layer and they did not replace C atoms in the honeycomb structure. Contrary to the C–K-edge NEXAFS spectra, the F–K-edge spectra did not exhibit variations with the degree of fluorination. Thus, the interaction of the F atoms with the MWNTs proceeded through covalent attachment of F atoms to the tube skeleton, without its destruction, although hybridization changed from sp^2 to sp^3. The effect of thermal annealing on defluorination was also reported in the same paper.
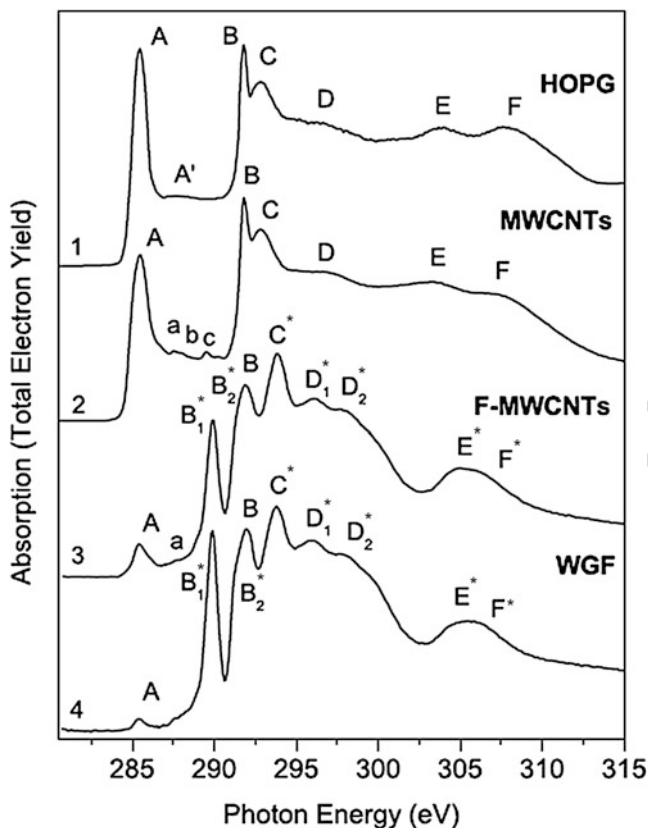
Fig. 4.26 C–K-edge NEXAFS spectra of (*1*) the HOPG, (*2*) pristine MWNTs, (*3*) fluorinated MWNTs, and (*4*) WGF (Reprinted figure with permission from M. M. Brzhezinskaya, V. E. Muradyan, N. A. Vinogradov, A. B. Preobrajenski, W. Gudat, and A. S. Vinogradov, Physical Review B, **79**, 155439, 2009)

The hydrogenation efficiency of SWNTs and their potential for applications in H storage was accessed with C–K-edge NEXAFS [194]. It was found that upon hydrogenation, the intensity of the π* resonance decreased and spectral features due to C–H bonding appeared. The ability of the liquid solvent SOCl$_2$ to remove the oxidized groups from SWNTs has been also studied [195]. Direct comparison of the C–K-edge NEXAFS spectra of pristine and SOCl$_2$-treated nanotubes revealed that the bands attributed to the π* states of C=O (288.5 eV) and σ* states of C–O (289.5 eV), which appear in-between the π* and σ* resonances, disappear after the treatment.

Another important issue in CNTs concerns their doping, i.e., the incorporation of atoms in the hexagonal lattice. It has been reported that nitrogen doping increases the CNT reactivity toward deposition of Pt nanoparticles for catalytic applications. N-doped CNTs were studied by means of C–K-edge NEXAFS [196]. A comparison
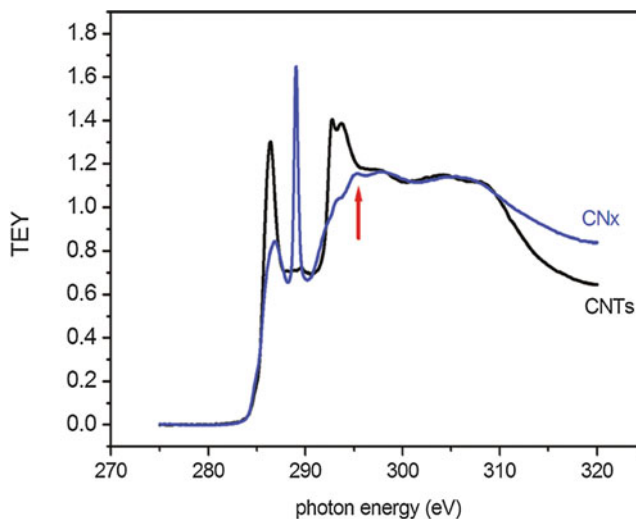
Fig. 4.27 C–K-edge NEXAFS spectra of undoped (*CNT*) and N-doped (*CN$_x$*) carbon nanotubes (Reprinted with permission from Y. Chen, J. Wang, H. Liu, M. Norouzi Banis, R. Li, X. Sun, T.-K. Sham, S. Ye, and S. Knights, Nitrogen doping effects on carbon nanotubes and the origin of the enhanced electrocatalytic activity of supported Pt for proton-exchange membrane fuel cells. Journal of Physical Chemistry C, 2011. **115**(9): 3769–3776. Copyright 2011, American Chemical Society)

of the spectra of doped (CN$_x$) and undoped CNTs is shown in Fig. 4.27. In N-doped nanotubes, the π^* resonance is significantly broadened and shifted to higher binding energies due to incorporation of N in the nanotube structure. The strong resonance at 289.1 eV is attributed to defects due to disruption of the sp^2 graphitic bonding induced by the N doping.

Low-pressure radio-frequency glow discharge was applied for the ex situ (post-deposition) N-doping of vertically aligned MWNTs [197]. Nitrogen can be incorporated in the graphitic network in various ways, e.g., substitutional, pyridinic, intercalated N$_2$ between the graphite layers, located in nonplanar sp^3 sites, or chemisorbed. From the angular dependence of the C–K-edge NEXAFS spectra, it was deduced that the vertical orientation of the nanotubes was preserved. In the N–K-edge spectra, three π^* resonances existed that evidenced the presence of various C–N bonds (pyridine-like, cyanic structure and substitutional, the graphite lattice). Their angular dependence revealed that N replaced C in the graphite rings, whereas a fraction of the N atoms formed cyanic structures. Annealing at 800 °C promoted incorporation of N in the graphitic planes and led in the formation of C–O/C=O bonds.

Intercalation of various compounds is also possible in CNTs. Encapsulation of Co-phthalocyanine (CoPc) in CNTs was studied by Schulte et al. [198]. Phthalocyanines comprise a group of blue-green pigments which can incorporate a number of different metals in their structure. They exhibit strong
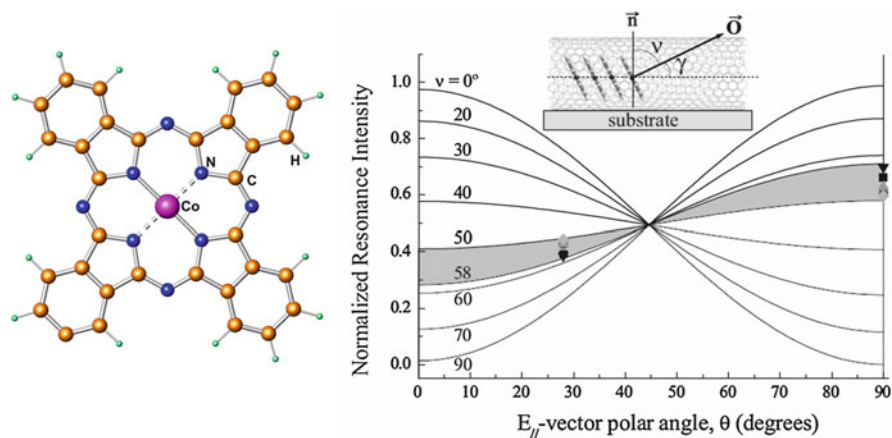
Fig. 4.28 (*Left*) Molecular structure of CoPc and (*right*) parametric curves of the dependence of the normalized, theoretically predicted intensities of the π^* resonance on the angle of incidence with angle ν as parameter. The *symbols* indicate the experimentally determined values. The geometry of the CoPc molecule encapsulated in the nanotube that lies on the substrate is also shown (The *right panel* of the figure is reprinted from Assembly of Cobalt Phthalocyanine Stacks inside Carbon Nanotubes, K. Schulte, J. C. Swarbrick, N. A. Smith, F. Bondino, E. Magnano, and A. N. Khlobystov. Advanced Materials, **19**(20): 3312–3316. © 2007 WILEY-VCH Verlag GmbH and Co. KGaA, Weinheim)

optical absorption and they are used in organic photovoltaic devices. Encapsulation of CoPc in CNTs permits the formation of one-dimensional molecular arrays that allow control of their optical and magnetic properties. Although transmission electron microscopy (TEM) can provide an image of the CNTs and verify the encapsulation of CoPc, the ordering of these planar molecules cannot be verified. In order to explore the N bonding geometry in the molecule, the orientation of the CoPc molecules was studied by means of N–K-edge NEXAFS spectroscopy (see Fig. 4.28). The lower unoccupied molecular orbital π^* is oriented perpendicular to the plane of the CoPc molecule, and since the initial state of the transition is a 1s (with spherical symmetry), it can be represented by a vector $\vec{O}$ normal to the molecule plane. The angular dependence of the resonance's intensity was studied as a function of two angles that determine the orientation of $\vec{O}$ relative to the sample surface, two angles that determine the orientation (inclination and rolling) of the molecule in the nanotube and the angle of incidence of the beam. These equations were simplified on the basis of microscopy observations for the orientation of the nanotubes on the substrate. In this way, the remaining dependence was on the angle of incidence θ and the angle ν formed by the planar molecule and the axis of the nanotube (see inset in Fig. 4.28). The theoretical curves that demonstrate the normalized θ-dependence of the resonance intensity using as parameter the ν angle are shown in Fig. 4.28. From the location of the experimentally determined intensities of the π^* resonance on these curves, the authors determined a ν angle equal to $54 \pm 5°$.

RuO$_2$-coated CNTs are functional nanocomposites that have potential applications as supercapacitors, in fuel cells, catalysts, and biosensors. The interaction of the RuO$_2$ with MWNT was studied with C–K-, O–K- and Ru–L$_3$-edge NEXAFS by Zhou et al. [199]. The results implied that the structure of the nanotube was not disturbed, Ru–O–C bonds were formed between the RuO$_2$ coating and the nanotube, and charge transfer from the RuO$_2$ to the nanotube took place.

Spectromicroscopic techniques were also applied for the study of CNTs. Felten et al. [200, 201] combined scanning transmission X-ray microscopy (STXM) and NEXAFS with a spatial resolution better than 40 nm (which was achieved using a Fresnel zone plate), for the study of individual MWNTs. The transmitted signal was measured with a single-photon counter using a phosphor converter and a high-performance photomultiplier tube. The STXM image can be recorded with beam energy that corresponds to a specific feature of the C 1s spectrum, for example, the 1s $\rightarrow$ π^* or 1s $\rightarrow$ σ^* transitions for sp^2-hybridized C atoms. Comparison of transmission electron microscopy (TEM) images with STXM reveals the type of the CNTs existing in the sample and can be used for easier selection of the sample spot for the acquisition of the NEXAFS spectra, for example, MWNT, carbon nanoparticles, or carbon support grid. In the spectra of the MWNTs, the width of the π^* resonance is smaller compared to the nanoparticles. The different chemical components identified by NEXAFS spectroscopy can be appropriately used to construct chemical maps that reveal the location and amount of each phase in the map. The authors discuss also the differences in the NEXAFS spectra of nanotubes prepared under different synthesis conditions. MWNTs selectively damaged by ion bombardment were also studied through spectromicroscopy by employing linear dichroism, i.e., the angular dependence of the NEXAFS signal. More specifically, the intensity of the π^* resonance is maximized (minimized) when the nanotubes are oriented with their axis perpendicular, $I_\perp$ (parallel, $I_\parallel$), to the polarization vector of the electric field of the beam. The ratio $I_R = I_\parallel/I_\perp$ varies with the defect content of the nanotubes. For a perfect nanotube and for 100 % linearly polarized SR beam, I_R approaches 0, whereas when the tube loses its sp^2 character through bonding with other tubes or loosing C atoms and buckling, I_R increases [202]. Irradiation of nanotubes with Ga$^+$ ions resulted in a higher value of I_R which increased further with the ion fluence. Furthermore, thicker tubes appeared more resistant to irradiation-induced amorphization.

6.5.2 Graphene and Graphene Oxide

Angle-resolved C–K-edge NEXAFS is extensively used for the characterization of graphene. Zhang et al. [203] applied angle-resolved C–K-edge NEXAFS spectroscopy for the study of a single layer of graphene on SiO$_2$. Although the intensity of the π^* resonance (285.5 eV) exhibited a linear dependence on cos$^2\theta$, where θ is the angle of incidence relative to the sample surface, it did not vanish completely at normal incidence indicating significant rippling or corrugation of the layer. Similar observations were reported by Lee et al. [204] for the orientation of a single graphene layer that was grown on Cu and transferred to a SiO$_2$/Si substrate. Although the dichroic ratio of the as-grown layer on Cu was −0.97 (i.e., very close to −1 for a
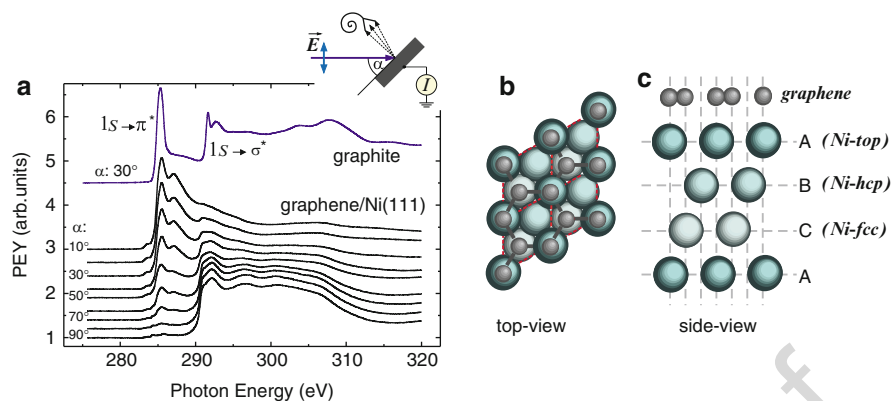
Fig. 4.29 (a) Angular-dependent C–K-edge NEXAFS spectra of graphene/Ni(111) layers compared with the reference spectrum of graphite measured at $\alpha = 30°$ (α is the angle between the incident beam and the sample surface). (b) Top and (c) side view of the top-*fcc* arrangement of carbon atoms in the graphene layer on Ni(111) (Reprinted with permission from M. Weser, Y. Rehder, K. Horn, M. Sicot, M. Fonin, A. B. Preobrajenski, E. N. Voloshina, E. Goering, and Yu. S. Dedkov, Induced magnetism of carbon atoms at the graphene/Ni(111) interface. Appl. Phys. Lett., 2010. **96**(1): 012505.1–012505.3. Copyright 2010, AIP Publishing LLC)

perfectly oriented and corrugation-free graphene layer), after transfer to the SiO_2/Si substrate, it reduced to -0.72. Residuals of the PMMA used for the transfer can be easily detected in the C–K-edge NEXAFS spectra as a strong peak at 288.6 eV. Graphene epitaxially grown on a Ni (111) substrate was also found to be corrugation or ripple-free. In the same paper, angular-dependent measurements were also performed to study the orientation of terephthalic acid molecules on graphene [205]. It should be pointed out that special care for the subtraction of the C–K-edge signal of graphene form that of the terephthalic acid was taken. In addition to the fact that metal substrates, such as Ni, are suitable for the growth of good quality graphene, certain metal/grapheme systems have the potential for other applications as well. For example, Ni(111)/graphene structures are promising for potential applications in spintronics: C–K-edge NEXAFS spectra of graphene on Ni(111) are shown in Fig. 4.29 for various angles of incidence along with the spectrum of a reference graphite sample [206]. The NEXAFS spectra also provide information on the interaction of graphene with the metal atoms. Thus, considerable broadening of the σ^* and π^* resonances was observed in the case of the graphene/Ni (111) and was attributed to the strong orbital hybridization and electron sharing at the graphene/Ni interface. A small shoulder observed in the spectra at 283.7 eV (i.e., below the π^* resonance) was associated with lowering of the Fermi level due to charge transfer. An additional characteristic is the splitting of the π^* resonance (two peaks at 285.5 and 287.1 eV). The splitting was attributed to hybridization of the C p_z with Ni three-dimensional orbital at the interface. In the same paper magnetization of Ni (111) was studied with XMCD measurements. Intercalation of one Fe monolayer between graphene and Ni (111) [207] does not result in the elimination of the second peak

in the π^* region. On the contrary, intercalation of Al causes elimination of the second peak indicating that this thin Al layer effectively decouples the graphene layer from the Ni (111) substrate, thus leading to the nearly free-standing behavior of graphene with small electron doping [208]. Similar splitting, which has been observed in graphene grown on Cu, is less pronounced in double graphene layers compared to single ones [204]. Voloshina et al. [209] applied simulation of the NEXAFS spectra, with various theoretical models, in order to understand the interaction mechanisms between the graphene and the metal.

Formation of interfaces between graphene and ultrathin dielectrics is important in a variety of microelectronic devices. However such interfacing may affect the transport properties of graphene. Schultz et al. [210] employed angle-resolved C–K-edge NEXAFS for the study of graphene on SiO_2 with TiO_2, ZrO_2, HfO_2, or TiN overlayers. The angular dependence of the spectra of the graphene layer on SiO_2 revealed its good orientation. However, deposition of a dielectric on top of graphene reduced the anisotropy of the spectra due to introduction of defects and corrugations. The authors compared the intensity of the π^* resonance for the various dielectrics and proposed that strong covalent bonding took place when a TiN overlayer was used, while only charge redistribution occurred in the case of a HfO_2 overlayer.

Graphene is a zero-gap semiconductor and therefore doping is applied to achieve gap opening. n- and p-doped graphene is a promising material for applications in biosensing, Li-batteries, and fuel cells [211]. Nitrogen is an n-type dopant, but it forms various types of defects when incorporated in graphene. N–K-edge NEXAFS spectra of N-doped graphene (pristine N-doped graphene on Ni(111), decoupled with gold intercalation and quasi-free standing after post-synthesis annealing) are shown in Fig. 4.30. Doping of graphene with N was achieved by introducing NH_3 in the gas flow during the chemical vapor deposition growth of graphene on Cu substrates. As shown in Fig. 4.30, three characteristic peaks appear in the spectra. Peak C, at ~401 eV, that is detected in the spectra of the annealed, Au-intercalated N-doped graphene was attributed to N 1 s $\rightarrow \pi^*$ of N in the graphitic environment. This particular peak gains intensity at grazing incidence. The angular dependence of peak B_1 (~405 eV) was the opposite and thus a σ^* character was assigned to it. Finally, peak A_1 (at ~399 eV) was ascribed to N 1 s $\rightarrow \pi^*$ transition of pyridinic moiety. The incorporation of nitrogen in the graphene layer is verified by the N–K-edge NEXAFS spectra where the peaks at 400.7 and 408 eV exhibit similar angular dependence with the π^* and σ^* peaks of the C–K-edge graphene spectra, respectively [212].

Cl doping was also investigated using C–K-edge NEXAFS. Cl, which is a p-type dopant, introduces a shoulder or a peak at approximately 0.8 eV below the π^* resonance [213].

Haberer et al. studied hydrogenated graphene (H-graphene) [214]. H-graphene exhibited the expected angular dependence of the π^* and σ^* resonances, although the intensity of the π^* resonance was slightly lower due to the formation of C–H bonds which reduced the sp^2 hybridization. The π^* resonance also appeared to have a weak shoulder in its low energy part which was assigned to an electronic state
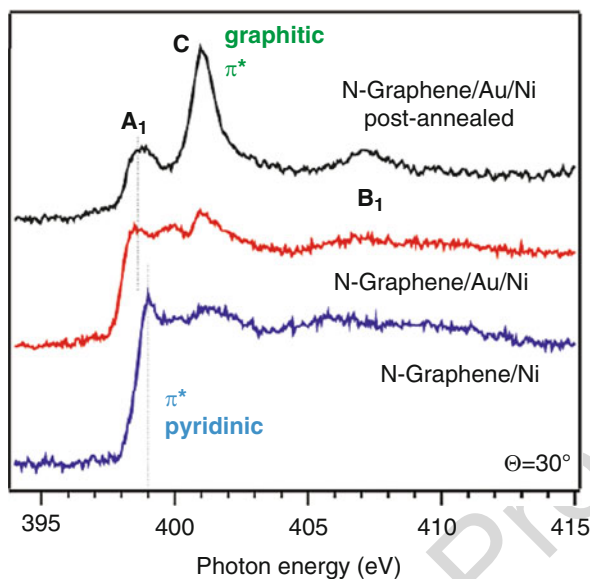
Fig. 4.30 N–K-edge NEXAFS spectra recorded at an angle of 30° between the polarization vector of the photons and the surface normal of N-doped graphene on Ni(111), intercalated with Au and annealed (Reprinted with permission from D. Usachov, O. Vilkov, A Grüneis, D. Haberer, A. Fedorov, V. K. Adamchuk, A. B. Preobrajenski, P. Dudin, A. Barinov, M. Oehzelt, C. Laubschat, and D. V. Vyalikh, Nitrogen-Doped Graphene: Efficient Growth, Structure, and Electronic Properties. Nano Letters 2011, **11**(12): 5401–5407. Copyright (2011), American Chemical Society)

in-between the π and π^* states. The results were verified by tight-binding calcula-
tions. Density functional theory calculations were also performed to simulate the
C–K-edge NEXAFS spectra of graphene and the effect of various defects [215].
Functionalization of graphene layers caused by 1 MeV electron irradiation was
studied by K.-j. Kim et al. [216]. Irradiation resulted in a decrease of the intensity
of the π^* resonance and evolution of resonances at 287.2 and 288.0 eV which were
attributed to C=O, i.e., irradiation resulted in oxidation of the graphene layer.

The effect of growth temperature on the structure of a few-layer graphene, grown
by molecular beam epitaxy, was also investigated using C–K-edge NEXAFS [217].
More specifically, when the growth temperature was 500 °C, only amorphous C
was observed. For temperatures higher than 700 °C, the characteristic π^* and σ^*
resonances evolved and they became sharper upon temperature increase up to
1300 °C. In addition to that, strong contribution from C–O bonds was observed.
Good quality graphene layers were grown on Si, instead of Al_2O_3, substrates, at
800 °C [218]. Graphite flakes consisting of a few graphene layers were investigated
using X-ray transmission imaging at the C–K-edge. The sample was illuminated by
the focused (using a capillary) quasi-monochromatic SR beam. The sample was
imaged by a zone plate objective with a CCD camera and the spatial resolution was
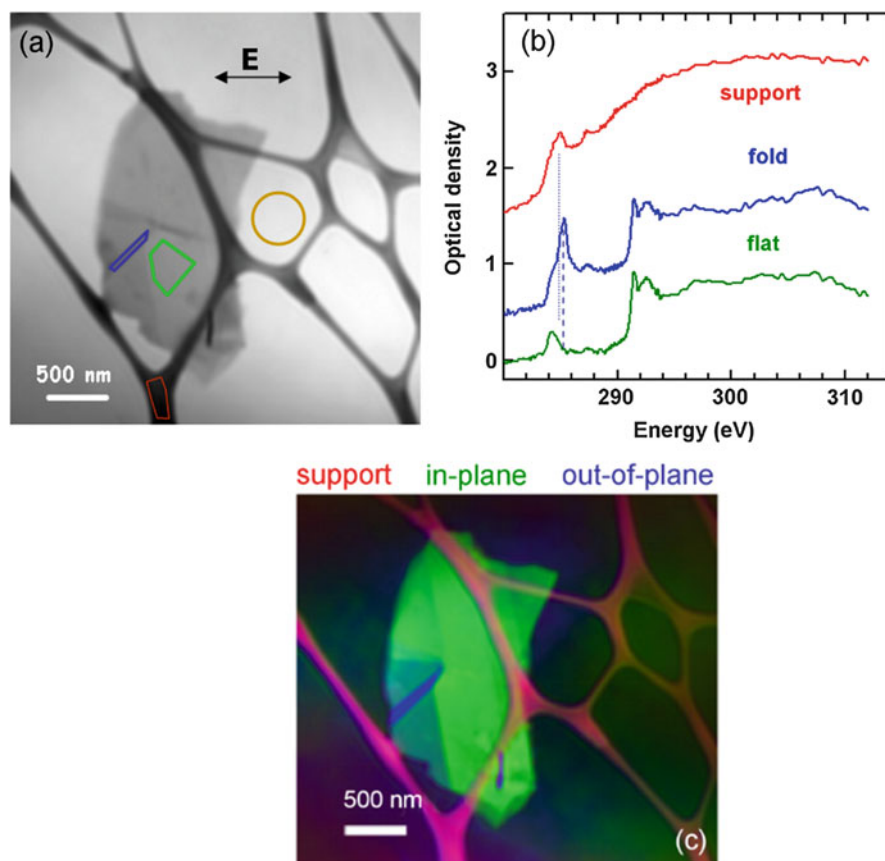
Fig. 4.31 (**a**) Average of aligned STXM images (283–311 eV). (**b**) Spectra extracted from the three regions indicated by the *colored shapes* in (**a**): the spectrum shown in *red* is from the lacey carbon support, and green is from the flat area of the sample, while *blue* is from the folded region. The signal intensity used to convert the measurements to optical density (OD) was taken from the *yellow* circular area. (**c**) Color-coded composite of the maps for lacey carbon (*red*), in plane, σ, (*green*) and out of plane, π, (*blue*), derived from a three-component fit of the carbon K-edge image sequence (Adopted from C. Bittencourt, A. P. Hitchock, X. Ke, G. Van Tendeloo, C. P. Ewels, and P. Guttmann, X-ray absorption spectroscopy by full-field X-ray microscopy of a thin graphite flake: imaging and electronic structure via the carbon K-edge. Beilstein J. Nanotechnol., 2012, **3**:345–350)

approximately 10 nm. Image stacks recorded at different energies in the C–K-edge NEXAFS region revealed variations in the chemical state of C [219]. Since the sample was positioned normal to the beam, flat and folded regions of the flake resulted in C–K-edge NEXAFS spectra with different intensities of the characteristic π* resonance. The spectrum of the lacey carbon support was considerably different. The spectra recorded from different regions are shown in Fig. 4.31b. A component image that shows in red the absorption of the lacey carbon support, in green the "in-

plane" absorption that corresponds to the σ* region, and in blue the "out-of-plane" absorption, which corresponds to the π* absorption, is shown in Fig. 4.31c. The "in-plane" signal is much stronger for the flat part of the graphite flake, whereas the "out-of-plane" signal is stronger for the folded part of the flake. SXTM images of single layer graphene grown by chemical vapor deposition revealed local variations in the intensity of the transmitted light. C–K-edge NEXAFS spectra from different sample spots identified variations in the intensity of the π* resonance. Nonzero intensity of the π* resonance indicates the presence of folds or ripples in the graphene layer [220]. Acquisition of C–K-edge NEXAFS spectra from different spots of a graphene sample, which were preselected from photoemission electron microscopy (PEEM) images, revealed the progressive variation of the spectra with the number of graphene layers [221].

Two-dimensional graphene oxide (GO), exfoliated from oxidized graphite, exhibits a behavior similar to that of a wide-band gap semiconductor. GO–metal oxide nanocomposites are suitable materials for supercapacitor applications. Similar to the case of graphene, the NEXAFS spectra of GO exhibit angular dependence that allow for the determination of the orientation of the O-related defects which give rise to additional peaks. Resonances that appeared at 286.5, 288.7, and 289.6 eV were assigned to π* excitations of C–O, C=O, and –O–C–OH, respectively [222]. The GO spectra were not significantly affected when nanocomposite structures with MnO_2 were formed. Reduction of GO resulted in the disappearance of the peak at 289.6 eV indicating the removal of the hydroxylated species with heat treatment. Reduction resulted also in enhancement of the π* resonance intensity, stronger angular dependence, and sharpening of the peaks in the σ* region indicating that an extended and less defective network was formed. Hybrid catalysts consisting of $MnCo_2O_4$ nanoparticles deposited on N-doped graphene were studied by means of XAFS at the C- and metal-absorption edges [223]. Initially, the metal precursors reacted with mildly oxidized graphene (mGO) and NH_4OH was added to provide the necessary N dopant. Next a hydrothermal treatment step was used to reduce the N-doped mGO and to promote crystallization of the metal nanoparticles. The π* and σ* resonances of graphitic C could be clearly resolved in C–K-edge spectra of the reduced N-doped GO. However, in the corresponding spectra of hybrid catalysts, features with considerable intensity due to C=N (~287.5 eV), O–C=O (~288.5 eV), and C–OH and C–O–C (~289.5 eV) appeared, indicating bonding of O and N to metal atoms in the oxide nanoparticles. Variations were also observed in the N–K-edge NEXAFS spectra where in the hybrid catalysts, enhanced intensity of π* resonance in the range of 398–402 eV (pyridinic, pyrrolic or amino, graphitic N) was observed compared to the spectra of N-doped reduced mGO. These variations were attributed to bonding of N to metal. The authors discussed also the $L_{2,3}$-edge spectra of Mn and Co.

Sulfur-graphene oxide (S–GO) nanocomposites are promising cathode materials for rechargeable Li/S cells. They were studied by means of S–K-, O–K-, and C–K-edge NEXAFS spectra recorded after different numbers of discharge–charge cycles in order to identify variations in the S and C bonding. In the S–K-edge spectra, peaks that correspond to transitions from 1 s to final π* states could be detected. The peaks

due to S–S (2472.2 eV) in elemental sulfur or C–S–S–C bonding in S–GO and due to C–S (2473.7 eV) of S–GO were identified. Acquisition of the spectra after discharge–charge cycles revealed changes that were attributed to loss of elemental S and/or S species bonded to GO, i.e., active S species, as a result of cycling as well as the presence of S^{2-}, SO_3^{2-}, and/or SO_4^{2-}. These products were formed at the expense of the active S species. Changes were also observed in the C–K-edge NEXAFS spectra upon cycling, with the characteristic π^* and σ^* peaks of graphene loosing intensity and giving place to peaks due to CO_3^{2-}, RO^-, and $-CH_2-$. The results supported the formation of lithium carbonate due to the Li/S–GO cell operation. Quantification of the variation of the different species, which could be identified from the NEXAFS spectra as a function of the discharge–charge cycle, was also provided after proper fitting of the spectra [224].

Graphene often results from the reduction of GO that can be exfoliated from oxidized graphite. Hydrothermal reduction of GO to graphene in the temperature range 120–180 °C resulted in partial restoration of the sp^2 bonding and removal of oxygen-containing functional groups [225]. Thermal treatment of GO with urea was also successfully used for the doping of graphene, as it was deduced from NEXAFS measurements at the C–N- and O–K-edges [226]. A C–K-edge NEXAFS study of the reduction of GO with hydrazine hydrate and a GO-paper intercalated with dodecylamine can be found in Ref. [227]. Hydrazine reduction of GO was also studied by Dennis et al. [228]. The observed increase of the π^* resonance intensity upon reduction signified improvement of the short-range order. Significant incorporation of N was observed in the form of pyridine-like and pyrrole-like moieties. Reduction of the oxygen-related species, e.g., epoxide, which can unzip the C–C bonds, took place. Epoxide and carboxyl are functional groups present on the surface of graphene that was obtained from oxidized graphite exfoliation. These groups cause electronic isolation of GO although in a number of applications, they are required since they act as anchoring sites, for example, for catalysts. SXTM images, with spatial resolution 30 nm, of GO reduced by annealing at 1050 °C under Ar flow [229] were recorded with circularly polarized SR light to avoid intensity variations related to local variations in the orientation. The observed intensity variations were assigned to the number of GO layers.

6.6 Nanomaterials and the Environment

The widespread applications of nanoparticles have raised considerable concern about potentially hazardous implications related to their release in the environment. On the other hand, a number of nanomaterials find important environment-friendly applications, e.g., for the removal of toxic elements from the environment, from the drinking water, or for the dissociation of toxic compounds.

6.6.1 Environmental Implications of Nanomaterials

Zn–K-edge XAFS was applied in order to investigate the structural changes in ZnO nanoparticles after their release in the environment and interaction with phosphates
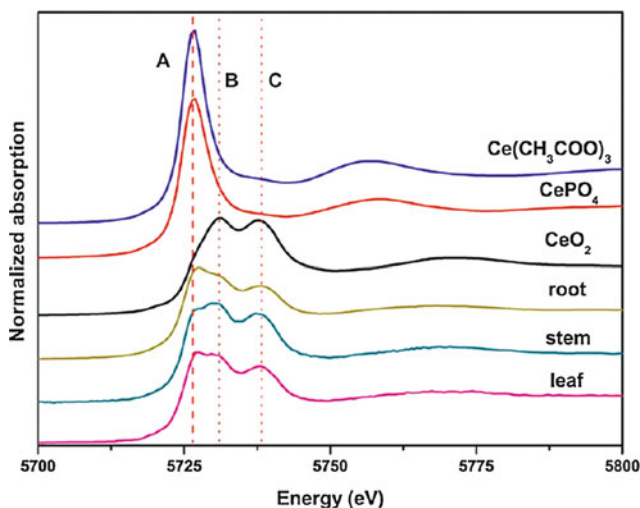
Fig. 4.32 Ce–L$_3$-edge XANES spectra of the root, stem, and leaf of cucumber plants treated with CeO$_2$ nanoparticle solutions for 21 days. *Vertical dashed* and *dotted lines* denote the energy positions of the characteristic peaks of Ce^{3+} (A) and Ce^{4+} (B,C), respectively (Reprinted with permission from P. Zhang, Y. Ma, Z. Zhang, X. He, J. Zhang, Z. Guo, R. Tai, Y. Zhao, and Z. Chai, Biotransformation of Ceria Nanoparticles in Cucumber Plants. ACS Nano, 2012. **6**(11): 9943–9950. Copyright (2012) American Chemical Society)

[230]. The XAFS measurements revealed that with increasing P/Zn ratio and reaction time, the reaction of ZnO nanoparticles with K$_2$HPO$_4$ solutions resulted in gradual transformation of ZnO to Zn$_3$(PO$_4$)$_2$ · 4H$_2$O. The quantification of the two phases was achieved by linear combination fitting of the χ(k) spectra using the spectra of pure compounds, i.e., ZnO and Zn$_3$(PO$_4$)$_2$ · 4H$_2$O.

CeO$_2$ nanoparticles, which are extensively used in biomedical applications, in cosmetics, as polishing materials, as well as in diesel–fuel additives, are considered toxic after their release in the environment. The biotransformation, i.e., biochemical modification by living organisms, of CeO$_2$ nanoparticles was studied by Zhang et al. [231]. The authors investigated the speciation of Ce in cucumber. Most of Ce in the plants accumulated in the roots, with the concentration of Ce in the leaves and stems being similar. The Ce–L$_3$-edge XANES spectra recorded from the root, stem, and leaf of the cucumber plant are shown in Fig. 4.32 along with spectra of reference compounds. The double peak with components denoted by B and C is a fingerprint of Ce^{4+}, whereas peak A is the characteristic of Ce^{3+}. The partial reduction of Ce^{4+} in the CeO$_2$ nanoparticles to Ce^{3+} in the plant can be easily deduced from the spectra, with the Ce^{3+}/Ce^{4+} ratio appearing to be higher in the roots. Linear combination fitting was applied for the determination of the corresponding ratios in various parts of the plant.

Ce was found to retain the form of CeO$_2$ nanoparticles in soybean plants grown in CeO$_2$-nanoparticle contaminated soil, while only a small amount was reduced to Ce^{3+} [232]. In the same study, ZnO nanoparticles were used to contaminate the soil. It was

found that Zn was bonded to O. The Zn–K-edge XANES spectra were well reproduced by a mixture of Zn nitrate and Zn citrate. In both cases, the XAFS spectra were recorded from metal-rich spots which were identified from micro-XRF maps. In a similar study on the uptake of coated CeO_2 nanoparticles by corn plants, significant reduction of Ce^{4+} to Ce^{3+} was not detected in the plant roots [233].

Ti–K-edge XAFS was used to study the accumulation and dissolution of TiO_2 nanoparticles, with diameters ranging from 14 to 655 nm, in wheat plants [234]. The spectra were recoded from Ti-rich plant parts which were identified from micro-XRF images. The spectrum profile and the relative intensity of the components of the pre-edge peak revealed that TiO_2 nanoparticles with anatase and rutile structures do not dissolve and retain their structure in the leaves and the roots of the plant.

Regarding the interaction of nanoparticles with tissues, Vaeronesi et al. [235] investigated the interaction of TiO_2 nanoparticles with cell cultures. More specifically, TiO_2 nanoparticles, with the structure of rutile and size of 21 nm, were incubated in gastric and intestinal fluids, to simulate the effect of gastrointestinal fluids on the structure of the nanoparticles. Micro-XRF was used for the selection of Ti-rich spots from where the XAFS spectra were recorded. Both the EXAFS and XANES spectra of the pristine nanoparticles and those internalized in the cells were similar, indicating that dissolution of the TiO_2 nanoparticles did not occur. The in vitro interaction of 7 nm CeO_2 nanoparticles with human dermal fibroblasts was also investigated and the reactions at the interface of nano-CeO_2 with the fibroblasts were studied with XAFS [236]. Partial reduction from Ce^{4+} to Ce^{3+} was deduced from the Ce–L_3-edge spectra.

6.6.2   Nanosized Adsorbents of Toxic Elements

Nanosized metal oxides are used for the adsorption of toxic elements, for example, As from drinking water. As in natural waters exists in the form of As^{3+} and As^{5+}. Trivalent As is considered as more toxic. The maximum allowed concentration of As in drinking water is 10 μg/l. Nanosized absorbents appear to be more effective compared to their macro-sized counterparts due to their large surface area. The ability of the adsorbents to oxidize As^{3+} to the less toxic As^{5+} and the trapping mechanism of As on the surface of the nanoparticles depend on the oxidation state of As, the chemical composition of the sorbent, and the solute pH. The As–K-edge XANES spectra (Fig. 4.33a) are characterized by a very intense white line whose energy position is a fingerprint of the oxidation state of As. The As–K-edge EXAFS spectra can provide additional information on the oxidation state of As. More specifically, As exists in water in the form of oxyanions. The As–O distance in the case of As^{3+} is longer compared to the corresponding distance in As^{5+}. The presence of further peaks in the Fourier transform (red and blue lines in Fig. 4.33b) is the characteristic of the adsorption of the oxyanion on the surface of the absorbent forming an inner sphere complex. Various modifications have been detected as either bidentate or monodentate, binuclear or mononuclear [237]. Another study was focused on the adsorption of As^{3+} on $Mg(OH)_2$. In this case layered structures by AsO_3 polymer chains (Fig. 4.33b) may be formed [238].
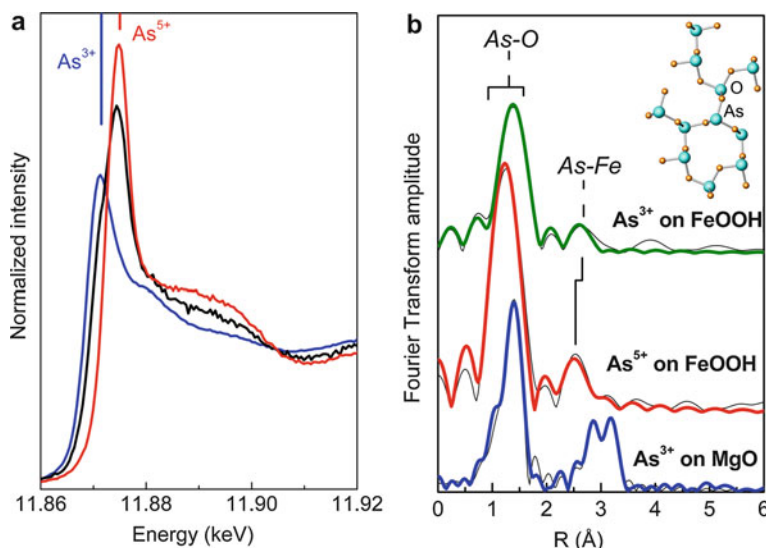
Fig. 4.33 (**a**) As–K-edge XANES spectra of As^{5+} (*red line*) and As^{3+} (*blue line*) adsorbed on nanoporous FeOOH (*red line*) and As^{3+} (*black line*) adsorbed on granular ferric oxide that caused partial oxidation of As. (**b**) Fourier transform of As–K-edge EXAFS signal of As^{3+} and As^{5+} adsorbed on FeOOH or MgO. The latter case is consistent with the formation of layered structures such as As_2O_3 shown in the *inset*. *Black* and *color lines* in (**b**) correspond to experimental and fitting curves, respectively

The efficiency of amorphous TiO_2 and TiO_2 nanoparticles, obtained by calcinations, in the adsorption of As was studied by Jegadeesan et al. [239]. It was found that As^{3+} oxidized to As^{5+} only when TiO_2 was amorphous. EXAFS analysis revealed that both As^{3+} and As^{5+} formed bidentate binuclear complexes. As–K-edge EXAFS study of the adsorption of As^{5+} by γ-alumina nanoparticles disclosed the formation of bidentate binuclear complexes bonded to the octahedra of the Al_2O_3 structure [240].

The As^{5+} trapping in magnetite nanoparticles was studied by means of absorption and precipitation methods [241]. In the adsorption samples, the arsenate (AsO_4) oxyanion was found to form bidentate binuclear complexes. In the precipitation samples and for high As^{5+} loading, the results demonstrated that part of the AsO_4 tetrahedra were incorporated in the magnetite structure. The study of the trapping mechanism of As^{3+} and As^{5+} from green rust $\left[Fe^{2+}_{1-x}Fe^{3+}_x(OH)_2\right](CO_3, Cl, SO_4)$ [242] revealed that oxidation of As^{3+} did not take place. Bidentate binuclear and monodentate mononuclear complexes were detected in the case of As^{5+} with the relative concentration depending on the As loading. Regarding As^{3+}, it was found that As forms dimmers of arsenite pyramids (As_2O_5) which are bonded to the layers of the green rust. Starch-stabilized magnetite nanoparticles were used for As^{5+} adsorption [243]. Starch plays the role of stabilizer of the magnetite nanoparticles,

affecting their size and surface properties. As was found to form bidentate binuclear and monodentate mononuclear complexes.

Since As^{3+} is more toxic than As^{5+}, processes that enhance the transformation of As^{3+} to As^{5+} and/or As retention are of interest for the remediation of As-contaminated groundwater. As–K-edge XANES verified the oxidation of As^{3+} to As^{5+} from magnetite nanoparticles in the presence of O_2. As^{3+} oxidation under similar oxic conditions was also achieved with ferrihydrite nanoparticles but only after addition of an aqueous solution of Fe^{2+} [244]. Oxidation of As^{5+} to As^{3+} and efficient trapping may be achieved by adding Mn (preferably tetravalent) in Fe oxides/hydroxides. Tresintsi et al. [245] studied the adsorption mechanism of As^{3+} and As^{5+} from mixed Fe/Mn oxy-hydroxide adsorbents. The Mn–K- and As–K-edge XANES spectra revealed that the oxidation state of Mn was 4+ and As^{3+} was successfully oxidized to As^{5+} by the Mn ions. The EXAFS analysis demonstrated that the As oxyanions were adsorbed in the bidentate mononuclear geometry, where the AsO_4 tetrahedron shares common edge with the FeO_6 octahedra. Similar observations were reported by Zhang et al. [246] who studied Fe/Mn binary oxides (of the type MnO_x–FeOOH) before and after the adsorption of As. The oxidation state of Mn was found between 3+ and 4+ and it was deduced that it efficiently oxidized As^{3+} to As^{5+}. The arsenate species were trapped in the form of bidentate binuclear complexes. Composite absorbents consisting of magnetite (Fe_3O_4) and Mn_3O_4 were also used for the adsorption of As^{3+} [247]. The As–K-edge XANES spectra disclosed that the adsorbed As was oxidized to As^{5+}, a process attributed to the presence of Mn. The Fe_3O_4 component offered the possibility for magnetic solid/liquid separation. Another application related to the oxidation of contaminant elements by Mn-containing nanoparticles is the oxidation of Sb^{3+} to Sb^{5+} by manganite (γ-MnOOH) nanoparticles, as it was verified by Sb–L_3-edge XANES [248].

Iron oxide nanoparticles have been also considered for the adsorption of other elements which are considered toxic above certain concentrations. The trapping mechanism of Se^{6+} on maghemite nanoparticles was studied with XAFS measurements at the Se–K-edge [249]. Similar to the case of As–K-edge spectra, a white line is present in the XANES spectra recorded at the Se–K-edge. From the position of the white line, it was deduced that the oxidation state of Se did not change after its sorption on the maghemite nanoparticles. EXAFS analysis demonstrated that the selenate tetrahedra formed bidentate binuclear complexes with the two corners of the Fe polyhedra. Nanoparticles produced by ball milling of red mud, a residue generated during the production of Al from bauxite, were used for the study of the trapping mechanism of Cd that is another toxic element [250]. Linear combination fitting of the XANES spectra recorded at the Cd–L_3-edge disclosed the formation of inner sphere complexes of the form XCd(OH) where X represents surface groups of the red mud.

Contamination of water resources by heavy metals, for example, Ni, Pb, and Hg, which are by-products of industrial activities, is also of great concern. Tinanate nanotubes (TNTs) were used for the removal of Ni^{2+} [251]. For low interaction times, only one neighboring shell of Ni, consisting of six O atoms, was detected

indicating that outer sphere complexes were formed via ion exchange with the TNTs. For higher interaction times, contribution of further shells (comprise of both Ti and Ni) was detected, indicating the formation of inner-sphere complexes and precipitates. Increase of the sorption pH promoted the formation of inner sphere complexes at lower interaction times.

7   Conclusions and Future Perspectives

XAFS spectroscopy, carried out using synchrotron radiation beams with beam size that ranges from hundreds of micrometers to few tens of nanometers, is a unique tool for the study of a plethora of materials developed for nanotechnology applications. Although in most of cases the XAFS signal provides average information from a certain sample volume, it is a versatile and attractive technique because it is element specific and nondestructive; it does not rely on the long-range order, as diffraction techniques do; and it is able to obtain signal from small quantities of a variety of materials, e.g., liquids, solids, quantum structures, composites, complexes, diluted samples, and elements that span almost the whole periodic table. The multitude of information that can be obtained is related to symmetry, electronic properties, charge transfer and oxidation state, element-specific magnetic properties, bonding configuration of elements, finite size effects and disorder, chemical effects, etc.

The development of quick-XAFS, with the improvement of acquisition electronics and detectors, offered the possibility to perform dynamical studies in the sub-second scale. The use of dispersive monochromator optics and CCD detectors permits measurements at even shorter time scales. When combined with proper sample environments for in situ characterization, unique information can be obtained on the dynamics of the material synthesis processes and the evolution of chemical reactions. Time-resolved measurements also permit the study of material response upon perturbation, for example, the application of external magnetic fields, laser light, mechanical stress, or mixing with a reactant. Time slicing is a relatively new method that offers sub-picosecond pulses of X-rays for the study of ultrafast phenomena.

Although microspectroscopy techniques enable XAFS measurements and XRF imaging of inhomogeneous samples with beam size of about 1 μm, still the size of the beam is 2–3 orders of magnitude larger than the size of nanomaterials. Toward the improvement of the spatial resolution, spectromicroscopy techniques are developed, where the XANES spectra are reconstructed from X-ray microscopy images with spatial resolution of approximately 50 nm. These images are recorded at different energies that span the XANES spectral region of the element and edge of interest.

Finally, the development of free electron lasers will improve dramatically the spatial and time resolution, thus enhancing the possibilities for advanced and intriguing XAFS-based methods for the study of nanomaterials of various kinds.

References

1. http://xdb.lbl.gov/
2. Ravel B, Newville M (2005) ATHENA, ARTEMIS, HEPHAESTUS: data analysis for x-ray absorption spectroscopy using IFEFFIT. J Synchrotron Radiat 12:537–541
3. Berger MJ, Hubbell JH, Seltzer SM, Chang J, Coursey JS, Sukumar R, Zucker DS, Olsen K Data obtained from the NIST Standard Reference Database XCOM
4. Barth T (1925) Die Kristallstruktur von Perowskit und verwandter Verbindungen. Nor Geol Tidsskr 8:201–216
5. Sevillano E, Meuth H, Rehr JJ (1979) Extended x-ray absorption fine structure Debye-Waller factors. I. Monatomic crystals. Phys Rev B 20(12):4908–4911
6. Dalba G, Fornasini P, Grisenti R, Purans J (1999) Sensitivity of extended x-ray absorption fine structure to thermal expansion. Phys Rev Lett 82(21):4240–4243
7. Bunker G (1983) Application of the ratio method of EXAFS analysis to disordered systems. Nucl Inst Methods B 207(3):437–444
8. Bunker G (2010) Introduction to XAFS: a practical guide to x-ray absorption fine structure spectroscopy. Cambridge University Press, Cambridge
9. Schnohr CS, Ridgway MC (eds) (2015) X-ray absorption spectroscopy of semiconductors. Springer Verlag, Berlin/Heidelberg
10. Teo B (1986) EXAFS: basic principles and data analysis. Springer Verlag, Berlin
11. Koningsberger DC, Prins R (1988) X-ray absorption: principles, applications, techniques of EXAFS, SEXAFS and XANES. Wiley, New York
12. Rehr JJ, Albers RC (2000) Theoretical approaches to x-ray absorption fine structure. Rev Mod Phys 72(3):621–654
13. Stöhr J (1992) NEXAFS spectroscopy. Springer, Heidelberg
14. Chen JG (1997) NEXAFS investigations of transition metal oxides, nitrides, carbides, sulfides and other interstitial compounds. Surf Sci Rep 30(1–3):1–152
15. Rehr JJ, Ankudinov AL (2005) Progress in the theory and interpretation of XANES. Coord Chem Rev 249(1–2):131–140
16. de Groot FMF (1994) X-ray absorption and dichroism of transition metals and their compounds. J Electron Spectrosc Relat Phenom 67(4):529–622
17. Fuggle JC, Inglesfield JE (eds) (1992) Unoccupied electronic states. Springer Verlag, Berlin/Heidelberg
18. Rehr JJ, Albers RC (1990) Scattering-matrix formulation of curved-wave multiple-scattering theory: application to x-ray absorption fine structure. Phys Rev B 41(12):8139–8149
19. Ankudinov AL, Ravel B, Rehr JJ, Conradson SD (1998) Real-space multiple-scattering calculation and interpretation of x-ray-absorption near-edge structure. Phys Rev B 58 (12):7565–7576
20. Kaznatcheev KV, Karunakaran C, Lanke UD, Urquhart SG, Obst M, Hitchcock AP (2007) Soft x-ray spectromicroscopy beamline at the CLS: commissioning results. Nucl Inst Methods A 582(1):96–99
21. Wiedemann H (2003) Synchrotron radiation. Springer, Berlin/Heidelberg
22. Mills DM (2002) Third-generation hard x-ray synchrotron radiation sources. Wiley, New York
23. Mills DM (ed) (2002) X-ray microbeam and microscopy techniques with hard x-rays in third-generation hard x-ray synchrotron radiation sources. Willey, New York
24. Lu K, Stern EA (1983) Size effect of powdered sample on EXAFS amplitude. Nucl Inst Methods 212(1–3):475–478
25. Tröger L, Arvanitis D, Baberschke K, Michaelis H, Grimm U, Zschech E (1992) Full correction of the self-absorption in soft-fluorescence extended x-ray absorption fine structure. Phys Rev B 46(6):3283–3288
26. Janssens KHA, Adams FCV, Rindby A (eds) (2000) Microscopic x-ray fluorescence analysis. Wiley, Chichester

27. Ertl G, Küppers J (1974) Low-energy electrons and surface chemistry. In: Monographs in modern chemistry, vol 4. Verlag Chemie, Weinheim

28. Krause MO (1979) Atomic radiative and radiationless yields for K and L shells. J Phys Chem Ref Data 8(2):307–327

29. Dent AJ (2002) Development of time-resolved XAFS instrumentation for quick EXAFS and energy-dispersive EXAFS measurements on catalyst systems. Top Catal 18(1–2): 27–35

30. Pascarelli S, Mathon O (2010) Advances in high brilliance energy dispersive x-ray absorption spectroscopy. Phys Chem Chem Phys 12(21):5535–5546

31. Grunwaldt J-D, Caravati M, Hannemann S, Beiker A (2004) X-ray absorption spectroscopy under reaction conditions: suitability of different reaction cells for combined catalyst characterization and time-resolved studies. Phys Chem Chem Phys 6(11):3037–3047

32. Webatoms Database, http://cars9.uchicago.edu/cgi-bin/atoms/atoms.cgi

33. American Mineralogist Crystal Structure Database, http://rruff.geo.arizona.edu/AMS/amcsd.php

34. The Landolt-Börnstein Database, http://www.springermaterials.com/

35. Crystallography Open Database, www.crystallography.net

36. Wyckoff RWG (1963) Crystal structures, vol 1, 2nd edn. Wiley, New York; Wyckoff RWG (1964) Crystal structures: inorganic compounds RX_n, R_nMX_2, R_nMX_3, vol 2, 2nd edn. Interscience Publishers, New York; Wyckoff RWG (1965) Crystal structures: $R_x(MX_4)_y$, $R_x(M_nX_p)_y$, hydrates and ammoniates, vol 3, 2nd edn. Interscience Publishers, New York; Wyckoff RWG (1968) Crystal structures: miscellaneous inorganic compounds, silicates, and basic structural information, vol 4, 2nd edn. Wiley Interscience, Chichester, New York

37. Tomić S, Searle BG, Wander A, Harrison NM, Dent AJ, Mosselmans JFW, Inglesfield JE (2004) New tools for the analysis of EXAFS: the DL_EXCURV package. Council for the Central Laboratory of the Research Councils, CCLRC technical report DL-TR-2005-001, pp 1–12

38. Binsted N, Cook SL, Evans J, Neville Greaves G, Price RJ (1987) EXAFS and near-edge structure in the cobalt K-edge absorption spectra of metal carbonyl complexes. J Am Chem Soc 109(12):3669–3676

39. Ankudinov AL, Rehr JJ (1997) Relativistic spin-dependent x-ray absorption theory. Phys Rev B 56(4):R1712–R1715

40. Di Cicco A (ed) (2009) GNXAS. Extended suite of programs for advanced X-ray absorption data-analysis: methodology and practice. Task, Gdansk

41. Filipponi A, Di Cicco A, Natoli CR (1995) X-ray-absorption spectroscopy and n-body distribution functions in condensed matter. I. Theory. Phys Rev B 52(21):15122–15134

42. de Groot F (2005) Multiplet effects in x-ray spectroscopy. Coord Chem Rev 249 (1–2):31–63

43. Benfatto M, Della Longa S, Natoli CR (2003) The MXAN procedure: a new method for analysing the XANES spectra of metallo-proteins to obtain structural quantitative information. J Synchrotron Radiat 10(Pt. 1):51–57

44. Greegor RB, Lylte FW (1980) Morphology of supported metal clusters: determination by EXAFS and chemisorption. J Catal 63(2):476–486

45. de Panfilis S, d'Acapito F, Haas V, Konrad H, Weissüller J, Boscherini F (1995) Local structure and size effects in nanophase palladium: an X-ray absorption study. Phys Lett A 201(6):397–403

46. Borowski M (1997) Size determination of small Cu-clusters by EXAFS. J Phys IV France 7 (C2):259–260

47. Traverse A (1998) X-ray absorption spectroscopy to study metallic clusters. New J Chem 22 (7):677–683

48. Frenkel AI, Yevick A, Cooper C, Vasic R (2011) Modeling the structure and composition of nanoparticles by extended x-ray absorption fine-structure spectroscopy. Annu Rev Anal Chem 4:23–39

49. Kuzmin A, Chaboy J (2014) EXAFS and XANES analysis of oxides at the nanoscale. Int Union Crystallogr J 1(Pt. 6):571–589

50. Brice-Profeta S, Arrio M-A, Tronc E, Menguy N, Letard I, Cartier dit Moulin C, Nogués M, Chanéac C, Jolivet J-P, Sainctavit P (2005) Magnetic order in γ-Fe_2O_3 nanoparticles: a XMCD study. J Magn Magn Mater 288:354–365

51. Katsikini M, Paloura EC, Moustakas TD (1998) Experimental determination of the N-p-partial density of states in the conduction band of GaN: determination of the polytype fractions in mixed phase samples. J Appl Phys 83(3):1437–1445

52. Sobczak JW, Sobczak E, Drelinkiewicz A, Hasik M, Wenda E (2004) Local structure of a Pd-doped polymer investigated using a linear combination of XANES spectra. J Alloys Compd 362(1–2):162–166

53. McNeill CR, Ade H (2013) Soft X-ray characterisation of organic semiconductor films. J Mater Chem C 1(2):187–201

54. Parratt LG (1959) Electronic band structure of solids by X-ray spectroscopy. Rev Mod Phys 31 (3):616–645

55. Pinakidou F, Katsikini M, Paloura EC (2007) On the thermal stability of vitrified industrial wastes using microscale synchrotron radiation based techniques. J Appl Phys 102 (11):113512.1–113512.11

56. Westre TE, Kennepohl P, DeWitt JG, Hedman B, Hodgson KO, Solomon EI (1997) A multiplet analysis of Fe K-Edge 1s → 3d pre-edge features of iron complexes. J Am Chem Soc 119(27):6297–6314

57. Wilke M, Frarges F, Petit P-E, Brown GE, Martin F (2001) Oxidation state and coordination of Fe in minerals: an Fe-XANES spectroscopic study. Am Mineral 86(5–6):714–730

58. Chalmin E, Farges F, Brown GE Jr (2009) A pre-edge analysis of Mn K-edge XANES spectra to help determine the speciation of manganese in minerals and glasses. Contrib Mineral Petrol 157(1):111–126

59. Katsikini M, Pinakidou F, Paloura EC, Wendler E, Wesch W, Manzke R (2009) N–K edge NEXAFS study of the defects induced by indium implantation in GaN. J Phys Conf Ser 190 (1):012065.1–012065.4

60. Waychunas GA, Fuller CC, Davis JA, Rehr JJ (2003) Surface complexation and precipitate geometry for aqueous Zn(II) sorption on ferrihydrite: II. XANES analysis and simulation. Geochim Cosmochim Acta 67(5):1031–1043

61. Katsikini M, Pinakidou F, Paloura EC, Boscherini F (2007) Modification of the N bonding environment in GaN after high-dose Si implantation: an x-ray absorption study. J Appl Phys 101(8):083510.1–083510.9

62. Qi B, Perez I, Ansari PH, Lu F, Croft M (1987) L_2 and L_3 measurements of transition metal 5d orbital occupancy, spin-orbit effects, and chemical bonding. Phys Rev B 36(5):R2972–R2975

63. Bare SR, Ressler T (2009) Chapter 6: characterization of catalysts in reactive atmospheres by X-ray absorption spectroscopy. In: Gates BC, Knözinger H (eds) Advances in Catalysis, vol 52. Academic, Amsterdam, pp 339–465

64. Gross E, Dean Toste F, Somorjai GA (2015) Polymer-encapsulated metallic nanoparticles as a bridge between homogeneous and heterogeneous catalysis. Catal Lett 145(1):126–138

65. Witkowska A, Greco G, Dsoke S, Marassi R, Di Cicco A (2014) Structural change of carbon supported Pt nanocatalyst subjected to a step-like potential cycling in PEM FC. J Non Cryst Solids 401:169–174

66. Witkowska A, Di Cicco A, Principi E (2007) Local ordering of nanostructured Pt probed by multiple-scattering XAFS. Phys Rev B 76(10):104110.1–104110.12

67. Shishido T, Nasu H, Deng L, Teramrua K, Tanaka T (2013) Study of formation process of metal nanoparticles on metal oxides by in-situ XAFS technique. J Phys Conf Ser 430:012060.1–012060.4

68. Asakura H, Teramura K, Shishido T, Tanaka T, Yan N, Xiao C, Yao S, Kou Y (2012) In situ time-resolved DXAFS study of Rh nanoparticle formation mechanism in ethylene glycol at elevated temperature. Phys Chem Chem Phys 14(9):2983–2990

69. Nishimura S, Takagaki A, Maenosono S, Ebitani K (2010) In situ time-resolved XAFS study on the formation mechanism of Cu nanoparticles using poly(N-vinyl-2-pyrrolidone) as a capping agent. Langmuir 26(6):4473–4479

70. Harada M, Inada Y (2009) In situ time-resolved XAFS studies of metal particle formation by photoreduction in polymer solutions. Langmuir 25(11):6049–6061

71. Shimizu K, Ohshima K, Tai Y, Tamura M, Satsuma A (2012) Size- and support-dependent selective amine cross-coupling with platinum nanocluster catalysts. Catal Sci Technol 2 (4):730–738

72. Shimizu K-i, Sugino K, Sawabe K, Satsuma A (2009) Oxidant-free dehydrogenation of alcohols heterogeneously catalyzed by cooperation of silver clusters and acid–base sites on alumina. Chem Eur J 15(10):2341–2351

73. Kuroda Y, Mori T, Sugiyama H, Uozumi Y, Ikeda K, Itadani A, Nagao M (2009) On the possibility of AgZSM-5 zeolite being a partial oxidation catalyst for methane. J Colloid Interface Sci 333(1):294–299

74. Miller JT, Kropf AJ, Zhac Y, Regalbuto JR, Delannoy L, Louis C, Bus E, van Bokhoven JA (2006) The effect of gold particle size on Au–Au bond length and reactivity toward oxygen in supported catalysts. J Catal 240(2):222–234

75. Kroner AB, Newton MA, Tromp M, Russell AE, Dent AJ, Evans J (2013) Structural characterization of alumina-supported Rh catalysts: effects of ceriation and zirconiation by using metal–organic precursors. ChemPhysChem 14(15):3606–3617

76. Einaga H, Kawarada J, Kimura K, Teraoka Y (2014) Preparation of platinum nanoparticles on TiO_2 from DNA-protected particles. Colloids Surf A 455:179–184

77. Yancey DF, Chill ST, Zhang L, Frenkel AI, Henkelman G, Crooks RM (2013) A theoretical and experimental examination of systematic ligand-induced disorder in Au dendrimer-encapsulated nanoparticles. Chem Sci 4(7):2912–2921

78. Roscioni OM, Zonias N, Price SWT, Russell AE, Comaschi T, Skylaris C-K (2011) Computational prediction of L_3 EXAFS spectra of gold nanoparticles from classical molecular dynamics simulations. Phys Rev B 83(11):115409.1–115409.18

79. Price SWT, Zonias N, Skylaris C-K, Hyde TI, Ravel B, Russell AE (2012) Fitting EXAFS data using molecular dynamics outputs and a histogram approach. Phys Rev B 85 (7):075439.1–075439.14

80. Christensen ST, Feng H, Libera JL, Guo N, Miller JT, Stair PC, Elam JW (2010) Supported Ru–Pt bimetallic nanoparticle catalysts prepared by atomic layer deposition. Nano Lett 10 (8):3047–3051

81. Wang H, Miller JT, Shakouri M, Xi C, Wu T, Zhao H, Cem Akatay M (2013) XANES and EXAFS studies on metal nanoparticle growth and bimetallic interaction of Ni-based catalysts for CO_2 reforming of CH_4. Catal Today 207:3–12

82. de Graaf J, van Dillen AJ, de Jong KP, Koningsberger DC (2001) Preparation of highly dispersed Pt particles in zeolite Y with a narrow particle size distribution: characterization by hydrogen chemisorption, TEM, EXAFS spectroscopy, and particle modelling. J Catal 203 (2):307–321

83. Kitagawa H, Ichikuni N, Okuno H, Hara T, Shimazu S (2014) XAFS and HAADF STEM combined characterization for size regulated Ni nanocluster catalyst and its unique size dependence for water gas shift reaction. Appl Catal A 478:66–70

84. Thole BT, Carra P, Sette F, van der Laan G (1992) X-ray circular dichroism as a probe of orbital magnetization. Phys Rev Lett 68(12):1943–1946

85. Carra P, Thole BT, Altarelli M, Wang X (1993) X-ray circular dichroism and local magnetic fields. Phys Rev Lett 70(5):695–697

86. Stöhr J, König H (1995) Determination of spin- and orbital-moment anisotropies in transition metals by angle-dependent x-ray magnetic circular dichroism. Phys Rev Lett 75(20): 3748–3751

87. Torchio R, Meneghini C, Mobilio S, Capellini G, Garcia Prieto A, Alonso J, Fdez-Gubieda ML, Turco Liveri V, Longo A, Ruggirello AM, Neisius T (2010) Microstructure and magnetic properties of colloidal cobalt nano-clusters. J Magn Magn Mater 322(21):3565–3571

88. Dupuis V, Blanc N, Diaz-Sanchez LE, Hillion A, Tamion A, Tournus F, Pastor GM, Rogalev A, Wilhelm F (2013) Finite size effects on structure and magnetism in mass-selected CoPt nanoparticles. Eur Phys J D 67(2):1–4

89. Han L, Wiedwald U, Biskupek J, Fauth K, Kaiser U, Ziemann P (2011) Nanoscaled alloy formation from self-assembled elemental Co nanoparticles on top of Pt films. Beilstein J Nanotechnol 2:473–485

90. Alba Venero D, Fernández Barquín L, Alonso J, Fdez-Gubieda ML, Rodríguez Fernández L, Boada R, Chaboy J (2013) Magnetic disorder in diluted Fe_xM_{100-x} granular thin films (M = Au, Ag, Cu; x < 10 at.%). J Phys Condens Matter 25(27):276001.1–276001.10

91. Schmitz-Antoniak C (2013) Characterisation of FePt nanomagnets by x-ray absorption spectroscopy. Phys Status Solidi A 210(7):1298–1304

92. Chang S-J, Yang C-Y, Ma H-C, Tseng Y-C (2013) Complex magnetic interactions and charge transfer effects in highly ordered Ni_xFe_{1-x} nano-wires. J Magn Magn Mater 332:21–27

93. Barthem VMTS, Rogalev A, Wilhelm F, Sant' Anna MM, Mello SLA, Zhang Y, Bayle-Guillemaud P, Givord D (2012) Spin fluctuations of paramagnetic Rh clusters revealed by x-ray magnetic circular dichroism. Phys Rev Lett 109(19):197204.1–197204.5

94. Selenska-Pobell S, Reitz T, Schönemann R, Herrmansdörfer T, Merroun M, Geißler A, Bartolomé J, Bartolomé F, García LM, Wilhelm F, Rogalev A (2011) Magnetic Au nanoparticles on archaeal S-layer ghosts as templates. Nanomater Nanotechnol 1(2):8–16

95. Suturin M, Fedorov VV, Banshchikov AG, Baranov DA, Koshmak KV, Torelli P, Fujii J, Panaccione G, Amemiya K, Sakamaki M, Nakamura T, Tabuchi M, Pasquali L, Sokolov NS (2013) Proximity effects and exchange bias in $Co/MnF_2(111)$ heterostructures studied by X-ray magnetic circular dichroism. J Phys Condens Matter 25(4):046002.1–046002.9

96. Gridneva L, Persson A, Niño MÁ, Camarero J, de Miguel JJ, Miranda R, Hofer C, Teichert C, Bobek T, Locatelli A, Heun S, Carlsson S, Arvanitis D (2008) Experimental investigation of the spin reorientation of Co/Au based magnetic nanodot arrays. Phys Rev B 77 (10):104425.1–104425.9

97. Harada M, Inada Y, Nomura M (2009) In situ time-resolved XAFS analysis of silver particle formation by photoreduction in polymer solutions. J Colloid Interface Sci 337 (2):427–438

98. Ma J, Zou Y, Jiang Z, Huang W, Li J, Wu G, Huang Y, Xu H (2013) An in situ XAFS study – the formation mechanism of gold nanoparticles from X-ray-irradiated ionic liquid. Phys Chem Chem Phys 15(28):11904–11908

99. Haug J, Dubiel M, Kruth H, Hofmeister H (2009) Structural characterization of bimetallic Ag–Au nanoparticles in glass. J Phys Conf Ser 190(1):012124.1–0.12124.4

100. Chen HM, Liu RS, Jang L-Y, Lee J-F, Hu SF (2006) Characterization of core–shell type and alloy Ag/Au bimetallic clusters by using extended x-ray absorption fine structure spectroscopy. Chem Phys Lett 421(1–3):118–123

101. Padovani S, Puzzovio D, Sada C, Mazzoldi P, Borgia I, Sgamellotti A, Brunetti BG, Cartechini L, D' Acapito F, Maurizio C, Shokoui F, Oliaiy P, Rahighi J, Lamehi-Rachti M, Pantos E (2006) XAFS study of copper and silver nanoparticles in glazes of medieval middle-east lusterware (10th–13th century). Appl Phys A 83(4):521–528

102. Smith AD, Pradell T, Roqué J, Molera J, Vendrell-Saz M, Dent AJ, Pantos E (2006) Color variations in 13th century hispanic lustre – an EXAFS study. J Non Cryst Solids 352 (50–51):5353–5361

103. Karatutlu A, Little WR, Sapelkin AV, Dent A, Mosselmans F, Cibin G, Taylor R (2013) OD-XAS and EXAFS: structure and luminescence in Ge quantum dots. J Phys Conf Ser 430 (012026):1–6

104. Erenburg SB, Trubina SV, Bausk NV, Nikiforov AI, Dvurechenskii AV, Mansurov VG, Zhuravlev KS, Nikitenko SG (2011) The microstructure of vertically coupled quantum dots ensembles by EXAFS spectroscopy. J Surf Invest 5(5):856–862

105. Piskorska-Hommel E, Holý V, Caha O, Wolska A, Gust A, Kruse C, Kröncke H, Falta J, Hommel D (2012) Complementary information on CdSe/ZnSe quantum dot local structure from extended x-ray absorption fine structure and diffraction anomalous fine structure measurements. J Alloys Compd 523:155–160

106. Demchenko IN, Chernyshova M, He X, Minikayev R, Syryanyy Y, Derkachova A, Derkachov G, Stolte WC, Piskorska-Hommel E, Reszka A, Liang H (2013) XANES: observation of quantum confinement in the conduction band of colloidal PbS quantum dots. J Phys Conf Ser 430(1):012030.1–012030.5

107. Wright JT, Meulenberg RW (2012) Modification of the conduction band edge energy via hybridization in quantum dots. Appl Phys Lett 101(19):193104.1–193104.3

108. Lee JRI, Meulenberg RW, Hanif KM, Mattoussi H, Klepeis JE, Terminello LJ, van Buuren T (2007) Experimental observation of quantum confinement in the conduction band of CdSe quantum dots. Phys Rev Lett 98(14):146803.1–146803.4

109. Wright JT, Meulenberg RW (2013) Effects of dopants on the band structure of quantum dots: a theoretical and experimental study. Phys Rev B 88(4):045432.1–045432.8

110. Chen L-Y, Chen C-H, Tseng C-H, Laia F-L, Hwang B-J (2011) Synthesis $CdSe_xS_{1-x}$ core/shell type quantum dots via one injection methods. Chem Commun 47(5):1592–1594

111. Chen L-Y, Yang P-A, Tseng C-H, Hwang B-J, Chen C-H (2012) Internal structure of tunable ternary $CdSe_xS_{1-x}$ quantum dots unravelled by x-ray absorption spectroscopy. Appl Phys Lett 100(16):163113.1–163113.3

112. Limpijumnong S, Jutimoosik J, Palakawong N, Klysubun W, Nukeaw J, Du M-H, Rujirawat S (2011) Determination of miscibility in MgO-ZnO nanocrystal alloys by x-ray absorption spectroscopy. Appl Phys Lett 99(26):126014.1–126014.1

113. Murphy MW, Zhou XT, Ko JYP, Zhou JG, Heigl F, Shamd TK (2009) Optical emission of biaxial ZnO–ZnS nanoribbon heterostructures. J Phys 130(8):084707.1–084707.8

114. Rammutla KE, Chadwick AV, Harding J, Sayle DC, Erasmus RM (2010) EXAFS and Raman scattering studies of Y and Zr doped nano-crystalline tin oxide. J Phys Conf Ser 249 (1):012054.1–012054.5

115. Segura-Ruiz J, Martínez-Criado G, Denker C, Malindretos J, Rizzi A (2014) Phase separation in single $In_xGa_{1-x}N$ nanowires revealed through a hard X-ray synchrotron nanoprobe. Nano Lett 14(3):1300–1305

116. Martínez-Criado G, Segura-Ruiz J, Chu M-H, Tucoulou R, López I, Nogales E, Mendez B, Piqueras J (2014) Crossed Ga_2O_3/SnO_2 multiwire architecture: a local structure study with nanometer resolution. Nano Lett 14(10):5479–5487

117. Wang SL, Chen L, Meng KK, Xu PF, Meng HJ, Lu J, Yan WS, Zhao JH (2010) Origin of ferromagnetism in self-assembled $Ga_{1-x}Mn_xAs$ quantum dots grown on Si. Appl Phys Lett 97 (24):242505).11–3242505).1

118. Kim HS, Cho YJ, Kong KJ, Kim CH, Chung GB, Park J, Kim J-Y, Yoon J, Jung M-H, Jo Y, Kim B, Ahn J-P (2009) Room-temperature ferromagnetic $Ga_{1-x}Mn_xAs$ ($x \leq 0.05$) nanowires: dependence of electronic structures and magnetic properties on Mn content. Chem Mater 21 (6):1137–1143

119. Seong H-K, Kim U, Kim M-H, Lee H-H, Lee D-R, Kim J-Y, Choi H-J (2009) Structural and chemical characterization of Mn doped GaN nanowires by X-ray absorption spectroscopy. J Nanosci Nanotechnol 9(11):6772–6776

120. Hegde M, Farvid SS, Hosein ID, Radovanovic PV (2011) Tuning manganese dopant spin interactions in single GaN nanowires at room temperature. ACS Nano 5(8):6365–6373

121. Zheng W, Singh K, Wang Z, Wright JT, van Tol J, Dalal NS, Meulenberg RW, Strouse GF (2012) Evidence of a $ZnCr_2Se_4$ spinel inclusion at the core of a Cr-Doped ZnSe quantum dot. J Am Chem Soc 134(12):5577–5585

122. Kumar S, Kim YJ, Koo BH, Sharma SK, Vargas JM, Knobel M, Gautam S, Chae KH, Kim DK, Kim YK, Lee CG (2009) Structural and magnetic properties of chemically synthesized Fe doped ZnO. J Appl Phys 105(7):07C520.1–07C520.3

123. Gautam S, Kumar S, Thakur P, Chae KH, Kumar R, Koo BH, Lee CG (2009) Electronic structure studies of Fe-doped ZnO nanorods by x-ray absorption fine structure. J Phys D Appl Phys 42(17):175406.1–175406.7

124. Segura-Ruiz J, Martínez-Criado G, Chu MH, Geburt S, Ronning C (2011) Nano-X-ray absorption spectroscopy of single Co-implanted ZnO nanowires. Nano Lett 11 (12):5322–5326

125. Guglieri C, Laguna-Marco MA, García MA, Carmona N, Céspedes E, García-Hernández M, Espinosa A, Chaboy J (2012) XMCD proof of ferromagnetic behavior in ZnO nanoparticles. J Phys Chem C 116(11):6608–6614

126. Ueno N, Nakanishi K, Ohta T, Egashira Y, Nishiyama N (2012) Low-temperature synthesis of ZnO nanorods using organic–inorganic composite as a seed layer. Thin Solid Films 520 (14–15):4291–4296

127. Briois V, Giorgetti C, Dartyge E, Baudelet F, Tokumoto MS, Pulcinelli SH, Santilli CV (2006) In situ and simultaneous nanostructural and spectroscopic studies of ZnO nanoparticle and Zn-HDS formations from hydrolysis of ethanolic zinc acetate solutions induced by water. J Sol-Gel Sci Technol 39(1):25–36

128. Caetano BL, Santillia CV, Pulcinellia SH, Briois V (2011) SAXS and UV-vis combined to Quick-XAFS monitoring of ZnO nanoparticles formation and growth. Phase Transit 84 (8):714–725

129. Song J, Zhang J, Xie Z, Wei S, Pan Z, Hub T, Xie Y (2010) In situ XAFS studies on the growth of ZnSe quantum dots. Nucl Inst Methods A 619(1–3):280–282

130. Fellowes JW, Pattrick RAD, Lloyd JR, Charnock JM, Coker VS, Mosselmans JFW, Weng T-C, Pearce CI (2013) Ex situ formation of metal selenide quantum dots using bacterially derived selenide precursors. Nanotechnology 24(14):145603.1–145603.10

131. Lu P, Zhang H, Satoh T, Ohkubo T, Yamazaki A, Takano K, Kamiya T, Zhu L, Huang Y, Jiang Z, Zheng Y, Yang M, Mi Y, Ren Q, Shen H (2011) Investigation on the stability of water-soluble ZnO quantum dots in KB cells by X-ray fluorescence and absorption methods. Nucl Inst Methods B 269:1940–1943

132. Protesescu L, Rossini AJ, Kriegner D, Valla M, de Kergommeaux A, Walter M, Kravchyk KV, Nachtegaal M, Stangl J, Malaman B, Reiss P, Lesage A, Emsley L, Copéret C, Kovalenko MV (2014) Unraveling the core_shell structure of ligand-capped Sn/SnO$_x$ nanoparticles by surface-enhanced nuclear magnetic resonance, Mössbauer, and x-ray absorption spectroscopies. ACS Nano 8(3):2639–2648

133. Chen CH, Hwang BJ, Do JS, Weng JH, Venkateswarlu M, Cheng MY, Santhanam R, Ragavendran K, Lee JF, Chen JM, Liu DG (2010) An understanding of anomalous capacity of nano-sized CoO anode materials for advanced Li-ion battery. Electrochem Commun 12:496–498

134. Zhong K, Zhang B, Luo S, Wen W, Li H, Huang X, Chen L (2011) Investigation on porous MnO microsphere anode for lithium ion batteries. J Power Sources 196(16):6802–6808

135. Frey K, Iablokov V, Sáfrán G, Osán J, Sajó I, Szukiewicz R, Chenakin S, Kruse N (2012) Nanostructured MnO$_x$ as highly active catalyst for CO oxidation. J Catal 287:30–36

136. Ma S-B, Nam K-W, Yoon W-S, Yang X-Q, Ahn K-Y, Oh K-H, Kim K-B (2008) Electro-chemical properties of manganese oxide coated onto carbon nanotubes for energy-storage applications. J Power Sources 178(1):483–489

137. Ha H-W, Hwang S-J (2010) Improvement of electrochemical performance of tin dioxide negative electrode materials upon cobalt substitution. Electrochim Acta 55(6):2841–2847

138. Choi A, Palanisamy K, Kim Y, Yoon J, Park J-H, Lee SW, Yoon W-S, Kim K-B (2014) Microwave-assisted hydrothermal synthesis of electrochemically active nano-sized Li$_2$MnO$_3$ dispersed on carbon nanotube network for lithium ion batteries. J Alloys Compd 591:356–361

139. Kim CH, Jung YS, Lee KT, Ku JH, Oh SM (2009) The role of in situ generated nano-sized metal particles on the coulombic efficiency of MGeO₃ (M═Cu, Fe, and Co) electrodes. Electrochim Acta 54(18):4371–4377

140. Woo MA, Kim TW, Kim IY, Hwang S-J (2011) Synthesis and lithium electrode application of ZnO–ZnFe₂O₄ nanocomposites and porously assembled ZnFe₂O₄ nanoparticles. Solid State Ion 182(1):91–97

141. Koziej D, Rossell MD, Ludi B, Hintennach A, Novák P, Grunwaldt J-D, Niederberger M (2011) Interplay between size and crystal structure of molybdenum dioxide nanoparticles – synthesis, growth mechanism, and electrochemical performance. Small 7(3):377–387

142. Mao Y, Kong Q, Guo B, Shen L, Wang Z, Chen L (2013) Polypyrrole–NiO composite as high-performance lithium storage material. Electrochim Acta 105:162–169

143. Zhou JG, Fang HT, Maley JM, Murphy MW, Peter Ko JY, Cutler JN, Sammynaiken R, Sham TK, Liue M, Li F (2009) Electronic structure of TiO2 nanotube arrays from x-ray absorption near edge structure studies. J Mater Chem 19:6804–6809

144. Akgul G, Aksoy Akgul F, Attenkofer K, Winterer M (2013) Structural properties of zinc oxide and titanium dioxide nanoparticles prepared by chemical vapor synthesis. J Alloys Compd 554:177–181

145. Yu Liao C, Wang S-T, Chang F-C, Wang HP, Lin H-P (2014) Preparation of TiO₂ hollow spheres for DSSC photoanodes. J Phys Chem Solids 75(1):38–41

146. Kityakarn S, Worayingyong A, Suramitr A, Smith MF (2013) Ce-doped nanoparticles of TiO₂: rutile-to-brookite phase transition and evolution of Ce local-structure studied with XRD and XANES. Mater Chem Phys 139(2–3):543–549

147. Doong R-a, Chang S-m, Tsai C-w (2013) Enhanced photoactivity of Cu-deposited titanate nanotubes for removal of bisphenol A. Appl Catal B 129:48–55

148. Mourão HAJL, Avansi Junior W, Ribeiro C (2012) Hydrothermal synthesis of Ti oxide nanostructures and TiO₂:SnO₂ heterostructures applied to the photodegradation of rhodamine B. Mater Chem Phys 135(2–3):524–532

149. Suwanchawalit C, Wongnawa S, Sriprang P, Meanha P (2012) Enhancement of the photocatalytic performance of Ag-modified TiO₂ photocatalyst under visible light. Ceram Int 38(6):5201–5207

150. He R, Hocking RK, Tsuzuki T (2012) Co-doped ZnO nanopowders: location of cobalt and reduction in photocatalytic activity. Mater Chem Phys 132(2–3):1035–1040

151. Bergmann A, Zaharieva I, Dau H, Strasser P (2013) Electrochemical water splitting by layered and 3D crosslinked manganese oxides: correlating structural motifs and catalytic activity. Energy Environ Sci 6(9):2745–2755

152. Acuña LM, Muñoz FF, Cabezas MD, Lamas DG, Leyva AG, Fantini MCA, Baker RT, Fuentes RO (2010) Improvement in the reduction behavior of novel ZrO₂-CeO₂ solid solutions with a tubular nanostructure by incorporation of Pd. J Phys Chem C 114(46):19687–19696

153. Park J-H, Kim B, Shin C-H, Seo G, Kim SH, Hong SB (2009) Methane combustion over Pd catalysts loaded on medium and large pore zeolite's. Top Catal 52(1–2):27–34

154. Johnston-Peck AC, Senanayake SD, Plata JJ, Kundu S, Xu W, Barrio L, Graciani J, Fdez Sanz J, Navarro RM, Fierro JG, Stach EA, Rodriguez JA (2013) Nature of the mixed-oxide interface in ceria–titania catalysts: clusters, chains, and nanoparticles. J Phys Chem C 117 (28):14463–14471

155. Masuda T, Fukumitsu H, Fugane K, Togasaki H, Matsumura D, Tamura K, Nishihata Y, Yoshikawa H, Kobayashi K, Mori T, Uosaki K (2012) Role of cerium oxide in the enhancement of activity for the oxygen reduction reaction at Pt–CeOₓ nanocomposite electrocatalyst – An in situ electrochemical x-ray absorption fine structure study. J Phys Chem C 116 (18):10098–10102

156. Nishimura S, Shishido T, Ohyama J, Teramura K, Takagaki A, Tanaka T, Ebitania K (2012) In situ observation of the dynamic behavior of Cu–Al–Oₓ catalysts for water gas shift reaction during daily start-up and shut-down (DSS)-like operation. Catal Sci Technol 2(8):1685–1693

157. Rodriguez JA, Hanson JC, Stacchiola D, Senanayake SD (2013) In situ/operando studies for the production of hydrogen through the water-gas shift on metal oxide catalysts. Phys Chem Chem Phys 15(29):12004–12025

158. Corrias A, Mountjoy G, Loche D, Puntes V, Falqui A, Zanella M, Parak WJ, Casula MF (2009) Identifying spinel phases in nearly monodisperse iron oxide colloidal nanocrystal. J Phys Chem C 113(43):18667–18675

159. Menard MC, Marschilok AC, Takeuchia KJ, Takeuchi ES (2013) Variation in the iron oxidation states of magnetite nanocrystals as a function of crystallite size: the impact on electrochemical capacity. Electrochim Acta 94:320–326

160. Mendoza Zélis P, Muraca D, Gonzalez JS, Pasquevich GA, Alvarez VA, Pirota KR, Sánchez FH (2013) Magnetic properties study of iron-oxide nanoparticles/PVA ferrogels with potential biomedical applications. J Nanopart Res 15(5):1613.1–1613.12

161. Piquer C, Laguna-Marco MA, Roca AG, Boada R, Guglieri C, Chaboy J (2014) Fe-K-edge X-ray absorption spectroscopy study of nanosized nominal magnetite. J Phys Chem C 118 (2):1332–1346

162. Filippousi M, Angelakeris M, Katsikini M, Paloura E, Efthimiopoulos I, Wang Y, Zamboulis D, Van Tendeloo G (2014) Surfactant effects on the structural and magnetic properties of iron oxide nanoparticles. J Phys Chem C 118(29):16209–16217

163. Bora DK, Braun A, Erat S, Safonova O, Graule T, Constable EC (2012) Evolution of structural properties of iron oxide nano particles during temperature treatment from 250 °C–900 °C: X-ray diffraction and Fe K-shell pre-edge x-ray absorption study. Curr Appl Phys 12 (3):817–825

164. Desautels RD, Skoropata E, Chen Y-Y, Ouyang H, Freeland JW, van Lierop J (2012) Increased surface spin stability in γ-Fe₂O₃ nanoparticles with a Cu shell. J Phys Condens Matter 24 (14):146001.1–146001.11

165. Aldea N, Turcu R, Nan A, Craciunescu I, Pana O, Yaning X, Wu Z, Bica D, Vekas L, Matei F (2009) Investigation of nanostructured Fe₃O₄ polypyrrole core-shell composites by X-ray absorption spectroscopy and X-ray diffraction using synchrotron radiation. J Nanopart Res 11(6):1429–1439

166. Gilbert B, Katz JE, Denlinger JD, Yin Y, Falcone R, Waychunas GA (2010) Soft X-ray spectroscopy study of the electronic structure of oxidized and partially oxidized magnetite nanoparticles. J Phys Chem C 114(50):21994–22001

167. Ding J, Fan T, Zhang D, Saito K, Guo Q (2011) Structural and optical properties of porous iron oxide. Solid State Commun 151(10):802–805

168. Rinaldi-Montes N, Gorria P, Martínez-Blanco D, Fuertes AB, Fernández Barquín L, Rodríguez Fernández J, de Pedro I, Fdez-Gubieda ML, Alonso J, Olivi L, Aquilanti G, Blanco JA (2014) Interplay between microstructure and magnetism in NiO nanoparticles: breakdown of the antiferromagnetic order. Nanoscale 6(1):457–465

169. Anspoks A, Kalinko A, Kalendarev R, Kuzmin A (2012) Atomic structure relaxation in nanocrystalline NiO studied by EXAFS spectroscopy: role of Ni vacancies. Phys Rev B 86 (17):174114.1–174114.11

170. Anspoks A, Kuzmin A, Kalinko A, Timoshenko J (2010) Probing NiO nanocrystals by EXAFS spectroscopy. Solid State Commun 150(45–46):2270–2274

171. Schultz-Sikma EA, Joshi HM, Ma Q, MacRenaris KW, Eckermann AL, Dravid VP, Meade TJ (2011) Probing the chemical stability of mixed ferrites: implications for magnetic resonance contrast agent design. Chem Mater 23(10):2657–2664

172. Fantechi E, Campo G, Carta D, Corrias A, de Julián Fernández C, Gatteschi D, Innocenti C, Pineider F, Rugi F, Sangregorio C (2012) Exploring the effect of Co doping in fine maghemite nanoparticles. J Phys Chem C 116(14):8261–8270

173. Carta D, Casula MF, Floris P, Falqui A, Mountjoy G, Boni A, Sangregorio C, Corrias A (2010) Synthesis and microstructure of manganese ferrite colloidal nanocrystals. Phys Chem Chem Phys 12(19):5074–5083

174. Vamvakidis K, Katsikini M, Sakellari D, Paloura EC, Kalogirou O, Dendrinou-Samara C (2014) Reducing the inversion degree of $MnFe_2O_4$ nanoparticles through synthesis to enhance magnetization: evaluation of their ^{1}H NMR relaxation and heating efficiency. Dalton Trans 43 (33):12754–12765

175. Nordhei C, Lund Ramstad A, Nicholson DG (2008) Nanophase cobalt, nickel and zinc ferrites: synchrotron XAS study on the crystallite size dependence of meta distribution. Phys Chem Chem Phys 10(7):1053–1066

176. Hellner Nilsen M, Nordhei C, Lund Ramstad A, Nicholson DG, Poliakoff M, Cabañas A (2007) XAS (XANES and EXAFS) investigations of nanoparticulate ferrites synthesized continuously in near critical and supercritical water. J Phys Chem C 111(17):6252–6262

177. Fábregas IO, Lamas DG (2011) Parametric study of the gel-combustion synthesis of nano-crystalline ZrO_2-based powders. Powder Technol 214(2):218–228

178. He P, Liu T, Möslang A, Lindau R, Ziegler R, Hoffmann J, Kurinskiy P, Commin L, Vladimirov P, Nikitenko S, Silveir M (2012) XAFS and TEM studies of the structural evolution of yttrium-enriched oxides in nanostructured ferritic alloys fabricated by a powder metallurgy process. Mater Chem Phys 136:990–998

179. Staab TEM, Klobes B, Kohlbach I, Korff B, Haaks M, Dudzik E, Maier K (2011) Atomic structure of pre-Guinier-Preston and Guinier-Preston-Bagaryatsky zones in Al-alloys. J Phys Conf Ser 265(1):012018.1–012018.15

180. Furlan A, Lu J, Hultman L, Jansson U, Magnuson M (2014) Crystallization characteristics and chemical bonding properties of nickel carbide thin film nanocomposites. J Phys Condens Matter 26(41):415501:1–415501:11

181. Furlan A, Jansson U, Lu J, Hultman L, Magnuson M (2015) Structure and bonding in amorphous iron carbide thin films. J Phys Condens Matter 27(4):045002.1–045002.9

182. Endrino JL, Abad MD, Gago R, Horwat D, Jiménez I, Sánchez-López JC (2010) Extended x-ray absorption fine structure (EXAFS) investigations of Ti bonding environment in sputter-deposited nanocomposite TiBC/a-C thin films. IOP Conf Ser Mater Sci Eng 12 (1):012012.1–012012.4

183. Pinakidou F, Katsikini M, Paloura EC, Akbari A, Riviere JP (2011) Nanostructural character-ization of TiN-Ni films: a XAFS study. Mater Sci Eng B 176(6):473–476

184. Pinakidou F, Katsikini M, Patsalas P, Abadias G, Paloura EC (2009) On the nanostructure of Cu in Ti_xCu_{1-x} and TiN/Cu films: a XAFS study. J Nano Res 6:43–50

185. Wepasnick KA, Smith BA, Bitter JL, Fairbrother DH (2010) Chemical and structural charac-terization of carbon nanotube surfaces. Anal Bioanal Chem 396(3):1003–1014

186. Brzhezinskaya MM, Vinogradov NA, Muradyan VE, Yu M, Shul'ga VP, Vinogradov AS (2008) Characterization of fluorinated multiwalled carbon nanotubes by X-ray absorption spectroscopy. Phys Solid State 50(3):587–594

187. Fleming L, Ulrich MD, Efimenko K, Genzer J, Chan ASY, Madey TE, Oh S-J, Zhou O, Rowe JE (2004) Near-edge absorption fine structure and UV photoemission spectroscopy studies of aligned single-walled carbon nanotubes on Si(100) substrates. J Vac Sci Technol B 22 (4):2000–2004

188. Li Z, Zhang L, Resasco DE, Mun BS, Requejo FG (2007) Angle-resolved x-ray absorption near edge structure study of vertically aligned single-walled carbon nanotubes. Appl Phys Lett 90(10):103115.1–103115.3

189. Schiessling J, Kjeldgaard L, Rohmund F, Falk LKL, Campbell EEB, Nordgren J, Bruhwiler PA (2003) Synchrotron radiation study of the electronic structure of multiwalled carbon nanotubes. J Phys Condens Matter 15:6563–6579

190. Hemraj-Benny T, Banerjee S, Sambasivan S, Balasubramanian M, Fischer DA, Eres G, Puretzky AA, Geohegan DB, Lowndes DH, Han W, Misewich JA, Wong SS (2006) Near-edge X-ray absorption fine structure spectroscopy as a tool for investigating nanomaterials. Small 2(1):26–35

191. Mittal V (ed) (2011) Surface modification of nanotube fillers. Wiley, Weinheim

192. Wang X, Li N, Webb JA, Pfefferle LD, Haller GL (2010) Effect of surface oxygen containing groups on the catalytic activity of multi-walled carbon nanotube supported Pt catalyst. Appl Catal B 101(1–2):21–30
193. Brzhezinskaya MM, Muradyan VE, Vinogradov NA, Preobrajenski AB, Gudat W, Vinogradov AS (2009) Electronic structure of fluorinated multiwalled carbon nanotubes studied using x-ray absorption and photoelectron spectroscopy. Phys Rev B 79 (15):155439.1–155439.12
194. Nikitin A, Ogasawara H, Mann D, Denecke R, Zhang Z, Dai H, Cho K, Nilsson A (2005) Hydrogenation of single-walled carbon nanotubes. Phys Rev Lett 95(22):225507.1–225507.4
195. Dettlaff-Weglikowska U, Skákalová V, Graupner R, Jhang SH, Kim BH, Lee HJ, Ley L, Park YW, Berber SA, Tománek D, Roth S (2005) Effect of SOCl$_2$ treatment on electrical and mechanical properties of single-wall carbon nanotube networks. J Am Chem Soc 127 (14):5125–5131
196. Chen Y, Wang J, Liu H, Norouzi Banis M, Li R, Sun X, Sham T-K, Ye S, Knights S (2011) Nitrogen doping effects on carbon nanotubes and the origin of the enhanced electrocatalytic activity of supported Pt for proton-exchange membrane fuel cells. J Phys Chem C 115 (9):3769–3776
197. Abbas G, Papakonstantinou P, Iyer GRS, Kirkman IW, Chen LC (2007) Substitutional nitrogen incorporation through rf glow discharge treatment and subsequent oxygen uptake on vertically aligned carbon nanotubes. Phys Rev B 75(19):195429.1–195429.9
198. Schulte K, Swarbrick JC, Smith NA, Bondino F, Magnano E, Khlobystov AN (2007) Assembly of cobalt phthalocyanine stacks inside carbon nanotubes. Adv Mater 19 (20):3312–3316
199. Zhou JG, Fang HT, Hu YF, Sham TK, Wu CX, Liu M, Li F (2009) Immobilization of RuO$_2$ on carbon nanotube: an X-ray absorption near-edge structure study. J Phys Chem C 113 (24):10747–10750
200. Felten A, Bittencourt C, Pireaux J-J, Reichelt M, Mayer J, Hernandez-Cruz D, Hitchcock AP (2007) Individual multiwall carbon nanotubes, individual multiwall spectroscopy by scanning transmission x-ray microscopy. Nano Lett 7(8):2435–2440
201. Felten A, Hody H, Bittencourt C, Pireaux J-J, Hernández Cruz D, Hitchcock AP (2006) Scanning transmission X-ray microscopy of isolated multiwall carbon nanotubes. Appl Phys Lett 89(9):09312.1–09312.3
202. Felten A, Gillon X, Gulas M, Pireaux J-J, Ke X, Van Tendeloo G, Bittencourt C, Najafi E, Hitchcock AP (2010) Measuring point defect density in individual carbon nanotubes using polarization-dependent x-ray microscopy. ACS Nano 4(8):4431–4436
203. Zhang L, Guo J, Zhu J (2015) Band mapping of graphene studied by resonant inelastic x-ray scattering. Fullerenes Nanotubes Carbon Nanostruct 23(5):471–475
204. Lee V, Park C, Jaye C, Fischer DA, Yu Q, Wu W, Liu Z, Bao J, Pei S-S, Smith C, Lysaght P, Banerjee S (2010) Substrate hybridization and rippling of graphene evidenced by near-edge X-ray absorption fine structure spectroscopy. J Phys Chem Lett 1(8):1247–1253
205. Zhang W, Nefedov A, Naboka M, Cao L, Wöll C (2012) Molecular orientation of terephthalic acid assembly on epitaxial graphene: NEXAFS and XPS study. Phys Chem Chem Phys 14:10125–10131
206. Weser M, Rehder Y, Horn K, Sicot M, Fonin M, Preobrajenski AB, Voloshina EN, Goering E, Dedkov YS (2010) Induced magnetism of carbon atoms at the graphene/Ni(111) interface. Appl Phys Lett 96(1):012505.1–012505.3
207. Weser M, Voloshin EN, Horna K, Dedkov YS (2011) Electronic structure and magnetic properties of the graphene/Fe/Ni(111) intercalation-like system. Phys Chem Chem Phys 13 (16):7534–7539
208. Generalov AV, Voloshina EN, Dedkova YS (2013) Structural and electronic properties of graphene-based junctions for spin-filtering: the graphene/Al/Ni(111) intercalation-like system. Appl Surf Sci 267:8–11

209. Voloshina E, Ovcharenko R, Shulakov A, Dedkov Y (2013) Theoretical description of X-ray absorption spectroscopy of the graphene-metal interfaces. J Chem Phys 138 (15):154706.1–154706.8

210. Schultz BJ, Lee V, Price J, Jaye C, Lysaght PS, Fischer DA, Prendergast D, Banerjee S (2012) Near-edge X-ray absorption fine structure spectroscopy studies of charge distribution at graphene/dielectric interfaces. J Vac Sci Technol B 30(4):041205.1–041205.6

211. Usachov D, Vilkov O, Grüneis A, Haberer D, Fedorov A, Adamchuk VK, Preobrajenski AB, Dudin P, Barinov A, Oehzelt M, Laubschat C, Vyalikh DV (2011) Nitrogen-doped graphene: efficient growth, structure, and electronic properties. Nano Lett 11(12):5401–5407

212. Zhao L, He R, Rim KT, Schiros T, Kim KS, Zhou H, Gutiérrez C, Chockalingam SP, Arguello CJ, Pálová L, Nordlund D, Hybertsen MS, Reichman DR, Heinz TF, Kim P, Pinczuk A, Flynn GW, Pasupathy AN (2011) Visualizing individual nitrogen dopants in monolayer graphene. Science 333(6045):999–1003

213. Vinogradov NA, Simonov KA, Generalov AV, Vinogradov AS, Vyalikh DV, Laubschat C, Mårtensson N, Preobrajenski AB (2012) Controllable p-doping of graphene on Ir(111) by chlorination with $FeCl_3$. J Phys Condens Matter 24(31):314202.1–314202.8

214. Haberer D, Petaccia L, Farjam M, Taioli S, Jafari SA, Nefedov A, Zhang W, Calliari L, Scarduelli G, Dora B, Vyalikh DV, Pichler T, Wöll C, Alfè D, Simonucci S, Dresselhaus MS, Knupfer M, Büchner B, Grüneis A (2011) Direct observation of a dispersionless impurity band in hydrogenated graphene. Phys Rev B 83(16):165433.1–165433.6

215. Ehlert C, Unger WES, Saalfrank P (2014) C K-edge NEXAFS spectra of graphene with physical and chemical defects: a study based on density functional theory. Phys Chem Chem Phys 16(27):14083–14095

216. Kim K-j, Choi J, Lee H, Lee H-K, Kang T-H, Han Y-H, Lee B-C, Kim S, Kim B (2008) Effects of 1 MeV electron beam irradiation on multilayer graphene grown on 6H-SiC(0001). J Phys Chem C 112(34):13062–13064

217. Liu Z, Tang J, Kang C, Zou C, Yan W, Xu P (2012) Effect of substrate temperature on few-layer graphene grown on Al_2O_3 (0001) via direct carbon atoms deposition. Solid State Commun 152(11):960–963

218. Tang J, Kang CY, Li LM, Yan WS, Wei SQ, Xu PS (2011) Graphene films grown on Si substrate via direct deposition of solid-state carbon atoms. Phys E 43(8):1415–1418

219. Bittencourt C, Hitchock AP, Ke X, Van Tendeloo G, Ewels CP, Guttmann P (2012) X-ray absorption spectroscopy by full-field x-ray microscopy of a thin graphite flake: imaging and electronic structure via the carbon K-edge. Beilstein J Nanotechnol 3:345–350

220. Schultz BJ, Patridge CJ, Lee V, Jaye C, Lysaght PS, Smith C, Barnett J, Fischer DA, Prendergast D, Banerjee S (2011) Imaging local electronic corrugations and doped regions in graphene. Nat Commun 2(372):1–7

221. Pacilé D, Papagno M, Fraile Rodríguez A, Grioni M, Papagno L, Girit ÇÖ, Meyer JC, Begtrup GE, Zettl A (2008) Near-edge x-ray absorption fine-structure investigation of graphene. Phys Rev Lett 101(6):066806.1–066806.4

222. Gandhiraman RP, Nordlund D, Javier C, Koehne JE, Chen B, Meyyappan M (2014) X-ray absorption study of graphene oxide and transition metal oxide nanocomposites. J Phys Chem C 118(32):18706–18712

223. Liang Y, Wang H, Zhou J, Li Y, Wang J, Regier T, Dai H (2012) Covalent hybrid of spinel manganese-cobalt oxide and graphene as advanced oxygen reduction electrocatalysts. J Am Chem Soc 134(7):3517–3523

224. Feng X, Song M-K, Stolte WC, Gardenghi D, Zhang D, Sun X, Zhu J, Cairns EJ, Guo J (2014) Understanding the degradation mechanism of rechargeable lithium/sulfur cells: a comprehensive study of the sulfur–graphene oxide cathode after discharge–charge cycling. Phys Chem Chem Phys 16(32):16931–16940

225. Chuang C-H, Wang Y-F, Shao Y-C, Yeh Y-C, Wang D-Y, Chen C-W, Chiou JW, Ray SC, Pong WF, Zhang L, Zhu JF, Guo JH (2014) The effect of thermal reduction on the photoluminescence and electronic structures of graphene oxides. Sci Rep 4(4525):1–7

226. Zhong J, Deng J-J, Mao B-H, Xie T, Sun X-H, Mou Z-G, Hong C-H, Yang P, Wang S-D (2012) Probing solid state N-doping in graphene by X-ray absorption near-edge structure spectroscopy. Carbon 50(1):321–341

227. Hunt A, Dikin DA, Kurmaev EZ, Boyko TD, Bazylewski P, Chang GS, Moewes A (2012) Epoxide speciation and functional group distribution in graphene oxide paper-like materials. Adv Funct Mater 22(18):3950–3957

228. Dennis RV, Schultz BJ, Jaye C, Wang X, Fischer DA, Cartwright AN, Banerjee S (2013) Near-edge X-ray absorption fine structure spectroscopy study of nitrogen incorporation in chemically reduced graphene oxide. J Vac Sci Technol B 31(4):041204.1–041204.4

229. Zhou JG, Wang J, Sun CL, Maley JM, Sammynaiken R, Sham TK, Pong WF (2011) Nanoscale chemical imaging of a single sheet of reduced graphene oxide. J Mater Chem 21 (38):14622–14630

230. Lv J, Zhang S, Luo L, Han W, Zhang J, Yang K, Christie P (2012) Dissolution and microstructural transformation of ZnO nanoparticles under the influence of phosphate. Environ Sci Technol 46(13):7215–7221

231. Zhang P, Ma Y, Zhang Z, He X, Zhang J, Guo Z, Tai R, Zhao Y, Chai Z (2012) Biotransformation of ceria nanoparticles in cucumber plants. ACS Nano 6(11):9943–9950

232. Hernandez-Viezcas JA, Castillo-Michel H, Andrews JC, Cotte M, Rico C, Peralta-Videa JR, Ge Y, Priester JH, Holden PA, Gardea-Torresdey JL (2013) In situ synchrotron X-ray fluorescence mapping and speciation of CeO$_2$ and ZnO nanoparticles in soil cultivated soybean (Glycine max). ACS Nano 7(2):1415–1423

233. Zhao L, Peralta-Videa JR, Varela-Ramirez A, Castillo-Michel H, Li C, Zhang J, Aguilera RJ, Keller AA, Gardea-Torresdey JL (2012) Effect of surface coating and organic matter on the uptake of CeO$_2$ NPs by corn plants grown in soil: insight into the uptake mechanism. J Hazard Mater 225–226:131–138

234. Larue C, Laurette J, Herlin-Boime N, Khodja H, Fayard B, Flank A-M, Brisset F, Carriere M (2012) Accumulation, translocation and impact of TiO$_2$ nanoparticles in wheat (Triticum aestivum spp.): influence of diameter and crystal phase. Sci Total Environ 431:197–208

235. Veronesi G, Brun E, Fayard B, Cotte M, Carriére M (2012) Structural properties of rutile TiO$_2$ nanoparticles accumulated in a model of gastrointestinal epithelium elucidated by micro-beam x-ray absorption fine structure spectroscopy. Appl Phys Lett 100(21):214101.1–214101.4

236. Auffan M, Rose J, Orsiere T, De Meo M, Thill A, Zeyons O, Proux O, Masion A, Chaurand P, Spalla O, Botte A, Wiesner MR, Bottero J-T (2009) CeO$_2$ nanoparticles induce DNA damage towards human dermal fibroblasts in vitro. Nanotoxicology 3(2):161–171

237. Fendorf S, Eick MJ, Grossl P, Sparks DL (1997) Arsenate and chromate retention mechanisms on goethite. 1. Surface structure. Environ Sci Technol 31(2):315–320

238. Tresintsi S, Simeonidis K, Katsikini M, Paloura EC, Bantsis G, Mitrakas M (2014) A novel approach for arsenic adsorbents regeneration using MgO. J Hazard Mater 265:217–225

239. Jegadeesan G, Al-Abed SR, Sundaram V, Choi H, Scheckel KG, Dionysiou DD (2010) Arsenic sorption on TiO$_2$ nanoparticles: size and crystallinity effects. Water Res 44 (3):965–973

240. Li W, Harrington R, Tang Y, Kubicki JD, Aryanpour M, Reeder RJ, Parise JB, Phillips BL (2011) Differential pair distribution function study of the structure of arsenate adsorbed on nanocrystalline γ-alumina. Environ Sci Technol 45(22):9687–9692

241. Wang Y, Morin G, Ona-Nguema G, Juillot F, Calas G, Brown GE Jr (2011) Distinctive arsenic (V) trapping modes by magnetite nanoparticles induced by different sorption processes. Environ Sci Technol 45(17):7258–7266

242. Wang Y, Morin G, Ona-Nguema G, Juillot F, Guyot F, Calas G, Brown GE Jr (2010) Evidence for different surface speciation of arsenite and arsenate on green rust: an EXAFS and XANES study. Environ Sci Technol 44(1):109–115

243. Zhang M, Pan G, Zhao D, He G (2011) XAFS study of starch-stabilized magnetite nanoparticles and surface speciation of arsenate. Environ Pollut 159(12):3509–3514

244. Ona-Nguema G, Morin G, Wang Y, Foster AL, Juillot F, Alas G, Brown GE Jr (2010) XANES evidence for rapid arsenic(III) oxidation at magnetite and ferrihydrite surfaces by dissolved O_2 via Fe^{2+}-mediated reactions. Environ Sci Technol 44(14):5416–5422

245. Tresintsi S, Simeonidis K, Estradé S, Martinez-Boubeta C, Vourlias G, Pinakidou F, Katsikini M, Paloura EC, Stavropoulos G, Mitrakas M (2013) Tetravalent manganese feroxyhyte: a novel nanoadsorbent equally selective for As(III) and As(V) removal from drinking water. Environ Sci Technol 47(17):9699–9705

246. Zhang G, Liu F, Liu H, Qu J, Liu R (2014) Respective role of Fe and Mn oxide contents for arsenic sorption in iron and manganese binary oxide: an x-ray absorption spectroscopy investigation. Environ Sci Technol 48(17):10316–10322

247. Silva GC, Almeida FS, Ferreira AM, Ciminelli VST (2012) Preparation and application of a magnetic composite (Mn_3O_4/Fe_3O_4) for removal of As(III) from aqueous solutions. Mater Res 15(3):403–408

248. Wang X, He M, Lin C, Gao Y, Zheng L (2012) Antimony(III) oxidation and antimony (V) adsorption reactions on synthetic manganite. Chem der Erde 72(S4):41–47

249. Jordan N, Ritter A, Foerstendorf H, Scheinost AC, Weiß S, Heim K, Grenzer J, Mücklich A, Reuther H (2013) Adsorption mechanism of selenium(VI) onto maghemite. Geochim Cosmochim Acta 103:63–75

250. Luo L, Ma C, Ma Y, Zhang S, Lv J, Cui M (2011) New insights into the sorption mechanism of cadmium on red mud. Environ Pollut 159(5):1108–1113

251. Sheng G, Yea L, Li Y, Dong H, Li H, Gao X, Huang Y (2014) EXAFS study of the interfacial interaction of nickel(II) on titanate nanotubes: role of contact time, pH and humic substances. Chem Eng J 248:71–78

The Characterization of Atomically Precise Nanoclusters Using X-Ray Absorption Spectroscopy

5

Lisa Bovenkamp-Langlois and Martha W. Schaefer

Contents

L. Bovenkamp-Langlois (✉)
CAMD (Center for Advanced Microstructures and Devices), Louisiana State University, Baton Rouge, LA, USA

Center for Atomic-Level Catalyst Design, Cain Department of Chemical Engineering, Louisiana State University, Baton Rouge, LA, USA
e-mail: lbovenkamp@lsu.edu

M.W. Schaefer
CAMD (Center for Advanced Microstructures and Devices), Louisiana State University, Baton Rouge, LA, USA

Department of Geology and Geophysics, Louisiana State University, Baton Rouge, LA, USA

Department of Physics and Astronomy, Louisiana State University, Baton Rouge, LA, USA
e-mail: mws@lsu.edu

1   Definition of the Topic

Overview of the methods and results of the application of X-ray absorption spectroscopy characterizing atomically precise nanoclusters.

2   Introduction

Interest in catalysts such as the atomically precise nanoclusters (APNCs) is growing. Much is still to be learned about the properties of these materials, however. At what point in cluster growth does a material change from the quantum behavior of a single atom or molecule to the ensemble behavior of a bulk metal [1]? Is the transition smooth with increasing cluster size, or is there an intermediate region where the clusters have properties that are neither metallic nor due to quantum size effects [2]? Is there a relationship between the size of the clusters and their electronic, optical, and catalytic properties [3]? Is there a correlation between structure and electronic properties [4]? How are structure and electronic properties affected by a complex environment (including different temperatures, pressures, or solvation effects) [5]? Since APNCs are the focus of this book, some answers to these questions are presented in other chapters.

However, a very brief introduction shall help the reader to understand the separation of the group of APNCs from the wider group of nanoparticles (NPs). The definition of NPs as mesoscopic systems between atoms or molecules and macroscopic bulk material can apply to a good number of structures with particle sizes of ≤ 100 nm. The term APNC means that these NPs have a precise number of atoms and generally implies that they are small (below 10 nm diameter). It is reported that the atomic precision of APNCs affects catalytic and optical properties and gives exceptional stability to the APNC (e.g., [4, 6–8]). A brief history of Au APNCs is given in Schaaff et al. [7].

The first step in understanding the correlation between the structure and the chemical and physical properties (which enable tailoring of the catalytic properties of the APNC [9]) is to gain precise knowledge about the structure of the clusters. X-ray diffraction (XRD) is the best method to determine the structure of a material. For APNCs, there is a certain degree of disorder [10] and fluidity [11] on the surface due to the presence of ligands. For this reason, it is mostly not possible to grow crystals and determine the structure using XRD [12]. In order to find some understanding of the structure for these cases, certain semiempirical models have been developed [13, 14]. For example, "staple fitness," concerning the highest structural stability of the staple motif [15], will be discussed later in this paper.

The most basic structural models were created on the basis of atomic packing structures (e.g., fcc) and are summarized by Benfield [16]. The atomic packing mode in metal NCs is in direct correlation with their size and other structural properties [4, 9, 17]. Specifically, the stability stands in direct relation to the so-called magic numbers [9]. Details will be discussed further below. New approaches using density functional theory (DFT) have made it possible to determine the structures of several

clusters, e.g., $Au_{25}(SR)_{18}$ [18], $Au_{38}(SR)_{24}$ [19], and $Au_{144}(SR)_{60}$ [20]. Challenges include the determination of the cluster size (more specifically the number of atoms) from the packing mode models and the understanding why smaller clusters have icosahedral structure in one case and cuboctahedral structure in another [11].

The most studied group among the APNCs is the gold clusters ($Au_x(SR)_y$) with thiol capping. This is because when the gold–sulfur interface can be understood (including atomic and electronic structure, properties of signal transmittance, excitations, and electron transport), then they can be applied to fields such as nanocatalysis, molecular electronics, biolabeling, photonics, and sensing [20]. Further, the extremely high surface-to-volume ratio of these gold clusters ($Au_x(SR)_y$) can help with the understanding of self-organization processes in self-assembled monolayers (SAM) [7]. Solution phase investigations of Au clusters can reveal the physical and chemical properties of atomically precise Au nanoclusters [21]. In contrast to the use of thiol ligands is a new method of NC stabilization with s: These dendrimer-encapsulated nanoclusters (DENs) show quite different properties compared to thiol-stabilized NCs [22].

The second step in the understanding of the physical and chemical properties (specifically the catalytic properties) of APNCs is the determination of their electronic properties, which depend on the basic structure (size, packing) and environment. In particular, the size of a cluster will determine whether its electronic properties are discrete, i.e., atoms, molecules, and small clusters or form a band structure, i.e., bulk metals [4]. Common techniques to determine the electronic structure of materials are UV–vis spectroscopy and X-ray photoelectron spectroscopy (XPS) (which needs ultrahigh vacuum (UHV) conditions [9]). Another procedure that is used is the calculation of density of states based on quantum chemistry [23].

The goal of the generation of APNC is not only the control of the size (e.g., number of atoms) but also the distribution of metals in the case of the bimetallic NC. The determination of the distribution of the two metals is another aspect of the concept of "active sites" which includes defects, sharp corners, and atomic steps, and its understanding can help control catalytic reactions further [6].

The electronic properties can change if the two metals are distributed in the certain way [24]. For example, alloys with Pd, Ag, Pt, or Cu based on $Au_{25}(SR)_{18}$ and $Au_{38}(SR)_{24}$ NC were synthesized and investigated by both theory and experiment and showed that the content and distribution of second metal (doping) have direct effects on the geometrical structure and electronic properties (e.g., [25–28]). In the cases of $Au_{24}Pt(SR)_{18}$ [25], $Au_{24}Ag(SR)_{18}$ [26], $Au_{24}Pd(SR)_{18}$ [27, 28], and $Au_{24}Cu(SR)_{18}$ [29, 30], the dopant atoms are believed to occupy the central site of the metal core. It is the precise knowledge of the structure and electronic properties of the NCs that is important in the understanding of the catalytic properties. To achieve this goal, methods to investigate the structure and electronic properties have to be developed constantly [31].

A powerful characterization technique for many materials is X-ray absorption spectroscopy (XAS). XAS has become a very important tool among the synchrotron-based techniques for the characterization of materials, especially metal nanoparticles

and catalysts [9, 32]. Because XAS is element specific, this gives a very special opportunity to observe the same sample from different points of view if several elements, e.g., metals in alloy, are used (more details below). XAS is applicable to a broad range of elemental concentrations (i.e., from tens of ppm to wt% levels) [32] for solids and liquids as well and does not require long-range order in the sample [33]. In addition to the oxidation state, the chemical environment and geometrical information can be extracted from XAS. One aspect of XAS that especially combines theoretical and experimental techniques is extended X-ray absorption fine structure (EXAFS) spectroscopy. The analysis of EXAFS can:

- Determine coordination numbers (CN) to the neighboring atoms in a NC
- Determine distances of Me–Me and Me–L bonding
- Compare structure models with experimental data
- Determine structural disorder (up to a degree)

These important structural details can even be extracted from amorphous materials [2]. The resolution of EXAFS regarding the bond distances is of the order of 0.001 Å within a distance of about 10 Å from the center to analyze the local structure [3]. In this respect, EXAFS can even extract structural information which is based on the atomic packing models above from systems that do not have a long-range order.

Using the other aspect of XAS, X-ray absorption near-edge structure (XANES, formerly called NEXAFS) spectroscopy, it is possible to:

- Analyze the electronic properties (i.e., density of electronic states above the Fermi level)
- Determine the effective oxidation state
- Determine the chemical speciation

In this review, we focus on the methods and problems that are connected with the characterization of APNCs using XAS. Correct structural models and purity of NP content are the most important aspects to highlight. Together EXAFS and XANES are very versatile (nondestructive, study both atomic and electronic structure) and can be applied to the characterization of all kinds of materials and reactions in situ, even if they require high temperatures, high pressures, or other environmental changes, e.g., solvation and vaporization [12]. XAS techniques can be combined with theoretical calculations to validate structural models [31].

Some questions that will be answered in this review are the following:

- When was EXAFS first used for the characterization of APNC?
- How is the atomic size (numbers of atoms) determined by using EXAFS?
- What is so different in the use of EXAFS to study APNC compared to normal NP?
- What is the effect of structural disorder on the EXAFS analysis technique?
- How can the electronic information contained in XANES be extracted?

This latest review focuses on the use of XAS to characterize the structure, electronic properties, and behavior of APNCs, including during heating, solvation, and catalytic activity.

Other recent reviews on related topics include the following: Bare and Ressler [32] and Frenkel et al. [34] discuss the broader field of catalysis and the application of catalytic reactors together with (in situ) XAS. A more specified discussion of the catalytic activity of metal DENs using catalytic reactors investigated with in situ XAS was published by Myers et al. [22]. The wider region of the characterization of NP using XAS was reviewed by Frenkel et al. [35], Lapresta-Fernandez et al. [36], and Modrow [9].

In the wide field of applications of EXAFS, theoretical methods especially the combination of EXAFS with other theoretical methods such as density functional theory (DFT) and molecular dynamics (MD) are progressing fast and are becoming the state of the art of the characterization techniques [34]. Some of these techniques will be discussed here later to present a complete as possible overview of the techniques currently available in the XAS toolbox.

The evolution of clusters from atomic to bulk including both theoretical and experimental discussions is found in Schmid [37]. The interplay of atomic and electronic structure from a more theoretical point of view is discussed by Hakkinen [38] and Pei and Zeng [39].

Frenkel [40] and Gao and Goodman [41] discussed the specifics of the characterization of bimetallic NP, while Jin and Nobusada [42] focused on the methods of alloying within NCs with respect to different elements. Zhang [43] summarized the research on gold APNCs that was done in his group using XAS methods in a very recent review. Zhang also sketched very briefly using excellent illustrations the advantages and results that can be drawn from XAS. There can be found many more reviews on the different aspects of APNC. However, these do not mention the characterizational strength of the XAS toolbox.

The sections of this chapter are organized as follows: A short introduction of the physics of XAS and the specifics of XANES and EXAFS is followed by a discussion of the experimental setup in the next section. The main section of this chapter discusses the techniques of the application of first, EXAFS and second, XANES that are used in order to gain structural and electronic information from investigations of APNCs and the key findings.

3   Experimental and Instrumental Methodology

3.1   The Physics of X-Ray Absorption Spectroscopy

X-ray absorption spectroscopy (XAS) is a sophisticated tool to analyze many different types of materials. It is especially useful because no long-range order is required, but only the local environment of the element of interest is significant. This qualifies XAS as an excellent tool for the investigation of noncrystalline systems.

The analysis of XAS spectra can give details on oxidation state, geometry, and the kinds of neighboring atoms. The element under investigation can be chosen because of the distinct electron binding energies. There are a number of introductory texts on XAS available in the literature, for example, Bunker [44], Calvin [45], Kelly et al. [46], Koningsberger, Prins [33], and Teo [47]. In a nutshell: The law of Lambert–Beer

$$I = I_0 e^{-\mu_l(E)x} \tag{5.1}$$

describes the attenuation of radiation of initial intensity I_0 with regard to intensity I at a distance x within a material. $\mu_l(E)$ (short, μ) is the linear absorption coefficient at energy E. For XAS experiments, bonding energies of inner shell electrons extend from UV light for light elements (≈ 50 eV) up to hard X-rays (≈ 100 keV) for heavy elements. In this typical energy range for XAS experiments, the absorption coefficient μ is dominated by the photoelectric effect. XAS involves the measurement of the absorption coefficient μ as a function of photon energy E close to the ionization energy of an inner shell electron in a material and reveals a fine structure (see Fig. 5.1). The energy at which the absorption rises abruptly is called the absorption edge, and the energetic position is denoted E_0. This fine structure is an oscillatory structure that modulates the (atomic) absorption coefficient of an isolated atom and originates from the interaction of an electron excited by photo absorption with the surrounding material. In the quantum mechanical picture of the photoelectron as a matter wave, the oscillatory structure can be explained as interference between waves, one wave leaving the absorbing atom and the other waves that are backscattered from the neighboring atoms according to the scattering effects of the chemical environment. Because electron binding energies are element specific, XAS is element specific.

The non-modulated absorption coefficient μ_0, related to an environment where no neighboring atoms are present, is called the atomic background. The atomic background can be approximated by an arc tangent curve but is, mostly, masked by the features of the main edge (cf. Fig. 5.1). Materials that can be examined with XAS are solids, fluids, or gases. XAS is divided into two aspects depending on the involvement of the type of scattering contribution and molecular orbitals to the signal. X-ray absorption near-edge structure (XANES) spectroscopy is the part of the fine structure close to the absorption edge E_0 (typical -20 eV to 50 eV with respect to E_0) showing intense features. In addition to the oxidation state, the chemical environment and geometrical information can be extracted from XANES using the fingerprinting technique. The XANES region is dominated by multiple scattering and transitions into molecular orbitals. The extended X-ray absorption fine structure (EXAFS) region extends out to 1000 eV above E_0 and is mainly contributed by single scattering. The analysis of the EXAFS signal provides local structural information such as distance and CN of neighboring atoms. The information contained in a XAS spectrum is averaged over all atoms (of the element under investigation) that are probed (i.e., the atoms within the sample that are hit by the photon beam).

Fig. 5.1 Fe K-XANES spectrum of metallic iron (—) and the atomic background (...)
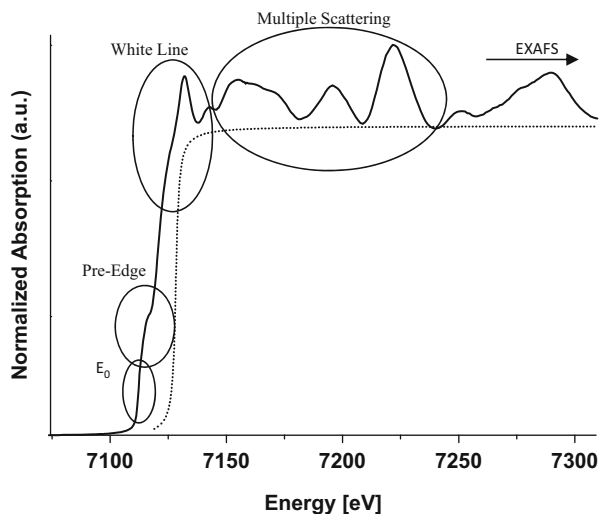
3.2   XANES

The fine structure of the near-edge (XANES, earlier NEXAFS) spectra consists of distinct characteristics such as pre-edge peaks, a white line (WL), shape resonances (SR), and the energy position of the absorption edge E_0 (cf. Fig. 5.1). The position of the edge E_0 is usually defined as the inflection point in the main rise of $\mu(E)$. In cases such as transition metals (Ti, Co, Fe, and so on), this position can be masked by pre-edge features. Figure 5.1 shows an example for iron metal. The position of the absorption edge E_0 can shift due to the oxidation state of the absorbing atom or electronegativity of the neighboring atoms [48]. The white line (WL) is named after the strong feature just above the absorption edge which was observed in photosensitive films used to record spectra in early XAS experiments. Pre-edge features and WL peaks arise from transitions into unoccupied atomic or molecular orbitals (MO) above the Fermi level. All other features after the WL (up to about 50 eV) are called shape resonances (SR). SR are also characteristic features, and they have their origin in multiple scattering with neighboring atoms. Together the shape and position of each of the characteristic features in the XANES spectrum comprise a fingerprint of the electronic and geometric environment of the absorbing element. This chemical environment can be determined by comparison to XANES spectra of compounds with known structures.

Additional information contained in the XANES spectrum comes from the correlation of the WL feature to molecular orbitals and density of states [33]. The density of states (DOS) describes the number density of available states as a function of energy [49]. Further, the l-projected DOS (l-DOS) only includes the DOS for a specific quantum number (l = 0, 1, 2, etc.) which corresponds to the classification of the orbitals due to their angular momentum (s, p, d, respectively). The shape of a

Fig. 5.2 The density of states (DOS) depicted on the top reflects the transitions of electrons from core levels into unoccupied states above the Fermi energy (E_FERMI). The transitions starting from specific core levels correspond to the absorption edges of XAS (Reprinted with permission from Rehr and Albers [50]. Copyright 2000 by the American Physical Society)
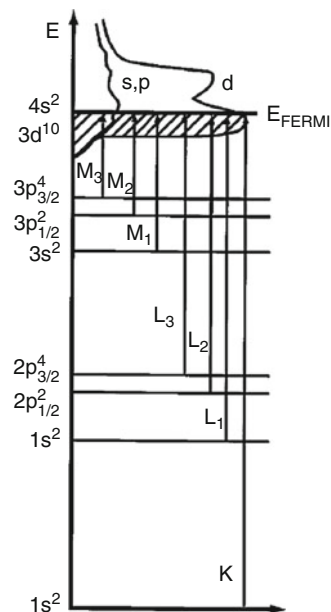
XANES spectrum reflects the projected electronic DOS of excited states because the XANES "function" $\chi(E)$ and the l-DOS $\rho(E)$ share the same fine structure:

$$\rho(E) \ = \rho_0(E) \left[1 \ + \chi(E)\right] \tag{5.2}$$

Here, E is the photoelectron energy, and $\rho_0(E)$ is the density of states for the atomic background [50]. The XANES spectrum is derived from the reflection of transitions into unoccupied states above the Fermi level. Figure 5.2 depicts the relationship between the transitions from core states and the absorption edges (K, L, M).

To correlate the unoccupied l-DOS $\rho(E)$ with experimental XANES, the relation

$$\rho(E) = \left[\rho_0(E)/\mu_0(E)\right] \mu(E) \tag{5.3}$$

can be used, where $\mu_0(E)$ describes the effects of the core–hole interaction. In general, unoccupied states show up as peaks (reflecting possible transitions between molecular orbitals), and hybridization of orbitals is revealed when peaks in different orbitals have the same energy [9].

3.3   EXAFS

More than 50 eV up to 1000 eV above the absorption edge (E_0), the fine structure is much reduced in intensity but not reduced in information content. Therefore, in order to extract the information, the smooth atomic background has to be removed, and $\chi(E)$, the fine structure function (Fig. 5.3), is calculated:
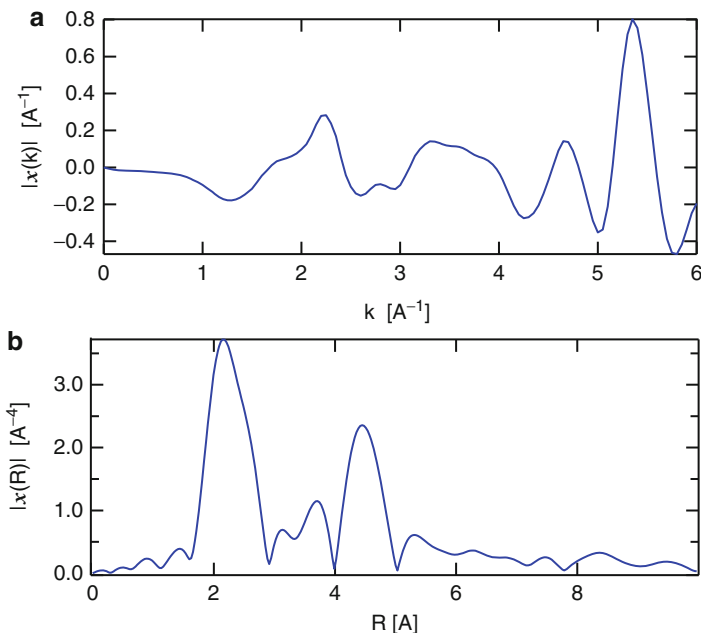
Fig. 5.3 Fine structure of the Fe metal EXAFS spectrum (**a**) $\chi(k)$ and (**b**) Fourier transformed, $\chi(R)$

$$\chi(E) \;=\; \frac{\mu(E) - \mu_0(E)}{\Delta\mu(E)} \tag{5.4}$$

where $\mu(E)$ is the measured absorption coefficient, $\mu_0(E)$ is the atomic background (a function calculated as a spline), and $\Delta\mu(E)$ is the edge step. Further, this function of the oscillations is converted into k-space using $k^2 = 2\,m/\hbar^2(E - E_0)$ (with m, the mass of the electron, and $\hbar$, the Planck constant (over 2π)) and using Fourier transformation into R-space (Fig. 5.3).

The interference between initial and backscattered waves as well as some examples for scattering paths is visualized in Fig. 5.4. Two main types of scattering paths are distinguished: single scattering and multiple scattering. Single scattering is in general sufficient to calculate the EXAFS part of the spectrum with the addition of some corrections regarding multiple scattering. Single scattering occurs only if the wavelength of the outgoing photoelectron wave λ is smaller than the interatomic bond distance R. Usually, this refers to a value of about +50 eV above E_0.

The EXAFS function $\chi(k)$ is directly connected to the parameters of the environment of the absorbing atom. These parameters are described in the EXAFS equation [50]:

$$\chi(k) = \sum_{R} S_0^2 N_R \frac{|f(k)|}{kR^2} * \sin\left(2kR + 2\delta_c + \Phi\right)e^{-2R/\lambda(k)}e^{-2\sigma^2 k^2} \tag{5.5}$$
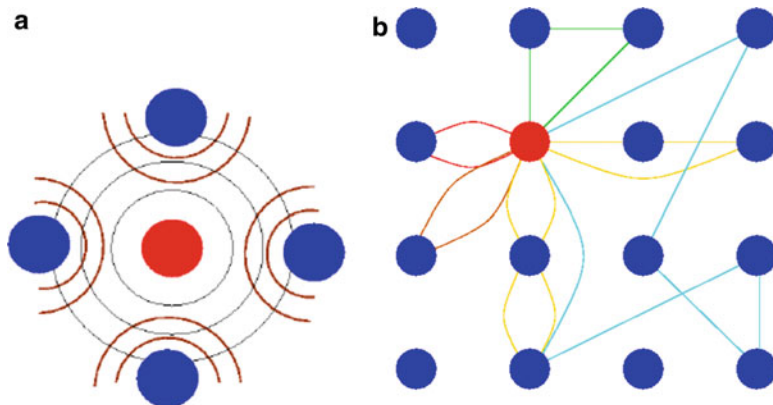
Fig. 5.4 (**a**) The interference between the outgoing wave and the backscattered waves is the source of the oscillatory structure in EXAFS, (**b**) examples for single scattering (*red, brown*) and multiple scattering paths (*green, yellow, blue*) in a crystal (From Ravel [51], used with permission)

where $\chi(k)$ represents the pure oscillations in k-space. S_0^2 is a factor that includes inelastic losses, N_R is the CN of neighbors at a certain radius, $f(k)$ is the scattering amplitude, R is the distance to the neighboring atoms, δ_e is the phase shift, λ is the mean free path for inelastic losses, and σ^2 is the Debye–Waller factor which relates to thermal and structural disorder. In order to extract the contributions of different backscattered waves, a Fourier transformation is performed, usually denoted FT $\chi(k)$ or just $\chi(R)$. From these parameters, bond lengths and coordination numbers can be extracted.

At present, EXAFS data are analyzed by refining the theoretically calculated EXAFS spectra of single paths using the sum of path rule:

$$\chi(k) = \sum_P \chi_P(k) \tag{5.6}$$

where χ_P denotes each path contributing to the spectrum.

The modern analysis of EXAFS data is done with programs such as Artemis (Demeter/Ifeffit) [52], WinXAS [53], or GNXAS [54]. The details of the application of these methods are described there. Briefly, the EXAFS spectrum in k-space is fitted using theoretically calculated scattering amplitudes and phase shifts from reference compounds with known structure. The parameters of the EXAFS equation are set as a relation to the structural values given for the known compounds. For the analysis of the EXAFS data, especially in the case of NCs, it is very important that the samples are 100 % NC and not containing by-products or precursors that contain the element under investigation [55]. For an EXAFS fit, it is important to have a model for the structure that is to be characterized. In the case of metallic NC, this model as a first-order approximation can be the metallic bulk structure. With a fit, distance and CNs with the first neighbors (up to five shells) are determined with the use of information about the Au–Au distance and CNs derived from the metal bulk.

The number of SS paths (also coordination numbers) and the number of multiple scattering paths are intercorrelated and depend on the size and shape of the crystallites (i.e., the NC).

For the EXAFS fitting approach for NP, the following constraints have been proposed previously [35, 56–59]:

1. The degeneracy of multiple scattering paths has to be optimized within a range obtained by the measured size distribution of the nanoparticles.
2. Due to the presence of surface, i.e., ill coordinated, atoms in NP systems, the bond distance and bond–angle distributions are affected; therefore, it must be possible to determine the bond distances separately from the bulk metal system.
3. Because the background is the same as in bulk crystalline metal foil, nonstructural parameters are fixed to the values obtained for bulk metal within their estimated uncertainty (S_O^2, ΔE_0).

The EXAFS analysis of bimetallic APNCs is even more challenging [55]. For alloy nanoclusters, the further following constraints are used on the heterometallic bonds based on Nashner et al., Frenkel, and Knecht et al. [40, 60–62]:

1. The CNs ($N_{Me1\text{-}Me2}$ and $N_{Me2\text{-}Me1}$ are heterometallic coordination numbers) of the *Me–Me* bonds for the two different metals (*Me1* and *Me2*) have to relate to their concentration c: $N_{Me1-Me2}/N_{Me2-Me1} = c_{Me2}/c_{Me1}$.
2. The distances R between atoms of the two metals in each shell have to be the same: $R_{Me1-Me2} = R_{Me2-Me1}$.
3. The disorder parameters (Debye–Waller factor, σ^2) for both metals in each shell have to be the same: $\sigma^2_{Me1-Me2} = \sigma^2_{Me2-Me1}$.

3.4 The XAS Experiment

Synchrotron radiation is monochromatized using a set of parallel crystals in a double crystal monochromator applying Bragg's law:

$$n \cdot \lambda \;=\; 2 \cdot d \cdot \sin\theta \tag{5.7}$$

with n being the order number, λ the wavelength of the reflected light, d the spacing of the crystal, and θ the Bragg angle. Slits are used to collimate and mirrors to focus the incoming beam onto the sample position.

A double crystal monochromator with parallel crystal setup is preferred for XAS experiments because the incoming and exiting beams are parallel to each other [63]. This way the monochromatized beam is fixed on the sample position, while the energy is scanned. The rest of this experimental setup consists of ionization chambers to measure the photon current before and after the sample and of an energy-dispersive semiconductor detector, positioned at a 90° angle with respect to
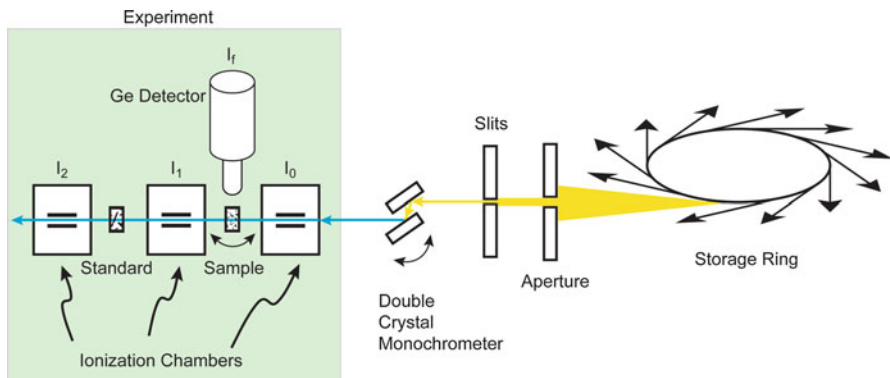
Fig. 5.5 Experimental setup of a XAS experiment

the incoming beam, to measure fluorescence photons coming from the sample. The layout is displayed in Fig. 5.5.

After monochromatizing, the photons pass through the two ionization chambers and the sample to measure $\mu(E)$. For concentrated samples, the absorption μ can be measured indirectly by applying the law of Lambert–Beer (cf. Eq. 5.1) – transmission mode:

$$\mu(E) \propto ln\left(\frac{I_0}{I_1}\right) \tag{5.8}$$

The absorption coefficient $\mu(E)$ is determined by measuring the photon current before the sample (I_0) and behind the sample (I_1). If another ionization chamber (I_2) is installed behind I_1, a standard (e.g., metal foil) can be measured at the same time with the sample. This standard is used for energy calibration purposes.

Diluted samples with less than 1 % concentration of the absorbing element are measured in fluorescence mode where the semiconductor detector collects the fluorescence photons (I_f) that are emitted as response to the absorption of the incident beam (I_0) by the sample. Fluorescence and Auger electrons are the two relaxation mechanisms of atoms excited by X-ray radiation. For fluorescence detection, the absorption coefficient $\mu(E)$ is described by

$$\mu(E) \propto \left(\frac{I_f}{I_0}\right) \tag{5.9}$$

Equation 5.9 is an approximation and only valid if the sample is thin and diluted so that no self-absorption occurs. Also, the sample should face in the direction of 45° with respect to the incoming beam (and therefore also the semiconductor detector) [44].

The sample preparation can have significant effects on the measurement. It is important that the samples are of the right average thickness and are homogeneous.

The thickness of the sample determines the total absorption, which ideally should be about 1. Homogeneity of the sample is important because a nonhomogeneous sample will have a distribution of absorption coefficients instead of a well-characterized single value. As discussed by Lee et al. [64] and Stern and Kim [65], if samples have, for example, little holes, the absorption coefficient cannot be the same at each point (see Eq. 5.1). Therefore, if the absorption coefficient μ is not measured correctly, the data evaluated from those measurements cannot be reliable, especially for the increased distortions in monocrystalline materials due to higher surface-to-volume ratio [66, 67].

4 Key Research Methods and Findings on APNCs Characterized Using XAS

4.1 EXAFS

The EXAFS analysis method is very important for the characterization of metal clusters and catalysts. EXAFS analysis is used to determine specific information about materials including the chemical identity, average bond lengths for the different shells, and ensemble-average CN of atoms in each shell around a central atom. To date, only APNCs containing Au, Pd, Pt, and some alloys (e.g., Au–Cu, Au–Pd, and Au–Pt) have been characterized by EXAFS. The literature reporting EXAFS used for the characterization of APNCs together with the details of the EXAFS analyses is summarized in Table 5.1.

4.1.1 Simple Structural Models

The first reports of the characterization of APNCs with EXAFS, i.e., Au_{55} clusters made by the Schmid [68] process by Cluskey et al. [69], Fairbanks et al. [70], and Marcus et al. [71], used early EXAFS analysis techniques where experimental phase shifts and amplitude of reference materials were compared with those of the unknown sample, and the software to make use of the EXAFS equation was just beginning to be developed. With time, a more complete understanding of the various effects that impact the spectra and the improvement of the analysis software has made possible a much more sophisticated approach to the analysis of EXAFS spectra. Better understanding of the effect of multiple scattering and curved wave effects [72] has improved the characterization of APNC with EXAFS. Early EXAFS results on Pd_{561} [72] and also Au_{55} [10] were revised and refined.

Several papers on the characterization of nanoparticles (not APNC) using EXAFS [17, 57–59, 73] form the basis for reliable results derived from EXAFS. In these publications, Frenkel and coworkers discuss the importance of multiple scattering effects [58] on the EXAFS analysis and models regarding the structural geometry of the nanoclusters [17, 59, 73], summarized in Frenkel et al. [35]. Together with the development of the FEFF code (specifically version 6), the calculation of multiple scattering paths became possible. This big improvement boosted the development of analysis software (e.g., WinXAS [53], Ifeffit, and Demeter [52]). The analysis of

Table 5.1 Summary of EXAFS data on APNCs

Nanocluster	EXAFS	1st shell M–M CN	1st shell M–M dist., r (Å)	Disorder param (10^-3 Å²)	Other shells, dopant data	Structure	k-range (Å^-1)	EXAFS fit plot?	Other techniques	Reference
GOLD										
$Au_{11}\{PPh_2(p\text{-}ClC_6H_4)\}_7I_3$ (80 K)	Au L₃-edge	1.4 ± 2	2.66 ± 0.01	4 ± 6	2nd Au-Au: CN = 2.4 ± 1, r = 2.87 ± 0.02 3rd Au-Au: CN = 3.2 ± 3, r = 4.68 ± 0.03 Au-P: CN = 0.8 ± 1, r = 2.27 ± 0.04 Au-I: CN = 2.6 ± 2, r = 2.64 ± 0.07	–	–	No	None	Clusky et al. 1993 [69]
$Au_{13}[PPh_3]_4[S(CH_2)_{11}CH_3]_2Cl_2$ $Au_{13}[PPh_3]_4[S(CH_2)_{11}CH_3]_4$ (not distinguished in results)	Au L₃-edge	6.5 ± 0.5	–	–	2nd Au-Au: CN = 0 3rd Au-Au: CN = 5 ± 1 Au-S: CN = 0.72 ± 0.05	–	–	Yes	XANES, HAADF-STEM, TEM	Frenkel et al. 2007 [89]
$Au_{13}[PPh_3]_4[S(CH_2)_{11}CH_3]_2Cl_2$	Au L₃-edge	SS1 path: 6.2 ± 0.6	SS1 path: 2.83 ± 0.01	Au-Au: 14 ± 1 Au-S: 5 ± 1	TR path: CN = 34 ± 26, r = 4.24 ± 0.05 SS3 path: CN = 8 ± 6, r = 4.75 ± 0.03 Au-S SS1 path: CN = 0.83 ± 0.08, r = 2.310 ± 0.007	–	3-12	Yes	XANES, HRTEM, HAADF-STEM	Menard et al. 2006 [3]

$Au_{13}[PPh_3]_4[S(CH_2)_{11}CH_3]_4$	Au L_3-edge	SS1 path: 6.7 ± 0.7	SS1 path: 2.85 ± 0.02	Au-Au: 15 ± 1 Au-S: 3 ± 1	TR path: CN = 21 ± 8, r = 4.26 ± 0.03 SS3 path: CN = 8 ± 4, r = 4.75 ± 0.02 Au-S SS1 path: CN = 0.76 ± 0.07, r = 2.324 ± 0.007	—	3-12	Yes	(As above)	Menard et al. 2006 [3]
Au_{13} P2VP in solution (P2VP = polystyrene-2-vinylpiridine)	Au L_3-edge	9.4	2.84 ± 0.01	12 ± 1	Au-X: CN = 0.2, r = 2.09 ± 0.03	—	2-12	Yes	XANES, FEFF DFT, XPS, HAADF-STEM, AFM	Behafarid et al. 2014 [106]
Au_{13} P2VP on Al_2O_3 (P2VP = polystyrene-2-vinylpiridine)	Au L_3-edge	8.2	2.79 ± 0.01	15 ± 2	Au-X: CN = 0.7, r = 2.11 ± 0.02	—	2-12	Yes	(As above)	Behafarid et al. 2014 [106]
$Au_{19}(SR)_{13}$	Au L_3-edge	1.05*	2.83 ± 0.01	4 ± 1	2nd Au-Au: CN = 1.89*, r = 3.04 ± 0.02 3rd Au-Au: CN = 1.89*, r = 3.37 ± 0.03 Au-S: CN = 1.37*, r = 2.33 ± 0.01	Icosahedral	2.5-11.5	Yes	XANES, XPS	Chevrier et al. 2012 [95]
$Au_{22}(SG)_{18}$	Au L_3-edge	0.7	2.67 ± 0.01	—	Au-S: CN = 1.7, r = 2.314 ± 0.004	Face-centered cubic	3.0-13.5	Yes	XANES, XPS	Yu et al. 2014 [146]
$Au_{24}Pt(SR)_{18}$	Pt L_3-edge	—	—	10 ± 1	Pt-S: CN = 2.6 ± 0.1, r = 2.319 ± 0.004 Pt-Au: CN = 5.5 ± 0.3, r = 2.750 ± 0.004	Icosahedral	3-8.8	No	MALDI, XPS, l-DOS	Christensen et al. 2012 [25]

(continued)

Table 5.1 (continued)

Nanocluster	EXAFS	1st shell M–M CN	1st shell M–M dist., r (Å)	Disorder param (10⁻³ Å²)	Other shells, dopant data	Structure	k-range (Å⁻¹)	EXAFS fit plot?	Other techniques	Reference
$Au_4Pt(SR)_{18}$	Au L_3-edge	2 ± 1^e	2.79 ± 0.01^e	13 ± 5	Au–S: CN = 1.7 ± 0.2, r = 2.315 ± 0.005	Icosahedral	3–12	Yes	(As above)	Christensen et al. 2012 [25]
$Au_4Pd(SC_{12}H_{25})_{18}$	Pd K-edge	–	–	–	Pd–Au: CN = 10.7 ± 0.9, r = 2.750 ± 0.005	–	3–15	No	None	Negishi et al. 2013 [28]
Au_{25}	Au L_3-edge	1.1 ± 0.2	2.81 ± 0.01	6 ± 1	Au–S: CN = 1.6 ± 0.1, r = 2.332 ± 0.007	Icosahedral	3–12	Yes	MALDI, XPS, l-DOS	Christensen et al. 2012 [25]
$[Au_{25}(TePh)_{-3}(SC_8H_{17})_{-15}]^-$	Au L_3-edge	0.9 ± 0.9	2.782 ± 0.025	1.0 ± 8.4	Au–S: CN = 1.4 ± 0.3, r = 2.299 ± 0.007 Au–Te: CN = 0.3 ± 0.2, r = 2.579 ± 0.019	–	3–15	No	XANES, ESI/MALDI, TEM, UV–vis	Kurashige et al. 2014 [110]
$[Au_{25}(TePh)_{-7}(SC_8H_{17})_{-11}]^-$	Au L_3-edge	1.0 ± 0.9	2.774 ± 0.031	0.6 ± 0.6	Au–S: CN = 1.2 ± 0.3, r = 2.299 ± 0.013 Au–Te: CN = 0.8 ± 0.3, r = 2.589 ± 0.013	–	3–15	No	(As above)	Kurashige et al. 2014 [110]
$[Au_{25}(PPh_3)_{10}(SC_{12}H_{25})_5Cl_2]^{2+}$ Au_{25}-bi	Au L_3-edge	6.9 ± 1.3	2.82 ± 0.03	–	Au–S: CN = 0.7 ± 0.4, r = 2.30 ± 0.05	Bi-icosahedral	2–11.5	No	XANES, UPS	Liu et al. 2013 [115]
$[Au_{25}(SCH_2CH_2Ph)_{18}]^-$ Au_{25}-i	Au L_3-edge	4.8 ± 1.3	2.80 ± 0.04	–	Au–S: CN = 1.2 ± 0.4, r = 2.30 ± 0.04	Icosahedral	2–11.5	No	(As above)	Liu et al. 2013 [115]

Sample	Edge					Structure	Range		Techniques	Reference
$[Au_{25}(SC_8H_{17})_{18}]^-$	Au L_3-edge	0.7 ± 0.5	2.738 ± 0.011	0.5 ± 3.3	Au-S: CN = 1.6 ± 0.2, r = 2.309 ± 0.003	–	3-15	No	XANES, ESI/MALDI, TEM, UV–vis	Kurashige et al. 2014 [110]
Au_{25}-BSA (BSA = bovine serum albumin)	Au L_3-edge	3.0 ± 0.4	2.81 ± 0.01	10 ± 1	Au-S: CN = 1.2 ± 0.1, r = 2.30 ± 0.01	Icosahedral	3-12	Yes	XANES, XPS, TEM	Simms et al. 2009 [84]
$[TOA]+$ $[Au_{25}(SCH_2CH_2Ph)_{18}]^-$ (TOA = tetraoctylammonium)	Au L_3-edge	1.44*	300 K: 2.82 ± 0.01 10 K: 2.80 ± 0.01	300 K: 8.4 10 K: 4.9	2nd Au-Au, 300 K: r = 2.97 ± 0.01, 10 K: r = 2.97 ± 0.01; 3rd Au-Au, 300 K: r = 3.14 ± 0.02, 10 K: r = 3.20 ± 0.02; Au-S, 300 K: r = 2.32 ± 0.01, 10 K: r = 2.32 ± 0.01	Icosahedral	3-12	Yes	XANES, l-DOS	MacDonald et al. 2011 [5]
Solvated $[TOA]+$ $[Au_{25}(SCH_2CH_2Ph)_{18}]^-$ (TOA = tetraoctylammonium) (a) Toluene (b) ACN = acetonitril	Au L_3-edge	1.44*	in toluene: 2.79 ± 0.01 in ACN: 2.79 ± 0.01	in toluene: 7.4 in AC: 7.2	2nd Au-Au, in toluene: r = 2.95 ± 0.01, in ACN: r = 2.95 ± 0.01; 3rd Au-Au, in toluene: r = 3.19 ± 0.02, in ACN: r = 3.14 ± 0.02; Au-S, in toluene: r = 2.33 ± 0.01, in ACN: r = 2.32 ± 0.01	Icosahedral	3-12	Yes	(As above)	MacDonald et al. 2011 [5]

(continued)

Table 5.1 (continued)

Nanocluster	EXAFS	1st shell M-M CN	1st shell M-M dist., r (Å)	Disorder param (10⁻³ Å²)	Other shells, dopant data	Structure	k-range (Å⁻¹)	EXAFS fit plot?	Other techniques	Reference
$Au_{25}(SR)_{18}$	Au L_3-edge	300 K: 1.44*	300 K: 2.80 ± 0.01	300 K: 9 ± 1	300 K: Au-S: CN = 1.44*, r = 2.321 ± 0.005	Icosahedral	3-11.3	Yes	XANES, FEFF, l-DOS	Chevrier et al. 2014 [99]
$Au_{25}(SR)_{18}$	Au L_3-edge	300 K: 1.44* 50 K: 1.44*	300 K: 2.790 ± 0.005 50 K: 2.784 ± 0.006	300 K: 4.8 ± 0.5 50 K: 3.0 ± 0.4	300 K: Au-S: CN = 1.44*, r = 2.333 ± 0.002 2nd shell Au-Au: CN = 1.92*, r = 2.97 ± 0.01 3rd shell Au-Au: CN = 2.88*, r = 3.22 ± 0.06 50 K: Au-S: CN = 1.44*, r = 2.327 ± 0.003 2nd shell Au-Au: CN = 1.92*, r = 2.955 ± 0.08 3rd shell Au-Au: CN = 2.88*, r = 3.16 ± 0.01	Icosahedral	3-13	Yes	XANES, l-DOS	Chevrier et al. 2014 [96]

$Au_{25}(SeR)_{18}$	Au L_3-edge	300 K: 1.44* 50 K: 1.44*	300 K: 2.70 ± 0.01 50 K: 2.775 ± 0.009	300 K: 5.0 ± 1.0 50 K: 5.4 ± 0.7	300 K: Au-Se CN = 1.44*, r = 2.417 ± 0.009 2nd shell Au-Au, 300 K: CN = 1.92*, r = 2.87 ± 0.02 3rd shell Au-Au, 300 K: CN = 2.88*, r = 3.46 ± 0.04 50 K: Au-Se CN = 1.44*, r = 2.428 ± 0.004 2nd shell Au-Au: CN = 1.92*, r = 2.98 ± 0.01 3rd shell Au-Au: CN = 2.88*, r = 3.60 ± 0.03	–	3-13	Yes	(As above)	Chevrier et al. 2014 [96]
$Au_{25}(SeR)_{18}$	Se K-edge	–	no Au-Au/no Se-Se	–	300 K: Au-Se: CN: 2, r = 2.408 ± 0.009 Se-C: CN: 1, r = 1957 ± 0.002 50 K: Au-Se: CN: 2.41 ± 0.01 Se-C: CN: 1, r = 1.87 ± 0.003	–	3-13	Yes	(As above)	Chevrier et al. 2014 [96]
CeO_2 rod supported $Au_{25}(SR)_{18}$ (SR = $-SCH_2CH_2Ph$)	Au L_3-edge	2-3	–	–	Au-S: CN-1, r = 2.31 (avg)	–	3-16	No	XANES, Raman, FTIR, MALDI-MS, HAADF-TEM	Wu et al. 2014 [91]

(continued)

Table 5.1 (continued)

Nanocluster	EXAFS	1st shell M–M CN	1st shell M–M dist., r (Å)	Disorder param (10⁻³ Å²)	Other shells, dopant data	Structure	k-range (Å⁻¹)	EXAFS fit plot?	Other techniques	Reference
Carbon-Supported $Au_{25}(SR)_{18}$ MPCs SR = Phenylethanethiolate	Au L_3-edge	25 °C: 1.44*	25 °C: 2.760 ± 0.002	25 °C: 7.9 ± 0.5	2nd Au–Au, 25 °C: CN = 1.92* r = 3.01 ± 0.02	Icosahedral	3–12.5	Yes	UV–vis, TEM, XPS, MALDI, TGA	Shivhare et al. 2013 [21]
		125 °C: 6.3 ± 0.5	125 °C: 2.848 ± 0.004	125 °C: 8.9 ± 0.5	3rd Au–Au, 25 °C: CN = 2.88*, r = 3.3 ± 0.1					
		150 °C: 7.3 ± 0.8	150 °C: 2.852 ± 0.003	150 °C: 8.9 ± 0.5	Au–S, 25 °C: CN = 2.0*, r = 2.32*					
		200 °C: 9.3 ± 0.3	200 °C: 2.855 ± 0.002	200 °C: 8.8 ± 0.2	Au–S, 125 °C: CN = 1.11 ± 0.09, r = 2.325 ± 0.004					
		250 °C: 10.1 ± 0.5	250 °C: 2.855 ± 0.002	250 °C: 8.6 ± 0.3	Au–S, 150 °C: CN = 0.75 ± 0.09, r = 2.331 ± 0.005					
					Au–S, 200 °C: CN = 0.63 ± 0.08, r = 2.342 ± 0.008					
					Au–S, 250 °C: CN = 0.5 ± 0.1, r = 2.33 ± 0.02					

Carbon Supported Au$_{25}$(SR)$_{18}$ MPCs SR = Hexanethiolate	Au L$_3$-edge	25 °C: 1.44*	25 °C: 2.805 ± 0.004	25 °C: 7.2 ± 0.2	2nd shell Au-Au, 25 °C: CN = 1.92*, r = 3.02 ± 0.01	Icosahedral	3–12.5	Yes	(As above)	Shivhare et al. 2013 [21]
		125 °C: 3.6 ± 0.3	125 °C: 2.855 ± 0.003	125 °C: 9.1 ± 0.5	3rd shell Au-Au, 25 °C: CN = 2.88*, r = 3.32 ± 0.02					
		150 °C: 6.7 ± 0.4	150 °C: 2.857 ± 0.005	150 °C: 8.4 ± 0.3	Au-S, 25 °C: CN = 1.8*, r = 2.315*					
		200 °C: 9.0 ± 0.7	200 °C: 2.851 ± 0.005	200 °C: 8.5 ± 0.5	Au-S, 125 °C: CN = 1.58 ± 0.06, r = 2.315 ± 0.002					
					Au-S, 150 °C: CN = 1.0 ± 0.1, r = 2.329 ± 0.006					
					Au-S, 200 °C: CN = 0.8 ± 0.2, r = 2.32 ± 0.02					
Au$_{28}$(SR)$_{20}$	Au L$_3$-edge	300 K: 1.71*	300 K: 2.732 ± 0.002	300 K: 5 ± 1	300 K: Au-S: CN = 1.43*, r = 2.322 ± 0.009	Face-centered cubic	3–11.3	Yes	XANES, FEFF, l-DOS	Chevrier et al. 2014 [99]
		90 K: 1.71*	90 K: 2.73 ± 0.01	90 K: 6 ± 1	2nd shell Au-Au: CN = 2.09*, r = 2.93 ± 0.03					
					90 K Au-S: CN = 1.43*, r = 2.328 ± 0.006					
					2nd shell Au-Au: CN = 2.09*, r = 2.99 ± 0.003					

(continued)

Table 5.1 (continued)

Nanocluster	EXAFS	1st shell M–M CN	1st shell M–M dist., r (Å)	Disorder param (10^{-3} Å²)	Other shells, dopant data	Structure	k-range (Å^{-1})	EXAFS fit plot?	Other techniques	Reference
$Au_{16}(SR)_{24}$	Au L$_3$-edge	295 K: 2.06* 90 K: 2.06*	295 K: 2.732 ± 0.004 90 K: 2.746 ± 0.003	295 K: 8.0 ± 0.3 90 K: 3.7 ± 0.9	Au-S, 295 K: CN = 1.33*, r = 2.322 ± 0.002 2nd shell Au-Au, 295 K: CN = 2.56*, r = 2.89 ± 0.01 Au-S, 90 K: CN = 1.33*, r = 2.329 ± 0.002 2nd shell Au-Au, 90 K: CN = 2.56*, r = 2.951 ± 0.005	Icosahedral	3–13.7	Yes	XANES, XPS, l-DOS	Chevrier et al. 2013 [98]
$Au_{38}(SCH_2CH_2Ph)_{24}$ (solid)	Au L$_3$-edge	3.3*	2.789 ± 0.007	7.4 ± 0.8	Au-S: CN = 1.26*, r = 2.325 ± 0.004	Icosahedral	3–12.5	No	XANES, l-DOS	MacDonald et al. 2011 [85]
$Au_{38}(SCH_2CH_2Ph)_{24}$ (liquid)	Au L$_3$-edge	3.3*	2.820 ± 0.007	9.7 ± 0.6	Au-S: CN = 1.26*, r = 2.346±0.003	Icosahedral	3–12.5	No	(As above)	MacDonald et al. 2011 [85]
$Au_{38}(SeC_{12}H_{25})_{24}$	Au L$_3$-edge	1.8 ± 0.8	2.773 ± 0.008	0 ± 22	Au-Se: CN = 1.4 ± 0.2, r = 2.429 ± 0.002	–	3–13.5	Yes	XANES, ESI/MALDI, TGA, XPS, UV–vis, TEM, XRD	Kurashige et al. [96]
$Au_{38}(SC_{12}H_{25})_{24}$	Au L$_3$-edge	1.7 ± 0.5	2.747 ± 0.005	7 ± 12	Au-S: CN = 1.6 ± 0.2, r = 2.319 ± 0.003	–	3–13.5	Yes	(As above)	Kurashige et al. 2013 [97]
$Au_{38}(SC_{12}H_{25})_{24}$	Au L$_3$-edge	1.7 ± 0.2	2.791 ± 0.006	2 ± 3	Au-S: CN = 1.4 ± 0.1), r = 2.342 ± 0.006	–	3–13	No	Maldi, TEM,XPS, UV–vis, XRD	Nishigake et al. 2012 [147]

$Au_{41}(S\text{-Eind})_{12}$	Au L_3-edge	4.1 ± 0.4	2.720 ± 0.005	12 ± 5	Au-S: CN = 0.9 ± 0.4, r = 2.353 ± 0.005	–	3-13	No	(As above)	Nishigake et al. 2012 [147]
$Au_{55}(PPh_3)_{12}Cl_6$ (8 K)	Au L_3-edge	7.8 ± 1	2. 803 + 0.01	5.7	AuCl: CN = 0.2 ± 0.2, r = 2.31 ± 0.1	–	2.5-16.5	No	XANES	Marcus et al. 1990 [71]
$Au_{55}(PPh_3)_{12}Cl_6$	Au L_3-edge	6.5 ± 0.4	2.785 ± 0.003	–		Face-centered cubic	2-18	Yes	XANES, UV–vis, WAXS	Benfield et al. 2001 [10]
$Au_{55}(PPh_3)_{12}Cl_6$ (two samples)	Au L_3-edge	7.0 ± 2.5, 7.3 ± 2.5	2.76 ± 0.02, 2.78 ± 0.02	11.5 ± 0.4, 11.0 ± 0.4		–	3.5-14.5	Yes	–	Fairbanks et al. 1990 [70]
$Au_{55}(PPh_3)_{12}Cl_6$ (80 K)	Au L_3-edge	7.6 ± 1	2.75 ± 0.01	9.5 ± 0.2	2nd Au-Au: CN = 5.0 ± 8 r = 3.93 ± 0.04; 3rd Au-Au: CN = 0.60 ± 0.5 r = 4.88 ± 0.01; Au-P: CN = 0.66 ± 0.3, r = 2.30 ± 0.02; Au-Cl: CN = 2.3 ± 1, r = 2.50 ± 0.01	–	–	No	–	Clusky et al. 1993 [69]
$Au_{55}(PPh_2C_6H_4SO_3Na)_{12}Cl_6$ (80 K)	Au L_3-edge	5.55 ± 0.7	2.79 ± 0.01	8.5 ± 0.1	2nd shell Au-Au: CN = 3.5 ± 4.4, r = 3.97 ± 0.03; 3rd shell Au-Au: CN = 1.1 ± 1.2, r = 4.90 ± 0.02; Au-P: CN = 0.87 ± 0.6, r = 2.26 ± 0.02; Au-Cl: CN = 5.0 ± 3.5, r = 2.47 ± 0.02	–	–	No	–	Clusky et al. 1993 [69]

(continued)

Table 5.1 (continued)

Nanocluster	EXAFS	1st shell M–M CN	1st shell M–M dist, r (Å)	Disorder param (10^{-3} Å^2)	Other shells, dopant data	Structure	k-range (Å^{-1})	EXAFS fit plot?	Other techniques	Reference
Au$_{55}$(T8-OSS-SH)$_{12}$CL$_6$	Au L$_3$-edge	6.3 ± 0.5	2.794 ± 0.003	8.5	–	Face-centered cubic	2-18	Yes	XANES, UV–vis, WAXS	Benfield et al. 2001 [10]
Au$_{55}$(PPh$_3$)$_{12}$Cl$_6$ in Al$_2$O$_3$	Au L$_3$-edge	7 ± 2	2.84 ± 0.01	–	–	Face-centered cubic	2-18	Yes	(As above)	Benfield et al. 2001 [10]
Au$_{55}$-thiol (size: 10–30 ± 15 Å)	Au L$_3$-edge	7.5-8.5 ± 1	2.845-2.860 ± 0.005	–	–	Face-centered cubic	2-12	Yes	TEM	Frenkel et al. 2005 [12]
Au$_{144}$(SR)$_{60}$ (SR = PhC$_2$H$_4$S)	Au L$_3$-edge	7.0 ± 0.4	2.831 ± 0.002	13.8 ± 0.4	Au-S: CN = 0.83 ± 0.06, r = 2.340 ± 0.003	Icosahedral	3–11.7	Yes	XANES, l-DOS, XPS	MacDonald et al. 2010 [93]
Au147@Sn* DEN G6-OH)† containing an average of 147 atoms per particle (Au147), functionalized with 2ME, where n is the number of surface 2ME ligands per particle (thiols/DEN))	Au L$_3$-edge	N = 0: 8.8 ± 0.9 N = 12: 8.8 ± 1.4 N = 24: 8.5 ± 1.0 N = 50: 8.0 ± 1.0 N = 72: 6.6 ± 0.9	N = 0: 2.811 ± 0.005 N = 12: 2.815 ± 0.007 N = 24: 2.822 ± 0.005 N = 50: 2.826 ± 0.005 N = 50: 2.826 ± 0.005	11.9 ± 1.0 12.7 ± 1.4 13.1 ± 1.0 12.7 ± 1.1 12.7 ± 1.1	– Au-S, n = 12: CN = 0.31 Au-S, n = 24: CN = 0.46 Au-S, n = 50: CN = 0.66 Au-S, n = 72: CN = 0.95	–	–	Yes	UV–vis, TEM	Yancey et al. 2013 [101]

Sample	Edge	SS1 path CN	SS1 path r	CN	Higher shell paths	Structure	CN range		Techniques	References
Au$_x$ MPCs (183 ± 116 Au atoms)	Au L$_3$-edge	SS1 path: 8.9 ± 0.5	SS1 path: 2.83 ± 0.01	13 ± 1	SS2 path: CN = 3 ± 2, r = 4.01 ± 0.02	–	3-12	Yes	XANES, HRTEM, HAADF-STEM	Menard et al. 2006 [3]
				1 ± 1	TR path: CN = 35 ± 18, r = 4.25 ± 0.02; SS3 path: CN = 9 ± 3, r = 4.91 ± 0.02; Au-S SS1 path: CN = 0.7 ± 0.1, r = 2.310 ± 0.005					
Au$_{147}$-thiol (size: 20–25 ± 10 Å)	Au L$_3$-edge	8.5 ± 1	2.855-2.860 ± 0.005	–	–	Face-centered cubic	2-12	Yes	TEM	Frenkel et al. 2005 [12]
Au$_{561}$-thiol (size: 30–50 ± 15 Å)	Au L$_3$-edge	10.7 ± 1	2.863-2.875 ± 0.005	–	–	Face-centered cubic	2-12	Yes	(As above)	Frenkel et al. 2005 [12]
Au$_x$(SR)$_y$: 2 nm	Au L$_3$-edge	7 ± 1	2.854 ± 0.008	5.8 ± 0.8	–	Face-centered cubic	3.4-16	No	XANES, TEM	Zanchet et al. 2000 [87]
Au$_x$(SR)$_y$: 3.2 nm		6 ± 1	2.862 ± 0.005	2.4 ± 0.5						
Au$_x$(SR)$_y$: 4.1 nm		8 ± 1	2.866 ± 0.003	1.6 ± 0.5						
COPPER										
Cu$_{13}$ (RNH$_2$)$_y$	Cu K-edge	7.3 ± 1.4	2.56 ± 0.04	9.8 ± 1.7	–	Icosahedral	2-14	Yes	XANES, DFT, AFM	Oyanagi et al. 2014 [107]
Cu$_{13}$ (RNH$^-$)$_y$	Cu K-edge	3.5 ± 0.6	2.56 ± 0.05	7.6 ± 1.3	Cu-N: CN: 0.7 ± 0.3, r = 1.90 ± 0.02	Icosahedral	2-14	Yes	(As above)	Oyanagi et al. 2014 [107]
PALLADIUM										
[Pd$_9$L(O)$_3$(OAc)$_3$]m (L = 1,10-phenanthroline; m = 63.5 ± 3.5; 570 ± 30 Pd atoms in cluster)	Pd K-edge	–	2.60 ± 0.04	–	2nd Pd-Pd: r = 3.10 ± 0.10; 3rd Pd-Pd: r = 3.66 ± 0.10; 4th Pd-Pd: r = 4.08 ± 0.10	Icosahedral	–	No	XRD, TEM	Vargaftik et al. 1985 [74]

(continued)

Table 5.1 (continued)

Nanocluster	EXAFS	1st shell M–M CN	1st shell M–M dist., r (Å)	Disorder param (10^{-3} Å^2)	Other shells, dopant data	Structure	k-range (Å^{-1})	EXAFS fit plot?	Other techniques	Reference
$Pd_4(CO)_4(OAc)_4$	Pd K-edge	–	2.64	–	2nd Pd-Pd: r = 2.99 Pd-C: r = 1.92 Pd-O: r = 2.20	Several	–	No	SAXS, TEM, ED, MS, NMR	Vargaftik et al. 1991 [75]
$(Pd_{29}Au_{118})$ DEN (G6-OH)[†]	Pd K-edge	1 ± 2	2.83 ± 0.07	0 ± 5	–	–	–	Yes	UV–vis	Knecht et al. 2008 [62]
	Au L$_3$-edge	10 ± 2	2.85 ± 0.07	–						
$(Pd_{29}Au_{118})$ MPC[‡]	Pd K-edge	–	–	4 ± 5	–	–	–	Yes	(As above)	Knecht et al. 2008 [62]
	Au L$_3$-edge	7.0 ± 1.5	2.80 ± 0.02	–						
$(Pd_{60}Au_{87})$ DEN (G6-OH)[†]	Pd K-edge	2.5 ± 1	2.78 ± 0.04	14 ± 11	–	–	–	Yes	(As above)	Knecht et al. 2008 [62]
	Au L$_3$-edge	8 ± 2	2.84 ± 0.08	–						
$(Pd_{60}Au_{87})$ MPC[‡]	Pd K-edge	2 ± 2	2.95 ± 0.03	12 ± 3	–	–	–	Yes	(As above)	Knecht et al. 2008 [62]
	Au L$_3$-edge	8 ± 2	2.77 ± 0.02	–						
$(Pd_{73}Au_{73})$ DEN (G6-OH)[†]	Pd K-edge	3 ± 2	2.78 ± 0.04	9 ± 6	–	–	–	Yes	(As above)	Knecht et al. 2008 [62]
	Au L$_3$-edge	6 ± 3	2.84 ± 0.08	–						

(Pd73Au73) MPC‡	Pd K-edge	3 ± 2	2.90 ± 0.05	12 ± 3	–	–	–	Yes	(As above)	Knecht et al. 2008 [62]
	Au L3-edge	7 ± 2	2.75 ± 0.02	–						
(Pd87Au60) DEN (G6-OH) †	Pd K-edge	3 ± 1	2.79 ± 0.04	12 ± 2	–	–	–	Yes	(As above)	Knecht et al. 2008 [62]
	Au L3-edge	7 ± 5	2.85 ± 0.07	–						
(Pd87Au60) MPC‡	Pd K-edge	2 ± 2	2.9 ± 0.1	14 ± 2	–	–	–	Yes	(As above)	Knecht et al. 2008 [62]
	Au L3-edge	7.5 ± 2.0	2.70 ± 0.02	–						
(Pd119Au29) DEN (G6-OH) †	Pd K-edge	5 ± 2	2.79 ± 0.04	12 ± 2	–	–	–	Yes	(As above)	Knecht et al. 2008 [62]
	Au L3-edge	3 ± 2	2.77 ± 0.1	–						
(Pd119Au29) MPC‡	Pd K-edge	2 ± 2	2.9 ± 0.1	14 ± 2	–	–	–	Yes	(As above)	Knecht et al. 2008 [62]
	Au L3-edge	4.5 ± 2.0	2.70 ± 0.02	–						
Pd561(phen)36O200	Pd K-edge	–	2.742 ± 0.003	300 K: 7.3 ± 0.3	average CN = 6.8 ± 0.5	Face-centered cubic	2.5–17.5	No	–	Benfield et al. 1995 [72]
			2.743 ± 0.003	190 K: 5.5 ± 0.3						
			2.743 ± 0.003	80 K: 3.7 ± 0.3						

(continued)

Table 5.1 (continued)

Nanocluster	EXAFS	1st shell M–M CN	1st shell M–M dist., r (Å)	Disorder param (10⁻³ Å²)	Other shells, dopant data	Structure	k-range (Å⁻¹)	EXAFS fit plot?	Other techniques	Reference
$Pd_{561}(phen)_{36}O_{200}$ (80 K)	Pd K-edge	5.0 ± 0.1	2.73 ± 0.01	4 ± 1	2nd Pd-Pd: CN = 2.0 ± 4, r = 3.83 ± 0.04 / 3rd Pd-Pd: CN = 2.3 ± 3, r = 4.74 ± 0.02 / 4th Pd-Pd: CN = 1.2 ± 3, r = 5.36 ± 0.03	–	–	No	–	Clusky et al. 1993 [69]
Pd7/8 (a ligand-stabilized Pd cluster with 7 or 8 shells)	Pd K-edge	–	300 K: 2.746 ± 0.003 / 190 K: 2.746 ± 0.003 / 80 K: 2.747 ± 0.003	6.6 ± 0.3 / 4.7 ± 0.3 / 3.1 ± 0.3	average CN = 7.8 ± 0.5	Icosahedral	2.5–17.5	No	–	Benfield et al. 1995 [72]
Pd_{147} DENs (G6-OH)†	Pd K-edge	8.4 ± 0.6	2.791 ± 0.003	8.4 ± 0.5	–	–	–	Yes	XANES, TEM, XPS, UV–vis	Anderson et al. 2013 [109]
$(Pd_{147}@Cu_{162})$ DENs (G6-OH)†	Pd K-edge	7.8 ± 0.7	2.752 ± 0.005	10 ± 2	Pd-Cu: CN = 1.7 ± 0.9, r = 2.64 ± 0.02	Face-centered cubic	–	Yes	(As above)	Anderson et al. 2013 [109]
PLATINUM										
Pt_{55} DENs (G6-OH)†	Pt L₃-edge	7.4 ± 0.8	–	–	–	–	–	Yes	XANES, TEM, XPS, UV–vis	Pande et al. 2011 [148]
$(Pt_{147}@Pd)$ DENs (G6-OH)†	Pt L₃-edge	10.9 ± 3.7	2.72 ± 0.02	11 ± 4	Pt-Pd: CN = 1.3 ± 00.6, r = 2.72 ± 0.02	Face-centered cubic	–	Yes	XANES, TEM, XPS, UV–vis	Anderson et al. 2013 [109]
	Pd K-edge	4.8 ± 1.1	2.72 ± 0.01	5 ± 1	Pd-Pt: CN = 2.6 ± 1.2, r = 2.72 ± 0.02	Face-centered cubic	–	Yes	(As above)	Anderson et al. 2013 [109]

	Edge	Voltage / CN	Distance	CN	Pt–O	Structure	Range		Characterization	Reference
Pt_{225} DENs (G6-OH)[†] O_2 exposure	Pt L_3-edge	0.3 V: 6.9 ± 0.5	2.751 ± 0.004	6.4 ± 0.5	Pt–O: CN = 0.7 ± 0.3	Face-centered cubic	3-13	Yes	XANES, TEM, XPS, UV–vis	Myers et al. 2012 [104]
		0.15 V: 7.0 ± 0.5	2.745 ± 0.004	6.0 ± 0.5	Pt–O: CN = 0.5 ± 0.2		3-12.5			
		0.05 V: 7.3 ± 0.4 / 9.2 ± 1.1	2.734 ± 0.003 / 2.745 ± 0.007	6.2 ± 0.4 / 6.7 ± 0.8	Pt–O: CN = 0.4 ± 0.2 / Pt–O: CN = 0.5 ± 0.4		3-12.5 / 3-12.0			
		−0.2 V: 8.1 ± 0.8 / 8.1 ± 0.6	2.747 ± 0.006 / 2.740 ± 0.003	6.0 ± 0.7 / 5.8 ± 0.3	Pt–O: CN = 0.8 ± 0.8 / Pt–O: CN = 0.4 ± 0.2		3-12 / 3-15			
Pt_{225} DENs (G6-OH)[†] N_2 exposure	Pt L_3-edge	0.3 V: 6.2 ± 0.8	2.752 ± 0.007	6.2 ± 0.4	Pt–O: CN = 0.6 ± 0.3	Face-centered cubic	3-12	Yes	(As above)	Myers et al. 2012 [104]
		0.15 V: 7.0 ± 0.7	2.748 ± 0.005	6.4 ± 0.6	Pt–O: CN = 0.6 ± 0.3		3-12			
		−0.2 V: 8.4 ± 0.6	2.747 ± 0.003	6.5 ± 0.9	Pt–O: CN = 0.5 ± 0.2		3-14			
Pt_{240} DENs (G6-OH)[†]	Pt L_3-edge	5.8 ± 1.3 (experiment 1)	N/A	N/A	Pt–O: CN = 1.6 ± 0.6 (experiment 1)	N/A	2-11	Yes	XANES, TEM, XPS, UV–vis	Weir et al. 2010 [90]
		9.9 ± 1.1 (experiment 2)			–(experiment 2)					
		10.5 ± 1.5 (experiment 3)			–(experiment 3)					
		8.9 ± 0.9 (experiment 4)			–(experiment 4)					

(continued)

Table 5.1 (continued)

Nanocluster	EXAFS	1st shell M–M CN	1st shell M–M dist., r (Å)	Disorder param (10^{-3} Å^2)	Other shells, dopant data	Structure	k-range (Å^{-1})	EXAFS fit plot?	Other techniques	Reference
Pt$_{399}$(phen*)$_{36}$O$_{30}$ (phen* is a sulphonated phenanthroline ligand)	Pt L$_3$-edge	300 K: 8.0 ± 3	300 K: 2.74 ± 0.03	300 K: 10 ± 1	–	Face-centered cubic	4-18	Yes	XANES	Benfield et al. 1999 [2]
		190 K: 8.0 ± 3	190 K: 2.74 ± 0.02	190 K: 7 ± 1	–					
		80 K: 7.0 ± 3	80 K: 2.74 ± 0.01	80 K: 4 ± 1	2nd Pt-Pt, 80 K: CN = 2.0 ± 1 r = 3.87 ± 0.02					
					3rd Pt-Pt, 80 K: CN = 7.0 ± 3 r = 4.75 ± 0.02					
					4th Pt-Pt, 80 K: CN = 3.0 ± 2 r = 5.46 ± 0.02					

*Value fixed from theory
†Dendrimer-encapsulated nanoparticle
‡Monolayer-protected cluster
ε Au and Pt shells not distinguishable

EXAFS spectra can only provide CN, bond distances, and disorder correlations. If a model provides predictions for these values, the validity of the model can be tested.

Specifically for the characterization of APNCs, basic structural models are important tools to determine the structure of the NCs with EXAFS. These models essentially derived from the fcc structure that is inherent to many metals in their bulk form. For their analysis of Au_{55} [10, 70], Pd_{561} [72], and Pt_{309} [2], they used the cuboctahedron (fcc) model and based the verification of the model on the comparison of the CN of the first-shell Me–Me bonding. This method is discussed extensively in Benfield [16] where a formula for the mean CN is derived. For each model system (cuboctahedron (fcc, hcp), icosahedral), the CNs of the atoms in the first shell close to the center atom are distinct. However, in some reports [2, 10, 70, 72], the CNs were always too low compared to the fcc model. The development in the understanding and description of the model system, specifically fcc vs. icosahedral, made it possible to include other features into the analysis. The Me–Me bond distances of the first shell in an icosahedral structure should show splitting of about 0.2 Å into two subshells, but Benfield et al. [10] could not resolve these subshells in their data.

In another early approach, Benfield et al. [2] and Vargaftik et al. [74, 75] used the ratios of the Me–Me distances for the first three shells derived from EXAFS in comparison with these ratios in cuboctahedral and icosahedral models. Vargaftik et al. [75] determine an icosahedral structure for the Pd_{561} cluster they reported, and Benfield et al. [2] reported that the Pt_{309} cluster has fcc structure.

This technique using the CNs of the first shell of the EXAFS analysis comparing to the fcc model was typically used in early EXAFS analyses [12]. Later this technique was expanded to the cubic (fcc) model with different shapes (such as spherical, hemispherical, rod, etc.) [59, 76], to hcp and icosahedral models [73], and to other structures [77]. Figure 5.6 shows the correlation between cluster size and CN of the first nearest neighbor for several structures. The packing structure of these models also implies distinct numbers of atoms in the clusters [16, 78]. An example of these "magic numbers" for a cuboctahedral structure (hcp packing) is shown in Fig. 5.7.

4.1.2 Nanoscale Structural Distortions

Coordination Number Truncation

The coordination number truncation model (CNT) demonstrates that atoms on the surface of the particle are surrounded by fewer neighbors than those in the bulk, and, hence, the average coordination number of the first nearest neighbors decreases [57]. This model was also discussed in Benfield et al. [10] explaining the lower CNs for NCs compared to bulk metal. Using this model, the size of APNCs can be determined by comparison with the coordination numbers of several first shells by assuming specific polyhedral shapes [12]. This CNT method was used by Frenkel [58] for nanoparticles using a hemispherical fcc structure and by Frenkel et al. [12] for APNCs using a spherical fcc structure to determine the cluster size of NCs. More extensive applications of the CNT model including cuboctahedral, icosahedral, and hemispherical cuboctahedral structures by Glasner and Frenkel [73] and pyramidal structures by Beale and Weckhuysen [77] have been reported.
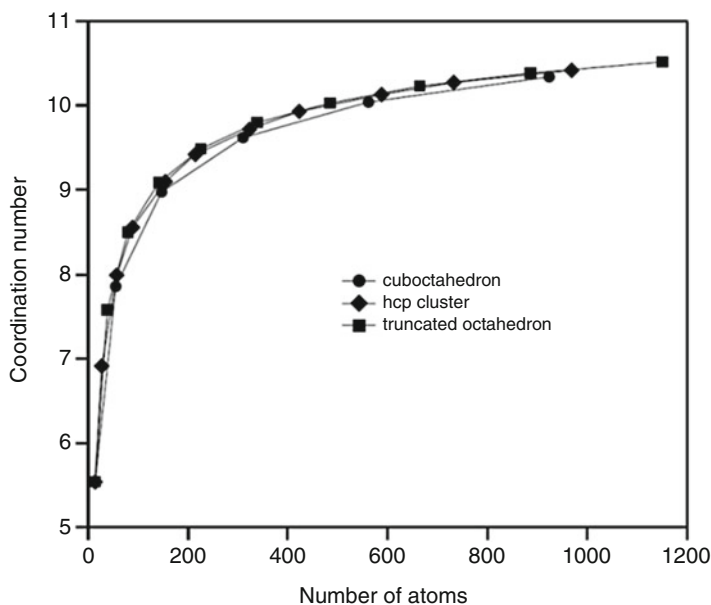
Fig. 5.6 The relation between number of atoms in a cluster and first-shell coordination number for a cuboctahedron, an hcp cluster, and a truncated octahedron (Based on data from Glasner and Frenkel [73])
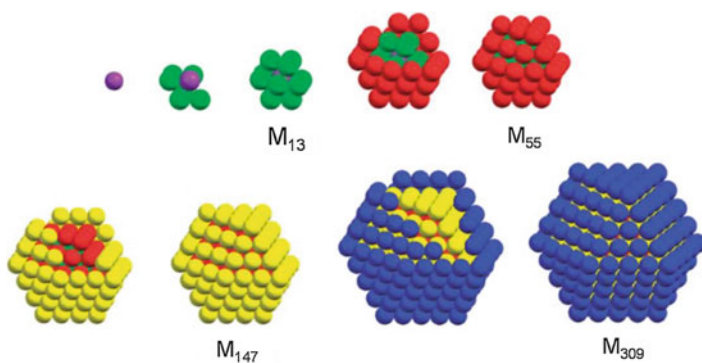
Fig. 5.7 Overview of structures and magic numbers of cuboctahedral clusters of different sizes (Reproduced from Schmid [79] with permission of the Royal Society of Chemistry on behalf of the Centre National de la Recherche Scientifique (CNRS) and the RSC)

Surface Tension

The surface-tension (ST) model was developed by Mays et al. [80]. Here the stress of the surface tension induces compression on the lattice which can be measured (in EXAFS) through the distances of the Me–Me coordination in the first shells if the data for the compressibility K and surface stress f_{rr} are available:

$$d = \frac{4}{3} \frac{f_{rr} K}{\alpha}, \tag{5.10}$$

where d is the particle diameter and $\alpha = \Delta R/R$ is the relative lattice contraction.

Me–Me bond length contraction that is directly related to this lattice contraction was observed not only by Frenkel et al. [12] but previously also by Benfield et al. [2, 10, 72] and Cluskey et al. [69]. Benfield et al. [2] found there to be different contraction rates for Au (4 %), Pt (1 %), and Pd (0.4 %) and related these to the results of differential scanning calorimetry measurements. They observed that bonding for Au–Au in NCs compared to bulk Au is stronger, while for Pd–Pd in NCs bonding is weaker than for bulk Pd. However, it was established by Häberlen et al. [81] and Kruger et al. [82, 83] using DFT calculations that the bond distances in small metal clusters (e.g., Pd, Au) are in direct and nearly linear relation to the mean nearest-neighbor CN and that the bond distances increase with cluster size. Later it was determined that as the particle size increases, the contraction decreases [12]. Further, it was found by Christensen et al. [25] that doping with Pt increased the Au–Au and Au–S contraction in the $Au_{24}Pt(SR)_{18}$ NC compared to the not doped $Au_{25}(SR)_{18}$.

Contraction of the first-shell Au–Au distance was observed by Menard et al. [3] for Au_{13} NCs. The contracted bond length was then used for geometrical calculations in order to determine the bond length of another Me–Me distance in accordance with a structural model, i.e., the distance to the third Au–Au shell which is on the surface of the cluster in an Au_{13} icosahedron. The discrepancies of their model with the experimental data led to the assumption that due to the ligands, there is a relaxation effect and therefore reduced contraction of this third shell distance. One of the objectives of the investigations by Simms et al. [84] was to understand the influence of the thiol ligand structure on the staple motif in Au_{25} NCs and the relationship of this structure toward physiochemical properties. The gigantic bovine serum albumin (BSA) molecule with tertiary structure as a ligand affects the structure of the Au_{25} NCs directly via contraction of the Au–S and Au–Au bonds: The Au–S bonds are shorter than in the theoretical model, while the Au–Au bond lengths agree with the model.

MacDonald et al. [5, 85] studied the effects of temperature and solvation of $Au_{25}(SR)_{18}$ and $Au_{38}(SR)_{24}$ nanoclusters. They observed that although the first two core shells were possibly contracted at lower temperature relative to room temperature, the third shell was expanded. On the other hand, although the nanoparticles solvated in toluene and acetonitrile (ACN) also had the first two core shells contracted, only the nanoparticles solvated in toluene showed an expansion (relaxation), and the Au–Au distance of the third shell solvated in ACN was the same as the solid. The effect that relaxation is sometimes observed for longer Au–Au distances with regard to the ligands is due to surface stabilization [86].

Self-Consistent Analysis

Frenkel et al. [12] were the first to characterize APNCs by applying the two above models (CNT and ST) independently. This self-consistent analysis uses the

comparison of results from two independent methods to give more reliable results than the use of a single model alone when applying a fitting procedure. A spherical fcc structure was used to determine the cluster size for the CNT model. Then, using the EXAFS data from their own experiment and experimentally determined values for f_{rr} and K from the literature, Frenkel and coworkers [12] determined the cluster size of thiol-stabilized gold nanoparticles according to the ST model. These findings by use of the ST model together with EXAFS are in agreement with the works by Zanchet et al. [87] and refined by Zhang and Sham [88] who used the same synthesis method as Frenkel et al. [12] but with different Au/thiol ratios. The work of these three groups did not include specification of the actual numbers of Au atoms determined by other methods such as MALDI-MS and qualify as borderline between studies of regular nanoparticles and studies of specific APNC.

Using these two methods (CNT and ST), Frenkel et al. [12] were able to determine the number of atoms in the core and particle diameters of several thiol-protected very small NCs (close to Au_{55}, Au_{147}, and Au_{561}). The EXAFS results were internally consistent, while the TEM and XRD measurements showed some discrepancies. These differences show that while methods such as TEM and XRD have problems resolving nanoclusters of this size (TEM, poor sensitivity to very small NCs smaller than 2 nm; XRD/Scherrer analysis: When the samples are dispersed in size, higher values for the particle diameter are assumed), this is not the case for EXAFS spectroscopy. However, the size dispersity of the sample does affect the reliability of the EXAFS analysis. The average particle size may be underestimated using the CNT method for size-dispersed samples. This is not the case when the ST model is used because both the mean bond length and its standard deviation (Gaussian distribution, which is the static contribution of the Debye–Waller factor in EXAFS) are involved in the determination of the size [12]. Frenkel et al. [12] concluded that the Au clusters investigated had a cuboctahedral fcc structure (using the CNs of several shells together instead of just the first shell) and that the synthesis methods (with one step or two steps) had an effect on the size of the clusters for the same Au/thiol ratios.

Frenkel and coworkers also used this self-consistent model investigating the geometry of Au_{13} NCs capped with mixed ligands [89]. The EXAFS-derived CN for three shells resulted in an icosahedral structure of the Au_{13} NCs where the number of atoms in the cluster was determined with high-angle annular dark-field scanning transmission electron microscopy (HAADF-STEM). Contraction of Au–Au bonds was measured by EXAFS and compared with ideal icosahedral structures. The differences in contraction (5 % ideal vs. 3 % EXAFS) seem to indicate that a relaxation of the strain is related to the capping ligands [89]. Even though this self-consistent method is very reasonable, it is only not often used.

However, these studies show the importance of using several models for the characterization of APNCs because each method includes some disadvantages.

4.1.3 Synergy of Multiple Techniques: The Use of Complementary Experimental Methods

There are many different techniques for the characterization of materials, such as TEM (transmission electron microscopy), UV–vis (optical spectroscopy), FTIR (Fourier-transformed infrared spectroscopy), XAS, XPS, MALDI-MS (matrix-assisted laser desorption/ionization mass spectrometry), theoretical calculations, and others. It is desirable when possible to use more than one of these techniques for the characterization of APNCs, especially when XRD, which is the major tool for structure determination, is not applicable. In some cases, the different methods complement each other and increase the level of understanding of the system, while in other cases, the results can confirm each other or point out possible problems.

Weir et al. [90] used additional TEM, UV–vis, XPS, and XANES for their in situ EXAFS investigations on Pt_{240} dendrimer-encapsulated nanoclusters (DENs). The details of the in situ EXAFS analysis are discussed in Sect. 4.1.5. UV–vis and TEM results were not discussed as these results were in agreement with previous studies. However, these techniques confirm some properties of the material under investigation. The interrelations of EXAFS with XANES are significant for this analysis. Because the XANES spectra show an oxidized species for one of the experiments, the question of including Pt–O scattering paths in the fitting procedure of the EXAFS analysis can be answered positively. This detail was crucial in the understanding of the effect of the reactions (application to the electrode, with potential, CO adsorption, and CO desorption).

In the work of Simms et al. [84] investigating Au_{25} encapsulated in bovine serum albumin (BSA), a sulfur-rich protein, TEM, EXAFS, XANES, XPS, and l-DOS were used. Here, regular TEM (compared to high-resolution TEM (HRTEM) and HAADF-STEM) is presented and shows one of the drawbacks of this method which is due to the fact that the resolution of the TEM results can be obscured by the enveloping protein. The correlation of XPS, XANES, and l-DOS is discussed in Sect. 4.2. The comparison of these results using different techniques including EXAFS, TEM, and XRD shows that the limitations of the resolution (sizes below 2 nm) of TEM and XRD lead to an overestimation of the cluster size [12]. EXAFS (CNT method) tends to underestimate the size, and EXAFS (ST model) is more accurate [12]. However, TEM can give information about the dispersity of sizes which EXAFS and XRD cannot [12]. In most cases, TEM is employed to monitor the size distribution during a reaction or comparative experiments (e.g., [21, 31]) to observe if the APNCs show changes.

Multiple techniques were used by Menard et al. [3]. To overcome the poor contrast in TEM between the smallest metal nanoparticles and the support films on which they are deposited, high-angle annular dark-field scanning transmission electron microscopy (HAADF-STEM) was employed. Using HAADF-STEM, it was possible to determine the number of atoms in the core as a size distribution showing a homogeneity of the small Au clusters with a *ca.* 13 Au atom core. This information was important to confirm that the EXAFS-derived results of the

coordination numbers had no error. Wrong determination of CNs from EXAFS analysis can arise from a significant presence of other larger clusters (in this case with fcc structure). Due to the precise results from HAADF-STEM, this scenario could be ruled out which again supported that the Au_{13} clusters have icosahedral structure.

Using HRTEM electron diffraction techniques, Menard et al. [3] were able to observe the fcc pseudo-spherical structure of the Au_{147} MPCs, while HAADF-STEM showed a much wider atom number distribution of the core. Detailed modeling showed that the coordination numbers (including CN for Au–S) and distances derived from the EXAFS analysis comply with a truncated octahedral core (which includes that a path for the second single scattering shell is applied). Altogether, in their report, Menard and coworkers [3] show how important are the careful application of models for the EXAFS analysis and the involvement of multiple scattering paths.

Frenkel et al. [89] used the same methodology (HAADF-STEM, TEM, MS EXAFS analysis, and XANES (see Sect. 4.2) as Menard et al. [3] to investigate Au_{13} NCs with a multi-ligand shell. Applying this method, they could characterize the nanocluster sample extensively – since it was both homogeneous in size and of high purity. They determined an icosahedral structure for the Au_{13} clusters, where two thiolates are bound at on-top sites, two thiolates at bridge sites, and four phosphines at on-top sites.

Vargaftik et al. [75] used TEM and SAXS to determine the cluster size of the different Pd NCs investigated. Testing the agglomeration was done with TEM and ED, while NMR, MS, FTIR, and EXAFS were used to determine the structure when XRD was not possible (because no crystal could be grown).

Benfield et al. [10] used wide-angle X-ray scattering (WAXS) as complimentary technique to EXAFS and XANES (which will be discussed in detail in Sect. 4.2) comparing bond distances and crystallite size with the EXAFS-derived results. The results from WAXS measurements are systematically larger than from EXAFS. Longer bond distances (WAXS) can be explained twofold: (a) The WAXS measurements were conducted at room temperatures and EXAFS measurements at 80 K and (b) by aggregation of NCs. The WAXS spectra (being a method similar to XRD) of the NCs are rather broad due to their more amorphous long-range structure.

In other cases [21, 91], the synergetic use of several techniques (Raman, FTIR, MALDI-MS, DFT, HAADF-TEM) was focused on the in situ application of these techniques and will be discussed in Sect. 4.1.5.

4.1.4 Combining EXAFS Analysis with DFT and MD, DFT Modeling Methods, and EXAFS Simulations

EXAFS Simulations on the Basis of DFT-Calculated Structures
Theoretical EXAFS methods, i.e., simulations of EXAFS spectra, are an effective characterization technique. These methods are based on density functional theory (DFT) calculations, and this technique became possible after structural models on the basis of DFT methods of the APNCs $Au_{144}(SR)_{60}$, $Au_{102}(SR)_{44}$, $Au_{38}(SR)_{24}$, and
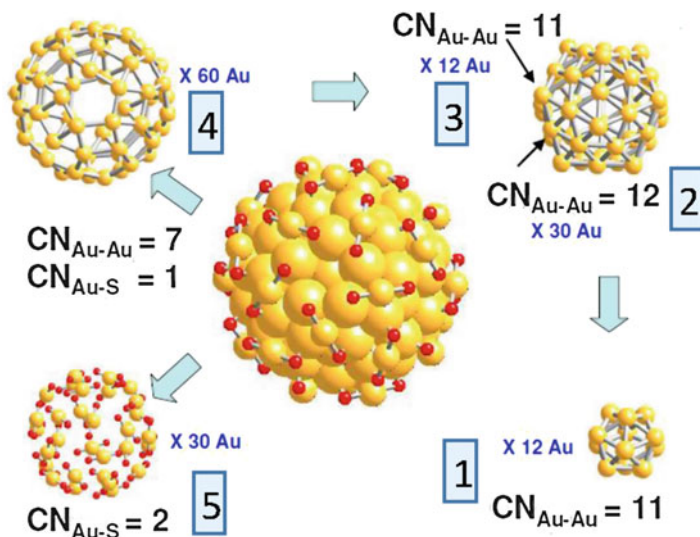
Fig. 5.8 Overview of Au sites (1–5) for the $Au_{144}(SR)_{60}$ NC (Reprinted with permission from MacDonald et al. [93] after Lopez-Acevedo et al. [20]. Copyright 2010 American Chemical Society)

$Au_{25}(SR)_{18}$ were developed by Lopez-Acevedo et al. [20], Jadzinsky et al. [92], Qian et al. [19], and Heaven et al. [18], respectively.

For the Au_{144} cluster, with well-established synthesis practices, MacDonald et al. [93] investigated the agreement of EXAFS in experiment and theory. In the theoretical structure model of the $Au_{144}(SR)_{60}$ cluster, the Au atoms are distinguished with regard to their bonding environment. Lopez-Acevedo et al. [20] proposed that the Au atoms occupy five different sites in this cluster, each of which represents a different environment for the Au atoms within the cluster. The details are shown in Fig. 5.8.

One central feature to the structure of $Au_x(SR)_y$ NCs is the so-called staple motif (Fig. 5.9). Two sulfur atoms of the thiol ligand lift a Au atom up out of the surface of the cluster like in a staple. This was proposed first by Jadzinsky et al. [92]. The staple motif is responsible for the structural stability of $Au_x(SR)_y$ NCs and can occur as monomer (RS–Au–SR) and dimer (RS–Au–(SR)–Au–SR) making Au NCs highly symmetrical [94]. The staple motif model was extended to "staple fitness" by Jiang [15] using combinatorics, and it was observed that the arrangement of the staple motifs on the surface of the NC affects the structure of the core and that the most stable configuration also protects a highly symmetrical core.

Because there are different sites for the Au atoms in the $Au_x(SR)_y$ NCs, theoretical investigations (by MacDonald et al. [93]), which were performed as simulations of EXAFS spectra (in k-space) using this structural information, have to be site specific. This means that for each site, a separate EXAFS spectrum has to be calculated, and these spectra averaged with regard to their number of degeneracy.

Fig. 5.9 Visualization of the "staple motif" as the thiolate ligand (here R = methanethiol) lifts one Au atom out of the surface (Reprinted with permission from Jiang et al. [94]. Copyright 2008 American Chemical Society)
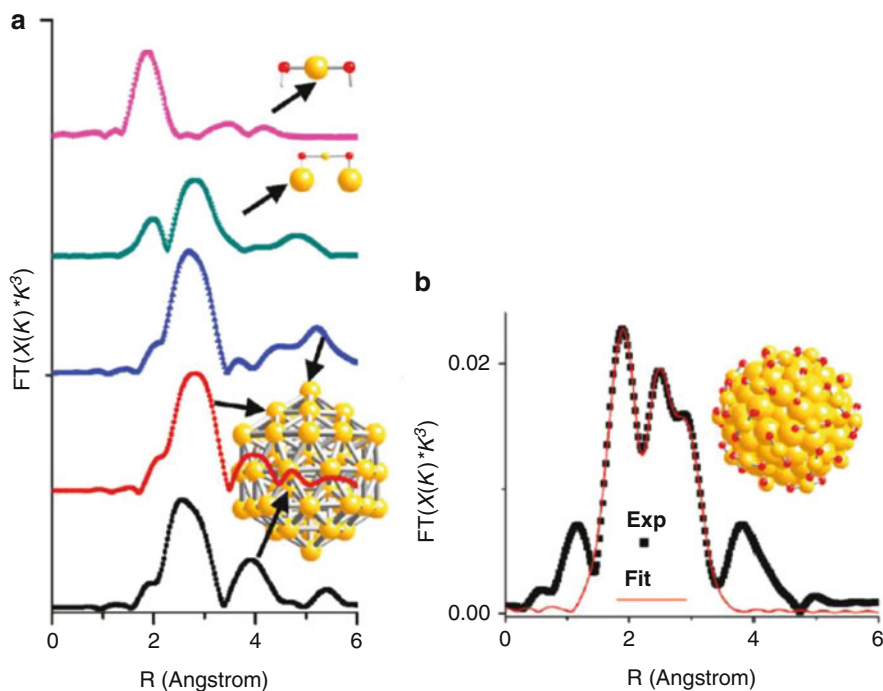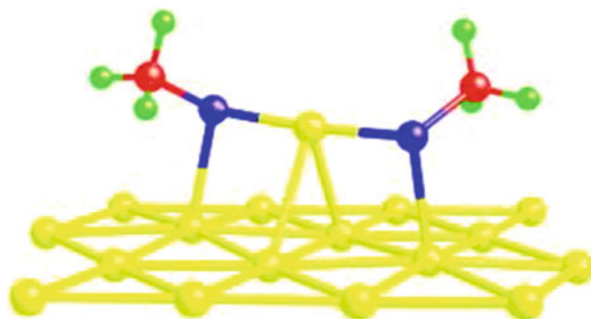
Fig. 5.10 (**a**) Examples of simulated EXAFS spectra for the five different Au sites from *bottom* to *top* (site 1–5) of the $Au_{144}(SR)_{60}$ NC, (**b**) experimental EXAFS spectrum and fit of the $Au_{144}(SR)_{60}$ NC (Reprinted with permission from MacDonald et al. [93]. Copyright 2010 American Chemical Society)

The site-specific EXAFS spectra calculated using this method and the experimental spectrum are shown in Fig. 5.10a. The correlation of the simulated EXAFS spectra with the experimental EXAFS spectra, i.e., $\chi(R)$ in R-space, is an important feature of this work [93]. Clearly, the feature around 2 Å (pink spectrum in Fig. 5.10a) is related to Au–S bonding at site 5 (staple motif), and the next feature (in the other spectra in Fig. 5.10a) at about 2.5 Å is related to the first-shell

Au–Au bonding (e.g., in the core or on the surface). This knowledge is used in all other reports for Au–thiol NCs based on the usual EXAFS fitting methods employing theoretical standards such as metal bulk. However, Fig. 5.10a with the EXAFS simulations showed this effect more visually and directly applied to the NCs. XPS results support this site-specific view of the $Au_{144}(SR)_{60}$ NC where Au atoms in the core show metallic features, Au atoms in the staple show nonmetallic features, and Au atoms on the surface of the NC show mixed features [93]. In addition, these data show that the whole cluster overall exhibits metallic behavior which is supported by the rather high intensity of the Au–Au first-shell peak in the EXAFS spectrum in Fig. 5.10b. Using the model structure of $Au_{102}(SR)_{44}$ [92] for the EXAFS fitting procedure (as standards) gives results for average Au–Au and Au–S CN that agree with the theoretical model of $Au_{144}(SR)_{60}$ from Lopez-Acevedo et al. [20].

Site-specific EXAFS simulations using the structure model of $Au_{25}(SR)_{18}$ cluster, proposed by Qian et al. [19], can show specifically that the first Au–Au shell in the core is split into three subshells. This splitting into subshells is a distinct feature for icosahedral structures, and it was observed in the experimental EXAFS spectra. The EXAFS results of $Au_{25}(SR)_{18}$ for the different environmental conditions show firstly that although the Au–Au bond length for the first Au–Au subshell decreases at low temperature, the Au–Au bond length for the third shell increases. This behavior is also observed in the solvation environments but only for toluene, with no change being observed for acetonitrile. The $Au_{25}(SR)_{18}$ NC is very special compared to the other $Au_x(SR)_y$ NCs. This cluster is characterized by six dimeric staple motifs [5], and these are expected to show significant changes in different solvation environments. For the Au–S bond length, no change can be observed in all cases which means that this stiff SR–Au–SR dimer is less responsive to the changes in the environment making this material (i.e., $Au_{25}(SR)_{18}$) more stable. Secondly, the Debye–Waller factor is much lower at lower temperature (which is to be expected) and also lower for the solvation environment (which is rather unexpected). And thirdly, upon solvation, the structural changes for the Au_{25} are not the same as observed for the Au_{38} cluster. For the Au_{38} cluster, all distances are longer (Au–S and Au–Au), and even splitting of the first Au–Au shell into two subshells for the solvated cluster was observed. The structural changes of Au_{25} are in agreement with the interactions between the aromatic solvent (i.e., toluene) and the ligand tailgroup vs. the polar solvent (i.e., acetonitrile) with the tailgroup. For the second interaction of the polar solvent with the ligand tailgroup, the ligand-induced strain on the core is not reduced as much compared with the results for toluene. There is a relaxation of the Au–Au bond distance in the third shell (and a slight lengthening for Au–S bonds) for the toluene-solvated Au_{25} only compared to the acetonitrile-solvated sample but on the other hand contraction of the first-shell Au–Au bond distance for both solvation environments. These observations confirm that there is an interplay between the Au–S bonding structure in the staple motif and the Au–Au bonding structure in the core [5]. These reports show the capabilities of EXAFS in distinguishing between the different (liquid vs. solid) environmental conditions due to the structural changes that have been observed with regard to tuning the properties of NCs.

Chevrier et al. [95] investigated $Au_{19}(SR)_{13}$ in comparison with $Au_{25}(SR)_{18}$ using EXAFS, XANES, l-DOS, and XPS. Again, XANES, l-DOS, and XPS are discussed in Sect. 4.2. The structure of $Au_{19}(SR)_{13}$ was reported by Jiang [15] (using DFT and XRD methods). Following the above technique of using this structural information from theory, the number of Au atoms in the core was varied in order to understand the structural evolution of NCs and structural stability. First, the EXAFS data were fit using only two shells in order to determine the CN for the Au–S and Au–Au coordination and to identify which of two structural scenarios agrees with the experiment. This step was necessary because the $Au_{19}(SR)_{13}$ cluster was shown to have 11 isomers [15]. Scenario 1 is that the center Au atom has a surface of only ten Au atoms (Au_{11} core) and eight Au atoms coordinate the S atoms in the staple motif (two monomers and three dimers). In scenario 2, the Au_{12} core does not have a center atom, and only seven Au atoms coordinate the S atoms in the staple motif (five monomers and one dimer). The EXAFS fitting procedure of the experimental data agreed better with scenario 1. For the refinement of the structural information, a multishell fitting where the CNs were calculated and fixed based on the $Au_{19}(SR)_{13}$ model (scenario 1) was performed. The Au–S and first Au–Au distance were found to be the same as for Au_{25}, and the second Au–Au distance was a bit longer. While the Au–S and the Au–Au bond distances for the center–surface bonding and surface–surface bonding agree very well with the fit, the long-range aurophilic distances do not. The Au–Au third shell was overestimated (meaning that the fixed CN was too high compared to the experimental data), and an incorrect Debye–Waller factor (being too large) was derived. The comparison with the $Au_{25}(SR)_{18}$ data discussed above shows the differences in the core structure (defective icosahedral) and higher structural disorder especially mixed (monomer and dimer) staple motifs [95]. This report shows that there are limitations of the EXAFS fitting technique in the presence of highly disordered system (in this case only for the long Au–Au bonds), but because of the systematic approach, reasonable conclusions still can be derived.

Exchanging the thiolate ligands for selenolate ligands, the structure of $Au_{25}(SeR)_{18}$ NCs was investigated by Chevrier and coworkers [96] based on the same multishell (three Au–Au shells) approach similar to their previous work discussed above. In addition, the analysis of Se K-edge data was included, which helped enhance the understanding of the Au–Se bond. Also, data on $Au_{25}(SR)_{18}$ were collected, reported, and analyzed again (compare [5]) to ensure consistency, which is very important. A Au–Se distance of 2.42 Å determined by Chevrier et al. was in agreement with the data from Kurashige et al. [97]. The Au–Se distance is longer than for Au–S in $Au_{25}(SR)_{18}$, which is presumed to be due to a larger covalent radius for the Se atom. The temperature dependence of the structure of $Au_{25}(SR)_{18}$ and $Au_{25}(SeR)_{18}$ was studied for 50 and 300 K. Strong contraction for the three Au–Au shells was determined for $Au_{25}(SeR)_{18}$ NCs for 300 K. This negative thermal expansion behavior was supported by DFT calculations (details for DFT calculations are discussed in section "The Relationship of DFT-MD Calculations and DFT Bases EXAFS Calculations"), and it was determined that the angle between the surface and the Au–Se–Au staples as well the angle of Au–Se in the staples changed due to the temperature change [96].
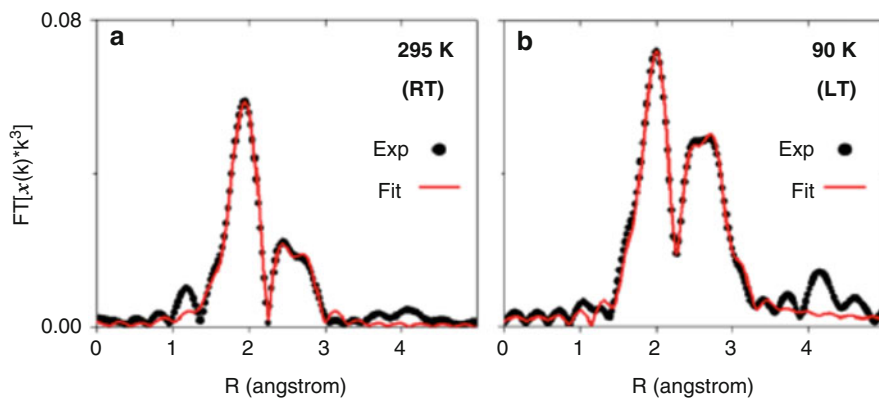
Fig. 5.11 FT-EXAFS data (*black dots*) and fit (*red line*) of the $Au_{36}(SR)_{24}$ NC at (**a**) room temperature and (**b**) low temperature. All peaks in the FT-EXAFS spectrum at low temperature are more intense and well resolved (Reprinted with permission from Chevrier et al. [98]. Copyright 2013 American Chemical Society)

This same EXAFS approach (theoretical model vs. experimental data) was used in the structural determination of $Au_{36}(SR)_{24}$ in comparison with $Au_{38}(SR)_{24}$ by Chevrier et al. [98]. They find that the Au_{36} clusters have an fcc-like core structure and bridging S atoms and four dimeric staple motifs compared to Au_{38} (icosahedral) with only staple motifs. Historically, investigations on the structure of the Au_{36} cluster exist because it is one of the few APNCs that can be grown into crystals and the structure resolved using XRD methods. The fcc-like structure of Au_{36} was verified with EXAFS using a new strategy: From a theoretical model with fcc core structure (Au_{28}), the EXAFS spectrum was simulated (k-space), and then Fourier transformed (R-space) and then backtransformed (k-space) calculated in order to compare this model data with the experimental data (isolated backtransformed signal for Au–Au bonding in the core only). These backtransformed spectra are an astonishingly good match.

Next to the Au–S shell, two Au–Au shells could be determined from the experimental EXAFS analysis. Again the CNs were fixed from the theoretical model, in this case a Au_{28} fcc core with 12 bridging and 8 Au atoms in staple motifs. For the first shell of Au–Au bonding, a much shorter distance compared to the Au_{38} cluster was observed. This experimental EXAFS data (see Fig. 5.11) show how well the scattering peaks at high R (>3.5 Å) are resolved for the low-temperature EXAFS spectra, which is directly correlated to precise (low Debye–Waller factors) values for the bond distances (when the k-range can be extended to about 16 $Å^{-1}$), and that the structural disorder increases quite much for room-temperature measurements (the Debye–Waller factor increases with temperature, and the shells are featured with much lower intensity and broadening in the R-space EXAFS spectra). It also shows that high purity of the samples is crucial for the reliability of the analysis. However, the two different Au–S bonding types (bridging and staple) did not result in different Au–S bond distances in this report [98].

The importance of the Au_4 units for the structure of the fcc-like $Au_{28}(SR)_{20}$ NCs was investigated in comparison with other $Au_x(SR)_y$ NCs in a very recent study by Chevrier et al. [99]. It was shown that site-specific EXAFS simulations can very well agree with experimental EXAFS results.

In another investigation, solely theoretical considerations of Au_{25} and Au_{102} NCs using site-specific EXAFS and l-DOS calculations were reported by Christensen et al. [100]. Due to size differences of the two NCs, the Au–Au coordination environments and also the electronic characters were found to be different. This pure theoretical discussion is important and can lead to valuable information about NC in the transition zone between atomic and bulk materials. In addition to the constant improvement of experimental techniques, the improvement of theoretical techniques is equally important. However, if these theoretical models are not compared with experiment, this information has to be regarded with caution.

The Relationship of DFT-MD Calculations and DFT Bases EXAFS Calculations

In another step to enhance the quality of EXAFS analysis and modeling, Yancey et al. [31] combined them with molecular dynamics (MD) and density functional theory (DFT). In this study, dendrimers were used to synthesize $Au_{147}S_n$ (NC with Au core and thiol shell where n gives Au/thiol ratio, also called thiol capped Au DEN). A similar system (Au–Pt DENs) was discussed in a theoretical way defining the DENs as a model system that is well defined, stable, homogeneous in size, and relatively simple (because they are not on a support) [101]. Yancey et al. [31] used the model system $Au_{147}S_n$ DEN to study the effects of different densities of the thiols on the Au surface (surface ligand density) on the structural disorder of the NCs. Along with EXAFS measurements of the $Au_{147}S_n$ DENs, theoretical EXAFS spectra were calculated based on DFT-MD simulations of the structure of the DENs as well as separate DFT-MD simulations of pair distribution functions (PDF). These methods were also reported by Yevick and Frenkel [102] and Roscioni et al. [103]. The simulated EXAFS spectra were fit using the same modeling strategy as for the experimental EXAFS spectra. More information was included by use of UV–vis and TEM. The size homogeneity was confirmed by TEM for all samples.

The EXAFS analysis shows that the CNs for Au–Au decrease and for Au–S increase when the surface density of thiols increases. This decrease in Au–Au CN with increasing surface density of thiols is in agreement with other results reported for disordered nanoparticle systems (e.g., Myers et al. [104], Price et al. [105]). For the Au–Au distances, a slight increase with higher thiol density was found which relates to a relaxation of the Au–Au bond length as discussed above. On the other hand, the increasing thiol density on the surface results in a decreasing Au–S bond length. This trend is consistent with the existence of the staple motif where the bonding of Au–S is stronger (and thus shorter). If we compare the Au–S bond in a Au–S lattice, the Au–S bond length is longer due to the fact that each S atom is pulling on several Au atoms isotropically (stellate) and vice versa in the three-dimensional lattice. Therefore, a shorter Au–S distance is highly correlated with the formation of staple motif on the surface of the DENs which is more likely for higher Au/thiol ratios. Finally, the Debye–Waller factors increase with increased surface thiol density [31]. The effects of structural disorder are discussed in detail below.

Among their results, Yancey et al. [31] find that using this method, the CNs, average bond lengths, and Debye–Waller factors are in agreement for the theoretical and experimental EXAFS data. Only in the results where the MD-derived parameters from the PDF are compared with the EXAFS-derived parameters (average bond lengths and Debye–Waller factors), there are some discrepancies. The main result of the study is that DFT-MD calculations can simulate complex experimental systems with control over structural disorder in nanoparticles and that this can improve EXAFS fitting methodologies for NC characterization. This combined technique using experimental and theoretical XAS with DFT was also used by Behafarid et al. [106]. Integrating different electron microscope techniques, they characterized Au NCs of different sizes prepared by their new synthesis method employing an inverse micelle encapsulation method with polymers. Distortions of the core structure (e.g., bond length contraction) were found to be size dependent for the ligand-protected NCs. Oyanagi et al. [107] also combined experimental and theoretical XAS with DFT to characterize Cu_{13} NCs synthesized using a new strategy of synchrotron radiolysis together with wet chemistry. Ahmadi et al. [108] also used DFT calculations, in this case on Ag and Cu NCs with cuboctahedral or Marks decahedral structure to determine lattice contraction and coordination. These calculations were though not accompanied by experimental EXAFS results.

4.1.5 In Situ EXAFS

Fast scanning techniques make it possible to observe reactions with EXAFS as they proceed (in situ). The strategic approach of using in situ EXAFS for temperature and extensive catalysis experiments consists of (1) gathering basic structural information about the system using EXAFS and (2) correlating this knowledge with chemical and structural changes of the APNCs during catalytic reactions [21]. UV–vis, MALDI-MS, TEM, and EXAFS together were applied in the examination of $Au_{25}(SR)_{18}$ MPCs on carbon support by Shivhare et al. [21] to determine that heating resulted in the removal of all of the thiolate stabilizers, while cluster integrity was maintained or until higher temperatures. The use of two different ligand thiols (phenylethanethiolate and hexanethiolate) for the experiments showed that higher activity was observed for phenylethanethiolate MPCs. A separate analysis of the $Au_{25}(SR)_{18}$ MPCs on the carbon support confirmed that the cluster kept structural integrity during the transfer process and bond lengths (Au–S and Au–Au) were not temperature dependent. However, the CNs changed (decrease for Au–S, increase for Au–Au bonds). There is a significant increase of the Au–Au CN, and the three Au–Au subshells that are characteristic for the Au_{25} cluster are not separated any longer. This is related to an increase in structural disorder and growth of the clusters, which was confirmed by TEM observing a small growth in the structures with increasing temperatures. Catalytic activation tests were performed with similar experimental conditions showing that the highest catalytic activity were observed at 250 °C where nearly all thiols have been removed from the surface [21].

Wu et al. [91] reported in situ EXAFS on $Au_{25}(SR)_{18}$ supported on CeO_2 including CO oxidation. Other methods used were UV–vis, FTIR, Raman spectroscopy, MALDI-MS, quadrupole-MS, DFT calculations, and HAADF-TEM methods.

While UV–vis, MALDI-MS, and HAADF-TEM were used to confirm the successful synthesis and loading on CeO_2 rods, the CO oxidation treatment was investigated in situ with MS, FTIR, Raman, XAS spectroscopy, and DFT calculations. In this report [91] with huge effort (many techniques) focusing on the CO oxidation effect on the Au_{25} NCs on CeO_2 support, unfortunately, no EXAFS fitting plots and/or table including fitting results were shown or discussed. Even the experimental EXAFS spectra before heating of the Au_{25} NCs on CeO_2 were not discussed. The only focus of the EXAFS analysis was a change in the Au–S bond distance (which did not occur) and the Au–S CN (a decrease was observed with heating). Since no values for Au–Au bonding and no Debye–Waller factors were given, the results derived from this EXAFS analysis can only qualitatively describe the reaction.

The structure of Pt_{240} DENs (on electrode support) during electrocatalytic oxidation of CO was investigated with in situ EXAFS, UV–vis, XPS, and TEM by Weir et al. [90]. UV–vis, XPS, and TEM results were used to confirm either data from previous reports or confirm the XAS data. Using only the CN of the first shell of the EXAFS results, the size of the Pt DENs was estimated to be about 240 atoms in agreement with TEM. After the first application of an electrical potential to the electrode, the Pt DENs were determined to be reduced. Weir et al. [90] observed that the Pt DENs were metallic (reduced) all further reactions. Especially important from this report is that the stability of the Pt DENs was not disrupted during the adsorption and subsequent oxidation of CO. The objective of this study is to understand if the catalyst (Pt DEN) can remain unchanged during the catalysis, which was successfully observed due to the stabilizing effect of the DENs. Immobilization on an electrode prevented agglomeration.

Myers et al. [104] report the in situ investigation of Pt_{225} DENs during electrocatalytic oxygen reduction reaction using EXAFS, XANES, TEM, and UV–vis. They successfully demonstrated the use of an in situ cell (like Weir et al. [90]) for electrometric experiments while recording EXAFS. Applying different potentials and gas conditions, the changes in the structure (Pt–Pt distances and CNs from EXAFS analysis) were observed but could not be fully explained. The structural disorder of the Pt NCs in these experiments can describe the discrepancy of low experimental CN compared to higher theoretical CN (fcc model clusters, size determined by TEM). This correlates well with EXAFS results, specifically multiple scattering contributions, if the core is ordered and the shell disordered. A rather fluid surface behavior for APNC was proposed by Schmid [11] using NMR techniques. This XAS cell and experimental method is promising for the analysis of such in situ experiments using EXAFS analysis. However, better quality and repeatable data is important which can be achieved by repeating measurements at the same conditions in order to make use of the correlation of electrical potential with structural effects.

4.1.6 Bimetallic APNCs

Bimetallic APNCs are discussed in Knecht et al. [62]. Using established synthesis procedures, bimetallic NCs were characterized using EXAFS. Here the synthesis employs dendrimers to form alloyed Au–Pd NCs and dodecane thiols for the extraction and stabilization of the NCs to form monolayer-protected clusters

(MPCs). Bimetallic NCs were generated in different Au/Pd ratios. EXAFS analysis is used to understand the structural changes before and after extraction for all (5) Au/Pd ratios. In their EXAFS analysis, the model for bimetallic NPs (see Sect. 3.3) was applied. Increasing CNs for Pd with increasing Pd concentration for the Au–Pd DENs show that these NCs are partly random alloy and partly in a core–shell structure (with Au in the core and Pd in the shell). For the Au–Pd MPCs, the CNs change drastically, which indicate a clear core–shell structure, where the Pd shell thickness increases with increasing Pd concentration. Additionally, coordination with sulfur was only observed for Pd atoms unless the Pd concentration was very low ($Au_{118}Pd_{29}$). However, the coordination numbers found for Pd–S bonding were much higher than anticipated for the NC model. This indicates the presence of small Pd–thiol complexes as a result of the high excess of thiol addition in the synthesis. The distances for the Au–Au, Pd–Pd, and Au–Pd bonds in the Au–Pd DENs are in agreement with other examples of binary alloys. However, for the Au–Pd MPCs, some distances (Pd–Pd) show some anomalous behavior. This behavior is either caused by relaxation effects in the Pd–S shell or due to misinterpretation cause by the presence of small Pd–S complexes that were found earlier. Detailed interpretation of UV–vis spectra supports the transformation of Au–Pd DENs into Au–Pd MPCs including the formation of a Pd–thiol compound. The analysis of bimetallic EXAFS spectra is very challenging not only because of the higher structural disorder of the system but also because these syntheses often involve the formation of a thiol species that masks the results of the bimetallic sample.

Anderson et al. [109] using in situ EXAFS, complemented by DFT calculations, XPS, UV–vis, XANES, and HRTEM and electrochemical experiments, monitored the three-step synthesis of DENs: (1) formation of a Pd core (Pd_{147} DEN), (2) deposition of a Cu shell ($Pd_{147}Cu_{162}$), and (3) galvanic exchange of Pt for Cu in the shell ($Pd_{1147}Pt_{162}$). The summarized result of this synthesis is instead structural inversion: The DENs with Pd–Cu core–shell structure change into a Pt-rich core and Pd-rich shell structure (Pt_{147} (core) $Pd_{147}Pt_{15}$ (shell)). DFT calculations were employed to help determine the structure of the Pt_{147} (core) $Pd_{147}Pt_{15}$ (shell) DENs after step 3.

Another approach based on site-specific structural considerations (such as in section "The Relationship of DFT-MD Calculations and DFT Bases EXAFS Calculations") can only be applied on very small NCs with only one doping atom. Investigations on $Au_{24}Pt(SR)_{18}$ are reported by Christensen et al. [25] using EXAFS, XPS, and l-DOS. The clusters were analyzed using Pt and Au L_3-edge EXAFS as well as previously published experimental data and theoretical knowledge about $Au_{25}(SR)_{18}$. The analysis of Au L_3-edge EXAFS spectra of the bimetallic cluster showed the contraction of Au–S and Au–Au bond distances in comparison with previous Au_{25} data. Using the Pt L_3-edge EXAFS data, the location of the doped Pt atom was determined to be in the center of the Au_{13} core. The presence of a second Pt species was determined by XPS compositional analysis. This unreacted Pt–thiolate oligomer present in the sample was also observed in the Pt L_3-EXAFS spectrum and causes a very intense Pt–S peak compared to the Pt–Au peak. This would not be possible for Pt in the center of an Au core. Further, while MALDI-MS

can in theory be a great tool to determine the cluster composition, a drawback here is that the Pt–S compound was not detected with MALDI-MS because the molecular mass of this compound was below the detection range of this device. In order to resolve this issue, instead of purifying the sample (which may not possible), Christensen et al. [25] used a theoretical approach to determine the possible CN for this mixture and, therefore, the position of the Pt atom within the Au cluster. Even though the EXAFS analysis was performed without the constraints for bimetallic clusters (as described in Sect. 3.3) and a short k-range only up to 8.8 Å^{-1} (which prevented them from resolving Au–Au vs. Au–Pt distances), this report shows that by use of several complementary methods, reasonable information for a complicated system can be derived.

Site-specific EXAFS simulations together with Mössbauer and EXAFS spectroscopy were used by Negishi et al. [28] in their report of bimetallic $Au_{24}Pd(SR)_{18}$ NC. Only EXAFS measurements at Pd K-edge are reported so only Pd–Au bonding can be discussed. The comparison of experimental with simulated EXAFS spectra of this cluster for Pd at different sites (center of the core, surface, staple) and the very high Pd–Au CN support the notion that the Pd atom is found mainly in the center of the core of the cluster. While no fits for the EXAFS analysis are shown (and the reported R-factor is 10 %, which is too high), this group makes an effort to determine the degree of purification of the synthesized clusters and improve the synthesis until the sample is purified. These findings show that effective use of EXAFS can give clear results even for the more complicated bimetallic system if great care is taken in confirming the purity of the sample and good EXAFS measurements.

4.1.7 EXAFS Analysis Is Not a Black Box

EXAFS analysis has a steep learning curve which is obvious if one watches the instruction videos or attends an EXAFS training workshop. The fitting technique using the analysis software is not "intuitive." At the same time, it is not enough to just press some buttons and the result is given. In these fast times where too much stress is laid on the number of publications, there seems to be not enough time to learn this technique by training to fit already-understood data. In this following section, a couple of problems are discussed to point out the difficulties of an EXAFS analysis that are rarely discussed.

Variety of Capping Ligands

One problem in the characterization of APNC by applying EXAFS fitting analysis, which is discussed in Menard et al. [3], is related to different and mixed ligands that are used for the stabilization of the NCs. Next to thiols (e.g., [3, 5, 89, 90, [93, 95, 98]), also phosphines [3, 89], acetates [75], selenides [97], and unoxidized tellurates [110] have been used in the literature reviewed. Also, chlorine can act as ligand as well if it is not carefully removed [69–71]. Specifically for the Au_{55} Schmid cluster, the gold atoms can have several different bonding partners in addition to gold (i.e., chlorine, triphenylphosphine, or nothing) [68]. The overview for this rather complex system is given in Table 5.2.

Table 5.2 Overview of Au sites and bonding ligand for the $Au_{55}(PPh_3)12Cl_6$ cluster

Gold site	Occupancy of site	CN
PPH3	12	5
Unbounded surface	24	7
CL	6	8
Central atom	1	12
Second central shell	12	12

Reprinted from Fairbanks [69]. Copyright (1990) with permission from Elsevier

The scattering amplitudes and phases that are calculated from theory (specifically by use of crystal structures of bulk compounds as an input for the FEFF calculations) are equivalent for elements such as P, S, Cl [3], N, C, O [90], and other elements that have similar atomic masses. The basis of the EXAFS single scattering model is that the backscattering of elements with similar atomic masses cannot be resolved within the EXAFS fitting analysis. This is connected to the principle of transferability of photoelectron phase shifts [111]. In the everyday typical EXAFS analysis, this means that a theoretical compound such as Au_2S can serve as a joint model for the determination of, for example, S and P contributions together or by themselves. It also means that S and P contributions cannot be separated. A complicated set of sites such as the Au_{55} NCs with Au–Cl, Au–P, and Au not bound (as in Table 5.2) cannot be completely specified with EXAFS. This is even more true when the surface is rather fluidic (Schmid [11]) causing structural disorder.

The Effect of Structural Disorder

Within the EXAFS data analysis technique as can be seen from the EXAFS equation (Eq. 5.5), structural disorder is parameterized in the form of the Debye–Waller factor (σ^2) (e.g., Calvin [45]). This total Debye–Waller factor includes thermal dynamic and static components that in turn represent changes in the configuration of the metal and ligand atoms in the NCs with time due to size dispersity [12]. EXAFS is only able to derive results for bond distances and bond length disorders from accurate structural and dynamic characteristics if the underlying distribution is quasi-Gaussian [31]. The effect of increased structural disorder for high temperatures as compared to low temperatures is discussed in Benfield et al. [2, 72], Chevrier et al. [98], and Shivhare et al. [21], specifically employing low temperatures (80 K). However, only in some cases, lower values for the Debye–Waller factor at low temperatures are reported [2, 72, 98]. Another aspect of this comparison is that the quality and reliability of the EXAFS analyses can be improved by taking data for the same sample at different temperatures [2, 21, 72]. The reliability of the EXAFS analysis technique can be tested observing certain ranges for the Debye–Waller factor values. For a reliable EXAFS analysis, σ^2 values for Au–Au bonding (most Me–Me bonding) need to be between 0.005 and 0.01 for the first shell and up to 0.02 for higher shells.

The effects of static structural disorder beyond the Gaussian case that are correlated to symmetric bond length distributions in the NCs are due to different bond

lengths in the core and on the surface of the NCs. This feature is called asymmetric bond length or the anharmonicity of the effective pair potential. This is reflected in the third cumulant parameter [3], a parameter included with modern EXAFS analysis software packages. The role of the third cumulant during the fitting procedure is to give an assessment of the significance of anharmonicity [12]. Symmetric bond length distributions are usually observed in bulk materials (i.e., without surface effects).

In the reports by Frenkel et al. [12], Menard et al. [3], and Yancey et al. [31], it was found that the role of the third cumulant was small. The main issue with this finding, addressed by Yancey et al. [31], is that EXAFS spectra provide only averaged information about the structure and dynamics of the environment of all absorbing atoms of the NC. If this "average" configuration is assumed to be the actual configuration, the EXAFS analysis cannot provide correct structural results. Specifically, this means that a broad distribution of sizes, shapes, crystal structures, and states of order will lead to misinterpretation of the EXAFS spectra. This effect of structural disorder on the EXAFS fit results was investigated in detail in the study by Yancey et al. [31]. One main result of this study is that the EXAFS fitting method which is based on the Gaussian bond length distribution is not able to describe highly disordered systems very well. Such systems can be described better in the PDF extracted from DFT-MD calculations, which can be asymmetric. In a report by Price et al. [105], experimental EXAFS and EXAFS simulations were combined with DFT-MD calculations for small Pt NPs in order to determine how the size determination for small NPs is affected by anharmonicity. They modeled the contraction of the surface layer was well as anisotropic disorder. In many cases, the use of the third cumulant, which should address this issue in the EXAFS fitting procedure, is not applicable because the Au–Au and Au–S bonding features (peaks) overlap and mask possible asymmetry. While it seems that this parameter does not "do" anything for some groups, it is important that it is reported together with errors and with a picture of the fit in k- and R-space in order to verify the reliability of the results.

The Importance of the k-Range and the Limitations of the Resolution of EXAFS

The limitations of the resolution of the EXAFS analysis are discussed in the report by Menard et al. [3]. While an EXAFS analysis can deliver results with a resolution of 0.001 Å for bond distances, this depends on the quality of the data measured. The knowledge that can be gathered from the EXAFS analysis can be limited when the k-range that is measured is too short or noise in high k region shortens the k-range. This results in the limitation of the spatial resolution of the EXAFS data (cf. Fig. 5.12). For example, because of the icosahedral structure of the Au_{13} NC, the Au atoms are distributed in two shells closest to the core (i.e., subshells). This multishell or splitting arises from a 5 % difference of the Au–Au distances in the distance range for the first shell [12] and could not be resolved by Menard et al. [3]. However, this group used a trick to overcome this problem: By calculating the ratios of the distances of the different shells (i.e., R_{3NN}/R_{1NN} third shell vs. first shell), the icosahedral structure for Au_{13} NCs and fcc structure for the Au_{147} MPCs
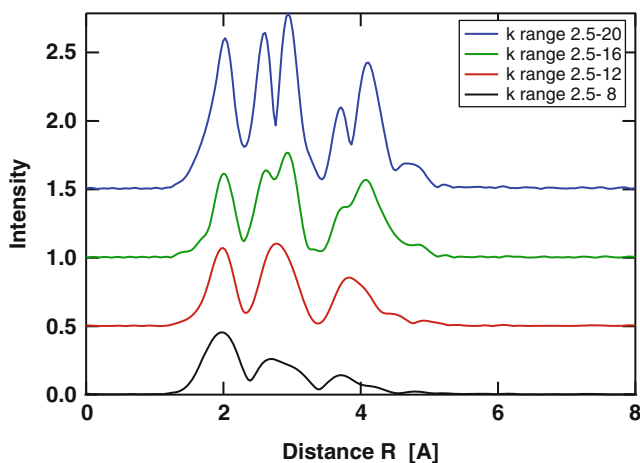
Fig. 5.12 FT-EXAFS spectra in R-space derived from the same EXAFS data (Au–S site in $Au_{102}(SR)_{44}$) for different k-ranges (from *bottom* to *top*, 2.5–8, 2.5–12, 2.5–16, and 2.5–20) (Structural data used from Jadzinsky et al. [92])

could be determined. Additionally, the fact that in the FT-EXAFS R-space spectra no single scattering for a second shell was observed helped with this assessment.

As a positive example where subshells could be observed in the experimental EXAFS spectra, the report by MacDonald et al. [5] is mentioned: The first Au–Au shell in the core is split into three subshells for the $Au_{25}(SR)_{18}$ icosahedron (determined by theoretical EXAFS). There is a discussion about the standardization to report XAS data among the XAFS community (cf. refs: IXS committee [112, 113]) ongoing. However, no agreement has been found yet.

The Requirement of Sample Purity

Menard et al. [3] also discuss discrepancies between the model (truncated octahedron) and the experimental EXAFS results (CN for Au–S) for the Au MPCs they investigated. These discrepancies are possible if the sample contains a thiolate precursor or if the NCs in the sample have degraded. Additional investigations by this group show that there are similarities in the EXAFS data between pure monomer gold (I) thiolate and the thiolate-protected Au MPCs. Menard et al. [3] point out that the EXAFS analysis technique is based on mass-weighted signals (which is nonstatistical). Therefore, with increasing metal cluster size, the CNs increase hyperbolically, and there is a higher sensitivity toward smaller clusters or low-coordination organometallic species. This means that suspiciously high Au–S and low Au–Au scattering magnitudes are related to the presence of a gold (I) thiolate species, making EXAFS uniquely sensitive to this impurity. Menard et al. [3] point out further several reports where the EXAFS data is attributed to pure NC samples; this data is actually identical to the EXAFS data of gold (I) dodecane thiolate and not NCs. The comparison of Au NCs with different cluster size (Au_{144} Au_{38} Au_{25}) by MacDonald et al. [93] confirms the sensitivity of EXAFS to the low-Z

elements because of the quite slow reduction in intensity of the Au–S peak in the EXAFS spectrum of the experimental samples.

The effect of mixed samples on EXAFS analysis is discussed extensively by Frenkel and coworkers, specifically in [55]. The importance (and verification) of the purification of the samples was shown by Negishi et al. [28]. This means that it is important to employ other techniques (e.g., XPS elemental analysis, ICP, EXAFS simulation) to confirm the purity of the sample or that the model applied agrees with the experimental data.

4.2 XANES

4.2.1 Experimental XANES and the Fingerprint Analysis

The measurement of XANES spectra can take less time than the measurement of EXAFS spectra, and more noise is acceptable for the data analysis using the fingerprint method (see Sect. 3.2). In order to gain structural information using the fingerprint method, effort has to be taken to find adequate reference spectra. In the case of APNCs, this is not always possible. In the studies when XANES data of APNCs have been reported, they were mainly shown compared with the bulk metal data (e.g., [28, 71, 84, 91, 93, 114]), which is always measured with the APNC sample simultaneously. Marcus et al. [71] used this comparison to confirm the fcc structure for the Au core in the $Au_{55}(PPh_3)_{12}Cl_6$ NCs since all the features of the bulk metal were observed in the XANES spectrum of the NC. The features (e.g., maxima) in the XANES spectrum were broadened and reduced in intensity which is known to be normal for nanoparticles [9]. Also, in MacDonald et al. [93], the metal character and fcc structure were observed for the $Au_{144}(SR)_{60}$ NCs by comparing the XANES spectra of bulk gold and the NCs. The metallic character of the one Pd atom in the bimetallic cluster $Au_{24}Pd(SR)_{18}$ was observed using Pd K-edge XANES spectra [28].

Another useful approach was reported by Frenkel et al. [89]. They acquired XANES spectra taken from the point of view of the ligand (in this case S and P K-edge) instead of metal core atoms (Au L_3-edge). The change in the chemical environment and, thus, the formation of the Me-ligand bond were confirmed because the features in the XANES spectra (at S or P K-edge) of the $Au_{13}[PPh_3]_4[S(CH_2)_{11}CH_3]_2Cl_2$ NCs were shifted to different energies compared to the pure ligand spectra. This approach was also used by Liu et al. [115]. Using also the ligand "point of view" using S K-edge XANES spectra, the increase in S–Au bonding with increasing cluster size was observed for several Au_xSR_y NCs [93].

Only in the report by Benfield et al. [10], quite a number of reference compounds for Au are presented. This group used the comparison of the XANES fingerprints to determine the metal-like chemical environment and oxidation state of the Au atoms in the $Au_{55}(PPh_3)_{12}Cl_6$ NCs. In addition to the standard reference compounds for the initial solution ($KAuCl_4$), ligand reference (PPh_3AuCl), and bulk gold, several NC and NP are collected in Fig. 5.13 showing how the features of the XANES spectra of the NCs (especially $Au_{55}(PPh_3)_{12}Cl_6$) are broadened as discussed above.
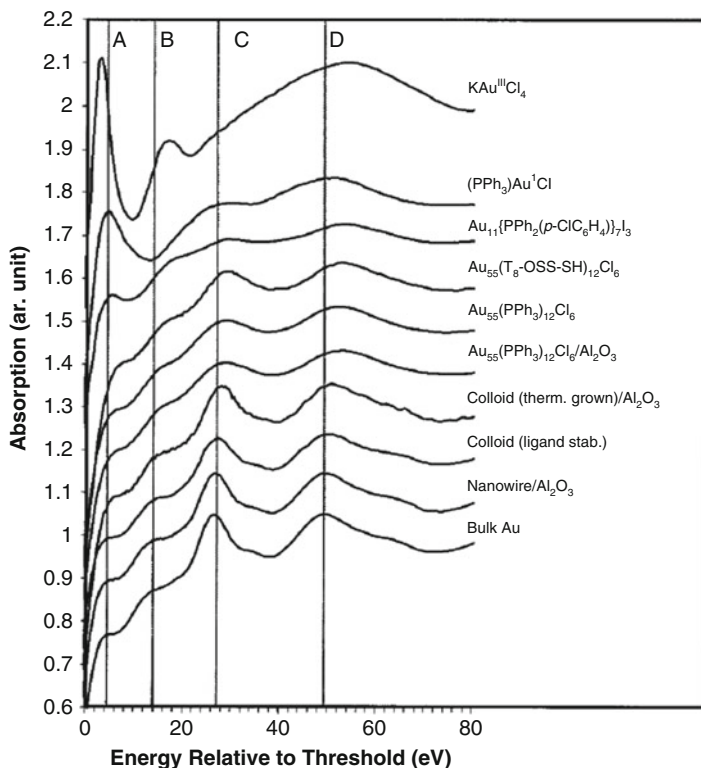
Fig. 5.13 XANES spectra at Au L_3-edge for different Au NP samples and reference compounds (Reprinted with permission from Benfield et al. [10]. Copyright 2001 American Chemical Society)

Even though not precisely about APNCs, Ohyama et al. [116] reported in situ XANES during the formation of (naked) Au NCs. This series of Au L_3-XANES spectra shows how the cluster formation starts with the precursor aurochloric acid (Au^{3+}) after addition of $NaBH_4$, reduction to Au(0), and formation of NP and how aggregation ends with the formation of Au bulk (Fig. 5.14). When the process starts, a broad peak at about 11,929 eV appears (characteristic for KAu(III)Cl) and is reduced in intensity during the reduction. An increase in WL intensity for Au L_3-edge XANES spectra at about 11,929 eV is reported for small NCs [3, 5, 28, 84, 85, 93, 95–98]. This feature is used quite extensively for the analysis of APNCs to determine the catalytic activity. The small difference of the intensity in the Au L_3-edge WL compared to bulk gold is used to indicate an increase in d-hole population.

However, caution must be applied when dealing with small differences. Although experimental XANES spectra are usually less affected by noise (because of the much more intense nature of the WL and SR) than EXAFS spectra, both EXAFS and XANES spectra always contain experimental errors that must be considered when making conclusions from the data. Firstly, there is an experimental error in the

Fig. 5.14 XANES spectra at
Au L_3-edge during the
formation of Au NPs
(Reprinted from Ohyama
et al. [116]. Copyright (2011)
with permission from
Elsevier)
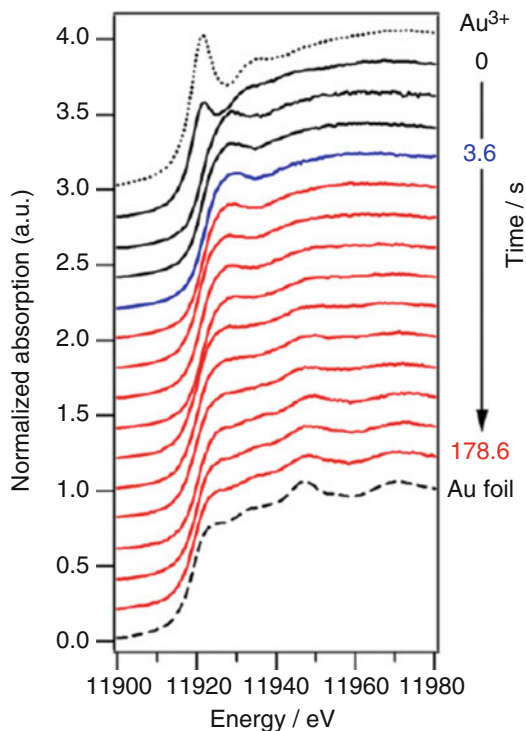
energy (E). If the energetic position of a peak maxima/minima (e.g., WL) or edge E_0
differs by more than the minimum step size (which was used for the measurements),
this difference is significant [117]. Therefore, an edge shift of 0.2 eV at Au L_3-edge
(11,919 eV) for XANES spectra of two different samples (e.g., at different temper-
atures) [96] cannot be significant because the minimum step size at Au L_3-edge is at
least 0.2 eV (more likely 0.5 eV). Secondly, there is an experimental error in the
absorption coefficient (μ) or line intensity. This was discussed in Benfield et al. [2,
10] where the differences in the intensity of the peaks were more than 5 %. An
experimental error analysis is always necessary, and this is especially true when
trying to make conclusions based on intensity differences of only a few percent. This
was crucial, e.g., in the analysis of plant samples by Bovenkamp et al. [118] at Pb
L_3-edge using a method to analyze the error contribution to XANES spectra by
Bovenkamp et al. [119]. The XAFS community is working toward the implementa-
tion of standards for XAS measurements for the last 20 years [112] in order to raise
awareness of the effect of the experimental error on the analysis of XAS experi-
ments. If small variations are reported, it should be self-evident to report the error
bars of this measurement.

L_3-edge XANES measurements are usually reported for transition metals such as
Au and Pt. The L_3-edge XANES spectra for these elements probe the transition
$2p \rightarrow 5d_{5/2}$ (or 6 s). Correspondingly, for the L_2-edge, the transition $2p \rightarrow 5d_{3/2}$

(6 s) is probed as discussed in Sect. 3.2. For the transition metals Au and Pt, the $L_{3,2}$-edge spectra are quite sensitive to electronic changes of the d-band which is especially observed in the WL region. These changes directly correlate to the oxidation state and d-band population of the material. In transition metals such as Pt and Au, the 5d-bands are filled in the metal state, and the XANES spectra (at $L_{3,2}$-edges) of these metals do not have a WL. For example, in the case of Au(III) compounds (with oxidation state 3+), the WL increases drastically due to the decrease in the occupancy of the d-orbitals (as d-electrons are transferred to the ligand) (Fig. 5.13: $KAuCl_4$). On the other hand, the Au(I) dodecane-thiolate polymer does not exhibit a strong white line even though the oxidation state of Au is 1+ [3]. This shows that the intensity of the WL does not solely depend on the oxidation state but also on the hybridization of the orbitals [3]. Additionally, stronger d–d interactions in Au NCs that increase the d-charge of Au atoms – as a "nanosize effect" [88] – might result in lower WL intensity compared to that for the bulk. Work by Zhang and Sham [120] shows also a more intense WL for Au NCs capped with thiols compared to capping with weakly interacting dendrimers (the clusters had identical size). The explanation for these effects lies in the difference in charge transfer for Au–S due to the different surface-to-volume ratios for small NCs compared to bigger ones [88] and that the size of the particle does influence this intensity due to broadening [33] as was discussed above.

In order to extract significant information from the shape (e.g., intensity differences of the WL) of the XANES spectrum, several methods intending to estimate densities of unoccupied 5d states around the Fermi level have been developed. These approaches do not just use the comparison of the intensity of the WL per se but the comparison of the intensity of the absorption edge calculated as the area under the peak [121–127]. According to Benfield and coworkers [10], only the method by Mattheiss and Dietz [125] as well as Tyson et al. [127] gives reliable semiquantitative estimates, whereas the others do not. Therefore, in two reports by Benfield et al. [2, 10], a method was used where the L_3-edge and L_2-edge spectra are compared with each other. This method employs the spin–orbit splitting effect between $d_{5/2}$ and $d_{3/2}$ orbitals to gain information on the occupancy of the $d_{5/2}$ orbital. The basis of this method is measurements of L_3-edge XANES spectra of gold, platinum, and iridium by Lytle et al. [128] showing WLs for compounds with metal oxidation state > 0, and band calculation measurements by Mattheiss and Dietz [125] show that spd hybridization causes unoccupied states in the $d_{5/2}$ and $d_{3/2}$ orbitals at the vicinity of the Fermi level.

In Benfield et al. [2], the L_3 to L_2 comparison is used to determine if Pt in the Pt_{309} NCs has molecular (oxidation state > 0) or metallic (oxidation state $= 0$) behavior. For this specific Pt_{309} NC, the comparison of the different area values for Pt foil, K_2PtCl_4, and Pt_{309} NCs resulted in the observation that the Pt atoms in the Pt_{309} NC have metallic character. In their report, Benfield and coworkers [10] investigate the oxidation state of Au in Au_{55} NCs with the same method. However, the area values for the Au_{55} NCs were smaller than those for Au bulk. The small cluster size resulting in stronger d–d interactions was the reason given why this method did not work for gold. This method was not used in any of the later reports. Possibly due to the extra time needed to measure both L_3-edge and L_2-edge XANES.

4.2.2   Theoretical XANES, l-DOS Calculations, and Charge Transfer

In a number of reports [5, 25, 84, 85, 93, 95, 98], mainly on Au APNCs, calculations of the projected DOS and charge transfer of electrons between orbitals have been discussed. The application of l-DOS and charge transfer calculations is useful because the knowledge about the DOS above and around the Fermi level makes it possible to probe the electronic structure dependent on the size of the NCs [3]. L-DOS and charge transfer calculations are used by more researchers because of the development of the theoretical description of XAS ab initio and the FEFF code as a program using those principles.

Without getting into much detail about the theory, which is covered by the literature (e.g., [9, 33, 50]), a short overview is presented here. Version FEFF6 made possible the successful calculation of EXAFS spectra based on single scattering and selected multiple scattering paths. The first time the multiple scattering expansion [129] was used to calculate XANES was in FEFF7, but only with the development of FEFF8 did the self-consistent (SCF) calculations of the scattering potential allow the determination of the Fermi energy and charge transfer. Since version FEFF8 with the development of better algorithms to calculate the matrix elements for the multiple scattering expansion and the development in computer capacity simulations of XANES spectra, l-DOS and charge transfer became easily calculable. Further, the multiple scattering calculations were extended to a real-space full multiple scattering routine [130] to prevent the divergence of the path expansion at low photon energy (which is exactly around the absorption edge). This important feature (real-space full multiple scattering) is crucial in any XANES calculation and, thus, l-DOS and charge transfer calculations. The real-space multiple scattering approach [130], which makes the FEFF8 (and later versions) code so user friendly (i.e., not difficult to use), needs the input of cluster data (of any compound or NC) in real space (xyz). This input can be derived from different atomic programs based on crystal structure.

Using the FEFF code to get a XANES spectrum is not too difficult. However, if something that looks somewhat like (the) data is calculated (and electron counts and l-DOS is calculated in any case), it is important to test its validity. These tests would include:

- Convergence of the SCF calculations (to determine the stability of the Fermi energy and thus electron transfer)
- Convergence of the full multiple scattering calculations (to determine the necessary cluster size)
- Agreement with the experimental data (to determine the validity of the cluster used and thus the l-DOS curves)

For typical compounds, it has been shown that 5–6 shells of atoms around the absorbing atom are required for a multiple scattering calculations in the full multiple scattering module so that the cluster can reproduce a XANES spectrum for that compound [131]. For more complicated structures such as NCs where the cluster size of one particle is effectively too small for the full multiple scattering calculation (e.g., with < 100 atoms in a cluster such as the Au_{25} or Au_{38} NCs), the convergence

Fig. 5.15 XANES spectra at Au L_3-edge of Au$_{13}$, Au$_{43}$, Au$_{55}$, and Au$_{78}$ clusters calculated with FEFF (Reprinted with permission from Chen et al. [133]. Copyright (2007) American Chemical Society)
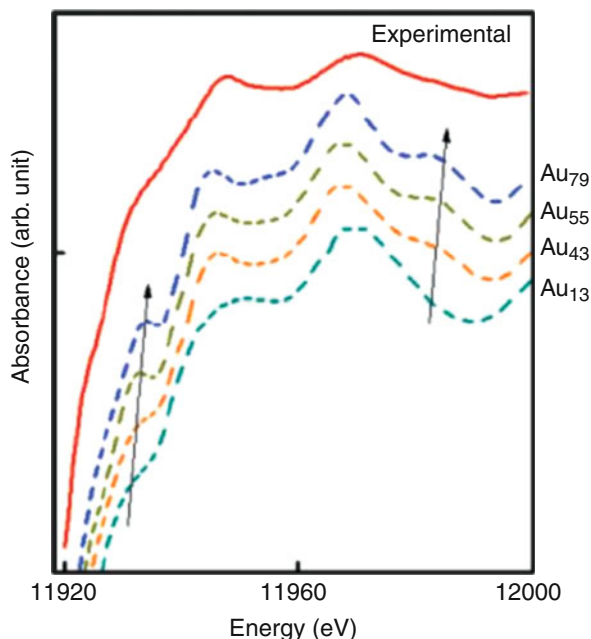
of the full multiple scattering calculations cannot be reached which means that the calculated XANES spectrum is not correct. This was described by Soldatov et al. [132] for small clusters at the Au L_3-edge.

The development of XANES features for small Au clusters was studied by Chen et al. [133] applying the XANES simulation tool of FEFF8 using a simple model of fcc gold. Figure 5.15 shows the simulated XANES spectra for several Au clusters created by restricting the cluster size for the full multiple scattering calculation (to shells 1–4) in comparison with the experimental XANES spectrum. Broadening washes out the features (e.g., maxima) of the XANES spectra for NCs (and other small nanoparticles, as was discussed above) similar to the effect of the different Au–Au bonding structure for the surface sites on NCs. Further, theoretical XANES investigations of small metal clusters were also done by Bazin and Rehr [1]. They find that the inner structure as well affects the XANES spectrum [1].

However, in the above report by Chen et al. [133], the XANES calculations are not completely correct, since the cluster size used was too small. The application of the full multiple scattering module, which is crucial for the XANES calculations, involves the inclusion of all multiple scattering contributions. Together with the muffin tin approximation, the center of the potential calculations, it is necessary to use large clusters for the calculations where the contributions of surface atoms can be neglected [1]. For a small cluster, this means that the contributions of (a) the Au–S staple motif atoms and (b) other nearby clusters have to be included.

There are discrepancies between experiment and FEFF calculations that are due to approximations. This fact is known, and the need for improvement of the FEFF

code for XANES calculations is discussed by the developers of FEFF (e.g., [130, 134, 135]). Including full potential calculations instead of spherical muffin tin calculations is necessary to accurately model for anisotropic systems. Also, better treatments of inelastic losses, self-energy, many-body corrections, and core–hole effects need to be implemented. These factors are rarely discussed within the community (because they know about it), but the new user might not be aware of these limitations and the connections between XANES and l-DOS. In a sequence of studies by Soldatov and coworkers [136–139], other software codes not using the muffin tin approximation were compared to FEFF for small clusters of Ti, Cu, and Nb. Oyanagi et al. [107] also used other software codes beyond the muffin tin approximation for their time-resolved characterization of radiolysis-irradiated Cu samples. These studies show the above-stated points.

To better understand the following discussions about l-DOS and charge transfer, some basics about Au are mentioned first. The electronic structure of Au was reported by Coulthard et al. [140] and Kuhn and Sham [141]: Due to the configuration of Au (as $[Xe]4f^{14}5d^{10}6s^1$), the d-band in metallic Au is nominally full. However, d and non-d (sp) rehybridization is possible and can create d-band holes where the Fermi level is then somewhere in the middle of the d-band 0.4 of the population for Au [88, 125]. Even for alloy formation, this rehybridization showed a significant effect in XPS and XANES [141]. Therefore, the first peak of the Au L_3-edge XANES spectrum (the WL, transition $2p \rightarrow 5d_{5/2}$) is related to the presence of d-holes [125, 140] (see Fig. 5.13) which, in turn, is related to a peak in the d-DOS. However, caution is necessary when interpreting features of the l-DOS curves as contributions to the XANES spectrum; not in all cases mixing (e.g., p–d mixing results in L_3 features [118]) is possible.

MacDonald et al. [5, 85, 93] used EXAFS, XANES, and XPS, and, in addition, l-DOS and charge transfer calculations, to study Au thiolate APNCs. The XANES spectra of the simulations were found to show features similar to those in the experimental spectra (Fig. 5.16a and b). However, it is not discussed why the experimental data shows a better resolution/less broadening compared to the simulations (usually it is reversed, and additional broadening has to be introduced with the simulated spectra). The strong S–Au/S–C (A and B) line in the S K-edge spectrum was inspected further. The l-DOS calculations here confirm that feature A originates from S–Au bonding and feature B originates from S–C bonding. The features a and a' in the simulated spectrum (Fig. 5.16c) are not resolved in the experimental spectrum (Fig. 5.16a). The discussion of similarities between calculated and experimental spectra in relationship to the presence and absence of S–C bonding is quite useful to confirm the bonding-type information reported by Chaudhuri et al. [142] and Zhang and Sham [88].

L-DOS and charge transfer calculations can be complemented with XPS and can extend the understanding of electronic properties [84]. XPS can also support the other results from MacDonald et al. [93] where the d-DOS of Au–S and Au–Au bonding shows the same behavior (molecular/nonmetallic = sharp singlet, metallic = wide doublet). Similar effects were observed by MacDonald et al. [85] for an Au_{38} cluster, by Chevrier et al. [95] for Au_{19} and Au_{25} clusters, and by Simms et al. [84] for Au_{25} clusters.
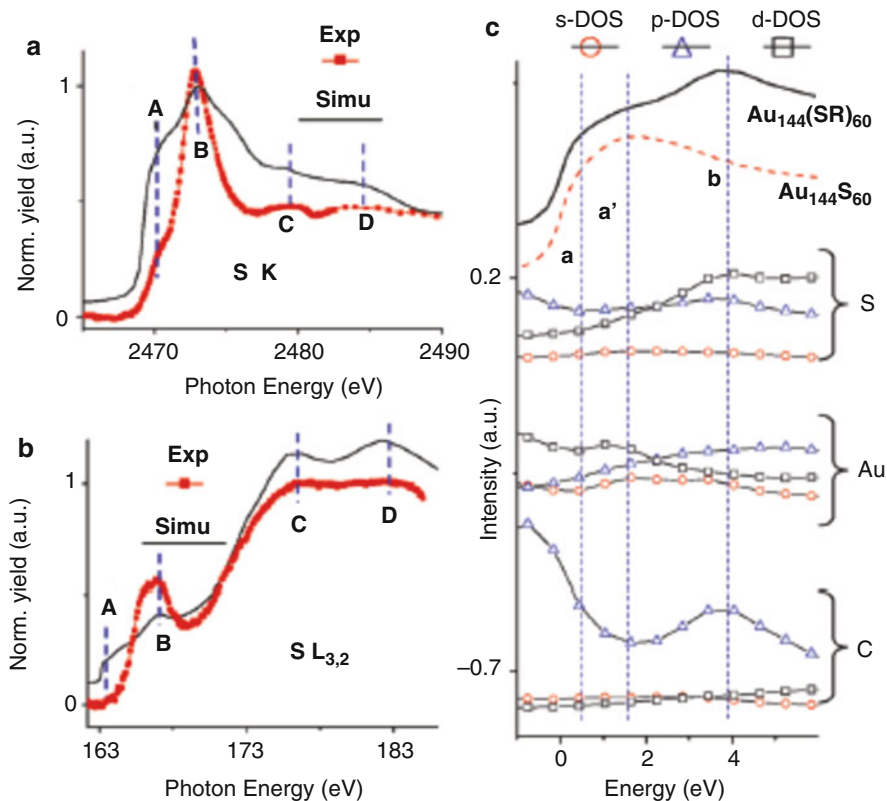
Fig. 5.16 Experimental and theoretical XANES spectra of $Au_{144}(SR)_{60}$ at (**a**) S K-edge, (**b**) S $L_{3/2}$-edge, and (**c**) calculated l-DOS of the S, Au, and C atoms of $Au_{144}(SR)_{60}$, with simulated XANES spectra of $Au_{144}(SR)_{60}$ (*black line*) compared to $Au_{144}S_{60}$ (*red dotted line*), over only about 2470–2476 eV (Reprinted with permission from MacDonald et al. [93]. Copyright 2010 American Chemical Society)

Site-specific d- and s-electron occupancy was used by MacDonald et al. [5, 85] to show similar properties of similar atomic sites for Au_{38} and Au_{25} NCs including charge transfer for Au in staple sites compared to Au in core sites. This is in agreement with a hypothesis of donation (3 s to Au 6 s) and back donation (Au 5d to S 3p) by Park and coworkers [143]. Also in this report, a theoretical model was used to represent solvation effects. The d-DOS curves of both the solid and the modeled (solvated) Au_{38} NC show that next to the narrowing of the d-band in the staple motif (as above) a shift to higher (closer to Fermi level) energies can be observed for the solvated model [85]. This hypothesis should be investigated more closely.

Chevrier et al. [95, 96, 98] compare the l-DOS curves (site specific) of $Au_{19}(SR)_{13}$ vs. $Au_{25}(SR)_{18}$, also $Au_{25}(SeR)_{18}$ vs. $Au_{25}(SR)_{18}$, and Au_{36} vs. ideal Au_{28} core, respectively, similar to the work by MacDonald et al. above. For the

comparison of the Au_{19} vs. Au_{25} NCs, the d-band for Au surface and Au center sites is broadened for Au_{25}. XPS results agree with this observation indicating that the Au_{11} core of Au_{19} has defects and has fewer Au–Au bonding interactions compared to the Au_{13} core of Au_{25} [95]. For the $Au_{25}(SeR)_{18}$ vs. $Au_{25}(SR)_{18}$ NCs, the 5d-band of the selenolate NCs shows higher electron counts compared to the 5d-band of the thiolated NCs which is linked to less charge transfer and more covalent behavior of the Au–Se bond [96]. The investigation of the electronic behavior of $Au_{36}(SR)_{24}$ and $Au_{38}(SR)_{24}$ resulted in the finding that for the Au_{36} cluster, the Au–Au bonding is more molecular compared to a rather metallic Au–Au bonding in Au_{38} NCs [98].

5 Conclusion and Future Perspectives

The quite young field of atomically precise nanoclusters started in the 1980s and was first addressed by the technique of EXAFS in 1985 [74] with early forms of analysis software. The boost of synchrotron radiation facilities and theoretical developments subsequentially has led to greatly improved analysis software and strategies to apply EXAFS to all kinds of systems.

One of the main uses for EXAFS became the determination of the size (number of atoms) of the APNCs. This was implemented using structural models based on atomic packing (e.g., fcc) and the proportionality of size and CN within these models. The successful application of this strategy made it possible to compare TEM, XRD, and EXAFS results.

The EXAFS strategies that were developed for the characterization of NP can be applied similarly to APNCs. However, *improvements* in EXAFS, such as the CNT model or the surface-tension model, were necessary due to the small size of the NCs. One important feature of all nanoparticle investigations is that the amplitudes of the EXAFS signals (in k-space and R-space) of the nanoparticles compared to the bulk metal are always reduced and in XANES even broadened. It has been shown that a self-consistent approach for the EXAFS analysis, using different models within the same technique, is a good method in order to validify the results characterizing the NCs.

Since XAS is a technique based on the *average configuration* of the sample under investigation, disorder within this configuration (more precisely disorder in the structure due to different bond distances) can lead to EXAFS analysis results that can be misleading.

XANES and EXAFS are not black boxes where a button just has to be pressed to measure the samples and spit out the results. Some understanding of the underlying physics of both methods (which includes an understanding of the errors involved) and a deeper understanding of the methods which are the basis of the technique have to be developed [144].

The techniques and methods that are presented here give a brief overview of the models that EXAFS analysis can use and how XANES and l-DOS calculations can be applied.

The application of complementary techniques (including HRTEM and HAADF-STEM to determine size homogeneity) is important to help validate the EXAFS results. Even more so can theoretical calculations using different techniques (DFT-EXAFS, DFT-MD) help to determine effects of structural disorder on the EXAFS analysis of experimental spectra.

The extraction of electronic information about APNCs from XAS can be done through L-DOS calculations based on FEFF. However, this has to be set in perspective with previous DOS calculations or XPS results to make proper analyses.

In conclusion, we find that a number of groups are using XAS techniques, especially EXAFS analysis for the characterization of APNCs. These reports are not just about understanding the structure of the NCs any longer but more so about tuning the properties of these NCs by varying the ligands. A particular driving force in these reports has been the understanding of the effect of the staple motif. EXAFS is a very powerful tool to study the changes in structure including bond length, coordination environment, and disorder that can be examined very powerfully. This use of the XAS toolbox (theoretical, experimental, in situ EXAFS and XANES, and l-DOS calculations) in its variety does help to gain more accurate information about the structural and electronic properties of APNC and their catalytic application.

Further improvements in the application of EXAFS/XANES in the characterization of APNCs lie in the development of reactors that can be installed in the XAS beamline to collect X-ray absorption spectra in situ as temperature and pressure are varied or other environmental conditions are needed or to observe the synthesis or a catalytic reaction itself. Such reactors to observe the synthesis can be, for example, milli-fluidic reactors (e.g., [145]) which bring the possibility of spatially resolved observation of the reaction. X-ray fluorescence mapping and X-ray microscopy using micro-focused beams are also useful.

Summarizing, we find that EXAFS and XANES are exciting and versatile techniques in the study of APNCs and their use in catalysis. The analysis of XAS data can be quite challenging, however, and it is important to have a thorough knowledge of the physics and possible sources of error involved and, in many cases, combine the EXAFS and XANES analyses with other techniques, and theoretical modeling, to produce the best understanding of the system under investigation.

References

1. Bazin D, Rehr JJ (2003) Limits and advantages of x-ray absorption near edge structure for nanometer scale metallic clusters. J Phys Chem B 107(45):12398–12402. doi:10.1021/Jp0223051

2. Benfield RE, Filipponi A, Morgante N, Schmid G (1999) Structural characterisation of the giant organometallic platinum cluster $Pt_{309}(phen^*)_{36}O_{30}$ using EXAFS. J Organomet Chem 573(1–2):299–304. doi:10.1016/S0022-328x(98)00878-X

3. Menard LD, Xu HP, Gao SP, Twesten RD, Harper AS, Song Y, Wang GL, Douglas AD, Yang JC, Frenkel AI, Murray RW, Nuzzo RG (2006) Metal core bonding motifs of monodisperse icosahedral Au_{13} and larger Au monolayer-protected clusters as revealed by X-ray absorption

spectroscopy and transmission electron microscopy. J Phys Chem B 110(30):14564–14573. doi:10.1021/Jp060740f

4. Zhu M, Aikens CM, Hollander FJ, Schatz GC, Jin R (2008) Correlating the crystal structure of a thiol-protected Au25 cluster and optical properties. J Am Chem Soc 130(18):5883. doi:10.1021/ja801173r

5. MacDonald MA, Chevrier DM, Zhang P, Qian H, Jin R (2011) The structure and bonding of Au25(SR)18 nanoclusters from EXAFS: the interplay of metallic and molecular behavior. J Phys Chem C 115(31):15282–15287. doi:10.1021/jp204922m

6. Qian HF, Jin RC (2009) Controlling nanoparticles with atomic precision: the case of Au144(SCH2CH2Ph)60. Nano Lett 9(12):4083–4087. doi:10.1021/nl902300y

7. Schaaff TG, Shafigullin MN, Khoury JT, Vezmar I, Whetten RL (2001) Properties of a ubiquitous 29 kDa Au:SR cluster compound. J Phys Chem B 105(37):8785–8796. doi:10.1021/jp011122w

8. Jin RC (2010) Quantum sized, thiolate-protected gold nanoclusters. Nanoscale 2(3):343–362. doi:10.1039/B9nr00160c

9. Modrow H (2004) Tuning nanoparticle properties – the X-ray absorption spectroscopic point of view. Appl Spectrosc Rev 39(2):183–290. doi:10.1081/Asr-120030955

10. Benfield RE, Grandjean D, Kroll M, Pugin R, Sawitowski T, Schmid G (2001) Structure and bonding of gold metal clusters, colloids, and nanowires studied by EXAFS, XANES, and WAXS. J Phys Chem B 105(10):1961–1970. doi:10.1021/Jp0028812

11. Schmid G (1985) Developments in transition-metal cluster chemistry – the way to large clusters. Struct Bond 62:51–85. doi:10.1007/BFb0009185

12. Frenkel AI, Nemzer S, Pister I, Soussan L, Harris T, Sun Y, Rafailovich MH (2005) Size-controlled synthesis and characterization of thiol-stabilized gold nanoparticles. J Chem Phys 123(18):184701. doi:10.1063/1.2126666

13. Deheer WA (1993) The physics of simple metal-clusters – experimental aspects and simple-models. Rev Mod Phys 65(3):611–676. doi:10.1103/RevModPhys.65.611

14. Hakkinen H, Walter M, Gronbeck H (2006) Divide and protect: capping gold nanoclusters with molecular gold-thiolate rings. J Phys Chem B 110(20):9927–9931. doi:10.1021/Jp0619787

15. Jiang D-e (2011) Staple fitness: a concept to understand and predict the structures of thiolated gold nanoclusters. Chem Eur J 17(44):12289–12293. doi:10.1002/chem.201102391

16. Benfield RE (1992) Mean coordination numbers and the nonmetal metal transition in clusters. J Chem Soc Faraday Trans 88(8):1107–1110. doi:10.1039/Ft9928801107

17. Frenkel A (2007) Solving the 3D structure of metal nanoparticles. Zeitschrift Fur Kristallographie 222(11):605–611. doi:10.1524/zkri.2007.222.11.605

18. Heaven MW, Dass A, White PS, Holt KM, Murray RW (2008) Crystal structure of the gold nanoparticle [N(C8H17)4][Au25(SCH2CH2Ph)18]. J Am Chem Soc 130(12):3754–3755. doi:10.1021/ja800561b

19. Qian H, Eckenhoff WT, Zhu Y, Pintauer T, Jin R (2010) Total structure determination of thiolate-protected Au38 nanoparticles. J Am Chem Soc 132(24):8280–8281. doi:10.1021/ja103592z

20. Lopez-Acevedo O, Akola J, Whetten RL, Gronbeck H, Hakkinen H (2009) Structure and bonding in the ubiquitous icosahedral metallic gold cluster Au144(SR)60. J Phys Chem C 113(13):5035–5038. doi:10.1021/jp8115098

21. Shivhare A, Chevrier DM, Purves RW, Scott RWJ (2013) Following the thermal activation of Au25(SR)18 clusters for catalysis by X-ray absorption spectroscopy. J Phys Chem C 117(39):20007–20016. doi:10.1021/jp4063687

22. Myers VS, Weir MG, Carino EV, Yancey DF, Pande S, Crooks RM (2011) Dendrimer-encapsulated nanoparticles: new synthetic and characterization methods and catalytic applications. Chem Sci 2(9):1632–1646. doi:10.1039/C1sc00256b

23. Behrens P (1992) X-ray absorption-spectroscopy in chemistry 2. X-ray absorption near edge structure. TrAC-Trend Anal Chem 11(7):237–244. doi:10.1016/0165-9936(92)87056-P

24. Zhu Y, Qian HF, Drake BA, Jin RC (2010) Atomically precise $Au_{25}(SR)_{18}$ nanoparticles as catalysts for the selective hydrogenation of α, β-unsaturated ketones and aldehydes. Angew Chem Int Ed 49(7):1295–1298. doi:10.1002/anie.200906249

25. Christensen SL, MacDonald MA, Chatt A, Zhang P, Qian H, Jin R (2012) Dopant location, local structure, and electronic properties of $Au_{24}Pt(SR)_{18}$ nanoclusters. J Phys Chem C 116(51):26932–26937. doi:10.1021/jp310183x

26. Negishi Y, Iwai T, Ide M (2010) Continuous modulation of electronic structure of stable thiolate-protected Au_{25} cluster by Ag doping. Chem Commun 46(26):4713–4715. doi:10.1039/C0CC01021A

27. Negishi Y, Igarashi K, Munakata K, Ohgake W, Nobusada K (2012) Palladium doping of magic gold cluster $Au_{38}(SC_2H_4Ph)_{24}$: formation of $Pd_2Au_{36}(SC_2H_4Ph)_{24}$ with higher stability than $Au_{38}(SC_2H_4Ph)_{24}$. Chem Commun 48(5):660–662. doi:10.1039/C1CC15765E

28. Negishi Y, Kurashige W, Kobayashi Y, Yamazoe S, Kojima N, Seto M, Tsukuda T (2013) Formation of a $Pd@Au_{12}$ superatomic core in $Au_{24}Pd_1(SC_{12}H_{25})_{18}$ probed by ^{197}Au Mössbauer and Pd K-edge EXAFS spectroscopy. J Phys Chem Lett 4(21):3579–3583. doi:10.1021/jz402030n

29. Negishi Y, Munakata K, Ohgake W, Nobusada K (2012) Effect of copper doping on electronic structure, geometric structure, and stability of thiolate-protected Au_{25} nanoclusters. J Phys Chem Lett 3(16):2209–2214. doi:10.1021/jz300892w

30. Kurashige W, Munakata K, Nobusada K, Negishi Y (2013) Synthesis of stable Cu_nAu_{25}-n nanoclusters (n = 1–9) using selenolate ligands. Chem Commun 49(48):5447–5449. doi:10.1039/C3CC41210E

31. Yancey DF, Chill ST, Zhang L, Frenkel AI, Henkelman G, Crooks RM (2013) A theoretical and experimental examination of systematic ligand-induced disorder in Au dendrimer-encapsulated nanoparticles. Chem Sci 4(7):2912. doi:10.1039/c3sc50614b

32. Bare SR, Ressler T (2009) Characterization of catalysts in reactive atmospheres by X-ray absorption spectroscopy. Adv Catal 52:339–465. doi:10.1016/S0360-0564(08)00006-0

33. Koningsberger DC, Prins R (1987) X-ray absorption: principles, applications, techniques of EXAFS, SEXAFS, and XANES. Wiley, New York, Chemical analysis, vol. 92

34. Frenkel AI, Cason MW, Elsen A, Jung U, Small MW, Nuzzo RG, Vila FD, Rehr JJ, Stach EA, Yang JC (2014) Critical review: effects of complex interactions on structure and dynamics of supported metal catalysts. J Vac Sci Technol A 32(2) 020801:1–17. doi:10.1116/1.4820493

35. Frenkel AI, Yevick A, Cooper C, Vasic R (2011) Modeling the structure and composition of nanoparticles by extended X-ray absorption fine-structure spectroscopy. Annu Rev Anal Chem 4:23–39. doi:10.1146/annurev-anchem-061010-113906

36. Lapresta-Fernandez A, Salinas-Castillo A, de la Llana SA, Costa-Fernandez JM, Dominguez-Meister S, Cecchini R, Capitan-Vallvey LF, Moreno-Bondi MC, Marco MP, Sanchez-Lopez JC, Anderson IS (2014) A general perspective of the characterization and quantification of nanoparticles: imaging, spectroscopic, and separation techniques. Crit Rev Solid State Mater Sci 39(6):423–458. doi:10.1080/10408436.2014.899890

37. Schmid G (2010) Nanoparticles: from theory to application, 2nd edn. Wiley-VCH, Weinheim

38. Hakkinen H (2008) Atomic and electronic structure of gold clusters: understanding flakes, cages and superatoms from simple concepts. Chem Soc Rev 37(9):1847–1859. doi:10.1039/B717686b

39. Pei Y, Zeng XC (2012) Investigating the structural evolution of thiolate protected gold clusters from first-principles. Nanoscale 4(14):4054–4072. doi:10.1039/C2nr30685a

40. Frenkel AI (2012) Applications of extended X-ray absorption fine-structure spectroscopy to studies of bimetallic nanoparticle catalysts. Chem Soc Rev 41(24):8163–8178. doi:10.1039/C2cs35174a

41. Gao F, Goodman DW (2012) Pd-Au bimetallic catalysts: understanding alloy effects from planar models and (supported) nanoparticles. Chem Soc Rev 41(24):8009–8020. doi:10.1039/C2cs35160a

42. Jin R, Nobusada K (2014) Doping and alloying in atomically precise gold nanoparticles. Nano Res 7(3):285–300. doi:10.1007/s12274-014-0403-5

43. Zhang P (2014) X-ray spectroscopy of gold–thiolate nanoclusters. J Phys Chem C 118 (44):25291–25299

44. Bunker G (2010) Introduction to XAFS: a practical guide to X-ray absorption fine structure spectroscopy. Cambridge University Press, Cambridge/New York

45. Calvin S (2013) XAFS for everyone. CRC press, Boca Raton

46. Kelly SD, Hesterberg D, Ravel B (2008) Analysis of soils and minerals using X-ray absorption spectroscopy. In: Ulery AL (ed) Mineralogical methods. Methods of soil analysis, vol 5. Soil Science Society of America, Madison, pp 387–464

47. Teo BK (1986) EXAFS: basic principles and data analysis. Inorganic chemistry concepts, vol 9. Springer, Berlin/New York

48. Pantelouris A, Kuper G, Hormes J, Feldmann C, Jansen M (1995) Anionic gold in Cs_3auo and Rb_3auo established by X-ray-absorption spectroscopy. J Am Chem Soc 117 (47):11749–11753. doi:10.1021/Ja00152a016

49. Kuno M (2011) Introductory nanoscience – physical and chemical concepts, 1st edn. Garland Science, New York

50. Rehr JJ, Albers RC (2000) Theoretical approaches to x-ray absorption fine structure. Rev Mod Phys 72(3):621–654. doi:10.1103/RevModPhys.72.621

51. Ravel B (2000) Introduction to EXAFS experiments and theory. Open access. doi:http://feff. phys.washington.edu/~ravel/

52. Ravel B, Newville M (2005) ATHENA, ARTEMIS, HEPHAESTUS: data analysis for X-ray absorption spectroscopy using IFEFFIT. J Synchrotron Radiat 12:537–541. doi:10.1107/S0909049505012719

53. Ressler T (1998) WinXAS: a program for X-ray absorption spectroscopy data analysis under MS-Windows. J Synchrotron Radiat 5:118–122

54. Westre TE, Di Cicco A, Filipponi A, Natoli CR, Hedman B, Solomon EI, Hodgson KO (1995) GNXAS, a multiple-scattering approach to EXAFS analysis: methodology and applications to iron complexes. J Am Chem Soc 117(5):1566–1583. doi:10.1021/ja00110a012

55. Frenkel AI, Wang Q, Sanchez SI, Small MW, Nuzzo RG (2013) Short range order in bimetallic nanoalloys: an extended X-ray absorption fine structure study. J Chem Phys 138(6) 064202:1–7. doi:10.1063/1.4790509

56. Calvin S, Carpenter E, Ravel B, Harris V, Morrison S (2002) Multiedge refinement of extended x-ray-absorption fine structure of manganese zinc ferrite nanoparticles. Phys Rev 66(22) 224405:1–13. doi:10.1103/PhysRevB.66.224405

57. Calvin S, Miller MM, Goswami R, Cheng SF, Mulvaney SP, Whitman LJ, Harris VG (2003) Determination of crystallite size in a magnetic nanocomposite using extended x-ray absorption fine structure. J Appl Phys 94(1):778. doi:10.1063/1.1581344

58. Frenkel AI (1999) Solving the structure of nanoparticles by multiple-scattering EXAFS analysis. J Synchrotron Radiat 6:293–295. doi:10.1107/S0909049598017786

59. Frenkel AI, Hills CW, Nuzzo RG (2001) A view from the inside: complexity in the atomic scale ordering of supported metal nanoparticles. J Phys Chem B 105(51):12689–12703. doi:10.1021/Jp012769j

60. Nashner MS, Frenkel AI, Adler DL, Shapley JR, Nuzzo RG (1997) Structural characterization of carbon-supported platinum-ruthenium nanoparticles from the molecular cluster precursor $PtRu_5C(CO)_{16}$. J Am Chem Soc 119(33):7760–7771. doi:10.1021/Ja971039f

61. Frenkel A (2007) Solving the 3D structure of metal nanoparticles. Zeitschrift für Kristallographie 222(11/2007). doi:10.1524/zkri.2007.222.11.605

62. Knecht MR, Weir MG, Frenkel AI, Crooks RM (2008) Structural rearrangement of bimetallic alloy PdAu nanoparticles within dendrimer templates to yield core/shell configurations. Chem Mater 20(3):1019–1028. doi:10.1021/Cm0717817

63. Lemonnier M, Collet O, Depautex C, Esteva JM, Raoux D (1978) High-vacuum two crystal soft-X-ray monochromator. Nucl Instrum Methods 152(1):109–111. doi:10.1016/0029-554x(78) 90246-X

64. Lee PA, Citrin PH, Eisenberger P, Kincaid BM (1981) Extended X-ray absorption fine-structure – its strengths and limitations as a structural tool. Rev Mod Phys 53(4):769–806. doi:10.1103/RevModPhys.53.769

65. Stern EA, Kim K (1981) Thickness effect on the extended-X-ray-absorption-fine-structure amplitude. Phys Rev B 23(8):3781–3787. doi:10.1103/PhysRevB.23.3781

66. Boscherini F, de Panfilis S, Weissmuller J (1998) Determination of local structure in nanophase palladium by x-ray-absorption spectroscopy. Phys Rev B 57(6):3365–3374. doi:10.1103/PhysRevB.57.3365

67. Stern EA, Yacoby Y (1996) Structural disorder in perovskite ferroelectric crystals as revealed by XAFS. J Phys Chem Solids 57(10):1449–1455. doi:10.1016/0022-3697(96)00012-1

68. Schmid G, Pfeil R, Boese R, Bandermann F, Meyer S, Calis GHM, Vandervelden WA (1981) $Au_{55}[P(C_6H_5)_3]_{12}cl_6$ – a gold cluster of an exceptional size. Chem Ber 114(11):3634–3642. doi:10.1002/cber.19811141116

69. Cluskey PD, Newport RJ, Benfield RE, Gurman SJ, Schmid G (1993) An EXAFS study of some gold and palladium cluster compounds. Z Phys D At Mol Clusters 26:8–11. doi:10.1007/BF01425601

70. Fairbanks MC, Benfield RE, Newport RJ, Schmid G (1990) An EXAFS study of the cluster molecule $Au_{55}(PPh_3)_{12}Cl_6$. Solid State Commun 73(6):431–436. doi:10.1016/0038-1098(90)90045-D

71. Marcus M, Andrews M, Zegenhagen J, Bommannavar A, Montano P (1990) Structure and vibrations of chemically produced Au_{55} clusters. Phys Rev B 42(6):3312–3316. doi:10.1103/PhysRevB.42.3312

72. Benfield RE, Filipponi A, Bowron DT, Newport RJ, Gurman SJ, Schmid G (1995) EXAFS investigations of high-nuclearity Pd clusters. Phys B Condens Matter 208(1–4):671–673. doi:10.1016/0921-4526(94)00783-R

73. Glasner D, Frenkel AI (2007) Geometrical characteristics of regular polyhedra: application to EXAFS studies of nanoclusters. AIP Conf Proc 882(1):746–748. doi:10.1063/1.2644651

74. Vargaftik MN, Zagorodnikov VP, Stolyarov IP, Moiseev II, Likholobov VA, Kochubey DI, Chuvilin AL, Zaikovsky VI, Zamaraev KI, Timofeeva GI (1985) A novel giant palladium cluster. J Chem Soc Chem Commun 14:937–939. doi:10.1039/C39850000937

75. Vargaftik MN, Moiseev II, Kochubey DI, Zamaraev KI (1991) Giant palladium clusters – synthesis and characterization. Faraday Discuss 92:13–29. doi:10.1039/Fd9919200013

76. Jentys A (1999) Estimation of mean size and shape of small metal particles by EXAFS. Phys Chem Chem Phys 1(17):4059–4063. doi:10.1039/A904654b

77. Beale AM, Weckhuysen BM (2010) EXAFS as a tool to interrogate the size and shape of mono and bimetallic catalyst nanoparticles. Phys Chem Chem Phys 12(21):5562–5574. doi:10.1039/B925206a

78. Teo BK, Sloane NJA (1985) Magic numbers in polygonal and polyhedral clusters. Inorg Chem 24(26):4545–4558. doi:10.1021/Ic00220a025

79. Schmid G (2008) The relevance of shape and size of Au_{55} clusters. Chem Soc Rev 37(9):1909–1930. doi:10.1039/B713631P

80. Mays CW, Vermaak JS, Kuhlmann D (1968) On surface stress and surface tension. 2. Determination of surface stress of gold. Surf Sci 12(2):134. doi:10.1016/0039-6028(68)90119-2

81. Häberlen OD, Chung S-C, Stener M, Rösch N (1997) From clusters to bulk: a relativistic density functional investigation on a series of gold clusters Au_n, n = 6,...,147. J Chem Phys 106(12):5189–5201. doi:10.1063/1.473518

82. Kruger S, Vent S, Rosch N (1997) Size dependence of bond length and binding energy in palladium and gold clusters. Ber Bunsen Phys Chem 101(11):1640–1643. doi:10.1002/bbpc.19971011115

83. Kruger S, Vent S, Nortemann F, Staufer M, Rosch N (2001) The average bond length in Pd clusters Pd_n, n = 4-309: a density-functional case study on the scaling of cluster properties. J Chem Phys 115(5):2082–2087. doi:10.1063/1.1383985

84. Simms GA, Padmos JD, Zhang P (2009) Structural and electronic properties of protein/thiolate-protected gold nanocluster with "staple" motif: a XAS, L-DOS, and XPS study. J Chem Phys 131(21):214703. doi:10.1063/1.3268782

85. MacDonald MA, Zhang P, Chen N, Qian HF, Jin RC (2011) Solution-phase structure and bonding of $Au_{38}(SR)_{24}$ nanoclusters from X-ray absorption spectroscopy. J Phys Chem C 115(1):65–69. doi:10.1021/Jp1102884

86. Fritsche HG, Buttner T (1999) Modification of the lattice contraction of small metallic particles by chemical and/or geometrical stabilization. Z Phys Chem 209:93–101

87. Zanchet D, Tolentino H, Alves MCM, Alves OL, Ugarte D (2000) Inter-atomic distance contraction in thiol-passivated gold nanoparticles. Chem Phys Lett 323(1–2):167–172. doi:10.1016/S0009-2614(00)00424-3

88. Zhang P, Sham T (2003) X-ray studies of the structure and electronic behavior of alkanethiolate-capped gold nanoparticles: the interplay of size and surface effects. Phys Rev Lett 90(24) 245502:1–4. doi:10.1103/PhysRevLett.90.245502

89. Frenkel AI, Menard LD, Northrup P, Rodriguez JA, Zypman F, Glasner D, Gao SP, Xu H, Yang JC, Nuzzo RG (2007) Geometry and charge state of mixed-ligand Au_{13} nanoclusters. AIP Conf Proc 882(1):749–751. doi:10.1063/1.2644652

90. Weir MG, Myers VS, Frenkel AI, Crooks RM (2010) *In situ* X-ray absorption analysis of approximately 1.8 nm dendrimer-encapsulated Pt nanoparticles during electrochemical CO oxidation. Chemphyschem Eur J Chem Phys Phys Chem 11(13):2942–2950. doi:10.1002/cphc.201000452

91. Wu Z, Jiang DE, Mann AK, Mullins DR, Qiao ZA, Allard LF, Zeng C, Jin R, Overbury SH (2014) Thiolate ligands as a double-edged sword for CO oxidation on CeO_2 supported $Au_{25}(SCH_2CH_2Ph)_{18}$ nanoclusters. J Am Chem Soc 136(16):6111–6122. doi:10.1021/ja5018706

92. Jadzinsky PD, Calero G, Ackerson CJ, Bushnell DA, Kornberg RD (2007) Structure of a thiol monolayer-protected gold nanoparticle at 1.1 Å resolution. Science 318(5849):430–433. doi:10.1126/science.1148624

93. MacDonald MA, Zhang P, Qian HF, Jin RC (2010) Site-specific and size-dependent bonding of compositionally precise gold-thiolate nanoparticles from X-ray spectroscopy. J Phys Chem Lett 1(12):1821–1825. doi:10.1021/Jz100547q

94. Jiang DE, Tiago ML, Luo WD, Dai S (2008) The "Staple" motif: a key to stability of thiolate-protected gold nanoclusters. J Am Chem Soc 130(9):2777. doi:10.1021/Ja710991n

95. Chevrier DM, MacDonald MA, Chatt A, Zhang P, Wu Z, Jin R (2012) Sensitivity of structural and electronic properties of gold–thiolate nanoclusters to the atomic composition: a comparative X-ray study of $Au_{19}(SR)_{13}$ and $Au_{25}(SR)_{18}$. J Phys Chem C 116(47):25137–25142. doi:10.1021/jp309283y

96. Chevrier DM, Meng X, Tang Q, Jiang D-e, Zhu M, Chatt A, Zhang P (2014) Impact of the selenolate ligand on the bonding behavior of Au_{25} nanoclusters. J Phys Chem C 118 (37):21730–21737. doi:10.1021/jp508419p

97. Kurashige W, Yamazoe S, Kanehira K, Tsukuda T, Negishi Y (2013) Selenolate-protected Au_{38} nanoclusters: isolation and structural characterization. J Phys Chem Lett 4 (18):3181–3185. doi:10.1021/jz401770y

98. Chevrier DM, Chatt A, Zhang P, Zeng C, Jin R (2013) Unique bonding properties of the $Au_{36}(SR)_{24}$ nanocluster with FCC-like core. J Phys Chem Lett 4(19):3186–3191. doi:10.1021/jz401818c

99. Chevrier DM, Zeng C, Jin R, Chatt A, Zhang P (2014) Role of Au_4 units on the electronic and bonding properties of $Au_{28}(SR)_{20}$ nanoclusters from X-ray spectroscopy. J Phys Chem C 119 (2):1217–1223. doi:10.1021/jp509296w

100. Christensen SL, Cho P, Chatt A, Zhang P (2014) A site-specific comparative study of Au_{102} and Au_{25} nanoclusters using theoretical EXAFS and l-DOS. Can J Chem 93:1–5. doi:10.1139/cjc-2014-0271

101. Yancey DF, Zhang L, Crooks RM, Henkelman G (2012) Au@Pt dendrimer encapsulated nanoparticles as model electrocatalysts for comparison of experiment and theory. Chem Sci 3(4):1033–1040. doi:10.1039/C2sc00971d

102. Yevick A, Frenkel AI (2010) Effects of surface disorder on EXAFS modeling of metallic clusters. Phys Rev B 81 115451:1–7. doi:10.1103/PhysRevB.81.115451

103. Roscioni OM, Zonias N, Price SWT, Russell AE, Comaschi T, Skylaris C-K (2011) Computational prediction of L_3 EXAFS spectra of gold nanoparticles from classical molecular dynamics simulations. Phys Rev B 83 115409:1–8. doi:10.1103/PhysRevB.83.115409

104. Myers VS, Frenkel AI, Crooks RM (2012) *In situ* structural characterization of platinum dendrimer-encapsulated oxygen reduction electrocatalysts. Langmuir 28(2):1596–1603. doi:10.1021/la203756z

105. Price SWT, Zonias N, Skylaris CK, Hyde TI, Ravel B, Russell AE (2012) Fitting EXAFS data using molecular dynamics outputs and a histogram approach. Phys Rev B 85(7), 075439:1–14. doi:10.1103/Physrevb.85.075439

106. Behafarid F, Matos J, Hong S, Zhang L, Rahman TS, Roldan Cuenya B (2014) Structural and electronic properties of micellar Au nanoparticles: size and ligand effects. ACS Nano 8(7):6671–6681. doi:10.1021/nn406568b

107. Oyanagi H, Orimoto Y, Hayakawa K, Hatada K, Sun Z, Zhang L, Yamashita K, Nakamura H, Uehara M, Fukano A, Maeda H (2014) Nanoclusters synthesized by synchrotron radiolysis in concert with wet chemistry. Sci Rep 4. doi:10.1038/srep07199

108. Ahmadi S, Zhang X, Gong Y, Sun CQ (2014) Effect of atomic under-coordination on the properties of Ag and Cu nanoclusters. Proc SPIE 9165, Phys Chem Interfaces Nanomaterials XIII, 91650. doi:10.1117/12.2059745

109. Anderson RM, Zhang L, Loussaert JA, Frenkel AI, Henkelman G, Crooks RM (2013) An experimental and theoretical investigation of the inversion of Pd@Pt core@shell dendrimer-encapsulated nanoparticles. ACS Nano 7(10):9345–9353. doi:10.1021/Nn4040348

110. Kurashige W, Yamazoe S, Yamaguchi M, Nishido K, Nobusada K, Tsukuda T, Negishi Y (2014) Au_{25} clusters containing unoxidized tellurolates in the ligand shell. J Phys Chem Lett 5 (12):2072–2076. doi:10.1021/jz500901f

111. Citrin P, Eisenberger P, Kincaid B (1976) Transferability of phase shifts in extended X-ray absorption fine structure. Phys Rev Lett 36(22):1346–1349. doi:10.1103/PhysRevLett.36.1346

112. IXS_Committee (2000a) Error reporting recommendation: a report of the International XAFS Society standards and criteria committee. http://ixs.iit.edu/subcommittee_reports/sc/

113. IXS_Committee (2000b) Report of the International XAFS Society standards and criteria committee. http://ixs.iit.edu/subcommittee_reports/sc/

114. Weir MG, Knecht MR, Frenkel AI, Crooks RM (2010) Structural analysis of PdAu dendrimer-encapsulated bimetallic nanoparticles. Langmuir 26(2):1137–1146. doi:10.1021/La902233h

115. Liu J, Krishna KS, Losovyj YB, Chattopadhyay S, Lozova N, Miller JT, Spivey JJ, Kumar CSSR (2013) Ligand-stabilized and atomically precise gold nanocluster catalysis: a case study for correlating fundamental electronic properties with catalysis. Chem-Eur J 19 (31):10201–10208. doi:10.1002/chem.201300600

116. Ohyama J, Teramura K, Shishido T, Hitomi Y, Kato K, Tanida H, Uruga T, Tanaka T (2011) *In Situ* Au L_3 and L_2 edge XANES spectral analysis during growth of thiol protected gold nanoparticles for the study on particle size dependent electronic properties. Chem Phys Lett 507(1–3):105–110. doi:10.1016/j.cplett.2011.03.020

117. Chauvistre R (1987) Absorptionsspektroskopie an Atomen und kleinen Molekülen im weichen Röntgengebiet. Diplom thesis, University of Bonn

118. Bovenkamp GL, Prange A, Schumacher W, Ham K, Smith AP, Hormes J (2013) Lead uptake in diverse plant families: a study applying X-ray absorption near edge spectroscopy. Environ Sci Technol 47(9):4375–4382. doi:10.1021/Es302408m

119. Bovenkamp GL, Prange A, Roy A, Schumacher W, Hormes FJ (2009) X-ray absorption near edge structure spectra as a basis for the speciation of lead. J Phys Conf Ser 190:012190. doi:10.1088/1742-6596/190/1/012190

120. Zhang P, Sham TK (2002) Tuning the electronic behavior of Au nanoparticles with capping molecules. Appl Phys Lett 81(4):736. doi:10.1063/1.1494120

121. Behrens P, Assmann S, Bilow U, Linke C, Jansen M (1999) Electronic structure of silver oxides investigated by AgL XANES spectroscopy. Z Anorg Allg Chem 625(1):111–116. doi:10.1002/(Sici)1521-3749(199901)625:1<111::Aid-Zaac111>3.0.Co;2-7

122. Evans J, Mosselmans JFW (1991) L-edge studies on molybdenum. J Phys Chem 95(24): 9673–9676. doi:10.1021/J100177a015

123. Hlil EK, BaudoingSavois R, Moraweck B, Renouprez AJ (1996) X-ray absorption edges in platinum-based alloys 2. Influence of ordering and of the nature of the second metal. J Phys Chem 100(8):3102–3107. doi:10.1021/Jp951440t

124. Mansour AN, Cook JW, Sayers DE (1984) Quantitative technique for the determination of the number of unoccupied d-electron states in a platinum catalyst using the $L_{2,3}$ X-ray absorption-edge spectra. J Phys Chem 88(11):2330–2334. doi:10.1021/J150655a029

125. Mattheiss LF, Dietz RE (1980) Relativistic tight-binding calculation of core-valence transitions in Pt and Au. Phys Rev B 22(4):1663–1676. doi:10.1103/PhysRevB.22.1663

126. Moraweck B, Renouprez AJ, Hlil EK, Baudoingsavois R (1993) Alloying effects on X-ray absorption edges in $Pt_{1-x}Nix$ single-crystals. J Phys Chem 97(17):4288–4292. doi:10.1021/J100119a009

127. Tyson CC, Bzowski A, Kristof P, Kuhn M, Sammynaiken R, Sham TK (1992) Charge redistribution in Au-Ag alloys from a local perspective. Phys Rev B 45(16):8924–8928. doi:10.1103/PhysRevB.45.8924

128. Lytle FW, Wei PSP, Greegor RB, Via GH, Sinfelt JH (1979) Effect of chemical environment on magnitude of x-ray absorption resonance at L_{III} edges. Studies on metallic elements, compounds, and catalysts. J Chem Phys 70(11):4849. doi:10.1063/1.437376

129. Zabinsky SI, Rehr JJ, Ankudinov A, Albers RC, Eller MJ (1995) Multiple-scattering calculations of X-ray-absorption spectra. Phys Rev B 52(4):2995–3009. doi:10.1103/PhysRevB.52.2995

130. Ankudinov AL, Ravel B, Rehr JJ, Conradson SD (1998) Real-space multiple-scattering calculation and interpretation of x-ray-absorption near-edge structure. Phys Rev B 58 (12):7565–7576. doi:10.1103/PhysRevB.58.7565

131. Ravel B (2005) A practical introduction to multiple scattering theory. J Alloy Compd 401 (1–2):118–126. doi:10.1016/j.jallcom.2005.04.021

132. Soldatov MA, Ascone I, Congiu-Castellano A, Messori L, Cinellu MA, Balerna A, Soldatov AV, Yalovega GE (2009) Potential antitumor gold drugs: DFT and XANES studies of local atomic and electronic structure. J Phys Conf Ser 190:012210. doi:10.1088/1742-6596/190/1/012210

133. Chen HM, Liu RS, Asakura K, Jang LY, Lee JF (2007) Controlling length of gold nanowires with large-scale: X-ray absorption spectroscopy approaches to the growth process. J Phys Chem C 111(50):18550–18557. doi:10.1021/Jp0770615

134. Kas JJ, Sorini AP, Prange MP, Cambell LW, Soininen JA, Rehr JJ (2007) Many-pole model of inelastic losses in x-ray absorption spectra. Phys Rev B 76 195116:1–10. doi:10.1103/Physrevb.76.195116

135. Rehr JJ (2006) Theory and calculations of X-ray spectra: XAS, XES, XRS, and NRIXS. Radiat Phys Chem 75(11):1547–1558. doi:10.1016/j.radphyschem.2005.11.014

136. Mazalova V, Kravtsova A, Yalovega G, Soldatov A, Piseri P, Coreno M, Mazza T, Lenardi C, Bongiorno G, Milani P (2007) Free small nanoclusters of titanium: XANES study. Nucl Instrum Methods Phys Res, Sect A 575(1–2):165–167. doi:10.1016/j.nima.2007.01.058

137. Mazalova VL, Soldatov AV, Adam S, Yakovlev A, Möller T, Johnston RL (2009) Small copper clusters in Ar shells: a study of local structure. J Phys Chem C 113(21):9086–9091. doi:10.1021/jp809401r

138. Mazalova VL, Soldatov AV (2008) Geometrical and electronic structure of small copper nanoclusters: XANES and DFT analysis. J Struct Chem 49(1):107–115. doi:10.1007/s10947-008-0208-z

139. Kravtsova AN, Lomachenko KA, Soldatov AV, Meyer J, Niedner-Schatteburg G, Peredkov S, Eberhardt W, Neeb M (2014) Atomic and electronic structure of free niobium nanoclusters: simulation of the $M_{4,5}$-XANES spectrum of Nb_{13}^+. J Electron Spectrosc Relat Phenom 195:189–194. doi:10.1016/j.elspec.2014.07.005

140. Coulthard I, Degen S, Zhu YJ, Sham TK (1998) Gold nanoclusters reductively deposited on porous silicon: morphology and electronic structures. Can J Chem 76(11):1707–1716. doi:10.1139/cjc-76-11-1707

141. Kuhn M, Sham T (1994) Charge redistribution and electronic behavior in a series of Au-Cu alloys. Phys Rev B 49(3):1647–1661. doi:10.1103/PhysRevB.49.1647

142. Chaudhuri A, Odelius M, Jones RG, Lee TL, Detlefs B, Woodruff DP (2009) The structure of the Au(111)/methylthiolate interface: new insights from near-edge x-ray absorption spectroscopy and x-ray standing waves. J Chem Phys 130(12) 124708:1–11. doi:10.1063/1.3102095

143. Park YS, Whalley AC, Kamenetska M, Steigerwald ML, Hybertsen MS, Nuckolls C, Venkataraman L (2007) Contact chemistry and single-molecule conductance: a comparison of phosphines, methyl sulfides, and amines. J Am Chem Soc 129(51):15768. doi:10.1021/Ja0773857

144. Ravel B (2014) Deeper understanding of EXAFS. Private communication

145. Krishna KS, Navin CV, Biswas S, Singh V, Ham K, Bovenkamp GL, Theegala CS, Miller JT, Spivey JJ, Kumar CSSR (2013) Millifluidics for time-resolved mapping of the growth of gold nanostructures. J Am Chem Soc 135(14):5450–5456. doi:10.1021/Ja400434c

146. Yu Y, Luo Z, Chevrier DM, Leong DT, Zhang P, Jiang D-e, Xie J (2014) Identification of a highly luminescent $Au_{22}(SG)_{18}$ nanocluster. J Am Chem Soc 136(4):1246–1249. doi:10.1021/ja411643u

147. Nishigaki JI, Tsunoyama R, Tsunoyama H, Ichikuni N, Yamazoe S, Negishi Y, Ito M, Matsuo T, Tamao K, Tsukuda T (2012) A new binding motif of sterically demanding thiolates on a gold cluster. J Am Chem Soc 134(35):14295–14297. doi:10.1021/Ja305477a

148. Pande S, Weir MG, Zaccheo BA, Crooks RM (2011) Synthesis, characterization, and electrocatalysis using Pt and Pd dendrimer-encapsulated nanoparticles prepared by galvanic exchange. New J Chem 35(10):2054–2060. doi:10.1039/C1nj20083f

X-Ray Absorption Spectroscopic Characterization of Nanomaterial Catalysts in Electrochemistry and Fuel Cells

6

Kotaro Sasaki and Nebojsa Marinkovic

Contents

K. Sasaki
Chemistry Department, Brookhaven National Laboratory, Upton, NY, USA
e-mail: ksasaki@bnl.gov

N. Marinkovic (✉)
Department of Chemical Engineering, Columbia University, New York, NY, USA
e-mail: marinkov@bnl.gov

315

1   Definition of Topic

X-ray absorption spectroscopy is a nondestructive synchrotron-based technique that measures the changes in x-ray absorption coefficient of a material as a function of energy of the x-rays. The technique has an advantage over other spectroscopy techniques as it can resolve the short-range arrangement of atoms. Since many of today's catalysts for electrochemical systems are in particles of a few nanometers in size (nanoparticles) and the technique can resolve the inner atomic structure of the nanoparticle, XAS quickly became a powerful tool for studying electrochemical catalysts, particularly in the field of fuel cells.

2   Overview

The chapter describes operation principles of x-ray absorption spectroscopy (XAS) technique and its application to atomic arrangement in nanoparticles, with a special interest in electrochemistry.

XAS is a nondestructive technique that measures the changes in x-ray absorption coefficient of a material as a function of energy. X-rays of a narrow energy resolution are shone on the sample, and the incident and transmitted x-ray intensity are recorded as the incident x-ray energy is incremented. When the incident x-ray energy matches the binding energy of an electron of an atom within the sample, the number of x-rays absorbed by the sample increases dramatically, causing a drop in the transmitted x-ray intensity; this is referred to as an absorption edge. Each element has a set of unique absorption edges giving XAS element selectivity. Because it requires a tunable x-ray source, XAS spectra are usually collected at synchrotrons. The x-rays are highly penetrating and allow studies of gases, solids, or liquid at concentrations of as low as a few ppm. When applied to nanoparticles, the technique can resolve inner arrangement of atoms within. XAS can be separated into two parts, depending on the range it covers with respect to the absorption edge, i.e., x-ray absorption near-edge spectroscopy and extended x-ray absorption fine structure (XANES and EXAFS).

As it is element specific, XANES can resolve the oxidation state of the element, as well as its coordination environment and subtle changes in it. EXAFS analyzes the local structure of the atoms in all physical states (solid, liquid, and gas), but the unique power of the spectroscopy is found in metal clusters, particularly in nanomaterials. It can resolve the inner structure of the nanoparticle clusters composed of two or more elements, i.e., solid solution, aggregate mixtures, or core–shell particle in which one metal is present mostly in the center of the particle (core) and the other forms a shell around it. These nanoparticle systems are of a special interest in catalytic electrochemical oxidation and/or reduction, as most of these systems require expensive noble metals and minimizing their content is the goal of the present technology development. Since the atoms in the core of the particle are not exposed to the electrochemical environment, they can be substituted by non-noble

materials. This chapter deals with electrochemical catalysts composed of two or more metal atoms and shows the basics of the analysis of these systems.

3   Introduction

While catalytic oxidation or reduction of species in electrochemistry involves the surface of the catalyst, there are a limited number of techniques that can study the catalyst surface during the electrochemical potential excursion, i.e., in situ. Vacuum techniques such as Auger electron spectroscopy (AES), x-ray photoelectron spectroscopy (XPS), and low-energy electron diffraction (LEED) are ideal for probing the solution/surface interface, but can only be used before and after the catalytic process. In situ electrochemical techniques like infrared reflection–absorption spectroscopy and differential electrochemical mass spectroscopy can reveal species adsorbed on the surface and/or in solution, but provide limited insight on the changes of the catalyst. X-ray absorption spectroscopy (XAS) is an ideal method for in situ studies of electrochemical systems because both the solution and the catalyst can be probed by penetrating x-rays. The technique yields both structural and chemical information. Since it is element specific, XAS permits investigation of the chemical environment of a constituent element in a composite material such as alloy catalysts. The chemical environment of the constituents can be studied by tuning the beam energy to the specific absorption edge of the element. Unlike x-ray diffraction (XRD) that probes the long-range order of atoms in the sample and therefore cannot yield information of nanoparticles smaller than *ca.* 3 nm, XAS probes the short-range order, and it can provide structural information on nanoparticles of practically any size. It can be also used to study amorphous materials, liquids, gases, adsorbed monolayers, and hydrated ions and complexes in aqueous solution or in dilute systems.

XAS is also sometimes called x-ray absorption fine structure (XAFS), where the fine structure refers to the details on the absorption of x-rays by an atom at energies in the vicinity of the core-level energy of the atom. Its spectra are especially sensitive to the formal oxidation state and coordination chemistry of absorbing atom, as well as the distances, coordination number, and nature of species in its immediate surroundings. XAS is routinely used in a wide range of scientific fields, including biology, environmental science, catalyst research, and material science. One major advantage of XAS in the study of electrocatalysts is its ability to probe the *d* states of Pt catalysts. The technique and its applications have been described in books, review articles, and online tutorials [1–5].

4   X-Ray Absorption Spectroscopy: Interaction with Matter

Matter interacts with x-ray light by the photoelectric effect. An atom in its ground state absorbs the x-ray energy and ejects an electron (called "photoelectron") from the atom's inner shell (K, L, or M) into continuum, Fig. 6.1. The atom is in an excited
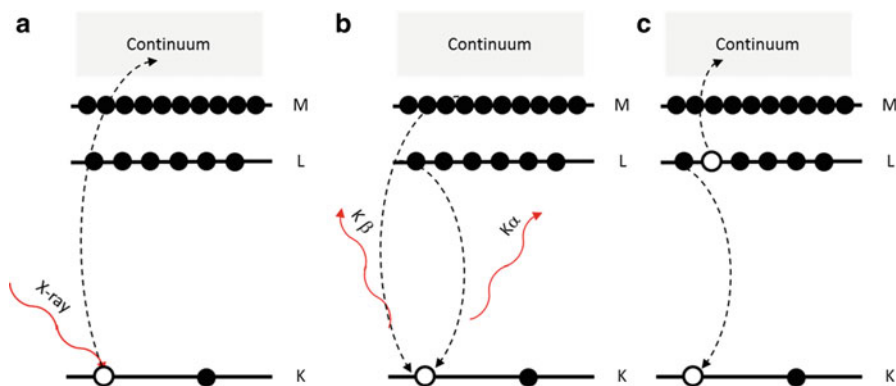
Fig. 6.1 Absorption of x-ray energy (**a**) and relaxation of the atom to the ground state by x-ray fluorescence (**b**) and Auger effect (**c**)

state because it has an empty place ("hole") in its core. The excited atom relaxes back to the ground state once an electron from the higher energy states jumps into the hole. The difference in energy of the two levels is either emitted by a radiative process called x-ray fluorescence or absorbed by another electron that has the sufficient energy to be ejected from the atom. As an atom has discrete K, L, or M energies, the energy difference that is being emitted or absorbed by another electron is characteristic of the absorbing atom and is used in vacuum spectroscopy to identify it by XPS and AES. Depending on where the electron resided before it filled the core hole in the K shell, L, or M, two characteristic energies are possible in XPS or in x-ray fluorescence spectroscopy: K_α, characteristic of the transition $L \rightarrow K$, or K_β, for the process $M \rightarrow K$.

In XAS, K transition, or "K-edge," corresponds to the ejection of an electron from $1s$ subshell. By the same principle, L_1 edge corresponds to the excitation of an electron from $2s$ subshells. Transitions L_2 and L_3 correspond to the ejection of an electron from the $2p$ subshells. There are two transitions as the orbital momentum (l) and the spin momentum (s) are coupled to give $j = l - s$ (for transition L_2) or $j = l + s$ (transition L_3). The selection rules of x-ray absorption determine that in dipole transitions the orbital quantum number of the final state must differ by 1 from the initial state ($\Delta l = \pm 1$, i.e., transition $s \rightarrow p$, $p \rightarrow s$, $p \rightarrow d$, etc.), whereas the spin must be conserved ($\Delta s = 0$). The same system of labeling is used for transitions from higher shells, e.g., M_1 edge corresponds to the excitation of $3s$ electrons, M_2 and M_3 edges correspond to the transition of $3p$ electrons, and M_4 and M_5 correspond to the transition of $3d$ electrons. The K and L edges are mostly used in XAS.

4.1 XAS Techniques: EXAFS and XANES

X-ray absorption spectroscopy refers to the modulation of the x-ray absorption coefficient at energies near and above an x-ray absorption edge. The term "edge,"
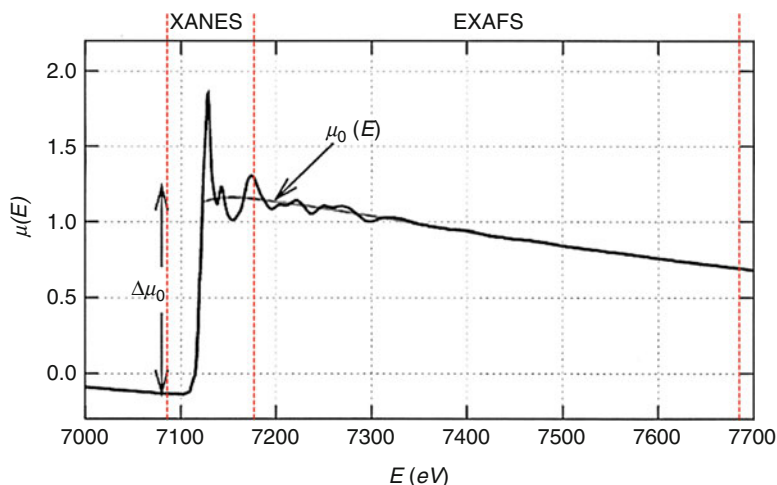
Fig. 6.2 $\mu(E)$ plot of Fe K-edge in condensed phase (metal foil), showing the ranges of XANES and EXAFS regimes, as well as characteristic oscillations about the smooth background $\mu_0(E)$ produced by the neighboring atoms and the edge step $\Delta\mu_0$

corresponding to the ejection of a core electron (photoelectron), is somewhat ambiguous as it depends on the nature of the matter: in metals, it is usually defined as the Fermi level, whereas in insulators it stands for the chemical potential. The part above the edge is divided in two regimes: x-ray absorption near-edge spectroscopy (XANES) and extended x-ray absorption fine structure (EXAFS). The two regimes contain related but somewhat different information about the element's local coordination and chemical state.

While there is no sharp boundary in the energy ranges corresponding to XANES and EXAFS spectroscopies, it is usually considered that XANES spans from a few tens of eV below the edge up to about 50 eV above the edge, while EXAFS covers a wide energy region (as much as 1.5 keV) that extends from 50 eV above the edge, as shown in Fig. 6.2. In practice, the spectra of both techniques include the pre-edge region of about 150 eV and the edge itself and extend to a user-defined limit.

The difference between the two spectroscopy techniques arises due to the processes that happen in the different energy ranges. It can be explained in terms of the relationship of the photoelectron wavelength λ and the interatomic distance R between the atom that interacts with the x-ray photon (photoabsorber) and the nearby atom (backscatterer). The photoelectron kinetic energy depends on the incident photon energy $h\nu$ and the electron binding energy in the atom:

$$E_{\text{kinetic}} = h\nu - E_{\text{binding}} = (2\pi)^2 \hbar^2 / (2m\lambda^2)$$

where h is the Planck's constant in $\hbar = h/2\pi$, and m is the mass of the photoelectron. For high E_{kinetic}, the photoelectron wavelength is shorter than the interatomic

distance, and the EXAFS region corresponds to a single scattering process; conversely, for lower energies, λ is larger than R and the XANES region is associated with a multiple-scattering regime.

XANES is often used in material science and engineering to resolve structure of layered materials and can be used to identify both surface and undersurface monolayers based on different core-level energies of different elements, unlike vacuum surface science techniques (AES and XPS) that are sensitive to surface only. XANES is also sensitive to the chemical state of elements which can be present even in minute quantities and gives the information on valence state of the element, its coordination environment, as well as geometrical distortions of it. XANES is mostly used in fingerprinting of sample mixtures by linear combination analysis (LCA) if the components are known or to acquire the information of the principal components in the mixture by principal component analysis (PCA), if the components are unknown.

EXAFS provides evidence on atomic arrangements, bond lengths, and coordination numbers in much the same way as XRD and LEED. EXAFS finds applications in all areas of science such as chemistry (e.g., in catalysis to distinguish catalytic steps and intermediate states in a complex reaction and catalytic active sites), physics (e.g., in solids, to resolve structure of alloys and amorphous/disordered solids, as well as phase transformations), materials science and engineering, structural biology, pharmaceutical industry, environmental science, etc.

4.2   Theoretical Interpretation of EXAFS

Due to complexity of the multiple-scattering events, no simple equation that characterizes the XANES region has been described yet. On the other hand, deriving the EXAFS equation is relatively simple. It is based on the single-particle theory approximation, in which the system is separated into a single electron residing in the core levels of the selected atomic species that is excited by the x-ray photon and N-1 passive electrons.

As x-ray passes through a material of a thickness t, its intensity exponentially decreases from the initial value I_0 to the value I in a way similar to the absorption of the UV/VIS radiation described by the Beer–Lambert law:

$$I = I_0 \exp\left(-\mu t\right) \tag{6.1}$$

The absorption coefficient of the material μ depends on the energy E of the x-ray radiation, as well as on the properties of the material, i.e., its atomic number Z, atomic mass A, and density ρ, as:

$$\mu \approx \left(\rho Z^4 / A E^3\right) \tag{6.2}$$

Since the properties of the material are independent on the x-ray energy, the absorption coefficient smoothly decreases with the increase of energy of the x-rays; however, at absorption edge the absorption coefficient rises sharply (see Fig. 6.3).
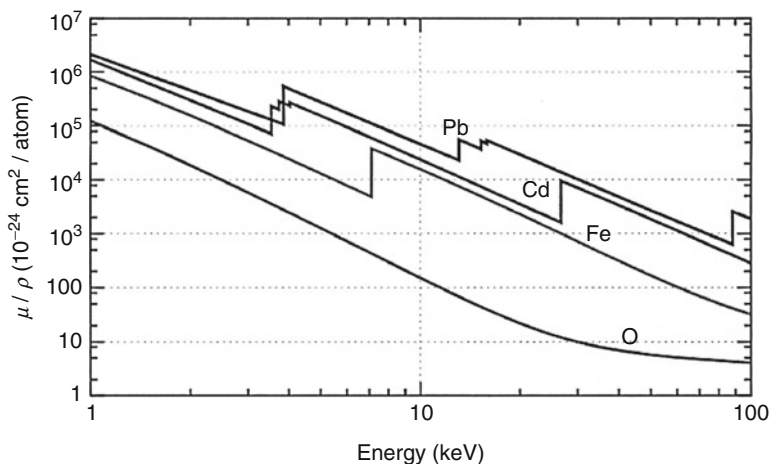
Fig. 6.3 Dependence of absorption coefficient of an isolated atom on energy of x-rays. Atom of O contains core electrons in the first shell only, and the energy needed to eject one of them (512 eV) lies outside the energy range of the plot. In contrast, the spectrum of a heavy atom like Pb contains multiple edges, i.e., five M edges around 3 keV which are too close to be resolved, three L edges around 12 keV, and a K-edge at 88 keV

If the photoabsorbing atom were completely isolated, i.e., not in any kind of environment, the sudden rise in absorption coefficient would be followed with the smooth decrease in the $\mu - E$ plot, according to Eq. 6.2. However, in condensed phases the electron wave travels to the neighboring atom (backscatterer) and reflects off of it, and the backscattered wave interferes with another wave coming from the photoabsorber; this interference produces oscillations in the $\mu(E)$ pattern as in Fig. 6.2.

The $\mu(E)$ oscillations obviously depend on the 3D surrounding of the absorbing atom, i.e., the "fine structure" in EXAFS. Thus, we define EXAFS as

$$\chi(E) = \frac{\mu(E) - \mu_0(E)}{\Delta \mu_0(E_0)} \tag{6.3}$$

where the bare atom background $\mu_0(E)$ was subtracted out and divided with the edge step $\Delta\mu_0(E_0)$ to produce oscillations in $\chi(E)$ normalized to one absorption event.

Instead of the energy E of the photoelectron, it is more convenient to express the EXAFS oscillations as a function of photoelectron wave number k:

$$k = \sqrt{\frac{2m(E - E_0)}{\hbar^2}} \tag{6.4}$$

where m is the mass of the photoelectron, E_0 is the energy of the edge, and h is the Planck's constant in $\hbar = h/2\pi$. For E in eV, $k = 0.512 (E - E_o)^{1/2}$ (in Å^{-1}). Because the oscillations in $\chi(k)$ quickly diminish, $\chi(k)$ is often multiplied by k^2 or k^3 to
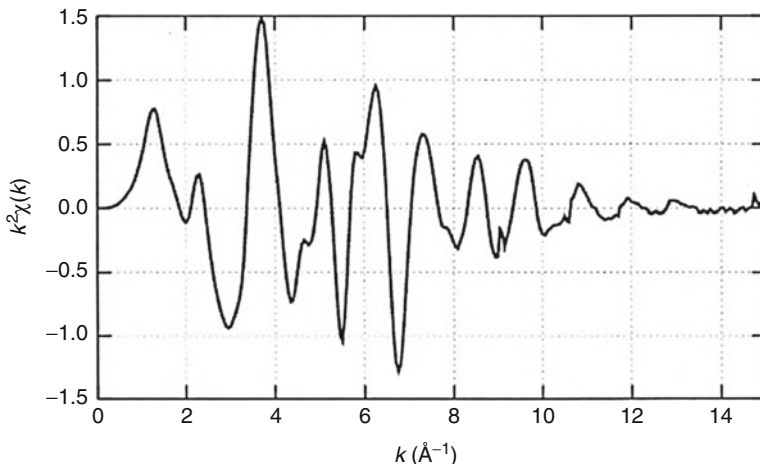
Fig. 6.4 EXAFS spectrum: k^2-weighted normalized absorption $\chi(k)$ as a function of photoelectron momentum k

amplify the oscillations at higher k values. This is called k-weighting, and the plot shown in Fig. 6.4 is often referred to as "k-space," to distinguish from the plots in "R-space," representing Fourier transform magnitudes described below.

The EXAFS equation has been first derived by Edward Stern [6]:

$$\chi(k) = \sum_j S_0^2 \, N_j \frac{f_{j^{(k)}}}{kR_j^2} \exp\left(-\frac{2R_j}{\lambda(k)}\right) \exp\left(-2k^2\sigma_j^2\right) \, \sin\left[2kR_j + \delta_j(k)\right] \qquad (6.5)$$

A real system has neighboring atoms at different distances to the absorbing atom and of different nature, and they all contribute to the oscillations in $\chi(E)$, and all those scattering events are summed. In every scattering event, the amplitude factor of Eq. 6.5 depends on the distance to the backscatterer atom R and the coordination number N of identical backscatterers, as well as the amplitude reduction factor S_0^2; these factors are taken to be independent on the x-ray beam energy. In addition, the amplitude linearly depends on the probability that the scattering takes place at the nearby atom, $f_j(k)$. The phase shift $\delta_j(k)$ is the consequence of the photoelectron moving in a varying potential induced by both central and backscattering atoms, i.e., with higher speeds around the atoms than in the space between them. Both $f_j(k)$ and $\delta_j(k)$ depend on the photon energy (or wave number k) and on the nature of the scattering atoms. As Z increases, peaks in $f(k)$ slowly shift toward higher k; for scatterers heavier than $3d$ transition elements, $f(k)$ shows multiple peaks, which in turn split peaks in the magnitude of Fourier transform even when only a single absorber–scatterer are present, as shown in the case of Pt below.

Besides the above parameters, there are additional semiempirical factors that affect the oscillations in the $\chi(k)$ plot. The term $\exp(-2R_j/\lambda(k))$ represents the probability that the photoelectron traverses the distance $2R$ from the photoabsorber

to the backscatterer and back without loss of energy. The mean free path of the photoelectron λ is within 5–30 Å and depends almost linearly on wave number in the region $k = 2$–15 Å^{-1}. The exponential term $\exp\left(-2k^2\sigma_j^2\right)$ is called Debye–Waller factor and allows for both static and thermal disorder of the condensed system due to the mean square variation in distance σ_j^2. The two exponential terms affect the $\chi(k)$ such that inelastic losses diminish the amplitude of the sine wave at low values of k, whereas the Debye–Waller disorder factor dampens the amplitude at high k values.

The amplitude reduction factor S_0^2 accounts for the losses in EXAFS amplitude due to many-electron excitations at the absorbing atom, thus representing the probability that each of the passive electrons surrounding the excited one remains in its initial state. While S_0^2 is generally taken to be a constant (typical values are within 0.7–1) for a certain element, it is actually energy dependent.

5   Experimental and Instrumental Methodology

For a good XAS spectrum, the signal to noise (S/N) ratio should be better than a thousand. In order to obtain such a spectrum in a reasonable time (several minutes), an intense beam of the order of 10^{10} photons/s and a bandwidth of about 1 eV are essential; these requirements are only met with synchrotron sources. Fortunately, there are several tens of synchrotron sources around the world [7], and many of them have more than one beamline (x-ray output) designed for XAS experiments.

A typical XAS setup is shown in Fig. 6.5. It consists of a synchrotron source, a monochromator, and at least two detectors for measuring the incident intensity of the x-ray beam I_0 and the intensity of transmitted beam I_t as it passes through the sample of thickness t. The most common detectors are ionization chambers, in which the x-ray beam is measured by the ionization of the gas in the chamber. The absorption coefficient $\mu = (1/t) \ln (I_0/I_t)$ is plotted against the x-ray energy, producing the spectrum similar to that shown in Fig. 6.2. For energy calibration purposes, the x-ray beam is usually allowed to pass through the reference material (usually a foil of the same element as the photoabsorber), and the transmitted beam is collected at the third ion chamber I_r; the absorption coefficient of the reference material $\mu_r = (1/t_r) \ln$
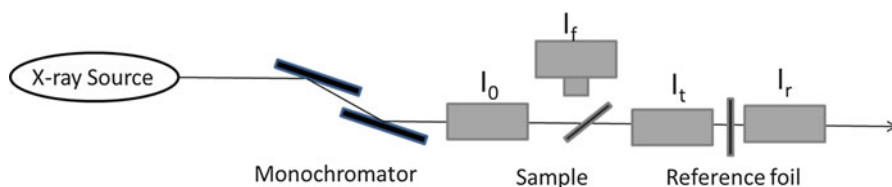
Fig. 6.5 EXAFS setup. Monochromatic x-ray beam passes through the sample, reference foil, and three ion chambers measuring the x-ray intensities I_0, I_t, and I_r. For thick or low-concentrated samples, fluorescence signal I_f can be observed

(I_t/I_r) is also plotted against the energy. The concentration of the sample for a good EXAFS transmission signal should be such that the edge step $(\Delta\mu_0 t)$ should be around one, i.e., the transmitted beam is about 1/3 of the incident beam. This however is only a rough estimate, as good XAS spectra can be obtained for edge steps anywhere between 0.2 and 1.2.

If the transmission experiment is not practical, e.g., when the sample concentration is too low, or the sample is too absorbing or too thick, the x-ray fluorescence signal I_f can be monitored by means of a fluorescence detector. In that case, the absorption coefficient is directly proportional to the fluorescence: $\mu t \propto I_f$. A number of fluorescence detectors are available, including semiconductor detectors like passivated implanted planar silicon (PIPS), solid-state array detectors (Ge or Si), as well as an ion chamber fluorescence x-ray detector with Stern–Heald slit assembly, also known as the Lytle detector. For the fluorescence measurement, the sample and the detector are oriented at 45° and 90° with respect to the incoming beam (Fig. 6.5) to minimize the scattered incoming x-rays at the detector. The fluorescence detector captures all x-rays, including the scattered primary monochromatic beam as well as the fluorescence signal coming from other atoms in the sample, if present. As the intensity of these by-signals varies little with the energy, the changes in the signal measured by the fluorescence detector depend mostly on the change in the fluorescence intensity of the measured element. In addition, solid-state detectors often have electronic energy discrimination, allowing only the fluorescence signal to be counted.

XAS measurements are usually done at K-edge up to about 40 keV, which includes low-Z elements of the first and second row of transition metals. Most synchrotron sources have the maximum of the photon flux near 10 keV; the flux at higher energies is reduced, sometimes by orders of magnitude, rendering measurements above 40 keV impractical. For third row transition metals, K-edge is too high, so measurements are usually conducted at L_3 edge. For instance, Pt K-edge is around 78 keV, while L edges are within 11–14 keV. The lowest-laying L_3 edge is mostly used as the probability (and therefore the intensity) of L_3; transition is much higher than that of other L edges.

In the dipole approximation, the transition is restricted by the selection rule $\Delta l = \pm 1$ and $\Delta j = 0, \pm 1$, where l is the orbital angular momentum quantum number and J is the total angular momentum quantum number $j = l \pm \frac{1}{2}$. In the case of Pt, the L_2 absorption edge is associated with transitions to empty $s_{1/2}$ and $d_{3/2}$ states above the Fermi level. The L_3 edge corresponds to transitions to empty $s_{1/2}$, $d_{3/2}$, and $d_{5/2}$ states. The contribution of s-symmetric final states is normally small and is spread over a wide energy range, whereas the d-symmetric portion of the density of final states is large and confined to a narrow energy range. Assuming no significant hybridization, the L_2 edge probes empty final states characterized by a total angular momentum quantum number of $j = 3/2$, whereas L_3 edge probes states with $j = 3/2$ and $j = 5/2$. Spin–orbit coupling effects cause a splitting of the final d states. This shifts the $d_{5/2}$ states to a higher energy with a corresponding shift of the $d_{3/2}$ states to lower energies. As a result, the unoccupied d states above the Fermi level are predominantly those with $j = 5/2$. This accounts for the enhanced peak at
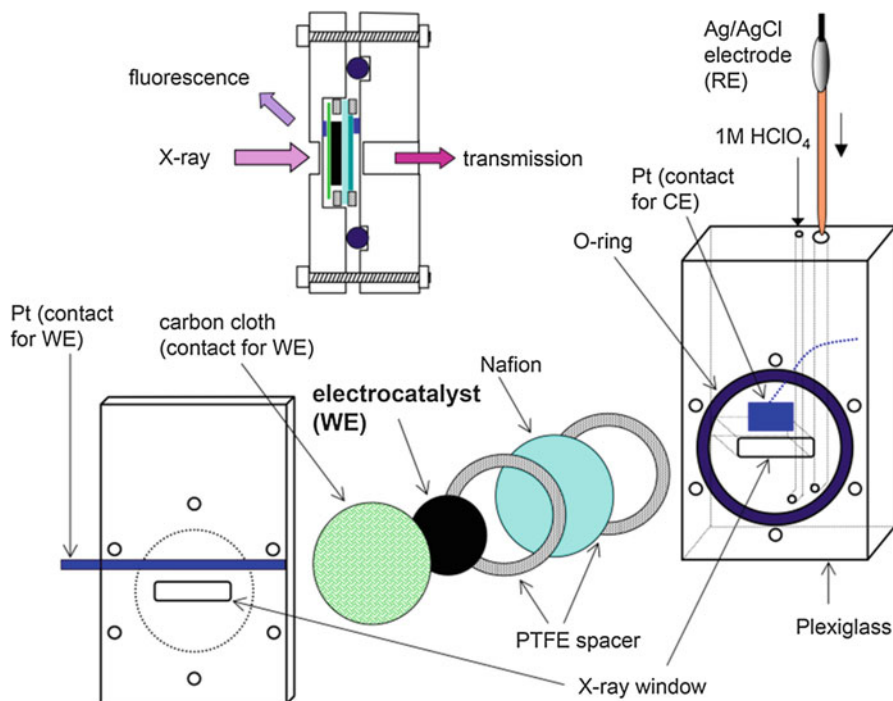
Fig. 6.6 Exploded view of the in situ electrochemical cell used in EXAFS experiments (From Ref. [9])

the L_3 edge for Pt that corresponds to ejection of an electron from a $2p_{3/2}$ core state. This feature is referred to as a "white line" as it showed up as such in the days when photographic plate was used as the detector.

5.1   Electrochemical Cell

The cell used for the in situ electrochemical measurements presented in later sections is a modified version of the one described by McBreen et al. [8]. The modified electrochemical cell allows XAS data acquisition in both transmission and fluorescence modes and is presented in Fig. 6.6 [9]. A carbon cloth, carbon-supported electrocatalyst, proton exchange membrane (Nafion 117, DuPont Chemical Co., DE), and two PTFE gaskets were sandwiched together and inserted in the thicker plastic body. All those components were clamped tightly by the two acrylic plastic bodies with an O-ring. Each plastic body has an opening for the passage of x-rays and an x-ray transparent window that is glued by a thin acrylic film. A Pt foil on the thicker plastic body acts as a counter electrode, while a Pt ribbon on the thinner plastic body achieves electrical contact with the electrocatalyst (working electrode) through the carbon cloth. Two capillaries are drilled in the thicker plastic block; one

is used for adding electrolyte into the cell, whereas the other provides a contact of the solution with an Ag/AgCl leak-free reference electrode. All the potentials in this chapter are reported with respect to reversible hydrogen electrode (RHE). The assembled cell is positioned 45° toward the incoming beam to allow fluorescence measurements [9].

6 Data Analysis of XAS Spectra

6.1 Interpretation of XANES

Even though no simple equation exists for the XANES region, the XANES spectrum can always be modeled qualitatively and in certain instances also quantitatively by LCA or PCA analysis. The edge shift toward higher or lower energies is the consequence of the oxidation state of the photoabsorber and can be modeled as well. Furthermore, XANES spectrum often shows unique "pre-edge" features that are easily identified and can be used in fingerprinting.

In the fingerprinting technique, the obtained spectrum is visually compared to the spectra of the same element in various oxidation states and environments, to see if they match. The technique gives the proper answer only if the sample has predominantly the same composition as one of the standards. At the K-edges of the first row transition elements, the transition is mostly from $1s$ to $4p$ states. However, small pre-edge peaks due to the weaker quadrupole ($\Delta l = \pm 2$) are often observed in cases where there is an inversion of symmetry (e.g., the rock–salt structure). These correspond to $1s$ to $3d$ transitions that become allowed due to, the p–d hybridization. For instance, in the case of chromium compounds, the tetrahedral Cr^{6+} ion shows an extremely large pre-edge peak, whereas it is much smaller in octahedral Cr^{3+} [5]. Thus, sometimes only visual observation of the XANES and/or pre-edge region can be used for identifying the oxidation state and/or structure. When the changes in XANES are too subtle to be seen directly, the $\Delta\mu$ XANES technique, based on subtraction of edges, can be used. By carefully aligning the spectra in order to remove initial- and final-state effects to separate the electronic and structural information hidden within, it was successfully used to elucidate Pt–H structure, as well as surface and subsurface oxygen on Pt [10, 11].

If the sample is a mixture of two or more components, one can carry on the LCA technique in an attempt to make a match of the spectrum of the sample by adding together fractions of the spectra of various standards. As a computer technique, the routine is easy and works well as long as the standards for all constituents are given. An example of XANES interpretation, $\Delta\mu$ analysis, and LCA technique will be shown in Sect. 7.1.

If one has a limited knowledge of the sample but plenty of related spectra, as in a series of samples with various compositions or a single sample under different conditions, the PCA computer routine can be used to identify the set of components that account for the spectra in decreasing order of importance. The technique provides information whether individual constituents are present and how many of them

are in the sample. It is most often used when the spectra are taken "in operando" while conditions like temperature, pressure, voltage, or concentration cause the change in the XANES spectra.

6.2   EXAFS Spectrum Processing

Processing of an EXAFS spectrum is based on fitting the spectrum to a predicted structure. While there are several computer programs for this purpose, the one used in the interpretation of the examples given later in this chapter is based on the Demeter package. The freeware includes Athena program containing LCA and PCA routines for XANES analysis, as well as data reduction and extraction of the sinusoidal EXAFS wave, Artemis program for fitting the EXAFS spectrum to a certain structure predicted on a reasonable assumption or other information about the sample, an automated program for ab initio multiple-scattering calculations for clusters of atoms (FEFF), as well as a number of helpful programs for data acquisition and processing [12].

6.2.1   Fitting of Bulk Materials

Data reduction is done in Athena program, by subtracting the spectrum of an isolated atom $\mu_0(E)$ from the real spectrum $\mu(E)$ and normalizing the obtained sinusoidal wave to 1 as in Eq. 6.3. The $\chi(E)$ spectrum is then converted to $\chi(k)$ by the Eq. 6.4 and plotted against the photoelectron momentum k as in Fig. 6.4. Data fitting of the EXAFS spectrum is done by Artemis program. It involves the determination of R_j, $S_0^2 N_j$, and σ_j^2. Parameters δ_j, f_j, and λ are obtained by theoretical calculations based on the predicted structure.

Peak fitting is based on matching the experimentally obtained spectrum to the theoretical one, based on the predicted structure. The structure can be either inputted directly using Atoms routine in the Artemis program or using Atoms input archive available on the Web [13]. For instance, Fig. 6.7a shows the input window of Atoms for cassiterite (SnO_2) using the input file from the above Web site. After filling the required fields for the known structure (here: SnO_2, crystal structure p 42/m n m, lattice parameters a = b = 4.73727 Å, c = 3.186383 Å, $\alpha = \beta = \gamma = 90$, defining the relative positions of Sn and O atoms and indicating Sn as the absorber) and running Atoms, the routine calculates the distances of backscatterer atoms surrounding the photoabsorber (display not shown); this list is the input file for FEFF calculation. FEFF calculates the single-and multiple-scattering paths by Fourier analysis and outputs the table of the paths ordered in increasing distances from the photoabsorber, and their amplitudes are scaled to the highest scattering event (Fig. 6.7b). One can choose the paths to be included in the fit, taking care that the distance from the photoabsorber in the path is within the "window" in which the fitting is done. If one has limited knowledge of the sample, the default parameters are sufficient to produce a reasonable first fit. The graphic display gives the original spectrum and the fitted one in either k-space (the oscillatory pattern as in Fig. 6.4) or
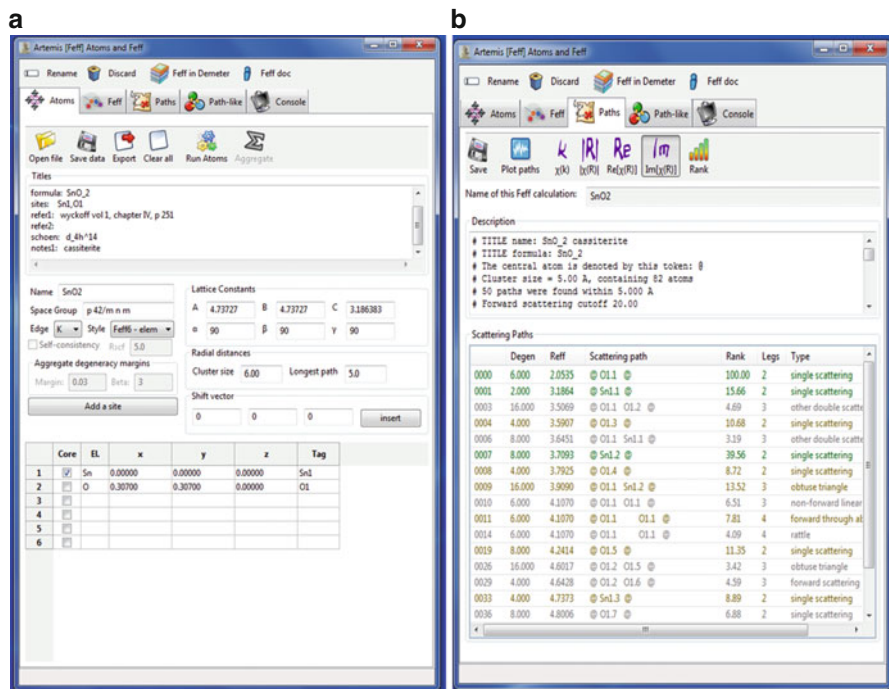
Fig. 6.7 (**a**) Input window of atoms routine in Artemis program. (**b**) FEFF routine in Artemis calculates scattering events and lists them in the increasing distance from the absorber; the events

"*R*-space" (Fourier transform magnitude plotted as a function of half path length *R*). Although *R* is measured in angstroms (Fig. 6.7c), the half path length does not correspond to the true distances between the photoabsorber and the backscatterer, but it is related to it. In most cases, the half path length is smaller than the real distance from the absorber by 0.3–0.5 Å. For instance, the FEFF output table (Fig. 6.7b) shows that the highest-amplitude peak, corresponding to the scattering path from the photoabsorber (Sn) to backscatterer (O), is at 2.052 Å, whereas the peak in Fig. 6.7c is at ~ 1.6 Å. The real distances are found in the list of fitted parameters, displayed along the graphic output.

6.2.2   Fitting of Monometallic Nanoparticles

Metallic nanoparticles have unique physical and chemical properties attractive for use in various research areas, in particular as the active component in supported metal catalysis [14]. Their small size makes them difficult to characterize by ordinary techniques like transmission electron microscopy (TEM), XRD, or chemisorption. Instead, EXAFS became the technique of choice for the characterization because of its unique ability to (a) elucidate the distances between atoms, (b) reveal the average particle size or particles smaller than *ca.* 3 nm (unlike XRD), (c) provide details on the shape of the nanoparticle (unlike chemisorption or XRD), as well as because (d) it can be used under in situ or *in operando* conditions (unlike TEM). Mathematical formulas for calculation of average coordination numbers for face-centered cubic (fcc) nanoparticles of complete concentric shells (cuboctahedron and icosahedron) as well as the distribution of surface atoms of cuboctahedron and icosahedron as a function of particle size were derived [2, 15]. Table 6.1 shows the average coordination numbers calculated for Pt nanoparticles up to 6 nm in diameter. It can be seen that the average coordination numbers for the two structures are within 10 % of each other even for the smallest nanoparticle containing 13 atoms (the central atom and its 12 nearest neighbors), becoming comparable for larger particles.

Fcc lattice structure is one of the most important for catalysis not only because many catalytically important metals (Pt, Au, Rh, etc.) crystallize in it but also as solid solutions of metals of which one is the fcc metal which often assumes fcc lattice [15]. However, nanoparticles can assume various shapes (decahedron, dodecahedron, cuboctahedron, icosahedron, etc.) that have a different number of surface atoms, so their average coordination numbers (ACN) vary. The average coordination numbers for various shapes of nanoparticles and for all three types of lattices (fcc, hcp, and bcc) were recently shown [16]. For metal particles crystallizing in close-packed lattice structures with the bulk coordination number of 12 (fcc and hcp) that account for about 2/3 of all metals in the periodic system, it was shown that the hyperbolic functions of ACN vs. the number of total atoms are similar. Furthermore,

Fig. 6.7 (continued) with the highest intensity (rank) are highlighted in green. (**c**) Fourier transform magnitude EXAFS spectrum of Sn K-edge for the $PtRhSnO_2/C$ electrocatalyst in 1 M $HClO_4$ solution at 0.41 V and first-shell fit

Table 6.1 Number of atoms, particle size (enclosed sphere with the diameter of 2n−1 atoms), and average coordination numbers for icosahedron and cuboctahedron for platinum, calculated by the formulae given in Ref. [15]

Number of shells (n)	Total atoms	Surface atoms	% of surface atoms	Particle size (nm)	$\overline{N}$ (icos)	$\overline{N}$ (cuboct)
1	1	1	100	0.28	−	−
2	13	12	92.3	0.83	6.46	5.54
3	55	42	76.4	1.39	8.51	7.85
4	147	92	62.6	1.94	9.47	8.98
5	309	162	52.4	2.50	10.02	9.63
6	561	252	44.9	3.10	10.37	10.05
7	923	362	39.2	3.61	10.62	10.35
8	1415	492	34.8	4.16	10.8	10.57
9	2057	642	31.2	4.72	10.94	10.73
10	2869	812	28.3	5.27	11.05	10.87
11	3871	1002	25.9	5.83	11.14	10.97
12	5083	1212	23.8	6.38	11.22	11.06

Core/Shell   Alloys   Aggregate Mixtures
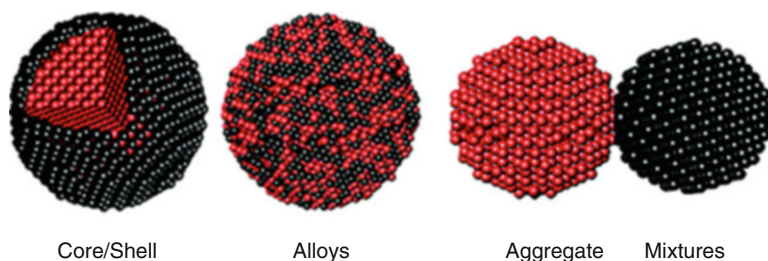
Fig. 6.8 Three types of bimetallic mixtures of two metals (From Ref. [18])

because of intrinsic uncertainty of EXAFS due to the high correlation of N with other parameters in Eq. 6.5, the number of atoms in nanoparticle of practically any structure falls within the error bars of experimentally obtained ACN. For instance, ACN of 9 represents a particle of approximately 170 atoms (fcc or hcp) regardless of its shape [16]. For bcc metals in which the coordination number of a bulk atom is 8, the hyperbolic function assumes the similar shape but is shifted to lower coordination numbers with respect of other two lattices [16].

6.2.3   Fitting of Bimetallic Nanoparticles

For metal–metal nanoparticles, it was shown that the coordination numbers and distances between metals can reveal its internal structure [16, 17]. Three structure types, a homogeneous solid solution (alloy) and two heterogeneous mixtures (see Fig. 6.8), can be easily distinguished by EXAFS by the relations below.

For the homogeneous solid solution of metals M_1 and M_2 where the atomic radius of M_1 is larger than that of M_2, the following relations can be used:

$$N(M_1M_1) = \frac{x(M_1)}{x(M_2)}N(M_1M_2) \tag{6.6a}$$

$$\sum_j N(M_1M_j) = \sum_j N(M_2M_j) \tag{6.6b}$$

$$R(M_2M_2) < R(M_1M_2) < R(M_1M_1) \tag{6.6c}$$

where $N(M_1M_2)$ is the coordination number between the metals M_1 and M_2, $x(M_1)$ and $x(M_2)$ are the mole fractions of the metal M_1 and M_2, and $R(M_iM_j)$ is the interatomic distance between atoms i and j.

Heterogeneous mixtures consisting of two segregated metals can form either a core–shell nanoparticle, in which one metal is preferentially found in the core of the nanoparticle and the other forms a shell around it, or an aggregate mixture, where each metal makes its own nanoparticle with minimal, if any, mixing with the other.

In core–shell nanoparticle, an atom of the core metal (M_{core}) is surrounded mostly with atoms of the same type, whereas the M_{shell} atom feels the presence of both the atoms of the same type that form the shell, as well as that of the other type of atoms forming the core; however, atoms in the shell always have lower coordination number. In addition, for a core–shell nanoparticle of a certain size, the total coordination number of the core atoms should be similar to the average coordination number for the nanoparticle of the same size composed of core atoms only, $N(M_{core\_nanoparticle})$. Finally, the distance between two atoms in the core should be similar to their bulk interatomic distance R (M_{core_bulk}), while the distance between two atoms in the shell can be either smaller or larger than bulk interatomic distance R_{shell_bulk}, depending on the relative sizes of the two metals comprising the core–shell particle. Thus, the following equations apply:

$$N(M_{core}M_{core}) > N(M_{shell}M_{shell}) \tag{6.7a}$$

$$\sum_j N(M_{core}M_j) \approx N(M_{core\_nanoparticle}) \tag{6.7b}$$

$$R(M_{core}M_{core}) \approx R(M_{core\_bulk}) \tag{6.7c}$$

$$R(M_{shell}M_{shell}) \neq R(M_{shell\_bulk}) \tag{6.7d}$$

Aggregate mixtures consist of two nanoparticles completely separated from one another, each consisting of one type of metal atoms only. Hence, the following relations describe it:

$$N(M_1M_2) \approx N(M_2M_1) \approx 0 \tag{6.8a}$$

$$R(M_1M_1) \approx R(M_{1\_bulk}) \tag{6.8b}$$

$$R(M_2M_2) \approx R(M_{2\_bulk}) \tag{6.8c}$$

where R (M_{1_bulk}) represents the distance of two atoms of metal 1 in the bulk.

a

b
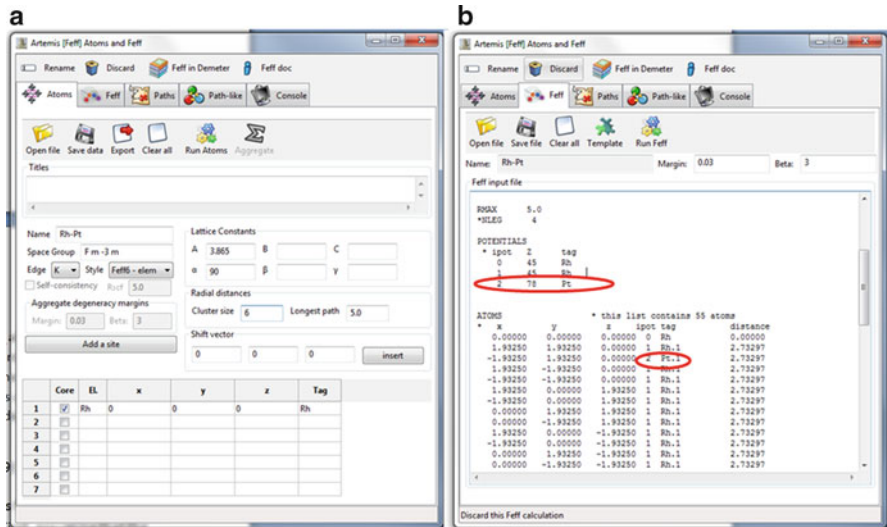
Fig. 6.9 (**a**) Atoms routine filled with the appropriate parameters for bimetallic Pt–Rh alloy; space group = F m −3 m, a = b = c = 3.865 Å, α = β = γ = 90°. Edge = K, cluster_size = 6 Å, core_atom = Rh at coordinates (0, 0, 0). Running the Atoms subroutine generates the FEFF input file (**b**), i.e., the list of atoms surrounding the absorber (Rh). To make the alloy, one adds ipot = 2, Z = 78, element = Pt under potentials; also, out of 12 Rh scattering atoms (ipot = 1, tag = Rh.1) in the first coordination shell, one is changed to Pt (ipot = 2, tag = Pt.1). FEFF then generates a list of scattering events (FEFF1); only the first two paths (Rh.1 and Pt.1) should be included in the fit

Fitting of a bimetallic nanoparticle can be done relatively easily using Artemis. In the example below, the procedure for simultaneous fitting of the alloy of two fcc metals (Pt and Rh) is described. To reduce the number of fitted parameters and thus obtain a more reliable fit, supporting information on the size and the mole fraction of Pt and Rh in the particle were obtained by independent techniques, TEM, and inductively coupled plasma (ICP).

One starts by inputting the Rh K-edge EXAFS sinusoidal wave (derived by Athena) into Artemis. In Atoms routine, one inputs the space group and the crystal structure parameters. Assuming that the Pt–Rh distance would be the average between Pt–Pt and Rh–Rh bond distances, which are R(Pt–Pt) = 277.5 pm and R(Rh–Rh) = 269.0 pm, respectively, the R(Pt–Rh) = 273.3 pm = 2.733 Å, and the lattice parameter of Pt–Rh is $a = 2^{1/2} R_{Pt–Rh}$ = 3.865 Å. Filling the Atoms page with appropriate parameters shown in Fig. 6.9a and running the Atoms subroutine, one gets the list of coordinates of all atoms surrounding the absorber. In the example used in Fig. 6.9a, only one type of atom needs to be specified, as Rh is both the absorber and scatterer. To make the FEFF scattering events for a bimetallic particle, a modification of the FEFF input file is necessary: one atom in the first shell is replaced with another scatterer (Pt), as shown in Fig. 6.9b. Running FEFF will then generate the list of scattering events (FEFF1) that include both Rh–Rh and Rh–Pt scatterings.

The same procedure is run once again, starting from the loading of the Athena-processed Pt L_3 edge spectrum and filling the Atoms routine with the same parameters as before using Pt as the absorber atom. In the FEFF input file, one Pt atom in the first shell is replaced with Rh; running the FEFF one obtains another list of scattering events (FEFF2).

Since one atom was replaced with the different scatterer in FEFF input files only in the list of first nearest neighbors, the fit is only valid for the first coordination shell. Thus, only the first two scattering events (or paths) should be taken from the both FEFF scattering lists, i.e., one path in which the scatterer is the same atom type as the absorber and the other path with different absorber–scatterer pair.

The generated FEFF files are the theoretical scattering events, and Artemis fits the experimentally obtained spectra to it. Since each scattering path contains four fitting parameters (ΔE_0, ΔR, σ^2, and $NS_0{}^2$), the first-shell fitting of a bimetallic particle has 16 parameters. However, the number of fitted parameters cannot be larger than the number of independent points, n_{ip}:

$$n_{ip} = (2/\pi)\,\Delta k \Delta R \tag{6.9}$$

where Δk and ΔR are the windows in k-space and R-space. Assuming typical values for a first-shell fit ($\Delta k \approx 12$ and $\Delta R \approx 2$), the number of independent points is $n_{ip} \approx 15$. Fortunately, certain parameters can be fixed. First, assuming that the Pt and Rh form solid solution and their mole fractions are found by ICP, the coordination number of one of the metals can be expressed in terms of the other one by Eq. 6.6a, so that only one coordination number is fitted. Second, both the change in the distance ΔR and the Debye–Waller factor σ^2 affecting the Pt–Rh scattering path are the same irrespective of the absorbing atom, so $\Delta R(\text{Pt–Rh}) = \Delta R(\text{Rh–Pt})$ and $\sigma^2(\text{Pt–Rh}) = \sigma^2(\text{Rh–Pt})$. And third, the ΔE_0 must be the same for both paths in one FEFF. Taking all these assumptions into the account, the number of fitted parameters reduces to 11. In addition, by fitting two edges concurrently, n_{ip} becomes substantially larger than the number of fitted parameters, producing a reliable fit.

It should be noted that Artemis fits the product of the coordination number and the amplitude reduction factor, NS_0^2. To find the coordination number N, one determines the amplitude reduction factor S_0^2 for both Pt and Rh by fitting the spectrum of the pure metal (metal foil), and use them in all subsequent fittings for that metal.

7   Selected Examples

Although the XAS technique is routinely used in a number of different scientific disciplines, in the examples shown below, only those of interest to electrocatalysis are illustrated. However, the similar XAS processing procedures can be applied to other areas of science, especially in those where nanomaterials are used. We start by explaining how to obtain relevant information from subtle changes in XANES spectra, as well as the procedure to quantitatively derive the number of atoms in a nanoparticle shell that become oxidized during an electrochemical reaction. Selected

examples on EXAFS processing data obtained during electrochemical reactions on both anode and cathode catalysts are given further, together with the correlation of XAS results to that obtained by other spectroscopy techniques.

7.1   In Situ XANES for Pt Oxidation of Carbon-Supported Pt Nanoparticles

Platinum undoubtedly is the best catalyst for both the anode and cathode. However, its catalytic activity degrades easily with oxidation of the surface. It is also known that the gradual decline in performance of low-temperature fuel cells is caused by the dissolution of carbon-supported Pt nanoparticles at the cathode during potential cycling, resulting in the loss of the electrochemical surface area. A detailed understanding of oxidation/dissolution mechanisms of Pt is therefore critical in designing durable catalysts.

Figure 6.10 shows in situ XANES spectra for Pt L_3 edge of carbon-supported Pt nanoparticles at potentials ascending from 0.41 to 1.51 V (Fig. 6.10a), followed by descending from 1.51 to 0.41 V in 1 M $HClO_4$ (Fig. 6.10b) [19]. The intensity of the white line increases considerably with elevating potentials as a consequence of depleting Pt's d-band due to the Pt oxide formation, and it starts to decrease with declining potentials as a result of filling d-band due to reduction of the oxide. The intensity of the white line at 0.41 V is almost identical before and after the potential cycling, but irreversible reduction during descending potentials gives hysteresis in a relative change of white-line intensity as a function of potentials. A similar hysteresis was reported elsewhere [20]. Also shown in the figure is a XANES spectrum of a commercial PtO_2 sample. Three distinct isosbestic points at 11576, 11605, and 11628 eV are observed in the XANES, indicating the existence of Pt species in two different chemical forms, having the same total concentration. We envisage that the surface of Pt nanoparticles is oxidized from metallic Pt (at 0.41 V) toward a form of PtO_2 as the potential increases; no clear intermediates are visually seen in the XANES spectra.

We should note that the electrochemical cell (Fig. 6.6) allows us to measure XAS and XRD of the same sample at the same electrochemical potentials. In situ XRD patterns from the same specimen measured immediately after the XAS at each electrochemical potential showed fairly small broadening of the peaks with increasing potentials [19]; the particle size changed from 2.6 to 2.1 nm by applying potentials from 0.41 to 1.51 V, indicating that the thickness of the oxide formed is approximately monolayer thick or less. Although the potential to 1.51 V significantly enhances the white line due to oxidation, the oxide is confined only to the top surface layer on the nanoparticles.

The delta mu ($\Delta\mu$) technique has been developed as a surface-sensitive method to identify surface/adsorbate interactions [11, 21]. By subtracting spectra of a sample at two different potentials, the $\Delta\mu$ method isolates surface/adsorbate interactions since bulk metal–metal interactions are eliminated by the subtraction. The obtained $\Delta\mu$ spectra are interpreted by comparing with theoretical $\Delta\mu$ curves on the basis of
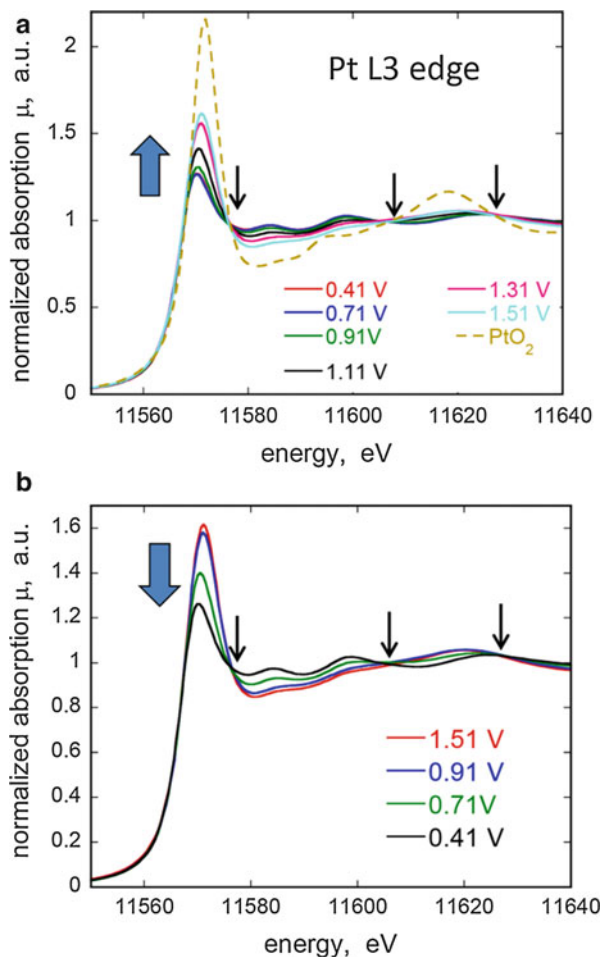
crystallographic models. Figure 6.11 depicts the $\Delta\mu$ spectra of the Pt/C catalyst at
$V = 0.71$, 0.91, and 1.11 V, calculated using the equation $(\Delta\mu(V) = \mu(V) -
\mu(0.41\ V))$, where $\mu(0.41\ V)$ is the reference signal of Pt/C considered free from
any adsorbates on the Pt surface. The $\Delta\mu(0.71\ V)$ shows a small positive peak at a
few eV above the E_0. With a further increase in potential, the intensity of $\Delta\mu$
increases significantly, and the peak position shifts slightly toward higher energy
values. The observation is interpreted as O or OH adsorption in atop sites of Pt at
0.71 V, followed by n-fold bonded configuration at higher potentials. Another
marked feature is that a negative peak slightly below the E_0 starts to appear above
0.91 V, which could be attributed to the formation of subsurface O due to a "place-
exchange" process, as indicated by comparison to the theoretically calculated $\Delta\mu$
spectral signatures [11, 21–23]. The interfacial place exchange of the adsorbed O
(OH) and platinum atoms then forms a Pt–O quasi-3D lattice at higher potentials.

Fig. 6.11 Pt L_3 edge $\Delta\mu(V) (= \mu(V) - \mu(0.41\ V))$ spectra of carbon-supported Pt nanoparticles at $V = 0.71$, 0.91, and 1.11 V in 0.1 M $HClO_4$ (Taken from Ref. [19])
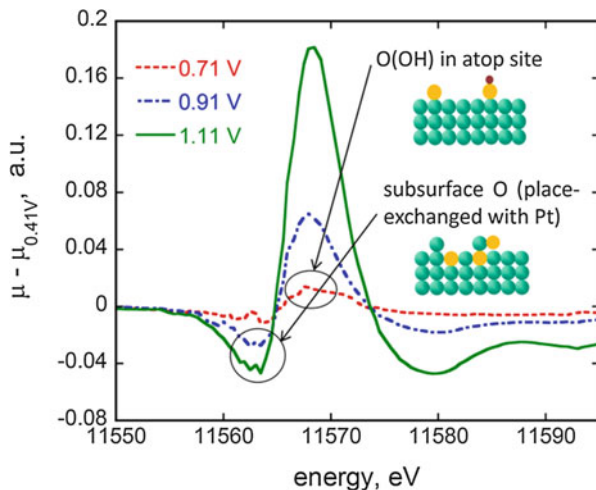
In situ XANES revealed that Pt nanoparticles are basically oxidized from a metallic state at 0.41 V to a PtO_2-type oxide structure during the potential excursion up to 1.51 V. Although the changes in the XANES spectra caused by the adsorbate formation and the place-exchange process are subtle, they could be amplified and analyzed by the above $\Delta\mu$ method. In the further example, we employ the linear composition analysis (LCA) technique to determine the fraction of metallic Pt and PtO_2 components at different potentials.

Figure 6.12a shows a XANES Pt L_3 spectrum from Pt/C at 1.31 V, together with oxide-free spectrum of Pt/C at 0.41 V and commercial PtO_2. The fitting analysis determined that the molar content of Pt metal and PtO_2 is 74 % and 26 %, respectively. PtO_2 percentage (%) involved in the catalyst as a function of applied potentials is shown in Fig. 6.12b. As in situ XRD measurements revealed, the oxide formation at 1.51 V is confined only to the top surface layer on the nanoparticles. The ratio of surface atoms (N_s) to total atoms (N_t) is a function of particle size (Table 6.1), and the N_s/N_t is *ca.* 0.50 for icosahedron and cuboctahedron nanoparticles with a diameter of 2.6 nm. This indicates that 76 % of surface atoms were oxidized at 1.51 V, if the oxidation takes place only on the top layer of the nanoparticles.

7.2 Application of EXAFS in Fuel Cells

Schematic diagram of a fuel cell in acidic medium is presented in Fig. 6.13. The electrochemical cell consists of two electrodes containing electron-conductive catalysts, separated by an electrolyte or proton conductor. The fuel (e.g., ethanol) is supplied at the anode side, and the oxygen (either pure gas or from air) is supplied at the cathode side. Electrons liberated at the anode by the oxidation of the fuel pass through the external electrical circuit and arrive at the cathode where they are used in
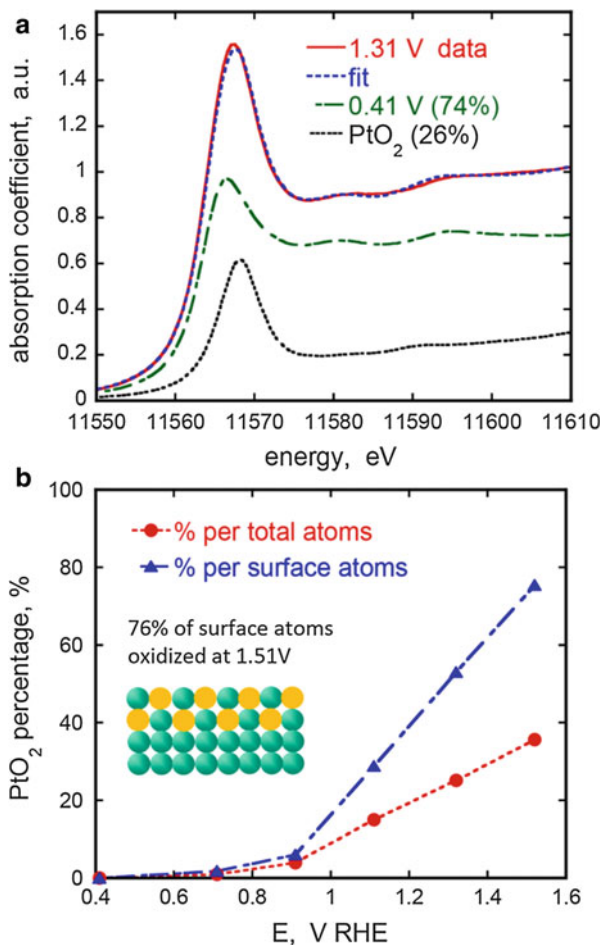
the reduction of oxygen. The circuit is closed by the transport of protons (H^+) from the anode to the cathode. The best catalyst for both anode and cathode sides is platinum. Unfortunately, platinum alone cannot deliver appreciable currents on either cathode or anode side due to a number of factors, and a series of investigations have been conducted over the past decades to improve the overall activity. The electrochemistry group at Brookhaven National Laboratory routinely uses XAS techniques in pursuit of active catalysts for both anode and cathode half-cells, and some will be presented in the examples below.

7.3   Ethanol Oxidation on Pt and Pt–M Bimetallic Anodes

Ethanol is considered as an ideal combustible for fuel cells because of its high energy–density, likely production from renewable sources, as well as ease of storage
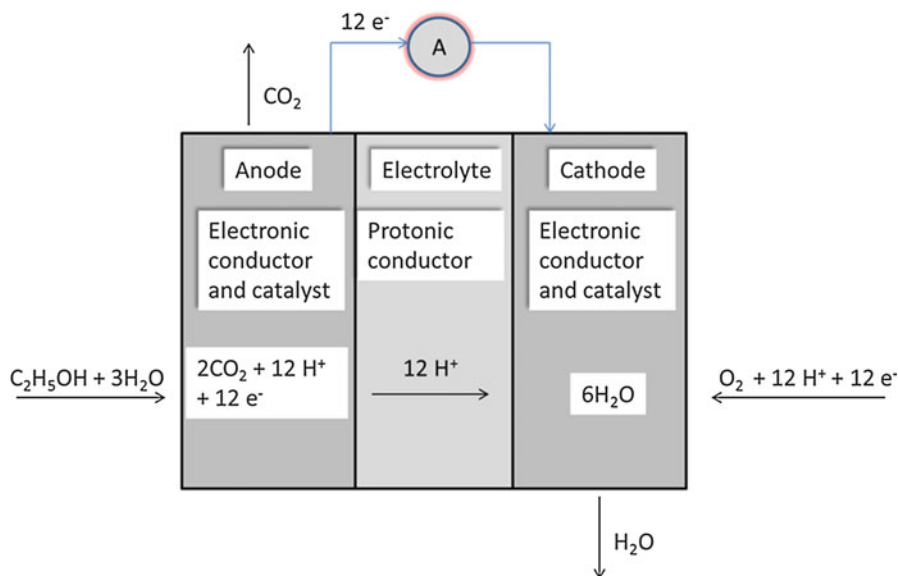
Fig. 6.13 Schematic representations of ethanol fuel cell for acidic solutions

and transportation [24]. Ethanol oxidation reaction (EOR) occurring at the fuel cell anode is the main impediment to practical application of the direct ethanol fuel cell (DEFC) because it is slow and incomplete. Other obstacles that have restrained the more rapid development and applications of direct alcohol fuel cells are, for example, alcohol crossover from the anode to the cathode, relatively low activity and complex reaction mechanism of most alcohols, high costs of precious metals, and CO poisoning of Pt catalysts at lower temperature in acidic media. In addition, apart from methanol, it is particularly difficult to break the C–C bond in alcohols during electrochemical oxidation. The complete oxidation of any aliphatic mono-alcohol can be written as

$$C_nH_{2n+1}OH + (2n-1)H_2O \rightarrow n\,CO_2 + 6n\,H^+ + 6n^{e-} \qquad (6.10)$$

The total oxidation of ethanol ($n = 2$) delivers 12 electrons and 12 protons. However, as shown in Fig. 6.14, EOR is a complex reaction occurring in a pattern of parallel reaction pathways [25]. Although mechanistic details are still debated, the prevailing view is the electrooxidation of ethanol at a Pt electrode in acidic solutions mostly follows the partial oxidation pathway at moderately positive potentials up to 0.6 V, yielding the products in which the C–C bond remains intact, i.e., acetaldehyde (CH_3CHO) and acetic acid (CH_3COOH). The total oxidation pathway to CO_2 requires the cleavage of the C–C bond, and the process on Pt proceeds mostly through re-adsorption of acetaldehyde, yielding adsorbed carbon monoxide CO_{ads} as an intermediate [26]. A study by Behm et al. showed that the on Pt particles adsorbed on carbon (Pt/C), the product yields range 20–65 %, 27–79 %, and

Fig. 6.14 Schematic representation of the parallel pathways during ethanol oxidation reaction (From [25])
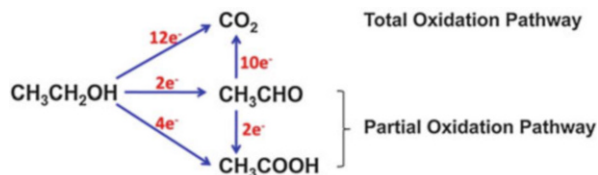
0.7–7.5 %, for acetic acid, acetaldehyde, and carbon dioxide, respectively, depending on the initial concentration of ethanol [27].

Pt surface is an exceptional catalyst in the sense that it adsorbs most species in an electrochemical solution. Carbon-containing species like CO_{ads} are especially strongly adsorbed; thus, blocking Pt sites for further adsorption of reactants. CO_{ads} can only be removed by oxidation which occurs at high electrode potentials. When the Pt surface becomes covered by Pt–OH or Pt–O species by oxidation of water, they react with CO_{ads} yielding CO_2 as the final product. The water oxidation occurs at potentials higher than 0.6 V which are impractical for fuel cell uses. Thus, Pt is an inadequate electrocatalyst for DEFC, and efforts to improve its activity have been concentrated on the addition of co-catalysts that supply oxygen-containing species at lower potentials and donate them to Pt for the oxidative removal of CO-like species. Of binary alloys, Pt–Sn and Pt–SnO_2 show the best oxidation rates that are about three times higher than on Pt, as Sn or SnO_2 supply OH groups from water. Nevertheless, the oxidation of ethanol is still incomplete as products with C-C bond intact are formed [28]. An overview of bimetallic alloy catalysts for EOR was given by Demirci [29]. However, the overall conclusion was that further investigation should be focused on ternary catalysts. Addition of a third element indeed enhances the oxidation currents with respect to the Pt–Sn, as shown for Pt–Ru–W, Pt–Sn–Ni, and Pt–Sn–Rh [30]. Yet, the overall CO_2 yield was still relatively low in comparison to the partial oxidation products.

7.3.1   Pt/Rh/SnO_2 Ternary Catalyst for Ethanol Oxidation

Rhodium has been used for decades in three-way catalytic converters in vehicles for its catalytic reduction of nitrogen oxides. Recently, metal/gas interface studies revealed that Rh is active in splitting C–C bond [31]. In electrochemical oxidation of ethanol, Rh was used for the first time in a multifunctional ternary Pt–Rh–SnO_2 electrocatalyst that effectively splits the C–C bond at room temperature without production of CO_{ads} [32]. The catalyst was prepared by preparing SnO_2 from $SnCl_2$, by adsorbing it on carbon support and depositing Pt and Rh on top of the SnO_2 surface from their soluble chlorides by chemical displacement of previously deposited lead nanoparticles. TEM measurement revealed SnO_2 clusters larger than 10 nm in diameter and Pt–Rh clusters between 1 and 3 nm [32].

Electrochemical measurements of ethanol oxidation demonstrated a considerably higher EOR activity of the ternary Pt–Rh–SnO_2 catalyst with respect to that of the binary Pt–SnO_2 catalyst, highlighting the importance of the Rh component [33, 34]. The catalytic property of the ternary catalyst is attributed to the synergistic effect

among all three constituents, where Pt provides sites for ethanol dehydrogenerative adsorption and SnO_2 supplies oxygen-containing species and simultaneously keeps Pt and Rh metallic, while Rh cleaves the C–C bond. DFT calculations of ethanol decomposition on the $PtRh/SnO_2(110)$ model catalysts propose that Rh adsorbs and stabilizes the key intermediate through an oxametallacyclic conformation ($*CH_2CH_2O$) that entails direct breakage of the C–C bond yielding $*CH_2$ and $*CH_2O$ radicals and two protons, with a reasonable energy barrier of 1.29 V. Pathway leading through acetaldehyde is unfavorable as its barrier is by 0.66 V higher than that for CH_2CH_2O intermediate, and furthermore, the C–C bond splitting from acetaldehyde requires an extremely high energy of 3.82 V. Furthermore, the DFT calculations on Rh(111) provided insights in electronic effect of Pt in RhPt alloy that weakens the C–Rh interaction and helps the C removal in the form of CO_2 [35]. In situ IR study of the ethanol oxidation confirmed these conclusions showing considerable production of CO_2 at potentials as low as 0.2 V, with negligible production of CO and a relatively low amount of partial oxidation products in the whole potential excursion [32].

EXAFS studies were conducted *in operando* to reveal the internal structure of the catalyst. Sn K-edge spectrum (Fig. 6.7c) revealed only a minor change in the intensity of the Sn–O scattering path during the potential excursion. This is not surprising because oxide surfaces behave as nonpolarizable interfaces in which the electrical state is controlled by the solution's pH and the effect of the electrode potential is negligible even for conductive oxides [36]. Water molecules are adsorbed on metal Sn^{4+} with the transfer of one of the protons to a neighboring oxygen atom, so that a "carpet" of OH groups mediates the interaction between the SnO_2 surface and its environment [37]. - Furthermore, OH groups present on the SnO_2 surface in aqueous solutions probably cause a shift in surface oxidation of both Rh and Pt (Rh–OH or Pt–OH formation) to positive potentials. They may be the cause for the minor changes in the in situ XANES spectra of Pt and Rh edges during the potential excursion from 0.21 to 1.11 V, i.e., between potentials at which no oxidation of ethanol is expected to that at which ethanol oxidation is in full progress. We conclude that both Pt and Rh surfaces stay in metallic form during the whole potential region practical for fuel cells and beyond.

7.3.2   EXAFS Fitting of Pt–Rh–SnO$_2$ Nanocatalyst

EXAFS studies were conducted to reveal the internal structure of Pt/Rh nanoclusters. The FEFF paths were constructed as described in Sect. 6.2. The results of the fit are shown in Fig. 6.15. The coordination numbers N(Pt–Rh) and N(Rh–Pt) were intentionally left to be fitted in order to compare them with those obtained by the inductively coupled plasma (ICP) mass spectrometric technique. Both edges were fitted concurrently, so the number of independent data points (~30) was sufficiently larger than the number of fitted parameters (two E_0, four coordination numbers, three ΔR, and three σ^2), yielding a reliable fit. The amplitude reduction factors S_0^2 were obtained by independent fitting of the metal foils; they were found to be 0.87 for Pt and 0.86 for Rh. These values were defined and kept as such in all following fittings.
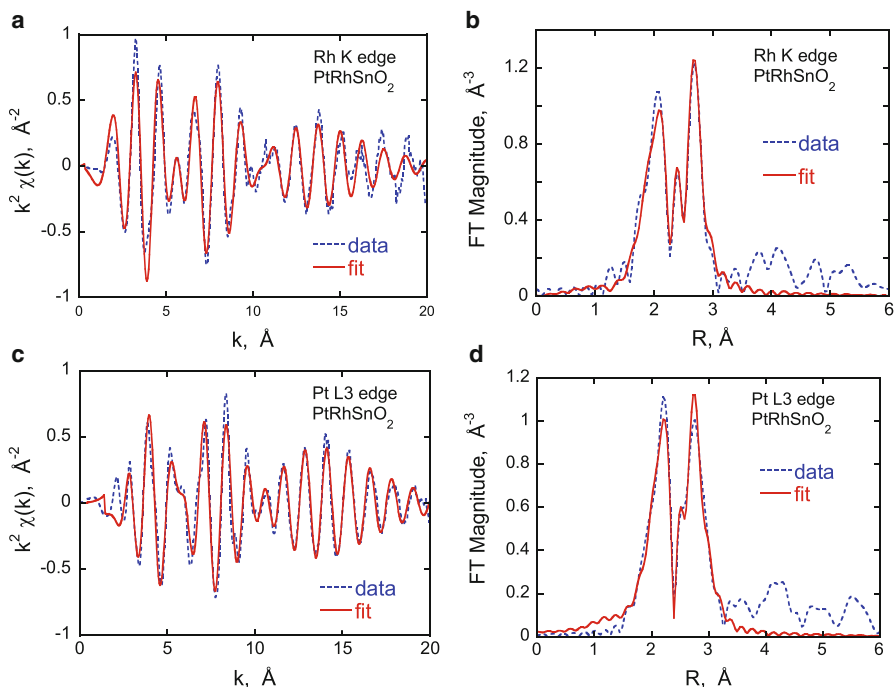
Fig. 6.15 Results of the first-shell fitting of the EXAFS spectra obtained during electrochemical oxidation of ethanol on the PtRhSnO$_2$/C electrocatalyst: (**a**) and (**b**) Rh K-edge; (**c**) and (**d**) Pt L$_3$ edge. The fits are presented in k-space (**a** and **c**), and Fourier transform magnitudes (**b** and **d**) for the catalyst held at 0.41 V vs. RHE. The Rh K-edge and Pt L$_3$ edge data were fitted concurrently to the theoretical signals while applying physically reasonable constraints (From Ref. [32])

Coordination numbers N(Rh–Pt) and N(Pt–Rh) revealed the average composition of the nanoparticles, $x(\text{Pt})/x(\text{Rh}) = N(\text{Rh} - \text{Pt})/N(\text{Pt} - \text{Rh}) = 2.1 \pm 0.3$, which is in reasonable agreement with the ICP data $x(\text{Pt})/x(\text{Rh}) = 1.5 \pm 0.2$. The obtained Pt–metal and Rh–metal coordination numbers were $N(\text{Pt} - \text{M}) = N(\text{Pt} - \text{Pt}) + N(\text{Pt} - \text{Rh}) = 9.5 \pm 0.8$ and $N(\text{Rh} - \text{M}) = N(\text{Rh} - \text{Rh}) + N(\text{Rh} - \text{Pt}) = 10.8 \pm 0.8$. Their close values are consistent with homogeneous distribution of Pt and Rh throughout the particles (see Eq. 6.6b). Also, as the N(Pt–Pt)/N(Pt–Rh) and N(Rh–Pt)/N(Rh–Rh) ratios were found to be consistent within the uncertainties, with the bulk ratios of Pt and Rh concentrations obtained independently by EXAFS and ICP, we conclude that the Pt and Rh formed a quasi-random alloy. This is also supported by the similarity between the Pt–Pt, Pt–Rh, and Rh–Rh bond lengths found by the EXAFS analysis: 2.743 ± 0.003, 2.725 ± 0.004, and 2.705 ± 0.005 Å, respectively, that is, characterized by a much smaller spread than between pure Pt (2.775 Å) and Rh (2.689 Å). Finally, the average of total coordination numbers for Pt–metal and Rh–metal (10.0 ± 0.8) suggests that the size of the nanoparticles is within 1.5 and 3.5 nm, which is in good agreement with the range found by TEM (1–3 nm) [32].

7.3.3   Optimizing Pt–Rh–SnO$_2$ Nanocatalyst

Further improvement of the catalytic properties of the ternary catalyst was done by optimizing the molar fractions of the three constituents in Pt/Rh/SnO$_2$. The composition and the particle size were controlled by simultaneous codeposition onto carbon support of all three metals by reduction of their soluble chlorides by ethylene glycol and oxidizing Sn to SnO$_2$ by heating in air. This technique produces PtRh particles of an average size of 1.5 nm with a narrow distribution [33].

Figure 6.16a shows the comparison of infrared spectroelectrochemical spectra of four catalysts with different Rh mole fractions, taken in 1 M HClO$_4$ at 0.6 V, the highest practical potential for DEFC. The Pt and Sn fractions were kept the same in all four catalysts, i.e., Pt:Sn = 1:1, whereas the mole fraction of Rh varied from ¼ to 1. The dominant peak at ~2340 cm^{-1} is the asymmetric stretch of CO$_2$ in aqueous solutions, the product of the total oxidation pathway. The other strong band around 1110 cm^{-1} presents the triply degenerate stretch of perchlorate anions, drawn into the electrochemical double layer to compensate the positive polarization charge of the catalyst surface. Besides these two strong bands, other smaller ones are also present. Those smaller bands are due to presence of acetic acid or acetaldehyde, the products of the incomplete oxidation of ethanol (the C $=$ O stretching band of both acetic acid and acetaldehyde in solution and adsorbed at the catalyst, at 1705 and 1625 cm^{-1}, respectively; the O–C–O stretching and CH$_3$ bending modes of adsorbed acetate at 1350 and 1400 cm^{-1}; the C–O stretching band of acetic acid in the solution at 1280 cm^{-1}; and C–C–O asymmetric stretch of acetaldehyde at 933 cm^{-1}). Although the direct comparison of the intensity of the bands in different spectra is difficult to use for quantification purposes as it depends on the positioning of the catalyst in the spectroelectrochemical cell [38], the ratio of bands in a single spectrum can be used to compare the activity of the electrocatalyst. The spectra of catalysts with mole Pt:Rh mole fractions of ¼ and 1 show a considerable amount of acetaldehyde and acetic acid and a relatively low peak of CO$_2$. The latter peak is the highest in the spectrum of the catalyst with Pt:Rh = 1:0.5 mol ratio, but the products of the incomplete EOR are still present. The spectrum of the catalyst with the Pt:Rh = 1:⅓ also shows a large peak of carbon dioxide, but a negligible amount of products of the incomplete oxidation pathway. The latter catalyst appears to have the optimal mole ratio of the noble metals. This conclusion is in accord with a study of three binary PtRh alloys, in which the catalyst with Pt:Rh ratio of 1:0.37 showed the largest production of CO$_2$ [39].

The catalyst with Pt:Rh = 1:⅓ also shows the best selectivity toward the total oxidation pathway in the EOR of ethanol, as shown in Fig. 6.16b. This phenomenon was ascribed to the electronic effect between Pt and Rh through which the *d*-band states of Rh are partially emptied, providing moderate bonding to ethanol intermediates with broken C–C bond. More mobile intermediates are promptly moved to the oxygen-containing species covering the SnO$_2$ sites at the surface of the ternary catalyst and further oxidized to CO$_2$ [40].

Electrochemical measurements were conducted on two catalysts with stoichiometric atomic ratio of Pt$_{21}$Rh$_5$Sn$_{39}$ and Pt$_{23}$Rh$_5$Sn$_{26}$ (both adsorbed on carbon), and
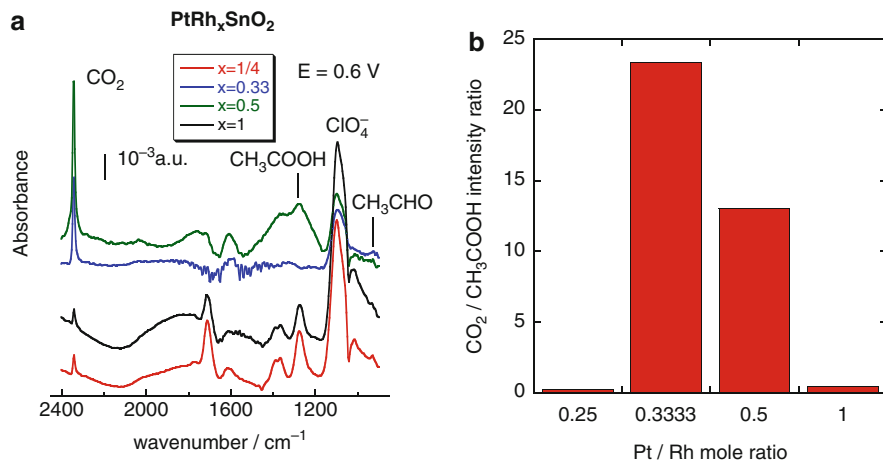
Fig. 6.16 (**a**) In situ infrared spectroelectrochemical spectra of $PtRh_xSnO_2$ ($x = \frac{1}{4}$, $\frac{1}{3}$, $\frac{1}{2}$, and 1) catalysts with varied mole fraction of Rh at 0.6 V vs. RHE. (**b**) Selectivity of the $PtRh_xSnO_2$ catalysts represented as the intensity ratios of the bands at 2340 cm^{-1} (C = O stretch in CO_2) and 1280 cm^{-1} (C–O stretch of acetic acid). Not published previously

their activity compared to the commercially available Pt/C and PtRu/C. The results show that the oxidation currents of the ternary catalysts, normalized to the noble metal loading, are considerably greater than that of the commercial ones and show lower oxidation onset. Between the two ternary catalysts, the one with the lower Sn loading shows better activity, lower onset of ethanol oxidation, and greater stability in chronoamperometric tests. As the two catalysts have roughly the same Pt:Rh ratio, the difference is ascribed to change in the SnO_2 content.

Figure 6.17 depicts relative changes in white-line peaks of Pt L_3 and Rh K-edges from two ternary catalysts as a function of applied potential. Figure 6.17a illustrates that the intensity of the white line of Pt shows no effect on potential excursions up to 0.41 V in either catalyst. At more positive potentials, the white lines of both catalysts are affected, but the one with higher Sn content shows more abrupt change with potentials [41]. On the other hand, while the white line of Rh in the catalyst with lower Sn content is unaffected by the potential excursion up to 0.41 V, that of $Pt_{21}Rh_5Sn_{39}$/C starts to change as early as 0.21 V and continues to increase with a steeper slope over the whole potential excursion (Fig. 6.17b).

The changes in the white line of both Pt and Rh may be correlated to the metal–SnO_2 spillover process in the ternary system that affects the oxidation of the noble metals. While the SnO_2 shifts the oxidation of noble metals to positive potentials, it appears that a too high content of SnO_2 at the catalysts surface lowers its activity for oxidation of alcohols. At potentials higher than 0.41 V, Pt sites in PtRh nanoclusters form bonds with OH provided by the SnO_2 and become unavailable for adsorption of ethanol. Similarly, too high content of SnO_2 in the ternary catalyst affects the Rh oxidation, which is evident at Rh XANES spectra obtained during the potential excursion from 0.06 to 0.91 V that show isosbestic points, a prima facie
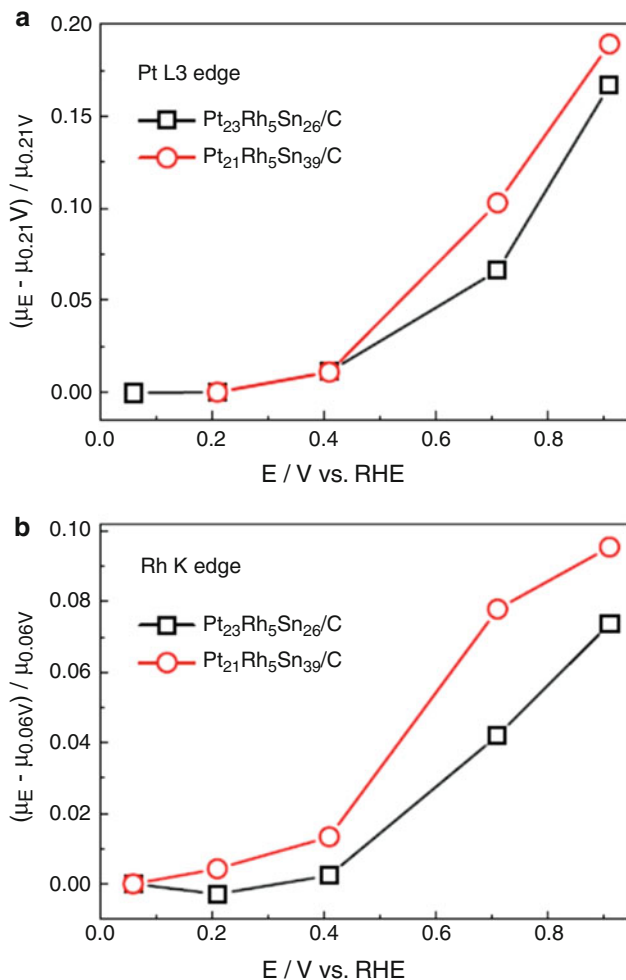
Fig. 6.17 Comparison of the change in absorption peaks at Pt L_3 edge (**a**) and at Rh K-edge (**b**) for the two Pt–Rh–SnO$_2$/C electrocatalysts with different stoichiometry, plotted as a function of applied potentials (From [41])

evidence of the existence of Rh species in two different chemical forms while their total concentration stays the same. The Rh changes its oxidation state directly from Rh^0 to Rh^{n+} (where n is most likely 3), without passing through reaction intermediates having lower oxidation state [41].

Secondary refinement of the ternary catalyst was carried out to discover the optimal ratio between Pt and Sn mole fractions. In these studies, the mole ratio of Pt and Rh was fixed to 1:$\frac{1}{3}$ while that of Pt:Sn was varied from 1:0.67 to 1:2. The activity of the series of catalysts was followed by a number of techniques including cyclic voltammetry and in situ infrared electrochemistry, while their constitution was
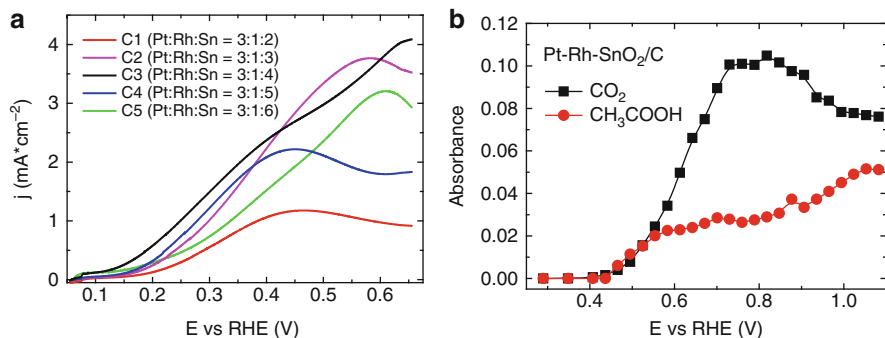
Fig. 6.18 (**a**) Electrochemical polarization curves of $Pt_3Rh(SnO_2)_x$ ($x = 2-6$) catalysts with varied mole fraction of Sn. (**b**) Integrated band intensities of CO_2 and CH_3COOH from Pt–Rh–SnO_2/C with the atomic ratio Pt:Rh:Sn = 3:1:4 (From Ref. [33])
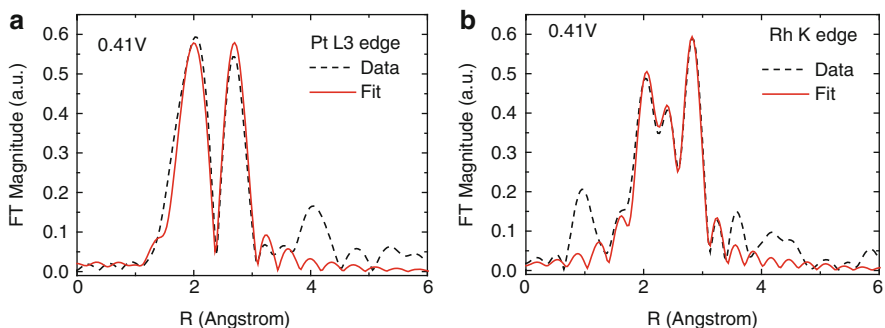
Fig. 6.19 Fourier transform magnitudes of Pt L_3 edge (**a**), and Rh K-edge (**b**), for Pt–Rh–SnO_2/C electrocatalyst with the atomic ratio Pt:Rh:Sn = 3:1:4 held at 0.41 V in 1 M $HClO_4$, and the respective first-shell fits (From Ref. [33])

resolved by EXAFS. Figure 6.18a shows the electrochemical polarization curves of ethanol oxidation on Pt/Rh/SnO_2 catalysts with varied Sn mole ratio. Among five catalysts, Pt_3RhSn_4 shows the lowest oxidation onset and the highest oxidation currents at most potentials practical for fuel cell applications. The in situ IR spectroelectrochemistry shows a large production of CO_2 (Fig. 6.18b).

The first-shell fitting results of the Pt–Rh–SnO_2/C (with Pt:Rh:Sn = 3:1:4 atomic ratio) electrocatalyst at a potential of 0.41 V are shown in Fig. 6.19. A reasonably good agreement between the fits and the original spectra is seen; the results of coordination numbers and bond lengths are summarized in Table 6.2. In these analyses, all parameters except for the passive electron reduction factors, S_0^2 (Pt) and S_0^2 (Rh), were allowed to vary with no constraints. As seen in the Table, the ratio of coordination numbers $N(Pt–Pt)/N(Pt–Rh) = 3.0$ is in excellent agreement with the mole fraction ratio $x(Pt)/x(Rh) = 3$. Concomitantly, the ratio of coordination numbers $N(Rh–Rh)/N(Rh–Pt)$ is determined to be 0.37, which is also in good agreement with $x(Rh)/x(Pt) = 0.33$. Furthermore, $N(Pt–Pt) + N(Pt–Rh) =$

Table 6.2 Bond lengths and coordination numbers of Pt and Rh metals in the Pt–Rh–SnO$_2$/C catalyst held at 0.41 V in 1 M HClO$_4$ obtained by the first-shell fitting and comparison to those of bulk metals (From Ref. [33])

	Bond length	Coordination number
Pt (bulk)	2.775	12
Rh (bulk)	2.689	12
Pt–Pt	2.740 ± 0.004	5.1 ± 0.9
Rh–Rh	2.683 ± 0.006	1.9 ± 0.9
Pt–Rh	2.715 ± 0.004	1.7 ± 0.9
Rh–Pt	2.715 ± 0.004	5.1 ± 1.0

6.8, and N(Rh–Rh) + N(Rh–Pt) = 7.0, thus within the experimental error N(Pt–M) = N(Rh–M), consistent with homogeneous distribution of both Pt and Rh atoms throughout the particles without preferential accumulation of one metal around the other. Clearly, the EXAFS analysis demonstrates the formation of homogeneous Pt–Rh random alloy nanoparticles. The particle size can be estimated from the total coordination numbers of the two metals. Assuming N(Pt–M) = N (Rh–M) = 7.0, the particle size is found to be about 1.4 nm, in good agreement with the HR-STEM data.

7.3.4 Substituting Rh with Ir

Because almost 80 % of the world production of Rh is used in vehicles and its price is higher than that of Pt, further work was aimed to substitute the Rh metal with a cheaper and possibly more abundant metal so that the electrocatalyst can be used in mass production of portable fuel cells. Iridium is a likely candidate for replacement of Rh, as the two metals are in the same group of periodic system and have similar chemical characteristics. Although Ir is one of the rarest elements in the Earth's crust, its current price is less than a half of that for Pt and Rh.

Electrochemical and in situ IR experiments performed on a series of Pt–M–SnO$_2$ catalysts adsorbed on carbon showed that Ir has the ability to split the C–C bond in ethanol [42]. To increase the activity of the catalysts, a series of Pt/Ir/Rh/Sn catalysts were also investigated. The highest activity among the Pt/Ir/Sn catalysts was found for the catalyst having Pt:Ir:Sn = 1:1:1 atomic ratio. Among all the catalysts with and without Rh, the highest CO$_2$ production was found for the catalyst that contained both Rh and Ir, with atomic ratio Pt:Ir:Rh:Sn = 1:1:1:1. However, both the activity and CO$_2$ production of all Ir catalysts were lower than those of the optimized Pt–Rh–SnO$_2$/C catalyst.

XAS experiments were conducted to reveal the internal structure of the Pt–Ir–Sn catalyst. However, since the L$_3$ absorption edges of Pt and Ir are very close, Ir L$_3$ edge cannot be extended beyond Pt edge that lays ca. 400 eV higher in energy which is insufficient for EXAFS analysis, and Pt L$_3$ edge oscillations are difficult to separate from that of Ir L$_3$. The XANES spectra revealed an oxidized state of Ir at all potentials. Both Ir and Pt spectra show a potential dependence so that their white lines increase at higher potentials, indicating their oxidation (Fig. 6.20).
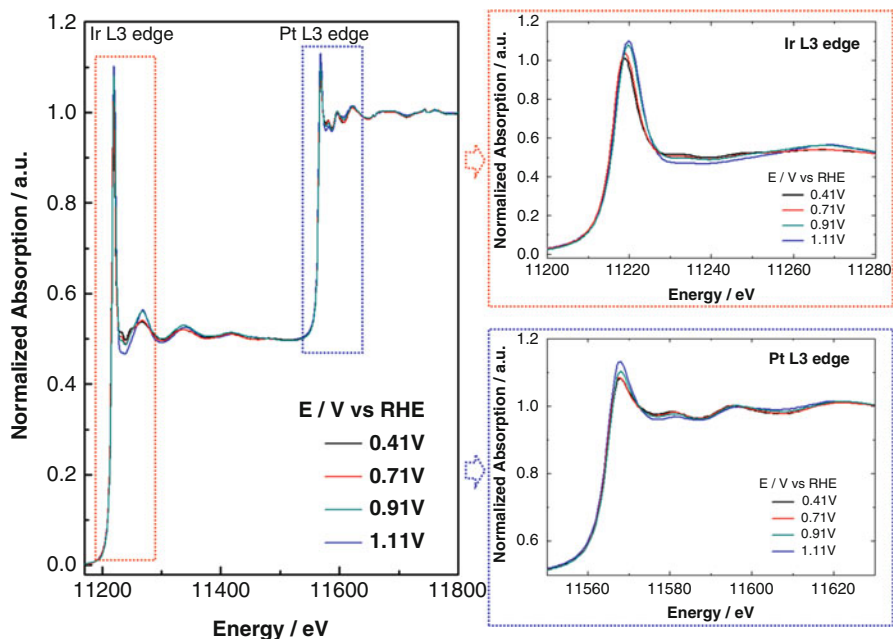
Fig. 6.20 In situ XANES spectra of Pt L_3 and Ir L_3 edges of PtIr/SnO$_2$/C electrocatalyst under different applied potentials (Taken from Ref. [42])

The ratio between the absorption intensities of Pt and Ir is ca. 0.95, measured from the XAS spectra. This ratio can be used to approximate the composition of the Pt/Ir electrocatalyst since their absorption coefficients are similar. Since the edge step ($\Delta\mu_0$, c.f. Fig. 6.2) of Ir L_3 is approximately equal to that of Pt L_3 (both ca. 0.5), the Pt/Ir ratio is close to 1, which is consistent with the nominal value [43].

7.4 Oxygen Reduction Reaction on Cathodes

The proton exchange membrane fuel cell (PEMFC) is widely considered as a high efficient and clean energy system. However, technical and economic barriers still exist in the development of oxygen reduction reaction (ORR) cathodes [44]; the principal drawbacks involve slow kinetics, high Pt loading, and poor long-term stability. Numerous studies have reported that Pt alloys (mostly with transition metals such as Co, Ni, and Fe) are more active for the ORR than pure Pt [45, 46]. However, the Pt loading in these alloys is still very high, and the non-noble metals in these alloys often dissolve in the acid environment of the PEMFC. In order to alleviate these impediments, a new class of electrocatalysts comprising a Pt monolayer deposited on nanoparticles of a suitable metal or alloy substrate has been developed. We employed a synthesis method of galvanic displacement of
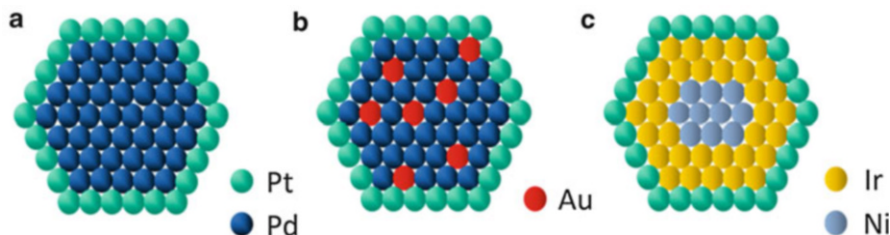
Fig. 6.21 Pt monolayer on (**a**) Pd, (**b**) PdAu alloy, and (**c**) IrNi core–shell nanoparticle catalysts

underpotentially deposited (UPD) Cu adatoms on substrate metal surfaces by a Pt monolayer. In the following sections, we will discuss how the atomic structures and electrochemical properties are mutually related using three examples of (i) Pt monolayer on Pd nanoparticle catalyst (Pt_{ML}/Pd/C) (Fig. 6.21a), (ii) Pt monolayer on PdAu alloy nanoparticle catalyst (Pt_{ML}/PdAu/C) (Fig. 6.21b), and (iii) Pt monolayer on IrNi core–shell nanoparticle catalysts (Pt_{ML}/IrNi/C) (Fig. 6.21c).

7.4.1 Pt_{ML}/Pd/C

The activity of Pt monolayer electrocatalysts for the ORR is strongly substrate metal dependent. The volcano-type plot is obtained from the activity of Pt monolayers on various substrates plotted as a function of calculated *d*-band center of Pt monolayer [47]. Pd imparts the highest activity of Pt monolayers, while Au, Ru, Re, and Rh cause a decrease in activity although they are stable supports. We have carried out the core–shell characterization of the Pt_{ML}/Pd/C electrocatalyst by in situ EXAFS [9]. The diameter of the Pt/Pd nanoparticles is *ca* 4.2 nm. Figures 6.22 and 6.23 show in situ EXAFS of Pt L_3 and Pd K-edges from the Pt/Pd/C electrocatalyst in 1 M $HClO_4$ at a potential of 0.41 V together with those from reference foils, respectively. The difference between the Pt deposited on Pd nanoparticles and Pt foil is clearly shown in Fig. 6.22, particularly in oscillation behavior in *k*-space (Fig. 6.22b). Two major differences are seen: one is that amplitude of oscillation from Pt deposits on Pd nanoparticles is much smaller than that of Pt foil, indicating that the size of Pt deposition is considerably small [48]. The other is that the phase in oscillation of the Pt deposits is markedly shifted from that of Pt foil, indicating that the atomic structure of the Pt deposited on Pd nanoparticles is significantly different from 3D Pt bulk. On the other hand, the *k*-space spectrum from Pd nanoparticles (Fig. 6.23b) shows somewhat smaller amplitude than that of Pd foil, but their oscillation behavior is approximately the same. This indicates that there may be only the size effect between these Pd components.

Pt L_3 and Pd K data were fitted concurrently using Artemis software [12] by applying the following physically reasonable constraints [17]: (i) the ratio of coordination numbers of Pt–Pd (N(Pt–Pd)) and Pd–Pt (N(Pd–Pt)) pairs is related with actual mole ratio of x(Pt)/x(Pd) that is determined to be 0.32 by ICP analysis; (ii) the Pt–Pd distance is the same as measured from either edge, i.e., R(Pt–Pd) $= R$(Pt–Pd); and (iii) the bond length disorder parameters of heterogeneous metal bonds are the

same as measured from opposite atoms, i.e., σ^2(Pt–Pd) = σ^2(Pd–Pt). The results of
fitting are shown in Fig. 6.24; the obtained *N*(Pt–Pt) is 5.8 ± 0.8 and the *N*(Pt–Pd) is
2.7 ± 0.7. Let us envisage a complete Pt monolayer on a Pd(111) surface; in this
case, the Pt–Pt coordination number is 6 and the Pt–Pd coordination number is
3. These numbers may be slightly different for monolayers on nanoparticles [4,
49]. For instance, the surface of a cubo-octahedron nanoparticle comprises (111) and
(100) planes and edges, leading to an average surface coordination number of 4.8
and an average surface–core coordination number of 3.2 for nanoparticles with
4 ~ 5 nm diameter [17]. On the other hand, the surface of icosahedron nanoparticles
comprises (111) planes and edges, resulting in an average surface coordination
number of 6 and an average surface–core coordination number of 2.7 for
nanoparticles with 4 ~ 5 nm diameter. These ratios between the planes and edges
change with the particle size, and actual nanoparticles may have more complicated
surface planes and combinations. For 4.2 nm diameter nanoparticles, it is inferred the
Pt–Pt CN may lay between 5 and 6, and the Pt–Pd CN around 3 for Pt monolayer.

Fig. 6.23 (**a**) In situ EXAFS and (**b**) (k^2-weighted) *k*-space spectra of Pd K-edge obtained from Pt$_{ML}$/Pd/C electrocatalysts in 1 M HClO$_4$ at a potential of 0.41 V (*solid lines*), together with those from a Pd foil (*dotted lines*) (Taken from Ref. [9])
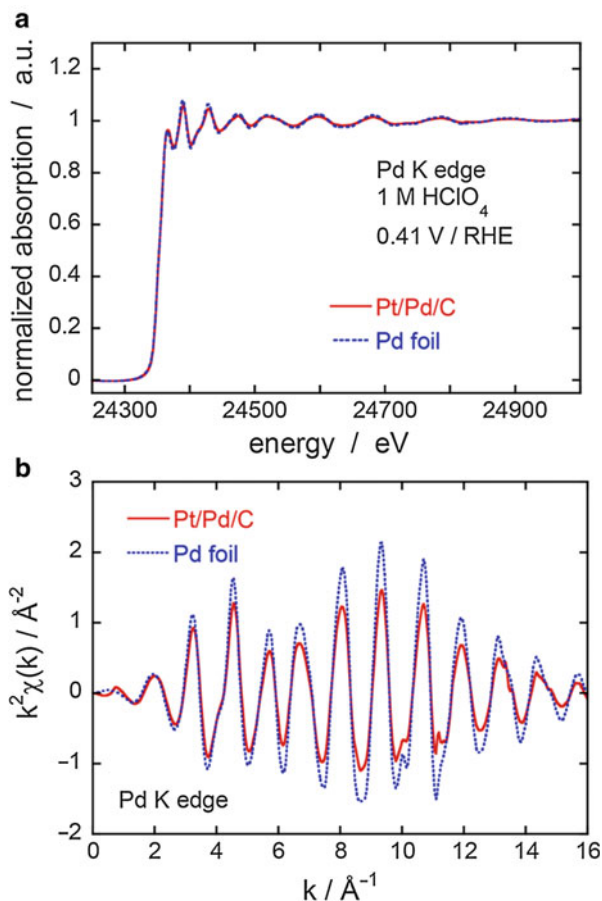
We consider that the *N*(Pt–Pt) and *N*(Pt–Pd) obtained from the present analysis thus verify the Pt monolayer formation on Pd nanoparticle surfaces. The analysis also determined that the Pt–Pt and Pt–Pd bond lengths are 2.729 ± 0.005 Å and 2.724 ± 0.007 Å, respectively; thus, both are smaller than that of pure Pt (2.775 Å). The slight contraction in Pt–Pt bond length of Pt$_{ML}$/Pd catalysts results in the enhancement of ORR activity compared with that of Pt.

Figure 6.25a depicts the results of the accelerated fuel cell stability tests of the Pt$_{ML}$/Pd/C electrocatalyst by plotting Pt mass activity as a function of the number of potential cycles [50]. The test involved potential step cycling between 0.7 and 0.9 V with a 30 s dwell time at 80 °C. After 100,000 cycles, the Pt mass activity had decreased by 37 %, indicating the superb durability of this electrocatalyst. In comparison, the Pt mass activity of two commercial Pt/C catalysts was about three times smaller than that of the Pt$_{ML}$/Pd/C electrocatalyst. After 60,000 potential cycles, the activity of the Pt/C had fallen by almost 70 %, compared with less than

Fig. 6.24 Fourier transform magnitudes of the data (*dotted red*) and first-shell fit (*solid blue*) of (**a**) Pt L$_3$ and (**b**) Pd K-edges from Pt$_{ML}$/Pd/C electrocatalysts in 1 M HClO$_4$ at a potential of 0.41 V (Taken from Ref. [9])
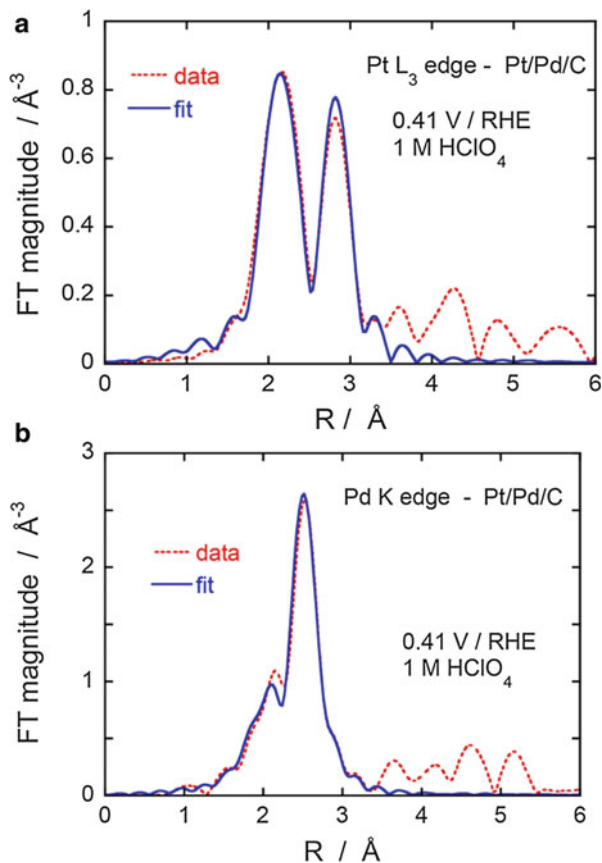
20 % for the Pt$_{ML}$/Pd/C catalyst; the activity of Pt/Ketjen black carbon had fallen more than 40 % after only 10,000 cycles. It is particularly important and informative that at 60,000 cycles, the Pt mass activity of our Pt$_{ML}$/Pd/C catalyst had risen from its initial threefold to a fivefold enhancement over that of Pt/C. This fact clearly illustrates the enhanced stability of the Pt$_{ML}$/Pd/C.

The EXAFS analysis revealed that the core–shell structure of the Pt$_{ML}$/Pd/C catalyst still exists after the potential cycling, despite a considerable loss of Pd [50]. Figure 6.25b presents the ex situ EXAFS spectrum of the Pt L$_3$ edge obtained from the Pt$_{ML}$/Pd/C electrocatalyst after a fuel cell test of 60,000 potential cycles, together with the in situ EXAFS spectrum measured at a potential of 0.41 V before the cycle test. As described above, we confirmed the formation of a Pt monolayer on the Pd nanoparticle surface of the sample prior to the potential cycles by in situ EXAFS [9]. After these cycles, the signal from the Pd K-edge became too small to concurrently fit Pt L$_3$ and Pd K data and to allow us to examine the atomic structures in detail. However, the general appearance of both Pt spectra is similar (except for

Fig. 6.25 (**a**) The Pt mass activity of the Pt_{ML}/Pd/C electrocatalyst for the ORR at 0.9 V versus the number of potential cycles during fuel cell test of the potential cycle between 0.7 and 0.9 V with a 30 s dwell time at 80 °C. Pt loadings in the cathodes: 0.085 mg cm^{-2} for Pt_{ML}/Pd/C, 0.133 mg cm^{-2} for Pt/C, and 0.30 mg cm^{-2} for Pt/Ketjen. (**b**) K^2-weighted EXAFS spectra of Pt L_3 edge from the Pt_{ML}/Pd/C electrocatalyst before and after 60,000 potential cycles. (**c**) Scheme showing Pd dissolution from the core, followed by the formation of a hollow structure (Taken from Ref. [50])
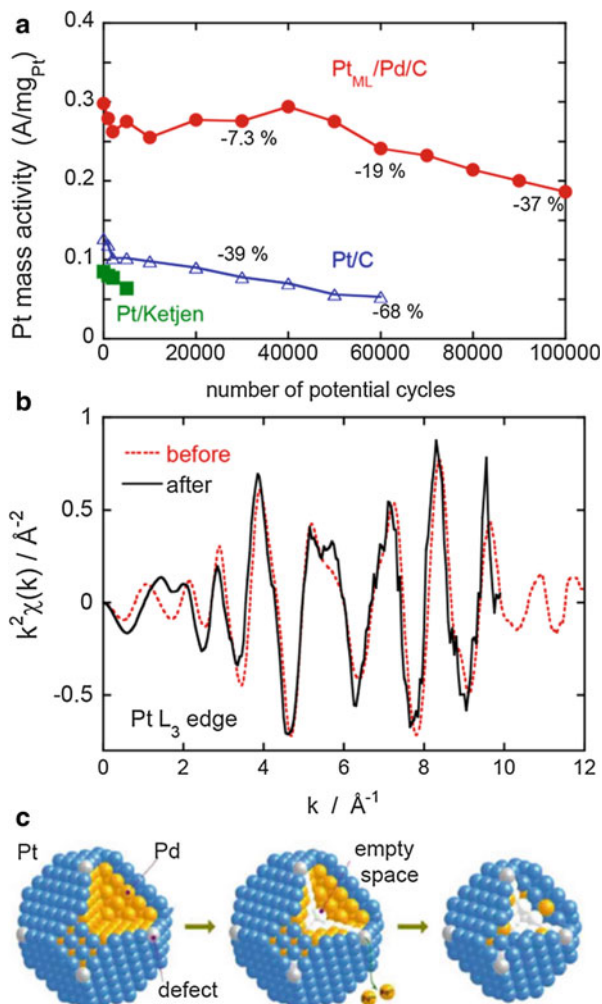
$k^2 < 2$ Å^{-1}, reflecting the oxidation of Pt), so pointing to the near retention of the structure of Pt shells throughout 60,000 cycles. The energy-dispersive x-ray spectroscopy (EDS) line analysis and electron energy loss spectroscopy (EELS) data also revealed the retention of the Pt shell and the significant loss of Pd during the potential cycles.

The evidence that the Pt shell remains on the surface of nanoparticles, and that the core–shell nanocatalyst is more active and stable than pure Pt, is very important. With the progression of Pd dissolution from the cores, the nanoparticles shrink gradually, and the Pt monolayers collapse inwardly, which may engender the formation of a Pt bilayer/multilayer, as well as that of a hollow structure (Fig. 6.25c). It may well be that Pd dissolution prevents the cathode potential from reaching high values at which Pt dissolution easily takes place. In other words, Pd
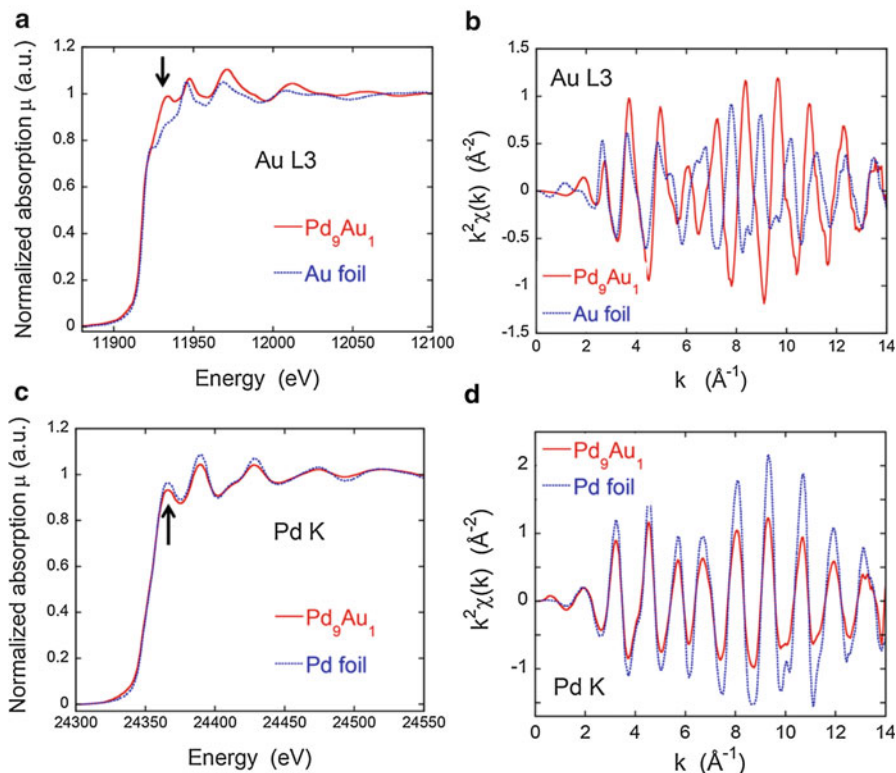
Fig. 6.26 (**a**, **b**) XANES and EXAFS k-space spectra (k^2-weighted) from Au L$_3$, and (**c**, **d**) from Pd K-edges from the Pd$_9$Au$_1$ nanoparticles measured in 1 M HClO$_4$ at a potential of 0.41 V (*red lines*), together with those from reference foils (*blue lines*) (Taken from Ref. [52])

may exert a certain degree of cathodic protection on Pt. In addition, the formation of a hollow structure might induce a slight contraction in Pt bonds and thereby enhance ORR activity [50, 51]. The density functional theory (DFT) calculations support the experimental data and indicate that hollow structures that form under these conditions would have the highest dissolution potentials.

7.4.2   Pt$_{ML}$/PdAu/C

We improved further the stability and activity of the Pt$_{ML}$/Pd/C monolayer electrocatalyst by alloying Pd with a small amount of gold to obtain a Pd$_9$Au$_1$ alloy core [52]. Figure 6.26 depicts the in situ XAS of the Au L$_3$ and Pd K-edges from the Pd$_9$Au$_1$ nanoparticles (without the Pt monolayers) in 1 M HClO$_4$ at a potential of 0.41 V, together with those from their respective reference foils. The mean diameter of the Pd$_9$Au$_1$ nanoparticles is 3.8 nm. There is a prominent difference between Au from the Pd$_9$Au$_1$ nanoparticles and the Au foil, both in the XANES region and in the EXAFS region (k-space), respectively, in Fig. 6.26a, b. We note that the XANES of Au in the Pd$_9$Au$_1$ nanoparticles (Fig. 6.26a) also differs from

Fig. 6.27 Fourier transform
EXAFS spectra of Pd K-edge
from (**a**) carbon-supported
Pd$_9$Au$_1$ alloy nanoparticles
and (**b**) Pd nanoparticles
(30 wt-%) in 1 M HClO$_4$ with
different applied potentials
(Taken from Ref. [52])
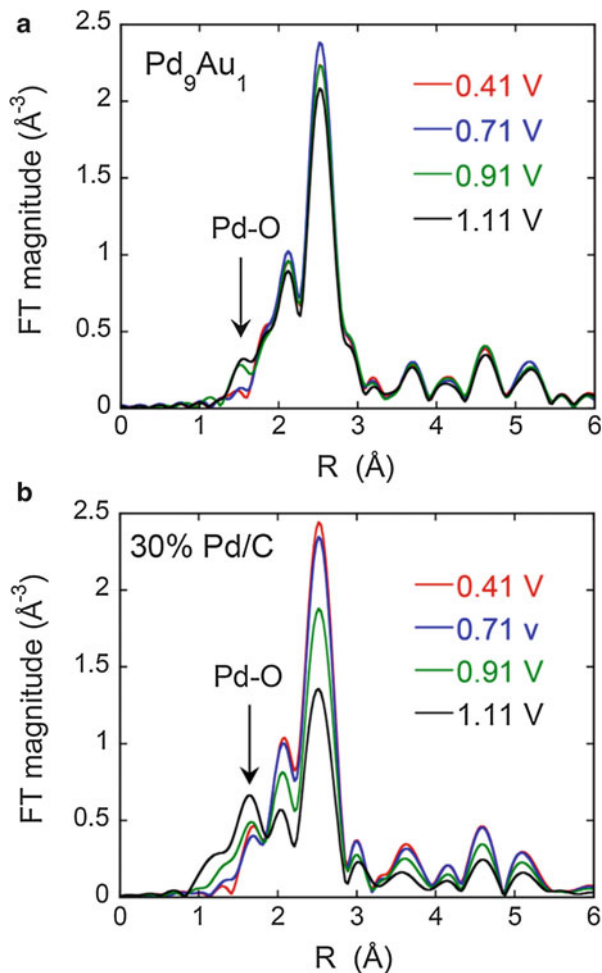
those observed by others in gold oxides [12, 48]. We attribute these dissimilarities to
changes in Au electronic states due to the interactions with Pd atoms. In the k-space
(Fig. 6.26b), the phase in oscillation of Au from the Pd$_9$Au$_1$ nanoparticles is shifted
markedly from that of Au foil, indicating that the atomic structure significantly
differs from that of an Au bulk. The XANES of Pd from Pd$_9$Au$_1$ nanoparticles
(Fig. 6.26c) is quite distinguishable from that from Pd foil, pointing to electronic
interference from Au atoms. On the other hand, the phase in oscillation in the
k-space (Fig. 6.26d) is not particularly unlike from those from a Pd foil, although
the amplitude of the former is slightly smaller than that of the Pd foil (the effect due
to particle size).

Figure 6.27 shows the findings from in situ EXAFS studies of Pd$_9$Au$_1$/C and
Pd/C nanoparticles measured at different potentials (0.41–1.12 V). The peak around
1.6 Å in the figures reflects the formation of Pd oxide. Clearly, Pd$_9$Au$_1$/C has much

Table 6.3 Coordination numbers (N), bonding distances (R), and bond length disorder parameters (δ) Pd_9Au_1 nanoparticles determined by the EXAFS experiment (Taken from Ref. [52])

	N	R (Å)	δ (Å^2)
Pd–Pd	9.2 ± 0.4	2.756 ± 0.002	0.0066 ± 0.0003
Pd–Au	0.9 ± 0.1	2.760 ± 0.007	0.0059 ± 0.0008
Au–Pd	8.1 ± 1.1	2.760 ± 0.007	0.0059 ± 0.0008
Au–Au	2.3 ± 1.6	2.771 ± 0.029	0.0063 ± 0.0038

lower potential dependence than does Pd/C, and Pd oxidation/dissolution in acid media is inhibited considerably by alloying Pd with a small concentration of Au (10 at-%). One of the origins is likely to be the electronic effect from the alloying element of Au, as we discussed above.

The results of first-shell fitting for the Pd_9Au_1 nanoparticles at a potential of 0.41 V with similar constraints discussed above are summarized in Table 6.3. We obtained the ratios of the coordination numbers $N(Au–Au)/N(Au–Pd) = 0.28$ and $N(Pd–Pd)/N(Pd–Au) = 10.2$, i.e., in reasonably good agreement with the mole fraction ratios, $x(Au)/x(Pd) = 0.16$ and $x(Pd)/x(Au) = 9.0$, each within the range of their experimental errors. Furthermore, the sum of coordination numbers for Pd ($N(Pd–Pd) + N(Pd–Au)$) is 10.1, which agrees well with that of Au ($N(Au–Au) + N(Au–Pd)$) at 10.4, indicating a homogeneous distribution of Pd and Au atoms in the particles without any preferential accumulation of one metal around the other, according to Eq. 6.6b. The EXAFS analysis demonstrates the formation of homogeneous PdAu alloy nanoparticles. We believe that the higher homogeneity may impart the better stability as discussed below.

Figure 6.28a depicts the results from stability tests of this $Pt_{ML}/Pd_9Au_1/C$ electrocatalyst, plotting Pt mass activity as a function of the number of potential cycles. The accelerated fuel cell stability test involved potential step cycling between 0.6 and 1.0 V with a 10 s dwell time at 80 °C. The stability of the electrocatalyst was excellent. After 100,000 cycles, the Pt mass activity had decreased by only 8 %. As shown in a STEM/EDS line-profile analysis (Fig. 6.28b) on a nanoparticle, the core–shell structure remains fairly unchanged after the test. While the Pt mass activity of the $Pt_{ML}/Pd/C$ electrocatalyst was almost comparable to that of the $Pt_{ML}/Pd_9Au_1/C$ electrocatalyst up to 40,000 cycles (Fig. 6.28a), they differ considerably in their behavior after 100,000 cycles, presumably due to the fact that the addition of a small amount of Au to Pd cores prevents the dissolution of Pd and thus effectively enhances the catalyst's stability.

Pd atoms may dissolve through imperfection sites (vacancies) in the Pt monolayers. The DFT calculation indicates that Au atoms segregate preferentially at defect sites in Pt monolayers [52]; if Au atoms mend the defective sites, Pd dissolution from the cores is effectively suppressed (the inset in Fig. 6.28b). This healing effect by Au atoms is the major factor improving stability of the $Pt_{ML}/Pd_9Au_1/C$ nanocatalyst. The segregated Au atoms on the surfaces also are beneficial in bettering the durability of the Pt monolayers. We demonstrated the stabilization of Pt nanoparticles in the presence of Au clusters under potential cycling conditions [43]. These clusters may

Fig. 6.28 (**a**) The Pt mass activity of the Pt$_{ML}$/Pd$_9$Au$_1$/C electrocatalyst for the ORR at 0.9 V versus the number of potential cycles during fuel cell test of potential cycles between 0.6 and 1.0 V with a 10 s dwell time at 80 °C. The results with Pt$_{ML}$/Pd/C and Pt/C catalysts are shown for comparison. (**b**) Distribution of components in a Pt$_{ML}$/Pd$_9$Au$_1$/C nanoparticle obtained by the line-scan analysis using EDS/STEM after the 100,000 potential cycle test (Taken from Ref. [52])
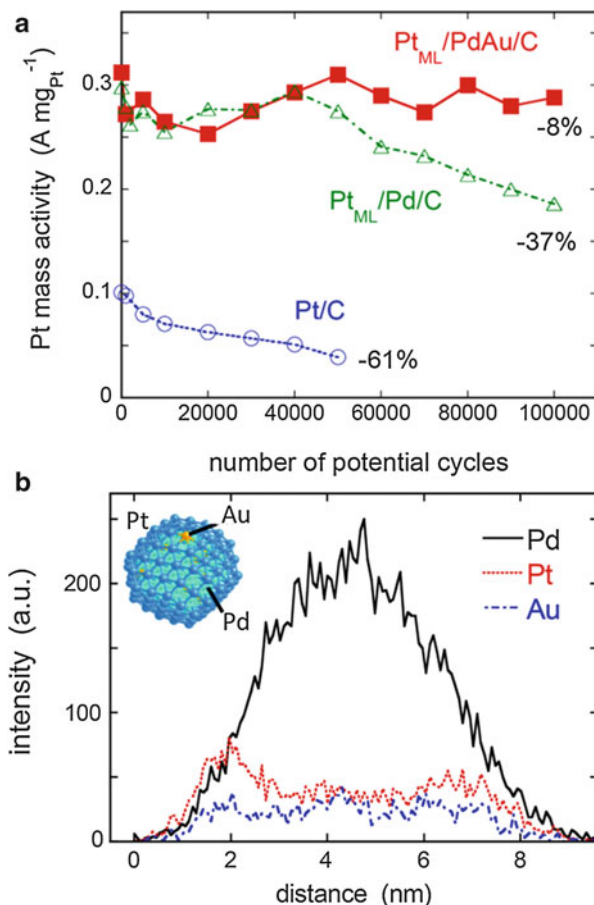
be deposited preferentially at low-coordinated sites, such as defects and edges on the
nanoparticles, thereby minimizing the total free surface energy; thus, the Au clusters
may block the initiation of Pt oxidation/dissolution and stabilize the Pt surfaces.

7.4.3 Pt Monolayer on IrNi Core–Shell Nanoparticle Catalysts (Pt$_{ML}$/IrNi/C)

Using non-noble metal – noble metal core–shell nanoparticles as supports facilitates a
further reduction of the content of the noble metal in ORR electrocatalysts. In addition,
by properly selecting the noble metal shell underneath the Pt monolayer, activity of the
latter, can be heightened through electronic and/or geometric effects. This new
approach represents a viable way of designing electrocatalysts with enhanced
activity and stability and with very low precious metal loading. We have devised
carbon-supported iridium–nickel core–shell structured nanoparticles [53], which are
demonstrated to be suitable substrates for Pt monolayer electrocatalysts for ORR [54].

Fig. 6.29 In situ XANES of (**a**) Ir L$_3$ edge and (**b**) Ni K-edges from the IrNi nanoparticles in 1 M HClO$_4$ at potentials of 0.41 V for (**a** and **b**) and 1.11 V for (**b**). Also shown are spectra from (**a**) Ir black and (**b**) a Ni foil (Taken from Ref. [53])
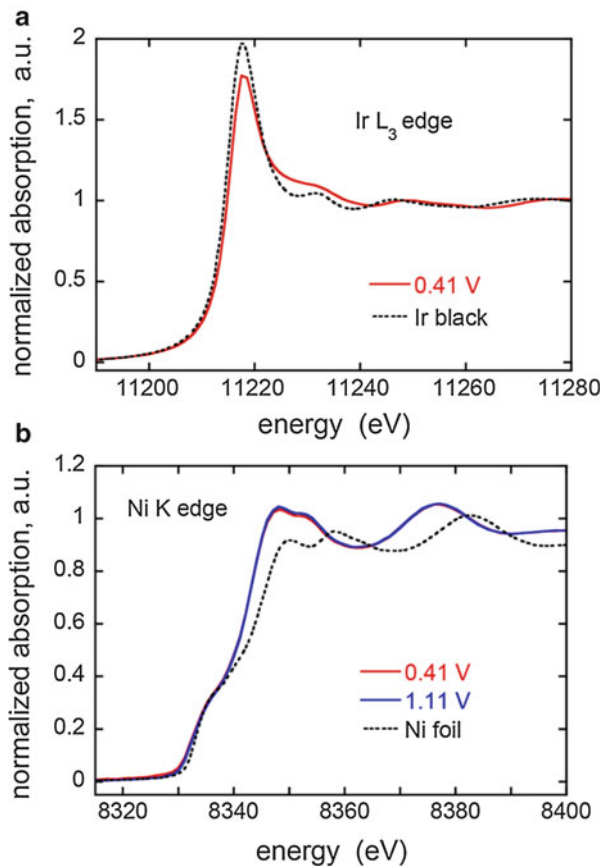
The IrNi core–shell nanoparticles were synthesized by chemical reduction and subsequent thermal annealing in H$_2$ [50]. Curves *a* and *b* of Fig. 6.29 show the in situ XANES of the Ir L$_3$ and Ni K-edges from the IrNi nanoparticles in 1 M HClO$_4$ at a potential of 0.41 V, together with those from reference materials, viz., Ir black (the particle diameter = 5 μm) and Ni foil (the thickness = 10 μm), respectively. Both Ir and Ni in the IrNi nanoparticles are considered to be metallic because the E_0 coincides with that of their respective bulk (11215 eV and 8333 eV for Ir and Ni, respectively). The Ni spectrum from the IrNi nanoparticles (Fig. 6.29b) also exhibits three peaks at 8348, 8353, and 8378 eV; the energy values of the peaks are lower, and their intensities are higher than those of the Ni foil, consistent with the reasonable assumption that alloying with Ir may change the electronic states of Ni atoms. This is in agreement with a number of XANES studies that have reported electronic interaction between alloy components [18, 55]. Also shown in Fig. 6.29b is the Ni K-edge spectrum from the IrNi nanoparticles at a potential of 1.11 V. Surprisingly, little change is observed between the two spectra at 0.41 and 1.11 V. On the other hand, the in situ XANES of Ir L$_3$ edge from the IrNi nanoparticles at 0.41 V displays

a decrease in intensity of the white line compared with that from the Ir black (Fig. 6.26a); this suggests that electronic properties of Ir may change by alloying with Ni. As the height of the white line is inversely proportional to the d-electron occupancy, it seems that both the Ir and Ni spectral changes in the alloy point to the d-electron transfer from Ni to Ir, which is in line with the electronegativities of the two elements.

Fourier transform EXAFS from the IrNi nanoparticles indicate that the highest peak in Ni from the IrNi nanoparticles is shifted to higher R values compared to that of the Ni foil, while the highest peak in Ir from the IrNi nanoparticles is displaced to a lower R than that from the Ir black. These data represent the expansion in the Ni bonds and the contraction in the Ir bonds as a consequence of the formation of IrNi solid solution alloy cores; the result is in line with those obtained from the XRD measurements [50] and the EXAFS fitting discussed below. The XAS spectra of Ni K-edge from the IrNi nanoparticles show little change occurring with increasing potentials and no characteristic signature of Ni oxides and/or Ni ions. As shown in Pourbaix diagrams [56], Ni cannot be present in a metallic state when exposed to acid solutions, unless the potential applied is below 0.4 V. The experimental result from the in situ XAS indicates that Ni atoms constituting the IrNi cores are not exposed to the electrolyte since the Ir shell completely encapsulates the IrNi core; Ni in the IrNi solid solution cores therefore is protected from oxidation or corrosion. The cyclic voltammetry curve of IrNi nanoparticles also revealed no anodic currents that can be ascribed to the oxidation/dissolution of Ni.

The Ir L_3 and Ni K-edge data were fitted concurrently with similar constraints discussed above. Figure 6.30 displays the fitting results of the IrNi nanoparticles. Good agreement is observed between the fits and the original spectra for both Ir L_3 (Fig. 6.30a) and Ni K (Fig. 6.30b) edges. Table 6.4 summarizes the coordination numbers obtained. We note that the length of the Ir–Ir bond obtained (2.664 Å) is shorter than that of pure Ir (2.714 Å), while the Ni–Ni bond obtained (2.562 Å) is longer than that of pure Ni (2.492 Å), indicating their alloying, vide supra.

The interpretation of the coordination numbers obtained is not straightforward since they are the ensemble average values from both the shells and cores, except for N(Ni–Ni) that is derived only from the cores. According to Eq. 6.6a, the ratio of the coordination number $N(M_1–M_1)/N(M_1–M_2)$ is equal to the mole fraction ratio $x(M_1)/x(M_2)$ for an $M_1–M_2$ binary solid solution alloy. As listed in Table 6.4, the ratio of coordination numbers N(Ni–Ni)/N(Ni–Ir) is 1.2, which is much larger than the actual mole fraction ratio x(Ni)/x(Ir) $= 0.56$. This finding indicates that more Ni–Ni bonds (and fewer Ni–Ir bonds) are present than in a random alloy wherein the two atoms have statistical distribution; this finding is well consistent with the STEM observations showing the Ir-rich (or Ni-depleted) shells; in the cores, the number of Ni–Ni bonds should be larger than on the average.

We used a suite of programs that model polyhedral nanoparticles with different diameters, different Ir shell thicknesses, and different molar ratios of IrNi cores to calculate the atomic coordination numbers for various core–shell structures [57, 58]. We then compared the coordination numbers in the model with those derived from
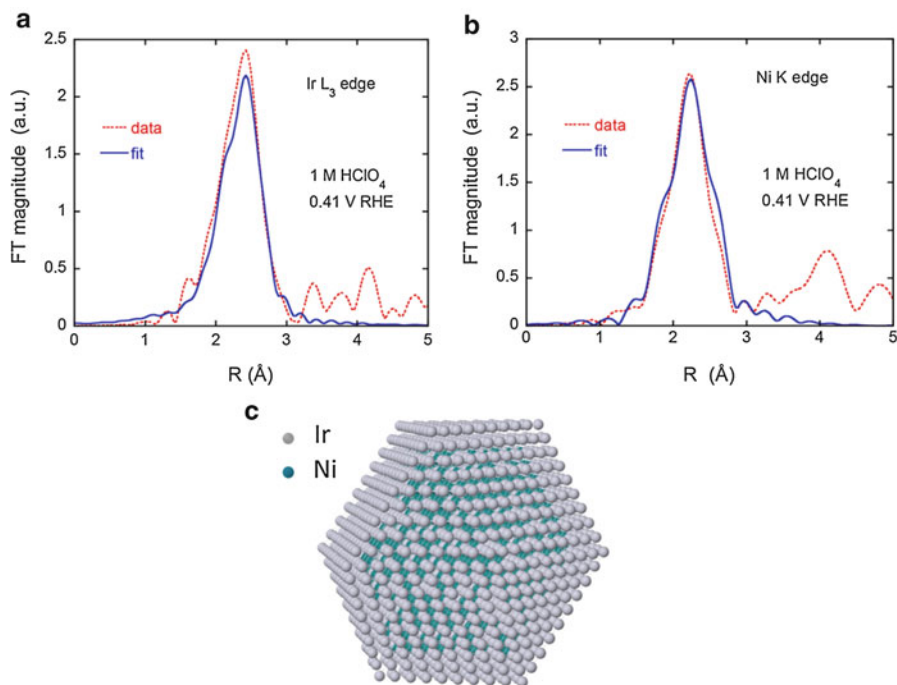
Fig. 6.30 Fourier transform magnitudes of the data (*dotted red*) and first-shell fit (*solid blue*) of (**a**) Ir L_3 and (**b**) Ni K-edges from IrNi nanoparticles in 1 M $HClO_4$ at a potential of 0.41 V. (**c**) Atomic configuration of two shell layers of Ir (1454 atoms) on an IrNi alloy core (1030 Ni and 385 Ir atoms). Ir: *gray* spheres. Ni: *green* spheres. Atomic ratio of Ni/Ir: 0.56. Diameter: 4.68 nm. Average metal–metal coordination number: 11 (Taken from Ref. [53])

Table 6.4 Coordination numbers determined by the EXAFS experiment and one-layer Ir shell and two-layer Ir shell models (Taken from Ref. [53])

	N(Ir–Ir)	N(Ir–Ni)	N(Ni–Ni)	N(Ni–Ir)	N(Ir–Ni)/N (Ni–Ir)	N(Ni–Ni)/N (Ni–Ir)
EXAFS	8.1 ± 0.7	2.9 ± 0.7	5.9 ± 0.7	5.1 ± 0.7	0.56	1.2 ± 0.2
One-layer Ir shell	6.47	3.76	5.28	6.72	0.56	0.79
Two-layer Ir shell	7.82	2.42	7.69	4.31	0.56	1.78

the EXAFS analysis in order to determine the most probable core–shell structure. We employed the polyhedron model to approximate a sphere-shaped particle for the present system. Table 6.4 also lists the calculated coordination numbers from two core–shell models: one comprises a one-layer Ir shell (812 atoms) on an IrNi alloy core (1027 Ni and 1030 Ir atoms), while the other represents a two-layer Ir shell (1454 atoms) on an IrNi alloy core (1030 Ni and 385 Ir atoms). Ir and Ni atoms in the

Fig. 6.31 (a) A HAADF–STEM image of a PtIrNi nanoparticle and (b) a comparison of the EELS intensities for the Pt and Ir M-edge and Ni Ledge along the scanned line, indicated in (a) (Taken from Ref. [54])
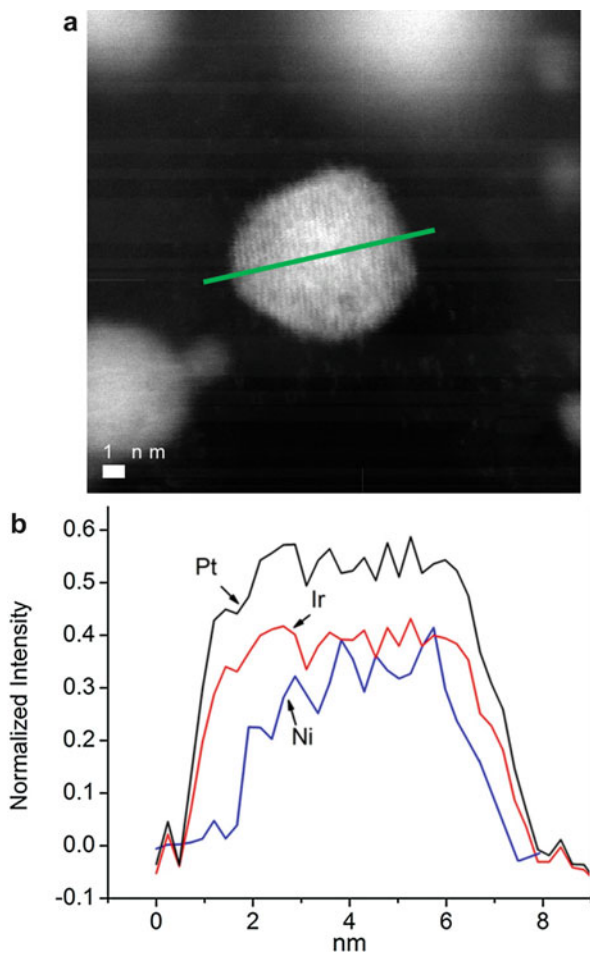
cores are randomly alloyed via a random number generator. For both models, the atomic ratio of Ni/Ir was set at 0.56, the diameter was calculated as 4.68 nm, and the average (metal–metal) coordination numbers were estimated to be 11. The two-layer model fits most of the EXAFS data much better cumulatively than does the one-layer model. Thus, the EXAFS analysis is consistent with the model wherein the IrNi nanoparticles are composed of two-layer Ir shells and IrNi alloy cores, as Fig. 6.27c schematically shows. On the basis of this result together with those from the XRD and the STEM–EELS measurements, we conclude that the nanoparticles comprise core–shell structure with Ir-rich top layers on the surfaces of IrNi solid solution alloy cores.

We deposited Pt monolayers on the surfaces of IrNi core–shell nanoparticles by a galvanic replacement of Cu UPD adatoms [54]. Figure 6.31 illustrates the line-profile analysis by STEM/EELS showing the distribution of Pt, Ir, and Ni components in a single nanoparticle (Fig. 6.31a). The EELS profile (Fig. 6.31b)

Table 6.5 Mass activity, half-wave potentials, and % loss in Pt surface area for the $Pt_{ML}/IrNi/C$ catalyst before and after potential cycling (Taken from Ref. [54])

	Synthesis on glassy Carbon electrode						Scale-up synthesis Method					
	Mass activity (j_k/A mg^{-1})		Half-wave potential (mV)		% loss in surface area		Mass activity (j_k/A mg^{-1})		Half-wave potential (mV)		% loss in surface area	
	Initial (0.9 V)	After 30,000 cycles (0.9 V)	Initial	After 30,000 cycles	After 30,000 cycles		Initial (0.9 V)	After 50,000 cycles (0.9 V)	Initial	After 50,000 cycles	After 50,000 cycles	
Pt	1.4	0.48	890	872	45		0.71	0.57	851	851	23	
PGM	0.78	0.27					0.22	0.17				

demonstrated that both the intensities of Ir and Ni are approximately constant around the center of the nanoparticle and Ni is depleted at both edges of the nanoparticles; the observation is in line with the EXAFS analyses. The differences in the Pt and the Ir profile, measured at the half value of the intensities are from 0.27 to 0.33 nm, corresponding to roughly one monolayer Pt shell on the IrNi alloy core.

Table 6.5 summarizes the ORR activity and stability of the Pt_{ML}/IrNi/C catalyst prepared by the carbon disk electrode and scale-up synthesis methods. The Pt mass activity of this catalyst at 0.9 V by the scale-up synthesis method is 0.71 A/mg, which is more than three times that of a commercial Pt/C catalyst. The enhancement in activity may be due to electronic modifications induced by strain, ligand, and segregation effects from the IrNi core–shell nanoparticles. The long-term stability of ORR electrocatalysts is another critical requirement for application in fuel cells. We evaluated the stability of the electrocatalyst by an accelerated test involving potential cycling between 0.6 and 1.0 V at a scan rate of 50 mV/s in an air-saturated $HClO_4$ solution. The Pt_{ML}/IrNi/C catalyst showed only a 20 % decrease in the Pt mass activity, a 23 % loss in the Pt surface area, and no loss in half-wave potential even after 50,000 cycles, which are much better performances than those of a commercial Pt/C catalyst. This demonstrates the advantages of depositing Pt monolayers on well-defined IrNi core–shell nanoparticles in enhancing both the activity and stability for ORR.

8   Conclusions and Future Perspective

A brief overview of in situ XAS techniques to characterize the nanostructured catalysts was described in the chapter, followed by discussion of selected examples involving XANES analysis of Pt nanoparticles, and EXAFS investigations of catalysts consisting of Pt–Rh solid solution deposited on SnO_2 for the EOR, as well as Pt monolayer catalysts for the ORR. The information on atomic structures, oxidation/ electronic states, and adsorbate species of catalytic surface during the course of a reaction, obtained by XAS analysis, provides a direct insight of the activity–structure relationship, as well as the origins for the activity and stability. The in situ XAS is thus an indispensable tool for catalysis studies because the data it furnishes can enhance our understanding of the mechanisms of electrocatalytic reactions at surfaces and provide a rational approach to the design of new active and durable electrocatalysts. With new synchrotrons developing worldwide, the technique has the promise to be widespread in scientific community.

References

1. Bunker G (2010) Introduction to XAFS: a practical guide to X-ray absorption fine structure spectroscopy. Cambridge University Press, Cambridge, UK
2. Calvin S (2013) XAFS for everyone. CRC Press/Taylor and Francis Group, Boca Raton
3. Koningsberger DC, Prins R (eds) (1988) X-ray absorption: principles, applications, techniques of EXAFS, SEXAFS, and XANES, in chemical analysis, vol 92. Wiley, New York
4. McBreen J, Mukerjee S (1999) In situ x-ray absorption studies of carbon-supported Pt and Pt alloy nanoparticles. In: Wieckowski A (ed) Interfacial electrochemistry: theory, experiment and applications. Marcel Dekker, New York, pp 895–914
5. See URL: xafs.org/Tutorials
6. Stern EA (1974) Theory of the extended x-ray-absorption fine structure. Phys Rev B 10 (8):3027–3037
7. See URL: lightsources.org
8. McBreen J, O'Grady WE, Pandya KI, Hoffman RW, Sayers DE (1987) EXAFS study of the nickel oxide electrode. Langmuir 3(3):428–433
9. Sasaki K, Wang JX, Naohara H, Marinkovic N, More K, Inada H, Adzic RR (2010) Recent advances in platinum monolayer electrocatalysts for oxygen reduction reaction: scale-up synthesis, structure and activity of Pt shells on Pd cores. Electrochim Acta 55(8):2645–2652
10. Ramaker DE, Koningsberger DC (2010) The atomic AXAFS and $\Delta\mu$ XANES techniques as applied to heterogeneous catalysis and electrocatalysis. Phys Chem Chem Phys 12 (21):5514–5534
11. Arruda TM, Shyam B, Ziegelbauer JM, Mukerjee S, Ramaker DE (2008) Investigation into the competitive and site-specific nature of anion adsorption on Pt using in situ X-ray absorption spectroscopy. J Phys Chem C 112(46):18087–18097
12. Ravel B, Newville M (2005) ATHENA, ARTEMIS, HEPHAESTUS: data analysis for X-ray absorption spectroscopy using IFEFFIT. J Synchrotron Radiat 12(4):537–541
13. See URL: http://cars9.uchicago.edu/~newville/adb/search.html
14. Bell AT (2003) The impact of nanoscience on heterogeneous catalysis. Science 299 (5613):1688–1691
15. Benfield RE (1992) Mean coordination numbers and the non-metal–metal transition in clusters. J Chem Soc Faraday Trans 88(8):1107–1110
16. Beale AM, Weckhuysen BM (2010) EXAFS as a tool to interrogate the size and shape of mono and bimetallic catalyst nanoparticles. Phys Chem Chem Phys 12(21):5562–5574
17. Frenkel A (2007) Solving the 3D structure of metal nanoparticles. Zeistchrift für Kristallographie 222(11):605–611
18. Alayoglu S, Zavalij P, Eichorn B, Wang Q, Frenkel AI, Chupas P (2009) Structural and architectural evaluation of bimetallic nanoparticles: a case study of Pt–Ru core-shell and alloy nanoparticles. ACS Nano 3(10):3127–3137
19. Nagamatsu S, Arai T, Yamamoto M, Ohkura T, Oyanagi H, Ishizaka T, Kawanami H, Uruga T, Tada M, Iwasawa Y (2013) Potential-dependent restructuring and hysteresis in the structural and electronic transformations of Pt/C, Au(core)-Pt(shell)/C, and Pd(core)-Pt(shell)/C cathode catalysts in polymer electrolyte fuel cells characterized by in situ X-ray absorption fine structure. J Phys Chem C 117(25):13094–13107
20. Sasaki K, Marinkovic NS, Isaacs HS, Adzic RR (2016) Synchrotron-based in situ characterization of carbon-supported Pt electrocatalysts ACS Catal 6(1): 69–76
21. Teliska M, O'Grady WE, Ramaker DE (2005) Determination of O and OH adsorption sites and coverage in situ on Pt electrodes from Pt L$_{23}$ X-ray absorption spectroscopy. J Phys Chem B 109 (16):8076–8084
22. Conway BE (1995) Electrochemical oxide film formation at noble metals as a surface-chemical process. Prog Surf Sci 49(4):331–452
23. Jerkiewicz G, Vatankhah G, Lessard J, Soriaga MP, Park YS (2004) Surface-oxide growth at platinum electrodes in aqueous H$_2$SO$_4$. Reexamination of its mechanism through combined

cyclic-voltammetry, electrochemical quartz-crystal nanobalance, and Auger electron spectroscopy measurements. Electrochim Acta 49(9–10):1451–1459

24. Lamy C, Coutanceau C, Leger J-M (2009) The direct ethanol fuel cell: a challenge to convert bioethanol cleanly into electric energy. In: Barbaro P, Bianchini C (eds) Catalysis for sustainable energy production. WILEY-VCH Verlag GmbH & Co. kGaA, Weinheim

25. Iwasita T, Pastor E (1994) A dems and FT*ir* spectroscopic investigation of adsorbed ethanol on polycrystalline platinum. Electrochim Acta 39(4):531–543; *ibid* (1994) D/H exchange of ethanol at platinum electrodes. Electrochim Acta 39(4):547–552

26. Camara GA, Iwasita T (2005) Parallel pathways of ethanol oxidation: the effect of ethanol concentration. J Electroanal Chem 578(2):315–321

27. Wang H, Yusus Z, Behm RJ (2004) Ethanol electrooxidation on a carbon-supported Pt catalyst: reaction kinetics and product yields. J Phys Chem B 108(50):19413–19424

28. Lamy C, Rousseau S, Belgsir EM, Coutanceau C, Léger JM (2004) Recent progress in the direct ethanol fuel cell: development of new platinum–tin electrocatalysts. Electrochim Acta 49 (22–23):3901–3908

29. Demirci UB (2007) Theoretical means for searching bimetallic alloys as anode electrocatalysts for direct liquid-feed fuel cells. J Power Sources 173(1):11–18

30. Antolini E (2007) Platinum-based ternary catalysts for low temperature fuel cells: part II. Electrochemical properties. Appl Catal B 74(3–4):337–350

31. Idriss H (2004) Ethanol reactions over the surfaces of noble metal/cerium oxide catalysts. Platin Met Rev 48(3):105–115

32. Kowal A, Li M, Shao M, Sasaki M, Vukmirovic MB, Zhang J, Marinkovic NS, Liu P, Frenkel AI, Adzic RR (2009) Ternary Pt/Rh/SnO$_2$ electrocatalysts for oxidizing ethanol to CO$_2$. Nat Mater 8(4):325–330

33. Li M, Kowal A, Sasaki K, Marinkovic NS, Su D, Korach E, Liu P, Adzic RR (2010) Ethanol oxidation on the ternary Pt–Rh–SnO$_2$/C electrocatalysts with varied Pt:Rh:Sn ratios. Electrochim Acta 55(14):4331–4338

34. Kowal A, Gojkovic SL, Leed KS, Olszewski P, Sung Y-E (2009) Synthesis, characterization and electrocatalytic activity for ethanol oxidation of carbon supported Pt, Pt–Rh, Pt–SnO$_2$ and Pt–Rh–SnO$_2$ nanoclusters. Electrochem Commun 11(4):724–727

35. Choi YM, Liu P (2011) Understanding of ethanol decomposition on Rh(1 1 1) from density functional theory and kinetic Monte Carlo simulations. Catal Today 165(1):64–70

36. Trasatti S (1999) Interfacial Electrochemistry of Conductive Oxides for Electrocatalysis. In: Wieckowski A (ed) Interfacial electrochemistry: theory, experiment, and applications. Marcel Dekker, New York, pp 769–788

37. Batzill M, Diebold U (2005) The surface and materials science of tin oxide. Prog Surf Sci 79 (2–4):47–154

38. Faguy PW, Marinkovic NS (1995) Sensitivity and reproducibility in infrared spectroscopic measurements at single-crystal electrode surfaces. Anal Chem 67(17):2791–2799

39. de Souza JPI, Queiroz SL, Bergamaski K, Gonzalez ER, Nart FC (2002) Electro-oxidation of ethanol on Pt, Rh, and PtRh electrodes. A study using DEMS and *in-situ* FTIR techniques. J Phys Chem B 106(38):9825–9830

40. Li M, Zhou W-P, Marinkovic NS, Sasaki K, Adzic RR (2013) The role of rhodium and tin oxide in the platinum-based electrocatalysts for ethanol oxidation to CO$_2$. Electrochim Acta 104 (1):454–461

41. Li M, Cullen D, Sasaki K, Marinkovic NS, More K, Adzic RR (2013) Ternary electrocatalysts for oxidizing ethanol to carbon dioxide: making Ir capable of splitting C–C bond. J Am Chem Soc 135(1):132–141

42. Li M, Marinkovic N, Sasaki K (2012) *In situ* characterization of ternary Pt–Rh–SnO$_2$/C catalysts for ethanol electrooxidation. Electrocatalysis 3(3–4):376–385

43. Zhang J, Sasaki K, Sutter E, Adzic RR (2007) Stabilization of platinum oxygen-reduction electrocatalysts using gold clusters. Science 315(5809):220–222

44. Gasteiger HA, Kocha SS, Sompalli B, Wagner FT (2005) Activity benchmarks and requirements for Pt, Pt-alloy, and non-Pt oxygen reduction catalysts for PEMFCs. Appl Catal B Environ 56(1–2):9–35
45. Mukerjee S, Srinivasan S, Soriaga M, McBreen JM (1995) Effect of preparation conditions of Pt alloys on their electronic, structural, and electrocatalytic activities for oxygen reduction - XRD, XAS, and electrochemical studies. J Phys Chem 99(13):4577–4589
46. Stamenkovic VR, Fowler B, Mun BS, Wang G, Ross PN, Lucas CA, Markovic NM (2007) Improved oxygen reduction activity on Pt$_3$Ni(111) via increased surface site availability. Science 315(5811):493–497
47. Zhang JL, Vukmirovic MB, Xu Y, Mavrikakis M, Adzic RR (2005) Controlling the catalytic activity of platinum-monolayer electrocatalysts for oxygen reduction with different substrates. Angew Chem Int Ed 44(14):2132–2135
48. Frenkel A, Hills CW, Nuzzo RG (2001) A View from the inside: complexity in the atomic scale ordering of supported metal nanoparticles. J Phys Chem B 105(51):12689–12703
49. Frische HG, Benfield RE (1993) Extract analytical formulae for mean coordination numbers in clusters. Z Phys D Atom Mol Clusters 26(1):S15–S17
50. Wang JX, Ma C, Choi YM, Su D, Zhu Y, Liu P, Si R, Vukmirovic MB, Zhang Y, Adzic RR (2011) Kirkendall effect and lattice concentration in nanoparticles: a new strategy to enhance sustainable activity. J Am Chem Soc 133(34):13551–13557
51. Sasaki K, Naohara H, Cai Y, Choi YM, Liu P, Vukmirovic MB, Wang JX, Adzic RR (2010) Core-protected platinum monolayer shell high-stability electrocatalysts for fuel-cell cathodes. Angew Chem Int Ed 49(46):8602–8607
52. Sasaki K, Naohara H, Choi YM, Cai Y, Chen W-H, Liu P, Adzic RR (2012) Highly stable Pt monolayer on PdAu nanoparticle electrocatalysts for the oxygen reduction reaction. Nat Commun 3. doi:10.1038/ncomms2124
53. Sasaki K, Kuttiyiel KA, Barrio L, Su D, Frenkel A, Marinkovic N, Mahajan D, Adzic RR (2011) Carbon-supported IrNi core-shell nanoparticles: synthesis, characterization, and catalytic activity. J Phys Chem C 115(20):9894–9902
54. Kuttiyiel KA, Sasaki K, Choi YM, Su D, Liu P, Adzic RR (2012) Bimetallic IrNi core platinum monolayer shell electrocatalysts for the oxygen reduction reaction. Energ Environ Sci 5 (1):5297–5304
55. Sasaki K, Adzic RR (2009) XAS of platinum monolayer fuel cell electrocatalysts – unambiguous, direct correlation of spectroscopy data with catalytic properties. Synchrotron Radiat News 22(1):17–21
56. Pourbaix M (1966) Atlas of electrochemical equilibria in aqueous solutions. CEBELCOR, Oxford
57. Glasner D, Frenkel AI (2007) Geometrical characteristics of regular polyhedra: application to EXAFS studies of nanoclusters. AIP Conf Proc 882:746–748
58. Coordinates of polyhedral clusters are available from: http://www3.bnl.gov/frenkel/coords.html. For the program to calculate the properties of bimetallic nanoparticles please contact A. I. Frenkel (anatoly.frenkel@yu.edu).

In Situ SXS and XAFS Measurements of Electrochemical Interface

7

Toshihiro Kondo, Takuya Masuda, and Kohei Uosaki

Contents

T. Kondo
Global Research Center for Environment and Energy based on Nanomaterials Science (GREEN), National Institute for Materials Science (NIMS), Tsukuba, Japan

Graduate School of Humanities and Sciences, Ochanomizu University, Bunkyo-ku, Tokyo, Japan
e-mail: kondo.toshihiro@ocha.ac.jp

T. Masuda
Global Research Center for Environment and Energy based on Nanomaterials Science (GREEN), National Institute for Materials Science (NIMS), Tsukuba, Japan

Advanced Key Technologies Division, National Institute for Materials Science (NIMS), Tsukuba, Japan

Precursory Research for Embryonic Science and Technology (PRESTO), Japan Science and Technology Agency (JST), Kawaguchi, Japan
e-mail: masuda.takuya@nims.go.jp

K. Uosaki (✉)
Global Research Center for Environment and Energy based on Nanomaterials Science (GREEN), National Institute for Materials Science (NIMS), Tsukuba, Japan

International Center for Materials Nanoarchitectonics (MANA), National Institute for Materials Science (NIMS), Tsukuba, Japan
e-mail: UOSAKI.kohei@nims.go.jp

1   Overview

In this chapter, we focus on structural studies at electrode/electrolyte solution interfaces by means of surface x-ray scattering (SXS) and x-ray absorption fine structure (XAFS) measurements using synchrotron radiation (SR) light as an x-ray source. After describing the importance of these techniques for structural studies at the electrode/electrolyte interface as an introduction, we explain the fundamental principles and experimental methodologies of these techniques. Finally, we describe trends in the development of these techniques and review the latest topics.

2   Introduction

Many important processes such as crystal and thin film growth, corrosion, electrode reactions, and biological processes take place at electrode/electrolyte interfaces. In order to precisely understand the reaction mechanisms of these processes and to apply them to modern nanotechnology, it is essential to clarify the geometric and electronic structures at these interfaces with atomic resolution, in situ and in real time [1, 2]. Surface analysis techniques such as electron microscopies (scanning electron microscopy (SEM) and transmission electron microscopy (TEM)), low-energy electron diffraction (LEED), and x-ray photoelectron spectroscopy (XPS), which are powerful methods to evaluate the surface structures and/or electronic states using electrons as a probe, however, cannot be employed to study electrode/electrolyte interfaces, because of the requirement of vacuum. As the recognition of the importance of electrode/electrolyte interfaces increased, several techniques, such as scanning probe microscopy (SPM) [3, 4] and nonlinear spectroscopies (second harmonic generation (SHG) and sum frequency generation (SFG)) [5, 6], for analyzing the geometric structures and electronic states at electrode/electrolyte interfaces have been developed, as well as the use of clean single-crystal electrodes. However, SPM measurements provide geometric structure information at an atomic level but of the outermost layer only, and therefore, the electrode surface structure cannot be determined by SPM when the electrode surface is covered with adsorbates such as water molecules and ions. Information obtained by optical spectroscopies has a high time resolution but not high enough spatial resolution.

The x-ray techniques such as surface x-ray scattering (SXS) and x-ray absorption fine structure (XAFS), which will be explained in detail in the next sections, using synchrotron radiation (SR) light [7–9] provide a lot of information about both the three-dimensional geometric structures and electronic states at electrode/electrolyte interfaces with atomic resolution, both in situ and in real time [1, 2, 10, 11]. Because the wavelength of x-rays (0.001–10 nm) is equivalent to the size of atoms and ions, they are an excellent probe that can be used for structure analysis at atomic dimensions. Moreover, x-rays are considered to be ideal for the analysis of electrode/electrolyte interfaces because they transmit through the

electrolyte solutions without any significant interactions. It is impossible, however, to selectively get information at an electrode/electrolyte interface with a high signal-to-noise (S/N) ratio using laboratory x-ray sources due to their low intensity and directionality, and therefore, the application of x-ray techniques to electro-chemical reactions using such low-intensity x-ray sources was limited to the study of material layers with a certain thickness of less than a few nanometers. Because SR light has high brilliance and directionality in addition to a continuous wave-length distribution, which is an important property especially for XAFS, it has brought a revolutionary change in the use of x-rays in electrochemistry since the 1980s.

In the following sections, we first explain the fundamental principles and experimental methodologies of SXS and XAFS. Then, we describe the develop-mental trends of these techniques and review the latest topics in these fields. Because SXS requires a sample with long-range order, such as a single crystal, structural studies of the fundamental surface science and electrochemistry of surface reactions have used single-crystal metal electrodes. These studies have focused on topics such as reconstruction/relaxation and surface oxide formation/reduction, electrodeposition/dissolution reactions on the electrode surfaces, several electrode reactions including electrocatalytic reactions, and the adsorbed ion layer on the electrode surfaces and the electrical double layers formed on/above them. On the other hand, XAFS is applicable to various materials, even those without long-range order, such as polycrystal surfaces, nanoparticles, and metal complexes in both liquid and solid phases, and has been employed to investigate the latest topics in the structural studies of those materials in relation to industrial applications.

3   Experimental and Instrumental Methodology

3.1   Surface X-Ray Scattering (SXS)

3.1.1 Fundamental Principles of SXS

Surface x-ray scattering (SXS) technique includes surface x-ray diffraction (SXRD), from which the surface two-dimensional structure is obtained, and crystal truncation rod (CTR) analysis, which provides the structure normal to the surface [1, 2, 10–15]. Thus, we can find precise three-dimensional geometric structures at electrode/electrolyte interfaces from SXS data analysis. In this section, we explain the fundamental principles and experimental procedures of these two techniques.

3.1.2 Surface X-Ray Diffraction (SXRD) Measurements

In the general x-ray diffraction (XRD) method for three-dimensional crystals, the incident angle of the x-rays is higher than the critical angle, where total reflection starts to take place, and then, the bulk structure of three-dimensional crystals can be
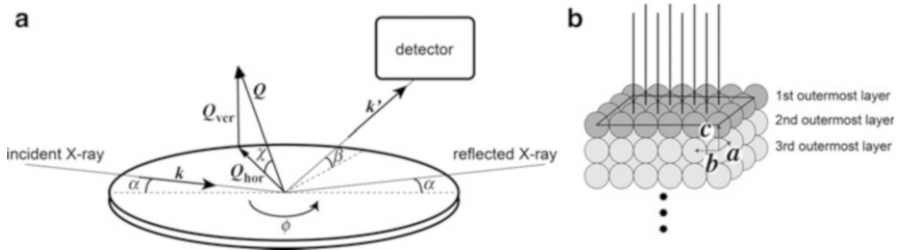
Fig. 7.1 (a) Sample geometry of the SXRD experiments. The electrode orientation is given by the azimuthal angle, ϕ, and the polar angle, χ, between the sample surface and $\boldsymbol{Q}$. (b) Schematic illustration of the semi-infinite crystal. Because the periodicity in the $\boldsymbol{c}$ axis direction is lost due to the existence of the surface, a scattering intensity along the vertical rod from the surface is observed

determined by analyzing the diffraction peak positions. In SXRD measurements, on the other hand, the incident angle of the x-rays is less than 2–3 mrad, below the critical angle. Because, in this case, x-rays can penetrate only 1–10 nm into the sample and most of the x-rays are specularly reflected, two-dimensional surface structure information can be obtained. When a two-dimensionally ordered structure exists on the sample surface, a small part of the x-rays which penetrate into the sample surface are two-dimensionally diffracted by that ordered surface structure. Figure 7.1 shows a typical SXRD experimental configuration. In Fig. 7.1a, the incident and diffracted x-ray vectors are $\boldsymbol{k}$ and $\boldsymbol{k}'$, respectively, and they have a magnitude,

$$k = k' = 2\pi/\lambda \tag{7.1}$$

where λ is the x-ray wavelength. The important variable for SXRD is the scattering vector, $\boldsymbol{Q}$, which is given by

$$\boldsymbol{Q} = \boldsymbol{k}' - \boldsymbol{k} \tag{7.2}$$

and has a magnitude

$$\boldsymbol{Q} = (4\pi/\lambda)\ \sin\theta \tag{7.3}$$

where the scattering angle, 2θ, is the angle between $\boldsymbol{k}$ and $\boldsymbol{k}'$. $\boldsymbol{Q}$ is divided into a lateral component, $\boldsymbol{Q}_{\text{hor}}$, and a vertical component, $\boldsymbol{Q}_{\text{ver}}$. ϕ is the azimuth of the sample surface, χ is the angle between the sample surface and $\boldsymbol{Q}$, and α and β are the angles between the sample surface and $\boldsymbol{k}$ and $\boldsymbol{k}'$, respectively. In the actual SXRD measurements, the intensity of diffracted x-rays is measured when $\boldsymbol{Q}_{\text{hor}}$ is varied by changing the position of the detector (2θ) and/or by rotating the sample (changing ϕ) at a very small $\boldsymbol{Q}_{\text{ver}}$ (β and/or χ). When $\boldsymbol{Q}_{\text{hor}}$ becomes equal to one of the reciprocal lattice vectors of the laterally ordered structure of the sample surface, a diffraction peak is observed. The atomic row spacing, d, can be determined from the value of $\boldsymbol{Q}_{\text{hor}}$ that corresponds to the peak. In addition to d, the orientation of the

structure with d can be determined by rotating only the sample (changing ϕ) while keeping 2θ (constant Q_{hor}, i.e., constant d). Thus, the two-dimensional average atomic positions of the sample surface can be determined from the dependence of the intensity of diffracted x-rays on Q_{hor} and ϕ.

3.1.3 Crystal Truncation Rod (CTR) Measurements

Diffraction and scattering from the flat surface of a crystal can be expressed using the reciprocal lattice rod called a "crystal truncation rod." Consider the diffraction conditions when the unit cell is defined by the unit lattice vectors, a, b, and c, where vectors, a and b, are parallel to the surface and vector c is normal to the surface, as shown in Fig. 7.1b, and x-rays are incident on this surface. Since the unit cells are infinitely arranged in a two-dimensional periodic lattice along the lateral direction, for any integer pair $(H\ K)$,

$$q = Ha^* + Kb^* \tag{7.4}$$

x-ray diffraction takes place only in the direction satisfying Eq. (7.4), using the reciprocal lattice vectors, a^*, b^*, and c^*, which can be calculated from a, b, and c. This diffraction corresponds to the peak position of SXRD as mentioned above. On the other hand, along the c^* direction which is normal to the surface, because the surface (or interface) is present, the periodicity is broken, and the diffraction condition is eliminated in the vertical direction and then scattering always occurs. In other words, due to the presence of the surface, a diffraction intensity distribution is observed along the rods which extend vertically from the two-dimensionally ordered surface. This is called a reciprocal lattice rod and this phenomenon is referred as CTR scattering, because the scattering is caused by truncation of the surface. Using a set of H and K, which represent the two-dimensional plane, each rod is referred as an $(H\ K)$ rod. Positions on each rod are represented using the continuous quantity, L (i.e., Q_{ver} in Fig. 7.1a), in units of $|c^*|$. For a totally smooth surface, the Q_{ver} dependence of the scattered x-ray intensity, $F(Q_{ver})$, is refined as in the following equation:

$$|F(Q_{ver})|^2 = N_a^2 N_b^2 / \{2\ \sin^2(1/2Q_{ver})\} \tag{7.5}$$

where N_a and N_b are the number of unit cells in the a and b directions, respectively.

3.1.4 Electrochemical Cell for In Situ SXS Measurements

Figure 7.2a shows a schematic illustration of an electrochemical cell used for normal in situ SXS measurements. In order to minimize the x-ray absorption by the electrolyte solution and the scattering of x-rays from the solution and window, the SXS measurements are carried out with highly intense x-rays and with a "thin-layer" configuration, where the thickness of the solution layer should be less than a few tens of μm and ultrathin polymer layer (thickness: μm order) should be used as a window [15]. Because a too thin electrolyte solution layer results in a nonuniform potential distribution and high cell resistance, the SXS measurements are generally
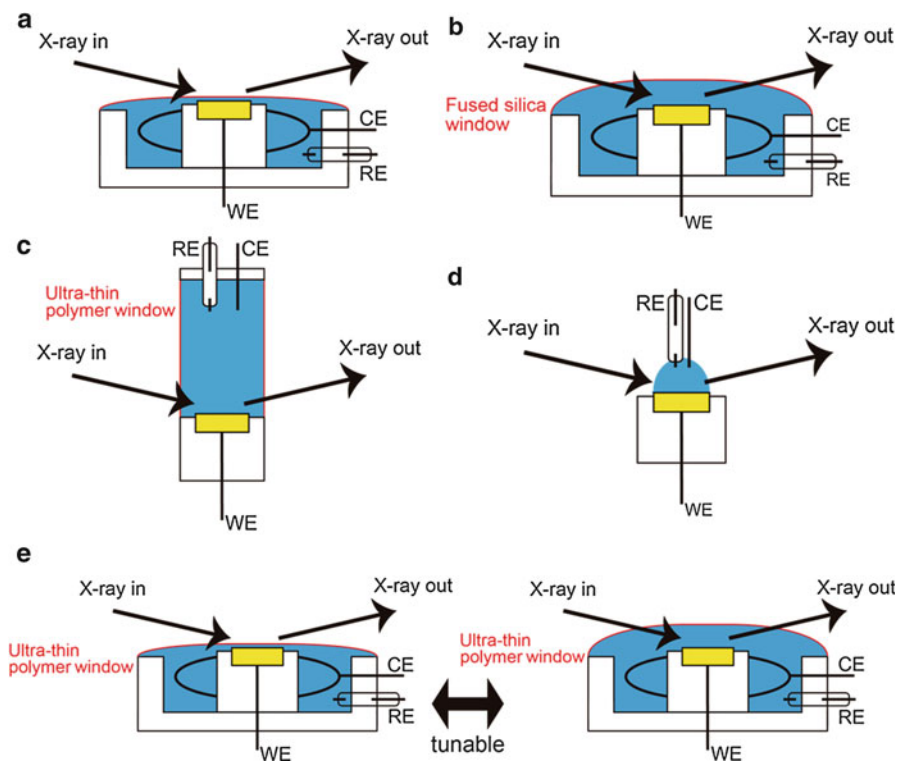
Fig. 7.2 Schematic illustrations of electrochemical cells for SXS measurements. (**a**) Thin-layer type [15] and thick-layer type with (**b**) a dome-shaped window [17], (**c**) a cylindrical-shaped window [18], (**d**) a drop type [20–22], and (**e**) tunable type between thin-layer and thick-layer types [19]. WE, RE, and CE represent working electrode, reference electrode, and counter electrode, respectively

carried out after increasing the thickness of the solution layer by introducing the solution into the cell. A certain potential is applied to the electrode for a predetermined period so that the electrochemical reaction uniformly proceeds. After that, the thickness of the electrolyte solution layer is decreased and the SXS measurements are carried out.

As mentioned above, the electrode potential should be kept constant during the SXS measurements, which means that potential-dependent structure changes at the electrode/electrolyte interface cannot be measured using the general SXS configuration. Therefore, various ideas and improvements of the experimental configuration have been made. Zegenhagen et al. [16, 17] and Nagy and You [18] used a dome-shaped fused silica window (Fig. 7.2b) and a cylindrical-shaped polymer window (Fig. 7.2c), respectively, and high-energy x-rays for high transmittance. Under these conditions, real-time potential-dependent structure changes can be measured with a high time resolution. We have improved such a "thick-layer" configuration to easily control the thickness of the electrolyte solution layer using a thin polymer window (Fig. 7.2e) and then succeeded to measure not only detailed

potential-dependent static interfacial structures in a "thin-layer" configuration but also in situ real-time potential-dependent interfacial structure changes in a "thick-layer" configuration [19].

On the other hand, Tamura et al. [20] and Magnussen et al. [21, 22] employed a drop cell (Fig. 7.2d) to carry out in situ SXS with high time resolution. However, a drop-type cell configuration has several technical difficulties, such as the requirement that the surface area of the counter electrode and the cell resistance should be large and low enough, respectively, to allow high time resolution for the electrochemical measurements and that the surface area of the working electrode should be kept constant for any diffractometer arrangements.

3.2 X-Ray Absorption Fine Structure (XAFS)

3.2.1 Fundamental Principles of XAFS

X-ray absorption fine structure (XAFS) is a powerful technique to investigate the local geometric structures and electronic states of materials of interest with very high sensitivity and elemental specificity by using x-rays to excite electrons from a core level to an unoccupied electronic state [23]. In short, XAFS is basically an absorption spectroscopy using x-rays as a probe. Although SXS is only applicable to crystalline surfaces because it utilizes the diffraction induced by structures with long-range order, XAFS can be applied to various materials without long-range order, such as polycrystal surfaces, nanoparticles, metal complexes, and biomolecules, both in liquid and solid phases.

The fundamental theory of XAFS had been established by Lytle, Sayers, and Stern in the early 1970s and is summarized in a review and references therein [24] and was immediately applied to various systems. However, it was not immediately utilized for surfaces due to the insufficient intensity of laboratory x-ray sources. After the advent of the second-generation high-brilliance SR light sources, XAFS techniques have been rapidly expanded to many systems.

XAFS is divided into two regions as shown in Fig. 7.3. One is the x-ray absorption near-edge structure (XANES), typically approximately 100 eV around the absorption edge, and the other is the extended x-ray absorption fine structure (EXAFS), typically up to several hundreds eV to 1000 eV above the absorption edge.

In the XANES region, electrons in a core level are excited to an unoccupied state. Since those unoccupied states are sensitive to the atomic arrangement and surrounding potential, the position of the absorption edge and the intensity of the peak just above the absorption edge, the so-called white line (WL), reflect the oxidation state and local coordination of the x-ray absorbing atom. Thus, the XANES spectra are used as fingerprints for the identification of the electronic structure, density of unoccupied states, and bonding geometry around the x-ray absorbing atom.

In the energy region higher than the XANES region, electrons in a core level can be excited to the continuum and photoelectrons are then ejected. The photoelectrons act as a spherical wave source that can be backscattered by the atoms surrounding the x-ray absorbing atom and those photoelectron waves interfere

Fig. 7.3 XAFS spectrum at the Pt L$_{III}$ absorption edge of a Pt foil
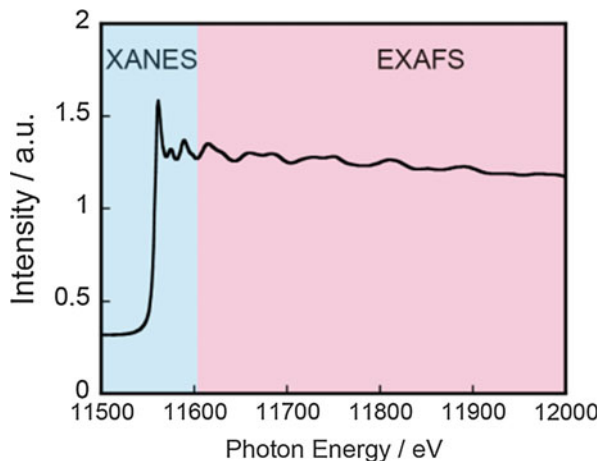
with each other. This interference causes a change in the transition probability and induces an oscillatory structure in the EXAFS region. Since the backscattering factor depends on the kind of the surrounding atoms, the analysis of the EXAFS oscillations reveals the local structure, including neighboring atomic species, their coordination number, and bond length between the x-ray absorbing and surrounding atoms.

To date, various methods have been developed to perform in situ XAFS analysis.

3.2.2 Transmission Mode

The XAFS spectra are generally obtained in a transmission mode in which the intensity of x-rays before and after transmission through the sample is monitored to yield absorbance as a function of the incident x-ray energy, as is the case of absorption spectra in ultraviolet and visible-light regions. A typical experimental configuration for the transmission mode is illustrated in Fig. 7.4. An ionization chamber composed of a gas-filled chamber with two electrodes is the most typically used detector for XAFS measurements in the transmission mode. When x-rays penetrate into the ionization chamber filled with specific gases, the gas molecules are ionized to cations and electrons. The cations and electrons move to the cathode and anode, respectively, under the high voltage applied between the two electrodes so that the intensity of x-rays can be detected as an ionization current. A sample is mounted between two ionization chambers and the intensity of the x-rays at each ionization chamber is monitored as the x-ray energy is scanned through the absorption edge. The absorbance, μt, is given from

$$\mu t = \log \left(I_0 / I \right) \tag{7.6}$$

where μ is the absorption coefficient, t is the thickness of the sample, and I_0 and I are the intensities of the incident and transmitted x-rays, respectively.

The transmission mode is applicable to thin solid films or solutions in thin-layer cells. The cells are similar in configuration to those used for UV/Vis spectroscopy.
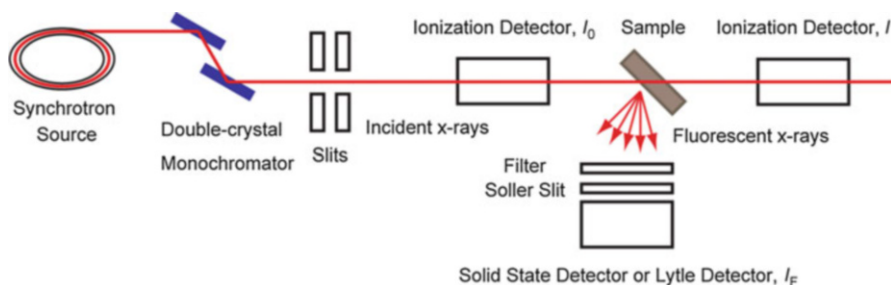
Fig. 7.4 Schematic illustration of experimental setup for XAFS measurements in transmission and fluorescence modes

Whereas quartz is commonly used as a window in UV/Vis spectroscopy, polymer films such as polyimides (Kapton®) and polyesters (Mylar®), with a thickness of several micrometers, are used as windows in the XAFS measurements because of their transparency for x-rays. In addition to the use of thin film windows, the thickness of cells needs to be small to minimize absorption loss due to the windows and electrolyte solutions.

The basic configuration of in situ electrochemical cells in the transmission mode was developed in the 1980s [25–27]; thin metal layers are deposited on the thin film windows of above-mentioned thin-layer liquid cells as working electrodes. This configuration is still widely used for various applications [28]. Recently, in situ electrochemical cells equipped with ultrathin membranes such as Si_3N_4 and graphene with a thickness of 10–100 nm, which serve not only as a window but also as a separator between vacuum and ambient, were developed for in situ TEM [29–32], x-ray emission spectroscopy (XES) [33, 34], and XPS [35]. Those are also utilized for in situ XAFS measurements [36–39] especially in the soft x-ray region because soft x-ray XAFS measurements require vacuum. In research on electrocatalysts for polymer electrolyte membrane fuel cells (PEMFCs), membrane electrode assemblies (MEAs) which are constructed by binding carbon-supported catalyst layers on both sides of electrolyte membranes were straightforwardly measured to clarify the reaction mechanisms [40–45].

3.2.3 Fluorescence Mode

When a material is irradiated with x-rays, electrons in a core level are excited to the continuum and/or photoelectrons are ejected, leading to the formation of core level holes. When such holes are created in a core level by the absorption of x-rays, electrons in an outer orbital can relax to the core hole, leading to the emission of fluorescence x-rays. In the fluorescence mode, the intensity of the fluorescence x-rays, I_F, is compared with that of the incident x-rays, I_0, to obtain "quasi-absorbance" as a function of the incident x-ray energy, instead of the transmitted x-ray intensity, I, based on the assumption that I_F is proportional to I. It should be

noted that this assumption is valid for a thick dilute sample or a thin concentrated sample. If the sample does not meet this requirement, spectra can be distorted due to the self-absorption of fluorescence x-rays.

A typical experimental configuration for the fluorescence mode is illustrated in Fig. 7.4. I_F is monitored by a Lytle detector or solid-state detector (SSD), whereas I_0 is monitored by an ionization chamber, as in the case of the transmission mode.

Using the fluorescence mode for XAFS measurements is beneficial for the following reasons: (1) when the concentration of the material of interest is very low, (2) the thickness of the sample is too thin to detect the difference between I_0 and I, or (3) the sample is too thick for x-rays to transmit, i.e., the surface of bulk materials. For example, it can detect Pt complexes with a surface concentration of ca. 10^{-10} mol cm^{-2}, incorporated within an organic molecular layer on a Si surface when the SSD is used in a total-reflection fluorescence configuration [46].

The cells for in situ SXS measurements in the thin-layer configuration shown in the previous section can be also used for XAFS measurements in the fluorescence mode [46–48]. Although this configuration enables us to employ conventional bulk materials as working electrodes, effective mass transfer can be often prevented because the electrolyte solution layer has to be as thin as <100 μm to minimize the absorption and scattering of x-rays. Another approach is the backside illumination fluorescence configuration where a thin film window coated with a thin metal layer as a working electrode is exposed to incident x-rays and fluorescent x-rays emitted at the interface between the metal layer and electrolyte solution can be detected through the window [49, 50]. In this configuration, adsorption and scattering of x-rays can be avoided and measurements can be performed with a thick solution layer. Recently, thin films such as Si_3N_4 [51–54], polyimide [55], poly(dimethylsiloxane) (PDMS) [56], and graphite layer peeled from HOPG [57] were also utilized for in situ electrochemical XAFS measurements [52, 57].

3.2.4 Total-Reflection Fluorescence Mode

Since the penetration depth of x-rays is much longer than that of other probes, such as the electrons used in XPS and Auger electron spectroscopy (AES), XAFS is rather "surface insensitive." When the x-rays are passing through a boundary between two media, they change the direction in accordance with Snell's law. As the incident angle becomes larger, the x-rays are bent toward the boundary, and total internal reflection occurs at the critical angle. When the incident x-rays are totally reflected from the sample surface, the penetration depth into the sample is typically several tens of angstrom, and therefore, surface-sensitive measurements can be achieved by utilizing total reflection.

Although the alignment required to yield total reflection needs special equipment and skills, total-reflection XAFS enables surface-sensitive in situ analysis and polarization-dependent measurements by utilizing polarized x-rays as an incident light source.

The EXAFS oscillation has a polarization dependence. For the EXAFS oscillation at the K absorption edge, the effective coordination number, N^*, can be expressed as [23]

$$N^* = 3\sum_i^N \cos^2(\theta_i) \tag{7.7}$$

where θ_i is the angle between the ith bond and the polarization vector of the incident x-rays. Thus, the bond orientation can be determined by measuring EXAFS data with both p-polarization and s-polarization, that is, polarization-dependent total-reflection fluorescence (PTRF) XAFS [58, 59].

For the EXAFS oscillation at the $L_{III, II}$ absorption edges, the coordination number does not dramatically depend on the polarization. The effective coordination number, N^*, can be expressed as [23]

$$N^* = \frac{1}{2}N + \frac{3}{2}\sum_i^N \cos^2(\theta_i) \tag{7.8}$$

Thus, even if the polarization vector of the incident x-rays is perpendicular to the ith bond, the oscillation can be detected, although its amplitude is 1/3 of that in the parallel case.

3.2.5 Time-Resolved Measurements

In the conventional step-scan XAFS technique, the energy of the monochromator is kept constant during each data acquisition and swept to the next acquisition point. Thus, it usually takes a long time, typically more than 10 min, to collect a whole spectrum. On the other hand, in the quick-XAFS (QXAFS) mode, a double-crystal monochromator is continuously swept over the energy range through the absorption edge during the data acquisition, so that time-resolved XAFS measurements can be performed [60–63]. The time resolution of the QXAFS mode is governed by the mechanical motion of the monochromator and is typically in a range of $\sim$1 ms to a few seconds when the concentration of sample is high enough.

Unlike the conventional XAFS and QXAFS techniques in which mechanical motion of the double-crystal monochromator is required to monochromatize the incident white x-rays, in the energy-dispersive XAFS (DXAFS) method, a polychromator, typically a bent crystal, is used to disperse the incident white x-rays and all the data in the energy range through the absorption edge is simultaneously collected by a position-sensitive multichannel detector [64–67]. Generally, the DXAFS technique has a better time resolution than the QXAFS technique since it does not rely on the mechanical motion of the monochromator, although QXAFS has a better energy resolution.

The combination of XAFS and a multichannel detector also enables two-dimensional imaging of XAFS spectra [68–71]. The QXAFS or DXAFS technique is used for this purpose, because acquisition of a series of XAFS spectra point by point over the entire area often requires a substantial time.

4 Key Research Findings

4.1 SXS

4.1.1 Trends of In Situ SXS

SXS measurements utilizing diffraction phenomenon require that the substrate should have long-range order, i.e., a single-crystal substrate, and it also requires a highly brilliant x-ray source. Therefore, structural studies at electrode/electrolyte interfaces using in situ SXS were not started until the late 1980s, when Clavilier found a simple method to prepare single-crystal electrodes [72] and the second-generation SR facilities with highly intense x-rays were developed [7–9]. At the same time, the SPM, which is capable of observing atoms even in a solution, was developed, and studies in electrochemistry using single-crystal electrodes became an active research area.

One of the pioneering investigations at the electrode/electrolyte interface using the in situ SXS technique is a structural study by Ocko et al. on the reconstruction of gold single crystals [15, 73, 74]. They not only precisely determined the $(23 \times \sqrt{3})$ reconstructed structure of the Au(111) electrode surface in the electrolyte solution, which had not been clearly observable in in situ scanning tunneling microscopic (STM) images until then, but also showed the incommensurate lifting process through the $(p \times \sqrt{3})$ structure in detail. The other pioneering research effort using this technique is by Toney et al. [11, 75–78]. They reported the precise atomic arrangement of underpotentially deposited (UPD) Bi on Ag(111).

After these pioneering efforts, with the advent of the third-generation SR facilities as even more intense x-ray sources, the improvements in the electrochemical cells for in situ SXS measurements described in the above section and the development of SPM techniques, in situ SXS has significantly contributed to fundamental electrochemistry, such as electrode surface reactions, UPD layers formed on the electrode surfaces, and ion layers adsorbed on the electrode. However, the number of electrochemical systems which have been investigated are limited by the available beam time and there are still unresolved issues at present. In this section, the latest topics in structural studies on the surface reactions of single-crystal metal electrodes, such as reconstruction/relaxation and surface oxide formation/reduction, electrodeposition/dissolution reactions including UPD processes on electrode surfaces, several electrode reactions including electrocatalytic reactions, and adsorbed ion layers on the electrode surfaces and electrical double layers formed on/above the electrode surfaces, summarized in Table 7.1, will be reviewed.

4.1.2 Electrode Surface Reactions (Reconstruction/Relaxation and Surface Oxide Formation/Reduction)

Comparison of Surface Reactions at Au(111) and Au(100)

Because Au is one of the most important metals, potential-dependent structures at the Au single-crystal electrode/electrolyte interfaces have been extensively studied

Table 7.1 Summary of recently reported in situ SXS studies at electrode/electrolyte interfaces

Methods	Systems	Beamlines at SR facility	Ref.
CTR	Au(111) and Au(100) surfaces	BL4C at PF	[79]
SXRD, CTR	Au(111) and Au(100) surfaces	ID32 at ESRF	[19]
SXRD, CTR	Au(111) surface	BM28 and ID3 at ESRF, BM12 at APS, and 7-2 at SSRL	[80]
CSXS	Au(100) surface	8ID at APS	[81]
CTR	Pt(111)/ionomer	BL13XU at SPring-8	[82]
SXRD	Au(111)/ionic liquids	BL14B1 at SPring-8	[83]
CTR	Pt(331) and Pt(511) surfaces	BL13XU at SPring-8	[84]
RSXS	Pt on Au(111)	BL3A at PF	[85, 86]
CTR	Pd on Au(111) and Au(100)	BL4C at PF and BL14B1 at SPring-8	[87]
SXRD	Bi on Au(100)	ID32 at ESRF	[88]
SXRD	Cu on Cu(100)	ID32 at ESRF	[89–91]
SXRD	Au on Au(111) and Au(100)	ID32 at ESRF and BW2 at HASYLAB	[92]
SXRD, CTR	Ag/AgCl on Ag/Au(111)	BL4C at PF and BL14B1 at SPring-8	[93]
CTR	ORR on Pd(111) and Pd(100)	BL13XU at SPring-8	[94]
CTR	Hydrogen insertion on Pd/Pt(111)	D2AM at ESRF	[95–97]
CTR	Oxygen species on Pt(111) and Pt3Ni(111)	ID32 at ESRF	[98]
SXRD, CTR	Chloride anion on Cu(111) and Cu(100)	ID32 at ESRF	[91]
CTR	EDL on Pt(111) and Au(111)	11ID-D at APS	[99]
CTR	EDL on Ag(100)	BL13XU at SPring-8	[100]
SXRD, CTR	EDL on Ag(111)	BM28 at ESRF and I07 at diamond	[101]
CTR	EDL on Cu(100)	X04SA at SLS	[102, 103]

using various techniques, including conventional electrochemical methods [104–110], STM [111–122], and several optical techniques [122–130] as well as SXS [11, 15, 19, 73, 74, 79, 131]. Using a newly designed spectro-electrochemical cell for in situ real-time SXS measurements, in which the electrolyte solution thickness was tunable by using a flexible thin polymer film as a window (Fig. 7.2e), as explained in Sect. 3.1.3, we succeeded to precisely determine not only potential-dependent static structures but also in situ real-time potential-dependent structure changes at Au(111) and Au(100) single-crystal electrode/sulfuric acid electrolyte solution interfaces [19, 79].

From in situ CTR measurements using a "thin-layer" configuration, we initially precisely determined the potential-dependent static structures at the Au(111) and Au(100) single-crystal electrodes/sulfuric acid solution interfaces at several potentials (Fig. 7.5) [19, 79]. At the Au(111)/sulfuric acid interface (see cyclic
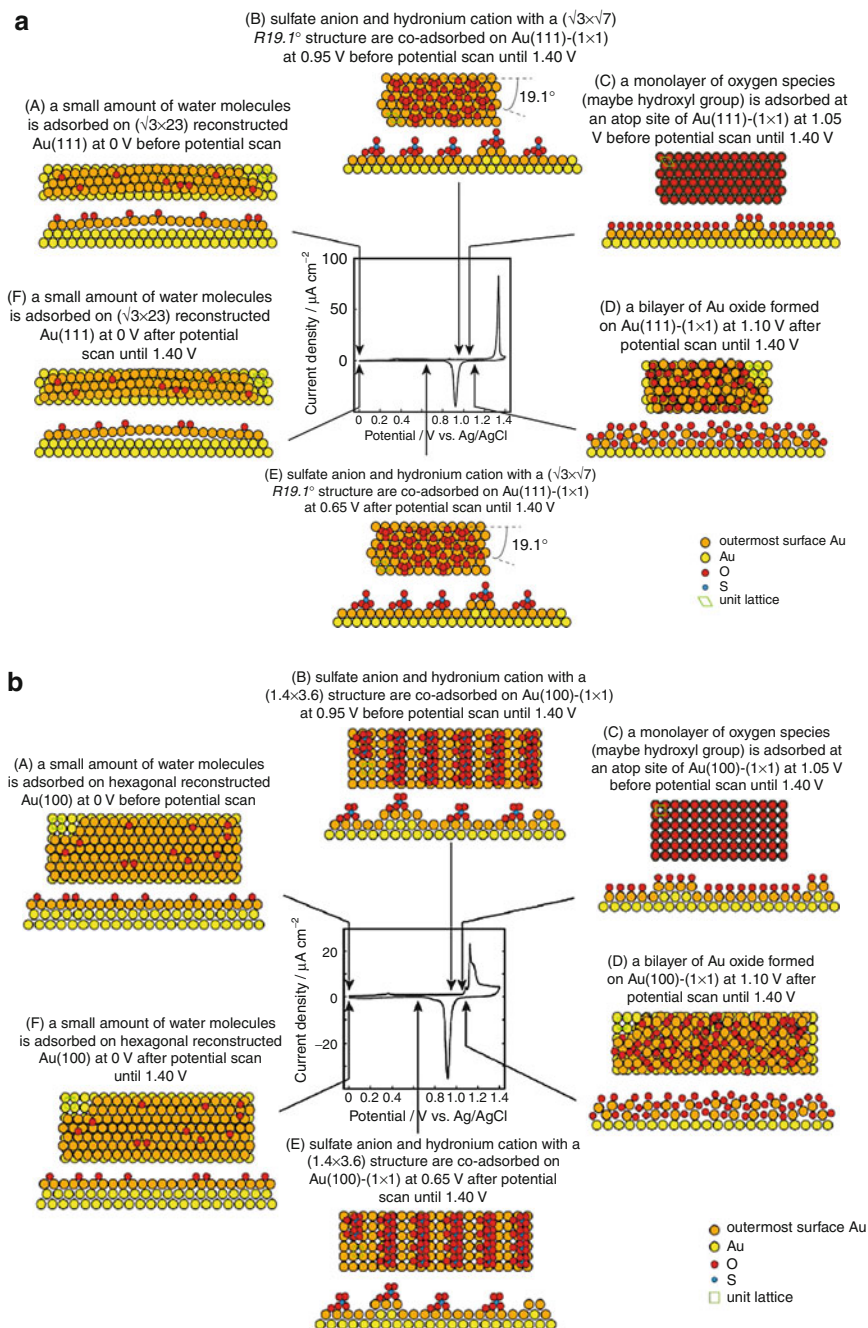
Fig. 7.5 Schematic top (*upper*) and side views (*lower*) of (**a**) the Au(111) and (**b**) Au(100) electrodes in 50 mM H$_2$SO$_4$ solutions at various potentials together with cyclic voltammograms

voltammogram (CV) in inset of Fig. 7.5a), the Au(111) surface just after annealing with a hydrogen flame and quenching with ultrapure water is reconstructed to $(23 \times \sqrt{3})$ at 0 V (vs. Ag/AgCl), and a small amount of oxygen species (maybe water molecules) is adsorbed on this reconstructed surface (Fig. 7.5a (A)). This reconstructed structure of the Au(111) surface was well studied by SXRD [15, 73, 74] and STM [116, 121, 122]. When the potential is made positive to 0.95 V, the reconstructed surface is lifted to (1 × 1) and sulfate anion and hydronium cations are coadsorbed on this surface with a $(\sqrt{3} \times \sqrt{7})R19. 1°$ structure (Fig. 7.5a (B)). This lateral ordered structure of adsorbed ions was observed by STM [111, 115, 120, 122] and the presence of adsorbed ions was established by vibrational spectroscopy [122, 123, 129]. When the potential is made more positive to 1.05 V, adsorbed ions are removed from the surface, and a monolayer of oxygen species (maybe OH groups) is adsorbed at an atop site of the Au(111)-(1 × 1) surface (Fig. 7.5a (C)). When the potential is made more positive to 1.40 V, the surface is oxidized and a bilayer of Au oxide forms on the Au(111)-(1 × 1) surface (Fig. 7.5a (D)). At 0.65 V after 1.40 V is applied, sulfate anion and hydronium cation are coadsorbed on the Au(111)-(1 × 1) surface in a similar manner that observed at 0.95 V before 1.40 V is applied (Fig. 7.5a (E)). When the potential is made more negative to 0 V after 1.40 V is applied, a small amount of oxygen species (maybe water molecules) is adsorbed on the $Au(111) - (23 \times \sqrt{3})$ reconstructed surface (Fig. 7.5a (F)).

At the Au(100)/sulfuric acid interface (see CV in inset of Fig. 7.5b), the Au(100) surface just after annealing and quenching is reconstructed to the hexagonal close-packed structure at 0 V and a small amount of water molecules is adsorbed on it (Fig. 7.5b (A)). The lateral structure of this reconstructed surface was well studied by SXRD [131] and STM [116]. At 0.95 V, the reconstructed surface is lifted to (1 × 1) and sulfate anion and hydronium cations are coadsorbed on this Au(100)-(1 × 1) surface with a (1.4 × 3.6) structure (Fig. 7.5b (B)). Adsorbed sulfate anions were investigated by vibrational spectroscopy [123] and the lateral structure of adsorbed ions was observed by STM [115]. When the potential is made more positive to 1.05 V, a monolayer of hydroxyl groups is adsorbed at the atop site on the Au(100)-(1 × 1) surface (Fig. 7.5b (C)). At 1.40 V, the surface is oxidized and a bilayer of Au oxide forms on the Au(100)-(1 × 1) surface (Fig. 7.5b (D)). When the potential is made negative to 0.65 V after 1.40 V is applied, sulfate anion and hydronium cations with a (1.4 × 3.6) structure are coadsorbed on the Au(100)-(1 × 1) surface in a similar way to that observed at 0.95 V before 1.40 V is applied (Fig. 7.5b (E)). At 0 V after 1.40 V is applied, a small amount of water molecules is adsorbed on the Au(100)-hexagonal reconstructed surface (Fig. 7.5b (F)).

Fig. 7.5 (continued) measured with a scan rate of 10 mV s^{-1}. The outermost surface Au atoms are displayed in a different color from the others. *Green rhomboids* in (**a**) and *green squares* in (**b**) represent the (1 × 1) surface unit lattice, to which the scattering intensity at (0 1 0.2) corresponds (From [19]. With permission from Elsevier)

Based on the above static structures at the Au(111) and Au(100)/sulfuric acid interfaces, in situ real-time SXS measurements using a "thick-layer" configuration were carried out [19]. We monitored the in-plane x-ray scattering intensity at (0 1 0.2) as a probe of surface structure change, because it monitors the formation and disappearance of the atomic arrangements corresponding to the surface (1 × 1) unit lattices, which are shown by green rhomboids in Fig. 7.5a on Au(111) and green squares in Fig. 7.5b on Au(100), respectively. Thus, we know that a surface structure change, such as reconstruction lifting, adsorption of oxygen species at the atop site, and reduction of the surface oxide lead to an increase of the (0 1 0.2) intensity. Based on the results of in situ real-time SXS measurements using a "thick-layer" configuration, it can be concluded that the phase transition between the reconstruction and lifting, adsorption of oxygen species, and surface oxide formation/reduction on Au (100) proceed much slower, slightly slower, and faster, respectively, than those on Au(111). This behavior is probably caused by the difference in the surface density of Au atoms at the lifted and reconstructed structures of Au(111) and Au(100).

Temperature Effect on Atomic Arrangement at Au(111)

The Au(111) surface reconstruction shows the well-known $(p \times \sqrt{3})$ phase in an electrolyte solution as mentioned in the above section [15, 19, 73, 79]. Although a great number of ultrahigh vacuum (UHV) studies have already been performed using LEED [132], SXS [133], STM [134], and computational simulations [135], there were still some differences between the $(p \times \sqrt{3})$ reconstructed phase in UHV and electrolyte solution; for example, the ordered array of kinks, the so-called chevron phase, was observed in the former [133] but not observed in the latter [15]. In the former case, the surface structures are induced only by temperature but they are controlled by potential in the latter.

In order to clarify such phenomenon, Gründer et al. tried to measure the effect of temperature on the reconstructed structure of the Au(111) surface using a temperature-controlled electrochemical cell for in situ SXS [80]. Figure 7.6a shows SXRD profiles along the <1 1 0> direction through the (0 1 0.52) reciprocal lattice position measured at −0.75 V (vs. RHE), where the surface is fully reconstructed, measured in 0.1 M KOH at two different temperatures (low temperature, LT, was 281 K and high temperature, HT, was 313 K). Two peaks were observed at $H = 0$ and $K = 1$, corresponding to the surface (1 × 1) structure, and at $H \sim 0.02$ and $K \sim 1.02$, corresponding to the $(p \times \sqrt{3})$ reconstructed structure. As can be clearly seen in this figure, the amount of the surface that was reconstructed was lowest at the low temperature. There was no statistically significant difference between the measurements at ambient temperature (299 K, data not shown) and at high temperature. The shift in peak position from low temperature to high temperature also showed that the surface at the high temperature is more compressed than that at low temperature, corresponding to p values of 23 and 24, respectively. The difference in the fitted peak fwhm values indicates that the reconstruction domain size at the high temperature is slightly larger than that at the low temperature. In addition to the data of Fig. 7.6a, potential dependencies of
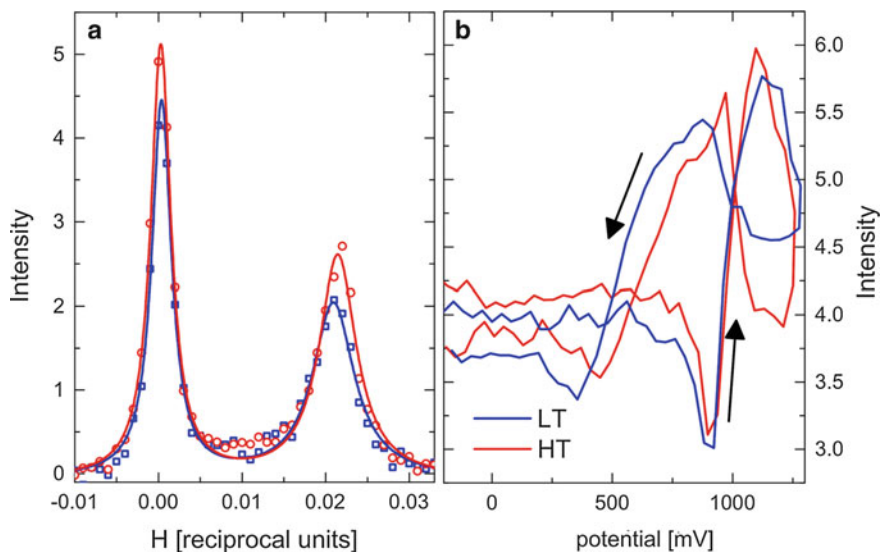
Fig. 7.6 (**a**) In-plane diffraction along the <1 1 0> direction, measured at −0.9 V, through the (0 1 0.52) position showing the peak due to the (0 1 L) CTR and the peak due to the Au surface reconstruction measured at 281 K (*blue*) and 313 K (*red*) in 0.1 M KOH. The *solid lines* are the results of fitting a double Lorentzian line shape to the data. (**b**) Potential dependence of x-ray intensity at (0 1 0.52) position at 281 K (*blue*) and 313 K (*red*). The *arrows* indicate the sweep direction and the scan rate was 1 mV s^{-1} (From [80]. With permission from Elsevier)

the x-ray scattering intensity at (0 1 0.52) were obtained at two different temperatures (Fig. 7.6b) to investigate the temperature effect on the phase transition between $Au(111) - (p \times \sqrt{3})$ and Au(111)-(1 × 1) structures, i.e., reconstructed and lifted structures, respectively. The effect of reducing the temperature appeared to slow down the kinetics of the reconstruction/lifting process, i.e., the data at low temperature is "smeared out" over a broader potential window and shows a decrease of the ordering of the reconstructed layer. In UHV, two distinct phases were observed; one, which is a surface structure that consists of an equilibrium density of kinks between rotationally equivalent domains of a uniaxial reconstruction, was observed at temperatures lower than 865 K and the other, in which atomic positions are microscopically well-defined but the arrangement of discommensurations and kinks is disordered, was observed at temperatures higher than 880 K [133]. Moreover, the phase transition between $Au(111) - (p \times \sqrt{3})$ and Au(111)-(1 × 1) structures was not observed reversibly in UHV. These should be caused by the differences between working in UHV and in an electrolyte solution.

Dynamics of Reconstruction/Lifting Process at Au(100) by Coherent SXS

As mentioned in Sect. 3.1.4, in order to increase the time resolution of in situ SXS, various improvements in in situ SXS measurements have been made, including an improved electrochemical cell. You et al. proposed a coherent surface x-ray

Fig. 7.7 (**a**) A single reflection from a flat terrace. (**b**) Two split reflections from two adjacent terraces. Each pixel is equivalent to a detector angle position and the center of the image is at $\nu = 0°$; $\delta = 12.4°$ and $\Delta\delta = 0.030°$; $\Delta\nu = 0.015°$, where ν and δ are the angles of the reflected x-ray vector with respect to the incident x-ray vector along the direction normal and parallel, respectively, to the electrode surface (From [136]. With permission from Elsevier)
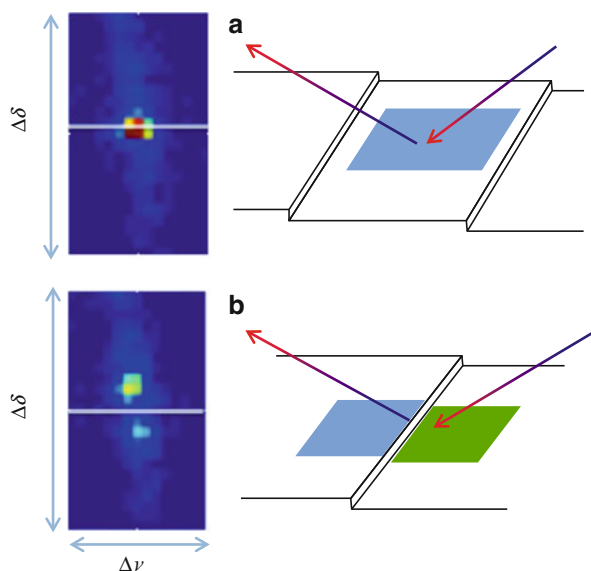
scattering (CSXS) technique that allows in situ measurements of electrode surface dynamics [81, 136]. In ordinary SXS, the x-ray scattering intensity, even under anti-Bragg conditions, is not sensitive to the position of a step. In CSXS, however, the intensity is sensitive to the position of a step relative to the x-ray illumination area, as shown in Fig. 7.7 [136]. In Fig. 7.7a where there is no step, x-rays reflect as if reflecting from a mirror and produce a single spot on the two-dimensional CCD detector. In Fig. 7.7b, a photon splits and interferes across both terraces, and then, the detected image on the CCD also splits. Therefore, the image oscillates between the single and double spots whenever a step passes through the illumination area. By utilizing this phenomenon, not only the transient dynamics of phase relaxation from one phase to another upon changing electrochemical conditions but also the dynamics of microstates can be measured by this technique, even if the macroscopic state of the electrode is apparently static.

You et al. employed this CSXS technique to study the dynamics of the phase transition between reconstruction and lifting at the Au(100) surface in 0.1 M HClO$_4$ electrolyte solution [81]. They found that edges of steps and islands on the Au(100) surface are highly dynamic in the solution and evolve continuously, even at room temperature. The evolving speed increased nearly two orders of magnitude when the quasi-hexagonal reconstruction is lifted during a slow potential sweep and was higher by more than four orders of magnitude than the speed measured in UHV [136]. In addition, they found that surface lattice dynamics appear when the reconstruction is lifted, and those are faster by two orders of magnitude than the edge dynamics. They also confirmed these behaviors by complementary STM measurements.

Pt(111)/Ionomer Interface

The polymer electrolyte membrane (PEM) fuel cell, which is abbreviated here to PEMFC, is one of the most promising candidates for a new-generation energy conversion device because of its high theoretical efficiency for the conversion of chemical energy to electrical energy [137–140]. The PEMFC is composed of a membrane electrode stack assembly (MEA), which is constructed by binding carbon-supported platinum catalyst layers with perfluorosulfonated ionomer (PFSI) on both sides of the PEM. Degradation control of Pt catalysts at an ionomer/Pt interface is one of the major issues of the PEMFC affecting their widespread use. One of the key solutions to control Pt dissolution is the surface oxide layer, which can protect Pt from dissolution, and therefore, it is essential to clarify the origin of the degradation of Pt and to design a long-lived catalyst. To this end, studies have been performed on the oxide formation process at a well-defined Pt single-crystal electrode/ionomer interface [139]. Since the SPM, which is a very powerful tool to probe the surface structure, cannot observe a surface structure covered by an overlayer such as an ionomer membrane, details of this process at an atomic level are still unknown.

In this respect, we constructed an MEA-like configuration of a PEMFC, i.e., a vacuum-evaporated Pt layer/PEM (Nafion® membrane)/PFSI (adhesion Nafion® layer)/Pt(111) system, as shown in Fig. 7.8a, and the structures at the PFSI/Pt (111) interface with and without induced-bias were investigated by in situ SXS [82]. Results of the CTR measurements showed that fluorocarbon groups of PFSI adsorbed on the Pt(111)-(1 × 1) surface without bias (Fig. 7.8b (A)) but the PFSI
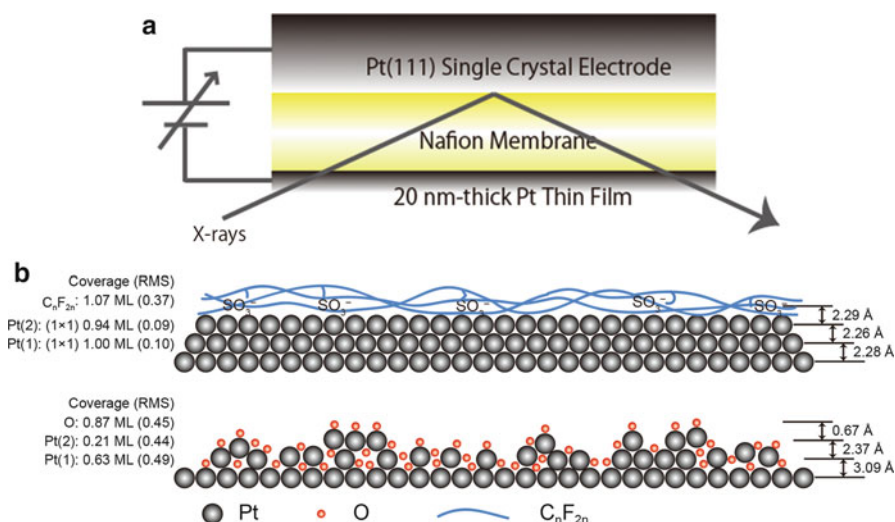
Fig. 7.8 (**a**) A Pt/PEM/PFSI/Pt(111) sandwich configuration. (**b**) Schematic models based on structural parameters obtained from the best fit data of (A) without bias and (B) when a positive bias was applied (Reprinted with permission from [82]. Copyright (2013) American Chemical Society)

layer was detached from the Pt surface and oxygen atoms penetrated into the Pt lattice by turnover between Pt and O atoms, i.e., the surface oxide layer formed, when a positive bias was applied (Fig. 7.8b (B)).

Au(111)/Ionic Liquid Interface

Since room-temperature ionic liquids (RTILs) have unique features, such as tunability and designability, RTILs have been considered as an alternate liquid to water and organic solvents [141]. A variety of RTIL's characteristics related to their electrochemical properties, such as potential window, viscosity, conductivity, and hydrophobicity, can be tuned by designing their molecular structure [142–144], and therefore, there have been many investigations of the electrochemical characteristics of RTILs using SPM [145] and vibration spectroscopies [146, 147]. However, due to the limitation of the SPM and spectroscopy measurements as mentioned above, the reconstruction/relaxation process in RTILs is still unknown.

Tamura et al. investigated the potential-dependent surface structures of Au(111) electrodes in the hydrophobic ionic liquids, 1-butyl-1-methylpyrrolidinium bis (trifluoromethylsulfonyl)amide ([BMP]TFSA) and 1-butyl-3-methylimidazolium bis(trifluoromethylsulfonyl)amide ([BMIM]TFSA), using in situ SXS [83]. In both [BMP]TFSA and [BMIM]TFSA, a reconstruction of the surface structure was observed and a reversible phase transition between the (1×1) and the reconstructed $(p \times \sqrt{3})$ structure took place. However, the electrode area of the reconstructed structure in [BMP]TFSA was larger than that in [BMIM]TFSA. This difference suggested that the [BMIM]$^{+}$–Au interaction is stronger than the [BMP]$^{+}$–Au interaction.

High-Index Surfaces of Metal Electrodes

The catalytic activity and selectivity of electrochemical reactions strongly depend on the surface structures of the electrodes [148–151]. Well-defined single-crystal electrodes play a key role in the determination of the structures of the active sites involved in the reactions. The structures occurring during the reconstruction/relaxation processes of the low-index planes of Pt in electrolyte solutions were precisely determined by SPM [152–154] and SXS [155–157] as follows: (i) Pt(111) and Pt (100) have an unreconstructed (1×1) structure, whereas Pt(110) has a (1×1) or (1×2) structure depending on the cooling conditions after annealing; (ii) the interlayer spacing between the first and second layers, d_{12}, is the same as that of the bulk in the double-layer potential region on Pt(111) and Pt(100), whereas it is expanded in the adsorbed hydrogen potential region; (iii) the topmost rows of Pt atoms on Pt(110) are expanded in the double-layer region, and additional expansion occurs because of the adsorption of hydrogen atoms, with an expansion that increases as Pt(111) (2 %) < Pt(100) (2.5 %) < Pt(110) (10 %) in 0.5 M H_2SO_4. On the other hand, there were few reports on the real structures present in electrolyte solutions on the high-index planes of Pt [158].

Hoshi et al. reported the surface structures of the high-index planes of Pt with three atomic rows of terraces (Pt(331) = 3(111)-(111) and Pt(511) = 3(100)-

(111) (111) (111) (111) (111)   (111)   (111) (111)   (111)(111)

Pt(511) (1×1)   Pt(511) (1×2)

(111)   (111)   (111)   (111)
       (111)   (111)
Pt(331) (1×1)   Pt(331) (1×2)
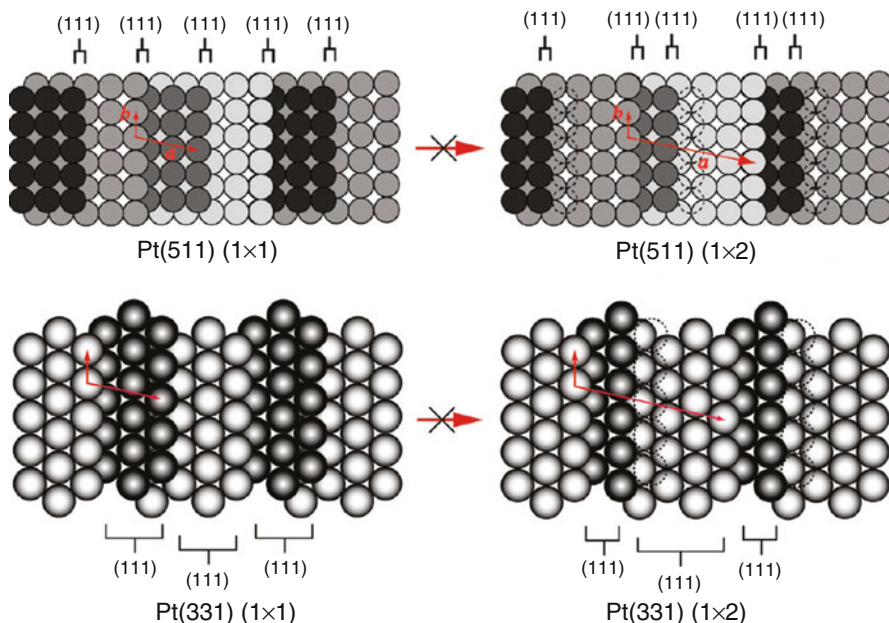
Fig. 7.9 Hard-sphere models of the unreconstructed (*left*) and reconstructed (*right*) structures of the high-index planes of Pt surface with three atomic rows of terraces (Reprinted with permission from [84]. Copyright (2011) American Chemical Society)

(111)) in a 0.1 M $HClO_4$ electrolyte solution by in situ SXS [84]. According to previous reports [157, 158], the surfaces with two atomic rows of terraces, Pt (110) = 2(111)-(111) and Pt(311) = 2(100)-(111) = 2(111)-(100), are reconstructed to a (1 × 2) structure. Small shifts of the peak position in the SXRD profiles of both electrodes showed, however, that the surfaces with three atomic rows of terraces have pseudo-(1 × 1) structures. Based on CTR measurements, the interlayer spacing, d_{12}, is expanded by 13 % on Pt(331) compared to that of the bulk, whereas it is contracted by 37 % on Pt(511). The surface structures did not depend on the applied potential for either surface. The authors explained these results using hard-sphere models (Fig. 7.9). Using in situ SXS, they also investigated the surface structures of the high-index planes of Pd (Pd(110) = 2(111)-(111) and Pd(311) = 2(100)-(111)) and compared them with the Pt results [159].

4.1.3 Electrodeposition/Dissolution on Electrode Surfaces

Pt on Au(111)
Ultrathin metal layers formed on foreign metal substrates have been attracting interest because of their unique physical and chemical properties, particularly their high electrocatalytic activities [160, 161]. Such high electrocatalytic activities presumably result from the geometric and electronic structures of the interfacial
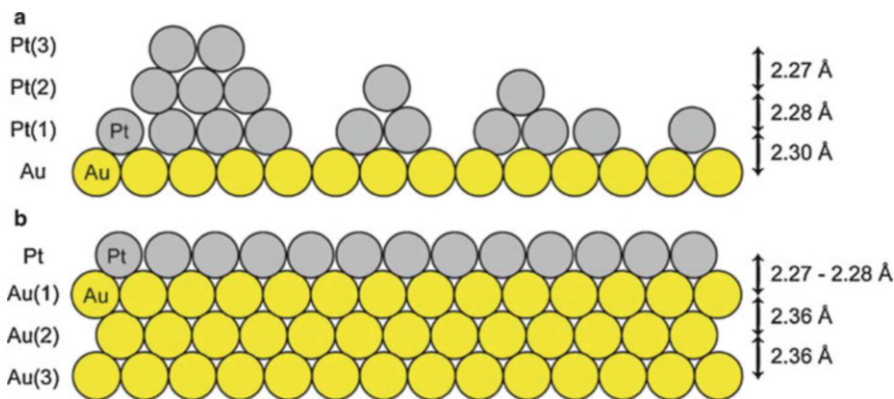
Fig. 7.10 Schematic side views of Pt layers electrodeposited on the Au(111) surface proposed by (**a**) Waibel et al. [164] and Strbac et al. [165] and (**b**) Naohara et al. [163] (From [85]. With permission from Elsevier)

layers being different from those of the bulk [162], and therefore, it is very important to know the interfacial structures at atomic dimensions in situ. Although the structural studies of electrochemically deposited Pt ultrathin layers on Au(111) have been carried out using STM by several groups [163–166], the results differed from each other. While Naohara et al. reported that Pt grows on an atomically flat Au(111) surface in the Frank–van der Merwe (FM; layer by layer) mode [163], Waibel et al. [164] and Strbac et al. [165] reported that Pt grows on the Au(111) surface in the Volmer–Weber (VW, islanding) mode. In order to clarify such differences, we evaluated the surface structures of the ultrathin Pt layers formed on Au(111), which were prepared under two sets of extremely different conditions, using SXS. However, since the atomic number and, therefore, the scattering parameters of Pt are very close to those of Au, the interfacial structure of the Pt layer formed on the Au surface cannot be precisely determined from the SXS data obtained using an incident x-ray energy that does not correspond to an absorption energy of Au and Pt, used as a substrate and deposited material, respectively, as is usually used in the ordinary SXS method [19, 79, 167–171]. We employed the resonance surface x-ray scattering (RSXS) method, in which the incident x-ray energy is close to the Pt L_{III} absorption edge (11.55 keV), in order to use the anomalous scattering parameter effect [172–175] and succeeded to demonstrate the former [163] to form an atomically flat Pt layer and the latter [164, 165] to form a rough Pt layer [85] (Fig. 7.10).

Epitaxial growth of a well-defined metal layer has been achieved by vapor deposition, molecular beam epitaxy (MBE), and metal-organic chemical vapor deposition (MOCVD) under UHV conditions. Compared to metal deposition by these techniques in UHV, however, electrochemical metal deposition is economical and easy because expensive equipment is not required in this process. The conditions for electrochemical deposition of an atomically flat, pseudomorphic Pt layer

on a Au(111) electrode surface were established based on electrochemical and in situ RSXS studies on the potential dependence of Pt deposition [86]. When Pt was deposited at a relatively large overpotential, a three-dimensional rough Pt layer was formed on Au(111). When the overpotential was very small, Pt nuclei formed but did not grow further. At an appropriate overpotential between these two potentials, the RSXS data showed that an atomically flat, pseudomorphic Pt layer grew in the FM mode (Figs. 7.11 and 7.12).

Pd on Au(111) and Au(100)

The structure of Pd thin films electrodeposited on the Au(111) and Au(100) electrodes in a solution containing tetrachloropalladate and sulfate anions was investigated by in situ SXS [87, 167]. Comparison of Pd/Au(111) and Pd/Au(100) growth modes showed a similarity in the first-layer deposition. On both Au(111) and Au(100), Pd follows the crystal structure of the substrates and forms a pseudomorphic monolayer, meaning that deposited Pd atoms occupy the threefold hollow cubic closest packing (ccp) sites, not the hexagonal closest packing (hcp) and atop sites, on Au(111) and the fourfold hollow site, not the atop site, on Au(100). Beyond 2 ML, however, Pd thin films electrodeposited on Au(111) are relaxed (Fig. 7.13a), although there is still a small amount of pseudomorphic layers at the interface (Fig. 7.13b). In contrast, Pd thin films electrodeposited on Au(100) continue to grow pseudomorphically over 30 ML. The difference in the growth mode between the Au(111) and Au(100) surfaces is not ascribable only to anisotropy in the elasticity of the thin film. The relationship between a growing surface and an allowed gliding plane in misfit dislocations was proposed as a crucial factor to determine the critical thickness of the Pd thin films.

When Pd layers were electrodeposited on the Au(111) electrode in an electrolyte solution containing chloride anions, on the other hand, it was reported that Pd layers pseudomorphically grew on Au(111) over 2 ML [176]. Sibert et al. reported that the growth of the Pd layers electrodeposited in a chloride-containing solution on Au (111) was investigated by cyclic voltammetry, potential step experiments, and time-resolved in situ SXS. The first UPD layer growth proceeds by several processes with different kinetics. The first reaction, characterized by a quite fast kinetics below 1 s, is followed by a slow adsorption process and then by instantaneous nucleation-and-growth. Almost complete layer-by-layer growth up to two pseudo-morphic layers was observed, even if the third and following relaxed layers started to grow before the full completion of the second, forming huge 3D islands. Sibert et al. were able to unambiguously assign the current peaks observed in the electro-chemical characterization of the Pd ultrathin layers on Au(111) in 0.1 M H_2SO_4.

Bi on Au(100)

Although Toney et al. reported the growth of electrodeposited Bi on Ag [11, 75–78], the UPD Bi adlayers formed on Au single-crystal electrode surfaces have also received much attention [20, 177–181], because of its similarity to the other metals such as Pb and Tl, as well as by its interesting catalytic properties for oxygen and peroxide reduction at intermediate UPD coverages. Although the detailed potential-dependent structures of UPD Bi on Au(111) were studied by
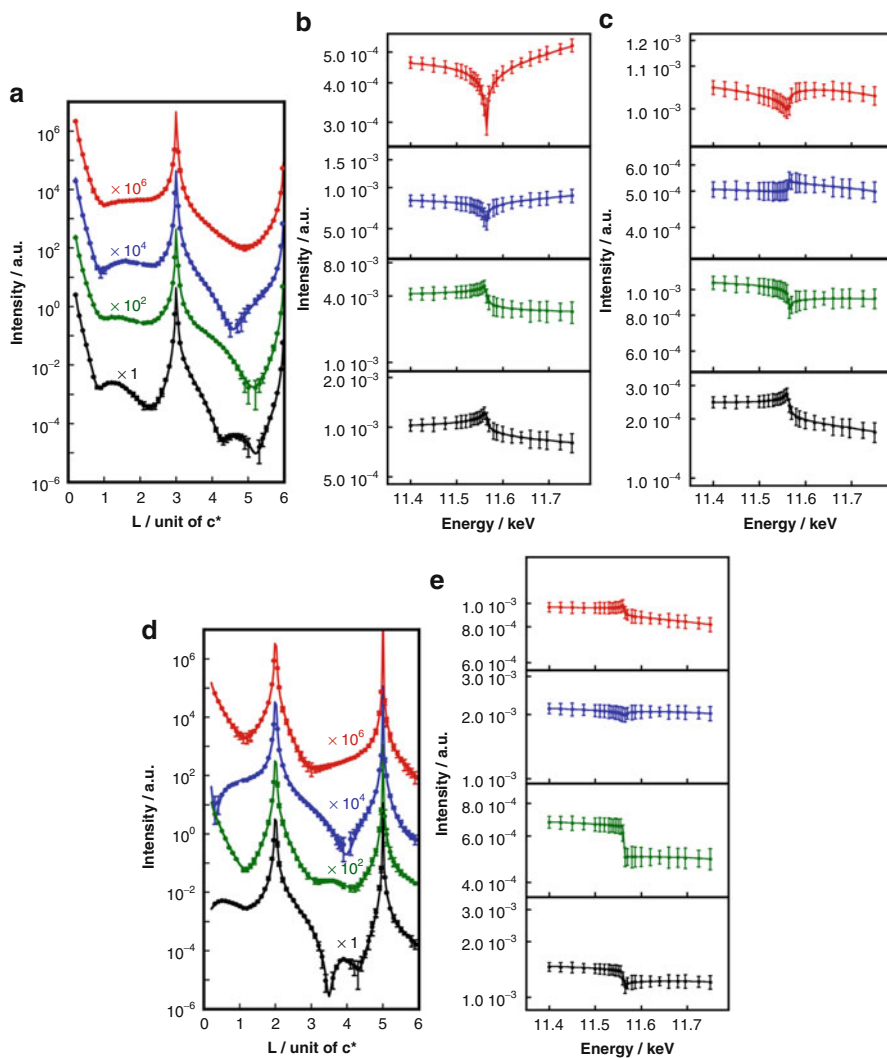
Fig. 7.11 In situ RSXS profiles of (**a**) (00) rod, incident energy dependencies of the scattering x-ray intensity at (**b**) (0 0 0.8) and (**c**) (0 0 2.7), (**d**) (01) rod, and incident energy dependence of the scattering x-ray intensity at (**e**) (0 1 1.7) of Pt electrodeposited on Au(111), which were prepared at open circuit potential (OCP) just after dipping (*red*), at 0.90 V (vs. RHE) for 400 s (*blue*), for 2000 s (*green*), and for 3000 s (*black*). *Closed circles* and *solid lines* represent experimental data points and fitted curves, respectively. The vertical scales of (**a**) and (**d**) are adjusted to present all data in one figure by multiplying the intensity by numbers shown in the figures (Reprinted with permission from [86]. Copyright (2012) American Chemical Society)
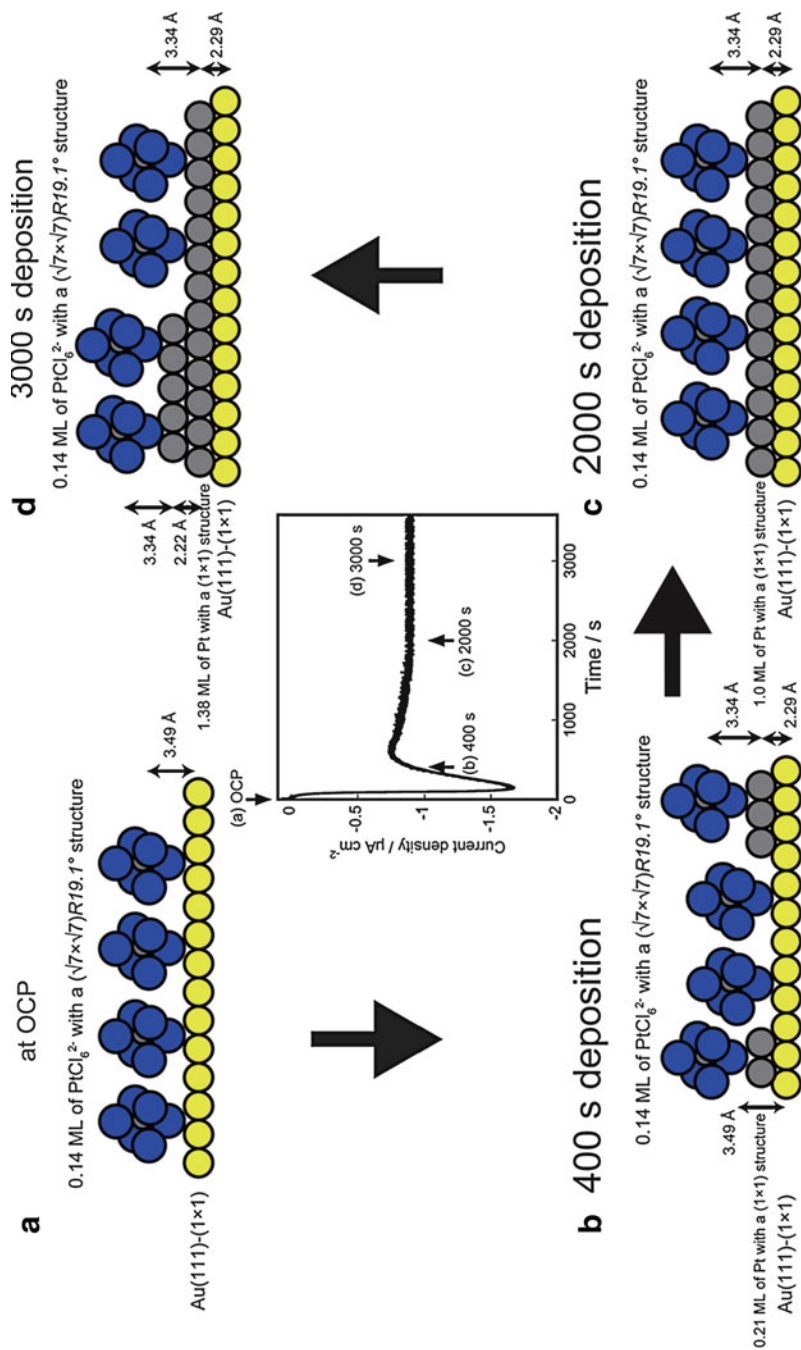
Fig. 7.12 The time course of cathodic current density at Au(111) electrode during Pt deposition at 0.90 V (vs. RHE) in 0.1 M HClO₄ solution containing 0.05 mM H₂PtCl₆ and structural models of Pt electrodeposited on the Au(111) surfaces for several deposition periods (Reprinted with permission from [86]. Copyright (2012) American Chemical Society)
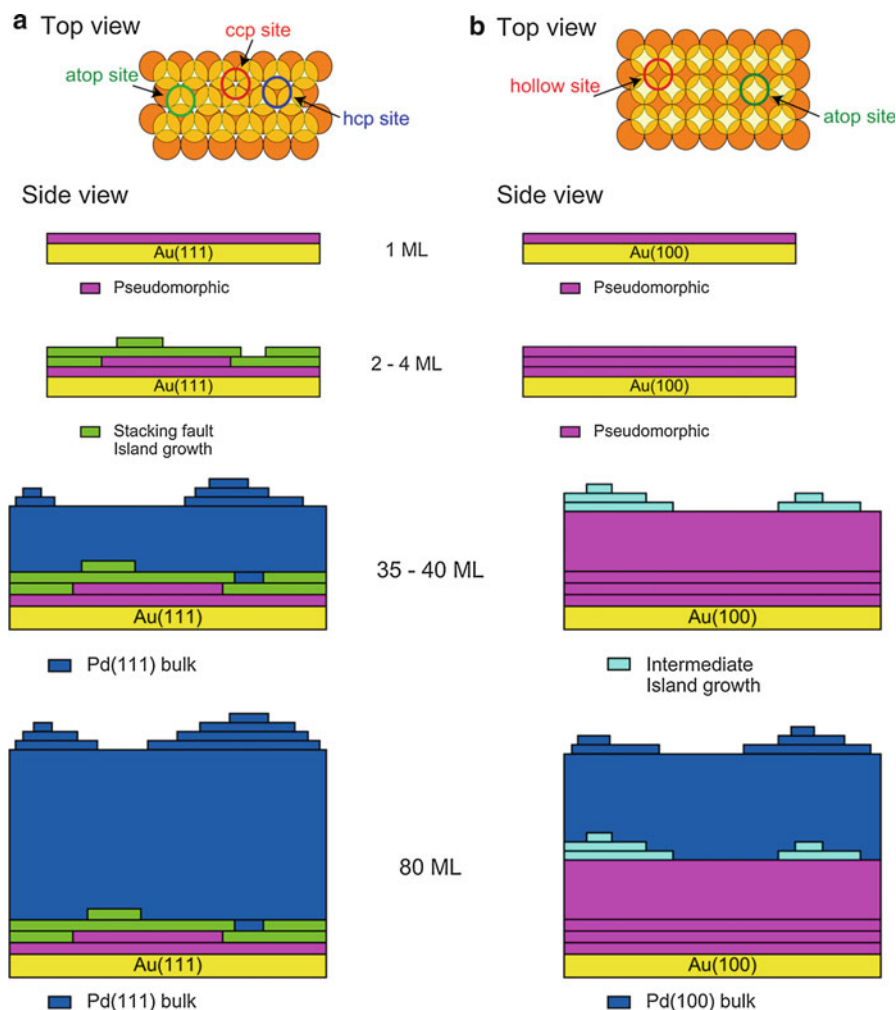
Fig. 7.13 Schematic illustrations of the electrodeposited Pd layers on (**a**) Au(111) and (**b**) Au (100) in a deaerated 0.1 M H_2SO_4 solution containing 1 mM K_2PdCl_4

STM [179] and SXS [20, 180], those on Au(100) were only little investigated by STM [181], in spite of the higher electrocatalytic activity of Bi on Au(100) than that on Au(111). Thus, Zhang et al. examined the potential-dependent structures of the Bi UPD adlayer on Au(100) in 0.1 M $HClO_4$ in detail using in situ SXS [88]. Bi initially adsorbs on the Au(100) surface forming a disordered adlayer. With a negative shift in the potential, three ordered adlayer phases were found (Fig. 7.14): a (3×3) structure consisting of square Bi quadrumers (Fig. 7.14a); a $c(\sqrt{2} \times 3\sqrt{2})R45°$ structure (Fig. 7.14b), where the Bi adatoms are arranged in zigzag chains; and a quasi-hexagonal close-packed $c(p \times 2)$ adlayer (Fig. 7.14c),
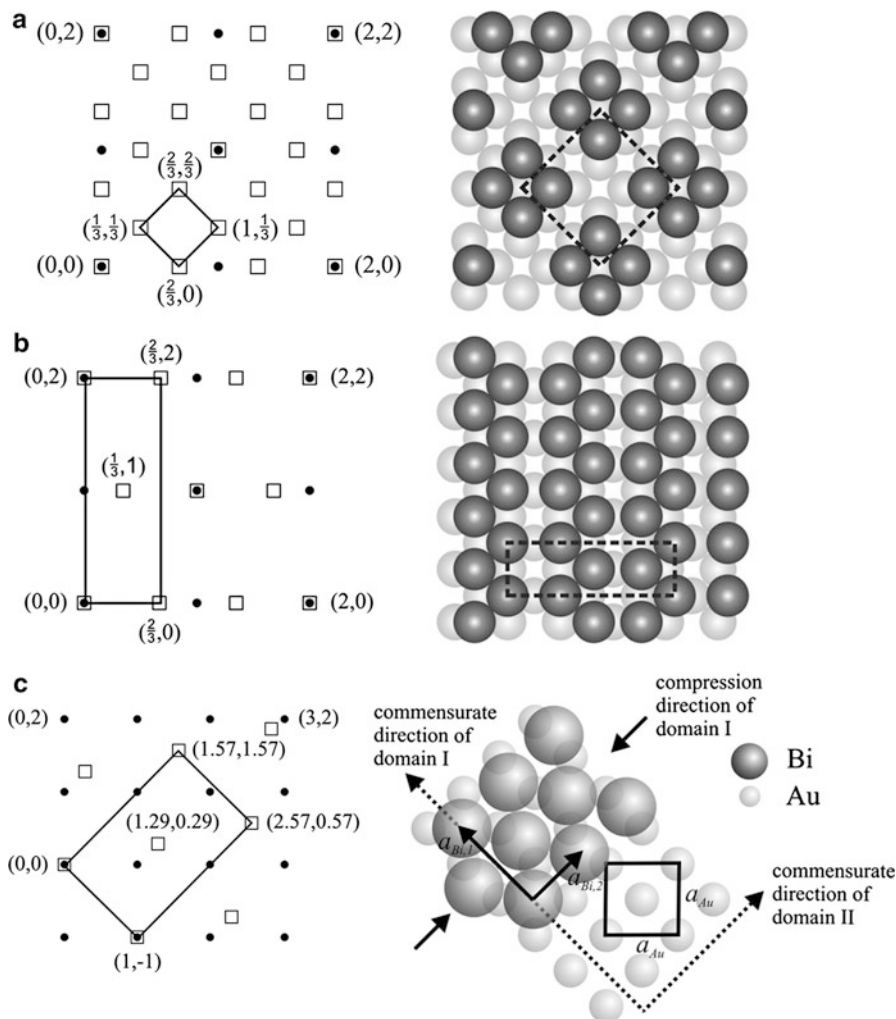
Fig. 7.14 In-plane diffraction patterns and corresponding real space models of (**a**) (3×3), (**b**) $c(\sqrt{2} \times 3\sqrt{2})R45°$, and (**c**) $c(p \times 2)$ structures of Bi adlayers on Au(100). In the patterns, *solid circles* and *open squares* represent the Au(100) substrate and the deposited Bi superstructure reflections, respectively. In the models, *light* and *dark gray spheres* represent outermost surface Au and deposited Bi atoms, respectively (From [88]. With permission from Elsevier)

which is uniaxially incommensurate and compresses by ~ 2 % over the 30 mV stability potential range. The local atomic arrangement in the first phase resembles that in the bulk Bi crystal. Furthermore, it was found that only the $c(\sqrt{2} \times 3\sqrt{2})R45°$ structure is active for electrocatalytic peroxide reduction.

The relationship between the Bi adlayer structures on Au(111) and electrocatalytic activity for hydrogen peroxide reduction was also investigated by Nakamura et al. using SXS, STM, and density functional theory (DFT) calculation [182].

Cu on Cu(100)

Since the successful implementation of Cu as a silicon chip interconnect material in the 1990s [183, 184], renewed interest in the Cu electrodeposition process triggered extensive researches. The advances achieved in this process have played a major role in the downscaling of today's storage media, chip interconnects, microelectronic packaging, and micro-mechanical components [185]. Besides a Cu ion source, an important constituent in the acidic electroplating bath is chloride ion in varying concentrations to influence the deposit properties [22, 89].

Homoepitaxial Cu electrodeposition on Cu(100) in the electrolyte solution containing chloride ion was investigated [89] by time-resolved in situ SXS using transmission geometry [90]. On shifting the Cu deposition potential positively, transitions from step-flow to layer-by-layer and then to multilayer growth modes were observed (Fig. 7.15). This potential dependence was opposite to that expected theoretically and found experimentally for the homoepitaxial electrodeposition of Au on Au(100) [20]. This anomalous behavior was rationalized by a decisive influence of the ordered $c(2 \times 2)$-Cl adlayer [91] on the surface energy landscape, specifically on the effective change in dipole moment during adatom diffusion. Golks et al. also investigated the influence of chloride anion on the atomic-scale interfacial processes during Cu electrodeposition on Cu(100) in an electrolyte solution containing 1 mM or 5 mM $Cu(ClO_4)_2$ by in situ SXS [89]. By time-resolved in situ SXS measurements, insight into the underlying atomic-scale processes was gained up to growth rates of 38 ML/min, revealing a pronounced mutual interaction of the Cl adlayer ordering and Cu growth behavior. At the negative potential limit, where the Cl adlayer is disordered, step-flow growth was observed. Toward more positive potentials, in the regime of the $c(2 \times 2)$-Cl adlayer phase, transitions to layer-by-layer and then 3D growth were found [186]. In turn, the
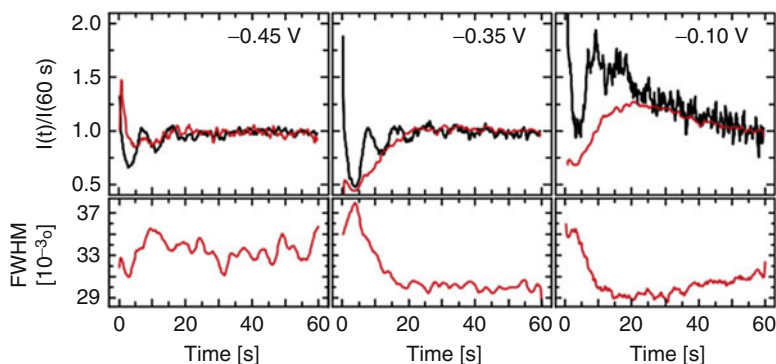
Fig. 7.15 Time-dependent integrated intensities (*top panel*, *red* and *black* curves) and fwhm (*bottom panel*, *red* curve) of the $c(2 \times 2)$ superstructure rod at (1 0 0.1) (*red* curves) and at (1 1 0.1) (*black* curve) after potential steps of Cu(100) from -0.60 V (vs. Ag/AgCl) to the indicated potentials in a 0.1 M $HClO_4$ aqueous solution containing 1 mM $Cu(ClO_4)_2$ and 1 mM HCl. The intensity values were normalized to the intensity at 60 s for better comparability (From [89]. With permission from Elsevier)

kinetics of the $c(2 \times 2)$-Cl adlayer ordering during Cu deposition was substantially slowed down as compared with a Cu-free solution. Furthermore, from a detailed analysis of the anti-Bragg peak shape during layer-by-layer growth, an oscillatory average strain in the surface layer was estimated, which was tentatively rationalized by a model considering strain induced by step edges and adatoms.

Au on Au(111) and Au(100)

Homoepitaxial electrodeposition of Au on Au(111) and Au(100) in an electrolyte solution containing chloride anion was reported by Magnussen et al. using in situ SXS in transmission geometry [92]. Employing diffusion-limited deposition conditions to separate the effects of potential and deposition rate, it was found that there was a mutual interaction between the interfacial structure and the growth behavior. Time-dependent in situ SXS measurements during Au(100) homoepitaxy using negatively scanning potential revealed transitions from step-flow to layer-by-layer growth, then to multilayer growth, and finally back to layer-by-layer growth (Fig. 7.16). This complex growth behavior can be explained within the framework of kinetic growth theory due to the effect of potential, Cl adsorbates, and the Au surface structure, specifically the presence of the surface reconstruction, on the Au surface mobility. Conversely, the electrodeposition

Fig. 7.16 X-ray intensity at Au(100) surface at different potentials in 0.1 M HCl containing 0.5 mM HAuCl₄ as a function of deposition time. The data were obtained at (1 1 0.1) (From [92]. With permission from Elsevier)
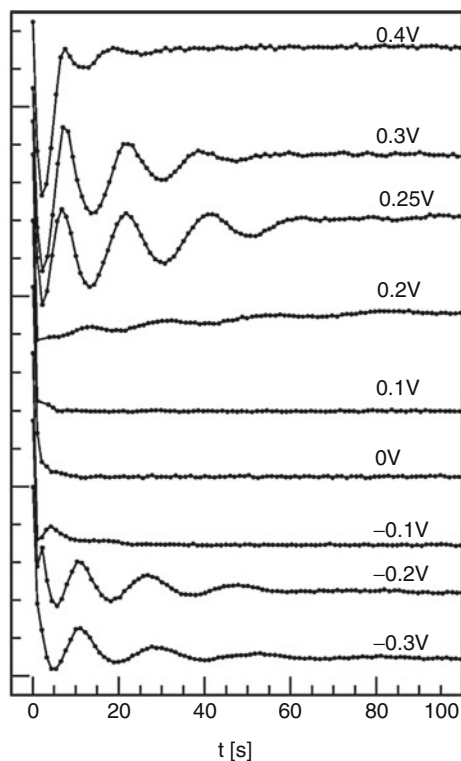
process influences the structure of the reconstructed Au surface, where a significant deposition-induced compression of the Au surface layer occurs as compared to Au(111) surfaces under UHV conditions or in Au-free electrolyte solution. This compression increased toward more negative potentials, which may be explained by a release of potential-induced surface stress.

Electrochemical dissolution of Au from the Au(111) surface at technologically relevant rates in an electrolyte solution containing chloride anion was also investigated with high time resolution by monitoring the time-dependent x-ray intensity at selected scattering points and by simultaneously recording high-quality electrochemical data [90]. This phenomenon had previously been studied only by in situ STM [119] with relatively low time resolution. With positive dissolution potential shifts, transitions from step-flow to layer-by-layer dissolution modes, manifesting as layer oscillations in the x-ray intensity as well as in electrochemical current–time transients, were observed prior to surface passivation due to formation of the surface oxide. A quantitative analysis based on an atomic-scale structure model showed that the dissolution process proceeds via progressive vacancy island nucleation over the whole active dissolution regime with next-layer nucleation occurring at a comparatively low critical coverage, θ_c, between 0.29 and 0.44. This dissolution behavior showed the same characteristics as the intermediate "smooth multilayer growth" regime recently introduced in kinetic growth theories.

4.1.4 Electrochemical Reactions on Electrode Surfaces

Ag/AgCl Reaction on Ag/Au(111)
The Ag/AgCl reaction (Eq. (7.9)) is one of the most fundamental reactions in electrochemistry and is the basis for the Ag/AgCl reference electrode.

$$\text{Ag} + \text{Cl}^- \leftrightarrow \text{AgCl} + \text{e}^- \tag{7.9}$$

In spite of this importance, until recently there were no reports about the Ag/AgCl reaction at an atomic level, although several structural studies of a Cl monolayer on a Ag single-crystal surface with atomic resolution were available [187–193]. This is because when the potential is made positive so that the chlorination reaction (forward reaction of Eq. (7.9)) proceeds at an Ag single-crystal electrode, the reaction takes place not only at the surface but also in the bulk, and aggregates of AgCl clusters, in which atomic arrangements should be random, are formed. Furthermore, the electrochemical reduction of AgCl does not result in an atomically flat single-crystal surface of Ag. We already found that the structure of the pseudomorphic Ag UPD bilayer on Au(111) is so stable even without potential control [169, 170] that the Ag/AgCl reaction can be investigated using this stable Ag film as an electrode. Thus, we were able to study the Ag/AgCl reaction at the Ag UPD bilayer on the Au(111) surface, with atomic resolution using electrochemical, electrochemical quartz crystal microbalance (EQCM), and STM measurements combined with in situ SXS measurements [93]. When the potential was scanned positively from −200 mV (vs. Ag/AgCl), the chloride anion was adsorbed on the Au(111) surface around 0 mV, and then the phase transition of the adsorbed chloride
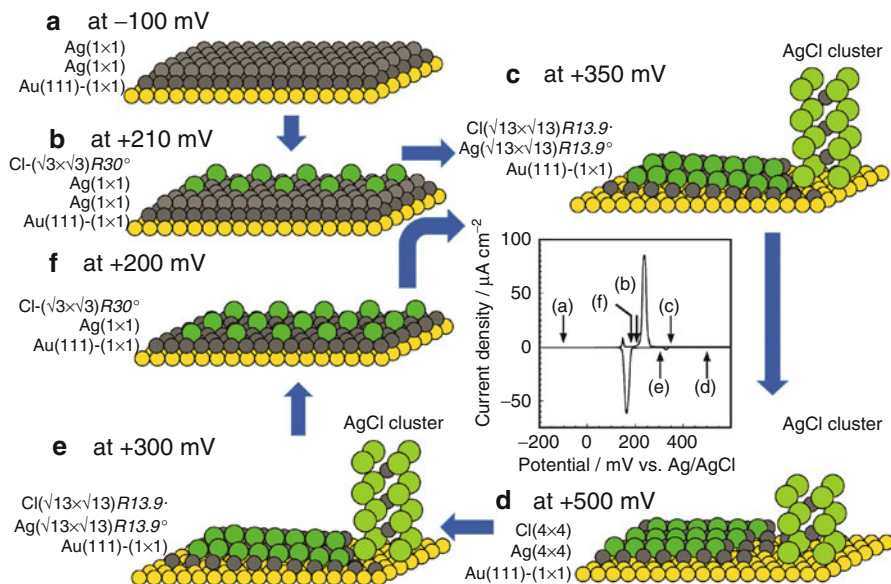
Fig. 7.17 CV of the Au(111) electrode measured in 50 mM H_2SO_4 solution containing 2 mM NaCl and schematic illustrations of surface structure at various potentials shown in CV. Ag UPD bilayer was electrodeposited on Au(111) just before the CV was measured (Reprinted with permission from [93]. Copyright (2011) American Chemical Society)

anion layer from random orientation to ($\sqrt{3} \times \sqrt{3}$) structure took place at around +130 mV. The Ag bilayer and chloride anions were oxidatively reacted to form the AgCl monolayer with a ($\sqrt{13} \times \sqrt{13}$)$R13.9°$ structure around +200 mV, accompanied by the formation of AgCl monocrystalline clusters on the AgCl monolayer surface. The structure of the AgCl monolayer on the Au(111) surface changed from a ($\sqrt{13} \times \sqrt{13}$) $R13.9°$ structure to a (4×4) structure around +500 mV. When the potential was scanned back negatively, the AgCl monolayer was electrochemically reduced, and a Ag monolayer, not a bilayer, was formed on the Au(111) surface. These structure changes, together with simultaneously recorded CV, are schematically shown in Fig. 7.17. In the subsequent potential cycles, the structural change between the Ag monolayer and the AgCl monolayer was reversibly observed. We also found that all oxidative structural changes were much slower than the reductive ones.

Electrocatalytic Reactions on Pd(111) and Pd(100)

The electrocatalytic oxygen reduction reaction is one of the key issues for the development of the PEMFC [137–140, 194], as mentioned in Sect. 4.1.2. Naito et al. studied the surface structures of Pd(111) and Pd(100) electrodes using in situ SXS, whose electrocatalytic activity for the oxygen reduction reaction (ORR) is as high as that of Pt, at 0.50 V (vs. RHE) in 0.1 M $HClO_4$ saturated with Ar or O_2 [94]. Both Pd(111) and Pd(100) electrode surfaces are unreconstructed at 0.50 V in

both Ar- and O_2-saturated solutions: Pd atoms are accurately located at (1×1) positions in the in-plane structure. On the other hand, the interlayer spacing behaviors are different. The values of interlayer spacing between the first and second Pd layers, d_{12}, agree with those of the Pd bulk in Ar-saturated solution. In O_2-saturated solution, however, the d_{12} values are expanded on both Pd(111) and Pd(100). The degree of expansion of Pd(100) is much larger than that of Pd(111), indicating that the interaction of oxygen with the Pd(100) surface is stronger than that with Pd(111). The authors suggested that this is the reason that the electrocatalytic activity for ORR on Pd(100) is higher than that on Pd(111) [195].

Hydrogen Insertion on Pd/Pt(111)

Pd thin films are of interest as a protective barrier against oxidation and/or as a promoter for hydrogen insertion complex hydrides from compounds of light elements such as Mg_2Ni, $LaNi_5$, $NaAlH_4$, and $LiAlH_4$ [196–199]. Soldo-Oliver et al. studied the hydrogen electro-insertion process into Pd thin films electrodeposited on Pt(111) in detail by in situ SXS [95–97]. First, they made clear that the role of chloride in the deposition solution is to promote the growth of a Pd thin film on Pt(111) in a layer-by-layer mode [95]. Then, the structures of about 20 ML thick Pd films electrodeposited on Pt(111) before and after hydrogen electro-insertion and after hydrogen electro-desorption were investigated [96]. They also determined the influence of the substrate on the pseudomorphic character of the palladium deposits thicker than about 10 Pd layers and on the structure change during the hydrogen insertion/desorption processes. After hydrogen insertion, an asymmetric expansion of the Pd film, almost four times larger normal to the surface, was observed. The presence of two differently ordered regions (a two-phase region) in the hydride film and of a morphological irreversibility after hydrogen desorption was confirmed. These hydrogen insertion/desorption process behaviors are schematically shown in Fig. 7.18.

In order to get a thorough understanding of the mechanisms governing hydrogen insertion into the Pd layers, Soldo-Olivier et al. also studied the hydrogen electro-insertion process using ultrathin Pd layers on Pt(111) by an original method allowing the measurement of hydrogen insertion electrochemical isotherms [97]. The use of a hanging meniscus rotating disk electrode and a new calculation approach permitted them to remove the contributions to the insertion charge of both the hydrogen evolution reaction (HER) and hydrogen oxidation reaction (HOR). Applying this method, hydrogen insertion isotherms for Pd films on Pt(111) from 14 ML down to 4 ML can be measured. Independent of the film thickness, the maximum hydrogen insertion rate, $(H/Pd)_{max}$, is smaller than that of bulk Pd. The so-called two-phase region, as mentioned above, was still observed, but contrary to bulk Pd, it was characterized by a slope. Both the hydrogen solubility and the two-phase domain width diminished with a decrease of the Pd film thickness. The behavior of the hydrogen electro-insertion isotherms was interpreted in the light of the Pd nanofilm structures obtained with in situ SXS. The lattice constraints induced by the substrate resulted in a lower insertion rate in the Pd layers close to the Pt–Pd interface. Only the outermost region of the Pd film was relaxed and behaved like bulk Pd. This description
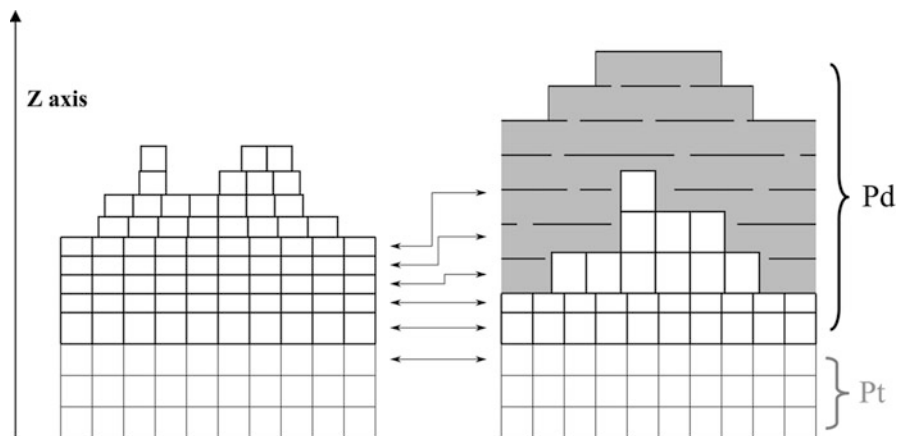
Fig. 7.18 Out-of-plane schematic representation of the Pd film structure before (*left*) and after (*right*) hydrogen insertion, where the in-plane "disordered" region in the hydride Pd film is indicated by the *gray* zone (Reprinted with permission from [96]. Copyright (2011) American Chemical Society)

quantitatively accounted for the experimental behavior of $(H/Pd)_{max}$ as a function of the Pd film thickness. The structure of Pd films obtained on Pt(111) also corresponded to the presence of nonequivalent hydrogen insertion sites, surely contributing to the slope observed in the two-phase domain.

4.1.5 Adsorbed Ion and Double-Layer Structures on Electrode Surfaces

Adsorption of Oxygen Species on Pt(111) and Pt₃Ni(111)

Adsorption of Oxygen Species on Pt(111) and $Pt_3Ni(111)$

An understanding of the role of hydration water molecules at the electrode/electrolyte interface is of great importance to reveal their structures under control of the electrode potential. However, although the structures of adsorbed water molecules on a metal surface can be observed by LEED in UHV, the electrochemical interface is much harder to study due to the presence of the bulk electrolyte. In electrolyte solutions free of strongly adsorbing anions, such as KOH, the electrochemical interface offers the opportunity of controlling the surface coverage by hydrogen, water, and OH species simply by controlling the applied electrode potential. To probe the structure of the water layer at the electrode/electrolyte interface in situ is a technically challenging experiment as the scattering signal from the ordered oxygen atoms is relatively small compared to the diffuse scattering from the bulk of the electrolyte solution. In this context, Lucas et al. reported the results obtained using a UHV transfer system to provide unprecedented control over the electrode surface structure during transfer from UHV to the electrochemical environment [98]. Initially, a well-defined Pt(111) surface was prepared in UHV, dosed with oxygen to form a $p(2 \times 2)$ oxygen adlayer and then studied by SXS, initially under UHV conditions and then in a nitrogen atmosphere before a droplet of water was placed

Table 7.2 Structural parameters for the fitting to the Pt(111) CTR data (From [98]. With permission from Royal Society of Chemistry)

System	θ_O, θ_{OH}	$d_{Pt\text{-}O}$/Å	ε_1/Å	ε_2/Å	σ_{xy}/Å	σ_z/Å
Pt(111)–O	0.25f	1.5 (0.2)	+0.05 (0.005) (2.2 %)	0.005 (0.005)	0.06 (0.01)	0.0
Pt(111)–H$_2$O	0.7 (0.3)	1.9 (0.4)	+0.03 (1.3 %)	0.01	0.10	0.0
Pt(111)–KOH ($E=-1.0$ V)	0	–	+0.05 (2.2 %)	0.005	0.06	0.0
Pt(111)–KOH ($E = -0.1$ V)	0.55 (0.2)	2.1 (0.4)	+0.04(1.8%)	0.0	0.06	0.0

f indicates a parameter that was fixed. Uncertainties are indicated in brackets. ε_1 is also quoted as a percentage of the Pt(111) atomic layer spacing. d, θ, and σ represent layer spacing, coverage, and root mean square (RMS), respectively, of the corresponding layers shown as subscripts

on the surface. Measurements of the surface structures were then performed on the surface modified by the bulk water overlayer before the water was exchanged with 0.1 M KOH electrolyte solution and the Pt(111) electrode put under potential control to allow potential-dependent studies of the interfacial structure. In UHV, the SXS data clearly showed the structure of the oxygen adlayer with the $p(2 \times 2)$ structure, as same as that previously investigated by LEED [200]. When the sample was contacted with a droplet of pure water, however, it was not possible to observe any ordered structures of oxygen species at the Pt(111)/water interface because of the weakness of the expected signal compared to the background scattering from the water droplet. Detailed analysis of the CTR data showed systematic changes in the measured intensities associated with restructuring at the interface. The data was reproduced by a simple structural model showing a reduced outward relaxation in the Pt surface accompanied by an increased in-plane distortion of the surface Pt layer and an increased coverage by oxygen species. Their results measured in 0.1 M KOH at -1 V (vs. Ag/AgCl) and -0.1 V were consistent with previous SXS results [150, 201, 202] and gave insight into the adsorption of hydrogen and oxygen species. The data obtained in their study [98] are summarized in Table 7.2. Their experiments on Pt(111) indicated the possibility of studying a range of model electrocatalysts using this methodology, and they also reported the results at a Pt$_3$Ni(111)/0.1 M HClO$_4$ interface obtained from similar experiments.

Adsorbed Chloride Anion on Cu(111) and Cu(100)

Strongly adsorbed layers of chemically bound anions such as halide and sulfate have been investigated in detail, revealing a complex, potential-dependent two-dimensional phase behavior, which can significantly affect electrochemical reactions, such as deposition, etching, corrosion, and electrocatalytic processes [203]. Chloride adlayers on Cu electrodes are of major importance in corrosion and electroplating, in particular for the on-chip metallization of ULSI microchips, where chloride and organic additives form an inhibiting adsorbate layer that controls the growth process, leading to superconformal growth. Thus, Gründer et al. investigated the structures of specific adsorbed chloride and its induced Cu substrate buckling on Cu(100) [91] and Cu(111) [204] using in situ SXS, in addition to the studies on Cu electrodeposition on Cu reviewed in section "Cu on Cu(100)".

The interface of Cu(100) electrode surfaces in 10 mM HCl solution was studied by in situ SXS and DFT calculations, focusing on a precise structure analysis of the $c(2 \times 2)$ Cl adlayer formed at positive potentials [91]. CTR measurements in this adsorbate phase at -0.20 V (vs. Ag/AgCl) showed distinct differences to the corresponding data reported by Tolentino et al. [205] for the $c(2 \times 2)$ Cl structure formed at the Cu(100)–vacuum interface. Although the atoms in the second Cu layer exhibit a small vertical corrugation in both environments, the sign of this corrugation is reversed. Furthermore, the Cu–Cl bond distance and the average Cu interlayer spacing also differ. Ab initio calculations performed for this adsorbate system reproduced these effects, specifically the reversal of the subsurface second-layer buckling caused in the presence of coadsorbed water molecules and cations in the outer part of the electrochemical double layer. In addition, studies at more negative potentials showed a continuous surface phase transition from the ordered $c(2 \times 2)$ to a disordered Cl adlayer at -0.62 V but also indicated a substantial Cl coverage even at the onset of hydrogen evolution.

The specific adsorption of chloride on Cu(111) in an acidic aqueous electrolyte solution (pH 3) was also investigated by in situ SXS, revealing an incommensurate hexagonal rotated Cl adlayer. The structure and its potential dependence suggested a strong adsorbate–adsorbate interaction as compared to other halide adlayers on (111)-oriented metal electrode surfaces. The orientational epitaxy can be rationalized by the model proposed by Grey and Bohr [206], which is based on symmetry considerations [91].

Adsorbed Cation and Anion (Electrical Double Layer) on Pt, Au, Ag, and Cu
Strmcnik et al. indicated that hydrated cations that are not in direct contact with the electrode surface but are still located well within the electric double layer, which consists of the inner Helmholtz layer (IHL) and outer Helmholtz layer (OHL) [207–213], are just as important as the covalently bound adsorbates when it comes to electrocatalytic properties [214–219]. This is especially true in alkaline environments, which are of major importance both in chlor-alkali electrolysis and water electrolysis, as well as in energy conversion systems such as alkaline fuel cells. Thus, it is very important to study the potential-dependent structures of cation layers and also anion and water layers, adsorbed on the electrode surface, where these are collectively referred to the electrical double layer, not only for understanding the fundamental surface science but also for industrial applications.

Strmcnik et al. reported novel findings on the influence of non-covalent interactions at the electrochemical interface [99]. Their in situ SXS data of Pt and Au single-crystal electrodes measured in alkaline solution clearly showed metal-adsorbed OH (OH_{ad}) covalent bonding, as well as corresponding OH_{ad}-hydrated metal ion ($M^{n+}(H_2O)_x$) interactions and the formation of OH_{ad}–cation complexes with the cation centered at 3.48 ± 0.05 Å away from the Pt surface. Then, they proposed that cations bound to OH_{ad} are partially dehydrated, showing the predominant role of the direct ion–dipole interaction that increases in the same
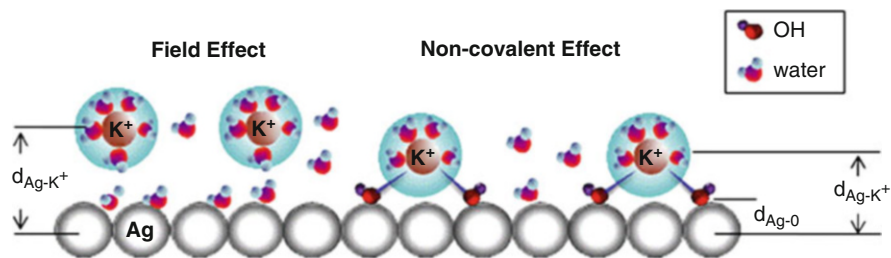
Fig. 7.19 A schematic illustration of the interfacial structure of the Ag(111) electrode in 0.1 M KOH at the negatively charged (*left*) and positively charged (*right*) surface. The layer separations obtained from the CTR measurements are indicated (From [101]. With permission from Elsevier)

order as the OH interaction energy with the corresponding cations ($Ba^{2+} > Li^+ \gg K^+$). These trends are inversely proportional to the activities of the ORR and are much more significant for Pt than Au systems.

An in situ SXS study on the Ag(100)/alkaline solution interface performed by Nakamura et al. [100] made clear the structure of Cs^+ in the OHL, which is located above a $c(2 \times 2)$ Br layer adsorbed on Ag(100). The coverage of Cs^+ and the distance of the Cs^+ layer from the electrode surface depends on the electrode potential. They also found that single water layer is intercalated between IHP and OHP ion layers.

Lucas et al. structurally studied the electrochemical double layer at the Ag(111)/ 0.1 M KOH electrolyte interface using in situ SXS [101]. A schematic illustration of their proposed interfacial structure is shown in Fig. 7.19. At a negative potential (-1.0 V vs. SCE), where there is no chemisorbed species on the electrode surface, the CTR results are consistent with the presence of a hydrated cation adlayer at a distance of 4.1 Å above the Ag surface. At a positive potential (-0.2 V), however, OH_{ad} stabilizes the hydrated K^+ cations, at a distance of 3.6 Å above the Ag surface, through a non-covalent (van der Waals) interaction.

The structure of the electric double layer has also been studied in an acidic solution by in situ SXS. Keller et al. investigated the structuring impact of an anion-modified Cu electrode surface on the near-surface liquid electrolyte [102, 103]. This templating effect of the IHL of specifically adsorbed anions not only affects the interfacial structure parallel to the surface normal by layering the liquid in the near-surface regime but also induces moreover a lateral ordering of water dipoles and solvated counter ions in the OHL. In this respect, they observed a symmetry transfer from the IHL into the liquid electrolyte next to the electrode surface [102]. Their prototypical model system was a Cu(100) surface on which chloride adsorbs with the formation of a simple $p(1 \times 1)$ adlayer phase that serves as a structural template for the coadsorption of monovalent K^+ and hydronium cations from the acidified supporting electrolyte. A layer of interfacial water is interpreted as a part of the remaining solvation shell of K^+ in the OHL.

In the acidic solution, the full 3D structure of a Cu(100)/10 mM HCl electrolyte interface, where adsorption of alkali metal ion is explicitly excluded, was also clarified and compared with the alkali metal data by the same authors as above using in situ SXS [103]. Chloride anions chemically adsorb on the Cu(100) surface

at positive potentials forming a $p(1 \times 1)$ structure. This Cl chemisorption layer serves as a structural template for the lateral ordering of water molecules and hydronium cations in the near-surface liquid electrolyte, the same situation as above. Evidence for this interfacial geometry is mainly derived from the intensity distribution of surface-sensitive SXS data along the (1 0 L) adlayer rod. The characteristic oscillating intensity distribution along the (1 0 L) rod is due to a centered bilayer system consisting of the anionic IHL of chemisorbed chloride and the cationic OHL. The latter is constituted in this case by hydronium cations that preferentially populate fourfold hollow sites of the underlying chloride lattice. IHL and OHL are separated by an extra interfacial water layer. Anions and cations in the IHL and OHL, respectively, compete for these water species as part of their solvation shell. The Cl/water/hydronium layers can be considered as a prototypical model system where the anions and cations in the coupled bilayer system are sharing the interfacial water as part of their solvation shell. In this respect, the Cl$^-$/water/hydronium "bilayer" considerably differs from the above Cl$^-$/water/K$^+$ system [102] where the interfacial water was clearly assigned to the solvation shell of the alkali metal cation in the OHL. The accumulation of non-chemisorbing species in the OHL and the interfacial water layer clearly depends on the chemical nature of the chemisorbed anion, their lateral structure on the electrode surface, and chemical nature of the adsorbing cations. In this sense, the authors denoted the observed phenomenon as specific cation adsorption on the layer of specifically adsorbed anions.

4.2   XAFS

4.2.1 Trends of In Situ XAFS

Since in situ XAFS does not require long-range order, in contrast to in situ SXS, it is applicable not only to single-crystal electrodes but also to various materials such as nanoparticles, metal complexes, and biomolecules adsorbed on polycrystal electrode surfaces and, of course, polycrystal electrodes themselves. Thus, taking advantage of the XAFS method, there have been many structural studies on polycrystalline types of electrodes, especially metal and alloy nanoparticles, in recognition of their technological applications to electrocatalysts.

Since XAFS is not inherently surface sensitive because of the relatively long penetration length of x-rays, various techniques were combined to selectively extract the information from the surfaces of interest. At the very early stage, most of the XAFS studies on surface analysis were performed using electron detection techniques which are surface sensitive but are not suitable for interfaces buried under liquid layers. Thus, various tailor-made in situ electrochemical cells suitable for each application have been developed as summarized in Sects. 3.2.2 and 3.2.3.

Pioneering structural studies at electrode/electrolyte interfaces using in situ XAFS were reported in the late 1980s by several groups [220] in relation to surface passivation films on metal surfaces [49, 50, 221], metal complexes [27], chemisorbed species [47, 222], and UPD metal monolayers [223–226] on single-crystal substrates, metal oxides [26, 227, 228], and materials for batteries and fuel cells [25].

Since one of the most attractive points of in situ measurements is detection and identification of intermediate species adsorbed on electrode surfaces, surface-adsorbed layers became a primary object of study. Abruña et al. successfully detected the Pt–I bond at an iodine monolayer adsorbed on a Pt(111) single-crystal surface in contact with an electrolyte solution [222]. Their initial experiment was performed with an incident angle of 45°, resulting in obscure signals due to Compton and elastic scatterings from the substrate. Subsequently, a configuration with a grazing angle was adopted, where total external reflection occurs, leading to significant suppression of Compton and elastic scatterings and an improvement in the signal-to-noise ratio. They also applied this technique for a structural determination of the Cu UPD layer formed on the Au(111) surface [223]. Fitting of the EXAFS oscillation at the Cu K edge showed that Cu atoms sit in the threefold hollow site of Au(111) with an oxygen species on top of the deposited Cu.

In research on corrosion/inhibition, McBreen et al. measured potential cycle dependence of the structures of the surface Ni-OH species of the Ni oxide poly-crystal electrode using the transmission mode, which was explained in Sect. 3.2.2. In addition, time-resolved DXAFS was readily adopted for this system after its development. They also utilized the DXAFS technique to monitor the continuous change of oxidation states and local coordination structures of the Ni oxide [229, 230]. Davenport et al. measured the potential-dependent oxidation number of Cr in a polycrystal Al–Cr alloy using the fluorescence mode, which was explained in Sect. 3.2.3.

Since these pioneering studies were reported, many structural researches at the electrode/electrolyte interface involving species such as metal complexes [231–235], metal nanoparticles [236–239], deposited metal on foreign metal [240–248], and semiconductor electrodes [249–251] have been carried out using the in situ XAFS technique. In particular, in situ XAFS started to be applied to the structural determination of electrocatalysts for PEMFCs [252, 253] and electrode materials for lithium ion batteries (LIBs) [254] under operating conditions.

Structural studies of Pt and Pt-based nanoparticles under potential control have been an important subject because these materials are the most active electrocatalysts for the cathode and anode reactions in PEMFCs [252]. The potential-dependent change of the WL intensity and local structural parameters were investigated in detail by several groups [255–258]. Herron et al. carried out XAFS measurements of carbon-supported platinum catalysts, which are the most widely used electrocatalysts in PEMFCs, in sulfuric acid solution at various electrochemical potentials and detected the formation of a Pt–O bond in the positive potential region, associated with oxide formation [255]. Subsequently, a series of in situ XAFS measurements were performed over a broader potential range to discuss the potential dependence of the occupied d-state and local structural parameters; a widening of the high-energy side of the WL at negative potential and increase in the WL intensity at positive potential were attributed to adsorption of hydrogen and oxide formation, respectively [256–258]. The potential-induced structural changes of Pt nanoparticles were recently examined in detail by Imai et al. with a

combination of XAFS and XRD [259]. Iwasawa and Tada et al. applied spatially resolved μ-XAFS [69] and time-resolved QXAFS [40–42, 44] techniques to investigate the distribution and dynamic structural changes, respectively, of Pt embedded in the MEA configuration.

One of the most important requirements for positive electrodes in LIBs is a reversible lithiation/delithiation capability without drastic structural changes because it is a governing factor of the cycle characteristics of batteries. Nakai et al. conducted a series of in situ XAFS structural studies on various lithium-transition metal complex oxides (Li metal oxides), which are the most widely used positive electrode materials in LIBs, after charge/discharge processes [260–267]. Changes in the oxidation states of transition metals and a phase transition caused by the electrochemical deintercalation of Li were identified from the XANES and EXAFS analysis in conjunction with XRD. Recently, Ogumi and Uchimoto et al. have been measuring a wide variety of electrode materials [55, 268–277] by means of various techniques to clarify the mechanisms of lithiation/delithiation processes as well as accompanying degradation processes [68, 278]. Thus, one of the recent trends is the application of in situ XAFS analysis to a broader range of materials for energy conversion devices, especially electrocatalysts and electrode materials actually used in LIBs and PEMFCs. Among the many structural investigations at the electrode/electrolyte interface performed using the in situ XAFS technique, we review in the following section the latest findings in the areas of fuel cells, batteries, and a few other important systems, summarized in Table 7.3.

4.2.2 Electrocatalysts for Polymer Electrolyte Membrane Fuel Cells (PEMFCs)

PEMFCs are one of the key energy conversion devices because of their very high theoretical efficiency and relatively low emissions, as mentioned in Sect. 4.1.2. [137–140, 319]. Pt and other Pt-based materials are the most widely used electrocatalysts for both anode and cathode electrodes because of their excellent catalytic activity for the HOR [320, 321], ORR [322], and methanol oxidation reaction (MOR) [323]. However, potential loss at the cathode caused by the slow kinetics of the ORR is a critical issue to be solved for the development of the next-generation PEMFC with an improved efficiency. Another important issue involving the electrocatalysts in connection with the widespread commercialization of PEMFCs is degradation control [139, 324] Particle growth via Ostwald ripening due to dissolution and redeposition of Pt is widely recognized to be a primary factor contributing to the deterioration of the ORR activity because it decreases the electrochemically active surface area. In order to develop electrocatalysts with very high activity and durability, an understanding of those processes at the electrocatalyst/electrolyte interfaces is essential, and XAFS has been utilized for in situ analysis of various model PEMFC systems because of the above-mentioned advantages [236, 237, 239, 252, 256–259, 287, 325–330].

Table 7.3 Summary of recently reported in situ XAFS studies at electrode/electrolyte interfaces

Methods	Systems	Beamlines at SR facility	Remarks	Ref.
XAFS in transmission mode	Pt/Au core–shell nanoclusters	BL16B2 at SPring-8	A new spectroelectrochemical cell equipped with Kapton window	[28, 279]
Soft XAS in transmission mode	Liquid water, $Fe^{2+/3+}$ in aqueous solutions, methanol–water binary solutions	BL3U at UVSOR-III	A thickness adjustable spectroelectrochemical cell equipped with 100 nm thick Si_3N_4 window	[36–39]
SXTM, micro-spot XAS and XRF	Ionic liquid/Ni thin film interfaces	TwinMic beamline at Elettra		[53, 280]
XAFS in fluorescence mode	MnO_x thin film for ORR and OER electrocatalysts	BL10.3.2 at ALS	A spectroelectrochemical cell equipped with 1 μm thick Si_3N_4 window	[52]
Soft XAS in total fluorescence yield	$Cu^{0/+/2+}$ in aqueous solutions, graphene in aqueous solutions	BL 8.0.1 ALS	A spectroelectrochemical cell	[51, 281, 282]
Fluorescence XAS	Lithium metal oxide for positive electrodes	BL 10 at SR center of Ritsumeikan University	A spectroelectrochemical cell equipped with 7.5 μm polyimide window	[55]
Transmission XAFS	Pt electrocatalysts for ORR	X19A at NSLS	A microstructured PDMS pouch-type spectroelectrochemical cell	[56]
Fluorescence XAFS	Pt/HOPG	BL9A at KEK PF	Backside illumination fluorescence XAFS	[57]
Fluorescence XAFS	Size-selected Pt nanoparticles, Pt/Rh(111), Pt/Au(111), Cu/Au(111)	BL 6-2 at SSRL	High-energy-resolution fluorescence-detected XAFS	[283–285]
XAFS	Fuel cell research		Review	[253]
Fluorescence XAFS	Pt/CeO_x electrocatalysts for ORR and Pt molecular catalysts for HER	BL 14B1 at SPring-8	Thin-layer configuration	[48]

Time-resolved QXAFS and DXAFS	Pt-based electrocatalysts for ORR	BL 01B1, 36XU, and 40XU at SPring-8	MEA-type configuration	[40, 42–45]
Spatially resolved XAFS	Pt-based electrocatalysts for ORR	BL 36XU at SPring-8	MEA-type configuration	[69]
3D laminography–XAFS	Pt-based electrocatalysts for ORR	BL47XU at SPring-8	MEA-type configuration	[286]
Time-resolved XAFS and XRD	Pt-based electrocatalysts for ORR	BL16XU, 16B2, and 28B2 at SPring-8	Configuration	[259, 287]
XAFS	Pt nanoparticles	XOR 9BM at APS	Transmission configuration	[288]
XAFS	Pt nanoparticles	X11A at NSLS	MEA-type configuration	[289]
Fluorescence XAFS	Cu/Au(111) and Zn/Au(111)	Station 16.5 at SRS	Thin-layer cell	[290, 291]
Fluorescence XAFS	Pb/Ni and Sn/Au(111)	BL16B2 at SPring-8	Kapton window cell. Thickness of solution layer: 1 mm	[292, 293]
Fluorescence XAFS	Pd/Au	BLB18 at Diamond Light Source	Pd/Au core–shell particles painted onto carbon paper	[294]
Fluorescence XAFS	MnO_x/Nb:SrTiO$_3$	BL12C at KEK PF and BL01B1 at SPring-8	Thin-layer configuration	[295–298]
Fluorescence XAFS	Pt molecular catalysts for HER	BL12C at KEK PF	Thin-layer configuration	[46]
Fluorescence XAFS	Cobalt phosphate and nickel borate for OER	BL7-3 and 9–3 at SSRL and BL 10.3.2 at ALS	Cell equipped with ITO-coated PET window	[299, 300]
XAFS	LIB research		Review	[254]
XAFS	Lithium metal oxides for LIB	BL7C and 11A at KEK PF and BL01B1, 28XU, and 37XU at SPring-8	Ex situ XAFS characterization	[274, 276, 301–305]
Total-reflection fluorescence XAFS and depth-resolved XAFS	$LiCoO_2$	BL01B1 and 37XU at SPring-8	Lithium sheet/Electrolyte_Separator/LiCoO$_2$ film/Platinum substrate	[268, 269]

(continued)

Table 7.3 (continued)

Methods	Systems	Beamlines at SR facility	Remarks	Ref.
Time-resolved XRD and XAFS	$LiFePO_4$, $LiNi_{0.5}Mn_{1.5}O_4$	BL01B1, 14B2, 28XU, and 46XU at SPring-8	Transmission configuration	[270–272, 277]
Time-resolved XAFS	$LiFePO_4$	X18A at NSLS	CR2032 coin cell	[306]
Time-resolved XRD and XAFS	$LiFePO_4$	BL01C2 at National Synchrotron Radiation Research Center	Coffee-bag cell or CR2032 coin cell	[307]
XRD and time-resolved XAFS	$LiFePO_4$	BL01B1 at SPring-8	Transmission configuration	[308]
Time-resolved XRD and XAFS	$LiMn_3O_4$ and sulfur/carbon composite electrode	BLA2 at CHESS and X19A at NSLS	CR2032 coin cell with Kapton window	[309]
Time and spatially resolved XAFS	$LiFePO_4$	SAMBA, ODE, and LUCIA at SOLEIL	Transmission configuration	[310]
XRD and XAFS	Li_2MnSiO_4, $LiFeSiO_4$, and $Li_{2-x}VTiO_4$	HASYLAB at DESY	Transmission configuration	[311, 312]
XAFS	$LiFePO_4$ and $Li(Ni_{0.4}Co_{0.15}Al_{0.05}Mn_{0.4})O_2$	Beamline station D of the DND-CAT (sector 5) at APS	Transmission configuration	[313–315]
XAFS	$LiFe_{0.4}Mn_{0.6}PO_4$	BL7C at PLS	Transmission configuration	[316]
XAFS	$LiMg_{0.05}Ni_{0.45}Mn_{1.5}O_4$	Station 7.1 at SRS	Transmission configuration	[317]
XAFS	$LiFe_{0.33}Mn_{0.67}PO_4$	XAFS beamline at ELETTRA	Transmission configuration	[318]
XAFS	Mg/Mg^{2+} at Pt	BL6.3.1 at ALS	Spectroelectrochemical cell equipped with Si_3N_4 window	[54]

Important Role of Cocatalysts in Enhancement of the ORR

One of the effective approaches to enhance the ORR activity and reduce the amount of Pt loading is utilization of cocatalysts in combination with Pt. From the 1990s, a variety of transition metals [331–337] and metal oxides [338–350] have been used as cocatalysts and several binary and ternary Pt-based electrocatalysts have been proved to be more active for the ORR than pure Pt. Recently, cerium oxide (CeO_x), which is known to be an excellent additive for exhaust gas catalysts of automobiles, has been utilized as a cocatalyst with a Pt catalyst for the ORR in PEMFCs and the ORR activity has been proved to be enhanced. Although the enhancement effect of CeO_x on the ORR activity was considered to be due to its unique oxygen storage capability and substantial interaction between Pt and CeO_x, the details of the role of CeO_x in the promotion of the ORR was not well understood. To clarify the role of CeO_x in the enhancement of the ORR activity, in situ XAFS measurements at the Pt L_{III} and Ce L_{III} absorption edges of the Pt–CeO_x/C catalyst at various conditions were performed in the fluorescence mode [48]. Figure 7.20 shows normalized XANES spectra at the Pt L_{III} edge before and after the pretreatment, that is, oxidation/reduction cycles in N_2-saturated 0.5 M H_2SO_4 solution and the Ce L_{III} edge after each treatment step, respectively.

A peak corresponding to the Pt metal was observed around 11560 eV at the Pt L_{III} edge and almost no change was observed before and after the pretreatment, showing that the amount and oxidation state of Pt were not affected by the pretreatment. On the other hand, significant change was observed in the XANES spectra at the Ce LIII edge after the pretreatment.

While typical doublet peaks corresponding to Ce^{4+} were observed at 5733 and 5740 eV for pure CeO_2 powder, confirming that the CeO_2 is the dominant species, an additional peak corresponding to Ce^{3+} is observed at around 5729 eV in the spectrum of the Pt–CeO_x/C catalyst, showing the formation of Ce^{3+} species as a result of the incorporation of Pt.

After the Pt–CeO_x/C catalyst was immersed in a 0.5 M H_2SO_4 solution for the pretreatment, the absorbance, μt, significantly decreased (inset of Fig. 7.20) and the peak due to the Ce^{3+} became dominant, showing the preferential dissolution of Ce^{4+} species as only the Ce^{3+} peak was observed. Thus, a Ce^{3+} species was formed at the interface when Pt was incorporated with CeO_2, and the residual CeO_2 was dissolved in sulfuric acid solution during the pretreatment. The TEM image of the Pt–CeO_x/C catalyst after the pretreatment was presented in a previous report, and it showed the presence of Pt nanoparticles with a diameter of 3–5 nm coated with a few CeO_x layers.

Figure 7.21 shows the potential-dependent XANES spectra at the Pt L_{III} edge of the Pt/C catalyst and at the Pt L_{III} and Ce L_{III} edges of the Pt–CeO_x/C catalyst. At the Pt L_{III} edge, whereas the WL intensities of the Pt/C catalyst gradually increased as the potential goes more positive than 1.0 V, not much change was observed in the XANES spectrum of the Pt–CeO_x/C catalyst. Since the Pt L_{III} absorption is attributed to the transitions of electron from the *2p* to the *d* state, the WL intensity reflects the amount of *d*-band vacancies. It suggests that although Pt oxide was formed at the Pt/C catalyst, the formation of Pt oxide was significantly suppressed at the

Fig. 7.20 Normalized XANES spectra at the (**a**) Pt L$_{III}$ edge of the Pt–CeO$_x$/C before (*blue*) and after (*red*) the potential cycles and at the (**b**) Ce L$_{III}$ edge of the Pt–CeO$_x$/C before (*blue*) and (*red*) after immersing in 0.5 M H$_2$SO$_4$ solution for 30 min for the oxidation reduction cycle (ORC) together with a reference spectrum for (*black*) CeO$_2$ powder. *Insets*: raw data of the corresponding spectra (Reprinted with permission from [48]. Copyright (2012) American Chemical Society)
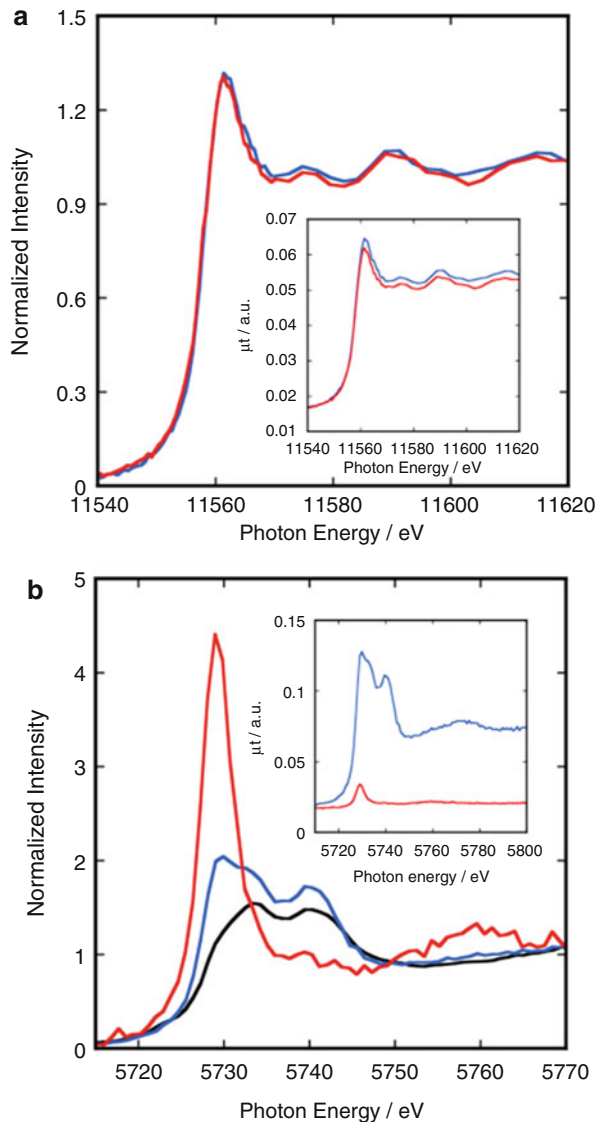
Pt–CeO$_x$/C catalyst. Instead, the shape of the XANES spectra at the Ce L$_{III}$ of the Pt–CeO$_x$/C catalyst dramatically changed: at 0.5 V, the doublet peaks corresponding to Ce^{4+} are hardly visible and only the peak corresponding to Ce^{3+} was observed at 5729 eV. When the potential was made more positive than 1.1 V, not only the Ce^{3+} single peak but also the doublet peak corresponding to Ce^{4+} was observed. The potential dependencies of the WL intensity of Pt in the Pt/C catalyst and the WL intensities of Pt and the intensities of Ce^{3+} and Ce^{4+} in
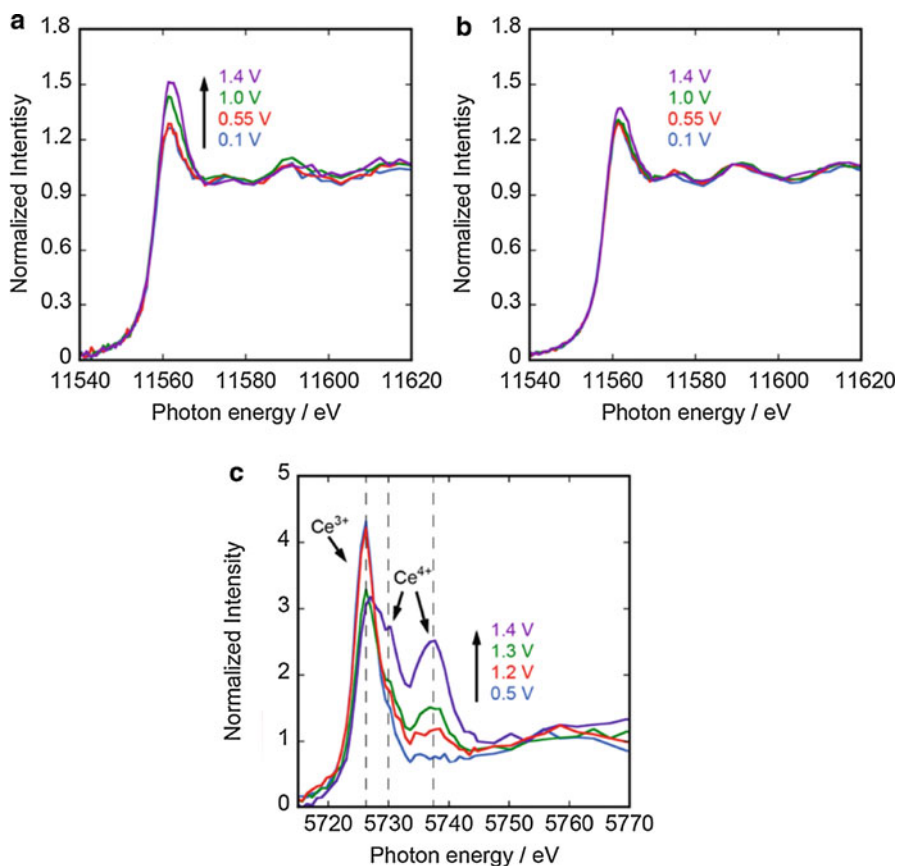
Fig. 7.21 Potential-dependent XANES spectra at the (**a**, **b**) Pt L$_{III}$ and (**c**) Ce L$_{III}$ edges of (**a**) Pt/C and (**b**, **c**) Pt–CeO$_x$/C in a 0.5 M H$_2$SO$_4$ solution saturated with O$_2$ [48]

the Pt–CeO$_x$/C catalyst are summarized in Fig. 7.22. In the case of the Pt/C catalyst, the Pt surface is partly covered by Pt oxide at the potentials where the ORR takes place. In contrast, in the case of the Pt–CeO$_x$/C catalyst, formation of the Pt oxide is significantly suppressed and the Ce^{3+} species was oxidized to the Ce^{4+} species as the potential goes more positive. It was suggested that the Ce^{3+} species was oxidized instead of Pt due to the electronic communication between Pt and CeO$_x$ at the Pt–CeO$_x$ interface, leading to the suppression of Pt oxide formation. The ORR activity at the Pt surface is known to be higher than that at the Pt oxide surface. Hence, it can be concluded that the Pt–CeO$_x$/C catalyst shows higher electrocatalytic activity for the ORR because the intrinsic catalytic activity of the Pt surface is exerted through the suppression of Pt oxide formation by CeO$_x$.
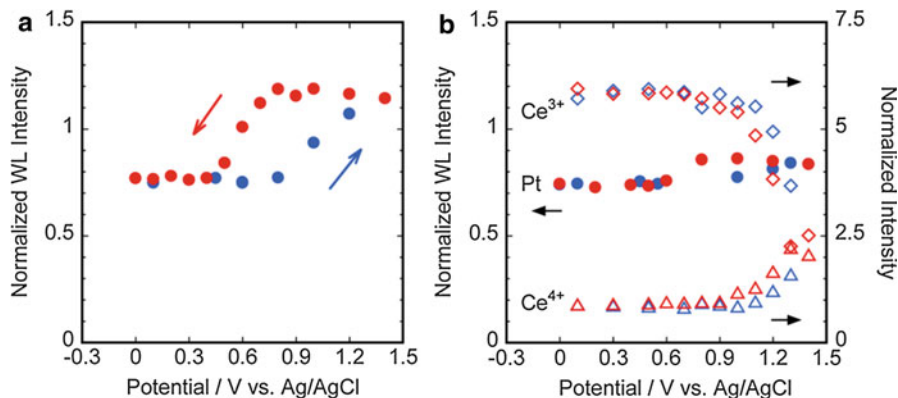
Fig. 7.22 Normalized WL intensities of (**a**) Pt/C and (**b**) Pt–CeO$_x$/C in a 0.5 M H$_2$SO$_4$ solution saturated with O$_2$ as a function of the potential in the positive (*blue*)- and negative (*red*)-going scans (Reprinted with permission from [48]. Copyright (2012) American Chemical Society)

Potential-Dependent Structural Changes of Pt-Based Electrocatalysts for the ORR

Because the fuel cell reactions take place at the electrocatalyst/electrolyte interfaces, understanding of various interfacial processes, which affect the reaction kinetics and stability of the electrodes, is a key to the improvement of cell performance and durability. Extensive research has been performed to understand the ORR mechanism and identify the major cause for degradation of the ORR activity, by various techniques including TEM [351–356], XRD [357–360], XPS [361–364], and XAFS. The effect of structural changes of the catalyst layer on the cell performance and degradation of the PEM fuel cell has been already well documented in review papers [139, 324], and not many new important findings have been made by XAFS analysis in the last several years. However, various new techniques have been utilized to confirm those previously reported results.

Iwasawa and his coworkers utilized DXAFS and QXAFS techniques for in situ time-resolved analysis of the structural changes of Pt-based electrocatalysts [40–45]. The time-resolved QXAFS procedure and schematics of the experimental setup are shown in Fig. 7.23.

XANES and EXAFS of the electrocatalysts were typically recorded every 100 ms and 500 ms, respectively, together with the current response after the potential step, and the structural parameters such as the WL intensity and coordination numbers of Pt–O and Pt–Pt bonds were determined for each spectrum by curve fitting of the normalized XANES and Fourier-transformed EXAFS oscillations, respectively, to yield the time courses of these parameters [42, 43, 45]. Figure 7.24 shows a typical series of XAFS spectra and time courses of electric charge and structural parameters.

It should be noted, however, that since the estimated parameters were averages of the overall Pt species, the change of each parameter was attributed to numerous
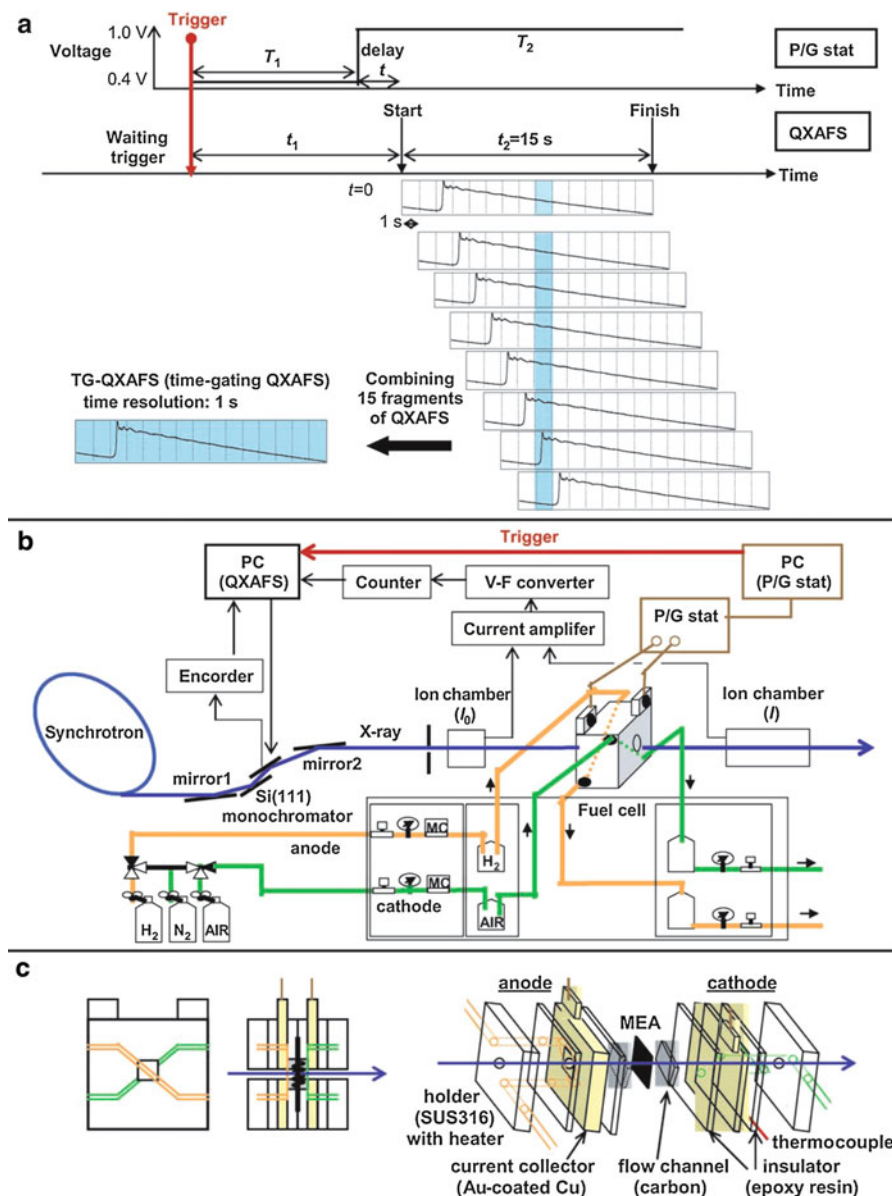
Fig. 7.23 (**a**) Procedure for time-resolved QXAFS measurements. Schematics of (**b**) the experimental setup and (**c**) in situ XAFS cell (From [40]. With permission from John Wiley and Sons)

elementary steps including the adsorption/desorption of water, oxygen molecules, atomic oxygen, and other oxygen species. Moreover, one has to be very careful about the definition of electron transfer rates in this work. Although detection of intermediate species at electrode surfaces is one of the most attractive points of in
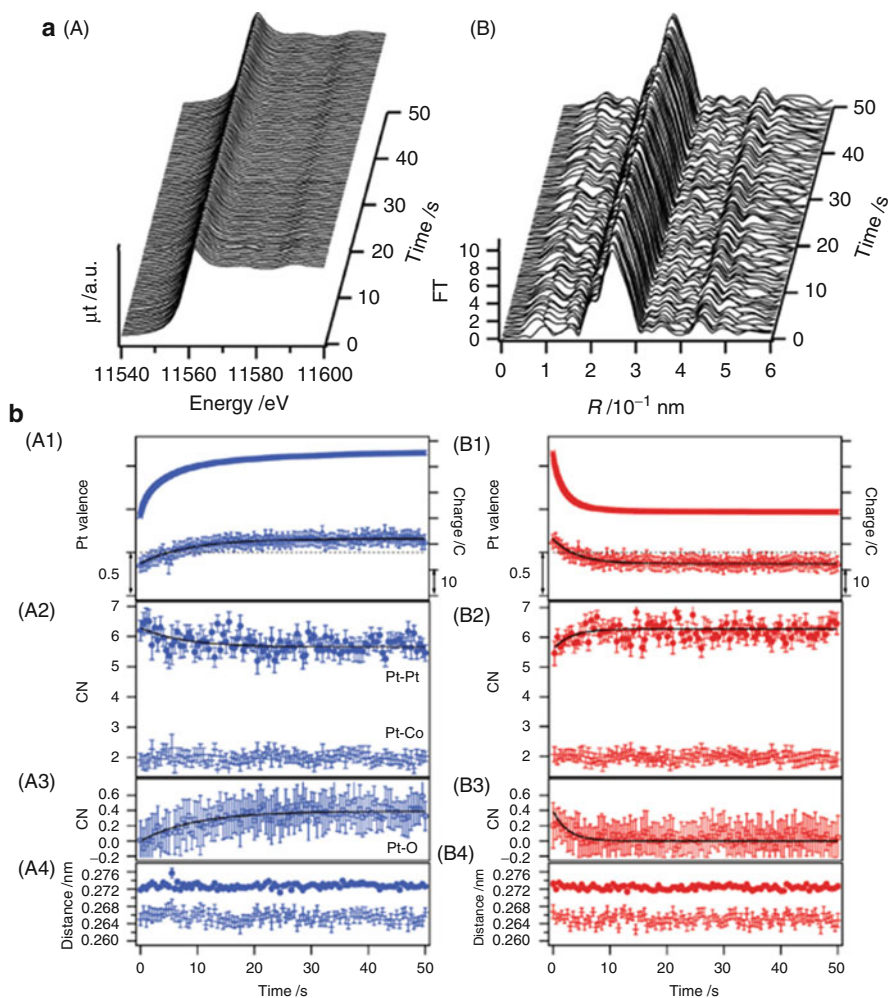
Fig. 7.24 (continued)

situ dynamic measurements, new species which cannot be detected by conventional steady-state measurements were not observed at present.

Iwasawa and his coworkers also utilized the QXAFS technique in combination with mapping [69] and x-ray computed tomography (XCT), namely, 3D laminography–XAFS [365], to visualize the 2D and 3D distributions of Pt in the MEA at a micrometer scale before and after durability tests, including oxidation states and local structures of Pt (Fig. 7.25).

The combination of XAFS and spatially resolved techniques provided experimental support for early reports of phenomenon such as dissolution, migration, and

C   **(A) Pt-Co/C**

e$^-$ transfer (k_{e2} = 0.258 s^{-1})

Pt-Pt bond breaking (k_{Pt-Pt} = 0.13 s^{-1})

e$^-$ transfer (k_{e1} = 2.86 s^{-1})   changing in Pt charge density (k_{Pt} = 0.12 s^{-1})

Pt-O bond formation (k_{Pt-O} = 0.10 s^{-1})

changing in Pt charge density   e$^-$ transfer (k'_{e1} = 3.68 s^{-1})

(k'_{Pt} = 0.24 s^{-1})

● Pt

● Co   Pt-Pt bond re-formation (k'_{Pt-Pt} = 0.3 s^{-1})   e$^-$ transfer (k'_{e2} = 0.484 s^{-1})

● O   Pt-O bond breaking (k'_{Pt-O} = 0.4 s^{-1})

0.4 V   1.0 V

(B) Pt/C

e$^-$ transfer (k_{e2} = 0.167 s^{-1})   Pt-Pt bond breaking (k_{Pt-Pt} = 0.088 s^{-1})

Pt-O bond formation (k_{Pt-O} = 0.076 s^{-1})

e$^-$ transfer (k_{e1} = 1.84 s^{-1})   changing in Pt charge density

(k_{Pt} = 0.073 s^{-1})

e$^-$ transfer (k'_{e1} = 2.16 s^{-1})

Pt-Pt bond re-formation (k'_{Pt-Pt} = 0.078 s^{-1})

● Pt   Pt-O bond breaking (k'_{Pt-O} = 0.11 s^{-1})   e$^-$ transfer (k'_{e2} = 0.259 s^{-1})

● O   changing in Pt charge density (k'_{Pt} = 0.14 s^{-1})

0.4 V   1.0 V

Fig. 7.24 (**a**) A series of time-resolved XAFS spectra at the Pt L_{III} edge of Pt$_3$Co/C assembled in MEA. (**b**) Time courses of electric charge and structural parameters. (**c**) Proposed structural kinetics of the surface events (Reprinted with permission from [42]. Copyright (2012) American Chemical Society)

agglomeration of Pt during the durability test. In particular, the mapping XAFS found the segregation of Pt^{2+} components coordinated with four oxygen species in a microcrack area of the MEAs.

Oxide Formation Process at Pt-Based Electrocatalysts During the ORR

Degradation of Pt catalysts has been extensively studied, and agglomeration due to the dissolution/redeposition of Pt catalysts at the ionomer/Pt interface is known to be the primary origin. It was proposed that the dissolution of Pt was affected by the potential, particle size of catalysts, and oxide formation. Thus, an understanding of the oxidation states and local structures of Pt catalysts at an atomic level is essential to design a long-lived catalyst. Although oxide formation at Pt electrode surfaces seems a very basic issue not only in fuel cell research but also for fundamental electrochemistry, it has been discussed for a long period of time [366, 367].
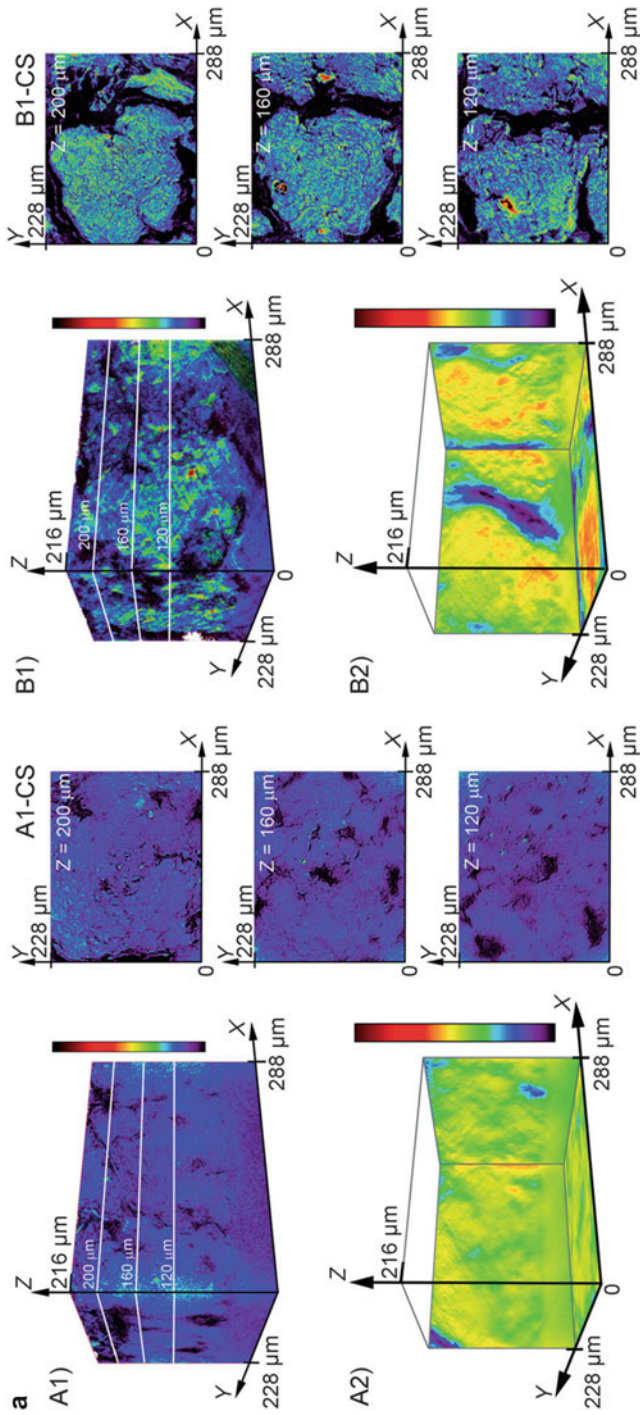
Fig. 7.25 (continued)
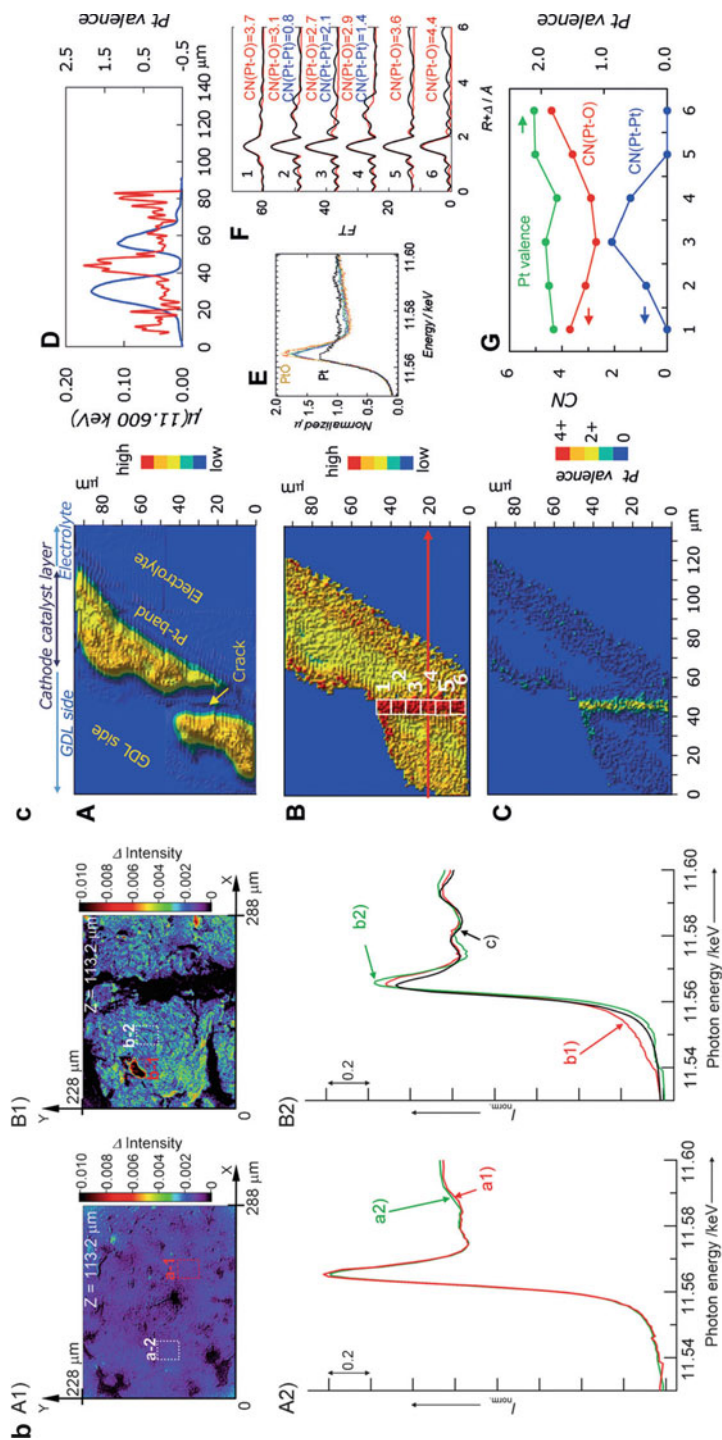
Fig. 7.25 (**a**) The distribution of Pt in the cathode catalyst layer in an MEA (**a**) before and (**b**) after degradation, observed by 3D laminography–XANES (From [286]. With permission from John Wiley and Sons). (**b**) Spatially resolved laminography–XANES at the Pt L$_{III}$ edge of the catalyst layer (From [286]. With permission from John Wiley and Sons). (**c**) Mappings of (A) the Pt L$_{III}$ edge jump, (B) WL intensity, (**c**) Pt valence of the MEA after degradation (From [69]. With permission from John Wiley and Sons), (**d**) Line profile of the absorbance (From [69]. With permission from John Wiley and Sons), (**e**) XANES spectra (From [69]. With permission from John Wiley and Sons), (**f**) Fourier-transformed EXAFS spectra, and (**g**) structural parameters at each area [69]

Imai and his coworkers systematically investigated the oxidation behaviors of the platinum nanoparticles and platinum skin layers of Pt–Co bimetallic nanoparticles in sulfuric acid solutions by in situ time-resolved XRD and DXAFS [259, 287]. The combination of the two complementary techniques enabled them to track both the structural changes and oxidation state of Pt during the formation of a few monolayers of Pt oxide. At the early stage of Pt oxide formation, relatively longer Pt–O bonds, 2.2–2.3 Å, probably corresponding to the adsorption of intermediate species such as OHH and/or OH species, were formed by partial oxidation of water, and then the surface oxygen species was oxidized to atomic oxygen with a Pt–O bond length of 2.0 Å. The atomic oxygen was exchanged with an outermost layer of the Pt nanoparticles, forming an initial monolayer oxide in a α-PtO$_2$-like structure, that is, place exchange [368]. Finally, the 3D Pt oxide in a β-PtO$_2$-like structure was formed by repeating the adsorption of oxygen species on the outermost Pt, followed by the place exchange.

Kongkanand et al. investigated the oxide formation processes at Pt in perchloric acid solution in the presence of molecular oxygen and found that place exchange occurs at a potential more negative than that in the absence of molecular oxygen [288]. Substantial roughening at relatively negative potentials, probably due to the place exchange, was also observed by electrochemical STM (EC-STM) only when O$_2$ was present, and Pt dissolution was significantly enhanced in this case [369]. Thus, it was proposed that this potential shift may affect the ORR activity and Pt dissolution. Formation of PtO$_2$ via the place exchange was confirmed in the MEA configuration where carbon-supported Pt nanoparticles were bound to a Nafion® membrane by Redmond et al. [289].

4.2.3 In Situ XAFS Characterization of Well-Defined Metal Layers Deposited on Foreign Metals

Well-defined metal layers deposited on single-crystal electrode surfaces, such as a UPD metal monolayer, are one of the electrochemical interfaces most studied by various in situ techniques, including SXS. There are a few advantages of XAFS over SXS to investigate electrochemically deposited metal layers: (1) XAFS is applicable not only to single-crystal surfaces but also to nanoparticles, and (2) XAFS can selectively probe the oxidation state and local structure of the outermost layer by utilizing bulk penetrating hard x-rays if a well-defined metal monolayer can be formed on a foreign metal substrate. Currently, determination of the electronic structure and local geometry of those metal layers on single-crystal surfaces and nanoparticles is of great interest not only for fundamental science but also for their potential applications for electrocatalysts in PEMFCs [290, 293, 294, 370, 371].

Vacuum-Deposited Metal Layers on Single-Crystal Surfaces

Friebel and Nilsson et al. prepared a well-defined Pt monolayer on a Rh(111) electrode by vacuum deposition. After confirming the formation of a perfect 2D monolayer of Pt, the Pt oxide formation process at the Pt/Rh(111) surface was investigated by means of the high-energy-resolution fluorescence detection (HERFD) XAS technique and ab initio multiple-scattering calculations using the

FEFF code [284]. As compared to conventional XAS spectra, spectral features such as an increase in both width and intensity of WL due to adsorption of oxygen species and the formation of Pt oxide are significantly enhanced, so that adsorbed oxygen species can be distinguished from Pt oxides. Formation of the Pt oxide was confirmed by a decrease of the number of the Pt–Pt and Pt–Rh bonds and the appearance of a new peak corresponding to a Pt–O bond. According to the WL intensity, the coverage of the oxygen species is less than 25 %, implying a relatively low oxygen affinity. In addition, it was proposed that the Pt oxide formed at the Pt/Rh(111) substrate is not PtO_2, as was proposed in other papers [259, 289] discussed in section "Oxide Formation Process at Pt-Based Electrocatalysts During the ORR", but was actually an ultrathin Pt oxide film composed of square planar PtO_4 with the Pt in a higher oxidation state than in PtO. This contradiction with the situation for pure Pt nanoparticles is probably due to ligand and strain effects of the underlying Rh(111) substrate. To study the effect of nanostructuring of the deposited Pt layer on the adsorption strength of chemisorbed species such as atomic hydrogen and oxygen species (OH groups and atomic oxygen), 3D Pt islands were prepared on a Rh(111) surface by a wet chemical approach involving a redox displacement of a Cu UPD monolayer with Pt. On the 3D Pt/Rh(111) surface, the ligand and strain effects became significantly smaller than on the 2D Pt/Rh(111) surface due to the formation of multilayers of Pt which can serve as pure Pt. Consequently, the adsorption energies return to the values found for pure Pt.

Friebel and Nilsson et al. also carried out in situ HERFD XAS of the 3D Pt islands formed on Rh(111) and Au(111) surfaces, as model systems for bimetallic electrocatalysts in PEMFCs, at various potentials to elucidate the degradation mechanism of Pt [372]. Adsorption of oxygen species and the formation of Pt oxide were slow at the Pt/Rh(111) surface as observed at the 2D monolayer of Pt on the Rh(111) surface. In contrast, dissolution of Pt was promoted at the Pt/Au(111) surface because of the mismatch of surface energies, so that Au is preferentially exposed.

Electrochemically Deposited Metal Layers on Single-Crystal Surfaces

Since the original work of Abruña et al. [226], a Cu UPD monolayer on a Au(111) surface is one of the UPD metal monolayer systems most studied by in situ XAFS analysis [226, 373–377]. Not only is the Cu UPD on a Au(111) surface still of great interest [290, 378] but various other systems [291–293] also. It was proposed that a Cu adlayer that has Cu adatoms located on threefold hollow sites on the Au(111) substrate in a $(\sqrt{3} \times \sqrt{3})R30°$ structure ($\theta sc = 0.67$) with coadsorbed sulfate in a $(\sqrt{3} \times \sqrt{3})R30°$ structure ($\theta sc = 0.33$) was formed prior to formation of a (1×1) structure [290, 375, 376]. A conflicting model, in which Cu adatoms adopt a $(\sqrt{3} \times \sqrt{3})R30°$ structure at lower coverage and then transform to a (1×1) structure via a $c(5 \times 5)$ structure, was also proposed [373, 374].

Rayment et al. performed in situ XAFS characterization of a Cu UPD monolayer formed on a Au(111) surface premodified with a self-assembled monolayer (SAM) of butanethiol [290]. XAFS spectra were collected in both the p- and s-polarizations. Analysis of the p-polarization EXAFS data suggested that Cu

ions penetrate between the SAM and Au(111) surface and that Cu adatoms sit on the face-centered cubic threefold hollow sites of the Au(111) surface with a coadsorbed overlayer of butanethiol sulfur atoms in a $(\sqrt{3} \times \sqrt{3})R30°$ structure on the Cu UPD monolayer. However, the S/N ratio of the spectra obtained in the s-polarization was too low to allow it to be analyzed and any information about the Cu-Cu bond, which is perpendicular to the surface normal, was absent because the EXAFS oscillations at the K absorption edge is polarization sensitive (see Sect. 3.2.4).

Friebel and Nilsson et al. investigated the interfacial structure of Cu mono- and multilayer deposited Au(111) surfaces in alkaline solutions and found significant differences in their redox behaviors [378]. In situ Cu K edge HERFD XAS spectra of the Cu 1ML/Au(111) and 7ML/Au(111) systems showed that Cu monolayers deposited on a Au(111) surface are expanded by 12.5 % and their oxidation occur at more positive potential than pure Cu and structurally relaxed Cu multilayers. It is thought that Cu monolayers on a Au(111) surface is more stable against oxidation due to the modulation of the electronic structure caused by the tensile strain. In addition, the Cu monolayer in a metallic state was directly converted to CuO, whereas a Cu multilayer was oxidized to CuO via an intermediate Cu_2O phase. They also proposed that deposited Cu atoms are unstable with respect to place exchange with underlying Au atoms.

Electrochemically Deposited Metal Layers on Nanoparticles

Electrochemically deposited metal layers on nanoparticles have attracted much attention as more practical materials. Various core–shell-type nanoparticles have been synthesized to modulate the electronic structure of outermost layers and have been characterized by in situ XAFS analysis.

Asakura et al. prepared Pt-shell Au-core electrocatalysts on carbon supports by depositing Pt on Au nanoparticles and found that the ORR activity of the Pt/Au core–shell electrocatalyst is higher than that of conventional carbon-supported Pt catalysts [28, 279]. In situ XAFS analysis of the Pt/Au core–shell catalysts was conducted in a N_2-saturated solution at the potential where the ORR takes place in an O_2-saturated solution. Although XANES spectra at the Pt and Au L_{III} absorption edges can provide useful information of their d-band states, the Pt L_{III} edge EXAFS oscillation for the Pt/Au core–shell catalysts cannot be measured to perform a reliable curve-fitting analysis because Au L_{III} edge rises only ca. 350 eV above the Pt L_{III} edge. Thus, XAFS spectra at the Pt and Au K edges were measured in the present work. According to the analyses of EXAFS oscillation by two-shell curve fitting, in the Pt/Au core–shell catalysts, the coordination number of Pt–Pt is much smaller than that of Au–Au, confirming a core–shell structure in which more Pt than Au is on the surface. One may expect that the Pt–Pt bond length would be elongated due to the strain effect from the underlying Au since the lattice constant of Au is longer than that of Pt. However, both the Pt–Pt and Au–Au bond lengths for the Pt/Au/C were smaller than those for corresponding metal foils. They attributed this unusual result to the contraction of the Au core induced by strong Pt–Pt bonds and claimed that the formation of

contracted core–shell catalysts is a primary reason for the improved ORR activity. Although all the measurements were performed in the absence of O_2, the effect of O_2 on the core–shell structure seems very important because recent studies have suggested that Pt dissolution was significantly enhanced in the presence of O_2, as introduced in section "Oxide Formation Process at Pt-Based Electrocatalysts During the ORR" [288, 369].

Russell et al. prepared Au-core Pt-shell nanoparticles by two methods based on the combination of thiol encapsulation and displacement of a Cu UPD layer with Pd: (1) a Cu UPD layer was first formed on Au nanoparticles prepared by a thiol encapsulation method and then displaced with Pd ions, and (2) a Cu UPD and its displacement with Pd were simultaneously performed in a one-pot method [294]. In situ Au L_{III} and Pd K edge XAFS measurements of these Pd/Au nanoparticles were carried out at various potentials. At the Au L_{III} edge for both samples, only Au-Au bonds were detected and Au–Pd bonds were absent. In addition, the coordination number and bond length of the first shell Au–Au bond are independent of the applied potential, showing the formation of Au cores. At the Pd K edge, both Pd–Pd and Pd–Au bonds were observed, confirming the formation of a Pd-core Au-shell structure. When the potential was swept to -0.655 V vs. Hg/Hg_2SO_4, at which hydrogen absorption in the Pd lattice occurs, expansion of the Pd–Pd bond was observed only for Pd/Au (1) system, suggesting the formation of segregated Pd islands at the Au core surface. In contrast, such expansion of Pd–Pd bonds was not observed for the Pd/Au (2) system, and the coordination number of Pd–Pd is smaller than that of Pd–Au, showing the formation of a Au core surrounded by alloyed Pd/Au shell.

4.2.4 In Situ XAFS Characterization of Materials for Rechargeable Batteries

Rechargeable LIBs hold a prominent position as electrical energy storage devices in a sustainable energy scheme. Lithium-transition metal complex oxides (Li metal oxides) are the most widely used positive electrode materials. One of the most important requirements as positive electrodes for LIBs is a reversible lithiation/delithiation capability without drastic structural changes, which is a determining factor for long-term durability. To date, most research has focused on the improvement of battery performance by synthesizing new materials for positive electrodes. However, an understanding of the reaction mechanism, including undesirable side reactions, may provide new insights to design more reliable positive electrode materials. The usefulness of the in situ XAFS analysis for energy devices such as batteries and fuel cells had been recognized early [25], and it is still one of the major applications [254].

Phase Transition and Valence Change of Transition Metal in Positive Electrodes During Charging/Discharging Processes

Many groups have used in situ XAFS, often in combination with XRD, to investigate the electronic and local structural conversion of transition metals in various Li metal oxides such as $LiCoO_2$ [268, 269, 274], $LiNi_xMn_{1-x}O_4$ [270, 277], $LiMn_3O_4$ [309], $LiFePO_4$ [271, 272, 306, 308, 310, 379], $Li_{2-x}VTiO_4$ [312],

$LiFe_xMn_{1-x}PO_4$ [316, 318], $LiNi_xCu_yMn_{2-x-y}O_4$ [380], Li_2MnSiO_4 [311], Li_2FeSiO_4 [273, 311], $Li_3V_2(PO_4)_3$ [381], and other complicated oxides [315, 317] induced by lithiation/delithiation processes. Although the target materials are different, most of the recent studies are basically repetitions of the work performed by Nakai et al. in the 1990s [260–267].

$LiCoO_2$ has been the most widely used positive electrode material in LIBs since its development by Goodenough and his coworkers [382, 383]. Takamatsu et al. carried out the in situ XAFS analysis of $LiCoO_2$ for the first time after the initial charging and discharging process in the total-reflection fluorescence mode [268]. Two incident angles were adopted to obtain information not only from the surface ($\sim$3 nm to the surface) but also from the bulk (greater than 100 nm to the surface). In situ XANES spectra showed that Co ions in the bulk underwent a reversible interconversion between Co^{3+} and Co^{4+} after charging and discharging processes, suggesting that the layered structure was maintained. In contrast to the bulk, when the material was soaked in a 1:1 volumetric mixture of ethylene carbonate and diethyl carbonate containing 1 M $LiClO_4$, surface Co ions of the $LiCoO_2$ were reduced and were oxidized by charging. The oxidized Co ions did not recover to the original state after discharging. The authors attributed this to the initial degradation of the electrode, although the resulting material was not identified. Later, they reported that this initial degradation can be avoided by coating the $LiCoO_2$ surface with a ZrO_2 layer [269].

Time-resolved in situ XAFS techniques have been utilized to track the dynamic electronic and local structural changes of the $LiFePO_4$ during electrochemical lithium extraction and insertion [271, 272, 306, 308]. During the extraction/insertion of Li, an isosbestic point was observed, confirming the two-phase reaction between Li-rich ($LiFePO_4$) and Li-poor ($FePO_4$) phases. The corresponding transient change of the lattice constant was successfully observed by time-resolved in situ XRD [271, 272, 307, 384].

Abruña et al. carried out in situ XAFS measurements of Mn_3O_4 during insertion and extraction of Li to identify the structure of the Mn oxide species in each process [309]. The authors more quantitatively assigned electrochemical features to specific reactions, although most of the other researches mainly paid attention to the phase transitions and valence changes of the metal oxides during lithiation/delithiation and their reversibility. As a result, a significant fraction of the charge was consumed not by the desired lithiation/delithiation in the Mn oxide compounds but by conversion reaction of non-Mn-centered species.

Komaba and his coworkers have also extensively applied XAFS to a new class of electrode materials not only for rechargeable lithium batteries but also for sodium ion batteries, such as Nb_2O_5 [385], FeF_3 [386], $Na_{1-x}Ni_{0.5}Mn_{0.5}O_2$ [387] and Li_2MnO_3-$LiCoO_2$-$LiCrO_2$ [388].

4.2.5 Other Applications

The photoelectrochemical and photocatalytic HER, the oxygen evolution reaction (OER), and the carbon dioxide reduction reaction on semiconductors have been extensively studied because of the interest in solar to chemical energy conversion.

Most of the semiconductors with a suitable bandgap for solar energy conversion are corrosive in aqueous solutions and are not catalytically active for these complicated multi-electron transfer reactions. Although many groups have examined the modification of the semiconductor surfaces by catalytic layers with metals, metal oxides, and/or organic molecules, both the efficiency and durability are still very far from practical use. A critical requirement for its practical use is the development of highly efficient and durable catalysts from earth-abundant materials.

Various interesting processes are involved in the photoelectrochemical and photocatalytic multi-electron transfer reactions, such as light absorption, formation of electrons and holes, transfers of those carriers to the reaction sites, and multi-electron transfer reactions. Hence, an understanding of the structural change and oxidation states of those materials during photoelectrochemical and photocatalytic processes is still very important from the viewpoint of fundamental science, and in situ XAFS measurements have been utilized to identify the local structure and oxidation states of reaction active sites.

Photoelectrochemical Hydrogen Evolution Reaction

Recently, we have demonstrated that an efficient photoelectrochemical HER can be achieved at Si(111) electrodes modified with an ordered molecular layer containing viologen moieties and a Pt complex as electron transfer mediator and catalyst, denoted as a Pt–V^{2+}–Si(111) surface [389, 390]. A hydrogen-terminated Si(111) surface was modified with the multilayer of viologen moieties by sequential surface chemical reactions, and the viologen-modified Si(111) surface was then immersed in an aqueous solution containing K_2PtCl_4 to replace the counteranions of viologen moieties with $PtCl_4^{2-}$ by an ion exchange reaction, to yield the Pt–V^{2+}–Si(111) surface, as shown in Fig. 7.26.

The HER rate is significantly enhanced after the incorporation of Pt complexes within the molecular layer. Since the HER took place at a potential much more negative than the redox potential of most Pt complexes, e.g., +0.51 V vs. Ag/AgCl for $PtCl_4^{2-}$, we concluded that the Pt complexes were reduced to form Pt metallic
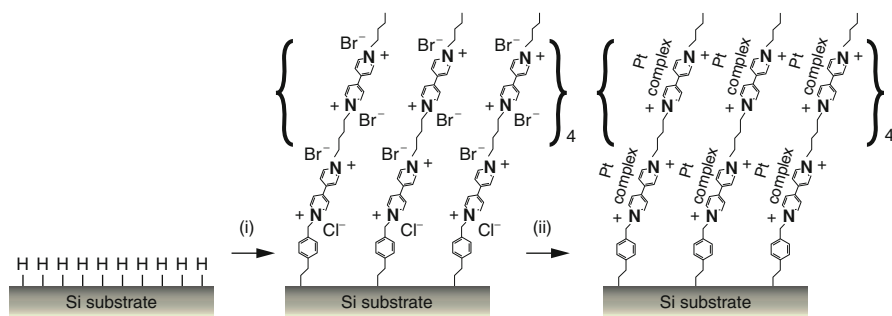
Fig. 7.26 Schematic illustration of surface modification steps to produce a Pt–V^{2+}–Si(111) surface (From [46]. With permission from John Wiley and Sons)
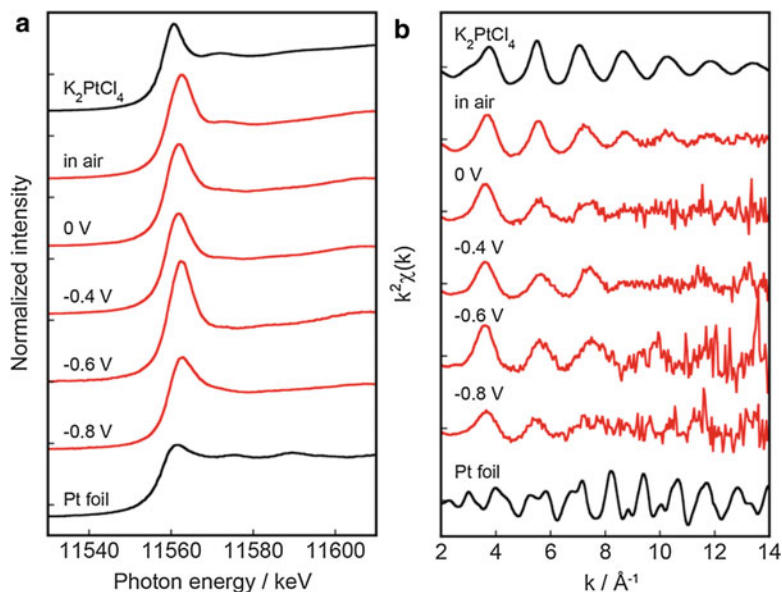
Fig. 7.27 XANES and EXAFS oscillations of the Pt–V^{2+}–Si(111) surface in air and in contact with 0.1 M Na_2SO_4 solution at various potentials, together with those for K_2PtCl_4 and Pt foil as references (From [46]. With permission from John Wiley and Sons)

nanoparticles and that Pt metallic nanoparticles are the actual catalyst for the HER [390]. However, such nanoparticles were not observed by SEM, and the peak position of the Pt 4f peaks in the XPS spectrum of the Pt–V^{2+}–Si(111) surface after use for the HER was at a higher binding energy than that of Pt in the metallic state by ca. 2 eV. Thus, since these observations suggested that the Pt complexes serve as a molecular catalyst without being converted into Pt nanoparticles, in situ PTRF-XAFS analysis of the Pt–V^{2+}–Si(111) surface was performed to precisely identify the local structure and oxidation state of the Pt catalysts [46]. Figure 7.27 shows the XANES and EXAFS oscillations of the Pt–V^{2+}–Si(111) surface in air and in contact with 0.1 M Na_2SO_4 solution at various potentials, together with those for K_2PtCl_4 and Pt foil as references.

In the Pt–V^{2+}–Si(111) surface measured in air, a small shoulder which is characteristic of Pt–Cl bonds was observed just above the WL peak in the XANES spectra, and the period of EXAFS oscillations is in reasonable agreement with that for K_2PtCl_4, confirming that $PtCl_4^{2-}$ was successfully inserted into the molecular layers. When the Pt–V^{2+}–Si(111) surface was kept at 0 V and the potential goes more negative, the shoulder attributable to the Pt–Cl bonds gradually decreased and disappeared at -0.6 V. In addition, three waves in the region of $k = 8 - 12$ of the EXAFS oscillation weakened and became two waves at -0.6 V. These results showed that the Pt–Cl bonds were replaced by oxygen species but no Pt–Pt bonds were formed, which was supported by a FEFF simulation. Thus, Pt nanoparticles were not formed even when the HER took place and the Pt complexes

acted as molecular catalysts for the HER while confined within the molecular layer. Probably, the migration and aggregation of Pt complexes to form Pt nanoparticles were inhibited since the complexes were separated by molecular layers.

Photoelectrochemical Water Oxidation for Photocatalytic Water Splitting

Modification of semiconductor surfaces by metal oxides is an effective approach to enhance the catalytic activity for multi-electron transfer reactions. Among the various metal oxides, Mn oxides, which are analogs of the water oxidation center of photosynthesis, $CaMn_4O_x$, bound to the Photosystem II (PSII), have attracted much attention, not only because of their high electrocatalytic activity for the water oxidation reaction, i.e., OER, but also because of the interest in a unique role of $CaMn_4O_x$ in the water oxidation.

A variety of Mn-based compounds were synthesized, but most of them tested in homogeneous solution did not catalyze the OER. Recently, Hocking and coworkers synthesized a tetranuclear manganese cluster embedded in a Nafion matrix, inspired by the CaMn4O4 cluster of PSII, and achieved efficient catalytic activity for the OER [391–395]. They also demonstrated its reversible interconversion between a reduced Mn^{2+} state and disordered $Mn^{3+/4+}$ oxide phase by XAFS analysis, as shown in Fig. 7.28.

Whereas a reduced Mn^{2+} state was formed by dissociation of the cluster upon photoirradiation, a disordered $Mn^{3+/4+}$ oxide phase was formed by reoxidation
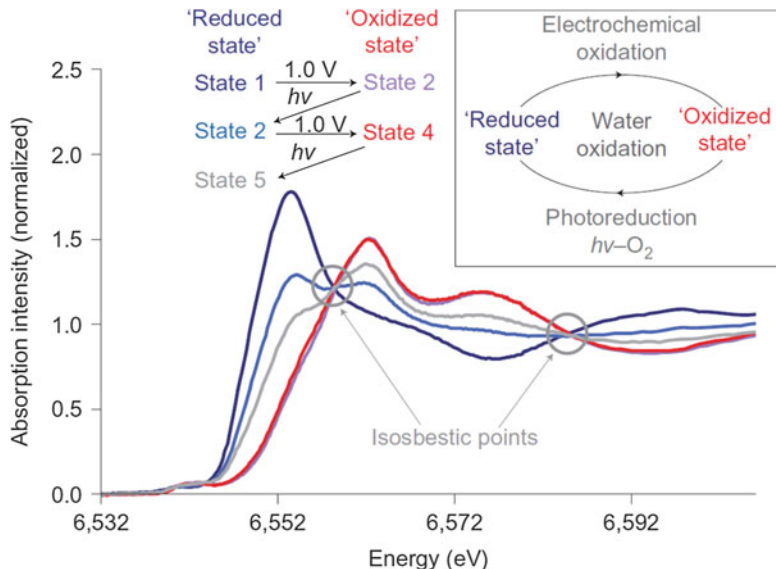
Fig. 7.28 XANES spectra at the Mn K edge of a Nafion-coated $[Mn_4O_4L_6]^+$-loaded glassy carbon (state 1) without any treatment and after (states 2 and 4) keeping the potential at 1.0 V vs. Ag/AgCl in 0.1 M Na_2SO_4 aqueous solution and (states 3 and 5) irradiation (From [391]. With permission from Nature Publishing Group)

Fig. 7.29 XANES spectra at the Mn K edge of the photodeposited MnO$_x$ on n-type SrTiO$_3$ in Ar-saturated 0.1 M Na$_2$SO$_4$ solution at (**a**) 0.5 V and (**b**) 0 V vs. RHE under UV irradiation (Reprinted with permission from [297]. Copyright (2014) American Chemical Society)
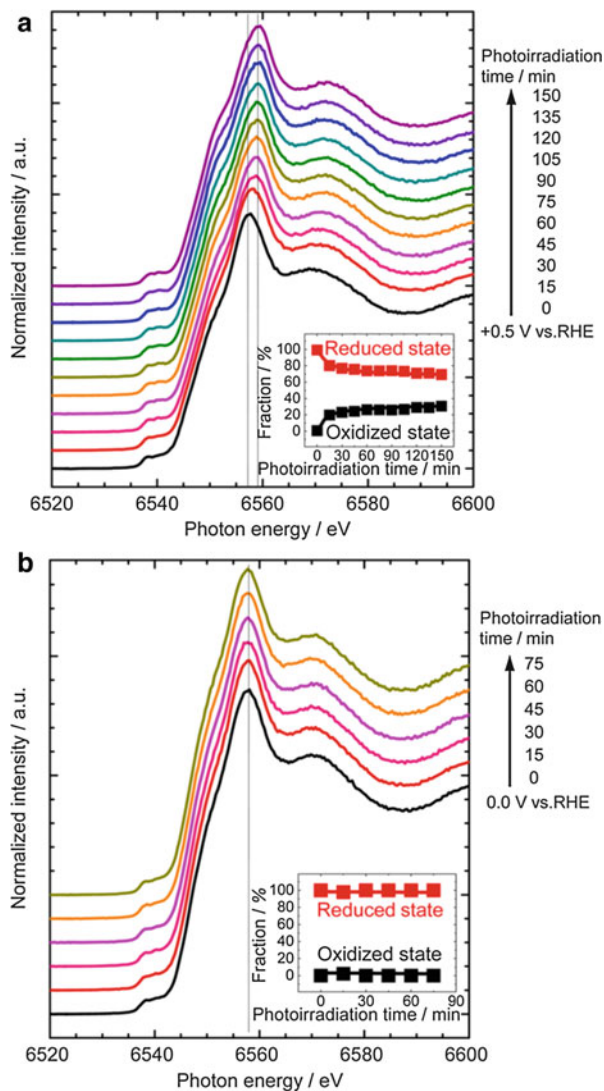
under an applied positive potential. They proposed an analogy of this cycle to the Mn biogeochemical cycling where the formation of solid Mn$^{3+/4+}$ oxides by the bacterial oxidation of the soluble Mn^{2+} species and photoreduction of the oxides to the soluble Mn^{2+} species cycles take place. They also suggested the future possible capability of Mn-based compounds as self-healing water oxidation catalysts.

Yoshida and Kondoh et al. measured in situ XAFS at the Mn K absorption edge of the photodeposited MnOx layers on n-type SrTiO3 substrates in collaboration with our group and found that the absorption edge was gradually shifted to a higher energy during photoirradiation (Fig. 7.29) [295, 297].
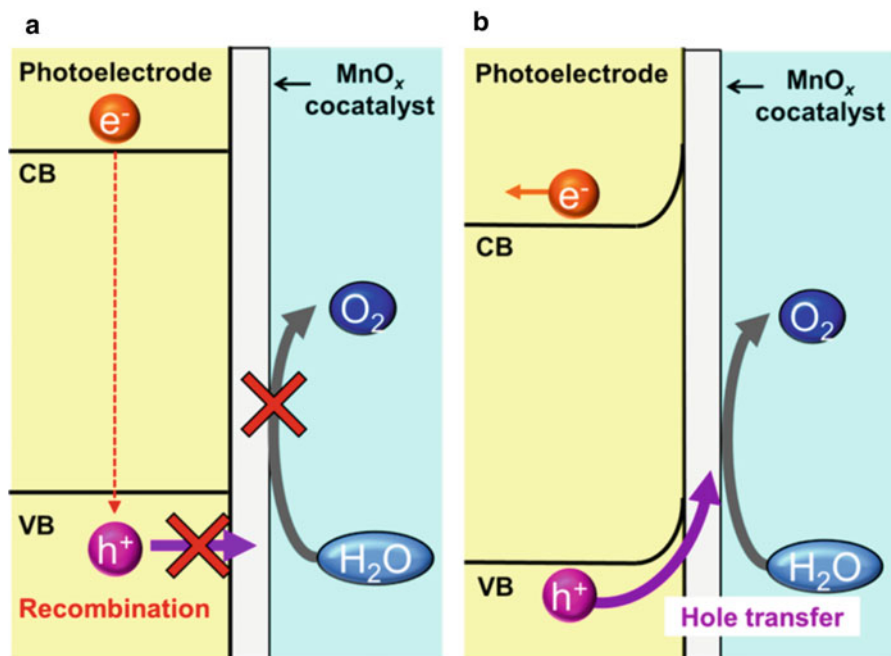
Fig. 7.30 Possible models for photoexcited carrier transfer from $SrTiO_3$ to MnO_x at (**a**) 0 V and (**b**) 1.0 V vs. RHE under photoirradiation (Reprinted with permission from [297]. Copyright (2014) American Chemical Society)

This shift was observed at a potential more positive than 0.5 V where photoexcited holes can be transferred to the interface, and the shift became more pronounced as the potential was made more positive. This shift was attributed to the oxidation of the MnO_x due to the injection of the photoexcited holes as schematically shown in Fig. 7.30.

One would expect, however, that the oxidation states of the MnO_x need to be maintained because the photoexcited holes are consumed to oxidize water immediately after their injection into the MnO_x if it serves as an active catalyst for the OER. In addition, since all the experiments were performed in the conventional step-scan mode under potentiostatic conditions, only relatively slow structural changes were detected at present, while photoinduced processes are generally much faster than the time constant. In order to clarify these points, time-resolved in situ measurements are desirable to track the dynamic photo-responses of the XANES spectra.

Jaramillo and his coworkers synthesized a nanostructured Mn oxide film which serves as an electrocatalyst not only for the ORR but also for the OER [396] and identified the active sites during these reactions by in situ XAFS measurements [52]. A disordered $Mn_3^{II,III,III}O_4$ and a mixture of two types of MnO_x, ca. 20 % of unchanged $Mn_3^{II,III,III}O_4$ and 80 % of more oxidized phase, were observed under the ORR and OER conditions, respectively.

The structures and oxidation states of other electrocatalysts for the OER such as cobalt phosphate [299] and nickel borate [300] have also been investigated by in situ XAFS measurements.

5   Conclusions and Future Perspective

The application of surface x-ray scattering (SXS) and x-ray absorption fine structure (XAFS) techniques using synchrotron radiation (SR) to structural studies at electrode/electrolyte interfaces was described, from fundamental principles and experimental methodologies to reviews of recent topics. In order not only to fundamentally understand electrochemical reactions such as surface reaction of the electrodes, crystal growth, metal deposition/dissolution, and corrosion but also to apply accumulated electrochemical knowledge to the modern nanotechnology such as batteries, fuel cells, sensors, and molecular devices, we need to know the potential-dependent structures present at the electrode/electrolyte interface, with both high spatial and high time resolution. For this purpose, it is essential to combine these in situ SXS and in situ XAFS techniques with scanning probe microscopies (SPMs) and several optical spectroscopies, in addition to theoretical calculations. When the sensitivity and the resolution of these in situ in real-time structure analysis techniques based on the technological developments increase and combination with other methods proceeds, nanotechnology will be more advanced; for example, energy density and lifetime of the batteries will become higher and longer, respectively, and sensitivity and size of the sensors will become higher and smaller, respectively. Therefore, advances in these techniques lead to our future prosperity.

References

1. Uosaki K (2015) In situ real-time monitoring of geometric, electronic, and molecular structures at solid/liquid interfaces. Jpn J Appl Phys, Part 1 54(3):030102/1–030102/14
2. Jerkiewicz G, Soriaga MP, Uosaki K, Wieckowski A (1997) Solid–liquid electrochemical interfaces. American Chemical Society, Washington, DC
3. Gewirth AA, Niece BK (1997) Electrochemical applications of in situ scanning probe microscopy. Chem Rev 97(4):1129–1162
4. Szklarczyk M, Strawski M, Bienkowski K (2008) 25 years of the scanning tunneling microscopy. Mod Aspects Electrochem 42:303–368
5. Tadjeddine A, Peremans A (1998) Non-linear optical spectroscopy of the electrochemical interface. Adv Spectrosc 26:159–217
6. Shen YR (1989) Surface-properties probed by 2nd-harmonic and sum-frequency generation. Nature 337(6207):519–525
7. Brown GS, Moncton DE (1991) Handbook on synchrotron radiation, vol 3. North Holland, Amsterdam
8. Margaritondo G (1991) Introduction to synchrotron radiation. Oxford University Press, New York
9. Willmott P (2011) An introduction to synchrotron radiation: techniques and applications. John Wiley & Sons Ltd, West Sussex

10. Melendres CA, Tadjeddine A (1994) Synchrotron techniques in interfacial electrochemistry. Springer, Dordrecht
11. Toney MF, McBreen J (1993) In situ synchrotron x-ray techniques for determining atomic structure at electrode/electrolyte interfaces. Electrochem Soc Interface 2(Spring):22–31
12. Feidenhansl R (1989) Surface-structure determination by x-ray-diffraction. Surf Sci Rep 10(3):105–188
13. Als-Nielsen J, McMorrow D (2001) Elements of modern x-ray physics. John Wiley & Sons Ltd, Chichester
14. Robinson J (1988) X-ray techniques. In: Gale RJ (ed) Spectroelectrochemistry: theory and practice. Plenum Press, New York, pp 9–40
15. Wang J, Ocko BM, Davenport AJ, Isaacs HS (1992) In situ x-ray-diffraction and x-ray-reflectivity studies of the Au(111) electrolyte interface – reconstruction and anion adsorption. Phys Rev B 46(16):10321–10338
16. Scherb G, Kazimirov A, Zegenhagen J (1998) A novel thick-layer electrochemical cell for in situ x-ray diffraction. Rev Sci Instrum 69(2):512–516
17. Scherb G, Kazimirov A, Zegenhagen J, Lee TL, Bedzyk MJ, Noguchi H, Uosaki K (1998) In situ x-ray standing-wave analysis of electrodeposited Cu monolayers on GaAs(001). Phys Rev B 58(16):10800–10805
18. Nagy Z, You H (2002) Applications of surface x-ray scattering to electrochemistry problems. Electrochim Acta 47(19):3037–3055
19. Kondo T, Zegenhagen J, Takakusagi S, Uosaki K (2015) In situ real-time study on potential induced structure change at Au(111) and Au(100) single crystal electrode/sulfuric acid solution interfaces by surface x-ray scattering. Surf Sci 631:96–104
20. Tamura K, Wang JX, Adzic RR, Ocko BM (2004) Kinetics of monolayer Bi electrodeposition on Au(111): surface x-ray scattering and current transients. J Phys Chem B 108(6):1992–1998
21. Ayyad AH, Stettner J, Magnussen OM (2005) Electrocompression of the Au(111) surface layer during Au electrodeposition. Phys Rev Lett 94(6):066106/1–066106/4
22. Krug K, Stettner J, Magnussen OM (2006) In situ surface x-ray diffraction studies of homoepitaxial electrochemical growth on Au(100). Phys Rev Lett 96(24):246101/1–246101/4
23. Iwasawa Y (1996) X-ray absorption fine structure for catalyst and surfaces. World Scientific, Singapore
24. Lytle FW (1999) The EXAFS family tree: a personal history of the development of extended x-ray absorption fine structure. J Synchrotron Radiat 6:123–134
25. McBreen J, O'Grady WE, Pandya KI (1988) EXAFS – a new tool for the study of battery and fuel-cell materials. J Power Sources 22(3–4):323–340
26. McBreen J, O'Grady WE, Pandya KI, Hoffman RW, Sayers DE (1987) EXAFS study of the nickel-oxide electrode. Langmuir 3(3):428–433
27. Dewald HD, Watkins JW, Elder RC, Heineman WR (1986) Development of extended x-ray absorption fine-structure spectroelectrochemistry and its application to structural studies of transition-metal ions in aqueous-solution. Anal Chem 58(14):2968–2975
28. Kaito T, Mitsumoto H, Sugawara S, Shinohara K, Uehara H, Ariga H, Takakusagi S, Asakura K (2014) A new spectroelectrochemical cell for in situ measurement of Pt and Au K-edge x-ray absorption fine structure. Rev Sci Instrum 85(8):084104/1–084104/8
29. Holtz ME, Yu YC, Gunceler D, Gao J, Sundararaman R, Schwarz KA, Arias TA, Abruña HD, Muller DA (2014) Nanoscale imaging of lithium ion distribution during in situ operation of battery electrode and electrolyte. Nano Lett 14(3):1453–1459
30. Mehdi BL, Gu M, Parent LR, Xu W, Nasybulin EN, Chen XL, Unocic RR, Xu PH, Welch DA, Abellan P, Zhang JG, Liu J, Wang CM, Arslan I, Evans J, Browning ND (2014) In-situ electrochemical transmission electron microscopy for battery research. Microsc Microanal 20(2):484–492
31. White ER, Singer SB, Augustyn V, Hubbard WA, Mecklenburg M, Dunn B, Regan BC (2012) In situ transmission electron microscopy of lead dendrites and lead ions in aqueous solution. ACS Nano 6(7):6308–6317

32. Wu F, Yao N (2015) Advances in sealed liquid cells for in-situ TEM electrochemical investigation of lithium-ion battery. Nano Energ 11:196–210

33. Niwa H, Kiuchi H, Miyawaki J, Harada Y, Oshima M, Nabae Y, Aoki T (2013) Operando soft x-ray emission spectroscopy of iron phthalocyanine-based oxygen reduction catalysts. Electrochem Commun 35:57–60

34. Asakura D, Hosono E, Niwa H, Kiuchi H, Miyawaki J, Nanba Y, Okubo M, Matsuda H, Zhou H, Oshima M, Harada Y (2015) Operando soft x-ray emission spectroscopy of $LiMn_2O_4$ thin film involving Li–ion extraction/insertion reaction. Electrochem Commun 50:93–96

35. Masuda T, Yoshikawa H, Noguchi H, Kawasaki T, Kobata M, Kobayashi K, Uosaki K (2013) In situ x-ray photoelectron spectroscopy for electrochemical reactions in ordinary solvents. Appl Phys Lett 103(11):111605/1–111605/4

36. Nagasaka M, Hatsui T, Horigome T, Hamamura Y, Kosugi N (2010) Development of a liquid flow cell to measure soft x-ray absorption in transmission mode: a test for liquid water. J Electron Spectrosc Relat Phenom 177(2–3):130–134

37. Nagasaka M, Yuzawa H, Horigome T, Hitchcock AP, Kosugi N (2013) Electrochemical reaction of aqueous iron sulfate solutions studied by Fe L-edge soft x-ray absorption spectroscopy. J Phys Chem C 117(32):16343–16348

38. Nagasaka M, Yuzawa H, Horigome T, Kosugi N (2014) In operando observation system for electrochemical reaction by soft x-ray absorption spectroscopy with potential modulation method. Rev Sci Instrum 85(10):104105/1–104105/7

39. Nagasaka M, Mochizuki K, Leloup V, Kosugi N (2014) Local structures of methanol–water binary solutions studied by soft x-ray absorption spectroscopy. J Phys Chem B 118(16):4388–4396

40. Tada M, Murata S, Asakoka T, Hiroshima K, Okumura K, Tanida H, Uruga T, Nakanishi H, Matsumoto S, Inada Y, Nomura M, Iwasawa Y (2007) In situ time-resolved dynamic surface events on the Pt/C cathode in a fuel cell under operando conditions. Angew Chem Int Ed 46(23):4310–4315

41. Uemura Y, Inada Y, Bando KK, Sasaki T, Kamiuchi N, Eguchi K, Yagishita A, Nomura M, Tada M, Iwasawa Y (2011) In situ time-resolved XAFS study on the structural transformation and phase separation of Pt_3Sn and PtSn alloy nanoparticles on carbon in the oxidation process. Phys Chem Chem Phys 13(35):15833–15844

42. Ishiguro N, Saida T, Uruga T, Nagamatsu S, Sekizawa O, Nitta K, Yamamoto T, Ohkoshi S, Iwasawa Y, Yokoyama T, Tada M (2012) Operando time-resolved x-ray absorption fine structure study for surface events on a Pt_3Co/C cathode catalyst in a polymer electrolyte fuel cell during voltage-operating processes. ACS Catal 2(7):1319–1330

43. Ishiguro N, Saida T, Uruga T, Sekizawa O, Nagasawa K, Nitta K, Yamamoto T, Ohkoshi S, Yokoyama T, Tada M (2013) Structural kinetics of a Pt/C cathode catalyst with practical catalyst loading in an MEA for PEFC operating conditions studied by in situ time-resolved XAFS. Phys Chem Chem Phys 15(43):18827–18834

44. Nagasawa K, Takao S, Higashi K, Nagamatsu S, Samjeske G, Imaizumi Y, Sekizawa O, Yamamoto T, Uruga T, Iwasawa Y (2014) Performance and durability of Pt/C cathode catalysts with different kinds of carbons for polymer electrolyte fuel cells characterized by electrochemical and in situ XAFS techniques. Phys Chem Chem Phys 16(21):10075–10087

45. Kityakarn S, Saida T, Sode A, Ishiguro N, Sekizawa O, Uruga T, Nagasawa K, Yamamoto T, Yokoyama T, Tada M (2014) In situ time-resolved XAFS of transitional states of Pt/C cathode electrocatalyst in an MEA during PEFC loading with transient voltages. Topics Catal 57(10–13):903–910

46. Masuda T, Fukumitsu H, Takakusagi S, Chun WJ, Kondo T, Asakura K, Uosaki K (2012) Molecular catalysts confined on and within molecular layers formed on a Si(111) surface with direct Si-C bonds. Adv Mater 24(2):268–272

47. Albarelli MJ, White JH, Bommarito GM, Mcmillan M, Abruña HD (1988) In situ surface EXAFS at chemically modified electrodes. J Electroanal Chem 248(1):77–86

48. Masuda T, Fukumitsu H, Fugane K, Togasaki H, Matsumura D, Tamura K, Nishihata Y, Yoshikawa H, Kobayashi K, Mori T, Uosaki K (2012) Role of cerium oxide in the enhancement of activity for the oxygen reduction reaction at Pt-CeOx nanocomposite electrocatalyst – an in situ electrochemical x-ray absorption fine structure study. J Phys Chem C 116(18):10098–10102

49. Kordesch ME, Hoffman RW (1984) Electrochemical-cells for in situ EXAFS. Nucl Instrum Methods Phys Res Sect A 222(1–2):347–350

50. Davenport AJ, Isaacs HS, Frankel GS, Schrott AG, Jahnes CV, Russak MA (1991) In situ X-ray absorption study of chromium valency changes in passive oxides on sputtered AlCr thin-films under electrochemical control. J Electrochem Soc 138(1):337–338

51. Velasco-Velez JJ, Chuang CH, Han HL, Martin-Fernandez I, Martinez C, Pong WF, Shen YR, Wang F, Zhang YG, Guo JH, Salmeron M (2013) In-situ XAS investigation of the effect of electrochemical reactions on the structure of graphene in aqueous electrolytes. J Electrochem Soc 160(9):C445–C450

52. Gorlin Y, Lassalle-Kaiser B, Benck JD, Gul S, Webb SM, Yachandra VK, Yano J, Jaramillo TF (2013) In situ x-ray absorption spectroscopy investigation of a bifunctional manganese oxide catalyst with high activity for electrochemical water oxidation and oxygen reduction. J Am Chem Soc 135(23):8525–8534

53. Bozzini B, Gianoncelli A, Kaulich B, Kiskinova M, Mele C, Prasciolu M (2011) Corrosion of Ni in 1-butyl-1-methyl-pyrrolidinium bis (trifluoromethylsulfonyl) amide room-temperature ionic liquid: an in situ x-ray imaging and spectromicroscopy study. Phys Chem Chem Phys 13(17):7968–7974

54. Arthur TS, Glans PA, Matsui M, Zhang RG, Ma BW, Guo JH (2012) Mg deposition observed by in situ electrochemical Mg K-edge x-ray absorption spectroscopy. Electrochem Commun 24:43–46

55. Nakanishi K, Kato D, Arai H, Tanida H, Mori T, Orikasa Y, Uchimoto Y, Ohta T, Ogumi Z (2014) Novel spectro-electrochemical cell for in situ/operando observation of common composite electrode with liquid electrolyte by x-ray absorption spectroscopy in the tender x-ray region. Rev Sci Instrum 85(8):084103/1–084103/6

56. Erickson EM, Thorum MS, Vasic R, Marinkovic NS, Frenkel AI, Gewirth AA, Nuzzo RG (2012) In situ electrochemical x-ray absorption spectroscopy of oxygen reduction electrocatalysis with high oxygen flux. J Am Chem Soc 134(1):197–200

57. Uehara H, Uemura Y, Ogawa T, Kono K, Ueno R, Niwa Y, Nitani H, Abe H, Takakusagi S, Nomura M, Iwasawa Y, Asakura K (2014) In situ back-side illumination fluorescence XAFS (BI-FXAFS) studies on platinum nanoparticles deposited on a HOPG surface as a model fuel cell: a new approach to the Pt-HOPG electrode/electrolyte interface. Phys Chem Chem Phys 16(27):13748–13754

58. Asakura K (2003) Recent developments in the in situ XAFS and related work for the characterization of catalysts in Japan. Catal Surv Asia 7(2–3):177–182

59. Chun WJ, Tanizawa Y, Shido T, Iwasawa Y, Nomura M, Asakura K (2001) Development of an in situ polarization-dependent total-reflection fluorescence XAFS measurement system. J Synchrotron Radiat 8:168–172

60. Frahm R (1989) New method for time-dependent x-ray absorption studies. Rev Sci Instrum 60(7):2515–2518

61. Frahm R (1989) QEXAFS – x-ray absorption studies in seconds. Phys B Condens Matter 158 (1–3):342–343

62. Iwasawa Y (2003) In situ characterization of supported metal catalysts and model surfaces by time-resolved and three-dimensional XAFS techniques. J Catal 216(1–2):165–177

63. Nonaka T, Dohmae K, Araki T, Hayashi Y, Hirose Y, Uruga T, Yamazaki H, Mochizuki T, Tanida H, Goto S (2012) Quick-scanning x-ray absorption spectroscopy system with a servo-motor-driven channel-cut monochromator with a temporal resolution of 10 ms. Rev Sci Instrum 83(8):083112/1–083112/5

64. Kaminaga U, Matsushita T, Kohra K (1981) A dispersive method of measuring extended x-ray absorption fine-structure. Jpn J Appl Phys 20(5):L355–L358

65. Matsushita T, Phizackerley RP (1981) A fast x-ray absorption spectrometer for use with synchrotron radiation. Jpn J Appl Phys 20(11):2223–2228

66. Flank AM, Fontaine A, Jucha A, Lemonnier M, Williams C (1982) Extended x-ray absorption fine-structure in dispersive mode. J Phys Lett 43(9):L315–L319

67. Flank AM, Fontaine A, Jucha A, Lemonnier M, Raoux D, Williams C (1983) EXAFS in dispersive mode. Nucl Instrum Methods Phys Res 208(1–3):651–654

68. Tanida H, Yamashige H, Orikasa Y, Oishi M, Takanashi Y, Fujimoto T, Sato K, Takamatsu D, Murayama H, Arai H, Matsubara E, Uchimoto Y, Ogumi Z (2011) In situ two-dimensional imaging quick-scanning XAFS with pixel array detector. J Synchrotron Radiat 18:919–922

69. Takao S, Sekizawa O, Nagamatsu S, Kaneko T, Yamamoto T, Samjeske G, Higashi K, Nagasawa K, Tsuji T, Suzuki M, Kawamura N, Mizumaki M, Uruga T, Iwasawa Y (2014) Mapping platinum species in polymer electrolyte fuel cells by spatially resolved XAFS techniques. Angew Chem Int Ed 53(51):14110–14114

70. Beale AM, Jacques SDM, Weckhuysen BM (2010) Chemical imaging of catalytic solids with synchrotron radiation. Chem Soc Rev 39(12):4656–4672

71. Grunwaldt JD, Schroer CG (2010) Hard and soft x-ray microscopy and tomography in catalysis: bridging the different time and length scales. Chem Soc Rev 39(12):4741–4753

72. Clavilier J (1999) Flame-annealing and cleaning technique. In: Wieckowski A (ed) Interfacial electrochemistry: theory, experiment, and applications. Marcel Dekker, New York, pp 231–248

73. Wang J, Davenport AJ, Isaacs HS, Ocko BM (1992) Surface-charge induced ordering of the Au(111) surface. Science 255(5050):1416–1418

74. Ocko BM, Wang J (1994) Surface structure of the Au(111) electrode. In: Melendres CA, Tadjeddine A (eds) Synchrotron techniques in interfacial electrochemistry (Nato Science Series C). Springer, Dordrecht, pp 127–155

75. Toney MF, Melroy OR (1991) Surface x-ray scattering. In: Abruña HD (ed) Electrochemical interfaces modern techniques for in-situ interface characterization. VCH Publishers, New York/Weinheim/Cambridge, pp 55–129

76. Toney MF (1994) Studies of electrodes by in situ x-ray scattering. In: Melendres CA, Tadjeddine A (eds) Synchrotron techniques in interfacial electrochemistry. Kluwer Academic Publishers, Dordrecht, pp 109–125

77. Toney MF, Gordon JG, Samant MG, Borges GL, Wiesler DG, Yee D, Sorensen LB (1991) In situ surface x-ray-scattering measurements of electrochemically deposited Bi on Ag(111) – structure, compressibility, and comparison with exsitu low-energy electron-diffraction measurements. Langmuir 7(4):796–802

78. Toney MF (1991) In-situ surface x-ray scattering of metal monolayers adsorbed at solid–liquid interfaces. Proc SPIE Int Soc Opt Eng 1550:140–150

79. Kondo T, Morita J, Hanaoka K, Takakusagi S, Tamura K, Takahasi M, Mizuki J, Uosaki K (2007) Structure of Au(111) and Au(100) single-crystal electrode surfaces at various potentials in sulfuric acid solution determined by in situ surface x-ray scattering. J Phys Chem C 111(35):13197–13204

80. Gründer Y, Markovic NM, Thompson P, Lucas CA (2015) Temperature effects on the atomic structure and kinetics in single crystal electrochemistry. Surf Sci 631:123–129

81. Pierce MS, Komanicky V, Barbour A, Hennessy DC, Zhu CH, Sandy A, You H (2012) Dynamics of the Au (001) surface in electrolytes: in situ coherent x-ray scattering. Phys Rev B 86(8):085410/1–085410/7

82. Masuda T, Fukumitsu H, Kondo T, Naohara H, Tamura K, Sakata O, Uosaki K (2013) Structure of Pt(111)/ionomer membrane interface and its bias-induced change in membrane electrode assembly. J Phys Chem C 117(23):12168–12171

83. Tamura K, Miyaguchi S, Sakaue K, Nishihata Y, Mizuki J (2011) Direct observation of Au (111) electrode surface structure in bis(trifluoromethylsulfonyl)amide-based ionic liquids using surface x-ray scattering. Electrochem Commun 13(5):411–413

84. Hoshi N, Nakamura M, Sakata O, Nakahara A, Naito K, Ogata H (2011) Surface x-ray scattering of stepped surfaces of platinum in an electrochemical environment: Pt(331)=3 (111)-(111) and Pt(511)=3(100)-(111). Langmuir 27(7):4236–4242

85. Kondo T, Shibata M, Hayashi N, Fukumitsu H, Masuda T, Takakusagi S, Uosaki K (2010) Resonance surface x-ray scattering technique to determine the structure of electrodeposited Pt ultrathin layers on Au(111) surface. Electrochim Acta 55(27):8302–8306

86. Shibata M, Hayashi N, Sakurai T, Kurokawa A, Fukumitsu H, Masuda T, Uosaki K, Kondo T (2012) Electrochemical layer-by-layer deposition of pseudomorphic Pt layers on Au(111) electrode surface confirmed by electrochemical and in situ resonance surface x-ray scattering measurements. J Phys Chem C 116(50):26464–26474

87. Takahasi M, Tamura K, Mizuki J, Kondo T, Uosaki K (2010) Orientation dependence of Pd growth on Au electrode surfaces. J Phys Condens Matter 22(47):474002/1–474002/9

88. Zheng SH, Krug K, Golks F, Kaminski D, Morin S, Magnussen OM (2010) Study of B1 UPD structures on Au(1 0 0) using in situ surface x-ray scattering. J Electroanal Chem 649 (1–2):189–197

89. Golks F, Gründer Y, Stettner J, Krug K, Zegenhagen J, Magnussen OM (2015) In situ surface x-ray diffraction studies of homoepitaxial growth on Cu(100) from aqueous acidic electrolyte. Surf Sci 631:112–122

90. Krug K, Kaminski D, Golks F, Stettner J, Magnussen OM (2010) Real-time surface x-ray scattering study of Au(111) electrochemical dissolution. J Phys Chem C 114(43):18634–18644

91. Gründer Y, Kaminski D, Golks F, Krug K, Stettner J, Magnussen OM, Franke A, Stremme J, Pehlke E (2010) Reversal of chloride-induced Cu(001) subsurface buckling in the electrochemical environment: an in situ surface x-ray diffraction and density functional theory study. Phys Rev B 81(17):174114/1–174114/10

92. Magnussen OM, Krug K, Ayyad AH, Stettner J (2008) In situ diffraction studies of electrode surface structure during gold electrodeposition. Electrochim Acta 53(9):3449–3458

93. Uosaki K, Morita J, Katsuzaki T, Takakusagi S, Tamura K, Takahasi M, Mizuki J, Kondo T (2011) In situ electrochemical, electrochemical quartz crystal microbalance, scanning tunneling microscopy, and surface x-ray scattering studies on Ag/AgCl reaction at the underpotentially deposited Ag bilayer on the Au(111) electrode surface. J Phys Chem C 115(25):12471–12482

94. Naito K, Nakamura M, Sakata O, Hoshi N (2011) Surface x-ray scattering of Pd(111) and Pd (100) electrodes during the oxygen reduction reaction. Electrochemistry 79(4):256–260

95. Lebouin C, Soldo-Olivier Y, Sibert E, De Santis M, Maillard F, Faure R (2009) Evidence of the substrate effect in hydrogen electroinsertion into palladium atomic layers by means of in situ surface x-ray diffraction. Langmuir 25(8):4251–4255

96. Soldo-Olivier Y, Lafouresse MC, De Santis M, Lebouin C, de Boissieu M, Sibert E (2011) Hydrogen electro-insertion into Pd/Pt(111) nanofilms: an in situ surface x-ray diffraction study. J Phys Chem C 115(24):12041–12047

97. Soldo-Olivier Y, Sibert E, Previdello B, Lafouresse MC, Maillard F, De Santis M (2013) H electro-insertion into Pd/Pt(111) nanofilms: an original method for isotherm measurement coupled to in situ surface x-ray diffraction structural study. Electrochim Acta 112:905–912

98. Lucas CA, Cormack M, Gallagher ME, Brownrigg A, Thompson P, Fowler B, Grunder Y, Roy J, Stamenkovic V, Markovic NM (2008) From ultra-high vacuum to the electrochemical interface: x-ray scattering studies of model electrocatalysts. Faraday Discuss 140:41–58

99. Strmcnik D, van der Vliet DF, Chang KC, Komanicky V, Kodama K, You H, Stamenkovic VR, Markovic NM (2011) Effects of Li$^+$, K$^+$, and Ba^{2+} cations on the ORR at model and high surface area Pt and Au surfaces in alkaline solutions. J Phys Chem Lett 2(21):2733–2736

100. Nakamura M, Sato N, Hoshi N, Sakata O (2011) Outer Helmholtz plane of the electrical double layer formed at the solid electrode-liquid interface. ChemPhysChem 12(8):1430–1434

101. Lucas CA, Thompson P, Gründer Y, Markovic NM (2011) The structure of the electrochemical double layer: Ag(111) in alkaline electrolyte. Electrochem Commun 13 (11):1205–1208

102. Keller H, Saracino M, Nguyen HMT, Broekmann P (2010) Templating the near-surface liquid electrolyte: in situ surface x-ray diffraction study on anion/cation interactions at electrified interfaces. Phys Rev B 82(24):245425/1–245425/7

103. Keller H, Saracino M, Nguyen HMT, Thi MTH, Broekmann P (2012) Competitive anion/water and cation/water interactions at electrified copper/electrolyte interfaces probed by in situ x-ray diffraction. J Phys Chem C 116(20):11068–11076

104. Angersteinkozlowska H, Conway BE, Hamelin A, Stoicoviciu L (1986) Elementary steps of electrochemical oxidation of single-crystal planes of Au.1. Chemical basis of processes involving geometry of anions and the electrode surfaces. Electrochim Acta 31(8):1051–1061

105. Angersteinkozlowska H, Conway BE, Hamelin A, Stoicoviciu L (1987) Elementary steps of electrochemical oxidation of single-crystal planes of Au.2. A chemical and structural basis of oxidation of the (111) plane. J Electroanal Chem 228(1–2):429–453

106. Bourkane S, Gabrielle C, Huet F, Keddam M (1993) Investigation of gold oxidation in sulfuric medium.1. Electrochemical impedance techniques. Electrochim Acta 38(7):1023–1028

107. Bourkane S, Gabrielli C, Keddam M (1993) Investigation of gold oxidation in sulfuric medium.2. Electrogravimetric transfer-function technique. Electrochim Acta 38(14):1827–1835

108. Conway BE (1995) Electrochemical oxide film formation at noble-metals as a surface-chemical process. Prog Surf Sci 49(4):331–452

109. Dickertmann D, Schultze JW, Vetter KJ (1974) Electrochemical formation and reduction of monomolecular oxide layers on (111) and (100) planes of gold single-crystals. J Electroanal Chem 55(3):429–443

110. Tremiliosi-Filho G, Dall'Antonia LH, Jerkiewicz G (2005) Growth of surface oxides on gold electrodes under well-defined potential, time and temperature conditions. J Electroanal Chem 578(1):1–8

111. Schneeweiss MA, Kolb DM (1997) Oxide formation on au(111) – an in situ STM study. Solid State Ion 94(1–4):171–179

112. Vitus CM, Davenport AJ (1994) In-situ scanning-tunneling-microscopy studies of the formation and reduction of a gold oxide monolayer on Au(111). J Electrochem Soc 141(5):1291–1298

113. Honbo H, Sugawara S, Itaya K (1990) Detailed in situ scanning tunneling microscopy of single-crystal planes of gold(111) in aqueous-solutions. Anal Chem 62(22):2424–2429

114. Gao XP, Hamelin A, Weaver MJ (1991) Atomic relaxation at ordered electrode surfaces probed by scanning tunneling microscopy – Au(111) in aqueous-solution compared with ultrahigh-vacuum environments. J Chem Phys 95(9):6993–6996

115. Cuesta A, Kleinert M, Kolb DM (2000) The adsorption of sulfate and phosphate on Au(111) and Au(100) electrodes: an in situ STM study. Phys Chem Chem Phys 2(24):5684–5690

116. Kolb DM (1996) Reconstruction phenomena at metal-electrolyte interfaces. Prog Surf Sci 51(2):109–173

117. Schneeweiss MA, Kolb DM, Liu DZ, Mandler D (1997) Anodic oxidation of Au(111). Can J Chem 75(11):1703–1709

118. Magnussen OM, Hagebock J, Hotlos J, Behm RJ (1992) In-situ scanning-tunneling-microscopy observations of a disorder–order phase-transition in hydrogensulfate adlayers on Au (111). Faraday Discuss 94:329–338

119. Ye S, Ishibashi C, Uosaki K (1999) Anisotropic dissolution of an Au(111) electrode in perchloric acid solution containing chloride anion investigated by in situ STM – the important role of adsorbed chloride anion. Langmuir 15(3):807–812

120. Sato K, Yoshimoto S, Inukai J, Itaya K (2006) Effect of sulfuric acid concentration on the structure of sulfate adlayer on Au(111) electrode. Electrochem Commun 8 (5):725–730

121. Takakusagi S, Kitamura K, Uosaki K (2008) In situ real-time monitoring of electrochemical Ag deposition on a reconstructed Au(111) surface studied by scanning tunneling microscopy. J Phys Chem C 112(8):3073–3077

122. Edens GJ, Gao XP, Weaver MJ (1994) The adsorption of sulfate on gold(111) in acidic aqueous-media – adlayer structural inferences from infrared-spectroscopy and scanning-tunneling-microscopy. J Electroanal Chem 375(1–2):357–366

123. de Moraes IR, Nart FC (1999) Sulfate ions adsorbed on Au(hkl) electrodes: in situ vibrational spectroscopy. J Electroanal Chem 461(1–2):110–120

124. Horkans J, Cahan BD, Yeager E (1974) Electrode potential scanning ellipsometric spectroscopy – study of formation of anodic oxide film on noble-metals. Surf Sci 46(1):1–23

125. Kolb DM (1988) UV-visible reflectance spectroscopy. In: Gale RJ (ed) Spectroelectrochemistry: theory and practice. Plenum Press, New York, pp 87–188

126. Beden B, Lamy C (1988) Infrared reflectance spectroscopy. In: Gale RJ (ed) Spectroelectrochemistry: theory and practice. Plenum Press, New York, pp 189–262

127. Birke RL, Lombardi JR (1988) Surface-enhanced Raman scattering. In: Gale RJ (ed) Spectroelectrochemistry: theory and practice. Plenum Press, New York, pp 263–446

128. Kolb DM, Mcintyre JD (1971) Spectrophotometric determination of optical properties of an adsorbed oxygen layer on gold. Surf Sci 28(1):321

129. Zhumaev U, Rudnev AV, Li JF, Kuzume A, Vu TH, Wandlowski T (2013) Electro-oxidation of Au(111) in contact with aqueous electrolytes: new insight from in situ vibration spectroscopy. Electrochim Acta 112:853–863

130. Shi Z, Lipkowski J, Gamboa M, Zelenay P, Wieckowski A (1994) Investigations of SO_4^{2-} adsorption at the Au(111) electrode by chronocoulometry and radiochemistry. J Electroanal Chem 366(1–2):317–326

131. Ocko BM, Wang J, Davenport A, Isaacs H (1990) In situ x-ray reflectivity and diffraction studies of the Au(001) reconstruction in an electrochemical-cell. Phys Rev Lett 65(12):1466–1469

132. Perdereau J, Biberian JP, Rhead GE (1974) Adsorption and surface alloying of lead monolayers on (111) and (110) faces of gold. J Phys F-Met Phys 4(5):798

133. Sandy AR, Mochrie SGJ, Zehner DM, Huang KG, Gibbs D (1991) Structure and phases of the Au(111) surface – x-ray-scattering measurements. Phys Rev B 43(6):4667–4687

134. Barth JV, Brune H, Ertl G, Behm RJ (1990) Scanning tunneling microscopy observations on the reconstructed Au(111) surface – atomic-structure, long-range superstructure, rotational domains, and surface-defects. Phys Rev B 42(15):9307–9318

135. Wang Y, Hush NS, Reimers JR (2007) Simulation of the Au(111)-(22 × √3) surface reconstruction. Phys Rev B 75(23):233416/1–233416/4

136. You H, Pierce M, Komanicky V, Barbour A, Zhu CH (2012) Study of electrode surface dynamics using coherent surface x-ray scattering. Electrochim Acta 82:570–575

137. Kordesch KV, Simader GR (1995) Environmental-impact of fuel-cell technology. Chem Rev 95(1):191–207

138. Winter M, Brodd RJ (2004) What are batteries, fuel cells, and supercapacitors? Chem Rev 104(10):4245–4269

139. Borup R, Meyers J, Pivovar B, Kim YS, Mukundan R, Garland N, Myers D, Wilson M, Garzon F, Wood D, Zelenay P, More K, Stroh K, Zawodzinski T, Boncella J, McGrath JE, Inaba M, Miyatake K, Hori M, Ota K, Ogumi Z, Miyata S, Nishikata A, Siroma Z, Uchimoto Y, Yasuda K, Kimijima KI, Iwashita N (2007) Scientific aspects of polymer electrolyte fuel cell durability and degradation. Chem Rev 107(10):3904–3951

140. Wagner FT, Lakshmanan B, Mathias MF (2010) Electrochemistry and the future of the automobile. J Phys Chem Lett 1(14):2204–2219

141. Ohno H (2005) Electrochemical aspects of ionic liquids. John Wiley & Sons Inc, Hoboken

142. Rollins JB, Conboy JC (2009) Kinetics and thermodynamics of hydrogen oxidation and oxygen reduction in hydrophobic room-temperature ionic liquids. J Electrochem Soc 156(8): B943–B954

143. Xiang HF, Yin B, Wang H, Lin HW, Ge XW, Xie S, Chen CH (2010) Improving electrochemical properties of room temperature ionic liquid (RTIL) based electrolyte for Li-ion batteries. Electrochim Acta 55(18):5204–5209

144. Sugimoto T, Atsumi Y, Kono M, Kikuta M, Ishiko E, Yamagata M, Ishikawa M (2010) Application of bis(fluorosulfonyl)imide-based ionic liquid electrolyte to silicon-nickel-carbon composite anode for lithium-ion batteries. J Power Sources 195(18):6153–6156

145. Kubo K, Hirai N, Tanaka T, Hara S (2003) In situ observation on Au(100) surface in molten EMImBF(4) by electrochemical atomic force microscopy (EC-AFM). Surf Sci 546(1): L785–L788

146. Bozzini B, Bund A, Busson B, Humbert C, Ispas A, Mele C, Tadjeddine A (2010) An SFG/DFG investigation of CN- adsorption at an Au electrode in 1-butyl-1-methyl-pyrrolidinium bis (trifluoromethylsulfonyl) amide ionic liquid. Electrochem Commun 12(1):56–60

147. Brandao CRR, Costa LAF, Breyer HS, Rubim JC (2009) Surface-enhanced Raman scattering (SERS) of a copper electrode in 1-n-butyl-3-methylimidazolium tetrafluoroborate ionic liquid. Electrochem Commun 11(9):1846–1848

148. Adzic R (1990) Reaction kinetics and mechanisms on metal single-crystal electrode surfaces. In: Modern aspects of electrochemistry, vol 21. Plenum Press, New York

149. Lamy C, Leger JM (1991) Electrocatalytic oxidation of small organic-molecules at platinum single-crystals. J Chim Phys Phys -Chim Biol 88(7–8):1649–1671

150. Markovic NM, Ross PN (2002) Surface science studies of model fuel cell electrocatalysts. Surf Sci Rep 45(4–6):121–229

151. Ye S, Kondo T, Hoshi N, Inukai J, Yoshimoto S, Osawa M, Itaya K (2009) Recent progress in electrochemical surface science with atomic and molecular levels (vol 77, pg 2, 2009). Electrochemistry 77(4):322–340

152. Sashikata K, Furuya N, Itaya K (1991) In situ electrochemical scanning tunneling microscopy of single-crystal surfaces of Pt(111), Rh(111), and Pd(111) in aqueous sulfuric-acid-solution. J Vac Sci Technol B 9(2):457–464

153. Villegas I, Weaver MJ (1994) Carbon-monoxide adlayer structures on platinum(111) electrodes – a synergy between in-situ scanning-tunneling-microscopy and infrared-spectroscopy. J Chem Phys 101(2):1648–1660

154. Itaya K (1998) In situ scanning tunneling microscopy in electrolyte solutions. Prog Surf Sci 58(3):121–247

155. Tidswell IM, Markovic NM, Ross PN (1994) Potential-dependent surface-structure of the Pt (111) vertical-bar-electrolyte interface. J Electroanal Chem 376(1–2):119–126

156. Tidswell IM, Markovic NM, Ross PN (1993) Potential-dependent surface relaxation of the Pt (001) electrolyte interface. Phys Rev Lett 71(10):1601–1604

157. Lucas CA, Markovic NM, Ross PN (1996) Surface structure and relaxation at the Pt(110)/ electrolyte interface. Phys Rev Lett 77(24):4922–4925

158. Nakahara A, Nakamura M, Sumitani K, Sakata O, Hoshi N (2007) In situ surface x-ray scattering of stepped surface of platinum: Pt(311). Langmuir 23(22):10879–10882

159. Hoshi N, Naito K, Nakamura M, Sakata O (2014) Surface x-ray scattering of Pd(110) and Pd (311) in electrochemical environments. Electrochemistry 82(5):351–354

160. Somorjai GA (1994) Introduction to surface chemistry and catalysis. John Wiley & Sons, Inc, New York

161. Adamson AW, Gast AP (1997) Physical chemistry of surfaces. John Wiley and Sons, Inc, New York

162. Naohara H, Ye S, Uosaki K (2001) Thickness dependent electrochemical reactivity of epitaxially electrodeposited palladium thin layers on Au(111) and Au(100) surfaces. J Electroanal Chem 500(1–2):435–445

163. Uosaki K, Ye S, Naohara H, Oda Y, Haba T, Kondo T (1997) Electrochemical epitaxial growth of a Pt(111) phase on an Au(111) electrode. J Phys Chem B 101(38):7566–7572

164. Waibel HF, Kleinert M, Kibler LA, Kolb DM (2002) Initial stages of Pt deposition on Au (111) and Au(100). Electrochim Acta 47(9):1461–1467

165. Strbac S, Petrovic S, Vasilic R, Kovac J, Zalar A, Rakocevic Z (2007) Carbon monoxide oxidation on Au(111) surface decorated by spontaneously deposited Pt. Electrochim Acta 53(2):998–1005

166. Mathur A, Erlebacher J (2008) Effects of substrate shape, curvature and roughness on thin heteroepitaxial films of Pt on Au(111). Surf Sci 602(17):2863–2875

167. Takahasi M, Hayashi Y, Mizuki J, Tamura K, Kondo T, Naohara H, Uosaki K (2000) Pseudomorphic growth of Pd monolayer on Au(111) electrode surface. Surf Sci 461 (1–3):213–218

168. Uosaki K, Ye S, Kondo T, Naohara H (2002) Electrochemical epitaxial growth, structure, and electrocatalytic properties of noble metal thin films on Au(111) and Au(100). In: Soriaga MP, Stickney JL, Bottomley LA, Kim Y-G (eds) Thin films: preparation, characterization, applications. Kluwer Academic/Plenum Publishers, New York, pp 17–35

169. Kondo T, Morita J, Okamura M, Saito T, Uosaki K (2002) In situ structural study on underpotential deposition of Ag on Au(111) electrode using surface x-ray scattering technique. J Electroanal Chem 532(1–2):201–205

170. Kondo T, Takakusagi S, Uosaki K (2009) Stability of underpotentially deposited Ag layers on a Au(111) surface studied by surface x-ray scattering. Electrochem Commun 11(4):804–807

171. Kondo T, Tamura K, Takakusagi S, Kitamura K, Takahasi M, Mizuki J, Uosaki K (2009) Partial stripping of Ag atoms from silver bilayer on a Au(111) surface accompanied with the reductive desorption of hexanethiol SAM. J Solid State Electrochem 13 (7):1141–1145

172. Tweet DJ, Akimoto K, Tatsumi T, Hirosawa I, Mizuki J, Matsui J (1992) Direct observation of Ge and Si ordering at the Si/B/Gexsi1-X (111) interface by anomalous x-ray-diffraction. Phys Rev Lett 69(15):2236–2239

173. Chu YS, You H, Tanzer JA, Lister TE, Nagy Z (1999) Surface resonance x-ray scattering observation of core-electron binding-energy shifts of Pt(111)-surface atoms during electrochemical oxidation. Phys Rev Lett 83(3):552–555

174. Takahasi M, Mizuki J (2006) Element-specific surface x-ray diffraction study of GaAs(001)-c (4x4). Phys Rev Lett 96(5):055506/1–055506/4

175. Menzel A, Chang KC, Komanicky V, You H, Chu YS, Tolmachev YV, Rehr JJ (2006) Resonance anomalous surface x-ray scattering. Radiat Phys Chem 75(11):1651–1660

176. Sibert E, Wang L, De Santis M, Soldo-Olivier Y (2014) Mechanisms of the initial steps in the Pd electro-deposition onto Au(111). Electrochim Acta 135:594–603

177. Schultze JW, Dickertmann D (1976) Potentiodynamic desorption spectra of metallic monolayers of Cu, Bi, Pb, Tl, and Sb adsorbed at (111), (100), and (110) planes of gold electrodes. Surf Sci 54(2):489–505

178. Juttner K (1986) Surface structural effects in electrocatalysis. Electrochim Acta 31(8):917–927

179. Chen CH, Kepler KD, Gewirth AA, Ocko BM, Wang J (1993) Electrodeposited bismuth monolayers on Au(111) electrodes – comparison of surface x-ray-scattering, scanning-tunneling-microscopy, and atomic-force microscopy lattice structures. J Phys Chem 97 (28):7290–7294

180. Tamura K, Ocko BM, Wang JX, Adzic RR (2002) Structure of active adlayers on bimetallic surfaces: oxygen reduction on Au(111) with Bi adlayers. J Phys Chem B 106(15):3896–3901

181. Hara M, Nagahara Y, Yoshimoto S, Inukai J, Itaya K (2004) Underpotentially deposited layers of Bi on Au-(100) in $HClO_4$ investigated by in situ STM. J Electrochem Soc 151(3): E92–E96
182. Nakamura M, Sato N, Hoshi N, Sakata O (2010) Catalytically active structure of Bi deposited on a Au(111) electrode for the hydrogen peroxide reduction reaction. Langmuir 26(7): 4590–4593
183. Andricacos PC, Uzoh C, Dukovic JO, Horkans J, Deligianni H (1998) Damascene copper electroplating for chip interconnections. IBM J Res Dev 42(5):567–574
184. Edelstein D, Heidenreich J, Goldblatt R, Cote W, Uzoh C, Lustig N, Roper P, McDevitt T, Motsiff W, Simon A, Dukovic JO, Wachnik R, Rathore H, Schulz R, Su L, Luche S, Slattery JP (1997) Full copper wiring in a sub-0.25 μm CMOS ULSI technology. Technical Digest – International Electron Devices Meeting
185. Datta M (2009) Electrodeposition. In: Shacham-Diamon Y, Osaka T, Datta M, Ohba T (eds) Advanced nanoscale ULSI interconnects: fundamentals and applications. Springer, New York, pp 63–72
186. Golks F, Stettner J, Gründer Y, Krug K, Zegenhagen J, Magnussen OM (2012) Anomalous potential dependence in homoepitaxial Cu(001) electrodeposition: an in situ surface x-ray diffraction study. Phys Rev Lett 108(25):256101/1–256101/5
187. Schott JH, White HS (1994) Halogen adlayers on Ag(111). J Phys Chem 98(1):291–296
188. Aloisi G, Funtikov AM, Will T (1994) Chloride adsorption on Ag(111) studied by in-situ scanning-tunneling-microscopy. J Electroanal Chem 370(1–2):297–300
189. Sneddon DD, Gewirth AA (1995) In situ characterization of halide adsorption and Ag-halide growth on Ag(111) electrodes using atomic force microscopy. Surf Sci 343(3):185–200
190. Ocko BM, Magnussen OM, Wang JX, Adzic RR, Wandlowski T (1996) The structure and phase behavior of electrodeposited halides on single-crystal metal surfaces. Phys B -Condens Matter 221(1–4):238–244
191. Hecht D, Strehblow HH (1997) A surface analytical investigation of the electrochemical double layer on silver electrodes in chloride solutions. J Electroanal Chem 436(1–2):109–118
192. Shimooka T, Inukai J, Itaya K (2002) Adlayer structures of cl and br and growth of bulk AgBr layers on Ag(100) electrodes. J Electrochem Soc 149(2):E19–E25
193. Bozzini B, Giovannelli G, Mele C (2007) Electrochemical dynamics and structure of the Ag/AgCl interface in chloride-containing aqueous solutions. Surf Coat Technol 201(8):4619–4627
194. Wieckowski A (2009) Fuel cell catalysis: a surface science approach. John Wiley & Sons, Inc, Hoboken
195. Kondo S, Nakamura M, Maki N, Hoshi N (2009) Active sites for the oxygen reduction reaction on the low and high index planes of palladium. J Phys Chem C 113 (29):12625–12628
196. Barsellini D, Visintin A, Triaca WE, Soriaga MP (2003) Electrochemical characterization of a hydride-forming metal alloy surface-modified with palladium. J Power Sources 124(1): 309–313
197. Kumar P, Malhotra LK (2004) Electrochemical loading of hydrogen in palladium capped samarium thin film: structural, electrical, and optical properties. Electrochim Acta 49 (20):3355–3360
198. Ambrosio RC, Ticianelli EA (2005) Studies on the influence of palladium coatings on the electrochemical and structural properties of a metal hydride alloy. Surf Coat Technol 197 (2–3):215–222
199. Pitt MP, Blanchard D, Hauback BC, Fjellvag H, Marshall WG (2005) Pressure-induced phase transitions of the $LiAlD_4$ system. Phys Rev B 72(21):214113/1–214113/9
200. Materer N, Starke U, Barbieri A, Doll R, Heinz K, Vanhove MA, Somorjai GA (1995) Reliability of detailed leed structural-analyses – Pt(111) and Pt(111)-P(2x2)-O. Surf Sci 325 (3):207–222
201. Marinkovic NS, Markovic NM, Adzic RR (1992) Hydrogen adsorption on single-crystal platinum-electrodes in alkaline-solutions. J Electroanal Chem 330(1–2):433–452

202. Lucas CA (2002) Surface relaxation at the metal/electrolyte interface. Electrochim Acta 47 (19):3065–3074
203. Magnussen OM (2002) Ordered anion adlayers on metal electrode surfaces. Chem Rev 102 (3):679–725
204. Gründer Y, Drunkler A, Golks F, Wijts G, Stettner J, Zegenhagen J, Magnussen OM (2011) Structure and electrocompression of chloride adlayers on Cu(111). Surf Sci 605 (17–18):1732–1737
205. Tolentino HCN, De Santis M, Gauthier Y, Langlais V (2007) Chlorine chemisorption on Cu(001) by surface x-ray diffraction: geometry and substrate relaxation. Surf Sci 601(14):2962–2966
206. Grey F, Bohr J (1992) A symmetry principle for epitaxial rotation. Europhys Lett 18 (8):717–722
207. von Helmholtz HLF (1879) Studies of electric boundary layers. Ann Phys 243(7):337–382
208. Gouy G (1910) Construction of the electric charge at the surface of an electrolyte. J Phys II 9:457–467
209. Chapman DL (1913) A contribution to the theory of electrocapillarity. Phylos Mag 25:475–481
210. Stern O (1924) The theory of the electrolytic double-layer. Z Elektrochem Angew Phys Chem 30:508–516
211. Frumkin A (1926) The influence of an electric field on the adsorption of neutral molecules. Z Phys 35:792–802
212. Bockris JOM, Devanathan MAV, Muller K (1963) On the structure of charged interfaces. Proc Roy Soc Lond A 274:91–121
213. Grahame DC (1947) The electrical double layer and the theory of electrocapillarity. Chem Rev 41(3):441–501
214. Adzic RR, Markovic NM (1979) Reflectance study of cation adsorption on oxide layers of gold and platinum-electrodes. J Electroanal Chem 102(2):263–270
215. Strmcnik D, Escudero-Escribano M, Kodama K, Stamenkovic VR, Cuesta A, Markovic NM (2010) Enhanced electrocatalysis of the oxygen reduction reaction based on patterning of platinum surfaces with cyanide. Nat Chem 2(10):880–885
216. Strmcnik D, Kodama K, van der Vliet D, Greeley J, Stamenkovic VR, Markovic NM (2009) The role of non-covalent interactions in electrocatalytic fuel-cell reactions on platinum. Nat Chem 1(6):466–472
217. Stoffelsma C, Rodriguez P, Garcia G, Garcia-Araez N, Strmcnik D, Markovic NM, Koper MTM (2010) Promotion of the oxidation of carbon monoxide at stepped platinum single-crystal electrodes in alkaline media by lithium and beryllium cations. J Am Chem Soc 132(45):16127–16133
218. van der Vliet DF, Koper MTM (2010) Electrochemistry of Pt (100) in alkaline media: a voltammetric study. Surf Sci 604(21–22):1912–1918
219. Escudero-Escribano M, Michoff MEZ, Leiva EPM, Markovic NM, Gutierrez C, Cuesta A (2011) Quantitative study of non-covalent interactions at the electrode-electrolyte interface using cyanide-modified Pt(111) electrodes. ChemPhysChem 12(12):2230–2234
220. Abruña HD (1991) X-ray absorption spectroscopy in the study of electrochemical systems. In: Abruña HD (ed) Electrochemical interfaces: modern techniques for in-situ interface characterization. VCH Publishers, New York/Weinheim/Cambridge, pp 1–54
221. Bardwell JA, Sproule GI, Macdougall B, Graham MJ, Davenport AJ, Isaacs HS (1992) In situ XANES detection of Cr(VI) in the passive film on Fe-26Cr. J Electrochem Soc 139(2):371–373
222. Gordon JG, Melroy OR, Borges GL, Reisner DL, Abruña HD, Chandrasekhar P, Blum L (1986) Surface EXAFS of an electrochemical interface iodine on platinum (111). J Electroanal Chem 210(2):311–314
223. Blum L, Abruña HD, White J, Gordon JG, Borges GL, Samant MG, Melroy OR (1986) Study of underpotentially deposited copper on gold by fluorescence detected surface EXAFS. J Chem Phys 85(11):6732–6738

224. Samant MG, Borges GL, Gordon JG, Melroy OR, Blum L (1987) In situ surface extended x-ray absorption fine-structure spectroscopy of a lead monolayer at a silver(111) electrode electrolyte interface. J Am Chem Soc 109(20):5970–5974

225. White JH, Albarelli MJ, Abruña HD, Blum L, Melroy OR, Samant MG, Borges GL, Gordon JG (1988) Surface extended x-ray absorption fine-structure of underpotentially deposited silver on Au(111) electrodes. J Phys Chem 92(15):4432–4436

226. Melroy OR, Samant MG, Borges GL, Gordon JG, Blum L, White JH, Albarelli MJ, Mcmillan M, Abruña HD (1988) Inplane structure of underpotentially deposited copper on gold(111) determined by surface EXAFS. Langmuir 4(3):728–732

227. Pandya KI, Hoffman RW, McBreen J, O'Grady WE (1990) In situ x-ray absorption spectroscopic studies of nickel-oxide electrodes. J Electrochem Soc 137(2):383–388

228. Pandya KI, O'Grady WE, Corrigan DA, McBreen J, Hoffman RW (1990) Extended x-ray absorption fine structure investigations of nickel hydroxides. J Phys Chem 94(1):21–26

229. McBreen J, O'Grady WE, Tourillon G, Dartyge E, Fontaine A, Pandya KI (1989) In situ time-resolved x-ray absorption near edge structure study of the nickel-oxide electrode. J Phys Chem 93(17):6308–6311

230. Guay D, Tourillon G, Dartyge E, Fontaine A, McBreen J, Pandya KI, O'Grady WE (1991) In situ time-resolved EXAFS study of the structural modifications occurring in nickel-oxide electrodes between their fully oxidized and reduced states. J Electroanal Chem 305(1):83–95

231. Yamaguchi T, Mitsunaga T, Yoshida N, Wakita H, Fujiwara M, Matsushita T, Ikeda S, Nomura M (1993) XAFS study with an in situ electrochemical-cell on manganese Schiff-base complexes as a model of photosystem-II. Jpn J Appl Phys Part 1 32:533–535

232. Yamaguchi T, Valli M, Miyata S, Wakita H (1997) In-situ x-ray absorption spectroelectrochemistry for determination of the oxidation states and the local structure of metalloprotein model compounds. Anal Sci 13:37–40

233. Bae IT, Scherson DA (1998) In situ x-ray absorption of a carbon monoxide-iron porphyrin adduct adsorbed on high-area carbon in an aqueous electrolyte. J Phys Chem B 102 (14):2519–2522

234. Totir D, Mo YB, Kim S, Antonio MR, Scherson DA (2000) In situ CoK-edge x-ray absorption fine structure of cobalt hydroxide film electrodes in alkaline solutions. J Electrochem Soc 147(12):4594–4597

235. Mo YB, Antonio MR, Scherson DA (2000) In situ Ru K-edge x-ray absorption fine structure studies of electroprecipitated ruthenium dioxide films with relevance to supercapacitor applications. J Phys Chem B 104(42):9777–9779

236. Mukerjee S, Srinivasan S, Soriaga MP, McBreen J (1995) Role of structural and electronic-properties of Pt and Pt alloys on electrocatalysis of oxygen reduction – an in-situ XANES and EXAFS investigation. J Electrochem Soc 142(5):1409–1422

237. McBreen J, Mukerjee S (1995) In-situ x-ray-absorption studies of a Pt-Ru electrocatalyst. J Electrochem Soc 142(10):3399–3404

238. Sanjeev M, McBreen J (1999) An in situ x-ray absorption spectroscopy investigation of the effect of Sn additions to carbon-supported Pt electrocatalysts. Part I. J Electrochem Soc 146(2):600–606

239. Mukerjee S, McBreen J (1996) Hydrogen electrocatalysis by carbon supported Pt and Pt alloys – an in situ x-ray absorption study. J Electrochem Soc 143(7):2285–2294

240. Yee HS, Abruña HD (1993) In-situ x-ray-absorption spectroscopy studies of copper underpotentially deposited in the absence and presence of chloride on platinum(111). Langmuir 9(9):2460–2469

241. Yee HS, Abruña HD (1993) In situ x-ray studies of the underpotential deposition of copper on platinum(111). J Phys Chem 97(23):6278–6288

242. Yee HS, Abruña HD (1994) Ab-initio XAFS calculations and in-situ XAFS measurements of copper underpotential deposition on Pt(111) – a comparative-study. J Phys Chem 98(26):6552–6558

243. Gómez R, Yee HS, Bommarito GM, Feliu JM, Abruña HD (1995) Anion effects and the mechanism of Cu Upd on Pt(111) – x-ray and electrochemical studies. Surf Sci 335 (1–3):101–109

244. Herrero E, Li J, Abruña HD (1999) Electrochemical, in-situ surface EXAFS and CTR studies of Co monolayers irreversibly adsorbed onto Pt(111). Electrochim Acta 44 (14):2385–2396

245. Tadjeddine A, Tourillon G (1992) Characterization of metal monolayers electrodeposited on gold single-crystals using x-ray absorption-spectroscopy. Analusis 20(6):309–318

246. Bommarito GM, Acevedo D, Rodriguez JF, Abruña HD (1994) Potential-dependent structural-changes of underpotentially deposited copper on an iodine-treated platinum surface determined in-situ by surface EXAFS and its polarization dependence. J Electroanal Chem 379(1–2):135–150

247. Prinz H, Strehblow HH (2002) The structure of Cu- and Cd-UPD-layers on a stepped Pt(533) single crystal surface studied by grazing incidence XAFS, XRD and XPS. Electrochim Acta 47(19):3093–3104

248. Soldo Y, Sibert E, Tourillon G, Hazemann JL, Levy JP, Aberdam D, Faure R, Durand R (2002) In situ x-ray absorption spectroscopy study of copper under potential deposition on Pt(111): role of the anions on the Cu structural arrangement. Electrochim Acta 47(19):3081–3091

249. Kondo T, Tamura K, Koinuma M, Oyanagi H, Uosaki K (1997) Coverage dependent structure of electrochemically deposited Cu on p-GaAs(100) in H_2SO_4 solution determined by in situ surface x-ray absorption fine structure spectra. Chem Lett 8:761–762

250. Uosaki K, Kondo T, Koinuma M, Tamura K, Oyanagi H (1997) Structural study of electrochemically deposited copper on p-GaAs(001) by atomic force microscopy and surface x-ray absorption fine structure measurement. Appl Surf Sci 121:102–106

251. Tamura K, Oyanagi H, Kondo T, Koinuma M, Uosaki K (2000) Structural study of electrochemically deposited Cu on p-GaAs(100) in H_2SO_4 solution by in situ surface-sensitive x-ray absorption fine structure measurements. J Phys Chem B 104(38):9017–9024

252. Russell AE, Rose A (2004) X-ray absorption spectroscopy of low temperature fuel cell catalysts. Chem Rev 104(10):4613–4635

253. Croze V, Ettingshausen F, Melke J, Soehn M, Stuermer D, Roth C (2010) The use of in situ x-ray absorption spectroscopy in applied fuel cell research. J Appl Electrochem 40(5):877–883

254. McBreen J (2009) The application of synchrotron techniques to the study of lithium-ion batteries. J Solid State Electrochem 13(7):1051–1061

255. Herron ME, Doyle SE, Pizzini S, Roberts KJ, Robinson J, Hards G, Walsh FC (1992) In situ studies of a dispersed platinum on carbon electrode using x-ray absorption-spectroscopy. J Electroanal Chem 324(1–2):243–258

256. Yoshitake H, Mochizuki T, Yamazaki O, Ota K (1993) Study of the density of the D-state and structure transformation of Pt fine particles dispersed on carbon electrodes by in-situ x-ray-absorption spectroscopy. J Electroanal Chem 361(1–2):229–237

257. Yoshitake H, Yamazaki O, Ota K (1994) In-situ x-ray-absorption fine-structure study on structure transformation and electronic-state of various Pt particles on carbon electrode. J Electrochem Soc 141(9):2516–2522

258. Mukerjee S, McBreen J (1998) Effect of particle size on the electrocatalysis by carbon-supported Pt electrocatalysts: an in situ XAS investigation. J Electroanal Chem 448(2):163–171

259. Imai H, Izumi K, Matsumoto M, Kubo Y, Kato K, Imai Y (2009) In situ and real-time monitoring of oxide growth in a few monolayers at surfaces of platinum nanoparticles in aqueous media. J Am Chem Soc 131(17):6293–6300

260. Shiraishi Y, Nakai I, Tsubata T, Himeda T, Nishikawa F (1997) In situ transmission x-ray absorption fine structure analysis of the charge–discharge process in $LiMn_2O_4$, a rechargeable lithium battery material. J Solid State Chem 133(2):587–590
261. Nakai I, Takahashi K, Shiraishi Y, Nakagome T, Izumi F, Ishii Y, Nishikawa F, Konishi T (1997) X-ray absorption fine structure and neutron diffraction analyses of de-intercalation behavior in the $LiCoO_2$ and $LiNiO_2$ systems. J Power Sources 68(2):536–539
262. Nakai I, Takahashi K, Shiraishi Y, Nakagome T, Nishikawa F (1998) Study of the Jahn-Teller distortion in $LiNiO_2$, a cathode material in a rechargeable lithium battery, by in situ x-ray absorption fine structure analysis. J Solid State Chem 140(1):145–148
263. Nakai I, Shiraishi Y, Nishikawa F (1999) Development of a new in situ cell for the x-ray absorption fine structure analysis of the electrochemical reaction in a rechargeable battery and its application to the lithium battery material, $Li_{1+y}Mn_{2-y}O_4$. Spectrochim Acta Part B 54(1):143–149
264. Shiraishi Y, Nakai I, Tsubata T, Himeda T, Nishikawa F (1999) Effect of the elevated temperature on the local structure of lithium manganese oxide studied by in situ XAFS analysis. J Power Sources 81:571–574
265. Terada Y, Yasaka K, Nishikawa F, Konishi T, Yoshio M, Nakai I (2001) In situ XAFS analysis of $Li(Mn, M)_2O_4$ (M = Cr, Co, Ni) 5 V cathode materials for lithium-ion secondary batteries. J Solid State Chem 156(2):286–291
266. Terada Y, Nishiwaki Y, Nakai I, Nishikawa F (2001) Study of Mn dissolution from $LiMn_2O_4$ spinel electrodes using in situ total reflection x-ray fluorescence analysis and fluorescence XAFS technique. J Power Sources 97–98:420–422
267. Nakai I, Yasaka K, Sasaki H, Terada Y, Ikuta H, Wakihara M (2001) In situ XAFS study of the electrochemical deintercalation of Li from $Li_{1-x}Mn_{2-y}Cr_yO_4$ (y = 1/9, 1/6, 1/3). J Power Sources 97–98:412–414
268. Takamatsu D, Koyama Y, Orikasa Y, Mori S, Nakatsutsumi T, Hirano T, Tanida H, Arai H, Uchimoto Y, Ogumi Z (2012) First in situ observation of the $LiCoO_2$ electrode/electrolyte interface by total-reflection x-ray absorption spectroscopy. Angew Chem Int Ed 51(46):11597–11601
269. Takamatsu D, Mori S, Orikasa Y, Nakatsutsumi T, Koyama Y, Tanida H, Arai H, Uchimoto Y, Ogumi Z (2013) Effects of ZrO_2 coating on $LiCoO_2$ thin-film electrode studied by in situ x-ray absorption spectroscopy. J Electrochem Soc 160(5):A3054–A3060
270. Arai H, Sato K, Orikasa Y, Murayama H, Takahashi I, Koyama Y, Uchimoto Y, Ogumi Z (2013) Phase transition kinetics of $LiNi_{0.5}Mn_{1.5}O_4$ electrodes studied by in situ x-ray absorption near-edge structure and x-ray diffraction analysis. J Mater Chem A 1(35):10442–10449
271. Orikasa Y, Maeda T, Koyama Y, Murayama H, Fukuda K, Tanida H, Arai H, Matsubara E, Uchimoto Y, Ogumi Z (2013) Transient phase change in two phase reaction between $LiFePO_4$ and $FePO_4$ under battery operation. Chem Mater 25(7):1032–1039
272. Orikasa Y, Maeda T, Koyama Y, Minato T, Murayama H, Fukuda K, Tanida H, Arai H, Matsubara E, Uchimoto Y, Ogumi Z (2013) Phase transition analysis between $LiFePO_4$ and $FePO_4$ by in-situ time-resolved x-ray absorption and x-ray diffraction. J Electrochem Soc 160(5):A3061–A3065
273. Masese T, Orikasa Y, Mori T, Yamamoto K, Ina T, Minato T, Nakanishi K, Ohta T, Tassel C, Kobayashi Y, Kageyama H, Arai H, Ogumi Z, Uchimoto Y (2014) Local structural change in Li_2FeSiO_4 polyanion cathode material during initial cycling. Solid State Ion 262:110–114
274. Takamatsu D, Koyama Y, Orikasa Y, Mori S, Nakatsutsumi T, Hirano T, Tanida H, Arai H, Uchimoto Y, Ogumi Z (2014) Electrochemical and spectroscopic characterization of $LiCoO_2$ thin-film as model electrode. J Electrochem Soc 161(9):A1447–A1452
275. Yamamoto K, Minato T, Mori S, Takamatsu D, Orikasa Y, Tanida H, Nakanishi K, Murayama H, Masese T, Mori T, Arai H, Koyama Y, Ogumi Z, Uchimoto Y (2014) Improved cyclic performance of lithium-ion batteries: an investigation of cathode/electrolyte interface via in situ total-reflection fluorescence x-ray absorption spectroscopy. J Phys Chem C 118(18):9538–9543

276. Katayama M, Sumiwaka K, Miyahara R, Yamashige H, Arai H, Uchimoto Y, Ohta T, Inada Y, Ogumi Z (2014) X-ray absorption fine structure imaging of inhomogeneous electrode reaction in LiFePO$_4$ lithium-ion battery cathode. J Power Sources 269:994–999

277. Kawaura H, Takamatsu D, Mori S, Orikasa Y, Sugaya H, Murayama H, Nakanishi K, Tanida H, Koyama Y, Arai H, Uchimoto Y, Ogumi Z (2014) High potential durability of LiNi$_{0.5}$Mn$_{1.5}$O$_4$ electrodes studied by surface sensitive x-ray absorption spectroscopy. J Power Sources 245:816–821

278. Tanida H, Fukuda K, Murayama H, Orikasa Y, Arai H, Uchimoto Y, Matsubara E, Uruga T, Takeshita K, Takahashi S, Sano M, Aoyagi H, Watanabe A, Nariyama N, Ohashi H, Yumoto H, Koyama T, Senba Y, Takeuchi T, Furukawa Y, Ohata T, Matsushita T, Ishizawa Y, Kudo T, Kimura H, Yamazaki H, Tanaka T, Bizen T, Seike T, Goto S, Ohno H, Takata M, Kitamura H, Ishikawa T, Ohta T, Ogumi Z (2014) RISING beamline (BL28XU) for rechargeable battery analysis. J Synchrotron Radiat 21:268–272

279. Kaito T, Mitsumoto H, Sugawara S, Shinohara K, Uehara H, Ariga H, Takakusagi S, Hatakeyama Y, Nishikawa K, Asakura K (2014) K-edge x-ray absorption fine structure analysis of Pt/Au core-shell electrocatalyst: evidence for short Pt-Pt distance. J Phys Chem C 118(16):8481–8490

280. Gianoncelli A, Kaulich B, Kiskinova M, Prasciolu M, Urzo BD, Bozzini B (2011) An in situ electrochemical soft x-ray spectromicroscopy investigation of Fe galvanically coupled to Au. Micron 42(4):342–347

281. Jiang P, Chen JL, Borondics F, Glans PA, West MW, Chang CL, Salmeron M, Guo JH (2010) In situ soft x-ray absorption spectroscopy investigation of electrochemical corrosion of copper in aqueous NaHCO$_3$ solution. Electrochem Commun 12(6):820–822

282. Jiang P, Prendergast D, Borondics F, Porsgaard S, Giovanetti L, Pach E, Newberg J, Bluhm H, Besenbacher F, Salmeron M (2013) Experimental and theoretical investigation of the electronic structure of Cu2O and CuO thin films on Cu(110) using x-ray photoelectron and absorption spectroscopy. J Chem Phys 138(2):024704/1–024704/6

283. Merte LR, Behafarid F, Miller DJ, Friebel D, Cho S, Mbuga F, Sokaras D, Alonso-Mori R, Weng TC, Nordlund D, Nilsson A, Cuenya BR (2012) Electrochemical oxidation of size-selected Pt nanoparticles studied using in situ high-energy-resolution x-ray absorption spectroscopy. ACS Catal 2(11):2371–2376

284. Friebel D, Miller DJ, O'Grady CP, Anniyev T, Bargar J, Bergmann U, Ogasawara H, Wikfeldt KT, Pettersson LGM, Nilsson A (2011) In situ x-ray probing reveals fingerprints of surface platinum oxide. Phys Chem Chem Phys 13(1):262–266

285. Friebel D, Viswanathan V, Miller DJ, Anniyev T, Ogasawara H, Larsen AH, O'Grady CP, Norskov JK, Nilsson A (2012) Balance of nanostructure and bimetallic interactions in Pt model fuel cell catalysts: in situ XAS and DFT study. J Am Chem Soc 134 (23):9664–9671

286. Saida T, Sekizawa O, Ishiguro N, Hoshino M, Uesugi K, Uruga T, Ohkoshi S, Yokoyama T, Tada M (2012) 4D visualization of a cathode catalyst layer in a polymer electrolyte fuel cell by 3D laminography-XAFS. Angew Chem Int Ed 51(41):10311–10314

287. Imai H, Matsumoto M, Miyazaki T, Kato K, Tanida H, Uruga T (2011) Growth limits in platinum oxides formed on Pt-skin layers on Pt-Co bimetallic nanoparticles. Chem Commun 47(12):3538–3540

288. Kongkanand A, Ziegelbauer JM (2012) Surface platinum electrooxidation in the presence of oxygen. J Phys Chem C 116(5):3684–3693

289. Redmond EL, Setzler BP, Alamgir FM, Fuller TF (2014) Elucidating the oxide growth mechanism on platinum at the cathode in PEM fuel cells. Phys Chem Chem Phys 16(11):5301–5311

290. Lee JRI, O'Malley RL, O'Connell TJ, Vollmer A, Rayment T (2009) X-ray absorption spectroscopy characterization of Cu underpotential deposition on Au(111) and organothiol-self-assembled-monolayer-modified Au(111) electrodes from sulfate supporting electrolyte. J Phys Chem C 113(28):12260–12271

291. Lee JRI, O'Malley RL, O'Connell TJ, Vollmer A, Rayment T (2010) X-ray absorption spectroscopy characterization of Zn underpotential deposition on Au(111) from phosphate supporting electrolyte. Electrochim Acta 55(28):8532–8538

292. Seo M, Fushimi K, Aoki Y, Habazaki H, Inaba M, Yokomizo M, Hayakawa T, Nakayama T (2012) In situ x-ray absorption spectroscopy for identification of lead species adsorbed on a nickel surface in acidic perchlorate solution. J Electroanal Chem 671:7–15

293. Seo M, Habazaki H, Inaba M, Yokomizo M, Wakabayashi T, Nakayama T (2014) In situ x-ray absorption spectroscopy study of Sn underpotential deposition on Ni from perchloric acid. J Electrochem Soc 161(4):H195–H202

294. Price SWT, Rhodes JM, Calvillo L, Russell AE (2013) Revealing the details of the surface composition of electrochemically prepared Au@Pd Core@Shell nanoparticles with in situ EXAFS. J Phys Chem C 117(47):24858–24865

295. Yoshida M, Yomogida T, Mineo T, Nitta K, Kato K, Masuda T, Nitani H, Abe H, Takakusagi S, Uruga T, Asakura K, Uosaki K, Kondoh H (2013) In situ observation of carrier transfer in the Mn-oxide/Nb:SrTiO$_3$ photoelectrode by x-ray absorption spectroscopy. Chem Commun 49(71):7848–7850

296. Yoshida M, Gon N, Maeda S, Mineo T, Nitta K, Kato K, Nitani H, Abe H, Uruga T, Kondoh H (2014) In situ XAFS study of the photoinduced potential shift of a MnO$_x$ cocatalyst on a SrTiO$_3$ photocatalyst. Chem Lett 43(11):1725–1727

297. Yoshida M, Yomogida T, Mineo T, Nitta K, Kato K, Masuda T, Nitani H, Abe H, Takakusagi S, Uruga T, Asakura K, Uosaki K, Kondoh H (2014) Photoexcited hole transfer to a MnO$_x$ cocatalyst on a SrTiO$_3$ photoelectrode during oxygen evolution studied by in situ x-ray absorption spectroscopy. J Phys Chem C 118(42):24302–24309

298. Yoshida M, Kondoh H (2014) In situ observation of model catalysts under reaction conditions using x-ray core-level spectroscopy. Chem Rec 14(5):806–818

299. Kanan MW, Yano J, Surendranath Y, Dinca M, Yachandra VK, Nocera DG (2010) Structure and valency of a cobalt-phosphate water oxidation catalyst determined by in situ x-ray spectroscopy. J Am Chem Soc 132(39):13692–13701

300. Bediako DK, Lassalle-Kaiser B, Surendranath Y, Yano J, Yachandra VK, Nocera DG (2012) Structure-activity correlations in a nickel-borate oxygen evolution catalyst. J Am Chem Soc 134(15):6801–6809

301. Okumura T, Fukutsuka T, Matsumoto K, Orikasa Y, Arai H, Ogumi Z, Uchimoto Y (2011) Role of local and electronic structural changes with partially anion substitution Lithium manganese spinel oxides on their electrochemical properties: x-ray absorption spectroscopy study. Dalton Trans 40(38):9752–9764

302. Orikasa Y, Ina T, Nakao T, Mineshige A, Amezawa K, Oishi M, Arai H, Ogumi Z, Uchimoto Y (2011) X-ray absorption spectroscopic study on La$_{0.6}$Sr$_{0.4}$CoO$_3$-delta cathode materials related with oxygen vacancy formation. J Phys Chem C 115(33):16433–16438

303. Okumura T, Nakatsutsumi T, Ina T, Orikasa Y, Arai H, Fukutsuka T, Iriyama Y, Uruga T, Tanida H, Uchimoto Y, Ogumi Z (2011) Depth-resolved x-ray absorption spectroscopic study on nanoscale observation of the electrode-solid electrolyte interface for all solid state lithium ion batteries. J Mater Chem 21(27):10051–10060

304. Okumura T, Fukutsuka T, Yanagihara A, Orikasa Y, Arai H, Ogumi Z, Uchimoto Y (2011) Electronic and local structural changes with lithium-ion insertion in TiO$_2$-B: x-ray absorption spectroscopy study. J Mater Chem 21(39):15369–15377

305. Orikasa Y, Ina T, Nakao T, Mineshige A, Amezawa K, Oishi M, Arai H, Ogumi Z, Uchimoto Y (2011) An x-ray absorption spectroscopic study on mixed conductive La$_{0.6}$Sr$_{0.4}$Co$_{0.8}$Fe$_{0.2}$O$_3$-delta cathodes. I. Electrical conductivity and electronic structure. Phys Chem Chem Phys 13(37):16637–16643

306. Yu XQ, Wang Q, Zhou YN, Li H, Yang XQ, Nam KW, Ehrlich SN, Khalid S, Meng YS (2012) High rate delithiation behaviour of LiFePO$_4$ studied by quick x-ray absorption spectroscopy. Chem Commun 48(94):11537–11539

307. Chang HH, Chang CC, Wu HC, Yang MH, Sheu HS, Wu NL (2008) Study on dynamics of structural transformation during charge/discharge of $LiFePO_4$ cathode. Electrochem Commun 10(2):335–339

308. Inoue K, Fujieda S, Shinoda K, Suzuki S, Waseda Y (2010) Chemical state of iron of $LiFePO_4$ during charge–discharge cycles studied by in-situ x-ray absorption spectroscopy. Mater Trans 51(12):2220–2224

309. Lowe MA, Gao J, Abruña HD (2013) In operando x-ray studies of the conversion reaction in Mn_3O_4 lithium battery anodes. J Mater Chem A 1(6):2094–2103

310. Ouvrard G, Zerrouki M, Soudan P, Lestriez B, Masquelier C, Morcrette M, Hamelet S, Belin S, Flank AM, Baudelet F (2013) Heterogeneous behaviour of the lithium battery composite electrode $LiFePO_4$. J Power Sources 229:16–21

311. Dominko R, Arcon I, Kodre A, Hanzel D, Gaberscek M (2009) In-situ XAS study on Li_2MnSiO_4 and Li_2FeSiO_4 cathode materials. J Power Sources 189(1):51–58

312. Dominko R, Garrido CVA, Bele M, Kuezma M, Arcon I, Gaberscek M (2011) Electrochemical characteristics of $Li_{2-x}VTiO_4$ rock salt phase in Li-ion batteries. J Power Sources 196(16):6856–6862

313. Deb A, Bergmann U, Cairns EJ, Cramer SP (2004) X-ray absorption spectroscopy study of the Li_xFePO_4 cathode during cycling using a novel electrochemical in situ reaction cell. J Synchrotron Radiat 11:497–504

314. Deb A, Bergmann U, Cairns EJ, Cramer SP (2004) Structural investigations of $LiFePO_4$ electrodes by Fe x-ray absorption spectroscopy. J Phys Chem B 108(22):7046–7049

315. Rumble C, Conry TE, Doeff M, Cairns EJ, Penner-Hahn JE, Deb A (2010) Structural and electrochemical investigation of $Li(Ni_{0.4}Co_{0.15}Al_{0.05}Mn_{0.4})O_2$ cathode material. J Electrochem Soc 157(12):A1317–A1322

316. Nedoseykina T, Kim MG, Park SA, Kim HS, Kim SB, Cho J, Lee Y (2010) In situ x-ray absorption spectroscopic study for the electrochemical delithiation of a cathode $LiFe_{0.4}Mn_{0.6}PO_4$ material. Electrochim Acta 55(28):8876–8882

317. Lafont U, Locati C, Borghols WJH, Lasinska A, Dygas J, Chadwick AV, Kelder EM (2009) Nanosized high voltage cathode material $LiMg_{0.05}Ni_{0.45}Mn_{1.5}O_4$: structural, electrochemical and in situ investigation. J Power Sources 189(1):179–184

318. Perea A, Castro L, Aldon L, Stievano L, Dedryvere R, Gonbeau D, Tran N, Nuspl G, Breger J, Tessier C (2012) Study of C-coated $LiFe_{0.33}Mn_{0.67}PO_4$ as positive electrode material for Li-ion batteries. J Solid State Chem 192:201–209

319. Wang CY (2004) Fundamental models for fuel cell engineering. Chem Rev 104(10):4727–4765

320. Gasteiger HA, Markovic NM, Ross PN (1995) H2 and CO electrooxidation on well-characterized Pt, Ru, and Pt-Ru.1. Rotating-disk electrode studies of the pure gases including temperature effects. J Phys Chem 99(20):8290–8301

321. Gasteiger HA, Markovic NM, Ross PN (1995) H2 and CO electrooxidation on well-characterized Pt, Ru, and Pt-Ru.2. Rotating disk electrode studies of Co/H2 mixtures at 62-degrees-C. J Phys Chem 99(45):16757–16767

322. Markovic NM, Schmidt TJ, Stamenkovic V, Ross PN (2001) Oxygen reduction reaction on Pt and Pt bimetallic surfaces: a selective review. Fuel Cells 1(2):105–116

323. Burstein GT, Barnett CJ, Kucernak AR, Williams KR (1997) Aspects of the anodic oxidation of methanol. Catal Today 38(4):425–437

324. Zhang SS, Yuan XZ, Hin JNC, Wang HJ, Friedrich KA, Schulze M (2009) A review of platinum-based catalyst layer degradation in proton exchange membrane fuel cells. J Power Sources 194(2):588–600

325. Mukerjee S, Srinivasan S, Soriaga MP, McBreen J (1995) Effect of preparation conditions of Pt alloys on their electronic, structural, and electrocatalytic activities for oxygen reduction-XRD, XAS, and electrochemical studies. J Phys Chem 99(13):4577–4589

326. Mukerjee S, Urian RC (2002) Bifunctionality in Pt alloy nanocluster electrocatalysts for enhanced methanol oxidation and CO tolerance in PEM fuel cells: electrochemical and in situ synchrotron spectroscopy. Electrochim Acta 47(19):3219–3231

327. Kotobuki M, Shido T, Tada M, Uchida H, Yamashita H, Iwasawa Y, Watanabe M (2005) XAFS characterization of Pt-Fe/zeolite catalysts for preferential oxidation of CO in hydrogen fuel gases. Catal Lett 103(3–4):263–269
328. Teliska M, Murthi VS, Mukerjee S, Ramaker DE (2005) Correlation of water activation, surface properties, and oxygen reduction reactivity of supported Pt-M/C bimetallic electrocatalysts using XAS. J Electrochem Soc 152(11):A2159–A2169
329. Wiltshire RJK, King CR, Rose A, Wells PP, Hogarth MP, Thompsett D, Russell AE (2005) A PEM fuel cell for in situ XAS studies. Electrochim Acta 50(25–26):5208–5217
330. Wiltshire RJK, King CR, Rose A, Wells PP, Davies H, Hogarth MP, Thompsett D, Theobald B, Mosselmans FW, Roberts M, Russell AE (2009) Effects of composition on structure and activity of PtRu/C catalysts. Phys Chem Chem Phys 11(13):2305–2313
331. Mukerjee S, Srinivasan S (1993) Enhanced electrocatalysis of oxygen reduction on platinum alloys in proton-exchange membrane fuel-cells. J Electroanal Chem 357(1–2):201–224
332. Tamizhmani G, Capuano GA (1994) Improved electrocatalytic oxygen reduction performance of platinum ternary alloy-oxide in solid-polymer-electrolyte fuel-cells. J Electrochem Soc 141(4):968–975
333. Toda T, Igarashi H, Uchida H, Watanabe M (1999) Enhancement of the electroreduction of oxygen on Pt alloys with Fe, Ni, and Co. J Electrochem Soc 146(10):3750–3756
334. Toda T, Igarashi H, Watanabe M (1999) Enhancement of the electrocatalytic O_2 reduction on Pt-Fe alloys. J Electroanal Chem 460(1–2):258–262
335. Paulus UA, Wokaun A, Scherer GG, Schmidt TJ, Stamenkovic V, Radmilovic V, Markovic NM, Ross PN (2002) Oxygen reduction on carbon-supported Pt-Ni and Pt-Co alloy catalysts. J Phys Chem B 106(16):4181–4191
336. Stamenkovic VR, Mun BS, Arenz M, Mayrhofer KJJ, Lucas CA, Wang GF, Ross PN, Markovic NM (2007) Trends in electrocatalysis on extended and nanoscale Pt-bimetallic alloy surfaces. Nat Mater 6(3):241–247
337. Stamenkovic VR, Fowler B, Mun BS, Wang GF, Ross PN, Lucas CA, Markovic NM (2007) Improved oxygen reduction activity on $Pt_3Ni(111)$ via increased surface site availability. Science 315(5811):493–497
338. Ioroi T, Siroma Z, Fujiwara N, Yamazaki S, Yasuda K (2005) Sub-stoichiometric titanium oxide-supported platinum electrocatalyst for polymer electrolyte fuel cells. Electrochem Commun 7(2):183–188
339. Lim DH, Lee WD, Choi DH, Kwon HH, Lee HI (2008) The effect of cerium oxide nanoparticles on a Pt/C electrocatalyst synthesized by a continuous two-step process for low-temperature fuel cell. Electrochem Commun 10(4):592–596
340. Lee KH, Kwon K, Roev V, Yoo DY, Chang H, Seung D (2008) Synthesis and characterization of nanostructured PtCo-CeO_x/C for oxygen reduction reaction. J Power Sources 185 (2):871–875
341. Elezovic NR, Babic BM, Radmilovic VR, Gojkovic SL, Krstajic NV, Vracar LM (2008) Pt/C doped by MoO_x as the electrocatalyst for oxygen reduction and methanol oxidation. J Power Sources 175(1):250–255
342. Elezovic NR, Babic BM, Radmilovic VR, Vracar LM, Krstajic NV (2009) Synthesis and characterization of MoO_x-Pt/C and TiO_x-Pt/C nano-catalysts for oxygen reduction. Electrochim Acta 54(9):2404–2409
343. Sasaki K, Zhang L, Adzic RR (2008) Niobium oxide-supported platinum ultra-low amount electrocatalysts for oxygen reduction. Phys Chem Chem Phys 10(1):159–167
344. Baturina OA, Garsany Y, Zega TJ, Stroud RM, Schull T, Swider-Lyons KE (2008) Oxygen reduction reaction on platinum/tantalum oxide electrocatalysts for PEM fuel cells. J Electrochem Soc 155(12):B1314–B1321
345. Chhina H, Campbell S, Kesler O (2009) Ex situ and in situ stability of platinum supported on niobium-doped titania for PEMFCs. J Electrochem Soc 156(10):B1232–B1237

346. Xiong LF, More KL, He T (2010) Syntheses, characterization, and catalytic oxygen electroreduction activities of carbon-supported PtW nanoparticle catalysts. J Power Sources 195(9):2570–2578
347. Huang SY, Ganesan P, Popov BN (2010) Electrocatalytic activity and stability of niobium-doped titanium oxide supported platinum catalyst for polymer electrolyte membrane fuel cells. Appl Catal B Environ 96(1–2):224–231
348. Fugane K, Mori T, Ou DR, Suzuki A, Yoshikawa H, Masuda T, Uosaki K, Yamashita Y, Ueda S, Kobayashi K, Okazaki N, Matolinova I, Matolin V (2011) Activity of oxygen reduction reaction on small amount of amorphous CeO_x promoted Pt cathode for fuel cell application. Electrochim Acta 56(11):3874–3883
349. Lim DH, Lee WD, Choi DH, Lee HI (2010) Effect of ceria nanoparticles into the Pt/C catalyst as cathode material on the electrocatalytic activity and durability for low-temperature fuel cell. Appl Catal B Environ 94(1–2):85–96
350. Garsany Y, Epshteyn A, Purdy AP, More KL, Swider-Lyons KE (2010) High-activity, durable oxygen reduction electrocatalyst: nanoscale composite of platinum-tantalum oxyphosphate on vulcan carbon. J Phys Chem Lett 1(13):1977–1981
351. Ferreira PJ, la O' GJ, Shao-Horn Y, Morgan D, Makharia R, Kocha S, Gasteiger HA (2005) Instability of Pt/C electrocatalysts in proton exchange membrane fuel cells – a mechanistic investigation. J Electrochem Soc 152(11):A2256–A2271
352. Yasuda K, Taniguchi A, Akita T, Ioroi T, Siroma Z (2006) Platinum dissolution and deposition in the polymer electrolyte membrane of a PEM fuel cell as studied by potential cycling. Phys Chem Chem Phys 8(6):746–752
353. Xie J, Wood DL, More KL, Atanassov P, Borup RL (2005) Microstructural changes of membrane electrode assemblies during PEFC durability testing at high humidity conditions. J Electrochem Soc 152(5):A1011–A1020
354. Schulze M, Schneider A, Gulzow E (2004) Alteration of the distribution of the platinum catalyst in membrane-electrode assemblies during PEFC operation. J Power Sources 127(1–2):213–221
355. Akita T, Taniguchi A, Maekawa J, Sirorna Z, Tanaka K, Kohyama M, Yasuda K (2006) Analytical TEM study of Pt particle deposition in the proton-exchange membrane of a membrane-electrode-assembly. J Power Sources 159(1):461–467
356. Yasuda K, Taniguchi A, Akita T, Ioroi T, Siroma Z (2006) Characteristics of a platinum black catalyst layer with regard to platinum dissolution phenomena in a membrane electrode assembly. J Electrochem Soc 153(8):A1599–A1603
357. Wilson MS, Garzon FH, Sickafus KE, Gottesfeld S (1993) Surface-area loss of supported platinum in polymer electrolyte fuel-cells. J Electrochem Soc 140(10):2872–2877
358. Borup RL, Davey JR, Garzon FH, Wood DL, Inbody MA (2006) PEM fuel cell electrocatalyst durability measurements. J Power Sources 163(1):76–81
359. Ascarelli P, Contini V, Giorgi R (2002) Formation process of nanocrystalline materials from x-ray diffraction profile analysis: application to platinum catalysts. J Appl Phys 91(7): 4556–4561
360. Giorgi R, Ascarelli P, Turtu S, Contini V (2001) Nanosized metal catalysts in electrodes for solid polymeric electrolyte fuel cells: an XPS and XRD study. Appl Surf Sci 178(1–4):149–155
361. Wakisaka M, Mitsui S, Hirose Y, Kawashima K, Uchida H, Watanabe M (2006) Electronic structures of Pt-Co and Pt-Ru alloys for Co-tolerant anode catalysts in polymer electrolyte fuel cells studied by EC-XPS. J Phys Chem B 110(46):23489–23496
362. Wakisaka M, Suzuki H, Mitsui S, Uchida H, Watanabe M (2008) Increased oxygen coverage at Pt-Fe alloy cathode for the enhanced oxygen reduction reaction studied by EC-XPS. J Phys Chem C 112(7):2750–2755
363. Wakisaka M, Suzuki H, Mitsui S, Uchida H, Watanabe M (2009) Identification and quantification of oxygen species adsorbed on Pt(111) single-crystal and polycrystalline Pt electrodes by photoelectron spectroscopy. Langmuir 25(4):1897–1900

364. Wakisaka M, Udagawa Y, Suzuki H, Uchida H, Watanabe M (2011) Structural effects on the surface oxidation processes at Pt single-crystal electrodes studied by x-ray photoelectron spectroscopy. Energy Environ Sci 4(5):1662–1666

365. Ishiguro N, Uruga T, Sekizawa O, Tsuji T, Suzuki M, Kawamura N, Mizumaki M, Nitta K, Yokoyama T, Tada M (2014) Visualization of the heterogeneity of cerium oxidation states in single Pt/Ce$_2$Zr$_2$O$_x$ catalyst particles by nano-XAFS. ChemPhysChem 15(8):1563–1568

366. Jerkiewicz G (1999) Surface oxidation of noble metal electrodes. In: Wieckowski A (ed) Interfacial electrochemistry: theory, experiment, and applications. Marcel Dekker, New York, pp 559–576

367. Markovic NM, Ross PN (1999) In: Wieckowski A (ed) Interfacial electrochemistry: theory, experiment, and applications. Marcel Dekker, New York, pp 821–842

368. You H, Zurawski DJ, Nagy Z, Yonco RM (1994) In-situ x-ray reflectivity study of incipient oxidation of Pt(111) surface in electrolyte-solutions. J Chem Phys 100(6):4699–4702

369. Matsumoto M, Miyazaki T, Imai H (2011) Oxygen-enhanced dissolution of platinum in acidic electrochemical environments. J Phys Chem C 115(22):11163–11169

370. Carino EV, Crooks RM (2011) Characterization of Pt@Cu Core@Shell dendrimer-encapsulated nanoparticles synthesized by Cu underpotential deposition. Langmuir 27(7):4227–4235

371. Taguchi S, Kondo M, Mori H, Aramata A (2013) Formation of zinc-oxianion complex adlayer by underpotential deposition of Zn on Au(111) electrode: preferential formation of zinc monohydrogen phosphate complex in weakly acidic solutions. Electrochim Acta 111:642–655

372. Friebel D, Miller DJ, Nordlund D, Ogasawara H, Nilsson A (2011) Degradation of bimetallic model electrocatalysts: an in situ x-ray absorption spectroscopy study. Angew Chem-Int Ed 50(43):10190–10192

373. Tadjeddine A, Guay D, Ladouceur M, Tourillon G (1991) Electronic and structural characterization of underpotentially deposited submonolayers and monolayer of copper on gold (111) studied by in situ x-ray-absorption spectroscopy. Phys Rev Lett 66(17):2235–2238

374. Tadjeddine A, Tourillon G, Guay D (1991) Structural and electronic characterization of underpotentially deposited copper on gold single-crystal probed by in situ x-ray absorption-spectroscopy. Electrochim Acta 36(11–12):1859–1862

375. Gordon JG, Melroy OR, Toney MF (1995) Structure of metal electrolyte interfaces – copper on gold(111), water on silver(111). Electrochim Acta 40(1):3–8

376. Wu S, Lipkowski J, Tyliszczak T, Hitchcock AP (1995) Effect of anion adsorption on early stages of copper electrocrystallization at Au(111) surface. Prog Surf Sci 50(1–4):227–236

377. Wu S, Shi Z, Lipkowski J, Hitchcock AP, Tyliszczak T (1997) Early stages of copper electrocrystallization: electrochemical and in situ x-ray absorption fine structure studies of coadsorption of copper and chloride at the Au(111) electrode surface. J Phys Chem B 101(49):10310–10322

378. Friebel D, Mbuga F, Rajasekaran S, Miller DJ, Ogasawara H, Alonso-Mori R, Sokaras D, Nordlund D, Weng TC, Nilsson A (2014) Structure, redox chemistry, and interfacial alloy formation in monolayer and multilayer Cu/Au(111) model catalysts for CO$_2$ electroreduction. J Phys Chem C 118(15):7954–7961

379. Love CT, Korovina A, Patridge CJ, Swider-Lyons KE, Twigg ME, Ramaker DE (2013) Review of LiFePO$_4$ phase transition mechanisms and new observations from x-ray absorption spectroscopy. J Electrochem Soc 160(5):A3153–A3161

380. Yang MC, Xu B, Cheng JH, Pan CJ, Hwang BJ, Meng YS (2011) Electronic, structural, and electrochemical properties of LiNi$_x$Cu$_y$Mn$_{2-x-y}$O$_4$ (0 < x < 0.5, 0 < y < 0.5) high-voltage spinel materials. Chem Mater 23(11):2832–2841

381. Yoon J, Muhammad S, Jang D, Sivakumar N, Kim J, Jang WH, Lee YS, Park YU, Kang K, Yoon WS (2013) Study on structure and electrochemical properties of carbon-coated monoclinic Li$_3$V$_2$(PO$_4$)$_3$ using synchrotron based in situ x-ray diffraction and absorption. J Alloys Compd 569:76–81

382. Mizushima K, Jones PC, Wiseman PJ, Goodenough JB (1981) LixCoO2 ($0 < x \leq 1$): a new cathode material for batteries of high-energy density. Solid State Ion 3–4(Aug):171–174

383. Mizushima K, Jones PC, Wiseman PJ, Goodenough JB (1980) LixCoO2 ($0 < x \leq 1$): a new cathode material for batteries of high-energy density. Mater Res Bull 15(6):783–789

384. Shin HC, Chung KY, Min WS, Byun DJ, Jang H, Cho BW (2008) Asymmetry between charge and discharge during high rate cycling in $LiFePO_4$ – in situ x-ray diffraction study. Electrochem Commun 10(4):536–540

385. Kodama R, Terada Y, Nakai I, Komaba S, Kumagai N (2006) Electrochemical and in situ XAFS-XRD investigation of Nb_2O_5 for rechargeable lithium batteries. J Electrochem Soc 153(3):A583–A588

386. Yabuuchi N, Sugano M, Yamakawa Y, Nakai I, Sakamoto K., Muramatsu H, Komaba S (2011) Effect of heat-treatment process on FeF3 nanocomposite electrodes for rechargeable Li batteries. J Mater Chem 21(27):10035–10041

387. Komaba S, Yabuuchi N, Nakayama T, Ogata A, Ishikawa T, Nakai I (2012) Study on the Reversible Electrode Reaction of $Na_{1-x}Ni_{0.5}Mn_{0.5}O_2$ for a Rechargeable Sodium-Ion Battery. Inorg Chem 51(11):6211–6220

388. Yabuuchi N, Yamamoto K, Yoshii K, Nakai I, Nishizawa T, Omaru A, Toyooka T, Komaba S (2013) Structural and Electrochemical Characterizations on Li_2MnO_3-$LiCoO_2$-$LiCrO_2$ System as Positive Electrode Materials for Rechargeable Lithium Batteries. J Electrochem Soc 160(1):A39–A45

389. Masuda T, Uosaki K (2004) Construction of organic monolayers with electron transfer function on a hydrogen terminated Si(111) surface via silicon-carbon bond and their electrochemical characteristics in dark and under illumination. Chem Lett 33(7):788–789

390. Masuda T, Shimazu K, Uosaki K (2008) Construction of mono- and multimolecular layers with electron transfer mediation function and catalytic activity for hydrogen evolution on a hydrogen-terminated Si(111) surface via Si-C bond. J Phys Chem C 112(29):10923–10930

391. Dismukes GC, Brimblecombe R, Felton GAN, Pryadun RS, Sheats JE, Spiccia L, Swiegers GF (2009) Development of bioinspired Mn_4O_4-cubane water oxidation catalysts: lessons from photosynthesis. Acc Chem Res 42(12):1935–1943

392. Brimblecombe R, Swiegers GF, Dismukes GC, Spiccia L (2008) Sustained water oxidation photocatalysis by a bioinspired manganese cluster. Angew Chem Int Ed 47(38):7335–7338

393. Brimblecombe R, Kolling DRJ, Bond AM, Dismukes GC, Swiegers GF, Spiccia L (2009) Sustained water oxidation by $[Mn_4O_4]^{7+}$ core complexes inspired by oxygenic photosynthesis. Inorg Chem 48(15):7269–7279

394. Brimblecombe R, Dismukes GC, Swiegers GF, Spiccia L (2009) Molecular water-oxidation catalysts for photoelectrochemical cells. Dalton Trans 43:9374–9384

395. Hocking RK, Brimblecombe R, Chang LY, Singh A, Cheah MH, Glover C, Casey WH, Spiccia L (2011) Water-oxidation catalysis by manganese in a geochemical-like cycle. Nat Chem 3(6):461–466

396. Gorlin Y, Jaramillo TF (2010) A bifunctional nonprecious metal catalyst for oxygen reduction and water oxidation. J Am Chem Soc 132(39):13612–13614

Gas-Phase Near-Edge X-Ray Absorption Fine Structure (NEXAFS) Spectroscopy of Nanoparticles, Biopolymers, and Ionic Species

Aleksandar R. Milosavljević, Alexandre Giuliani, and Christophe Nicolas

Contents

A.R. Milosavljević (✉)
Institute of Physics Belgrade, University of Belgrade, Belgrade, Serbia
e-mail: vraz@ipb.ac.rs

A. Giuliani
Synchrotron SOLEIL, L'Orme des Merisiers, Gif-sur-Yvette, France

UAR1008, CEPIA, INRA, Nantes, France
e-mail: alexandre.giuliani@synchrotron-soleil.fr

C. Nicolas
Synchrotron SOLEIL, L'Orme des Merisiers, Gif-sur-Yvette, France
e-mail: christophe.nicolas@synchrotron-soleil.fr

1   Definition of the Topic

Near-edge X-ray absorption fine structure (NEXAFS) spectroscopy probes directly or indirectly the photoabsorption cross section of a system under study as a function of the photon energy around the core–shell ionization thresholds. When the photon energy matches the difference between the core level and an unoccupied valence level, the photoabsorption cross section increases. The core levels are associated with particular atoms within the system under the study; therefore, NEXAFS spectroscopy appears to be a very sensitive probe of physicochemical and structural properties of molecules and materials. It has been intensively applied to investigate gaseous, liquid, and solid species. In this chapter, we describe methods to perform *gas-phase* NEXAFS spectroscopy of large systems, such as nanoparticles, clusters, and biopolymers, as well as of ionic species. We also review recent research findings.

2   Overview

The development of third-generation synchrotron radiation (SR) sources, providing extremely bright and energy-resolved X-ray beams, established NEXAFS spectroscopy as a powerful and widely used technique to investigate electronic and structural properties of both organic and inorganic samples of increasing complexity. Particularly, gas-phase NEXAFS studies allow for an investigation of well-defined targets prepared under desired conditions.

Unfortunately, gas-phase NEXAFS spectroscopy of large species such as biopolymers (e.g., proteins and DNA) and nanoparticles, as well as ionic species, is experimentally very challenging due to great difficulties in both bringing large molecules or particles intact into the gas phase and providing high-enough target density, photon flux, and interaction time needed to distinguish K-shell excitation processes. Only recently, the development of new experimental techniques has allowed performing gas-phase NEXAFS of nanoparticles, biopolymers, and ionic species.

Herein, we present the basic principles of NEXAFS spectroscopy and describe the state-of-the-art experimental approaches that allow for NEXAFS spectroscopy of large biopolymers and nanoparticles isolated in the gas phase. Finally, we present some key research finding spanning from relatively small biomolecules to large biopolymers and nanoparticles.

3   Introduction

NEXAFS spectroscopy has been used to study systems of increasing complexity, from small isolated molecules to large biological objects and materials; and it has been successfully applied to gaseous, liquid, thin-layer, nanoscopic, and solid targets. There is a substantial literature on the subject, from comprehensive graduate-level textbooks presenting both the fundamental principles and the

applications of NEXAFS spectroscopy (e.g., [1]) to more specialized reviews that deal with, for example, the application of the technique in studying thin organic films and liquids [2] or DNA components [3]. Herein, the focus is on recently developed NEXAFS action spectroscopy of ionic targets as well as large species such as nanoparticles and biopolymers isolated in vacuo.

The strength of inner-shell spectroscopic techniques is based on the excitation of core-level electrons providing a highly localized nature of the triggering process and, thus, sensitive and selective probe of the electronic, chemical, and structural properties of the system [4]. With this aim, NEXAFS spectroscopy of thin molecular films has been used in recent years to investigate properties of large biologically important molecules, such as proteins, for example [5–9]. However, spectroscopic study of solid or aqueous samples may be limited in cases where intrinsic electronic and structural information is to be measured without interferences from the environment. Moreover, condensed matter samples may suffer severe radiation damage from the energetic X-ray radiation, which, in turn, may affect the results (see [10] and references therein). Gas-phase spectroscopy, on the other hand, allows studying isolated system in vacuo under well-defined conditions. Furthermore, a constant sample renewal practically prevents any radiation damage effects. Nevertheless, the crucial issue here is the kind of objects that can be transferred and isolated in vacuo with a high-enough density for inner-shell spectroscopy to be efficiently conducted.

There are tremendous amounts of results from gas-phase NEXAFS spectroscopy, which has been routinely performed on relatively small targets that can be easily brought into the gas phase. This incredible rise of the X-ray-based spectroscopy is dominantly due to the increasing number of new-generation bright SR sources. However, gas-phase X-ray spectroscopy of large targets has been reported only recently, after development of modern methods allowing for bringing such large species into the gas phase. For example, one way to obtain an intact protein in the gas phase and to submit it to X-rays is to use the electrospray ionization (ESI) [11], where protonated or deprotonated protein ions are extracted into the gas phase directly from the solution. Nevertheless, since the ionic target density is too low to measure the photon beam attenuation, NEXAFS spectroscopy must be performed as an action spectroscopy, by indirectly recording processes resulting from the X-ray absorption. A very efficient action spectroscopy is based on tandem mass spectrometry (MS^2). With the advent of modern ionization techniques, MS^2 has become one of the most powerful tools to probe the structure of biopolymers [12]. In MS^2 a desired ionic compound is isolated, activated, and mass analyzed. NEXAFS MS^2 is, therefore, based on recording the tandem mass spectra produced upon photon activation of the precursor ions, as a function of the photon energy scanned around the core ionization edge. Figure 8.1 schematically presents soft X-ray absorption processes, leading to the formation of a core hole triggering either resonant or normal Auger decays and resulting in ejection of Auger electrons and ionization of the precursor, which, finally, can be detected by mass spectrometry (see Sect. 4.2.4 for more details).

The principles of SR sources are described in Sect. 4.1. The common spectroscopic techniques are presented and shortly described in Sect. 4.2. The sources of
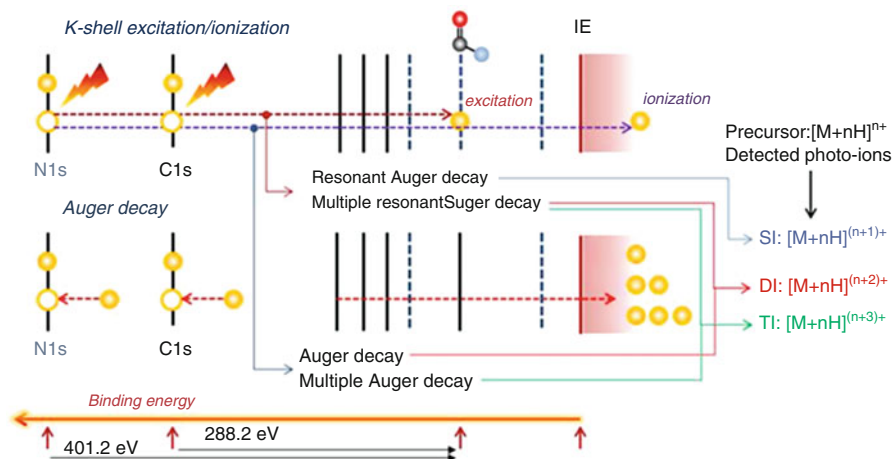
Fig. 8.1 Schematic representation of the X-ray K-shell excitation/ionization of a multiply proton-ated protein ion, followed by Auger decays and production of ionized cations that are detected in the experiment (Adopted from Milosavljević et al. [13])

gas-phase targets are described in Sect. 4.3. Typical experimental setups for coupling the sources of large gas-phase targets with the synchrotron X-ray beam are the subject of Sect. 4. Finally, key research findings are reviewed in Sect. 5.

4 Experimental and Instrumental Methodology

4.1 X-Ray Sources

4.1.1 Synchrotron Radiation Facilities

There are many different ways to produce X-ray photons, from laboratory X-ray tubes to the latest generation of synchrotron radiation storage rings and free-electron lasers. In this chapter, we will concentrate on accelerator-based sources. Synchrotron radiation (SR) is an electromagnetic radiation produced by the acceleration of charged particles of relativistic velocities. SR is intimately connected to a high-energy particle accelerator. Indeed, SR is the main mechanism of energy lost by the accelerated particles, due to photon emissions all along their trajectories. Ivanenko and Pommeranchuck in 1944 [14] and independently Schwinger in 1946 [15, 16] have reported the theory of SR for circular particle accelerators. SR has been observed for the first time in 1946 at the General Electric synchrotron in the United States. However, due to the complexity of the accelerator technologies and also to the dedication of these machines primarily to high-energy physics, it was only in the 1960s that SR was used for the first time for spectroscopic studies [17–20]. There-after, storage rings started to be progressively dedicated to SR studies, and due to the specific properties of SR light, synchrotron facilities have become one of the most

useful sources of spectroscopic studies in the twentieth century. Kuntz et al. [21] give a good overview of the early stages of SR development but also the basis of synchrotron radiation theory. The important properties of SR are:

1. A wide wavelength coverage, from THz to hard X-rays. Moreover, with the advent of the third-generation installations (see below), SR radiation can be optimized over a given energy range (vacuum ultraviolet, soft X-rays, hard X-rays).
2. A high brilliance, due to the high collimation of the emitted radiation.
3. The time structure of the pulsed light.
4. An adjustable polarization, from classic linear polarization with the electric vector parallel to the orbit plan (classic bend magnet radiation) to various polarizations including circular or elliptical (by using an insertion device such as an undulator; see below).

Figure 8.2 depicts a typical third-generation synchrotron storage ring, such as SOLEIL, the latest French synchrotron facility. The electron bunches are created by an electron gun and then first accelerated in the LINAC (linear accelerator) up to 100 MeV. Then, they are brought to the nominal energy of the storage ring in the booster ring (2.75 GeV, in the case of SOLEIL). When they reach this final energy, they are injected into the storage ring, which is composed of a succession of straight sections connected by bending magnets. Compared to second-generation installations, which use exclusively the bending magnets to produce SR radiation, the third generations use magnetic insertion devices such as undulators or wigglers [22–24], made with a periodic structure of dipole magnets. In this case, the electron bunches experience a periodic magnetic field that radially accelerates them several times, giving them an oscillatory trajectory and thus producing SR. This radiation is orders of magnitudes higher than the one produced by a standard bending magnet. Moreover, by adjusting the design parameters of the insertion device, the emission can be optimized in a narrower region around the photon energy of interest [25]. As an example, a brilliance of 10^{15} photons/s 0.1 % bw mm^2 $mrad^2$ can be achieved in the soft X-ray regime, thanks to insertion devices, such as the Apple II. These kinds of photon fluxes have made possible new studies on low-density samples under vacuum by different spectroscopic techniques and will be discussed below.

With the forthcoming generation of storage rings, the ultimate storage ring light sources [26], the diffraction limit of the machine electron optics should be achieved. With the decrease in the horizontal emittances thus reached, an additional gain of several orders of magnitude in brilliance is expected compared to existing light sources, and therefore new studies on gas-phase isolated biomolecules, clusters, and nanoparticles, which are particularly photon demanding, should be boosted. In particular, pump–probe experiments involving optical lasers would be facilitated.

In parallel with the development of synchrotron light sources, another type of installation based on the same technology is developing. Free-electron laser (FEL) sources use a linear accelerator followed by one or more undulators in series, in which the electron bunches are dumped after they emit their SR pulse. Initially used

Fig. 8.2 Schematic drawing of a third-generation synchrotron machine (SOLEIL synchrotron, France)

in the IR or in the VUV and EUV ranges, in the last decade, the X-ray FELs made available high-intensity femtosecond X-ray pulses of coherent SR to the user's community. The brilliance of FELs are orders of magnitudes higher than existing or future storage rings. As an example, the LCLS installation is capable of reaching an average brilliance of 10^{22} photon/s 0.1 % bw mm^2 $mrad^2$. These X-ray pulses are:

- Ultra-intense
- Coherent
- Ultrashort
- Having a high spatial resolution

These properties have made possible single-shot diffraction experiments of labile objects such as biomolecules or membrane proteins [27, 28] but also of nanoscale objects such as viruses [29–31] or soot particles [32]. The possibility of coupling diffraction techniques (structural information) with spectroscopic or spectrometric techniques is very promising.

4.1.2 Soft X-Ray Beamlines

SR, after being emitted by an undulator or a bending magnet, is collected tangentially to the storage ring into a beamline, which comprises a set of optical and mechanical devices used to transport, select the photon energy, and focalize the monochromatic light to the desired area in the experimental chamber. The new-generation synchrotrons can host more than 20 beamlines, each one specializing in specific scientific fields. We will concentrate in this chapter only on the soft X-ray beamlines opened to users and that are specialized in dilute matter studies. Presently, there are 16 soft X-ray beamlines of this type around the world. With the

later-generation beamlines, the synchrotron beam can be focused into a spot with dimensions of around a few hundred micrometers; even focusing to a few tens of micrometers can now be easily achieved. Also, the geometric dimensions of these synchrotron beams at the focal point are now matching the dimension of nanoparticle beams (few hundreds of micrometers) or even liquid microjet beams (tens of micrometers). Moreover, the brilliance on the sample can reach 10^{13} photon/s mm^2 0.1 % bw mrad^2. The resolving powers of the photon beam have also increased. Nowadays, a beamline designed for high resolution can reach a maximum resolving power of 100 000.

4.2   General Techniques

4.2.1   X-Ray Absorption Spectroscopy

NEXAFS spectroscopy is a commonly used technique in gas phase or surface science experiments [1]. A core electron is excited to an unoccupied molecular orbital or to the continuum, and then a de-excitation occurs, via Auger decay or fluorescence, to fill the core hole created. In the soft X-ray regime and with low Z-elements, the fluorescent channel remains weak. Usually in NEXAFS spectroscopy, spectra exhibit π^* or σ^* resonances when the energy difference between the core level and one unoccupied molecular orbital equals the photon energy. Additionally, Rydberg series converging toward the K-edge ionization threshold may also be observed for isolated species. Thus, information about the electronic structure may be obtained from such experiments. Moreover, with NEXAFS spectroscopy, specific bonds such as C–C, C=C, C=O, etc., can be identified. It is important to note that the position of the σ^* resonances compared to the absorption onset has been related to the bond length [33–35]. The simplest way to measure NEXAFS spectra is to record total ion or electron yields as a function of the photon energy. A basic setup consists of two polarizable grids that attract the cations (or the electrons, depending on the chosen mode), a multichannel plate chevron stack, and a 50 Ω adapted full metal anode.

The absorption of a photon just below or just above the core ionization threshold promotes a molecule to an energetic core-excited state that dominantly relaxes via Auger decay [10, 36, 37]. Below the threshold, the core electron is promoted to an unoccupied molecular orbital, triggering the resonant Auger decay or an X-ray fluorescence process [37], leading mostly to a single-ionization process (an Auger electron emission) [10] but also a multiple ionization. When the photon energy is above the core ionization threshold, the core electron is ejected directly into the ionization continuum, and the system may relax via a normal Auger decay, producing a multiply charged ion (emission of both a core ejected and Auger electron(s)). In all cases, X-ray absorption produces ionized species that can be detected by means of mass spectrometry methods (see Fig. 8.3). Fine-tuning of the photon energy over the resonant excitation energies and the core ionization threshold may result in a drastic change in the fragment ion yields, since the intensive ionization/fragmentation is actually triggered by the resonant photon absorption or the ionization.
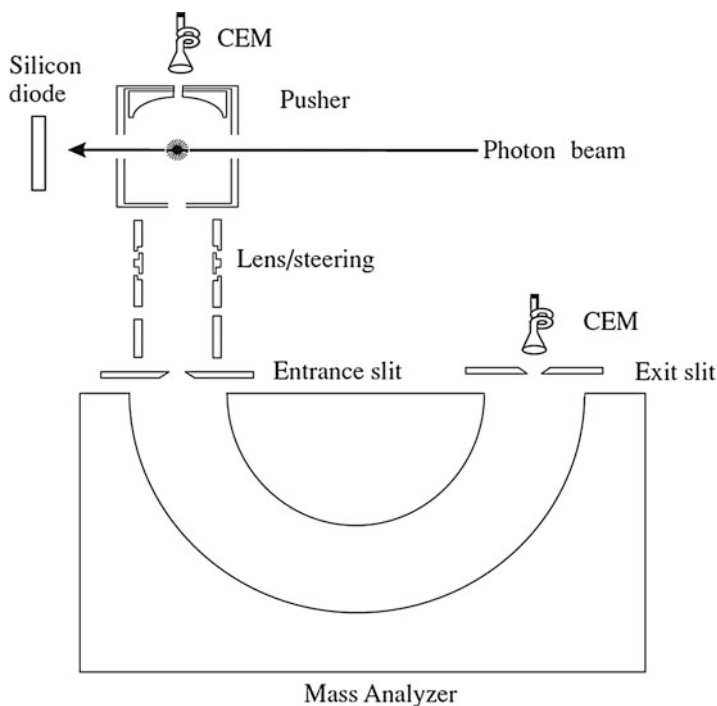
Fig. 8.3 Schematic representation of the experimental setup used for the partial-ion-yield measurements (Reprinted from Guillemin et al. [38]. © IOP Publishing. Reproduced with permission. All rights reserved)

In the case of relatively small gaseous molecules, X-ray absorption generally leads to an intensive fragmentation of the target. Therefore, the results represent partial-ion-yield curves of selected fragments, possessing rich spectroscopic structure below the ionization threshold corresponding to the excitation energies of the target molecule. Also, doubly charged fragment ions have increased yield above the ionization threshold. The application of X-ray absorption mass spectrometry has been limited until recently only to relatively small molecules, owing to difficulties to place in gas-phase large species such as neutral biomolecules (see the Introduction and the following section about sources of gas-phase targets).

4.2.2   X-Ray Photoemission Spectroscopy

With NEXAFS spectroscopy, there is no analysis of the kinetic energy (E_{Kin}) of the electron detected. Indeed, the absorption cross section is a sum over all the electrons ejected belonging to shells with a binding energy (E_{BD}) lower than or equal to the photon energy (E_{Photon}). In photoemission experiments, the kinetic energy of the electron is analyzed. The relation between the kinetic energy (E_{Kin}) of the emitted electron and the binding energy (E_{BD}) is given by Eq. 8.1:

$$E_{Kin} = E_{Photon} - E_{BD} \tag{8.1}$$

Various kinds of spectrometers have been developed in order to analyze the kinetic energy of the emitted electrons [39, 40]. Either the time of flight of the electron is measured and its correspondent kinetic energy is calculated or energy-dispersive elements (electrodes) are used to deflect the electrons according to their kinetic energy. In this last case, an electron lens system is needed to collect, transport, and focus the photoelectrons on the entrance slit of the analyzer. Information on the electronic structure of matter can be obtained through measurement of the electron binding energies and their chemical shifts [41]. Atoms and molecules [42, 43], clusters [44–50] or nanoparticles, and bulk material [51–56] are investigated with this technique. As shown by Eq. 8.1, for a given electronic state, increasing the energy of the incoming photon will increase the kinetic energy of the emitted electron. Moreover, according to the universal inelastic mean free path curve of an electron, the surface sensitivity can be tuned. This is an important point, as it explains the extreme surface sensitivity of nanoparticle studies in the soft X-ray regime (see Sect. 5.3).

4.2.3   Coincident Measurements

Compared to conventional electron spectroscopy, an electron–electron or electron–ion coincidence measurement is always much more powerful in providing a direct view of the interaction processes [57–62]. Different experimental setups are used with soft X-ray synchrotron radiation [60, 63–65]. One of the key points in such a measurement requires that both electrons and ions are collected and detected as efficiently as possible, hence to maximize coincidence efficiency. Fragmentation of gas-phase molecules [62] or small biomolecules (see Sect. 4.1), clusters [66, 67], condensed matter [68–71], and nanoparticles [52] has been investigated with this technique.

4.2.4   X-Ray Action Spectroscopy of Trapped Ions

Recently, the use of ion-trapping devices has attracted a growing interest, as it allows performing mass and charge-selected spectroscopy [72]. These experiments are sequential in nature. Ions of interest are generated in a variety of ion sources (described in Sect. 4.3.3), which may be pulsed (such as laser desorption) or continuous (such as electrospray ionization). The ions are then selected and stored in an appropriate ion trap. When the storage capacity of the trap is reached, X-ray beam from a beamline is admitted to the trap and irradiates the ions for a controlled amount of time. After the interactions, the ion trap is emptied, and its content analyzed. The whole sequence is described in Fig. 8.4.

The steps described in Fig. 8.4 may be repeated several times until satisfactory statistic is reached before the photon energy is changed and the cycle is reiterated.

The ion spectroscopy experiments belong to the class of action spectroscopy, in which specific photophysical or photochemical reaction giving a detectable product ion is used to derive partial yields over the photon energy range of interest [10, 73, 74] (see Fig. 8.5). Thus, monitoring each particular process as a function of the

Fig. 8.4 The typical time frame of an ion trap-based experiment. Ion production may be either pulsed (as depicted by the *dashed lines*) or continuous (*solid line*)
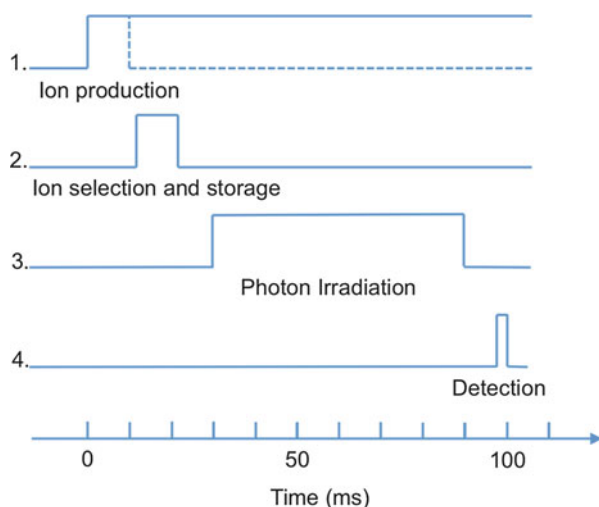
photon energy offers the possibility to selectively study molecular core-level processes. Nevertheless, great care should be taken to avoid sequential two-photon reactions, in which photoproducts absorb a photon and react. Usually, the yields of photoproducts are maintained low enough for these sequential reactions to be negligible. When the photon energy is scanned over the K-edges, in analogy with NEXAFS spectroscopy, the technique has been referred to by a group as near-edge X-ray absorption mass spectrometry (NEXAMS) [73].

4.3 Sources of Gas-Phase Targets and Their Coupling with X-Ray Beam

4.3.1 Neutral Molecules

Relatively small molecules and biomolecules, existing as liquids or solids at room temperature and possessing low vapor pressure, are commonly vaporized into the gas phase and introduced into the vacuum conditions using ovens. The design of the oven must ensure, on the one hand, an increased vapor pressure needed to produce a satisfactory high intensity of the molecular beam, and on the other hand, it must prevent overheating and thermal decomposition of the molecules. In the case of crossed-beam experiments, the oven design also needs to ensure the formation of a geometrically well-defined target molecular beam. More details about the design of the ovens can be found in a number of previous publications and books (e.g., see [75] and references therein).

Experiments using ovens should be carefully performed when thermally fragile targets are investigated, such as some amino acids or oligosaccharides, for example. Still, with a fine regulation of the temperature, this approach may have some advantages over other soft-evaporation techniques. For example, Touboul
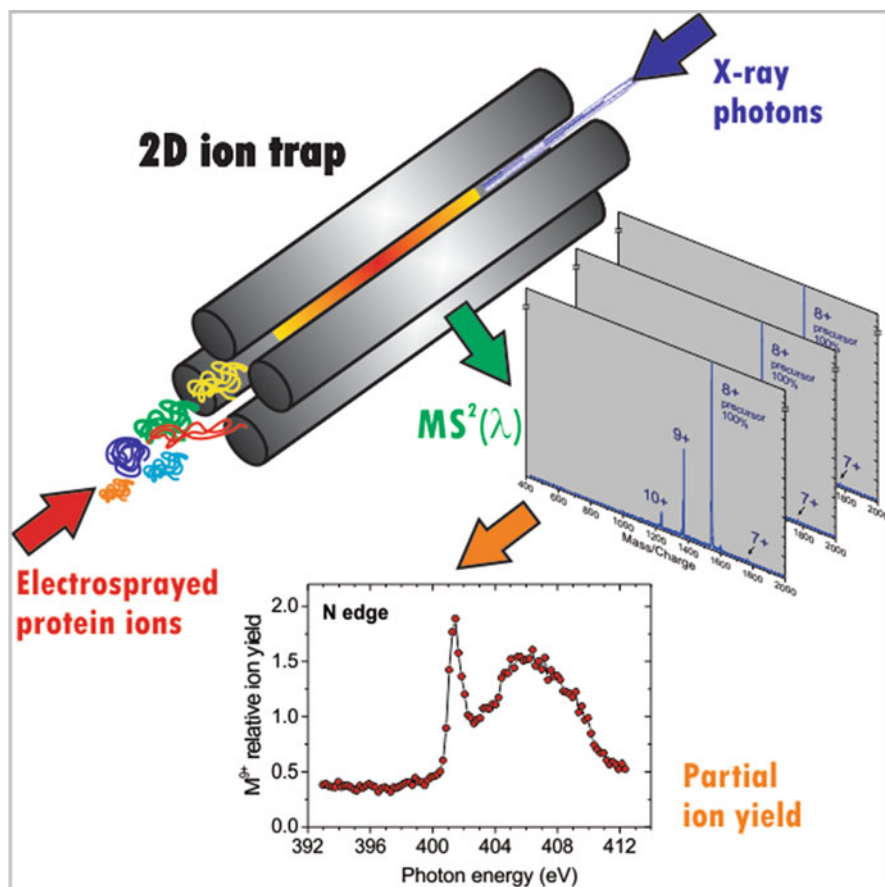
Fig. 8.5 Schematic representation of the near-edge X-ray absorption tandem mass spectrometry experimental method using a linear ion trap fitted with an ESI source (Reprinted with permission from Milosavljević et al., The Journal of Physical Chemistry Letters (2012) 3, 1191 [10]. Copyright (2012) American Chemical Society)

et al. [76] have recently investigated VUV photoionization of gas-phase amino acids adenine and cytosine. In this work, the authors have compared two different techniques to obtain intact gas-phase amino acids, namely, a temperature-controlled oven placed under vacuum and an aerosol setup coupled to a thermodesorber module (see section "Aerosol Technique Used for Neutral Biomolecule Production"). They concluded that although the aerosol thermodesorption allowed for lower sample consumption while still providing a satisfactory sensitivity, it resulted on relatively lower overall experimental energy resolution in comparison with the oven vaporization followed by beam expansion, due to the higher internal energy deposited on the neutral target molecules. It should be noted, however, that the same authors [76] suggested that the aerosol thermodesorption technique could be improved and be

more suitable for large and thermolabile neutral biological compounds (nucleotides, oligopeptides, polysaccharides, etc.).

4.3.2 Nanoparticles and Large/Fragile Neutral Biomolecules and Clusters

Laser Ablation
One way to isolate nanoparticles or clusters is to produce them directly under the vacuum. For example, a pulsed laser may be focused on a rotating target sample comprising a rod or disk of the material under study, which is placed in front of a molecular beam nozzle where a carrier gas is expanding [77]. This expansion is either free or confined in a channel (from a few millimeters in diameter to over a centimeter long) in order to reach a higher average of the cluster size distribution. Nanoparticles with a diameter of a few nanometers can be generated. The beam is then skimmed before entering the spectrometer chamber. However, to obtain sufficient energy per pulse, mostly nanosecond or picosecond low repetition rate lasers (from 10 to 1000 Hz) are used. The very unfavorable duty cycle (the SR is usually pulsed around few hundred of MHz) may account for small number of studies using this technique with SR [78].

Aerosol Techniques
There are different kinds of nanoparticle generators (atomizers, vibrating orifices, etc.), each one with their specificity and optimized for a certain type of nanoparticle. Some are able to disperse directly nanoparticle powders, while others produce liquid droplets containing nanoparticles, such as those developed to study aerosols.

Usually, the nanoparticle sample is diluted in water or alcoholic solution. The solution is sprayed at the atmospheric pressure via an atomizer into small droplets, which contain the nanoparticles. The atomization is based on the Venturi effect, where a high-velocity gas (usually air with a pressure of 1–2 bar expanding through a diaphragm of few hundred microns) sucks the solution through a capillary placed orthogonally to the gas flow. The liquid is then transformed into small droplets under the action of the high-velocity jet. This generator is well suited to nanoparticles with a diameter of 10–2000 nm. Densities of particles from 10^6 up to 10^8 particles/cm^3 can be reached. It is the most commonly used method in synchrotron studies owing to its continuous mode of generation, but also because constant particle size distribution is generated. One drawback is the relatively high quantity of nanoparticles needed for an experiment. Indeed, concentrations around 1 g/L are usually required, which prevent from using of nanoparticles that cannot be produced in high quantity or those with a high cost. To remove the solvent, the aerosols pass through diffusion dryers, made of a stainless steel mesh tube surrounded by silica gels. After solvent removal, the dried nanoparticle beam is sent to the aerodynamic lens (see section "Aerosol Technique Used for Neutral Biomolecule Production", Fig. 8.6) to be focused under vacuum. The aerosol distribution exiting an atomizer is polydisperse in size.
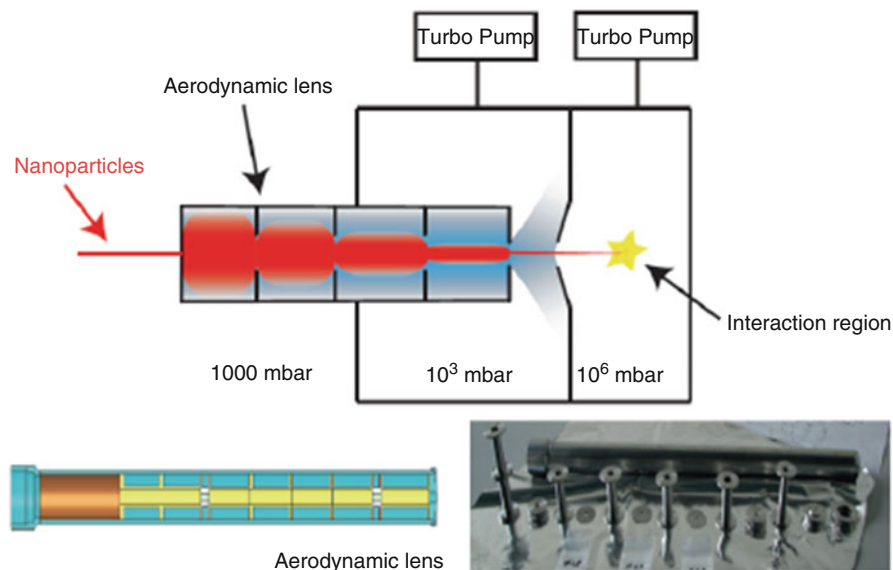
Fig. 8.6 *Top*: schematic drawing of an aerodynamic lens to focus a nanoparticle beam under vacuum. *Bottom*: details of the current aerodynamic lens used by PLEIADES beamline [79] and a picture of the easily interchangeable apertures and spacers that allow quick switching between different lens geometries

For smaller-sized nanoparticles, from 2 to 100 nm, an electrospray source (see section "Aerosol Technique Used for Neutral Biomolecule Production") followed by an ionizer (radioactive source or X-ray lamp) can be used. In this case the suspension of nanoparticles with a buffer is pushed through a capillary. The electric field applied to the capillary tip creates a Taylor cone producing small droplets. A sheath flow of CO_2 and air transports the droplets to a chamber, where their high number of charges created by electrospray ionization will be reduced by the ionizer source. The sheath flow participates also in the evaporation of the solvent. At the end, a very narrow size distribution of nanoparticles (almost monodispersed) can be reached, with a density of up to 10^7 particles/cm^3. The liquid consumption compares favorably to that required for an atomizer source. However, this type of source has not been used often in a synchrotron facility. This is probably because only a ^{210}Po ionization source was available when those experiments started, which leads to difficulties due to nuclear safety regulations. This problem was recently solved by the possibility of using an X-ray lamp as an ionizer. However, as will be discussed in section "Aerosol Technique Used for Neutral Biomolecule Production", the difficulty of focusing under vacuum nanoparticles with a diameter smaller than 30 nm represents a major limitation in the use of the electrospray as a conventional nanoparticle source for soft X-ray synchrotron studies.

Aerosol Technique Used for Neutral Biomolecule Production

Kevin et al. [80] demonstrated for the first time that an aerosol technique could be used to produce under vacuum fragile neutral biomolecules in order to be studied by SR. The biomolecule is simply dissolved into a solution (1.5 g/L), which is sprayed with an atomizer. After passing through the diffusion dryer, the aerosol of bio-nanoparticle has a size distribution centered on 280 nm. After being focused under vacuum by an aerodynamic lens (Fig. 8.6), the nanoparticle beam impacts a hot tip placed a few millimeters from the synchrotron beam, in the spectrometer chamber. The hot tip is usually a rod of a few millimeters in diameter and made from copper or porous tungsten (for better efficiency of vaporization). A proportional–integral–derivative controller drives a heater cartridge to adjust and stabilize the temperature. The bio-nanoparticles, impacting the hot tip, are flash vaporized and create an almost continuous plume of neutral, intact biomolecules, if the temperature of the hot tip is properly chosen. Peptides, polypeptides (such as gramicidin), fragile organic molecules, and beta-carotene have been produced [76, 80–83]. One drawback of this technique is the perturbation induced by the hot tip on the pulsed high-voltage fields applied to the mass spectrometers to extract the photoions, inducing a loss in its resolution. If only mass spectrometry is required, decoupling the position of the ion created by the SR and the ion's mass spectrometer acceleration region has solved this problem [84]. Flash vaporization of bio-nanoparticles has been used only with VUV SR as an ionization source. An attempt to use this technique with the soft X-ray photon was tried at PLEIADES beamline (see Fig. 8.7). A reflectron time-of-flight spectrometer was used to detect any ions coming from the ionization of the neutral parent molecule. If it was still possible to detect ion signals for photon energy up to 100 eV (corresponding to the maximum photon flux of the beamline), measurements around the different K-edges were not successful. This is probably due to the difference in ionization cross sections between valence electrons and core electrons. Also, it seems that the density of neutral molecules created by this technique is insufficient to be able to run experiments that include electron spectroscopy or coincidence measurement.

Coupling Nanoparticle Sources to X-Ray Beam

The development, by McMurry and coworkers [85–88], of aerodynamic lens systems built from a succession of orifices with decreasing diameters along the stream flow marked an important milestone in the possibility of focusing particles under vacuum. Indeed, the submillimeter-sized particle beams created this way are intense, due to the high transmission efficiency of the lens over a wide range of NP diameters (30–1000 nm), and collimated, which make them particularly compatible with under vacuum diagnostic techniques such as mass spectrometry or photoelectron spectroscopy.

In brief, an aerosol source (see Sect. 4.3.2) transfers into gas phase, from the atmospheric pressure, NPs mixed with a carrier gas (air, N_2, He, Ar, etc.). After passing through a diffusion dryer, the aerosol obtained is directed by a split flow
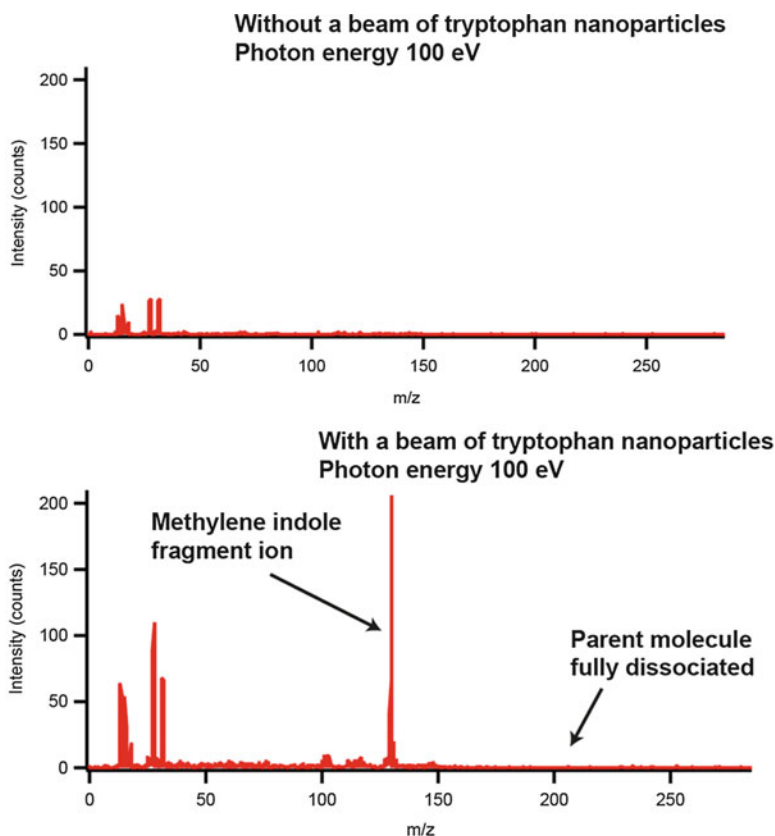
Fig. 8.7 Signal of tryptophan obtained at 100 eV at the PLEIADES beamline by the technique of flash vaporization of bio-nanoparticles. *Left*: without nanoparticle beam. *Right*: when the particles impact the hot tip. At this high photon energy, the parent molecule is completely dissociated

device into three different flows: one going to the aerodynamic lens system, one to a granulometry analyzer for characterization of the nanoparticles' concentration and size distribution, and one toward a gas exhaust line to equilibrate the gas flow. The gas–particle mixture enters the aerodynamic lens via the critical orifice (or chocked inlet orifice), a calibrated hole of around 200 μm, followed by a relaxation chamber. Its role is to fix the mass flow rate into the system and to reduce the ambient pressure to the operating pressure of the lens system. Focusing is accomplished by successive compression and expansion of a carrier gas through the series of coaxial orifices (thin plates) with different diameters (in the millimeter range). The NPs are progressively separated from the gas streamlines, due to the inertia principle, and focused along the lens symmetry axis. After exiting the accelerating nozzle of the lens into a differentially pumped chamber, the collimated nanoparticle beam passes through a skimmer

to reach the interaction region inside the spectrometer chamber. The skimmer, in this case, does not skim the nanoparticle beam, but has a role of limitation of conductance to assure that the pressure in the spectrometer does not exceed 10^{-5} mbar. The nanoparticle beam, focused with the aerodynamic lens, provides a continuously renewed sample. Charging effects, or degradation of the sample via interaction with energetic radiation, cannot happen in this case. Figure 8.6 shows a principle drawing of a typical aerodynamic lens arrangement and a dismounted lens from [79].

The aerodynamic lens is able to focus nanoparticles into a beam of diameters < 500 μm (FWHM). The beam is also highly collimated (sometimes less than 1 mrad). Different types of aerodynamic lenses exist, which have been experimentally [86, 87, 89–92] or theoretically [85, 88, 93–95] characterized. Theoretical simulations are complex and therefore are mainly limited to spherical nanoparticles, quite often far from the real object under study, considering, for example, soot or agglomerated particles. One important parameter is the Stokes number, which describes a particle's behavior in fluid flow when they are meeting an obstacle, such as the element of an aerodynamic lens. This dimensionless number is a ratio between the characteristic of the particle and the characteristic of the obstacle. It can be express as the ratio between the kinetic energy of the nanoparticle and the dissipated energy due to the friction forces with the fluid. If the Stokes number is equal to zero, the particles will follow perfectly the fluid flow, but if the Stokes number is much bigger than one, the particles are not influenced by the fluid flow and they can impact either the diaphragm or the inner part of the lens and be lost. In reference [85], different trajectories of an identical set of particles are presented, but with different Stokes numbers. The best focalization is achieved with a Stokes number equal to one. In order to test new geometries of lenses, Wang and McMurry developed an "aerodynamic lens calculator" simulation software, where the geometry of the lens can be defined, as well as the different conditions of operation (carrier gas properties, nanoparticle properties, and lens conditions) [91].

Each set of orifices with different diameters will be able to focus different sizes of particles. Ideally, by stacking a sufficient number of orifices, an aerodynamic lens should be able to focus a wide range of nanoparticles. The lens geometries cited above are able to focus and have transmission efficiencies close to 100 % for particles with diameters above 30 nm. Below 30 nm, the Brownian motion of the nanoparticles starts to play a non-negligible role and tends to defocus the beam inside the lens, but also after the nozzle, which degrades the density and collimation of the created beam. Being able to create an intense beam of nanoparticles with a diameter below 10 nm is of crucial importance, since size and quantum effects start to be present only in particles close to nanometer size [52, 96]. It is important to note that most of the first calculations on a particle's trajectories inside the aerodynamic lens did not take into account diffusion effects [85, 86, 88]; this has been corrected by newest studies [94, 95, 97]. However, it is possible to find lenses that have been designed especially for focusing particles to below 30 nm [93, 98–100]. Another approach, concerning charged nanoparticles, is to use the radio-frequency ions guide technique to store and concentrate the nanoparticle at the SR interaction region

before their analysis. Various kinds of nanoparticles have been studied with this technique, which is more complex than a simple aerodynamic lens but does not have a size limitation [101–104]. Also, different synchrotron radiation-based experimental setups with an aerodynamic lens system can be found [52, 79, 82, 84, 105].

4.3.3   Ionic Species

Today, the variety of ion sources available is very important, with new developments appearing regularly and giving easier access to new classes of molecules. A typical ion source comprises a desorption/desolvation method to place the species of interest in the gas phase, and an ionization means to produce charged species. It is, however, possible to categorize ion sources into two main classes: atmospheric pressure ionization (API) sources and vacuum sources.

Sources functioning under reduced pressure include electron impact ionization of vapor gas phase, as used by Thissen and coworkers [106]. This method, which may be either pulsed or continuous, is applicable to gases and to sample with a sufficient vapor pressure. Electron beam ion trap (EBIT) sources create highly charged ions at rest by passing high current density electrons into drift tubes in which ions are confined by magnetic and electrical fields [107]. An EBIT source has been used by Epp and coworkers to perform soft X-ray spectroscopy on trapped highly charged ions [108]. Lau and coworkers have used magnetron sputtering by argon atoms of targeted metallic species to produce intense beams of neutral and ions [109]. Gas-phase aggregation is achieved in a volume cooled by liquid nitrogen and leads to an abundant cluster production. Owing to the relatively high flow of gases, the source has to be vigorously differentially pumped by high-capacity turbomolecular pumps. Laser vaporization has also been successfully used to produce intense cluster ion beams [110] suitable for spectroscopy at FLASH [50].

API sources are newcomers in this field and are based on the generation of ions at atmospheric pressure prior to their introduction into the vacuum through an orifice or a capillary differentially pumped. These ion sources have been successfully used by Giuliani and coworkers [72] and by Schlathölter and coworkers [73, 111]. Both of these groups have taken profit from the capabilities of electrospray ionization (ESI) to place in the gas-phase variety of molecules and clusters [112]. The mechanism of ESI has been a subject of considerable study [11, 113]. In ESI, a solution containing a molecule of interest at concentrations of 10^{-4} to 10^{-6} mol/L is pushed through a stainless steel needle at flow rates typically in the 1–20 μL/min. The needle is polarized at 3–5 kV with respect to the sampling orifice of the mass spectrometer. In combination with ion funnels, high ionization and transmission efficiencies can be reached for electrosprayed ions [114]. Nanospray ionization, a variation on the theme of electrospray, has drastically reduced consumption of matter, as flow rates in the nanoliters per minute are required.

Other API ion sources appear particularly interesting, although they have not been used for ion spectroscopy purposes. Atmospheric pressure photoionization (APPI) is a method giving access to very hydrophobic compounds [115] and has proven its potential in ionization of polycyclic hydrocarbons and fullerenes [116].

Fig. 8.8 Scheme of the MAIA merged-beam experimental setup on the PLEIADES beamline. The ion optics used for the ion beam transport are represented in *red. ECRIS* electron cyclotron ion source, *E* einzel lens, *St* set of horizontal and vertical steerers, *S* collimating slits, *FC* Faraday cup, *ED* electrostatic deflector, *IR* interaction region, *EQ* electrostatic quadrupole, *SR* synchrotron radiation, *PD* photodiode (Figure graciously provided by Jean-Marc Bizau, Orsay)

Coupling the Ion Sources with the X-Ray Beam

The main difficulty encountered when performing mass-selected ion spectroscopy lies in the confinement of high-enough quantity of ion in a precise region of space where the interaction with the incident X-ray photon beam will take place. Photon sources of high brilliance are required for this kind of spectroscopy, such as delivered by SR sources and FELs. Three different kinds of experimental arrangements have been combined with SR and FELs to perform X-ray spectroscopy: crossed-beam, merged-beam, and ion-trapping setups.

Historically, mass and charge-resolved action spectroscopy has been achieved using the so-called merged-beam technique. This method was developed by Peart and coworkers in the 1970s for the study of electron impact processes on atomic ions [117]. Later on, the method was adapted to the study of photoionization processes using synchrotron radiation by Lyon and coworkers using the Synchrotron Radiation Source (SRS) at Daresbury, UK [118]. In merged-beam experiments, ions, produced from a plasma ion source, for example, are accelerated, selected by a magnetic mass filter, and merged over tens of centimeters with monochromatic photons from synchrotron radiation beamlines. Ion current in the 1–100 nA is produced after mass selection at keV kinetic energy. Both ion and photon beams are allowed to interact over 50 cm or more, in the μs time range [119–121]. Figure 8.8 presents a typical merged-beam setup, as found on the PLEIADES beamline at SOLEIL [122]. Fairly high target densities are obtained, but relatively elevated background is generated by collisions of the fast ions with residual background gases. The use of ion-trapping devices for X-ray spectroscopy has brought an interesting and

Fig. 8.9 Experimental setup for cluster ion photoelectron spectroscopy (Reprinted with permission from Bahn et al. [50]. © IOP Publishing & Deutsche Physikalische Gesellschaft. CC BY-NC-SA)

complementary alternative to merged-beam setup for atomic, cluster, and molecular ion studies [106, 121, 123].

Photoelectron spectroscopy has appeared as a subsequent development of the merged-beam setup, with the pioneering work of Bizau and coworkers at Super ACO in the 1990s in the VUV [124, 125]. However, recently crossed-beam arrangements have appeared at FLASH for photoelectron studies on anions in the VUV [126] and soft X-ray range [50]. In this kind of arrangements, ion beam is crossed with the FEL radiation from FLASH. The photoelectron distributions are measured with a hemispherical electron analyzer, as shown in Fig. 8.9, and ions are time-of-flight analyzed. By matching the ion acceleration and the delay-line detectors with the FEL pulsing frame, photoelectrons can be assigned to a specific ion mass, without upstream ion selection.

Ion traps are devices using a combination of electric and/or magnetic fields to confine charged species in vacuum. These devices, widely used in various fields of analytical mass spectrometry, have found applications in spectroscopy [72, 74, 127–129]. Several setups based on ion trapping have been used to probe ions in the X-ray regimes, using Penning traps [106, 130, 131], Paul traps [73, 111, 132] or linear ion traps [10, 109, 133].

Ion-trapping experiments complement advantageously the merged-beam techniques. First, these devices can be associated with a variety of ion sources, such as electron impact ionization in vapor phase, sputtering sources, laser desorption, or electrospray ionization. Second, ion traps compensate for a lower amount of ions in

the interaction region by longer interaction times, which may be extended up to tens of seconds. Third, ion traps may be associated with other mass analyzers in hybrid instruments, such as with time of flight or as stand-alone spectrometers. Finally, the ability to repeat n-times the selection and activation steps opens up the possibility to do successive tandem mass spectrometry (MS^n).

The first coupling of an ion trap with synchrotron radiation was originally reported in 1991 by Kravis and coworkers [134]. In this experiment, performed at the National Synchrotron Light Source facility in Brookhaven (USA), the authors investigated inner-shell photoionization and sequential ionization of atomic dications produced by electron impact and stored in a Penning trap. In this pioneering work, the incident radiation was not monochromatic, which complicated the analysis of the results. The first coupling of ion-trapping devices with mono-chromatic synchrotron radiation appeared almost simultaneously using a Penning trap at Elettra (Italy) [106] and a linear ion trap at Bessy (Helmholtz-Zentrum Berlin, Germany) [133]. In the Elettra experiment, a portable FT-ICR mass spec-trometer (MICRA) was coupled to the gas-phase beamline [106]. Xenon radical cations were produced by electron impact on xenon inside the trap and were selected subsequently. Irradiation of these precursor ions with monochromatic radiation in the extreme UV proved to be possible and is compared favorably with merged-beam experiments. The MICRA mass spectrometer has very appeal-ing capabilities. Its high mass resolving power of 73,000 may be very useful to separate signal from the background. However, FT instruments suffer from lower dynamics than ion-counting mass spectrometer, which makes detection limits around 200 ions [131]. Nevertheless, the magnetic field used in Penning trap to confine the ions has been elegantly used to perform X-ray magnetic circular dichroism using the 7 T from the Bruker APEX mass spectrometer [131]. Fig-ure 8.10 shows the setup, which was placed 4 m downstream the U52-PGM at Bessy. Clusters were prepared by laser desorption on a rotating foils combined with adiabatically expansion under vacuum of the clusters mixed with helium. XAS measurements were performed with linear polarized radiation and XMCD with circularly polarized radiation.

Alternatively, linear ion traps offer the advantage of higher detection dynamics and higher column density, as interaction lengths up to 265 mm have been achieved [109]. In this last setup, presented in Fig. 8.11, storage and irradiation take place in a linear ion trap, and ion detection is achieved by a time of flight, giving a mass resolving power of 300 in the Wiley–McLaren configuration and 1700 in the reflectron configuration [109]. A similar coupling, based on a Paul trap and time-of-flight detection of the ions, has been coupled to VUV and soft X-ray beamline [73, 132, 135, 136].

In 2012 Milosavljevic et al. [10, 137] reported the coupling of a commercial linear ion trap with synchrotron radiation beamlines in the soft X-rays at the SOLEIL synchrotron radiation facility, as shown in Fig. 8.12. This commercial machine (LTQ XL from Thermo Finnigan) allows performing isolation, storage, irradiation, and detection using the same linear ion trap device, making the system
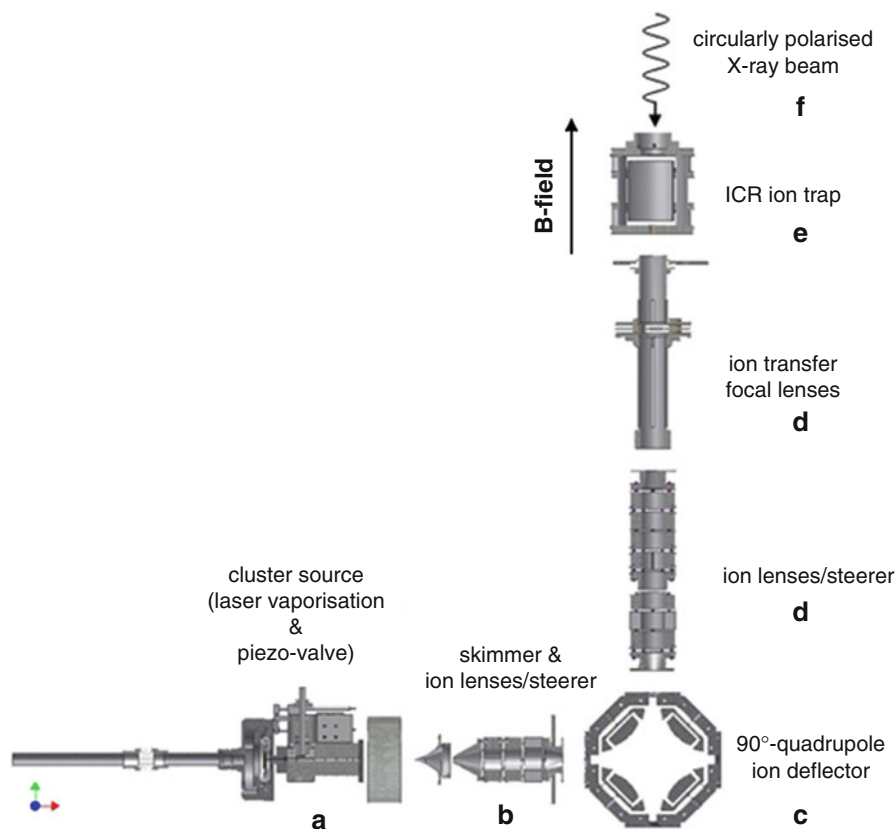
Fig. 8.10 XMCD setup based on a Bruker APEX III mass spectrometer for metal cluster X-ray spectroscopy (Reprinted from Peredkov et al. (2011) *Journal of Electron Spectroscopy and Related Phenomena*, *184*, 113 [131]. Copyright (2011), with permission from Elsevier)

very compact. The quadrupole consists of rods with a hyperbolic profile, and each rod is cut into three axial sections of 12, 37, and 12 mm length [138]. The ion trapping is achieved by a combination of DC and RF fields applied to each rod. The ion ejection is made through 0.25 mm height slots that had been cut along the middle side electrodes. The ejected ions are converted using conversion dynodes and the electron signal detected by two electron multipliers. Such ion ejection is mandatory for the irradiation of the ion packet. This mass spectrometer is able to reach a mass resolving power above 25,000 [139]. The LTQ from Thermo operates in a helium gas bath at 10^{-3} mbar inside the trap, in contrast to the other ion-trapping systems for which helium was pulsed to collisionally cool the ions. Such a permanent helium pressure in the trap has been shown to lead to minor evaporation of weakly bound clusters [112]. Another interesting feature of this
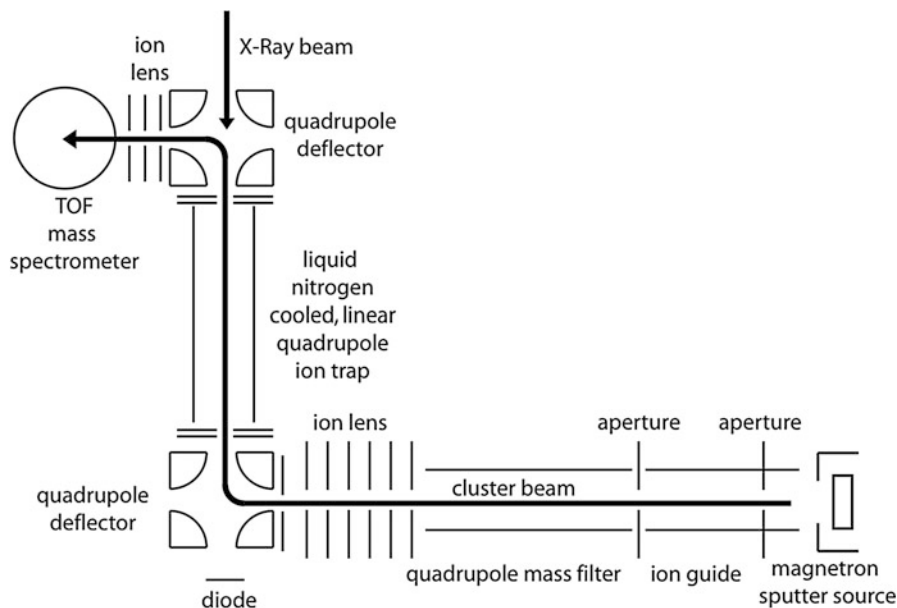
Fig. 8.11 Setup based on a linear ion trap (Reprinted from Hirsch et al. [109]. © IOP Publishing. Reproduced with permission. All rights reserved)
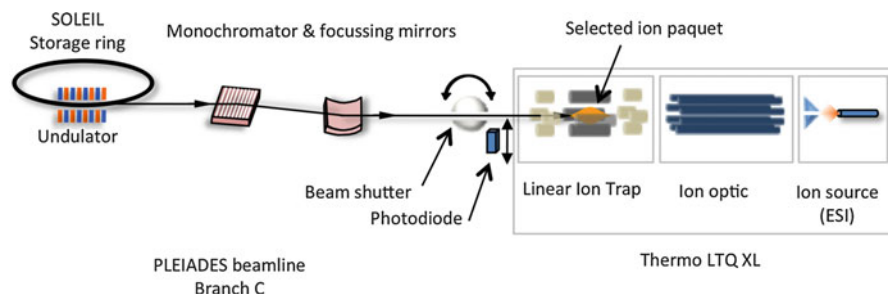
Fig. 8.12 Scheme of the coupling of a LTQ XL mass spectrometer with the soft X-ray beamline PLEIADES at SOLEIL synchrotron facility (Adapted with permission from Milosavljević et al. [137])

commercial instrument is the availability of various ion sources, such as atmospheric pressure chemical ionization (APCI), atmospheric pressure photoionization (APPI), atmospheric pressure matrix-assisted laser desorption/ionization (AP-MALDI), and electrospray ionization (ESI). Such a diversity of reliable ion sources allows accessing a variety of targets, ranging from biomolecules [140–144], weakly bound aggregates [145, 146], or clusters [112].

5 Key Research Findings

5.1 Small Biomolecules

Gas-phase NEXAFS spectroscopy of biologically relevant molecules has attracted a great deal of attention in recent years. The general idea is that gas-phase experiments of relatively small molecules under very well-defined conditions can provide a fundamental understanding of the structure and physicochemical properties of certain compounds, as well as reliable data sets on their interactions with X-ray irradiation. The latter can serve as a benchmark for theoretical modeling and, hopefully, an extrapolation of the conclusions to real biological objects, thus allowing modeling their interaction with X-rays. As an introduction to gas-phase NEXAFS spectroscopy of large vital biopolymers such as DNA/RNA and proteins, discussed in more detail later on, this subsection reviews recent results on biomolecules representing building blocks of biopolymers. These relatively small molecules such as nucleobases and amino acids can be brought into the gas phase by using simple thermal vaporization techniques (Sect. 4.3.1) and studied by inner-shell spectroscopy. We also include a short paragraph (Sect. 5.1.2) reviewing recent results on partial-ion-yield spectroscopy of small organic molecules, which is out of scope of the present work. However, the experimental technique and the characteristic ion yields are relevant to the X-ray absorption tandem mass spectrometry of large biomolecules presented in Sect. 5.5.

5.1.1 Gas-Phase X-Ray Spectroscopy of DNA Components and Amino Acids

Nucleic Acid Components
A number of studies on X-ray interaction with isolated DNA and RNA nucleobases or with some of their derivatives have been reported so far, since a beam of free nucleobases in the gas phase can be routinely formed using ovens and submitted to tunable X-ray synchrotron radiation. A more detailed review on the recent progress in the application of synchrotron-based spectroscopic techniques such as NEXAFS, for the study of nucleic acids, can be found in Wu et al. [3].

Bolognesi et al. have performed both X-ray photoemission and NEXAFS spectroscopy of pyrimidine and halogenated pyrimidines, supported by calculations [147–149]. The authors assigned and tabulated detailed N and C K-edge spectroscopic results, presenting core excitation energies obtained both from the experiment and from the calculations, for pyrimidine and substituted pyrimidines. They have shown that in fact all the carbon and nitrogen atoms in pyrimidine are affected by halogenation due to the higher electronegativity of the halogen atoms compared to substituted hydrogen. For example, a chemical shift of the π^* core excitation to higher energies at the substituted C atom due to an antiscreening effect has been observed; also, the substitution of an H atom with a larger halogen atom induces a chemical shift of the σ^* core excitation to lower energies due to an increase of the bond length [148]. Moreover, using resonant Auger electron-ion coincidence

spectroscopy, Bolognesi et al. [149] have shown that the fragmentation of pyrimidine triggered by a resonant core excitation depends only on the final state of the singly charged ion.

Comprehensive gas-phase core-level studies on other isolated nucleobases, including cytosine, uracil, and guanine, as well as their derivatives, have also been performed recently. Feyer, Plekan, and coauthors have investigated tautomerism in cytosine, uracil, guanine, 4-hydroxypyrimidine, S-methyl-2-thiouracil, and 2-thiouracil [150–154]. They have shown, for example, that population of tautomers in the gas phase can significantly vary over the nucleobases and that a substitution of hydrogen by a halogen atom can strongly influence the dominance of particular tautomer. It should be also noted that Hua et al. [155] performed first calculations of the N 1s NEXAFS spectra of the guanine and cytosine nucleobases and their tautomers in order to investigate the potential of NEXAFS analysis to study hydrogen-bond structure in DNA.

Fragmentation of DNA components following core ionization has been also investigated in the Kukk group using synchrotron radiation in combination with coincident detection of energy-resolved electrons and mass-resolved ions. They have investigated site-selective carbon core ionization of gas-phase pyrimidine derivatives [156], thymine and uracil and its derivatives [157, 158], and even thymidine [159], which is the only neutral nucleoside to be investigated by X-rays in vacuo due to its higher vapor pressure. The use of coincident spectroscopy allowed authors to resolve an intensity of specific fragmentation channels as a function of the initial core ionization site and the correlation between the ionized site and the bond breakage locations. Moreover, in the case of a more complex thymidine molecule, the authors reported a strong difference between valence and core ionization-induced fragmentation, demonstrating a specificity of X-ray interaction with biomolecules [159]. Along the same line of research, the group also investigated fragmentation of DNA and RNA sugars following C 1s and O 1s ionization [160].

Amino Acids

Gas-phase X-ray spectroscopy of amino acids has been attracting great deal of attention in recent years, since these biomolecules are still small enough to be brought into the gas phase relatively easily using classical temperature-controlled ovens, in contrast to their polymers – peptides and proteins. Recent studies include coincident X-ray spectroscopy [161–163], as well as both core-level photoemission and C, N, and O K-edge NEXAFS spectroscopy [164–167].

NEXAFS spectroscopic studies of isolated gas-phase amino acids allow for an investigation of inherent properties of these compounds, without intermolecular interactions occurring in solid or solvated samples that inevitably influence their electronic structure and physicochemical characteristics. On the other hand, gas-phase NEXAFS spectroscopy of relatively short chains of amino acids (peptides) also allows for a controlled study of the intramolecular interactions in biopolymers defining their structure and properties. For example, Feyer et al. [164] reported detailed comparison between NEXAFS spectra of isolated amino acid glycine (Gly) and a corresponding dipeptide glycylglycine (see Fig. 8.13). The
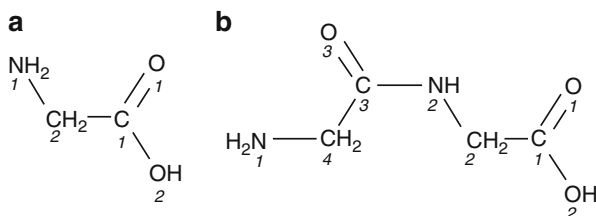
Fig. 8.13 Chemical structures of (**a**) glycine and (**b**) glycylglycine. *Italics* indicate the numbering of heavy atoms (Reprinted with permission from Feyer et al. (2009) *The journal of physical chemistry. A*, *113*, 10726 [164]. Copyright (2009) American Chemical Society)
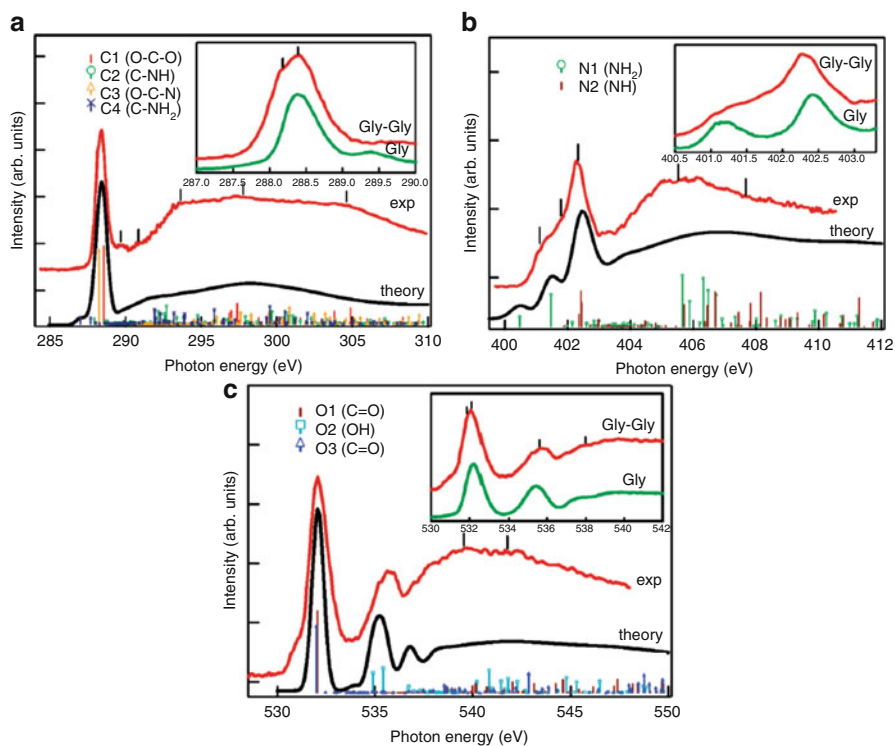
Fig. 8.14 NEXAFS of Gly-Gly compared to Gly (*insets*) for different K-edges. (Reprinted with permission from Feyer et al. (2009) *The journal of physical chemistry. A*, *113*, 10726 [164]. Copyright (2009) American Chemical Society)

later study is important as investigating the influence of polymerization of amino acids to the NEXAFS spectra. Figure 8.14 presents NEXAFS C, N, and O K-edge spectra of Gly-Gly compared to Gly [164]. The calculated transitions are also indicated in the same figure. The might of NEXAFS spectroscopy is that it is chemically sensitive – the resonant transitions associated with different C, N, and

O atoms (chemical shift) can be distinguished, which is particularly expressed in the case of the resonant transition to π^*_{CN} orbital either from N1 or N2. Moreover, the dimerization of the molecule and its three-dimensional rearrangement also affect the NEXAFS spectra, as with the internal hydrogen bonding between NH_2 and NH groups, the resonance associated with the N1 $1s \rightarrow \pi^*_{CN}$ transition shifts with respect to Gly by ~ 0.6 eV to a lower photon energy.

5.1.2 Partial-Ion-Yield Spectroscopy of Small Biomolecules

The absorption of a soft X-ray photon by a relatively small gaseous molecule produces a highly energetic core-excited state, which dominantly decays by a nonradiative Auger process leading to molecular ionization and intensive fragmentation due to the Coulomb repulsion [38]. Below the core ionization threshold, the resonant photon absorption thus leads to an increased fragment ion yield, allowing for NEXAFS action spectroscopy. Furthermore, the possibility to monitor the yield of a selected ionic fragment as a function of the photon energy – the partial-ion-yield spectroscopy [38, 168] – offers a number of advantages with respect to total electron or total ion yield such as investigating channels that are highly selective with respect to different types of resonances or detecting transitions otherwise hidden. This method has been applied to study very interesting phenomena but, until recently, only to small gaseous organic molecules such as formic acid [38] or phenol [169].

5.2 Clusters

Gas-phase clusters are a logical bridge between isolated species in the gas phase and bulk materials. Inner-shell spectroscopy can provide deep insight into the electronic structure of clusters thanks to its chemical specificity. The technique has proven to be a very powerful tool for gas-phase spectroscopy and surface science, but its application to clusters, either free or immobilized, is recent. For clusters, it is well known that the bulk picture is at least partially inadequate. Indeed, in clusters a large part of the atoms belong to the surface, where the electronic structure is different from the rest of the material [170]. The study of cluster properties as a function of size provides fundamental insights of importance in chemistry and physics. The first observation of metal clusters in an ion trap was made by laser vaporization [171].

5.2.1 Atomic Clusters

Gas-phase optical spectroscopy of isolated clusters is not a trivial task. Measurement of photon beam attenuation through dilute sample represents a straightforward mean of accessing optical and magneto-optical properties of isolated cluster ions. Such measurements have been reported for Mn^+ [172, 173] and silver cluster ions using cavity ring-down spectroscopy [174, 175]. However, the so-called photon-trap method is hitherto restricted to the near UV range. Using action spectroscopy, Lau and coworkers have reported the first X-ray absorption of size-selected free metal clusters [109, 133]. This group has studied a variety of mass-selected atomic cluster ions produced by a sputter-magnetron gas-aggregation source, such as titanium [133, 176], vanadium

Fig. 8.15 X-ray absorption spectra of size-selected titanium species, showing the trend from isolated atomic ion to bulk titanium (Reprinted figure with permission from Lau et al., *Physical Review Letters*, 101, 153401 (2008) [133]. Copyright (2008) by the American Physical Society)
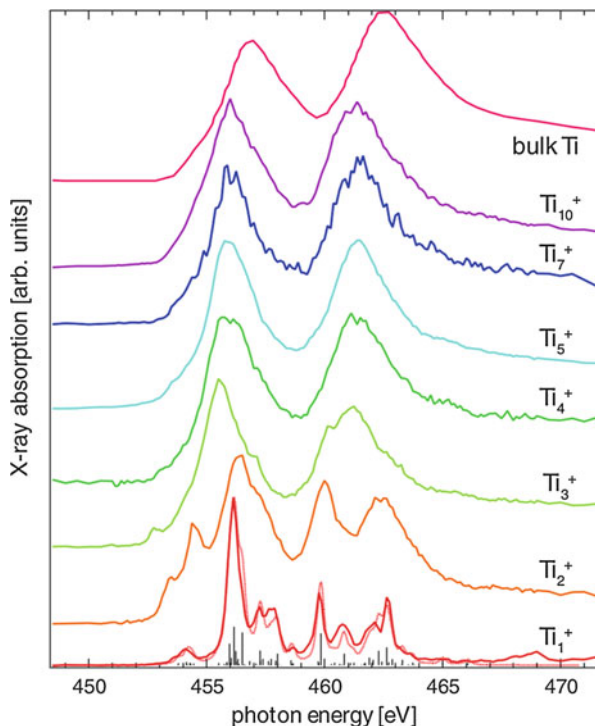
[131, 133, 176], cobalt [131, 133, 176], chromium [109, 176], manganese [176], silicon [177, 178], iron [176], nickel [179], and niobium [131]. Following X-ray photoabsorption, the mass-selected clusters may decay through emission of Auger electrons leading to multiply charged clusters, which, in turn, may further evaporate. Monitoring of the product ion abundance as a function of the photon energy provides a mean for measuring absorption spectra. X-ray action spectroscopy combined with mass and charge-selected targets has been used to derive fundamental properties and trends from the isolated atomic ion to increasing cluster size and up to the bulk. Inner-shell electron binding energy spectra and HOMO–LUMO band gap have been measured for doped silicon clusters [177]. Energy core-level shifts appear to be sensitive to the local electron density and can lead to structural assignments. A comprehensive study on metallic clusters on homonuclear 3d transition metal ranging from Ti to Ni and composed of 1–200 atoms has been carried out at the 2p X-ray absorption edge, as exemplified for titanium in Fig. 8.15.

In combination with an applied magnetic field, this powerful technique has allowed X-ray magnetic circular dichroism (XMCD) spectroscopy to be performed on mass-selected clusters [130, 131, 180–182]. The feasibility of such implementation has been demonstrated on Co_{22}^+ clusters [131]. Spin and angular momentum could be determined for Co clusters composed of 8–22 atoms as a function of the temperature [130]. The magnetism of Fe [180, 182], Co [182], and Ni [182] clusters

has been investigated as a function of the number of constituting atoms. The effect of a single impurity in silicon clusters could also be observed on magnetic moments [181].

Photoelectron spectroscopy of isolated and mass-selected metallic clusters has been recently reported using free-electron lasers, which allows compensating the low target density with increased photon fluxes within the pulse. In a pioneering study at FLASH in the VUV, the binding energy of 5d electrons of Pb cluster anions has been measured as a function of size [126]. A metal to non-metal transition has been evidenced, in agreement with previous theoretical calculations. Further refinement of the electron spectrometer has allowed accessing higher photon energy in the soft X-ray regime at 263.5 eV in Pb anionic clusters [50]. In contrast to valence-shell ionization, inner-shell ionization produces a short-lived highly excited neutral. This technique might provide information about the different relaxation dynamics of valence and core-level holes.

5.2.2 Molecular Clusters

The fine structure of X-ray absorption spectra provides unique insights into the electronic structure of molecular systems; core electron binding energies are particularly sensitive to the local chemical environments (chemical shift). Efforts in X-ray action spectroscopy of ionic clusters have been focused on atomic clusters, and we are not aware of any studies of this kind for molecular clusters. Ryding et al. [112] have studied ammonium bisulfate clusters at oxygen and nitrogen 1s and at the sulfur 2p edges, as shown in Fig. 8.16, and at selected stoichiometries, using the commercial linear ion trap system coupled to the PLE-IADES beamline at the SOLEIL facility (described in Sect. 4.3). In this work, careful analysis has allowed identifying X-ray-induced dissociation (XRID) from collisionally activated dissociation. The ion trap used in this work operates at relatively high helium pressure. Interestingly, XRID leads to loss of several constituting units from the clusters. The effect of photoelectrons produced by helium photoionization has been investigated and shown to be negligible. This preliminary work has paved the way for the establishment of action spectroscopy on mass-selected clusters as a general-purpose method for detailed structural analysis of small molecular clusters. These species are of interest in atmospheric chemistry for nucleation processes and represent model systems for hydrogen bonds and intramolecular protolysis.

Daly and coworkers [183] have used ESI to produce silver-based nanoclusters in the gas phase and studied the optical properties of this material using the SOLEIL device coupled to a VUV beamline. Studies in the X-ray range of these clusters are very likely to develop in a near future.

5.3 Nanoparticles

Nowadays, nanotechnologies are widespread in our daily lives. This has become possible because even though syntheses of nanoparticles are complex, they can still
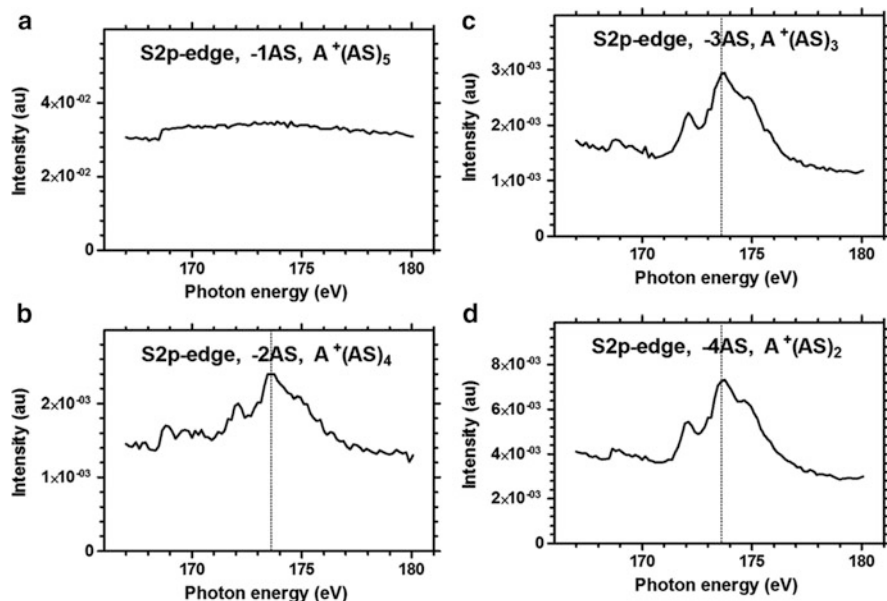
Fig. 8.16 Soft X-ray spectra for losses of increasing number of monomers from ammonium sulfate $A(AS)_6^+$ cluster around the sulfur 2p-edge (Reprinted with permission from Ryding et al. [112]. Published by The Royal Society of Chemistry)

be transposed into mass production units. The final size and composition of nanoparticles can be well tailored by their production processes, whether colloidal or polymer chemistry [184, 185] or laser pyrolysis [186, 187] is used. Thus, using the aerosols techniques to transfer them into gas phase does not need further size selection, assuming that no agglomeration process is present in the solution.

As discussed above, one of the main benefits of studying free nanoparticles is the avoidance of the influence of a substrate on their physical and chemical properties. An additional reason is the possibility of running in situ measurements of nanomaterials which can, for example, easily react with oxygen. A striking example is given by the recent study on pre-fullerenic nanoparticles by Ravagnan et al. [188]. This NEXAFS spectroscopy study on free carbon nanoparticles generated by a pulsed microplasma source clearly demonstrated, for the first time, the presence of distinct sp hybridization resonance [78]. It may sound surprising that only two recent studies in which special care was taken to avoid sample oxidation, either by in situ measurement [189] or by transporting the sample under vacuum [190], claimed the eventual presence of two distinct sp and sp^2 hybridization resonances. By varying the time between the detection of electron and the discharge in the plasma source, for which the NP size and structure evolve, Ravagnan et al. demonstrated that the relative amount of sp and sp^2 bonds varies all along the growth of the NPs. This discovery may have an important impact in fields such as astrochemistry or combustion.

Fig. 8.17 Total electron yields from freestanding sodium sulfate nanoparticles, which present a Glauber's salt structure (given in *inset*) for Na$_2$SO$_4$ (Reprinted from Antonsson et al. (2013) *Chemical Physics Letters*, *559*, 1 [52]. Copyright (2013), with permission from Elsevier)
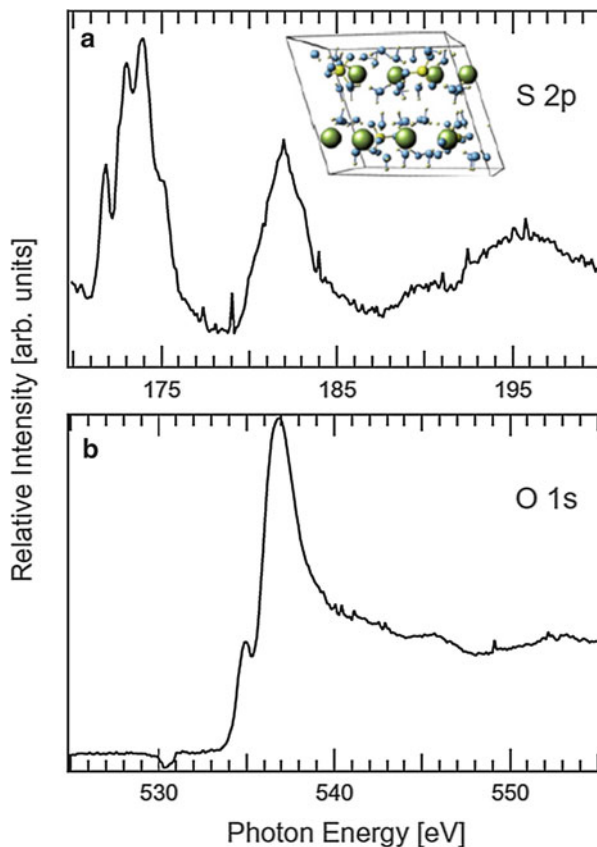
A detailed review of free nanoparticles studied by soft X-ray synchrotron radiation is given by Antonsson et al. [52], gathering all the studies done before 2013. We will concentrate on the two studies of near-edge spectroscopy reported by the authors.

The first study is on solid nanoparticles produced from a sprayed aqueous solution of sodium sulfate. When drying, the droplets give rise to Glauber's salts: Na$_2$SO$_4$.10H$_2$O. This example highlights the ability of near-edge absorption spectroscopy in probing the local electronic structure of the absorbing atom. Indeed, if the near-edge spectra of the sodium sulfate taken at the S 2p-edge (see Fig. 8.17) display an identical structure to that obtained for the dry sodium sulfate [191], a shift in photon energy of around 0.8 eV toward the higher photon energy is observed for the Glauber's salt structure. This could indicate a difference in the local chemical environment of the absorbing sulfur atom between the dry and wet sample. Moreover, there exists a difference in shape of the feature at 181 eV, assigned to the S 2p → d shape resonance [192]. In the absorption spectra at the O 1s-edge, features associated with bound oxygen in the sulfate group, as well as in crystalline water, are present, but signatures of liquid water are also visible. All these findings are in favor
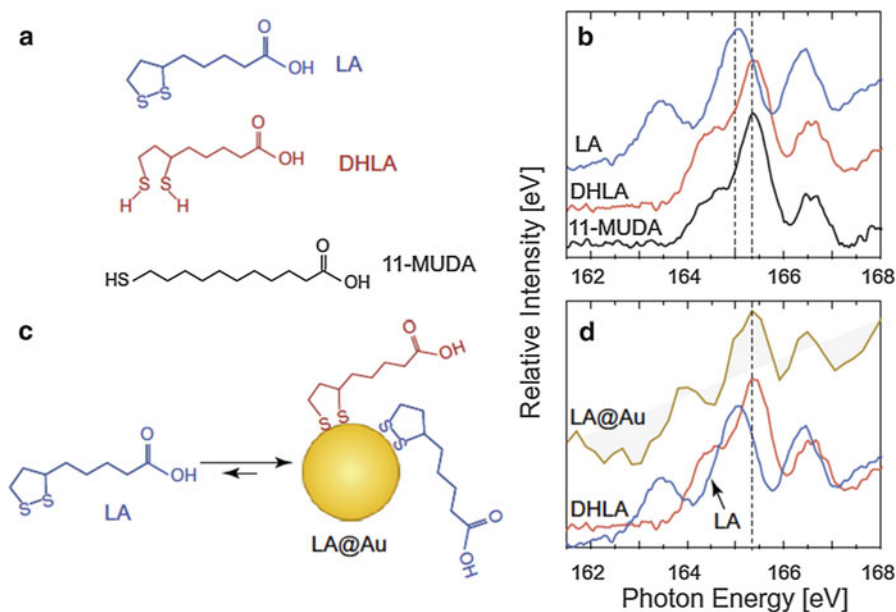
Fig. 8.18 Near-edge absorption spectra at the S 2p-edge, for (**b**) pure ligand nanoparticles (see *text*) and for (**d**) functionalized gold nanoparticles with lipoic acid (LA), according to the schematic reaction depicted in (**c**) (Reprinted from Antonsson et al. (2013) *Chemical Physics Letters*, *559*, 1 [52]. Copyright (2013), with permission from Elsevier)

of a higher number of water molecules than in pure Glauber's salts. In addition, they do not bind exclusively within the crystal water. Bonds with the sulfate group may also exist, which induce the energy shift observed in the near-edge spectrum at the S 2p-edge. A very interesting point raised by the authors is that NaCl nanoparticles, prepared in the same way, do not display strong evidence of water inclusion [193]. Also, the in situ preparation of nanoparticles, by an atomization of a solution, still conserves some of the properties of the solute.

The second study focuses on functionalized gold nanoparticles with mono- or divalent thiol ligands and, more precisely, on how the ligands bind to the 47 nm +/− 10 nm gold nanoparticles. This work is in line with previous S 1s-edge NEXAFS and XPS studies that demonstrate that dihydrolipoic acid is bonding with both sulfur sites to gold nanoparticles [194, 195]. First, the absorption spectra of pure ligand nanoparticles were recorded (see Fig. 8.18 a and b) for comparison to spectra obtained with free functionalized gold nanoparticles (see Fig. 8.18 c and d). Three different thiols were selected for this study: lipoic acid (LA), dihydrolipoic acid (DHLA), and 11-mercaptoundecanoic acid (11-MUDA). All the features for the pure ligand nanoparticle spectra are in accordance with the previous work of Dezarnaud et al. [196]. The peak at 163.3 eV corresponds to the S $2p_{3/2} \rightarrow \sigma^*$ (S–S) transition, which is why it can be observed only in the LA spectrum, and the most intense feature of all the different spectra corresponds to a superposition of the S $2p_{1/2} \rightarrow \sigma^*$

(C–S) and S $2p_{1/2} \rightarrow \sigma^*$ (C–S) transition. Even if the signal from the functionalized nanoparticle (LA@Au) is lower than the pure ligand nanoparticle signal due to a low density of ligand bound to the gold nanoparticles, interesting features in the spectra can be seen. The authors report slight shifts of 0.15 eV and 0.30 eV toward higher photon energies for 11-MUDA@Au and LA@Au, respectively, indicating chemical bonding between the ligands and the nanoparticles. Moreover, the reaming feature assigned to S 2p3/2 $\rightarrow$ sigma* (S–S), with a relative intensity identical to the one obtained with pure nanoparticles of LA, indicates that the S–S distance remains constant when lipoic acid is bound to the gold nanoparticle. With deeper analysis of the spectrum, the authors estimate that DHLA ligand could be present up to 20 %. With this study, the authors demonstrate that LA binds mostly as dithiolane to gold nanoparticles, which is in agreement with previous studies made with other spectroscopic techniques [197, 198].

In these two examples, the authors demonstrated the possibilities and the sensitivity of near-edge absorption spectroscopy when free nanoparticles are coupled with soft x-ray radiation. The element and the surface selectivity of the soft X-ray regime, coupled with near-edge absorption or photoemission studies, could play an important role in improving knowledge of the physical chemistry occurring at the surface of the nanoparticles. Even if the number of these studies to date remains still marginal, in the framework of nanomaterial studies, it should increase rapidly, as dedicated source and end stations are now available for users in several synchrotrons [47, 52, 79, 82, 84, 101].

5.4   Small Ions

In their pioneer work, Kravis and coworkers have investigated photoionization of dication of argon [134] and xenon [199] stored in a Penning trap. The doubly charged precursor ions were formed by electron impact ionization of neutral gas in the trap, stored, and photoionized by a broadband synchrotron radiation beam (white beam) from a bending magnet. The distribution of photoion charge states following K-shell photoionization could be measured and showed abundant sequential photoionization as a function of the irradiation time. This technique has the potential of producing highly charged ions.

The first reports of monochromatic photoionization on atomic ions were produced in parallel by Lau and coworkers on transition metal at Bessy synchrotron [133] and by Thissen and coworkers on xenon radical ion at Elettra synchrotron (Trieste) [106]. These studies have been extended to krypton ion at SOLEIL synchrotron [121, 123], as well as 3d elements such as calcium and copper at Bessy synchrotron [179]. Ion trap experiments showed the potential to offer control on the initial state of the target ion, allowing photoionization studies on either electronic ground state or on metastable species. This specificity complements nicely previous merged-beam experiment, in which the use of electron cyclone resonance sources produces a manifold of excited species [121, 200].

5.5   Biopolymer Ions

NEXAFS spectroscopy of large isolated gaseous biopolymer ions such as peptides, proteins, and DNA has become possible only recently with development of ion trap-based experiments (see Sect. 4). The method consists of coupling an ion trap with brilliant third-generation soft X-ray synchrotron sources, allowing to reach both a sufficient target density and preservation of the ion packet for a sufficient time (for more details and an extended reference list on the coupling of an ion trap mass spectrometer with a synchrotron photon beam, see a recent review article by Giuliani et al. [72]). Large biopolymers are introduced into the gas phase by use of modern ionization techniques such as electrospray ionization (ESI) (see Sect. 4).

Ion traps allow performing tandem mass spectrometry at the *n*th level. Therefore, the NEXAFS spectroscopy of a particular precursor is actually performed as an action spectroscopy, by collecting tandem mass spectra as a function of the activation photon energy (see Sect. 4.2.4).

The results represent a number of tandem mass spectra recorded as a function of the photon energy scanned over C, N, or O K-edge in small steps. The NEXAFS partial ion yields are finally obtained after normalization to the total ion current and the photon flux.

Two experimental setups coupling ion traps with SR have been developed more or less at the same time (see [72] for more details): Schlathölter and coworkers have developed a setup that couples a Paul ion trap with the SR and using a time-of-flight (ToF) analysis of the ionic products [135], and Giuliani and coworkers have developed a setup based upon coupling of a linear quadrupole ion trap mass spectrometer ("Thermo Scientific LTQ XL"), equipped with ESI and nano-ESI probes, with SR [143, 144]. In this section, we review recent results from NEXAFS action spectroscopy of large biopolymer ions, namely, peptides, proteins, oligonucleotides, and polycyclic aromatic hydrocarbons (PAHs).

5.5.1   Peptides

González-Magaña and coauthors have reported a pioneering study on the dissociation of the gas-phase protonated peptide leucine-enkephalin (Leu-Enk) [YGGFL + H]$^+$ ion upon soft X-ray absorption in the vicinity of the C K-edge [73]. The experiment has been performed by coupling a Paul ion trap with a SR beamline and by recording tandem mass spectra as a function of the X-ray energy. From the MS^2 spectra both the total photoabsorption yield and the partial ion yields of specific fragments have been extracted and discussed. The authors named the technique as near-edge X-ray absorption mass spectrometry (NEXAMS), since it corresponds to NEXAFS spectrometry performed on condensed phase targets. Except that NEXAMS is performed on gas-phase species, the advantage of incorporating the mass spectrometry into the method allows the study of resonant core excitations and core ionizations with respect to fragment specificity, i.e., specific bond breaking (see Fig. 8.19). The authors could distinguish specific electronic transitions, such as C 1s → π* excitations in aromatics at 284.4 eV or C 1s → π*$_{C=O}$ transitions corresponding to amide group along the peptide backbone at 288.4 eV. They could
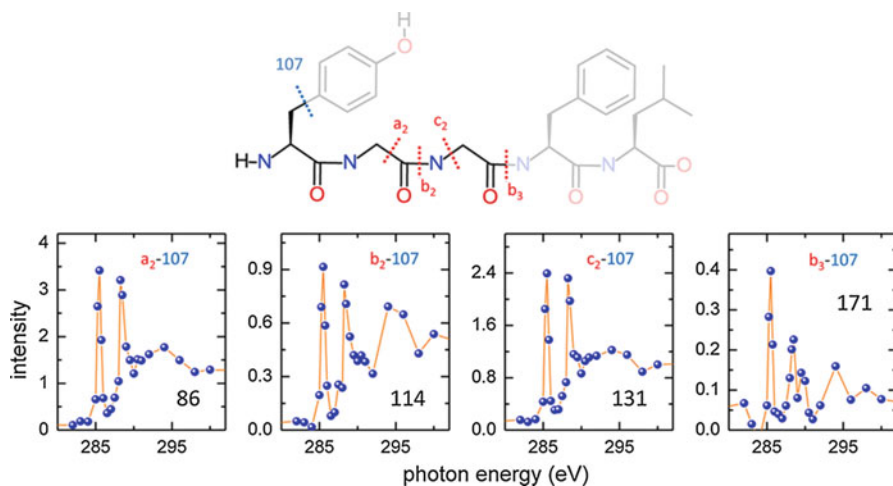
Fig. 8.19 Near-edge X-ray absorption mass spectrometry of a gas-phase protonated peptide leucine-enkephalin [YGGFL+H]$^+$ (Reprinted with permission from O. González-Magaña et al. (2009) *The journal of physical chemistry. A*, *116*, 10745 [73]. Copyright (2012) American Chemical Society)

also correlate specific transitions to specific fragmentation channels and fragmentation intensity. Interestingly, it has been found that excitations in the aromatic side chains lead to relatively little fragmentation in comparison with such excitations along the peptide backbone. It should be also pointed out that the study reported by González-Magaña and coauthors [73] clearly shows an intensive fragmentation of a relatively short peptide chain (a pentapeptide) upon soft X-ray absorption, similarly as found for its constituents – the isolated amino acids (see Sect. 5.1.1). However, this is in contrast to the larger polymer, proteins [10], and will be discussed below.

We have recently studied NEXAMS of protonated substance P peptide (Arg-Pro-Lys-Pro-Gln-Gln-Phe-Phe-Gly-Leu-Met-NH$_2$), as well as its nanosolvation by a controlled amount of water molecules produced by nanospray ionization using a linear ion trap coupled with the PLEIADES beamline (Giuliani et al., *to be published*). Preliminary results suggest that yield of specific fragments can be strongly dependent on the location where photon energy is injected, i.e., on C, N, or O atoms. Moreover, upon nanosolvation, the 1s excitation of oxygen atoms related to water cluster seems to become very intensive process leading to abundant water evaporation. Gas-phase NEXAFS of such systems allows distinguishing characteristic resonances.

5.5.2 Proteins

To our knowledge, the first near-K-edge X-ray spectroscopy of a protein isolated in the gas phase has been reported by Milosavljevic et al. in 2012 [10]. Using the coupling of a linear ion trap with the PLEIADES soft X-ray beamline at the SOLEIL synchrotron facility, we have performed C, N, and O near-edge ion yield
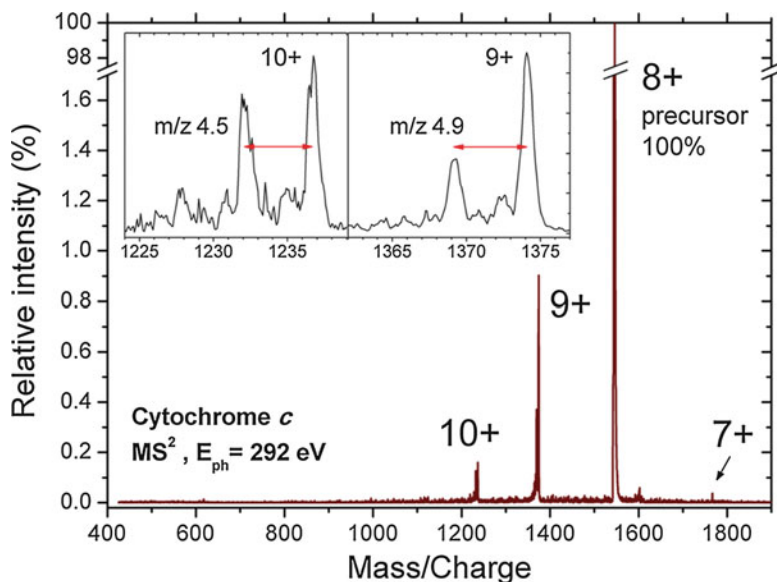
Fig. 8.20 Tandem ESI/photoionization mass spectrum of 8+ (m/z 1546) ions of cytochrome c protein from equine heart, obtained after 600 ms of irradiation at a photon energy of 292 eV (Reproduced from Milosavljević et al. [10]). The *inset* shows a zoom in the mass regions around 9+ (m/z 1374) and 10+ (m/z 1237) charge states, normalized to the same dominant peak intensity. The *arrows* mark the peaks' separations of about m/z 4.9 ± 0.1 and 4.5 ± 0.3 for the 9+ and 10+ channels, respectively, corresponding to 44 Da, tentatively assigned to CO_2 loss (Reprinted with permission from Milosavljević et al., The Journal of Physical Chemistry Letters (2012) 3, 1191 [10]. Copyright (2012) American Chemical Society)

spectroscopy of 8+ electrosprayed cations of cytochrome *c* protein (about 12 kDa). The tandem mass spectra were recorded for defined photon energies that were changed in small steps below and above the 1s core ionization thresholds.

Figure 8.20 shows a tandem ESI/photoionization mass spectrum of 8+ charge state of cytochrome *c* protein recorded at the photon energy of 292 eV. Interestingly, the protein ion appeared to be drastically less prone to fragmentation upon soft X-ray irradiation in comparison with amino acids (Sect. 5.1.1) and peptides (Sect. 5.5.1). Indeed, the main relaxation channels represent single and multiple ionization (electron ejection) accompanied with small neutral losses, which have been tentatively assigned to CO_2 losses according to the m/z difference, although it could also correspond to detachment of neutral amino acid residues. The ejected electrons from the Auger process can further trigger radiation damage [201].

Figure 8.21 shows the spectroscopy of the selected 8+ charge state precursor of the cytochrome c protein over the C, N, and O K-edges [10]. As explained above, the single precursor ionization can be exclusively a result of the resonant Auger decay upon core 1s electron resonant excitations. Indeed, the partial ion yields that correspond to the single ionization (blue circles in Fig. 8.21a–c) reveal spectral features that perfectly correspond to the NEXAFS data obtained from thin organic

Fig. 8.21 (continued)

protein films [6, 7, 202]. In the C 1s energy domain, the peak at about 285.5 eV (denoted as A in Fig. 8.21a) can be clearly assigned to the C 1s → π* transitions associated with the aromatic rings of amino acid residues. Furthermore, the next closely lying shoulder at about 286.05 (denoted by an arrow in Fig. 8.21) has been assigned to C 1s(C − R) → π*$_{C=C}$ of the Trp residue [6]. The structure at 287.0 eV can be assigned to σ*$_{C-H}$ resonance. The strong peak at 288.3 eV (denoted as B in Fig. 8.21a) has been assigned to the C 1s → π*$_{amide}$ transition. The energy position of the later structure is in perfect agreement with the previously reported values for NEXAFS spectroscopy on thin film of proteins (albumin, fibrinogen, lysozyme, ovalbumin, collagen) [6, 7]. However, interestingly, the relative intensity of this transition appeared to be much lower than expected. Indeed, the peaks corresponding to a C 1s → π*$_{amide}$ transition, as by a rule, dominate the NEXAFS spectra of solid protein samples, peptides, and amino acids. The lower intensity can be thus either a specificity that corresponds to the spectroscopy of large gaseous and multiply charged biopolymer ions or an experimental artifact. The authors suggested that an experimental influence could be due to carbon pollution of the different optical elements of the SR beamline [10], which induces a very low photon flux around the C 1s absorption edge (the so-called carbon deep), which was difficult to handle in the data treatment. This possibility is also supported by the fact that corresponding N and O 1s → π*$_{amide}$ transitions are dominant, as expected; moreover, the same was measured for the C K-edge for other trapped protein ions in further experiments, after cleaning the photon optics (see Fig. 8.22). The broad feature centered at about 293 eV (denoted as C in Fig. 8.21) is due to the overlap of various transitions, mainly associated with the σ* resonance (C−C, C−N, C−O, etc.) and dominantly related to valence and Rydberg transitions of amino acid residues merging into a broad band. Single-ionization spectra over the N 1s and O 1s K-edges are also very similar to previous NEXAFS data on proteins and polypeptides. The 1s → π*$_{amide}$ [1s → π*$_{C=O}$(C = ONH)] transitions centered at about 401.4 eV and 531.4 eV for N and O 1s, respectively, dominate the spectra.

The experimental results by Milosavljevic et al. [10] have shown that ions of large biopolymers, such as proteins, can be investigated by means of the powerful NEXAFS spectroscopy method, isolated under well-defined conditions in the gas phase. For example, the typical resonant transitions have been well resolved by using the present method, directly pointing to the primary protein structure, in line with previous solid film NEXAFS studies. But at the same time, the present technique avoids the drawbacks related to NEXAFS spectroscopy on thin organic films and liquids, such as radiation damage occurring in condensed matter samples and an uncontrolled influence of the environmental effects in the case of studying condensed crystalline or aqueous samples.

Fig. 8.21 Single, double, and total C, N, and O K-edge photoionization yields of the 8+ charge state precursor of equine cytochrome c protein (Reprinted with permission from Milosavljević et al., The Journal of Physical Chemistry Letters (2012) 3, 1191 [10]. Copyright (2012) American Chemical Society)

Fig. 8.22 Single (*blue circles*) and double (*black squares*) C K-edge photoionization yields of the 5+ (*top*) and 9+ (*bottom*) charge state precursor of ubiquitin protein. The single-ionization yield is normalized to the double-ionization yield
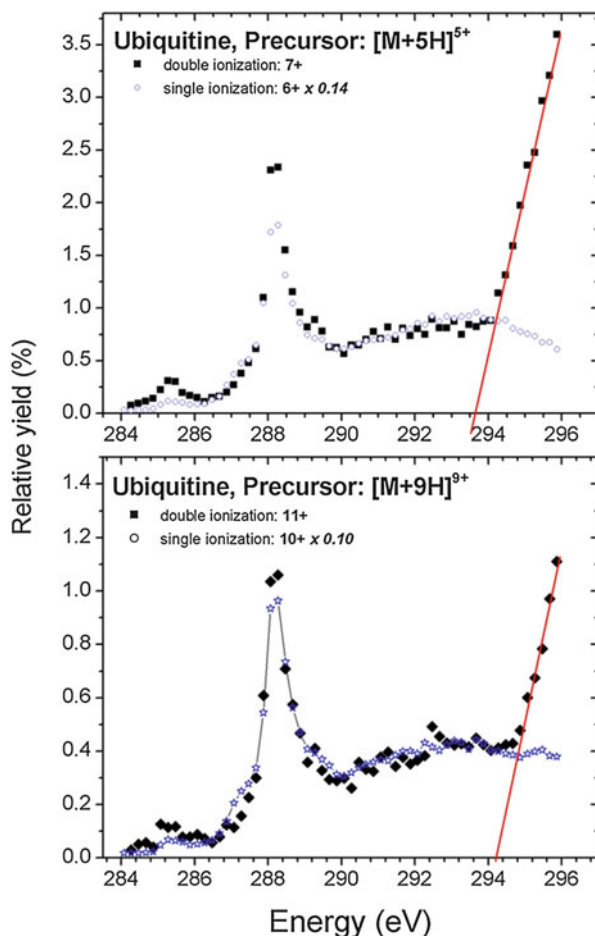
It is interesting to note that the gas-phase NEXAFS spectra of an isolated multiply protonated (8+) protein agree perfectly with NEXAFS spectroscopy on neutral thin-film protein samples. This may seem in contrast with previous microjet studies on solvated amino acids (protein building blocks), where the changing of solution pH (thus protonation/deprotonation of the biomolecule under study) has shown to affect significantly the NEXAFS resonant lines [203–205]. However, one should keep in mind that in the present case of a large gaseous protein ion, only a few protonated amino acids (according to the charge state) inside the precursor actually contribute to a possible chemical shift of the resonant transition; and resonant energy is additionally smeared out due to the contribution from different C atoms, with respect to their distance from the protonation site. Therefore, the overall effect can be negligible. Indeed, this is shown in more recent measurements for different charge states of ubiquitin protein [13]. Figure 8.22 presents single- and double-ionization yields of the 5+ and 9+ protonated precursors of ubiquitin. The experiment was performed by

coupling a commercial linear LTQ XL ion trap to the soft X-ray beamline PLEIA-DES at the SOLEIL synchrotron facility. For both charge state precursors (5 and 9), the ionization yields show the characteristic NEXAFS features corresponding to the C 1s → π* transitions in the aromatic amino acids at about 285.5 eV and the strong peak at 288.3 eV due to the C 1s → π*$_{amide}$ transitions in the peptide backbone. Clearly, these resonant excitation energies appear to be the same for both charge states, even though the level of protonation is significantly different.

The fact that the resonant core 1s transition energies to frontier molecular orbitals of a large protein are not affected by its protonation appears to be even more interesting if we consider the ternary structure of the protein. Actually, the protonation can alter its structural arrangement if the protein is free to unfold, as a consequence of minimizing the potential energy of the system [142]. Particularly, the 5+ protonated ubiquitin ion in the gas phase is still dominantly folded, while the increase of protonation to 9+ induces the unfolding of the protein [142]. Therefore, the tertiary structure of the 5+ ubiquitin precursor is drastically different from the 9+ precursor. On the other hand, there is no measurable difference in their C K-edge excitation to the molecular π* orbitals associated with aromatics and the peptide backbone. Since the core 1s electron is localized in the vicinity of the C atom, the present experiment shows that the frontier protein orbitals also appear to be rather localized and do not depend strongly on the tertiary protein structure.

Double-ionization yields of both precursors presented in Fig. 8.22 seem to exactly follow the shape of the corresponding single-ionization yields below the core ionization threshold. This confirms that double ionization below the threshold is due to the multiple resonant Auger decay – the relaxation of the core-excited species preceded by ejection of two Auger electrons. But, since the process is triggered by the same electronic transition, the spectroscopic signature is the same, as seen in Fig. 8.22. Nevertheless, above the threshold the 1s electron is directly ejected into the vacuum, and normal Auger decay becomes operative, thus reducing drastically single-ionization events on behalf of the double ionization. Therefore, the double-ionization yield allows determination of the K-edge ionization threshold of a protein under study. It is interesting to note that, in contrast to the resonant excitation, the 1s threshold energies do depend on the precursor charge state. Clearly, the ionization energy of the 9+ precursor is shifted upwards with respect to the 5+ one. However, the shift should not be the consequence of the change in the electronic structure. In the case of the protonated (positively charged) target, the departing electron also needs to overcome the Coulomb barrier, which depends both on the protonation level and the protein ternary structure [142].

5.5.3   Oligonucleotides

González-Magaña et al. [132] have investigated photon-induced fragmentation of protonated oligonucleotides in a large energy domain from 30 eV to 600 eV. The precursors under study were doubly protonated oligonucleotides $[dGCAT + 2H]^{2+}$ or $[dGTAT + 2H]^{2+}$ (the letters G, C, A, and T denoting the nucleobases guanine, cytosine, adenine, and thymine, respectively), which were isolated in a Paul trap and submitted to either soft X-ray radiation or the highly charged ions [132]. In this way,

Fig. 8.23 Ratios between protonated and nonprotonated nucleobase yields for T, A, and G as a function of the photon energy (Reprinted figure with permission from Lau et al., *Physical Review A*, 87, 032702 (2013) [132]. Copyright (2013) by the American Physical Society)
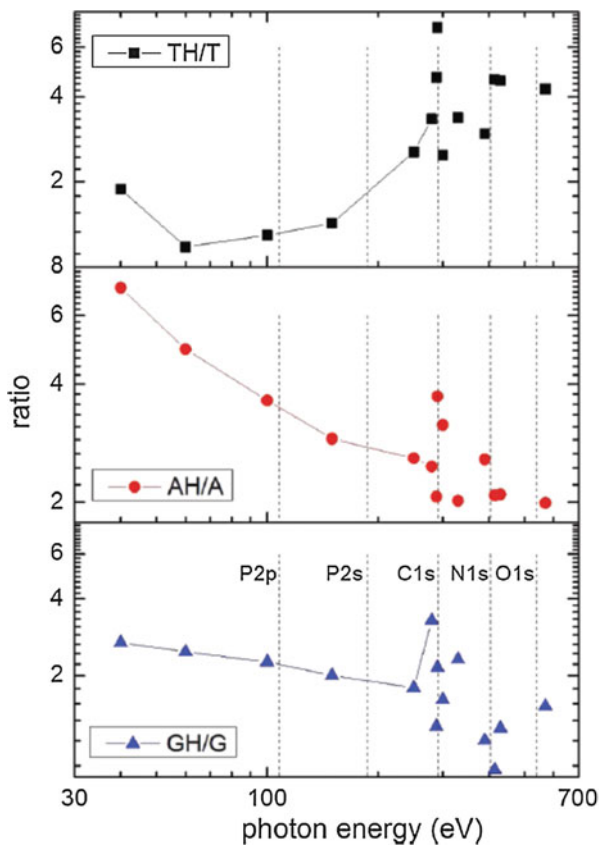
the authors aimed at performing a systematic study on differences and similarities between ion- and photon-induced excitation and fragmentation mechanisms in DNA. They found qualitatively similar fragmentation patterns for both types of projectiles (ions and energetic X-ray photons). The measured fragmentation patterns revealed that nucleobases appeared to be rather stable, while deoxyribose fragments dominated the spectra.

The relative photoabsorption cross sections, as well as the photofragmentation yields for protonated and nonprotonated nucleobases spanning over a wide photon energy range, clearly show an expected increased ion production in the vicinity of C and N core 1s ionization thresholds, as a consequence of the inner-shell core formation triggering the Auger processes. However, the energy step was too coarse for fine near K-edge spectroscopic structures to be studied. Still, the authors could compare the yields of protonated and nonprotonated nucleobases as a function of the photon energy. Interestingly, they found that the ratio between protonated and nonprotonated yields depends strongly on ion velocity and photon energy. For example, a significant increase of the yield of protonated bases relative to the nonprotonated fragments is measured at resonant 1s excitation of the molecule (see Fig. 8.23).

5.5.4   Polycyclic Aromatic Hydrocarbons

Gas-phase polycyclic aromatic hydrocarbons (PAHs) have been also investigated by means of near-edge X-ray absorption mass spectrometry [111, 206, 207]. The PAHs are of great interest in many research fields such as astrochemistry/astrophysics and combustion and analytical chemistry [111]. Moreover, the investigation of the electronic properties of PAHs and the influence of certain processes such as hydrogenation to the electronic structure, under well-defined conditions, may be relevant for both the fundamental and applied nanosciences.

The experiments of Reitsma et al. [111, 207] have been performed by coupling an ion trap time-of-flight (ToF) instrument with the soft X-ray beamline U49/2-PGM1 at the BESSY II synchrotron facility. The ions were produced by an ESI, trapped in an RF Paul trap, and the product ions were analyzed using ToF. The authors have investigated the photoexcitation, photoionization, and photodissociation of gas-phase coronene cations $C_{24}H_{12}^{+}$ upon soft X-ray absorption in the C K-edge region. The relaxation of superhydrogenated gas-phase coronene cation upon resonant carbon (1s) $\rightarrow \pi^*$ transition at 285 eV was investigated by means of NEXAMS and compared to calculations [207]. The results allowed for postulating the effect of superhydrogenation on the ionization and fragmentation of PAHs. It has been found that superhydrogenation acts as a buffer that protects PAH molecules against X-ray-induced destruction. NEXAMS of coronene is further investigated by the same authors in more details [111]. NEXAMS spectra for a number of different fragmentation channels, resulting from the inner-shell excitation or ionization of the coronene precursor $C_{24}H_{12}^{+}$, were presented. The excitation of the carbon 1s electron triggers the Auger process that leads to the formation of intermediate vibrationally excited $C_{24}H_{12}^{2+}$ and $C_{24}H_{12}^{3+}$ cations that can relax by means of ejecting H atoms. Figure 8.24 presents NEXAMS spectra for different coronene dications as a function of the number of H atoms lost [111]. Figure 8.24 shows that while the formation of intact dications is mainly triggered by C 1s $\rightarrow \pi^*$ transition at about 285 eV, the formation of dications that lose 2, 4, and 6 H atoms occurs also at higher photon energies, as a consequence of different resonant processes that can be associated to σ^* and Rydberg transitions. Moreover, the dications that lost H atoms can be detected even above the core ionization threshold.

It should be noted that the gas-phase NEXAFS spectroscopy of neutral PAH molecules has been reported, as well [206]. In their experiment, Fronzoni et al. [206] used a custom-built resistively heated furnace made of stainless steel to sublimate PAH samples into the vacuum chamber. The authors could regulate the sublimation temperature and monitor the vaporization by measuring the valence photoelectron spectrum of the heated sample. The experimental setup was based on a crossed photon/molecular beam arrangement, allowing the core-level photoelectron spectroscopy. The measurements were performed at the gas-phase photoemission (GAPH) beamline at Elettra synchrotron using a VG 150 mm hemispherical electrostatic analyzer. The reported work represents a combination of experimental and theoretical study of the C1s NEXAFS and X-ray photoelectron spectroscopy allowing for a detailed investigation of the vibronic coupling in PAHs and the role of this effect in such systems.
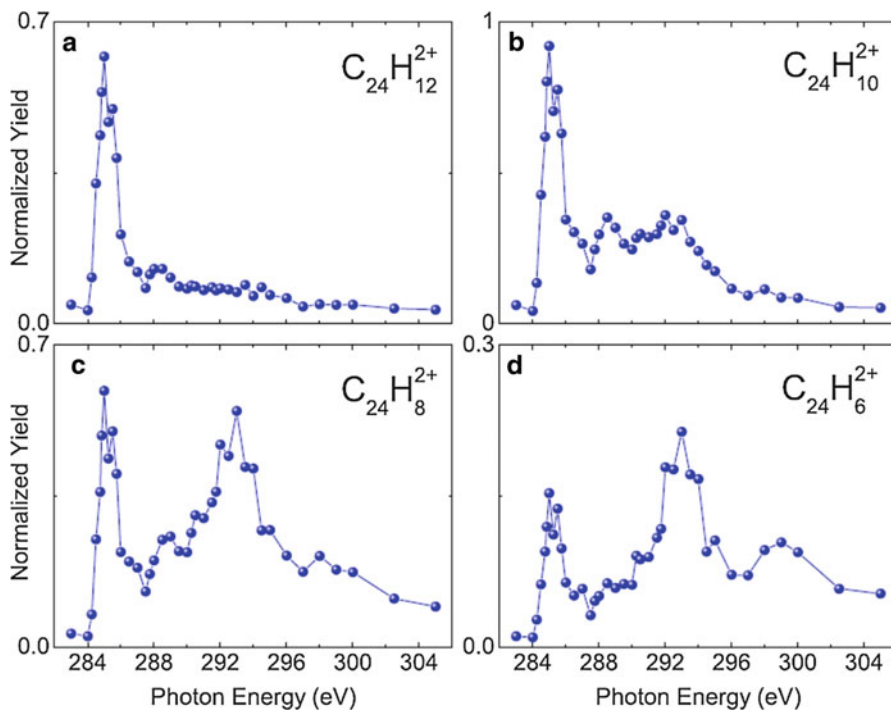
Fig. 8.24 NEXAMS spectra for $C_{24}H_{12}^{+}$ (**a**), $C_{24}H_{10}^{+}$ (**b**), $C_{24}H_8^{+}$ (**c**), and $C_{24}H_6^{+}$ (**d**), illustrating the strong dependence of the dehydrogenation on the photon energy (Reprinted with permission from Reitsma et al. (2012) *The Journal of chemical physics*, *142*, 024308 [111]. Copyright (2012), AIP Publishing LLC)

6   Conclusions and Perspectives

In recent years, the gap between NEXAFS spectroscopy studies of condensed and gas-phase matter has been shrinking. Indeed, the development of techniques allowing placement of intact species of increasing size and complexity in the gas phase has emerged, allowing study of polymers or nanoparticles. More recently, the advent of ion-trapping experiments has opened up a new area in the study of mass-selected targets.

In this chapter, we have reviewed novel experimental methods allowing performance of gas-phase NEXAFS spectroscopy of large complex species. The chapter includes a short presentation of SR sources that can provide a high-brilliance X-ray photon beam. The inner-shell studies of diluted matter are extremely photon demanding, particularly in the case of large particles that can be collected in the gas phase with extremely low partial pressures. Therefore, development of new-generation X-ray SR sources was a necessary step needed to perform such studies. The chapter further includes descriptions of general techniques used to perform inner-shell studies, with a

particular focus on X-ray action spectroscopy. Indeed, the more recent methods based on action spectroscopy offer significant improvements regarding both the sensitivity and selectivity of the technique in the case of low-density complex targets. We have also described novel techniques for sources of gas-phase targets, as well as experimental setups coupling the sources of large gas-phase targets with an X-ray beam. Finally, we review results spanning from relatively small metallic and organic molecular ions, over isolated DNA basis and amino acids representing building blocks of large biopolymers and finally including full proteins and molecular clusters.

In the present chapter, we also review the results on gas-phase NEXAFS spectroscopy of nanoparticles. Nanoparticles play an important role in our everyday lives, and in order to obtain the maximum amount of useful information on one specific system, spectroscopic and imaging techniques are often used in parallel. It has been shown that under-vacuum beams of nanoparticle have the advantages of preserving the integrity of the targets, as well as cancelling any detrimental influence of the substrate on the physical properties of the nanosystem, but also the advantage of removing any aging problem as the sample is continuously renewed. Even if the density of nanoparticles remains low in the beam, near-edge absorption spectroscopy can be performed. Moreover, it offers a mean to probe functionalized free nanoparticles where a sub-monolayer of ligands is attached to the particle. It is important to note that another way to introduce nanoparticles under vacuum is to couple the spectrometers with a liquid microjet, in which a solution containing nanoparticles forms a jet under vacuum through a capillary. The liquid jet then intercepts the synchrotron beam inside the spectrometer chamber, following which the electrons created can be analyzed [208, 209]. A recent review on the different experiments performed on nanoparticles can be found in Brown et al. [210], and this clearly highlights the capabilities of this complementary technique in tackling different questions regarding the nanoparticle/liquid interface. Moreover, wide varieties of different kinds of nanoparticles can be studied, from multilayered to functionalized or homogeneous nanoparticles. In addition, different synchrotrons are now offering liquid microjet sources or even dedicated end stations [211–213].

The variety of samples that will be accessible to X-ray spectroscopy will undoubtedly increase in the forthcoming years. Indeed, analytical chemists have developed a wide range of ionization techniques, such as atmospheric pressure MALDI, and atmospheric pressure photoionization or ASAP probe, from which the atomic and molecular community can profit. The current tendency is to increase the control on the target. The benefit of mass and charge-selected spectroscopy has allowed to gradually bridge the gap between the isolated atomic ion up to the bulk through the study of continuously controlled cluster composition. For biomolecules, the effect of the charge state on the spectroscopic properties could be evidenced for the first time. However, control on the mass and charge may not be sufficient, and conformation-specific experiments could be necessary. It is very likely that in the near future, experiments will combine mass-selected targets using ion traps in combination with ion mobility to reach conformationally selected targets. Thus, further studies will allow for reaching unprecedented control of the target to gain deeper understanding of the physicochemical and structural properties of complex systems.

References

1. Stöhr J (1992) NEXAFS spectroscopy, vol 25, Springer series in surface sciences. Springer, Berlin
2. Hähner G (2006) Near edge X-ray absorption fine structure spectroscopy as a tool to probe electronic and structural properties of thin organic films and liquids. Chem Soc Rev 35 (12):1244–1255. doi:10.1039/b509853j
3. Wu P, Yu Y, McGhee CE, Tan LH, Lu Y (2014) Applications of synchrotron-based spectroscopic techniques in studying nucleic acids and nucleic acid-functionalized nanomaterials. Adv Mater 26(46):7849–7872. doi:10.1002/adma.201304891
4. Brena B, Siegbahn PEM, Agren H (2012) Modeling near edge fine structure X-ray spectra of the manganese catalytic site for water oxidation in photosystem II. J Am Chem Soc. doi:10.1021/ja306794p
5. Zubavichus Y, Shaporenko A, Grunze M, Zharnikov M (2007) NEXAFS spectroscopy of homopolypeptides at all relevant absorption edges. J Phys Chem B 111(33):9803–9807
6. Stewart-Ornstein J, Hitchcock AP, Hernández Cruz D, Henklein P, Overhage J, Hilpert K et al (2007) Using intrinsic X-ray absorption spectral differences to identify and map peptides and proteins. J Phys Chem B 111(26):7691–7699
7. Zubavichus Y, Shaporenko A, Grunze M, Zharnikov M (2008) Is X-ray absorption spectroscopy sensitive to the amino acid composition of functional proteins? J Phys Chem B 112 (15):4478–4480. doi:10.1021/jp801248n
8. Aziz EF (2011) X-ray spectroscopies revealing the structure and dynamics of metalloprotein active centers. J Phys Chem Lett 2(4):320–326. doi:10.1021/jz1014778
9. Baio JE, Jaye C, Fischer DA, Weidner T (2014) High-throughput analysis of molecular orientation on surfaces by NEXAFS imaging of curved sample arrays. ACS Comb Sci 16 (9):449–453. doi:10.1021/co5001162
10. Milosavljević AR, Canon F, Nicolas C, Miron C, Nahon L, Giuliani A (2012) Gas-phase protein inner-shell spectroscopy by coupling an ion trap with a soft X-ray beamline. J Phys Chem Lett 3(9):1191–1196. doi:10.1021/jz300324z
11. Fenn JB, Mann M, Meng CK, Wong SF, Whitehouse CM (1990) Electrospray ionization-principles and practice. Mass Spectrom Rev 9(1):37–70. doi:10.1002/mas.1280090103
12. Aebersold R, Mann M (2003) Mass spectrometry-based proteomics. Nature 422 (6928):198–207. doi:10.1038/nature01511
13. Milosavljević AR, Nicolas C, Ranković MLJ, Canon F, Miron C, Giuliani A (2015) K-shell excitation and ionization of a gas-phase protein: interplay between electronic structure and protein folding. J Phys Chem Lett 6:3132. doi:10.1021/acs.jpclett.5b01288
14. Ivanenko DD, Pommeranchuck I (1944) On the maximal energy, obtainable in a betatron. Phys Rev 65:343
15. Schwinger J (1949) Phys Rev 75:1912
16. Schwinger J (1946) Electron radiation in high energy accelerators. Phys Rev 70:798
17. Hartman P, Tomboulian D (1952) Ultraviolet radiation from the Cornell synchrotron. Phys Rev 87(1):233
18. Codling K, Madden RP (1965) Characteristics of the "synchrotron light" from the NBS 180-MeV machine. J Appl Phys 36(2):380
19. Madden RP, Codling K (1964) Recently discovered auto-ionizing states of krypton and xenon in the λ380–600-Å region. J Opt Soc Am 54(2):268
20. Madden RP, Codling K (1963) New autoionizing atomic energy levels in He, Ne, and Ar. Phys Rev Lett 10(12):516. doi:10.1103/PhysRevLett.10.516
21. Kuntz C, Rowe EM, Gudat W, Kotani A, Toyozawa Y, Codling K et al (1979) Synchrotron radiation techniques and applications. In: Kuntz C (ed) Topics in current physics. Springer, Berlin/Heidelberg/New York
22. Motz H (1951) Applications of the radiation from fast electron beams. J Appl Phys 22(5):527

23. Motz H, Thon W, Whitehurst RN (1953) Experiments on radiation by fast electron beams. J Appl Phys 24(7):826

24. Winick H, Brown G, Halbach K, Harris J (1981) Wiggler and undulator magnets. Phys Today 34(5):50. doi:10.1063/1.2914568

25. David A (2000) Soft X-rays and extreme ultraviolet radiation: principles and applications. Cambridge University Press, Cambridge

26. Borland M (2013) Progress toward an ultimate storage ring light source. J Phys Conf Ser 425:042016

27. Johansson LC, Arnlund D, White TA, Katona G, Deponte DP, Weierstall U et al (2012) Lipidic phase membrane protein serial femtosecond crystallography. Nat Methods 9(3):263–265

28. Arnlund D, Johansson LC, Wickstrand C, Barty A, Williams GJ, Malmerberg E, Neutze R et al (2014) Visualizing a protein quake with time-resolved X-ray scattering at a free-electron laser. Nat Methods 11(9):923–926. doi:10.1038/nmeth.3067

29. Seibert MM, Ekeberg T, Maia FR, Svenda M, Andreasson J, Jönsson O et al (2011) Single mimivirus particles intercepted and imaged with an X-ray laser. Nature 470(7332):78–81

30. Chapman HN, Fromme P, Barty A, White TA, Kirian RA, Aquila A, Spence JC et al (2011) Femtosecond X-ray protein nanocrystallography. Nature 470(7332):73–77

31. Koopmann R, Cupelli K, Redecke L (2012) In vivo protein crystallization opens new routes in structural biology. Nat Methods 9(3):259

32. Loh ND, Hampton CY, Martin AV, Starodub D, Sierra RG, Barty A et al (2012) Fractal morphology, imaging and mass spectrometry of single aerosol particles in flight. Nature 486 (7404):513–517

33. Hitchcock AP, Beaulieu S, Steel T, Stöhr J, Sette F (1984) Carbon K-shell electron energy loss spectra of 1- and 2-butenes, trans-1,3-butadiene, and perfluoro-2-butene. Carbon–carbon bond lengths from continuum shape resonances. J Chem Phys 80(9):3927

34. Sette F, Stöhr J, Hitchcock AP (1984) Determination of intramolecular bond lengths in gas phase molecules from K shell shape resonances. J Chem Phys 81(11):4906

35. Stöhr J, Gland J, Kollin E, Koestner R, Johnson A, Muetterties E, Sette F (1984) Desulfurization and structural transformation of thiophene on the Pt(111) surface. Phys Rev Lett 53 (22):2161–2164

36. Guillemin R, Stolte WC, Piancastelli MN, Lindle DW (2010) Jahn-Teller coupling and fragmentation after core-shell excitation in CF_4 investigated by partial-ion-yield spectroscopy. Phys Rev A 82(4):043427. doi:10.1103/PhysRevA.82.043427

37. Piancastelli M (1999) The neverending story of shape resonances. J Electron Spectrosc Relat Phenom 100(1–3):167–190. doi:10.1016/S0368-2048(99)00046-8

38. Guillemin R, Stolte WC, Lindle DW (2009) Fragmentation of formic acid following photoexcitation around the carbon K edge. J Phys B Atomic Mol Phys 42(12):125101. doi:10.1088/0953-4075/42/12/125101

39. Kock E-E (ed) (1983) Handbook on synchrotron radiation. North Holland Pub Co, Amsterdam

40. Quack M, Merkt F (eds) (2011) Handbook of high-resolution spectroscopy. John Wiley, New York, p 2182

41. Bagus PS, Ilton ES, Nelin CJ (2013) The interpretation of XPS spectra: insights into materials properties. Surf Sci Rep 68(2):273–304

42. Ueda K (2003) High-resolution inner-shell spectroscopies of free atoms and molecules using soft-x-ray beamlines at the third-generation synchrotron radiation sources. J Phys B Atomic Mol Phys 36(4):R1–R47. doi:10.1088/0953-4075/36/4/201

43. Miron C, Morin P (2011) High-resolution inner-shell photo-ionization photoelectron and coincidence spectroscopy. In: Quack M, Merkt F (eds) Handbook of high-resolution spectroscopy, vol 3. John Wiley, New York, pp 1655–1689

44. Björneholm O, Öhrwall G, Tchaplyguine M (2009) Free clusters studied by core-level spectroscopies. Nucl Instrum Methods Phys Res, Sect A 601(1–2):161–181. doi:10.1016/j.nima.2008.12.222

45. Makarova AA, Grachova EV, Krupenya DV, Vilkov O, Fedorov A, Usachov D et al (2014) Insight into the electronic structure of the supramolecular "rods-in-belt" AuICuI and AuIAgI self-assembled complexes from X-ray photoelectron and absorption spectroscopy. J Electron Spectrosc Relat Phenom 192:26–34

46. Miron C, Patanen M (2014) Synchrotron-radiation-based soft X-ray electron spectroscopy applied to structural and chemical characterization of isolated species, from molecules to nanoparticles. Adv Mater 26:7911–7916. doi:10.1002/adma.201304837

47. Schramm T, Ganteför G, Bodi A, Hemberger P, Gerber T, von Issendorff B (2014) Photoelectron spectroscopy of size-selected cluster ions using synchrotron radiation. Appl Phys A 115 (3):771–779. doi:10.1007/s00339-014-8434-z

48. Tchaplyguine M, Peredkov S, Rosso A, Schulz J, Öhrwall G, Lundwall M et al (2007) Direct observation of the non-supported metal nanoparticle electron density of states by X-ray photoelectron spectroscopy. Eur Phys J D 45(2):295–299

49. Tchaplyguine M, Zhang C, Andersson T, Björneholm O (2014) Tuning the oxidation degree in sub-10nm silver-oxide nanoparticles: from Ag2O monoxide to AgOx(x > 1) superoxide. Chem Phys Lett 600:96–102

50. Bahn J, Oelßner P, Köther M, Braun C, Senz V, Palutke S et al (2012) Pb 4f photoelectron spectroscopy on mass-selected anionic lead clusters at FLASH. New J Phys 14(7):075008

51. Sublemontier O, Nicolas C, Aureau D, Patanen M, Kintz H, Liu X et al (2014) X-ray photoelectron spectroscopy of isolated nanoparticles. J Phys Chem Lett 5(19): 3399–3403

52. Antonsson E, Bresch H, Lewinski R (2013) Free nanoparticles studied by soft X-rays. Chem Phys Lett 559:1–11

53. Baer DR, Engelhard MH (2010) XPS analysis of nanostructured materials and biological surfaces. J Electron Spectrosc Relat Phenom 178–179:415–432

54. Meinen J, Khasminskaya S, Eritt M, Leisner T, Antonsson E, Langer B, Rühl E (2010) Core level photoionization on free sub-10-nm nanoparticles using synchrotron radiation. Rev Sci Instrum 81(8):085107

55. Mysak ER, Starr DE, Wilson KR, Bluhm H (2010) Note: A combined aerodynamic lens/ ambient pressure x-ray photoelectron spectroscopy experiment for the on-stream investigation of aerosol surfaces. Rev Sci Instrum 81(1):016106

56. Wilson KR, Bluhm H, Ahmed M (2011) Fundamentals and applications in aerosol spectroscopy, "Aerosol photoemission", fundamentals and applications in aerosol spectroscopy. In: Signorell R, Reid JR (eds). Taylor & Francis Inc, Philadelphia, p 367

57. Shigemasa E, Adachi J, Oura M, Yagishita A (1995) Angular distributions of 1sσ{} photoelectrons from fixed-in-space {{\mathrm N}}_{2} molecules. Phys Rev Lett 74(3):359–362. doi:10.1103/PhysRevLett.74.359

58. Dörner R, Bräuning H, Feagin JM, Mergel V, Jagutzki O, Spielberger L et al (1998) Photo-double-ionization of He: fully differential and absolute electronic and ionic momentum distributions. Phys Rev A 57(2):1074–1090. doi:10.1103/PhysRevA.57.1074

59. Ueda K, Simon M, Miron C, Leclercq N, Guillemin R, Morin P, Tanaka S (1999) Correlation between nuclear motion in the core-excited CF4 molecule and molecular dissociation after resonant auger decay. Phys Rev Lett 83(19):3800–3803

60. Prümper G, Carravetta V, Muramatsu Y, Tamenori Y, Kitajima M, Tanaka H et al (2007) Electron transfer during the dissociation of CH_{3}F^{+} produced by resonant photoemission following F 1s excitation. Phys Rev A 76(5):52705. doi:10.1103/PhysRevA.76.052705

61. Liu XJ, Prümper G, Kukk E, Sankari R, Hoshino M, Makochekanwa C et al (2005) Site-selective ion production of the core-excited CH_{3}F molecule probed by Auger-electron–ion coincidence measurements. Phys Rev A 72(4):42704. doi:10.1103/PhysRevA.72.042704

62. Miron C, Morin P (2009) High-resolution inner-shell coincidence spectroscopy. Nucl Instrum Methods Phys Res Sect A, 601(1–2, Sp. Iss. SI):66–77. doi:10.1016/j.nima.2008.12.104

63. Dörner R, Mergel V, Jagutzki O, Spielberger L, Ullrich J, Moshammer R, Schmidt-Böcking H (2000) Cold target recoil ion momentum spectroscopy: a 'momentum microscope' to

view atomic collision dynamics. Phys Rep 330(2–3):95–192. doi:10.1016/S0370-1573(99)00109-X

64. Ullrich J, Moshammer R, Dorn A, Dörner R, Schmidt LPH, Schmidt-Böcking H (2003) Recoil-ion and electron momentum spectroscopy: reaction-microscopes. Rep Prog Phys 66:1463. doi:10.1088/0034-4885/66/9/203

65. Ceolin D, Miron C, Simon M, Morin P (2004) Auger electron-ion coincidence studies to probe molecular dynamics. J Electron Spectrosc Relat Phenom, 141(2–3, Sp. Iss. SI):171–181. doi:10.1016/j.elspec.2004.06.014

66. Rühl E, Schmale C, Schmelz HC, Baumgärtel H (1992) The double ionization potentials of argon clusters. Chem Phys Lett 191(5):430–434

67. Mucke M, Braune M, Barth S, Förstel M, Lischke T, Ulrich V et al (2010) A hitherto unrecognized source of low-energy electrons in water. Nat Phys 6(2):143–146

68. Biester H, Besnard M, Dujardin G, Hellner L, Koch E (1987) Photoemission of pairs of electrons from rare-gas solids. Phys Rev Lett 59(12):1277–1280

69. Herrmann R, Samarin S, Schwabe H, Kirschner J (1998) Two electron photoemission in solids. Phys Rev Lett 81(10):2148–2151. doi:10.1103/PhysRevLett.81.2148

70. Huth M, Chiang C-T, Trützschler A, Schumann FO, Kirschner J, Widdra W (2014) Electron pair emission detected by time-of-flight spectrometers: recent progress. Appl Phys Lett 104(6):061602

71. Schumann FO, Behnke L, Li CH, Kirschner J (2013) Exploring highly correlated materials via electron pair emission: the case of NiO/Ag(100). J Phys Condens Matter 25(9):094002. doi:10.1088/0953-8984/25/9/094002

72. Giuliani A, Milosavljević AR, Canon F, Nahon L (2014) Contribution of synchrotron radiation to photoactivation studies of biomolecular ions in the gas phase. Mass Spectrom Rev 33(6):424–441. doi:10.1002/mas.21398

73. González-Magaña O, Reitsma G, Tiemens M, Boschman L, Hoekstra R, Schlathölter T (2012) Near-edge X-ray absorption mass spectrometry of a gas-phase peptide. J Phys Chem A 116(44):10745–10751. doi:10.1021/jp307527b

74. Baer T, Dunbar RC (2010) Ion spectroscopy: where did it come from; where is it now; and where is it going? J Am Soc Mass Spectrom 21(5):681–693. doi:10.1016/j.jasms.2010.01.028

75. Lucas CB (2013) Atomic and molecular beams: production and collimation. CRC Press, 6000 Broken Sound Pkwy NW - Boca Raton FL, p 392

76. Touboul D, Gaie-Levrel F, Garcia GA, Nahon L, Poisson L, Schwell M, Hochlaf M (2013) VUV photoionization of gas phase adenine and cytosine: a comparison between oven and aerosol vaporization. J Chem Phys 138(9):094203. doi:10.1063/1.4793734

77. Bernstein ER (1990) Atomic and molecular clusters. In: Bernstein ER (ed). Elsevier, Amsterdam/Oxford/New York/Tokyo, p 805

78. Wegner K, Piseri P, Tafreshi HV, Milani P (2006) Cluster beam deposition: a tool for nanoscale science and technology. J Phys D Appl Phys 39(22):R439–R459

79. Lindblad A, Söderström J, Nicolas C, Robert E, Daniel G, Miron C (2013) A multi purpose source chamber at the PLEIADES beamline at SOLEIL for spectroscopic studies of isolated species: cold molecules, clusters, and nanoparticles. Rev Sci Instrum 84:113105. doi:10.1063/1.4829718

80. Wilson KR, Jimenez-Cruz M, Nicolas C, Belau L, Leone SR, Ahmed M (2006) Thermal vaporization of biological nanoparticles: fragment-free vacuum ultraviolet photoionization mass spectra of tryptophan, phenylalanine-glycine- glycine, and β-carotene. J Phys Chem A 110(6):2106–2113

81. Wilson KR, Belau L, Nicolas C, Jimenez-Cruz M, Leone SR, Ahmed M (2006) Direct determination of the ionization energy of histidine with VUV synchrotron radiation. Int J Mass Spectrom 249–250:155–161

82. Gaie-Levrel F, Garcia GA, Schwell M, Nahon L (2011) VUV state-selected photoionization of thermally-desorbed biomolecules by coupling an aerosol source to an imaging photoelectron/photoion coincidence spectrometer: case of the amino acids tryptophan and phenylalanine. Phys Chem Chem Phys 13(15):7024–7036

83. Tia M, Cunha de Miranda B, Daly S, Gaie-Levrel F, Garcia GA, Nahon L, Powis I (2014) VUV photodynamics and chiral asymmetry in the photoionization of gas phase alanine enantiomers. J Phys Chem A 118(15):2765–2779

84. Isaacman G, Wilson KR, Chan AWH, Worton DR, Kimmel JR, Nah T et al (2012) Improved resolution of hydrocarbon structures and constitutional isomers in complex mixtures using gas chromatography-vacuum ultraviolet-mass spectrometry. Anal Chem 84(5):2335–2342

85. Liu P, Ziemann PJ, Kittelson DB, McMurry PH (1995) Generating particle beams of controlled dimensions and divergence. 1. Theory of particle motion in aerodynamic lenses and nozzle expansions. Aerosol Sci Technol 22(3):293–313. doi:10.1080/02786829408959748

86. Liu P, Ziemann PJ, Kittelson DB, McMurry PH (1995) Generating particle beams of controlled dimensions and divergence. 2. Experimental evaluation of particle motion in aerodynamic lenses and nozzle expansions. Aerosol Sci Technol 22(3):314–324. doi:10.1080/02786829408959749

87. Zhang XF, Smith KA, Worsnop DR, Jimenez JL, Jayne JT, Kolb CE et al (2004) Numerical characterization of particle beam collimation: part II – integrated aerodynamic-lens-nozzle system. Aerosol Sci Technol 38(6):619–638. doi:10.1080/02786820490479833

88. Zhang XF, Smith KA, Worsnop DR, Jimenez J, Jayne JT, Kolb CE (2002) A numerical characterization of particle beam collimation by an aerodynamic lens-nozzle system: part I. An individual lens or nozzle. Aerosol Sci Technol 36(5):617–631. doi:10.1080/02786820252883856

89. Jayne JT, Leard DC, Zhang XF, Davidovits P, Smith KA, Kolb CE, Worsnop DR (2000) Development of an aerosol mass spectrometer for size and composition analysis of submicron particles. Aerosol Sci Technol 33(1–2):49–70. doi:10.1080/027868200410840

90. Headrick JM, Schrader PE, Michelsen HA (2013) Radial-profile and divergence measurements of combustion-generated soot focused by an aerodynamic-lens system. J Aerosol Sci 58:158–170. doi:10.1016/j.jaerosci.2013.01.002

91. Wang X, Kruis FE, McMurry PH (2005) Aerodynamic focusing of nanoparticles: I. Guidelines for designing aerodynamic lenses for nanoparticles. Aerosol Sci Tech 39(7):611–623

92. Tafreshi HV, Benedek G, Piseri P, Vinati S, Barborini E, Milani P (2002) A simple nozzle configuration for the production of low divergence supersonic cluster beam by aerodynamic focusing. Aerosol Sci Tech 36(5):593–606

93. Lee D, Lee KS (2010) Aerodynamic lens. Google Patents, US 7652247 B2

94. Wang X, Gidwani A, Girshick S, McMurry P (2005) Aerodynamic focusing of nanoparticles: II. Numerical simulation of particle motion through aerodynamic lenses. Aerosol Sci Technol 39(7):624–636

95. Tafreshi H, Piseri P, Barborini E, Benedek G, Milani P (2002) Simulation on the effect of Brownian motion on nanoparticle trajectories in a pulsed microplasma cluster source. J Nanoparticle Res 4(6):511–524

96. Lewinski R, Graf C, Langer B, Flesch R, Bresch H, Wassermann B, Rühl E (2009) Size-effects in clusters and free nanoparticles probed by soft X-rays. Eur Phys J Spec Top 169(1):67–72

97. Shrivastava M, Gidwani A, Jung HS (2009) Modeling oxidation of soot particles within a laminar aerosol flow reactor using computational fluid dynamics. Aerosol Sci Tech 43(12):1218–1229

98. Wang X, McMurry PH, Kruis E (2009) Aerodynamic focusing of nanoparticle or cluster beams. Google Patents, US 7476851 B2

99. Piseri P, Tafreshi HV, Milani P (2004) Manipulation of nanoparticles in supersonic beams for the production of nanostructured materials. Curr Opin Solid State Mater Sci 8(3–4):195–202

100. Piseri P, Podestà A, Barborini E, Milani P (2001) Production and characterization of highly intense and collimated cluster beams by inertial focusing in supersonic expansions. Rev Sci Instrum 72(5):2261

101. Martinez F, Bandelow S, Breitenfeldt C, Marx G, Schweikhard L, Vass A, Wienholtz F (2014) Upgrades at ClusterTrap and latest results. Int J Mass Spectrom 365–366:266–274

102. Sturm S, Wagner A, Schabinger B, Blaum K (2011) Phase-sensitive cyclotron frequency measurements at ultralow energies. Phys Rev Lett 107(14):143003
103. Grimm M, Langer B, Schlemmer S, Lischke T, Becker U, Widdra W et al (2006) Charging mechanisms of trapped element-selectively excited nanoparticles exposed to soft X rays. Phys Rev Lett 96(6):066801
104. Gerlich D (2003) Molecular ions and nanoparticles in RF and AC traps. Hyperfine Interact 146/147(1–4):293–306
105. Shu J, Wilson KR, Ahmed M, Leone SR (2006) Coupling a versatile aerosol apparatus to a synchrotron: vacuum ultraviolet light scattering, photoelectron imaging, and fragment free mass spectrometry. Rev Sci Instrum 77(4):043106
106. Thissen R, Bizau J, Blancard C, Coreno M, Dehon C, Franceschi P et al (2008) Photoionization cross section of Xe+ ion in the pure 5p5 P3/22 ground level. Phys Rev Lett 100(22):223001. doi:10.1103/PhysRevLett.100.223001
107. Marrs R, Elliott S, Knapp D (1994) Production and trapping of hydrogenlike and bare uranium ions in an electron beam ion trap. Phys Rev Lett 72(26):4082–4085. doi:10.1103/PhysRevLett.72.4082
108. Epp S, López-Urrutia J, Brenner G, Mäckel V, Mokler P, Treusch R et al (2007) Soft X-Ray laser spectroscopy on trapped highly charged ions at FLASH. Phys Rev Lett 98(18):183001. doi:10.1103/PhysRevLett.98.183001
109. Hirsch K, Lau JT, Klar P, Langenberg A, Probst J, Rittmann J et al (2009) X-ray spectroscopy on size-selected clusters in an ion trap: from the molecular limit to bulk properties. J Phys B Atomic Mol Phys 42(15):154029. doi:10.1088/0953-4075/42/15/154029
110. Heiz U, Vanolli F, Trento L, Schneider W-D (1997) Chemical reactivity of size-selected supported clusters: an experimental setup. Rev Sci Instrum 68(5):1986. doi:10.1063/1.1148113
111. Reitsma G, Boschman L, Deuzeman MJ, Hoekstra S, Hoekstra R, Schlathölter T (2015) Near edge X-ray absorption mass spectrometry on coronene. J Chem Phys 142(2):024308. doi:10.1063/1.4905471
112. Ryding MJ, Giuliani A, Patanen M, Niskanen J, Simões G, Miller GBS et al (2014) X-ray induced fragmentation of size-selected salt cluster-ions stored in an ion trap. RSC Adv 4(88):47743–47751. doi:10.1039/C4RA09787D
113. Cole RB (2010) Electrospray and MALDI mass spectrometry: fundamentals, instrumentation, practicalities, and biological applications, 2nd edn. Wiley, Hoboken, p 896
114. Cox JT, Marginean I, Smith RD, Tang K (2015) On the ionization and ion transmission efficiencies of different ESI-MS interfaces. J Am Soc Mass Spectrom 26(1):55–62. doi:10.1007/s13361-014-0998-5
115. Robb D, Covey T, Bruins A (2000) Atmospheric pressure photoionization: an ionization method for liquid chromatography-mass spectrometry. Anal Chem 72(15):3653–3659
116. Song L, Wellman AD, Yao H, Adcock J (2007) Electron capture atmospheric pressure photoionization mass spectrometry: analysis of fullerenes, perfluorinated compounds, and pentafluorobenzyl derivatives. Rapid Commun Mass Spectrom 21(8):1343–1351. doi:10.1002/rcm.2963
117. Peart B, Stevenson JG, Dolder KT (1973) Measurements of cross sections for the ionization of Ba+ by energy resolved electrons. J Phys B Atomic Mol Phys 6(1):146–149. doi:10.1088/0022-3700/6/1/016
118. Lyon IC, Peart B, West JB, Dolder K (1986) Measurements of absolute cross sections for the photoionisation of Ba+ ions. J Phys B Atomic Mol Phys 19(24):4137–4147. doi:10.1088/0022-3700/19/24/015
119. Kjeldsen H, Folkmann F, Elp JV, Knudsen H, West JB, Andersen T (2005) Absolute measurements of photoionization cross-sections for ions. Nucl Instrum Methods Phys Res Sect B 234(3):349–361. doi:10.1016/j.nimb.2005.01.011
120. Kjeldsen H (2006) Photoionization cross sections of atomic ions from merged-beam experiments. J Phys B Atomic Mol Phys 39(21):R325–R377. doi:10.1088/0953-4075/39/21/R01

121. Bizau JM, Cubaynes D, Al Shorman MM, Guilbaud S, Blancard C, Lemaire J et al (2012) Photoionization of atomic and molecular positively charged ions. J Phys Conf Ser 399:012002. doi:10.1088/1742-6596/399/1/012002

122. Gharaibeh MF, Bizau JM, Cubaynes D, Guilbaud S, El Hassan N, Al Shorman MM et al (2011) K-shell photoionization of singly ionized atomic nitrogen: experiment and theory. J Phys B Atomic Mol Phys 44:175208. doi:10.1088/0953-4075/44/17/175208

123. Bizau JM, Blancard C, Coreno M, Cubaynes D, Dehon C, El Hassan N et al (2011) Photo-ionization study of Kr+ and Xe+ ions with the combined use of a merged-beam set-up and an ion trap. J Phys B Atomic Mol Phys 44(5):055205. doi:10.1088/0953-4075/44/5/055205

124. Bizau JM, Cubaynes D, Richter M, Wuilleumier F, Obert J, Putaux JC (1992) The combined use of a singly charged ion-beam and undulator radiation for photoelectron spectrometry studies on atomic ions. Rev Sci Instrum 63:1389–1392, Univ Paris 11, Inst Phys Nucl, F-91405 Orsay, France

125. Bizau JM, Cubaynes D, Richter M, Wuilleumier FJ, Obert J, Putaux JC et al (1991) First observation of photoelectron spectra emitted in the photoionization of a singly charged-ion beam with synchrotron radiation. Phys Rev Lett 67(5):576–579

126. Senz V, Fischer T, Oelßner P, Tiggesbäumker J, Stanzel J, Bostedt C et al (2009) Core-Hole Screening as a Probe for a Metal-to-Nonmetal Transition in Lead Clusters. Phys Rev Lett 102 (13):138303. doi:10.1103/PhysRevLett.102.138303

127. Dunbar RC (2014) In the beginning was H2+: mass spectrometry and the molecular spectros-copy of gas-phase ions. Int J Mass Spectrom. doi:10.1016/j.ijms.2014.07.049

128. Dunbar RC (2000) Photodissociation of trapped ions. Int J Mass Spectrom 200:571–589

129. Antoine R, Dugourd P (2011) Visible and ultraviolet spectroscopy of gas phase protein ions. Phys Chem Chem Phys 13(37):16494–16509. doi:10.1039/c1cp21531k

130. Peredkov S, Neeb M, Eberhardt W, Meyer J, Tombers M, Kampschulte H, Niedner-Schatteburg G (2011) Spin and orbital magnetic moments of free nanoparticles. Phys Rev Lett 107(23):233401. doi:10.1103/PhysRevLett.107.233401

131. Peredkov S, Savci A, Peters S, Neeb M, Eberhardt W, Kampschulte H et al (2011) X-ray absorption spectroscopy of mass-selected transition metal clusters using a cyclotron ion trap: an experimental setup for measuring XMCD spectra of free clusters. J Electron Spectrosc Relat Phenom 184(3–6):113–118. doi:10.1016/j.elspec.2010.12.031

132. González-Magaña O, Tiemens M, Reitsma G, Boschman L, Door M, Bari S et al (2013) Fragmentation of protonated oligonucleotides by energetic photons and Cq+ ions. Phys Rev A 87(3):032702. doi:10.1103/PhysRevA.87.032702

133. Lau JT, Rittmann J, Zamudio-Bayer V, Vogel M, Hirsch K, Klar P et al (2008) Size depen-dence of L2,3 branching ratio and 2p core-hole screening in X-ray absorption of metal clusters. Phys Rev Lett 101(15):153401. doi:10.1103/PhysRevLett.101.153401

134. Kravis SD, Church D, Johnson B, Meron M, Jones K, Levin J et al (1991) Inner-shell photoionization of stored positive ions using synchrotron radiation. Phys Rev Lett 66 (23):2956–2959. doi:10.1103/PhysRevLett.66.2956

135. Bari S, Gonzalez-Magaña O, Reitsma G, Werner J, Schippers S, Hoekstra R, Schlathölter T (2011) Photodissociation of protonated leucine-enkephalin in the VUV range of 8–40 eV. J Chem Phys 134(2):024314. doi:10.1063/1.3515301

136. González-Magaña O, Reitsma G, Bari S, Hoekstra R, Schlathölter T (2012) Length effects in VUV photofragmentation of protonated peptides. Phys Chem Chem Phys 14(13):4351–4354. doi:10.1039/c2cp23470j

137. Milosavljević AR, Nicolas C, Gil J, Canon F, Réfrégiers M, Nahon L, Giuliani A (2012) VUV synchrotron radiation: a new activation technique for tandem mass spectrometry. J Synchro-tron Radiat 19(Pt 2):174–178. doi:10.1107/S0909049512001057

138. Schwartz JC, Senko MW (2002) A two-dimensional quadrupole ion trap mass spectrometer. J Am Soc Mass Spectrom 13(6):659–669. doi:10.1016/S1044-0305(02)00384-7

139. Thelen JJ, Miernyk JA (2012) The proteomic future: where mass spectrometry should be taking us. Biochem J 444(2):169–181

140. Canon F, Milosavljević AR, van der Rest G, Réfrégiers M, Nahon L, Sarni-Manchado P et al (2013) Photodissociation and dissociative photoionization mass spectrometry of proteins and noncovalent protein-ligand complexes. Angew Chem Int Ed Engl 52(32):8377–8381. doi:10.1002/anie.201304046

141. Canon F, Milosavljevic AR, Nahon L, Giuliani A (2015) Action spectroscopy of a protonated peptide in the ultraviolet range. Phys Chem Chem Phys. doi:10.1039/C4CP04762A

142. Giuliani A, Milosavljević AR, Hinsen K, Canon F, Nicolas C, Réfrégiers M, Nahon L (2012) Structure and charge-state dependence of the gas-phase ionization energy of proteins. Angew Chem Int Ed Engl 51(38):9552–9556. doi:10.1002/anie.201204435

143. Milosavljević AR, Nicolas C, Lemaire J, Dehon C, Thissen R, Bizau J-M et al (2011) Photoionization of a protein isolated in vacuo. Phys Chem Chem Phys 13 (34):15432–15436. doi:10.1039/c1cp21211g

144. Milosavljević AR, Giuliani A, Nicolas C, Gil J-F, Lemaire J, Réfrégiers M, Nahon L (2010) Gas-phase spectroscopy of a protein. J Phys Conf Ser 257(1992):012006. doi:10.1088/1742-6596/257/1/012006

145. Milosavljević AR, Cerovski VZ, Canon F, Nahon L, Giuliani A (2013) Nanosolvation-induced stabilization of a protonated peptide dimer isolated in the gas phase. Angew Chem Int Ed Engl 52(28):7286–7290. doi:10.1002/anie.201301667

146. Milosavljević AR, Cerovski VZ, Canon F, Ranković ML, Škoro N, Nahon L, Giuliani A (2014) Energy-dependent UV photodissociation of gas-phase adenosine monophosphate nucleotide ions: the role of a single solvent molecule. J Phys Chem Lett 5:1994–1999. doi:10.1021/jz500696b

147. Bolognesi P, Mattioli G, O'Keeffe P, Feyer V, Plekan O, Ovcharenko Y et al (2009) Investigation of halogenated pyrimidines by X-ray photoemission spectroscopy and theoretical DFT methods. J Phys Chem A 113(48):13593–13600. doi:10.1021/jp908512v

148. Bolognesi P, O'Keeffe P, Ovcharenko Y, Coreno M, Avaldi L, Feyer V et al (2010) Pyrimidine and halogenated pyrimidines near edge x-ray absorption fine structure spectra at C and N K-edges: experiment and theory. J Chem Phys 133(3):034302. doi:10.1063/1.3442489

149. Bolognesi P, O'Keeffe P, Feyer V, Plekan O, Prince K, Coreno M et al (2010) Inner shell excitation, ionization and fragmentation of pyrimidine. J Phys Conf Ser 212:012002. doi:10.1088/1742-6596/212/1/012002

150. Feyer V, Plekan O, Richter R, Coreno M, Vall-llosera G, Prince KC et al (2009) Tautomerism in cytosine and uracil: an experimental and theoretical core level spectroscopic study. J Phys Chem A 113(19):5736–5742. doi:10.1021/jp900998a

151. Plekan O, Feyer V, Richter R, Coreno M, Vall-Llosera G, Prince KC et al (2009) An experimental and theoretical core-level study of tautomerism in guanine. J Phys Chem A 113(33):9376–9385. doi:10.1021/jp903209t

152. Feyer V, Plekan O, Richter R, Coreno M, de Simone M, Prince KC et al (2010) Tautomerism in cytosine and uracil: a theoretical and experimental X-ray absorption and resonant auger study. J Phys Chem A 114(37):10270–10276. doi:10.1021/jp105062c

153. Giuliano BM, Feyer V, Prince KC, Coreno M, Evangelisti L, Melandri S, Caminati W (2010) Tautomerism in 4-hydroxypyrimidine, S-methyl-2-thiouracil, and 2-thiouracil. J Phys Chem A 114:12725–12730

154. Feyer V, Plekan O, Kivim A, Prince KC, Moskovskaya TE, Zaytseva IL et al (2011) Comprehensive core-level study of the effects of isomerism halogenation, and methylation on the tautomeric equilibrium of cytosine. J Phys Chem A 115(26):7722–7733

155. Hua W, Gao B, Li S, Ågren H, Luo Y (2010) Refinement of DNA structures through near-edge X-ray absorption fine structure analysis: applications on guanine and cytosine nucleobases, nucleosides, and nucleotides. J Phys Chem B 114:13214–13222. doi:10.1021/jp1034745

156. Itälä E, Ha DT, Kooser K, Huels MA, Rachlew E, Nõmmiste E et al (2011) Molecular fragmentation of pyrimidine derivatives following site-selective carbon core ionization. J Electron Spectrosc Relat Phenom 184(3–6):119–124. doi:10.1016/j.elspec.2011.01.007

157. Itälä E, Ha DT, Kooser K, Rachlew E, Huels MA, Kukk E (2010) Fragmentation patterns of core-ionized thymine and 5-bromouracil. J Chem Phys 133(15):154316. doi:10.1063/1.3505140

158. Itälä E, Ha DT, Kooser K, Nõmmiste E, Joost U, Kukk E (2011) Fragmentation patterns of core ionized uracil. Int J Mass Spectrom 306(1):82–90. doi:10.1016/j.ijms.2011.07.006

159. Itälä E, Huels MA, Rachlew E, Kooser K, Hägerth T, Kukk E (2013) A comparative study of dissociation of thymidine molecules following valence or core photoionization. J Phys B Atomic Mol Phys 46(21):215102. doi:10.1088/0953-4075/46/21/215102

160. Ha DT, Huels MA, Huttula M, Urpelainen S, Kukk E (2011) Experimental and ab initio study of the photofragmentation of DNA and RNA sugars. Phys Rev A 84(3):033419. doi:10.1103/PhysRevA.84.033419

161. Itälä E, Kooser K, Rachlew E, Huels MA, Kukk E (2014) Soft x-ray ionization induced fragmentation of glycine. J Chem Phys 140(23):234305. doi:10.1063/1.4882648

162. Laksman J, Kooser K, Levola H, Ita E, Ha DT, Rachlew E, Kukk E (2014) Dissociation pathways in the cysteine dication after site-selective core ionization. J Phys Chem B 118(40):11688–11695

163. Ha DT, Wang Y, Alcamí M, Itälä E, Kooser K, Urpelainen S et al (2014) Fragmentation dynamics of doubly charged methionine in the gas phase. J Phys Chem A 118(8):1374–1383. doi:10.1021/jp4113238

164. Feyer V, Plekan O, Richter R, Coreno M, Prince KC, Carravetta V (2009) Photoemission and photoabsorption spectroscopy of glycyl-glycine in the gas phase. J Phys Chem A 113(40):10726–10733. doi:10.1021/jp906843j

165. Feyer V, Plekan O, Richter R, Coreno M, Prince KC, Carravetta V (2008) Core level study of alanine and threonine. J Phys Chem A 112(34):7806–7815. doi:10.1021/jp803017y

166. Zhang W, Carravetta V, Plekan O, Feyer V, Richter R, Coreno M, Prince KC (2009) Electronic structure of aromatic amino acids studied by soft x-ray spectroscopy. J Chem Phys 131(2009):035103. doi:10.1063/1.3168393

167. Li H, Hua W, Lin Z, Luo Y (2012) First-principles study on core-level spectroscopy of arginine in gas and solid phases. J Phys Chem B 116:12641–12650. doi:10.1021/jp302309u

168. Stolte W, Hansen D, Piancastelli M, Dominguez Lopez I, Rizvi A, Hemmers O (2001) Anionic photofragmentation of CO: a selective probe of core-level resonances. Phys Rev Lett 86(20):4504–4507. doi:10.1103/PhysRevLett.86.4504

169. Lin Y-S, Lu K-T, Lee YT, Tseng C-M, Ni C-K, Liu C-L (2014) Near-edge X-ray absorption fine structure spectra and site-selective dissociation of phenol. J Phys Chem A 118(9):1601–1609. doi:10.1021/jp500284r

170. Billas IM, Châtelain A, de Heer WA (1994) Magnetism from the atom to the bulk in iron, cobalt, and nickel clusters. Science 265(5179):1682–1684. doi:10.1126/science.265.5179.1682

171. Krückeberg S, Beiersdorfer P, Dietrich G, Lützenkirchen K, Schweikhard L, Walther C (1997) First observation of multiply charged vanadium clusters in a Penning trap. Rapid Commun Mass Spectrom 11(5):455–458

172. Terasaki A, Majima T, Kondow T (2007) Photon-trap spectroscopy of mass-selected ions in an ion trap: optical absorption and magneto-optical effects. J Chem Phys 127(23):231101. doi:10.1063/1.2822022

173. Majima T, Terasaki A, Kondow T (2008) Optical pumping by a laser pulse traveling in a cavity. Phys Rev A 77(3):033417. doi:10.1103/PhysRevA.77.033417

174. Terasaki A, Majima T, Kasai C, Kondow T (2009) Photon-trap spectroscopy of size-selected free cluster ions: "direct" measurement of optical absorption of Ag+ 9. Eur Phys J D 52(1–3):43–46. doi:10.1140/epjd/e2008-00274-0

175. Egashira K, Bartels C, Kondow T, Terasaki A (2011) Optical absorption spectrum of the silver dimer ion: temperature dependence measured by photodissociation and photon-trap spectroscopy. Eur Phys J D 63(2):183–187. doi:10.1140/epjd/e2011-10525-6

176. Hirsch K, Zamudio-Bayer V, Rittmann J, Langenberg A, Vogel M, Möller T et al (2012) Initial- and final-state effects on screening and branching ratio in 2p x-ray absorption of size-selected free 3d transition metal clusters. Phys Rev B 86(16):165402. doi:10.1103/PhysRevB.86.165402

177. Lau JT, Vogel M, Langenberg A, Hirsch K, Rittmann J, Zamudio-Bayer V et al (2011) Communication: highest occupied molecular orbital-lowest unoccupied molecular orbital gaps of doped silicon clusters from core level spectroscopy. J Chem Phys 134(4):41102. doi:10.1063/1.3547699

178. Vogel M, Kasigkeit C, Hirsch K, Langenberg A, Rittmann J, Zamudio-Bayer V et al (2012) 2p core-level binding energies of size-selected free silicon clusters: chemical shifts and cluster structure. Phys Rev B 85(19):195454. doi:10.1103/PhysRevB.85.195454

179. Hirsch K, Zamudio-Bayer V, Ameseder F, Langenberg A, Rittmann J, Vogel M et al (2012) 2p x-ray absorption of free transition-metal cations across the 3d transition elements: calcium through copper. Phys Rev A 85(6):062501. doi:10.1103/PhysRevA.85.062501

180. Niemeyer M, Hirsch K, Zamudio-Bayer V, Langenberg A, Vogel M, Kossick M et al (2012) Spin coupling and orbital angular momentum quenching in free iron clusters. Phys Rev Lett 108(5):057201. doi:10.1103/PhysRevLett.108.057201

181. Zamudio-Bayer V, Leppert L, Hirsch K, Langenberg A, Rittmann J, Kossick M et al (2013) Coordination-driven magnetic-to-nonmagnetic transition in manganese-doped silicon clusters. Phys Rev B 88(11):115425. doi:10.1103/PhysRevB.88.115425

182. Langenberg A, Hirsch K, Ławicki A, Zamudio-Bayer V, Niemeyer M, Chmiela P et al (2014) Spin and orbital magnetic moments of size-selected iron, cobalt, and nickel clusters. Phys Rev B 90(18):184420. doi:10.1103/PhysRevB.90.184420

183. Daly S, Krstic M, Giuliani A, Antoine R, Nahon L, Zavras A, et al. (2015) Gas-phase VUV photoionization and photofragmentation of the silver deuteride nanocluster [Ag10D8L6]2+ (L=bis(diphenylphosphino)methane). A joint experimental and theoretical study. Phys Chem Chem Phys 17(39):25772–25777. doi:10.1039/c5cp01160d

184. Burda C, Chen XB, Narayanan R, El-Sayed MA (2005) Chemistry and properties of nanocrystals of different shapes. Chem Rev 105(4):1025–1102. doi:10.1021/cr030063a

185. Schliehe C, Schliehe C, Thiry M, Tromsdorf UI, Hentschel J, Weller H, Groettrup M (2011) Microencapsulation of inorganic nanocrystals into PLGA microsphere vaccines enables their intracellular localization in dendritic cells by electron and fluorescence microscopy. J Control Release 151(3):278–285. doi:10.1016/j.jconrel.2011.01.005

186. Flagan RC, Lunden MM (1995) Particle structure control in nanoparticle synthesis from the vapor phase. Mater Sci Eng A 204(1–2):113–124

187. Sublemontier O, Kintz H, Lacour F, Paquez X, Maurice V, Leconte Y et al (2011) Synthesis and on-line size control of silicon quantum dots. Kona Powder Part J 29:236–250

188. Ravagnan L, Mazza T, Bongiorno G, Devetta M, Amati M, Milani P et al (2011) sp hybridization in free carbon nanoparticles–presence and stability observed by near edge X-ray absorption fine structure spectroscopy. Chem Commun (Camb) 47(10):2952–2954

189. Ravagnan L, Bongiorno G, Bandiera D, Salis E, Piseri P, Milani P et al (2006) Quantitative evaluation of sp/sp(2) hybridization ratio in cluster-assembled carbon films by in situ near edge X-ray absorption fine structure spectroscopy. Carbon 44(8):1518–1524. doi:10.1016/j.carbon.2005.12.015

190. Diaz J, Monteiro OR, Hussain Z (2007) Structure of amorphous carbon from near-edge and extended x-ray absorption spectroscopy. Phys Rev B 76(9):094201. doi:10.1103/PhysRevB.76.094201

191. Kasrai M, Brown JR, Bancroft GM, Yin Z, Tan KH (1996) Sulphur characterization in coal from X-ray absorption near edge spectroscopy. Int J Coal Geol 32(1–4):107–135. doi:10.1016/S0166-5162(96)00033-X

192. Sutherland DGJ, Kasrai M, Bancroft GM, Liu ZF, Tan KH (1993) Si L-edge and K-edge X-ray-absorption near-edge spectroscopy of gas-phase Si(CH3)(x)(OCH3)(4-X) – models for solid-state analogs. Phys Rev B 48(20):14989–15001. doi:10.1103/PhysRevB.48.14989

193. Bresch H (2007) Doctoral thesis. Freie Universität Berlin

194. Garcia B, Salome M, Lemelle L, Bridot JL, Gillet P, Perriat P et al (2005) Sulfur K-edge XANES study of dihydrolipoic acid capped gold nanoparticles: dihydrolipoic acid is bound by both sulfur ends. Chem Commun 3:369–371. doi:10.1039/b411231h

195. Roux S, Garcia B, Bridot JL, Salome M, Marquette C, Lemelle L et al (2005) Synthesis, characterization of dihydrolipoic acid capped gold nanoparticles, and functionalization by the electroluminescent luminol. Langmuir 21(6):2526–2536. doi:10.1021/la048082i

196. Dezarnaud C, Tronc M, Hitchcock AP (1990) Inner shell spectroscopy of the carbon—sulfur bond. Chem Phys 142(3):455–462

197. Mei BC, Susumu K, Medintz IL, Delehanty JB, Mountziaris TJ, Mattoussi H (2008) Modular poly(ethylene glycol) ligands for biocompatible semiconductor and gold nanocrystals with extended pH and ionic stability. J Mater Chem 18(41):4949–4958. doi:10.1039/b810488c

198. Volkert AA, Subramaniam V, Ivanov MR, Goodman AM, Haes AJ (2011) Salt-mediated self-assembly of thioctic acid on gold nanoparticles. ACS Nano 5(6):4570–4580. doi:10.1021/nn200276a

199. Kravis SD, Church DA, Johnson BM, Levin JC, Azuma Y, Sellin IA et al (1991) Sequential photoionization of ions using synchrotron radiation and a Penning ion trap. Nucl Instrum Methods Phys Res Sect B 56–57:396–399. doi:10.1016/0168-583X(91)96054-Q

200. West JB (2001) Photoionization of atomic ions. J Phys B Atomic Mol Phys 34(18):R45–R91

201. Gokhberg K, Kolorenč P, Kuleff AI, Cederbaum LS (2014) Site- and energy-selective slow-electron production through intermolecular Coulombic decay. Nature 505(7485):661–663. doi:10.1038/nature12936

202. Zubavichus Y, Shaporenko A, Grunze M, Zharnikov M (2009) NEXAFS spectroscopy of biological molecules: from amino acids to functional proteins. Nucl Instrum Methods Phys Res Sect A 603(1–2):111–114. doi:10.1016/j.nima.2008.12.171

203. Messer BM, Cappa CD, Smith JD, Wilson KR, Gilles MK, Cohen RC, Saykally RJ (2005) pH dependence of the electronic structure of glycine. J Phys Chem B 109(11):5375–5382. doi:10.1021/jp0457592

204. Nolting D, Aziz EF, Ottosson N, Faubel M, Hertel IV, Winter B (2007) pH-induced proton-ation of lysine in aqueous solution causes chemical shifts in X-ray photoelectron spectroscopy. J Am Chem Soc 129(45):14068–14073. doi:10.1021/ja072971l

205. Ottosson N, Børve KJ, Spångberg D, Bergersen H, Sæthre LJ, Faubel M et al (2011) On the origins of core-electron chemical shifts of small biomolecules in aqueous solution: insights from photoemission and ab initio calculations of glycine(aq). J Am Chem Soc 133 (9):3120–3130. doi:10.1021/ja110321q

206. Fronzoni G, Baseggio O, Stener M, Hua W, Tian G, Luo Y et al (2014) Vibrationally resolved high-resolution NEXAFS and XPS spectra of phenanthrene and coronene. J Chem Phys 141:044313. doi:10.1063/1.4891221

207. Reitsma G, Boschman L, Deuzeman MJ, González-Magaña O, Hoekstra S, Cazaux S et al (2014) Deexcitation dynamics of superhydrogenated polycyclic aromatic hydrocarbon cations after soft-x-ray absorption. Phys Rev Lett 113(5):053002. doi:10.1103/PhysRevLett.113.053002

208. Winter B (2009) Liquid microjet for photoelectron spectroscopy. Nucl Instrum Methods Phys Res Sect A 601(1–2):139–150. doi:10.1016/j.nima.2008.12.108

209. Faubel M, Siefermann KR, Liu Y, Abel B (2012) Ultrafast soft X-ray photoelectron spectros-copy at liquid water microjets. Acc Chem Res 45(1):120–130

210. Brown MA, Jordan I, Beloqui Redondo A, Kleibert A, Wörner HJ, Van Bokhoven JA (2013) In situ photoelectron spectroscopy at the liquid/nanoparticle interface. Surf Sci 610:1–6. doi:10.1016/j.susc.2013.01.012

211. Brown MA, Redondo AB, Jordan I, Duyckaerts N, Lee MT, Ammann M et al (2013) A new endstation at the Swiss Light Source for ultraviolet photoelectron spectroscopy, X-ray photoelectron spectroscopy, and X-ray absorption spectroscopy measurements of liquid solutions. Rev Sci Instrum 84(7):073904
212. Winter B, Faubel M (2006) Photoemission from liquid aqueous solutions. Chem Rev 106 (4):1176–1211
213. Bergersen H, Marinho RRT, Pokapanich W, Lindblad A, Björneholm O, Sæthre LJ, Öhrwall G (2007) A photoelectron spectroscopic study of aqueous tetrabutylammonium iodide. J Phys Condens Matter 19(32):326101

In Situ X-Ray Reciprocal Space Mapping for Characterization of Nanomaterials

9

Peter Siffalovic, Karol Vegso, Martin Hodas, Matej Jergel, Yuriy Halahovets, Marco Pelletta, Dusan Korytar, Zdeno Zaprazny, and Eva Majkova

Contents

1   Definition of Topic

In this chapter, we will focus on the small-angle X-ray scattering (SAXS) technique performed on planar samples in the grazing-incidence small-angle X-ray scattering (GISAXS) geometry. This particular method of SAXS allows a fast, nondestructive analysis of the near-surface electron density variations on the lateral length scale ranging from several angstroms up to several hundreds of nanometers with adjustable in-depth sensitivity down to several nanometers. Special emphasis will

P. Siffalovic (✉) • K. Vegso • M. Hodas • M. Jergel •
Y. Halahovets • M. Pelletta • E. Majkova
Institute of Physics, Slovak Academy of Sciences, Bratislava, Slovakia
e-mail: peter.siffalovic@savba.sk; karol.vegso@savba.sk; martin.hodas@savba.sk; matej.jergel@savba.sk; fyzihala@savba.sk; marco.pelletta@savba.sk; eva.majkova@savba.sk

D. Korytar • Z. Zaprazny
Institute of Electrical Engineering, Slovak Academy of Sciences, Bratislava, Slovakia
e-mail: elekdkor@savba.sk; zdenko.zaprazny@savba.sk

507

be given to GISAXS experiments with laboratory X-ray sources as these are much more easily accessible as compared to synchrotron facilities.

2   Overview

The steadily growing research field of applied nanomaterials calls for development of advanced analytical methods for rapid and nondestructive structural characterization. A relatively simple grazing-incidence small-angle X-ray scattering (GISAXS) technique is an efficient analytical tool for structural studies of layered nanomaterials and self-assembled nanostructures. The feasibility to obtain statistically relevant parameters that characterize position correlations and size distributions in the surface or embedded nanoparticle assemblies or interface correlations in the layered nanostructures render the GISAXS technique a valuable complementary tool to the standard real-space investigation methods like transmission electron microscopy (TEM), scanning tunneling microscopy (STM), scanning electron microscopy (SEM), atomic force microscopy (AFM), etc. While a sophisticated sample preparation is often required for the real-space imaging techniques, the GISAXS has no special requirements. This technique is especially valuable for a real-time tracking of the nucleation and growth phases of nanomaterials preparation due to the long X-ray attenuation length in air and absence of special requirements for the experimental setup.

In this chapter, we will review applications of GISAXS for in situ studies of nanomaterial formation including the nucleation, agglomeration, self-assembly, and reassembly phenomena. Majority if not all in situ GISAXS experiments of nanomaterial formation have been performed at synchrotron facilities, taking the advantage of their high X-ray photon flux and low beam divergence. Only the advent of new micro-focusing X-ray sources coupled with high-performance reflective X-ray optics has allowed such GISAXS in situ experiments in a laboratory as will be demonstrated on several examples in this chapter.

3   Introduction

The tracking of temporal evolution of nanomaterials formation opens new possibilities to tailor their properties for the envisaged application. As a representative example, we quote formation of metallic nanoclusters on the substrates with different surface energies that are popular as nucleation templates for carbon nanotubes or dedicated substrates for surface-enhanced Raman scattering (SERS). The metal deposition time has to be precisely controlled to avoid cluster coalescence into larger domains. Here, the in situ GISAXS provides a precise monitoring of the metallic nanoparticle growth in real time. Another example is an in situ GISAXS monitoring of etching the nanoparticle surfactant shell by the UV/ozone processing. We can precisely identify the stop time for the surfactant etching in order to avoid oxidation and agglomeration of nanoparticles.

The chapter is organized as follows. In the section *Theoretical Background*, we discuss the essential theoretical ansatz suitable for description of the measured

GISAXS reciprocal space maps. In the section *Experimental and Instrumental Methodology*, we define basic GISAXS experimental geometry common to synchrotron beamlines. We highlight the latest advances in the laboratory GISAXS instrumentation. The section *Key Research Finding* is devoted to diverse in situ GISAXS experiments. We illustrate the usefulness of the in situ GISAXS technique for tracking the nanoparticles self-assembly at solid and liquid surfaces. A special attention will be paid to ex situ and in situ GISAXS analyses of multilayers. The coming trends in the GISAXS in situ experiments are compiled in *Future Perspective. Conclusions* summarize the presented topic.

4   Theoretical Background

The analysis of elastically scattered X-rays is performed in the reciprocal space. The reciprocal space is defined by the transfer wave vector $\vec{q} = \vec{k}_f - \vec{k}_i$ where $\vec{k}_i$ and $\vec{k}_f$ are the wave vectors of the incoming and scattered X-ray waves, respectively (Fig. 9.1).

Generally, the amplitude $F\left(\vec{q}\right)$ of the scattered X-rays at the reciprocal point $\vec{q}$ is given by the Fourier transform of the electron density $\rho\left(\vec{r}\right)$ [1–3]:

$$F\left(\vec{q}\right) = \iiint \rho\left(\vec{r}\right) e^{-i\vec{q}\,\vec{r}} dV \tag{9.1}$$

The scattered intensity $I\left(\vec{q}\right)$ in the first Born approximation can be calculated as follows:

$$I\left(\vec{q}\right) = F\left(\vec{q}\right).F^*\left(\vec{q}\right) = \iiint \iiint \rho(\vec{r_1})\rho(\vec{r_2}) e^{-i\vec{q}\,(\vec{r_1}-\vec{r_2})} dV_1 dV_2$$
$$= \iiint \tilde{\rho}\left(\vec{r}\right) e^{-i\vec{q}\,\vec{r}} dV \tag{9.2}$$
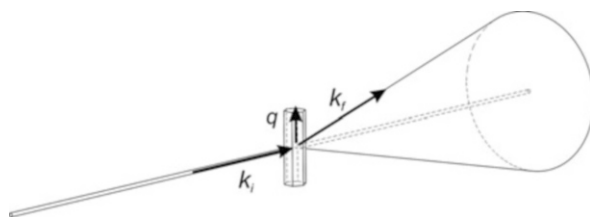
Fig. 9.1 Simplified geometry of a general SAXS experiment showing the incoming X-ray beam with the initial wave vector $\vec{k}_i$, the studied specimen having the transfer wave vector $\vec{q}$, and the scattered X-ray radiation with the final wave vector $\vec{k}_f$

This equation states that the measured intensity of the scattered X-rays in the reciprocal space is directly proportional to the Fourier transform of the electron density autocorrelation function $\tilde{\rho}(\vec{r})$ in real space. As in the following discussion, we focus on the in situ studies of the nanoparticle assemblies and growing interfaces, and we introduce simplifications of Eq. (9.2). In the case of particles or clusters, we deal with ensemble of similar scattering entities and their position correlations. For monodisperse systems it is reasonable to introduce a function $P\left(\vec{q}\right) = \left|F\left(\vec{q}\right)\right|^2$ also called form-factor function, describing the distribution of scattered X-ray intensity in the reciprocal space by a single entity of ensemble, i.e., particle or cluster. In the case of ensemble with no particle correlations, known as dilute system, the final scattered intensity is simply given by [1–3]:

$$I\left(\vec{q}\right) = NP\left(\vec{q}\right) \tag{9.3}$$

where N is the total number of scattering entities in ensemble. In the case of polydisperse particle systems, a further generalization is required that is systematically handled in the literature [1–3]. In the case of dense particle assemblies where the particle position correlations play a role, we define the pair-correlation function $g(r)$ which gives the probability of finding the neighboring particle at the distance r. For spherical particles we can simplify the observed scattered X-ray intensity to the form [1–3]

$$I(q) \approx P(q)S(q) \tag{9.4}$$

where $S(q)$ is the interference function given by the integral transformation of the pair-correlation function $g(r)$ as follows [4]:

$$S(q) = 1 + 4\pi N \int_0^\infty (g(r) - 1) \frac{\sin qr}{qr} r^2 dr \tag{9.5}$$

From the experimental point of view, the pair-correlation function of particle assembly with a low size dispersion is easily accessible if the average particle form-factor is available. In many cases the average particle form-factor can be directly measured in dilute system using Eq. (9.3). The aim of the in situ SAXS experiments is to track the changes of the particle correlations in the assembly and/or the agglomeration of individual particles into larger entities. Here, the interference function $S(q)$ gives access to the temporal changes in the particle position correlations. On the other hand, the changes in the form-factor function $P(q)$ give information on the temporal changes of the average particle shape and size. The GISAXS in situ experiments are aimed to track the evolution of the particles or clusters on a surface or buried in the subsurface region [5]. The typical GISAXS experimental geometry is shown in Fig. 9.2.

The presence of sample surface in the GISAXS measurement geometry breaks the symmetry in the reciprocal space. It is suitable to define the parallel component $q_\parallel$ of the transfer wave vector $\vec{q}$ that lies in the x-y plane and the perpendicular

Fig. 9.2 A sketch of
GISAXS measurement
geometry
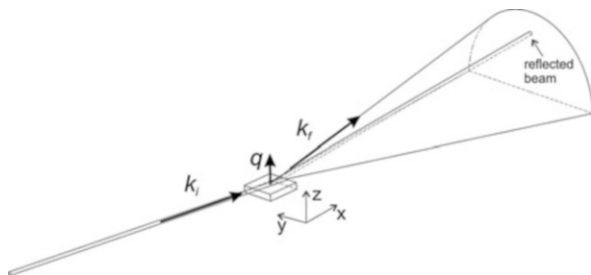
component q_z which is projection of $\vec{q}$ onto z axis in the reciprocal space. A specific
feature of GISAXS geometry is the existence of the specularly reflected X-ray beam
accompanied by the diffuse scattering originating from surface roughness and
subsurface defects. In the case of particle/cluster assembly on a surface, generally,
four scattering channels add up coherently with different phase shifts and produce
the observed scattering pattern. Moreover, a strong interplay between the X-ray
waves scattered by the particle assembly and the surface occurs at the incident and
scattered angles close to the critical angle for total external reflection from the
surface [6]. This significant enhancement of the scattered intensity at the critical
angle also known as the Yoneda peak [7] is routinely employed to increase the
sensitivity of the in situ GISAXS measurements. It is not the intention of this chapter
to explain the theoretical basis of the multiple scattering events typical for GISAXS
geometry. A detailed treatment of the X-ray scattering within the framework of the
distorted wave Born approximation (DWBA) can be found elsewhere [8–12]. Let us
just remark that the number of multiple scattering channels can be reduced and the
probing X-ray depth increased by increasing the angle of incidence above the critical
angle for total external reflection [13]. Moreover, if the scattering angles from the
particle/cluster assembly are 2–3 times larger than the critical angle, the data
evaluation using the first-order Born approximation given by the Eq. (9.2) has a
good validity. If the full DWBA theory has to be used, a large number of numerical
computer codes with graphical user interface are freely available [12, 14–17].

Another system of interest for the in situ GISAXS studies are interfaces between
two materials, e.g., in layered nanostructures. Using the in situ GISAXS, we can
elucidate the interface formation, its modification, and diffusion processes occurring
along and across the interface. The scattered X-ray intensity from a single isotropic
rough interface can be obtained by rewriting the Eq. (9.2) [6, 8, 11, 18]:

$$I\left(\vec{q}\right) \approx \int \left(e^{i|q_z|^2 C(r_{\|})} - 1\right) e^{iq_{\|}r_{\|}} dr_{\|} \qquad (9.6)$$

Here, $C(r)$ is the autocorrelation function of the interface height function $z(r)$ which
is directly accessible by surface scanning probe techniques [19–21]. The subscripts $\|$
and z refer to the parallel (in-plane) and perpendicular (out-of-plane) components,
respectively, of the real and reciprocal space vectors (Fig. 9.2). In the case of small

surface roughness defined by the condition $|q_z|^2 C(r_\parallel) \ll 1$, the Eq. (9.6) can be further simplified and reads

$$I\left(\vec{q}\right) \approx \int C(r_\parallel) e^{iq_\parallel r_\parallel} dr_\parallel \qquad (9.7)$$

In this case, the scattered X-ray intensity profile along $q_\parallel$ is proportional to the power spectral density (PSD) of the interface roughness that is Fourier transform of the surface autocorrelation function $C(r)$. A direct implication of Eq. (9.7) for the in situ GISAXS experiments is the possibility to track temporal evolution of the interface PSD in the low roughness limit. The absence of the q_z component in Eq. (9.7) plays an important role in data interpretation near the Yoneda peak. Even though the existing multiple scattering channels add up with a different but constant phase shift along $q_\parallel$, the final intensity profile still can be related to the PSD of surface roughness. Moreover, utilizing a small grazing-incidence angle near to the critical angle, we can restrict the scattering volume to the subsurface region of few nanometers given by the penetration depth of the evanescent X-ray wave. This allows surface-sensitive in situ GISAXS observation of the roughness evolution during the interface growth or the etching process.

In the case of multiple interfaces, the constructive interference of all partially scattered X-ray waves by local roughness has to be taken into account. Summing up all relevant scattering terms, one can derive the following formula for the total scattered X-ray intensity [8, 11, 18]:

$$I\left(\vec{q}\right) \approx \sum_{j,k}^{N} Q_{jk} \left| T_j^i T_k^i T_j^f T_k^f \right| e^{i\left(q_{jz}z_j - q_{kz}z_k\right)} \qquad (9.8)$$

$$Q_{jk} = \frac{1}{q_{jz}q_{kz}^*} e^{-\frac{1}{2}\left(\left(\sigma_j q_{jz}\right)^2 + \left(\sigma_k q_{kz}^*\right)^2\right)} \Delta\rho_j \Delta\rho_k \int_0^\infty r J_0\left(q_\parallel r_\parallel\right) \left(e^{q_{jz}q_{kz}^* C_{jk}(r_\parallel)} - 1\right) dr \qquad (9.9)$$

The position of the j-th interface within the multilayer stack is given by z_j. The Fresnel transmission coefficients for the incident wave to reach the j-th interface and for the scattered wave to reach the detector are given by T_j^i and T_j^f, respectively. The $C_{jk}(r)$ is the generalized cross-correlation function that correlates the roughness between the j-th and k-th interfaces [8, 11, 18]. The Eq. (9.8) is summing up all the scattered X-ray waves with the respective phase shifts and transmitted amplitudes from N interfaces. Experimentally, extraction of a single interface roughness of a particular layer is difficult due to many cross-correlation terms in Eq. (9.9). Theoretical models describing the growing interface show dominance of the roughness replication at longer spatial frequencies over the shorter ones that leads to a strong attenuation of high spatial frequencies of interface roughness during the growth process and significant attenuation of $C_{jk}(r)$ cross-correlation function at small r values [20]. Therefore, even in the simplest case of interfaces with similar autocorrelation functions, the final scattered intensity along $q_\parallel$ cannot be easily related to the average PSD of the interfaces. The situation is even more complicated in the case of grazing-incidence and grazing-exit geometry. Here, a full DWBA with

multiple scattering events at critical incidence and exit angles has to be taken into account as described elsewhere [8, 11, 18]. Employing the grazing-incidence and grazing-exit geometry, we can tune the penetration depth and limit the number of interference terms in the formulas (9.8) and (9.9) [13]. In this way the in situ GISAXS can provide unique roughness information of each individual interface during the growth process.

5   Instrumentation

The small-angle X-ray scattering instrumentation can be divided into two major groups: synchrotron-based and laboratory instruments. The key difference is in the source of X-rays. The synchrotron insertion devices like wiggler and undulators produce the X-ray radiation with high brilliance and low divergence [6, 22]. High photon fluxes of the order of 10^{12} photons/s at the sample position are available, allowing in situ SAXS/GISAXS/GIWAXS experiments [23–25]. The X-ray-induced sample damage becomes a serious issue at such high photon fluxes and has to be always checked and avoided [26]. On the other hand, the limited exposure does not allow systematic studies and many times only the proof-of-principle experiments are possible. The brilliance of available tabletop X-ray sources is compared to the brilliance of insertion devices at the second-generation synchrotron facility in Fig. 9.3.

The major drawback of the laboratory SAXS/GISAXS instrumentation is low brilliance of the X-ray sources. From our experience, the flux of 10^8 photons/s at sample position is the lowest acceptable limit to perform realistic in situ SAXS/GISAXS experiments with temporal resolution of few seconds on strongly scattering systems, like metallic nanoparticles and thin metallic films. The aim of this chapter is to provide information on possible in situ SAXS/GISAXS experiments with contemporary laboratory instrumentation.

The laboratory SAXS/GISAXS system is composed of four main parts starting with an X-ray source (Fig. 9.4). The standard SAXS/GISAXS systems are operating at characteristic Cu K_α ($E(K_{\alpha 1}) = 8047$ eV) lines, but the alternatives based on lower (Cr, $E(K_{\alpha 1}) = 5414$ eV) or higher (Ga, $E(K_{\alpha 1}) = 9251$ eV) X-ray energies are also available [27–29]. The conventional water-cooled sealed-off X-ray tubes with line focus are utilized preferentially in line collimating SAXS systems based on Kratky block collimator [1]. Their low brilliance excludes application with point collimating systems. The most frequent laboratory SAXS/GISAXS systems are equipped with various micro-focusing X-ray sources. These allow a higher electron beam power load at the anode than the conventional line-focusing X-ray tubes. A low total power of the order of 50 W allows even air-cooled operation of micro-focusing X-ray sources (Incoatec). The modern micro-focusing X-ray sources coupled with the reflective X-ray optics achieve the total flux of 10^8 photons/s [30, 31]. The reflective optics is based on elliptically or parabolically shaped multilayer mirrors with laterally graded period of the Goebel type in the single- or double-bounce configuration also termed as Montel optics [32, 33]. The available collimating Montel optics with
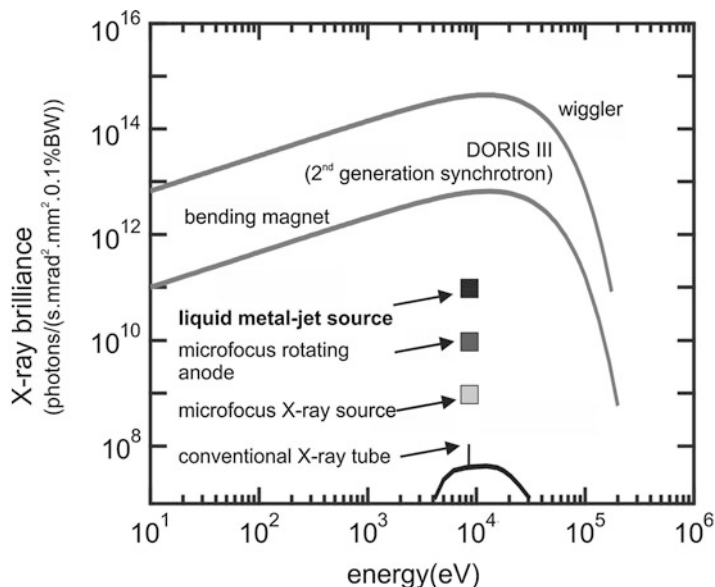
Fig. 9.3 A chart comparing the X-ray brilliance of available tabletop X-ray sources with synchrotron
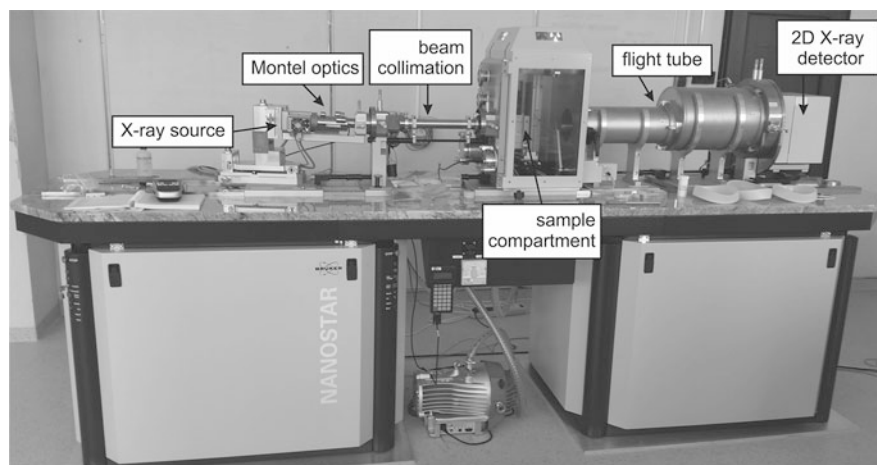
Fig. 9.4 The SAXS/GISAXS laboratory installation of NanoSTAR system (Bruker AXS) at the Institute of Physics, SAS (Slovakia)

parabolic mirrors delivers the X-ray beam of the 1 mm diameter with the angular divergence as low as 0.5 mrad. The beam size has to be further restricted by collimating slits or pinholes. The focusing Montel optics with elliptical mirrors is capable of producing focused X-ray beams with the sizes below 250 μm in diameter

(FWHM). However, the typical beam divergence of 5 mrad seriously restricts the achievable resolution in the reciprocal space. In particular cases such as the in situ studies of nanoparticle colloids with the average size below 20 nm, this kind of optics provides higher photon flux density than the parallel-beam optics [29]. The high-performance micro-focusing rotating X-ray anodes (Rigaku) and liquid-metal-jet X-ray sources (Excillum) [34–37] provide the highest X-ray brilliance for the presently available laboratory SAXS/GISAXS setups.

The second important part of each SAXS/GISAXS system is the collimator. The main role of collimator is to reduce the beam size and divergence. Moreover, it removes parasitic scattering surrounding the primary X-ray beam. The best angular resolution is achieved with the beam size matched to the point spread function of the X-ray detector and the beam divergence of the order of 0.1 mrad. These strict criteria are, however, in many cases sacrificed in order to preserve higher photon flux at the sample position. In general, the collimator unit is composed of two pinholes or motorized slits in an evacuated tube. The final divergence is given by the geometrical restraints set by the size of pinholes and their distance [38]. The primary disadvantage of the pinhole collimating units are inherently long evacuated tubes and inability to provide further monochromatization to the X-ray beam exiting Montel optics. The SAXS/GISAXS systems using vacuum collimators reach the resolution limit of approximately 200 nm in real space. Any enhancement of this number is possible only at the cost of very large and bulky installations. The conventional collimating pinholes are fabricated from polycrystalline metals like Pt, Ir, or W. The side effect of pinhole collimators based on polycrystalline metals is a strong small-angle parasitic scattering that is usually suppressed by a third dedicated anti-scatter pinhole placed directly in front of the measured sample [39]. The latest advances in collimating pinhole research allowed fabrication of scatterless slits with a very low parasitic scattering made of single crystal Si or Ge [40]. Hence, the modern SAXS/GISAXS systems based on single crystal pinhole collimator do not require the third anti-scatter pinhole anymore. The high-performance SAXS/GISAXS systems based on the liquid-metal-jet anode X-ray generator and vacuum collimator equipped with single crystal pinholes reach the total flux of 10^8 photons/s at the sample position.

An alternative approach in the design of beam collimation system is the use of compressing X-ray diffractive optics [41, 42]. In contrary to the pinhole or slit collimation systems, where the spatial filtering is employed to reduce the size and divergence of incoming beam (Fig. 9.5a), the diffraction collimator uses two successive X-ray diffractions to compress the beam size, one of them at least being asymmetric (Fig. 9.5b). Monolithic channel-cut design is used to guarantee mechanical and thermal stability. Compression ratio up to 20 times can be achieved by sophisticated design. The two X-ray diffractions eliminate inherently the parasitic scattering from the Montel multilayer optics and provide a high-quality primary beam for the SAXS/GISAXS experiments. The added value of the channel-cut collimation is monochromatization depending on the X-ray diffraction used. For example, the channel-cut compressor based on Ge 220 diffraction provides a clean $K_{\alpha 1}$ X-ray line at the exit. Utilizing Ge 111 diffraction with larger intrinsic integral
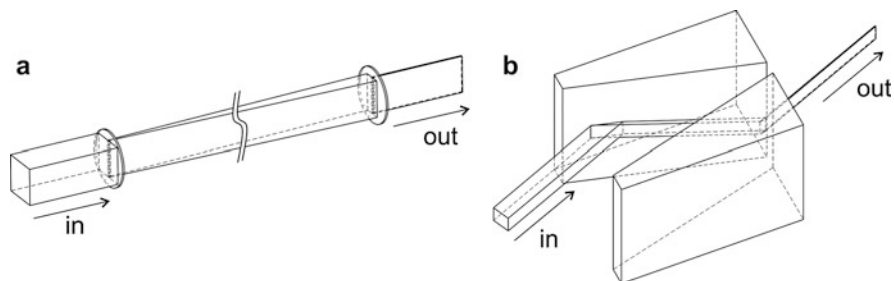
Fig. 9.5 Collimator setups: (**a**) slit collimation based on spatial filtering, (**b**) crystal collimation based on the asymmetric X-ray diffraction

intensity improves the throughput but worsens the spectral purity as the characteristic X-ray lines $K_{\alpha1}$ and $K_{\alpha2}$ are not separated completely and $K_{\alpha2}$ leak is present after the channel-cut compressor tuned at $K_{\alpha1}$. For the GISAXS experiments, the one-dimensional compression is fully sufficient as the angular sample acceptance in the perpendicular plane is inherently strongly limited at small incidence angles typical in the grazing-incidence geometry. The laboratory SAXS/GISAXS system equipped with an asymmetric channel-cut collimator can reach the resolution of 500 nm in real space at the 2.5 m overall instrumental length [42]. Such a space-saving setup is another advantage of the channel-cut compressors comparing to the long-slit or pinhole collimation systems.

The third basic part of each SAXS/GISAXS system is the evacuated experimental chamber. It usually accommodates a sample alignment positioner composed of linear and rotation stages. Recently, the hexapod positioning unit with six degrees of freedom has become popular for the sample alignment due to its compact dimensions compared to conventional sample positioners (Fig. 9.6). The experimental chamber for in situ SAXS/GISAXS studies has usually enough room for various testing units including tensile stage for stress–strain measurement, humidity chamber, heating and cooling plates, and similar. The standards for absolute calibration of the reciprocal space and intensity should be implemented in the experimental chamber as well. An independent evacuation option for the collimator and flight tubes should enable SAXS/GISAXS measurements in ambient air conditions.

The flight tube connects the experimental chamber and a two-dimensional (2D) X-ray detector – the last basic part of the SAXS/GISAXS system. The length of the flight tube together with the beam size, beam divergence, and point spread function of the 2D detector defines the achievable resolution in the reciprocal space. In front of the 2D detector, two movable beamstops are located – one for the primary beam and the other one for the specularly reflected beam in the case of GISAXS measurement. The beamstops protect the 2D detector against the damage coming from the high-intensity primary and reflected beams and allow prolonged exposure without overflow of A/D converters. Traditional 2D X-ray detectors for the SAXS/GISAXS measurements are imaging plates, multiwire gas detectors, and
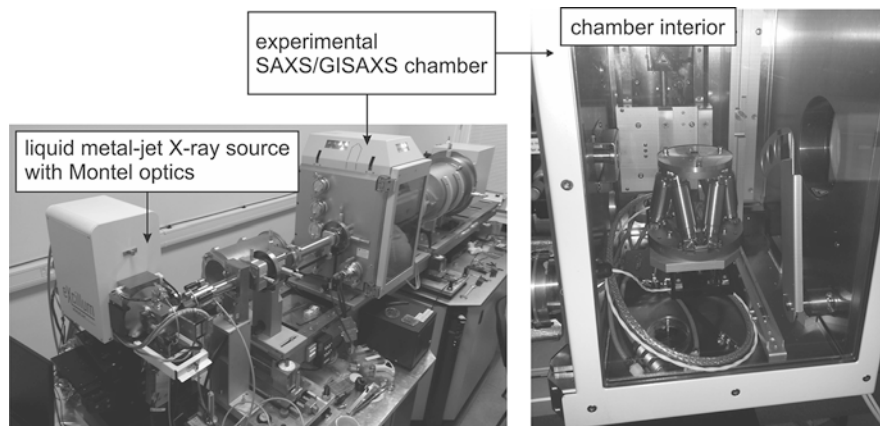
Fig. 9.6 The high-performance laboratory SAXS/GISAXS system equipped with 250 W liquid-metal-jet X-ray source (Excillum). The experimental vacuum chamber uses a hexapod to align the sample in the X-ray beam. Installation at the Institute of Physics, SAS (Slovakia)

scintillators coupled to CCD or CMOS cameras [38]. The imaging plates are not suitable for the in situ operation due to a long readout time. The multiwire or multistrip gas detectors filled with Xe gas are suitable for lower intensities as their global counting rate is typically 10^6 photons/s which is a serious limitation especially for the time-resolved GISAXS studies. Here, the scintillators coupled to CCD or CMOS detectors are the most suitable with the limitations imposed only by the background noise and the usual 16-bit dynamic range. Recently, the PILATUS series detectors with directly coupled CMOS to biased Si chips have proved to be useful for in situ operation due a fast readout time in milliseconds and adjustable zero background operation [43–45]. For GISAXS measurements, the detector should be mounted on a translation stage as there is no relevant information below the sample horizon (see Fig. 9.2). The SAXS/GISAXS systems may be complemented by synchronized detectors for diffraction (WAXS) placed directly behind the sample stage [23].

For some applications of the SAXS/GISAXS technique, the nature of the sample requires a special design of the setup. The first example is the in situ GISAXS monitoring of the thin-film growth in a dual ion-beam sputtering chamber shown in Fig. 9.7.

Here, a micro-focusing X-ray source (Incoatec, 30 W IμS source) is attached to the frame of the deposition vacuum chamber and precisely aligned using a heavy-duty hexapod positioner. The chamber is equipped with UHV compatible Be entry and exit windows for the X-rays. The anti-scatter pinhole is mounted on a three-axis vacuum manipulator placed directly in the vacuum chamber. The elliptical Montel optics with the focus located on the sample is utilized in order to maximize the scattered X-ray intensity. The angle of incidence and the sample position can be finely adjusted by the vacuum manipulator with three degrees of freedom. The scattered X-rays are recorded by a 2D PILATUS 200 K detector mounted directly
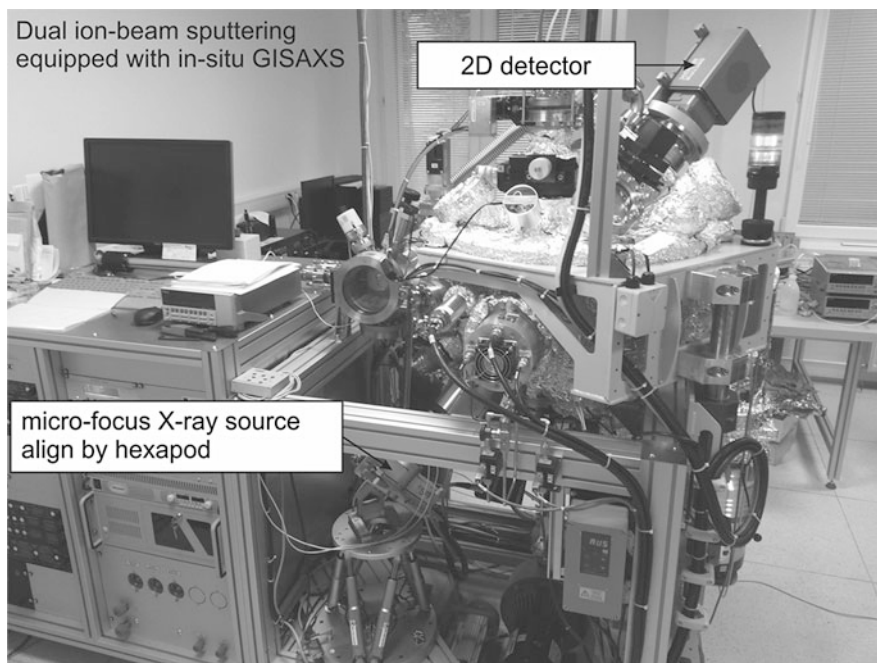
Fig. 9.7 Installation of in situ GISAXS solution attached to dual ion-beam sputtering equipment at the Institute of Physics, SAS (Slovakia)

on the vacuum flange. This system allows the monitoring of the thin-film growth on the time scale of a few seconds for taking one GISAXS pattern. The acquired GISAXS patterns provide information on the evolution of interface roughness, while the thickness information is monitored simultaneously by the in situ spectroscopic ellipsometry.

Another custom-designed solution is the adaption of GISAXS measurement geometry to studies of nanomaterials confined to the air/water interface. In particular, the self-assembled mono- and multilayer arrays of metallic and metal-oxide nanoparticles at the air/water interface are attractive templates for many applications [46]. Figure 9.8 shows a laboratory GISAXS setup with a Langmuir trough with high compression ratio [47].

Precise adjustment of the incidence angle is provided by robust translation and rotation stages holding a micro-focusing X-ray source (Incoatec, 30 W IµS source). The X-rays scattered from the air/water interfaces are passing inside an evacuated flight tube and are detected by a PILATUS 100 K detector. The GISAXS data are correlated with the other in situ techniques including spectroscopic reflectometry, surface tension measurement, and optical microscopy installed at a common workbench.
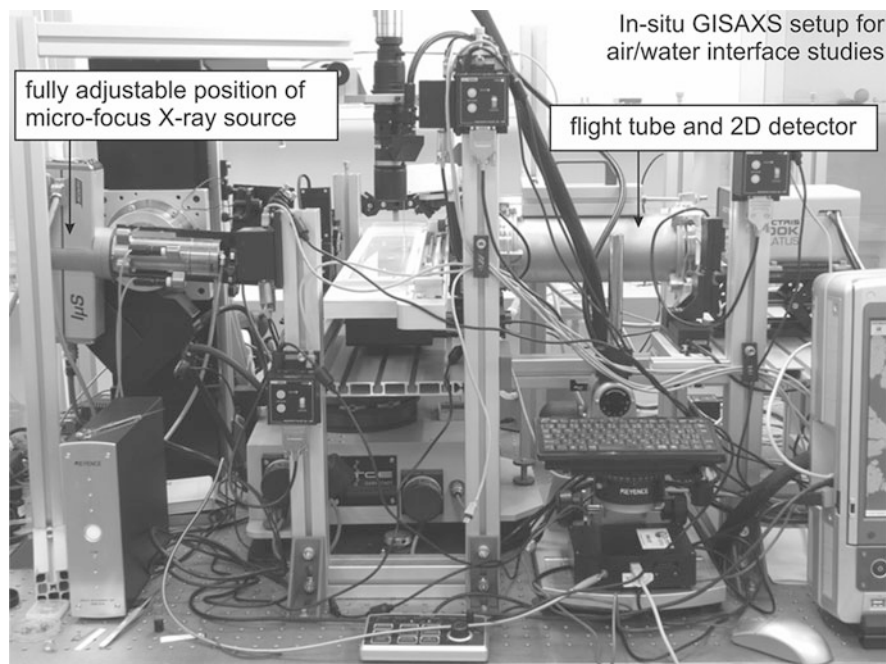
Fig. 9.8 Installation of in situ GISAXS for liquid interface studies at the Institute of Physics, SAS (Slovakia)

6 Some Topical Applications

6.1 Time-Resolved Studies of Nanoparticle Self-Assembly

The metallic, metal-oxide, and oxide nanoparticles have been studied intensively for many applications [48–53]. In particular, their ability to spontaneously order called self-assembly opens new possibilities for a simple and effective *bottom-up* approach to formation large ordered templates of macroscopic dimensions. The self-assembled nanoparticle arrays find applications in gas sensors [54], strain gauges [55, 56], surface-enhanced Raman probes [57, 58], calibration standards, and future electronic and spintronic devices. In the following section, we will illustrate how the time-resolved in situ GISAXS technique helps to clarify physical and chemical processes behind the nanoparticle self-assembly [47].

The first example documents the self-assembly of colloidal iron oxide nanoparticles. These nanoparticles with low size dispersion less than 10 % are easily produced as colloidal solutions in large quantities by wet chemical synthesis methods [59]. The iron oxide nanoparticles are synthesized as the core–shell particles with a crystalline core and a shell composed of organic molecules. The outer organic shell,
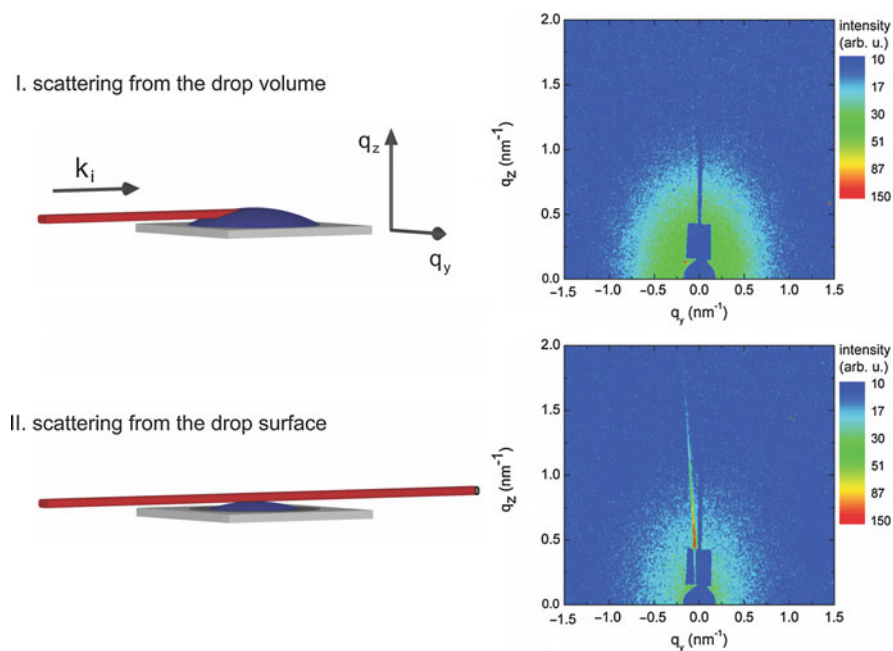
Fig. 9.9 The GISAXS measurement geometry and snapshots of the GISAXS pattern taken during evaporation of the colloidal nanoparticle drop [60]

so-called surfactant shell, prevents from the nanoparticle agglomeration. A stable nanoparticle colloidal solution can be produced in a polar or nonpolar organic solvent. A simple evaporation of the colloidal solution is known to produce the self-assembled nanoparticle mono- and multilayers depending on the nanoparticle concentration of the initial solution. A relatively long penetration depth of X-rays in common organic solvents predetermines them as a good local probe of the nanoparticle ordering. Therefore, the GISAXS technique can be used to study selectively the nanoparticle self-assembly in the volume of a colloidal drop or close to its surface. It is also possible to adjust the nanoparticle concentration to form a self-assembled monolayer as utilized in the following example of the time-resolved in situ GISAXS studies of the nanoparticle agglomeration and ordering in the drying colloidal drop [60]. The sketch of the experimental geometry along with the selected GISAXS patterns is shown in Fig. 9.9.

The probing X-ray beam was aligned to hit sample surface at the grazing-incidence angle of $0.1°$ and was subsequently translated upward in order to avoid the X-ray scattering from the sample surface. In this experimental configuration, we were able to distinguish between the nanoparticle self-assembly in the colloidal drop volume (Fig. 9.9, case I) and at the drop surface (Fig. 9.9, case II). The X-ray scattering from the drop surface was accompanied by an intense scattering streak originating from the long-range surface roughness correlations visible as a narrow streak along q_z direction in the GISAXS pattern (Fig. 9.9, case II). The GISAXS pattern was evaluated and successfully fitted with the form-factor function of a single
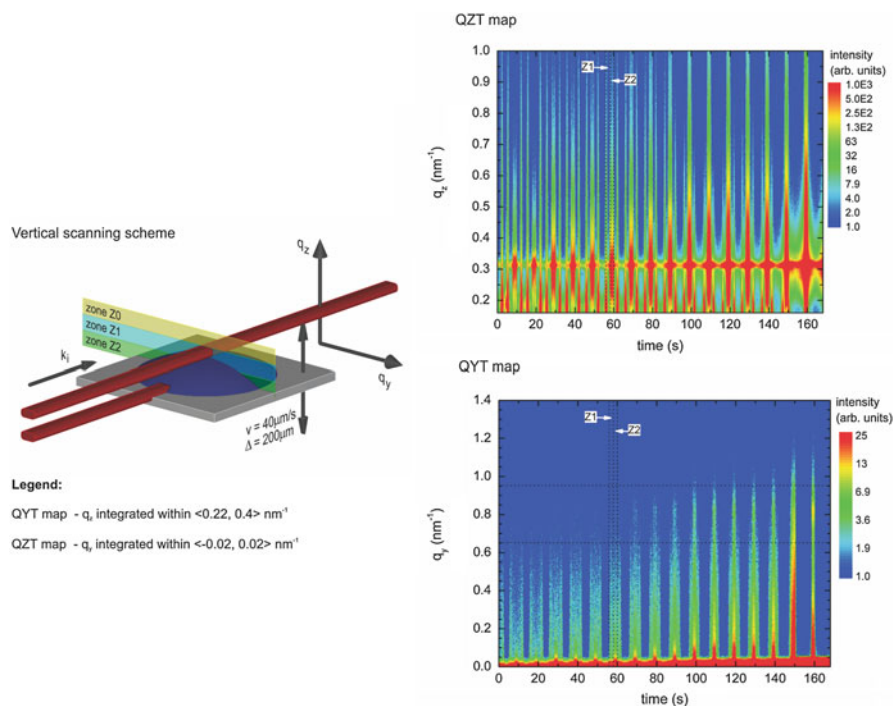
Fig. 9.10 The principle of the vertical scanning mode. The plots show temporal evolution of selected cuts of the GISAXS patterns [61]

spherical nanoparticle and a constant interference function. This means that no positive evidence of the nanoparticle self-assembly in the drop volume or close to the drop surface was found [60]. In order to identify the region of nanoparticle self-assembly in the drying colloidal nanoparticle drop, we developed a time-resolved scanning measurement mode [61]. The principle of the vertical scanning together with the reduced GISAXS reciprocal space maps is shown in Fig. 9.10.

The vertical scanning scheme is based on a fast and repeated acquisition of many GISAXS patterns during the vertical oscillation of the sample surface across the primary X-ray beam. Adjusting a suitable scanning speed and the detector acquisition time so as to avoid smearing effects, we were able to collect a large number of reciprocal space maps from different evaporation stages of the drying colloidal drop. During one oscillation loop, we were able to distinguish between three types of scattering from the drying drop that corresponded to three zones in real space labeled as Z0, Z1, and Z2 (Fig. 9.10). The experimentally relevant zones Z1 and Z2 can be assigned to the scattering from the drying drop surface and volume, respectively. The time-resolved integrated cuts in the reciprocal space along q_z and q_y directions are also shown in Fig. 9.10. Similarly to the case II in Fig. 9.9, we observe a strong scattering streak when passing from the zone Z0 to Z1, corresponding to surface scattering from the drop surface. No nanoparticle self-assembly could be identified

from the scattering data along q_y direction when the X-ray beam passed the drop surface. Similarly, the time-resolved data originating from the drop volume were fully described by a model based exclusively on the nanoparticle form-factor function. Using the additional time-resolved horizontal scanning mode, the drop contact line was finally identified as the origin of the nanoparticle self-assembly [61].

A drying colloidal drop provides the self-assembled nanoparticle monolayer over a very limited area. Large and homogenous areas of self-assembled nanoparticles can be prepared as Langmuir films at the air/water interface. Using a modified Langmuir-Schaefer deposition, such self-assembled nanoparticle layers can be reliably transferred onto an arbitrary support [47]. The time-resolved GISAXS can provide valuable data on the formation of a self-assembled nanoparticle monolayer at the air/water interface [62]. Figure 9.11 shows GISAXS patterns (i.e., reciprocal space maps) for Langmuir layer of silver nanoparticles at different surface pressures measured with a laboratory GISAXS equipment (Fig. 9.8). For low surface pressures below 16 mN/m, we observe the Bragg truncation rods [6] of self-assembled nanoparticles modulated only by the nanoparticle form-factor function. For higher surface pressures, the maximum of truncation rod intensity progressively shifts from the critical exit angle, given by the Yoneda peak position, toward the higher q_z values as can be seen in Fig. 9.11 at surface pressure of 20 mN/m. This is a clear indication of a transition from the closed nanoparticle monolayer to a bilayer that is accompanied by appearance of a new interference function along the q_z direction comprising the vertical correlation of nanoparticles in the second layer. At even higher surface pressures ($\Pi = 26$ mN/m in Fig. 9.11), the appearance of individual Bragg diffraction spots confirms the existence of the vertically correlated nanoparticle multilayer. Theoretical simulations of the intensity distributions in the reciprocal space can unambiguously determine the kind of the observed nanoparticle vertical correlations [63].

Figure 9.12 shows the calculated GISAXS reciprocal space maps for three different cases of vertically correlated nanoparticle multilayers. The stacking of nanoparticle monolayers without any lateral offsets between the two successive nanoparticle layers is shown in Fig. 9.12a. In this case the Bragg spots positioned along the Bragg truncation rods are vertically aligned with the Bragg spots located along q_z direction at $q_y = 0$ also termed as the detector scan direction. In the case of ABAB stacking, the Bragg maxima along the Bragg truncation rods are vertically offset with respect to the Bragg maxima along the detector scan as can be seen in Fig. 9.12b. The last case shown in Fig. 9.12c is the reciprocal space map of the vertically uncorrelated nanoparticle multilayer. Here, the intensity along the Bragg truncation rods is smeared which indicates a constant interference function along the q_z direction.

In the following we will describe in more detail the temporal evolution of the changes in reciprocal space during a continuous compression of the nanoparticle film at the air/water interface employing the high acquisition rate of modern PILATUS detectors [62]. Knowing the speed of barriers compressing the nanoparticle layer, the time can be recalculated to surface area of the nanoparticle layer. Figure 9.13 shows the evaluated intensity, maximum position, and width (FWHM) of the Bragg truncation rod as a function of the surface area occupied by the nanoparticle layer
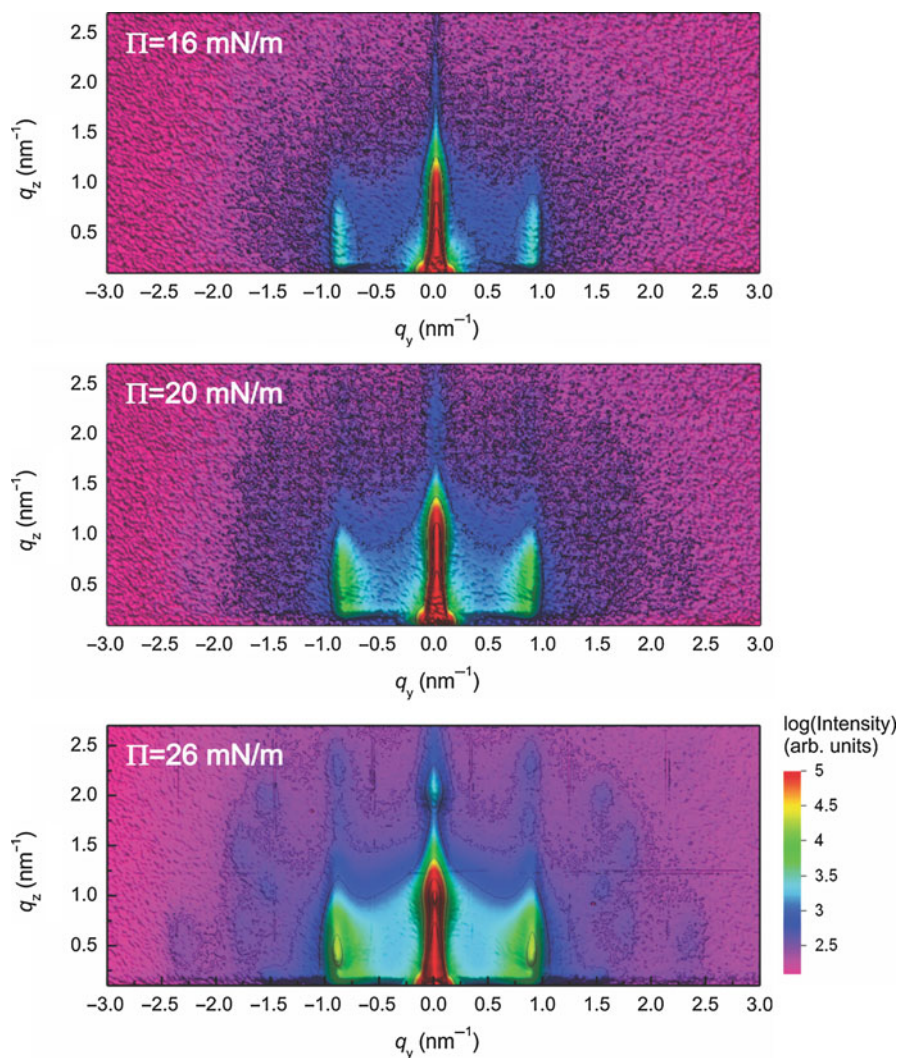
Fig. 9.11 The GISAXS reciprocal space maps of the self-assembled nanoparticle layer at the air/water interface measured at different surface pressures

during its continuous compression. During the initial compression stage, the isolated self-assembled islands of nanoparticles are merging into continuous nanoparticle monolayer. This stage is indicated by a continuous increase of the Bragg truncation rod intensity. The mean nanoparticle distance is constant at this stage. Approaching the surface pressures above 10 mN/m, we observe a slight compression of the interparticle distance. The possibility to observe directly this highly nonequilibrium transient stage in the nanoparticle self-assembly process is a unique ability of the
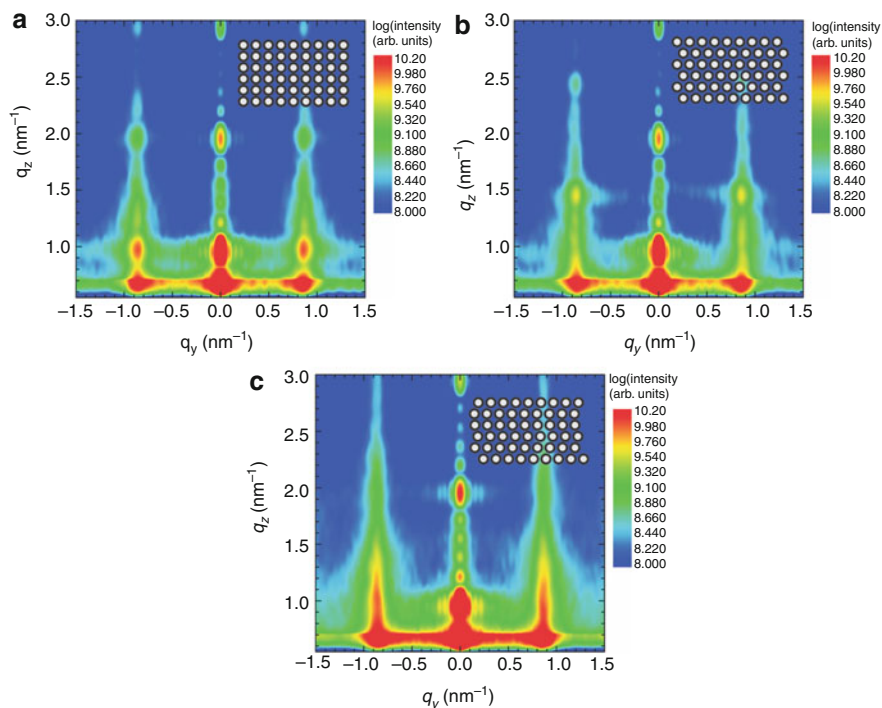
Fig. 9.12 The calculated reciprocal space maps of the nanoparticle multilayers with different vertical correlations [63]

time-resolved GISAXS measurement scheme as this transition stage would relax under the steady-state conditions. The nanoparticle monolayer collapse and formation of the second nanoparticle layer is observed as reversal in the apparent interparticle distance and changed slope in the Bragg truncation rod intensity (Fig. 9.13b). The comprehensive interpretation of the measured GISAXS data and supplementary simulations can be found elsewhere [62].

A repeated application of the Langmuir-Blodgett technique gives possibility to prepare nanoparticle multilayers with different kinds of vertical correlation between the successive monolayers as described above. In the case of vertical correlation, these ordered assemblies are nothing else than three-dimensional nanoparticle crystals in the language of crystallography. A simpler and faster method of their preparation is the solvent evaporation-driven growth from highly concentrated colloidal solutions. Here, we give example of the time-resolved GISAXS study of the kinetics of the three-dimensional nanoparticle crystal growth from a colloidal solution of silver nanoparticles dropped onto silicon substrate [64]. The time-resolved GISAXS measurements were performed at the photon energy of 12.65 keV. This energy is high enough to penetrate the drying colloidal drop and at the same time is still sufficient to provide reasonably high scattering cross section to perform time-resolved measurements with a single-frame exposure of 0.5 s. Further experimental details can be found elsewhere [64].
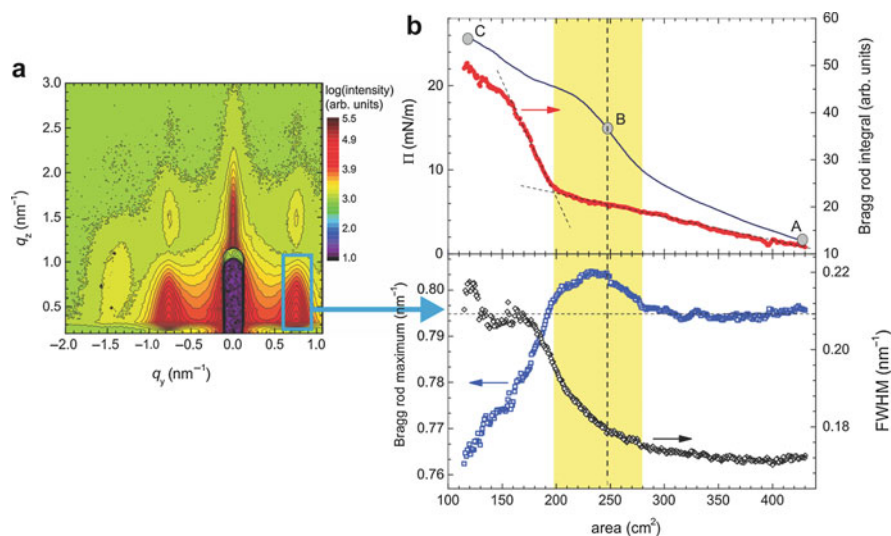
Fig. 9.13 The intensity, maximum position, and width of the Bragg truncation rod during continuous compression of the nanoparticle layer

The measured GISAXS reciprocal space map of the nanoparticle three-dimension crystal with a large number of Bragg maxima is shown in Fig. 9.14a. The measured diffraction maxima correspond to the nanoparticle crystal with the face-centered cubic (fcc) symmetry and the [111] direction oriented along the substrate normal. In the following we will focus on the temporal evolution of the Bragg diffraction maxima indexed as 111 and 222. Figure 9.14b shows the difference between the fitted widths (FWHM) of 111 and 222 Brag maxima as a function of the drying time. The colloidal nanoparticle solution was dropped in situ at time 0 s and completely dried at the times longer than 300 s. The observed colloidal crystal (i.e., before complete solvent evaporation) can be successfully described by the short-range order paracrystalline model [65] with the exception of the interval 125–155 s when a nonequilibrium transient phase with the long-range order appears. This is indicated by equal widths of 111 and 222 Bragg peaks which is in contradiction with the cumulative disorder of paracrystalline model. A systematic explanation of the observed phenomena is given in reference [64]. This in situ example also demonstrates how an adequate temporal resolution can help to reveal a short-living transient phase in the crystallization process.

The post-processing of self-assembled nanoparticle templates by annealing, etching, or overcoating by another material is important for many applications [66]. In the following two examples, we will illustrate how the in situ GISAXS can help to analyze the nanoparticle reassembly processes accompanying the UV/ozone etching used for the surfactant shell removal of self-assembled iron oxide nanoparticles. This is essential, e.g., for gas sensing applications. Figure 9.15 shows the measured GISAXS reciprocal space maps of the self-assembled iron oxide nanoparticles before and after etching in UV/ozone reactor [61].
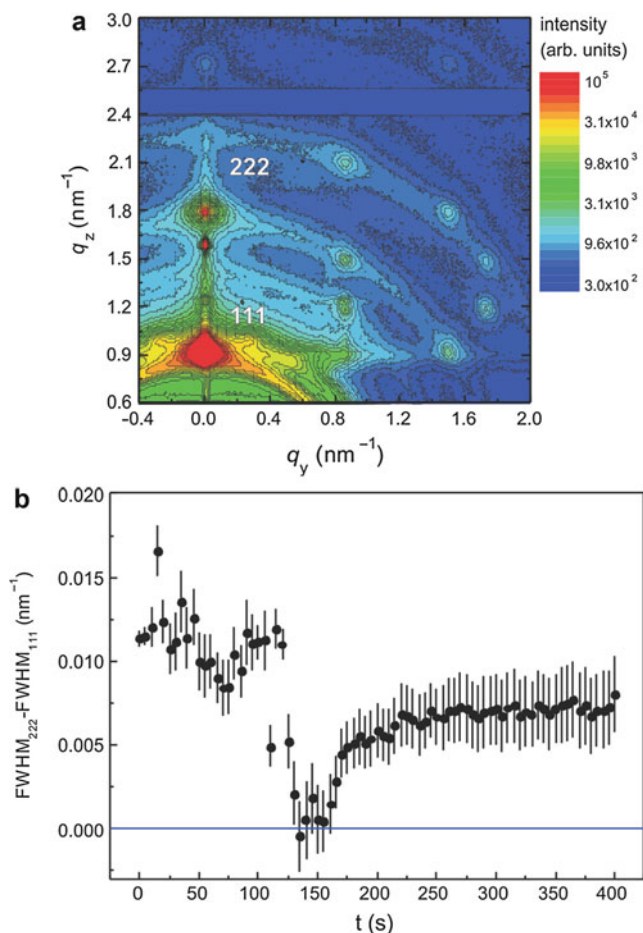
Fig. 9.14 (**a**) The measured GISAXS pattern of the three-dimensional nanoparticle crystal composed of self-assembled silver nanoparticles. (**b**) The temporal evolution of difference of the Bragg peak widths of 111 and 222 diffractions

The removal of the nanoparticle surfactant shell leads to the nanoparticle reassembly evidenced by the appearance of a new broader Bragg truncation rod at lower q_y values. The scanning electron microscope (SEM) studies revealed agglomerated nanoparticle clusters with a characteristic percolation length that corresponds to the measured Bragg truncation rod at $q_y = 0.2$ nm^{-1}. The time-resolved GISAXS provides a unique insight into the kinetics of the nanoparticle reassembly directly in the UV/ozone reactive environment. Figure 9.16a shows the temporal evolution of the integrated cuts in the reciprocal space along q_y direction at the critical exit angle.

The etching of the nanoparticle surfactant shells reduces the lateral correlation length and hence the nanoparticle short-range order as indicated by a gradual decrease of the Bragg truncation rod intensity at $q_y = 0.9$ nm^{-1}. The analysis of
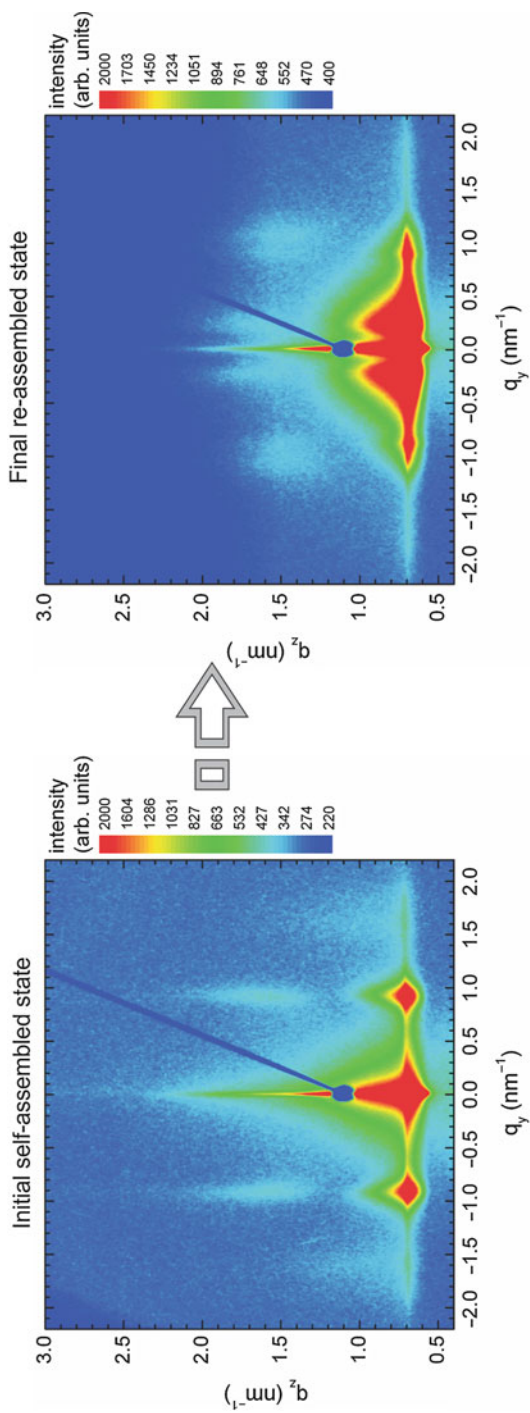
Fig. 9.15 The GISAXS patterns measured before and after exposure in UV/ozone reactor [61]
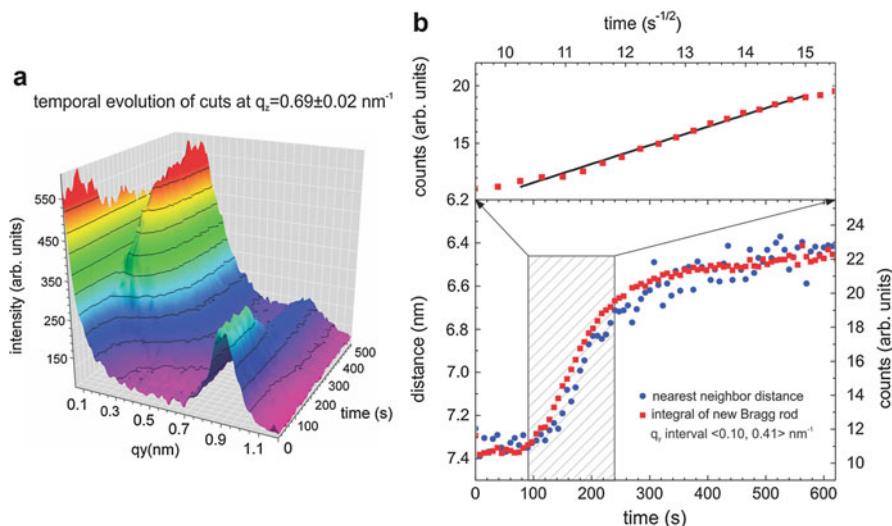
Fig. 9.16 (**a**) The temporal evolution of the reciprocal space cuts along q_y direction. (**b**) The integral intensity of the newly formed Bragg truncation rod and the interparticle distance as a function of the etching time

the GISAXS data also shows that the truncation rod shifts toward higher q_y values which indicates a shortening of the interparticle distance by 1 nm during the etching, in accord with the SEM observations of the final reassembled state [61]. The intensity increase of the newly formed Bragg truncation rod at $q_y = 0.2$ nm^{-1} follows the same kinetics as the interparticle distance reduction (Fig. 9.16b bottom) and scales linearly with the square root of time in initial stages (Fig. 9.16b top) which suggests the diffusion-like agglomeration of nanoparticles during the surfactant shell removal. The second example demonstrates how the in situ GISAXS combined with the in situ GIWAXS probes the silver nanoparticle oxidation and reassembly simultaneously during the UV/ozone etching process [61]. The GISAXS pattern cuts at the critical exit angle along the q_y direction are shown in Fig. 9.17a and b.

We distinguish here the two GISAXS regions due to considerably different length scales addressed in real space. The first one, termed as GISAXS (Fig. 9.17b), shows the initial nanoparticle correlations of the order of few nanometers. Assuming the hexagonally close-packed order of silver nanoparticles, the initial interparticle distance is estimated to be 9.4 nm. The second one, termed as HR-GISAXS (Fig. 9.17a), shows the correlations in the nanoparticle assembly of the order of hundreds of nanometers. Here, the lateral correlation length of approximately 240 nm in real space corresponds to the agglomerated clusters of silver oxide nanoparticles. The temporal evolution of pie-integrated GIWAXS patterns is shown in Fig. 9.17c. Based on the available time-resolved reciprocal space data, we can propose the following etching scenario of the silver nanoparticle monolayer. In the first phase the UV/ozone etching removes the surfactant shell of silver nanoparticles. This is observed as a steady decrease of the Bragg truncation rod
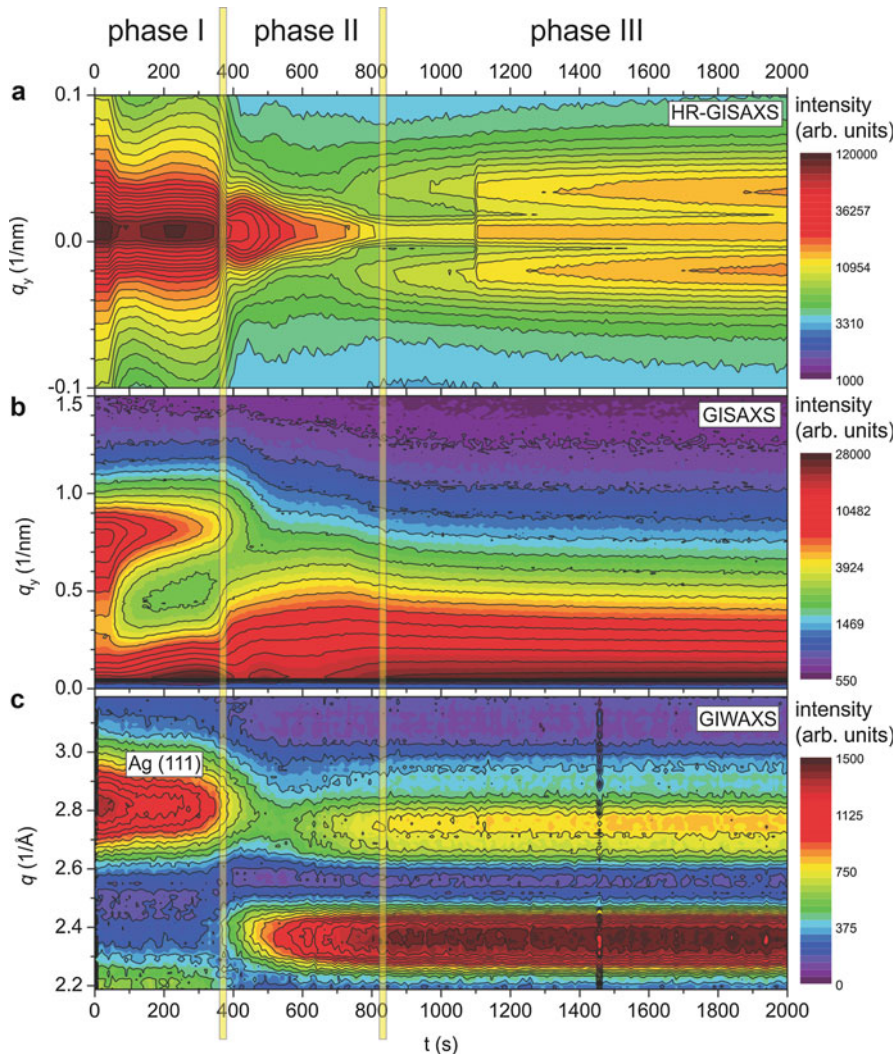
Fig. 9.17 Temporal evolution of selected cuts along q_y in the reciprocal space during the etching of silver nanoparticle monolayer at three different length scales [67]

intensity (Fig. 9.17b) which indicates extinction of the nanoparticle short-range order. The second phase is controlled by the ozone oxidation of the exposed silver nanoparticle cores. Here, Ag 111 diffraction is gradually replaced by several AgO diffraction lines. The third phase is characterized by a slowly proceeding agglomeration of the silver oxide nanoparticles into ordered clusters as indicated by the gradual formation of a new Bragg truncation rod at $q_y = 0.026$ nm^{-1} shown in Fig. 9.17c. A comprehensive data analysis supported by a simulation based on the paracrystal model is given in reference [67].

6.2   Time-Resolved Studies of Thin-Film Growth

The nucleation and growth of thin films is of utmost importance for functionality of current electronic and photonic devices. The ability of the real-time GISAXS thin-film growth monitoring opens new possibilities to tailor the final film parameters. For example, the in situ monitoring of the interface morphology of the GMR/TMR (giant and tunnel magnetoresistance) devices [68] and X-ray mirrors [69] is crucial for achieving their good performance. In this section we will demonstrate how the in situ GISAXS in laboratory conditions can probe the nucleation and growth of thin films.

The growth of thin films is conventionally divided into the three representative groups based on the balance of surface energies [20, 21, 70–74]. The Frank–van der Merwe (FM) growth model is described by continuous lateral growth of a single atomic layer on the previously closed atomic layer. The opposite case is the growth of layers in the form of islands also known as Volmer–Weber (VW) growth model. A combination of the layer-by-layer and island growth mechanisms is termed as Stranski–Krastanov (SK) growth model. Experimentally, the measured power spectra density (PSD) of surface roughness for the FM growth mode is well described by a monotonously decreasing function, whereas the PSD of surface roughness for the VW and SK growth modes has a maximum that corresponds to the lateral correlation length of the surface islands. The in situ GISAXS offers the time-resolved measurements of the surface roughness PSD as described by Eq. (9.6). The competing surface characterization techniques such as the atomic force microscopy (AFM), scanning tunneling microscopy (STM), scanning electron microscopy (SEM), high-resolution low-energy electron diffraction (HRLEED), or reflection high-energy electron diffraction (RHEED) are either too slow to follow the real-time growth process or unable to work at relatively high processing pressures typical for sputtering or chemical vapor deposition (CVD). Here, the in situ GISAXS offers an exceptional capability to track the interface morphology in the reciprocal space in real time [5, 11, 75].

The synchrotron-based in situ GISAXS monitoring of deposition process provides the highest-quality data with the millisecond time resolution [24, 75] but cannot be used for everyday needs of technology because of obvious reasons. Figure 9.18 shows the scheme of a dual ion-beam sputtering apparatus equipped with GISAXS probe and spectroscopic ellipsometry for in situ monitoring [76] that was implemented in the laboratory (Fig. 9.7).

In the first example, we present studies of the W layer growth by the ion-beam sputtering that was performed as a part of development of W/B_4C multilayer X-ray mirrors with ultrashort period. Based on the balance between the temporal resolution and the GISAXS data quality, the 8 s integration time for one GISAXS pattern was used. Assuming the W deposition rate of 0.14 Å/s, the sub-monolayer sensitivity of the real-time deposition monitoring was achieved. Figure 9.19a and b show selected GISAXS patterns of the W layer growing on the SiO$_2$ and Si substrates taken at the thicknesses of 0.5 nm, 1 nm, and 2 nm. The growth of W on SiO$_2$ follows the VW island-like growth model. This is especially well visible from the distinct side maxima at the W thicknesses of 0.5 nm and 1 nm. On the other hand, the growth of W on Si is characterized by a low surface roughness and absence of any side
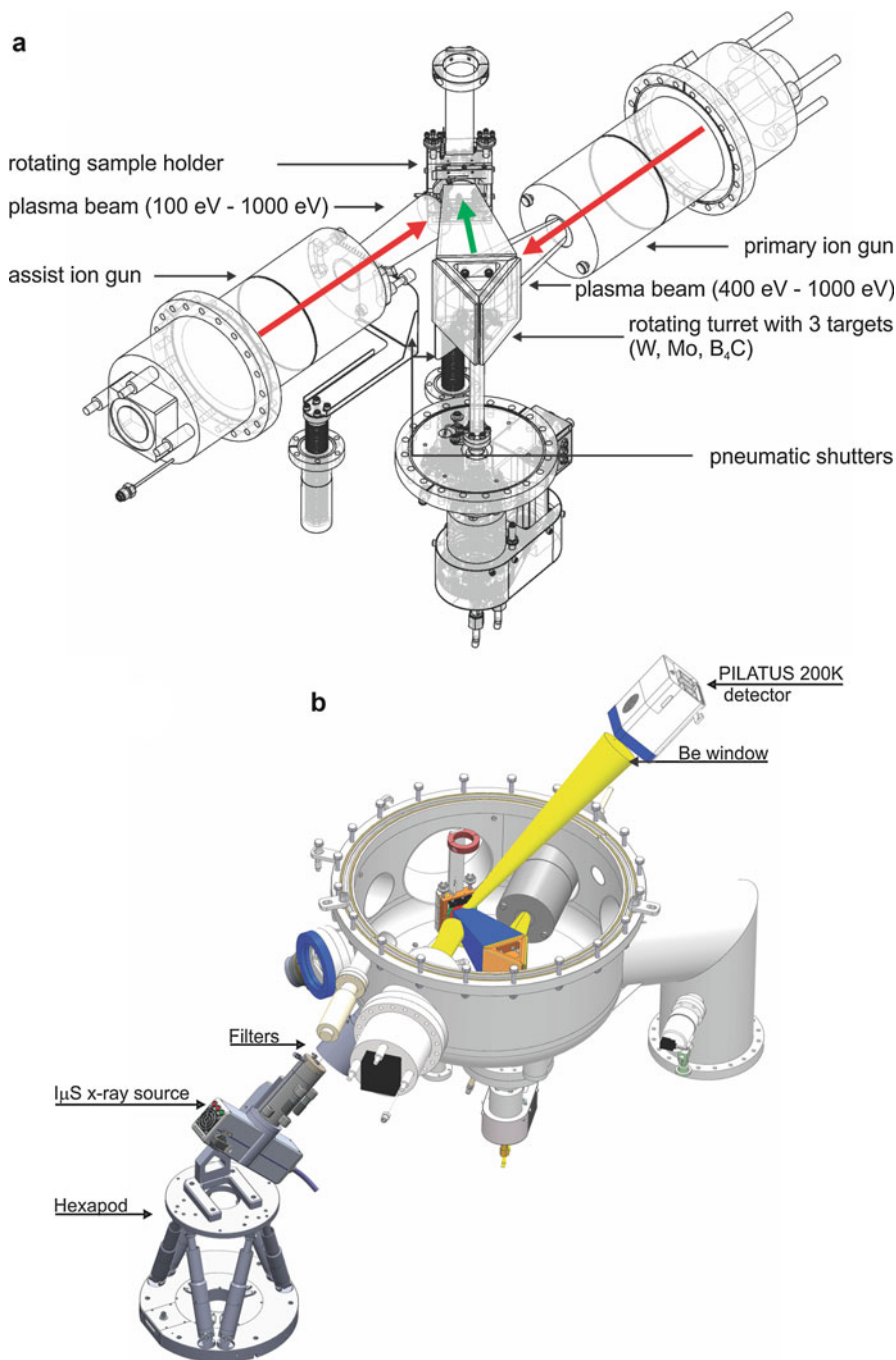
Fig. 9.18 (**a**) Geometry of a dual ion-beam sputtering equipment. (**b**) The 3D view of in situ GISAXS mounted on the sputtering chamber

maxima in the GISAXS patterns at the early stages of the layer growth that suggests applicability of the FM growth model.

The growth of the W islands and their coalescence into continuous layer can be analyzed in the reciprocal space. Figure 9.20 shows series of the reciprocal space cuts along the q_y axis at the critical exit angle as a function of the deposited average W thickness. The evolution of the side maximum position as obtained from the cut fits is shown as well. It shifts to the lower q_y values with the increasing average W thickness. This suggests that the initial small separation between the isolated W islands is steadily increasing due to the coalescence of smaller islands into larger ones [77].

In the following, we present the GISAXS measurements on periodic multilayers composed of two different materials. A simplified representation of the reciprocal space of a periodic multilayer is shown in Fig. 9.21. The most remarkable features are the Bragg points due to the multilayer periodicity surrounded by the Bragg sheets coming from resonant diffuse scattering on rough and at least partly correlated interfaces. The positions of the Bragg points are given by the Bragg equation and the intensity distribution along the Bragg sheets is given by the Eq. (9.8).

The intensity and width of the Bragg sheets along the q_z axis at the different $q_\parallel$ values are given by the number of vertically correlated interfaces at particular PSD spatial frequency. Therefore, the cross-correlation function in a multilayer stack affects any lateral cut along $q_\parallel$ in the reciprocal space, and straightforward extraction of PSD of a particular interface is impossible. Another limitation that precludes an unambiguous determination of the PSD function of a particular interface is the loss of the phase information in the GISAXS pattern. Using appropriate growth models we can, however, estimate an average PSD of interfaces in the multilayer stack [20, 79–84]. A comprehensive discussion of the problem is out of the scope of this chapter and is given elsewhere [8, 78].

An example of the GISAXS pattern of Mo/Si multilayer with a series of periodically spaced Bragg sheets is shown in Fig. 9.22a. The Bragg condition for constructive interference is not fulfilled at the grazing angle of incidence of 0.7°; hence, the Bragg sheets originate exclusively due to coherent interference of the X-rays diffusely scattered on multiple interfaces of the multilayer stack. The average thickness and rms roughness of the Mo and Si layers were determined by simulation of the X-ray reflectivity (XRR) that is shown in Fig. 9.22b. The determination of the layer thicknesses by XRR is preferred to GISAXS because of a simple simulation relying exclusively on Fresnel equations. Figure 9.22c shows the fitted width (FWHM) of the second Bragg sheet along the q_z axis as a function of q_y values. The Bragg sheet width is inversely proportional to the number of vertically correlated layers at the particular roughness spatial frequency assuming the autocorrelation functions of each contributing interfaces are similar. The intensity decay of the second Bragg sheet along the q_y values is shown in Fig. 9.22d. The plot in Fig. 9.22c shows that the number of vertically correlated interfaces N_{eff} is quite constant up to q_y values of approximately 0.2 nm^{-1}. Within this q_y range, we can assume fully correlated interfaces and estimate the autocorrelation function of an average interface. A good model for the average autocorrelation function is the one proposed by
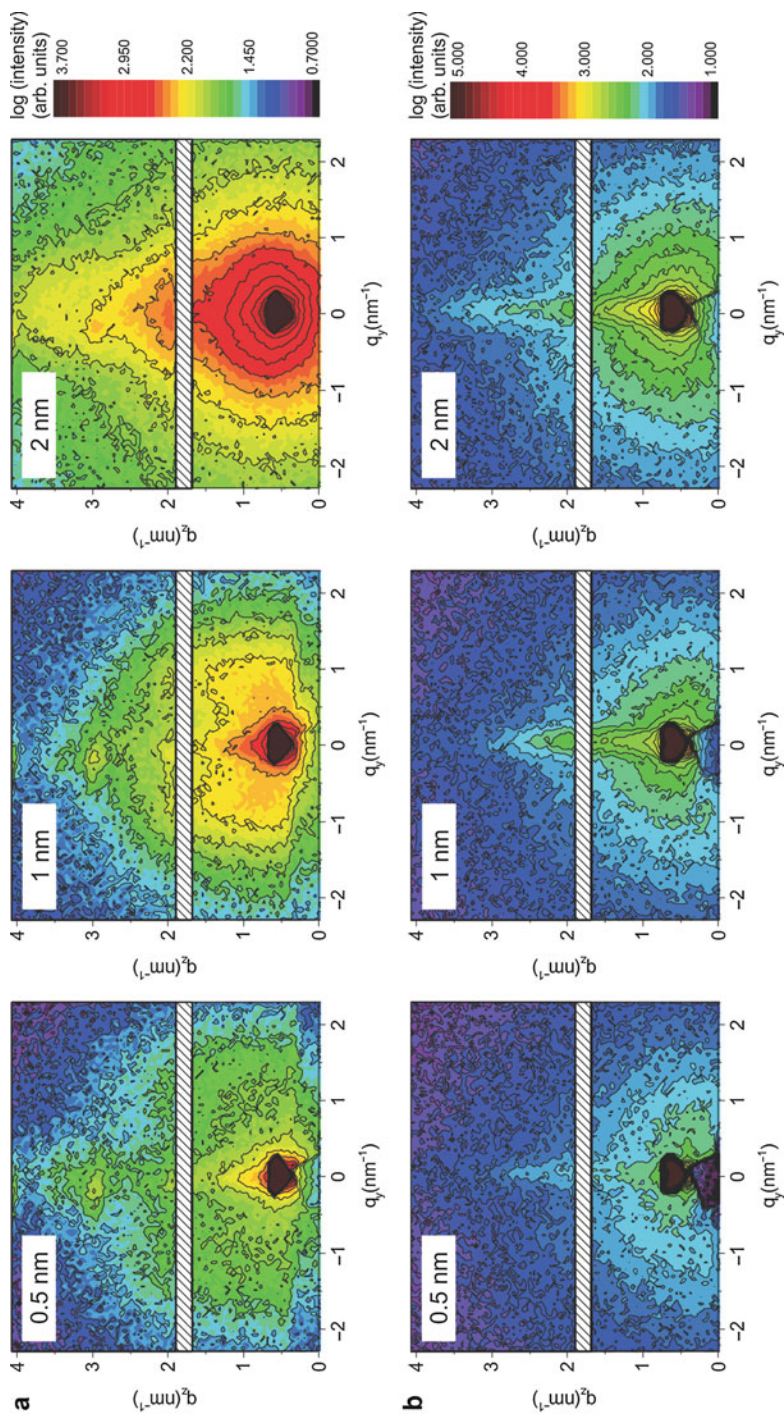
Fig. 9.19 Selected GISAXS patterns of the W layer growing on (**a**) SiO$_2$ and (**b**) Si
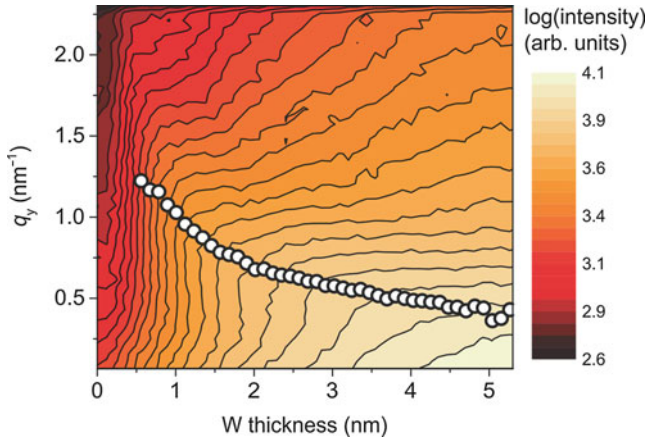
Fig. 9.20 The reciprocal space cuts at the critical exit angle as a function of the deposited W thickness. The *white dots* indicate the position of side maximum in the measured intensity profile
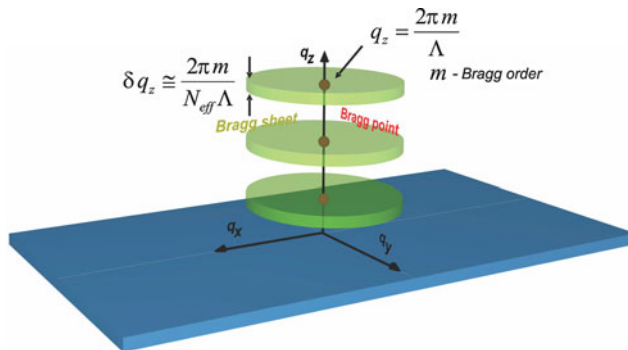
Fig. 9.21 Schematic representation of the reciprocal space for a periodic multilayer [78]

Sinha [86] having only two key parameters: the lateral correlation length ξ and the scaling parameter H (Hurst parameter). A simulation of the second Bragg sheet intensity together with the best suited parameters of the average autocorrelation function is shown in Fig. 9.22d. A more precise estimation of the average autocorrelation function using the GISAXS pattern would include an appropriate growth model like that of Edwards–Wilkinson [87] and can be found elsewhere in literature [88].

The in situ GISAXS measurement significantly simplifies the interface morphology characterization. During the growth of the multilayer stack, we can distinguish independently the contribution of each particular interface to the total scattered X-ray intensity. Moreover, adjusting the angle of incidence close or even below the critical reflection angle, we can significantly suppress the scattered X-rays originating from the already deposited layers. The observation at the critical exit
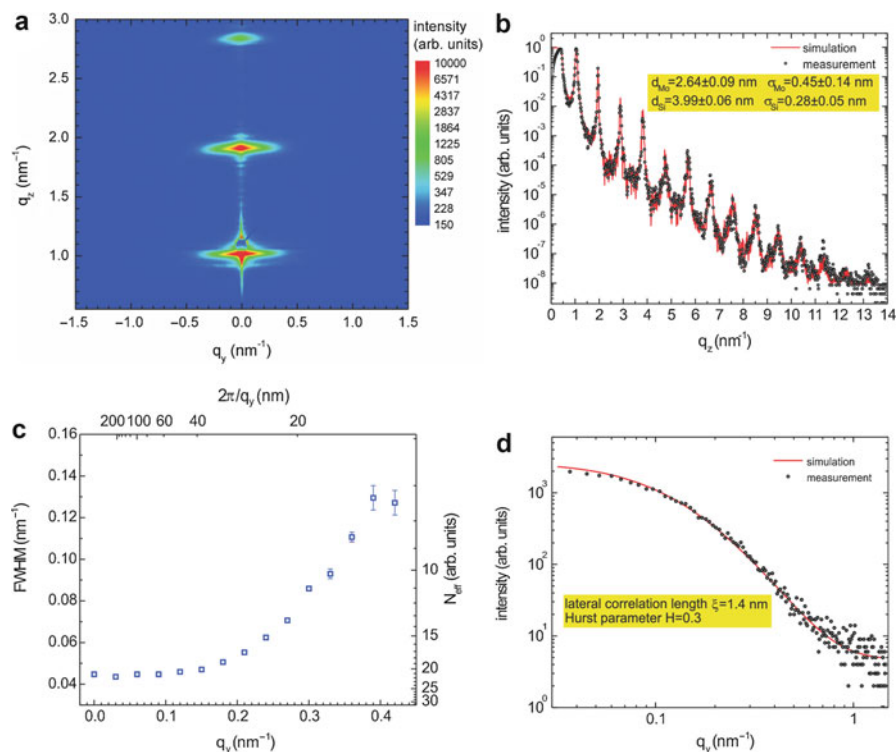
Fig. 9.22 X-ray characterization of the sputtered Mo/Si multilayer: (**a**) GISAXS pattern, (**b**) X-ray reflectivity and simulation, (**c**) measured width of the second Bragg sheet as a function of q_y, and (**d**) the intensity of the second Bragg sheet as a function of q_y [85]

angle on the other hand amplifies the scattered X-ray intensity due to the Yoneda resonance and allows short acquisition times. The impact of the multiple scattering channels on the distribution of the total scattered X-ray intensity was already discussed in the theoretical section within the DWBA approach.

The last example concerns the in situ GISAXS studies of a periodic W/B_4C multilayer growth in the dual ion-beam sputtering equipment shown in Fig. 9.18. The multilayer has nominal period thickness of 2.1 nm. Figure 9.23 shows the GISAXS data obtained during the deposition of the first 15 periods. The final GISAXS reciprocal space map after deposition of 15 periods is shown in Fig. 9.23a. The integral cuts along the q_z and q_y directions as a function of time are shown in Fig. 9.23b and c, respectively. The integrated areas are denoted by the two white boxes in Fig. 9.23a. The temporal evolution of the cuts along the q_z axis, also called detector scans, reveals 15 deposited periods that are distinguished by periodic abrupt changes in the scattered X-ray intensity when the W layers are deposited. This happens due to a much larger scattering cross section of W than B_4C. On the other hand, the accumulated phase shifts during deposition of the B_4C layers are responsible for a regular but slow intensity drifts in the reciprocal space. The appearance of Fig. 9.23b is affected also by different deposition
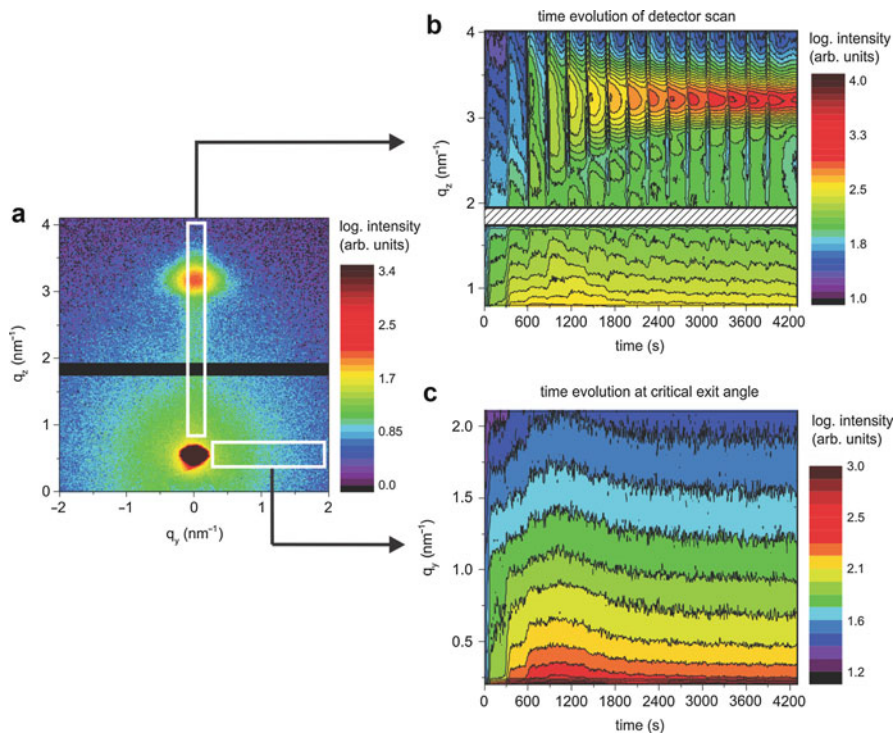
Fig. 9.23 Time-resolved reciprocal space probing by GISAXS during the growth of W/B$_4$C multilayer. (**a**) The final GISAXS reciprocal space map. (**b**) The temporal evolution of (**b**) *vertical* cuts at $q_y = 0$ nm^{-1} and (**c**) *horizontal* cuts at the critical exit angle

rates for W and B$_4$C. The deposition time of W is shorter because of a higher sputtering rate of 0.14 Å/s for W when compared to 0.06 Å/s for B$_4$C. The q_z position of the first Bragg sheet evolves during the first five periods and then stays constant, while the width of the Bragg sheets is getting narrower with the increasing number of periods, being finally restricted by a shallow probing depth of the incoming X-ray beam. This depth was adjusted by the angle of incidence of 0.2° which is below the critical angle for W reflection at the Cu K$_\alpha$ X-ray line. The most interesting information stems from the temporal evolution of the cuts along the q_y reciprocal space axis which can be identified with the shape of the integral roughness PSD function of interfaces within the probing X-ray depth (Fig. 9.23c). Here, we can notice a transient state in the scattered X-ray intensity that persists up to the deposition of approximately the first seven periods as can be seen in Fig. 9.23c. As already shown at the beginning of this section, the growth of W layer on the SiO$_2$ substrate can be described by the VW growth model. The growth of the W islands is, however, interrupted by the FM growth of the first B$_4$C layer. The second W layer cannot fully recover the VW growth due to the B$_4$C spacing layer. This situation repeats in less and less extent unless a sufficient number of periods is deposited (approximately seven in our case). Subsequently, the steady-state FM-like

growth of W and B_4C layers leads to a high-quality multilayer with low interfacial roughness. A more detailed analysis accompanied by simulations will be published elsewhere [76]. Here, it has been shown that the in situ GISAXS technique provides information on transient stages of the multilayer growth and individual roughness of each interface comparable only to ex situ transmission electron microscopy studies of the multilayer cross sections. Nevertheless, the nondestructive character and inherently statistical information provided by GISAXS are unique features of GISAXS.

7   Future Perspectives

In the previous section we demonstrated that the modern X-ray sources with photon fluxes at the level of 10^8 photons/s can be employed for the in situ time-resolved GISAXS studies of sufficiently scattering samples, typically containing metal atoms. The latest advances in the development of high-flux laboratory sources including progress in the liquid-metal-jet X-ray generators opened new possibilities to perform the time-resolved in situ studies also on weakly scattering materials such as polymers.

As an example we introduce a GISAXS/GIWAXS study of the annealing of the P3HT–PCBM (poly(3-hexylthiophene)) and ([6, 6]-phenyl-C61-butyric acid methyl ester) polymer blend used as the active layer in organic solar cells. The time-resolved GISAXS/GIWAXS studies performed on synchrotron [89, 90] were able to track the crystallization of P3HT and the formation of a percolated structure with P3HT- and PCBM-rich domains known as the bulk heterojunction (BHJ). The laboratory GISAXS/GIWAXS apparatus (Fig. 9.6) based on the liquid-metal-jet X-ray generator delivers 10^9 photons/s after collimating Montel optics. The ex situ GISAXS/GIWAXS measurements on the P3HT–PCBM films before and after thermal and solvent annealings were performed. The measured GISAXS and GIWAXS patterns are shown in Fig. 9.24a and c, respectively. The solvent and thermal annealings support phase separation and formation of BHJ with a typical distance of 30 nm between the two phases that is visible as a pronounced broad peak at approximately $0.2 \, nm^{-1}$ in GISAXS (Fig. 9.24b). The BHJ phase separation is accompanied by an increase of the P3HT crystalline phase which is evidenced by the enhanced intensity of P3HT 100 and 200 diffraction peaks (Fig. 9.24d). The 20-fold higher intensity of the liquid-metal-jet X-ray generator comparing with the conventional micro-focus X-ray tube allows GISAXS/GIWAXS time-resolved studies on the polymer thin films with the temporal resolution better than 10 s.

Resolution improvement of the laboratory SAXS/GISAXS equipments is another important development during recent years. Our studies using the channel-cut diffractive optics for the X-ray beam compression demonstrated possibility of ultracompact GISAXS setups with the resolution up to 500 nm in real space. The standard commercially available SAXS/GISAXS systems achieve maximum resolution of approximately 200 nm in real space. Using a linearly compositionally graded GeSi channel cut with the compression ratio of 21, we were able to produce the X-ray beam with the size $1.3 \times 0.2 \, mm^2$, divergence 0.5×0.07 mrad, and intensity 1×10^6 photons/s [41, 42]. For the tests of resolution, periodic ripples on
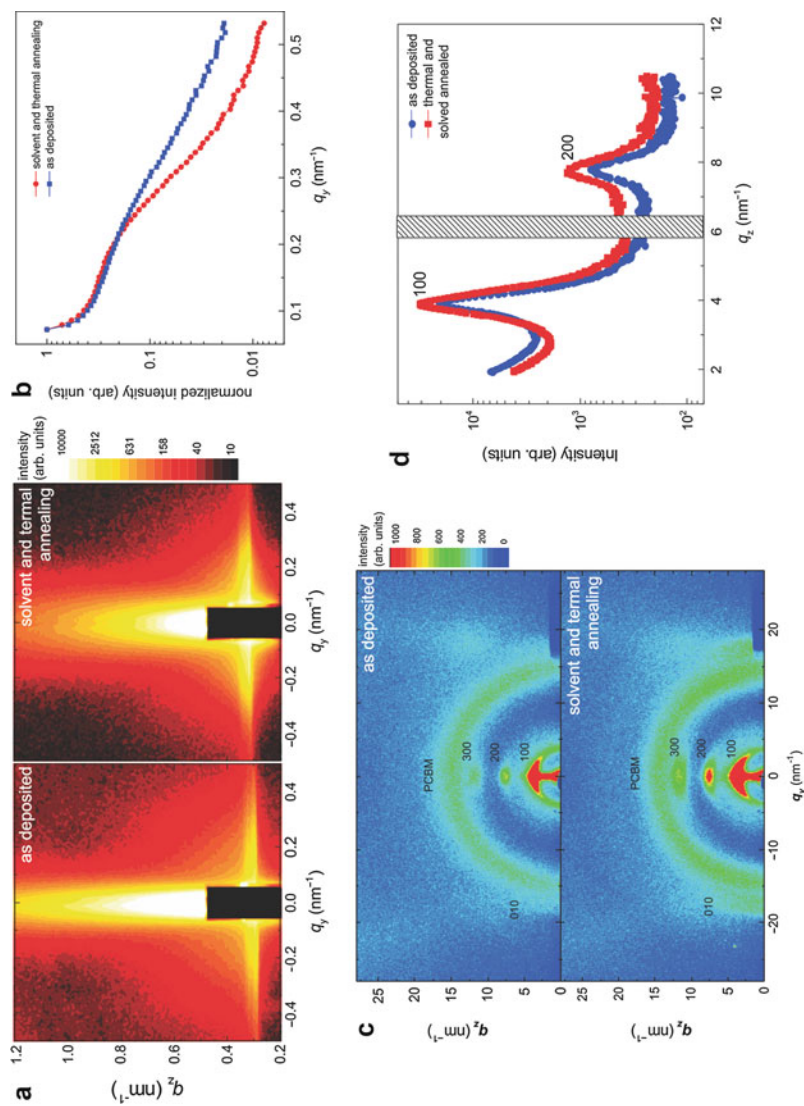
Fig. 9.24 Laboratory GISAXS/GIWAXS measurements of the P3HT–PCBM thin film before and after solvent and thermal annealings
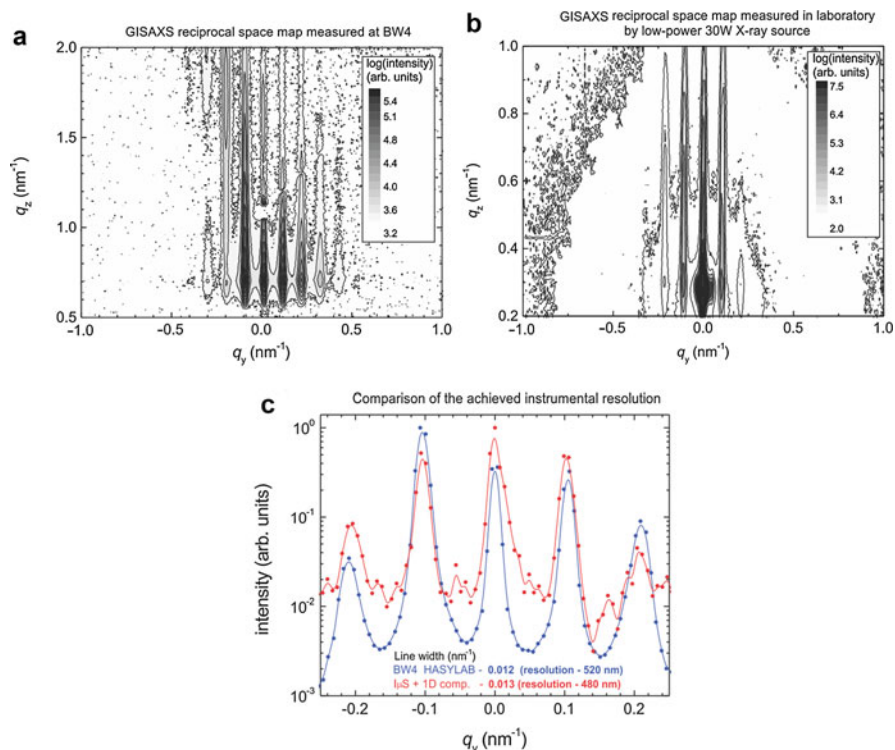
Fig. 9.25 GISAXS patterns of identical sample measured on (**a**) synchrotron and (**b**) laboratory setup. (**c**) Comparison of the reciprocal space cuts along the q_y direction

Si substrate produced by ion-beam etching [91] with a period of 60 nm were used. The GISAXS patterns measured on a synchrotron beamline and on the laboratory setup are shown in Fig. 9.25a and b, respectively.

The lower photon flux of the laboratory setup is responsible for the lower number of visible Bragg truncation rods in the GISAXS pattern when compared to the synchrotron measurement. On the other hand, the fitted width of the Bragg truncation rods is comparable to that from the synchrotron measurement. The high background of the laboratory GISAXS measurement results from air scattering as the setup was not evacuated. The synchrotron quality Montel optics coupled to the liquid-metal-jet X-ray sources (Fig. 9.6) holds promise of more than 20-fold intensity enhancement after the compression by the channel-cut optics which can open a new field for high-resolution time-resolved in situ SAXS/GISAXS laboratory measurements confined solely to synchrotrons before.

The highest brilliance laboratory X-ray sources based on the liquid metal jets are limited to few characteristic emission lines. In the following we outline a strategy toward a future laboratory high-brilliance, multiple-wavelength X-ray source capable of generating X-rays at common K lines of metals like Cu, Co, and Cr which are suitable for anomalous SAXS/GISAXS studies. These experiments have been
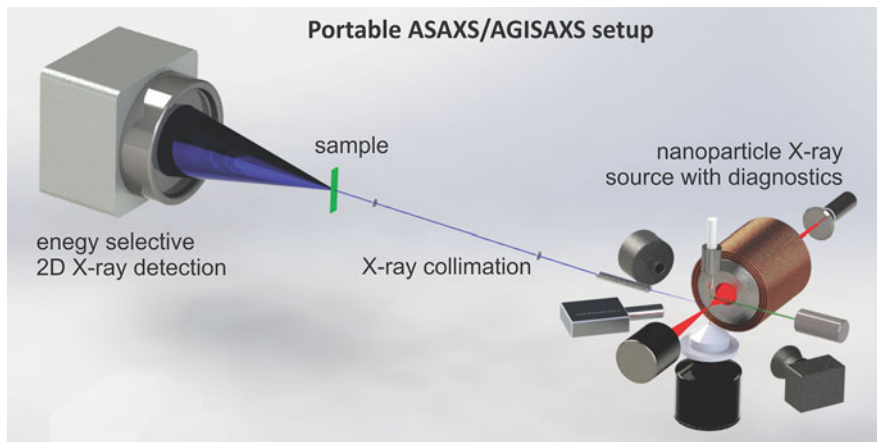
Fig. 9.26 Sketch of a nanoparticle-powered, dual-wavelength X-ray source

widely employed at synchrotron beamlines by tuning the X-ray radiation close to the absorption edges of specific elements. The anode of the new laboratory X-ray source will be based on a liquid jet of colloidal metallic nanoparticles. A highly concentrated dispersion of colloidal nanoparticles is injected into a focused electron beam. If required, an infrared laser will be used to evaporate the nanoparticle-supporting solvent. Using different kinds of the nanoparticles, we can effectively tune the X-ray wavelength emission. Moreover, a mixture of two or more kinds of nanoparticles will generate the dual- or multi-wavelength X-ray emission. The point-like, micrometer-size X-ray source can be simply collimated or focused using two-dimensional hybrid Montel X-ray optics. The breaking nature of this nanoparticle X-ray source is the ability to emit continuously X-ray radiation at two or more characteristic energies at the same time. Such a laboratory source for the anomalous SAXS/GISAXS measurements is schematically shown in Fig. 9.26.

Large changes of the atomic scattering factor at the absorption edges of chemical elements are used to enhance the scattering signal from particular atoms and/or clusters and provide additional chemical sensitivity to the SAXS/GISAXS techniques. The energy-selective, two-dimensional solid-state detector will be used to measure simultaneously scattering patterns at two X-ray energies. A successful implementation of this nanoparticle-powered X-ray source will enable new physics, chemistry, and biology in laboratories and will rationalize exploitation of the synchrotron and free-electron laser beamtimes.

8   Conclusions

In this chapter we have addressed various in situ time-resolved SAXS/GISAXS studies of nanomaterials including nanoparticles and thin films. At the beginning we reviewed a standard SAXS/GISAXS instrumentation and presented a wide range of

setups suitable for the time-resolved studies in laboratories. The basic theory required to understand the reciprocal space data measured by GISAXS was presented. A significant part of the chapter was devoted to various examples of the in situ nanoparticle self-assembly studies. We demonstrated how the pair-correlation function of the nanoparticle assembly can be probed in situ during various processes affecting the nanoparticle ordering. A special emphasis was given to the analyses of the X-ray scattering from surfaces and buried interfaces. The experimental data of the time-resolved in situ GISAXS study of the multilayer growth were presented and discussed. Finally, we have shown how the last generation of laboratory high-flux X-ray generators can stimulate further development of the time-resolved in situ SAXS/GISAXS studies in laboratory conditions.

References

1. Glatter O, Kratky O (1982) Small angle x-ray scattering. Academic, London/New York
2. Guinier A, Fournet G (1955) Small-angle scattering of X-rays. Wiley, New York
3. Feigin LA, Svergun DI, Taylor GW (1987) Structure analysis by small-angle X-ray and neutron scattering. Plenum Press, New York
4. Brumberger H (1995) Modern aspects of small-angle scattering. Kluwer Academic Publishers, Dordrecht/Boston
5. Renaud G, Lazzari R, Revenant C, Barbier A et al (2003) Real-time monitoring of growing nanoparticles. Science 300:1416
6. Als-Nielsen J, MacMorrow D (2011) Elements of modern X-ray physics. Wiley, Chichester
7. Yoneda Y (1963) Anomalous surface reflection of X rays. Phys Rev 131:2010
8. Holý V, Pietsch U, Baumbach T (1999) High-resolution X-ray scattering from thin films and multilayers. Springer, Berlin/New York
9. Holy V, Baumbach T (1994) Nonspecular X-ray reflection from rough multilayers. Phys Rev B 49:10668
10. Holy V, Kubena J, Ohlidal I, Lischka K et al (1993) X-ray reflection from rough layered systems. Phys Rev B 47:15896
11. Renaud G, Lazzari R, Leroy F (2009) Probing surface and interface morphology with grazing incidence small angle X-ray scattering. Surf Sci Rep 64:255
12. Lazzari R (2002) IsGISAXS: a program for grazing-incidence small-angle X-ray scattering analysis of supported islands. J Appl Crystallogr 35:406
13. Birkholz M, Fewster PF, Genzel C (2006) Thin film analysis by X-ray scattering. Wiley-VCH, Weinheim
14. http://www.bornagainproject.org/
15. http://www.pprime.fr/?q=fr/nanoparticules-nanostructures
16. Tate MP, Urade VN, Kowalski JD, Wei T-c et al (2006) Simulation and interpretation of 2D diffraction patterns from self-assembled nanostructured films at arbitrary angles of incidence: from grazing incidence (above the critical angle) to transmission perpendicular to the substrate. J Phys Chem B 110:9882
17. Chourou ST, Sarje A, Li XS, Chan ER et al (2013) HipGISAXS: a high-performance computing code for simulating grazing-incidence X-ray scattering data. J Appl Crystallogr 46:1781

18. Daillant J, Gibaud A (2009) X-ray and neutron reflectivity: principles and applications. Springer, Berlin/Heidelberg
19. Bennett JM, Mattsson L (1989) Introduction to surface roughness and scattering. Optical Society of America, Washington, DC
20. Pelliccione M, Lu TM (2008) Evolution of thin film morphology: modeling and simulations. Springer, New York/London
21. Franceschetti G, Riccio D (2007) Scattering, natural surfaces, and fractals. Elsevier Academic Press, Amsterdam/Boston
22. Onuki H, Elleaume P (2003) Undulators, wigglers, and their applications. Taylor & Francis, London/New York
23. Liu D-G, Chang C-H, Liu C-Y, Chang S-H et al (2009) A dedicated small-angle X-ray scattering beamline with a superconducting wiggler source at the NSRRC. J Synchrotron Radiat 16:97
24. Döhrmann R, Botta S, Buffet A, Santoro G et al (2013) A new highly automated sputter equipment for in situ investigation of deposition processes with synchrotron radiation. Amsterdam 84:043901
25. Santoro G, Buffet A, Döhrmann R, Yu S et al (2014) Use of intermediate focus for grazing incidence small and wide angle x-ray scattering experiments at the beamline P03 of PETRA III, DESY. Rev Sci Instrum 85:043901
26. Borsali R, Pecora R (2008) Soft-matter characterization. Springer, New York
27. Zschornack G (2006) Handbook of X-ray data. Springer, New York
28. Otendal M, Tuohimaa T, Vogt U, Hertz HM (2008) A 9 keV electron-impact liquid-gallium-jet x-ray source. Rev Sci Instrum 79:016102
29. Siffalovic P, Vegso K, Jergel M, Majkova E et al (2010) Measurement of nanopatterned surfaces by real and reciprocal space techniques. Meas Sci Rev 10:153
30. Michaelsen C, Wiesmann J, Hoffmann C, Wulf K et al (2002) Recent developments of multilayer mirror optics for laboratory x-ray instrumentation. X-Ray Mirrors, Crystals, and Multilayers Ii 4782:143
31. Wiesmann J, Graf J, Hoffmann C, Hembd A et al (2009) X-ray diffractometry with low power microfocus sources – new possibilities in the lab. Part Part Syst Charact 26:112
32. Michaelsen C, Wiesmann J, Hoffmann C, Oehr A et al (2003) Optimized performance of graded multilayer optics for X-ray single crystal diffraction. Advances in Mirror Technology for X-Ray, Euv Lithography, Laser, and Other Applications 5193:211
33. Hertlein F, Oehr A, Hoffmann C, Michaelsen C et al (2006) State-of-the-art of multilayer optics for laboratory X-ray devices. Part Part Syst Charact 22:378
34. Hemberg O, Otendal M, Hertz HM (2003) Liquid-metal-jet anode electron-impact x-ray source. Appl Phys Lett 83:1483
35. Hemberg O, Otendal M, Hertz HM (2004) Liquid-metal-jet anode X-ray tube. Opt Eng 43:1682
36. De Caro L, Altamura D, Vittoria FA, Carbone G et al (2012) A superbright X-ray laboratory microsource empowered by a novel restoration algorithm. J Appl Crystallogr 45:1228
37. De Caro L, Altamura D, Sibillano T, Siliqi D et al (2013) Rat-tail tendon fiber SAXS high-order diffraction peaks recovered by a superbright laboratory source and a novel restoration algorithm. J Appl Crystallogr 46:672
38. He BB (2009) Two-dimensional x-ray diffraction. Wiley, Hoboken
39. Wignall GD, Lin JS, Spooner S (1990) Reduction of parasitic scattering in small-angle X-ray scattering by a three-pinhole collimating system. J Appl Crystallogr 23:241
40. Li Y, Beck R, Huang T, Choi MC et al (2008) Scatterless hybrid metal-single-crystal slit for small-angle X-ray scattering and high-resolution X-ray diffraction. J Appl Crystallogr 41:1134
41. Korytar D, Vagovic P, Vegso K, Siffalovic P et al (2013) Potential use of V-channel Ge(220) monochromators in X-ray metrology and imaging. J Appl Crystallogr 46:945
42. Jergel M, Siffalovic P, Vegso K, Majkova E et al (2013) Extreme X-ray beam compression for a high-resolution table-top grazing-incidence small-angle X-ray scattering setup. J Appl Crystallogr 46:1544

43. Schlepütz CM, Herger R, Willmott PR, Patterson BD et al (2005) Improved data acquisition in grazing-incidence X-ray scattering experiments using a pixel detector. Acta Crystallogr Sect A Found Crystallogr 61:418

44. Kraft P, Bergamaschi A, Broennimann C, Dinapoli R et al (2009) Performance of single-photon-counting PILATUS detector modules. J Synchrotron Radiat 16:368

45. Wernecke J, Gollwitzer C, Muller P, Krumrey M (2014) Characterization of an in-vacuum PILATUS 1M detector. J Synchrotron Radiat 21:529

46. Chitu L, Siffalovic P, Majkova E, Jergel M et al (2010) Modified Langmuir-Blodgett deposition of nanoparticles – measurement of 2D to 3D ordered arrays. Meas Sci Rev 10:162

47. Siffalovic P, Majkova E, Jergel M, Vegso K et al (2012) Self-assembly of nanoparticles at solid and liquid surfaces. In: Hashim A (ed) Smart nanoparticles technology. INTECH, Rijeka, pp 441–466

48. Sun SH, Murray CB, Weller D, Folks L et al (2000) Monodisperse FePt nanoparticles and ferromagnetic FePt nanocrystal superlattices. Science 287:1989

49. Bigioni TP, Lin XM, Nguyen TT, Corwin EI et al (2006) Kinetically driven self assembly of highly ordered nanoparticle monolayers. Nat Mater 5:265

50. Shevchenko EV, Talapin DV, Kotov NA, O'Brien S et al (2006) Structural diversity in binary nanoparticle superlattices. Nature 439:55

51. Talapin DV, Shevchenko EV, Bodnarchuk MI, Ye X et al (2009) Quasicrystalline order in self-assembled binary nanoparticle superlattices. Nature 461:964

52. Fan JA, Wu C, Bao K, Bao J et al (2010) Self-assembled plasmonic nanoparticle clusters. Science 328:1135

53. Macfarlane RJ, Lee B, Jones MR, Harris N et al (2011) Nanoparticle superlattice engineering with DNA. Science 334:204

54. Luby S, Chitu L, Jergel M, Majkova E et al (2012) Oxide nanoparticle arrays for sensors of CO and NO2 gases. Vacuum 86:590

55. Herrmann J, Müller KH, Reda T, Baxter GR et al (2007) Nanoparticle films as sensitive strain gauges. Appl Phys Lett 91:183105

56. Siffalovic P, Chitu L, Vegso K, Majkova E et al (2010) Towards strain gauges based on a self-assembled nanoparticle monolayer-SAXS study. Nanotechnology 21:385702

57. Nie S, Emory SR (1997) Probing single molecules and single nanoparticles by surface-enhanced Raman scattering. Science 275:1102

58. Santoro G, Yu S, Schwartzkopf M, Zhang P et al (2014) Silver substrates for surface enhanced Raman scattering: correlation between nanostructure and Raman scattering enhancement. Appl Phys Lett 104:243107

59. Capek I (2004) Preparation of metal nanoparticles in water-in-oil (w/o) microemulsions. Adv Colloid Interface Sci 110:49

60. Siffalovic P, Majkova E, Chitu L, Jergel M et al (2007) Self-assembly of iron oxide nanoparticles studied by time-resolved grazing-incidence small-angle x-ray scattering. Phys Rev B 76:195432

61. Siffalovic P, Majkova E, Chitu L, Jergel M et al (2008) Real-time tracking of superparamagnetic nanoparticle self-assembly. Small 4:2222

62. Vegso K, Siffalovic P, Majkova E, Jergel M et al (2012) Nonequilibrium phases of nanoparticle Langmuir films. Langmuir 28:10409

63. Vegso K, Siffalovic P, Benkovicova M, Jergel M et al (2012) GISAXS analysis of 3D nanoparticle assemblies-effect of vertical nanoparticle ordering. Nanotechnology 23:045704

64. Vegso K, Siffalovic P, Jergel M, Weis M et al (2014) A non-equilibrium transient phase revealed by in situ GISAXS tracking of the solvent-assisted nanoparticle self-assembly. J Nanopart Res 16:2536

65. Eads JL, Millane RP (2001) Diffraction by the ideal paracrystal. Acta Crystallogr A 57:507

66. Capone S, Manera MG, Taurino A, Siciliano P et al (2014) Fe3O4/γ-Fe2O3 nanoparticle multilayers deposited by the Langmuir–Blodgett technique for gas sensors application. Langmuir 30:1190

67. Siffalovic P, Vegso K, Benkovicova M, Jergel M et al (2014) Reassembly and oxidation of a silver nanoparticle bilayer probed by in situ X-ray reciprocal space mapping. J Phys Chem C 118:7195
68. Hirota E, Sakakima H, Inomata K (eds) (2002) Giant magneto-resistance devices. Springer, Berlin/Heidelberg
69. Spiller E (1994) Soft X-ray optics. SPIE Optical Engineering Press, Bellingham
70. Venables J (2000) Introduction to surface and thin film processes. Cambridge University Press, Cambridge; New York
71. Lüth H (2010) Solid surfaces, interfaces and thin films. Springer, Heidelberg/New York
72. Freund LB, Suresh S (2009) Thin film materials: stress, defect formation, and surface evolution. Cambridge University Press, Cambridge/New York
73. Ohring M (2001) Materials science of thin films. Elsevier Science, Singapore
74. Barabási A-L, Stanley HE (1995) Fractal concepts in surface growth. Press Syndicate of the University of Cambridge, New York
75. Renaud G, Ducruet M, Ulrich O, Lazzari R (2004) Apparatus for real time in situ quantitative studies of growing nanoparticles by grazing incidence small angle X-ray scattering and surface differential reflectance spectroscopy. Nucl Inst Methods Phys Res B 222:667
76. Hodas M 2015 doi:10.1117/12.2187999
77. Schwartzkopf M, Buffet A, Korstgens V, Metwalli E et al (2013) From atoms to layers: in situ gold cluster growth kinetics during sputter deposition. Nanoscale 5:5053
78. Siffalovic P, Jergel M, Majkova E (2011) GISAXS – probe of buried interfaces in multilayered thin films. In: Bauwens CM (ed) X-ray scattering. Nova Science Publishers, New York, pp 1–54
79. Stearns DG (1992) X-ray-scattering from interfacial roughness in multilayer structures. J Appl Phys 71:4286
80. Salditt T, Lott D, Metzger TH, Peisl J et al (1996) Observation of the Huygens-principle growth mechanism in sputtered W/Si multilayers. Europhys Lett 36:565
81. Salditt T, Metzger TH, Peisl J, Reinker B et al (1995) Determination of the height-height correlation-function of rough surfaces from diffuse-X-ray scattering. Europhys Lett 32:331
82. Salditt T, Lott D, Metzger TH, Peisl J et al (1996) Characterization of interface roughness in W/Si multilayers by high resolution diffuse X-ray scattering. Phys B Condens Matter 221:13
83. Salditt T, Metzger TH, Brandt C, Klemradt U et al (1995) Determination of the static scaling exponent of self-affine interfaces by nonspecular X-ray-scattering. Phys Rev B 51:5617
84. Salditt T, Metzger TH, Peisl J (1994) Kinetic roughness of amorphous multilayers studied by diffuse-X-ray scattering. Phys Rev Lett 73:2228
85. Siffalovic P, Majkova E, Chitu L, Jergel M et al (2009) Characterization of Mo/Si soft X-ray multilayer mirrors by grazing-incidence small-angle X-ray scattering. Vacuum 84:19
86. Sinha SK, Sirota EB, Garoff S, Stanley HB (1988) X-ray and neutron-scattering from rough surfaces. Phys Rev B 38:2297
87. Edwards SF, Wilkinson DR (1982) The surface statistics of a granular aggregate. Proc R Soc A 381:17
88. Siffalovic P, Jergel M, Chitu L, Majkova E et al (2010) Interface study of a high-performance W/B4C X-ray mirror. J Appl Crystallogr 43:1431
89. Wu W-R, Jeng US, Su C-J, Wei K-H et al (2011) Competition between fullerene aggregation and poly(3-hexylthiophene) crystallization upon annealing of bulk heterojunction solar cells. ACS Nano 5:6233
90. Li G, Yao Y, Yang H, Shrotriya V et al (2007) "Solvent annealing" effect in polymer solar cells based on poly(3-hexylthiophene) and methanofullerenes. Adv Funct Mater 17:1636
91. Ziberi B, Cornejo M, Frost F, Rauschenbach B (2009) Highly ordered nanopatterns on Ge and Si surfaces by ion beam sputtering. J Phys Condens Matter 21:224003

X-Ray Powder Diffraction Characterization of Nanomaterials

Antonio Cervellino, Ruggero Frison, Norberto Masciocchi, and Antonietta Guagliardi

Contents

A. Cervellino (✉)
Swiss Light Source, Paul Scherrer Institut, Villigen, Switzerland
e-mail: Antonio.Cervellino@psi.ch

R. Frison
Istituto di Cristallografia and To.sca.Lab., Consiglio Nazionale delle Ricerche, Como, Italy

Department of Chemistry, University of Zurich, Zurich, Switzerland
e-mail: ruggero.frison@ic.cnr.it; ruggero.frison@uzh.ch

N. Masciocchi
Dipartimento di Scienza e Alta Tecnologia and To.sca.Lab., Università dell'Insubria, Como, Italy
e-mail: norberto.masciocchi@uninsubria.it

A. Guagliardi (✉)
Istituto di Cristallografia and To.sca.Lab., Consiglio Nazionale delle Ricerche, Como, Italy
e-mail: antonella.guagliardi@ic.cnr.it

1   Definition of the Topic

We discuss here what important knowledge can be gained by X-ray diffraction (of course, more specifically, we talk of X-ray powder diffraction) experiments on nanoparticles and nanomaterials in general. Historically, the uses of X-ray diffraction have been to investigate (a) the crystal structure of materials at the atomic scale and (b) their microstructure, a broad term meaning deviations from perfect crystalline order on a scale that is larger than the atomic one but still microscopic. In fact, macroscopic properties of materials tend to depend on both of those. For nanomaterials, the focus is to understand how the small crystal domain extension and related phenomena influence properties that differ – often in a very useful way – from the parent crystalline material. This means that the focus is on the microstructure, due to the fact that reduced domain extension is a (strong) deviation from crystal order – this is by definition something that extends to infinity. Of course there exist crystalline phases that are stable only at the nanoscale – and in such case, the crystal structure determination still is very important. In this contribution, we shall review all modern experimental methods and especially – as this is the core of the method – the data analysis techniques currently used, from the oldest, based on the Bragg formalism to interpret crystal diffraction, to the newest, relying on atomic-scale modeling.

2   Overview

2.1   Nanoparticle Characterization

The great discovery that for many materials a crystal size in the nanometer range strongly affects properties and opens large avenues to applications has spurred a concerted effort to understand why and how that happens, in the way that the resulting changes in properties can be understood and optimized for applications. If we think of the reduced size as an imperfection or a defect of the crystal structure (by definition, a perfect crystal extends to infinity), this is a case in which structural defects determine the material properties. To understand the importance of defects on tuning materials properties, the example of silicon is illuminating: all modern electronics – up to computers and handheld devices – are made possible by careful insertion of defects (doping) in otherwise perfect silicon crystals. Therefore, a complete and meaningful characterization of a nanoparticle (NP) must include its ideal atomic structure – that of an infinite crystal of which the NP represents a small portion – and its defects, starting from the finite and rather small size, the shape, and other defects which may be induced by the small size (as surface distortion and reconstruction) or independent from it.

2.1.1   The Goal: Atomic Structure and Microstructure
The most important analysis goal for NP is to determine the *complete* structure of a NP (or a system thereof), how that is affected by the synthesis method, and how that

correlates with materials properties. With complete structure here we mean both the atomic structure of the "parent" crystal (*crystal structure*), of which the NPs represent small portions, and the *microstructure*, including all the defects – first of all, size and shape – that differentiate NPs from the parent perfect crystal. While crystal structure is of course an average property, and therefore it is the same for all individual NPs contained in a macroscopic sample, microstructure is stochastic in nature. A defect with a small probability will be present in some NPs and absent in many more. Surface amorphization will lead to as many differently structured NPs as there are in the sample, even if all the rest is identical. Size and shape themselves in most cases are statistically distributed in a synthesized NP batch, so much that in many cases synthesis progress is measured with respect to the narrowness of the resulting size/shape distribution. Therefore, while the detailed global atomic structure of a *single* NP is very informative, it automatically excludes the most important information – that about the statistical distribution of defects. X-ray powder diffraction (XRPD) measures, instead, the averaged diffraction signal from a huge (macroscopic) ensemble of NPs; therefore, it contains information about the statistics of the NPs in the sample. While experimentally XRPD is an "easy" method, data analysis is a complex endeavor, especially when complex statistical microstructural information is desired. In the following, we will illustrate the state of the art in the experimental and data analysis methods for XRPD, showing the wealth of information that can be obtained therefrom.

2.1.2   Diffraction Versus Microscopy

Nanomaterials are complex systems. This makes their physicochemical characterization a rather difficult task, the smaller the NPs, the complex the task. Therefore, extracting information about crystal structure, defects, size, shape, and composition is commonly performed through the combination of different characterization techniques, typically spanning from microscopy, diffraction, and spectroscopy. Among these, transmission electron microscopy (TEM), often used in high-resolution mode or in combination with electron diffraction, has been playing the role of leading technique, particularly for characterizing the distribution of NP size and their morphology. The successful impact of (HR)TEM in the field of nanoscience and nanotechnology in the last decades, particularly when compared to that of X-ray diffraction techniques, is easily understandable after considering (i) the importance of directly visualizing unpredictable sizes and shapes of newly synthesized NPs (although just a 2D projection becomes available, unless an extremely time-consuming tomographic 3D reconstruction is carried out) and (ii) the deficiency of conventional XRPD Bragg-based methods in characterizing very small NPs, which has typically limited their use to verifying the phase purity of new materials and, sometimes, to rough domains size estimation. However, since one of the goals of nanomaterials characterization is achieving the statistical distribution of defects, then investigating a larger sample volume using diffraction (or scattering) techniques should be considered a more appropriate approach, bringing the analysis to the most suitable statistical level. In this view, in fact, we have to consider the local nature of the microscopy probe, which typically involves a number of investigated NPs as

small as 500, i.e., extremely shrunk if compared to the several thousands of NPs sampled by X-ray scattering techniques. An additional important advantage of X-ray diffraction versus microscopy refers to its sensitivity to atomic species, which makes the technique a valuable route to investigate sample stoichiometry and phase composition of complex mixtures of NPs or multiple nanosized components of different chemical composition. We will show, throughout this chapter, that diffraction is a powerful complementary tool to microscopy for nanomaterials characterization, particularly when the so-called total scattering methods are used.

3 Experimental and Instrumental Methodology

3.1 X-Ray Powder Diffraction (XRPD)

3.1.1 General Theory

We will consider a parallel beam (plane wave) of monochromatic radiation, that is, with a single constant wavelength λ (if we think about a particle beam, as it is allowed by the De Broglie ambiguity, all particles travel parallel to each other and have the same speed and energy). When the beam interacts with something (an obstacle or target) placed in its path, some particles will deviate and perhaps exchange energy with the target. Here we will only consider the case when no energy exchange happens (*elastic scattering*) – that is, the outgoing particles have the same energy as the incoming ones (or, identically, the same wavelength λ). Therefore, only the direction of motion of the scattered particles is affected. We define now the wave vector $\boldsymbol{k}$ of the incoming particles as the vector that has the same direction as the incoming beam and length $k = |\boldsymbol{k}| = 1/\lambda$; similarly, the wave vector $\boldsymbol{k'}$ of a scattered particles has also length $k' = |\boldsymbol{k'}| = k = 1/\lambda$, while its direction is now the one of the scattered particle. Define also $\boldsymbol{q} = \boldsymbol{k'} - \boldsymbol{k}$ as the *scattering vector* (see Fig. 10.1). [Note: physicist prefer alternative definitions of the wave vectors and scattering vectors; these differ by a factor 2π, and as both definitions are broadly used, we will hereafter use capital symbols for the physicists' vectors, as $\boldsymbol{Q} = 2\pi \, \boldsymbol{q}$, $\boldsymbol{K} = 2\pi \, \boldsymbol{k}$, ...]. We will also assume that there is no delay between collision and scattering; this means that the scattered wave starts with the same phase as the incoming one (*coherent scattering*). In the X-ray case, elastic scattering is always coherent, while with other widely used diffraction probes (neutrons), this may not be the case. If 2θ is the angle between $\boldsymbol{k}$ and $\boldsymbol{k'}$, the length of $\boldsymbol{q}$ is $q = |\boldsymbol{k} - \boldsymbol{k'}| = 2k \sin\theta = 2 \sin\theta/\lambda$ [and of course, $Q = 4\pi \sin \theta/\lambda$].

In a diffraction experiment, we measure then the angular distribution of the scattered particles. The quantity we measure is the *differential cross-section* $d\sigma/d\Omega$, defined as follows: if I_0 is the intensity (number of particles per unit area and per unit time) incident on the target, the number of particles detected per unit time in a small detector window covering a small solid-angle $d\Omega$ around any given $(2\theta, \varphi)$ direction is equal to $I_0 \times d\sigma/d\Omega(2\theta, \varphi) \times d\Omega$ (Fig. 10.2).
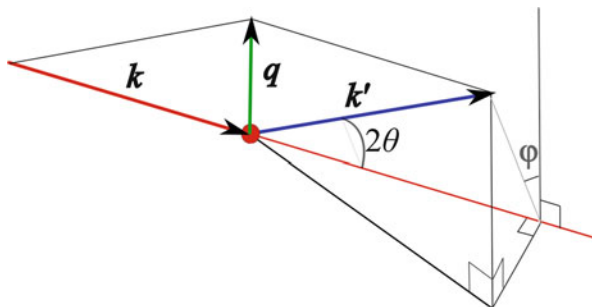
Fig. 10.1 Representation of the three wave vectors k, *red*; k', *blue*; and $q = k - k'$, *green*, for a probe coming from the k direction which is elastically and coherently scattered by a target (*red circle*) in the k' direction, which forms angles 2θ with the k direction and φ around k with respect to a reference (here vertical) plane
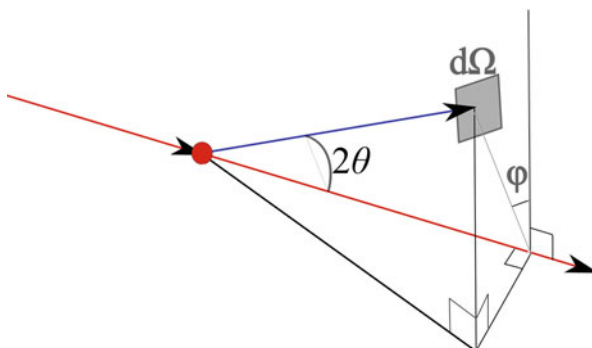
Fig. 10.2 The scattered radiation is collected in a small detector window placed around direction $(2\theta,\varphi)$ with respect to the incoming beam. If the window is placed at a distance R from the target and has a (small) area dS and the normal to its surface forms an angle ψ with the direction of the scattered beam, then it covers a solid-angle $d\Omega = dS\,\cos\psi/R^2$. If I_0 is the incident intensity on the target, then the observed intensity is defined as the product of $I_0 \times d\Omega \times d\sigma/d\Omega(2\theta,\varphi)$

The measured $d\sigma/d\Omega$ at several directions contains information about the structure of the target. To see how precisely, we must go into the scattering process for waves.

The incoming beam is represented by a plane wave, whose amplitude in any point r is given by $I_0^{1/2}\exp(2\pi i k r)$. The scattered wave from a point target located at r_1 is represented instead by a spherical wave, whose amplitude in any point R is given by

$$I_0^{1/2} b \frac{e^{2\pi i k r_1}\; e^{2\pi i k|R-r_1|}}{|R - r_1|}$$

at large $\boldsymbol{R}$,
again $\approx$ plane wave

$\sqrt{I_0}\,\dfrac{b}{|\boldsymbol{R}-\boldsymbol{r_1}|}\,\mathrm{e}^{2\pi i k\cdot r_1}\,\mathrm{e}^{2\pi i k'\cdot\,(\boldsymbol{R}\text{-}r_1)}$

$\boldsymbol{R}-\boldsymbol{r}_1$

ψ

solid angle : $\mathrm{d}\Omega = \mathrm{d}S\cos\psi$

$\boldsymbol{R}$

2θ

Incoming beam
plane wave

$\sqrt{I_0}\ \mathrm{e}^{2\pi i k\cdot r}$

$\boldsymbol{r}_1$

Scattered spherical wave

O

$\sqrt{I_0}\ \dfrac{b}{|\boldsymbol{R}-\boldsymbol{r}_1|}\ \mathrm{e}^{2\pi i k\cdot r_1}\,\mathrm{e}^{2\pi i k|\boldsymbol{R}-\boldsymbol{r}_1|}$
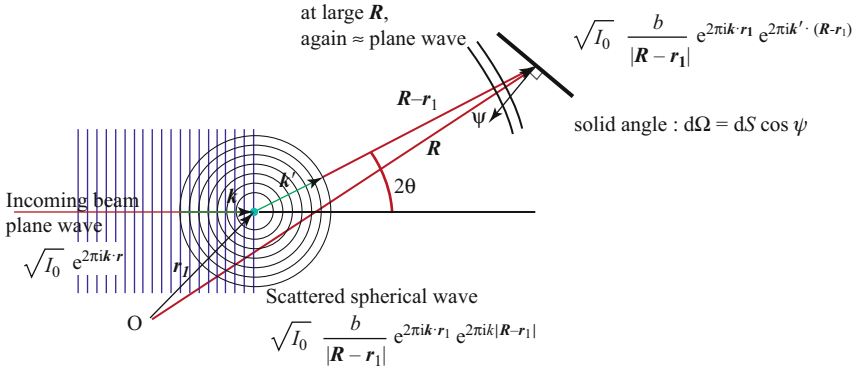
Fig. 10.3 Elastic scattering process – from plane wave (incident beam) to spherical wave (scattered beam) to plane wave once more (detected beam)

Here b is the *scattering length* of the point scatterer; it is a measure of its scattering effectiveness. For large $\boldsymbol{R}$ and small $\boldsymbol{r}_1$, the spherical wavefronts become again approximately planar, so there we can approximate it as

$$I_0^{1/2}b\,\frac{\mathrm{e}^{2\pi i k r_1}\ \mathrm{e}^{2\pi i k|\boldsymbol{R}-\boldsymbol{r}_1|}}{|\boldsymbol{R}-\boldsymbol{r}_1|}\approx I_0^{1/2}b\,\frac{\mathrm{e}^{2\pi i k r_1}\ \mathrm{e}^{2\pi i k'(\boldsymbol{R}-\boldsymbol{r}_1)}}{R}$$

Here we used the fact that, by definition, $(\boldsymbol{R}-\boldsymbol{r}_1)$ and $\boldsymbol{k}'$ are parallel. See Fig. 10.3 for clarity. If we have N point scatterers, we have to sum the amplitudes of the resulting waves, obtaining

$$\frac{I_0^{1/2}}{R}\mathrm{e}^{2\pi i k'R}\sum_{j=1}^{N}b_j\mathrm{e}^{-2\pi i(k'-k)r_j}=\frac{I_0^{1/2}}{R}\mathrm{e}^{2\pi i k'R}\sum_{j=1}^{N}b_j\mathrm{e}^{-2\pi i q\,r_j}$$

Now suppose we capture this wave on a small surface $\mathrm{d}S$, whose normal forms an angle ψ with the scattered wave direction. The signal per unit time measured on $\mathrm{d}S$ is then the square modulus of the wave amplitude times the area orthogonal to the wavefront $\mathrm{d}S\cos\psi$. This yields

$$\left|\frac{I_0^{1/2}}{R}\mathrm{e}^{2\pi i k'R}\sum_{j=1}^{N}b_j\mathrm{e}^{-2\pi i\,q\,r_j}\right|^2\mathrm{d}S\cos\psi = I_0\frac{\mathrm{d}S\cos\psi}{R^2}\left|\sum_{j=1}^{N}b_j\mathrm{e}^{-2\pi i q r_j}\right|^2$$

$$= I_0\mathrm{d}\Omega\left|\sum_{j=1}^{N}b_j\mathrm{e}^{-2\pi i q r_j}\right|^2$$

and from the definition, the sum within the square modulus in the last term is just the elastic coherent scattering differential cross section

$$\frac{\mathrm{d}\sigma}{\mathrm{d}\Omega}(\boldsymbol{q}) = \left| \sum_{j=1}^{N} b_j \mathrm{e}^{-2\pi i \boldsymbol{q} \boldsymbol{r}_j} \right|^2$$

Before removing some approximations (like, that the atoms are point scatterers), we specialize the former equation to the case of an infinite perfect crystal. Then instead of a finite set of N atoms, we have an infinite repetition of a set of N atoms that represent the content of one unit cell, translated by all the vectors of an infinite lattice. A lattice vector $\boldsymbol{L}$ is an integer linear combination of three basis vectors $\boldsymbol{a}$, $\boldsymbol{b}$, $\boldsymbol{c}$, $\boldsymbol{L} = l_1\boldsymbol{a} + l_2\boldsymbol{b} + l_3\boldsymbol{c}$, where l_1, l_2, l_3 are any integer. The position vector of a generic atom is then $\boldsymbol{L} + \boldsymbol{r}_j$ and

$$\frac{\mathrm{d}\sigma}{\mathrm{d}\Omega}(\boldsymbol{q}) = \left| \sum_{\boldsymbol{L}} \sum_{j=1}^{N} b_j \mathrm{e}^{-2\pi i \boldsymbol{q}(\boldsymbol{r}_j + \boldsymbol{L})} \right|^2 + U \sum_{\boldsymbol{H}} \left| \sum_{j=1}^{N} b_j \mathrm{e}^{-2\pi i \boldsymbol{H} \boldsymbol{r}_j} \right|^2 \delta(\boldsymbol{q} - \boldsymbol{H})$$

Here we have used Poisson's summation formula and

- U is a constant (theoretically infinite) representing the total number of lattice nodes.
- $\delta(x)$ is the "infinitely sharp peak" (Dirac's δ) function.
- H is a node of the reciprocal lattice. This is another lattice, with $\boldsymbol{H} = h_1\boldsymbol{a}^* + h_2\boldsymbol{b}^* + h_3\boldsymbol{c}^*$, with h_1, h_2, h_3 integers and related to the crystal (direct) lattice by relations $\boldsymbol{a}\boldsymbol{a}^* = \boldsymbol{b}\boldsymbol{b}^* = \boldsymbol{c}\boldsymbol{c}^* = 1$ and $\boldsymbol{a}\boldsymbol{b}^* = \boldsymbol{a}\boldsymbol{c}^* = \boldsymbol{b}\boldsymbol{c}^* = \boldsymbol{a}^*\boldsymbol{b} = \boldsymbol{a}^*\boldsymbol{c} = \boldsymbol{b}^*\boldsymbol{c} = 0$. Therefore, $\mathrm{d}\sigma/\mathrm{d}\Omega$ is represented by a lattice of sharp peaks (*Bragg peaks*) whose weights (intensities) are given by the sum in $|.|^2$ in the last term.

Now we specialize a bit more into X-ray scattering. This affects only the scattering lengths b_j. X-rays interact with electrons, and the elastic coherent scattering length of one electron is the classical (Thompson) electron radius $r_e = e^2/(4\pi\varepsilon_0 \, m_e c^2) = 2.8179 \times 10^{-15}$ m [SI units]. The scattering length of an atom with Z electrons would then be $Z \, r_e$. This is true only at very small q, however; because the electron cloud of an atom is relatively not small compared to X-ray wavelengths, the atoms are not point scatterers for X-rays. However, to good approximation, the electron cloud is spherically isotropic, so we can simply substitute the fixed scattering lengths b with the X-ray atomic form factors $f(q)$, one for each atomic species, depending only on the magnitude q of the scattering vector $\boldsymbol{q}$ and with $f(0) = Z \, r_e$. [Hereafter we will adopt the usual crystallographic scattering length units, or *electron units*, in which $r_e = 1$ so it can be omitted, and it will never be mentioned any more]. Similarly, to account for uncorrelated harmonic thermal motion, a factor $T(q)$ for each atom (Debye–Waller factor) is sufficient. Finally, considering also that some atoms may be present with a probability $o < 1$, we have the corrected expression

$$\frac{d\sigma}{d\Omega}(\boldsymbol{q}) = \left| \sum_{j=1}^{N} f_j(q) T_j(q) o_j e^{-2\pi i \boldsymbol{q} \boldsymbol{r}_j} \right|^2 \tag{10.1}$$

Last but not least, we specialize to X-ray powder diffraction. A powder is a very large ensemble of particles (crystals) with all possible spatial orientations and with a spherically uniform distribution of orientations. So we need to average the differential cross section over all possible orientations. This is done easily and it results to

$$\left\langle \frac{d\sigma}{d\Omega} \right\rangle (q) = \sum_{j=1}^{N} f_j^2(q) o_j^2 + 2 \sum_{j>k=1}^{N} f_j(q) f_k(q) T_j(q) T_k(q) o_j o_k \mathrm{sinc}\left(2\pi q d_{jk}\right) \tag{10.2}$$

where $d_{jk} = |\boldsymbol{r}_j - \boldsymbol{r}_k|$ is the interatomic distance between the jth and kth atom and sinc $(x) = \sin(x)/x$ is the sine cardinal function. This is the Debye scattering equation for a general set of atoms. If we start from the expression from an infinite crystal, we have instead

$$\left\langle \frac{d\sigma}{d\Omega} \right\rangle (q) = \sum_{\boldsymbol{H}} \left| \sum_{j=1}^{N} f_j(q) T_j(q) o_j e^{-2\pi i \boldsymbol{H} \boldsymbol{r}_j} \right|^2 \delta(q - H) \tag{10.3}$$

Here averaging only affects the $\delta-$function argument, where the lengths q and H replace the vectors $\boldsymbol{q}$ and $\boldsymbol{H}$.

Comparing the two forms of the XRPD scattering equation leads to some important conclusions. We need, however, to address also the effects brought about by crystal defects. Generally, crystal defects will lead to replace the $\delta-$function with a broadened profile. This will be clarified better in Sect. 3.1. Moreover, additional scattering will appear also between the Bragg peaks (*diffuse scattering*). [Note that the distinction between Bragg and diffuse scattering is heuristic only, being there no way to differentiate them exactly]. The integrated intensities of the Bragg peaks, however, will not be affected by crystal defects, and they depend only on the (average) content of the unit cell. At variance, the Bragg peak shape and breadth will encode all information on crystal defects, crystal size, and shape. This has been the basis of classical Bragg analysis methods – both for structure solution (finding out the positions of the atoms in the unit cell, their thermal vibration factors and site occupancies) and of defect analysis, as it will be recalled in the next sections. For small NPs, however, this distinction starts to lose meaning. Bragg peaks broaden enough that they are not separable and integrated intensity values have considerable errors. Moreover, the "diffuse scattering" increases and becomes very difficult to separate. Discarding it, moreover, would mean discarding an important part of information. Therefore, in recent years, the use of the full Debye scattering equation – without the simplifications deriving from an assumption of periodicity – has been more and more frequently used, in spite of its complexity, as the sinc sum nominally contains a number of terms proportional to the *square* of the number of atoms in the *whole NP*. We will expand on this topic in Sect. 4.2.2.

As a last remark, X-rays are scattered also inelastically and incoherently (i.e., actually, the vast majority of the X-ray scattering processes with matter). Of particular importance are processes where an X-ray photon is converted into another X-ray photon with lower energy. The main processes in this category are Compton scattering and fluorescence. Fluorescence lines are known for all elements, and with careful choices of incident energy and detector setup, they can be eliminated – at least at synchrotron sources. Compton scattering is quite weak and very close in energy to the incident radiation, so it cannot be eliminated with existing methods; however, it is fairly easy to calculate it and subtract it from the elastic scattering signal. Other forms of scattering do not cause spurious signals in an X-ray detector, but still they cause absorption of the primary and scattered beam while they travel through the sample, so special corrections have to be devised in order to obtain undistorted data.

3.2   Instrumentation: Laboratory and Synchrotron

As most other experimental techniques based on the radiation–matter interaction, also XRPD requires a source of radiation, a sample holder (with its specific environment), and a radiation detector; the latter is meant to measure the diffracted intensity not directly down the impinging direction (as in most absorption-based spectroscopies), rather at different scattering angles (in the most common situations). Of course, beam conditioning (limitation of beam divergence, filtering or monochromatization, positioning of antiscatter slits avoiding spurious radiation, etc.) is also necessary and heavily depends on the overall diffraction geometry, equipment, and radiation source. Since there exist many different combinations of *sources*, *optics*, *sample nature*, *size and shape*, and *detectors*, the instrumentation part is here split into "independent" portions, which, after being assembled in suitable configurations, can give rise to a large variability of versatile equipment (the *diffractometers*). The interested reader can find more details on XRPD instrumentation in the nice book by Guinebretière [1].

Sources The most common radiation source in the lab is the *X-ray tube*, which, operating at a typical power of 2 kW, can provide photon fluxes at the sample close to 10^8 ph/s. Commercially available anode materials are Ag, Mo, Cu, Co, Fe, and Cr, spanning, with their Kα characteristic lines, the 22.2–5.4 keV energy range (λ = 0.559–2.290 Å). Unless specific requirements are necessary (e.g., to avoid Fe/Ni/Co fluorescence effects or to reach high Q values, $Q = 4\pi\sin\theta/\lambda$, for pair distribution function studies; *see below*), nearly ubiquitous is the use of Cu-Kα radiation (λ = 1.5416 Å for the unresolved $\alpha_{1,2}$ doublet). This gives a good range of accessible *d* values, a limited overlap (for moderately complex materials), and reasonably treatable transparency/absorption effects.

Boosted sources, allowing a *max.* tenfold increase of flux, at the expenses of a significantly higher cost and maintenance requirements, are *rotating anodes*. While originally developed for point focus experiments (small molecule or protein

single-crystal diffractometry), they have also been recently adapted, and improved, for other kinds of instrumentation: as highly brilliant microfocus sources (down to diameters of 70 μm) for scanning SAXS and WAXS (small and wide-angle X-ray scattering) experiments or for providing line-focus beams for XRPD. In these cases, only Cu, Co, Cr, and Mo radiation sources are available on the market, with the interesting option of double-element anodes, providing two-wavelength beams.

Definitely more appealing for the material scientist, and for the nanoworld, are X-rays generated at *synchrotron* sources, where extremely high brilliance, energy tunability, nearly null beam divergence, polarization, and "flashing" time structure can be independently, or simultaneously, exploited in devising specific advanced experiments. Fluxes at the sample close to 10^4–10^6 higher than lab sources are normally achieved, making fast data collections on nanomaterials possible. For a high-quality pattern from poorly scattering nanomaterials, with the best detectors (see below), acquisition times of minutes are normal; when fast transformations are to be qualitatively observed, acquisition times down to 1 ms are currently possible. The wavelength (or the energy) of modern synchrotron sources is continuously tunable in a given range (5–38 keV for the X04SA-MS beamline at SLS [2], 6–80 keV for the ID22 beamline at ESRF [3]). The X-ray beam is commonly very parallel (divergence roughly down to 0.001°, depending on conditions) and narrow (from few mm to <1 μm with specialized optics).

Detectors Disregarding the physical nature of the X-ray detection event and its conversion into a machine-readable electrical current, several different kinds of detectors are normally used:

(i) *Point* detectors (*0D*), capable of measuring a tiny solid angle (typically, a few seconds of a solid radians – or less), used in scanning mode, either by a continuous movement of the motors of the arm on which they are set (and sampling the integrated intensity at predefined time intervals corresponding to typical 2θ steps of 0.001–0.02°) or in a step-scanning mode, by measuring for a *fixed* time each *fixed* 2θ point, sequentially over a large angular range. Sometimes such detectors can be equipped with collimators or even (multi)analyzer crystals that bring the angular resolution down to 0.001° or less, at the cost of a huge loss in intensity. For this reason, (multi)analyzer crystals are usually only installed at synchrotron sources [4]. Analyzers not only increase the angular resolution but also select only the scattered radiation coming at a given angle from a very narrow region at the geometrical instrument center, so reducing drastically the background. However, sequential acquisition mode and very poor detection efficiency lead to very long acquisition times.

(ii) *1D (strip)* detectors, which typically possess a large number (>100) of measuring channels, typically covering from 1 to over 120° (2θ), mounted on a moving arm [as in (i)] but providing (at least) >50 times larger total counts. This is due to two factors: (a) there is no possibility of introducing a collimator or analyzer on the diffracted beam; therefore, no efficiency loss is introduced in this way, while other measures must be undertaken to safeguard the data

quality; (b) the number of parallel channels can be quite large (e.g., over 60,000 in the large Mythen II detector (120° coverage, 0.0037° resolution) installed at the X04SA-MS beamline of the Swiss Light Source [2, 5]), and of course the efficiency is proportional to the number of channels. In order to cover the unavoidable blind spots, the total acquisition time is often partitioned between two or more slightly different detector positions. The time spent in moving the detector can be kept to a small fraction of the total time.

(iii) *2D imaging* detectors, based on a number of different technologies, which simultaneously collect either entire Debye–Scherrer rings (form which clear textural features are likely to emerge) or large arcs thereof. This increases in a significant manner the collected intensity and the direct visualization of the reciprocal space, which sometimes provides valuable information, well beyond the aseptic list of angles and intensity counts within a *xy* file. Such detectors can be easily shifted away from, or close to, the sample, or moved on a goniometer circle, so that different angular ranges become available, at the expenses of resolution changes if a too short distance is chosen (though making a large $2\theta_{max}$ value accessible) and of time spent on moving and acquiring in different positions. For powder diffraction at synchrotrons, very valuable are 2D detectors coupled with high-energy (40–100 keV) beams, where the sample is in a flat transmission container (vide infra) and the detector is frontally located. The high-energy beam overcomes the difficulty of a small $2\theta_{max}$ (30–45°) by still reaching a high $Q = 4\pi \sin\theta/\lambda$ through the shorter wavelength λ – and this is the setup of most PDF-specialized beamlines like the 11-ID-B at the Advanced Photon Source.

(iv) Static *energy-dispersive* detectors ($E = hc/\lambda$), which are used in "crowded" sample environments (e.g., high pressure cells), where, at fixed $2\theta_0$ position(s) in the presence of a non-monochromatic ("white") beam, the XRD pattern is collected as an intensity versus energy trace [using Bragg's law, $\lambda = 2d \sin\theta$, in its equivalent formulation: $E = hc/(2d \sin\theta_0)$].

Samples Typically constituted by incoherent particles of sizes below 10 μm (down to a few nm for very small nanoparticle specimens), powder samples need to be confined in suitable sample holders, which must not disturb, or affect, the collected data, ideally giving no contribution at all. While this is possible if thick (or, better said, nontransparent to X-rays) specimens are deposited as flat plates in the hollow of a so-called Zero Background Plate (suitably cut silicon or quartz monocrystals) in the Bragg–Brentano geometry (depicted in Fig. 10.4a), conventional powder diffractometry typically uses aluminum, plastic, or glass sample holders (for flat samples in reflection mode) or thin capillaries (borate glass, or, more rarely, Kapton or silica, for specific experiments) in transmission mode (Debye–Scherrer geometry; see Fig. 10.4b). Accordingly, the contribution of the scattering of these materials adds up to the true sample-dependent XRPD trace, from which it must be eliminated prior to (or modeled within) the final data analysis. This is normally done using a phenomenological description (e.g., in classical Rietveld-like approaches) or requires an intense series of parallel experiments and data treatment if a total
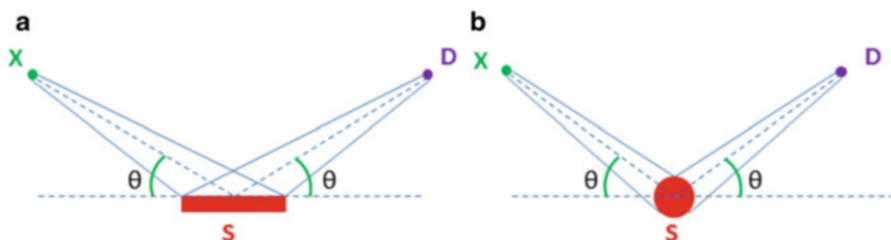
Fig. 10.4 Schematics of the basic geometries used for X-ray powder diffraction (diffraction from polycrystalline materials), *not to scale*: (**a**) *Bragg–Brentano* geometry, with flat sample mode in parafocussing geometry (the standard mode for phase identification and quantitative analyses performed in the laboratory); (**b**) *Debye–Scherrer* geometry, with cylindrical sample in transmission mode, suitable for colloidal suspensions of nanoparticles and/or air-sensitive materials confined within a glass, plastic, or quartz capillary (the custom geometry for nanomaterials studies at synchrotrons). X, X-ray source; S, Sample; D, Detector; θ, Bragg angle as for Bragg equation. Sample to detector distance may vary from *ca.* 150 mm for bench (transportable) X-ray diffractometers to more than 700 mm in large synchrotron setups. Also beam divergence (here exaggerated) can vary, from >1° (in the lab) to less than 0.01° (at synchrotrons)

scattering method, highly relevant for nanomaterials, is adopted [6]. At synchrotrons, the Bragg–Brentano geometry is impossible due to the parallel nature of the beam; a similar geometry (but with fixed-incidence angle α (small, 1–10°) and variable reflection angle $2\theta-\alpha$) is sometimes used, although it is very difficult to correct the data, especially when an analyzer is not used. The Debye–Scherrer geometry (Fig. 10.5b) is very often used, and with high-energy sources (>40 keV), often also the thin-plate transmission geometry (Fig. 10.5b) is used in combination with 2D detectors.

Summarizing, without taking into account the many variations which can be devised for samples of different nature (bulk materials, thin films, colloidal suspensions, etc.), for different optical elements geometrically defining, filtering, and monochromatizing the X-ray beam, Table 10.1 summarizes the most useful, and popular, combinations (a few rarer ones, requiring, in some cases, *curved* samples, are also included for completeness). *In fact, the geometry of a powder diffractometer is mainly determined by the shapes of the sample and of the beam and does not depend upon the source or the other components.*

4 Key Research Findings

4.1 Bragg Methods of Analysis: An Overview

4.1.1 Crystal Structure Solution

The determination of the crystal and molecular structure for crystalline materials (inorganic, organic, and organometallic species) has become, in the last 20 years, a pervasive activity; this has been favored by the dissemination of automatic X-ray
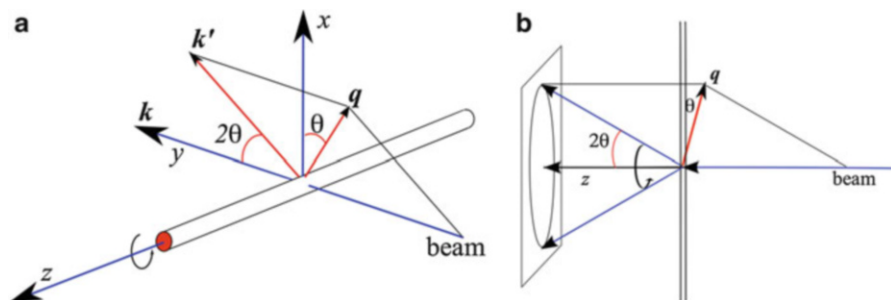
Fig. 10.5 Schematics of the most important geometries used for X-ray powder diffraction at synchrotrons with parallel beam, *not to scale*: (**a**) *Debye–Scherrer* geometry, with cylindrical sample in transmission mode, suitable for powders as well as colloidal suspensions of nanoparticles and/or air-sensitive materials confined within a glass, plastic, or quartz capillary. (**b**) *Thin-plate transmission* geometry, with a flat sample container (consisting of a box with two closely spaced flat surfaces orthogonal to the beam, here schematized with two vertical parallel lines) in transmission mode with frontally installed 2D detector. The third (fixed incidence on flat sample, not shown) resembles the Bragg–Brentano configuration (Fig. 10.4a) except that the beam is parallel and much smaller than the sample area, the incidence angle (α) is fixed and small (1–$10°$), and the reflection angle ($2\theta - \alpha$) is variable. This geometry is better suited to analyzer detectors and even so it needs important angle-dependent corrections because the sample-illuminated volume changes with 2θ

Table 10.1 Summary of the different X-ray powder diffraction geometries for laboratory and synchrotron sources. In the latter case, diffractometers are mostly one-off constructions and therefore not especially named; we list the ideal detector type, instead

Laboratory sources		
Sample shape	Geometry	Diffractometer
Cylindric	Debye–Scherrer *(Transmission)*	Debye chamber, parallel-beam diffractometer
Curved	Guinier *(Focusing)*	Guinier chamber, Seeman-Bohlin diffractometer
Flat	Bragg–Brentano *(Mostly in reflection mode; rarely in transmission)*	Parafocussing diffractometer
Synchrotron sources		
Sample shape	Geometry	Ideal detector type
Cylindric	Debye–Scherrer *(Transmission)*	0D (analyzer), 1D detectors
Flat	Fixed incidence *(Reflection)*	0D (analyzer)
Flat	Thin-plate *(Transmission)*	2D detectors, high energy

diffractometers, efficient structure solution and refinement software, and, as sad as it can appear, by the quest for low-quality (or low-relevance) papers by newly founded journals accepting, mostly for commerce, nearly all contributions. The tremendous increase of "small molecules" structural knowledge is witnessed by the exponential increase of the structures deposited in the Cambridge Structural Database [7], paralleled by that of the Inorganic Crystal Structural Database managed by FIZ in

Karlsruhe [8], per se significant in terms of strengthening the statistical value of structural correlation methods [9], conformational analyses [10], and crystal engineering studies [11].

Of lower *numerical* impact (less than 0.5 % of the total), crystal structures determined by powder diffraction methods also began to appear in the last decade. Ab initio structural determination by XRPD [12] becomes indeed necessary only when the size and quality of the "single crystalline domains" lower to a level that crystal mounting, conventional data collection, and diffraction data analyses (in the "single-crystal" mode) are not a viable choice. In these cases, provided that the "molecular" complexity is not too large (typically, <30 nonhydrogen atoms in the asymmetric unit, though striking exceptions to this rule-of-thumb are known), structures can be solved, and (approximate) models defined, to an accuracy level way below that attainable by conventional single-crystal techniques. However, as often proposed, *poor information is better than no information at all*.

Noteworthy, structure solution from a single nanocrystal or a collection thereof, by X-ray diffraction methods in the standard Bragg approach (in which the integrated intensities of well-separated peaks, or disentangled overlapping reflections are used as the primary source of information), is not possible, as it turns out to be extremely difficult to deal with extremely broad, and often asymmetric, peaks in reciprocal space, no matter which radiation source (X-ray tubes, rotating anodes, or synchrotrons), diffraction geometry, and X-ray detectors are adopted.

Therefore, nearly all X-ray diffraction studies of nanocrystalline matter rely on structural models taken from the bulk, and, whenever possible, only slight modifications of the pertinent parameters [lattice periodicity, stoichiometry and (dis)ordering, thermal agitation] are introduced in model refinement procedures, normally (but not uniquely) performed by least-squares methods in whole-pattern profile matching procedures (the Rietveld method [13]). In this approach, peak positions are determined by strict symmetry and metrical relationships, (integrated) peak intensities depend on the atomic positions within the unit cell, and peak shapes are modeled by (flexible) analytical functions, phenomenologically describing the intensity spread in the angular space.

Accordingly, the final models, derived from initial guess of the structure, heavily depend on what is normally assumed for the bulk structure, only minor modifications being expected. Under these circumstances, we cannot speak of "true" crystal structure solution by diffraction methods (if powders, suspensions, or polycrystalline thin films are employed). However, recent advances in the instrumental and (nano) crystal handling (mounting and centering) have shown that down to the limit of 10 μm^3 [14] (still larger than those used by precession electron diffraction methods on nanosized samples [15]), single-crystal techniques can fruitfully be employed. Therefore, if pushed to these limits, the structure of nanomaterials can be solved (i.e., determined) on samples of very limited size. However, an important question still remains open: *Is such a specimen representative of the entire sample?* As naïve as it can appear, questions of this type are only rarely considered, or answered, particularly in the immense field of nanoscopic (imaging) techniques which encompass the nanoworld.

More importantly, while nanocrystals and nanoparticles are often viewed as small portions of the bulk materials, this has been proven to be an erroneous oversimplification. Numerous studies have shown that even nominally single-phase NPs (e.g., Au, CdSe, PbS, Fe_3O_4, etc.) contain core and shell regions that are very different in the atomic order and/or stoichiometry (see, e.g., [16]). While only an average crystal structure (in terms of lattice periodicity) is maintained, local distortions, changes in stoichiometry, compositional gradients, and size-dependent strains may (jointly) occur. In these cases, their accurate analysis and *quantitative* estimation become difficult by conventional methods, opening the way to a bevy of unconventional techniques, including total scattering methods (widely discussed later in this chapter).

4.1.2   Traditional Methods for Size and Shape Analysis

As early as 1918, at the verge of the development of diffraction methods for the study of crystalline materials by diffraction methods, Scherrer [17] proposed a simple formula relating the broadening of diffraction peaks in powder diffraction patterns to crystallite size (L). Scherrer's equation reads as

$$L = \frac{K\lambda}{\beta \cos\theta}$$

where 2θ is the Bragg angle, λ is the radiation wavelength, and β is the peak breadth, obtained after subtracting the instrumental line broadening, in radians; K is a dimensionless factor, with a typical value of about 0.9 (but varies with the actual shape of the crystallites – from 0.62 to 2.08) [18]. The peak breadth is also sometimes denoted as $\Delta(2\theta)$. Strictly speaking, L is the *volume-averaged* crystal dimension normal to the diffracting *hkl* plane under consideration, and β is the *integral breadth* of the full intensity distribution (originating from the sample *only*), i.e., the width of a rectangle having the same area and the same height as the peak. Interestingly, upon changing the 2θ-axis into the scattering vector modulus $s = 2\sin\theta/\lambda$, simple algebraic transformations lead to a simplified version of Scherrer's equation which allows the straightforward estimate of L by $L = K/\beta(s)$.

When crystals possess a significantly anisotropic shape, that is, when their "sizes" cannot be described by a scalar quantity L, a more complex treatment becomes necessary. This is particularly true for platy shaped or acicular materials, which typically show severely broadened peaks in the presence of the narrow(er) ones. Even under the assumptions that these effects are attributed to size effects only (and not to crystal strain or other kind of defectiveness) and that monodisperse crystal size/shapes are present in the actual specimen (both hypotheses being difficult to verify), several numerical techniques have been used to properly model, in reciprocal space, the peak width variability, mostly by a phenomenological approach. Indeed, L is then described by a vectorial approach (i.e., $L = L_{hkl}$ or $L = L_{\theta\phi}$, in polar coordinates), for example, by linear combinations of Miller indexes products (as implemented in the GSAS [19] and PSSP [20] Rietveld-refinement codes) or by

symmetrized spherical harmonics (as found in other popular programs, from TOPAS [21] to FULLPROF [22] and MAUD [23]).

The basic equations for the two approaches are

– for Stephens' model [24]

$$L_{hkl}^{-1} \propto \sum_{HKL} S_{HKL} h^H k^K l^L$$

with H + K + L = 4 and up to 15 independent S_{HKL} coefficients in the triclinic case (symmetry conditions apply for higher symmetry crystal systems), although more simplified versions have been proposed in earlier literature.

– for spherical harmonics, in Järvinen's formulation [25]

$$L_{hkl}^{-1} \propto \sum_{ij} C_{ij} Y_{ij}(\theta_{hkl}, \phi_{hkl})$$

with C_{ij} taken as coefficients (set to zero for specific crystal systems) for the real spherical harmonics of *even* order, Y_{ij}, i = 0, 2, 4, ... and j = $-i$, $-i+1$, ... , $i-1$, i (as in hydrogen atomic orbitals). Also here, slightly different formulations, relying on alternative algebraic descriptions, have been used. Significantly, a parallel formulation for cubic materials showing high-order "shapes" of a particular property P_{hkl} (say, domain size in nanocrystalline tetrapods, specific crystal morphology inducing textural effects, etc.) exist, in which cubic harmonics $K_{ij}(\theta_{hkl}, \phi_{hkl})$ are used, in

$$P_{hkl} = P\left[\sum_{ij} k_{ij} K_{ij}(\theta_{hkl}, \phi_{hkl})\right]$$

where k_{ij} are the coefficients, i = 0, 4, 6, 8, ... (*but not 2*), j = 1 (only occasionally, 2, in Laue class *m-3*), and $K_{ij}(\theta_{hkl}, \phi_{hkl})$ typically contain polynomials in $x^n + y^n + z^n$, with n even and $0 \le n \le i$ (x, y, z being the Cartesian coordinates related to θ and ϕ by the usual trigonometric transformations).

A more modern approach to size-broadening anisotropy has been proposed by Popa and Balzar, [26] who combined the spherical harmonics approach to predefined size-distribution models, here, the nearly ubiquitous (for nanomaterials) *lognormal* function. Still phenomenological, this new complex method was proven to be able to fit difficult patterns where conventional profiles fail and to provide accurate estimates of both the volume- and area-averaged apparent crystallites. These estimates can be further used in least-squares refinements of physically sound models, even if the complexity of the approach does not ensure the uniqueness of the provided solution, which can be (partially) validated by additional microscopic, say TEM, information.

Another popular, though old, method developed for estimating size effects is the Warren–Averbach analysis [27], which, based on Fourier transformation of the whole peak profile(s), can be used to extract size information of simple materials,

such as metals and alloys, and, simultaneously, strain effect. After careful background subtraction, the entire experimental profile, *h(x)*, is subjected to removal of the instrumental contribution *g(x)* by the so-called Stokes decomposition; practically, given that $h(x) = \int f(x)g(x{-}u)du$, the pure sample-dependent *f(x)* can be retrieved by using the convolution theorem of Fourier transforms, which turns the Fourier coefficients into simple factors of conventional multiplications. Then, the cosine coefficients of *f(x)* $A_n(L)$ are retained, and, if strain is considered negligible, the plot of $A_n(L)$ versus L leads, ideally, to a concave curve $(d^2 A_n(L)/dL^2 \propto P(n) > 0$, $P(n)$ being the distribution of column lengths – n cells long – in the *hkl* direction). Extrapolation onto the L axis of the line tangent to the $A_n(L)$ curve at $L = 0$ gives $<L>_a$, the sought average *area-weighted* crystal size. It is however well known that experimental artifacts twist the overall shape of this curve toward an unphysical "hook effect" [28]. In such a case, estimation of accurate size values becomes cumbersome. Actually, the method is able to provide other important microstructural information: the full $P(n)$ (i.e., size) distribution and, if an accurate measurement of *well-separated* diffraction peaks, belonging to different orders of the same "diffraction plane" (*hkl*, 2*h*2*k*2*l*, etc.) is available, also strain parameters. The method is exact if the strain distribution in the crystallites is Gaussian and is still a good approximation otherwise provided the crystallite lattice distortions are small.

More recently, using the whole powder pattern modeling (WPPM) approach, Scardi and Leoni [29] have proposed a physically based convolutory approach, in which the entire profile is reproduced by the following formula:

$$I(d^*) = k(d^*) \int dL\, C(L)\, e^{2\pi i L d^*_{hkl}}$$

where *d** is the modulus of the diffraction vector in reciprocal space (*d**$_{hkl}$ in Bragg conditions); k(*d**) includes constant, or known, *d**-dependent geometrical and structural terms (Lp, $|F|^2$, absorption, etc.); L is the Fourier length (the conjugate variable of *d**); and C(L) can be factorized into terms describing different instrumental and physical effects (nanocrystal size and shape, strain, faults, etc.). This Fourier-based approach is made convenient by the mathematical simplicity of the convolutory approach, which turns into simple multiplication of suitable functions in reciprocal space.

In the absence of other broadening sources, the size and shape of crystalline domains (taken as simple convex forms, like a sphere or any other regular solid defined by a unique size parameter D – diameter or edge) generate an intensity distribution defined by

$$I(d^*, D) = k(d^*) \int_0^{D'_{hkl}} dL\, A^S(L, D) e^{2\pi i L d^*_{hkl}}$$

Here, $A^S(L, D)$ is the Fourier transform of the diffraction profile, and D'_{hkl} is the maximum Fourier length (which depends on the actual shape of the crystal domain).

Values of $A^S(L, D)$ and D'_{hkl} for simple shapes can be computed and can be found in Ref. [30]. More complex formulae are required if a polydisperse system with known (or refinable) column length distribution needs to be considered. A detailed analysis can be found in Ref. [31].

Finally, a very recent report [32] proposed a global approach to phase identification, structure refinement, characterization of anisotropic crystallite sizes and shapes, and texture analysis using TEM scattering patterns, incorporated in a Rietveld-like approach and using Popa's formalism [26].

4.1.3 An Overview of Traditional Methods for Strain and Defects Analysis

Size effects are often accompanied, in real materials, by lattice strain and by variable (chemical and metrical) defectiveness. Therefore, a number of tools have been devised to tackle the quantitative determination of the structural parameters defining deviation from ideal periodicity, which, depending on their nature, require specific, and versatile, approaches.

A simple and, to some extent, very general use of the peak width variation in reciprocal space, determined by independent profile fitting procedures, and possibly expressed in terms of the integral breadth β (defined above), allows evaluation of size and (micro)strain (the latter being defined as $\varepsilon = \Delta L/L$). Taking into account that the size (β_L) and strain (β_e) effects have a different functional dependence on θ, ($1/\cos\theta$ and $\tan\theta$, respectively), and assuming their additivity in breadth $\beta = \beta_L + \beta_e$, it is possible to disentangle both contributions, by plotting $\beta\cos\theta$ versus $\sin\theta$; since $\beta\cos\theta = k\lambda/L + 4\varepsilon^s \sin\theta$ ($\varepsilon^s = <\varepsilon^2>^{1/2}$, the root mean-square strain), the intercept and the slope of the best linear regression allows the derivation of L and ε^s. This is the so-called Williamson–Hall method, originally proposed more than 50 years ago [33] and subsequently modified [34, 35] to include more subtle effects. A couple of examples are provided in Fig. 10.6, for data collected of heavily strained ball-milled Ni powders [36]. A recent case in the realm of nanocrystalline materials (magnetite nanocrystals, possessing a partially oxidized maghemitic shell) can be found in Frison et al. [16], from which Fig. 10.7 is taken.

As anticipated, the WPPM approach can include a number of physical effects – other than size and shape, provided that an analytical expression of the Fourier coefficients of the peak broadening is known (both the real and imaginary term contributions – the A^D_{hkl} and iB^D_{hkl} terms – become necessary). To this goal, strain, dislocation, and even twin and deformation faults have been properly included in the WPPM code, following Warren–Averbach (or Stokes–Wilson [38], Ungár [39], and Warren–Velterop [40] formulations, respectively). The field has been nicely reviewed in *The "state of the art" of the diffraction analysis of crystallite size and lattice strain* [41], where the interested reader is referred to.

1D defects are normally related to the presence of planar subunits or slabs of finite thickness, stacking in space along their normal direction, with possible in-plane shifts. Beyond the well-known case of "classical" stacking faults of metals, alloys, and layered metal sulfides (widely treated by Bragg as well as by non-Bragg approaches), other kinds of defects, such as polytypism, antiphase domains,

Fig. 10.6 *Top*: conventional Williamson–Hall plot for ball-milled nickel, with *s* and *d** coordinates replacing the original θ-dependent parameters. *Bottom*: modified Williamson–Hall plot, [37] taking into account the nature and the dependence on the crystallographic directionality of the strain fields caused by lattice defects (Reprinted with permission from P. Scardi, M. Leoni, R. Delhez, *Line broadening analysis using integral breadth methods: a critical review*, J. Appl. Cryst. 2004, **37**: p. 381–390. Copyright 2004, IUCr)
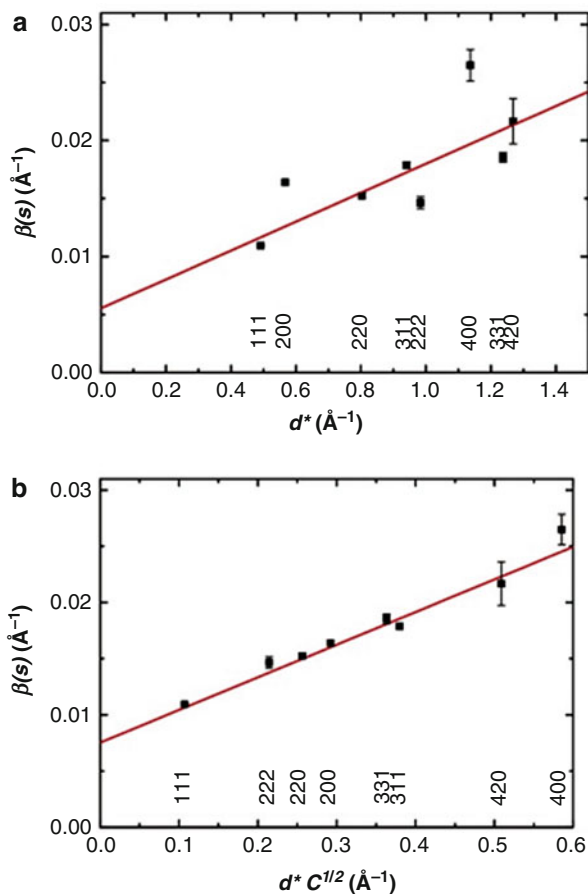
intergrowth, and polysynthetic twinning, can affect several other classes of materials. They include important technological-functional materials such silicon carbide, micas, metal oxides, layered double hydroxides, and, recently, even molecular solids like the drug cimetidine [42]. Inspired to the work of Warren for an infinite sequence of layers [43], innovative approaches have been implemented in recursive algorithms, taking a finite sequence of stacking into account. An example is represented by the *Diffax* approach [44], originally developed by Treacy et al. back in the 1990s, mostly for zeolites intergrowth, and later modified by Leoni (*Diffax+*, [45]).

Whole pattern profile matching for faulted materials has also been proposed by Tsybulya et al. [46] who recognized that, in the field of nanostructured materials, the principal limitation of the Rietveld approach lies in its fundamental assumption, which implies a 3D-ordered structural model. With a specific interest toward 1D-faulted stacking of regular, biperiodic layers, an innovative approach, based on
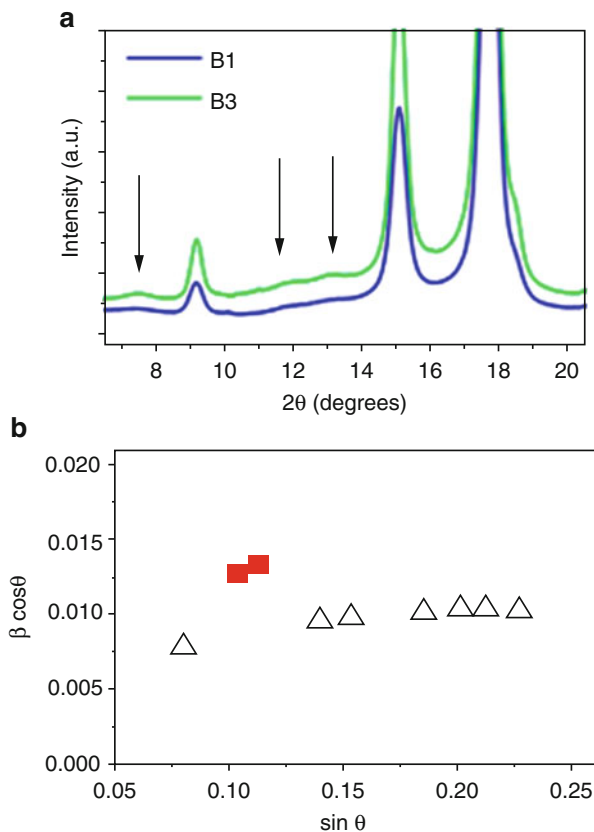
Fig. 10.7 (a) Low-angle region synchrotron XRPD data of two oxidized $Fe_{3-\delta}O_4$ nanomagnetite samples, labeled B1 and B3 in the original paper, showing very broad (110), (210), and (211) superstructure peaks (marked by the *arrows*), attributed to cation vacancies ordering. (b) Integral breadths (β) versus angle ($\sin\theta$) in the Williamson–Hall plot for B3 sample: *red* points refer to the superstructure peaks. From the $\sin\theta = 0$ intercept and the slope of the regression line on the empty triangles data, average size and strain values can easily be derived (Reprinted with permission from R. Frison, G. Cernuto, A. Cervellino, O. Zaharko, G. M. Colonna, A. Guagliardi, N. Masciocchi, *Magnetite–Maghemite Nanoparticles in the 5–15 nm Range: Correlating the Core–Shell Composition and the Surface Structure to the Magnetic Properties. A Total Scattering Study*, Chem. Mater. 2013, **25**: p. 4820–4827; Copyright 2013, American Chemical Society)

the Kakinoki–Komura theory [47], taking into account stacking probabilities of random (i.e., *uncorrelated*) faults, has been developed and implemented in a software code [48]. Examples of applications of the method include metals and alloys, layered minerals, and nanostructured carbons [49]. An alternative approach, based on the Rietveld method, has been briefly proposed by Casas–Cabanas et al. in 2006 [50], with little follow-up.

The case of *2D defects* is treated in detail in Sect. 4.2.2.

4.2   Total Scattering Methods

Total scattering methods refer to the measurement and the subsequent analysis of the complete diffraction pattern, which – in the case of imperfect crystalline materials, as NPs always are – contains (if we adopt the usual heuristic partition) both elastic scattering contributions coming from the average periodicity (Bragg scattering) and from local nonperiodic deviations from the average (diffuse elastic scattering). These methods were first routinely applied for the analysis of liquid and amorphous systems and only lately to powders of crystalline materials displaying disorder. As explained in Sect. 3.1, in nanocrystalline materials, in addition to the reduced coherent domain size, a large variety of structural defects may be observed, and therefore the application of the total scattering methods is an appropriate way to study such kind of systems disentangling the contribution of the different kinds of defects and quantifying their amount. In any experimental pattern, however, the diffuse scattering produced, by definition, by defects and disorder adds to the unavoidable background produced by the parasitic scattering (e.g., sample holder and air scattering). In the course of a total scattering analysis, it is therefore mandatory either to perform an accurate data correction in order to disentangle the sample scattering from the total observed diffraction pattern or to model and calculate the extrinsic background. For the data correction, nowadays dedicated experimental procedures and software packages have been developed to perform this task, the main ones being GudrunX and PDFGetX3 [51, 52]. Typically, in addition to the standard sample measurement, the diffraction patterns of the extrinsic background sources (e.g., sample holder, air, or when present the suspending liquid) are acquired and then subtracted from the first after properly scaling each experimental pattern for the angle-dependent absorption effects.[1] In Sect. 2.1.1, the Debye scattering equation (DSE, Eq. 10.2) was introduced; it is the basic equation of total scattering analysis and it can be derived, under the assumption described therein, by a spherical average of the coherent elastic scattering differential cross section. The DSE spans both the reciprocal (q) and, via the correlation distances $d_{ij} = |r_i - r_j|$ between the positions of the ith and jth atom, the real space (r). As it will be shown later, the correlation distances are one of the most important quantities in the total scattering analysis since they also define the pair distribution function (PDF). In this section, the two main topics of total scattering analysis will be presented: the *direct space approach* – known as PDF analysis – and the *reciprocal space approach* or DSE method. This distinction arises from the space, direct or reciprocal, in which the observed data are analyzed. In both cases, there are pros and cons which will be also discussed in the following, and, as one might expect, we suggest that, rather than alternative, they are

---

[1]To determine experimentally the absorption coefficients of the sample and sample holder, transmission measurement can be performed before or after the diffraction measurement. PDFGetX3 is quite successful, however, in performing heuristic absorption corrections avoiding those additional measurements.

complementary in that the combination of the two methods may be often the best way to get the "full" picture of real NPs.

4.2.1 Direct Space Analysis: The Pair Distribution Function

The first real space approach in crystal structure determination based on the use of the pair distribution function (PDF) was suggested by Warren in the 1930s [53], but it was only much later that the PDF analysis found its rigorous definition and almost systematic application through the work of Egami and coworkers [54].

What the PDF Is and How to Obtain It

The distribution of N point-like atoms at positions $r_j, j = 1 \ldots N$, can be described by the atomic local density function $n(r)$

$$n(\boldsymbol{r}) = \sum_{j=1}^{N} b_j \delta(\boldsymbol{r} - \boldsymbol{r_j})$$

where b_j are the atoms' scattering lengths. The autocorrelation function of $n(r)$ provides the atomic pair density function $\rho(r)$

$$\rho(\boldsymbol{r}) = \frac{1}{N} \int d\boldsymbol{r}' n(\boldsymbol{r}') n(\boldsymbol{r}' - \boldsymbol{r}) = \frac{1}{N} \sum_{i,j=1}^{N} b_i b_j \delta(\boldsymbol{r} - \boldsymbol{d_{ij}}), \quad \boldsymbol{d_{ij}} = \boldsymbol{r_i} - \boldsymbol{r_j}$$

and the latter's spherical average $\rho(r)$ is given by

$$\rho(r) = \frac{1}{4\pi r^2 N} \sum_{i,j=1}^{N} b_i b_j \delta(r - d_{ij}), \quad d_{ij} = |\boldsymbol{d_{ij}}| = |\boldsymbol{r_i} - \boldsymbol{r_j}|$$

$\rho(r)$ is the pair distribution function (PDF). The PDF is a one-dimensional function that has peaks at positions corresponding to the interatomic distances; thus, it is a histogram-like pattern that, because of the large number of atoms in the crystal, becomes a quasi-continuous distribution function. It therefore provides a very intuitive but essential picture of the structure of the material, which is independent from its ordered state. The fact that atoms (for X-rays at least) are extended objects having a (spherically isotropic) scattering length density leads to complications, however; each term $b_i b_j \delta(\boldsymbol{r} - \boldsymbol{d_{ij}})$ must be replaced by an appropriate function which is the convolution of the densities of the two atoms. This complication is not needed in the case of (elastic nuclear) neutron scattering, for instance, where the scatterers (the nuclei) extend over a few fm, which is much less than the typical diffraction wavelengths (~1 Å), while the electron cloud that scatters X-rays extends over a few Å. Each term still is a peaked function, however less sharp than a Dirac's δ. Analytically it can be very complex, much more so after spherical averaging. A successful simplification is to assume that all atomic density functions are proportional to each other, so the convolution-square profile can be factored out. Moreover, we have

to take into account the atomic thermal motion, which further spreads the atomic positions by a Gaussian function with a rms amplitude equal to that of the atomic motion. However, in reciprocal space, the picture is much simpler. In fact, the Fourier transform of $\rho(r)$ is (apart from a trivial factor) the differential cross section (cf. Eq. 10.1)

$$\int d^3r \rho(r) e^{-2\pi i q \cdot r} = \frac{1}{N} \sum_{i,j=1}^{N} f_i(q) f_j(q) T_i(q) T_j(q) o_i o_j e^{-iQ \cdot d_{ij}} = \frac{1}{N} \frac{d\sigma}{d\Omega}(Q)$$

Hereafter we will use the capital variable $Q = 2\pi q$ ($Q = |Q| = 2\pi q$) as much as possible, as it is far more popular, while keeping the lowercase variable for the Fourier transforms as they are much simpler this way. Here we have also reintroduced the Debye–Waller factors T_j and the site occupancies o_j, in agreement with Eqs. 10.1 and 10.2 (in the following, we will however assume that all the site occupancies o_j are 1 so we eliminate them). To see that the equality holds, it is sufficient to write the square modulus in Eq. 10.1 as a double sum, as here. The spherical average of the differential cross section is given in Eq. 10.2, where this operation results simply in the substitution of the complex exponential with (real) sinc functions. Now, as in Eq. 10.2, we can split the double sum in a part (*self-scattering*) containing only the terms with $i = j$ and another containing all the rest, that is,

$$\frac{1}{N} \sum_{j=1}^{N} f_j^2(Q) = \langle F^2 \rangle(Q)$$

where we emphasize that the self-scattering is just the average of the squared scattering factors. The Debye–Waller factors T_j here have been intentionally dropped, as it is correct, because no thermal motion can change the distance of one atom from itself (i.e., $d_{jj} = 0$). Now we can define the scattering function

$$S(Q) = \frac{1}{\langle f^2 \rangle(Q)} \frac{1}{N} \frac{d\sigma}{d\Omega}(Q)$$

$$= 1 + \frac{1}{N} \sum_{i \neq j=1}^{N} \frac{f_i(Q) f_j(Q)}{\langle f^2 \rangle(Q)} T_i(Q) T_j(Q) \text{sinc}(Q d_{ij}) \qquad (10.4)$$

Here, assuming that the *f*s are proportional to each other, the terms $f_i f_j / \langle f^2 \rangle$ are approximately constant (no Q dependence). So we have recovered a situation close to a set of point scatterers. The $S(Q)$ can be obtained directly from the data; the only operations needed are (a) calculating $\langle f^2 \rangle$ (easily done knowing even approximately the composition of the sample) and (b) evaluating the proper scale factor, which also can be done if the maximum experimental Q is sufficiently high so that $S(Q) \sim 1$ in the high Q part of the pattern. In fact, the nontrivial part of $S(Q)$ goes to zero at high Q because of the Debye–Waller factors, which are Gaussians. These

tasks can be entrusted to widespread programs, like the above-cited GudrunX and PDFGetX3.

Once we have the $S(Q)$, we still need to see what it corresponds to in direct space. We recall the orthogonality relationship between sinc functions:

$$\int_0^{+\infty} 4\pi q^2 dq \; \text{sinc}(2\pi qr) \, \text{sinc}\,(2\pi qr') = \frac{1}{2\pi^2} \int_0^{+\infty} Q^2 dQ \, \text{sinc}\,(Qr) \, \text{sinc}\,(Qr')$$

$$= \frac{\delta(r - r')}{4\pi r r'} \tag{10.5}$$

This is obtained recalling that $\text{sinc}(x) = \sin(x)/x$ is the spherical Bessel function of order 0, $j_0(x)$ and using the relevant relationship [55]. We can use this to transform $S(Q) - 1$ (the constant 1 would make the integral divergent). Especially, we are interested in the reduced scattering function

$$G(r) = 4\pi r \frac{1}{2\pi^2} \int_0^{+\infty} Q^2 dQ \, \text{sinc}(Qr)[S(Q) - 1]$$

$$= \frac{2}{\pi} \int_0^{+\infty} Q dQ \sin\,(Qr)[S(Q) - 1] \tag{10.6}$$

This is the most common form of the PDF as a sine-Fourier transform. Another widely used form is $g(r) = G(r)/(4\pi r n_0)$, where n_0 is simply the number density N/V, V being the volume occupied by the NP. There are still two points to be clarified:

1. In $S(Q) - 1$ (Eq. 10.4), there appear other Q-dependent factors, namely, the Debye–Waller factor products $T_i(Q)T_j(Q)$. Their effect is that, instead of a scaled Dirac's δ function as in Eq. 10.5, each sinc term results in a sharp Gaussian

$$\frac{1}{d_{ij}\sqrt{2\pi\left(\left\langle u_i^2 \right\rangle + \left\langle u_j^2 \right\rangle\right)}} \exp\left(-\frac{\left(r - d_{ij}\right)^2}{2\left(\left\langle u_i^2 \right\rangle + \left\langle u_j^2 \right\rangle\right)}\right)$$

where $<u_j^2>$ is simply the mean-square thermal oscillation amplitude of atom j. The δ peaks are hence Gaussian-broadened and their width contains information about the thermal motion amplitudes.

2. The integration cannot be extended to 0 and to $+\infty$, because of obvious experimental limitations. The most important is the truncation at the maximum experimental Q_{max} value; in fact, if $S(Q_{max})$-1 has not substantially reached its asymptotic value (0), fast truncation oscillations result that may obscure the interatomic distance peaks of $G(r)$. The same holds for the truncation at the minimum Q_{min}, with slow oscillations that do not disturb so much. Another consequence of the Q_{min} truncation is that the small-angle (SAXS) signal is almost always entirely lost. This results in a smooth negative baseline for $g(r)$ and $G(r)$ (for $g(r)$ we must subtract a correction term $\gamma_0(r)$ and accordingly a term

$4\pi r n_0 \gamma_0(r)$ to $G(r)$ [56]. This small negative baseline goes quickly to zero at large r, however, and does not hamper the PDF analysis.

The Local Structure

A consolidated trend in modern technology is pointing toward getting more and more structurally complex and/or disordered nanomaterials. Thus, in the context of the structural analysis of such systems, the expression *local structure*, which refers to the atomic neighboring environment at the length scale of nanometers or less, clearly gets its full meaning and importance. In fact, in a system with very limited size, the modification of the atomic positions and/or composition of even a small part of it is exactly what makes it functional. The structural analysis of such systems clearly cannot be performed on the simplifying assumption of an extended periodic lattice but requires a complex modeling of the many effects determined by the given structural complexity, such as surface relaxation and/or compression, atomic displacement, lattice expansion, contraction and distortion, and interface effect. The following section reports a selection of some recent results in the modeling and analysis of NP systems by the PDF analysis.

Modeling and NP Analysis

The most popular approach in the PDF analysis probably is the so-called real-space Rietveld, a full-profile fitting method analogous to the Rietveld method but where the function being fit is the PDF, nowadays integrated in well-known software like PDFfit2 and PDFgui [57]. Parameters in the structural model, and other experiment-dependent parameters, are allowed to vary until a best fit of the PDF calculated from the model and the data-derived PDF is obtained, using a least-squares approach. The structural parameters included in the PDF model are the unit cell parameters, atomic positions in the unit cell expressed in fractional coordinates, anisotropic thermal ellipsoids, and the average atomic occupancy factor for each site – thus, exactly the same as those obtained from a Rietveld analysis, but with the *local* structure, in the sense defined above, being fit as a difference, which contains information about short-range atomic correlations. The similarity of such approach with the conventional Rietveld method is also the reason of its success; in fact, if the Rietveld analysis provides evidences suggesting that a local structural distortion of the average structure exists, then it is easy to incorporate it in the PDF model and proceed with the analysis using a very similar approach, but in real space.

The "real-space Rietveld" approach was used by Michel and coworkers [58] in a highly cited work to obtain the structure of ferrihydrite, an important nanomineral component of many environmental and biological systems. They performed a PDF total scattering analysis on synthetic ferrihydrite with three distinct average coherent scattering domain sizes of about 2, 3, and 6 nm (Fhyd2, Fhyd3, and Fhyd6 samples, respectively). Using the $G(r)$ against the observed data, they refined the unit cell dimensions, atomic positions, displacement, site occupancy factors, and other model-dependent parameters, obtaining, for all the three samples, a single-phase model with the hexagonal space-group $P6_3mc$, a unit cell with average dimensions of a ~5.95 Å and c ~9.06 Å, and chemical formula $Fe_{10}O_{14}(OH)_2$. They described
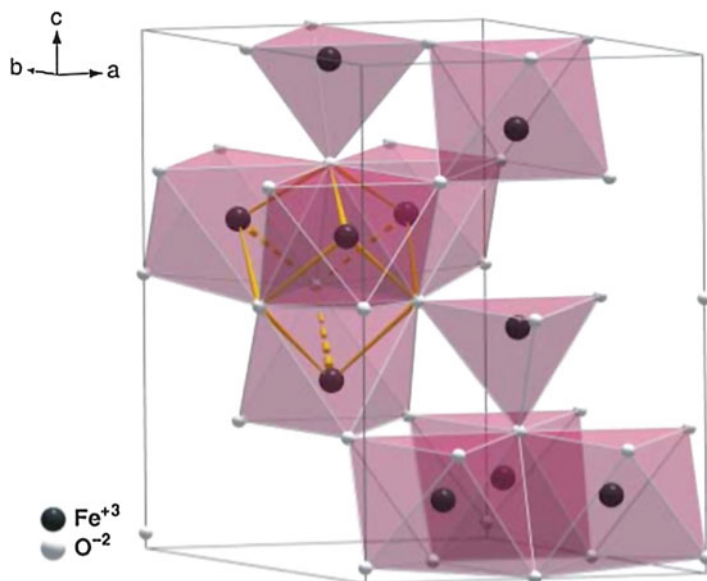
Fig. 10.8 Polyhedral representation of the hexagonal unit cell for ferrihydrite. The bonded atoms (*yellow*) define a cubane-like moiety that connects the basic structural motif of the model (Reprinted with permission from: F.M. Michel, L. Ehm, S.M. Antao, P.L. Lee, P.J. Chupas, G. Liu, D.R. Strongin, M.A.A. Schoonen, B.L Phillips, J.B. Parise, *The Structure of Ferrihydrite, a Nanocrystalline Material*, Science, 2007, **316**: p. 1726–1729, Copyright 2007, AAAS)

the ferrihydrite nanoparticles as 3D packing of clusters of 13 iron atoms and 40 oxygen atoms, with a central tetrahedrally coordinated Fe, connected by m_4-oxo bridges to 12 peripheral octahedrally coordinated Fe atoms; these are in turn arranged in edge-sharing groups of three, with adjacent clusters connected by a common pair of edge-shared octahedra, the overall arrangement creating a cubane-like moiety corresponding to four edge-shared Fe octahedra (see Fig. 10.8). Worthy of note, the proposed model has been questioned, opening a thick debate on the subject [59]. The best fit for the three datasets are shown in Fig. 10.9.

Chupas and Chapman have obtained excellent results applying the PDF method to study, in situ, several systems of high-functional relevance like TiO_2- and Al_2O_3-supported catalytic Pt NPs [60, 61], silver-containing zeolite mordenite for radiological iodine capture [62], and solid acids [63]. At the basis of their results, performed by means of synchrotron total scattering measurement, there is an extensive use of the differential-PDF (d-PDF). The idea underlying the d-PDF closely refers to the data correction mentioned in the introduction of this section, whereby the scattering signal of the support is being subtracted by the experimental total scattering pattern in order to recover the atom–atom correlations arising from the supported clusters only. To this aim, however, great care has to be taken since any changes in the structure of the support during chemical and/or thermal treatment
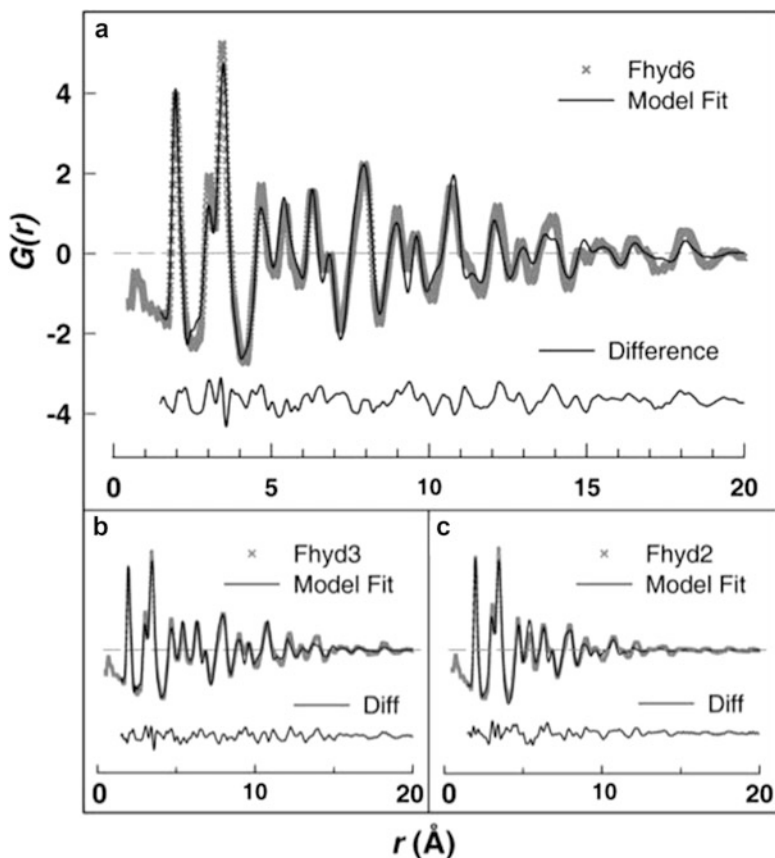
Fig. 10.9 Plots of the observed PDF G(r) (*gray line*), refined fit of the model overlaid (*solid black*) and difference up to 20 Å for each of the three samples: Fhyd6 (**a**), Fhyd3 (**b**), and Fhyd2 (**c**) (Reprinted with permission from: F.M. Michel, L. Ehm, S.M. Antao, P.L. Lee, P.J. Chupas, G. Liu, D.R. Strongin, M.A.A. Schoonen, B.L Phillips, J.B. Parise, *The Structure of Ferrihydrite, a Nanocrystalline Material*, Science, 2007, **316:** p. 1726–1729. Copyright 2007, AAAS)

need to be quantified. Thus, first the PDFs of the support samples are measured to guarantee that the support does not change during the experimental conditions and then it is subtracted from other experimental patterns acquired. Example of such d-PDF is shown in Fig. 10.10.

In Fig. 10.11, we show an example of an in situ PDF and its corresponding d-PDF, which was used by Chupas and coworkers to successfully follow the reduction or Pt^{IV} and examine the mechanism of particle formation and growth during in situ measurements [59]. However, as the authors pointed out, the weakness of this kind of PDF studies is the difficulty in analyzing particle shape and size in real samples where dispersion of particle sizes/shapes is present.
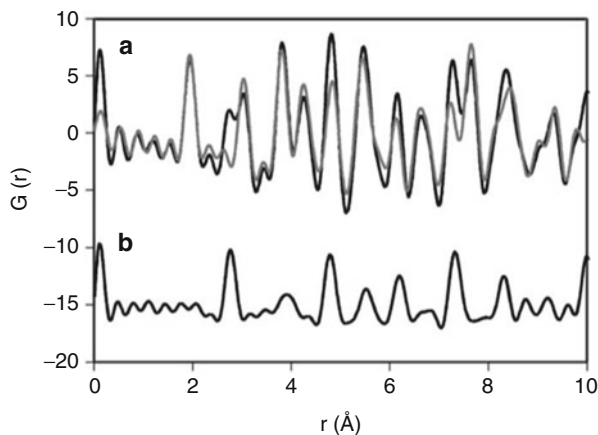
Fig. 10.10 An example of a differential-PDF approach: (**a**) measured G(r) for the TiO$_2$ support (*gray line*) and the measured G(r) for a 2.5 % Pt on TiO$_2$ calcined under a flow of 5 % H$_2$ in Ar; (**b**) the differential-PDF calculated between the two measured PDFs, [G(r) 2:5 %Pt/TiO$_2$ – G(r) TiO$_2$]; for details refer to Ref. [59] (Reprinted with permission from P. J. Chupas, K. W. Chapman, H. Chen, C. P. Grey, C. P. *Application of high-energy X-rays and Pair-Distribution-Function analysis to nano-scale structural studies in catalysis*, Catal. Today, 2009, **145**: p. 213–219, Copyright 2009, Elsevier)

In the track of PDF early studies, dedicated to truly disordered and/or noncrystalline materials, Chapman and coworkers reported [64, 65] the formation of an ordered noncrystalline phase obtained by rapid solidification of the melt Al–Fe–Si alloy studied by ex situ as well as in situ experiments. On a related subject, Doan-Nguyen and coworkers [66] investigated nickel NPs, finding that, below a certain size, the scattering signal and the resulting PDF from these systems changed from that of the bulk close-packed FCC structure to an amorphous-like scattering signal closely matching, after properly rescaling, that observed in bulk metallic glasses. However, their work presented an inception of advance use of the PDF method since they eventually calculated the G(r) from an atomistic model of icosahedral Ni particles (see Fig. 10.12) demonstrating that the calculated pattern was consistent with the observed one. Such results interestingly prove the power of the total scattering approach in modeling noncrystallographic structures even though, as stressed by the authors their selves, the PDF modeling requires samples having great structural, dimensional, and shape uniformity; otherwise sample polydispersity may limit the information available in the PDF.

A further alternative for performing a PDF analysis is shown by the work of Farrow and colleagues [67], which focused on the microstructure of CoPi and CoBi catalysts films by X-ray PDF analysis correlating then the results with catalytic activity measurements. The PDF experimental data were analyzed by means of atomistic nanoparticle models created from the CoO(OH) structure and the authors' recently developed SRREAL and SRFIT programs [68]. NP models were created using a nanoparticle template approach where a geometric shape is used to carve out
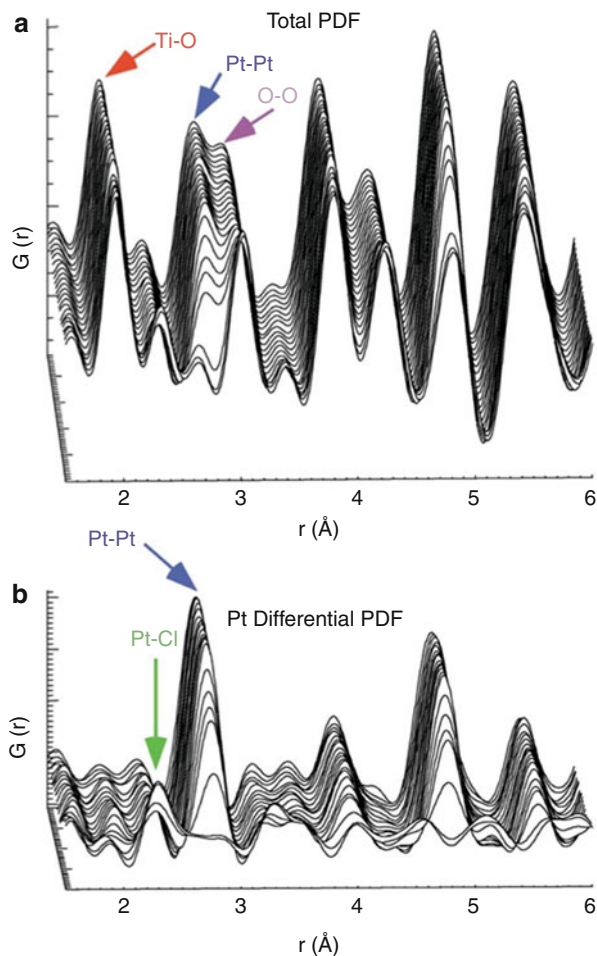
a finite-size nanoparticle model from the 3D crystal structure, thus obtaining the
control not only of the crystal structure but also of the dimensions of the nanopar-
ticle. They used a template of variable dimensions and location, with the axis of the
cylinder aligned with the c-axis of the CoO(OH) structure and performing circular
cuts in the hexagonal layers. Having the atomistic nanoparticle models, the final PDF
pattern was then calculated from the Debye pattern, thus dropping the periodic
boundary conditions used in the examples presented above and typical of many
crystallographic approaches. Figure 10.13 shows the refined PDF fits and the
extracted average models for CoBi and CoPi catalysts (grown from borate- and
phosphate-rich solutions, respectively). In particular, the CoBi model was charac-
terized by three layers and a diameter of the layers being approximately 35 Å.
Interestingly, despite the modeling allowed CoPi the flexibility to form layers, the
fit results excluded such configuration, suggesting that the coherent domains of the
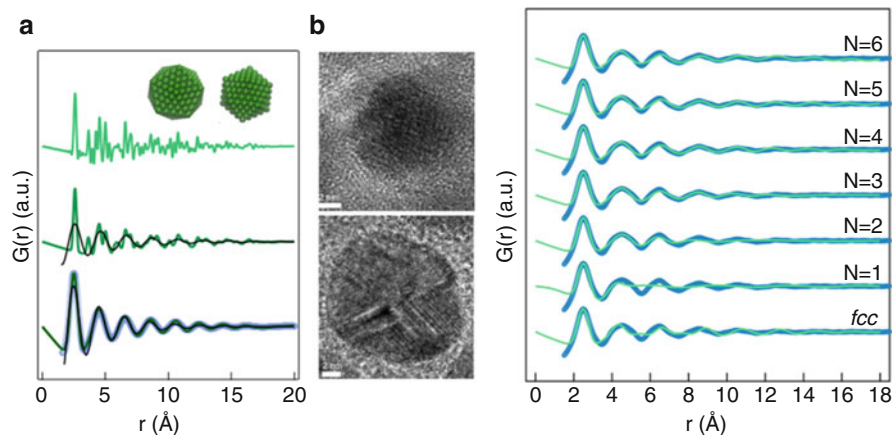
Fig. 10.12 *Left panel*: (**a**) PDFs of icosahedral models: green curves are PDFs from 309-atom icosahedral model shown in the *inset*. From top to bottom, PDFs were calculated with atomic displacement parameter of 0.001, 0.01, and 0.1 Å^2, respectively. The *black curves* are fits of a damped single-mode sine wave to the icosahedral PDFs. The *blue curve* in the bottom plot is the measured PDF from the 5 nm Ni NPs. (**b**) High-resolution TEM images of 5 nm (*top*) and 17.7 nm (*bottom*) Ni NPs note the lattice fringes, indicating the existence of twinning and local ordering within the nanostructures. *Right panel*: calculated G(r) for icosahedral clusters with increasing number of shells (N) and experimental total scattering data for 5 nm NPs (*blue*) (Reprinted with permission from V.V. Doan-Nguyen, S.A.J. Kimber, D. Pontoni, D. Reifsnyder Hickey, B.T. Diroll, X. Yang, M. Miglierini, C.B. Murray, S.J.L. Billinge, *Bulk Metallic Glass-like Scattering Signal in Small Metallic Nanoparticles,* ACS Nano, 2014, **8:** p. 6163–6170, Copyright 2014, American Chemical Society)

catalyst consist of single-layer clusters like those shown in Fig. 10.13, whose arrangements were thus disordered within the film. Finally they could prove that the dimensional reduction of cobalt oxide catalysts can extend beyond the Co oxide cluster units.

Finally, Petkov and coworkers have complemented their resonant PDF experiment on metallic nanoparticle alloys, like PtAu [69] and PtPd [70], with an extensive use of computer simulations. Even though far from being trivial, the PDF experiment are used to obtain the so-called partial PDF, that is, the PDF pattern where only the atom–atom correlations of a selected atomic species are present. Resonant PDF experiment are usually performed far above and just below the K-absorption edge of a specific element, the contribution to the total measured intensity of the selected atom being suppressed in the pattern collected below the edge. The partial PDF is then obtained after weighing two experimental atomic PDFs and taking a difference between them to eliminate particular atomic pair correlations that appear in the two PDFs but with different weight contributions. The task of extracting of a partial PDF is nowadays implemented in dedicated software, like MIXSCAT [71]. On the computational side, they strengthened their modeling, employing the Reverse Monte Carlo technique in order to access disordered atomic configurations which would be otherwise prohibited by the translational symmetry encoded in the PDFgui
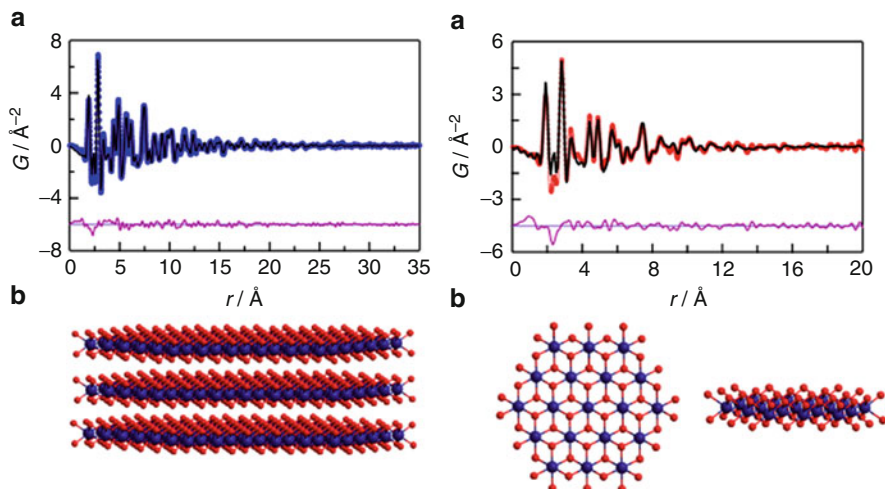
Fig. 10.13 *Left panel*: (**a**) Cylindrical atomistic model fit (*black line*) to the CoBi catalyst PDF data (*blue circles*) and difference curve (*purple*, offset for clarity). (**b**) Model for the refined average coherent domain in CoBi films. Right panel: (**a**) Cylindrical atomistic model fit (*black line*) to the CoPi catalyst PDF data (*red circles*) and difference curve (*purple*, offset for clarity). (**b**) Two views of the model for the refined average coherent domain in CoPi films (Reprinted with permission from C.L. Farrow, D.K. Bediako, Y. Surendranath, D.G. Nocera, S.J.L. Billinge, *Intermediate-Range Structure of Self-Assembled Cobalt-Based Oxygen-Evolving Catalyst*, J. Amer. Chem. Soc., 2013, **135**: p. 6403–6406, Copyright 2014, American Chemical Society)

approach. Such approach allowed them to compare different models: perfectly ordered, randomly disordered, and core–shell structure (which is a kind of partial order). Once more, however, the size and shape of the NPs were estimated by TEM analyses, whose statistical robustness, as stated in Sect. 2.1.2, is by far lower than an X-ray scattering experiment.

4.2.2 Reciprocal Space Analysis: The Debye Scattering Formula

Another way of analyzing the XRPD data within the total scattering approach is to build up an atomistic model of the NP(s) in the sample and then use the Debye scattering equation or DSE (Eq. 10.2) to calculate the XRPD diffraction pattern of the model NP system. Upon a good match with the data, one can be satisfied that the model realistically describes the sample. This method has several advantages upon the former:

1. The sample can be anything. It can contain one or more kinds of NPs, each distributed in a range of different sizes and shapes. Parameters that depend on the NP dimensions can be accounted for easily; the size dependence of lattice parameters, for instance, can only be analyzed in this way [72]. Amorphous parts can be included in the modeling too or measured separately and considered as a fractional component of the sample. This means that complex samples,

including NP polymorphs or composite and hybrid materials, which are very important for applications, can also be analyzed this way [73, 113, 120, 123], provided that the various components each leave some signature in the diffraction pattern.

2. There is no need to measure the pattern to high Q values, up to where the $S(Q)$ is already "dead," having reached its asymptotic constant value. In fact, while the high Q-tail region is very important for a successful Fourier transformation from $S(Q)$ to $G(r)$, it contains only scant information compared to that already included in the medium-Q range. The higher Q-range, as it is well known, allows for a more precise resolution of the atomic positions. Of course, there is scant need of that if the atomic positions are themselves statistically "blurred" by disorder, as it is often the case with NPs.

3. Although a proper background subtraction, including instrumental (sample container and environment scattering) and sample background (Compton, on occasion the suspension liquid), is always better, it is in principle not needed. A phenomenological modeling of the background is sufficient in many cases, at least when the background is a simple, smooth curve, easily reproduced with a polynomial of low to moderate degree.

4. The sensitivity to the NP shape and size distribution is unrivaled and has been proven in very complex cases. In fact, anisotropic Bragg peak broadening has been shown to be a very powerful and accurate method for revealing particle shape even using conventional Bragg methods [26]. The higher accuracy of DSE-based methods has broadened the horizon of size/shape analysis to include bivariate distributions and multiphase mixtures [113, 120].

Since reciprocal space modeling is more convenient from the experimental point of view, it allows for a more detailed insight into the microstructure, and especially it is suitable also for complex samples. The drawback is only one – complexity. First, building atomic-scale models of NPs is not a trivial task. Second, and more importantly, evaluating the Debye scattering equation (Eq. 10.2) where the summation extends on a number of terms that is formally equal to the *square* of the number of atoms (or the sixth power (!) of the NP diameter) is a daunting endeavor. Nowadays it can be performed also on large-scale atomic ensembles, obtained e.g., from MD simulations [74, 75]. Of course, increasing computer power [76] is a reason of this success; other reasons are algorithms that permit to pre-encode the huge interatomic distance set (growing as N^2) into a much smaller binned/sampled set that grows only as $N^{1/3}$.

Theory and Implementations in Data Analysis Software Tools

The problem of evaluating the DSE for large atomic clusters means taking into account a large number of interatomic distances and the associated scattering lengths. Of course, in situations where there is a minimum of symmetry, one expects many of the distances to be exactly the same; therefore, the distances that are equal can be taken as one and the associated scattering lengths summed. This is helpful in cases with high symmetry, but not really a solution, as the number of distances

anyway increases as N^2. However, the freely distributed software `DISCUS` [141] is able to handle small NPs in this way. The first breakthrough was in 1991 [77], when binning of the large set of interatomic distances was applied. In this case, all distances that fall in a discrete interval from $(k-1/2)\Delta$ to $(k + 1/2)\Delta$ (with k integer) are considered as one, equal to $k\Delta$, and the associated scattering lengths summed. The main advantage is that the set of interatomic distances is converted into a set of binned distances, whose cardinality grows as the NP diameter or as $N^{1/3}$ only. However, binning requires Δ to be kept very small (0.001–0.0001 Å) not to lose information. The implementation is simple, so this is the most commonly used method. For instance, the freely distributed `Debyer` (http://debyer.readthedocs.org) software package uses this method. A much better solution is to sample the 1D scattering length density $\rho(r)$. Sampling here is meant in the sense of the Whittaker–Nyquist–Kotelnikov–Shannon sampling theorem [78]. A difficulty that arises is the very large bandwidth (the domain extension of the Fourier transform) of $\rho(r)$. The bandwidth is infinity for a Dirac's δ function; even when thermal motion is accounted for and the δs are smoothed to narrow Gaussians, the bandwidth is still very large. This means using a small sampling step, even smaller than that used for binning. Cleverer – and more complex – is the convolution–sample–sharpen method [79], where a positive peaked function with positive band-limited Fourier transform (a Gaussian, most commonly) is pre-convoluted to the $\rho(r)$. The bandwidth is then reduced to that of the convoluting Gaussian, and this can be chosen to be equal or slightly larger than the bandwidth of the data (i.e., $2\,q_{max}$ or Q_{max}/π). The sampling step then can be chosen as about $\Delta = \pi/Q_{max}$, that is, the Shannon–Nyquist limit (10–20 % less is recommended for numerical reasons) which yields $\Delta \sim 0.03$–1.0 Å, as extremes, typically 0.1–0.3 Å. Finally, once the diffraction pattern of the sampled density is evaluated, it can be divided by the Fourier transform of the convoluting function – removing all effects of the convolution (dividing in reciprocal space is equivalent to deconvoluting in direct space). Note that division requires a positive Fourier transform, and this is why binning fails (the Fourier transform of a bin – a rectangle function – is not positive). The details and numerical analysis of the Gaussian sampling method can be found in [80, 81], together with a long list of early applications of the DSE method. Other very important algorithmic improvements in the evaluation of powder diffraction patterns via the DSE are:

– Exploiting lattice periodicity for crystalline NPs in order to reduce from the start the number of interatomic distances to be sampled or binned. Take a NP consisting of L lattice points, with each unit cell containing C atoms. Then we first evaluate the distinct interatomic distances between the atoms in the unit cell; these will be at most $C^2/2$, often much less depending on cell symmetry. The distances between lattice points will be at most $8\,L$ ($4\,L$ taking inversion symmetry into account), because of a fundamental property of lattices (the distance vectors between the lattice points limited by a finite region of space are just the lattice points contained in a doubly extended space region) See [80, 82] for details. At the end, we must consider only $2LC^2$ original vector distances instead of L^2C^2.

– Chemical disorder, represented as site occupancy disorder, where the probability that an atom in a given site is smaller than one, is already intrinsically implemented in the DSE (Eq. 10.2), and it is a simple matter to factor out the occupancy factors o_j. Then they can be changed and refined separately. Correlation between occupancy of neighbor sites must be taken into account separately, however, depending on the nature of the interaction. In its simple form, alternative occupation of sites that are too close together to be simultaneously occupied can be taken into account (exactly!) by lower-thresholding the interatomic distances and "shifting" those that are too short to the "self-scattering" term (see Sect. 3.2.1), omitting, of course, the sinc and T factors, as it is appropriate.

– Fast transform of a sampled scattering density having a uniform step Δ. Details are given in [79, 80]. As all fast transforms, this not only speeds up greatly the evaluation of the diffraction pattern, it is also more robust with respect to roundoff errors, a delicate argument when using Gaussian-sampled scattering densities.

– Finally, the effect of various kinds of disorder (paracrystallinity, elastic strain, stacking disorder) can be much more efficiently represented in correlation space instead of configuration space. In fact, disorder is stochastic in nature. Powder diffraction gives the average diffraction pattern of a huge number of NPs, and each of them will have a different atomic configuration (even assuming that they have the same size and shape to begin with!). Therefore, modeling disorder in configuration space means considering a vast number of configurations (large enough to be representative) and repeating the DSE calculation as many times. Instead, one can work in correlation space. In a (nano)crystal, each of the d_{ij} interatomic distance vectors will be found exactly identical in very many copies. Disorder will change the "exactly identical" to "approximately equal." If the spread is not large, the set of approximately equal vectors can be represented by a (generally anisotropic) Gaussian distribution, whose first and second 3D moments coincide with the original distribution. Therefore, only one distance again needs to be considered. The Gaussian broadening (or its 1D equivalent after spherical averaging that must be evaluated numerically – but this is a small burden) can be then introduced in the DSE in a way that is similar to the Debye–Waller factors. The main difference to that case is that the Gaussian variance will be a function of d. This would lead to any sort of complications, except that in the Gaussian sampling method, we already broaden every distance d – the length of each vector d – by a Gaussian of fixed variance; it is simple then to add the intrinsic (disorder-related) variance to the fixed sampling variance and obtain a sampled set that already contains disorder. Of course, evaluating the intrinsic variance for each d vector slows slightly the generation of the sampled scattering distribution, but it is still extremely faster than considering a large (and statistically representative) number of starting configurations. This trick works with paracrystallinity [83] (even strongly anisotropic [84]) and microstrain [82, 85]. For stacking disorder [82], similar tricks are known, as the probability of finding two crystal planes of specified types at any given separation can be calculated, and then the interplanar interatomic distances can be evaluated and

averaged using the computed probabilities between the possible different pairs of planes. Note also that the intraplanar interatomic distances need not be computed more than once. Again, as before, a slightly more complex calculation involving a single-disordered cluster replaces the necessity of averaging over a huge number of configurations.

Debussy [71] is the only available DSE software packages that implements all of these algorithmic improvements (or shall do so in the forthcoming version 2.0). It is because of these accelerations that it can be used to compose a diffraction pattern as a sum of several thousands of separate NP patterns. Many of those (those corresponding to a single phase) are separately summed according to a parametrized uni- or bivariate size distribution, where also the lattice parameter, Debye–Waller factors, and site occupancies are left free to vary, depending on particle size/shape according to a specified (parametrized) law. Disorder (anisotropic paracrystallinity, soon stacking disorder) is also implemented, although at the Gaussian sampling stage, so without the possibility of parametrization and refinement while fitting the observed pattern. The resulting summed patterns, together with calculated and separately measured background components, are then scaled together to fit the observed data using SVD, which is extremely precise and robust. All this can be cyclically repeated within a suitable refinement algorithm, optimizing the parameters governing the size/shape distribution of each separate phase and the related lattice parameter, occupancy, and size-dependent laws. In the next section, we will exemplify those unique capabilities.

Characterization of Different Classes of Materials and Complex Systems

Most of the recent pertinent literature reports on the Debye function analysis of noble metals and semiconductors, in the characterization of small defective nanoparticles investigation [86–91] and metal-supported catalysts [92], and for the advanced modeling of specific structural defects (see the next paragraph). Very few are the examples in which DFA has been the main characterization tool for a more complete analysis. However, DFA is a highly versatile approach, which has been successfully applied by us to characterize different classes of nanosized materials, each of them showing its own level of complexity. Cases of application refer to metals, oxides, ceramics, organic compounds, and metal-organic polymers; the investigated systems include single or multiple phases and complex nanocomposites. The characterization typically enabled a multiple scale study providing quantitative (sample volume-averaged) information on (i) the crystal structure (atomic arrangement, defects and strain, at the atomic scale), (ii) the NP size and shape and their distributions (nanometer scale), and (iii) the composition (phase amount and NP stoichiometry). In the systems we have investigated, the extracted values have played an important role in the interpretation of the material functional properties. This paragraph is dedicated to the presentation of some paradigmatic cases; additional examples can be found in Refs. [93–95]. All the experimental data used in the applications here presented, unless differently specified, underwent the data treatment procedure described in Sect. 3.2 before the

complete DFA was performed. Therefore, patterns were corrected for (angle-dependent) offsets and absorption effects, and extra-sample scattering contributions were subtracted. Unless differently specified, a pattern modeling free of any phenomenological component was also carried out.

Characterization of Magnetite–Maghemite Core–Shell NPs in the 5–15 nm Size Regime Thanks to their peculiar magnetic properties, iron oxide NPs are materials of great interest in many technological (high-density storage media, ferrofluids, electronic devices, catalysis) and biomedical applications (magnetic resonance imaging, hyperthermia, targeted drug delivery) [96, 97]. We focused our interest on Fe_3O_4 (magnetite) NPs and on its oxidized counterpart, γ-Fe_2O_3 or, equivalently, $Fe_{2.67}O_4$ (maghemite), whose super-paramagnetic properties originate from a rather complex interplay of structural, compositional, and surface effects, depending on both NP size and oxidation state. In order to facilitate the comprehension of the DFA on these nanomaterials, it is useful to briefly describe the main features of their crystal structures. Magnetite shows an inverse spinel structure (*Fd-3m*) in which oxygen atoms (Wyckoff position 32*e*) form a closed-packed cubic lattice, Fe^{3+} ions (Wyckoff position 8*a*) are located in the tetrahedral sites, and a 1:1 mix of Fe^{2+} and Fe^{3+} ions (Wyckoff position 16*d*) fill the octahedral sites. The easy oxidation of Fe^{2+} in air is well known to cause (i) iron diffusion outwards (leaving vacant sites in the crystal lattice); (ii) lattice parameter contraction ($a_{\text{Magnetite}} = 8.3967(3)$ Å [98], shrinks to $a_{\text{Maghemite}} = 8.3457(-)$ Å [99]), and (iii) formation of nonstoichiometric magnetite–maghemite core–shell NPs ($Fe_{3-\delta}O_4$, $\delta < 1/3$), or of pure maghemite ($\delta = 1/3$), as a consequence of partial and complete oxidation, respectively. Moreover, iron vacancies can either be randomly distributed, without any change of the starting crystal space group, or partially/totally ordered; in these cases, the space-group transforms into cubic $P4_132$ [100] or tetragonal $P4_12_12$ [101]. Within such a framework, the physicochemical characterization of these NPs and the correct assessment of the core–shell magnetite–maghemite composition is not an easy task. Indeed, a combination of complementary techniques, typically including XRPD (structure and phase purity), TEM (NP size distribution), and Mössbauer or other spectroscopies (sample oxidation state) is commonly used. Our DFA [16, 102] was applied to a large set of samples prepared according to suitable modifications of the coprecipitation protocol [103] and under a variety of synthetic conditions (concentration, pH, T, oxygen-rich or oxygen-free environments). Synchrotron X-ray scattering data were collected at the X04SA-MS beamline of SLS, in Debye–Scherrer geometry, using the beam energy of 15 and 16 keV and 0.3 mm glass capillaries. The DFA of these materials has been addressed to two main goals: (a) simultaneously characterizing the iron oxide NPs in terms of structure, stoichiometry, core–shell composition, average size, and size distribution, all within an organic framework. Such a characterization was then used to correlate structural and microstructural sample properties to their magnetic behavior; (b) predicting NP size and stoichiometry effects on lattice parameter variations. This study enabled us to derive, within reasonable approximations, a global law that might be applied to similar systems.

The pattern modeling was performed by applying the two-stage strategy of the Debussy Suite and three main computational steps: (1) atomistic models of pure Fe_3O_4 nanocrystals of spherical shape were generated ending up with the sampled interatomic distances of a discrete population of NPs of increasing size, Δr of subsequent spheres being equal to ≈ 0.33 nm; (2) pattern simulations were calculated by assuming a lognormal size-distribution function with adjustable average size ($<D>$) and width (σ), a size dependence for the lattice parameter, atomic Debye–Waller factors, and *sof* of Fe in the octahedral site [Fe(oct)]; (3) model parameters were optimized through the simplex method [104]. Adopting the lognormal function is justified by experimental observations and many theoretical models; using a single lattice parameter for a core–shell NP is, in this case, an acceptable approximation, thanks to the close similarity of either the end-member lattice values or their bulk moduli, as also confirmed by the lack of evident peak broadening attributable to strain. Despite the very close similarity of magnetite and cubic maghemite in terms of crystal structures and lattice parameters, and the peak broadening due to the very small crystal domains, the total scattering approach and the DFA, for the first time applied to this kind of iron oxide NPs, allowed many relevant results to be achieved. Among these, both the number-based and the mass-based NP size and size distribution are derived, whose average values may show a large discrepancy when sizes are broadly distributed, as in our samples (showing a monodispersity index $\sigma_M / <D>_M$ in the 0.3–0.5 range – Fig. 10.14, panel D – and $<D>_M \approx 1.7 <D>_N$). This is an important issue when NP size is to be correlated to volume-based magnetic properties. During the analysis, a (never detected before) lattice expansion emerged in the majority of the samples upon decreasing the crystal domain size below 5 nm (magenta curve in Fig. 10.13, panel A) while simultaneously the Fe(oct) *sof* undergoes a progressive decrease due to the NP oxidation (green curve in Fig. 10.14, panel A), according to which a lattice contraction is expected. The lattice expansion is therefore attributed to surface relaxation effects, a phenomenon that will be later discussed. However, it does not influence too much the *average* lattice parameters which, indeed, show a very good linear mutual correlation with the sample stoichiometry ($<3-\delta>$) calculated from the Fe(oct) *sof* values (Fig. 10.14, panel C) and spanning from pure maghemite [$<3-\delta> = 2.675(4)$] to barely oxidized magnetite [$<3-\delta> = 2.988(6)$]. Moreover, adopting an idealized model with a uniformly oxidized shell (i.e., neglecting any compositional gradient), both the average and the size-dependent core–shell composition of all investigated samples have been determined in terms of R_{core} and R_{shell} (Fig. 10.14, panel E). These values play an important role in the interpretation of the magnetic properties, which were explored in samples showing low (C3), medium (B9), and high (B1, B3, B10, and B11) oxidation levels and, for the B subset, a rather similar size ($<D>_M \approx 10$ nm).

The magnetization (M) curves versus applied field (H) at 2 and 300 K are shown for the 10 nm-sized B9 and the 20 nm-sized C3 samples in Fig. 10.15 (panel A), both approaching at 2K the saturation magnetization (M_s) of bulk magnetite M_{sB} ~92 emu/g. Zero-field-cooled and field-cooled (ZFC, FC) magnetization curves, obtained as a function of the temperature (2–300 K) at the applied field
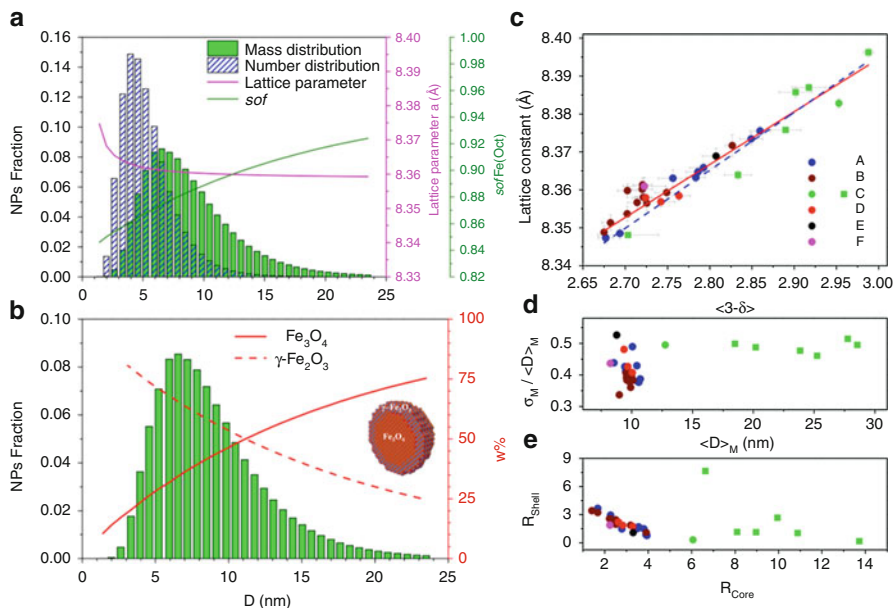
Fig. 10.14 (**a**) Number- and mass-based frequency distributions (*shaded* and *solid* histograms, respectively) for a selected sample of magnetic iron oxide nanoparticles. *Green* and *magenta lines* represent the dependence of the octahedral Fe site occupancy factor and a_0 lattice parameter on NP size, respectively. (**b**) For the same sample shown in (**a**), the *red curves* indicate the weight % partitioning of the core (magnetitic) and shell (maghemitic) regions versus NP size (*continuous* and *dashed lines*, respectively). In both **a** and **b** panels, the abscissa is the NP diameter, in nm. (**c**) Linear correlation (*red line*) of the average lattice parameters with the sample stoichiometry ($<3−δ>$), calculated from the Fe(oct) *sof* values and spanning from pure maghemite [$<3−δ> = 2.675(4)$] to barely oxidized magnetite [$<3−δ> = 2.988(6)$]; the *blue dashed line* refers to the subset of NPs with sizes above 10 nm. For the meaning of the A to F labels (referring to different groups of materials), see the original paper [101]. (**d**) Plot of the monodispersity index of the different samples versus NP size. (**e**) Size-dependent core–shell composition of all investigated samples in terms of R_{shell} versus R_{core} correlation (Reprinted with permission from: R. Frison, G. Cernuto, A. Cervellino, O. Zaharko, G. M. Colonna, A. Guagliardi, N. Masciocchi, *Magnetite − Maghemite Nanoparticles in the 5–15 nm Range: Correlating the Core − Shell Composition and the Surface Structure to the Magnetic Properties. A Total Scattering Study*, Chem. Mater. 2013, **25**: p. 4820–4827; Copyright 2013, American Chemical Society)

$H = 200$ Oe, are shown in panel B and clearly indicate that the broadness of the maxima of the ZFC curves strongly depend on the sample average particle size and the degree of polydispersity (these values are also reported in the Table, in Fig. 10.15). Interestingly, the NP core diameter provided by DFA well matches the diameter of magnetic domains ($<D>_{Mag}$), independently derived from the magnetization curves through Chantrell's equations [105] (see Table in Fig. 10.15), highlighting a prevailing role of the magnetite core in determining the NP magnetization. Such a hypothesis is further supported by two additional results: (i) the dependence of M_s on increasing the thickness of the oxidized shell for samples

Fig. 10.15 (**a**) *Left*: the magnetization (M) versus applied field (H) at 2 and 300 K for two selected magnetic iron oxide NPs (B9, 10 nm and C3, 20 nm). *Right*: Field- and zero-field-cooled temperature-dependent magnetization curves for samples of different size and nature (detailed in

having similar average size and different R_{core}/R_{shell} ratio (Fig. 10.15, panel B) and (ii) the observation of very broad "superstructure" peaks in the diffraction pattern of many samples, which reveal a partial ordering of the Fe ion vacancies in the oxidized shell and suggest the occurrence of smaller coherent domains forming a polycrystalline layer at the NP surface. Such a "fragmented" maghemite shell (possessing a partial structural order), never detected – to the best of our knowledge – on samples oxidized at room temperature (as in this case), might explain its negligible contribution to the magnetization of the investigated samples. As a final remark of this brief description of structure–property correlations, an additional advantage provided by the DFA characterization is the possibility of estimating an "effective" magnetic anisotropy constant, typically taken as $K_M = 25$ k_B T_B/V (k_B is the Boltzmann constant, T_B the blocking temperature, and V the NP volume). This relation is valid for a collection of NPs within an ideally perfect monodisperse sample [106]. However, since our samples show relatively broad particle size distributions, we modified it to include the complete mass-based size distribution of a collection of spherical NPs (as provided by DFA) and evaluated the magnetic anisotropy constant K'_M. The reader can appreciate the two sets of values in the Table of Fig. 10.2 and refer to the original paper for more details.

To complete this paragraph dedicated to the DFA of iron oxide NPs, we present an overall general law, with a single adjustable parameter (Ω):

$$a = \left[(1 - x)a_{\text{Maghemite}} + x\, a_{\text{Magnetite}}\right]\left(1 - \frac{\Omega}{D}\right)$$

where $\Omega = 4\gamma/(3B)$, γ is the surface tension, B the bulk modulus, and $x = 3(<3-\delta> - 8)$ ($x = 0$ for maghemite and $x = 1$ for magnetite). This law has been derived from the entire ensemble of NPs, under the main assumption that the surface conditions of *all* particles in *all* samples are identical. In such a case, the lattice parameter variations due to stoichiometry and to particle size can be usefully combined, taking into account the interplay between bulk elastic energy and surface tension [107]. The derivation of the law, as detailed in the original paper [16], relies on the following additional assumptions: (1) the magnetite–maghemite system can be considered an ideal solid solution (Vegard's law); (2) each nanocrystal behaves as an isotropic medium, which makes the uniform isotropic strain a scalar parameter;

Fig. 10.15 (continued) the *bottom panel*). (**b**) Dependence of the saturation magnetization versus the R_{shell}/R ratio. In the top insert, the experimental detection of broad superstructure diffraction peaks, indicative of partial vacancy ordering; in the bottom one, the R_{core}/R_{shell} versus R trend for the various samples described in the *bottom panel*. Here, different physicochemical parameters of the studied materials are synoptically collected (Reprinted with permission from: R. Frison, G. Cernuto, A. Cervellino, O. Zaharko, G. M. Colonna, A. Guagliardi, N. Masciocchi, *Magnetite − Maghemite Nanoparticles in the 5–15 nm Range: Correlating the Core − Shell Composition and the Surface Structure to the Magnetic Properties. A Total Scattering Study*, Chem. Mater. 2013, **25:** p. 4820–4827; Copyright 2013, American Chemical Society)

(3) Ω does not change with respect to x (this assumption is largely justified by the similarity of the bulk moduli (B): 186 GPa for magnetite [108] and 203 GPa for maghemite [109]). Worthy of note, this law predicts *an inflation* of the cell parameter upon decreasing the NP size while keeping constant the oxidation degree. According to Ref. [106], this is a common behavior for oxides, meaning that the surface tension must be *negative*.

Investigating the Role of Citrate in Biomimetic Apatite Nanoparticles Biomineralization is the very complex process by which living organisms assemble organic–inorganic composites, typically forming structures with hierarchical organizations able to show exceptional functional properties and aptitude to adaptation [110]. Bone is one of the most representative systems in which the organic matrix of collagen microfibrils (alternating the so-called overlap and gap zones) acts as a template where the deposition of the mineralized component (a nanosized and defective hydroxyl calcium phosphate) takes place. Intrafibrillar mineralization is thought to form from an amorphous precursor (spherical nanoparticles are commonly reported), infiltrating the gap region and subsequently transforming into thin platelets of nanometer sized nonstoichiometric apatite crystals [111, 112]. However, the comprehension of the mechanisms enabling the strict control over these minerals in terms of structure, composition, growth, and morphology are still far from being clearly understood. On this side, there is a great deal of interest for the relevance both on the fundamental knowledge and as source of inspiration for preparing biomimetic materials with advanced biomedical applications. One of the open debates concerns the role of either non-collagenous proteins or small molecules such as citrate. In a recent solid-state NMR study, citrate has been estimated to amount about 5.5 wt% of the total organic component and to play the role of stabilizing the thickness and the morphology of apatite platelets, through hydroxyl citrate groups strongly binding to Ca^{2+} ions on (10–10) crystal facets [113]. However, considering the hexagonal symmetry of the apatite crystal structure, citrate molecules cannot induce the peculiar platy morphology of bone apatite (which develops parallel to the hexagonal axis rather than orthogonal to it, as one would expect). We therefore investigated citrate-bio-inspired apatite NPs, precipitated at increasing maturation times (5 min, 4 h, and 96 h), by ex situ X-ray total scattering modeling and quantitatively characterized the NCs in terms of structure, composition, size, and morphology [114]. We also cross coupled the DFA results on the size and shape of crystal domains with those obtained by atomic force microscopy (AFM), i.e., we used a microscopic technique whose nanometer length scale resolution disregards the NP crystalline or amorphous nature. The goal of this combination was to reconstruct the ACP-to-apatite transformation process at molecular scale resolution and to disclose a plausible mechanism inducing the platy morphology of crystals.

Synchrotron X-ray scattering data (collected at the X04SA-MS of SLS using a beam energy of 16 KeV and 0.5 mm glass capillaries) were processed by the DFA, adopting a three-component model: the crystal structure of calcium-deficient hydroxyapatite (CDHA) [115] was used to generate two distinct bivariate

populations of nanocrystals, having hexagonal (Hex) and platy morphologies (Fig. 10.16, panel A), and the experimental pattern of an amorphous (ACP) powder was added to the pattern model to account for this additional component (the blue trace in the best fit shown in Fig. 10.16, panel B). To best match the experimental data, a number of adjustable parameters were involved in the pattern model. In particular, the size and shape distributions of the bivariate population of CDHA nanocrystals were modeled through the bivariate lognormal function with five adjustable parameters (the average/standard deviation pairs of the size distributions along two growth directions and their correlation angle); among the structural parameters, we refined the atomic site occupancy factors of the two Ca and the hydroxyl O atoms and all the isotropic atomic Debye − Waller factors, while, to limit the number of parameters, those of the phosphate O atoms were constrained to the same value.

From a modeling point of view, it is useful for the reader to have more details about how we managed the platy morphology without introducing a trivariate size-distribution function, which in itself is too complex to be extracted from even the best possible diffraction data. We firstly generated the population of hexagonal prisms through a layer-by-layer construction and under the assumption of two independent "growth" directions, one along the sixfold symmetry c-axis and the second one in the orthogonal ab plane, up to 15 nm in ab and 50 nm along c. In order to deal with the platy CDHA shapes, *bivariate* populations, addressed by L_c along c, and, in ab, by anisotropic parallelogram-shaped bases with fixed 1:2 a/b ratio, were built. These populations were used *together* with the hexagonal base prisms previously defined and constrained to the same NC size distribution and stoichiometry values, in a *biphasic* (crystalline) pattern model. Such a combination of hexagonal and platy shapes is a way to approximate a trivariate size distribution through estimation of the shape anisotropy of the ab-base (in addition to the anisotropy due to the crystal elongation in the c-axis direction), without introducing too many unnecessary parameters. Such anisotropy can be measured by the ratio A of the base polygon principal inertia moments (in our model, A = 1 for the hexagonal base, A = 6.17 for the platelet base). Since this measure is linear in the mass fraction, an effective average base anisotropy <A> was derived through the mass fractions of the two populations, hexagonal and platelet (normalized to the total crystalline components, which differ only for the anisotropy of the ab-base shape). Therefore, mass fractions % reported in the table of Fig. 10.16 also contain information about the degree of anisotropy in the ab plane (the corresponding values of the <A> parameter range between 2.6 and 5.8 for the subset of carbonated apatite samples – cAp – here shown).

For the investigated samples, the DFA provided the following: (i) the relative abundance of ACP and hexagonal-/platy-shaped CDHA (table of Fig. 10.16), which are detected as distinct components at each maturation time; (ii) the bivariate size-distribution maps (Fig. 10.17) and the average crystal size and shape (Fig. 10.16, panels C and D); (iii) the (size-dependent) site occupancy and Debye–Waller factors
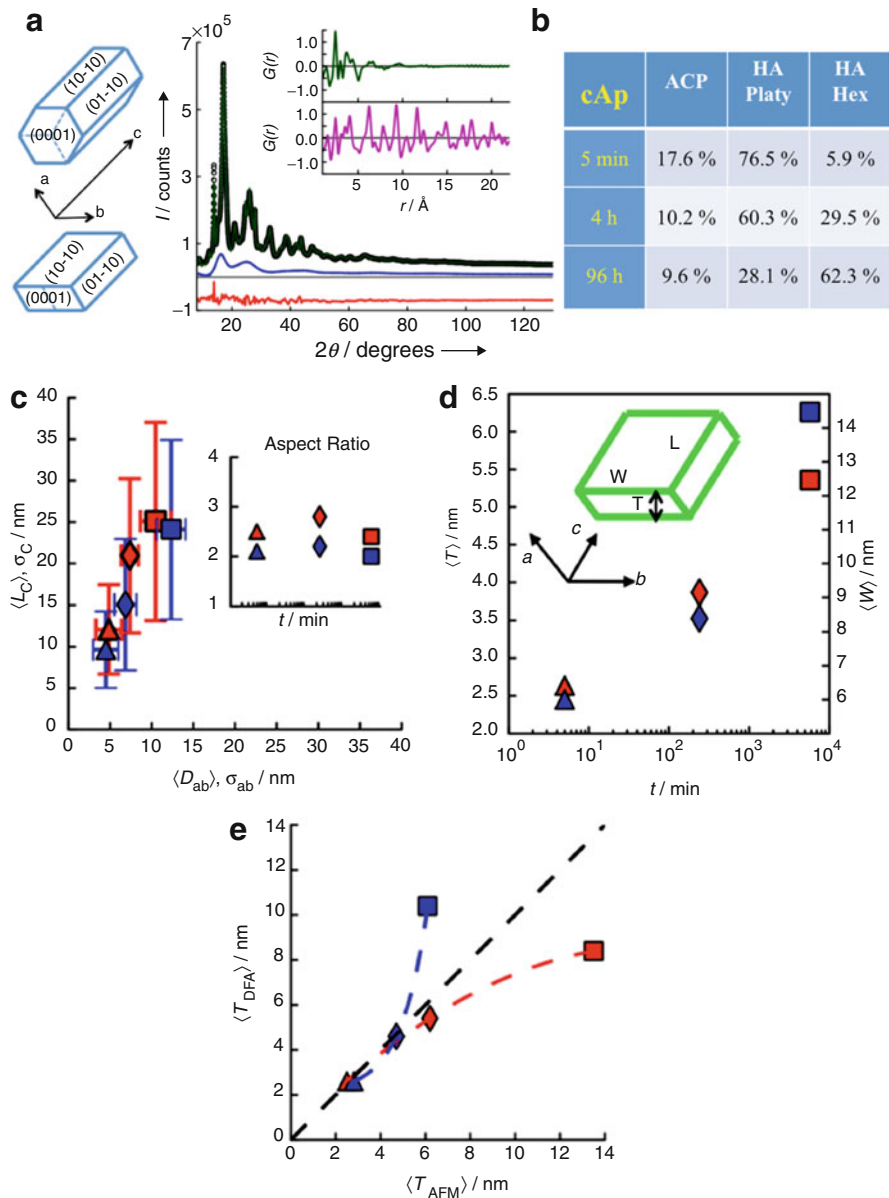
Fig. 10.16 (**a**) Ideal shape of hexagonal and platy CDHA NPs, with reference axes and face indexing. (**b**) An example of the DFA best fit of the observed data by a sum of two nanocrystalline (hex- and platy) phases and of the ACP component (*blue trace*); the wavy *red trace* at the bottom is the difference plot. In the insert, the *real-space* G(r) functions calculated for the ACP (*top*) and mature CDHA (*bottom*) samples show clear similarities at low r values. The table in the *top-right*
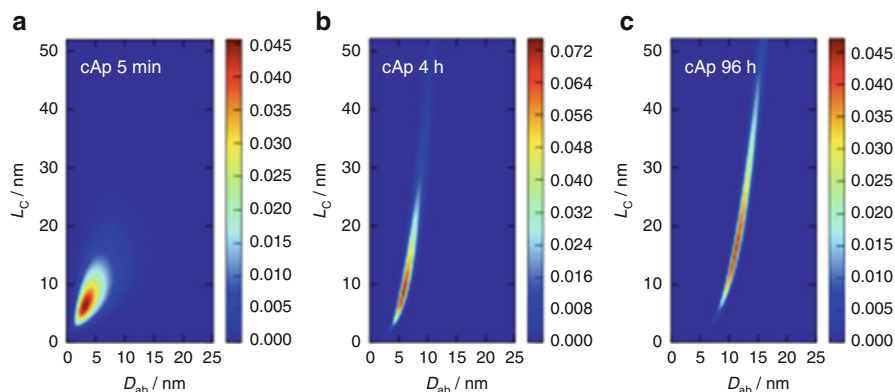
Fig. 10.17 Two-dimensional maps illustrating the number-based frequency distribution of the NP size and shapes of three carbonated hydroxyapatites recovered at different maturation times. The peak heights are shown by the color-code bars at the *right*. A bivariate lognormal distribution, including a correlation angle term between the two normal growth directions (*c* and *ab*), has been assumed

of CDHA Ca and hydroxyl O atoms (the Ca/P ratio controls the NP dissolution properties; see [116] and the original paper [113] for more details), and (iv) the citrate surface density. Looking at the evolution of the samples with the precipitation time, DFA results indicate, after 5 min, a nonnegligible amount of ACP (ca. 18 wt%) coexisting with a majority of tiny, platy CDHA crystalline domains, ca. 2.5 nm thick, 6.0 nm wide, and 9.6 nm long. Upon maturation, larger crystals of preferential hexagonal shape develop, while the content of ACP progressively decreases. Moreover, apatite crystals show also the tendency to become more stoichiometric. Interestingly, all samples show a broad distribution of crystal lengths along the *c*-axis, while they are narrowly distributed in the *ab* plane (Fig. 10.17c). Such a finding agrees well with the mechanism, hypothesized in bone mineralization, of citrate molecules stabilizing the apatite crystals thickness. Moreover, the citrate surface density of 1 molecule/$(n \text{ nm})^2$ was estimated, with $1.6 < n < 2.0$, very close to the value previously reported for avian and bovine bone [112].

←

Fig. 10.16 (continued) location contains the DFA quantitative estimates of the weight fractions in the carbonated CDHA samples. (**c**) Size estimates of the hex- component (bars refer to the width of the lognormal distribution, and not to the statistical errors) of the six samples characterized in [113]: $<L_c>$ is average length along c, $<D_{ab}>$ is the diameter of the equivalent circle in the *ab* plane. The insert summarizes the aspect ratios $<L_c>/<D_{ab}>$. (**d**) Maturation time dependence of the average thickness, $<T>$, of the platy NPs. (**e**) Correlation between NP thicknesses measured by DFA and AFM experiments

Even more interesting is the comparison between DFA and AFM results. AFM analysis shows that unusual tiny platelets form at the earliest stages of precipitation, amorphous in nature, as witnessed by the ACP diffraction trace in Fig. 10.16b. The coherence length of these NPs was estimated by the reduced G(r) function (shown in the inset of Fig. 10.16b, green top curve) and well matches the slightly polydisperse ACP NP thicknesses of 1.1 ± 0.5 nm measured by AFM. On increasing the maturation time, NPs appear in the AFM images (not shown here) as thicker but still platy NPs. Unexpected results were obtained when we compared the average thickness (T_{DFA}), width (W_{DFA}), and length (L_{DFA}) of *crystal domains* provided by DFA and those determined by AFM. The inset of Fig. 10.16, D, clarifies how thickness (T), width (W), and length (L) are assigned to the platelets (either crystals or NPs) and the mutual orientation of crystallographic axes and NP surface. Importantly, crystal thickness systematically fits that of NPs ($T_{DFA} \approx T_{AFM}$) until 4 h maturation (Fig. 10.16e), while width and length are systematically smaller in crystals than in NPs (not shown here). Therefore, at low and medium maturation time, the NPs *must be* single-crystal domains along T_{AFM} and multiple crystal domains along W_{AFM} and L_{AFM}. Moreover, the coincidence of T_{DFA} and T_{AFM} (the shortest sizes) indicates that crystals are oriented with their (10–10) plane parallel to the NP surface imaged by AFM (compare Fig. 10.16a). Therefore, assuming that crystal nuclei start to form within platy amorphous NPs, the results found in this study enabled us to infer the anisotropic growth of apatite along the crystallographic *a*- and *b*-axes (breaking the hexagonal symmetry and giving rise to platy crystals). Indeed, the growth is expected to stop in one direction, because of the finite thickness of the parent amorphous platelets (T_{AFM}) and the further binding of citrate on the surface, but to freely continue in the other directions within each NP, therefore increasing W_{DFA} and L_{DFA}. A more detailed description of a plausible mechanism inducing the platy morphology in bio-inspired apatite NCs can be found in the original paper. It shows, for the first time, the role of citrate in driving the formation of platy apatite NCs similar to those formed in bone under the control of acidic non-collagenous proteins, collagen fibrils, and, likely, citrate molecules.

Size and Shape Dependence of the Photocatalytic Activity of TiO_2 Nanocrystals The excellent photochemical activity of nanosized titanium dioxide crystals have attracted the interest of many for their potential applications in fields such as solar-energy capture, air and water pollutant decontamination, water-splitting reactions, and fabrication of smart textiles [117–119]. Many investigations have been addressed to clarify the dependence of the functional properties on the occurring polymorphs (anatase, rutile, and brookite) or on a mixture thereof, on the particle size and shape, and on the structural defects. In particular, structural and morphological anisotropy of nanocrystalline TiO_2 seems to deeply affect the local stereochemistry of the surface atoms and the development of defects and, therefore, to determine the optical bandgap value and the efficiency of charge separation and migration. In this view, TEM/HRTEM techniques are commonly applied to get

information about the particle shape and aspect ratio. However, the complete understanding of the structure–property relationship of this material seems not to be fully achieved [120]. In this study [121], the DFA approach has been used to quantitatively characterize a number of TiO_2 samples containing very small aniso-tropically shaped nanocrystals (NCs, with average sizes well below 10 nm) and to correlate the photocatalytic activity with both the average size and NCs aspect ratio, simultaneously derived within the coherent framework of the total scattering DFA characterization. Samples were prepared by the sol–gel route, employing different conditions for the A and C (acidic, HCl and CH_3COOH, respectively) subgroups and for the B (basic, NaOH) specimens (see the original paper for details). Since our interest in titania nanoparticles dealt with the appealing goal of tailoring suitable coatings for smart textiles, all preparations were carried out by keeping the temperature low enough to grant the formation of very small (still active) materials, while any heat treatment (which is well known to increase crystal size, crystal perfection, and photocatalytic activity) was deliberately avoided. Data were collected at rt at the X04SA Material Science Beamline at SLS, Paul Scherrer Institut, using a 0.3 mm glass capillaries and a 0.620639 Å X-ray beam. Differently from the previous cases, scattering signals from the empty glass capillary and from air were added to the model pattern and suitably scaled to the experimental trace rather than being subtracted.

All TiO_2 samples showed the evident trace of nanocrystalline anatase and, in the A- and B-type samples, a small amount of brookite (already evidenced by others in analogous preparations). Accordingly, bivariate sets of atomistic clusters of increasing size were created for anatase (sizes up 15 nm in the *ab* plane and 30 nm along the *c*-axis) and for brookite (up to 6 and 10 nm in *ab* and along *c*, respectively). Due to the importance, in this study, of the NCs aspect ratio, it is worth noting that the choice of prismatic crystals approximated by a simple square prism, although each NCs in our samples is expected to have its own shape, is justified by two main reasons: (1) the level of shape information that can reliably be extracted – as a statistical distribution – is the prism aspect ratio, as long as the principal axes of the base remain comparable, and finer details are likely lost in the experimental trace and (2) the crystal symmetry. For anatase (in agreement with the space-group $I4_1/amd$ and a recent report on NCs shape different from the bipyramidal morphology of macroscopic crystals), the chosen polyhedron might not be very far from reality. For brookite, the orthorhombic space group (*Pbca*) suggested us to use a trick: we permuted the axes of the ICSD entry 36408, in order to have **c** as the longest axis and **a** and **b** of nearly equal lengths, further treated by a common growth parameter to match the bivariate size-distribution model.

The most relevant findings of this analysis are summarized in Fig. 10.18. The best fit in panel **a** and the 2D maps of the bivariate lognormal size distribution (panels **b** and **c**) for the two polymorphs refer to the sample B1. The molar fraction (χ) of brookite was estimated in the 20–32 % range, when present. These values were used to normalize the sample photocatalytic activity (k, i.e., the kinetic constant of methylene blue degradation, in the first-order approximation) by assuming anatase
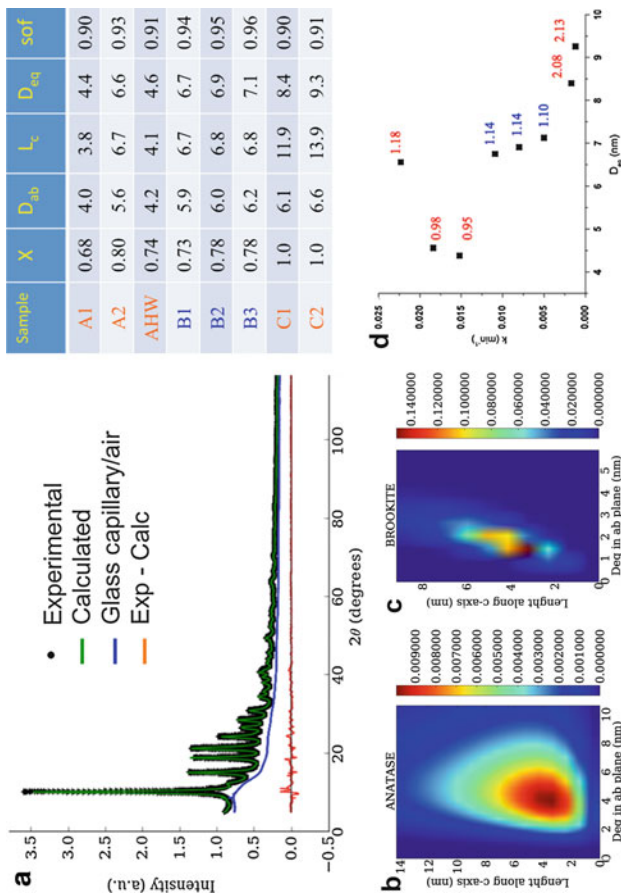
Fig. 10.18 (**a**) An example of the DFA best fit of the observed data by a sum of two nanocrystalline (anatase and brookite) phases and of an amorphous component (*blue trace*); the wavy red trace at the bottom is the difference plot. *Top-right table*: a summary of the size and shape parameters of the samples studied in Ref. 121; A, B and C groups in the table correspond to samples prepared using markedly different synthetic protocols. (**b**) Two-dimensional map illustrating the mass-based distribution of the NP size and shapes of the anatase polymorph within a selected sample. The peak heights are shown by the color-code bars at the *right*. A bivariate lognormal distribution function, including a correlation angle term between the two normal growth directions (*c* and *ab*), has been assumed. (**c**) Same as **b**, but for the minor brookite contaminant phase. (**d**) Plot correlating the apparent photocatalytic activity in methylene *blue* degradation (here expressed by the first-order kinetic constant *k*) versus the average size of the anatase NPs (D_{eq}). Numerical values are the DFA-derived aspect ratios

as the only active polymorph (this approximation does not change the validity of our results). The average sizes (the diameter of the equivalent circle in the *ab* plane, D_{ab}; the domain length along the *c*-axis, L_c; and the diameter of the equivalent sphere, D_{eq}), in nanometers, are reported in the table of Fig. 10.18. There is the clear effect of the different acid (CH_3COOH vs. HCl) in inducing larger particles with significantly increased anisotropy and aspect ratios well above 2 (C1 and C2 samples). To compare the photochemical activity of all the samples, the kinetic constants were derived from methylene blue (MB) discoloration under isothermal conditions. They are shown in Fig. 10.18, **D**, as a function of D_{eq} and exhibit a clear trend of k: it lowers at increasing size with the exception of A1 and AHW, the samples with the smallest crystal sizes also possessing the smallest (mass-derived) aspect ratios. This finding confirms that both size and shape affect the photochemical activity and that a rather complex interplay among NC facets extension and surface/volume atomic ratio controls the electron transfer to MB. Finally, the occurrence of metal ion vacancies in sol–gel titania NPs, also quoted in previous reports [119], was estimated in our samples in the range 0.90–0.96 (Ti *sofs* are given in the table of Fig. 10.18), the lower values being observed in acidic preparations. These defects, most likely distributed on the surface, have different concentration in small versus large clusters, as indirectly supported by the Debye–Waller factors that systematically show higher values at increasing size in the *ab* plane of the anatase NCs, which can be seen as a compensation to the surplus of intensity due to an average occupancy factor that is overestimated for larger clusters.

Amorphous–Crystalline Interplay in SiO_2–TiO_2 Nanocomposites One of the most appealing goal in the field of nanoscience and nanotechnology is designing multifunctional nano-objects able to synergistically combine distinct properties of individual components. Crystalline–amorphous composites are among the most interesting hybrids. Those combining amorphous silica and titanium dioxide NPs are of relevance for preparing materials with excellent photocatalytic activity (from the crystalline titania NPs) and remarkable adsorption properties (from the porous silica), in order to overcome the relatively low surface area of pure titania NPs, as required, for example, in environmental applications (wastewater and air pollution) [122, 123].

Sol–gel SiO_2/TiO_2 composites were prepared at low temperature (80 °C) by tuning the Si/Ti molar ratios (50:50, 65:35, and 80:20) and the samples aging time (24, 48, and 120 h). When embedded in an amorphous silica (am-SiO_2) matrix, the growth of pure anatase is favored, as we observed also in our samples. These systems were investigated through a combination of the DFA approach and the radial distribution function (RDF) method [124]. The pattern modeling was carried out, as in the previous cases, by generating a bivariate population of D_{4h} prismatic anatase crystals of variable shape and size (platelets to rods); in order to reproduce a satisfactory (and wavy) amorphous trace (see Fig. 10.19a), the experimental diffraction patterns of pure SiO_2 samples were used as an initial estimate, and 50 additional Chebyshev polynomial coefficients were also necessary (and refined
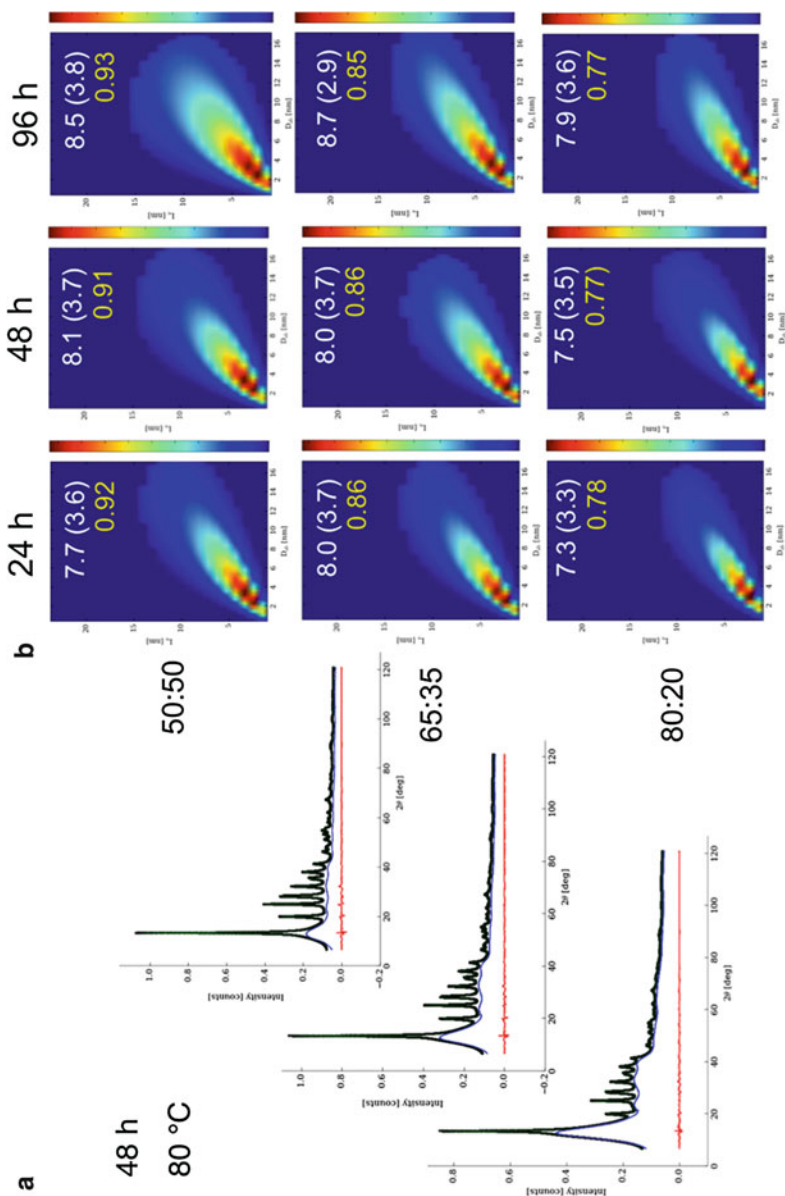
Fig. 10.19 (**a**) Three examples of the DFA best fit of the observed data obtained by the sum of one nanocrystalline (anatase) phase and of an amorphous component (*blue trace*); the wavy *red trace* at the bottom is the difference plot. (**b**) Two-dimensional maps illustrating the mass-based distribution of the NP size

by linear least squares). Satisfactory fits were obtained for all samples; Fig. 10.19a shows the best match of three of them (one for each of the three silica–titania nominal compositions at the medium aging time of 48 h). Disclosing the effect of the amorphous silica matrix on the NCs size and shape distributions upon varying the Si/Ti ratio and the aging time was one of the most interesting results. The 2D maps synoptically collected in Fig. 10.19b indicate a strong correlation, occurring in all samples, between the two independent growth directions (along the *c*-axis and in the orthogonal *ab* plane) and a clear dependence of the size/shape distribution on both the composition and the sample aging: the distribution becomes wider upon aging and narrower upon increasing the amorphous silica content. Average NCs size and shape (derived from the previous 2D distributions and reported in Fig. 10.19b as D_{eq}, σ_{eq}, and aspect ratios) show weak, but detectable, systematic effects: smaller sizes are formed at low aging times and at larger silica fractions; progressively more anisotropic shapes are favored from larger amorphous content.

The RDF analysis enabled us to investigate the sample amorphous component, once we realized that the corresponding calculated traces (provided by the Debussy as separate signals) did not exactly match the experimental patterns of pure SiO_2 (see Fig. 10.20a), suggesting the formation of possible short-range distortion of the amorphous matrix or the presence of some contamination. The G(r) curves are shown at the bottom of Fig. 10.20a for the three-sample group with increasing amount of silica and 96 h of aging time (the other samples show similar features). Unexpectedly, besides the Si–O and Si–Si interatomic distances (at 1.5 and 3.0 Å, respectively), a weak shoulder at 2.0 Å and a more pronounced one at 3.7 Å are clearly visible in the 50:50 sample and still weakly perceptible in the others (more TiO_2-diluted). These two distances correspond to the Ti–O and Ti–Ti distances in corner-sharing TiO_6 octahedra, respectively, thus giving evidence of the presence of amorphous titania (am-TiO_2). We also estimated its weight fraction (by comparing the DFA-derived integral areas under the crystalline and amorphous traces) for all the composites (see Fig. 10.20b). A significant percentage (about 16 %, 14 %, and 10 % of the total weight in the 50:50, 65:35, and 80:20 samples, respectively) turned out to be am-TiO_2, with small fluctuations depending on aging and on the accuracy of the method. A final part of this study has been dedicated to understand how the TiO_2/SiO_2 interplay influences the electronic, sorptive, and photocatalytic properties of the nanocomposites, which the interested reader can found in the original paper.

Defects and Strain Analysis in Nanoparticles and Nanomaterials

We here focus on the most relevant *structural* defects occurring in nanocrystalline materials, which are intended as deviations of the atomic arrangement from ideally periodic repetition of a unit cell content. As already mentioned in Sect. 4.1.3 for

Fig. 10.19 (continued) and shape of the anatase polymorph. The samples are all aged at 80 °C and prepared using the specified Si/Ti rations (*left*) and aging times (*top*). The values in each panel refer to size and shape parameters, in the $D_{eq}(\sigma_{eq})$ and aspect ratio form
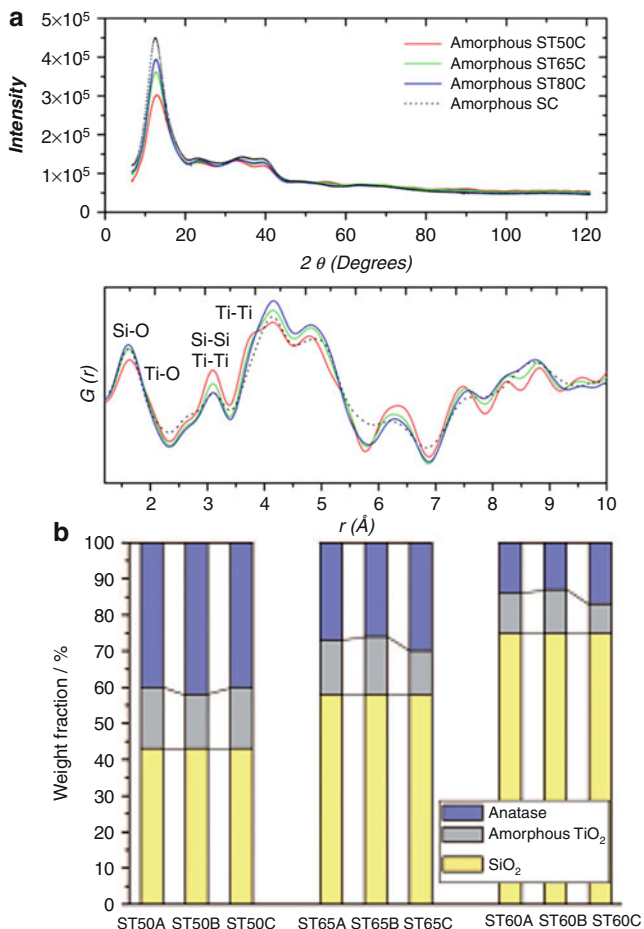
Fig. 10.20 (**a**) The amorphous components obtained during DFA analysis for three selected samples (*top*) and the reduced *G(r)* functions obtained therefrom, showing the effect of Ti inclusion in the amorphous silica matrix (*bottom*). (**b**) Weight percentage estimates of anatase, amorphous titania, and amorphous silica obtained by coupling analytical data and DFA analysis (Reprinted with permission from G. Cernuto, S. Galli, F. Trudu, G. M. Colonna, N. Masciocchi, A. Cervellino, A. Guagliardi, *Investigating the Amorphous–Crystalline Interplay in SiO₂/TiO₂ Nanocomposites by Total Scattering Methods*, Angew. Chem. Int. Ed. 2011, **50**: p. 10828–10833, Copyright 2011, Wiley)

Bragg methods, this kind of defects can be subdivided in different classes, depending on their origin and dimensionality. They can arise from local compositional changes (vacancies, substitutional, or interstitial variations), or by (geo)metrical modifications of structural subunits, related by random or correlated shifts. In small NPs, they usually form during crystals growth and/or as a consequence of volume to surface energy balance due to the largest fraction of atoms located at the surface layers compared to the interior of the NPs. In several cases, compositional, geometrical,

and surface aspects are simultaneously present and may be strongly correlated, making the theoretical approach, and the subsequent data analysis, highly complex. Different examples of structural defects affecting important classes of nanomaterials are here discussed. Due to the extent of the field, examples are mostly picked up from the cases in which the Debye and/or PDF approach has been used for data analysis.

Direct modeling by the Debye equation of (partially) disordered systems within 1D stacking fault approach has been pioneered by Espinat et al. [125] and Vogel and Gnutzmann [126] and progressively used for metals and metal alloys, kaolinite [127], and turbostratic carbons [128, 129]. Adopting the probability approach of Warren [42] combining different kinds of faulting, Debye simulations have been used by Oddershede et al. [130] to confirm the presence of deformation stacking faults in nitrogen-expanded austenite samples, at the same time ruling out the occurrence of growth faults. The effect of planar faults on the position and the broadening of diffraction peaks in *fcc* nanocrystalline materials have been recently theoretically revised considering the finite extent of the planar sequence and a new method to calculate the probability correlation function [131]. The most interesting result is that the fault position within a spherical NP affects the planar correlation in a different way, resulting in an almost perfect *fcc* sequence when it is located near the NP boundary and in a much large correlation when located near the center. Therefore, when dealing with 1D stacking fault defects, the assumption that the interplanar transitions are the same throughout the crystallite for any crystallite size is, in principle, incorrect. However, the method is limited to the case of a single fault occurrence within the NP, and its extension to higher density of faults becomes too complex, which turns its application to real cases less appealing.

A highly sophisticated model of closed-packed *fcc* and *hcp* sequences, where four-layer blocks influence in a probabilistic way the occurrence of the next layer, has been very recently proposed by Longo et al. [85] and applied to nanosized spherical cobalt NPs, the size and shape distributions of which are simultaneously refined within the Debye equation frame. Interestingly, the faulted sequences can be completely uncorrelated, or a range of correlation can also hold, defining (according to the Kakinoki's matrix formalism [132]) how many foregoing layers determine the statistical occurrence of the next one. A degree of local order is reported to appear in the completely random close packing after the assumption that a range of correlation is effective. Such a result corroborates the theoretical analysis that the *fcc* and *hcp* phases of cobalt evolve, with different growth mechanisms, from a disordered parent polytype in which ordered blocks and disordered stacking regions alternate [133]. Unraveling the cobalt close packing is of high relevance as many magnetic and catalytic properties depend critically on it.

A more general approach to stacking faults (*but not only*) has been implemented in the DISCUS suite of programs, which allows simulation, and refinement, of complex user-defined systems, at the expense of extremely long CPU usage and intense programming. Specifically, DISCUS can generate disordered atomic structures and compute the corresponding single crystal or powder diffuse scattering, both the Debye pattern simulation and the full atomic pair distribution function
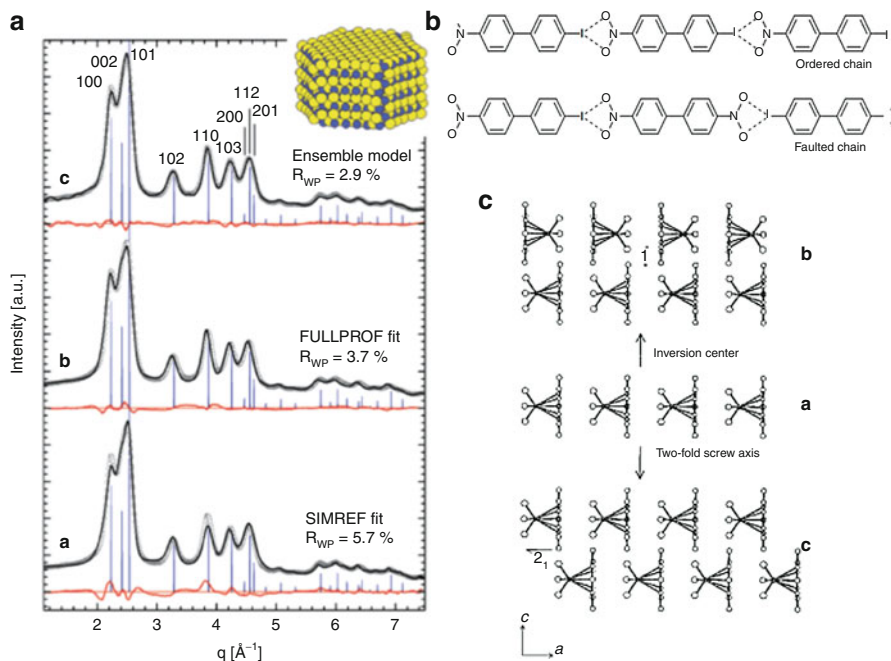
Fig. 10.21 (**a**) Best pattern matching of ZnO NP sample, performed with the DFA (*top trace*) and two alternative Rietveld methods (*middle* and *bottom traces*). The much better agreement obtained by total scattering (vs. Bragg) approaches can be easily appreciated. (**b**) The mechanism for chain reversal in the crystals of 4-iodo.4′-nitrobiphenyl, in the presence of small amounts of the 4,4′-dinitrobiphenyl contaminant. (**c**) Nearly equienergetic, i.e., nearly equiprobable packing of neighboring chains of Cp*ReO$_3$ molecules in 2D molecular polytypes (Reprinted with permission from: F. Niederdraenk, K. Seufert, A. Stahl; R.S. Bhalerao-Panajkar, S Marathe, S.K. Kulkarni, R.B. Neder, C. Kumpf, *Ensemble modeling of very small ZnO nanoparticles*, Phys. Chem. Chem. Phys., 2011, **13**: p. 498–505, Copyright 2011, Royal Society of Chemistry; N. Masciocchi, P. Cairati, F. Saiano, A. Sironi, *Two-Dimensional Polytypism of "Crystalline" (C$_5$Me$_5$)ReO$_3$*, Inorg. Chem., 2000, **35**: p. 460–463; Copyright 2000, American Chemical Society)

(PDF), with the aid of powerful Monte Carlo simulation capabilities and the generation of nanoparticles domain structures. Sophisticated imperfections in the lattice such as strain, fault probabilities, and relaxation effects, in particular at the NP surface (surface relaxation effects), can be also refined, besides fundamental properties (size, anisotropic shape, and atomic structure), by means of an evolutionary algorithm. DISCUS approach is reported mainly for II–VI semiconductor NPs. A nice application to thioglycerol-stabilized ZnO nanoparticles can be found in [134], where a further comparison of the Debye pattern simulation to the ones obtained using conventional Rietveld modeling is also presented (see Fig. 10.21, panel A).

A more complex multiple twinning effect is typically observed in noble metal NPs (Au, Ag, Pt, Pd), whose applications span from catalysis to optoelectronic and surface plasma resonance properties, therefore covering many fields of interest. At very small sizes, noble metal NPs are known to form particles having decahedral and

icosahedral symmetry, that is, atomic arrangements that the simple *fcc* unit cell of the corresponding bulk material is not able to describe, due to the occurrence of unconventional crystallographic features (like the presence of *local* fivefold symmetry axes) [135].[2] Reinhard et al. [136] reported on unsupported silver NPs that, at sizes smaller than 5 nm, show the icosahedral structure, while in larger NPs of 9 nm, the *fcc* structure of the bulk metal is found. The transition from fivefold symmetric to twinned *fcc* gold NPs during thermally induced growth is reported by Vogel et al. [91], while Kaszkur [86] applied the Debye equation to investigate the surface relaxation occurring in palladium nanocrystals on chemisorption of oxygen and interaction with inert gas and hydrogen. The coexistence of *fcc* and noncrystallographic structure types (which might be energetically favored) is also reported in very small thiol-passivated gold NPs (estimated size in the 2.0–4.1 nm range). In this case, the occurrence of icosahedral and decahedral structures made the DFA the only possible modeling approach, as reported by many authors [85–87].

Other classes of defective nanomaterials feature the formation of *2D defects*. This is the case of rod-shaped subunits, or extended polymeric chains, which typically arrange in parallel bundles, with stronger interactions within one direction than perpendicularly to it. Ideally, the extreme uncorrelated disorder is found in purely nematic phases, as found in several technologically relevant liquid crystalline phases [137]. However, partial crystallinity is sometimes preserved even if strongly anisotropic forces are at work, with specifically relevant stereochemical control. 2D polytypism is a generalization of the more common polytypic, monodimensional, stacking of 2D layer; it typically arises from the possibility of building a similar motif both with different packing operators, often related to the nearly equivalent packing of neighboring chains of equal or different polarity. While the overall "crystal size" can be micrometric (or even larger), coherent domains (of stereoregular sequence) are much smaller, thus suitably falling in the 10–50 nanometers range (and pertinent to this discussion). Though rarer than 1D counterparts, 2D polytypes are indeed experimentally found, also for truly molecular systems. Notable examples include the elusive 4-iodo-4′-nitrobiphenyl (INB) system [138] (the structure of which is driven by the stability of the Ar-NO$_2$···I-Ar supramolecular synthon – Ar = arene), where the presence of a small amount of the dinitro-derivative (DNB) contaminant occasionally reverts (max. *once* per chain) the ordered sequence. Modeling of the powder diffraction trace, performed by DISCUS using the explicit Fourier transform, the faulted chain model shown in Fig. 10.22, panel B, on 20 × 20 × 20 cells (about 10^6 atoms), afforded some diffuse scattering and markedly asymmetric (111) or split (022) peaks, fully consistent with the broadening and lowering of peak intensity (compared to the ideal *ordered Fdd2*

---

[2]Since these nanoparticles differ from the truly periodic *fcc* arrangement by folding, ideally, about their *centers of mass*, and not by extending their faults in 1D (along one *stacking direction*) or in 2D (in a *plane*), they can *nominally* be associated to 0D defectiveness (of a rather different type than point defects, typically associated to *strain*). Obviously, quasi-crystals of icosahedral or decagonal point symmetry (which can be considered periodic in a >3D hyperspace) belong to a completely different class than noble metal NPs.
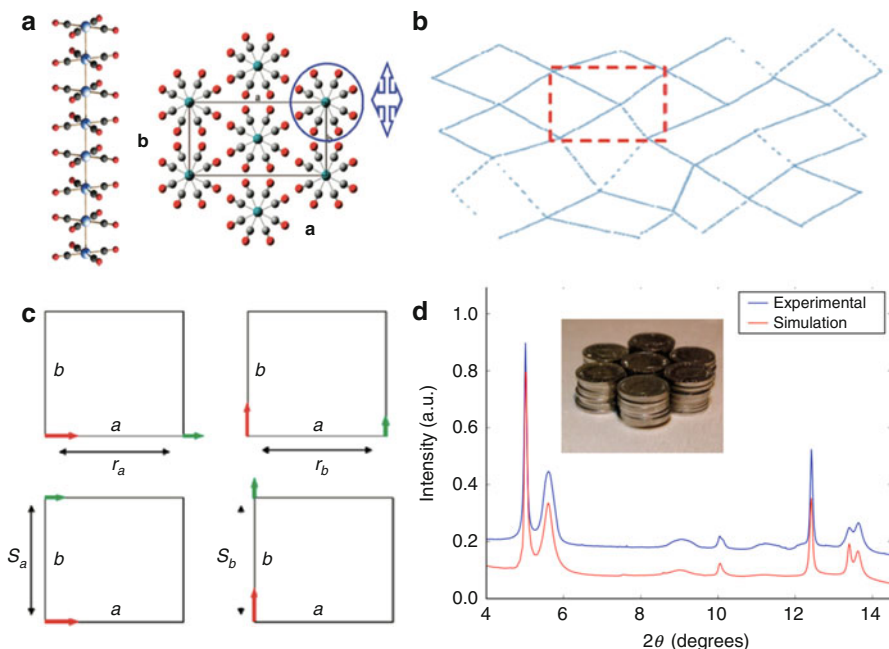
Fig. 10.22 (**a**) The structure of the $[Ru(CO)_4]_n$ polymer, built by a stacking of *trans-D_{4h}-Ru(CO)$_4$* fragments (staggered by 45° one to each other) along the **c**-axis of the (average, undistorted) orthorhombic *Ibam* structure (*left*) and pseudohexagonally packed in the *ab* plane (*right*); the *blue arrows* indicate the possible direction for independent shifts of the chain axes in ab. (**b**) A sketch of the C-centered paracrystalline net of the locations of the Ru_n chain axes in *ab*. (**c**) The geometrical representation of longitudinal and transversal correlation coefficients, relating the (*green*) shifts induced by arbitrary changes (*red arrows*) of one chain from its ideal location at the origin of the unperturbed planar lattice. (**d**) Observed (*blue*) and simulated (*red*) powder diffraction traces for the $[Ru(CO)_4]_n$ polymer. Simulation was performed by the DFA and the paracrystalline parameters described in the text. A plausible pictorial model of not strictly collinear ruthenium atoms (which our data do not allow to detect), causing a slight off-centering of the Ru atom location and, consequently, inducing evident paracrystallinity. That this deformation can indeed occur is also compatible with recent results on off-axis metal atoms in solid $Mn_2(CO)_{10}$ [139] (Reprinted with permission from: A. Cervellino, A. Maspero, N. Masciocchi, A. Guagliardi, *From Paracrystalline Ru(CO)$_4$ 1D Polymer to Nanosized Ruthenium Metal: A Case of Study through Total Scattering Analysis*, Cryst. Growth Des. 2012, **12**: p. 3631–3637; Copyright 2012, American Chemical Society)

structure) observed in the INB powder pattern. Significantly, depending on the extension of the ordered domains (i.e., on lowering the size of homopolar domains), a progressive change from polar *Fdd2* crystal (SHG active) to macrotwinned, and statistically disordered (microtwinned) crystals, can be generated.

On the same line, and driven by the similarity of the crystal packing energy of parallel and antiparallel chains of piano-stool molecules, falls the organometallic Cp^*ReO_3 molecule (Cp^* = pentamethylcyclopentadiene) [140], with a highly debated crystal structure. In that study [141], (i) the presence at low angles of

broad, but well-defined, space-group *forbidden* peaks, (ii) a marked asymmetric broadening of some peaks, and (iii) a structured background level were suitably simulated on nanocrystals, by the Debye interference function and by the explicit Fourier transform, [142] and on infinitely thick crystals, by the DiffaX recursive algorithms, all methods reinforcing the proposed polytypic arrangement (shown in Fig. 10.22, panel C).

As the final example of this paragraph, we discuss a *paracrystalline* approach to strain, which we proposed in a recent paper, aiming at defining specific microstructural features showing up, in the diffraction traces, as a not easily predictable peak broadening effect, not monotonic with θ, nor (apparently) determined by a simple (continuous) *hkl* dependence. This has been observed in a number of coordination polymers ($Ru(CO)_4$, [83] and porous metal-organic frameworks [143]) and has been attributed to *correlation* effects between polymetallic chains (Fig. 10.22, panel A, shows the undistorted model), with 1D motifs packing in a parallel fashion but with their center of mass – in the direction normal to chain propagation – nearly, but not exactly, periodic (see Fig. 10.22, panel B). Taking advantage of the seminal work by Hosemann, Bagchi, and Welberry [144, 145], the effects of two-dimensional *correlated* shifts were analyzed in reciprocal space upon modification of the Debye equation. Specifically, by defining damped correlations (in real space) between chain axes locations in *ab* (not any longer exactly C-centered), a probabilistic description of the interatomic vectors in that plane was considered. For simplicity, we report here the equation valid for a 2D net, with 1D displacements:

$$P_a(\boldsymbol{d}) = K_a \times \exp\left(-\frac{1}{2}\frac{(\boldsymbol{d}-\boldsymbol{d}_0)^2}{2\sigma_a^2\left(1 - r_a^{|m|}s_a^{|n|}\right)}\right)$$

where $\boldsymbol{d}$ is the vector separating two chains (in *ab*), r_a and s_a are the so-called longitudinal and transversal correlation coefficients, and m and n are the distance (in lattice units) of the pertinent chain. σ_a is the limiting statistical variance (i.e., the maximum amplitude of uncorrelated shifts) of the packing periodicity along the *a* axis. Deviation of r_a and s_a from unity represents the loss of correlation for moieties lying along *a* and for the laterally displaced ones, respectively. A similar definition relates $P_b(d)$ to r_b, s_b, and σ_b parameters, for shifts occurring along *b*, in the 2D displacements model (graphically shown in Fig. 10.22, panel C). The best match of the Debye simulation is shown in Fig. 10.22, panel D, and was obtained after adjusting the correlation coefficients to the values $r_a = 1.00$, $s_a = 0.97$, $r_b = 0.97$, $s_b = 1.00$, and $\sigma_a = \sigma_b = 3.0$ Å.

A similar approach was used to investigate the more complex structural features of $[Ag(4\text{-}NO_2\text{-}pz)]_3$ and $[Cu(4\text{-}NO_2\text{-}pz)]_3$ (4-NO_2-pz = 4-nitropyrazolate) in which the phenomenon of correlated shifts and faulted stacking of trimeric molecules of D_{3h} idealized geometry were found to simultaneously happen [146]. After determining the average crystal structure through ab initio X-ray powder diffraction techniques on high-resolution synchrotron data, randomly distributed defects within the molecular sequences were modeled and, then, crossed-coupled with the size and

shape information on nanocrystalline coherent domains derived from tailored Debye function simulations with those obtained from SEM images on significantly bent and polyfragmented multidomain particles. The multiple scale approach enabled us to infer the mechanism of structural disorder disrupting crystal periodicity.

5   Conclusions and Future Perspectives

In the complex field of NP characterization, XRPD stands as a fundamental pillar. It is a very old and very simple experimental method that is enjoying a new *Renaissance* because of constant improvements and incremental advances. These are due mainly to progress in instrumentation, especially at synchrotrons but also, very importantly, at the laboratory scale. XRPD is suited to almost every conceivable sample, from laboratory-created ideal samples to real-world wall scrapings, and the preparation requirements – apart from producing the sample itself, of course – are minimal. It is also a nondestructive tool and is well suited to follow sample evolution in non-ambient conditions. It is also fundamentally a "tail-heavy" method: data as collected are not immediately meaningful, and a more or less complex analysis procedure must be carried out to obtain the desired information. This makes XRPD a medal with two faces. The ugly face is that, even after the experiment has been successfully completed, most of the work must still be done. This is at variance with other methods – for instance, electron microscopy – that yield immediately understandable data. Note, however, that the process of inspecting and extracting information out of a large set of EM micrographs can be as burdensome or even more when some statistical information is needed. XRPD data contain already the properly averaged information, because a XRPD pattern contains signals from huge numbers of single NPs. The happy face is that the information contained in a XRPD pattern, and that is possible to extract there from, is quite large, as it is spread on a range of different scales, from the fine details of the atomic structure to microstructure effects that range up to the scale of NP size, which is several orders of magnitude larger. Depending on the sought-for information and on the nature of the system, various analysis methods can be applied which yield surprisingly detailed results. As the information is extracted from a simple 1D graph (the diffraction pattern), it is often a good rule – by common sense – to seek for at least partial confirmation of the results obtained by other methods, either imaging or spectroscopic or analytical methods. Nevertheless, the power of the XRPD technique is amazing, even being so simple and almost rough as experiment, being however able to supply detailed knowledge about very dirty and complex matter.

As future perspectives, the availability and development of data analysis software stands up in front. The number, kind, and capability of analytical programs available for XRPD is increasing constantly, eventually reducing, in the near future, the burden of data analysis. On the other hand, broad instrumental improvement is still expected in the medium term, on laboratory equipment, as well as on dedicated synchrotron beamlines, the former exploiting the technological fallout of the later. A larger step forward will happen – is happening – as the new FEL X-ray sources come

on line. In one of the many new applications of FELs, powder diffraction patterns are obtained by illuminating one by one with the FEL particles traveling in a jet. This extends the applicability of the method to materials that are not suited for conventional XRPD because of their tendency to coalesce or react whenever stuffed together in a confined volume. Again, a new infancy for this centenary method?.

References

1. Guinebretière R (2007) X-ray diffraction by polycrystalline materials. Wiley, New York
2. Willmott PR et al (2013) The materials science beamline upgrade at the Swiss Light Source. J Synchrotron Radiat 20:667–682
3. Hodeau J-L, Bordet P, Anne M, Prat A, Fitch AN, Dooryhee E, Vaughan G, Freund A (1998) Nine crystal multi-analyser stage for high-resolution powder diffraction between 6 and 40 keV. Proc SPIE 3448:353–361
4. Fitch AN (2004) The high resolution powder diffraction beam line at ESRF. J Res Natl Inst Stand Technol 109:133–142
5. Bergamaschi A, Cervellino A, Dinapoli R, Gozzo F, Henrich B, Johnson I, Kraft P, Mozzanica A, Schmitt B, Shi X (2010) The MYTHEN detector for x-ray powder diffraction experiments at the Swiss Light Source. J Synchrotron Radiat 17:653–668
6. Cervellino A, Frison R, Cernuto C, Guagliardi A (2012) Debye Function Analysis: Thererical and Experimental Aspcts. In: Guagliardi A, Masciocchi N (eds) Crystallography for Health and Biosciences. IUP, Varese
7. Groom CR, Allen FH (2014) The Cambridge Structural Database in retrospect and prospect. Angew Chem Int Ed Engl 53:662–671
8. Belsky A, Hellenbrandt M, Karen VL, Luksch P (2002) New developments in the Inorganic Crystal Structure Database (ICSD): accessibility in support of materials research and design. Acta Crystallogr B B58:364–369
9. Bürgi H-B (1975) Stereochemistry of reaction paths as determined from crystal structure data – a relationship between structure and energy. Angew Chem Int Ed Engl 14:460–473
10. Barton DHR, Cookson RC (1956) The principles of conformational analysis. Q Rev Chem Soc 10:44–82
11. Desiraju G (2013) Crystal engineering: from molecule to crystal. J Am Chem Soc 135:9952–9967
12. David WIF, Shankland K, McCusker LB, Baerlocher C (eds) (2006) Structure determination from powder diffraction data, IUCr monographs on crystallography. OUP, Oxford
13. Young RA (ed) (1995) The rietveld method, IUCr monographs on crystallography. OUP, Oxford
14. Holton JM, Frankel KA (2010) The minimum crystal size needed for a complete diffraction data set. Acta Crystallogr D Biol Crystallogr D66:393–408
15. Gemmi M, Galanis A, Karavassili F, Pratim Das P, Calamiotou M, Gantis A, Kollia M, Margiolaki I, Nicolopoulos S (2013) Structure determination of nano-crystals with precession 3D electron diffraction tomography in the transmission electron microscope. Microsc Anal 2:24–29

16. Frison R, Cernuto G, Cervellino A, Zaharko O, Colonna GM, Guagliardi A, Masciocchi N (2013) Magnetite–maghemite nanoparticles in the 5–15 nm range: correlating the core–shell composition and the surface structure to the magnetic properties. A total scattering study. Chem Mater 25:4820–4827

17. Scherrer P (1918) Bestimmung der Größe und der inneren Struktur von Kolloidteilchen mittels Röntgenstrahlen. Göttinger Nachrichten Gesell 2:98–100

18. For an excellent discussion of k, refer to Langford JI, Wilson AJC (1978) Scherrer after sixty years: a survey and some new results in the determination of crystallite size. J Appl Crystallogr 11:102–113

19. Larson AC, Von Dreele RB (2000) General structure analysis system (GSAS). Los Alamos National Laboratory report LAUR, 84–748

20. Pagola S, Stephens PW (2010) PSSP, a computer program for the crystal structure solution of molecular materials from x-ray powder diffraction data. J Appl Crystallogr 43:370–376

21. Coelho AA, Evans J, Evans I, Kern A, Parsons S (2011) The TOPAS symbolic computation system. Powder Diffr 26:S22–S25

22. Rodríguez-Carvajal J (2001) Commission on powder diffraction (IUCr). Newsletter 26:12–19

23. Ischia G, Wenk H-R, Lutterotti L, Berberich F (2005) Quantitative Rietveld texture analysis from single synchrotron diffraction images. J Appl Crystallogr 38:377–380

24. Stephens PW (1999) Phenomenological model of anisotropic peak broadening in powder diffraction. J Appl Crystallogr 32:281–289

25. Järvinen M (1993) Application of symmetrized harmonics expansion to correction of the preferred orientation effect. J Appl Crystallogr 26:525–531

26. Popa NC, Balzar D (2008) Size-broadening anisotropy in whole powder pattern fitting. Application to zinc oxide and interpretation of the apparent crystallites in terms of physical models. J Appl Crystallogr 41:615–627

27. Warren BE, Averbach BL (1950) The effect of cold-work distorsion on x-ray patterns. J Appl Phys 21:595–599

28. Dengfa L, Yuming W (1987) The "hook" effect of x-ray diffraction peak broadening of multilayer thin films. Powder Diffract 2:180–182

29. Scardi P, Leoni M (2002) Whole powder pattern modelling. Acta Crystallogr A58:190–200

30. Scardi P, Leoni M (2001) Diffraction line profiles from polydisperse crystalline systems. Acta Crystallogr A57:604–613

31. Scardi P, Leoni M (2003) Whole powder pattern modeling: theory and applications. In: Mittemeijer E, Scardi P (eds) Diffraction analysis of the microstructure of materials. Springer, Berlin

32. Boullay P, Lutterotti L, Chateigner D, Sicard L (2014) Fast microstructure and phase analyses of nanopowders using combined analysis of transmission electron microscopy scattering patterns. Acta Crystallogr A70:448–456

33. Williamson GK, Hall WH (1953) X-ray line broadening from filed aluminium and wolfram. Acta Metall 1:22–31

34. Ungár T, Borbély A (1996) The effect of dislocation contrast on x-ray line broadening: a new approach to line profile analysis. Appl Phys Lett 69:3173–3175

35. Monshi A, Foroughi MR, Monshi MR (2012) Modified Scherrer equation to estimate more accurately nano-crystallite size using XRD. World J Nano Sci Eng 2:154–160

36. Scardi P, Leoni M, Delhez R (2004) Line broadening analysis using integral breadth methods: a critical review. J Appl Crystallogr 37:381–390

37. Wilkens M (1970) The determination of density and distribution of dislocations in deformed single crystals from broadened X-ray diffraction profiles. Phys Status Solidi A 2:359–370

38. Stokes AR, Wilson AJC (1944) The diffraction of x rays by distorted crystal aggregates – I. Proc Camb Phys Soc 31:174–181

39. Ungár T, Dragomir I, Revesz A, Borbély A (1999) The contrast factors of dislocations in cubic crystals: the dislocation model of strain anisotropy in practice. J Appl Crystallogr 32:992–1002

40. Velterop L, Delhez R, De Keiser TH, Mittemeijer EJ, Reefman D (2000) X-ray diffraction analysis of stacking and twin faults in f.c.c. metals: a revision and allowance for texture and non-uniform fault probabilities. J Appl Cryst 33:296–306, and references therein

41. Mittemeijer EJ, Welzel U (2008) The "state of the art" of the diffraction analysis of crystallite size and lattice strain. Z Kristallogr 223:552–560

42. Arakcheeva A, Pattison P, Bauer-Brandl A, Birkedal H, Chapuis G (2013) Cimetidine, $C_{10}H_{16}N_6S$, form C: crystal structure and modelling of polytypes using the superspace approach. J Appl Crystallogr 46:99–107

43. Warren BE (1990) X-ray diffraction, Dover books on physics. Dover Publications, Mineola

44. Treacy MM, Newsam JM, Deem MW (1991) A general recursion method for calculating diffracted intensities from crystals containing planar faults. Proc R Soc London Ser A 433:499–520

45. Leoni M, Gualtieri AF, Roveri N (2004) Simultaneous refinement of structure and microstructure of layered materials. J Appl Crystallogr 37:166–173

46. Cherepanova SV, Tsybulya SV (2004) Simulation of x-ray powder diffraction patterns for one-dimensionally disordered crystals. Mater Sci Forum 443–444:87–90

47. Kakinoki J, Komura Y (1954) Intensity of x-ray diffraction by a one-dimensionally disordered crystal. II. General derivation in the case of the correlation range $S \geq 2$. J Phys Soc Jpn 9:166–176

48. Cherepanova SV, Tsybulya SV (2000) Simulation of x-ray powder diffraction patterns for low-ordered materials. J Mol Catal A 158:263–266

49. Drits VA, Tchoubar C (1990) X-ray diffraction by disordered lamellar structures: theory and applications to microdivided silicates and carbons. Springer, Berlin

50. Casas-Cabanas M, Rodríguez-Carvajal J, Palacín MR (2006) Faults, a new program for refinement of powder diffraction patterns from layered structures. Z Kristallogr S23:243–248

51. Soper AK (2011) GudrunN and GudrunX: programs for correcting raw neutron and x-ray diffraction data to differential scattering cross section. Science and Technology Facilities Council (Great Britain), Didcot

52. Juhàs P, Davis T, Farrow CL, Billinge SJL (2013) PDFgetX3: a rapid and highly automatable program for processing powder diffraction data into total scattering pair distribution functions. J Appl Crystallogr 46:560–566

53. Warren BE, Gingrich NS (1934) Fourier integral analysis of x-ray powder patterns. Phys Rev 46:368–372; Warren BE (1934) X-ray diffraction study of carbon black. J Chem Phys 2:551–555

54. Toby B, Dmowski W, Egami T, Jorgensen J, Subramanian MA, Gopalakrishnan J, Sleight AW (1989) Ordering in $Tl_2CaBa_2Cu_2O_8$ and $Tl_2Ba_2CuO_6$ studied by paid distribution function and Rietveld analysis. Physica C 162:101–102; Egami T, Rosenfeld H, Toby B, Bhalla A (1991) Diffraction studies of local atomic-structute in ferroelectric and superconducting oxides. Ferroelectrics 120:11–21; Billinge SJL, Davies PK, Egami T, Catlow C (1991) Deviations from planarity of copper-oxygen sheets in $Ca_{0.85}Sr_{0.15}CuO_2$. Phys Rev B 43:10340–10352; Toby B, Egami T (1992) Accuracy of pair distribution function analysis applied to crystalline and noncrystalline materials. Acta Crystallogr A48:336–356

55. NIST Digital Library of Mathematical Functions http://dlmf.nist.gov/1.17.E14, Release 1.0.9 of 29 Aug 2014. Online companion to: Olver FWJ, Lozier DW, Boisvert RF, Clark CW (eds) (2010) NIST handbook of mathematical functions. Cambridge University Press, New York

56. Guinier A, Fournet G, Walker C, Yudowitch K (1955) Small-angle scattering of x-rays. Wiley, New York

57. Farrow CL, Juhas P, Liu J, Bryndin D, Bozin ES, Bloch J, Proffen T, Billinge SJL (2007) PDFfit2 and PDFgui: computer programs for studying nanostructure in crystals. J Phys Condens Matter 19:33521

58. Michel FM, Ehm L, Antao SM, Lee PL, Chupas PJ, Liu G, Strongin DR, Schoonen MAA, Phillips BL, Parise JB (2007) The structure of ferrihydrite, a nanocrystalline material. Science 316:1726–1729

59. Manceau A, Skanthakumar S, Soderholm L (2011) PDF analysis of ferrihydrite: critical assessment of the under-constrained akdalaite model. Am Mineral 96:521–533
60. Chupas PJ, Chapman KW, Chen H, Grey CP (2009) Application of high-energy x-rays and pair-distribution-function analysis to nano-scale structural studies in catalysis. Catal Today 145:213–219
61. Newton MA, Chapman KW, Thompsett D, Chupas PJ (2012) Chasing changing nanoparticles with time-resolved pair distribution function methods. J Am Chem Soc 134:5036–5039
62. Chapman KW, Chupas PJ, Nenoff TM (2010) Radioactive iodine capture in silver-containing mordenites through nanoscale silver iodide formation. J Am Chem Soc 132:8897–8899
63. Chupas PJ, Chapman KW, Halder GJ (2011) Elucidating the structure of surface acid sites on γ-Al_2O_3. J Am Chem Soc 133:8522–8524
64. Chapman KW, Chupas PJ, Long GG, Bendersky L, Levine LE, Mompiou F, Stalick JK, Cahn JW (2014) An ordered metallic glass solid solution phase that grows from the melt like a crystal. Acta Mater 62:58–68
65. Long GG, Chapman KW, Chupas PJ, Bendersky LA, Levine LE, Mompiou F, Stalick JK, Cahn JW (2013) Highly ordered noncrystalline metallic phase. Phys Rev Lett 111:015502
66. Doan-Nguyen VV, Kimber SAJ, Pontoni D, Reifsnyder Hickey D, Diroll BT, Yang X, Miglierini M, Murray CB, Billinge SJL (2014) Bulk metallic glass-like scattering signal in small metallic nanoparticles. ACS Nano 8:6163–6170
67. Farrow CL, Bediako DK, Surendranath Y, Nocera DG, Billinge SJL (2013) Intermediate-range structure of self-assembled cobalt-based oxygen-evolving catalyst. J Am Chem Soc 135:6403–6406
68. Farrow CL, Billinge SJL (2009) Relationship between the atomic pair distribution function and small-angle scattering: implications for modeling of nanoparticles. Acta Crystallogr A65:232–239
69. Petkov V, Wanjala BN, Loukrakpam R, Luo J, Yang L, Zhong C-J, Shastri S (2012) PtAu alloying at the nanoscale. Nano Lett 12:4289–4291
70. Petkov V, Shastri SD (2010) Element-specific structure of materials with intrinsic disorder by high-energy resonant x-ray diffraction and differential atomic pair-distribution functions: a study of PtPd nanosized catalysts. Phys Rev B 81:165428
71. Wurden C, Page K, Llobet A, White CE, Proffen T (2010) Extracting differential pair distribution functions using it MIXSCAT. J Appl Crystallogr 43:635–638
72. Cervellino A, Giannini C, Guagliardi A (2010) DEBUSSY: a Debye user system for nano-crystalline materials. J Appl Crystallogr 43:1543–1547
73. Cervellino A, Schefer J, Keller L, Woike T, Schaniel D (2010) Identification of single photoswitchable molecules in nanopores of silica xerogels using powder diffraction. J Appl Crystallogr 43:1040–1045
74. Derlet PM, Van Petegem S, Van Swygenhoven H (2005) Calculation of x-ray spectra for nanocrystalline materials. Phys Rev B 71:024114
75. Leonardi A, Leoni M, Scardi P (2013) Directional pair distribution function for diffraction line profile analysis of atomistic models. J Appl Crystallogr 46:63–75
76. Gelisio L, Azanza Ricardo CL, Leoni M, Scardi P (2010) Real-space calculation of powder diffraction patterns on graphics processing units. J Appl Crystallogr 43:647–653
77. Hall BD, Monot R (1991) Calculating the Debye-Scherrer diffraction pattern for large clusters. Comput Phys 5:414–417
78. Shannon CE (1949) Communication in the presence of noise. Proc Inst Radio Eng 37:10–21
79. Ten Eyck LF (1977) Efficient structure-factor calculation for large molecules by the fast Fourier transform. Acta Crystallogr A33:486–492
80. Cervellino A, Giannini C, Guagliardi A (2006) On the efficient evaluation of Fourier patterns for nanoparticles and clusters. J Comput Chem 27:995–1008
81. Cervellino A, Guagliardi A (2010) Turning the Debye function into an efficient total scattering method for nanocrystals. In: Guagliardi A, Masciocchi N (eds) Diffraction at the nanoscale. IUP, Varese

82. Grover RF, McKenzie DR (2001) An efficient ab initio calculation of powder diffraction intensity using Debye's equation. Acta Crystallogr A57:739–740

83. Longo A, Martorana A (2008) Distorted f.c.c. arrangement of gold nanoclusters: a model of spherical particles with microstrains and stacking faults. J Appl Crystallogr 41:446–455

84. Cervellino A, Maspero A, Masciocchi N, Guagliardi A (2012) From paracrystalline Ru(CO)$_4$ 1D polymer to nanosized ruthenium metal: a case of study through total scattering analysis. Cryst Growth Des 12:3631–3637

85. Longo A, Sciortino L, Giannici F, Martorana A (2014) Crossing the boundary between face-centred cubic and hexagonal close packed: the structure of nanosized cobalt is unraveled by a model accounting for shape, size distribution and stacking faults, allowing simulation of XRD, XANES and EXAFS. J Appl Crystallogr 47:1562–1568

86. Hall BD (2000) Debye function analysis of structure in diffraction from nanometer-sized particles. J Appl Phys 87:1666–1675

87. Kaszkur Z (2000) Powder diffraction beyond the Bragg law: study of palladium nanocrystals. J Appl Crystallogr 33:1262–1270

88. Zanchet D, Hall BD, Ugarte D (2000) Structure population in thiol-passivated gold nanoparticles. J Phys Chem B 104:11013–11018

89. Cervellino A, Giannini C, Guagliardi A (2003) Determination of nanoparticle structure type, size and strain distribution from x-ray data for monatomic f.c.c.-derived non-crystallographic nano clusters. J Appl Crystallogr 36:1148–1158

90. Buljan M, Desnica UV, Radic N, Drazic G, Matej Z, Vales V, Holy V (2009) Crystal structure of defect-containing semiconductor nanocrystals – an x-ray diffraction study. J Appl Crystallogr 42:660–672

91. Beyerlein KR (2011) Simulation and modeling of the powder diffraction pattern from nanoparticles: studying the effects of faulting in small crystallites. Ph.D. thesis, University of Trento, Georgia Institute of Technology

92. Vogel W, Bradley J, Vollmer O, Abraham I (1998) Transition from five-fold symmetric to twinned FCC gold particles by thermally induced growth. J Phys Chem B 102:10853–10859

93. Aprea A, Maspero A, Masciocchi N, Guagliardi A, Figini Albisetti A, Giunchi G (2013) Nanosized rare-earth hexaborides: low-temperature preparation and microstructural analysis. Solid State Sci 21:32–36

94. Campi G, Ricci A, Guagliardi A, Giannini C, Lagomarsino S, Cancedda R, Mastrogiacomo M, Cedola A (2012) Early stage mineralization in tissue engineering mapped by high resolution x-ray microdiffraction. Acta Biomater 8:3411–3418

95. Guagliardi A, Cedola A, Giannini C, Ladisa M, Cervellino A, Sorrentino A, Lagomarsino S, Cancedda R, Mastrogiacomo M (2010) Debye function analysis and 2D imaging of nanoscaled engineered bone. Biomaterials 31:8289–8298

96. Reddy LH, Arias JL, Nicolas J, Couvreur P (2012) Magnetic nanoparticles: design and characterization, toxicity and biocompatibility, pharmaceutical and biomedical applications. Chem Rev 112:5818–5878

97. Laurent S, Forge D, Port M, Roch A, Robic C, Vander Elst L, Muller RN (2008) Magnetic iron oxide nanoparticles: synthesis, stabilization, vectorization, physicochemical characterizations, and biological applications. Chem Rev 108:2064–2110

98. Bosi F, Halenius U, Skogby H (2009) Crystal chemistry of the magnetite-ulvospinel series. Am Minerol 94:181–189

99. Shin H-S (1988) A study on the structure of maghemite (γ-Fe$_2$O$_3$). I – rietveld analysis of powder XRD patterns. J Korean Ceram Soc 35:1113–1119

100. Shmakov AN, Kryukova SV, Tsybulya SV, Chuvilin AL, Solovyeva LP (1995) Vacancy ordering in γ-Fe$_2$O$_3$: synchrotron x-ray powder diffraction and high-resolution electron microscopy studies. J Appl Crystallogr 28:141–145

101. Greaves C (1983) A powder neutron diffraction investigation of vacancy ordering and covalence in y-Fe$_2$O$_3$. J Solid State Chem 49:325–333

102. Cervellino A, Frison R, Cernuto G, Guagliardi A, Masciocchi N (2014) Lattice parameters and site occupancy factors of magnetite–maghemite core–shell nanoparticles. A critical study. J Appl Crystallogr 25:4820–4827

103. Massart R (1981) Preparation of aqueous magnetic liquids in alkaline and acidic media. IEEE Trans Magn 17:1247–1248

104. Nelder JA, Mead R (1965) A simplex method for function minimization. Comput J 27:308–316

105. Chantrell RW, Popplewell J, Charles SW (1978) A model of interaction effects in granular magnetic solids. IEEE Trans Magn 14:975–977

106. Park J, Lee E, Hwang N-M, Kang M, Kim SC, Hwang Y, Park J-G, Noh H-J, Kim J-Y, Park J-H, Hyeon T (2005) One-nanometer-scale size-controlled synthesis of monodisperse magnetic iron oxide nanoparticles. Angew Chem Int Ed 44:2872–2877

107. Diehm PM, Agoston P, Albe K (2012) Size-dependent lattice expansion in nanoparticles: reality or anomaly? ChemPhysChem 13:2443–2454

108. Finger LW, Hazen RM, Hofmeister AM (1986), High-pressure crystal chemistry of spinel ($MgAl_2O_4$) and magnetite (Fe_3O_4): Comparisons with silicate spinels. Phys Chem Miner 13:215–220

109. Jiang JZ, Olsen JS, Gerward L, Mørup S (1998) Enhanced bulk modulus and transition pressure in y-Fe_2O_3 nanocrystals. Europhys Lett 44:620–626

110. Nudelman F, Sommerdijk NAJM (2012) Biomineralization as an inspiration for materials chemistry. Angew Chem Int Ed 51:6582–6596

111. Mahamid J, Aichmayer B, Shimoni E, Li C, Siegel S, Paris O, Fratzl P, Weiner S, Addadi L (2010) Mapping amorphous calcium phosphate transformation into crystalline mineral from the cell to the bone in zebrafish fin rays. Proc Natl Acad Sci USA 107:6316–6321

112. Nudelman F, Pieterse K, George A, Bohmans PHH, Friedrich H, Brylka LJ, Hilbers PAJ, de With G, Sommerdijk NAJM (2010), The role of collagen in bone apatite formation in the presence of hydroxyapatite nucleation inhibitors. Nat Mater 9:1004–1008

113. Rawal HY, Schmidt-Rohr K (2010) Strongly bound citrate stabilizes the apatite nanocrystals in bone. Proc Natl Acad Sci USA 107:22425–22429

114. Delgado-López JM, Frison R, Cervellino A, Gómez-Morales J, Guagliardi A, Masciocchi N (2014) Crystal size, morphology, and growth mechanism in bio- inspired apatite nanocrystals. Adv Funct Mater 24:1090–1099

115. Leventouri T (2006) Crystal size, morphology, and growth mechanism in bio- inspired apatite nanocrystals. Biomaterials 27:3339–3342

116. Wang L, Nancollas GH (2008) Calcium orthophosphates: crystallization and dissolution. Chem Rev 108:4628–4669

117. Woolerton TW, Sheard S, Reisner E, Pierce E, Ragsdale SW, Armstrong FA (2010) Efficient and clean photo-reduction of CO_2 to CO by enzyme-modified TiO_2 nanoparticles using visible light. J Am Chem Soc 132:2132–2133

118. Szeifert JM, Feckl JM, Fattakhova-Rohlfing D, Liu Y, Kalousek V, Rathousky J, Bein T (2010) Ultrasmall titania nanocrystals and their direct assembly into mesoporous structures showing fast lithium insertion. J Am Chem Soc 132:12605–12611

119. Apfel UP, Weigand W (2011) Efficient activation of the greenhouse gas CO_2. Angew Chem Int Ed 50:4262–4264

120. Thompson TL, Yates Y (2006) Surface science studies of the photoactivation of TiO_2-new photochemical processes. Chem Rev 106:4428–4453

121. Cernuto G, Masciocchi N, Cervellino A, Colonna GM, Guagliardi A (2011) Size and shape dependence of the photocatalytic activity of TiO_2 nanocrystals: a total scattering Debye function study. J Am Chem Soc 133:3114–3119

122. Costi R, Saunders AE, Banin U (2010) Colloidal hybrid nanostructures: a new type of functional materials. Angew Chem Int Ed 49:4878–4897

123. Zelenàk V, Hornebecq V, Mornet S, Schäf O, Llewellyn P (2006) Mesoporous silica modified with titania: structure and thermal stability. Chem Mater 18:3184–3189

124. Cernuto G, Galli S, Trudu F, Colonna GM, Masciocchi N, Cervellino A, Guagliardi A (2011) Investigating the amorphous–crystalline interplay in SiO_2/TiO_2 nanocomposites by total scattering methods. Angew Chem Int Ed 50:10828–10833

125. Espinat D, Thevenot F, Grimoud J, El Malki K (1993) Powerful new software for the simulation of WAXS and SAXS diagrams. J Appl Crystallogr 26:368–383

126. Gnutzmann V, Vogel W (1990) Structural sensitivity of the standard platinum/silica catalyst EuroPt-1 to hydrogen and oxygen exposure by in situ x-ray diffraction. J Phys Chem 94:4991–4997

127. Thomas NW (2010) A new approach to calculating powder diffraction patterns based on the Debye scattering equation. Acta Crystallogr A66:64–77

128. Li ZQ, Lu CJ, Xia ZP, Zhou Y, Luo Z (2007) X-ray diffraction patterns of graphite and turbostratic carbon. Carbon 45:1686–1695

129. Dopita M, Rudolph M, Salomon A, Emme M, Aneziris CG, Rafaja D (2013) Simulations of x-ray scattering on two-dimensional, graphitic and turbostratic carbon structures. Adv Eng Mater 15:1280–1291

130. Oddershede J, Christiansen TL, Ståhl K (2008) Modelling the x-ray powder diffraction of nitrogen-expanded austenite using the Debye formula. J Appl Crystallogr 41:537–543

131. Beyerlein KR, Snyder RL, Scardi P (2011) Faulting in finite face-centered-cubic crystallites. Acta Crystallogr A67:252–263

132. Kakinoki J (1967) Diffraction by a one-dimensionally disordered crystal. II. Close-packed structures. Acta Crystallogr A23:875–885

133. Tolédano P, Krexner G, Prem M, Weber H-P, Dmitriev VP (2001) Theory of the martensitic transformation in cobalt. Phys Rev B 64:144104

134. Niederdraenk F, Seufert K, Stahl A, Bhalerao-Panajkar RS, Marathe S, Kulkarni SK, Neder RB, Kumpf C (2011) Ensemble modeling of very small ZnO nanoparticles. Phys Chem Chem Phys 13:498–505

135. Marks LD (1994) Experimental studies of small particle structures. Rep Prog Phys 57:603–649

136. Reinhard D, Hall BD, Ugarte D, Monot R (1997) Size-independent fcc-to-icosahedral structural transition in unsupported silver clusters: an electron diffraction study of clusters produced by inert-gas aggregation. Phys Rev B 55:7868–7881

137. Bahadur B (ed) (1992) Liquid crystals: applications and uses. World Scientiic, Singapore

138. Masciocchi N, Sironi A, Bergamo M (1998) Comments on the elusive crystal structure of 4-iodo-4′-nitrobiphenyl. Chem Commun:1347–1348

139. Macchi P, Casati N, Evans SR, Gozzo F, Simoncic P, Tiana D (2014) An "off-axis" Mn-Mn bond in $Mn_2(CO)_{10}$ at high pressure. Chem Commun 50:12824–12827

140. Burrell AK, Cotton FA, Daniels LM, Petricek V (1995) Structure of crystalline $(C_5Me_5)ReO_3$ and implied nonexistence of "$(C_5Me_5)Tc_2O_3$". Inorg Chem 34:4253–4255

141. Masciocchi N, Cairati P, Saiano F, Sironi A (2000) Two-dimensional polytypism of "crystal-line" $(C_5Me_5)ReO_3$. Inorg Chem 35:460–463

142. Proffen T, Neder RB (1997) DISCUS, a program for diffuse scattering and defect structure simulations. J Appl Crystallogr 30:171–175

143. Masciocchi N, Colombo V, Maspero A, Galli S (2011) Coordination polymers: what can diffraction tell us? 5th EuCheMS conference on nitrogen ligands, Granada, p 66

144. Hosemann R, Bagchi SN (1962) Direct analysis of diffraction by matter. North-Holland/Interscience, Amsterdam/New York

145. Welberry TR (2004) Diffuse x-ray scattering and models of disorder. Oxford University Press, Oxford

146. Bertolotti F, Maspero A, Cervellino A, Guagliardi A, Masciocchi N (2014) Bending by faulting: a multiple scale study of copper and silver nitropyrazolates. Cryst Growth Des 14:2913–2922

X-Ray Absorption Fine Structure Analysis of Catalytic Nanomaterials

11

Wang-Jae Chun, Satoru Takakusagi, Yohei Uemura,
Kyoko Bando, and Kiyotaka Asakura

Contents

W.-J. Chun (✉)
Graduate School of Arts and Sciences, International Christian University, Mitaka, Tokyo, Japan
e-mail: wchun@icu.ac.jp

S. Takakusagi • K. Asakura (✉)
Catalysis Research Center, Hokkaido University, Sapporo, Hokkaido, Japan
e-mail: takakusa@cat.hokudai.ac.jp; askr@cat.hokudai.ac.jp

Y. Uemura
Division of Electronic Structure, Department of Materials Science, Institute for Molecular
Science, Okazai, Aichi, Japan
e-mail: y-uemura@ims.ac.jp

K. Bando
Nanosystem Research Institute, National Institute of Advanced Industrial Science and Technology
(AIST), Tsukuba, Japan
e-mail: kk.bando@aist.go.jp

1   Definition of the Topic

X-ray absorption fine structure (XAFS) is an absorption spectroscopy which pro-
vides the material local structure with a bond distance of less than sub-Å precision.
It does not require any long-range order nor special environment. Therefore, it is the
suitable technique to characterize the catalytic nanomaterials under working con-
ditions. This chapter presents an overview of the principle, emerging technology,
and applications of XAFS in characterizing nanomaterials in catalysis.

2   Overview

Catalysts are materials that accelerate the reaction rate. The structure characteriza-
tions are difficult using diffraction methods because catalysts are often used as
nanoclusters highly dispersed on oxide surfaces. In addition, the structures before,
during, and after catalytic reactions are different from each other, and the in situ
observation techniques of catalyst structures are highly required. X-ray absorption
fine structure (XAFS) method is the most appropriate technique to investigate the
catalyst nanomaterial structure under working conditions. We will review the
history and principle of XAFS, followed by experimental setup and preparation
of the sample. The analysis of XAFS will be briefly described, where the error
estimations using Hamilton ratio method are discussed. We will mention its appli-
cation to nanoparticles – monometallic and bimetallic under reaction conditions.
We also describe the two emerging technologies in XAFS, called as ultrafast time-
resolved XAFS and polarization-dependent total reflection fluorescence XAFS
(PTRF-XAFS), which can provide new structural information we never have had
with other characterization methods. Finally, we discuss its future perspective.

3   Introduction

Catalysts are materials that accelerate chemical reactions which are widely used to
create energies and new materials as well as improve the environment. Catalysts
may be divided into three categories: molecular, heterogeneous, and biocatalysts.
Molecular catalysts and biocatalysts function primarily in solution, and their active
site structures are often determined by nuclear magnetic resonance (NMR) or by
X-ray crystallography following crystallization from a solvent. Heterogeneous
catalysts, in contrast, represent active species (primarily in a metallic state) dis-
persed on solid surfaces. Metal nanoclusters are particularly important as hetero-
geneous catalysts. In these materials, optimal catalytic performance is typically
obtained through intimate contact between the metal nanoclusters and its solid
support, and so the catalyst has to be characterized in its supported form. The
present review focuses on such heterogeneous catalysts, in which the surface
nanostructure is crucial. These materials do not exhibit long-range order and
hence are not readily analyzed via X-ray crystallography. Electron microscopy,

however, is a good candidate for the characterization of these catalysts, since it allows assessment of the morphologies of nanomaterials, as well as the atomic locations, in addition to chemical analysis on the nano-level as the result of newer developments in spherical aberration correction techniques [1]. Recently, electron microscope imaging under catalytic conditions has been made possible using differential pumping or electron transmission windows [2]. Even so, it remains challenging to measure bond lengths with 0.001 nm precision. If the nanoclusters are dispersed at a relatively high concentration, a partial distribution function (PDF) analysis can be applied as discussed later [3, 4], although the use of this technique with dilute samples on oxide supports such as SiO_2 and Al_2O_3 would be difficult.

In this chapter, we discuss the applications of X-ray absorption spectroscopy to the analysis of catalytic materials, in particular the use of X-ray absorption fine structure (XAFS). XAFS is a unique technique that provides useful information about both bond lengths and ligands. The XAFS phenomenon was first observed by Fricke in 1920 [5], although the initial theoretical analysis was performed by Kronig [6, 7]. Kronig considered the use of both long-range- and short-range-order theories in the understanding of XAFS and concluded that the long-range-order theory was the most appropriate. Following the work of Shiraiwa [8], Kostarev [9], and Kozlenkov [10], Lytle proposed a short-range-order interpretation of EXAFS [11] in the late 1960s, while in 1971 Sayers reported an analysis based on the Fourier transform in k-space [12]. At the same time, synchrotron radiation, a strong X-ray source well suited to XAFS measurements, became available at Stanford University [13, 14]. Subsequently, XAFS was widely applied to the analysis of nanomaterials. Lytle et al. applied XAFS to metal catalysts while performing an in situ characterization of Ru during an oxidation process [15] and also used XAFS to elucidate the inner structures of various bimetallic nanoparticles [16]. Koningsberger and Iwasawa observed the structural changes during various reactions and used these data to determine the associated reaction mechanisms [17, 18]. Since XAFS was found to provide information concerning the dynamic processes of nanomaterials under reaction conditions, it was increasingly applied to the analysis of catalysts.

Figure 11.1 shows a typical X-ray absorption spectrum for Pt foil around the Pt L-edges. In such spectra, the absorption coefficient, μ, is expressed as follows:

$$\mu t = \ln(I_0/I_t), \tag{11.1}$$

where Io, I_t, and t are the incident and transmitted X-ray intensities and the thickness of the sample, respectively. As the sample is irradiated with X-rays whose energy is scanned, μ abruptly increases at energy values specific to elements. This energy for a given element is known as its absorption edge and results from excitation of core electrons to unoccupied states and to the vacuum level (equal to the Fermi level in a solid) to generate free electrons or photoelectrons. The 1s, 2s, $2p_{1/2}$, and $2p_{3/2}$ core electron energy levels are the most often used and are termed the K-, L_1-, L_2-, and L_3-edges, respectively. XAFS provides information concerning local electronic states and geometric structures around the

Fig. 11.1 Pt L-edge X-ray absorption fine structure
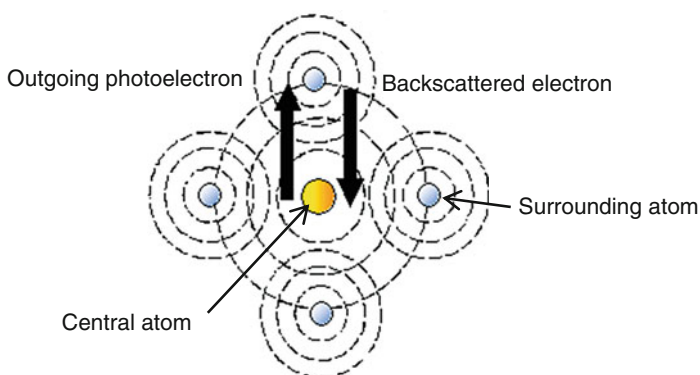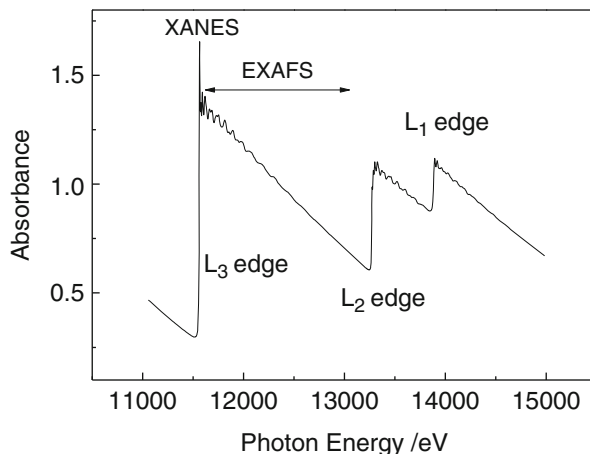
Fig. 11.2 An X-ray-excited photoelectron moving out of the central atom (*yellow*) is scattered by the surrounding atoms (*blue*). Some of the scattered electrons are reflected back to the central atom where they interfere with outgoing photoelectrons to produce EXAFS oscillations

X-ray-absorbing atom. The absorption spectrum near the edge (-10 to 50 eV) is complicated and is referred to as X-ray absorption near edge structure (XANES) where excited electrons are trapped by unoccupied states and/or undergo multiple scattering by surrounding atoms. On the other hand, the fine structures appearing more than 50 eV are referred to as extended X-ray absorption fine structure (EXAFS) which results from the interference between outgoing photoelectrons and the electrons backscattered by the surrounding atoms, as shown in Fig. 11.2.

The scattering in the EXAFS region can be explained in a simple manner by considering that the oscillation associated with a single-scattering event has a sinusoidal waveform, as expressed in Eq. (11.2):

$$\chi(k) = \frac{NS_0^2 F(k)}{kr^2} e^{-2k^2\sigma^2} e^{-2r/\lambda} \sin(2kr + \phi(k)). \tag{11.2}$$

Here, $F(k)$, $\Phi(k)$, N, σ, r, λ, and S_0^2 are the backscattering amplitude, phase shift function, coordination number, Debye–Waller factor or mean square displacement, bond length measured for the X-ray-absorbing atom, mean free path length, and amplitude reduction factor. The term k represents the wave number of the photoelectron calculated from

$$k = \sqrt{\frac{2m}{\hbar^2}(h\nu - E_B)}, \tag{11.3}$$

where m, $h\nu$, and E_B are mass of electron, photon energy, and binding energy of core electron, respectively.

EXAFS is sensitive to the local structure around the X-ray-absorbing atom and thus allows the specific structural analysis of elements by selecting a particular atom. The resulting EXAFS oscillation has a sinusoidal form against k such that the Fourier transform of the data generates a pseudo-radial distribution function in which the peaks correspond roughly to specific bonds. The exact bond length and coordination number are determined through curve fitting analysis in the r-space or k-space using the theoretically or empirically determined phase shift and background amplitude functions. The advantage of XAFS is that it does not require the sample to be in a particular form, and thus it is applicable to noncrystalline materials such as liquids and amorphous substances. Therefore, XAFS can be employed to determine the local structures of catalyst nanoclusters deposited on support surfaces.

A further advantage of XAFS is that it allows in situ analysis in the presence of various ambient gases, since the X-rays readily penetrate the gas phase. This is important with regard to the structural analysis of catalysts, since their structures may differ before, during, and after reaction.

Below, we discuss the applications of XAFS to the analysis of nanoparticle catalysts, in particular in situ and time-resolved XAFS studies, beginning with a summary of the history of XAFS and the associated experimental apparatus. In addition, a single-crystal oxide system using polarization-dependent XAFS capable of providing three-dimensional (3D) structures is considered.

4 Experimental and Instrumental for XAFS Measurements

XAFS spectra can be acquired in several modes – transmission, fluorescence, and electron yield – and choosing the appropriate mode for a given experiment is crucial. Here, we briefly describe the transmission mode, which is the most fundamental mode and also the most frequently used.

The first step of any XAFS measurement is sample preparation, and here, there are three important factors: a suitable edge jump value, a suitable absorption

coefficient, and sample uniformity. The total absorbance of a sample at the target wavelength can be calculated from the X-ray absorption cross sections [19] of all the elements in the sample. The difference in the absorption coefficient before the edge (pre-edge) and just after the edge (post-edge) is referred to as the edge jump ($\Delta\mu$). Since the amplitude of the EXAFS oscillation is proportional to the edge jump, a small edge jump value will generate a small oscillation in the EXAFS region, thus giving a poor signal-to-noise (S/N) ratio. It is thus recommended to adjust the sample thickness until the $\Delta\mu$ value is close to unity. This does not mean that the edge jump must always be unity; in the case of a sample with significant background X-ray absorption and a low concentration of the target element, the total absorbance will be quite large when $\Delta\mu$ is unity, and so the transmitted X-ray intensity will be too low to be detected with a suitable S/N ratio, and the effects of stray X-rays and higher harmonics will become important. Thus, the total absorbance of a sample should be maintained below 3 to 4 even if this means that $\Delta\mu$ will be less than unity. The first and second criteria are thus sometimes mutually exclusive, and a suitable absorption coefficient is generally the more important of the two. In fact, when using synchrotron radiation and/or a prolonged data acquisition time, it is possible to obtain suitably intense XAFS oscillations with a $\Delta\mu$ in the vicinity of 0.1. At values less than 0.1, however, it is advisable to instead use a fluorescence yield method [20]. The last factor, which remains extremely important, is the uniformity of the target samples, since an inhomogeneous sample thickness will result in severe distortion of the XAFS spectra. Powdered samples are most commonly used in XAFS measurements, and a mortar and pestle are typically employed to provide fine, homogeneous sample grains. In the case of small sample amounts, the specimen may be mixed with a filler or binder composed of elements with low atomic numbers, and this binder should be chemically inert to avoid any reaction with the sample. Carbon black, boron nitride, starch, flour, cellulose, and mineral oils are typically used for this purpose. There are three ways to prepare powdered samples. When working in the transmission mode, samples should be well dispersed and the areal density of the material as presented to the X-ray beam must be uniform. One useful means of assembling samples is to coat a commercial adhesive tape such as a Scotch® tape with the sample in the form of fine particles. Other approaches are to form a sample pellet using a tableting machine or to place a well-mixed sample into a sample cell with X-ray transparent windows, as in Fig. 11.3.

XAFS cells for holding liquid or powdered samples can be prepared rather simply by drilling a hole (several millimeters in diameter) and milling a slot in a plate of an appropriate material, such as a plastic, Teflon®, or a metal. To allow for a vacuum, threaded, sealable plugholes must also be included. Finally, a pair of thin Kapton® films may be affixed to either side of the cell as windows. The optimal window thickness is approximately 250 μm but will vary somewhat depending on the absorption energy of the target element. If the sample has to be cooled to cryogenic temperatures, the cell should be made of a material that exhibits good thermal conductivity, such as Cu or Al, and will require sufficient thermal contact, such as through an indium foil, with the cold finger of a helium cryostat.
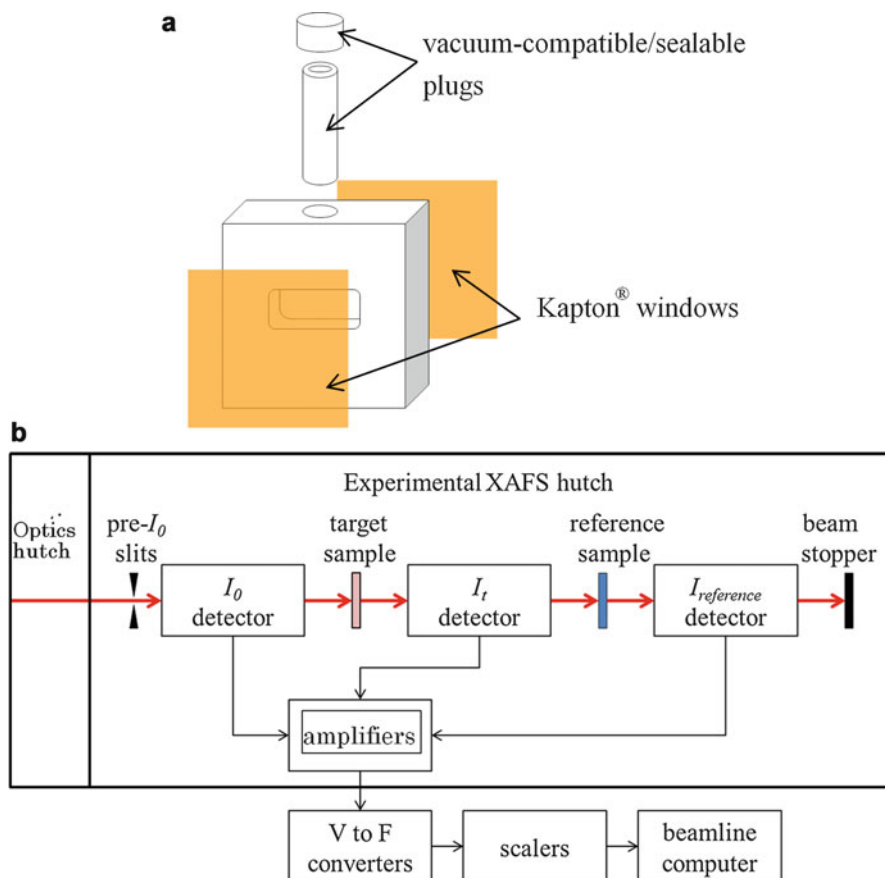
Fig. 11.3 Typical XAFS (**a**) cell and (**b**) measurement system

To allow the measurement of small variations in the absorption coefficient $\mu(E)$ in EXAFS spectra, the data acquisition process must generate an S/N ratio better than 10^3 in the region from 600 to 1000 eV above the absorption edge. As well, in order to resolve XANES features, the energy resolution of the X-ray beam should be less than 1 eV. Synchrotron radiation is an ideal light source for XAFS since it is able to provide 10^{10} photons/s with a small angular spread.

A typical configuration for transmission XAFS measurements is shown in Fig. 11.3b. The intensity of the X-ray flux is determined both before and after the sample, yielding I and I_0, respectively, by ionization chambers. A third ionization chamber can also be installed to obtain internal standard measurements using a reference metal foil or chemical compound for energy calibration. The data acquisition time required to obtain a complete XAFS spectrum varies between 20 and 60 min when using a conventional step-scanning monochromator. This can be reduced to several minutes by the Quick XAFS measurement or even several

seconds if an energy dispersive method (dispersive XAFS) is employed. These techniques will be reviewed in more detail in Sect. 6.3.

In order to obtain reliable results from EXAFS, it is important to acquire spectra using the largest possible k-range. The EXFAS equation implies that experimental data collected up to a high k_{max} will increase the number of independent fitting parameters as the available k-range (Δk) increases. As a result, we can reduce the correlation between the parameters N_i and σ_i, as will be discussed in the analysis section. Moreover, this allows improved discrimination between close peaks during the Fourier transform. The distance resolution in an EXAFS spectrum, ΔR, is expressed as

$$\Delta R = \frac{\pi}{2\Delta k}.$$

Therefore, a measurement requires a Δk value of approximately 16 $\mathring{A}^{-1}$ if two peaks for which $\Delta R = 0.1$ $\mathring{A}$ are to be resolved by the Fourier transform.

5   XAFS Analysis

As described in the "Introduction," EXAFS data allow analysis of the types of surrounding atoms and their structural parameters, including coordination numbers, bond lengths, and disorder. In contrast, the electronic states and symmetry of nanomaterials are obtained from the XANES region. In this section, we describe a standard data analysis procedure. Many EXAFS data analysis software packages are currently available [21]. Although each has its advantages and disadvantages, they all have a common feature with regard to the analytical procedure. A basic EXAFS oscillation is expressed by the following equation, the single coordination version of which has already been presented as Eq. (11.4):

$$\chi(k) = S_0^2 \sum_i \frac{N_i F_i(k_i)}{k_i r_i^2} e^{-2k_i^2 \sigma_i^2} e^{-2r_i/\lambda} \sin(2k_i r_i + \phi_i(k_i)). \qquad (11.4)$$

Here, the EXAFS oscillation is summed over the ith shell.

The standard EXAFS analysis procedure involves fitting the experimental data to determine a structural model, using Eq. (11.4), and applying a nonlinear least squares fitting method in which N_i, r_i, σ_i^2 and ΔE_{i0} are optimized. ΔE_{i0} represents the change in the original kinetic energy of the photoelectron as described in the following equation:

$$k_i = \sqrt{k^2 - \frac{2m}{\hbar^2} \Delta E_{i0}}. \qquad (11.5)$$

Since the original kinetic energy of the photoelectron in the unknown compound, E_0, is not always equal to the value used in the calculation of the phase shift
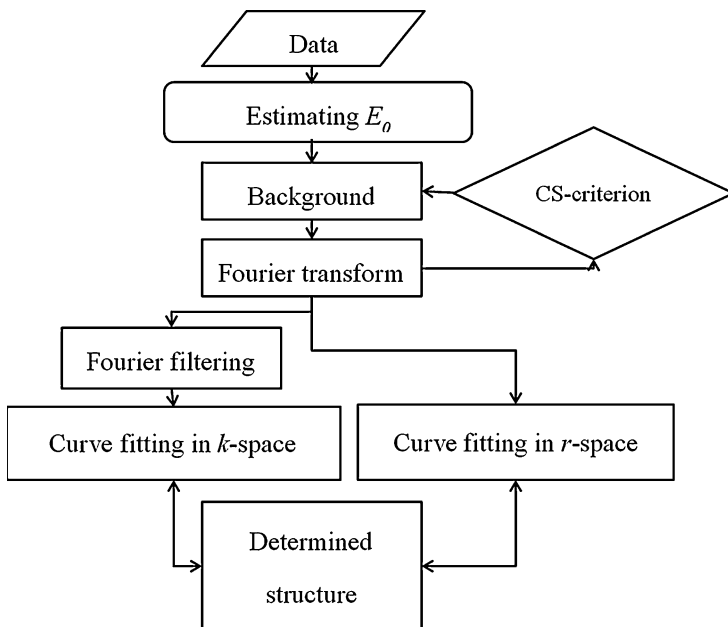
Fig. 11.4 Data analysis flow chart

and backscattering amplitude functions or that of the reference compound, it is necessary to adjust ΔE_{i0} during the curve fitting process.

The overall data analysis process is described by the flow chart presented in Fig. 11.4.

The first step is the estimation of the energy threshold, E_0, in which the first inflection point on the edge is typically used. Another means of approximating E_0 is to use the halfway point of the absorption edge jump. Rough estimations such as these are sufficient because the value of E_0 will be further refined during the curve fitting analysis. The EXAFS oscillation, $\chi(k)$, is obtained from the measured absorption coefficient $\mu(E)$ by the equation $\chi(k) = \frac{\mu(E) - \mu_{bkg}(E)}{\mu_0(E)}$, where $\mu_{bkg}(E)$ is the smooth portion of the absorption coefficient in the post edge region. The post-edge smooth curve can be obtained by polynomial fitting, moving average, cubic spline, and smoothing spline [22], and the goodness of smoothing can be estimated using the Cook–Sayers (CS) criterion [23]. The value of $\mu_0(E)$ is estimated from the edge jump, and its energy dependence can be calculated from Victoreen's coefficients [24].

EXAFS spectra consist of sums of damped sine waves corresponding to longer path lengths. The EXAFS data are weighted by k^1 or k^3 so as to emphasize the contributions of low or high Z (atomic number) neighbors, respectively. These weighted spectra are Fourier transformed to r-space. Since the EXAFS oscillation is the sum of sinusoidal curves, the Fourier transform generates peaks at positions

corresponding to the atom locations. The heights of these Fourier transform peaks represent the average k^n-weighted EXAFS amplitudes and are affected by the scattering atoms, the k-weighting, and the Fourier transform windows. The Fourier transform will have real and imaginary parts, although only the modulus of the Fourier transform is given in the literature. It is noteworthy that this modulus includes no phase information and will give unusual peaks if two shells are close to one another. In this case, it is recommended to present both the modulus and the imaginary part because these data are helpful with regard to distinguishing between true and ghost peaks by comparison of the imaginary part [22].

It should be noted that the position of the peak in r-space is shifted to shorter side by approximately 0.2–0.4 Å because of the negative slope of the phase shift function. Both accurate bond lengths and other structural parameters can be obtained by curve fitting procedures. This curve fitting analysis depends on the proposed model structures, meaning the pairs of absorbing-neighboring atoms chosen for analysis. The credibility of the data fitting relies on appropriate knowledge of the target system's chemical composition, which has been obtained by other techniques. Prior to the curve fitting, however, the $F_i(k_i)$ and $\Phi_i(k_i)$ functions must be obtained. There are two approaches. The first employs experimentally derived phase shifts and backscattering amplitudes extracted from the EXAFS data for reference compounds. These experimental standards are generally not complex but must be carefully prepared and handled, since the usefulness of the data they provide depends on the quality of the standard compound and the separation of the target atomic pairs from other neighbors in the standard compound. The sample purity has an especially direct effect on the credibility of the resulting data, and it is thus recommended to use a simple compound in which there is a single neighboring atom that has a single interatomic distance and for which the purity has been ascertained by X-ray diffraction. Another approach is to use a theoretical standard generated using a computer program such as FEFF, GNXAS, or EXCURVE. These theoretical standards can include multiple scattering if higher coordination shells are analyzed. Thus, if one wishes to analyze a complex system, the theoretical approach is desirable. Although the reliability of the theoretical approach has improved, it is necessary to apply these theoretical functions to the analysis of EXAFS data for standard compounds to evaluate their validity.

The EXAFS data will be fitted in k-space or r-space with the appropriate fitting parameters. The goodness of fit is estimated from the associated R_{factor}, expressed by the following equation:

$$R_{\text{factor}} = \frac{\sqrt{\sum_i \left(\chi_i^{\text{experiment}}(k) - \chi_i^{\text{fit}}(k, [\alpha]) \right)^2}}{\sqrt{\sum_i \left(\chi_i^{\text{experiment}}(k) \right)^2}}, \tag{11.6}$$

where $\chi_i^{\text{experiment}}(k)$, $\chi_i^{\text{fit}}(k)$, and $[\alpha]$ are the experimental data, the theoretical fitted data, and the fitting parameters, respectively. The goodness of fit can often be

estimated using the chi-square (χ^2) test, as in Eq. (11.7), below. Here, we use R_ν instead of χ:

$$|R_\nu|^2 = \frac{M}{N(M-n)} \sum_i \frac{\left(\chi_i^{\text{experiment}}(k) - \chi_i^{\text{fit}}(k, [\alpha])\right)^2}{\varepsilon_i^2}. \tag{11.7}$$

Here, N, n, and ε_i represent the number of data points used for data fitting, the number of fitting parameters, and the error of the ith data point. M is the degrees of freedom estimated from the Nyquist theorem, as follows:

$$M = \frac{2\Delta k \ \Delta r}{\pi} + m (m = 0, 1, 2), \tag{11.8}$$

where Δk and Δr are the k and the r window widths, respectively. Although Stern proposed a value of 2 for m [25], *one of the authors* (*KA*) recommends a conservative value of zero for m, which prevents the use of too many fitting parameters [26].

When $|R_\nu|^2$ is less than 1, the fitting is accepted, while a value greater than 1 signifies that the fitting is not acceptable. Although the χ^2-test is the most reasonable and absolute criterion for the goodness of fit, it is difficult to apply in practice because the error (ε_i^2) estimation (especially the systematic error estimation) for each data point is difficult.

In contrast, the R factor is calculated using Eq. (11.6) in a straightforward manner. Hamilton has proposed the use of a modified F test (termed the Hamilton test) to estimate the error and to assess the validity of the model structure in the analysis of X-ray diffraction data [27], and this test can also be applied to EXAFS analysis. Essentially, the Hamilton test is a relative statistical test method, in which the ratio of two R factors is compared as a means of ascertaining the validity of a new (or old) model based on an old (or new) one, using a confidence level and the F distribution. During this process, two fitting results are obtained for the same data applying two different degrees of freedom, thus generating two R factors. In the first fitting procedure, one obtains R_1 in the best fitting results with a quantity of data point and a quantity of fitting parameters equal to M (determined by Eq. (11.8)) and n, respectively. In the second fitting, certain fitting parameters are restricted under a specific hypothesis. The R_2, R factor obtained in this second fitting will be inferior. The ratio of the two R factors, $\overline{R} = R_2/R_1$, is then compared with a tabular value, $\overline{R}_{b, M-n, p}$, where b and p are the number of restricted fitting parameters and significance level, respectively. If $\overline{R} > \overline{R}_{b, M-n, p}$, the hypothesis "the two fitting results are essentially the same" is rejected, while if $\overline{R} < \overline{R}_{b, M-n, p}$, the hypothesis is accepted at the p significance level.

Here, we consider two examples in which the Hamilton test is employed.

(Example 1) Error Estimation
In this example, a curve fitting analysis is performed for which $\Delta k = 3\text{–}15 \ \text{Å}^{-1}$. The Fourier filtering range is $\Delta r = 1\text{–}2 \ \text{Å}$ with four adjustable parameters,

$N, r, \Delta E$, and σ, and the R for the best fit value is $R_1 = 0.02$. What, then, is the error in r? In this example, the r term is fixed at a value slightly different from the optimal value, $r + \Delta r$, and the other three parameters are optimized. Here, b = 1 since r is fixed. A value of $R_2 = 0.03$ is then obtained. In this case, M = 2 $\Delta r \Delta k / \pi$ = 8. In the initial optimization process, we used $n = 4$ parameters such that 4 (=(M − n)) degrees of freedom were left. When estimating the error bar at the 10 % significance level, the Hamilton ratio $\overline{R}_{1,4,0.1} = 1.462$ is approximately equal to 0.03/ 0.02 = 1.5. Thus, at the 10 % significance level, the error bar should be Δr.

(Example 2) Validity of Two-Shell Fitting
In this example, the presence of Pd–C in Pd nanoparticles is assessed, applying the curve fitting of Pd nanoparticles with two shells using eight parameters. The r-range and k-range are 1.197–3.007 Å and 3.00–16.75 Å^{-1}, respectively. Under these conditions, M becomes 15.85. One-shell fitting based on solely the Pd–Pd interaction is also carried out. In this case, the number of restricted parameters (b) is four since the parameters for Pd–C are fixed. The resulting R factors are $R_1 = 0.0038$ (with both Pd–C and Pd–Pd shells being adjusted) and $R_2 = 0.006$ (if only the Pd–Pd shell is adjusted and no Pd–C contribution is considered). Thus, $\overline{R} = \frac{0.006}{0.0038}$ = 1.57, $\overline{R}_{4,8,0.25} = 1.354$, $\overline{R}_{4,8,0.1} = 1.550$, and $\overline{R}_{4,8,0.05} = 1.838$. Therefore, the presence of Pd–C has been demonstrated at a significance level of 10 %.

6 Key Research Methods and Findings on Catalytic Nanomaterials Characterized Using XAFS

6.1 Application of XAFS to Nanoparticles

One of the most fundamental goals of nanoparticle (NP) studies is to understand the factors governing the 3D arrangements of atoms and their geometry in the NPs. A practical advantage of EXAFS is its sensitivity to the partial radial distribution function of the absorbing atoms and their neighbors within the local range (about 6Å). Due to the finite size effect, the differences between NPs and the bulk material produce dramatic changes in EXAFS results, including a reduced amplitude due to smaller coordination numbers and a different oscillation period due to the change in bond lengths compared to those in the bulk. In addition, important information concerning the disorder in NPs is also derived from EXAFS spectra. During the last decade, the combination of different structural analysis techniques, such as high-angle annular dark field scanning TEM (HAADF-STEM), high-energy XRD, time-of-flight mass spectrometry (TOF-MS), and density functional theory (DFT) calculations, with EXAFS has allowed quantification of the number of atoms in NPs, as well as visualization of their geometry on the sub-nm to 2–3 nm size range.
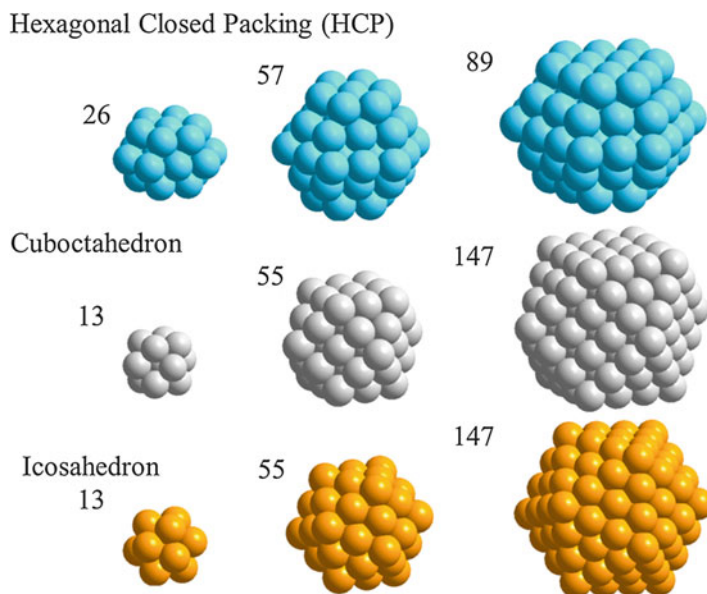
Fig. 11.5 Atomic configurations and magic numbers for several representative clusters [167]

6.1.1 Monometallic Nanoparticles

In this subsection, we review general analysis strategies and discuss recent studies in which the quantitative geometric properties of monometallic nanoparticles (MMNPs) have been elucidated.

A number of studies aimed at understanding both ligand-protected and oxide-supported MMNPs have been reported. The majority of these MMNPs possess a high degree of symmetry and their sizes and properties can be controlled by various synthetic approaches. As such, a regular polyhedron (including cuboctahedral, icosahedral, truncated decahedral, truncated octahedral, and hexagonal close packing) is a good approximation of a nanocluster. Many of these nanoclusters have a closed shell that are often characterized by "magic numbers" of metal atoms, as shown in Fig. 11.5. This approximation is justified for relatively small clusters (consisting of about 10–1000 atoms) and also by theoretical calculations that have shown that the regular polyhedron model is energetically the most favorable [28–31].

The strategies for elucidating the sizes and shapes of symmetrical MMNPs from EXAFS data can be roughly categorized as either the single-scattering (SS) or multiple-scattering (MS) path approach. The SS path approach allows determination of the first nearest coordination numbers (N_{1st}) of regular clusters (i.e., symmetrical nanoclusters). Montejano-Carrizales et al. have analytically characterized several regular polyhedral clusters as a function of the cluster size L (defined as $L = N_E-1$, where N_E is the number of atoms along the edge of a regular polyhedron) [32].

$$N_{1st}(\text{cubooctahderal (closed packed)}) = \frac{24L(5L^2 + 3L + 1)}{10L^3 + 15L^2 + 11L + 3}$$
$$N_{1st}(\text{icosahedral (non-closed packed)}) = \frac{6L(20L^2 + 15L + 7)}{10L^3 + 15L^2 + 11L + 3}$$

In contrast, Calvin et al. used a simple sphere with radius R for approximation purposes and obtained the value of N_{1st} by the following equation:

$$N_{1st} \approx \left[1 - \frac{3}{4}\left(\frac{r}{R}\right) + \frac{1}{16}\left(\frac{r}{R}\right)^3\right]N_{1st}^{bulk},$$

where r is the average bond length associated with the N_{1st} for the nanocluster and N_{1st}^{bulk} is the first coordination number for the bulk [33]. This approach can provide good estimations in the case of larger clusters if the number of atoms in the nanocluster is larger than 100, such that $L = 3$, and also if the size distribution is relatively broad. In practice, these two approaches work well for calculating the N_{1st} values for nanoclusters, but are not effective for the estimation of shells with longer bond lengths, such as the second, third, and fourth coordination numbers (N_{2nd}, N_{3rd}, N_{4th}) because the sizes, shapes, and surface orientations of nanoclusters are also affected by an MS contribution to the nanocluster EXAFS data [34]. Therefore, this MS contribution must be suitably described in order to extract the additional information from the EXAFS data.

Frenkel et al. have proposed a means of discriminating between models with different atomic packing and morphology [35]. This technique involves the calculation of the average pair radial distribution function (RDF, $Q(r)$) as in Eq. (11.9) for N_{1st}, N_{2nd}, N_{3rd} values and then comparing this calculated value with the RDF value derived from observed EXAFS data:

$$Q(r) = \frac{1}{n}\sum_{i=1}^{n} Q_i(r), \quad Q_i(r) = \frac{dn_i}{dR_i}. \tag{11.9}$$

Here, n is the number of identical atoms in a nanocluster, $Q_i(r)$ is the partial RDF for atom i, and dn_i is the number of neighbors within a spherical shell of thickness dR_i. The coordination numbers (N_{1st}, N_{2nd}, N_{3rd}) within a given shell in a model cluster can be estimated using

$$N_{order} = \int_{R_i}^{R_f} Q(r)dr, \tag{11.10}$$

where the *order* value will be the first, second, or third coordination number and R_i and R_f define the range of the spherical shell.

This RDF method has demonstrated superiority in determining monodispersed Au and Pt NPs with HAADF-STEM data [36–39]. Figure 11.6 presents the experimental results and model calculations for the coordination numbers (N_{1st}, N_{2nd}, N_{3rd}) within a
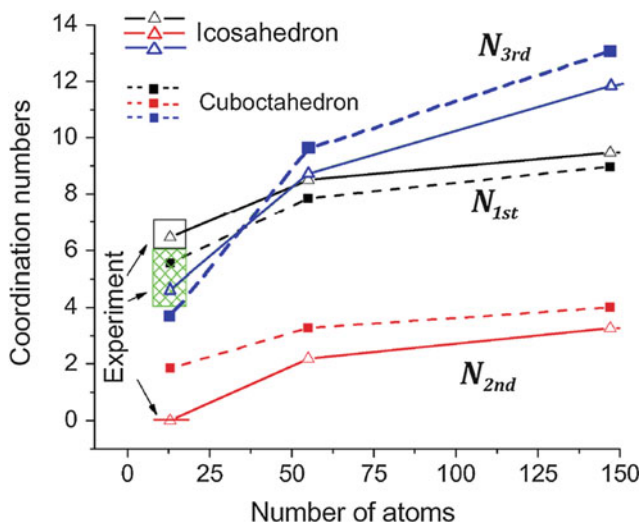
Fig. 11.6 Experimental results and model calculations for icosahedron and cuboctahedron clusters [39]. The values in *black* and *green* boxes and the *red line* are experimental values, and their uncertainties are compared against the model structures (Reproduced with permission from Ref. [39]. Copyright 2007, AIP Publishing LLC)

given shell for icosahedron and cuboctahedron clusters [37]. The experimental results for the coordination numbers were $N_{1st} = 6.5 \pm 1, N_{2nd} = 0, N_{3rd} = 8 \pm 1$. The coordination number for the first shell (N_{1st}) agreed with the calculated values of 6.46 and 5.54 for the icosahedron (Au13) and cuboctahedron (Au13) in the limit of error. In the case of the N_{2nd} value, however, dramatic differences were observed. For the icosahedron model, the value of N_{2nd} was zero, while the value obtained using a cuboctahedron or a truncated octahedron was 1.85.

Another important factor in the EXAFS analysis of NPs is the effect of disorder in the NP structure, as reflected in the Debye–Waller factor σ^2, since this disorder attenuates the EXAFS oscillations and may produce misleading data concerning the coordination number and thus lead to incorrect conclusions during nanocluster modeling. The σ^2 effect can be expressed as the simple sum of static and thermal (or dynamic) terms, as in Eq. (11.11).

$$\sigma^2 = \sigma^2_{static} + \sigma^2_{thermal} \tag{11.11}$$

A simple and practical means of reducing the thermal term is to acquire the EXAFS oscillations at cryogenic temperature. Figure 11.7a shows an example of this approach. This figure demonstrates that the amplitude intensity within the higher k region, which is often attenuated by the thermal term, is dramatically increased at cryogenic temperatures. Imaoka et al. have precisely synthesized both the Pt_{12} and Pt_{13} clusters shown in this figure by controlling their unique molecular level formula based on a stoichiometric adjustment [40]. The number of atoms and the
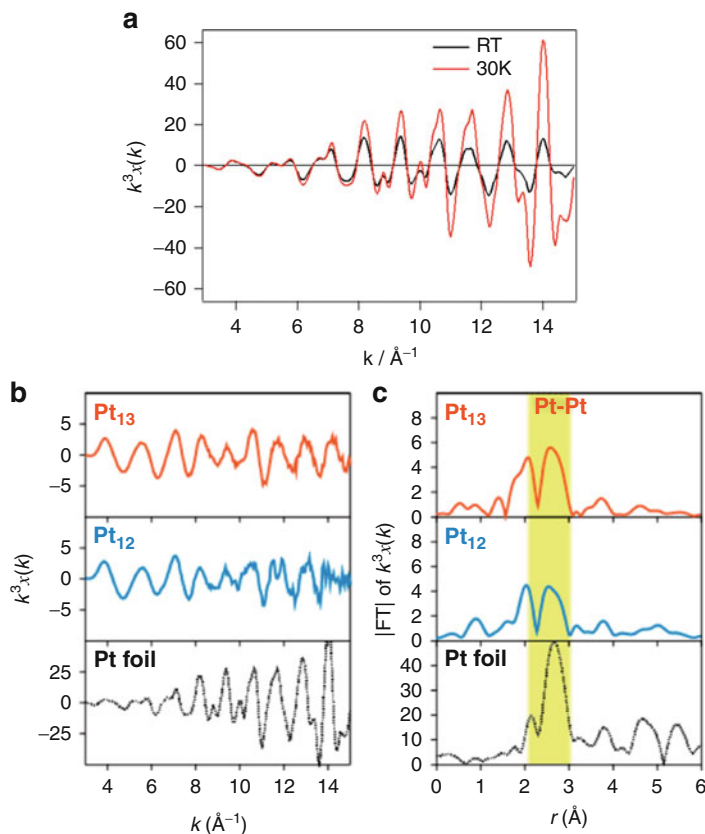
Fig. 11.7 (a) k^3-weighted Pt L_{III} EXAFS spectra of Pt_{12}, Pt_{13}, and Pt foil at 30 K and (b) Fourier transforms of the k^3-weighted Pt L_{III} EXAFS spectra [40] (Copyright 2013, American Chemical Society)

sizes of the clusters were subsequently determined by electrospray ionization (ESI)-TOF-MS and HAADF-STEM. In order to understand the unique oxygen reduction reaction (ORR) activity of the Pt_{12} and Pt_{13} clusters, EXAFS analyses were carried out at cryogenic temperatures below 30 K. Figure 11.7b shows that the oscillation amplitude for Pt_{12} is slightly smaller than that for Pt_{13}. Assuming the presence of light elements such as carbon or nitrogen near the surface platinum atoms, the first coordination number (N_{1st}) for the Pt–Pt interaction in the Pt_{13} clusters was found to be 6.5, which is in good agreement with the theoretical N_{1st} value calculated assuming an icosahedral cluster model ($N_{1st} = 6.46$). This result is also consistent with the particle sizes proposed by Frenkel et al. [34]. Conversely, the N_{1st} value of 5.2 obtained for the Pt_{12} clusters shows a minimal difference in the intrinsic ORR activities (a 2.5-fold higher activity for Pt_{12} compared to Pt_{13}). To ascertain the

Fig. 11.8 Debye temperature for γ-Al₂O₃-supported Pt NPs as a function of first-nearest-neighbor coordination number (N_{1st}). The insets show corresponding models of fcc-Pt NP shapes. S1 to S4 are the sample numbers. Diameters obtained by HAADFS-STEM: 1.0 ± 0.2 nm for S1, S2, and S4 and 0.8 ± 0.2 nm for S3 (Reproduced with permission from Ref. [38]. Copyright 2010, APS Journals)
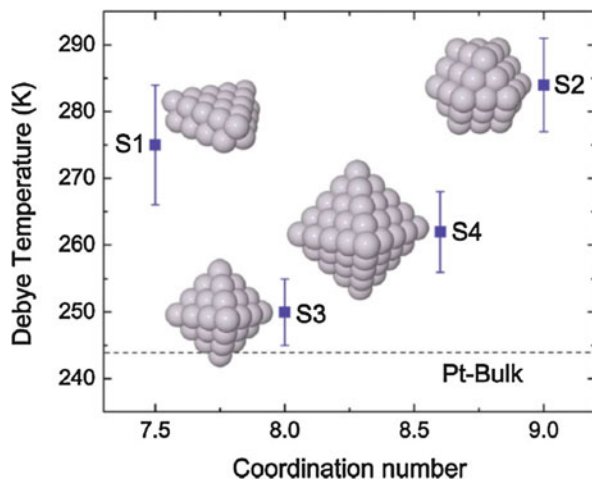
structure of Pt_{12}, several plausible models were examined based on DFT calculations. These models suggested that Pt_{12} has a deformed coordination, while Pt_{13} exhibits the well-known icosahedral atomic coordination found in stable cluster series.

The growth mechanisms and the resulting structures of nanoclusters under synthesis conditions such as H_2 reduction are also highly important issues in nanocluster studies. However, the disorder expressed by the Debye–Waller factor σ^2 directly affects the amplitude of EXAFS oscillations at higher temperatures. Therefore, it is important to select a reliable means of eliminating the correlation between σ^2 and S_0^2 or N. Correlated Einstein and Debye models are both commonly used to analyze thermal σ^2 terms. Sevillano et al., however, recommend the Debye model for nearly isotropic systems since this approach is both simple and reliable [41].

Roldan et al. estimated the Debye temperature of ligand-free, size- and shape-selected Pt NPs supported on γ-Al₂O₃, based on the correlated Debye model [38]. In the case of bulk Pt, they found that the increase in the Debye temperature was affected by size, shape, support interactions, and adsorbate effects, as shown in Fig. 11.8. It is worth noting that there is some correlation between the shapes of NPs and their Debye temperatures, even in the case of NPs having similar average sizes [38].

In addition to changes in the Debye–Waller factors for NPs, it is important to consider the apparent contraction of lengths due to the asymmetric radial distribution effect. The EXAFS formula given in Eqs. (11.2) and (11.4) is based on a Gaussian radial distribution. However, the real distribution deviates slightly from a Gaussian radial distribution, exhibiting a gentle slope on the longer bond length side. Clausen et al. demonstrated that Cu NPs exhibit an apparent bond contraction when analyzed using Eq. (11.2) [42]. Bunker et al. proposed a cumulant

analysis of EXAFS data in a non-Gaussian distribution system using the following equation [43]:

$$\chi(k) = \frac{N S_0^2 F(k)}{k r^2} e^{-2k^2\sigma^2 + 2/3 C_4 k^4} e^{-2r/\lambda} \sin\left(2kr + \phi(k) - \frac{4}{3}C_3 k^3\right). \qquad (11.12)$$

Here, the bond lengths are shortened due to the influence of the k^3 term. In the case of a moderately non-Gaussian system, therefore, Eq. (11.12) may be used. Yokoyama et al. reported that Pt NPs stabilized in NaY showed a shorter bond length after cumulant corrections had been applied [44]. Kang et al. found a negative thermal expansion effect in small Pt NPs (0.9 nm in diameter) [45] during EXAFS measurements between 165 and 573 K under He and H_2. Following the cumulant correction, they found bond lengths of 2.70 and 2.75 Å in He and H_2, respectively, at 165 K. At the higher temperature of 573 K, they observed shorter bond lengths than those measured at 165 K, suggesting that the unusual negative thermal expansion could be due to the metal–support bonding interaction.

Finally, it is helpful to briefly consider another potential tool for the characterization of NPs [46, 47]. Recently, Petkov et al. and Nishigaki et al. have demonstrated the possibility of applying a high-energy XRD (HEXRD) technique to the analysis of ligand-protected Au NPs. These groups investigated the atomic structure of Au NPs using a well-designed combination of HEXRD, EXAFS, matrix-assisted laser desorption/ionization (MALDI)-MS, TEM, and DFT. The resulting data showed that HEXRD together with the PDF analysis technique allows the analysis of diffuse (i.e., non-Bragg type) XRD patterns and generates 3D structural information, such as nearest neighbor atomic distances and coordination numbers, for noncrystalline materials exhibiting some degree of structural coherence and periodicity [4]. In addition, this approach allows elucidation of the structures of 3D NPs through the application of reverse Monte Carlo simulations followed by ab initio structural determination.

6.1.2 Bimetallic Nanoparticles

Fundamental Conditions Required for the Analysis of Bimetallic Nanoparticles

Several equations must be satisfied to allow for the analysis of bimetallic NPs. A bimetallic nanocluster is composed of two different elements, A and B, and the EXAFS oscillations correspond to the bond lengths and coordination numbers of both elements. In the analysis of bimetallic systems, therefore, several conditions must be satisfied, as follows [16, 48]:

1. The bond length determined for element A (R_{AB}) equals that determined for B (R_{BA}).
2. The coordination numbers determined for elements A and B satisfy the following relation:
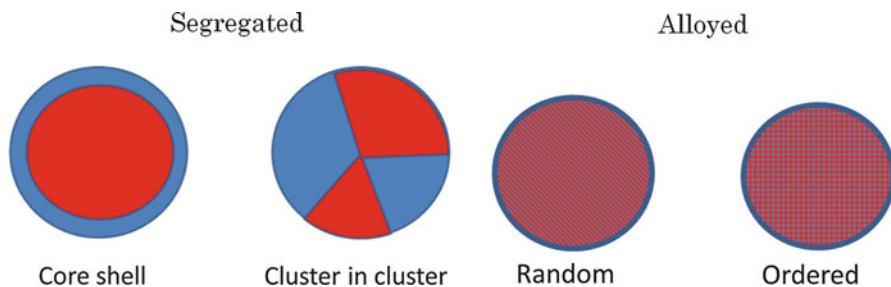
Fig. 11.9 Classification of bimetallic clusters

$$C_A N_{AB} = C_B N_{BA},$$

where C_A and C_B are, respectively, the molar coefficients of elements A and B in the chemical formula of the compound, which can be determined by chemical analysis using inductively coupled plasma (ICP), X-ray fluorescence, and other techniques.

If the above two conditions are not satisfied within the limits of error, the reliability of the results are in doubt.

In principle, the absolute values for the Debye–Waller factor as determined from each XAFS oscillation should be equal to one another within the limits of error. However, determination of the absolute value of the Debye–Waller factor can be challenging and so this is not always the case. However, if a reference compound containing the same atomic pair is analyzed, the difference between the squares of the Debye–Waller factors for the reference and unknown compounds at the two edges shown in Eq. (11.13) should be the same:

$$\begin{aligned}
\Delta\sigma^2_{A-B} &= \Delta\sigma^2_{A-B,\,\text{unknown}} - \Delta\sigma^2_{A-B,\,\text{ref}} \\
\Delta\sigma^2_{B-B} &= \Delta\sigma^2_{B-A,\,\text{unknown}} - \Delta\sigma^2_{B,\,\text{unknown}} \\
\Delta\sigma^2_{A-B} &= \Delta\sigma^2_{B-A}
\end{aligned} \quad . \tag{11.13}$$

Bimetallic nanoparticles (NPs) may be roughly classified into two categories, as shown in Fig. 11.9 [49, 50]. One category consists of segregated NPs, while the other contains alloyed NPs.

Alloyed Nanoparticles
Alloy nanoparticles may be classified as either random or ordered. In a random alloy, the ratio of the coordination numbers of homoatomic and heteroatomic pairs should equal the component ratio. However, an ordered alloy has a definite coordination number ratio derived from its ordered structure. For example, in bulk Cu_3Au, each Cu atom is surrounded by four Au and eight Cu atoms, while Au is completely surrounded by Cu. FePt has an ordered metallic form known as $L1_0$, and Shinoda et al. have prepared FePt nanoparticles using a polyol process [51] in which Pt and then Fe are sequentially reduced to give a core (Pt)–shell (Fe) structure. When a sample of this material was heated to 573 K, the PtFe nanoparticles transitioned to PtFe $L1_0$ ordered

Table 11.1 Coordination numbers for PdCu nanoparticles as determined from XAFS

Cu:Pd	Cu–Cu	Cu–Pd	Pd–Cu	Pd–Pd
4:1	6.0 (6.2/6.1)[a]	1.8 (1.6/1.8)	7.2 (6.2/7.0)	0.8 (1.6/0.7)
3:2	3.9 (4.7/3.2)	3.8 (3.1/4.2)	5.5 (4.7/6.3)	2.2 (3.1/2.2)
1:1	2.8 (3.9/2.7)	5.0 (3.9/5.1)	5.1 (3.9/5.1)	2.8 (3.9/2.7)
1:4	0.8 (1.6/0.7)	7.0 (6.2/7.0)	1.8 (1.6/1.8)	6.0 (6.2/6.1)

[a]The first and second numerals in parentheses show the coordination numbers derived from random alloy and heterobondphilic models
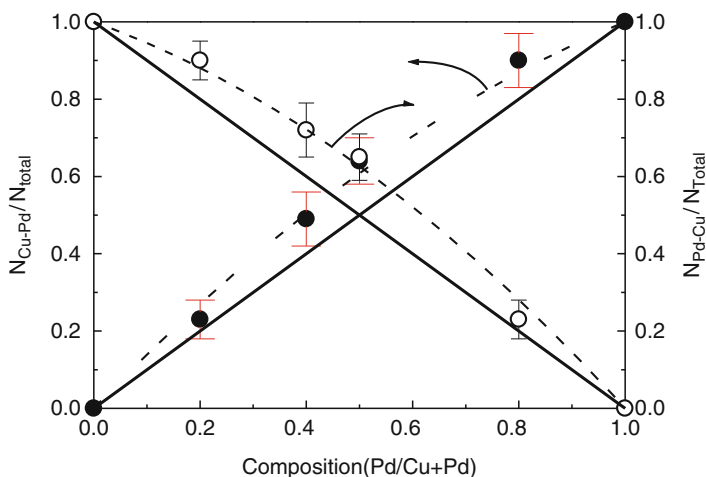
Fig. 11.10 Ratios of heterobonds to total coordination number as a function of composition [55] (Copyright 2002, American Chemical Society)

particles with Fe–Pt and Pt–Pt bond lengths of 0.269 and 0.272 nm, respectively [52]. Phase transitions may also occur as the result of gas-phase absorption [53]. Knecht et al. investigated PdAu in the form of dendrimers and found that the coordination number ratio changed linearly with the composition, indicating the formation of an alloy [54]. However, the total coordination number around Au was greater than that around the Pd atoms, and thus it was concluded that a quasi-random alloy with a Au-rich core was obtained.

The coordination numbers in Table 11.1 were obtained for PdCu nanoparticles and demonstrate a trend similar to that observed for a random alloy [49, 55], such that the coordination number tracks the metal composition. However, the coordination number for heteroatomic pairs is always larger than that for homoatomic pairs. Figure 11.10 summarizes the heterobond to homobond coordination number ratios. In the case of a random alloy, a linear plot results with a slope of 1 or −1, as shown by solid line in Fig. 11.10. However, the actual data plots tend to deviate from a straight line in an upward direction, indicating that the homoatomic pair is preferred over the heteroatomic pair. The coordination number trend can be simulated by assuming

that the energy of the Pd–Cu interaction (E_{PdCu}) is lower than those of the Pd–Pd and Cu–Cu (E_{PdPd}, E_{CuCu}) interactions and that the difference in these energy values may be described by ($\Delta E_{PdCu} = E_{PdCu} - (E_{PdPd} + E_{CuCu})/2) = 4RT$. PdCu is known to form intermetallic compounds or ordered alloys such as Pd_3Cu or PdCu. In the case of PdCu NPs, the structure is intermediate between a random and an ordered alloy due to the mobile character of the atoms in the NPs. Although an ordered alloy might be more stable than a random alloy, smaller particles will have more mobile atoms, especially at the surface, such that the entropy factor may concur with the energy term. The balance between an intermetallic compound and a solid solution may be quite subtle. PtRu nanoparticles, heated to 1173 K and rapidly cooled to RT, form a random alloy [56], while PdTe and RhTe NPs preferentially form heteroatomic pairs or intermetallic NPs [57].

Segregated Nanoparticles

In the case of a segregated cluster, the coordination numbers for homoatomic pairs are larger than those for heteroatomic pairs. These structures can be further divided into core–shell and cluster-in-cluster types. The "core" of the core–shell structure gives a total coordination number nearly equal to the bulk value, while the coordination numbers for the atoms in the "shell" are lower than the bulk value because the surface atoms are less coordinated. A cluster-in-cluster structure is formed when each element initially forms clusters of like atoms, following which these clusters agglomerate to form larger clusters. Clusters of both atoms may be located on the surface, and hence the total coordination numbers are less than those in the bulk, and the coordination number for the homoatomic pair is larger than that for the heteroatomic pair.

PtAu bimetallic nanoclusters have been prepared by the deposition of Pt onto Au nanoclusters previously prepared through a sputter deposition technique [58, 59]. Figure 11.11 shows the resulting Pt and Au K-edge EXAFS data for these clusters. Both the Pt and Au atoms were assessed using the L_3-edge, although these edges were separated by only 350 eV. For this reason, the Au L_3-edge appears in the center of the Pt EXAFS oscillations, meaning that the L_3-edge EXAFS analysis of these PtAu NPs did not generate useable data, even though these NPs were found to function very well as fuel cell cathode catalysts [59, 60]. The Pt and Au K-edges, however, were well separated such that the analysis of these PtAu NPs was possible, and the coordination numbers shown in Table 11.2 could be obtained.

In the case of both Pt and Au edges, homoatomic pairs were more favorable than heteroatomic pairs, such that $N_{Pt–Pt}$, $N_{Au–Au} > N_{Pt–Au}$, $N_{Au–Pt}$, indicating a segregated structure. The total numbers of atoms around the Pt and Au atoms were 9.2 and 12.4, respectively, demonstrating a Pt shell with a Au core. Table 11.2 presents the calculated values based on the core–shell model, which are evidently in good agreement with the experimentally observed data. These experimental values correspond well to the values derived from the model structure depicted in Fig. 11.12, in which two Pt shells cover an Au core.

PtPd NPs supported on SiO_2 with various compositions were prepared from PVP (polyvinylpyrrolidone)-protected bimetallic nanoclusters [61–63], and the associated coordination numbers determined by EXAFS were given in Table 11.3 [63].
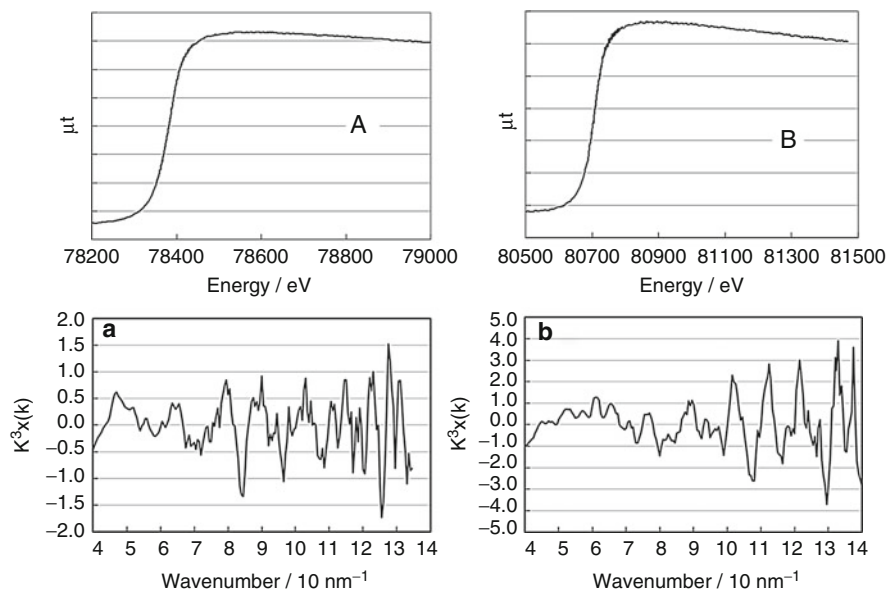
Fig. 11.11 (*A* and *B*) XAFS spectra and (*a* and *b*) oscillations derived from the Pt and Au K-edges

Table 11.2 Coordination numbers around Pt and Au atoms in NPs

	Coordination number for the scattering metal (Pt)		Coordination number for the scattering metal (Au)	
Absorber	Experimental	Calculated[a]	Experimental	Calculated[a]
Pt	7.2 ± 2.9	6.7	2.0 ± 0.8	2.1
Au	2.7 ± 2.7	2.3	9.7 ± 2.9	9.6

[a]Calculated based on the model structure depicted in Fig. 11.12

The coordination numbers of the homoatomic pair were larger than expected from the composition and random alloy model, indicating the segregation structure. However, the total coordination numbers of Pd and Pt were less than 12, indicating not a core–shell but a cluster-in-cluster-type structure [63]. Careful investigation of the coordination number determined by XAFS can provide information about the inner structures of bimetallic NPs.

6.2   In Situ XAFS

XAFS is a potentially suitable technique for in situ/*operando* experiments [64]. Due to the exceptional ability of X-rays to transmit through materials, various cell designs become possible, in which the incident, emitted, or transmitted X-rays are properly monitored by detectors. As a result, numerous cells have been

Fig. 11.12 Structural model for a PtAu nanocluster. *Gray* and *yellow* balls represent Pt and Au atoms, respectively
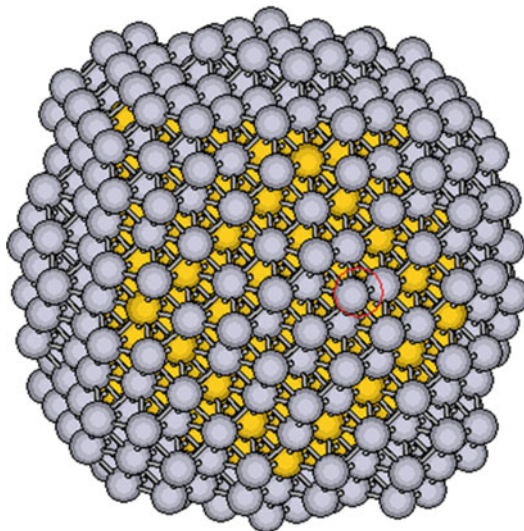
Table 11.3 XAFS data for PtPd bimetallic alloy nanoparticles

Pt:Pd	Pd–Pd	Pd–Pt	Pt–Pd	Pt–Pt
1:4	6.9 (7.7/8.2)[a]	1.4 (1.1/1.2)	6.1 (4.5/4.7)	4.1 (7.5/5.2)
1:2	6.2 (6.3/6.9)	2.8 (1.9/2.4)	5.0 (3.8/4.7)	5.7 (8.2/5.0)
1:1	5.1 (4.5/5.6)	3.7 (3.0/3.7)	3.2 (3.1/3.7)	6.5 (8.3/5.9)
2:1	5.2 (3.0/5.0)	5.8 (3.8/4.7)	2.7 (1.9/2.4)	5.6 (8.9/6.9)

[a]Values in parentheses indicate the coordination numbers derived from core–shell and cluster-in-cluster models, respectively [63]. The cluster-in-cluster model is shown to agree with the experimentally observed data

developed to date, and dynamic structural and electronic analyses of active species under working conditions have been conducted. This section primarily focuses on in situ XAFS studies applied to the analysis of catalysts under reaction conditions.

6.2.1 Principles of the In Situ XAFS Cell

The structure of a cell strongly depends on the X-ray energy, the reaction phase or atmosphere (vacuum, gas, or liquid), and the temperature. Since the cell is usually made on a smaller size scale than a realistic reactor and tuned to obtain the best spectrum, the chemical state of a catalyst might not be the same as in an actual reactor even if the temperature, gas atmosphere, and reaction time are finely adjusted. Therefore, to understand the catalysis more accurately, simultaneous evaluation of the catalytic performance is very important. The use of a conventional product analysis technique such as gas chromatography (GC) during the reaction would be one means of simultaneously evaluating the catalytic activity, although the time required for each analysis could be as long as 20–30 min, which is much longer than the time required for an XAFS measurement (less than 1 min per
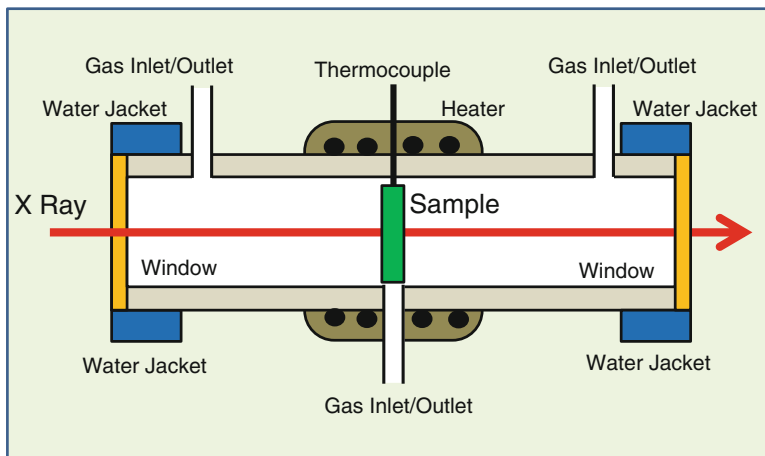
Fig. 11.13 Typical example of a type I XAFS sample cell

spectrum). If a transient process is being investigated by XAFS to determine how the active sites are formed or how they respond to changes in reaction conditions, gas-phase analyses using mass spectroscopy or gas-phase infrared (IR) spectroscopy are preferable because they have comparable time resolutions to that of XAFS [65]. In addition to the gas-phase analysis, simultaneous observations of the catalytic sample using XRD, IR, and Raman spectroscopy can be used to obtain information regarding the lattice, the adsorbates, and both, respectively, in conjunction with XAFS [66]. These techniques thus represent powerful tools for the investigation of various properties of catalysts under reaction conditions.

In Situ XAFS Cell for Gas-Phase Reactions over Solid Catalysts

When the sample is a solid and is well suited to analysis by transmission mode XAFS and the reaction is conducted in the gas phase, the design of the cell is very simple, and two types of cell are usually used. One type has almost the same structure as cells used for other spectroscopic analyses, such as IR spectroscopy (Fig. 11.13, type I) [67], while the other is a capillary type (Fig. 11.14, type II).

In the case of the type I cell, the body is made of glass [68] or a metal such as stainless steel [67]. The sample is pressed into a wafer (pellet) and set in the center of the cell, and heaters are attached around the wall at the center of the cell. Both ends of the cell are equipped with water jackets to cool the regions around the windows, and o-rings are often used to seal the cell. The X-rays enter through a window on either side of the cell and pass through the sample before exiting from the other side. The only substantial difference between this apparatus and an IR cell is the window material. The windows should be as transparent as possible to the X-rays and therefore should be composed of light elements such as beryllium [69] or certain plastics. Although the window part is cooled with water jackets, it is advisable to situate the windows far from the sample area. When the measurement

Fig. 11.14 Schematic of a type II cell
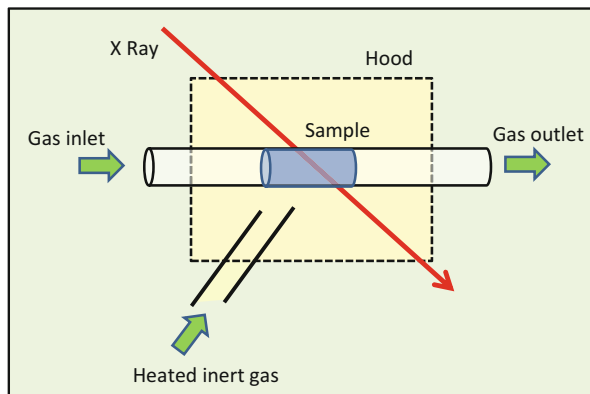
is conducted with high-energy X-rays (over 20 keV), attenuation by the reactant gases will have little effect. For example, when 20 keV X-rays pass through a cell filled with a gas mixture composed of 5 % thiophene in hydrogen at atmospheric pressure with a 300 mm path length, the μt value attributed to gas-phase absorption is approximately 0.02. It is therefore possible to construct an elongated cell in which the windows are situated far from the heaters so as to avoid direct contact between the heated gas and the windows [70]. In addition, this type of apparatus prevents direct contact of the heated gas with the windows when introducing the reactant gas from the side of the cell near the windows such that it flows to the center of the cell where high temperature reactions occur. Ichikuni et al. succeeded in observing the carburization of Nb supported on mesoporous silica up to 1223 K with this type of cell [70]. Using this structure, many types of plastics may be employed as windows. As an example, acrylic resin disks were used in a cell built for the analysis of Rh catalysts under high pressure (3 MPa) during CO_2 hydrogenation conditions where thickness of the disks was 3 mm ($\mu t = 0.15$ per disk in Rh K-edge) [67]. Acrylic resin is convenient because it is readily available, relatively hard, and transparent to visible light, making it possible to see the inside of the cell. Polyimide is also often used as a window material due to its good transparency to X-rays and tolerance to chemicals and high temperature (up to approximately 573 K) [71]. Consequently, this material would be suitable for the analysis of pressurized reactions of organic compounds. Type I cells are now widely used for XAFS experiments and some facilities are equipped with cells available to visiting users [72].

The type II cell is similar to the tubular reactors used for catalytic reaction tests. As shown in Fig. 11.14, the temperature of the cell is controlled by an inert gas pumped into a surrounding hood and the reactant gases pass through a catalyst bed. Therefore, if conditions such as temperature, pressure, and flow rate are properly controlled, it can be regarded as reproducing realistic reaction conditions. In the case of the type I cell, there are some pathways by which the gas can move without contacting the sample, while the type II cell avoids this problem. However, there
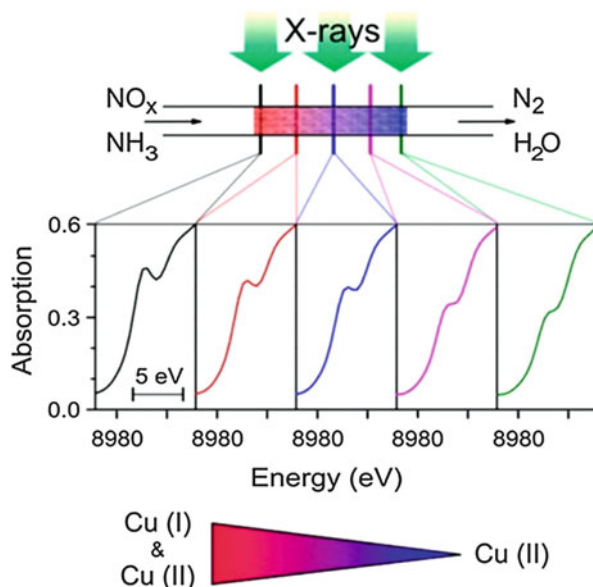
are still challenges with tubular cells. Firstly, the walls of the cell function as the
X-ray window and so must be made of a material that is transparent to X-rays. In
addition, the walls should be resistant to heat and internal pressurization. To
meet all these requirements, glass capillaries are often used [73], since these can
be used at 723 K under an internal pressure up to 5 MPa. Beryllium [74] and AlN
[75] have also been used for this type of cell. Usually these cells are made with very
thin tubes less than 1 mm in diameter, and therefore, the incident beam must be
properly focused and aligned. In addition, due to the tube curvature, the sample
thickness differs along the vertical direction. If an XAFS spectrum is obtained as
the sum of transmitted beams passing through different thicknesses, the spectrum
can be deformed compared with the one observed for a sample with a uniform
thickness. Deviation of the beam position can affect the spectrum as well, and the
ability to adjust the sample thickness is somewhat limited. Despite these issues,
experiments using tubular cells have reported good results to date, due to precise
alignment of the optical equipment and highly focused beams. In particular, the
tubular cell has been used to allow the spatial analysis of catalyst beds. It is
commonly believed that the chemical state of active species differs depending on
their position in the reactor, since the reactant gas composition varies between the
entrance and the exit. Doronkin et al. applied this technique to the study of a catalyst
during the selective catalytic reduction (SCR) of NOx by NH_3 [76]. They clearly
observed variations in the chemical states of active sites (Cu or Fe) even within a
10 mm long catalyst bed, as shown in Fig. 11.15. These results indicated that the
interpretation of XAFS data obtained for a bulk sample under working conditions
should be conducted with care, taking into account the presence of different phases.

Both of these cell types may be used for the *operando* analysis of catalysts, but they may also be employed for the observation of the phase transition processes of various materials under controlled atmospheres.

In Situ XAFS Cell for Liquid-Phase Reactions over Solid Catalysts

Liquid-phase reactions are also vital in the chemical industry, and so it is important to investigate the structural changes of catalysts under working conditions in order to determine the active phases and to elucidate the reaction mechanism. Compared to gas-phase reactions, cell designs for solid catalysts in liquids require special concepts for windows because of the higher X-ray absorption and heat conductivity of liquids. The same type II cells used for gas-phase reactions may be employed, but with some modifications. Recently, an experiment with supercritical water was reported in which an AlN tube was used as the cell [75]. As in the case of gas-phase reactions, real-world reaction conditions may be more closely reproduced with tubular cells. The diameter and the thickness of the walls should be optimized depending on the conditions, although the same apparatus used to study gas-phase reactions can be employed.

When a type I cell is used for liquid-phase reactions, the windows must be set close to the sample, as shown in Fig. 11.16, in which the inner space has a width of 2 mm.

In such cases, it is impossible to avoid direct contact of heated reactants with the windows, and therefore the window materials must be able to withstand high temperatures and pressures, as well as certain chemicals. Beryllium can meet all these requirements and so it has been used to form X-ray windows, although it is toxic when inhaled or absorbed through the skin, and so careful handling is
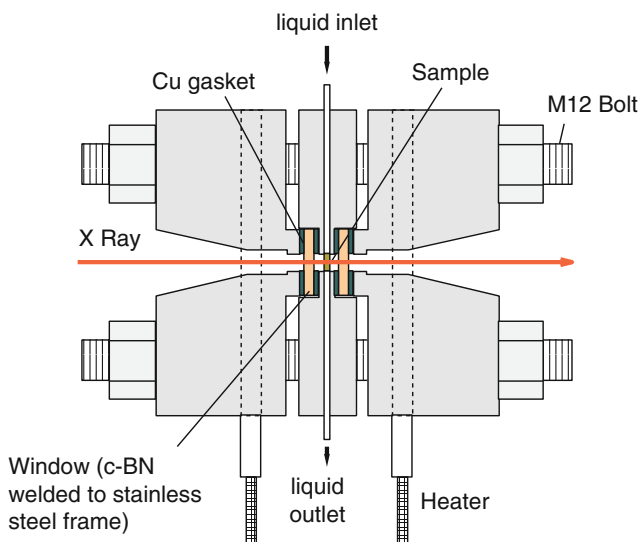
Fig. 11.16 Schematic drawing of the XAFS cell used for analysis of a high-pressure liquid phase
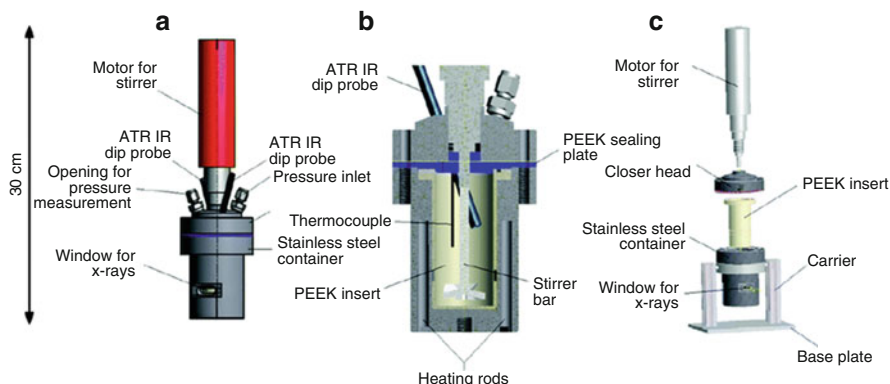
Fig. 11.17 *Operando* XAFS and ATR-FTIR cells for the Au L$_{III}$-edge XAFS of Au/CeO$_2$ during hydrogenation of nitrobenzene (Reproduced from Ref. [82] with permission of The Royal Society of Chemistry)

necessary, such as working in a ventilation hood with plastic gloves [77]. As noted in the previous section, polyimide is another good material for X-ray windows, since it will withstand exposure to many chemicals and tolerates heat up to 500 K. At approximately 573 K, however, polyimides soften and swell, which could lead to plugging of small inner spaces such as that in the cell shown in Fig. 11.16. Polybenzimidazole and other engineering plastics [78] exhibit good stability upon exposure to chemicals, heat, and pressure, such that no degradation is observed when disks of this material are used at 553 K under 4 MPa in direct contact with organic solvents [79]. However, this material may not be used above 723 K. Cubic boron nitride (c-BN) is a thermally and chemically stable inorganic material, and, in the apparatus in Fig. 11.16, sintered c-BN disks are used as windows (800 *μ*m thick, 4 mm wide) [80]. Theoretically, this material can resist temperatures up to 1625 K and pressures up to 10 MPa. In practice, the cell was found to tolerate 723 K at ambient pressure and 613 K at 3 MPa [81]. (Unluckily, the company (SEI) stopped supplying the material in 2015).

When studying reactions in which solid catalysts are suspended in a liquid, the catalysts should be kept uniformly mixed to allow for suitable XAFS analysis. An autoclave-type cell enables both XAFS and attenuated total reflectance Fourier transform infrared (ATR-FTIR) measurements in such cases [82]. Here, the sample is suspended in the solvent within the cell, and XAFS and ATR-FTIR data are acquired simultaneously while heating and stirring the reaction mixture (Fig. 11.17). Experiments using autoclaves are of interest, because the direct visual observations of reactions inside autoclaves are typically difficult, so indirect observation of the formation of new crystalline substances might provide useful information regarding the synthesis of new materials.

It is important to note that slight fluctuations in pressure will produce serious deformations in the XAFS background, due to the high density of the liquid medium, which could in turn affect the analysis of the XAFS spectra (Fig. 11.18).

Fig. 11.18 Pt L$_{III}$-edge XAFS data for a Pd–Pt/SiO$_2$ catalyst during the HDS reaction of a model oil at 553 K and 4 MPa. The baseline is deformed due to the liquid pump pulsations
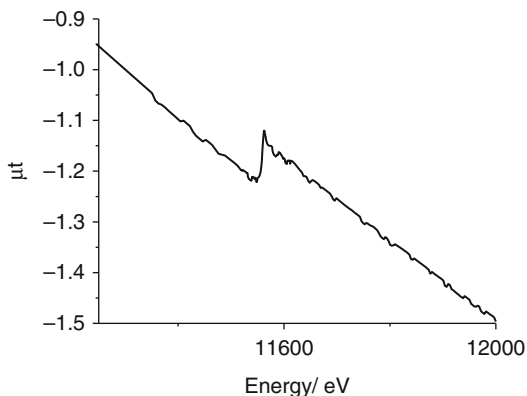
Precise control of the reactant flow rate is required to suppress this effect. When the reaction is between a gas and a liquid over a solid catalyst, it is advisable to stop the reaction and separate the solid catalyst from the liquid by sedimentation [83] or filtration [84] in order to reduce the density and composition fluctuations.

6.2.2 Simultaneous Measurements of Catalyst with Various Methods

XAFS gives information about local structures around the X-ray-absorbing atom. Usually, additional analyses with other techniques are conducted separately to study complimentary properties of the material. In such cases, due to the difference in conditions, including the shape of the reactor, the amount of sample, the gas flow rate, the temperature distribution, and so on, it is challenging to exactly reproduce the same reaction conditions with different instruments. Thus, obtaining a perfect time-resolved correspondence between multiple data sets requires much care. Simultaneous observations of the same sample under the same conditions with different spectroscopic methods are ideal and provide much useful information about catalysts, and in situ XAFS combined with XRD, UV, and IR spectroscopy has been reported [85]. In one example, combined *operando* XAFS and FTIR analyses of nickel phosphide catalysts were performed under hydrodesulfurization (HDS) reaction conditions [86, 87]. The supported Ni$_2$P catalyst was found to be active for the HDS of diesel fuel, and its performance was shown to be higher than that of industrial catalysts [88]. Significant work has performed with the aim of clarifying the cause of the high efficiency of Ni$_2$P during HDS. According to structural analysis of spent catalysts by ex situ XAFS and XRD, the bulk Ni$_2$P structure is stable under HDS reaction conditions [81, 89]. However, it was also found that sulfur was strongly bound to the Ni$_2$P surface and appeared to work as a promoter rather than as a poison. In order to confirm the role of sulfur species and elucidate the reaction mechanism, a combined *operando* XAFS and FTIR study was carried out, using the cross-shaped cell shown in Fig. 11.19. Here, both the X-ray and IR beams pass through a sample set in the center of the cell and both of the spectra are acquired in the transmission mode. The IR spectrometer was equipped with an optical fiber (ZnSe) capable of transmitting the IR beam to the
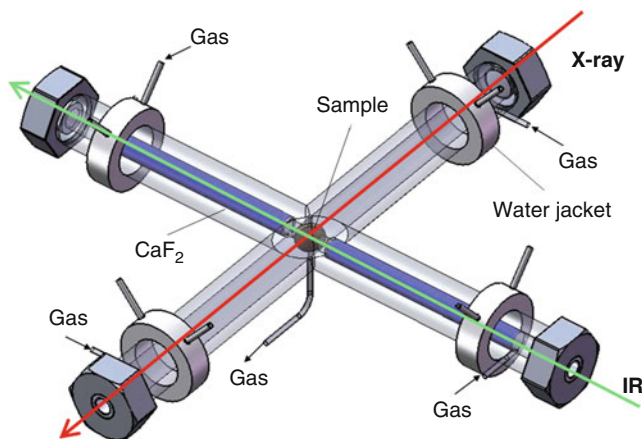
Fig. 11.19 Schematic of an in situ XAFS and IR cell [86]
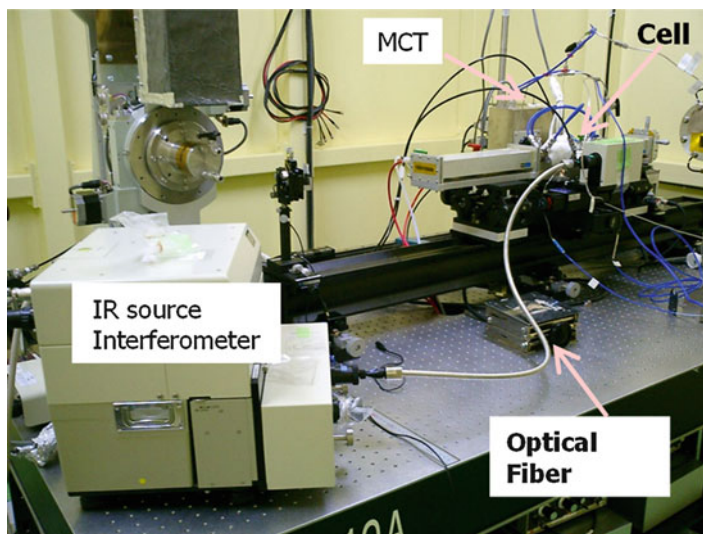
Fig. 11.20 Experimental apparatus consisting of an IR spectrometer (JASCO VIR-9500) inside an XAFS experimental hutch (PF-AR NW10A)

desired location, as shown in Fig. 11.20. Figure 11.21 presents the result of this combined analysis, at the onset of the HDS reaction over an MCM-41-supported Ni$_2$P catalyst. The green data points indicate changes in the XANES data at 8333.3 eV, which are proportional to the amount of surface Ni–S species [65]. These values can be directly compared to the IR adsorption due to the aliphatic ν(CH) region and the amount of H$_2$S produced as observed at m/z = 34 by mass spectrometry. It was found that Ni–S species were formed immediately after the

Fig. 11.21 XANES data at 8333.3 eV (*green circles*) together with IR absorption in the aliphatic ν(CH) region (*red stars*) and the formation of H_2S (*blue circles*) during HDS at 513 K [86]
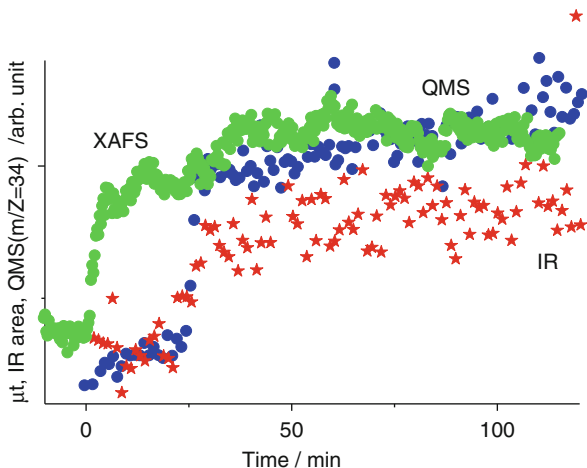
reaction started. Following approximately 5.5 min of reaction time, the XANES values exhibit a slower rate of change although S still accumulates. In contrast, the IR band absorption and production of H_2S are negligible up to 20 min, after which both suddenly increase. These results indicate that the sulfur introduced at the initial stage of the reaction formed Ni phosphosulfide (NiPS) and that, when the NiPS concentration reached a certain level, the catalytic HDS reaction of thiophene began and tetrahydrothiophene appeared as a reaction intermediate on NiPS.

The combination of time-resolved XAFS and FTIR elucidated the active structure and the intermediate species formed during the HDS of thiophene. In this example, consecutive events which could not be followed with a single method were captured using three techniques, allowing analysis of the overall reaction process on the catalyst. The catalyst substrate often consists of metal oxides that contain lighter elements such as silicon, aluminum, and magnesium. Since the absorption edge energies for these elements are typically low, measurements are usually conducted under ultrahigh vacuum (UHV) conditions. However, the substrates play an important role in the catalysis process, so it is of significant interest to know how these atoms behave under ambient conditions. For this reason, using a cell as thin as 0.8 mm, in situ Al K-edge XAFS measurements of USY and ZSM-5 zeolites have been performed [90].

Various electrochemical devices, including fuel cells and sensors, have also been investigated by XAFS [91]. The performance of these devices is evaluated while applying the currents or potentials expected under regular operating conditions. In the case of fuel cells, increasing the lifetime of the platinum catalyst on the electrode is a crucial step in developing marketable devices, and so the deactivation process mechanism has been intensively studied. Due to the complicated multilayered structure of a fuel cell, however, successful experimentation requires an apparatus in which there is a path by which X-rays can reach the active components [92].

6.2.3   General Notes Regarding In Situ XAFS

As synchrotron radiation facilities have progressed, the available X-ray beam
intensities have increased, and photon flux values much greater than $10^{10} \, \text{cm}^{-2} \, \text{s}^{-1}$
are available. Although such high-brilliance sources are necessary for high-quality
time- and space-resolved XAFS measurements, their use also requires special care
to prevent damage to the X-ray windows and the sample. Figure 11.22 shows a
photograph of an X-ray window made of acrylic resin following a 24 h XAFS
operando experiment with an X-ray energy of approximately 11 keV using a
focused bending beam line at the Photon Factory (a 2.5th-generation synchrotron
radiation source). Discoloration is observed at the center of the window. Very slight
but discernible discolorations are also seen when using inorganic materials such as
SiO_2 and Al_2O_3, presumably representing color centers due to oxygen defects.
There are currently many synchrotron radiation facilities that require special pre-
cautions to prevent radiation damage to cells and specimens.

   An important point regarding the Debye–Waller factor in in situ EXAFS
analysis should also be considered. Under reaction conditions, high temperature
may increase the Debye–Waller factors due to increasing levels of thermal
disorder (Fig. 11.23) [93]. The EXAFS amplitude at high temperatures decreases
such that the coordination number derived from EXAFS analysis becomes
smaller if the Debye–Waller factor estimation is invalid. The effect of deviation
of the Debye–Waller factor for an observed scattering can be estimated by
the analysis of standard compounds with similar structures at the same temper-
ature. Another means of addressing this problem is to apply a combination of
other experimental techniques, such as XRD, and simulation techniques such
as molecular dynamics (MD), Monte Carlo (MC), and reverse MC (RMC)
[94, 95]. The cumulant expansion analysis may be helpful though much care
about the convergence of the expansion should be paid at high temperatures.
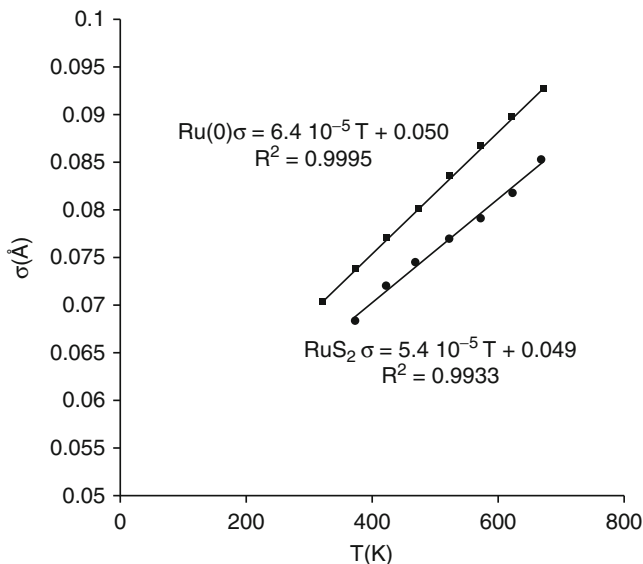
Fig. 11.23 Temperature dependencies of the Debye–Waller factors of bulk RuS_2 and Ru(0) (Reproduced from Ref. [93]. Copyright transfer 2007, with permission from Elsevier)

6.3 Time-Resolved XAFS

XAFS has the potential to elucidate the mechanisms of dynamic processes such as chemical reactions or phase transitions of materials, since XAFS spectra can be obtained from any material without long-range order in any environment, as noted in Sect. 6.2. To observe such dynamic processes, the XAFS spectrum should be obtained within a time span of several seconds or preferably milliseconds or shorter. However, a conventional XAFS system working in the step-scan mode cannot acquire an entire XAFS spectrum within such short timescales because the monochromator must stop at each discrete energy value to measure the signal. The energy range of an XAFS spectrum is usually more than 1000 eV, and thus several tens of minutes are required to acquire an XAFS spectrum. Figure 11.24 shows two typical time-resolved XAFS methods: Quick XAFS (QXAFS) and dispersive XAFS (DXAFS). In a QXAFS system, the monochromator is moved rapidly and the signals are measured continuously and simultaneously (known as "on the fly") [96]. The typical measurement time required for a QXAFS spectrum is between several hundred milliseconds and several seconds. QXAFS does not require any changes in the experimental setup from the conventional step-scan mode and various detection methods can be applied, such as the transmission mode, fluorescence mode, and electron yield method. QXAFS has been widely applied to observe the formation of Pd NPs [97], Pt NPs [98], and Au NPs [99], the catalytic reactions
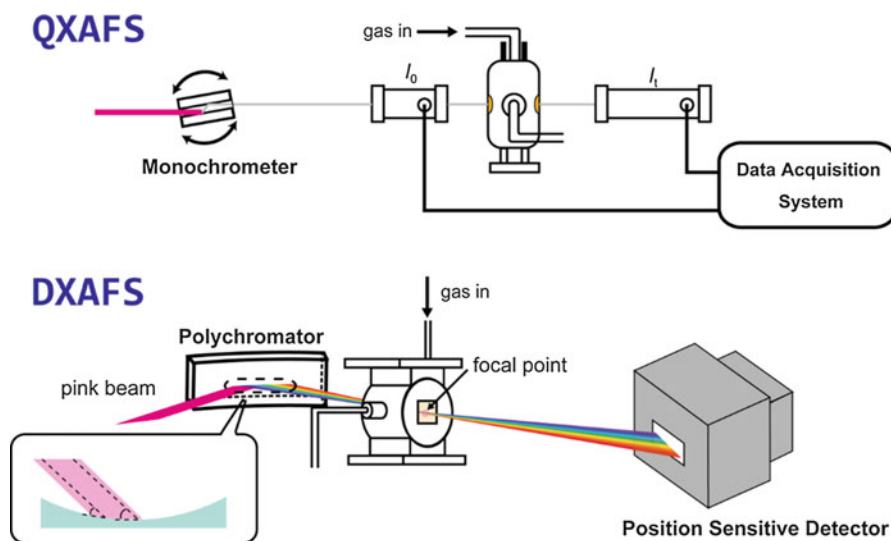
Fig. 11.24 Schematic of QXAFS and DXAFS instrumentation

of zeolite catalysts [100], the growth of Au thin films [101] and HfO$_x$ films [102], the reduction of hematite and calcium ferrite [103], and Pt catalysts on the cathode of a polymer electrolyte fuel cell under working conditions [104]. In contrast, monochromators are not used in DXAFS systems [105]. Rather, a curved single crystal, known as a polychromator, is used, and the incident X-ray direction is gradually moved against the lattice plane of the crystal to achieve different Bragg angles on the surface of the polychromator. X-rays with different energies are thus dispersed at different angles and focused at the sample location, as shown in Fig. 11.24. Transmitted X-rays from the sample with different energies are detected simultaneously by a position-sensitive detector such as a position-sensitive proportional counter (PSPC), a photodiode array detector (PAD), or a charge-coupled detector (CCD). Consequently, an entire XAFS spectrum can be acquired simultaneously. The time resolution of a DXAFS system depends on the detector time constant, since there are no physical movements of optical components as there are in the case of monochromators. The typical acquisition time per spectrum ranges from microseconds [106] to several seconds. In principle, fluorescent X-rays cannot be obtained with these systems. DXAFS has been also applied to the study of automobile catalysts [107, 108] and PtSn NPs on γ-Al$_2$O$_3$ [109] or active carbon [110], formation of PdZn nanoparticles on a ZnO substrate [111] or Rh nanoparticles in a liquid phase [112], a catalytic reaction of Re clusters [113] or Rh nanoparticles on γ-Al$_2$O$_3$ [114], the photodeposition of Rh NPs on TiO$_2$ [115], the decomposition of Rh clusters by CO absorption [116], and other processes. DXAFS and QXAFS can be applied to the study of irreversible changes on these timescales.

In the case of faster processes occurring in less than a microsecond, one may use a pump–probe method that requires reversible or repeatable processes. Both pump and probe lights produce pulse shapes. A laser is the most commonly used pump source and synchrotron radiation may be applied as the probe light. The typical pulse duration for a synchrotron light source is 100 ps

In the 1980s, the recovery of bonds between carbon monoxide (CO) and myogloobin (Mb) was observed by pump–probe XAFS [117]. The bonds were initially broken by irradiation with a pulsed Nd:YAG laser, and the reconstruction of the CO–Mb bonds was observed by measuring the Fe K-edge through XAFS spectra. Chen et al. employed a pulsed laser with a pulse duration of 5 ps and a wavelength of 351 nm [118], operating at a 1 kHz repetition rate. Only those X-ray signals synchronized with the laser irradiation were acquired. They observed photoexcitation of a Ni–porphyrin complex dissolved in piperizine. Two piperizine molecules were found to be bonded to one Ni atom in the ground state. The peperidine molecules detached from the Ni atom immediately following the laser excitation and then reconnected to the Ni atom. This work determined that the excited state of the Ni complex had a lifetime of 28 ns, based on the XAFS data, and also allowed estimation of the bond lengths between Ni and the porphyrin N by analyzing EXAFS oscillations [118]. There have been several studies focusing on excited states of metal complexes in the liquid phase. Chen et al. also observed the photoexcitation state of a Cu complex [119], and Chergui et al. studied the excited states of $Fe[bpy_3]^{2+}$ [120] and a Re complex [121], while Nozawa et al. observed Fe $[phen_3]^{2+}$ [122] and Sato et al. experimented with a $Ru[bpy_3]^{2+}$ [123] complex in the liquid phase. A photoexcitation state of an Os complex has also been reported [124]. In addition, dynamic processes in functionalized materials such as dye-sensitized solar cells and photocatalysts have been elucidated [125–127]. The photoexcitation state of WO_3 has also been studied by XAFS in conjunction with a 400 nm pulse laser [128]. WO_3 is a visible, light-sensitive photocatalyst used for the water splitting reaction with a band gap of approximately 2.6 eV. In WO_3, electrons in the valence band can be excited to the conduction band during the photoabsorption process. The valence and conduction bands are primarily composed of O 2p and W 5d orbitals, respectively, and the d electron density of W atoms is increased following photoexcitation. W L_{III} XANES spectra with and without laser excitation are shown in Fig. 11.25. The absorption intensity around 10,216 eV is observed to decrease 150 ps after the excitation, indicating an increase in the electron density of W.

Although transient XAFS measurements are a powerful tool for the observation and determination of short-lived species, practical experimentation is very challenging, since very long data acquisition times are needed to obtain XAFS spectra with good S/N ratios. Recently, drastic advances in transient XAFS methodology have been achieved in Advanced Photon Source (APS) at Argonne National Laboratory [129] and Swiss Light Source (SLS) at Paul Scherrer Institute [130]. Pumped lasers have normally been operated at 1 kHz; however, the rate of X-ray pulses obtained from a synchrotron facility is more than 1 MHz. Most of these X-rays are not used in transient XAFS measurements. However, the new APS

Fig. 11.25 XAFS spectra and differential XAFS spectra of photoexcited and ground-state WO_3
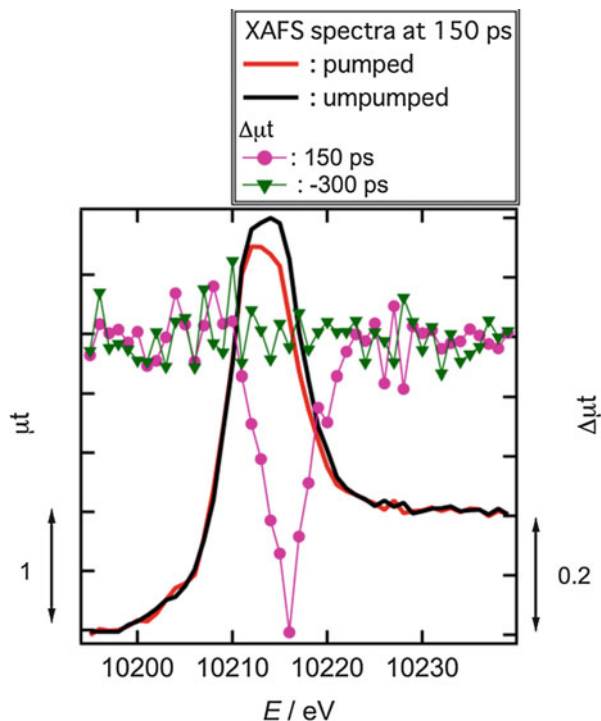
and SLS systems employ high-repetition, high-power lasers capable of emitting pulses at several hundreds of kHz up to several MHz. The repetition rates of transient XAFS measurements can thus be increased to more than several hundred kHz. This strategy has enabled the acquisition of transient XAFS signals in much shorter time spans [129] and the analysis of transient species that would not have been identified using a conventional 1 kHz system [127]. There has also been progress in transient XAFS experiments. The time resolution of transient XAFS experiments is usually equal to the pulse duration of the X-rays, which is typically 100 ps when employing a synchrotron radiation light source. A special operation [131] or special techniques [120] such as low alpha mode [132] or the slicing method [133] are necessary to achieve a time resolution less than 100 ps. X-ray free-electron lasers (XFEL), however, provide coherent, intense, and very short duration X-ray pulses, with durations of several tens of femtoseconds. The photoexcited state of Fe[bpy]$^{2+}$ was successfully observed using an XFEL at LCLS [134]. Photoexcitation of iron(III) oxalic acid in aqueous solution was also successfully observed by XFEL in a Japanese study at SACLA at Nishi-Harima area [135]. Additional XFEL facilities, such as the XFEL facility in Europe or the FEL facility in Switzerland, are now under construction. XFEL X-ray pulses thus have shown significant potential to allow progress in pump–probe XAFS experimentation.

6.4   PTRF-XAFS: Application of XAFS to Single-Crystal Model Surfaces

XAFS is a powerful technique capable of providing information about the local structure around an X-ray-absorbing atom with sub-Å resolution. The application of XAFS to metal species dispersed on an oxide single-crystal surface, which can be regarded as a good model of an actual oxide-supported metal catalyst, should provide helpful information about the structures of the metal species and metal–support interactions. In this section, polarization-dependent total reflection fluorescence (PTRF)-XAFS technique for determining 3D structure of metal species deposited on a single-crystal surface is described.

6.4.1   Basics of Polarization-Dependent Total Reflection Fluorescence (PTRF)-XAFS Technique

The angular dependence of EXAFS oscillations is expressed as in Eqs. (11.14) and (11.15) [136]:

$$\chi(k) = 3\sum_i \cos^2\theta_i \chi_i(k) \quad \text{for K-edge and L$_I$-edge absorption.} \tag{11.14}$$

$$\chi(k) = \sum_i \chi_i(k)(0.7 + 0.9\cos^2\theta_i) \quad \text{for L$_{II}$ and L$_{III}$-edge absorption.} \tag{11.15}$$

Here, $\chi(k)$, θ_i, and $\chi_i(k)$ are the overall EXAFS oscillation, the angle between the electric vector $\left(\vec{E}\right)$ of the incident X-rays and the ith bond direction, and the partial EXAFS oscillation accompanying the ith bond, respectively, as shown in Fig. 11.26a. When θ_i is 0°, the maximum contribution from the ith scattering atom is obtained.

The selection of the K-edge or L$_I$-edge is more effective as a means of assessing the polarization dependence of the bond direction compared to the use of the L$_{II}$- or L$_{III}$-edge, as can be predicted based on the dependence of $\chi(k)$ on θ_i. Various metal species have been studied in this manner on a TiO$_2$(110) single-crystal surface, since TiO$_2$ is a typical transition metal oxide and its single-crystal surfaces, especially TiO$_2$(110), have been extensively studied [137]. As shown in Fig. 11.26b, the TiO$_2$(110) surface has an anisotropic structure, and polarization-dependent XAFS data of metal species deposited on TiO$_2$(110) may be acquired by applying various polarization directions, such as [001], $\left[1\bar{1}0\right]$, and [110]. Consequently, we can obtain information regarding the orientations and bond directions of the metal species. Moreover, when the polarization is directed toward the substrate ($\vec{E}$ //[110] in Fig. 11.26c), we are able to elucidate the metal–support interaction more selectively. However, when XAFS is applied to a single-crystal system, we often face difficulties in terms of the low concentration of metal species on the small surface area in conjunction with high background scattering from the substrate. In conventional powder oxide-supported metal systems, the typical oxide
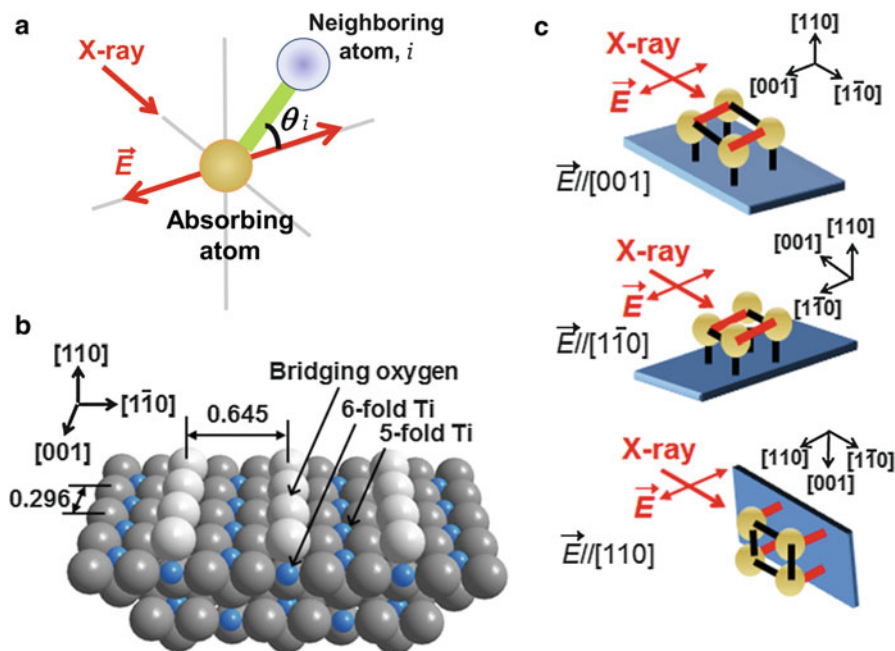
Fig. 11.26 (a) Definition of the angle θ_i between the polarization direction $\left(\vec{E}\right)$ and the ith bonding direction. (b) A TiO$_2$(110) surface with nomenclature (units are nanometers). (c) Three possible orientations for PTRF-XAFS measurements when using TiO$_2$(110) as a substrate surface

surface area is 100 m^2/g, such that it is possible to obtain suitable S/N ratios from XAFS data due to the abundance of metal species in the X-ray optical path. Conversely, a single-crystal oxide surface typically has an area of only a few cm^2, and the quantity of metal species contained thereon is only around 10^{-10} mol. Although surface XAFS using Auger electrons or secondary electrons has been developed, it is primarily applied to light elements such as C, N, and S [138, 139] because X-ray absorption edges of heavier elements (Ni and Cu) are above 4 keV, and thus the X-rays penetrate significantly into the bulk to create numerous background photoelectrons, which in turn greatly deteriorates the S/N ratio. In a grazing incidence X-ray configuration, the X-rays undergo total reflection and thus cannot penetrate into the bulk (or at least do not penetrate more than a few nanometers) [140]. Consequently, the surface sensitivity of the X-rays is enhanced. Thus, the total reflection and fluorescence detection XAFS modes have been combined. The fluorescence method provides the XAFS signal of the dilute system, since the probability of a fluorescence decay process for a core hole is greater than that for the Auger decay process in the hard X-ray region. Consequently, an XAFS signal can be obtained for a metal species on a single-crystal surface with a coverage as small as 10^{13} cm^{-2} [141]. Furthermore, in situ studies, which are not

Fig. 11.27 A 6-axis goniometer (X, Y, Z, θ, Φ, Ψ) for precise control of total reflection conditions [143] (Reproduced with permission of the International Union of Crystallography)
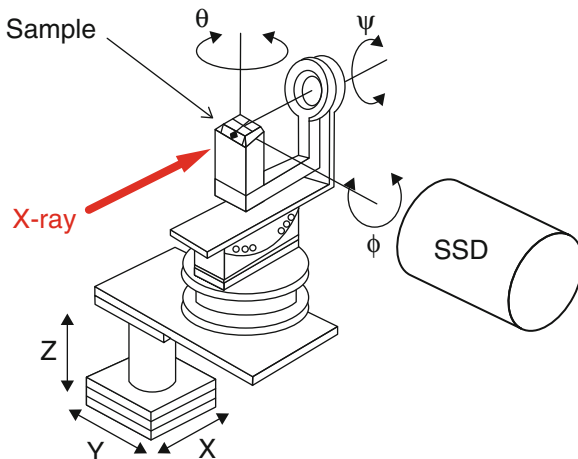
possible with the electron yield method, can be carried out. This technique is known as polarization-dependent total reflection fluorescence X-ray absorption fine structure (PTRF-XAFS) [142].

6.4.2   Setup for PTRF-XAFS Measurements

To achieve precise total reflection conditions, the sample is set on a 6-axis goniometer as shown in Figs. 11.27 and 11.28. When using ultra-high vacuum (UHV) PTRF-XAFS equipment [143], the goniometer is also placed under UHV conditions. The goniometer is made of aluminum in order to lessen the weight load on the stepping motors, and the rotational center of the goniometer is fixed to coincide with the sample surface. Three rotational axes (θ, Φ, and Ψ) are driven by bakeable vacuum stepping motors, while X, Y, and Z motions are introduced from outside the UHV chamber using standard stepping motors. After adjustment of the total reflection conditions, the fluorescence signal is collected by a multi-element solid-state detector (SSD) as illustrated in Fig. 11.27. The SSD is placed outside the chamber and the fluorescence signal is extracted through a Be window attached to the UHV flange.

Figure 11.28 shows the setup used for three different sample configurations, in which the electric vector is parallel to the surface (s-polarization) and perpendicular to the surface (p-polarization). If the surface symmetry is less than threefold, two directions parallel to the surface can be distinguished, a typical example being $TiO_2(110)$ as depicted in Fig. 11.26b, c.

6.4.3   Application of PTRF-XAFS to Metal Species on Single-Crystal Surfaces

The following sections review some of our group's work concerning metal species on single-crystal oxide surfaces as characterized by PTRF-XAFS.
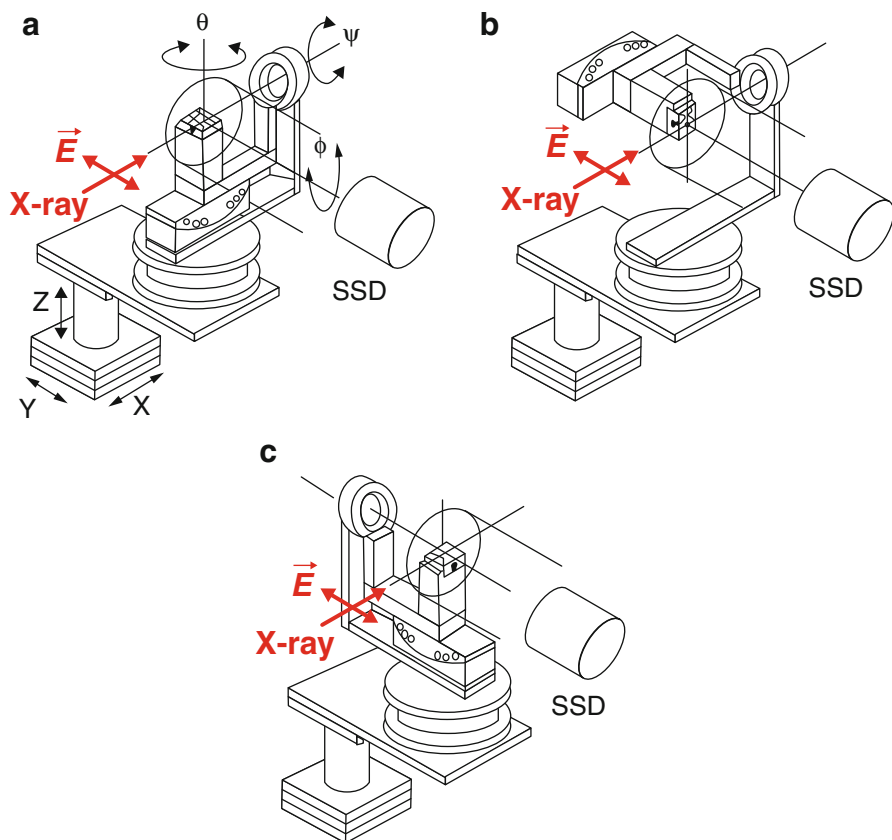
Fig. 11.28 Configuration of the 6-axis goniometer used for measurements against three different polarization directions: (**a**) *s*-polarization $\left(\vec{E}\,\|\text{surface}\right)$, (**b**) *p*-polarization $\left(\vec{E}\perp\text{surface}\right)$, and (**c**) a second *s*-polarization perpendicular to the direction of (**a**) [143] (Reproduced with permission of the International Union of Crystallography)

Metal Complexes on TiO$_2$(110)

Copper is one of the easily aggregated metals on a TiO$_2$(110) surface when evaporated at room temperature. This is due to the low stabilization energy of Cu on the TiO$_2$(110) surface and/or the small activation energy associated with Cu diffusion, suggesting that the strength of the Cu-bridging oxygen bond is not sufficient to fix the monatomic Cu. It is possible to obtain atomically dispersed Ni on TiO$_2$(110) because Ni has a greater formation energy with oxygen than with Cu [142]. Therefore, organometallic Cu may be used to stabilize metal complexes in the presence of suitable ligands [144, 145]. However, if the oxide support surface is premodified with an organic ligand that strongly fixes metal atoms through covalent bonds prior to the deposition of metal atoms, a well-defined atomically dispersed metal species can be obtained without the synthesis of organometallic
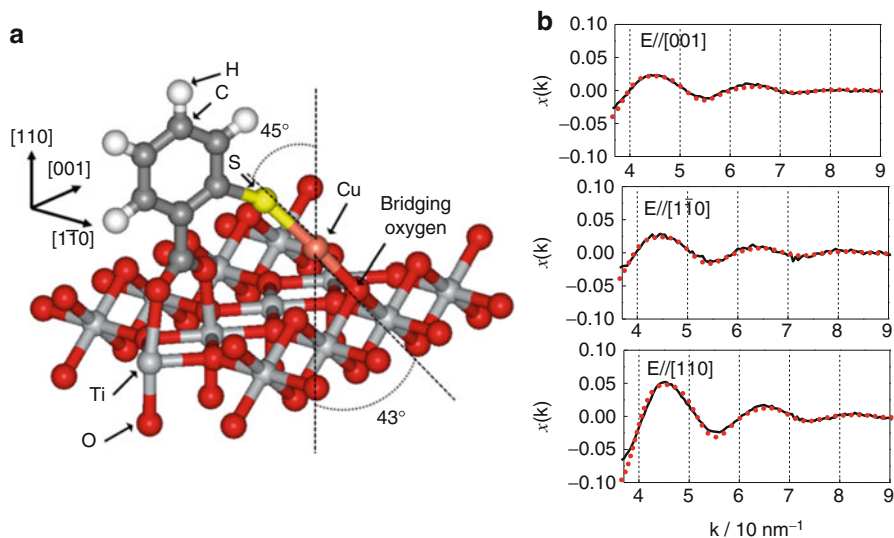
Fig. 11.29 (**a**) Structure of Cu/*o*-MBA/TiO$_2$(110). (**b**) Cu K-edge PTRF-EXAFS spectra, in which *black solid* and *red dotted curves* indicate observed and calculated EXAFS oscillations, respectively [147] (Reproduced by permission of the Royal Society of Chemistry)

compounds. This preparation method has been referred to as the premodified surface method and allows various organic compounds to be made available for premodification purposes and also provides fine-tuning of the surface metal structures [146–148]. As an example, we have successfully synthesized surface Cu complexes on TiO$_2$(110) through the evaporation of Cu on a surface premodified with *ortho*-mercaptobenzoic acid (*o*-MBA), as shown in Fig. 11.29a, such that the carboxylic group acts to bind to the TiO$_2$ substrate [147]. In this case, the monatomic Cu species was stabilized by bond formation with sulfur atoms of the corresponding MBA molecules and with bridging oxygen atoms on the TiO$_2$(110) substrate surface. The Cu–S bond length was found to be 2.19 Å, while the distance associated with the Cu–O interaction was 1.85 Å. The Cu–S and Cu–O bond angles to the surface normal were 45° and 43°, respectively. The 3D structure of the Cu species was determined by initially applying a preliminary curve fitting analysis to each spectrum for the three different polarization directions so as to confirm the formation of Cu–S and Cu–O bonds. An iteration method was subsequently employed, using the FEFF code [149] to simulate the polarization-dependent EXAFS oscillation of a given real-space structural model until a reasonable model was obtained that generated simulated spectra in good agreement with the observed spectra. As shown in Fig. 11.29b, the spectra calculated based on the final structural model (Fig. 11.29a) were in good agreement with all the observed spectra in all three different polarization directions. The S–Cu–O angle was also estimated to be 177°, which was quite close to the expected value of 180°.
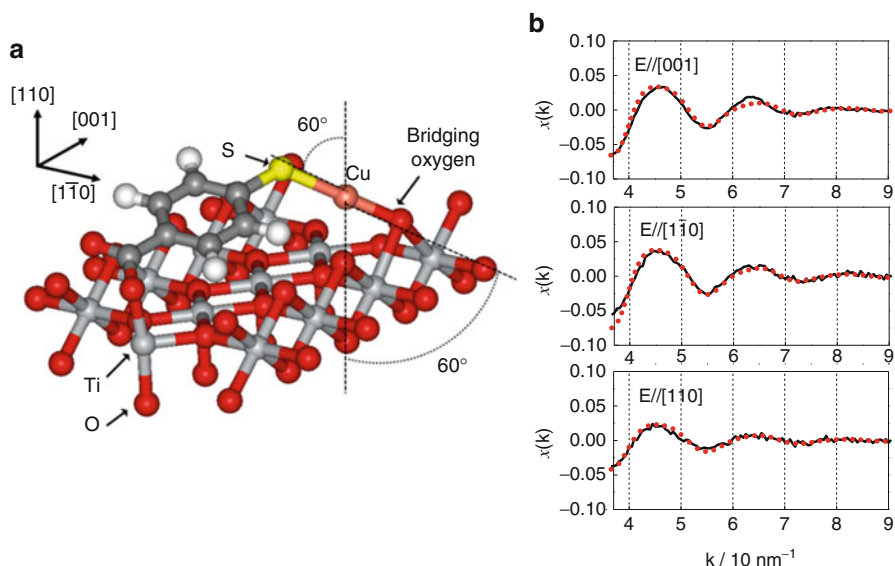
Fig. 11.30 (**a**) Structure of Cu/*p*-MBA/TiO$_2$(110). (**b**) Cu K-edge PTRF-EXAFS spectra, in which *black solid* and *red dotted curves* indicate observed and calculated EXAFS oscillations, respectively [147] (Reproduced by permission of the Royal Society of Chemistry)

The effect of the mercapto group position of MBA on the final Cu structure was also examined. This work demonstrated the formation of similar surface compounds (linear S–Cu–O) on *m*- and *p*-MBA-modified TiO$_2$(110) surfaces. However, the orientations of the S–Cu–O structure on the *o*- and *m*-MBA-modified TiO$_2$(110) surfaces (40–45° inclined from the surface normal) were different from that on the *p*-MBA-modified TiO$_2$(110) surface (60° from the surface normal). Figure 11.30a, b shows a model structure and the PTRF-EXAFS spectra for Cu/*p*-MBA/TiO$_2$(110). Note that the amplitude of the EXAFS oscillation in the [110] direction is smaller than that in the other two directions, which is in contrast to the results in Fig. 11.29b. This difference originates from the increased planar orientation of the Cu–S and Cu–O bonds of the Cu species compared with that in Cu/*o*-MBA/TiO$_2$(110) (see Eq. (11.14) regarding the polarization dependence of $\chi(k)$). These results suggest that the selection of an organic linker molecule enables fine-tuning of the orientations and configurations of metal structures. The chemical reactivity of the Cu species is also expected to vary with their configurations on the TiO$_2$(110).

The applicability of this premodification method was also extended to another metal. Following the premodification of the TiO$_2$ surface with *o*- or *m*-MBA compounds, atomically dispersed Au species were successfully obtained, even though Au normally aggregates to form 3D nanoclusters (see section "Three-Dimensional (3D) Nanoclusters on TiO$_2$(110)") when it is evaporated
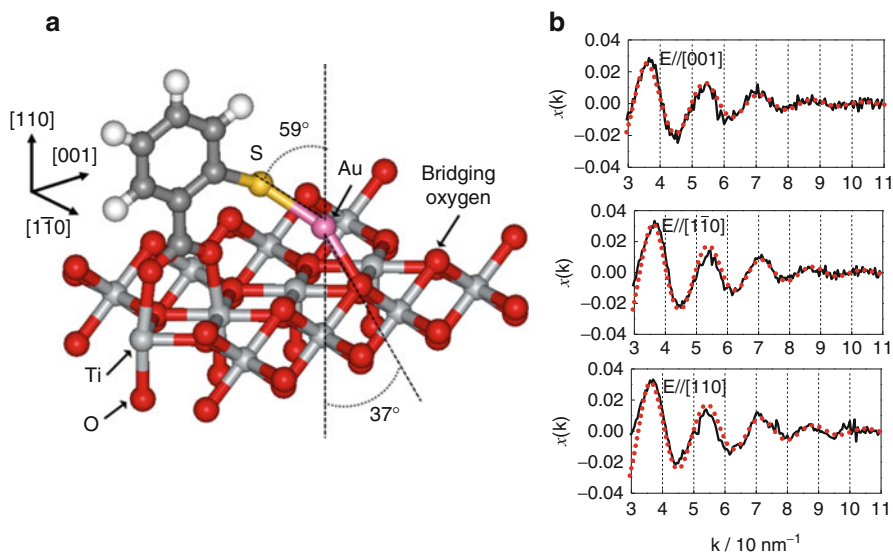
Fig. 11.31 (**a**) Structure of Au/*o*-MBA/TiO$_2$(110). (**b**) Au L$_3$-edge PTRF-EXAFS spectra, in which *black solid* and *red dotted curves* indicate observed and calculated EXAFS oscillations, respectively [148] (Reproduced by permission of the Royal Society of Chemistry)

directly onto a bare TiO$_2$(110) surface. Figure 11.31a, b shows the structural model and PTRF-EXAFS spectra for Au/*o*-MBA/TiO$_2$(110), respectively. In this case, Au atoms were sandwiched between a sulfur atom and a bridging oxygen atom, similar to the structure of Cu/MBA/TiO$_2$(110). In contrast, a TiO$_2$(110) surface premodified with thiophene carboxylic acid (TCA) did not generate atomically dispersed Au, although it was possible to disperse Cu on a TCA-pretreated surface [146, 148]. The failure of thiophene to fix atomic Au can be explained based on the different affinities of Au atoms for the S atoms in TCA and in MBA. To the best of our knowledge, no Au–thiophene compounds have been reported in the literature; however, there are many examples of Au–mercaptobenzene compounds.

Small Nanoclusters on TiO$_2$(110)

Goodman et al. have proposed that the Pd dimer is the most stable and also the smallest moiety that may be deposited on a TiO$_2$(110) surface [150]. Chun et al. observed Mo dimers on TiO$_2$(110) that had a similar local structure to that of bulk MoO$_3$ and found that the octahedral local structure was tetrahedrally distorted. The difference between the Mo and Pd dimers on TiO$_2$(110) is in the direction of the dimer axis in addition to the valence state. In the case of the Mo dimer, the Mo–Mo bond is directed in the $[1\bar{1}0]$ direction (perpendicular to the bridging oxygen row), while the Pd dimer is oriented in the [001] direction (parallel to the bridging oxygen row). These Mo dimers have been shown to change their

structure during the CH$_3$OH oxidation reaction, undergoing cleavage and reformation of Mo–Mo bonds [151, 152].

Tanizawa et al. created Cu trimers on a TiO$_2$(110) surface using the reaction of Cu(dpm)$_2$ (dpm = dipivaloylmethanate or 2,2,6,6,-tetramethyl-3,5-heptanedione) [144, 145] with bridging oxygen atoms, followed by low-temperature in situ reduction at 363 K, as shown in Fig. 11.32a [145]. The Cu trimer underwent strong interactions with the bridging oxygen atoms and exhibited an inclined molecular plane against the surface normal, with an inclination angle between the Cu$_3$ plane and TiO$_2$(110) surface normal of approximately 30°. The Cu trimer was transformed to a hexamer during in situ H$_2$ reduction at 473 K (Fig. 11.32b). In this process, Cu growth took place in the vertical direction, which corresponds to the [110] direction of fcc Cu. Recently, our group also identified Ni trimer growth along the [001] direction when a small amount of Ni was evaporated on a stepped TiO$_2$(110) surface. The Ni atoms in the trimer were located at the step edge, at which oxygen dangling bonds were present and directed toward the trimer [153].

Two-Dimensional (2D) Nanoclusters on TiO$_2$(110)

PTRF-XAFS is also a powerful tool for the investigation of nanoclusters containing from several to tens of atoms or of low-dimensional (2D or 1D) clusters on single-crystal surfaces. Fujikawa et al. observed self-regulated Ni growth on a TiO$_2$(110) surface by scanning tunneling microscopy [154]. They found that monolayers or bilayers of Ni clusters having specific sizes were produced in a stable manner and that the number of clusters increased with increasing deposition amounts below 0.2 monolayers (ML), suggesting the presence of a metal–support interaction that stabilized a defined cluster structure. Koike et al. investigated Ni cluster structures by PTRF-XAFS and determined that a one-atom-thick Ni layer was formed, with its fcc (110) plane parallel to the TiO$_2$(110) surface, as shown in Fig. 11.33 [155]. They proposed that the stability of this layer was based on multiple metal–oxygen bonds and lattice matching. Multiple metal–oxygen bonds (36 Ni–O bonds for the 42 Ni atoms in each cluster) stabilized the structure since the six Ni atoms associated with the bridging oxygen atoms (0.24 nm × 5 = 1.2 nm) were a good fit with the five oxygen atoms (0.296 nm × 4 = 1.18 nm) in the [001] direction, because the Ni−Ni distance in the $\left[1\bar{1}0 \right]$ direction between the Ni rows on the bridging oxygen atoms of 0.62 nm matched the separation of the bridging oxygen rows. Surface anions have also been found to play an important role in the structures and dispersion of metal species. An fcc (110) structure has been shown to be stable on a TiO$_2$(110) surface in the case of both Ni and Cu hexamers, evidently because the anion arrangements stabilize the fcc(110) structure. The Ni and Cu structures, however, exhibit different growth modes. In the case of Ni, 2D clusters are formed as shown in Fig. 11.33 and the cluster height begins to increase at 0.2 ML. In contrast, Cu trimers form on the surface and then undergo upward growth, as shown in Fig. 11.32. This difference could be due to the different
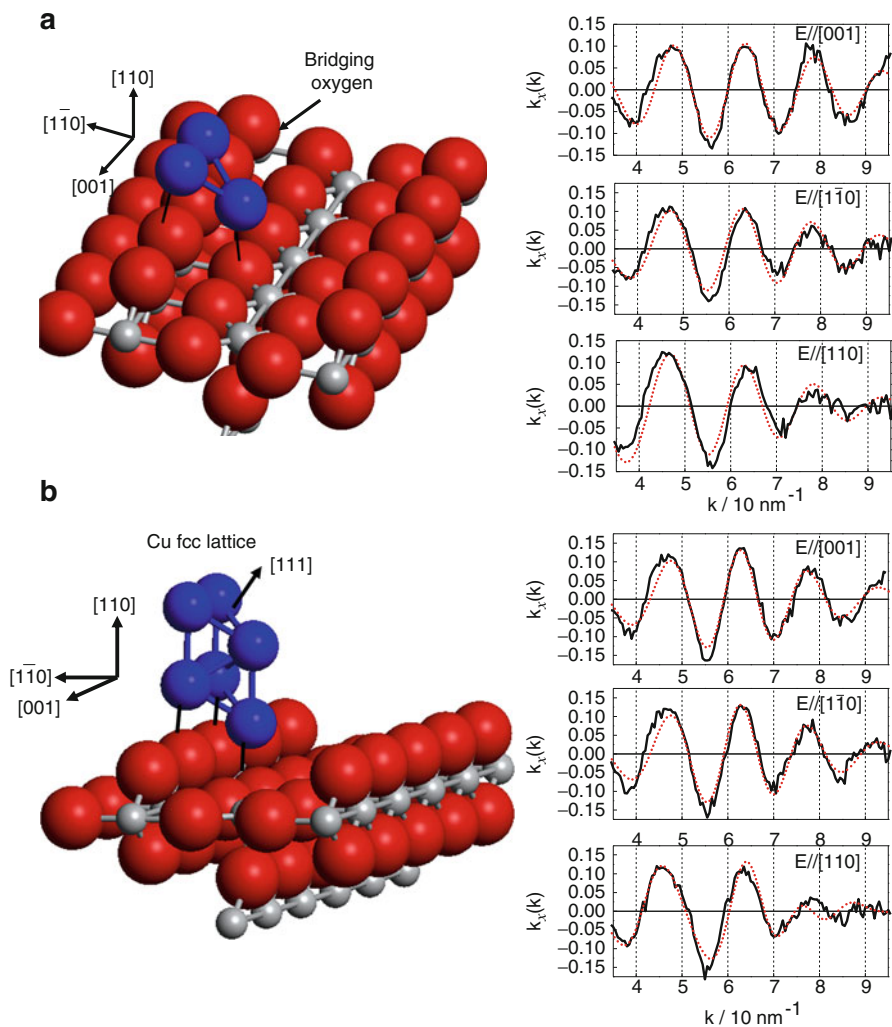
Fig. 11.32 (**a**) Cu trimer model structure (*left*) and its polarization-dependent EXAFS oscillations (*right*). *Black solid* and *red dotted* curves show the observed and simulated spectra, respectively. (**b**) Cu hexamer model structure (*left*) and its polarization-dependent EXAFS oscillations (*right*). *Red* and *gray* spheres indicate oxygen and Ti atoms, respectively, while Cu atoms are *blue* [145] (Copyright 2003, American Chemical Society)

strengths of the Cu–O and Ni–O interactions. The Ni–O interaction is stronger than that of Cu–O, and so Ni–O clusters grow in two dimensions, while Cu–Cu bonding is preferred over Cu–O bonding such that Cu–Cu bonds form in the vertical direction.

Fig. 11.33 Model structure
of the 2D Ni clusters on
TiO$_2$(110) derived from
PTRF-XAFS analysis. *Red*
and *purple* spheres indicate
oxygen, and *black* spheres
indicate Ti. *Blue* spheres are
Ni atoms [155] (Copyright
2008, American Chemical
Society)
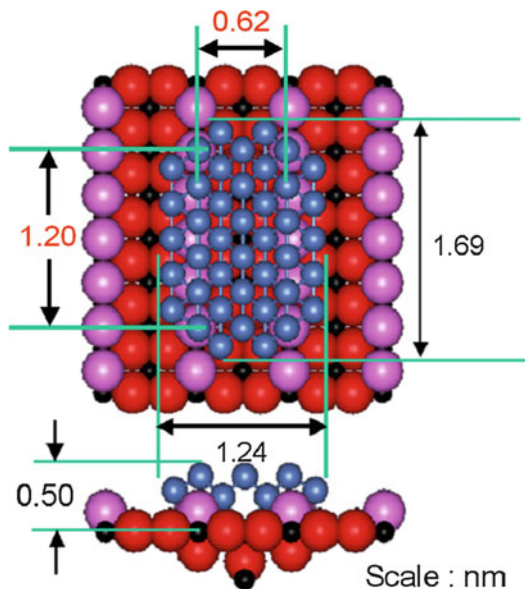
Three-Dimensional (3D) Nanoclusters on TiO$_2$(110)

Gold NPs deposited on oxide supports have attracted significant attention because
Au NPs show very different catalytic properties from those of bulk Au [156, 157].
Goodman et al. reported that a (1×3) Au bilayer was extraordinarily active for CO
oxidation [158]. Since the Au–oxide interaction is weak, 3D nanoclusters of this
metal are readily obtained. Our group applied angle-resolved total reflection
fluorescence XAFS (AR-TRF-XAFS), acquiring XAFS signals every 10–15°, as a
means of performing a precise structural analysis [159]. As a result, we determined
the size and morphology of Au nanoclusters on a TiO$_2$(110)-(1×1) surface and
found two possible structures for Au nanoclusters approximately 1 nm in size: a
cuboctahedron and an icosahedron. A detailed analysis by AR-TRF-XAFS revealed
that Au nanoclusters preferentially adopt the icosahedral Au$_{55}$ structure [160], and
this structure was also found on the more highly reduced TiO$_2$(110) $- (1 \times 2)$
surface [160].

Metal Species on Other Single-Crystal Oxide Surfaces

The PTRF-XAFS technique can also be applied to other single-crystal oxides such
as SiO$_2$, MgO, and Al$_2$O$_3$. Gota et al. studied Cu on Al$_2$O$_3$(0001) $- (1 \times 1)$ and
$(\sqrt{31} \times \sqrt{31})R \pm 9°$ surfaces using total reflection fluorescence XAFS [161]. They
found that Cu dimers and clusters were created on the (1×1) surface and that
larger Cu clusters were generated on the reconstructed surface. These results
suggested the absence of Cu–O interactions on the surfaces, although this was not
confirmed by assessing the polarization dependence of the XAFS data. Shirai
et al. applied PTRF-XAFS to the study of Co oxide on an α-Al$_2$O$_3$(0001) surface

prepared by chemical vapor deposition of $Co_2(CO)_8$ [162] and identified the epitaxial growth of seven layers of Co_3O_4 spinel particles, with the (001) plane of the Co_3O_4 parallel to the α-Al_2O_3(0001) surface. The (001) plane of Co_3O_4 showed high catalytic activity for the CO oxidation reaction at low temperatures. This same team also investigated Pt species on Al_2O_3(0001) and found that a one-atom-thick layer of Pt clusters was stabilized on the α-Al_2O_3(0001) surface [163]. Contrary to the results of Gota's work, the Pt–O bonds were found to lie along the [110] direction. Asakura and Ijima studied Mo species on MgO(001) and α-Al_2O_3(0001) − (1 × 1) surfaces and observed tetrahedral or square pyramidal Mo species, respectively [164].

7   Concluding Remarks and Future Perspective

The above discussion shows that XAFS is a powerful tool for the characterization of NPs dispersed on oxide surfaces, which represent very important materials in catalytic processes. Conventional XAFS provides the local structure around the active sites. The beauty of XAFS is that it allows the assessment of a catalytic system under actual reaction conditions and can determine changes in catalyst structures with a time resolution ranging from milliseconds to seconds, using Quick XAFS. Dispersive XAFS can also be used to follow faster processes if the transmission mode is available. If the material changes are repeatable, we can also apply the pump–probe method and obtain picosecond time resolution. Simultaneous measurements using XAFS in conjunction with other methods can allow analysis of the reaction mechanisms of NP catalysts. Although greater X-ray intensity values may be required to produce statistically valid data in some cases, it is important to pay attention to sample damage, especially when the beam is focused on the sample.

The PTRF-XAFS technique allows the determination of the 3D structures of highly dispersed metal species supported on single-crystal surfaces, together with an analysis of metal–support interfacial bonds. This technique thus provides insight into the structural chemistry and material functions, especially at catalyst surfaces. In the future, it would be beneficial to improve the time resolution of the PTRF-XAFS technique, since PTRF-XAFS usually requires acquisition times on the order of 10 h in order to obtain a good S/N ratio for each spectrum. Another drawback of PTRF-XAFS is its limited capability to assess liquid/solid interfaces since the liquid phase generates a large amount of scattering and deteriorates the S/N ratio. Recently, our group has developed a high-sensitivity polarization-dependent fluorescence XAFS method that works well even in the presence of a liquid phase, based on the use of a log spiral spectrometer for fluorescence signal detection [165].

Although this review has not considered high-energy-resolution emission spectroscopy [166], this is a promising technique for the study of nanomaterials with the aim of understanding the electronic states. In such applications, higher-performance fourth-generation X-ray sources, such as XFEL, ultimate synchrotron radiation, and energy recovery linacs (ERL), are required. It is anticipated that, over

the next decade, a more thorough understanding of the chemical behavior of nanomaterials will be obtained through the use of XAFS and its derivatives using such fourth-generation X-ray sources.

References

1. Hawkes PW (2009) Aberration correction past and present. Philos Trans R Soc A Math Phys Eng Sci 367:3637–3664
2. Creemer JF, Helveg S, Hoveling GH, Ullmann S, Molenbroek AM, Sarro PM, Zandbergen HW (2008) Atomic scale electron microscopy at ambient pressure. Ultramicroscopy 108:993
3. Chapman KW, Chupas PJ (2013) In-situ characterization of heterogeneous catalysts. Wiley, New Jersey p 147–168
4. Klug HP, Alexander LE (1974) X-ray diffraction procedures for polycrystalline and amorphous materials. John Wiley, New York
5. Fricke H (1920) The K-characteristic absorption frequencies for the chemical elements magnesium to chromium. Phys Rev 16:202
6. Kronig R d (1931) Zur Theorie der Feinstruktur in den Rontgenabsorptionsspektren. Z Phys 70:317
7. Kronig R d (1932) Zur Theorie der Feinstruktur in den Rontgenabsorptionsspektren III. Z Phys 75:468
8. Shiraiwa T, Ishimura T, Sawada M (1958) The theory of the fine structure of the X-ray absorption spectrum. J Phys Soc Jpn 13:847
9. Kostarev I (1941) Zh Eksp Teor Fiz 11:60
10. Kozlenkov A (1961) Bull Acad Soc USSR Phys Ser 25:968
11. Lytle FW (1966) Determination of interatomic distances from X-ray absorption fine structure. Adv X-ray Anal 9:398
12. Sayers DE, Stern EA, Lytle FW (1971) New technique for investigating noncrystalline structures: fourier analysis of the EXAFS. Phys Rev Lett 27:1204
13. Kincaid BM, Eisenberger P (1975) Synchrotron radiation studies of the K-edge photoabsorption spectra of Kr, Br_2, and $GeCl_4$: a comparison of theory and experiment. Phys Rev Lett 34:1361
14. Eisenberger P, Kincaid B (1978) EXAFS: new horizons in structure determinations. Science 200:1441
15. Lytle FW, Via GH, Sinfelt JH (1977) New application of EXAFS as a surface probe-nature of oxygen interaction with a ruthenium catalyst. J Chem Phys 67:3831
16. Via GH, Drake KF Jr, Meitzner G, Lytle FW, Sinfelt JH (1990) Analysis of EXAFS data on bimetallic clusters. Catal Lett 5:25–33
17. Van't Blik HFJ, Van Zon JBAD, Huizinga T, Vis JC, Koningsberger DC, Prins R (1983) An extended X-ray absorption fine structure spectroscopy study of a highly dispersed rhodium/aluminum oxide catalyst: the influence of carbon monoxide chemisorption on the topology of rhodium. J Phys Chem 87:2264
18. Iwasawa Y, Asakura K, Ishii H, Kuroda H (1985) Dynamic behavior of active sites of a SiO_2-attached Mo(VI)-dimer catalyst during ethanol oxidation observed by means of EXAFS. Z Phys Chem N F 144:105
19. McMaster WH, Kerr Del Grande N, Mallett JH, Hubbell JH (1969) Compilation of X-ray cross sections, U.S. Department of Commerce, vol. UCRL-50174, Section II, Revision I
20. Jaklevic J, Kirby JA, Klein MP, Robertson AS, Brown GS, Eisenberger P (1977) Fluorescence detection of EXAFS: sensitivity enhancement for dilute species and thin films. Solid State Commun 23:679
21. XAFS software catalog-ESRF keeps to update the list of EXAFS analysis software. http://www.esrf.eu/computing/scientific/exafs/xafs.html

22. Asakura K (1996) X-ray absorption fine structure for catalysts and surfaces. In: Iwasawa Y (ed) X-ray absorption fine structure for catalysts and surfaces, vol 2, 1st edn. World Scientific, Singapore, p 33
23. Cook JW, Sayers DE (1981) Criteria for automatic X-ray absorption fine structure background removal. J Appl Phys 52:5024
24. MacGillavry CH, Rieck GD (eds) (1968) International tables for x-ray crystallography, vol III. Kynoch, Birmingham, pp 171–173
25. Stern E (1993) Number of relevant independent points in XAFS spectra. Phys Rev B 48:9825
26. Asakura K (2012) Polarization-dependent total reflection fluorescence extended X-ray absorption fine structure and its application to supported catalysis. R Soc Chem 24:290, in Catalysis: Volume 24
27. Hamilton WC (1965) Significance tests on the crystallographic R factor. Acta Crystallogr 18:502
28. Arratoa-Perez R, Ramos AF, Mall GL (1989) Calculated electronic structure of Au13 cluster. Phys Rev B 39:3005
29. Cleveland CL, Landman U, Schaaff TG, Shafigullin MN, Stephens PW, Whetten RI (1997) Structural evolution of smaller gold nanocrystals: the truncated decahedral motif. Phys Rev Lett 79:18731876
30. Cleveland CL, Landman U, Shafigullin MN, Stephens PW, Whetten RI (1997) Structural evolution of smaller gold nanocrystals. Z Phys D 40:503
31. Köhn A, Weigned F, Ahlrichs R (2001) Theoretical study of clusters of magnesium. Phys Chem Chem Phys 3:711
32. Montejano-Carrizales JM, Aguilera-Granja F, Moran-Lopez JL (1997) Direct enumeration of the geometrical characteristics of cluster, Determination of crystallite size in a magnetic nanocomposite using EXAFS. NanoStructured Mater 8:269
33. Calvin S, Miller MM, Goswami R, Cheng S-F, Mulvaney SP, Whitman LJ, Harris VG (2003) Determination of crystallite size in a magnetic nanocomposite using EXAFS. J Appl Phys 94:778
34. Frenkel AI, Hills CW, Nuzzo RG (2001) A View from the Inside: complexity in the atomic scale ordering of supported metal nanoparticles. J Phys Chem B 105:12689
35. Glasner D, Frenkel AI (2007) Geometrical characteristics of regular polyhedra: application to EXAFS studies of nanoclusters. AIP Conf Proc 882:746
36. Frenkel A, Menard L, Northrup P, Rodriguez J, Zypman F, Glasner D, Gao S, Xu H, Yang J, Nuzzo R (2007) Geometry and charge state of mixed-ligand Au13 nanoclusters. AIP Conf Proc 882:749
37. Menard LD, Gao S-P, Xu H, Twesten RD, Harper AS, Song Y, Wang G, Douglas AD, Yang JC, Frenkel AI, Nuzzo RG, Murray RW (2006) Sub-nanometer au monolayer-protected clusters exhibiting molecule-like electronic behavior: quantitative high-angle annular dark-field scanning transmission electron microscopy and electrochemical characterization of clusters with precise atomic stoichiometry. J Phys Chem B 110:12874
38. Roldan Cuenya B, Frenkel AI, Mostafa S, Behafarid F, Croy JR, Ono LK, Wang Q (2010) Anomalous lattice dynamics and thermal properties of supported size- and shape-selected Pt nanoparticles. Phys Rev B 82:155450
39. Mostafa S, Behafarid F, Croy JR, Ono LK, Li L, Yang JC, Frenkel AI, Cuenya BR (2010) Shape-dependent catalytic properties of Pt nanoparticles. J Am Chem Soc 132:15714
40. Imaoka T, Kitazawa H, Chun W-J, Omura S, Albrecht K, Yamamoto K (2013) Magic Number Pt13 and misshapen Pt12 clusters: which one is the better catalyst. J Am Chem Soc 135:13089
41. Sevillano E, Meuth H, Rehr JJ (1979) Extended X-ray absorption fine structure Debye-Waller factors. I. Monatomic crystals. Phys Rev B 20:4908
42. Hansen LB, Stoltze P, Norskov JK, Clausen BS, Niemann W (1990) Is there a contraction of the interatomic distance in small metal particles. Phys Rev Lett 64:3155

43. Bunker G (1983) Application of the ratio method of EXAFS analysis to disordered systems. Nucl Instrum Methods 207:437
44. Yokoyama T, Kosugi N, Asakura A, Iwasawa Y, Kuroda H (1986) Temperature dependence of the Pt L_3-Edge EXAFS of platinum clusters supported on NaY-Zeolites. J Phys 47 C8:273
45. Kang JH, Mendard LD, Nuzzo RG, Frenkel AI (2006) Unusual non-bulk properties in nanoscale materials. J Am Chem Soc 128:12068
46. Petkov V, Bedford N, Knecht MR, Weir MG, Crooks RM, Tang W, Henkelman G, Frenkel A (2008) Noble-transition metal nanoparticle breathing in a reactive gas atmosphere. J Phys Chem C 112:8907
47. Nishigaki J-i, Yamazoe S, Kohara S, Fujiwara A, Kurashige W, Negishi Y, Tsukuda T (2014) A twisted bi-icosahedral Au_{25} cluster enclosed by bulky arenethiolates. Chem Commun 50:839
48. Bian CR, Suzuki S, Asakura K, Hei L, Toshima N (2002) EXAFS studies on the structure of the PVP-stabilized Cu/Pd particles colloidally dispersed in solution. J Phys Chem 106:8587
49. Beale AM, Weckhuysen BM (2010) EXAFS as a tool to interrogate the size and shape of mono and bimetallic catalyst nanoparticles. Phys Chem Chem Phys 12:5562
50. Hwang B-J, Sarma LS, Chen JM, Chen CH, Shih SC, Wang GR, Liu DG, Lee JF, Tang MT (2005) Structural models and atomic distribution of bimetallic nanoparticles as investigated. J Am Chem Soc 127:11140
51. Hisano M, Sato O, Urakawa K, Jeyadevan B, Tohji K (2005) Effect of additives on the direct synthesis of L10-FePt nanoparticles by polyol process. J Magn Soc Jpn 29:814
52. Shinoda K, Sato K, Jeyadevan B, Tohji K (2006) Polyol process for Fe-based hard (fct-FePt) and soft (FeCo) magnetic nanoparticles. Mag IEEE Trans 42:3051
53. Nakaya M, Kanehara M, Yamauchi M, Kitagawa H, Teranishi T (2007) Hydrogen-induced crystal structural transformation of FePt nanoparticles at low temperature. J Phys Chem C 111:7231
54. Knecht MR, Weir MG, Frenkel AI, Crooks RM (2007) Structural rearrangement of bimetallic alloy PdAu nanoparticles within dendrimer templates to yield core/shell configurations. Chem Mater 20:1019
55. Asakura K, Bian CR, Suzuki S, Chun WJ, Watari N, Ohnishi S, Lu P, Toshima N (2005) XAFS study on the polymer protected CuPd bimetallic nanoparticles: a novel heterobond-philic structure. Phys Scr T115:781
56. Takeguchi T, Yamanaka T, Asakura K, Muhamad EN, Uosaki K, Ueda W (2012) Evidence of nonelectrochemical shift reaction on a CO-tolerant high-entropy state Pt–Ru anode catalyst for reliable and efficient residential fuel cell systems. J Am Chem Soc 134:14508
57. Takahashi H, Konishi N, Ohno H, Takahashi K, Koike Y, Asakura K, Muramatsu A (2011) Preparation of well-crystallized Pd20Te7 alloy nanoparticulate catalysts with uniform structure and composition in liquid-phase. Appl Catal A Gen 392:80
58. Hatakeyama Y, Asakura K, Takahashi S, Judai K, Nishikawa K (2014) Microscopic structure of naked Au nanoparticles synthesized in typical ionic liquids by sputter deposition. J Phys Chem C 118:27973
59. Kaito T, Mitsumoto H, Sugawara S, Shinohara K, Uehara H, Ariga H, Takakusagi S, Hatakeyama Y, Nishikawa K, Asakura K (2014) K-edge X-ray absorption fine structure analysis of Pt/Au core–shell electrocatalyst: evidence for short Pt–Pt distance. J Phys Chem C 118:8481
60. Adzic RR, Zhang J, Sasaki K, Vukmirovic MB, Shao M, Wang JX, Nilekar AU, Mavrikakis M, Valerio JA, Uribe F (2007) Platinum monolayer fuel cell electrocatalysts. Top Catal 46:249
61. Toshima N, Yonezawa T, Harada M, Asakura K, Iwasawa Y (1990) The polymer-protected Pd-Pt bimetallic clusters having catalytic activity for selective hydrogenation of diene. Chem Lett 815–818
62. Toshima N, Harada M, Yonezawa T, Kushihashi K, Asakura K (1991) J Phys Chem 95:7448
63. Asakura K, Yamazaki Y, Kuroda H, Harada M, Toshima N (1993) A "cluster-in-cluster" structure of the SiO_2-supported PtPd clusters. Jpn J Appl Phys 32–2:448

64. Clausen BS, Topsoe H (1989) In-situ studies of catalysts by XAFS and Mössbauer spectros-copy. Hyperfine Interact 47:203–217
65. Wada T, Bando KK, Miyamoto T, Takakusagi S, Oyama ST, Asakura K (2012) Operando QEXAFS studies of Ni2P during thiophene hydrodesulfurization: direct observation of Ni-S bond formation under reaction conditions. J Synchrotron Radiat 19:205–209
66. Weckhuysen BM (ed) (2004) In-situ spectroscopy of catalysts. American Scientific Pub-lishers, Stevenson Ranch
67. Bando KK, Saito T, Sato K, Tanaka T, Dumeignil F, Imamura M, Matsubayashi N, Shimada H (2001) In situ XAFS analysis system for high-pressure catalytic reactions and its application to CO_2 hydrogenation over a Rh/Y-zeolite catalyst. J Synchrotron Radiat 8:581–853
68. http://support.spring8.or.jp/xafs/in-situ/in-situ_cell.html
69. Dalla Betta RA, Boudart M, Foger K, Loffer DG, Sanchez Arrieta J (1984) Cell fitted with thin beryllium windows for x-ray absorption under pressure up to 14 MPa and temperatures up to 700 K. Rev Sci Instrum 55:1910
70. Ichikuni N, Murayama H, Bando KK, Shimazu S, Uematsu T (2005) Preparation of mesoporous silica supported Nb catalysts and in-situ XAFS characterization during carburi-zation process. Phys Scr T115:807–809
71. http://www.dupont.com/content/dam/assets/products-and-services/membranes-films/assets/DEC-Kapton-general-specs.pdf
72. http://pfxafs.kek.jp/wp-content/uploads/2012/12/ASPF20_03.pdf, http://www.saga-ls.jp/?page=200#X1
73. Clausen BS, Steffensen G, Fabius B, Villadsen J, Feidenhans'l R, Topsøe H (1991) In-situ cell for combined XRD and on-line catalysis tests: studies of Cu based water gas shift and methanol catalysts. J Catal 132:524–535
74. Bare SR, Yang N, Kelly SD, Mickelson GE, Modica FS (2007) Catal Today 126:18
75. Dreher M, De Boni E, Nachtegaal M, Wambach J, Vogel F (2012) Design of a continuous-flow reactor for in situ x-ray absorption spectroscopy of solids in supercritical fluids. Rev Sci Instrum 83:054101
76. Doronkin DE, Casapu M, Gunter T, Muller O, Frahm R, Grunwaldt J-D (2014) Operando spatially- and time-resolved XAS study on zeolite catalysts for selective catalytic reduction of NOx by NH3. J Phy Chem C 118:10204–10212
77. Grunwaldt J-D, Ramin M, Rohr M, Michailovski A, Patzke GR, Baiker A (2005) High pressure in situ x-ray absorption spectroscopy cell for studying simultaneously the liquid phase and the solid/liquid interface. Rev Sci Instrum 76:054104
78. http://www.polypenco.co.jp/products_e/pp_pbi/product00_cha.html
79. Bando KK, Kawai T, Asakura K, Matsui T, Le Bihan L, Yasuda H, Yoshimura Y, Oyama ST (2006) In situ XAFS analysis of Pd-Pt catalysts during hydrotreatment of model oil. Catal Today 111:199–204
80. Kawai T, Chun WJ, Asakura K, Koike Y, Nomura M, Bando KK, Oyama ST, Sumiya H (2008) Design of a high-temperature and high pressure liquid flow cell for XAFS measure-ments under catalytic reaction conditions. Rev Sci Instrum 79:014101
81. Kawai T, Bando KK, Lee Y-K, Oyama ST, Chun W-J, Asakura K (2006) EXAFS measure-ments of a working catalyst in the liquid phase: An in situ study of a Ni_2P hydrodesul-furization catalyst. J Catal 241:20–24
82. Makosch M, Kartusch C, Sa J, Duarte RB, van Bokhoven JA, Kvashnina K, Glatzel P, Fernandes DLA, Nachtegaal M, Kleymenov E, Szlachetko J, Neuholda B, Hungerbuhler K (2012) HERFD XAS/ATR-FTIR batch reactor cell. Phys Chem Chem Phys 14:2164–2170
83. Niwa M, Katada N, Okumura K (2010) Characterization and design of zeolite catalysts: solid acidity, shape selectivity and loading properties. Springer Ser Mater Sci 141:9–27
84. Pinxt HHCM, Kuster BFM, Koningsberger DC, Marin GB (1998) On-line characterization by EXAFS of tin promoted platinum graphite catalysts in the aqueous phase. Catal Today 39:351–361

85. Newton MA, van Beek W (2010) Combining synchrotron-based X-ray techniques with vibrational spectroscopies for the in situ study of heterogeneous catalysts: a view from a bridge. Chem Soc Rev 39:4845–4863

86. Bando KK, Wada T, Miyamoto T, Miyazaki K, Takakusagi S, Koike Y, Inada Y, Nomura M, Yamaguchi A, Gott T, Ted Oyama S, Asakura K (2012) Combined in situ QXAFS and FTIR analysis of a Ni phosphide catalyst under hydrodesulfurization conditions. J Catal 286:165–171

87. Wada T, Bando KK, Oyama ST, Miyamoto T, Takakusagi S, Asakura K (2012) Operando observation of Ni_2P structural changes during catalytic reaction: effect of H2S pretreatment. Chem Lett 41:1238–1240

88. Li W, Dhandapani B, Oyama ST (1998) Synthesis, characterization, and reactivity studies of supported Mo_2C with phosphorus additive. Chem Lett 207–208

89. Kawai T, Bando KK, Lee Y-K, Oyama ST, Chun W-J, Asakura K (2007) In situ EXAFS studies on Ni_2P hydrodesulfurization catalysts in the presence of high pressure and high temperature oil. AIP Conf Proc 882:616

90. Drake IJ, Zhang Y, Gilles MK, Liu CNT, Nachimuthu P, Perera RCC, Wakita H, Bell AT (2006) An in situ Al K-edge XAFS investigation of the local environment of H^+ and Cu^+-exchanged USY and ZSM-5 zeolite. J Phys Chem B 110:11665–11676

91. Grunwaldt J-D, Hübner M, Koziej D, Barsan N, Weimar U (2013) The potential of operando XAFS for determining the role and structure of noble metal additives in metal oxide based gas sensors. J Phy Conf Ser 430:012078

92. Kaito T, Mitsumoto H, Sugawara S, Shinohara K, Uehara H, Ariga H, Takakusagi S, Asakura K (2014) A new spectroelectrochemical cell for in situ measurement of Pt and Au K-edge X-ray absorption fine structure. Rev Sci Instrum 85:084104

93. Blanchard J, Bando KK, Matsui T, Harada M, Breysse M, Yoshimura Y (2007) Ruthenium sulfide clusters in acidic zeolites: In situ XAS characterization during sulfidation and reaction. Appl Catal A 322:98–105

94. Tupy SA, Karim AM, Bagia C, Deng W, Huang Y, Vlachos DG, Chen JG (2012) Correlating ethylene glycol reforming activity with in situ EXAFS detection of Ni segregation in supported NiPt bimetallic catalysts. ACS Catal 2:2290–2296

95. Fujikawa K, Ariga H, Takakusagi S, Uehara H, Ohba T, Asakura K (2014) Micro reverse Monte Carlo approach to EXAFS analysis. e-J Surf Sci Nanotechnol 12:322–329

96. Frahm R (1989) New method for time dependent X-ray absorption studies. Rev Sci Instrum 60:2515

97. Groppo E, Agostini G, Borfecchia E, Wei L, Giannici F, Portale G, Longo A, Lamberti C (2014) Formation and growth of Pd nanoparticles inside a highly cross-linked polystyrene support: Role of the reducing agent. J Phys Chem C 118:8406

98. Shishido T, Nasu H, Deng L, Teramura K, Tanaka T (2013) Study of formation process of metal nanoparticles on metal oxides by in-situ XAFS technique. J Phys Conf Ser 430:012060

99. Tanaka T, Ohyama J, Teramura K, Hitomi Y (2012) Formation mechanism of metal nanoparticles studied by XAFS spectroscopy and effective synthesis of small metal nanoparticles. Catal Today 183:108

100. Doronkin DE, Casapu M, Günter T, Müller O, Frahm R, Grunwaldt JD (2014) Operando spatially- and time-resolved XAS study on zeolite catalysts for selective catalytic reduction of NOx by NH_3. J Phys Chem C 118:10204

101. Lützenkirchen-Hecht D, Stötzel J, Müller O, Just J, Frahm R (2013) Quick-scanning QEXAFS in grazing incidence: Surface science in sub-seconds. J Phys Conf Ser 430:092010

102. Liu M, Leichtweiß T, Janek J, Martin M (2013) In-situ structural investigation of non-stoichiometric HfO_2-x films using quick-scanning extended X-ray absorption fine structure. Thin Solid Films 539:60

103. Kimura M, Uemura Y, Takayama T, Murao R, Asakura K, Nomura M (2013) In situ QXAFS observation of the reduction of Fe_2O_3 and $CaFe_2O_4$. J Phys Conf Ser 430:012074

104. Ishiguro N, Saida T, Uruga T, Nagamatsu SI, Sekizawa O, Nitta K, Yamamoto T, Ohkoshi SI, Iwasawa Y, Yokoyama T, Tada M (2012) Operando time-resolved x-ray absorption fine structure study for surface events on a Pt_3Co/C cathode catalyst in a polymer electrolyte fuel cell during voltage-operating processes. ACS Catal 2:1319
105. Kaminaga U, Matsushita T, Kohra K (1981) A dispersive method of measuring extended X-ray absorption fine structure. Jpn J Appl Phys 20:L355
106. Headspith J, Salvini G, Thomas SL, Derbyshire G, Dent A, Rayment T, Evans J, Farrow R, Anderson C, Cliche J, Dobson BR (2003) Nuclear instruments and methods in physics research section A: accelerators, spectrometers, detectors and associated equipment. Nucl Instrum Methods A 512:239–244
107. Kimura M, Niwa Y, Uemura K, Nagai T, Inada Y, Nomura M (2013) In situ and simultaneous observation of palladium redox and oxygen storage/release in Pd/SrFeO perovskite catalysts using dispersive XAFS. Mater Trans 54:246
108. Matsumura D, Okajima Y, Nishihata Y, Mizuki J, Taniguchi M, Uenishi M, Tanaka H (2009) Dynamic structural change of Pd particles on $LaFeO_3$ under redox atmosphere and CO/NO catalytic reaction studied by dispersive XAFS. J Phys Conf Ser 190:012024
109. Uemura Y, Inada Y, Bando KK, Sasaki T, Kamiuchi N, Eguchi K, Yagishita A, Nomura M, Tada M, Iwasawa Y (2011) Core-shell phase separation and structural transformation of Pt 3Sn alloy nanoparticles supported on γ-Al_2O_3 in the reduction and oxidation processes characterized by in situ time-resolved XAFS. J Phys Chem C 115:5823
110. Uemura Y, Inada Y, Bando KK, Sasaki T, Kamiuchi N, Eguchi K, Yagishita A, Nomura M, Tada M, Iwasawa Y (2011) In situ time-resolved XAFS study on the structural transformation and phase separation of Pt_3Sn and PtSn alloy nanoparticles on carbon in the oxidation process. Phys Chem Chem Phys 13:15833
111. Uemura Y, Inada Y, Niwa Y, Kimura M, Bando KK, Yagishita A, Iwasawa Y, Nomura M (2012) In situ time-resolved XAFS study on the structural transformation and phase separation of Pt_3Sn and PtSn alloy nanoparticles on carbon in the oxidation process. Phys Chem Chem Phys 14:2152
112. Asakura H, Teramura K, Shishido T, Tanaka T, Yan N, Xiao C, Yao S, Kou Y (2012) In situ time-resolved DXAFS study of Rh nanoparticle formation mechanism in ethylene glycol at elevated temperature. Phys Chem Chem Phys 14:2983
113. Tada M, Uemura Y, Bal R, Inada Y, Nomura M, Iwasawa Y (2010) In situ time-resolved DXAFS for the determination of kinetics of structural changes of H-ZSM-5-supported active Re-cluster catalyst in the direct phenol synthesis from benzene and O_2. Phys Chem Chem Phys 12:5701
114. Newton MA (2009) Applying Dynamic and Synchronous DRIFTS/EXAFS to the Structural Reactive Behaviour of Dilute (≤ 1 wt%) Supported Rh/Al_2O_3 Catalysts using Quick and Energy Dispersive EXAFS. Top Catal 52:1410
115. Teramura K, Okuoka SI, Yamazoe S, Kato K, Shishido T, Tanaka T (2008) In situ time-resolved energy-dispersive XAFS study on photodeposition of Rh particles on a TiO_2 photocatalyst. J Phys Chem C 112:8495
116. Suzuki A, Inada Y, Yamaguchi A, Chihara T, Yuasa M, Nomura M, Iwasawa Y (2003) Time scale and elementary steps of CO-induced disintegration of surface rhodium clusters. Angew Chem Int Ed 42:4795
117. Mills DM, Lewis A, Harootunian A, Huang J, Smith B (1984) Time-resolved x-ray absorption spectroscopy of carbon monoxide-myoglobin recombination after laser photolysis. Science 223:811
118. Chen LX (2001) Capturing a photoexcited molecular structure through time-domain X-ray absorption fine structure. Science 292:262
119. Chen LX, Shaw GB, Novozhilova I, Liu T, Jennings G, Attenkofer K, Meyer GJ, Coppens P (2003) MLCT state structure and dynamics of a copper(I) diimine complex characterized by pump-probe X-ray and laser spectroscopies and DFT calculations. J Am Chem Soc 125:7022

120. Bressler C, Milne C, Pham VT, ElNahhas A, van der Veen RM, Gawelda W, Johnson S, Beaud P, Grolimund D, Kaiser M, Borca CN, Ingold G, Abela R, Chergui M (2009) Femtosecond XANES study of the light-induced spin crossover dynamics in an iron (II) complex. Science 323:489

121. El Nahhas A, van der Veen RM, Penfold TJ, Pham VT, Lima F a, Abela R, Blanco-Rodriguez a M, Záliš S, Vlček A, Tavernelli I, Rothlisberger U, Milne CJ, Chergui M (2013) X-ray absorption spectroscopy of ground and excited rhenium-carbonyl-diimine complexes: evidence for a two-center electron transfer. J Phys Chem A 117:361

122. Nozawa S, Sato T, Chollet M, Ichiyanagi K, Tomita A, Fujii H, Adachi S-i, Koshihara S-y (2010) Direct probing of spin state dynamics coupled with electronic and structural modifications by picosecond time-resolved XAFS. J Am Chem Soc 132:61

123. Sato T, Nozawa S, Tomita A, Hoshino M, Koshihara S-y, Fujii H, Adachi S-i (2012) Coordination and electronic structure of Ruthenium (II) – tris $-2, 2'$ – bipyridine in the triplet metal-to-ligand charge-transfer excited state observed by picosecond time-resolved Ru K -edge XAFS. J Phys Chem C 340:14232

124. Zhang X, Canton SE, Smolentsev G, Wallentin C-J, Liu Y, Kong Q, Attenkofer K, Stickrath AB, Mara MW, Chen LX, Wärnmark K, Sundström V (2014) Highly accurate excited-state structure of $[Os(bpy)_2dcbpy]_{2+}$ determined by x-ray transient absorption spectroscopy. J Am Chem Soc 136:8804

125. Zhang X, Smolentsev G, Guo J, Attenkofer K, Kurtz C, Jennings G, Lockard JV, Stickrath AB, Chen LX (2011) Visualizing interfacial charge transfer in Ru-dye-sensitized TiO_2 nanoparticles using x-ray transient absorption spectroscopy. J Phys Chem Lett 2:626

126. Katz JE, Zhang X, Attenkofer K, Chapman KW, Frandsen C, Zarzycki P, Rosso KM, Falcone RW, Waychunas GA, Gilbert B (2012) Electron small polarons and their mobility in iron (oxyhydr)oxide nanoparticles. Science 337:1200

127. Rittmann-Frank MH, Milne CJ, Rittmann J, Reinhard M, Penfold TJ, Chergui M (2014) Mapping of the photoinduced electron traps in TiO_2 by picosecond X-ray absorption spectroscopy. Angew Chem Int Ed 53:5858

128. Uemura Y, Uehara H, Niwa Y, Nozawa S, Sato T, Adachi S, Ohtani B, Takakusagi S, Asakura K (2014) In situ picosecond XAFS study of an excited state of tungsten oxide. Chem Lett 43:977

129. March AM, Stickrath A, Doumy G, Kanter EP, Krässig B, Southworth SH, Attenkofer K, Kurtz CA, Chen LX, Young L (2011) Development of high-repetition-rate laser pump/X-ray probe methodologies for synchrotron facilities. Rev Sci Instrum 82:073110

130. Lima F, Milne CJ, Amarasinghe DCV, Rittmann-Frank MH, van der Veen RM, Reinhard M, Pham V-T, Karlsson S, Johnson SL, Grolimund D, Borca C, Huthwelker T, Janousch M, van Mourik F, Abela R, Chergui M (2011) A high-repetition rate scheme for synchrotron-based picosecond laser pump/X-ray probe experiments on chemical and biological systems in solution. Rev Sci Instrum 82:063111

131. Radu I, Stamm C, Pontius N, Kachel T, Ramm P, Thiele JU, Dürr HA, Back CH (2010) Laser-induced generation and quenching of magnetization on FeRh studied with time-resolved X-ray magnetic circular dichroism. Phys Rev B 81:104415

132. Abo-Bakr M, Feikes J, Holldack K, Wüstefeld G, Hübers HW (2002) Steady-state far-infrared coherent synchrotron radiation detected at BESSY II. Phys Rev Lett 88:254801

133. Beaud P, Johnson SL, Streun A, Abela R, Abramsohn D, Grolimund D, Krasniqi F, Schmidt T, Schlott V, Ingold G (2007) Spatiotemporal stability of a femtosecond hard–X-ray undulator source studied by control of coherent optical phonons. Phys Rev Lett 99:174801

134. Lemke HT, Bressler C, Chen LX, Fritz DM, Gaffney KJ, Galler A, Gawelda W, Haldrup K, Hartsock RW, Ihee H, Kim J, Kim KH, Lee JH, Nielsen MM, Stickrath AB, Zhang W, Zhu D, Cammarata M (2013) Femtosecond X-ray absorption spectroscopy at a hard x-ray free electron laser: application to spin crossover dynamics. J Phys Chem A 117:735

135. Obara Y, Katayama T, Ogi Y, Suzuki T, Kurahashi N, Karashima S, Chiba Y, Isokawa Y, Togashi T, Inubushi Y, Yabashi M, Suzuki T, Misawa K (2014) Femtosecond time-resolved x-ray absorption spectroscopy of liquid using a hard X-ray free electron laser in a dual-beam dispersive detection method. Opt Express 22:1105
136. Shirai M, Iwasawa Y (1996) Total reflection fluorescence EXAFS. In: Iwasawa Y (ed) XAFS application to catalysis and surface. World Scientific, Singapore, p 332
137. Diebold U (2003) The surface science of titanium dioxide. Surf Sci Rep 48:53
138. Stohr J (1998) SEXAFS. In: Koningsberger DC, Prins R (eds) X-ray absorption principles, applications, techniques of EXAFS, SEXAFS, and XANES (vol 92) chemical analysis, vol 92. Wiley, New York, p 443
139. Stohr J (1993) NEXAFS spectroscopy, Springer series in surface sciences. Springer, Berlin
140. Parratt LG (1954) Surface studies of solids by total reflection of X-rays. Phys Rev 95:359
141. Koike Y, Ijima K, Chun WJ, Ashima H, Yamamoto T, Fujikawa K, Suzuki S, Iwasawa Y, Nomura M, Asakura K (2006) Structure of low coverage Ni atoms on the TiO2(110) surface polarization dependent total-reflection Fluorescence EXAFS study. Chem Phys Lett 421:27
142. Asakura K (2012) Polarization-dependent total reflection fluorescence extended X-ray absorption fine structure and its application to supported catalysis, Catalysis, vol 24. RSC Publishing, Cambridge, p 281
143. Chun WJ, Tanizawa Y, Shido T, Iwasawa Y, Nomura M, Asakura K (2001) Development of an in-situ polarization-dependent total reflection fluorescence XAFS measurement system. J Synchrotron Radiat 8:168
144. Tanizawa Y, Chun W-J, Shido T, Asakura K, Iwasawa Y (2001) Three-dimensional analysis of the local structure of Cu on TiO2(110) by in-situ polarization dependent total reflection fluorescence XAFS. J Synchrotron Radiat 8:508–510
145. Tanizawa Y, Shido T, Chun WJ, Asakura K, Nomura M, Iwasawa Y (2003) Three-dimensional local structure analysis of Cu species on TiO$_2$(110) surface studied by polarization-dependent total reflection fluorescence X-ray absorption fine structure(PTRF-XAFS). J Phys Chem B 107:12917
146. Chun WJ, Koike Y, Ijima K, Fujikawa K, Ashima H, Nomura M, Iwasawa Y, Asakura K (2007) Preparation of atomically dispersed Cu species on a TiO$_2$(110) surface premodified with an organic compound. Chem Phys Lett 433:345
147. Takakusagi S, Nojima H, Ariga H, Uehara H, Miyazaki K, Chun WJ, Iwasawa Y, Asakura K (2013) Fine tuning and orientation control of surface Cu complexes on TiO$_2$(110) premodified with mercapto compounds: the effect of different mercapto group positions. Phys Chem Chem Phys 15:14080
148. Asakura K, Takakusagi S, Ariga H, Chun WJ, Suzuki S, Koike Y, Uehara H, Miyazaki K, Iwasawa Y (2013) Preparation and structure of a single Au atom on the TiO$_2$(110) surface: control of the Au-metal oxide surface interaction. Faraday Discuss 162:165
149. Ankudinov AL, Ravel B, Rehr JJ, Conradson SD (1998) Real-space multiple scattering calculation and interpretation of XANES. Phys Rev B 58:7565
150. Xu C, Lai X, Zajac GW, Goodman DW (1997) Scanning tunneling microscopy studies of the TiO$_2$(110) surface: structure and the nucleation growth of Pd. Phys Rev B 56:13464
151. Asakura K, Chun WJ, Iwasawa Y (1999) Anisotropic arrangement of Mo species highly dispersed on TiO2(110) surface. Jpn J Appl Phys 38–1:40
152. Asakura K (2010) Catal today. Atomic aspects of surface chemical reactions. 157:2
153. Uehara H, bin Hanaffi MH, Koike Y, Fujikawa K, Suzuki S, Ariga H, Takakusagi S, Chun WJ, Iwasawa Y, Asakura K (2013) Anisotropic growth of a Nickel trimer formed on a highly-stepped TiO$_2$(110) surface. Chem Phys Lett 570:64
154. Fujikawa K, Suzuki S, Koike Y, Chun WJ, Asakura K (2006) Self-regulated Ni cluster formation on the TiO$_2$(110) terrace studied using scanning tunneling microscopy. Surf Sci 600:L117

155. Koike Y, Fujikawa K, Suzuki S, Chun WJ, Ijima K, Nomura M, Iwasawa Y, Asakura K (2008) Origin of self-regulated cluster growth on the $TiO_2(110)$ surface studied using polarization-dependent total reflection fluorescence XAFS. J Phys Chem C 112:4667

156. Hutchings GJ, Edwards JK (2012) Application of gold nanoparticles in catalysis. In: Roy LJ, Wilcoxon JP (eds) Frontiers of nanoscience, vol 3. Elsevier, Amsterdam, p 249

157. Haruta M (2004) Gold as a novel catalyst in the 21st century: preparation, working mechanism and applications. Gold Bull 37:27

158. Chen MS, Goodman DW (2004) The structure of catalytically active gold on titania. Science 306:252

159. Chun W-J, Miyazaki K, Watanabe N, Koike Y, Takakusagi S, Fujikawa K, Nomura M, Asakura K (2011) Angle resolved total reflection fluorescence XAFS and its application to Au clusters on $TiO_2(110)$ (1×1). J Ceram Soc Jpn 119:890

160. Chun W-J, Miyazaki K, Watanabe N, Koike Y, Takakusagi S, Fujikawa K, Nomura M, Iwasawa Y, Asakura K (2013) Au clusters on $TiO_2(110)$ (1×1) and (1×2) surfaces examined by polarization-dependent total reflection fluorescence XAFS. J Phys Chem C 117:252

161. Gota S, Gautiersoyer M, Douillard L, Duraud JP, Lefevre P (1996) The initial stages of the growth of copper on a (1×1) and a $(\sqrt{31} \times \sqrt{31})$ $R \pm 9°$ α-$Al_2O_3(0001)$ surface. Surf Sci 352:1016

162. Shirai M, Inoue T, Onishi H, Asakura K, Iwasawa Y (1994) Polarized total-reflection fluorescence EXAFS study of anisotropic structure analysis for Co oxides on α-$Al_2O_3(0001)$ as model surfaces for active oxidation catalysis. J Catal 145:159

163. Asakura K, Chun W-J, Shirai M, Tomishige K, Iwasawa Y (1997) In-situ polarization dependent total reflection fluorescence XAFS studies on the structure transformation of Pt clusters on α-$Al_2O_3(0001)$. J Phys Chem B 101:5549

164. Asakura K, Ijima K (2001) Polarization-dependent EXAFS studies on the structures of Mo oxides dispersed on single crystals. J Electron Spectrosc 119:185

165. Uehara H, Uemura Y, Ogawa T, Kono K, Ueno R, Niwa Y, Nitani H, Abe H, Takakusagi S, Nomura M (2014) In situ back-side illumination fluorescence XAFS (BI-FXAFS) studies on platinum nanoparticles deposited on a HOPG surface as a model fuel cell: a new approach to the Pt-HOPG electrode/electrolyte interface. Phys Chem Chem Phys 16:13748–13754

166. de Groot F, Kotani A (2008) Core level spectroscopy of solids. CRC Press, Boca Raton

167. Frenkel A (2007) Solving the 3D structure of metal nanoparticles. Z Krist 222:605

Contribution of Small-Angle X-Ray and Neutron Scattering (SAXS and SANS) to the Characterization of Natural Nanomaterials

12

Loïc Barré

Contents

1   Definition of the Topic

Small-angle neutron scattering (*SANS*) and small-angle X-ray scattering (*SAXS*) are well-established techniques that have been successfully used in nanoscale structure determination of synthetic or manufactured systems used in soft matter or materials domain. In this chapter, we examine the application of such techniques to determine features of natural nano-materials encountered in the petroleum and new energy industry.

L. Barré (✉)
IFP Energies Nouvelles, Rueil Malmaison, France
e-mail: loic.barre@ifpen.fr

2 Overview

Successful implementation of industrial processes depends partly on understanding of systems in use conditions. Hence, for transformation of natural materials, a good knowledge of structure and behavior of these materials in process conditions is desirable. Among natural materials, few of them are nanostructured, and very few techniques are available to characterize these systems in thermodynamic and hydrodynamic conditions close to one encountered in the industrial process.

Small-angle scattering (*SAS*) techniques, either X-ray or neutrons, has the potential, but its use is sometimes limited to manufactured or synthetic systems. Laboratory *SAXS* equipments become more popular but remain sparse, especially in industrial environment. Large-scale facilities such as synchrotron or neutron centers have been used for academic research but open now more and more to industrial issues. The aim of this chapter is to discuss the contribution of *SAXS* and *SANS* to the characterization of natural nano-materials.

Two different nanostructured materials will be examined here. The first one comes from heavy cuts of petroleum where the largest and most aromatic molecules – the asphaltenes – self-associate. The behavior of such aggregates generally impairs processes. This aggregation behavior will be examined in the bulk as well as at liquid/liquid or liquid/solid interfaces. A special attention will be paid to observation close to use conditions. The second ones are geomaterials, including sedimentary rocks and gas and oil shales. For these materials, the pore size distribution (open versus closed porosity, accessibility of pores to various fluids) is of primary interest leading to a better understanding of gas storage and transport mechanisms and their controls.

We will show, through the study of these two nanostructured materials, how *SAS* techniques contribute to the characterization of such systems.

3 Experimental and Instrumentation

This chapter doesn't intend to go in detail in small-angle scattering theory. Several references could be consulted [1–5] for that. In the same way, this section will not detail the advanced technology used in modern scattering instrumentation. The idea is rather to give keys that enable to appreciate the benefits and limitations of the techniques.

3.1 Basic of Small-Angle Scattering (*SAS*)

3.1.1 Description of *SAS* Experiment

A typical scattering experiment aims at measuring the scattering intensity produced by a sample illuminated by a monochromatic beam (λ) of X-ray or neutron (Fig. 12.1). This scattering intensity is related to the sample fluctuations or inhomogeneities at nanometer length scale. Assuming an elastic interaction, the
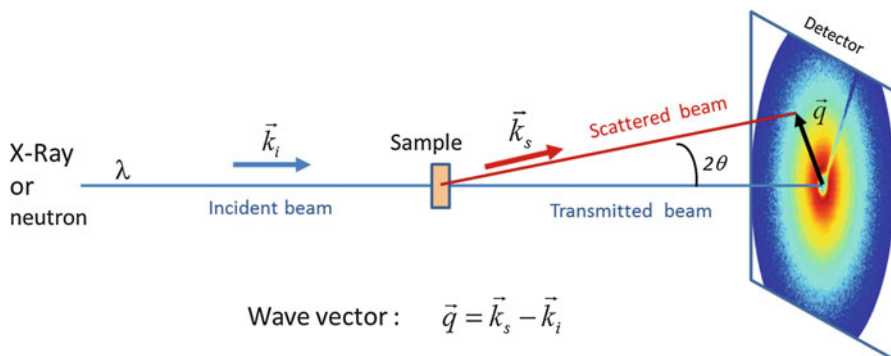
Fig. 12.1 Schematic representation of SAS experiment

difference between incident and scattered wave vectors at angle 2θ, respectively, k_i ($|k_i| = k_i = 2\pi/\lambda$) and k_s ($|k_s| = k_s = 2\pi/\lambda$), enables to define the scattering wave vector q ($q = k_s - k_0$). If fluctuations have no preferential orientation relatively to q, the scattering pattern will be isotropic. In the following, isotropic scattering is assumed and the module q of wave vector q will be used. By construction:

$$q = \frac{4\pi}{\lambda} \sin\theta \tag{12.1}$$

3.1.2 Length Scale and Wave Vector

For systems presenting periodic inhomogeneities, the scattering pattern will present a correlation peak. The Bragg law $2d \sin\theta = \lambda$ could be used to relate the period d of inhomogeneities to the observed scattering angle 2θ at peak maximum. By combining the Bragg law to Eq. 12.1, one finds:

$$q = \frac{2\pi}{d} \tag{12.2}$$

For a porous system, it was shown [6] that the linear scale of radius R of pores is related to the measured q scale by the relation:

$$q \approx \frac{2.5}{R} \tag{12.3}$$

More generally, q is related to the inverse of a characteristic length in direct space. It means that large particles or pores will scatter at small q values and conversely. The wave vector q is seen as an inverse length probe. The consequence is also that the multi-scale description of a structure requires acquiring data in a large q range. The usual q values accessible by SAXS or SANS instruments are in the range $5\ 10^{-3} - 0.5\ \text{Å}^{-1}$. This range could be extended with USAXS and USANS down to

Table 12.1 Main X-ray and neutron atomic scattering length (from Ref. [3])

| | | Scattering length b (10^{-12} cm) | |
Atom	Z	X-ray	neutron
H	1	0.28	−0.374
D	1	0.28	0.67
C	6	1.69	0.66
N	7	1.97	0.94
O	8	2.25	0.58
Na	11	3.09	0.36
Al	13	3.65	0.35
Si	14	3.93	0.42
S	16	4.50	0.28
K	19	5.34	0.37

10^{-4} Å^{-1}. The corresponding length in direct space varies from nanometer up to few micrometers.

3.1.3 Beam/Matter Interaction and Atomic Scattering Length

It is well known that X-ray interacts with electrons, whereas neutrons interact with nucleus. Atoms are often considered as individual scatterers, and atomic scattering length is used to quantify the magnitude of the interaction. For X-rays, the atomic scattering length b is simply the product of atomic number Z by the scattering length b_e of one electron ($b_e = 2.81 \; 10^{-13}$ cm). For neutrons, there are no simple rules and tabulated [3] values are used. Table 12.1 shows the main atomic scattering lengths for X-ray and neutron used here. It's worth noting that H and D have very different values.

3.1.4 Coarse Graining: Scattering Length Densities, Contrast

Scattering Length Density

As mentioned previously, small-angle scattering is sensitive to fluctuation down to the nanometer length scale. Nevertheless, this scale is almost one order of magnitude larger than the atomic scale, and atomic scattering length is usually averaged in order to simplify scattering intensity modeling. The way of averaging is to sum the atomic scattering length of each atom over a volume representative of a phase, a particle, or a region where the scattering properties of matter do not vary. We use for that *scattering length densities* (*SLDs* or noted ρ):

$$SLD = \rho = \frac{1}{V} \sum_i n_i b_i \tag{12.4}$$

where n_i is the number of atoms of type i in the volume V. This volume could be the unit cell for a crystal or the molecular volume for liquid or amorphous solid. Note that the calculation of *SLD* requires at least the knowledge of composition and mass density.

Using this definition, no fluctuation occurs if a simple liquid is considered and the resulting intensity should be null. Experiments confirm almost this point: a small scattering intensity is in fact observed. This small signal, ascribed to isothermal compressibility of the liquid, shows no or little q-dependence.

Contrast

If two phases are mixed but present fluctuations, we can calculate the magnitude of SLD fluctuations. If we consider silica nanoparticles (SiO_2, $d = 2.65$ g cm^{-3}) in water (H_2O, $d = 1$ g cm^{-3}), their X-ray $SLDs$ are, respectively, $\frac{2.65*6.02\ 10^{23}}{(28+2*16)}$ $(3.93 + 2*2.25)10^{-12} = 22.4\ 10^{10}$cm^{-2} and $\frac{1*6.02\ 10^{23}}{(16+2*1)}(2.25 + 2*0.281)10^{-12} = 9.4\ 10^{10}$cm^{-2}. From these values, the X-ray contrast $\Delta\rho = (SLD_{SiO2} - SLD_{H2O}) = 13\ 10^{10}$ cm^{-2} could be defined. The more important the contrast is, the more important the intensity is.

Due to very different neutron scattering lengths of H and D (Table 12.1), the SLD of hydrogenated solvent will be also very different from the corresponding deuterated one. For instance, if water (H_2O, $d = 1$g cm^{-3}) and heavy water (D_2O, d = 1.1 g cm^{-3}) are considered, their neutron $SLDs$ are, respectively, $\frac{1*6.02\ 10^{23}}{(16+2*1)}(2.25 + 2*0.281)10^{-12} = -0.56\ 10^{10}$cm^{-2} and $\frac{1.1*6.02\ 10^{23}}{(16+2*2)}$ $(2.25 + 2*0.281)10^{-12} = 6.4\ 10^{10}$cm^{-2} leading to *neutron contrasts* with silica, respectively, of 4.8 and 2.2 10^{10} cm^{-2}. From this peculiar example, we see that from a contrast viewpoint, *SAXS* should be preferred to *SANS* and that hydrogenated water gives stronger contrast than deuterated water (Fig. 12.2).
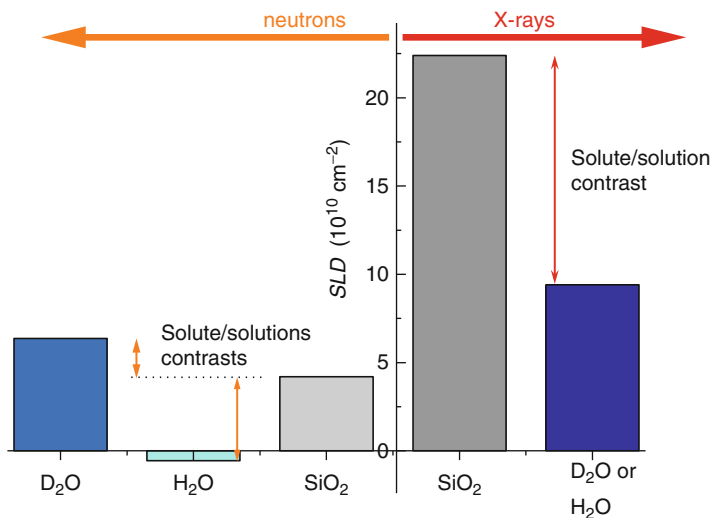
Fig. 12.2 X-ray and neutron SLD and contrasts considered for silica particles in water or heavy water

Mixing Rule for SLD

If two miscible liquids *1* and *2* are mixed, the resulting *SLD* is the sum of their *SLD* weighted by their respective volume fraction:

$$\rho_{mix} = \phi_1\rho_1 + \phi_2\rho_2 \tag{12.5}$$

This important property is extensively used in *SANS* where neutron *SLD* of usual solvents (water, toluene, heptane, etc.) could be adjusted at any desired value, while chemical properties are fixed, between the one of hydrogenated and deuterated solvent by mixing them. This practice, known as *contrast variation*, allows to:

1. Measure the *SLD* of unknown homogeneous species.
2. Simplify the data interpretation in the case of complex multiple component systems that present several regions of different *SLDs*. In this case, several experiments where different mixtures of specific isotopic solvents match the different regions of particles or aggregates are necessary.

3.1.5 Scattering Intensity Modeling

In the following part, expressions of the differential scattering cross section per unit volume ($d\Sigma/d\Omega$ (q) noted hereafter $I(q)$) will be given. The "Data Treatment" section will explicit how to relate measurements, i.e., number of photons or neutrons scattered, to $I(q)$.

Dilute System

General Expressions

The scattering amplitude $A(q)$ by a volume V where isotropic *SLD* fluctuations $\rho(r)$ occur is given by:

$$A(q) = \int_V \rho(r)e^{-iqr}dr \tag{12.6}$$

Variations in *SLD* $\rho(r)$ can be rewritten as the sum of an average *SLD* $<\rho>$ and a fluctuation part $\delta\rho(r)$ around the mean value, the average term $<\rho>$ giving no contribution to amplitude:

$$\rho(r) = \langle\rho\rangle + \delta\rho(r) \tag{12.7}$$

The detector measures an intensity which is the square of the amplitude. Scattered intensity per unit volume $I(q)$ is given by:

$$I(q) = \frac{A(q)A^*(q)}{V} = \frac{1}{V}\iint_{VV} \delta\rho(r)\delta\rho(r')e^{-iq(r-r')}drdr' \tag{12.8}$$

In a case of a two-phase system, one of *SLD* ρ_p and the second of *SLD* ρ_s, Eq. 12.8 becomes:

$$I(q) = \frac{1}{V}\left(\rho_p - \rho_s\right)^2 \iint\limits_{vv} e^{-iq(r-r')}drdr' = \frac{1}{V}\Delta\rho^2 \iint\limits_{vv} e^{-iq(r-r')}drdr' \qquad (12.9)$$

where *v* is the volume of the scatterer. For a dilute regime of N_p scatterers in the volume V, the scattering intensity collected by the detector is the sum of scattering intensity coming from all the individual scatterers (particles, pores, etc.), and Eq. 12.9 can be rewritten as:

$$I(q) = \frac{v^2}{V}N_p\Delta\rho^2[F(q)]^2, \text{ with } F(q) = \frac{1}{v}\int\limits_{v} e^{-iqr}dr \qquad (12.10)$$

By using notation where volume fraction ϕ ($\phi = N_p v/V = nv$) and form factor $P(q)$ of scatterers appear, Eq. 12.11 relates the main contributions to scattering in dilute systems:

$$I(q) = \phi V_p \Delta\rho^2 P(q) \qquad (12.11)$$

The contrast term $\Delta\rho$ being squared in this expression, we note the importance of its accurate knowledge for intensity modeling. $P(q)$, sometimes noted $F^2(q)$, is called the scatterer form factor and describes its geometry (size, shape, etc.). Note that for $q = 0, P(q) = 1$.

For heterogeneous particles in a solvent (*SLD* ρ_0) such as core–shell particles, Eq. 12.11 has to be modified in order to account for *SLD* and volume of the core and shell, respectively, noted ρ_C, ρ_S, v(R), and v (ΔR):

$$I(q) = n[(\rho_S - \rho_0)v(R + \Delta R)F(q, R + \Delta R) + (\rho_C - \rho_S)v(R)F(q, R)]^2 \qquad (12.12)$$

Equations 12.10, 12.11, 12.12, and 12.13 that are related to scattering by an assembly of isotropic, identical, and dilute scatterers could be developed according to the various *q* regimes considered.

Guinier Region

In the so-called *Guinier* region (at scales larger than the typical size of particles or, equivalently, at *q* values smaller than the reverse size of particles), the *Zimm* approximation [7] can be used to determine the scattering cross section at zero angle *I(0)* and the radius of gyration R_g of the particles:

$$\frac{1}{I(q)} = \frac{1}{I(0)}\left(1 + \frac{q^2 R_g^2}{3} + \dots\right), \text{ for } qR_g < 1 \qquad (12.13)$$

The validity of Eq. 12.13 can be extended for swollen particles. For polymers, Burchard [8] considers the *Zimm* approximation valid up to $qR_g = 2$.

From Eq. 12.11, $I(0)$ takes a simple form for dilute solutions from which the scatterer volume v can be extracted:

$$\frac{I(0)}{\phi \Delta \rho^2} = v \tag{12.14}$$

The "molar mass" M can be derived by using the usual expression:

$$M = dN_a v \tag{12.15}$$

with d the specific gravity of the solute and N_a the Avogadro number.

Combining Eqs. 12.13, 12.14, and 12.15 and considering concentration c in grams per unit volume, one obtains:

$$\frac{\Delta \rho^2}{d^2 N_a} \frac{c}{I(0)} = K \frac{c}{I(0)} = \frac{1}{M_w} \tag{12.16}$$

It is worth noting that expressions 12.14, 12.15, 12.16, and 12.17 are model independent.

Porod Domain

At large q values, in the q-regime where q^{-1} become smaller than the curvatures of the interfaces, they appear flat and the scattering intensity is proportional to the total surface area Σ independently of the shape of the two phases. Hence, for sharp interfaces (in the normal direction but smooth in any other directions), Porod [9] showed that intensity decreases as q^{-4} leading to:

$$\Sigma = \frac{1}{2\pi (\Delta \rho)^2} \lim_{q \to \infty} I(q) q^4 \tag{12.17}$$

where Σ is surface per unit volume developed by the interface, i.e., the specific area expressed in m^2/m^3. For a dispersion of spheres of radius R at volume fraction ϕ, the size of the sphere can be deduced from surface area measurement using:

$$R = \frac{3\phi}{\Sigma} \tag{12.18}$$

In the case of rough interfaces that could be described by surface fractal formalism, the scattering intensity follows at large q values a power law dependence. The power law exponent is then $-(6 - D_s)$ where D_s is the surface fractal dimension ($2 < D_s < 3$). The surface area Σ is related in this case to the measurement probe size r by:

$$\Sigma = \Sigma_X r^{2-D_S} \tag{12.19}$$

The pre-factor Σ_X can be determined from *SAS* experiments in the high q limit [10]:

$$\Sigma_X = \frac{1}{\pi \Delta \rho^2} \frac{\lim_{q \to \infty} I(q) q^{6-D_S}}{f(D_S)} \quad \text{with } f(D_S)$$
$$= \frac{\Gamma(5 - D_S) \sin\left[(3 - D_S)(\pi/2)\right]}{[3 - D_S]} \tag{12.20}$$

Intermediate Domain

In the intermediate domain, the q variations of scattering intensity are ascribed to form factor of individual scatterers. Analytic expressions of simple geometric and homogeneous objects are available [11]. For instance, for spheres:

$$F_{sphere}(q, R) = \left[3 \frac{\sin(qR) - (qR)\cos(qR)}{(qR)^3}\right]; \quad P_{sphere}(q, R) = \left[F_{spher}(q, R)\right]^2 \tag{12.21}$$

whereas for disorientated cylinders (radius R and height $2L$):

$$P(q) = \int_0^{\pi/2} \frac{\sin^2(qL \cos \alpha)}{(qL \cos \alpha)^2} \frac{4J_1^2(qR \sin \alpha)}{(qR \sin \alpha)^2} \sin \alpha \, d\alpha \tag{12.22}$$

In this last expression, α is the angle between the normal to the base cylinder and the scattering vector $\boldsymbol{q}$. Eq. 12.22 could be simplified in two limiting cases:

- For $L/R \ll 1$ and $q > \pi/R$, cylinders reduce to disks and the form factor decreases as q^{-2}. More generally, 2D objects such as lamellae or prolate ellipsoids behave the same.
- For $R/L \ll 1$ and $q > 1/L$, cylinders reduce to 1D objects and scattering intensity decreases as q^{-1}.

Intensity Modeling in the Whole q Range

The direct method assumes a shape (i.e., a scatterer form factor) and calculates the analytical expression of scattering intensity $I_{calc.}(q)$ which is compared to experimental data $I_{exp.}(q)$ in order to minimize the χ^2:

$$\chi^2 = \frac{\sum_{P-x} \left[\frac{(I_{calc.}(q) - I_{exp.}(q))}{Err(q)} \right]^2}{(P - x)} \qquad (12.23)$$

In this expression, $Err(q)$ represents the error on experimental intensity, P the number of intensities in the selected q range, and x the number of varying parameters such as size, radius, length, *SLD*, volume fraction, polydispersity, etc. Observation in direct space could help to select a realistic form factor. If no observations are available, several form factors will be tested in a q range as large as possible and the selection will be based on χ^2 values. The selectivity of the postulated model could also be assured by looking at the response of the model in varying contrast conditions, either by *SAXS* and *SANS* comparison or by contrast variation using *SANS*.

The intensity presents often a fast q-decaying behavior introducing a more important weight at small q values. For a better agreement at large q values, logarithm of intensities could be considered in the fitting procedure.

The indirect method [12, 13] uses the inverse Fourier transform of the measured intensity and doesn't require shape assumptions.

Polydispersity

For polydisperse systems, *SAS* measurements give the weight average molecular weight of scatterers $\overline{M_W}$ and the z-average radius of gyration $\overline{Rg_Z}$ defined by the following expressions:

$$\overline{M_w} = \frac{\sum_i m_i M_i}{\sum_i m_i} \qquad (12.24)$$

and

$$\overline{Rg_z} = \sqrt{\frac{\sum_i m_i M_i Rg_i^2}{\sum_i m_i M_i}} \qquad (12.25)$$

with m_i, M_i, and R_{gi} the mass, molar mass, and radius of gyration of the i fraction, respectively. The averaged values are sometimes difficult to handle, especially for uncontrolled polydispersity found in natural nano-materials, and polydispersity reduction is highly desirable. Examples will be given in Sect. 4.

Concentrate

When concentration of inhomogeneities increases, spatial correlations between scatterer mass centers appear and modulate the scattering intensity. To account

for this modulation, the structure factor $S(q)$ is introduced in the general expression of the scattering intensity:

$$I(q) = \phi v \Delta \rho^2 F^2(q) S(q) \tag{12.26}$$

$S(q)$ is related to the pair correlation function $g(r)$ that describes the local order of scatterers, i.e., the probability to find a scatterer at a given distance of another one. $g(r)$ depends on interaction potential $V(r)$:

$$g(r) = \exp^{-\frac{V(r)}{k_B T}} \tag{12.27}$$

And $S(q)$ is related to $g(r)$ by:

$$S(q) = 1 + 4\pi \frac{N}{V} \int_V (g(r) - 1) r^2 \frac{\sin(qr)}{(qr)} dr \tag{12.28}$$

From this expression, it appears that $S(q)$ is an oscillatory function that tends to be 1 for large q values and for dilute systems.

Structure Factor

Few structure factors are available in analytical form. Among them, the fractal structure factor will be used here. A mass fractal aggregate made of subunit (or primary particles) shows a self-similar structure between the size r_0 of primary particles and the size ξ of the aggregate. In this interval, the mass in sphere of radius r follows a power law $M(r) \propto r^D$ where D is defined as the fractal dimension. In the same way, the density at distance r from mass center scales as r^{D-3}. The corresponding scattering intensity shows a q^{-D} behavior in the $1/\xi - 1/r_0$ q range (Fig. 12.3).

One of the useful expressions of fractal structure factor has been proposed by Teixeira [15]:
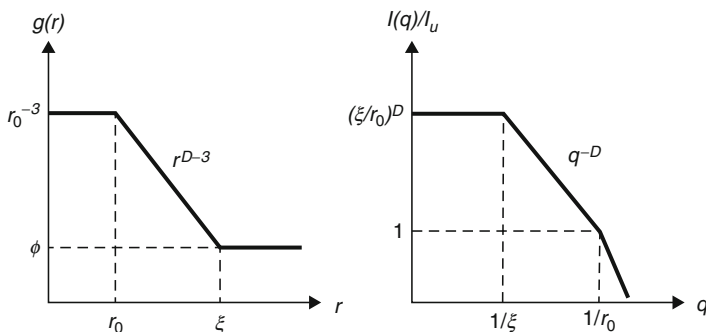
Fig. 12.3 (*left*) Pair correlation function $g(r)$ of a mass fractal; (*right*) corresponding scattering function (from Ref. [14])

$$S(q) = 1 + \frac{1}{(qr_0)^D} \frac{D\Gamma(D-1)}{\left[1 + 1/(q^2\xi^2)\right]^{(D-1)/2}} \times \sin\left[(D-1)\tan^{-1}(q\xi)\right] \quad (12.29)$$

In this expression, Γ is the gamma function, D is the fractal dimension of aggregates, and ξ is a characteristic distance above which the mass distribution is no longer described by the fractal law. ξ is related to the generalized radius of gyration Rg by [15]:

$$\xi^2 = \frac{2R_g^2}{D(D+1)} \quad (12.30)$$

Zimm Approach

For moderate concentration c of particles, interparticle interactions have to be taken into account, and the previous equations are modified through a virial expansion to give:

$$\frac{I_e\Delta\rho^2}{d^2N_a} \frac{c}{I(q)} = \frac{1}{M_w}\left(\left(1 + \frac{q^2R_g^2}{3}\right) + 2A_2M_wc + \dots\right) \quad A_2M_wc < 0.25 \quad (12.31)$$

This equation can be simplified in the *Guinier* region to yield:

$$\frac{I_e(\Delta\rho^2)}{N_ad^2} \frac{c}{I(0)} = \frac{1}{M_w}(1 + 2A_2M_wc) = \frac{1}{M_{app}} \qquad qR_g < 1; A_2M_wc < 0.25 \quad (12.32)$$

where A_2 is the second virial coefficient. Positive values of A_2, significant of repulsive interaction between objects, lead to a lowering of the $I(q)/\phi$ ratio at small q values as the concentration increases. This relation holds up to concentrations where interactions are described by pair interactions. The left-hand part of Eq. 12.32 can be used to define an "apparent" mass M_{app} which tends toward the real one at low concentration.

3.2 Instrumentation

SAS experiments require a specific instrumentation, and this section is not devoted to such a detailed description. Useful reviews are given for neutrons by Grillo [16] and for synchrotron by [17].

Nevertheless, this chapter aims at giving some tips for users in order to choose the adequate instrument and sample environment. The delicate issue of data reduction is also evoked.

3.2.1 General Considerations

Sample Thickness
The choice of sample thickness x has to fulfill several requirements.

- First of all, the counting time to get enough statistics on detector is closely related to sample thickness. The number of photons $N(q)$ recorded per unit time depends on:
  1. Number of scatterers in the beam, i.e., on optical path x ($N(q) \sim x$)
  2. Sample transmission $T = e^{-\mu x}$ where μ is the linear absorption coefficient ($N(q) \sim e^{-\mu x}$)

  The counting time optimization requires to maximize the product $x \, e^{-\mu x}$. This condition is fulfilled for $x = 1/\mu$ or equivalently $T = 1/e \approx 0.36$. Hence for *SAXS*, if aqueous solutions are considered, the optimal sample thickness is close to 1 mm, whereas it is roughly 2 mm for hydrocarbons.
- For *SANS*, the incoherent scattering has to be taken into account, and the rule of thumb is x = 1 mm for water and 2 mm for deuterated solvent. In any case, the transmission should be higher than 0.5.
- Finally, sample thickness has to be such that multiple scattering is absent. A practical way to avoid multiple scattering is to decrease thickness up to the point where the ratio $N(q)/x$ is constant. Multiple scattering is favored by large-size scatterers and high contrasts. A classical example is powders where large grains have large *SLD* compared to air. In this case, grains could be sprinkled on a scotch tape; in spite of ill defined thickness, data reduction for such powders is well documented [18].

Sample Environment
One of the major benefits of *SAS* technique is the fact that sample preparation is reduced. The various forms of samples such as liquids, solids, smokes, suspensions, gels, and foams to be analyzed make *SAS* one of the most versatile techniques.

Moreover, sample could be solicited during measurements. Control of thermodynamic conditions (temperature, pressure, relative humidity, etc.) as well as hydrodynamic conditions (flow, stretching, shear rate, etc.) is common.

Measurements: Data Treatment
Before starting an experiment, it is crucial to determine the required q range. It depends on the largest size of scatterer (observation in direct space could help). Experimentally, the q range could be varied by changing the detector-to-sample distance. If a large q range is needed, several acquisitions at different detector-to-sample distances (configuration) could be necessary. After data treatment, measurements from different configurations are merged, and superposition of absolute intensities in the recovery q ranges is a good indication of data treatment quality.

A rigorous data treatment is essential to convert number of photons or neutrons detected $N(q)$ into experimental differential scattering cross section per unit volume $I_{exp}(q)$ that can be compared to calculated intensity $I_{calc}(q)$. The usual steps of data treatment of *2D* raw images are the following:

1. *Centering and q calibration*. For that, a measurement of a sample giving Bragg peak at low angle (e.g., Ag behenate for X-ray) is often convenient. A geometrical measurement of sample-to-detector distance is also an alternative.
2. *Normalization of cell efficiency* could be necessary. In that case, a measurement of a sample giving a flat scattering (water for neutrons) is convenient. If a region of the detector is faulty (cells behind the beam stop or its support), it could be also masked.
3. *Subtraction of detector noise*.
4. *Normalization by the solid angle* of a cell.
5. *Normalization by sample transmission*. Counting time for transmission must be such that transmission is known at a precision of few per thousand.
6. *Radial averaging* in case of isotropic scattering.
7. *Subtraction of empty container*. For liquids, the container could be a capillary for X-ray, a quartz cell for neutrons, an empty beam for solid samples, or more generally an empty cell.
8. *Subtraction of the solvent*. The "solvent" to consider is the one where its empty container contribution has been subtracted. If solute is concentrate (volume fraction ϕ), the subtraction of the "solvent" has to be weighted by a factor $(1 - \phi)$.
9. *Normalization by the incident flux*. In practice, external standards of known absolute cross sections [19] are often used at this step.
10. *Normalization by sample thickness x*.

3.2.2   SANS

Neutron facilities are rather sparse, but *SANS* spectrometer is well represented within neutron centers. Most of the spectrometers are designed with a *2D* detector whose position could be varied in order to cover the usual q range of SANS (few 10^{-3}–0.5 Å^{-1}). Recently *USANS* instruments have been built in order to extend the q range down to 10^{-4} [20] or even 10^{-5} Å^{-1} [21].

The most common windows used for SANS experiments are made of quartz since they give high transmission and low level of scattering. The beam size depends on collimation conditions and is generally of few millimeters. The fluxes are rather modest (few 10^6 neutrons/s on sample) compared to SAXS synchrotron. The benefit is the preservation of the sample integrity, whereas the drawback is the long counting time – up to hours – for low contrasted systems. One feature of neutron is the ease to vary wavelength by changing the rotating velocity of wavelength selector. According to Eq. 12.1, the q domain may be changed in this way.

One of the major differences between the two techniques is the presence for neutrons of incoherent scattering that is notably important for ^{1}H. This incoherent

scattering doesn't wear any structural information. It occurs in all the directions and gives rise to flat background. The solute and the solvent incoherent contribution have to be taken into account in data treatment [22].

3.2.3   SAXS

Unlike *SANS*, *SAXS* equipments are found both in laboratory and on synchrotrons. For both equipments, samples are held in containers whose windows are often made of quartz (quartz capillaries), mica, or thin films of polymers such as polyimide (Kapton).

Laboratory Setup

Up to the 1980s, laboratory setup was frequently homemade equipments, and nowadays very good commercial equipments are available. The X-ray source (most of the time, $\lambda = \text{CuK}\alpha = 1.54$ Å) is either a sealed tube or a rotating anode microsource delivering on sample fluxes between 10^6 and few 10^7 photons/s in a submillimetric beam size. Few homemade laboratory setups have been designed in the *USAXS* domain [23].

Synchrotron

A lot of *SAXS* beamlines are now available on synchrotron. Compared to laboratory setups, the high fluxes (up to 10^{14} photons/mm^2 [24]) allow time-resolved measurements at frame rate of few milliseconds, and low divergence allows to reach q_{min} values as low as 10^{-3} Å^{-1}.

3.2.4   Conclusion

To conclude, a variety of equipments are now available. As a function of size heterogeneities, contrasts, available volume of sample, equilibrium, or dynamics, one can use at its best *SAS* or *USAS* techniques, X-ray or neutrons, laboratory setup, or synchrotron.

4   Key Research Finding

SAS experiments have been intensely used in *Soft Matter* and *Material Science* to characterize manufactured or synthetic systems of interest. The present chapter aims at showing that such powerful techniques could also be used to gain insight into natural nano-materials structure in spite of their size and composition complexity. Most of the examples shown here come from petroleum or new energy industries. It will be shown that knowledge of mesoscopic structure of natural systems is of paramount importance in respect to many industrial processes. The demarche proposed here could be easily extended to other systems relevant to other industries.

4.1 Solution of Asphaltene

Among natural nano-materials found in the petroleum industry, petroleum itself constitutes a natural colloidal system. In fact, petroleum is constituted of more than tens of thousands [25] of different hydrocarbon molecules. For such a complex liquid, separation methods are necessary for analytical purpose, and the one that prevails considers four classes of molecules: *s*aturate, *a*romatic, *r*esin, and *a*sphaltene known as the SARA method. The first step of separation is to contact crude oil with an excess volume of alkane (usually pentane or heptane): the precipitated material is called *asphaltene*, whereas the remaining part of crude oil is called *maltenes*. This latter fraction could be further separated by polarity contrast using chromatographic methods into saturates, aromatics, and resins.

In parallel, the first separation that occurs in a refinery plant is the distillation that separates molecules as a function of their ebullition points. It has been shown that asphaltene belongs to the less volatile fraction.

Asphaltenes represent a solubility class of industrial importance since they are known to increase the viscosities of crude oils, to phase separate from oil when they are mixed to low-polarity hydrocarbon fractions, or to be refractive to hydroconversion. *All these macroscopic properties are thought to be related to their ability to form aggregates in crude oils*. In this section, we will show how use of *SAS* methods improves the knowledge of aggregation behavior of asphaltene that could be relevant to better understand their macroscopic properties.

4.1.1 Molecular Aspects

Chemical composition of asphaltene fraction has been measured using elemental analysis [26]. The H/C ratio is close to 1 indicating aromatic molecules. The molecular mass has been subject of controversy, but there is now a consensus on mass ranging from 500 to 1000 g/mol. These estimations in dilute (~1 mg/l) solutions come from high-resolution mass spectrometry (*FT-ICRMS*) [27] or from fluorescence (*TRFD*) [28] measurements. Heteroelements such as O, N, and S are also present at few mass percent level. Aggregation properties observed at higher concentration limit the available investigation techniques.

Molecular structure is always a subject of debate. The *archipelago* model where few small aromatic regions (2–3 cycles) are linked by alkyl chains is opposed to the *continental* model where one larger aromatic domain (5–10 cycles) is surrounded by alkyl peripheral chains.

Several molecular interactions (π–π, H bonds, etc.) [29–31] have been invoked to explain aggregation properties.

4.1.2 Aggregated Material and Operational Definition of Asphaltene

One of the first observations of asphaltenic crude oil using *SAS* was by Dwiggins [32]. Thanks to a *Bonse–Hart* setup designed to probe the *USAXS* and *SAXS q* domain, he concluded that asphaltene colloids are present in crude oil in the form of few nanometer-size aggregates and absent in maltene. The dilution of crudes by

aromatic alkane or cycloalkane did not affect the radius of gyration of native colloids, whereas use of alcohols or n-alkanes shows a growth of aggregate sizes.

Several researchers [33–41] then used *SAS* methods to investigate the extracted asphaltene fraction in various solvents that mimic maltene behavior. Nevertheless, a recurrent question arises about the representativeness of such a simplification to approach the aggregation behavior of asphaltene in crude oils.

A contribution to this question is found in [42] where detailed comparisons of aggregated material in crude oil and extracted asphaltene are shown thanks to *SAS* experiments. In this study, permeates and retentates, differing in aggregate concentrations and sizes, were obtained from nanofiltration, using the method described by Zhao [43], of a vacuum residue at 200 °C with membranes of varying pore sizes. Abbreviations "P" and "R" refer to permeate and retentate, respectively, whereas the suffix "*nn*" refers to the pore size – 10, 20, or 50 nm – of the membrane. The entire *Safaniya* vacuum residue passed through the 100 nm membrane, while none passed through the 5 nm membrane. Elemental composition, density, and pentane and heptane asphaltene content were measured for each fraction.

In parallel, separation of asphaltene and maltene from precipitation using either pentane C5 or heptane C7 anti-solvents has been performed, leading to four fractions, namely, maltene (MC5 and MC7) and asphaltene (AC5 and AC7). The composition and mass density of these fractions have been also determined.

The combination of Eqs. 12.4 and 12.5 allows estimating the *SLD* of the different fractions. The results are plotted as a function of either AC5 or AC7 content (Fig. 12.4). The *SLD* of R and P fractions shows a linear behavior when plotted as a function of asphaltene volume fraction as expected from Eq. 12.5. When AC7 scale is considered, the extrapolated values are far from AC7 and MC7, whereas the AC5 scale gives satisfactory agreement between extrapolated P and R values and estimation of AC5 and MC5. *We concluded that, based on usual operational definition of asphaltenes, AC5 best represents the aggregated material in crude oil and MC5 best represents the solvent part of crude.* It is worth noting that using this approach, pentane resin fraction is part of the solvent. The direct
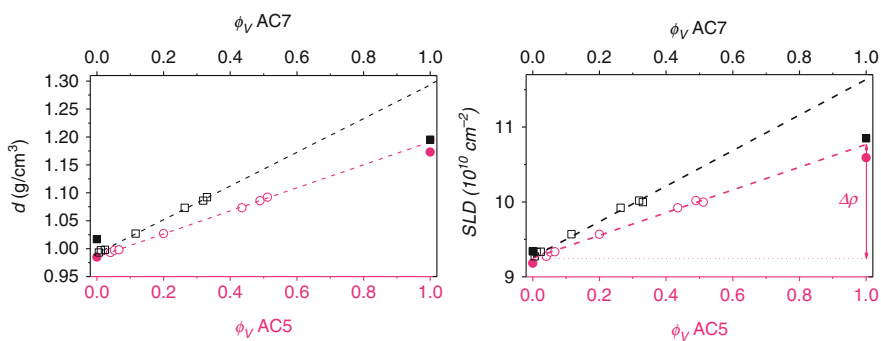
Fig. 12.4 Mass density (*left*) and estimated SLD (*right*) of permeate, retentate, asphaltene, and maltene fractions as a function of their AC5 or AC7 asphaltene content

consequence of this study is that aggregate concentration is readily determined using the ASTM method and that contrast is unambiguously determined by considering the *SLD* difference between extrapolated values at $\phi = 1$ and $\phi = 0$.

With concentration and contrast being known, the *WAXS*, *SAXS*, and *USAXS* signatures of the various fractions have been measured on the *ID02* synchrotron beamline of ESRF (Grenoble, France) at temperatures ranging from 80 to 300 °C. Samples were placed in an in-house brass cell with a 1.86 mm optical path and mica windows. The sample cell was placed vertically on a temperature-controlled hot stage (*HFS350V-MU, Linkam*) [44] with an upper operating temperature of 335 °C. Samples were kept under a nitrogen blanket to avoid oxidation during experiments. Data at 200 °C – the filtration temperature – were the focus of this study.

Figure 12.5a shows the scattering intensity on absolute scale of vacuum residue superimposed to permeate and maltene fractions. The lower scattering intensity and the most moderate *q*-dependence are obtained for MC5. These two observations are akin of solvent behavior in accordance with the above conclusions of *SLD* study. The subtraction of maltene contributions according to their concentration and the normalizations by volume fractions and contrast are shown in Fig. 12.5b. At small *q* values, data have been fitted to the *Zimm* approximation, and both mass and radii of gyration have been determined (Eq. 12.13, 12.14, 12.15, 12.16, and 12.17) for every fraction. Results are reported in Fig. 12.5c.

The main conclusions of this study could be summed up as follows:

- In crude oil, there are aggregate polydisperses that are at nm length scale.
- Based on the usual operational definition of asphaltenes, C5 asp. best represents the aggregated material in crude oils (id. maltene).
- The precipitation and redispersion in simple solvent approach seem to be valid and allow more detailed characterization.
- High temperature tends to disaggregate asphaltene but a structure at small length scale persists up to 300 °C.
- The M_W *vs.* R_g dependence for the largest aggregates suggests an aggregation mechanism leading to solvated aggregates.

4.1.3   Transient or Permanent Aggregation?

In opposition to the colloidal approach commonly applied to asphaltenes [33–42, 45, 46], which describes stabilized and permanent aggregates as detailed in the previous paragraph, asphaltenes in a good solvent are sometimes described as dispersed molecules near phase transitions [47], in which short-lifetime concentration fluctuations occur. The small-angle scattering signal is then associated to the correlation length of temporary fluctuations.

To discriminate between these two viewpoints and to gain insight into dynamic properties of asphaltene aggregates, we developed a methodology [48] based on the use of various scattering probes (i.e., *SANS* and *SAXS* and an in-house dynamic light scattering (*DLS*) setup adapted to dark and fluorescent solutions) and offering a subsequent degree of complementarities.
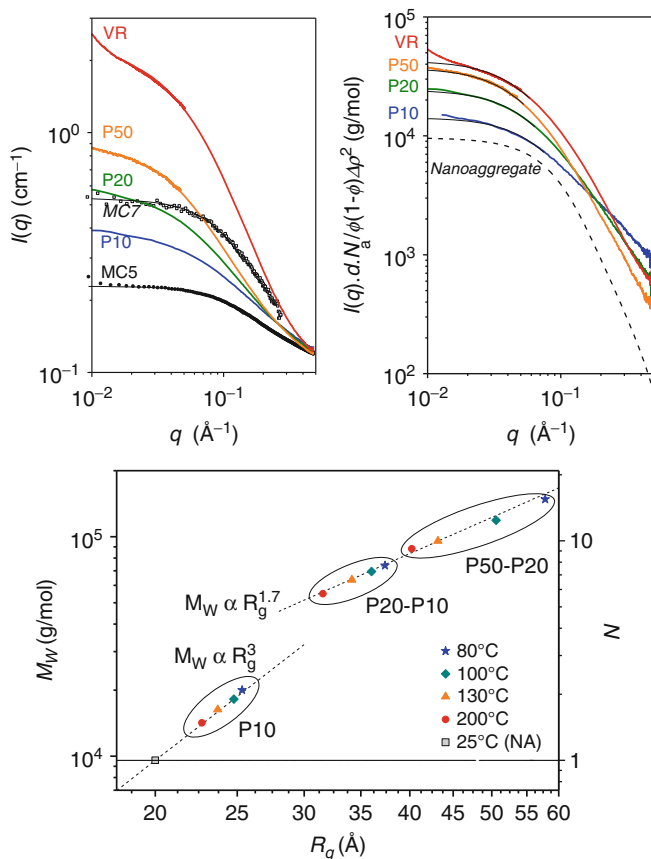
Fig. 12.5 (**a**) (*left*) Scattering intensity of vacuum residue compared to ultrafiltration and maltene fractions; (**b**) (*right*) scattering intensity of vacuum residue and fractions using maltene as solvent and corresponding Zimm approximation; (**c**) (*bottom*) mass/radius dependence of fractions at various temperatures

Samples are made of asphaltenes in toluene. A 3 wt% solution of asphaltenes in toluene was prepared, and two separations by ultracentrifugation were performed at 20 °C. The first centrifugation allowed to recover six fractions of the supernatant: F1 (top) down to F6 (bottom). The pellet of this preparation was not considered in this study. The second centrifugation allowed recovering the pellet which was hardly dissolved in deuterated toluene to generate the F7 fraction. Each of the seven fractions was characterized by (1) asphaltene concentration by weighting an aliquot before and after solvent evaporation, (2) chemical composition (CHONS), (3) asphaltene mass density at 20 °C as described elsewhere (18), and (4) *SAXS* or *SANS* and *DLS* measurements.

SAXS measurements of asphaltene fractions were processed at 23 °C on an in-house experimental setup as described elsewhere [51] in a flow-cell quartz

capillary. Two configurations allowed covering a total q range of 10^{-1}– 3 nm^{-1}. SANS measurements were carried out at the Laboratoire Leon Brillouin (LLB, Saclay, France) on the *PAXE* instrument, and the procedure is described elsewhere [52]. The wavelength was set at 1.7 nm, and the sample-to-detector distance was 5 m, allowing covering a complementary q range, relatively to in-house *SAXS*, of 3×10^{-2}–3×10^{-1} nm^{-1}.

DLS measurements were processed on homemade equipment: the incident beam ($\lambda = 656$ nm) goes through the sample placed in a 10 mm *Hellma* square quartz cell. The scattered and fluorescence light at 90 ° is filtered by a removable band-pass filter centered at 660 nm and recorded by an APD detector. The intensity of the scattered signal is optimized by positioning the laser and collecting the scattered signal in the vicinity of the wall, taking care to avoid heterodyne mixing mode. A single-mode fiber was used to collect the scattered signal in order to enhance the coherence factor β (see Eq. 12.33). The time-averaged scattered intensity, monitored all along the experiment duration, remains constant, which guaranties that no sedimentation or creaming occurs.

From time-dependent intensity fluctuations, the normalized autocorrelation function of the scattered intensity $G_2(q,t)$ (e.g., a correlogram) is built. $G_2(q,t)$ is related to the modulus of the normalized field autocorrelation function $g_1(q,t)$ by Siegert relationship:

$$G_2(q,t) = \alpha + \beta g_1^2(q,t) \tag{12.33}$$

where α is a baseline and β is the coherence factor. The time dependence of $g_1(q,t)$ is related to the dynamic properties of the solution. For Brownian, monodisperse, and noninteracting particles, $g_1(q,t)$ is an exponential decaying function:

$$g_1(q,t) = \exp(-\Gamma t) \tag{12.34}$$

where Γ is the decay rate. For a polydisperse system, $g_1(q, t)$ can be decomposed into a sum of exponential decaying functions:

$$g_1(q,t) = \sum_i A_i \exp(-\Gamma_i t) \tag{12.35}$$

where A_i represents the scattered intensity contribution of particles of class i and Γ_i its decay rate. To choose the number of characteristic decay times, we used a method based on *Padé* approximant. From this sum of exponential decaying functions, a standard *Levenberg–Marquardt* method is used to adjust the weight of each exponential decaying function. Good agreement between the data and the fit is reached when residual minimizing the Chi-square criterion is statistically distributed around zero without variations larger than a third the noise envelope. When the diffusion process is Brownian, the self-diffusion coefficient of the particles (D_i) is related to Γ_i by:
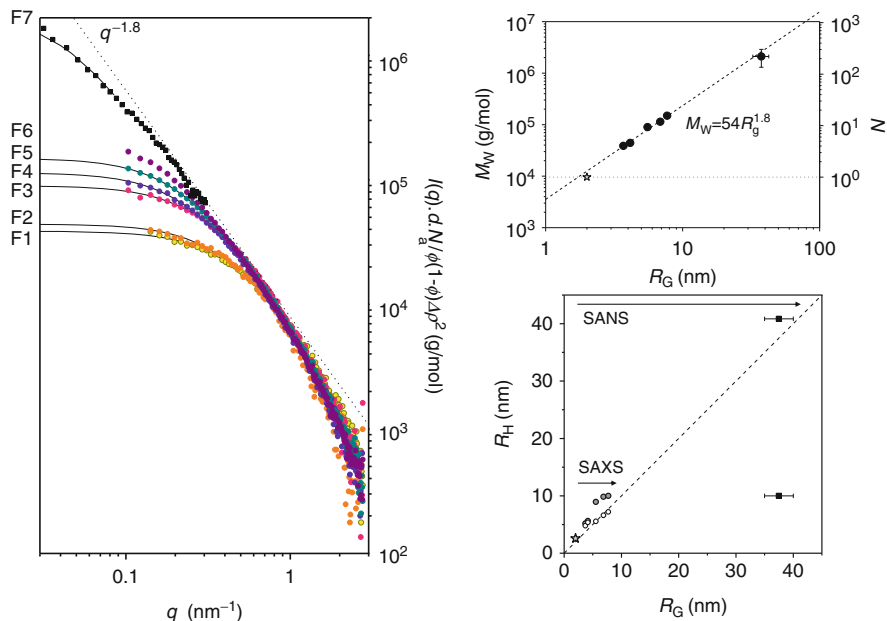
Fig. 12.6 (*left*) Normalized SAS data of fractions (symbols) and the corresponding Zimm approximation (*black full line*); (*right up*) M_W vs. RG dependence; (*right down*) RH vs. RG dependence

$$\Gamma_i = D_i q^2 \tag{12.36}$$

In the high dilution limit, the self-diffusion coefficient D_i enables calculation of the hydrodynamic radius R_{Hi} of the hard-sphere-equivalent noninteracting particles using the Stokes–Einstein equation:

$$D_i = \frac{k_B T}{6\pi\eta R_{Hi}} \tag{12.37}$$

where k_B and η are, respectively, the Boltzmann constant and the solvent viscosity.

Scattering intensities obtained from *SAXS* and *SANS* measurements are shown in Fig. 12.6. They are normalized to their asphaltene content and their contrast, allowing a direct comparison between *SAS* data:

- The small q regions allowed fitting data to the *Zimm* approximation (Eqs. 12.13, 12.14, 12.15, 12.16, and 12.17) as shown in Fig. 12.6 except for F6 fraction where the *Guinier* plateau is not reached even at the lowest q value scanned. The M_W and R_g values reported in Fig. 12.6 show that the fractions differ in molecular weight (3.9×10^4–2.1×10^6 g/mol) and sizes (3.7 nm up to 37.5 nm). Further, the rank of fraction follows rank of mass, suggesting that

separation occurs rather by mass than by density contrast. The large-size poly-dispersity could be appreciated from these values.

- The intermediate q region (0.2–1 nm^{-1}) shows that as far as aggregate grows, their scattering intensity collapses on a master power law curve ($I(q) \propto q^{-1.8}$). Moreover, as shown in Fig. 12.6, the mass M_W and the radius of gyration R_G are related through the relation $M_W \propto R_G^{1.8}$. These two observations are reminiscent of a fractal aggregation with mass fractal dimension $d_f = 1.8$.
- The large q region ($q > 1$ nm^{-1}) behaves the same for all fractions, suggesting that the structure at small length scale is independent of the size of the aggregates. The fractal concept suggests that aggregates are made of primary particles. It seems that the form factor of these primary particles is seen in this q region.

From DLS measurements, autocorrelation functions (not shown here) have been obtained. It was observed that baseline α (Eq. 12.33) was much higher for small aggregates (fractions F1 and F2) due to increasing contribution of fluorescence relatively to scattering intensity. For few samples, additional measurements on equipment allowing *DLS* measurements at $2\theta = 135°$ have been realized. For these samples, the decay rates scale linearly with q^2 (Eq. 12.36). *This observation and the fact that autocorrelation functions have been measured demonstrate that asphaltene forms permanent aggregates at least at time scale of experiments.* From decay rates, mean hydrodynamic radii R_H have been estimated using Eq. 12.37. Their comparison to radii of gyration R_G (Fig. 12.6) shows that $R_G \approx R_H$ on the whole range of sizes.

This study based on scattering measurements has demonstrated:

1. *The nanometric and large-size polydispersity of asphaltene aggregates in toluene solutions*
2. *The permanent character of aggregation in asphaltene-based systems*
3. *The mass fractal character of aggregates and, as a result, the existence of primary asphaltene particles*

4.1.4 Structure of Large-Scale Aggregates and Their Implication on Solution Viscosities

One of the most important industrial issues in asphaltenic crude oils or residues is the huge viscosity ascribed to the asphaltene fraction that impairs their transport properties. *The scientific question that arises is then to establish the relationship between mesoscale structure of aggregates and viscosity of the corresponding solutions.*

We have used [49] for that ultracentrifugation to produce, from a 3 wt% solution of asphaltene in toluene, reasonable quantities of asphaltene fractions of reduced polydispersity. Figure 12.7 shows the separation scheme, the name of fraction, and the mass balance of fractionation. For each fraction, the asphaltene concentration has been varied by adding or removing toluene.
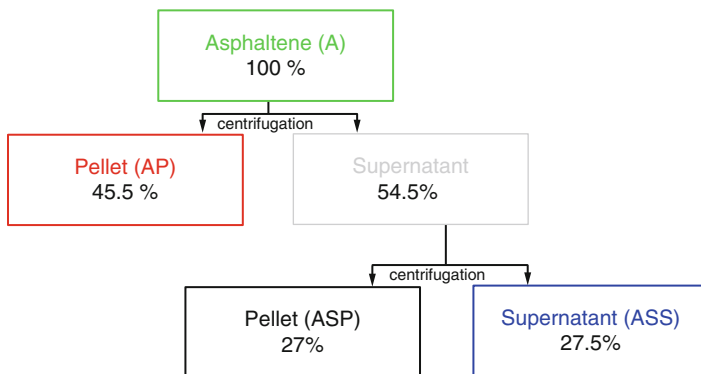
Fig. 12.7 Separation scheme of asphaltene by ultracentrifugation [Barré, Langmuir]

The viscosity and the structure of these asphaltene fraction solutions have been investigated using, respectively, rheological and X-ray scattering (SAXS) measurements as a function of concentration.

The viscosities η reported are the zero shear rate viscosities determined in the first Newtonian domain of asphaltene solutions using a *Contraves LS30* viscometer at 25 °C. From viscosity measurements, relative viscosities η_r, i.e., the ratio of solution-to-solvent η_0 viscosity, are formed and plotted as a function of asphaltene volume fraction ϕ (Fig. 12.8). For small ϕ values, the relative viscosity can be expressed by a virial expansion:

$$\eta_r = \frac{\eta}{\eta_0} = 1 + [\eta]\phi + k[\eta]^2\phi^2 + \dots \tag{12.38}$$

To obtain the k and $[\eta]$ parameters, Eq. 12.38 can be rearranged to yield:

$$\eta_{red} = \frac{\eta_{spe}}{\phi} = \frac{1}{\phi}\left(\frac{\eta}{\eta_0} - 1\right) = [\eta] + k[\eta]^2 \ \phi + \dots \tag{12.39}$$

where η_{red} and η_{spe} are, respectively, the reduced and specific viscosities. For a system of spheres without interactions, the $[\eta]$ value is 2.5. Equation 12.39 predicts that a plot of η_{spe}/ϕ versus ϕ should yield a straight line where the intercept is defined as the intrinsic viscosity $[\eta]$ and the slope is related to k known as Huggins' constant. Such a plot is presented in Fig. 12.8. Intrinsic viscosities are much higher than sphere values, 10.5–12, for pellet fraction (AP an ASP), whereas it is low, 5, for supernatant fraction ASS. The initial asphaltene solution A represents an intermediate case, 7, as expected.

For solvated particles or aggregates, the hydrodynamic "swollen" volume fraction ϕ_{eff}, often called "effective" volume fraction, is different from the "dry" solute volume fraction ϕ. The ratio of these quantities defines solvation constant k_S:
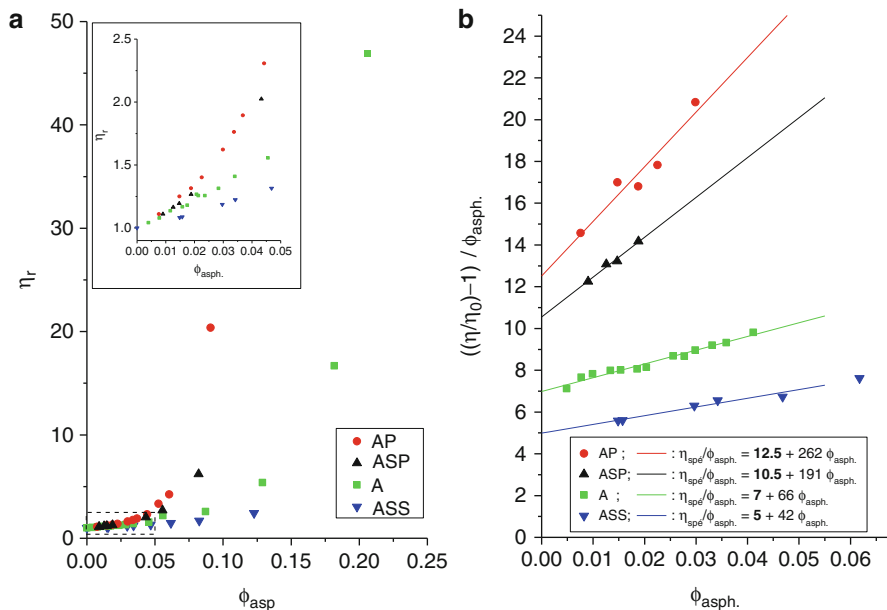
Fig. 12.8 Relative (**a**) and reduced (**b**) viscosities of the various fractions as a function of volume fraction of asphaltene

$$k_S = \frac{\phi_{eff}}{\phi} = \frac{n v_{eff}}{n v} = \frac{v_{eff}}{v} \qquad (12.40)$$

where n is the number of aggregates per unit volume, v_{eff} is the hydrodynamic volume of a solvated aggregate (solute plus solvent trapped in the aggregate), and v is the volume of a "dry" aggregate (solute only). If a spherical shape of aggregates is assumed, the ratio of their intrinsic viscosity to the one of hard spheres is again the k_s value $[\eta]/2.5 = k_s$. By combining the latter equation with Eq. 12.40, we obtain Eq. 12.41 which provides a practical way to renormalize concentration:

$$\phi_{eff} = \frac{[\eta]}{2.5} \phi \qquad (12.41)$$

This renormalization is particularly useful to compare the present system to the one of hard spheres that has been studied in detail. Hence, for more concentrated hard-sphere systems, Eq. 12.38 is no more appropriate. Instead, semiempirical models have been developed: they predict the viscosity divergence when the particle volume fraction approaches the dense random packing limit fraction ϕ_m. The Quemada equation, based on dissipated energy minimization by viscous effects, is frequently used because of its simplicity:

Fig. 12.9 Relative viscosities as a function of renormalized effective volume fractions. *Full lines* are the fit of the data to the Quemada Eq. 12.42
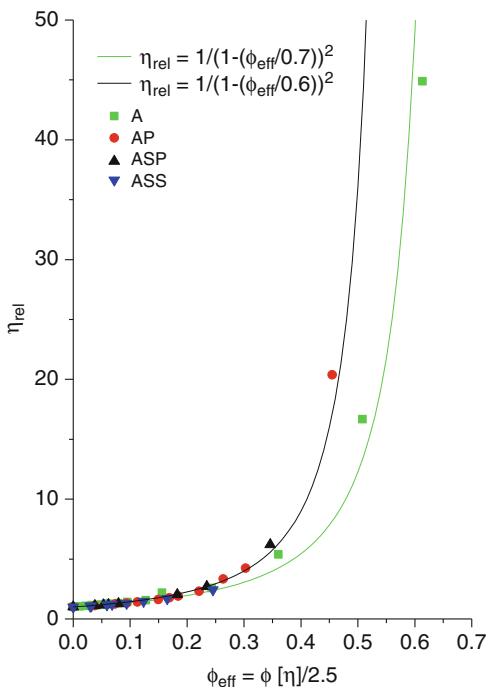
$$\eta_{rel} = \left(1 - \frac{\phi}{\phi_m}\right)^{-2} \tag{12.42}$$

Polydispersity can also have a significant effect on viscosity in the concentrated regime: the maximum packing fraction ϕ_m increases from about 0.63 for the monodisperse case up to values close to unity for large polydispersity systems (small spheres can fill the gap between the large ones in contact). Consequently, for a same volume fraction, a suspension of polydisperse spheres will exhibit a lower viscosity than the monodisperse one, especially at higher fractions (see Eq. 12.42).

Figure 12.9 shows the relative viscosities on the whole range of (renormalized) concentration. As expected, in the high dilution limit, all the curves merge on the "hard-sphere behavior," whereas at high concentration, the fit of the data to the Quemada Eq. 12.42 indicates a maximum packing fraction of 0.6 close to the monodisperse case for fractions and higher (0.7) for initial asphaltene solution.

In parallel, SAXS measurements have been conducted on the same solutions using a homemade equipment that allowed exploring the 0.01–0.22 Å^{-1} q range. The ASP fraction series, normalized to their asphaltene content and contrast, is shown in Fig. 12.10. At large q values, all curves are superimposed and behave as $q^{-2.1}$, whereas at small q values, normalized intensities decrease for most concentrated solutions. This last behavior indicates repulsive inter-aggregate interactions.
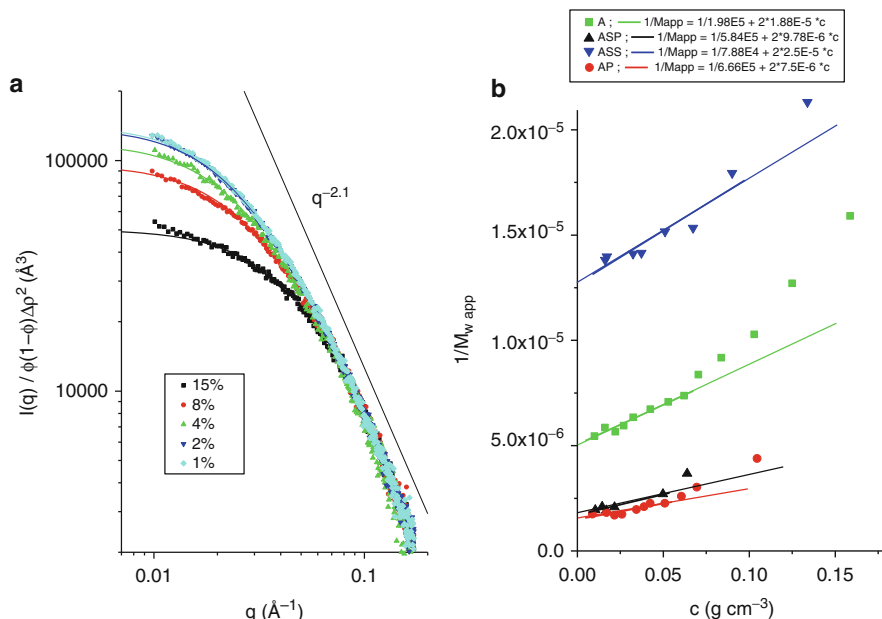
Fig. 12.10 Normalized SAXS data for ASP series (**a** *left*); reverse apparent mass as a function of asphaltene concentration (**b** *right*)

Indeed, the plots (Fig. 12.10b) of $1/M_{app}$ versus asphaltene concentration c according to Eq. 12.32 show positive slopes that mean repulsive interactions. From the same plot, M_w has been obtained by extrapolation to null concentration, and we reported values in the 79000–666000 g/mol range. Radii of gyration R_g have been estimated using Eqs. 12.13, 12.14, 12.15, 12.16, and 12.17 by considering for each fraction the most dilute solution. Numerical values go from 63 Å for ASS fraction up to 160 Å for AP fraction.

The $q^{-2.1}$ behavior, observed at large q values for each fraction, could be ascribed either to bidimensional or to mass fractal aggregates of fractal dimension 2.1. Viscosity measurements ruled out the assumption of flat aggregates. We will examine in the following the consistency and the robustness of mass fractal aggregate assumption.

For such a system, at much smaller scale than the typical size of aggregates, a simple expression of the scattering cross section is expected:

$$I(q) \propto q^{-d_f} \quad qR_g > 1 \tag{12.43}$$

Furthermore, a power law relation among the measured aggregate parameters, namely, radius of gyration, second virial coefficient, and molar mass, should be observed for these aggregates: [8]

Fig. 12.11 Dependence of A_2, $[\eta]$, and R_g as a function of M_w
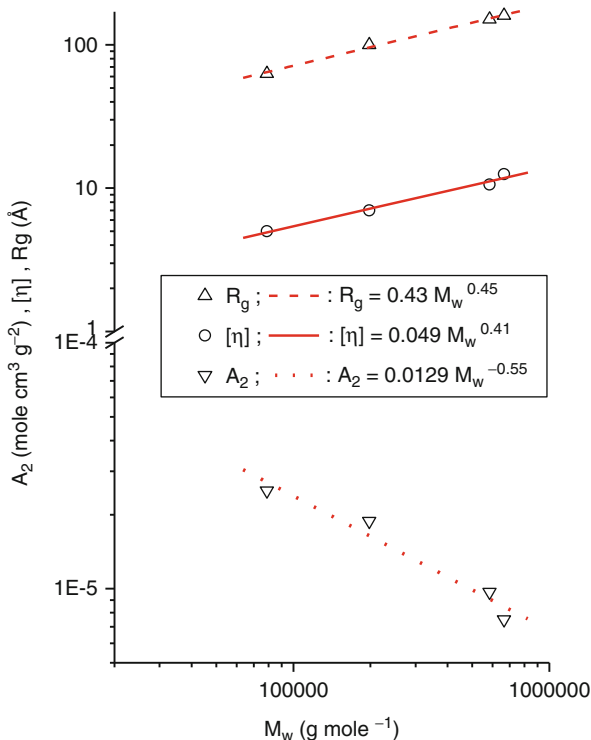
$$R_g = k_2 M_w^{1/d_f} \qquad (12.44)$$

$$A_2 = k_3 M_w^{-\left(\frac{3}{d_f}-2\right)} \qquad (12.45)$$

Finally, for such a system and by analogy with polymer solutions, the intrinsic viscosity should be related to the mass of aggregates by:

$$[\eta] = k_1 M_w^{\left(\frac{3}{d_f}-1\right)} \qquad (12.46)$$

Figure 12.11 shows the M_w dependence of R_g, A_2, and $[\eta]$ parameters. They all exhibit in log scale a reasonable linear behavior allowing experimental power law coefficient determination in spite of the restricted mass domain considered. The identification of exponents to one of Eqs. 12.44, 12.45, and 12.46 led to fractal dimension values $d_{f\,Rg}$, $d_{f\,[\eta]}$, and $d_{f\,A2}$, respectively, of 2.2, 2.13, and 2.02.

The closeness of the different independent determinations of fractal dimension, $d_{f\,Rg} \approx d_{f\,[\eta]} \approx d_{f\,A2} \approx d_{f\,I(q)}$, close to 2.1, is a very strong indication of the fractal nature of asphaltene aggregates. This polydispersion of solvated fractal aggregates has been confirmed by others [40, 41].

It can be concluded that asphaltene solution in toluene is described as a polydispersion of solvated aggregates of fractal dimension close to 2.1. Moreover, their viscosities at very low concentrations are controlled by size, mass, and fractal structure of the aggregates.

4.1.5   Asphaltene in Non-ambient Conditions

For crude oil production, transport, or refining applications, temperature of interest is in the range of -20–$400\,°C$, whereas pressures are in the range of atmospheric up to 500 bars. Characterization at temperature and pressure process conditions is highly desirable. One of the main advantages of scattering techniques is the possibility to do measurements when applying a constraint to the sample. The following section will detail some studies on asphaltene aggregation in non-ambient conditions.

In a first study [50], a high-temperature/high-pressure (293–573 $°C$, 0–400 bar) cell was built in order to perform *SANS* measurements. We took advantage of high-pressure strength, high transmission, and low scattering of sapphire to use this material as windows of a 2 mm path length cell. The latter was mounted on the PACE spectrometer operating at national neutron facility LLB (Saclay, France). Two configurations allowed to observe scattering in the 3.10^{-3}–$0.2\,\text{Å}^{-1}$ q range. A 3 wt% asphaltene in deuterated toluene solution was introduced in the cell.

For a given temperature, only minor effects of pressure on asphaltene aggregation are observed (Fig. 12.12), whereas aggregate mass changes noticeably (115 000 down to 33000) when temperature goes from 30 up to 290 $°C$.

Temperature effects have been recently studied on a vacuum residue diluted with its pentane maltene and using in-house SAXS experiments [51]. The brass cell associated to the hot stage (*HFS350V-MU, Linkam*) [44] described previously was used in the 80–240 $°C$ temperature range. Radius of gyration R_g, molecular weight M_W of asphaltenes, and second virial coefficients A_2 in vacuum residue are measured and are of the same magnitude as asphaltenes in toluene. Dimensions and masses decrease with temperature, while the small length scale remains unchanged, reinforcing the idea of same aggregation scheme previously described in toluene. In addition R_g, M_W, and $A2$ show power law dependence reminiscent of fractal aggregates.

Similar trends have been obtained by others using either *SAXS* [46] or *SANS* [45] in a restricted range of temperature.

It can be concluded that pressure has minor effects on asphaltene aggregation, whereas raising temperature disaggregates asphaltene to some extent, but small aggregates are still present at the highest probed temperatures (~300 $°C$).

4.1.6   The Nano-aggregate Fine Structure

Until now, only the *Guinier* region of *SAS* has been considered, and asphaltene aggregates have been described as mass fractal ones. This fractal aggregation implicitly assumes that the structure is self-similar between two characteristic sizes:

- The one of the aggregates that is roughly their radius of gyration
- The one of primary particles that scatter at large q values

Fig. 12.12 SANS of 3 wt% of asphaltenes in deuterated toluene as a function of pressure for various temperatures: (*full circle*) 303 K and 4 bar, (*open circle*) 303 K and 100 bar, (*full square*) 373 K and 100 bar, (*open square*) 373 K and 240 bar, (*full triangle*) 488 K and 60 bar, and (*open triangle*) 488 K and 100 bar
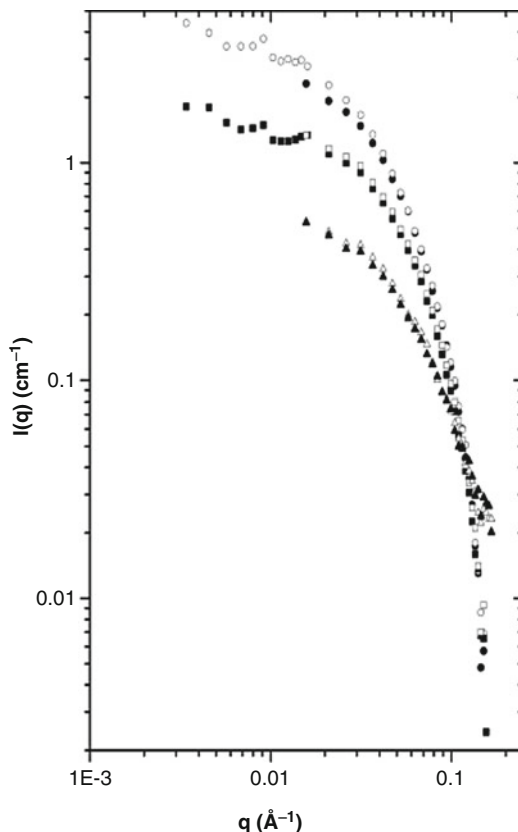
This chapter is dedicated to the structure of these primary particles. The main questions that arise concern their shape, their sizes, their composition, and their relation to the molecular level.

For that [52], we first compare scattering intensities of the same asphaltene in deuterated toluene measured by *SAXS* or *SANS* and normalized by their respective contrast term $\Delta\rho^2$ (Fig. 12.13). *SAXS* data have been obtained on *ID02* beamline of *ESRF* (Grenoble, France), whereas *SANS* data have been acquired on *D22* instrument of *ILL* (Grenoble, France). It's worth mentioning that data have been acquired with high signal to noise ratio in a large *q* range.

As expected, the *Guinier* regions are superimposed, and the usual calculations of size and mass of aggregates using the *Zimm* approximation conduct to the same results whatever technique used. At *q* values larger than $4 \, 10^{-2} \, \text{Å}^{-1}$, normalized intensity of *SANS* curve is smaller than *SAXS* and shows a large *q* oscillation centered about $0.3 \, \text{Å}^{-1}$ characteristic of a fine structure. The difference in normalized intensity at large *q* values is a proof of nonhomogeneous *SLD* at small length scales and suggests that at least two regions of different *SLDs* are necessary to describe the primary particles. Among analytical form factors of heterogeneous

Fig. 12.13 Scattering intensities normalized by contrast term of the same asphaltene in toluene solution measured by SAXS or by SANS
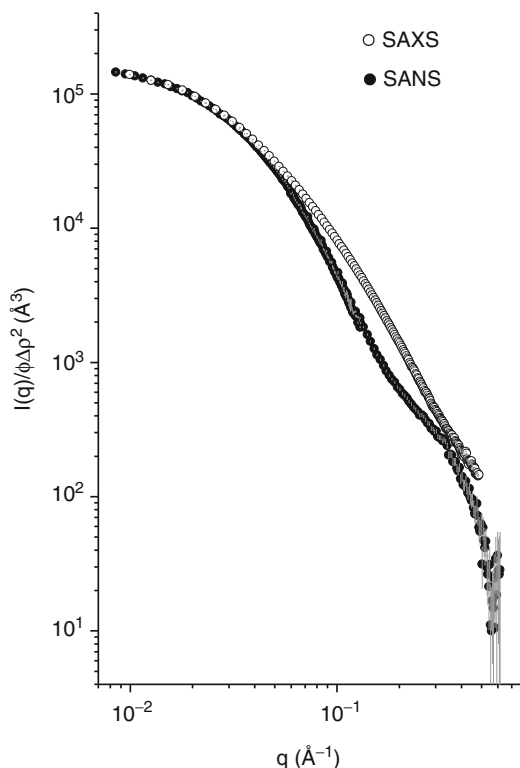
particles available, one of the core–shell spheres or cylinders is the simplest and will be considered in the following.

The usual way to determine form factors of particles presenting different *SLD* regions is the contrast variation. Additional measurements of the same asphaltene in various mixtures of deuterated and hydrogenated toluene were performed on the *PACE* spectrometer of *LLB*. A special attention was paid to get high signal to noise ratio data at large *q* values and to subtract realistic incoherent scattering backgrounds [22].

The general idea is to separate from $I(q)$ measurements the structure factor $S(q)$ and the form factor $P(q)$. The structure factor chosen here is the one of fractal aggregates, and the analytical expression (Eq. 12.30) of Teixeira [15] has been used here.

Regarding our previous work [49], fractal dimension $\boldsymbol{D}$ has been chosen as 2.1, and $\boldsymbol{\xi}$ is determined from combining R_g estimation obtained by the usual *Zimm* approximation and D (Eq. 12.31). The last unknown parameter in Eq. 12.30 is $\boldsymbol{r_0}$ which represents the gauge of the measurement and has a magnitude of the characteristic dimension of each individual primary particle. $\boldsymbol{r_0}$ has been varied between 10 and 28, and it has been shown [49] that a value of 18 Å gives the best agreement between measured and modeling intensities.
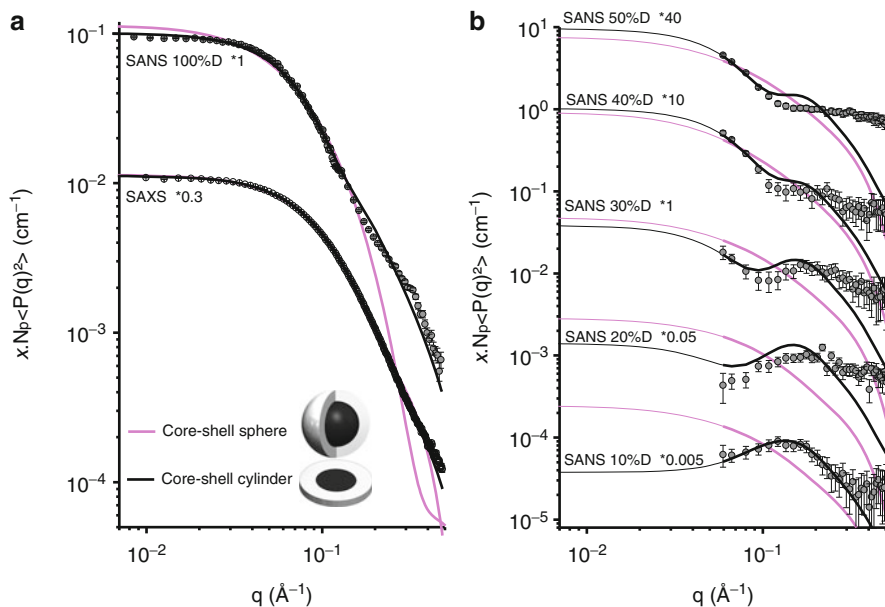
Fig. 12.14 (symbols) (**a**) SAXS and SANS 100%D (5 g/L in H and D-toluene, respectively) and (**b**) SANS contrast variation (50 g/L in toluene at various H/D ratios) asphaltene spectra divided by $S(q)$. (*lines*) fits with (i) core–shell sphere form factor and (ii) core–shell cylinder form factor. Spectra are rescaled for the sake of clarity

Assuming that decoupling approximation is valid, $I(q)/S(q)$ was estimated, and Fig. 12.14 presents the experimental form factor for both *SAXS* and *SANS* measurements including the one of contrast variation. The strong differences that appear at large *q* according to *SLD* values of toluene mixtures confirm the heterogeneous character of primary particles. Using the *SASfit* software developed at *PSI* [53], all the data were fitted *simultaneously* to form factor of core–shell polydisperse particles (Eq. 12.47):

$$\langle P^2(q) \rangle = \left\langle \left[(\rho_S - \rho_0)V(R + \Delta R)F_\alpha(q, R + \Delta R) + (\rho_C - \rho_S)V(R)F_\alpha(q, R) \right]^2 \right\rangle$$

(12.47)

where subscripts C, S, and 0 refer, respectively, to the core, the shell, and the solvent. R and ΔR are the radius of the core and the shell thickness, and V stands for the volume. Subscript α refers either to a sphere (Eq. 12.21) or to a cylinder (Eq. 12.22).

The sphere and cylinder geometries fit equally *SAXS* data, but regarding neutrons, core–shell cylinder geometry gives relatively good fits for all solvent conditions, contrary to the core–shell sphere geometry. The dimensions of the cylinder geometry reveal that the *particles are core–shell flat disks with a core radius of 18 Å rather monodisperse (σ = 0.3), a shell of 14.4 Å thickness, and a height of*

6.7 Å. The mass of the primary particles, easily estimated from their scattering intensity, is about 16 kDa, i.e., at least one order of magnitude larger than the estimated molecular weight of asphaltene. It shows that primary particles are in fact aggregates of molecules and they will be termed in the following *nano-aggregates*, according to the emerging denomination of asphaltene community and by opposition to (fractal) aggregates of which they constitute the building blocks.

The *SLD* of the core and shell have been also determined for both X-ray and neutrons from intensity modeling. Figure 12.15 sums up the results and shows that *SAXS* is mostly sensitive to core, whereas *SANS* in deuterated toluene is mostly sensitive to shell.

Fig. 12.15 SLD profile of asphaltene nano-aggregate for SANS (*top*) and SAXS (*bottom*)
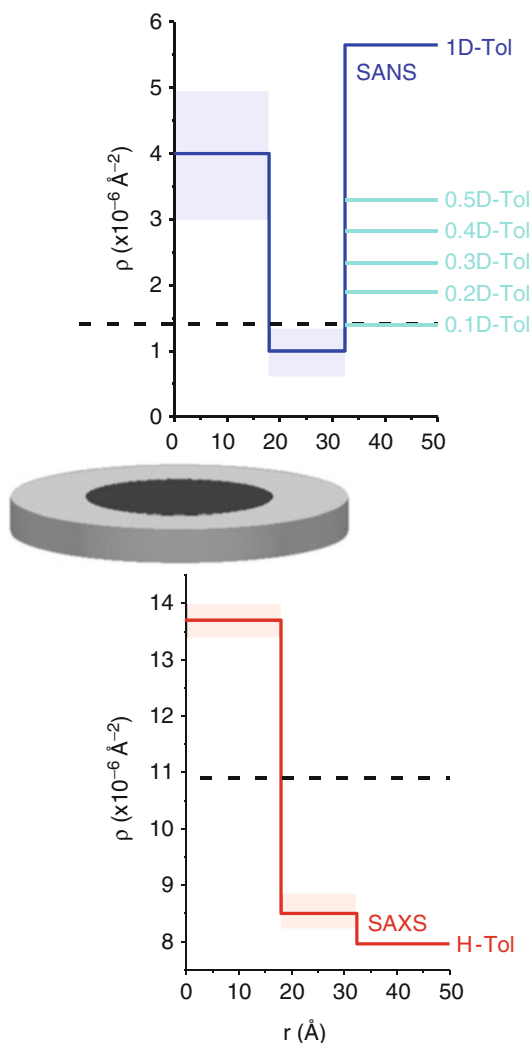
Neglecting the contribution of heteroelements[1] to *SLD*, the number n_C and n_H of C and H atoms in the volume of the core and shell could be estimated using Eq. 12.4. Note that this estimation is possible only if *SANS* and *SAXS* are used conjointly. Knowing n_C and n_H for each region allowed to estimate the aromaticity of the core and shell via the *H/C* ratio. Additionally, the knowledge of n_C, n_H, and the volume of each region allowed to estimate mass density of the core and shell. *It was found that the core is highly aromatic and dense (H/C ≈ 0.3; d_{core} ≈ 1.6 g cm^{-3}), whereas the shell is more aliphatic (H/C ≈ 1–1.6).* Furthermore, the combination of *H/C* or mass density *d* of the core and shell, weighted by their respective volume fraction, gives values averaged over the nano-aggregate close to the macroscopic measured values. The emerging picture of asphaltene nano-aggregates is summarized in Fig. 12.15. The geometry and dimensions of nano-aggregates have been found consistent with recent NMR measurements by Korb [54].

Coming back to the molecular level, it is clear that such a nano-aggregate is likely the result of island molecule aggregation through π–π interactions and that steric hindrance by peripheral chains will limit the extent of aggregation to few molecule layers. From the height of the disk (6.7 Å) and from the inter-aromatic plane distance of graphitic material (≈3.3 Å), the aggregation number in the stacking direction is ≈3 in fully agreement with recent results by molecular simulation.

4.1.7   Hierarchical Aggregation

From the previous sections, it was shown that *SAS* experiments are well-suited techniques to study the aggregation properties of asphaltene in the bulk that is summed up as:

1. Asphaltene form permanent aggregates in crude oil and solvents.
2. This aggregation is hierarchical going from molecules to nano-aggregates which form clusters at larger length scales.
3. The fine structure of nano-aggregates has been specified as core–shell disks, the core being aromatic and the shell aliphatic. This fine structure is in line with the island molecular model.
4. The cluster structure determines the viscosity properties of asphaltene solutions.
5. Clusters dissociate at high temperature, whereas nano-aggregates do not.

The contribution of *SAS* to the aggregation behavior knowledge appears central but still some questions remain as the arrangement of molecules inside the nano-aggregate core. Also few is known on the nature of molecular and aggregate interactions. Finally, all the conclusions have been drawn from asphaltenes of limited sources, and it will be interesting to extend the structural scheme to crude from various geochemical provenances.

---

[1]This assumption is justified in regard to their low content.

4.2   Asphaltene at Interfaces

If the aggregation behavior of asphaltene affects largely bulk properties of their parent crude oil, they are also known to accumulate at water and solid–crude interfaces influencing macroscopic properties such as emulsion stability or wettability.

4.2.1   Asphaltene at Liquid–Liquid Interfaces

In shearing conditions, when water is contacted with crude oil, water in crude oil emulsion is formed [55, 56]. If water droplets are objects, whose sizes vary from ~1 to 100 μm, not amenable to scattering methods, the emulsion films themselves are in the size range of 1–100 nm well suited to usual q range of *SAS*. Furthermore, from a scattering viewpoint, emulsion should be considered as a multicomponent system (water, interfacial film, and oil). As mentioned previously, oil is a complex mixture that could contain asphaltene but also indigenous water droplets or clay nanoparticles. In order to simplify the system and to study solely the influence of asphaltene on films, a model oily phase composed of extracted asphaltene in simple solvents could be considered. It allows by appropriate contrast matching reducing the number of scattering region to two. In these conditions, contrast matching *SANS* appears to be well adapted to directly probe the geometry and composition of interfacial films.

In a scattering-based emulsion study [57], emulsions were prepared by mixing water with asphaltene solution in xylene, the "asphaltene" being extracted either by n-pentane (AC5), n-heptane (AC7), or n-octane (AC8). After emulsification, the droplets were allowed to settle, and the supernatant was compared (Fig. 12.16) to their parent initial asphaltene solution using the neutron small-angle PACE spectrometer at Laboratoire Léon Brillouin. According to Eqs. 12.13, 12.14, 12.15, 12.16, and 12.17, data were fitted in the *Guinier* region to the *Zimm* approximation (Fig. 12.16a). The fitted parameters M_W and R_g, reported in Fig. 12.16b, show different trends.

Firstly, the longer the extracting alkane chains are, the higher the cluster size and mass are in the initial xylene solution. Secondly, the cluster size and mass are lower in supernatant than in initial solution suggesting that *the most aggregated species are in the interfacial film*. Lastly, the mass to radius of gyration dependence shows the same behavior than previously reported, reminiscent of mass fractal aggregates.

To gain insight into interfacial film structure, we directly measured the droplet sediments and applied contrast variation techniques. Two limiting cases were considered:

1. The case where *SLD* of mixture of heavy and light water is equal to the one of deuterated xylene ($5.9 \, 10^{10} \, \mathrm{cm}^{-2}$) and different from the *SLD* of asphaltene ($1.4 \, 10^{10} \, \mathrm{cm}^{-2}$). Then, the coherent intensity comes both from asphaltene aggregates in the oily phase (approximated by supernatant scattering) and from interfacial films. The subtraction of scattering intensity of supernatant to the one of settled droplets according to its volume fraction in the sedimented phase gives the
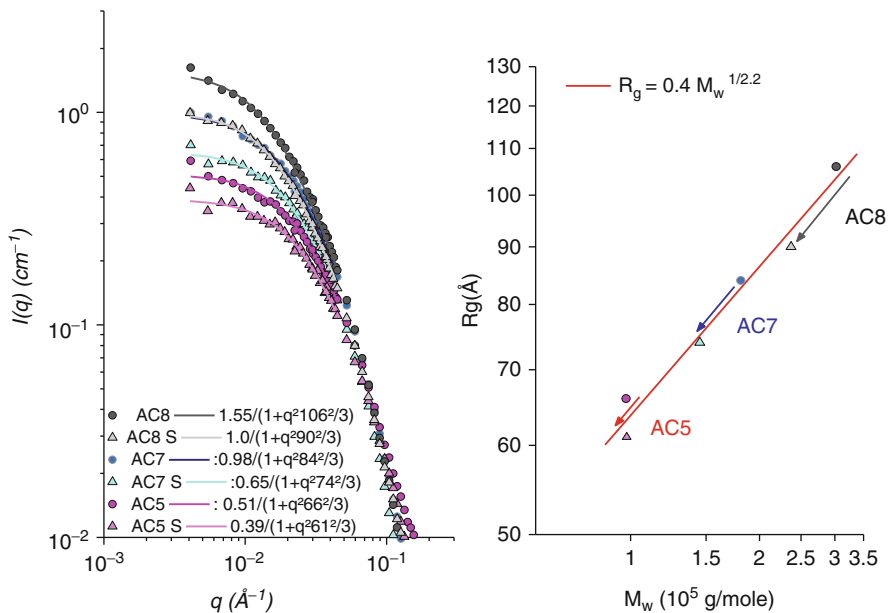
Fig. 12.16 (**a** *left*) SANS of supernatant (*triangles*) and initial (*circles*) AC5, AC7, and AC8 solutions in xylene; *lines* are fit to the Zimm approximation; (**b** *right*) corresponding radius of gyration to mass dependence

Fig. 12.17 Scattering intensity of settled emulsion, of incoherent H_2O background, and of supernatant. The scattering intensity of interface is obtained by considering the various individual contributions according to their volume fraction in the sediment
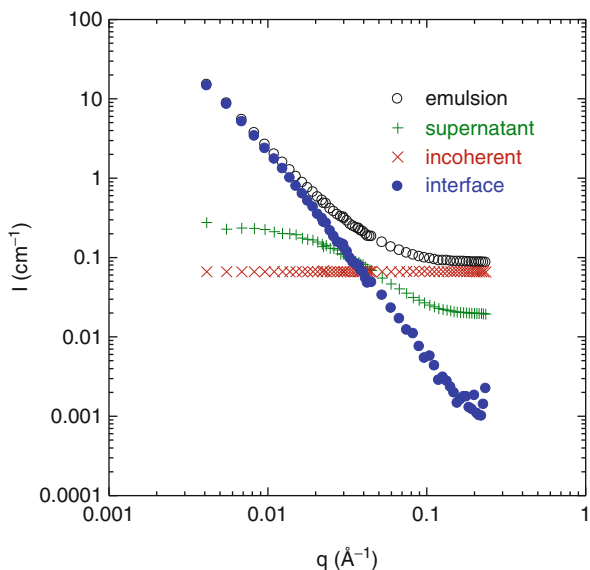
scattering contribution of the interfacial films. Such a procedure is illustrated in Fig. 12.17. In the q domain where q^{-1} is larger than the film thickness $2h$ but remains much smaller than the film extension R in the normal plane, the form factor of the film could be approximated by:

$$P(q) \propto \frac{2}{(qR)^2} \exp\left(-\frac{(qh)^2}{3}\right) \quad qh < 1; qR >> 1 \quad (12.48)$$

Plot of $Ln(q^2 I(q))$ versus q^2 presents a linear regime and from the slope, film thickness is estimated.

2. The case where *SLD* of mixture of hydrogenated and deuterated xylene is equal to the one of asphaltene and different from *SLD* of heavy water ($6.4 \ 10^{10}$ cm^{-2}). Then, scattering comes from water–oil interface and a *Porod* behavior is expected. Use of Eq. 12.17 allows estimating the surface area Σ of settled emulsion. If asphaltene concentrations are measured both in the supernatant and in the initial asphaltene in xylene solution, then surface excess Γ in mg/m^2 could be calculated.

Figure 12.18 shows the variation of film thickness for the AC5, AC7, and AC8 asphaltene. Not only the film thickness (113, 135, and 149 Å, respectively, for AC5, AC7, and AC8) seems to be proportional to aggregate size in the bulk (66, 84, and 106 Å), but also they are in the same order of magnitude suggesting again that larger aggregates adsorb at water–oil interface. The estimation of surface excess Γ using the surface area Σ determined with *SANS* gives typical values of 2 mg/m^2 in full agreement with values determined at liquid/solid interface for a monolayer of aggregates (see next section) [58]. From thickness and surface excess, the volume
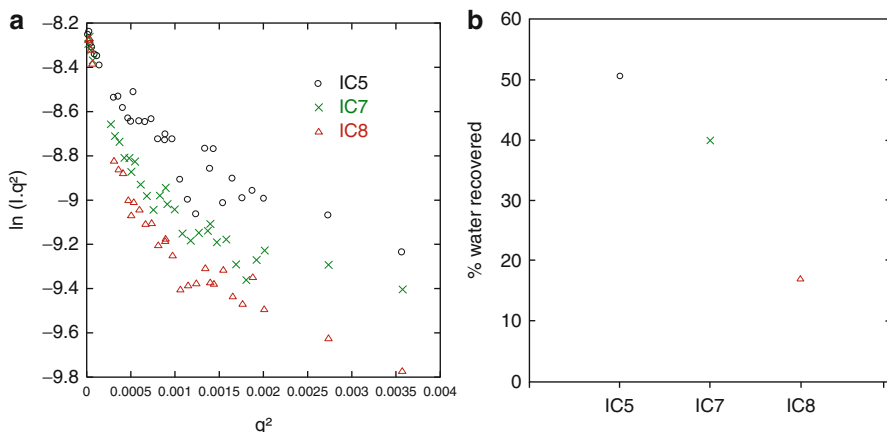
Fig. 12.18 (**a**) Scattering intensities of AC5, AC7, and AC8 interfacial films. In these scales film thickness is related to the slope of the curves at small q values. (**b**) Percentage of water resolved as a function of chain length precipitant

fraction of solvent in the film was estimated, and values (~0.1–0.2) are found higher than the one of bulk aggregates (~0.05–0.1 [58]) suggesting reorganization at interface in accordance with temporal evolution of the film rheology [59]. Finally, a criterion to classify the relative stability of emulsion has been determined (Fig. 12.18b). The results show that emulsion stability seems to be related to film thickness. Other parameters such as high pH or aging have been varied in this study.

Verruto et al. [60] used also the *SANS* contrast variation to study the influence of host solvent aromaticity on characteristics of asphaltene-based films. They used a more refined scattering intensity modeling by fitting the data to a core–shell model including as fitting parameters the film thickness size ΔR and its *SLD*; subsequent analysis of *SLD* gave directly composition of the film including asphaltene and water content. They found similar film thickness as ours and observed that the less aromatic solvent lead to the denser films. Finally Alvarez [61] used also *SANS* analysis to study in more details the influence of pH and ionic strength on film characteristics. They used the same methodology as ours and obtained a minimum film thickness at pH at which the charge of asphaltene in contact with water is zero. They also found that emulsion stability correlates with interfacial thickness.

In conclusion, the contrast matching SANS method has proved to be a valuable and unique technique to investigate directly interfacial film properties from model emulsion systems. This film seems to form from the largest aggregates present in bulk. The water in oil asphaltene emulsion stability is related to film characteristics and parameters such as film thickness, and density seems to play a major role. In the future, this technique could be used to investigate other parameters such as the water content and aging.

4.2.2 Asphaltene at Liquid–Solid Interfaces

The behavior of asphaltene at solid–liquid interface is of first importance regarding industrial processes. Indeed, crude oil–solid surface contact is ubiquitous in the petroleum industry going from crude oil generation in kerogen to nano-porous catalyst in hydroconversion units and passing through reservoirs, pipelines, surface facilities, or heat exchanger. This contact may cause variation in surface properties such as reservoir wettability alteration, deposition, and fouling of pipelines or equipments in contact with crude oils or retention [62].

Asphaltene is known to be the fraction of crude oil that accumulates at solid interface [62], and the purpose of this section is not to review asphaltene adsorption but rather to establish the structural modification between asphaltene in solution and in adsorbed layer.

Adsorption isotherms have been measured [58] from asphaltene solutions on silica particles, considered as hydrophilic. Asphaltene from different geographic and geochemical origins, as well as the same asphaltene in various simple solvents (toluene, xylene, 1 methylnaphthalene, toluene–heptane mixtures), has been considered. Adsorption isotherms share a nonlinear increase of the adsorbed amount for the lower concentrations, the slope of the curve decreasing to reach a plateau for higher concentrations. The plateau is indicative of surface saturation by a monolayer. Whatever the asphaltene or the solvent considered in this study, numerical

values of Γ_{pl} were in the range ~2.1–4.2 mg/m^2 in good accordance with other published values [62].

In parallel, the weight average molecular mass of asphaltene clusters M_W and their radii of gyration R_g have been determined from laboratory *SAXS* measurements using the *Zimm* approximation (Eqs. 12.13, 12.14, 12.15, 12.16, and 12.17). M_W were found to vary from 44 to 270 kDa, whereas R_g are in the 49–107 Å range. These two parameters were found to scale as:

$$R_g = 0.41 \ M_w^{0.45} \tag{12.49}$$

a behavior reminiscent of fractal organization of clusters.

Figure 12.19 shows a strong correlation between the plateau adsorbed amount and the cluster mass that evidence adsorption of a cluster monolayer. Fitting the data to a power law gives the following equation:

$$\Gamma_{pl} = 0.034 \ M_w^{0.37} \tag{12.50}$$

Using a simple geometrical model where all the available surfaces S are paved with aggregates without any further structural modifications, the relation between surface excess Γ_{pl} and a monolayer of n individual aggregates of size R_s and mass M_w is simply:
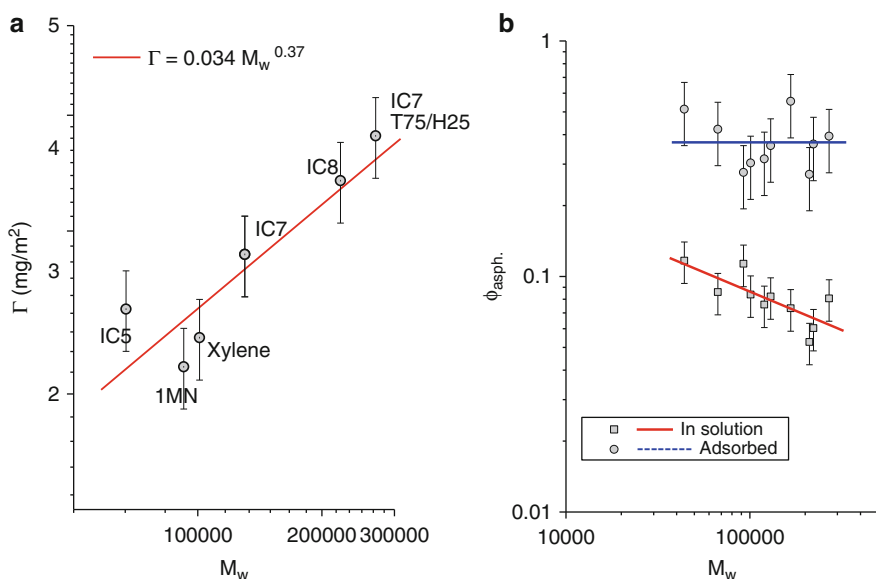
Fig. 12.19 (**a**) Relation between plateau adsorbed amount and mass of asphaltene clusters in the bulk. (**b**) Estimated asphaltene volume fraction in clusters or at solid interface

$$\Gamma_{pl} = \frac{M_{adsorbed}}{S} = \frac{nM_w}{nN_a\pi R_s^2} \qquad (12.51)$$

If we assume that no reorganization occurs during adsorption ($R_s = R_g$), we can combine Eqs. 12.49 and 12.51. The result, $\Gamma_{pl} \propto M_w^{0.1}$, is far from experimental measurement (Eq. 12.50) ruling out the assumption of no reorganization. Conversely, it could be shown that an exponent close to 0.37 requires a "fractal dimension" close to 3, i.e., a densification of cluster when adsorbed. Figure 12.19b compares the volume fraction of asphaltene in clusters or at solid interface as a function of mass of aggregates. It shows that asphaltene volume fraction goes from a power law dependence for cluster with values in the 0.05–0.1 range to nearly constant values close to 0.3, highlighting the densification and the loose of fractal organization upon adsorption.

In conclusion, the relevant species to be considered for asphaltene adsorption from stable crude oil is the cluster that tends to densify at solid contact.

To go further in adsorption studies, we coupled adsorption isotherm measurements from either stable or aggregating asphaltene solution onto hydrophilic or hydrophobic silica particles to measurements at the nanometer length scale using neutron reflectivity [63]. The technique is parent of *SANS* and aims at measuring the reflectivity – ratio of specular reflected to incident intensity – of a macroscopic interface (here an asphaltene in xylene–silicon interface) as a function of wave vector *q*. Measurements were performed on the *EROS* reflectometer of *LLB*.

For good-solvent conditions such as xylene, adsorption isotherms reveal that whatever the nature of silica surface (hydrophilic or hydrophobic) is, the shape of isotherm does not vary and the same plateau adsorbed amount is observed. At local scale, neutron reflectivity on bare (hydrophilic) or grafted (hydrophobic) silica evidences in both cases a rather dense adsorbed layer ($\phi_{asphaltene} \approx 0.6$) whose thickness is comparable to the radius of gyration of asphaltene clusters in the bulk solution. Densification is in line with the previous study [58], and layer thickness is similar to the one of films at liquid–liquid interfaces [57].

When bad solvent is added, the structure of the asphaltene adsorbed profile exhibits a transition from a monolayer to a multilayer structure when crossing the bulk flocculation threshold transition. This is thus a nice illustration of the strong relationship existing between the structure and the dynamics of growth of the asphaltene aggregates in solution and the adsorbed profiles at the solid–liquid interface.

In conclusion, neutron reflectivity could be an alternative technique to probe SLD profiles at liquid–solid interfaces.

We took advantage of specular neutron reflectivity (*SNR*) geometry to investigate the influence of shear rate on multilayer growth kinetics [64]. A rheometer was inserted on the horizontal time-of-flight reflectometer *EROS* at the *Laboratoire Léon Brillouin*. A sealed cell especially designed to be mounted on a rheometer, based on a cone–plate shearing geometry, has been built (see inset of Fig. 12.20b). The plate is a thick silicon wafer by which incident and reflected neutrons pass
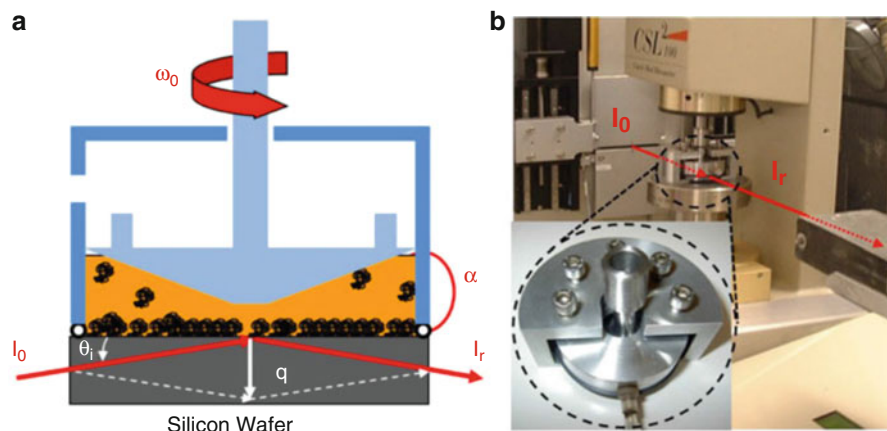
Fig. 12.20 (**a**) Principle of the experiment. The silicon wafer is represented in *gray*, the cone of the rheometer in *light blue*, the deuterated solvent in *orange*, and the asphaltene nano-aggregates in *black*. (**b**) Experimental setup. The neutron beam, schematized in *red*, outcoming from the exit slit of the collimator, crosses the cell where it is reflected. *Inset*: picture of the cell specifically designed for the experiment (*top view*)

through, whereas the cone is positioned by the rheometer slightly higher than the plate, ensuring homogeneous shear within the cell.

For a given shear rate, once bad solvent (deuterated dodecane) has been added to asphaltene in xylene solution, data were acquired as a function of time at a rate of one spectrum every 30 min. An example is given for a shear rate of 1200 s^{-1} (Fig. 12.21a). The *SNR* curves were fitted a posteriori using the optical matrix method resulting in the *SLD* profile (Fig. 12.21b) as a function of distance z from silicon oxide surface. *SLD* profiles of adsorbed layer were converted to asphaltene concentration profile (Fig. 12.21c) using Eq. 12.5.

The multilayer growth kinetics at bad (dodecane) to good (xylene) solvent ratio of 66:34 has been followed using *SNR* for two different shear rates (1200 and 2400 s^{-1}). The "neutron" surface excess has been estimated by integration over z of asphaltene concentration profiles. They are reported in Fig. 12.22 as a function of time and compared to the shift of frequency Δf of a quartz crystal microbalance (QCM), operating in similar cone–plate geometry.

First of all, we obtain a very good qualitative agreement between the two techniques, and it is clear from these data that shearing slows down the kinetics of multilayer growth. Second, after a quasi-linear behavior in the first times of adsorption, the curves tend to saturate for the long times suggesting that a stationary state could be reached. This equilibrium state could represent the balance between growth of layer by adsorption of new clusters coming from solution and desorption by the shear.

In conclusion, SNR – a parent technique of SANS – appears as a well-suited technique to study in situ the influence of shear rate on kinetics of multilayer layer growth. The study confirms the shear-limited character of asphaltene deposition

a

RQ⁴ (Å⁻⁴)

b

SLD 10⁻⁶(Å⁻²)

c

Φ
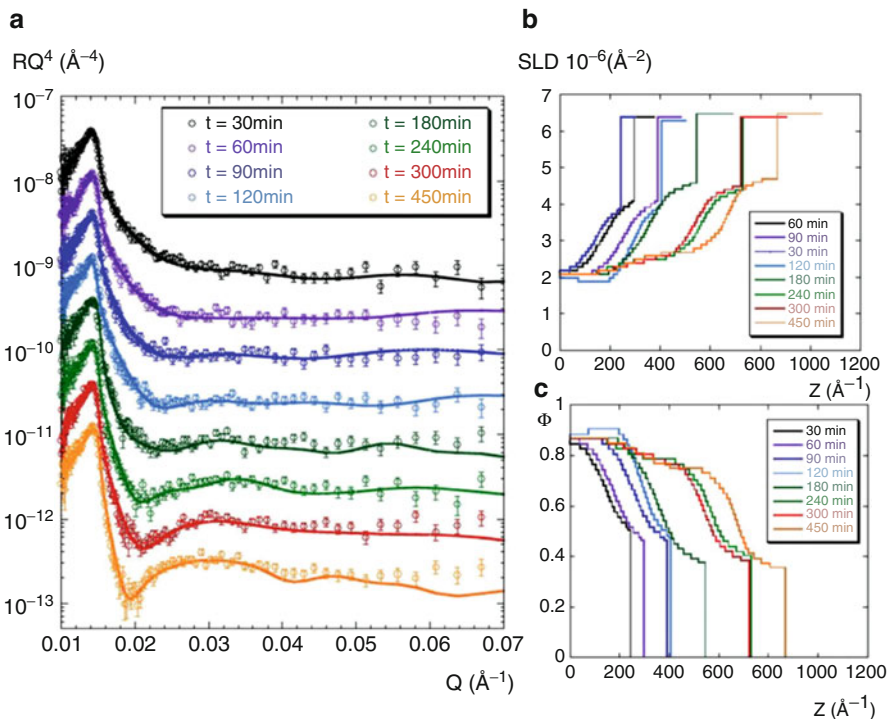
Fig. 12.21 (**a** *left*) Kinetic evolution of the SNR experimental curves (symbol) at 1200 s⁻¹ and the corresponding fits (*full lines*); (**b** *up right*) corresponding SLD profile; (**c** *bottom right*) corresponding asphaltene concentration profile

Fig. 12.22 Surface excess estimated from SNR measurements (symbol) for asphaltene in a 66/34 mixture of dodecane/xylene and measured at various shear rates. *Full lines* represent the shift of frequency obtained in a quartz crystal microbalance operating in similar cone–plate geometry
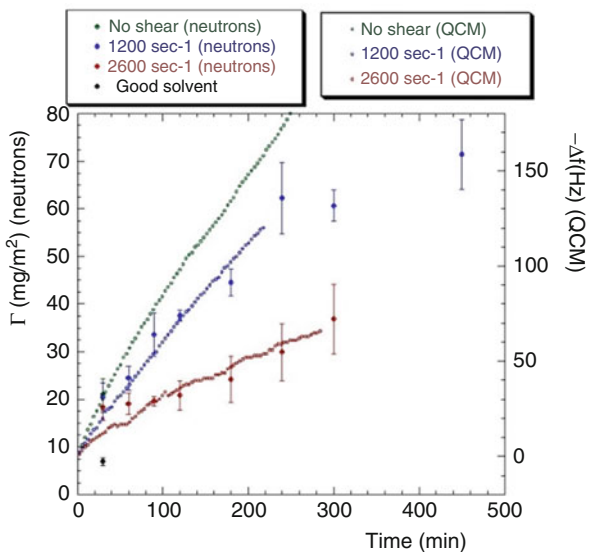
[65] *and is useful for modeling clogging in porous media (reservoir or catalyst). The technique enables to get concentration profiles within the layer that could help to explain irreversibility of asphaltene adsorption.*

4.3   Geomaterials

Geomaterials represent another class of natural nano-material encountered in the petroleum industry. *SAS* techniques enable to characterize their nanoscale organization in order to get understanding of their use properties.

4.3.1   Clay-Based Systems

One of the most studied geomaterials is the clay suspension. They are used as drilling fluid in the petroleum industry. They give rise to interesting behavior and are found in the form of sols, gels, glasses, and even liquid crystals. *SAS* has been intensely used to study their phase diagram as a function of concentration and ionic strength. A recent review by Bailey [66] summarizes the current status of research in this area.

4.3.2   Sedimentary Rocks

Sedimentary rocks such as sandstone, argillite, or carbonates are composed on the one hand of various minerals whose crystallite size varies in the 1–100 μm range and on the other of pores in the same size range. Porous sedimentary rocks are the most common reservoirs for oil and gas deposits. Knowledge of pore size distribution, fluid localization, fluid–mineral surface interactions, and flow within the porous medium is often of paramount importance for petrophysics properties involved in oil recovery methods.

At first sight, the multicomponent character of sedimentary rocks is not in line with the usual two-phase systems required to *SAS* data modeling. In the same way, the typical pore or crystallite sizes are not in the same size range as the inhomogeneities probed by *SAS* methods in the usual *q* range. Nevertheless, scattering methods have been applied to the sedimentary rock characterization [10, 67, 68].

Two-Phase System?

The fist point to consider is whether the minerals could be considered as a two-phase system (mineral and pores) regarding their scattering properties. For that, Clarkson [69] estimated the neutron *SLD* of the main minerals found in Triassic Montney tight gas reservoir in Western Canada.

It is clear from this table that SLDs are not constant. Nevertheless, for most of minerals, an *SLD* value close to ~3.8 10^{10} cm^{-2} could be considered. From Eq. 12.52, a generalization of Eq. 12.5:

$$<\rho> = \sum_i \phi_i \rho_i \qquad (12.52)$$
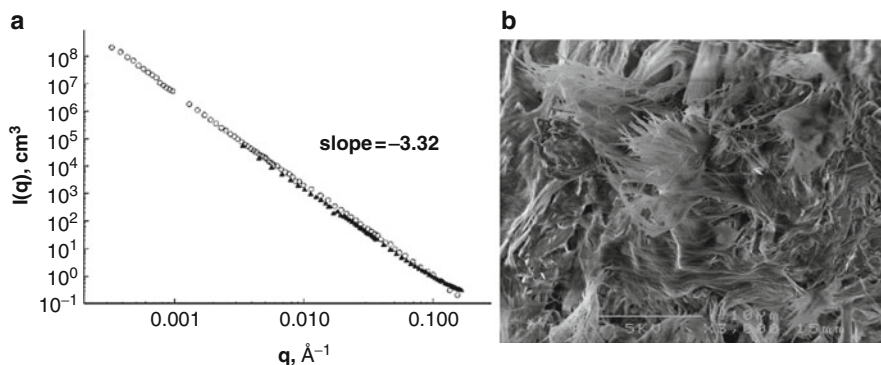
Fig. 12.23 (**a**) USAXS and SAXS (*circle*) and SANS (*triangles*) intensities normalized by their respective contrast terms from a "Vosges" sandstone; (**b**) SEM observation of a fracture in the same material

Table 12.2 Neutron scattering length densities for the usual minerals found in sedimentary rocks

Mineral	Formula	d (g cm^{-3})	Neutron SLD (10^{10} cm^{-2})
Illite		2.75	2.95
Muscovite		2.83	3.86
Quartz	SiO_2	2.65	4.18
Orthoclase	$KAlSi_3O_8$	2.55	3.64
Albite	$NaAlSi_3O_8$	2.62	3.97
Pyrite	FeS_2	5.01	3.81
Hematite	Fe_2O3		
Calcite	$CaCO3$	2.71	4.69
Dolomite	$CaMg(CO3)_2$	2.84	5.4
Smectite			

1. Mean *SLD* value $<\rho>$ can be estimated provided the volume fraction of each constituent is known. *XRD* analysis, including *Rietveld* refinement, could be used for that purpose [70].
2. The contribution $\phi_p\rho_p$ of a peculiar mineral p having an *SLD* value ρ_p far from $<\rho>$ could be estimated. If the contribution doesn't exceed few percent of mean value, the system is perceived by the radiation as a homogeneous phase.

This point is illustrated in Fig. 12.23 [68] where scattering intensity obtained by a *USAXS–SAXS* combination is compared to the one obtained by *SANS*. The sample, a "Vosges" sandstone, contains ~1 % of hematite Fe_2O_3 whose *SLD* (1.5 electron/Å^3) is far from the mean X-ray *SLD* value (0.8 electron/Å^3). For neutron, all the *SLDs* are close to the mean value (Table 12.2). When X-ray and neutron intensities are normalized by their respective mean *SLD*, they are almost superimposed suggesting that X-ray *SLD* fluctuation caused by hematite has limited influence on the scattering intensity.

In practice, most of the sedimentary rocks have been considered from a scattering point as a two-phase system.

Nanoscale?

The second point to consider is the length scale of *SAS* measurements (1–1000 nm) compared to pore size (1–100 μm) usually found in sedimentary rocks. It is clear that from *SAS* measurements, the asymptotic *Porod* domain will be mainly probed. From the general expression of scattering intensity (Eqs. 12.19 and 12.20) in the high q limit, *SAS* will give information on the roughness of mineral–air interface and on the corresponding surface area.

In practice, most of the investigated systems present rough interfaces giving power law q dependence with exponents $-\alpha$ ($\alpha = 6 - Ds$) larger than -4. For instance, "Vosges" sandstone [68] (Fig. 12.23a) shows a $q^{-3.32}$ (and therefore a surface fractal dimension Ds of 2.68) dependence on almost three decades in length scale and over nine decades in intensities. The roughness of interfaces is ascribed in this case to clay pore lining as shown by SEM micrograph of a fracture (Fig. 12.23b). According to Eqs. 12.19, 12.20, and 12.21, a surface area of 4–7 m^2/g was estimated in good agreement with value obtained from krypton adsorption measurements.

In these neutron or X-ray experiments, both the high values of scattering contrast, pore volume, and the pore volume fraction give for a neutron or a photon a very high probability to scatter. In these conditions, a special attention has to be paid to avoid multiple scattering. A parametric study by Radlinski et al. [10] shows that thickness of sedimentary rocks has to be reduced down to 0.5 mm.

Pfeifer and Avnir [71] demonstrated that a fractal surface can be considered to be equivalent to a polydisperse system of pores, with the number distribution of pore sizes given by:

$$f(r) \propto r^{-(D+1)} \tag{12.53}$$

In practice, the distribution in Eq. 12.53 is both upper and lower bound, i.e., extends only in the range $r_{min} < r < r_{max}$. The upper and lower bound in pore space are related to lower and upper limit in q space where the $q^{-(6-Ds)}$ behavior is observed. In order to capture the entire pore size distribution, scattering intensity measurements are often extended down to very low q values using *USANS* or *USAXS*. For uncorrelated and spherical pores, the scattering intensity is related to the pore size distribution by [72]:

$$I(q) = \Delta\rho^2 \phi \frac{\displaystyle\int_{r\mathrm{min}}^{r\mathrm{max}} v^2(r)f(r)P(q,r)dr}{\displaystyle\int_{r\mathrm{min}}^{r\mathrm{max}} v(r)f(r)dr} \tag{12.54}$$

Localization of Fluids Within Porous Media

We took advantage of the well-defined surface fractal "Vosges" sandstone to investigate the localization of water – considered as a wetting fluid – within the pores [68]. The control of water content was done in the following way: firstly, porous medium was imbibed with a mixture of H_2O/D_2O matching the mean neutron *SLD* of Vosges sandstone and secondly was left in contact with the vapor of a water liquid phase saturated with a given salt. In this process, some of the liquid water in the porous medium evaporated, down to an equilibrium value *Sw*. Varying the nature of saturating salt allowed to vary *Sw* from 14.2 down to 5 wt%. *SANS* data at various *Sw* values were acquired on the *PACE* spectrometer at Laboratoire Léon Brillouin (Saclay, France) in two configurations covering a total *q* range of $3 \ 10^{-3}$–$0.2 \ \text{Å}^{-1}$.

The dry, as well as water saturated, "Vosges" sandstone SANS spectra are shown in Fig. 12.24a. The dry porous medium exhibits a power law on the whole *q* range with an exponent of 3.32 (Ds = 2.68). During water filling, two regimes –namely, the fractal one and a Porod regime characterized by a q^{-4} behavior – appear separated by a crossover value *q**. The Porod regime, associated to sharp interfaces, is the signature of water capillary condensation. From a scattering viewpoint, the condensation of water having the same *SLD* as rocks "defractalizes"
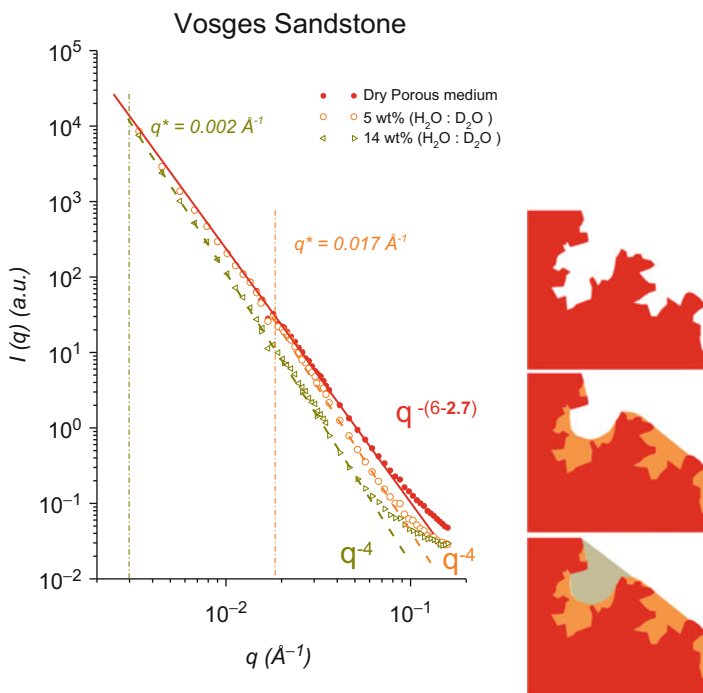
Fig. 12.24 (**a**) (*left*) Scattering intensity of a Vosges sandstone at various water saturation (Sw = 0, 5, 14.2 %); (**b**) (*right*) illustration of capillary condensation

the porous medium at small length scales as illustrated in Fig. 12.24b. The cross-over q^* is observed to move toward lower scattering vectors when the fluid content Sw increases.

The observation is interpreted in the following way: the wetting fluid occupies pores or surface concavities with radii of curvature smaller than $r \approx 1/q^*$, while all pores with radii $>r$ remain empty. For the particular porous rock used for this study, observations suggest that capillary wetting controls the fluid distribution within the pore space.

4.3.3 Oil and Gas Shales

Oil shale is a fine-grained sedimentary rock containing a solid mixture of organic compounds called kerogen. Pyrolysis of kerogen produces shale oil and ultimately shale gas. Recently, oil shales gained attention as potential abundant resource of oil and gas. From our perspective, they could be distinguished from usual sedimentary rocks by their inherent kerogen content and their broad pore size distribution (PSD) including nano-pores located in kerogen and meso-pores generated by small particle (mainly clays) compaction. Understanding the nature of the pore structure (PSD and open versus closed porosity) is a primary objective leading to a better understanding of gas storage and transport mechanisms and their controls. Recent advance in the detailed mesoscale organization of such a complex material benefits from application of *SAS* methods.

SANS measurements of kerogen of various geochemical types as well as of various thermal maturities were performed in order to estimate *SLD* of this material [73]. Kerogens were extracted using (1) Soxhlet extraction to remove soluble oil, (2) acid demineralization to remove minerals except pyrite, and (3) drying in an oven at 90 °C. Elemental analysis highlighted that a broad range of hydrogen-to-carbon atomic ratios, $0.5 < H/C < 1.4$, were obtained. *SLD* of kerogens (ρ_K) were estimated from elemental analysis and mass densities (Eq. 12.4) as well as measurements of ratio $R(q)$ of scattering intensities in both normal methanol (CH$_3$OH, scattering length density ρ_H) and deuterated methanol (CD$_3$OH, scattering length density ρ_D). The authors show that ρ_K is related to $R(q)$ by:

$$\rho_K = \frac{\rho_D \sqrt{R(q)} + \rho_H}{1 + \sqrt{R(q)}} \tag{12.55}$$

A good agreement between the two methods is found. Furthermore, ρ_K was found to vary almost linearly from 4 to 1 10^{10} cm^{-2} when H/C ratio varies from 0.5 to 1.4. A value of 4 10^{10} cm^{-2} is similar to the one of minerals (Table 12.2), and the modeling of scattering intensity from an oil shale will benefit of the two-phase approximation (solid and pores). A value of 0.5 is considered as very different from the one of minerals, and contrast variation methods should be used to simplify intensity modeling.

An alternative way to simplify such a complex system would be to extract kerogen without structural damage and to study the pore size distribution using

SAS methods. The traditional extraction procedure [74] includes heating for water removal, and it was shown [75] that heating damages the pore structure of kerogen. The authors recommend an alternative way to get rid of water based on critical point drying. Use of ethanol as intermediate fluid allowed using CO_2 as drying agent at pressure and temperature conditions slightly higher than critical.

Direct *USANS–SANS* measurements on oil shales were performed in 2000 by Radlinski et al. [6]. They mimic the natural maturity sequence by laboratory pyrolysis from 310 to 370 °C of an immature oil shale. The scattering intensities from the corresponding porous media show a marked reduction ascribed to contrast variations from rock/empty pores to rock/oil, i.e., primary migration. The authors measured also the same behavior in the natural maturity sequence, and the onset of phenomenon lies interestingly in a narrow maturity range within the geochemically determined region of the onset of hydrocarbon generation.

Recently, Ruppert et al. [76] used a combination of *USANS* and *SANS* measurements to probe the accessibility of pores in the Barnett shales to methane and water. They used ratio of scattering intensities of shale measured in the presence of fluids (either a mixture of H_2O/D_2O or deuterated methane CD_4 at 8000 psi) matching the *SLD* of shale to the one measured in vacuum. The following expression relates the fraction of accessible pores ϕ_{AC} at any q, $\phi_{AC}(q)$ to scattering intensities $I(q, \rho_{match})$ and $I(q, \rho_{vacuum})$, respectively, measured in matching and vacuum conditions:

$$\phi_{AC} = 1 - I(q, \rho_{match})/I(q, \rho_{vacuum}) \qquad (12.56)$$

It was shown that only 85 % of the pores were filled by water whatever their sizes. For methane, 85 % of the pores in the 10 μm–30 nm size range are filled, whereas it falls to ~60 % when pore sizes smaller than 30 nm are considered.

Another study by Bahadur [77] aims at measuring, by a combination of USANS and SANS, the pore size distribution (*PSD*) of Cretaceous shale samples from Alberta, Canada, collected from different depths with varying mineralogical compositions. The authors evidenced a contribution to "fractal" pores in a large size range but also contributions of meso- and micro-pores nonfractal in nature.

Lee et al. [78] has used *USAXS* measurements on Silurian black shales from the Baltic Basin, Poland from a wide range of depths along a burial diagenetic sequence. Their sample conditions were either equilibrated to 50 % of relative humidity or dehydrated at 200 °C. For both conditions, they observed "surface fractal" behavior – with different surface fractal dimensions – from which they estimate pore size distributions. They observed that porosity decreases with depth and porosity increase upon dehydration. This last point, ascribed to capillary and clay-bound water, affects the 100–1000 nm pore diameter.

From these recent contributions to oil shale characterization, it appears that SAS and USAS methods are perfectly adapted to the pore size found in these materials. Furthermore, the ability to control the sample environment allowed studying the affinity of various fluids to pores in the mineral or kerogen network. The possibility to vary contrast in SANS experiments is notably useful.

5 Conclusions and Future Perspectives

SAS techniques have been presented through characterization of various natural nano-materials. It appears that different instruments (*SAS* or *USAS*) could be used to probe materials at different length scales varying from 1 nm up to 10 μm.

SAXS and *SANS* differ by contrast considerations, beam size, and flux on the samples. Each technique could be used separately for its own advantage, but they can also be used together for their complementarity. The structure resolution of nano-aggregate of asphaltene constitutes a good example of such an association.

Two very different nano-materials have been discussed, and it was shown that *SAS* technique proved to be very well suited to the characterization of such heterogeneous systems. Nevertheless, separation techniques such as centrifugation, filtration, etc. are often required to simplify polydisperse systems. Again, the joint use of X-ray and neutron, as well as the possibility to vary contrast in *SANS*, constitutes a serious advantage for these complex natural nano-materials.

The reduced preparation of samples as well as their solicitation during observation is clearly an advantage. Examples such as high-temperature (300 °C) measurements of a vacuum residue, shear control of asphaltene solution during deposition, or simply humidity control in sandstone prove the demarche to be well founded.

Examination by these techniques of new nano-materials of industrial importance such as lingo-cellulosic biomass constitutes an exciting perspective.

References

1. Guinier A (1956) Théorie et Technique de la radiocristallographie. Ed Dunod, Paris
2. Guinier A, Fournet G (1955) Small angle scattering of X-rays. Wiley, New York
3. Feigin L, Svergun D (1987) Structure analysis by small angle X-ray and neutron scattering. Plenum Press, New York/London
4. Lindner P, Zemb T (eds) (2002) Neutron, X-rays and light: scattering methods applied to soft condensed matter. Elsevier, Amsterdam
5. Espinat D (1990) Revue de l'Institut Français du Pétrole 45:595–820
6. Radlinski AP, Boreham CJ, Lindner P, Randl O, Wignall GD, Hinde A, Hope JM (2000) Small angle neutron scattering signature of oil generation in artificially and naturally matured hydrocarbon source rocks. Org Geochem 31(2000):1–14
7. Zimm BH (1948) The scattering of light and the radial distribution function of high polymer solutions. J Chem Phys 16:1093–1099

8. Burchard W (1999) Solution properties of branched macromolecules. In: Branched Polymers II, vol 143, Advances in Polymer Science. Springer, Berlin, pp 113–194

9. Porod G, Kolloid Z (1951) 124(2):83

10. Radlinski AP, Radlinska EZ, Agamalian M, Wignall GD, Lindner P, Randl OG (1999) Fractal geometry of rocks. Phys Rev Lett 82:3078–3081

11. Pedersen JS (1997) Analysis of small-angle scattering data from colloids and polymer solutions: modeling and least-squares fitting. Adv Colloid Interf Sci 70:171–210

12. Glatter O (1977) New method for evaluation of small angle scattering data. J Appl Crystallogr 10:415–421

13. Forny-Le Follotec A, Glatter O, Barré L, Pezron I, Noïk C, Dalmazzone C, Metlas-Komunjer L (2012) Characterisation of micelles of small triblock copolymer by small angle scattering. Macromolecules 45:2874–2881

14. Cabane B (1991) Focussing on large scales. Growth: a brief guide for the use of scattering techniques. In: Lindner P, Zemb T (eds) Neutron, x-ray and light scattering: introduction to an investigative tool for colloidal and polymeric systems, vol 4, North-Holland, pp. 247–257.

15. Teixeira J (1988) Small-angle scattering by fractal systems. J Appl Crystallogr 21(6):781

16. Grillo I (2008) SANS and applications in soft condensed matter. In: Borsali R, Pecora R (eds) Soft matter characterization, pp 723–782

17. Diat O, Bosecke P, Ferrero C, Freund AK, Lambard J, Heintzmann R (1995) Ultra-small-angle X-ray-scattering with a Bonse-Hart camera on the high brilliance beamline at the ESRF. Nucl Inst Methods Phys Res Sect A 356:566–572

18. Spalla O, Lyonnard S, Testard F (2003) Analysis of the small-angle intensity scattered by a porous and granular medium. J Appl Crystallogr 36:338–347

19. Zemb T, Tache O, Ne F, Spalla O (2003) Improving sensitivity of a small-angle X-ray scattering camera with pinhole collimation using separated optical elements. Rev Sci Instrum 74:2456–2462

20. Désert S, Thevenot J, Oberdisse A, Brûlet J (2007) The new very-small angle neutron scattering spectrometer at Laboratoire Leon Brillouin. J Appl Crystallogr 40:S471–S473

21. http://www.nist.gov/ncnr/bt5-usans-ultra-small-angle-neutron-scattering.cfm

22. Brulet A, Lairez D, Lapp A, Cotton JP (2007) Improvement of data treatment in small-angle neutron scattering. J Appl Crystallogr 40:165–177

23. Lambard J, Lesieur P, Zemb T (1992) A triple axis double crystal multiple reflection camera for ultra- small angle X-ray scattering. J Phys I Fr 2(6):1363

24. http://www.esrf.eu/UsersAndScience/Experiments/CBS/ID02

25. Hughey C, Rodgers RP, Marshall AG (2002) Resolution of 11 000 compositionally distinct components in a single electrospray ionization fourier transform ion cyclotron resonance mass spectrum of crude oil. Anal Chem 74:4145–4149

26. Merdrignac I, Espinat D (2007) Physicochemical characterization of petroleum fractions: the state of the art. Oil Gas Sci Technol Revue d'IFP Energies nouvelles 62:7–32

27. Rodgers R, Schaub T, Marshall A (2005) Petroleomics: MS returns to its roots. Anal Chem 77:20A–27A

28. Groenzin H, Mullins O (1999) Asphaltene molecular size and structure. J Phys Chem A 103:11237–11245

29. Gray MR, Tykwinski RR, Stryker JM, Tan X (2011) Supramolecular assembly model for aggregation of petroleum asphaltenes. Energy Fuel 25:3125–3134

30. Mullins OC, Sabbah H, Eyssautier J, Pomerantz AE, Barre L, Andrews AB, Ruiz-Morales Y, Mostowfi F, McFarlane R, Goual L, Lepkowicz R, Cooper T, Orbulescu J, Leblanc RM, Edwards J, Zare RN (2012) Advances in asphaltene science and the modified yen model. Energy Fuels 26(7):3986–4003

31. Yarranton HW, Ortiz DP, Barrera DM, Baydak EN, Barré L, Frot D, Eyssautier J, Zeng H, Xu Z, Dechaine G, Becerra M, Shaw JM, McKenna AM, Mapolelo MM, Bohne C, Yang Z, Oake J (2013) On the size distribution of self-associated asphaltenes. Energy Fuel 27:5083–5106

32. Dwiggins CW (1978) J Appl Crystallogr 11:615
33. Espinat D, Rosenberg E, Scarsella M, Barre L, Fenistein D, Broseta D (1998) Colloidal structural evolution from stable to flocculated state of asphaltene solutions and heavy crudes. In: Mullins OC, Sheu EY (eds) Structures and dynamics of asphaltenes. Plenum Press, New York, pp 145–201
34. Sheu E (2002) Petroleum asphaltene-properties, characterization, and issues. Energy Fuel 16:74–82
35. Sheu E (2006) Small angle scattering and asphaltenes. J Phys Condens Matter 18(2006): S2485–S2498
36. Gawrys K, Blankenship G, Kilpatrick P (2006) Solvent entrainment in and flocculation of asphaltenic aggregates probed by small-angle neutron scattering. Langmuir 22:4487–4497
37. Gawrys K, Kilpatrick P (2005) Asphaltenic aggregates are polydisperse oblate cylinders. J Colloid Interface Sci 288:325–334
38. Morimoto M, Morita T, Takanohashi T, Nishikawa K (2013) Specific asphaltene aggregation in toluene around 50mg/L. J Jpn Pet Inst 56(1):58–59
39. Cosultchi A, Bosch P, Lara VH (2003) Small-angle X-ray scattering study of oil- and deposit-asphaltene solutions. Colloid Polym Sci 281:325–330
40. Hoepfner M, Vilas Boas Favero C, Haji-Akbari N, Fogler HS (2013) The fractal aggregation of asphaltenes. Langmuir 29:8799–8808
41. Hoepfner M, Fogler HS (2013) Multiscale scattering investigations of asphaltene cluster breakup, nanoaggregate dissociation, and molecular ordering. Langmuir 29:15423–15432
42. Eyssautier J, Espinat D, Gummel J, Levitz P, Becerra M, Shaw J, Barre L (2012) Mesoscale organization in a physically separated vacuum residue : comparison to asphaltenes in a simple solvent. Energy Fuels 26:2680–2687
43. Zhao B, Shaw JM (2007) Composition and size distribution of coherent nanostructures in athabasca bitumen and maya crude oil. Energy Fuel 21:2795–2804
44. http://www.linkam.co.uk/linkam-blog/2013/3/8/linkam-hfs350x-used-to-help-in-the-charac terisation-of-heavy.html
45. Headen TF, Boek ES, Stellbrink J, Scheven UM (2009) Small angle neutron scattering (SANS and V-SANS) study of asphaltene aggregates in crude oil. Langmuir 25:422–428
46. Hurtado J, Chodakowski M, Long B, Shaw JM (2011) Characterization of physically and chemically separated athabasca asphaltenes using small-angle X-ray scattering. Energy Fuel 25:5100–5112
47. Sirota EB (2005) Physical structure of asphaltenes. Energy Fuel 19:1290–1296
48. Eyssautier J, Frot D, Barré L (2012) Structure and dynamic properties of colloidal asphaltene aggregates. Langmuir 28:11997–12004
49. Barré L, Simon S, Palermo T (2008) Solution properties of asphaltenes. Langmuir 24:3709–3717
50. Espinat D, Fenistein D, Barre L, Frot D, Briolant Y (2004) Effects of temperature and pressure on asphaltenes agglomeration in toluene. a light, x-ray, and neutron scattering investigation. Energy Fuel 18:1243–1249
51. Eyssautier J, Hénaut I, Levitz P, Espinat D, Barré L (2012) Organization of asphaltenes in vacuum residue: a SAXS – viscosity approach at high temperature. Energy Fuel 26:2696–2704
52. Eyssautier J, Levitz P, Espinat D, Jestin J, Gummel J, Grillo I, Barre L (2011) Insight into asphaltene nanoaggregate structure inferred by small angle neutron and X-ray scattering. J Phys Chem B 115:68276837
53. Kohlbrecher J, Bressler I SASfit customized version of version 0.93.2, http://kur.web.psi.ch/ sans1/SANSSoft/sasfit.html
54. Korb J-P, Louis-Joseph A, Benamsili L (2013) Probing structure and dynamics of bulk and confined crude oils by multiscale NMR spectroscopy, diffusometry, and relaxometry. J Phys Chem B 117:7002–7014

55. Kilpatrick PK (2012) Water-in-crude oil emulsion stabilization: review and unanswered questions. Energy Fuel 26:4017–4026
56. Sjoblom J, Askea N, Harald Auflema I, Brandala O, Havrea T, Sæthera O, Westvikb A, Johnsenb E, Kallevikb H (2003) Our current understanding of water-in-crude oil emulsions. Recent characterization techniques and high pressure performance. Adv Colloid Interf Sci 100–102:399–473
57. Jestin J, Simon S, Zupancic L, Barré L (2007) A small angle neutron scattering study of the adsorbed asphaltene layer in water-in-hydrocarbon emulsions: structural description related to stability. Langmuir 23:10471–10478
58. Simon S, Jestin J, Palermo T, Barré L (2009) Relation between solution and interfacial properties of asphaltene aggregates. Energy Fuel 23:306–313
59. Yang X, Verruto V, Kilpatrick PK (2007) Dynamic asphaltene − resin exchange at the oil/water interface: time-dependent W/O emulsion stability for asphaltene/resin model oils. Energy Fuel 21(3):1343–1349
60. Verruto VJ, Kilpatrick PK (2008) Water-in-model oil emulsions studied by small-angle neutron scattering: interfacial film thickness and composition. Langmuir 24:12807–12822
61. Alvarez G, Jestin J, Argillier JF, Langevin D (2009) Small-angle neutron scattering study of crude oil emulsions: structure of the oil − water interfaces. Langmuir 25(7):3985–3990
62. Adams JJ (2014) Asphaltene adsorption, a literature review. Energy Fuel 28:2831–2856
63. Jouault N, Corvis Y, Cousin F, Jestin J, Barré L (2009) Asphaltene adsorption mechanisms on the local scale probed by neutron reflectivity: transition from monolayer to multilayer growth above the flocculation threshold. Langmuir 25:3991–3998
64. Corvis Y, Barré L, Cousin F, Gummel J, Jestin J (2012) Asphaltene adsorption mechanisms under shear flow probed by in-situ neutron reflectivity measurements. Eur Phys J Spec Top 213:295–302
65. Nabzar L, Aguiléra ME (2008) The colloidal approach. A promising route for asphaltene deposition modelling. Oil Gas Sci Technol Rev IFP 63:21–35
66. Bailey L, Lekkerkerker H, Maitland G (2014/2015) Smectite clay – inorganic nanoparticle mixed suspensions: phase behaviour and rheology. Soft Matter 11:222–236
67. Bale HD, Schmidt P (1984) Small-angle X-ray-scattering investigation of submicroscopic porosity with fractal properties. Phys Rev Lett 53(6):596–599
68. Broseta D, Barré L, Vizika O, Shahidzadeh N, Guilbaud JP, Lyonnard S (2001) Capillary condensation in a fractal porous medium. Phys Rev Lett 86:5313–5316
69. Clarkson CR, Freeman M, Heb L, Agamalian M, Melnichenko YB, Mastalerz M, Bustin RM, Radlinski AP, Blach TP (2012) Characterization of tight gas reservoir pore structure using USANS/SANS and gas adsorption analysis. Fuel 95:371–385
70. McCarty DK (2002) Quantitative mineral analysis of clay-bearing mixtures: the "Reynolds Cup" contest. Int Union Crystallogr Newslett 27:12–16
71. Pfeifer P, Avnir D, Chem J (1983) Phys Chem Chem Phys 79:3558–3565
72. Radlinski AP, Ioannidis MA, Hinde AL, Hainbuchner M, Baron M, Rauch H, Kline SR (2004) Angstrom-to-millimeter characterization of sedimentary rock microstructure. J Colloid Interface Sci 274:607–612
73. Thomas JJ, Valenza JJ, Craddock PR, Bake KD, Pomerantz AE (2014) The neutron scattering length density of kerogen and coal as determined by CH3OH/CD3OH exchange. Fuel 117:801–808
74. Durand B, Nicaise G (1980) Procedures for kerogen isolation. In: Durand B (ed) Kerogen: insoluble organic matter from sedimentary rocks. Editions Technip, Paris
75. Suleimenova A, Bake K, Ozkan A, Valenza J, Kleinberg R, Burnham A, Ferralis N, Pomerantz A (2014) Acid demineralization with critical point drying: a method for kerogen isolation that preserves microstructure. Fuel 135:492–497

76. Ruppert LF, Sakurovs R, Blach TP, He L, Melnichenko YB, Mildner D, Alcantar-Lopez L (2013) A USANS/SANS study of the accessibility of pores in the Barnett shale to methane and water. Energy Fuel 27:772–779
77. Bahadur J, Melnichenko YB, Mastalerz M, Furmann A, Clarkson C (2014) Hierarchical pore morphology of cretaceous shale: a small-angle neutron scattering and ultrasmall-angle neutron scattering study. Energy Fuel 28:6336–6344
78. Lee S, Fischer T, Stokes M, Klingler R, Ilavsky J, McCarty D, Wigand M, Derkowski A, Winans R (2014) Dehydration effect on pore size, porosity, and fractal parameters of shale rocks: USAXS study. Energy Fuel 28(11):6772–6779

Synchrotron Small-Angle X-Ray Scattering and Small-Angle Neutron Scattering Studies of Nanomaterials

<div style="text-align: right; font-size: 2em;">13</div>

Hiroyuki Takeno

Contents

1   Definition of the Topic

Small-angle scattering is a very powerful technique to probe structures of materials. X-ray, neutron, and light scattering techniques present structural information of materials in a wide range from nanometer to micrometer scale. Chemists, physicists, and engineers have used these techniques to study structures of various systems from hard to soft materials. In this topic, we focus upon soft materials such as polymers, gels, colloids, etc. We present a review of their recent studies with small-angle X-ray scattering (SAXS) and small-angle neutron scattering (SANS).

H. Takeno (✉)
Department of Chemistry and Chemical Biology, School of Science and Technology, Gunma University, Kiryu, Gunma, Japan
e-mail: takeno@gunma-u.ac.jp

2   Overview

In a typical experimental setup, synchrotron SAXS and SANS are capable of probing structures of aggregates in the range of 1–100 nm. The use of ultra-small-angle scattering techniques such as ultra-small-angle X-ray scattering (USAXS) and ultra-small-angle neutron scattering (USANS) makes it possible to probe structures of aggregates with larger size on a micrometer scale. Here we review some structural studies on various soft materials, which form a hierarchical organization. Recent development of synchrotron radiation source and neutron facility allows us to obtain scattering data on various length scales. It is shown that combination of various scattering methods provides us with information on hierarchical structures of soft materials from a microscopic to macroscopic level. The structural analysis on each level is also presented in the text. Furthermore, contrast variation and contrast-matching SAXS and SANS methods are very effective for structural investigation of multicomponent nanomaterials, e.g., these methods are very useful to probe internal structures of complex systems such as polymer micelles, polymer–inorganic nanocomposite gels, and rubber-filler systems swollen in an organic solvent.

3   Introduction

So far, many good books regarding experimental techniques and structural analysis by small-angle scattering have been published [1–6]. General data treatments, instrumentations, and data analysis by small-angle X-ray scattering (SAXS) are abundantly described by famous books of Guinier and Fournet [1], Glatter and Kratky [2], and Feigin and Svergun [3]. The book written by Higgins and Benoit presents a comprehensive data analysis of small-angle neutron scattering (SANS) in polymeric systems [4]. These books have provided many researchers with fundamentals of scattering techniques. Also, it is important to learn how their techniques could be used in practice. Recent development of brilliant X-ray sources and neutron facilities is striking, and there are progress and improvements in synchrotron X-ray and neutron scattering instruments. Thus, in this book chapter we introduce updated studies of soft materials with X-ray and neutron scattering. Recently, importance of SANS and SAXS is increasing more and more in the field of soft material science. As a matter of fact, in the past decade, there have been published a large number of review articles regarding SANS and SAXS studies of various soft materials such as copolymers, polymer blends, branched polymers [7], starch [8, 9], polyelectrolyte systems [10], polymer latexes [11], polymer gels [12], protein and peptide self-assembled materials [13], and three-dimensional periodic complex systems [14].

Though both SANS and SAXS have played an important role in probing structures of nanomaterials, each of the SAXS and SANS techniques has unique characteristics. The X-ray scattering is caused mainly by interactions of the incident beam with electrons, while the neutron scattering is done by those of the incident beam with nucleus [3]. As a consequence, the X-ray scattering from atoms increases with the increase of atomic number and has a scattering angle dependence, since

Table 13.1 Scattering length b of some elements for X-ray and neutron scattering [3, 15]

Element	b for X-ray (10^{-12} cm)	b for neutron (10^{-12} cm)
H	0.282	−0.374
D	0.282	0.667
C	1.69	0.665
N	1.97	0.94
O	2.26	0.58
S	4.51	0.28
Na	3.10	0.36
Cl	4.79	0.96

distribution of electrons spreads around nuclei. The absorption of X-rays also increases with the atomic number and the wavelength. On the other hand, neutron scattering from atoms is independent of the scattering angle due to the fact that dimensions of nucleus are much smaller in comparison with that of the neutron wavelength and does not have a definite relationship with the atomic number. The scattering length (or amplitude) b of main elements in soft materials for X-ray and neutron scattering is listed in Table 13.1. Note that the scattering intensity is proportional to the square of the scattering length. In neutron scattering, there are large differences between scattering lengths of hydrogen (H) and deuterium (D). Deuterium labeling is often utilized in neutron scattering experiments in order to change the scattering contrast.

Characteristics of synchrotron SAXS and SANS are compared in the following.

Synchrotron X-Rays
  (i) Heavier atoms have larger scattering length.
 (ii) The beam size is usually very small due to high photon fluxes (typically submillimeter), which enables us to obtain precise data with a very small amount of samples.
(iii) Energetic and angular resolutions are high.

Neutrons
  (i) Spatial information on light atoms such as hydrogen can be evaluated.
 (ii) Larger beam size in comparison with synchrotron X-rays is used (typically 5–10 mm).
(iii) Information on magnetic structures of condensed matter can be obtained from the magnetic scattering.
(iv) Contrast variation and contrast-matching techniques are very effective to probe the structure of complicated systems. Especially, in aqueous solutions and/or hydrogels, we can easily change scattering contrast by preparing H_2O/D_2O with different mixing ratios.

In the past two decades, high-performance materials have attracted material scientist's interest due to the potential applications in various fields. In many cases, functionality of materials is closely related to the internal structure. With the

high performance of materials, the system has grown more complex, and therefore, it is important to clarify the structure of the complicated system in the modern material science. We will show that combination of various scattering methods and contrast variation methods are useful to analyze structures of the complicated systems.

This book chapter deals with structural studies of complex soft materials such as polymeric systems, self-assembling systems, composite systems, etc. using X-ray and neutron scattering. Constitution of this book chapter is as follows: Sect. 4 briefly describes a fundamental of scattering methods. In Sects. 5.1 and 5.2, we briefly present an overview of scattering behaviors of hierarchically organized structures on each level. These are common to both of X-ray and neutron scattering. In Sect. 5.3, recent structural studies of soft materials using contrast variation SAXS and SANS are reviewed. Although the contrast variation method has been utilized from old times, recently, it largely has displayed the power against structural analysis of various complex materials. In Sects. 5.4 and 5.5, we introduce structural evolution using time-resolved scattering measurements and complementary use of X-ray scattering and neutron scattering. Complimentary use of neutron and X-ray scattering may be effective in the structural studies of various complex materials [16, 17].

4 Experimental and Instrumental Methodology

We show a schematic representation of typical small-angle scattering experiments in Fig. 13.1. In the synchrotron small-angle X-ray and neutron scattering experiments, the scattered intensity is usually measured with a two-dimensional detector such as CCD, imaging plate, and PILATUS. Therefore, we can obtain information about anisotropic structures of condensed matters [18–20], and the measurements are often performed under external fields, e.g., mechanical, electric, and magnetic fields.
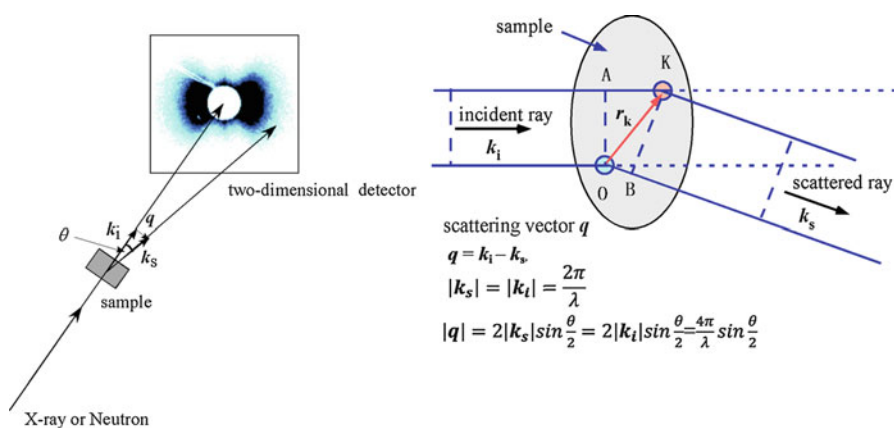
Fig. 13.1 A schematic diagram of a typical synchrotron small-angle X-ray or neutron scattering experiments and definition of scattering vector q

When an incident ray is scattered by particles located at positions of O and K, the path length difference between two scattered rays is presented by

$$AK - OB = \left(\boldsymbol{r_k} \cdot \frac{\boldsymbol{k_i}}{k_i} \right) - \left(\boldsymbol{r_k} \cdot \frac{\boldsymbol{k_s}}{k_s} \right), \tag{13.1}$$

and therefore, the phase difference ϕ_k is described by

$$\phi_k = \left(\frac{2\pi}{\lambda} \right) \left(\boldsymbol{r_k} \cdot \frac{\boldsymbol{k_i} - \boldsymbol{k_s}}{k} \right) = (\boldsymbol{r_k} \cdot \boldsymbol{q}), \tag{13.2}$$

where $\boldsymbol{k_i}$ and $\boldsymbol{k_s}$ are wavevectors of incident ray and scattered ray and the magnitudes are $k_i = k_s = k = \frac{2\pi}{\lambda}$. The scattering data are analyzed with scattering vector $\boldsymbol{q}$ defined by $\boldsymbol{q} = \boldsymbol{k_i} - \boldsymbol{k_s}$. The magnitude of the scattering vector is expressed by

$$q = 4\pi \frac{\sin(\theta/2)}{\lambda}, \tag{13.3}$$

where θ and λ represent the scattering angle and wavelength, respectively. The amplitude of the scattered wave at point K can be described by

$$A_k = A_0 b e^{-i(\omega t + \phi_k)} = A_0 b e^{-i(\omega t + \boldsymbol{r_k} \cdot \boldsymbol{q})}, \tag{13.4}$$

where A_0 is the amplitude of the incident wave and b is the scattering length. We can generalize Eq. (13.4) for the system composed of many identical scatterers, i.e., the total contribution A_t is described as follows:

$$A_t = \sum_k A_0 b e^{-i(\omega t + \boldsymbol{r_k} \cdot \boldsymbol{q})} = A_0 e^{-i\omega t} \sum_k b e^{-i\boldsymbol{r_k} \cdot \boldsymbol{q}}. \tag{13.5}$$

Thus, the scattering amplitude $F(q)$ is defined by

$$F(q) = \sum_k b e^{-i\boldsymbol{r_k} \cdot \boldsymbol{q}}, \tag{13.6}$$

and the scattering intensity is presented by

$$I(q) = F(q) \cdot F(q)^*. \tag{13.7}$$

When the scatterers are continuously distributed in a sample, $F(q)$ can be replaced by the following integral form:

$$F(q) = b \int n(r) e^{-i\boldsymbol{r} \cdot \boldsymbol{q}} \mathrm{d}\boldsymbol{r} \tag{13.8}$$

$n(r)$ is the local density of the scatterer at a point r. The relationship between the length scale of a structure in real space Λ and q is presented in the following form:

$$\Lambda = \frac{2\pi}{q}. \tag{13.9}$$

The data collection, data reduction, and data correction in SAXS experiments were recently written in details by a review article of Pauw [21, 22]. In a similar manner, reduction and correction of SANS data are conducted. Software tools for small-angle scattering data analysis are also important [23–25]. A lot of software packages to analyze small-angle scattering data can be found at the SAS portal (URL: http://smallangle.org).

5 Key Research Findings

In the following sections, we will review recent structural studies of soft materials investigated by combination of various scattering methods and by using a sophisticated analysis such as contrast variation SANS and SAXS methods and will show scattering functions from particles with various structural morphologies. Here although we introduce structural studies on polymer–nanoparticle composite gel, polymer micelles, and organogel comprising low molecular weight organogelator (LMOG), the analysis can be applied to other similar systems.

5.1 Hierarchical Structures of Various Soft Materials

Recently, facilities of synchrotron radiation and neutron sources around the world are remarkably developing. Combination of various scattering methods allows us to obtain structural information in a broad q range. Nowadays, simultaneous SAXS and wide-angle X-ray scattering (WAXS) measurements can be performed in many synchrotron beamlines over the world [26–30]. Ultra-small-angle X-ray scattering (USAXS), ultra-small-angle neutron scattering (USANS), and very-small-angle neutron scattering (VSANS) are used to extend scattering data in a very low q range, i.e., structural information on larger length scales. Conventional Bonse–Hart type of USAXS and USANS techniques had been limited to samples with high contrast and resolved only in one dimension [31, 32]. Therefore, they were not appropriate for measurements of anisotropic samples. However, development of recent USAXS/USANS instruments such as developed Bonse–Hart configuration using multiple reflection and a pinhole USAXS at very long camera length in synchrotron sources facilitates utilization of various soft materials [33–40]. Such instrumental improvement allows us to obtain two-dimensional scattering data and to probe structures of samples with low scattering contrast [18, 36, 41, 42]. USAXS studies in polymeric systems such as polymer gels, polymer solutions, polymer

Fig. 13.2 Hierarchical structures of low molecular weight organogel and length scale covered in various scattering methods
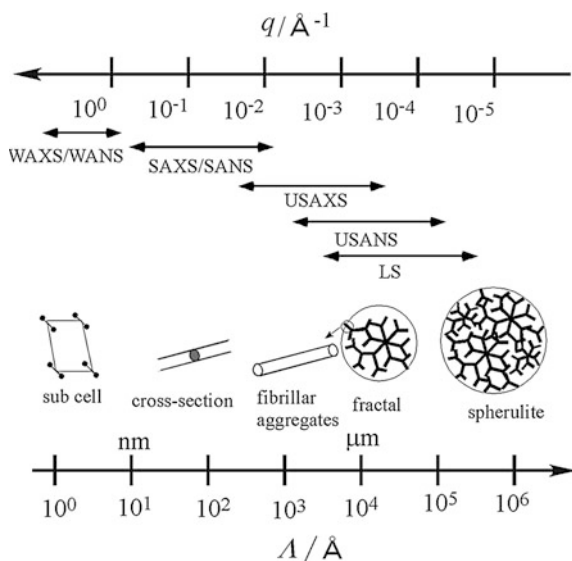
blends, polymer nanocomposites, colloidal gels, and rubber-filler systems can be found in review articles of Zhang and Ilavsky and Takenaka [42, 43].

As mentioned above, combining various scattering techniques makes it possible to obtain structural information of a broad length scale ranging from nanometers to micrometers [43]. Combination of these methods is useful to investigate hierarchical structures of soft matters on multilevels as shown in Fig. 13.2.

Here let us show a scattering profile combined by various scattering methods for an organogel composed of a LMOG, which entraps various organic solvents by self-assembly of the gelator molecules at very low concentrations [44, 45]. The self-assembly forms a fibrillar network, so that the solvents are immobilized. The self-assembled structure of a typical organogel is shown in Fig. 13.3. The graph depicts a scattering profile of 7 wt% 12-hydroxystearic acid (12-HSA)/toluene gel obtained by combining various scattering methods such as SAXS, SANS, focusing SANS [37, 38], and light scattering (LS). The profile shows that the structure caused by self-assembly of the LMOG molecules forms a hierarchical organization at various levels. The peaks at $q = 0.13$ and 0.38 Å^{-1} correspond to (001) and (003) peaks, respectively, which correspond to reflections from a long spacing of the long-chain fatty acids. The peak position is located in the same position as that of crystalline powder without any solvents [46, 47].

A shoulder peak at $q \sim 0.046$ Å^{-1} originates from cross-sectional scattering of fibrillar aggregates. The peak position suggests that the organogel is composed of nanofibers with a cross section of the radius of 8 nm with a comparatively narrow size distribution [48]. The scattering function from fibrillar aggregates (rod particles) exhibits a power law of q^{-1} in a small q range as shown in details later [2]. The scattering behavior of the organogel has an exponent of -1.2 larger than the absolute value of -1 in the small q range, which may suggest branching of fibrillar
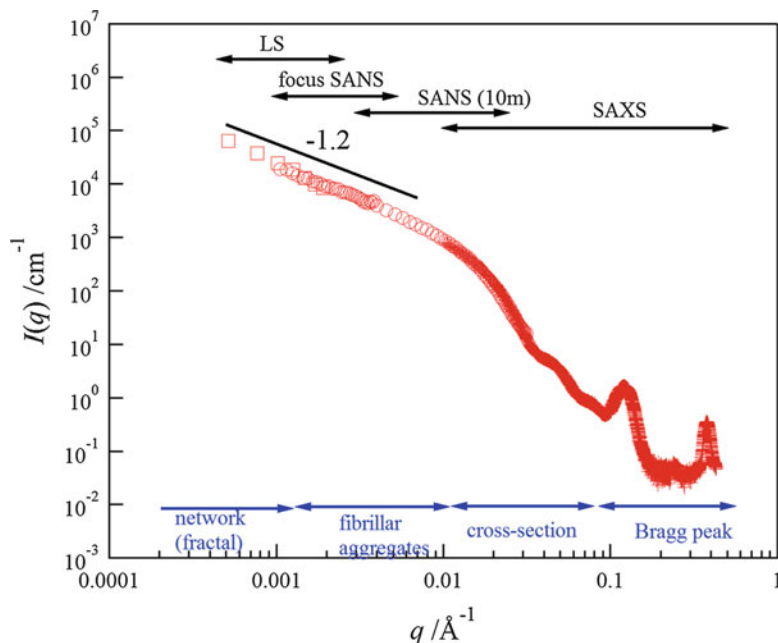
Fig. 13.3 A scattering profile of a low molecular weight organogel obtained by combining various scattering methods (*SAXS*, *SANS*, *focusing SANS*, and *LS*)

aggregates. The power-law scattering behavior in the small q range suggests that the network structure may exhibit a fractal nature [49, 50]. The schematic illustration of the hierarchical structures predicted from various scattering data is shown in Fig. 13.2. Various soft material systems other than LMOG also form hierarchical organization. Hierarchical structures of rubber-filler (carbon black or silica particles) systems were studied in depth by Takenaka et al. [43, 51–53]. They demonstrated by using combined scattering methods that the structures consist of multilevel structures such as (i) surface of primary particles, (ii) primary particles, (iii) aggregates composed of several fused primary particles, and (iv) mass-fractal agglomerate [51]. The combined scattering techniques are also effective for phase-separated polymer blends [54], colloidal silica and carbon [55], polymer electrolyte membranes [56], ceramics [57], spongelike polymer gels [58], clay suspension [59, 60], and cellulose synthesized via enzymatic polymerization [61, 62].

5.2 Structural Analysis of Soft Materials

Analysis of scattering data obtained by combination of various scattering methods is important. Here we shall show theoretical scattering function on each level and the unified approach to small-angle scattering of the multilevel structures such as the Beaucage model [63–66], which has been often used for analysis of multilevel

structures [67–69]. Scattering models for the multilevel structures other than the Beaucage model have been proposed by some researchers [70, 71]. In the following section, we shall briefly describe outline of these structural analyses.

5.2.1 Spherical Particles

The scattering intensity for spherical monodisperse particles can be written by

$$I(q) = n_P V_P^2 \Delta\rho^2 P(q) S(q), \tag{13.10}$$

where n_p and V_p^2 represent the number density of the particles and the square of the volume, respectively. $\Delta\rho$ is the scattering length density. $P(q)$ and $S(q)$ are the form factor of the particles and the structure factor. The former comes from the intraparticle interferences, while the latter comes from the interparticle interferences. In dilute systems the interactions between the particles can be ignored, and therefore, $S(q)$ approaches unity.

Series expansion of $P(q)$ in a small q range ($qR_g \ll 1$) leads to Guinier's law,

$$P(q) \cong P(0)\exp\left(-\frac{1}{3}R_g^2 q^2\right), \tag{13.11}$$

where R_g is the radius of gyration of a particle. Guinier's law is applicable to particulate systems with an arbitrary shape other than spherical particles. We can estimate R_g from the plot of $\ln(I(q))$ vs. q^2 for dilute systems. R_g of objects with various shapes is summarized in Table 13.2.

In the intermediate q range, $P(q)$ depends upon the size and the shape of the particles. $P(q)$ of spherical particles with radius R is presented by

$$P(q) = \left[\frac{3\{\sin(qR) - qR\cos(qR)\}}{(qR)^3}\right]^2. \tag{13.12}$$

Table 13.2 R_g of objects with various geometrical shapes

Sphere with radius R	$R_g = \left(\frac{3}{5}\right)^{1/2} R$
Spherical shell with radius $R_1 > R_2$	$R_g = \left(\frac{3}{5}\frac{R_1^5 - R_2^5}{R_1^3 - R_2^3}\right)^{1/2}$
Rectangular parallelepiped (sides $2a$, $2b$, $2c$)	$R_g = \left(\frac{a^2 + b^2 + c^2}{3}\right)^{1/2}$
Cylinder (half-length H, radius R)	$R_g = \left(\frac{R^2}{2} + \frac{H^2}{3}\right)^{1/2}$
Ellipsoid (half axis a, b, c)	$R_g = \left(\frac{a^2 + b^2 + c^2}{5}\right)^{1/2}$

Taking into consideration the size distribution of the radius, the scattering intensity is expressed by

$$I(q) = \int_0^\infty (\Delta\rho)^2 V_p{}^2 N(R) P(q) dR, \qquad (13.13)$$

where $N(R)$ represents the distribution function of the radius, and the lognormal distribution or the Gaussian distribution is often used.

$$N(R) = n_p \left(\frac{1}{R\sqrt{2\pi\ln\sigma}}\right) \exp\left[-\frac{(\ln R - \ln R_0)^2}{2\ln^2\sigma}\right] \qquad (13.14)$$

or

$$N(R) = n_p \left(\frac{1}{\sqrt{2\pi}\sigma}\right) \exp\left[-\frac{(R - R_0)^2}{(2\sigma^2)}\right] \qquad (13.15)$$

R_0 and σ are the geometric mean and the geometric standard deviation of the distribution, respectively.

5.2.2 Nonspherical Particles

For nonspherical monodisperse systems, the scattering intensity can be written by [72]

$$I(q) = n_P V_P^2 \Delta\rho^2 P(q) S_{\text{app}}(q) \qquad (13.16)$$

with

$$S_{\text{app}}(q) = 1 + \frac{|\langle F(q)\rangle|^2}{P(q)} [S(q) - 1]. \qquad (13.17)$$

Here the bracket in $|\langle F(q)\rangle|^2$ is an average weighed by the distribution of particle sizes and orientations. $S_{\text{app}}(q)$ behaves as an apparent interparticle structure factor. In dilute systems, since $S(q) = 1$, $S_{\text{app}}(q) = 1$.

It is known that self-assembly of small molecules and macromolecules in soft materials often forms fibrillar aggregates with various cross-sectional shapes. In the following sections, form factors of fibrillar aggregates with various cross-sectional shapes are briefly summarized.

Form Factor of Cylindrical Particles

Form factor $P(q)$ of randomly oriented cylinders (rods) with radius R and length $2H$,

$$P(q) = 4 \int_0^{\pi/2} \left[\frac{\sin^2(qH\cos\beta)}{(qH\cos\beta)^2}\right] \left[\frac{J_1^2(qR\sin\beta)}{(qR\sin\beta)^2}\right] \sin\beta d\beta, \qquad (13.18)$$

where β is the angle between the scattering vector q and the axis of the cylinder, and J_1 is the Bessel function of the first order. When the length of the fibrillar aggregates L is sufficiently long in comparison with the cross-sectional size, $P(q)$ can be approximated by [2, 3]

$$P(q) = \frac{L\pi}{q} I_c(q). \tag{13.19}$$

There is a relation of $L = 2H$. Here $I_c(q)$ represents the scattering intensity from cross section of cylindrical rod particles. In a q range much smaller than reciprocal of cross-sectional size but much larger than that of cylindrical rod length, i.e., for $2\pi/L << q << 2\pi/R_c$, $I_c(q)$ can be approximated by the Guinier type of representation,

$$I_c(q) = A^2 \exp\left(-\frac{R_c^2 q^2}{2}\right), \tag{13.20}$$

where R_c and A are the radius of the gyration and the area of the cross section of rod particles, respectively. Equation (13.20) is valid for cross section of arbitrary geometric shape. We can estimate R_c from slope in plot of $\ln(Iq)$ vs. q^2 [73, 74]. For circular cross section with monodisperse radius R, there is the following relation between R and R_c:

$$R_c = \frac{1}{\sqrt{2}} R. \tag{13.21a}$$

For particles with disk shape

$$R_c = \frac{1}{\sqrt{3}} H = \frac{1}{\sqrt{12}} L, \tag{13.21b}$$

Figure 13.4a shows scattering functions ($V_p^2 P(q)$) calculated without considering cross-sectional size distribution at various R's. The position of the oscillation in the scattering functions shifts toward small q with increasing cross-sectional size. The scattering function in the small q range shows a behavior of q^{-1}, indicating the scattering from cylindrical rod particles. Equation (13.13) is applicable to cylindrical particles as well as spherical particles. Figure 13.4b depicts the scattering function with the Gaussian size distribution of R, where we put $\Delta\rho^2 = 1$, $n_p = 1$ in Eqs. (13.13) and (13.15). The oscillation becomes ambiguous with increase of the distribution of the cross-sectional size, i.e., with increase of σ. Thus, we can estimate the cross-sectional size of rod particles and the size distribution from a peak position and the broadness of a scattering profile [75].

Figure 13.5 presents scattering functions of cylindrical particles at various rod lengths. In the case of long cylindrical rods ($H >> R$), the scattering functions in the small q range have the behavior of $I \propto q^{-1}$ as shown above. In a q range much smaller than $2\pi/L$, the scattering intensity becomes almost flat in the log–log plot.
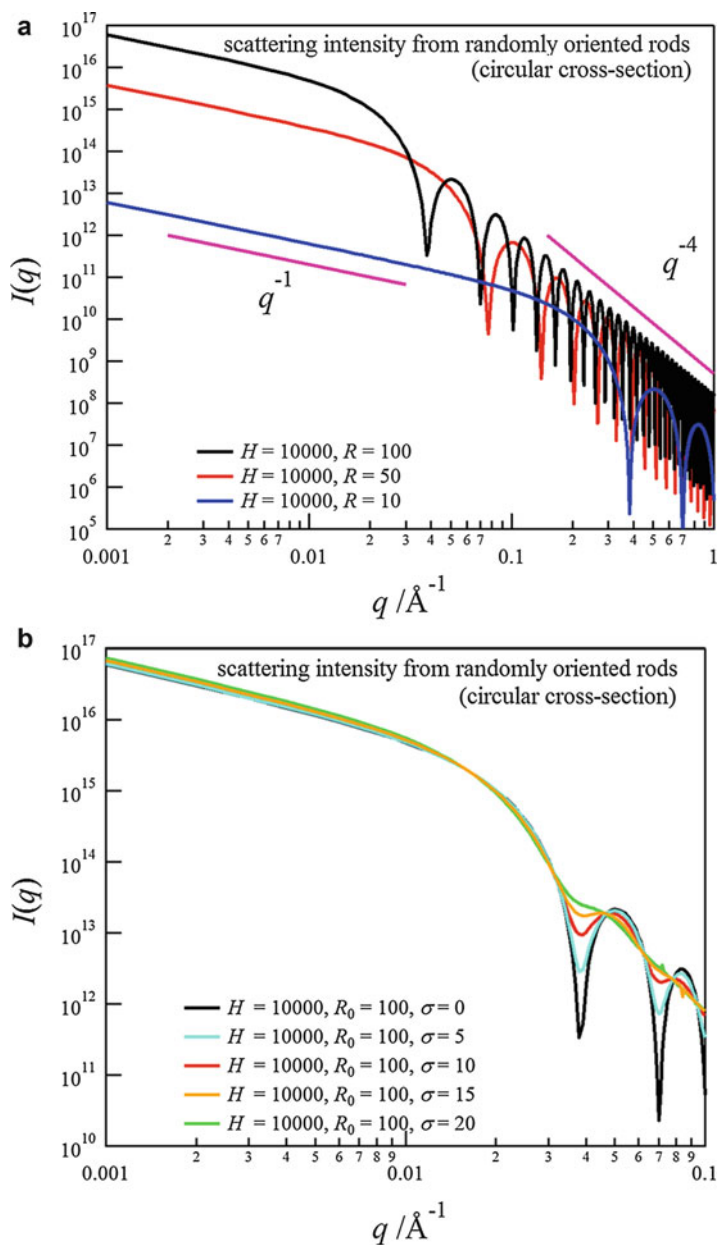
Fig. 13.4 Calculated scattering functions of monodisperse cylindrical particles at various R's (**a**) and those of cylindrical particles with the Gaussian size distribution at various σ's (**b**)
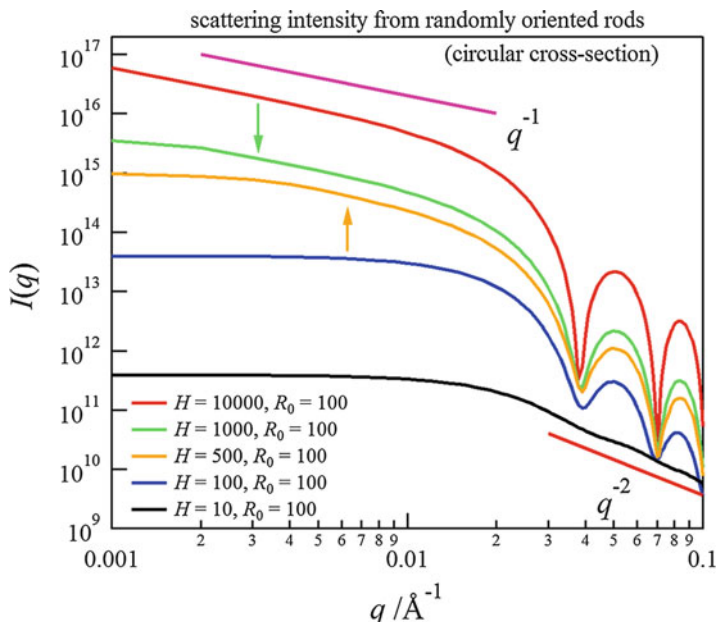
Fig. 13.5 Calculated scattering functions of randomly oriented cylindrical particles with circular cross section at various lengths. The *arrows* in the figure represent the position of $2\pi/L$

If R is much larger than H, i.e., cylindrical particles are regarded as disk particles rather than rod particles, the scattering function shows a behavior of q^{-2}.

Here let us show scattering curves of fibrillar aggregates formed by self-assembly of a low molecular weight organogelator in an organic solvent. Figure 13.6 shows combined SANS and focusing SANS profiles of 12-HSA/deuterated toluene gel over a wide temperature range from a gel state into a sol state [48].

The SANS data can be well described with the cylindrical form factor with the lognormal distribution (Eqs. (13.18) and (13.14)) over a broad q range. The fitted analysis leads to $R_0 = 80$ Å and $\sigma = 1.5$, which hardly change by temperature and concentration variations. The SANS result indicates that these gels form fibrillar aggregates with almost the same thickness at various temperatures and concentrations.

Form Factor of Rod Particles with Rectangular Cross Section
When the cross section has a rectangular Shape of the lengths of the sides a and b, $I_c(q)$ is presented by [76]

$$I_c = \frac{2}{\pi} \int_0^{\pi/2} \left[\frac{\sin(qa\sin\beta/2)}{qa\sin\beta/2} \right]^2 \left[\frac{\sin(qb\cos\beta/2)}{qb\cos\beta/2} \right]^2 d\beta. \qquad (13.22)$$
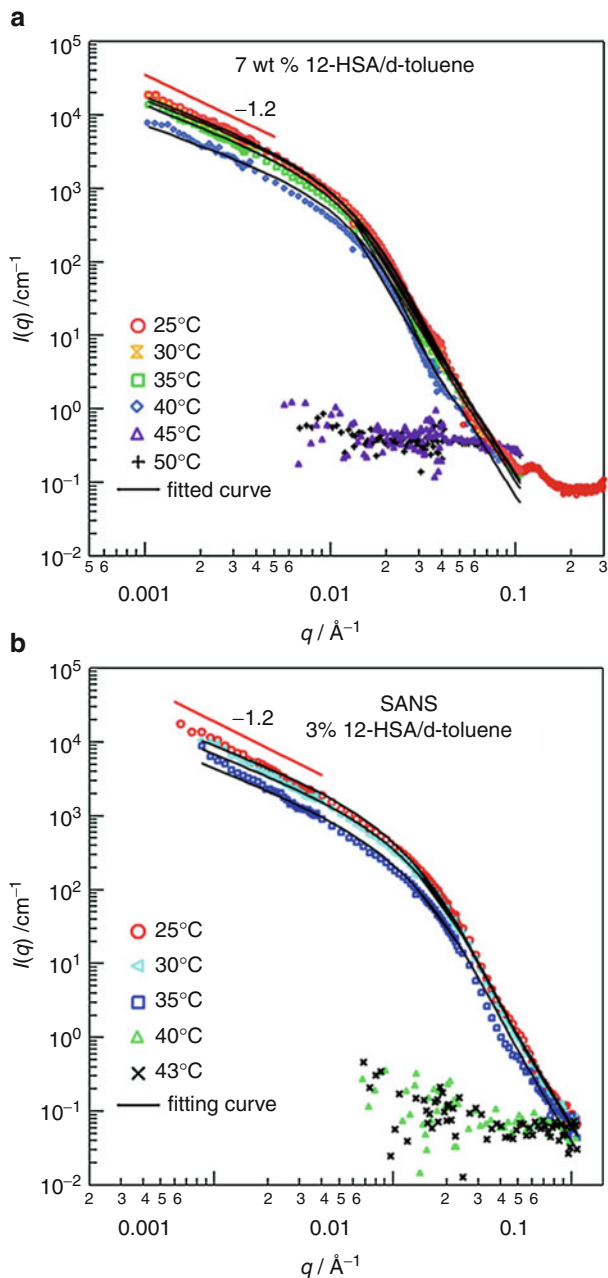
Fig. 13.6 SANS profiles at various temperatures for (**a**) 7 wt % 12-HSA gel and (**b**) 3 wt % 12-HSA gel. The *solid lines* represent the fitted curves (Reproduced with permission from *J Phys Chem* B [48]. Copyright (2012) American Chemical Society)
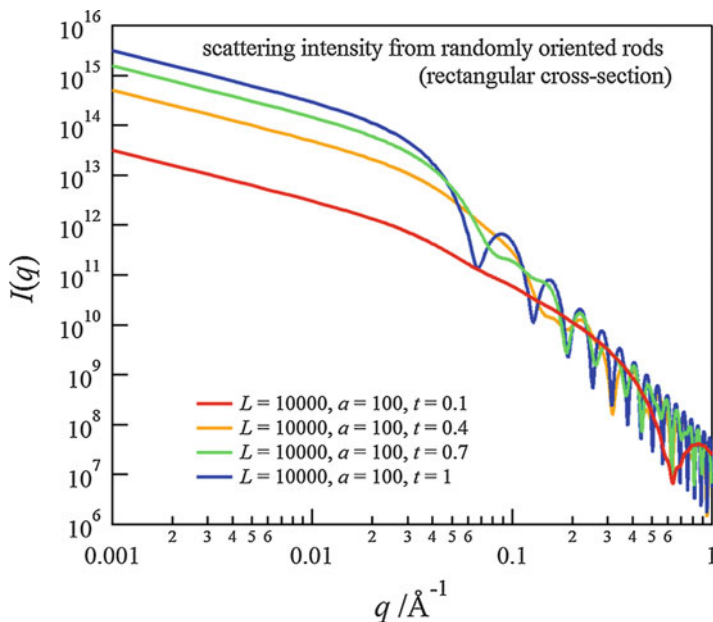
Fig. 13.7 Scattering profiles calculated with scattering function from rectangular cross section with ratio of $t = b/a$

Figure 13.7 depicts theoretical curves calculated with the scattering function from rectangular cross section at various ratios of $t = b/a$. The periodicity of the oscillation is modulated by variation of t.

Form Factor of Long Helices

Cross section of fibrillar aggregates has a variety of shapes such as hollow tube, helical ribbon, and double tube superhelix other than circular and rectangular cross sections [77–80]. The scattering function for infinitely long helices was derived by Pringle and Schmidt, which covers single, double, and hollow helices [81]. This model has been applied to various systems forming helical aggregates [79, 82, 83]. The scattering function can be described in the following form:

$$I(q) = \frac{\pi}{qL} \sum_{n=0}^{\infty} \varepsilon_n \cos^2(n\varphi/2) \frac{\mathrm{Sin}^2(n\omega/2)}{(n\omega/2)^2} [g_n(qR, a)]^2 \qquad (13.23\mathrm{a})$$

where

$$g_n(qR, a) = 2R^{-2} (1 - a^2)^{-1} \int_{aR}^{R} r J_n\left(qr\sqrt{1 - q_n^2}\right) dr \qquad (13.23\mathrm{b})$$

$$q_n = \frac{nb}{qR} \quad \text{for } qR \geq nb \tag{13.23c}$$

$$q_n = 1 \quad \text{for } qR \leq nb \tag{13.23d}$$

$$b = \frac{2\pi R}{P} \tag{13.23e}$$

$$\varepsilon_0 = 1 \text{ and } \varepsilon_n = 2 \quad \text{for } n \geq 1. \tag{13.23f}$$

$J_n(x)$ is the Bessel function of the first kind and order of n. L and P are the total length of the helix with its outer radius R and its inner radius aR and the helix period, respectively. The parameters φ and ω are the angle between the two sectors of a double helix and the angular part of the sector of a material, respectively. Although the summation in Eq. (13.23a) is described as infinite series, as a matter of fact, the terms for $n \geq qR/b$, i.e., $n \geq Pq/2\pi$, are zero.

The model can be extended to a helical tape consisted of N layers as shown by Teixeira et al. [82]. For a single helical tape with N shells (in this case $\varphi = 0$), the form factor of the helical tape can be expressed by

$$I(q) = \frac{\pi}{qLC_{n-shell}^2} \sum_{n=0}^{\infty} \varepsilon_n \frac{\mathrm{Sin}^2(n\omega/2)}{(n\omega/2)^2} \left[G_{shell,\,n}(R_m, \rho_m, P, q) \right]^2 \tag{13.24}$$

with

$$G_{shell,n}(R_m, \rho_m, P, q) = \sum_{m=1}^{N} (\rho_m - \rho_{m-1}) \times 2 \int_0^{R_m} r J_n\left(qr\sqrt{1-q_n^2}\right) dr \tag{13.25}$$

and

$$C_{n-shell} = \sum_{m=1}^{N} (\rho_m - \rho_{m-1}) R_m^2, \tag{13.26}$$

where R_m represents the radius of shell m with electron density ρ_m.

Teixeira et al. tried to fit theoretical scattering functions from helical model and from polydisperse cylindrical model to the scattering data from nanotube of hexa-*peri*-hexabenzocoronene (HBC)-based molecules in THF. They showed that the helical model with hexagonal structure factor is superior to the polydisperse cylindrical model in the fit of their SAXS data. The scattering curves from the helical model represent the width of the oscillator and the depth of the minima of the data very well as shown in Fig. 13.8.

Other than these models, recently, form factor of helical ribbons was derived by Hamley [84].
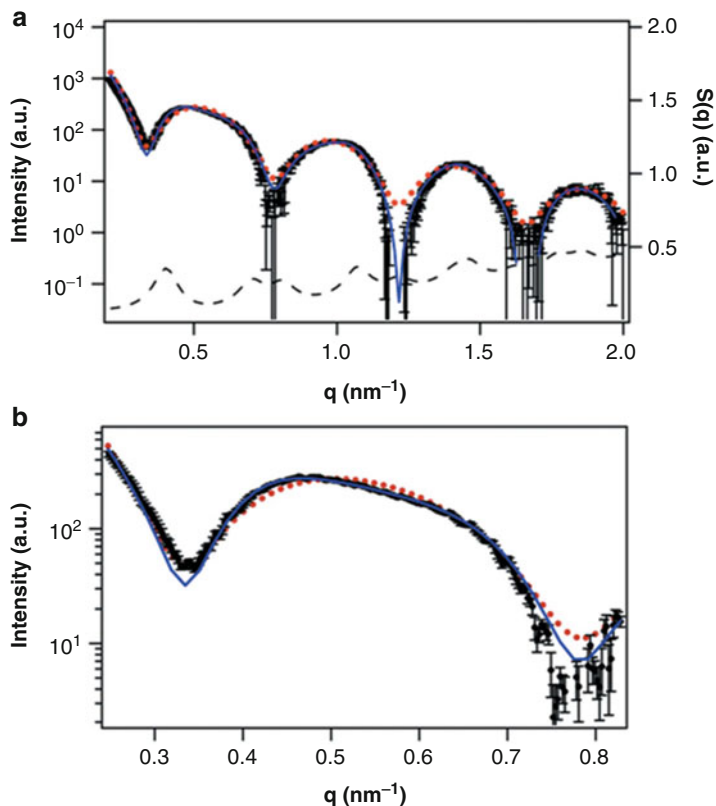
Fig. 13.8 Scattering curve of hexa-*peri*-hexabenzocoronene (HBC)/THF. Experimental curve (*black*), helix form factor (*red*), hexagonal structure factor (right axis; *dashed line*) (Reproduced with permission from *J Appl Crystallogr* [82]. Copyright (2010) International Union of Crystallography)

5.2.3   Structures at High *q*

Scattering intensity at high *q* follows the Porod law, which describes the scattering behavior from the interface of the particles [3, 4], and it comes from thermal concentration fluctuations (TCFs) inside the phase in the case of phase-separated systems:

$$I(q) = \frac{(\Delta\rho)^2 2\pi S}{q^4} + I_{\mathrm{TCF}}, \qquad (13.27)$$

where S is the total surface area of the particles. The scattering behavior from TCFs can be described by the Ornstein–Zernike representation,
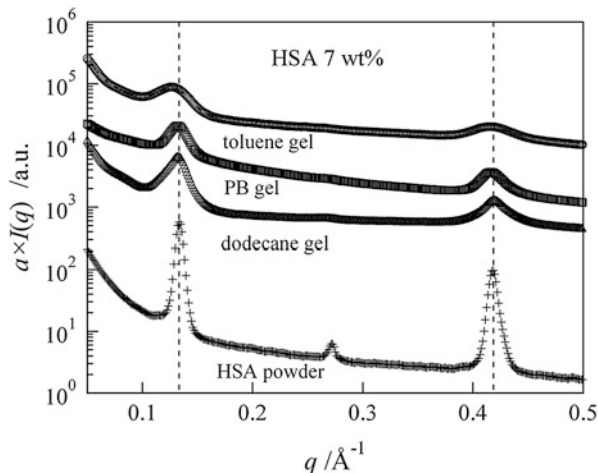
$$I_{\text{TCF}} = \frac{I_0}{1 + \xi^2 q^2} \tag{13.28}$$

where I_0 is a prefactor and ξ is the correlation length of TCFs. In the case of polymer
blends or polymer solutions, the scattering intensity from TCFs obeys the scattering
function calculated on the basis of the random phase approximation [85, 86].

If the aggregates exhibit a crystalline nature, e.g., self-assembled aggregates of
some LMOGs form crystalline fibers [46, 47, 87, 88], then the Bragg peaks are
observed, e.g., long spacing of fatty acids with long alkyl chains is usually in the
range of 3–5 nm measurable in the SAXS experiments. Figure 13.9 depicts com-
parison of SAXS profiles between 12-HSA gels in various solvents and the powder.
As shown in the figure, the profiles of gels for various solvents have the Bragg peaks
corresponding to (001) and (003) reflections at the same positions as the powder
sample (without any solvents), indicating that molecular arrangement of the LMOG
in the gel is similar to that of the crystalline powder. Wide-angle X-ray scattering
(WAXS) profiles for the gel also have the Bragg peaks at the same positions as the
crystalline powder [88]. Other than the q-dependent coherent scattering part as
shown above, the SANS intensity contains a q-independent incoherent scattering
part. Usually it is treated as background scattering in the SANS measurements,
although the incoherent scattering contains important dynamical information regard-
ing molecular vibrations and the rotations in neutron spectroscopy such as inelastic
and quasi-elastic neutron scattering measurements [4, 89].

5.2.4 Unified Approach of Multilevel Structures

The Beaucage unified model [63–66] is used to analyze multilevel structures inves-
tigated by combined various small-angle scattering measurements [43, 51, 52, 69,
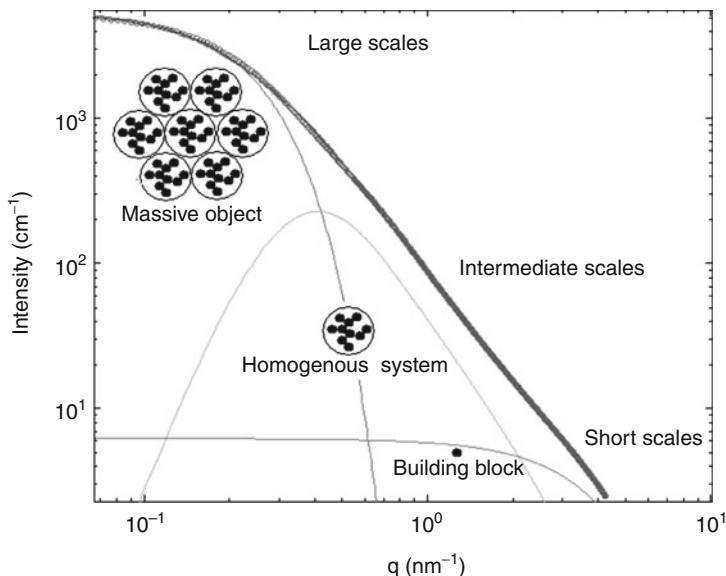
Fig. 13.10 A SAXS profile of an inorganic titania-based gel fitted with the Beaucage model (Reproduced with permission from *J Phys Chem* B [91]. Copyright (2010) American Chemical Society)

90, 91]. The model describes a smooth transition between the Guinier regime and a power-law regime such as the Porod regime. It can be extended to represent an arbitrary number of structures at different size scales,

$$
I(q) = \sum_{i=1}^{n} \left(G_i \exp\left(\frac{-q^2 R_{g(i)}^2}{3}\right) + B_i \exp\left(\frac{-q^2 R_{g(i+1)}^2}{3}\right) \times \left\{ \frac{\left[\mathrm{erf}\left(\frac{q R_{g(i)}}{6^{1/2}} \right) \right]^3}{q} \right\}^{P_i} \right),
$$

(13.29)

where G_i, B_i, $R_{g,i}$, and P_i represent the Guinier prefactor, a prefactor specific to the power-law scattering, the radius of gyration of the i-th level structure, and the exponent of the power-law scattering, respectively. In Eq. (13.29), $i = 1$ refers to the largest-size structural level. If the power-law scattering of the i-th level structure obeys the Porod law, then $P_i = 4$ and $B_i = 2\pi(\Delta\rho)^2 S$. The Beaucage model was recently compared with other models in depth by Hammouda [70, 71].

Pattier et al. investigated the structure of inorganic titania-based gels by SAXS and analyzed the SAXS data with the Beaucage model [91]. Figure 13.10 shows the SAXS data of an inorganic titania-based gel and the curve fitted with the Beaucage model. The Beaucage model well describes the multilevel structure of the gel.

5.3 Contrast-Matching and Contrast Variation Methods in SANS and SAXS

Contrast-matching [92–97] and contrast variation [16, 98–101] methods have so far been widely used to study complex structures of multicomponent systems. These methods are usually carried out by changing scattering length density of solvents. In the case of SAXS, the contrast variation experiments have been performed by changing the electron density of the solvent using substances inactive for latex particles, proteins, or macromolecules [3, 11, 102–104]. Substances such as sucrose and glycerol are often used as additives for the contrast variation. However, application of this method can be implemented only in a limited range, since addition of a substance for contrast variation may affect structures of the scattering objects. Otherwise anomalous or resonant contrast variation method is effective [16, 105]. Generally, the scattering length of a substance is an energy-dependent complex quantity and can be changed through variation of energies of incident X-ray near absorption edge of elements. Application of anomalous SAXS contrast variation method has been performed for various polymeric systems [64, 106–111]. The details of the anomalous SAXS method will be described in details in Sect. 5.3.4.

In the SANS experiments, contrast variation or contrast-matching methods are very effective to probe internal structures in multicomponent complex systems, since neutron scattering length of deuterium is largely different from that of hydrogen as mentioned in the Introduction. Therefore, hydrogen/deuterium replacement can easily change SANS contrast almost without modification of their chemical properties. This SANS contrast variation method has been widely utilized in various soft materials such as colloids, polymers, composites of polymer–inorganic substances, and biological systems. In the following sections, we shall describe details of SANS and SAXS contrast variation methods and the recent application.

5.3.1 Scattering Equation of Multicomponent Systems

The scattering intensity from the multicomponent systems with different $(p + 1)$ species $(0 \leq i \leq p)$ can be described in the following form [4]:

$$I(q) = \sum_{i=0}^{p} \rho_i^2 S_{ii}(q) + 2\sum_{i<j}^{p} \rho_i \rho_j S_{ij}(q) \qquad (13.30)$$

ρ_i is the scattering length density for i-th component, and S_{ij} is the partial structure factor, which is defined by

$$S_{ij}(q) = \iint n_i(r)n_j(r')exp[-iq \cdot (r' - r)]drdr' \qquad (13.31)$$

where $n_i(r)$ is the local density of component i at a position r. On the incompressible assumption, Eq. (13.30) is reduced to the following form:

$$I(q) = \sum_{i=1}^{p} (\rho_i - \rho_0)^2 S_{ii}(q) + 2\sum_{i<j}(\rho_i - \rho_0)(\rho_j - \rho_0)S_{ij}(q). \qquad (13.32)$$

Thus, the scattering intensity of multicomponent systems is composed of both self-terms and cross-terms of the partial structure factors. For the ternary system, the scattering intensity can be expressed by

$$
\begin{aligned}
I(q) = {} & (\rho_1 - \rho_0)^2 S_{11}(q) + (\rho_2 - \rho_0)^2 S_{22}(q) \\
& + 2(\rho_1 - \rho_0)(\rho_2 - \rho_0) S_{12}(q)
\end{aligned}
\tag{13.33}
$$

5.3.2 SANS Contrast-Matching and Contrast Variation Methods

In the small-angle scattering, the scattering length density is calculated from the chemical composition of the particles or the molecules.

$$
\rho = \frac{\sum_i b_i}{v},
\tag{13.34}
$$

where v and b_i are the volume considered in the chemical composition and the scattering length of the component i, respectively. Using the values of the scattering length shown in Table 13.1, it turns out that the neutron scattering length density of H_2O ($\rho_{H_2O} = -5.62 \times 10^9$ cm^{-2}) is largely different from that of D_2O ($\rho_{D_2O} = 6.40 \times 10^{10}$ cm^{-2}), while the X-ray scattering length of heavy water and light water is 9.44×10^{10} cm^{-2}. Thus, in SANS measurements we can easily change the scattering contrast of aqueous systems by adjusting mixing ratio between H_2O and D_2O.

First of all, let us consider a three-component system composed of an inorganic nanoparticle, a polymer, and a solvent (water). Here if components 0, 1, and 2 denote solvent, inorganic nanoparticle, and polymer, respectively, and the scattering contrast between the inorganic nanoparticle and the solvent is matched, i.e., $\rho_i = \rho_s$, then Eq. (13.33) leads to

$$
I(q) = (\rho_p - \rho_s)^2 S_{pp}(q).
\tag{13.35}
$$

Here subscripts i, p, and s denote inorganic nanoparticle, polymer, and solvent species, respectively.

In order to determine the scattering length density of the inorganic nanoparticles, the scattering intensity from the nanoparticles dispersed in H_2O/D_2O is measured. Since the scattering intensity $I(0)$ at $q = 0$ is proportional to the square of the scattering contrast as shown in Eq. (13.10), there is a linear relationship between $\sqrt{I(0)}$ and $\Delta\rho$. Therefore, the matching point can be obtained from a plot of $\sqrt{I(0)}$ vs. ϕ_D as shown in Fig. 13.11 [10]. Or it can be obtained from a fit to the scattering intensity with a quadratic function [95, 112]. In the case of SiO_2, since $\rho_{SiO_2} \cong 3.59 \times 10^{10}$ cm^{-2}, the scattering length density of the silica particles is matched by ~ 40/60 mixture of H_2O/D_2O [96]. If H/D exchange occurs on the inorganic nanoparticles, the scattering length density varies with the fraction of D_2O [113].

Fig. 13.11 A plot of square
of the scattering intensity
vs. fraction of deuterated
solvent to obtain contrast-
matching point
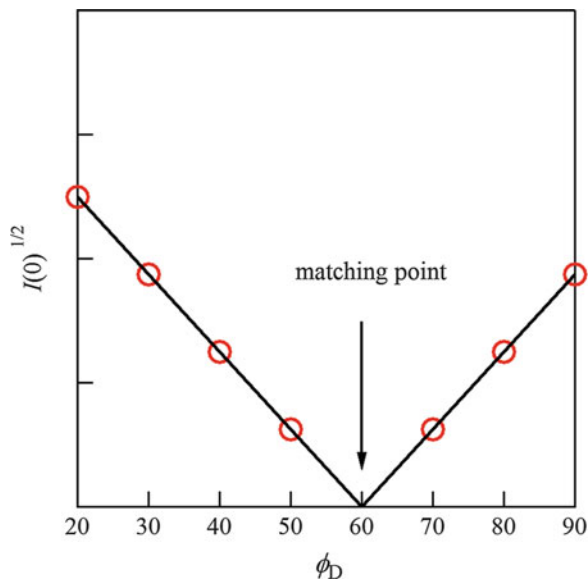
Contrast-matching SANS presents information on the chain conformation in a polymer nanocomposite [95]. However, if the inorganic nanoparticles are not homogeneous/inorganic, it is difficult to perfectly match the scattering contrast [95]. In a similar manner, contrast matching of a polymer and a solvent is also possible [114].

In the case of contrast variation method, scattering experiments with different scattering contrasts, e.g., changing ratio of H_2O/D_2O in aqueous systems are carried out.

Recently, Endo et al. developed SANS contrast variation method to evaluate partial structure factors in multicomponent systems such as microemulsion systems or block copolymer systems including inorganic materials [99, 100, 115]. Now, assuming that scattering measurements with n different contrasts are conducted, scattering intensity for each measurement can be expressed as follows:

$$I = M \cdot S \tag{13.36}$$

where I represents a vector of the scattering intensities at n different scattering contrasts, i.e.,

$$I = \begin{pmatrix} I_1(q) \\ \vdots \\ I_n(q) \end{pmatrix} \tag{13.37}$$

and M is a matrix related to scattering contrasts composed of the following form for ternary systems,

$$M = \begin{pmatrix} {}^1\Delta\rho_1^2 & 2\,{}^1\Delta\rho_1\,{}^1\Delta\rho_2 & {}^1\Delta\rho_2^2 \\ \vdots & \vdots & \vdots \\ {}^n\Delta\rho_1^2 & 2\,{}^n\Delta\rho_1\,{}^n\Delta\rho_2 & {}^n\Delta\rho_2^2 \end{pmatrix} \tag{13.38}$$

with

$$^j\Delta\rho_1 = \rho_1 - {}^j\rho_0 \tag{13.39}$$

and

$$^j\Delta\rho_2 = \rho_2 - {}^j\rho_0 \tag{13.40}$$

where ${}^j\rho_0$ is a scattering length density of the solvent in the j-th experiments ($j = 1, \cdots, n$).

S denotes a vector of partial structure factors

$$S = \begin{pmatrix} S_{11}(q) \\ S_{12}(q) \\ S_{22}(q) \end{pmatrix} \tag{13.41}$$

Thus, the partial structure factors can be obtained using orthogonal matrix M^T from Eq. (13.36):

$$S = M^T \cdot I \tag{13.42}$$

This sophisticated method has been applied to various soft materials such as polymer–clay nanocomposite hydrogels [101, 116, 117], rubber-filler systems [52, 53], polymer–inorganic particles, and fuel cells [118].

5.3.3 Application in Contrast Variation SANS Method

Recently, a variety of polymer nanocomposite systems have attracted many researchers from a viewpoint of potential application of materials in various fields. Accordingly, numerous studies have been made on polymer–inorganic nanocomposites [18, 52, 119], polymer–clay nanocomposite hydrogels [97, 119, 120], rubber-filler systems [18, 52, 121], and polymer–graphene composites [121–123]. Composite of polymer and inorganic substances causes enhancement of material properties such as thermal, mechanical, self-healing, and electrical properties. Recent SAXS, SANS, USAXS, and USANS studies reveal that these scattering methods are very useful to investigate structures of polymer nanocomposite materials.

Here let us show a structural analysis of polymer–clay nanocomposite hydrogels using the above contrast variation method. Haraguchi et al. developed polymer–clay nanocomposite hydrogels with excellent properties such as high extensibility, mechanical toughness, and self-healing by using in situ free radical polymerization

Fig. 13.12 The SAXS
profile of a 0.5 wt% Laponite
aqueous solution. The *solid
curve* represents the curve
fitted with Eq. (13.18),
considering the
inhomogeneity of the radius
of clay particles with the
Gaussian distribution
(Eq. 13.15) (Reproduced with
permission from *Colloid
Polym Sci* [130]. Copyright
(2013) Springer, Berlin/
Heidelberg)
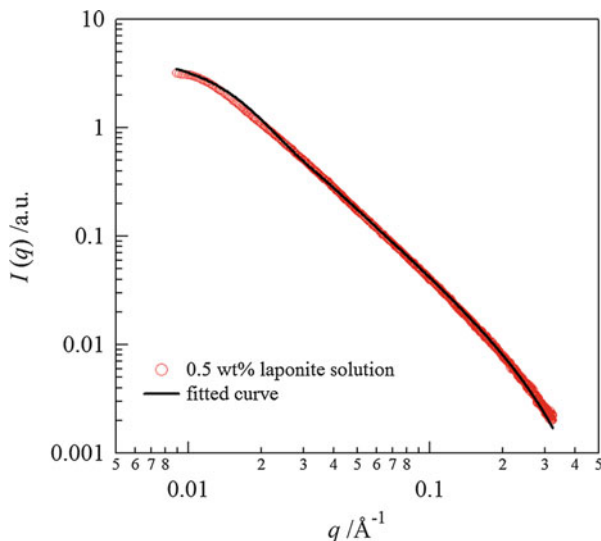
of N-alkylacrylamide in the presence of inorganic clay [124–128]. More recently, polymer–clay nanocomposite hydrogels with excellent mechanical properties were fabricated by simple mixing of clay with a cationic dendrimer [129] and a commercially available anionic polymer [130]. Since these materials are multicomponent, contrast variation method is useful. Synthetic hectorite (Laponite from Rockwood Ltd.) used as inorganic clay is a colloidal layered silicate made of the chemical composition of $Na_{0.66}[Mg_{5.34}Li_{0.66}Si_8O_{20}(OH)_4]$. The clay particles have a disk-shaped structure with a radius of 130–150 Å and thickness of 10 Å [59, 60, 130]. Figure 13.12 shows a SAXS profile for a 0.5 wt % Laponite aqueous solution. The profile can be well described by the form factor of cylindrical particles (Eq. 13.18) with radius of 130 Å and thickness of 10 Å with the Gaussian distribution (Eq. 13.15) in the radius ($\sigma = 30$ Å) [130].

The scattering contrast of the nanocomposite hydrogel in SANS can be easily changed by variation of mixing ratios between light water and heavy water. Endo, Shibayama, and Haraguchi et al. investigated structures of clay (Laponite)–poly(N-isopropylacrylamide) (PNIPAM) nanocomposite hydrogels with the sophisticated contrast variation SANS as shown in the previous section [101, 131]. They obtained the partial structure factors $S_{cc}(q)$, $S_{cp}(q)$, and $S_{pp}(q)$ from the scattering functions of samples prepared at seven different H_2O/D_2O ratios (Fig. 13.13a). Here the subscript c represents clay.

The scattering curves reconstructed from the partial structure factors obtained thus are in good agreement with the original experimental SANS curves (Fig. 13.13b).

Taking into consideration a layer of polymer chains adsorbed on clay particles as shown in Fig. 13.14, they analyzed the partial structure factors obtained from the contrast variation SANS.
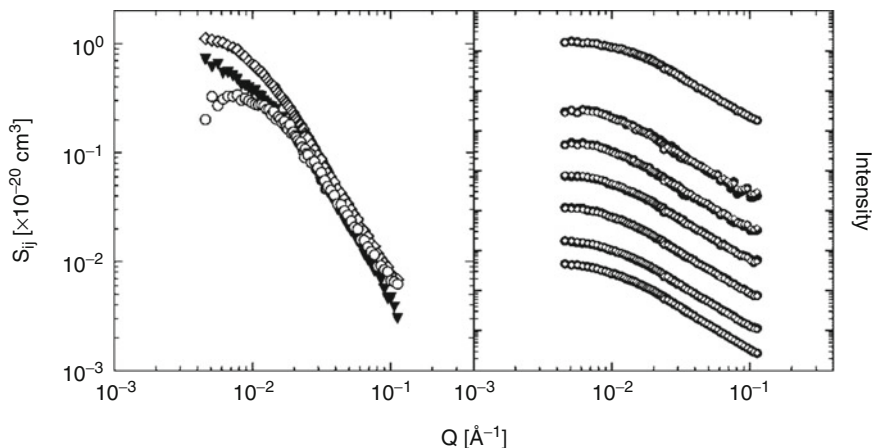
Fig. 13.13 (**a**) The partial structure factor obtained from Eq. (13.42); *circle* (S_{cc}), *filled inverse triangle* (S_{cp}), *lozenge* (S_{pp}). (**b**) Comparison between reconstructed scattering curves (*lozenge*) and experimental scattering curves (*solid circle*) (Reproduced with permission from *Macromolecules* [131]. Copyright (2008) American Chemical Society)

Fig. 13.14 A schematic illustration of a model of polymer layer adsorbed on clay particles
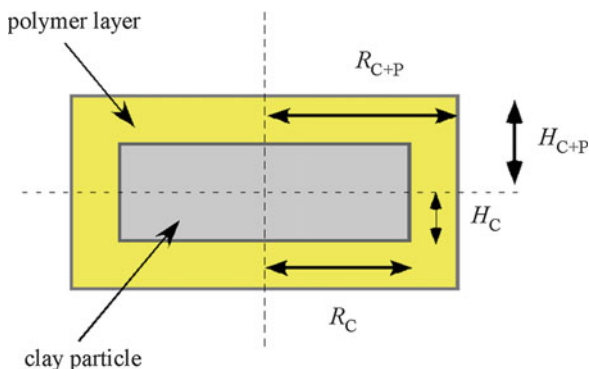
As the clay is cylindrical disk-shaped particles, the scattering amplitude of clay particles F_c is presented in the following form:

$$F_c(q) = 2 \frac{\sin(qH\ \cos\ \beta)}{qH\ \cos\ \beta} \frac{J_1(qR\ \mathrm{Sin}\ \beta)}{qR\ \mathrm{Sin}\ \beta} \tag{13.43}$$

β and J_1 are the same in Eq. (13.18).

The partial structure factor $S_{cc}(q)$ is written as follows:

$$S_{cc}(q) = n_c V_c^2 P_c(q) S_{c,\,app}(q) \tag{13.44}$$

$P_c(q)$ and $S_{c,app}(q)$ are the form factor of clay particles and the apparent structure factor, which are described by Eqs. (13.18) and (13.17), respectively. The partial
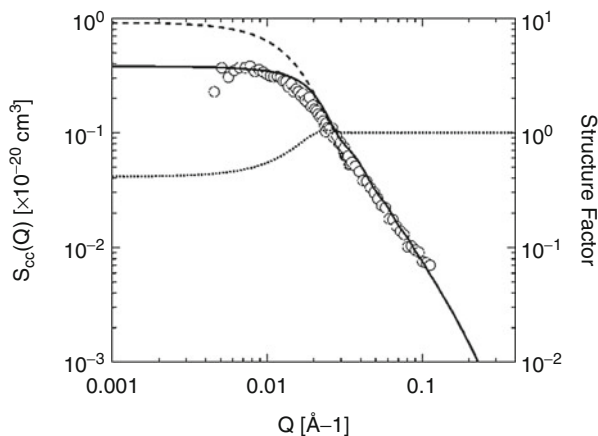
Fig. 13.15 Comparison between the partial structure factor $S_{cc}(q)$ and the fitted curve. The *broken* and the *dotted curves* show the form factor and the apparent structure factor, respectively (Reproduced with permission from *Macromolecules* [131]. Copyright (2008) American Chemical Society)

structure factor of polymer $S_{pp}(q)$ is composed of two contributions from the polymer adsorption layer and from the polymer network, which can be usually represented by the Lorentz function such as Eq. (13.28).

Figure 13.15 shows the analytical result of $S_{cc}(q)$ by Endo et al. The $S_{cc}(q)$ corresponds with the form factor of clay particles (broken curve) in high q range, while it deviates downward in a small q range due to effect of interparticle interference, i.e., $S_{app}(q)$.

The partial structure factor $S_{cc}(q)$ is similar to the overall SAXS profile of a clay–anionic polymer nanocomposite hydrogel for an unstretched sample as shown in Fig. 13.16 in spite of use of different polymer species, where the solid curve represents the form factor of cylindrical disk particles. The SAXS intensity in the small q range is also suppressed due to the interparticle interference in comparison with the form factor. Since clay particles are constituted of heavy atoms relative to polymers and water, the SAXS intensity of the polymer–clay nanocomposite hydrogel comes mainly from clay particles [130].

On the other hand, the cross-term $S_{cp}(q)$ reflects the structure of the adsorption layer. If there is no correlation between polymer and clay particles, i.e., no adsorption layer, $S_{cp}(q)$ becomes negative [99]. In fact, $S_{cp}(q)$ is positive as shown in Fig. 13.13. Thus, Endo et al. showed that the polymer chains are strongly adsorbed on the surfaces of clay particles from the analysis of the partial structure factor $S_{cp}(q)$ [131].

The sophisticated contrast variation SANS method is effective for other multicomponent systems. Takenaka et al. carried out structural analysis by using the contrast variation SANS method for swollen rubber–silica and rubber–carbon black systems, considering a polymer layer adsorbed on the particles [52, 53]. They
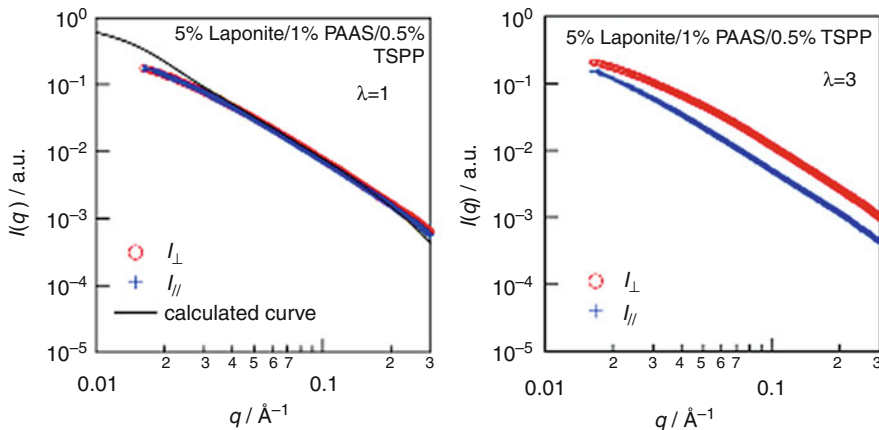
Fig. 13.16 SAXS profiles of a clay–anionic polymer nanocomposite hydrogel; *left* before stretching, *right* after stretching. The *solid line* represents the form factor of the randomly oriented disklike particles ($R = 13$ nm, $\sigma = 3$ nm, and $2H = 1.0$ nm) (Reproduced with permission from *Colloid Polym Sci* [130]. Copyright (2013) Springer, Berlin/Heidelberg)

adopted the Beaucage model for analysis of partial structure factors obtained with the contrast variation SANS and estimated structural parameters regarding interfacial properties in the rubber-filler systems.

5.3.4 Contrast Variation in SAXS: Anomalous SAXS

When SAXS measurements were conducted near absorption edge of elements, the scattering length $f(E)$ becomes a complex quantity as shown in Fig. 13.17 [132, 133]:

$$f(E) = f_0 + f'(E) + if''(E),\tag{13.45}$$

where f_0 is the nonresonant term which is proportional to the atomic number of the element and the resonant terms $f'(E)$ and $f''(E)$ are the real and imaginary components of the energy-dependent anomalous dispersion.

When anomalous SAXS measurements are performed, the scattering amplitude $F(q, E)$ is composed of two parts as follows [134]:

$$F(q,E) = \int \Delta\rho_0(\boldsymbol{r})\exp(-i\boldsymbol{qr})d\boldsymbol{r} + \int \Delta\rho_R(\boldsymbol{r},E)\exp(-i\boldsymbol{qr})d\boldsymbol{r}\tag{13.46}$$

where $\Delta\rho_0$ and $\Delta\rho_R$ are the electron density difference of the nonresonant and the resonant scattering atoms.

In the past, anomalous SAXS has been mainly applied to hard materials such as ceramics, metal catalyst, and metal alloys, which are composed of elements with a
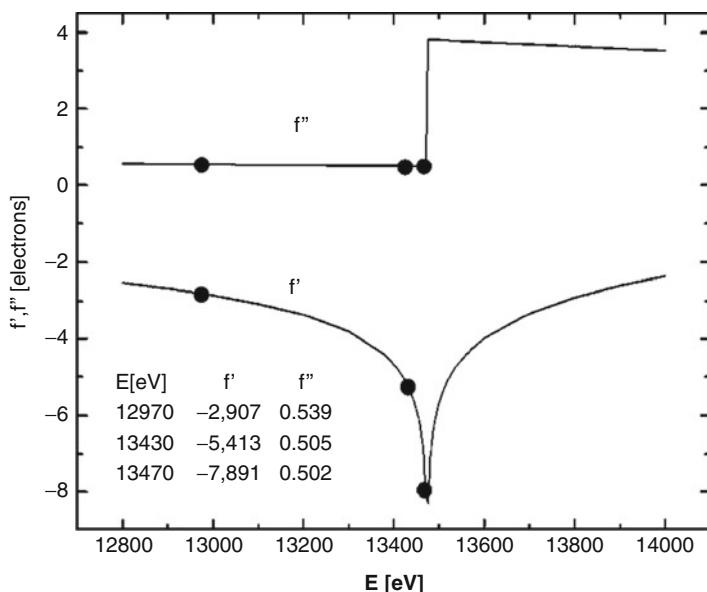
Fig. 13.17 Anomalous scattering factors of bromine (Reproduced with permission from *J Phys Chem B* [132]. Copyright (2006) American Chemical Society)

high atomic number [135–139]. This is because the absorption edge of the elements with high atomic number could be easily reached in the energy range of synchrotron X-rays. In the case of polymeric systems, the distribution and the number of counterion around a polyelectrolyte and DNA can be probed by anomalous SAXS [107, 109, 140]. Otherwise, absorption edge of K shell of bromine (Br) is often utilized [106, 132, 141, 142]. As mentioned above, the scattering amplitude $F(q, E)$ consists of two contributions of the nonresonant and resonant terms ($F_0(q)$ and $F_R(q, E)$):

$$F(q, E) = F_0(q) + F_R(q, E). \tag{13.47}$$

When the measurement is performed near the absorption edge of K shell of Br, $F_R(q, E)$ can be written as follows:

$$F_R(q, E) = [f'_{Br}(E) + if''_{Br}(E)]V(q). \tag{13.48}$$

$V(q)$ corresponds to the Fourier transform of the distribution function of Br, i.e., $V^2(q)$ corresponds to the form factor derived from the spatial distribution of Br.

Using Eq. (13.10), the anomalous scattering intensity $I(q, E)$ is presented by [106, 143]

$$I(q) = n_P V_P^2 \left[F_0^2(q) + 2f'_{Br}(E)F_0(q)V(q) + \left\{ f'^2_{Br}(E) + f''^2_{Br}(E) \right\} V^2(q) \right] S(q)$$

(13.49)

since $P(q, E) = F(q, E) F(q, E)^*$. In dilute systems, $S(q)$ approaches 1 as mentioned above. In practice $V^2(q)$ can be obtained from difference between different scattering profiles measured at different energies [106]. The difference in the scattering intensities at two different energies (E_i and E_j), ΔI_{ij}, is represented as follows:

$$\Delta I_{ij}(q, E_i, E_j) = n_P V_P^2 \left[2\left\{ f'_{Br}(E_i) - f'_{Br}(E_j) \right\} F_0(q)V(q) \right. \\ \left. + \left\{ f'^2_{Br}(E_i) - f'^2_{Br}(E_j) + f''^2_{Br}(E_i) - f''^2_{Br}(E_j) \right\} V^2(q) \right],$$

(13.50)

assuming $S(q) = 1$. Thus, using the scattering intensity measured at three different energies of X-rays (E_1, E_2, E_3), $V^2(q)$ can be obtained in the following form:

$$V^2(q) = \frac{1}{K} \left[\frac{\Delta I_{12}(q, E_1, E_2)}{f'_{Br}(E_1) - f'_{Br}(E_2)} - \frac{\Delta I_{13}(q, E_1, E_3)}{f'_{Br}(E_1) - f'_{Br}(E_3)} \right]$$

(13.51)

with

$$K = f'_{Br}(E_2) - f'_{Br}(E_3) + \frac{f''^2_{Br}(E_1) - f''^2_{Br}(E_2)}{f'_{Br}(E_1) - f'_{Br}(E_2)} - \frac{f''^2_{Br}(E_1) - f''^2_{Br}(E_3)}{f'_{Br}(E_1) - f'_{Br}(E_3)}$$

(13.52)

Akiba et al. performed anomalous SAXS measurements at three different energies of incident X-rays near the absorption edge of bromine (13.473 keV, 13.453 keV, 13.283 keV) in order to probe the internal structure of polymer micelles comprising poly(4-bromostyrene)-*block*-poly(ethylene glycol)-*block*-poly(4-bromostyrene) in an aqueous solution [106]. $V^2(q)$ obtained from the above analysis is shown in Fig. 13.18. The solid curve in Fig. 13.18 represents the scattering function calculated for a sphere with the radius of 10.2 nm, which is in good agreement with the data. Thus, the anomalous SAXS analysis revealed that the core composed of poly (4-bromostyrene) chains formed sphere with the radius of 10.2 nm.

5.4 Time-Resolved Scattering Measurements

Aggregated structures are developed via various processes such as liquid–liquid phase separation, crystallization, gelation, and micellization. Investigation of the kinetics is very important in order to understand the mechanism of their processes. Time-resolved scattering measurements have been performed for investigation of such kinetics. Especially, synchrotron SAXS technique is a very powerful tool to pursue a fast process, since high brilliance of synchrotron radiation makes it possible to obtain such precise data at a very short accumulation time [144, 145].
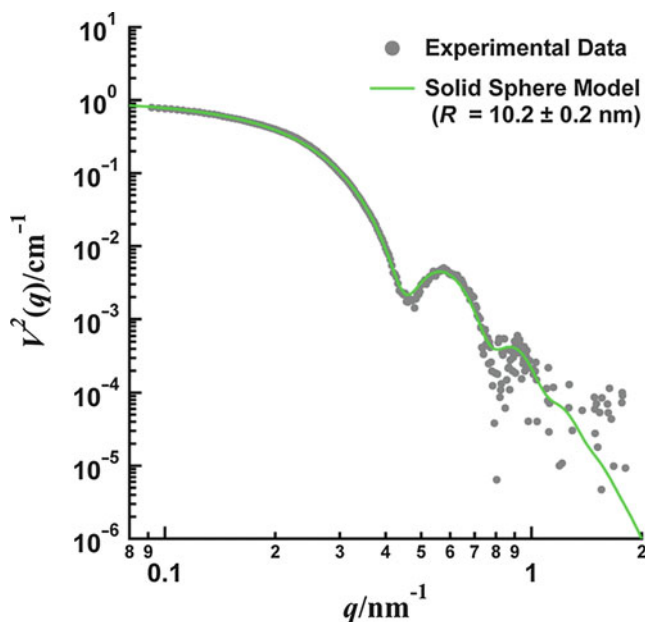
Fig. 13.18 Resonant term $V^2(q)$ of poly(4-bromostyrene)-*block*-poly(ethylene glycol)-*block*-poly (4-bromostyrene) micelles (Reproduced with permission from *Macromolecules* [106]. Copyright (2012) American Chemical Society)

Time-resolved SANS measurements also may be useful in some cases [146–151], although neutron sources are inherently weaker than synchrotron X-ray sources. Sometimes repeating experiments are performed in order to overcome a poor statistical accuracy, and the average scattering data are analyzed [149–151]. However, recent development of neutron sources makes it possible to follow the kinetics with a time resolution of subsecond [146, 152, 153]. Time-resolved synchrotron SAXS/SANS measurements are performed with specific cells such as temperature-jump or pressure-jump cells designed for synchrotron SAXS/SANS experiments [154, 155]. In synchrotron SAXS experiments, it is necessary to operate the cell by remote control outside a hutch.

Here we shall show a gelation process of a LMOG investigated by using time-resolved synchrotron SAXS. Figure 13.19 shows time course of the scattering profiles of a 12-HSA/xylene gel after quench from 55 °C (sol state) into 36 °C [74]. After crystalline nucleation occurred, i.e., (001) reflection appeared at a high q at $t = 31.9$ s, the scattering intensity increased with keeping almost the same shape in the double logarithmic plot (Fig. 13.19b). This result suggests that the crystalline fibers grow with keeping the thickness constant.

Figure 13.19c shows a picture of a temperature-jump cell used in the time-resolved synchrotron SAXS experiments. The *T*-jump cell is composed of two heated blocks, where we can separately control temperature. Instantaneous temperature jump can be performed by moving the heated blocks up and down with a remote controller.
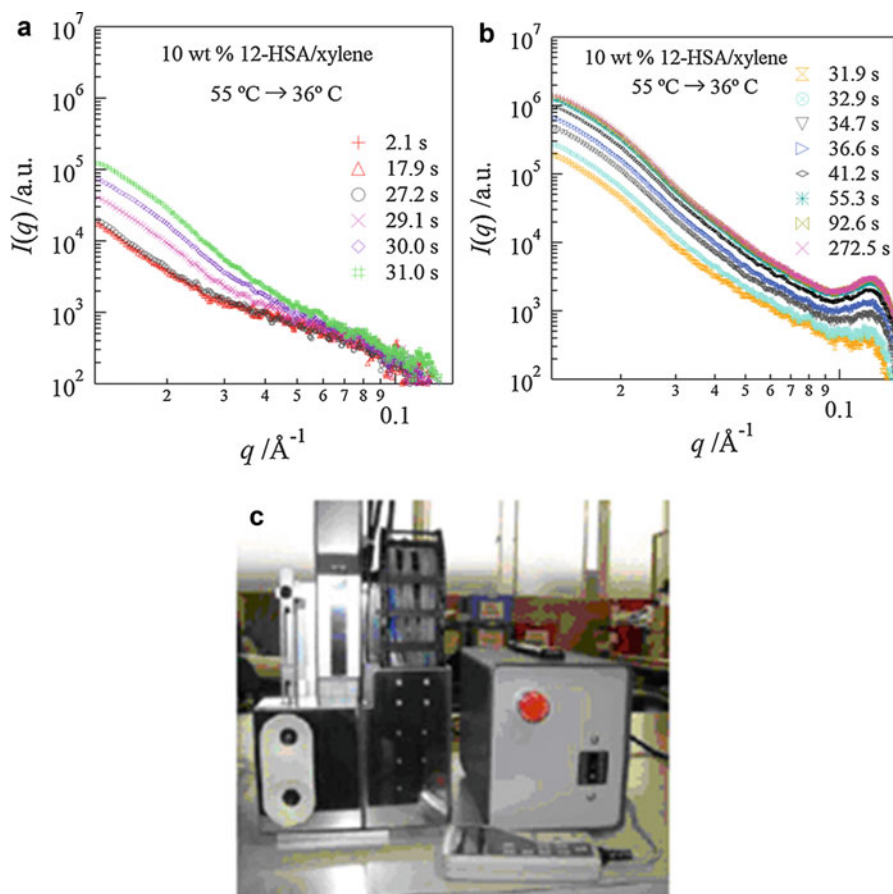
Fig. 13.19 Time evolution of SAXS profiles for 12-HSA/xylene gel at 36 °C in the regime (**a**) before crystalline nucleation and (**b**) after the nucleation (Reproduced with permission from *Colloid Polym Sci* [74]. Copyright (2013) Springer, Berlin/Heidelberg) (**c**) Picture of a temperature-jump cell designed for synchrotron small-angle X-ray scattering

Other than *T*-jump and *P*-jump cells, various cells and apparatuses have been designed for kinetic studies of fast processes [153, 156, 157]. The various cells for studies on the dynamics of lipidic nanostructures have been summarized by a review article of Yaghmur and Rappolt [157]. For crystalline polymers, polymer blends, block copolymers, and polymer gels, time-resolved SAXS and SANS have been used to pursue structural development during stretching and shear [19, 158–160]. In these studies, stress–strain curves and scattering data are simultaneously recorded.

Lund et al. designed a stopped-flow apparatus for rapid mixing and investigated the micellization kinetics of both surfactant and block copolymer micelles [153]. Figure 13.20 depicts an experimental setup with the stopped-flow apparatus (a), the time evolution of the SANS profiles after 1:1 mixing of 1.5 vol % micelle consisting
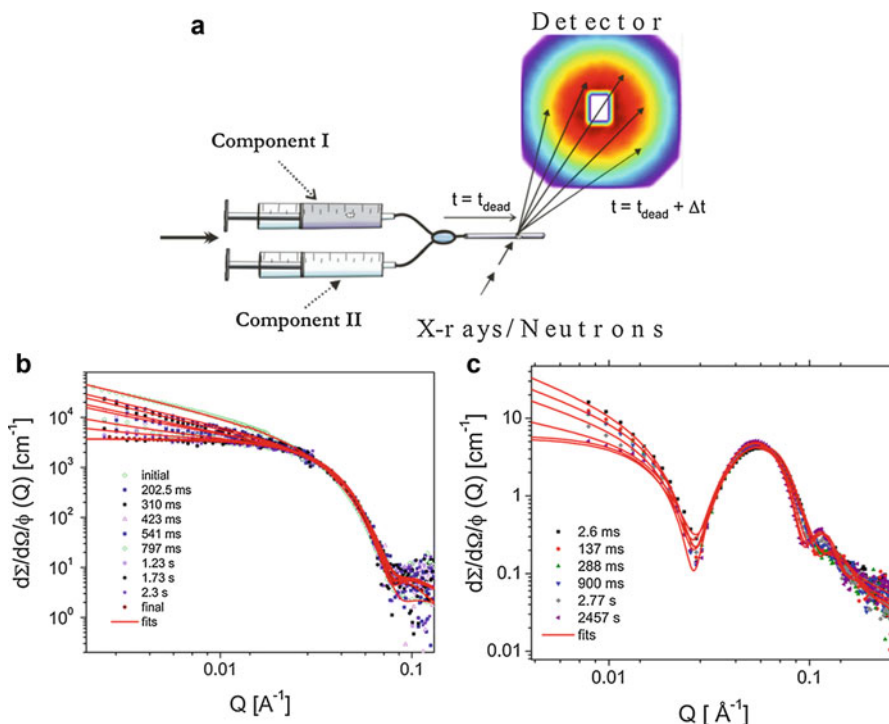
Fig. 13.20 (**a**) Schematic diagram of experimental setup using a stopped-flow apparatus. (**b**) Time-resolved SANS data after a rapid mixing of PEP1–PEO1 in 51 % dDMF/D$_2$O solution with pure dDMF obtained using the apparatus. (**c**) The time-resolved SAXS data (Reproduced with permission from *ACS Macro Letters* [153]. Copyright (2013) American Chemical Society)

of poly(ethylene-*alt*-propylene)–poly(ethylene oxide) (PEP1–PEO1) in 51 % dDMF/D$_2$O solution with pure dDMF (b), and the time evolution of the SAXS profiles after mixing it (c) [153]. The acquisition time of the SANS measurements is 200 ms. The five repeating experiments were performed, and their data were combined. On the other hand, the acquisition time of the SAXS measurements was 5 ms with a readout time of 140 ms between two acquisitions. They observed kinetics of the cylinder-to-sphere morphological transition for the block copolymer micelle on the millisecond range using the time-resolved SAXS and SANS.

5.5 Complementary Utilization of SAXS and SANS

In some soft material systems, complementary use between SAXS and SANS is effective to clarify the complex structures [161–168]. In Fig. 13.20, it is interesting to notice that the shape of the SANS profiles and the SAXS profiles for PEP1–PEO1 micelle in dDMF/D$_2$O solution is largely different, reflecting a large difference in both scattering contrasts [153]. All the SAXS intensities at various times have a
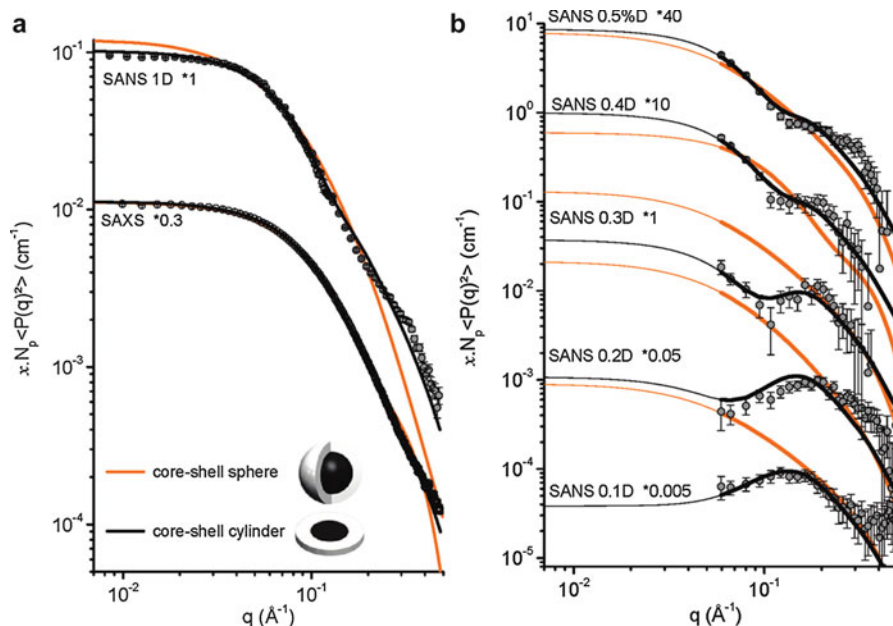
Fig. 13.21 (**a**) SAXS profiles for 5 g/L asphaltene in H-toluene and SANS profiles for 5 g/L asphaltene in D-toluene. (**b**) Contrast variation SANS for 50 g/L asphaltene in toluene at various h/d ratios. These *curves* were fitted by two models of the core–shell cylinder model and the core–shell sphere model (Reproduced with permission from *J Phys Chem B* [162]. Copyright (2011) American Chemical Society)

distinct scattering peak at high q range, while all the SANS intensities at various times monotonically decrease with increasing q. This behavior is often seen for a micelle in an aqueous solution [161]. In the SANS, the scattering length density of the polymeric core makes a negative contribution, while in the SAXS it makes a positive contribution. The SANS profiles show a behavior of $I \propto q^{-1}$ at the initial stage in a small q range, while they show a plateau-like behavior at the late stage. The former behavior indicates cylindrical-like behavior as shown in Fig. 13.4, while the latter suggests the Guinier-like behavior in the q range smaller than $2\pi/R_g$. Namely, these results show the cylinder-to-sphere morphological transition. On the other hand, the SAXS data show better resolution in comparison with the SANS data, although the time change in the intensity is much smaller, reflecting the small scattering contrast. Lund et al. obtained structural parameters from the fitting procedure to both SANS and SAXS data using a model of coexistence of sphere and cylindrical core–shell [153].

Eyssautier and Barre et al. performed SAXS and SANS measurements for precise structural analysis of nanoaggregates of asphaltene, which is high molecular substances in crude oil [162]. Figure 13.21 depicts (a) SAXS (5 g/L asphaltene in H-toluene) and SANS (5 g/L asphaltene in D-toluene) profiles and (b) the contrast

variation SANS (50 g/L asphaltene in toluene at various h/d ratios). Their fitting analysis shows that both models of core–shell sphere and core–shell cylinder describe their SAXS data well, i.e., it cannot be concluded from the fitting analysis which structural model is better. However, the fitting analysis of the SANS data reveals that the core–shell cylinder is the best model for asphaltene nanoaggregates. Furthermore, the contrast variation SANS clearly demonstrated that the core–shell cylinder model was superior to the core–shell sphere model.

Zemb and Diat pointed out importance of combined SAXS and SANS measurements of the same sample containing surfactants, which allow decomposition into form and structure factors [169]. Furthermore, they showed that combined SAXS and SANS measurements are useful for direct determination of the adsorption isotherm.

Complementary utilization of SAXS and SANS has been used in hard materials such as metal alloys as well as soft materials. Ohnuma et al. determined the chemical composition of the nanosized oxide in the steel matrix using the alloy contrast variation (ACV) method [166]. In both SAXS and SANS experiments, the intensity should be measured in absolute units. The chemical composition of the microstructure in the steel matrix is determined from the ratio of SAXS and SANS intensity [166, 170].

Besides, combination of small-angle scattering and other techniques such as in situ simultaneous SAXS and UV–vis, SAXS and Raman [171], simultaneous SAXS and FTIR [172], simultaneous fitting of SAXS and WAXS data [173], and combined SAXS/SANS with molecular dynamic simulations [174, 175] is also useful in addition to conventional complementary use of scattering technique and microscopy observation.

6   Conclusions and Future Perspective

In this chapter we have reviewed recent structural studies of soft materials such as polymeric micelles, low molecular weight organogels, polymer–clay nanocomposite gels, and so on. It has been shown that small-angle scattering methods such as synchrotron SAXS, USAXS, SANS, and USANS are powerful to probe structures of soft materials. Moreover, we have shown that combined scattering methods are very effective to clarify hierarchical structures. The hierarchical organization is composed of various structural levels, which depend upon the system, e.g., in the case of low molecular weight organogels, (i) spherulites, (ii) network (or fractal) structure, (iii) fibrous aggregates, (iv) cross-sectional structure of fibrous aggregates, and (v) crystalline organization in fibrous aggregates. Accompanying high performance of materials, their structures become more complicated. Therefore, it has been emphasized that sophisticated structural analysis for complex systems is indispensable. In general, however, structural analysis in multicomponent systems, e.g., that of three phases or more, becomes dramatically complex in comparison with two-phase or one-phase systems. We have shown that contrast variation SANS method using mixtures of hydrogenated and deuterated solvents with different ratios

and anomalous SAXS near the absorption edge of an element are suitable for internal structural studies of multicomponent systems. The scattering intensities measured with different scattering contrasts can be decomposed into partial structure factor of each component. The partial structure factors obtained thus presents important information on the self-correlation between nanoparticles, that between polymers, and the cross-correlation between nanoparticles and polymers.

In the future, importance of these combined methods and contrast variation methods will increase more and more with the development of high-performance materials. In practice the contrast variation SANS method introduced in this topic has been recently used for structural analysis of various high-performance materials, e.g., catalyst ink of fuel cell [118]. Anomalous SAXS may be useful for structural studies of drug delivery systems (DDS), since polymeric micelles have potential as drug carriers [176–178]. Recently, structures of polymer micelles that encapsulate drug-equivalent substances containing bromine atoms have been investigated by Sanada et al. [179]. Furthermore, anomalous X-ray scattering of light elements like sulfur and phosphorus atoms may be promising as pointed out by Stuhrmann, although the experiments are technically more difficult [105]. It may be useful especially for biological systems such as nucleoproteins and membrane proteins.

References

1. Guinier A, Fournet G (1955) Small-angle scattering of X-rays. Wiley, New York
2. Glatter O, Kratky O (1982) Small angle X-ray scattering. Academic, London
3. Feigin LA, Svergun DI, Taylor GW (1987) Structure analysis by small-angle X-ray and neutron scattering. Plenum Press, New York
4. Higgins JS, Benoît H (1994) Polymers and neutron scattering. Clarendon Press/Oxford University Press, Oxford/New York
5. Chu B (1997) Laser light scattering of polymer solutions. Appl Opt 36:7650–7656
6. Roe RJ (2000) Methods of X-ray and neutron scattering in polymer science. Oxford University Press, New York
7. Hammouda B (2010) SANS from polymers-review of the recent literature. Polym Rev 50:14–39
8. Blazek J, Gilbert EP (2011) Application of small-angle X-ray and neutron scattering techniques to the characterisation of starch structure: a review. Carbohydr Polym 85:281–293
9. Doutch J, Gilbert EP (2013) Characterisation of large scale structures in starch granules via small-angle neutron and X-ray scattering. Carbohydr Polym 91:444–451
10. Boué F, Cousin F, Gummel J, Oberdisse J, El Carrot G, Harrak A (2007) Small angle scattering from soft matter—application to complex mixed systems. C R Phys 8:821–844
11. Dingenouts N, Bolze J, Potschke D, Ballauff M (1999) Analysis of polymer latexes by small-angle X-ray scattering. Adv Polym Sci 144:1–47
12. Shibayama M (2011) Small-angle neutron scattering on polymer gels: phase behavior, inhomogeneities and deformation mechanisms. Polym J 43:18–34

13. Guilbaud JB, Saiani A (2011) Using small angle scattering (SAS) to structurally characterise peptide and protein self-assembled materials. Chem Soc Rev 40:1200–1210
14. Imperor-Clerc M (2012) Three-dimensional periodic complex structures in soft matter: investigation using scattering methods. Interface Focus 2:589–601
15. Sears VF (1992) Neutron scattering lengths and cross sections. Neutron News 3:26–37
16. Stuhrmann HB (2007) Contrast variation in X-ray and neutron scattering. J Appl Crystallogr 40:S23–S27
17. Belushkin AV, Kozlenko DP Rogachev AV (2011) Synchrotron and neutron-scattering methods for studies of properties of condensed matter: competition or complementarity? J Surf Invest-X-Ray 5:828–855
18. Shinohara Y, Kishimoto H, Inoue K, Suzuki Y, Takeuchi A, Uesugi K, Yagi N, Muraoka K, Mizoguchi T, Amemiya Y (2007) Characterization of two-dimensional ultra-small-angle X-ray scattering apparatus for application to rubber filled with spherical silica under elongation. J Appl Crystallogr 40:S397–S401
19. Takeno H, Uehara H, Murakami S, Takenaka M, Kim MI, Nagasawa N, Sasaki S (2007) Structural development of dynamically asymmetric polymer blends under uniaxial stretching. J Appl Crystallogr 40:S656–S661
20. Takeno H, Obuchi K, Maki Y, Kondo S, Dobashi T (2011) A structural study of polyelectrolyte gels in a unidirectionally swollen state. Polymer 52:2685–2692
21. Pauw BR (2013) Everything SAXS: small-angle scattering pattern collection and correction. J Phys Condens Matter 25:383201
22. Pauw BR (2014) Corrigendum: Everything SAXS: small-angle scattering pattern collection and correction (2013 J Phys Condens Matter 25:383201). J Phys Condens Matter 26:239501
23. Kline SR (2006) Reduction and analysis of SANS and USANS data using IGOR Pro. J Appl Crystallogr 39:895–900
24. Ilavsky J, Jemian PR (2009) Irena: tool suite for modeling and analysis of small-angle scattering. J Appl Crystallogr 42:347–353
25. Spinozzi F, Ferrero C, Ortore MG, Antolinos AD, Mariani P (2014) GENFIT: software for the analysis of small-angle X-ray and neutron scattering data of macromolecules in solution. J Appl Crystallogr 47:1132–1139
26. Kaneko F, Seto N, Sasaki K, Sakurai S, Kimura T (2013) Simultaneous SAXS and WAXS study on the guest exchange process of syndiotactic polystyrene: crystalline complex formation with triethylene glycol dimethyl ether. Macromol Chem Phys 214:1893–1900
27. Portale G, Cavallo D, Alfonso GC, Hermida-Merino D, van Drongelen M, Balzano L, Peters GWM, Goossens JGP, Bras W (2013) Polymer crystallization studies under processing-relevant conditions at the SAXS/WAXS DUBBLE beamline at the ESRF. J Appl Crystallogr 46:1681–1689
28. Tolentino A, León S, Alla A, Martínez de Ilarduya A, Muñoz-Guerra S (2013) The structure of poly(γ-glutamic acid)/nanoclay hybrids compatibilized by alkylammonium surfactants. Eur Polym J 49:2596–2609
29. Liu G, Schneider K, Zheng L, Zhang X, Li C, Stamm M, Wang D (2014) Stretching induced phase separation in poly(vinylidene fluoride)/poly(butylene succinate) blends studied by in-situ X-ray scattering. Polymer 55:2588–2596
30. Rath T, Novák J, Amenitsch H, Pein A, Maier E, Haas W, Hofer F, Trimmel G (2014) Real time X-ray scattering study of the formation of ZnS nanoparticles using synchrotron radiation. Mater Chem Phys 144:310–317
31. Bonse U, Hart M (1965) Tailless X-ray single-crystal reflection curves obtained by multiple reflection – (Si Ge crystals – E/T). Appl Phys Lett 7:238
32. Koga T, Hart M, Hashimoto T (1996) Development of a high-flux- and high-temperature-set-up Bonse-Hart ultra-small-angle X-ray scattering (USAXS) diffractometer. J Appl Crystallogr 29:318–324
33. Chaboussant G, Désert S, Brûlet A (2012) Recent developments and projects in SANS instrumentation at LLB-Orphée. Eur Phys J Spec Top 213:313–325

34. Dewhurst CD (2014) Novel multiple-beam very small angle neutron scattering (VSANS) using a conventional SANS instrument. J Appl Crystallogr 47:1180–1189

35. Freelon B, Suthar K, Ilavsky J (2013) A multi-length-scale USAXS/SAXS facility: 10–50 keV small-angle X-ray scattering instrument. J Appl Crystallogr 46:1508–1512

36. Ilavsky J, Jemian PR, Allen AJ, Zhang F, Levine LE, Long GG (2009) Ultra-small-angle X-ray scattering at the advanced photon source. J Appl Crystallogr 42:469–479

37. Koizumi S, Iwase H, Suzuki J, Oku T, Motokawa R, Sasao H, Tanaka H, Yamaguchi D, Shimizu HM, Hashimoto T (2006) Focusing and polarized neutron ultra-small-angle scattering spectrometer (SANS-J-II) at Research Reactor JRR3, Japan. Phys B Condens Matter 385–86:1000–1006

38. Koizumi S, Iwase H, Suzuki JI, Oku T, Motokawa R, Sasao H, Tanaka H, Yamaguchi D, Shimizu HM, Hashimoto T (2007) Focusing and polarized neutron small-angle scattering spectrometer (SANS-J-II). The challenge of observation over length scales from an angstrom to a micrometre. J Appl Crystallogr 40:S474–S479

39. Rehm C, Barker J, Bouwman WG, Pynn R (2013) DCD USANS and SESANS: a comparison of two neutron scattering techniques applicable for the study of large-scale structures. J Appl Crystallogr 46:354–364

40. Rehm C, Brule A, Freund AK, Kennedy SJ (2013) Kookaburra: the ultra-small-angle neutron scattering instrument at OPAL. J Appl Crystallogr 46:1699–1704

41. Sztucki M, Narayanan T (2007) Development of an ultra-small-angle X-ray scattering instrument for probing the microstructure and the dynamics of soft matter. J Appl Crystallogr 40:S459–S462

42. Zhang F, Ilavsky J (2010) Ultra-small-angle X-ray scattering of polymers. Polym Rev 50:59–90

43. Takenaka M (2013) Analysis of structures of rubber-filler systems with combined scattering methods. Polym J 45:10–19

44. Weiss RG (2014) The past, present, and future of molecular gels. What is the status of the field, and where is it going? J Am Chem Soc 136:7519–7530

45. Weiss RG, Terech P (2006) Molecular gels materials with self-assembled fibrillar networks. Springer, Dordrecht

46. Takeno H, Maehara A, Kuchiishi M, Yoshiba K, Takeshita H, Kondo S, Dobashi T, Takenaka M, Hasegawa H (2012) Structural and thermal properties of unpurified and purified 12-hydroxystearic acid solutions. Sen'i Gakkaishi 68:248–252

47. Takeno H, Mochizuki T, Yoshiba K, Kondo S, Dobashi T (2009) Self-assembling structures and sol–gel transition of optically active and racemic 12-hydroxystearic acids in organic solvents. Progr Colloid Polym Sci 136:47–53

48. Takeno H, Maehara A, Yamaguchi D, Koizumi S (2012) A structural study of an organogel investigated by small-angle neutron scattering and synchrotron small-angle X-ray scattering. J Phys Chem B 116:7739–7745

49. Liu XY, Sawant PD (2001) Formation kinetics of fractal nanofiber networks in organogels. Appl Phys Lett 79:3518–3520

50. Liu XY, Sawant PD (2002) Mechanism of the formation of self-organized microstructures in soft functional materials. Adv Mater 14:421–426

51. Koga T, Hashimoto T, Takenaka M, Aizawa K, Amino N, Nakamura M, Yamaguchi D, Koizumi S (2008) New insight into hierarchical structures of carbon black dispersed in polymer matrices: a combined small-angle scattering study. Macromolecules 41:453–464

52. Takenaka M, Nishitsuji S, Amino N, Ishikawa Y, Yamaguchi D, Koizumi S (2009) Structure analyses of swollen rubber-filler systems by using contrast variation SANS. Macromolecules 42:308–311

53. Takenaka M, Nishitsuji S, Amino N, Ishikawa Y, Yamaguchi D, Koizumi S (2012) Structure analyses of swollen rubber-carbon black systems by using contrast variation small-angle neutron scattering. Rubber Chem Technol 85:157–164

54. Hashimoto T (2004) Small-angle neutron scattering studies of dynamics and hierarchical pattern formation in binary mixtures of polymers and small molecules. J Polym Sci Pol Phys 42:3027–3062

55. Schaefer DW, Rieker T, Agamalian M, Lin JS, Fischer D, Sukumaran S, Chen CY, Beaucage G, Herd C, Ivie J (2000) Multilevel structure of reinforcing silica and carbon. J Appl Crystallogr 33:587–591

56. Iwase H, S-i S, Yamaki T, Koizumi S, Ohnuma M, Maekawa Y (2012) Hierarchical structure analysis of graft-type polymer electrolyte membranes consisting of cross-linked polytetra-fluoroethylene by small-angle scattering in a wide-Q range. Macromolecules 45:9121–9127

57. Allen AJ (2005) Characterization of ceramics by X-ray and neutron small-angle scattering. J Am Ceram Soc 88:1367–1381

58. Hashimoto T (2012) Combined small-angle scattering analysis of hierarchically self-assembled soft matters: unique "sponge-like" gel structure as an example of dissipative patterns formed in open non-equilibrium systems. Chin J Phys 50:171–192

59. Kroon M, Vos WL, Wegdam GH (1998) Structure and formation of a gel of colloidal disks. Phys Rev E 57:1962–1970

60. Pignon F, Magnin A, Piau JM, Cabane B, Lindner P, Diat O (1997) Yield stress thixotropic clay suspension: investigation of structure by light, neutron, and x-ray scattering. Phys Rev E 56:3281–3289

61. Hashimoto T, Koizumi S (2012) Polymer science: a comprehensive reference. Elsevier, Amsterdam

62. Tanaka H, Koizumi S, Hashimoto T, Kurosaki K, Kobayashi S (2007) Self-assembly of synthetic cellulose during in-vitro enzymatic polymerization process as studied by a combined small-angle scattering method. Macromolecules 40:6304–6315

63. Beaucage G (1995) Approximations leading to a unified exponential power-law approach to small-angle scattering. J Appl Crystallogr 28:717–728

64. Beaucage G (1996) Small-angle scattering from polymeric mass fractals of arbitrary mass-fractal dimension. J Appl Crystallogr 29:134–146

65. Beaucage G (2004) Determination of branch fraction and minimum dimension of mass-fractal aggregates. Phys Rev E 70:031401

66. Beaucage G, Schaefer DW (1994) Structural studies of complex-systems using small-angle scattering – a unified Guinier power-law approach. J Non-Cryst Solids 172:797–805

67. Beaucage G, Kammler HK, Pratsinis SE (2004) Particle size distributions from small-angle scattering using global scattering functions. J Appl Crystallogr 37:523–535

68. Mihara S, Datta RN, Dierkes WK, Noordermeer JWM, Amino N, Ishikawa Y, Nishitsuji S, Takenaka M (2014) Ultra small-angle X-ray scattering study of flocculation in silica-filled rubber. Rubber Chem Technol 87:348–359

69. Papagiannopoulos A, Zhao J, Zhang G, Pispas S, Radulescu A (2014) Thermoresponsive aggregation of PS–PNIPAM–PS triblock copolymer: a combined study of light scattering and small angle neutron scattering. Eur Polym J 56:59–68

70. Hammouda B (2010) Analysis of the Beaucage model. J Appl Crystallogr 43:1474–1478

71. Hammouda B (2010) A new Guinier-Porod model. J Appl Crystallogr 43:716–719

72. Kotlarchyk M, Chen SH (1983) Analysis of small-angle neutron-scattering spectra from polydisperse interacting colloids. J Chem Phys 79:2461–2469

73. Abreu MF, dos Santos DR, Gatts CEN, Giacomini R, Cardoso SL, Miranda PCML (2014) Small-angle X-ray scattering structural study of the nanofiber self-assembly process in supra-molecular gels based on glucopyranosides. J Appl Crystallogr 47:1284–1297

74. Takeno H, Mochizuki T (2013) A structural development of an organogel explored by synchrotron time-resolved small-angle X-ray scattering. Colloid Polym Sci 291:2783–2789

75. Takeno H, Kuribayashi Y (2015) A synchrotron small-angle X-ray scattering study on structures of 1,3:2,4-dibenzylidene sorbitol gels. Colloid Surf A 467:173–179

76. Mittelbach P, Porod G (1961) Zur Rontgenklein winkelstreung verdunnter kolloider Systeme. Die Berechung der Streukurven von Parallelpipeden. Acta Phys Austriaca 14:185–211

77. Lee HY, Oh H, Lee JH, Raghavan SR (2012) Shedding light on helical microtubules: real-time observations of microtubule self-assembly by light microscopy. J Am Chem Soc 134:14375–14381
78. Li Y, Li B, Fu Y, Lin S, Yang Y (2013) Solvent-induced handedness inversion of dipeptide sodium salts derived from alanine. Langmuir 29:9721–9726
79. Terech P, SKP V, Pernot P, Wiegart L (2012) Salt effects in the formation of self-assembled lithocholate helical ribbons and tubes. J Phys Chem B 116:11344–11355
80. Ziserman L, Lee HY, Raghavan SR, Mor A, Danino D (2011) Unraveling the mechanism of nanotube formation by chiral self-assembly of amphiphiles. J Am Chem Soc 133:2511–2517
81. Pringle OA, Schmidt PW (1971) Small-angle X-ray scattering from helical macromolecules. J Appl Crystallogr 4:290–293
82. Teixeira CV, Amenitsch H, Fukushima T, Hill JP, Jin W, Aida T, Hotokka M, Lindén M (2010) Form factor of an N-layered helical tape and its application to nanotube formation of hexa-peri-hexabenzocoronene-based molecules. J Appl Crystallogr 43:850–857
83. Terech P, Volino F, Ramasseul R (1985) Small-angle neutron-scattering study of steroidal gels. J Phys Paris 46:895–903
84. Hamley IW (2008) Form factor of helical ribbons. Macromolecules 41:8948–8950
85. de Gennes P-G (1979) Scaling concepts in polymer physics. Cornell University Press, Ithaca/London
86. Takeno H, Koizumi S, Hasegawa H, Hashimoto T (1996) Small-angle neutron scattering study of anomalous mixing behaviors in deuterated polystyrene poly(vinyl methyl ether) mixtures near the glass transition temperature. Macromolecules 29:2440–2448
87. Takeno H, Kuribayashi Y (2014) Structural studies of 1,3:2,4-dibenzylidene sorbitol gels. Adv Mater Res 896:300–304
88. Takeno H, Yanagita M, Motegi Y, Kondo S (2015) Relationship between helical aggregates and polymorphs in a 12-hydroxystearic acid gel: their thermal stability and formation kinetics. Colloid Polym Sci 293:199–207
89. Takeno H, Koizumi S (2006) Incoherent neutron scattering study on the local dynamics in polystyrene and poly(vinyl methyl ether) blends. Polymer 47:5946–5951
90. Long B, Chodakowski M, Shaw JM (2013) Impact of liquid–vapor to liquid–liquid–vapor phase transitions on asphaltene-rich nanoaggregate behavior in athabasca vacuum residue + pentane mixtures. Energy Fuel 27:1779–1790
91. Pattier B, Henderson M, Brotons G, Gibaud A (2010) Study of titanium oxide sol–gel condensation using small angle X-ray scattering. J Phys Chem B 114:5227–5232
92. Hollamby MJ, Borisova D, Brown P, Eastoe J, Grillo I, Shchukin D (2012) Growth of mesoporous silica nanoparticles monitored by time-resolved small-angle neutron scattering. Langmuir 28:4425–4433
93. Johansen D, Jeffries CM, Hammouda B, Trewhella J, Goldenberg DP (2011) Effects of macromolecular crowding on an intrinsically disordered protein characterized by small-angle neutron scattering with contrast matching. Biophys J 100:1120–1128
94. Jouault N, Dalmas F, Said S, Di Cola E, Schweins R, Jestin J, Boue F (2010) Direct measurement of polymer chain conformation in well-controlled model nanocomposites by combining SANS and SAXS. Macromolecules 43:9881–9891
95. Nusser K, Neueder S, Schneider GJ, Meyer M, Pyckhout-Hintzen W, Willner L, Radulescu A, Richter D (2010) Conformations of silica-poly(ethylene-propylene) nanocomposites. Macromolecules 43:9837–9847
96. Sharma KP, Aswal VK, Kumaraswamy G (2010) Adsorption of nonionic surfactant on silica nanoparticles: structure and resultant interparticle interactions. J Phys Chem B 114:10986–10994
97. Shibayama M, Karino T, Miyazaki S, Okabe S, Takehisa T, Haraguchi K (2005) Small-angle neutron scattering study on uniaxially stretched poly(N-isopropylacrylamide)-clay nanocomposite gels. Macromolecules 38:10772–10781

98. Avdeev MV (2007) Contrast variation in small-angle scattering experiments on polydisperse and superparamagnetic systems: basic functions approach. J Appl Crystallogr 40:56–70

99. Endo H (2006) Study on multicomponent systems by means of contrast variation SANS. Phys B Condens Matter 385:682–684

100. Endo H, Schwahn D, Colfen H (2004) On the role of block copolymer additives for calcium carbonate crystallization: small angle neutron scattering investigation by applying contrast variation. J Chem Phys 120:9410–9423

101. Miyazaki S, Endo H, Karino T, Haraguchi K, Shibayama M (2007) Gelation mechanism of poly(N-isopropylacrylamide)-clay nanocomposite gels. Macromolecules 40:4287–4295

102. Dingenouts N, Ballauff M (1993) Small-angle X-ray-analysis of latex-particles using contrast variation. Acta Polym 44:178–183

103. Hickl P, Ballauff M, Jada A (1996) Small-angle X-ray contrast-variation study of micelles formed by poly(styrene)-poly(ethylene oxide) block copolymers in aqueous solution. Macromolecules 29:4006–4014

104. Naruse K, Eguchi K, Akiba I, Sakurai K, Masunaga H, Ogawa H, Fossey JS (2009) Flexibility and cross-sectional structure of an anionic dual-surfactant wormlike micelle explored with small-angle X-ray scattering coupled with contrast variation technique. J Phys Chem B 113:10222–10229

105. Stuhrmann HB (2008) Small-angle scattering and its interplay with crystallography, contrast variation in SAXS and SANS. Acta Crystallogr A 64:181–191

106. Akiba I, Takechi A, Sakou M, Handa M, Shinohara Y, Amemiya Y, Yagi N, Sakurai K (2012) Anomalous small-angle X-ray scattering study of structure of polymer micelles having bromines in hydrophobic core. Macromolecules 45:6150–6157

107. Dingenouts N, Patel M, Rosenfeldt S, Pontoni D, Narayanan T, Ballauff M (2004) Counterion distribution around a spherical polyelectrolyte brush probed by anomalous small-angle X-ray scattering. Macromolecules 37:8152–8159

108. Lee B, Lo CT, Seifert S, Rago NLD, Winans RE, Thiyagarajan P (2007) Anomalous small-angle X-ray scattering characterization of bulk block copolymer/nanoparticle composites. Macromolecules 40:4235–4243

109. Pabit SA, Finkelstein KD, Pollack L (2009) Using anomalous small angle X-ray scattering to probe the ion atmosphere around nucleic acids. Methods Enzymol 469:391–410

110. Sztucki M, Di Cola E, Narayanan T (2012) Anomalous small-angle X-ray scattering from charged soft matter. Eur Phys J Spec Top 208:319–331

111. Thiyagarajan P (2003) Characterization of materials of industrial importance using small-angle scattering techniques. J Appl Crystallogr 36:373–380

112. Chevigny C, Jestin J, Gigmes D, Schweins R, Di-Cola E, Dalmas F, Bertin D, Boue F (2010) "Wet-to-dry" conformational transition of polymer layers grafted to nanoparticles in nanocomposite. Macromolecules 43:4833–4837

113. Suzuki T, Endo H, Shibayama M (2008) Analysis of surface structure and hydrogen/deuterium exchange of colloidal silica suspension by contrast-variation small-angle neutron scattering. Langmuir 24:4537–4543

114. Chevigny C, Gigmes D, Bertin D, Jestin J, Boue F (2009) Polystyrene grafting from silica nanoparticles via nitroxide-mediated polymerization (NMP): synthesis and SANS analysis with the contrast variation method. Soft Matter 5:3741–3753

115. Endo H, Mihailescu M, Monkenbusch M, Allgaier J, Gompper G, Richter D, Jakobs B, Sottmann T, Strey RIG (2001) Effect of amphiphilic block copolymers on the structure and phase behavior of oil–water-surfactant mixtures. J Chem Phys 115:580–600

116. Matsunaga T, Endo H, Takeda M, Shibayama M (2010) Microscopic structure analysis of clay-poly(ethylene oxide) mixed solution in a flow field by contrast-variation small-angle neutron scattering. Macromolecules 43:5075–5082

117. Nishida T, Endo H, Osaka N, Li H, Haraguchi K, Shibayama M (2009) Deformation mechanism of nanocomposite gels studied by contrast variation small-angle neutron scattering. Phys Rev E 80:030801

118. Shibayama M, Matsunaga T, Kusano T, Amemiya K, Kobayashi N, Yoshida T (2014) SANS studies on catalyst ink of fuel cell. J Appl Polym Sci 131:39842
119. Rose S, Dizeux A, Narita T, Hourdet D, Marcellan A (2013) Time dependence of dissipative and recovery processes in nanohybrid hydrogels. Macromolecules 46:4095–4104
120. Shibayama M, Suda J, Karino T, Okabe S, Takehisa T, Haraguchi K (2004) Structure and dynamics of poly(N-isopropylacrylamide)-clay nanocomposite gel. Macromolecules 37:9606–9612
121. Shinohara Y, Kishimoto H, Yagi N, Amemiya Y (2010) Microscopic observation of aging of silica particles in unvulcanized rubber. Macromolecules 43:9480–9487
122. Potts JR, Dreyer DR, Bielawski CW, Ruoff RS (2011) Graphene-based polymer nanocomposites. Polymer 52:5–25
123. Yoonessi M, Gaier JR (2010) Highly conductive multifunctional graphene polycarbonate nanocomposites. ACS Nano 4:7211–7220
124. Haraguchi K, Li HJ, Matsuda K, Takehisa T, Elliott E (2005) Mechanism of forming organic/ inorganic network structures during in-situ free-radical polymerization in PNIPA-clay nanocomposite hydrogels. Macromolecules 38:3482–3490
125. Haraguchi K, Takehisa T, Fan S (2002) Effects of clay content on the properties of nanocomposite hydrogels composed of poly(N-isopropylacrylamide) and clay. Macromolecules 35:10162–10171
126. Haraguchi K, Uyama K, Tanimoto H (2011) Self-healing in nanocomposite hydrogels. Macromol Rapid Commun 32:1253–1258
127. Okay O, Oppermann W (2007) Polyacrylamide-clay nanocomposite hydrogels: rheological and light scattering characterization. Macromolecules 40:3378–3387
128. Ren HY, Zhu M, Haraguchi K (2011) Characteristic swelling-deswelling of polymer/clay nanocomposite gels. Macromolecules 44:8516–8526
129. Wang Q, Mynar JL, Yoshida M, Lee E, Lee M, Okuro K, Kinbara K, Aida T (2010) High-water-content mouldable hydrogels by mixing clay and a dendritic molecular binder. Nature 463:339–343
130. Takeno H, Nakamura W (2013) Structural and mechanical properties of composite hydrogels composed of clay and a polyelectrolyte prepared by mixing. Colloid Polym Sci 291:1393–1399
131. Endo H, Miyazaki S, Haraguchi K, Shibayama M (2008) Structure of nanocomposite hydrogel investigated by means of contrast variation small-angle neutron scattering. Macromolecules 41:5406–5411
132. Varga Z, Bota A, Goerigk G (2006) Localization of dibromophenol in DPPC/water liposomes studied by anomalous small-angle X-ray scattering. J Phys Chem B 110:11029–11032
133. Stuhrmann HB (1985) Resonance scattering in macromolecular structure research. Adv Polym Sci 67:123–163
134. Goerigk G, Huber K, Mattern N, Williamson DL (2012) Quantitative anomalous small-angle X-ray scattering—the determination of chemical concentrations in nano-scaled phases. Eur Phys J Spec Top 208:259–274
135. Barnardo T, Hoydalsvik K, Winter R, Martin CM, Clark GF (2009) In situ double anomalous small-angle X-ray scattering of the sintering and calcination of sol–gel prepared yttria-stabilized-zirconia ceramics. J Phys Chem C 113:10021–10028
136. Bota A, Goerigk G, Drucker T, Haubold HG, Petro J (2002) Anomalous small-angle X-ray scattering on a new, nonpyrophoric Raney-type Ni catalyst. J Catal 205:354–357
137. Okuda H, Fukumoto T, Saida J, Ochiai S, Sasaki S, Masunaga H (2008) Anomalous small-angle scattering from nanoquasicrystalline precipitates in Zr80Pt20 ribbons. J Appl Crystallogr 41:675–679
138. Polizzi S, Riello P, Goerigk G, Benedetti A (2002) Quantitative investigations of supported metal catalysts by ASAXS. J Synchrotron Radiat 9:65–70
139. Rasmussen FB, Molenbroek AM, Clausen BS, Feidenhans R (2000) Particle size distribution of an Ni/SiO2 catalyst determined by ASAXS. J Catal 190:205–208

140. Pabit SA, Meisburger SP, Li L, Blose JM, Jones CD, Pollack L (2010) Counting ions around DNA with anomalous small-angle X-ray scattering. J Am Chem Soc 132:16334–16336

141. Sakou M, Takechi A, Handa M, Shinohara Y, Amemiya Y, Masunaga H, Ogawa H, Yagi N, Sakurai K, Akiba I (2011) Anomalous small-angle X-ray scattering study on aggregation of a block copolymer in a selective solvent. J Phys Conf Ser 272:012022

142. Varga Z, Berenyi S, Szokol B, Orfi L, Keri G, Petak I, Hoell A, Bota A (2010) A closer look at the structure of sterically stabilized liposomes: a small-angle X-ray scattering study. J Phys Chem B 114:6850–6854

143. Goerigk G, Mattern N (2010) Spinodal decomposition in Ni-Nb-Y metallic glasses analyzed by quantitative anomalous small-angle X-ray scattering. J Phys Conf Ser 247:012022

144. Gutsche A, Daikeler A, Guo X, Dingenouts N, Nirschl H (2014) Time-resolved SAXS characterization of the shell growth of silica-coated magnetite nanocomposites. J Nanoparticle Res 16:2475

145. Yan S, Wu Z, Yu H, Gong Y, Tan Y, Du R, Chen W, Xing X, Mo G, Chen Z, Cai Q, Sun D (2014) Time-resolved small-angle X-ray scattering study on the growth behavior of silver nanoparticles. J Phys Chem C 118:11454–11463

146. Adelsberger J, Metwalli E, Diethert A, Grillo I, Bivigou-Koumba AM, Laschewsky A, Muller-Buschbaum P, Papadakis CM (2012) Kinetics of collapse transition and cluster formation in a thermoresponsive micellar solution of P(S-b-NIPAM-b-S) induced by a temperature jump. Macromol Rapid Commun 33:254–259

147. Lu J, Bates FS, Lodge TP (2013) Chain exchange in binary copolymer micelles at equilibrium: confirmation of the independent chain hypothesis. ACS Macro Lett 2:451–455

148. Nishi K, Asai H, Fujii K, Han Y-S, Kim T-H, Sakai T, Shibayama M (2014) Small-angle neutron scattering study on defect-controlled polymer networks. Macromolecules 47:1801–1809

149. Takenaka M, Takeno H, Hasegawa H, Saito S, Hashimoto T, Nagao M (2002) Viscoelastic effects in relaxation processes of concentration fluctuations in dynamically asymmetric polymer blends. Phys Rev E 65:021806

150. Takenaka M, Takeno H, Hashimoto T, Nagao M (2003) Viscoelastic effects in dynamics of concentration fluctuations in dynamically asymmetric polymer blends. J Appl Crystallogr 36:642–645

151. Takenaka M, Takeno H, Hashimoto T, Nagao M (2006) Viscoelastic effects on early stage of spinodal decomposition in dynamically asymmetric polymer blends. J Chem Phys 124:104904

152. Kyriakos K, Philipp M, Adelsberger J, Jaksch S, Berezkin AV, Lugo DM, Richtering W, Grillo I, Miasnikova A, Laschewsky A, Müller-Buschbaum P Papadakis CM (2014) Cononsolvency of water/methanol mixtures for PNIPAM and PS-b-PNIPAM: pathway of aggregate formation investigated using time-resolved SANS. Macromolecules 47:6867–6879

153. Lund R, Willner L, Richter D, Lindner P, Narayanan T (2013) Kinetic pathway of the cylinder-to-sphere transition in block copolymer micelles observed in situ by time-resolved neutron and synchrotron scattering. ACS Macro Lett 2:1082–1087

154. Takenaka M, Miyazawa M, Miyajima T, Hashimoto T (2005) Synchrotron small-angle X-ray scattering of relaxation process in a nonentangled diblock copolymer. Macromolecules 38:8481–8485

155. Takeno H, Nagao M, Nakayama Y, Hasegawa H, Hashimoto T, Seto H, Imai M (1997) High pressure cell for small-angle neutron and light scattering studies of phase transitions in complex liquids. Polym J 29:931–939

156. Blazek J, Gilbert EP (2010) Effect of enzymatic hydrolysis on native starch granule structure. Biomacromolecules 11:3275–3289

157. Yaghmur A, Rappolt M (2012) Structural characterization of lipidic systems under nonequilibrium conditions. Eur Biophys J 41:831–840

158. Mao Y, Burger C, Li X, Hsiao BS, Mehta AK, Tsou AH (2012) Time-resolved synchrotron X-ray scattering study on propylene–1-butylene random copolymer subjected to uniaxial stretching at high temperatures. Macromolecules 45:951–961

159. Meins T, Hyun K, Dingenouts N, Fotouhi Ardakani M, Struth B, Wilhelm M (2012) New insight to the mechanism of the shear-induced macroscopic alignment of diblock copolymer melts by a unique and newly developed Rheo–SAXS combination. Macromolecules 45:455–472
160. Stribeck N, Zeinolebadi A, Ganjaee Sari M, Botta S, Jankova K, Hvilsted S, Drozdov A, Klitkou R, Potarniche C-G, Christiansen JD, Ermini V (2012) Properties and semicrystalline structure evolution of polypropylene/montmorillonite nanocomposites under mechanical load. Macromolecules 45:962–973
161. Arleth L, Ashok B, Onyuksel H, Thiyagarajan P, Jacob J, Hjelm RP (2005) Detailed structure of hairy mixed micelles formed by phosphatidylcholine and PEGylated phospholipids in aqueous media. Langmuir 21:3279–3290
162. Jl E, Levitz P, Espinat D, Jestin J, Jrm G, Grillo I, Lc B (2011) Insight into asphaltene nanoaggregate structure inferred by small angle neutron and X-ray scattering. J Phys Chem B 115:6827–6837
163. Hirai M (2007) Feasibility of complementary use of neutron and X-ray scattering techniques in research of lipid mixtures. J Phys Conf Ser 83:012003
164. Motokawa R, Suzuki S, Ogawa H, Antonio MR, Yaita T (2012) Microscopic structures of tri-n-butyl phosphate/n-octane mixtures by X-ray and neutron scattering in a wide q range. J Phys Chem B 116:1319–1327
165. Ogino Y, Fukushima H, Matsuba G, Takahashi N, Nishida K, Kanaya T (2006) Effects of high molecular weight component on crystallization of polyethylene under shear flow. Polymer 47:5669–5677
166. Ohnuma M, Suzuki J, Ohtsuka S, Kim SW, Kaito T, Inoue M, Kitazawa H (2009) A new method for the quantitative analysis of the scale and composition of nanosized oxide in 9Cr-ODS steel. Acta Mater 57:5571–5581
167. Schmiele M, Schindler T, Westermann M, Steiniger F, Radulescu A, Kriele A, Gilles R, Unruh T (2014) Mesoscopic structures of triglyceride nanosuspensions studied by small-angle X-ray and neutron scattering and computer simulations. J Phys Chem B 118:8808–8818
168. Sun YS, Jeng US, Huang YS, Liang KS, Lin TL, Tsao CS (2006) Complementary SAXS and SANS for structural characteristics of a polyurethethane elastomer of low hard-segment content. Phys B Condens Matter 385:650–652
169. Zemb T, Diat O (2010) What can we learn from combined SAXS and SANS measurements of the same sample containing surfactants? J Phys Conf Ser 247:012002
170. Oba Y, Koppoju S, Ohnuma M, Kinjo Y, Morooka S, Tomota Y, Suzuki J, Yamaguchi D, Koizumi S, Sato M, Shiraga T (2012) Quantitative analysis of inclusions in low carbon free cutting steel using small-angle X-ray and neutron scattering. ISIJ Int 52:457–463
171. Haas S, Plivelic TS, Dicko C (2014) Combined SAXS/UV–vis/Raman as a diagnostic and structure resolving tool in materials and life sciences applications. J Phys Chem B 118:2264–2273
172. Ratri PJ, Tashiro K (2013) Application of the simultaneous measurement system of WAXD, SAXS and transmission FTIR spectra to the study of structural changes in the cold- and melt-crystallization processes of trans-1,4-polyisoprene. Polym J 45:1019–1026
173. Gagin A, Allen AJ, Levin I (2014) Combined fitting of small- and wide-angle X-ray total scattering data from nanoparticles: benefits and issues. J Appl Crystallogr 47:619–629
174. Eremin RA, Kholmurodov K, Petrenko VI, Rosta L, Avdeev MV (2013) Effect of the solute–solvent interface on small-angle neutron scattering from organic solutions of short alkyl chain molecules as revealed by molecular dynamics simulation. J Appl Crystallogr 46:372–378
175. McDermott AG, Larsen GS, Budd PM, Colina CM, Runt J (2011) Structural characterization of a polymer of intrinsic microporosity: X-ray scattering with interpretation enhanced by molecular dynamics simulations. Macromolecules 44:14–16
176. Matsumura Y, Kataoka K (2009) Preclinical and clinical studies of anticancer agent-incorporating polymer micelles. Cancer Sci 100:572–579

177. Yang YQ, Zhao B, Li ZD, Lin WJ, Zhang CY, Guo XD, Wang JF, Zhang LJ (2013) pH-sensitive micelles self-assembled from multi-arm star triblock co-polymers poly(epsilon-caprolactone)-b-poly(2-(diethylamino)ethyl methacrylate)-b-poly(poly(ethylene glycol) methyl ether methacrylate) for controlled anticancer drug delivery. Acta Biomater 9:7679–7690
178. Yang YQ, Zheng LS, Guo XD, Qian Y, Zhang LJ (2011) pH-sensitive micelles self-assembled from amphiphilic copolymer brush for delivery of poorly water-soluble drugs. Biomacromolecules 12:116–122
179. Sanada Y, Akiba I, Sakurai K, Shiraishi K, Yokoyama M, Mylonas E, Ohta N, Yagi N, Shinohara Y, Amemiya Y (2013) Hydrophobic molecules infiltrating into the poly(ethylene glycol) domain of the core/shell interface of a polymeric micelle: evidence obtained with anomalous small-angle X-ray scattering. J Am Chem Soc 135:2574–2582

Quasielastic Neutron Scattering: An Advanced Technique for Studying the Relaxation Processes in Condensed Matter

14

Madhusudan Tyagi and Suresh M. Chathoth

Contents

M. Tyagi
NIST Center for Neutron Research, Gaithersburg, MD, USA

Department of Materials Science and Engineering, University of Maryland, College Park, MD, USA
e-mail: mtyagi@nist.gov

S.M. Chathoth (✉)
Department of Physics and Materials Science, City University of Hong Kong, Kowloon Tong, Hong Kong
e-mail: smavilac@cityu.edu.hk

1   Definition of the Topic

Quasi-elastic neutron scattering (QENS) is a part of more general inelastic neutron scattering and is a very powerful technique to explore the motions in biomolecules, polymers, simple liquids, alloy melts, and soft matter in general. In this chapter, we will discuss basic theoretical aspects of QENS, instrumentation, types of motion in liquids and solids, understanding these motions from the QENS data, and recent studies using QENS.

2   Overview

The QENS is a versatile technique to study the relaxation processes in the condensed materials, particularly in liquids. This technique typically uses cold neutrons as the energy of the cold neutrons is in a similar range with relaxation process in liquids and the wavelength is of the order of the interatomic distance in condensed materials. The QENS techniques can provide much more information on the relaxation processes (motions) as compared to other techniques, e.g., dielectric spectroscopy, nuclear magnetic resonance, and tracer diffusion measurements. The QENS technique is particularly helpful for understanding the microscopic dynamics of soft and biomaterials since these materials contain a large number of hydrogen atoms, and the hydrogen atom is very sensitive to neutron scattering due to a large scattering cross section.

Neutron scattering offers not only QENS but also other scattering techniques like diffraction, inelastic, reflectometry, triple axis, small-angle scattering, and neutron imaging. However, facilities available for neutron scattering research are very few in the world. The production of neutrons is very expensive and typically requires either a nuclear reactor or a target-based source and also detection of neutrons needs materials like ^{3}He, which is rare on earth, are the reason for it. Over the last few decades, few neutron scattering facilities like Spallation Neutron Source, National Institute of Standards and Technology (NIST) Center for Neutron Research (NCNR), Australian Neutron Scattering Facility, Forschungsreaktor Munchen (FRM)-II Germany, ISIS-UK, and JAPARK at Japan have been built. Also, there has been tremendous improvement in neutron scattering instrumentations, particularly building of new backscattering and spin echo spectrometers in the abovementioned facilities. At present relaxation process in a time scale of 0.1 ps–350 ns can be measured using neutron scattering.

In the beginning, QENS was mainly used to study the diffusion in simple liquids and hydrogen diffusion, in metals, etc. At present the QENS technique has been

used in many fields of science ranging from colloids, polymers, ionic liquids, hydrogen storage, food processing, biotechnology, and environments. In this chapter we will provide an overview of basic theoretical understanding of QENS, concepts of instrumentation, data analysis, identification of transport mechanism from QENS data, and recent research results using QENS.

3   Introduction

Atomic/molecular relaxation processes in condensed materials, particularly the long-range atomic/molecular diffusion process, are very important for many technological developments. For example, crystal growth from the melts, alloy design, nano-device fabrications, etc., require the knowledge of diffusion processes. In the field of basic science, glass transition is controlled by diffusion, and it is still an unresolved problem in condensed matter physics. Particularly, a reason for several-fold increase in the diffusivity of fragile glass-forming liquids in a short interval of temperature is not yet understood. Understanding the function of protein, DNA, and RNA is extremely important in life science, which is controlled by diffusion process. Therefore, accurately measuring the diffusion of atoms/molecules is unambiguously important in many fields of science and technology.

The atomic/molecular diffusion in condensed materials can be measured by several techniques, dynamic light scattering (DLS) [1], X-ray photon correlation spectroscopy (XPCS) [2], nuclear magnetic resonance (NMR) [3], tracer diffusion (TD) [4], dielectric spectroscopy (DS) [5], and QENS [6]. However, QENS is a unique technique; by this technique not only the diffusion coefficients of atoms/molecules in condensed materials can be measured, but also it provides detailed information on the atomic/molecular transport mechanism [7]. None of the abovementioned techniques other than the QENS are capable of providing detailed information about transport mechanisms in the condensed materials.

The DLS can only be used to study transparent or nearly transparent liquids, and DS and NMR cannot be used to study metallic liquids. The dynamic range of XPCS technique is few milliseconds to ten thousand seconds, and this technique is mainly used to understand the relaxation process in glassy materials. The main advantage of QENS is that the momentum transfer range in the interatomic distance can be measured which allows to distinguish between different types of atomic/molecular transport mechanism in liquids. For example, QENS can distinguish between Brownian and jump-diffusion processes based on the observed momentum transfer dependence of relaxation time. In the case of jump-diffusion process, in-cage rattling process (β-relaxation) and long-range diffusion process (α-relaxation) can be separately analyzed from QENS data. Additionally, the residence time and jump length in the jump-diffusion process can also be calculated from a QENS experiment. Measurements of these quantities are not possible with any other techniques. Moreover, the intermediate scattering function derived from a QENS experiment can readily be calculated by molecular dynamics simulation or ab initio molecular dynamics simulation; hence, there is a close correlation between theory and

experiments which will help further in the understanding of the dynamic processes in condensed materials [8].

4   Theory of Quasi-Elastic Neutron Scattering

In a typical neutron scattering experiment, a beam of neutrons with a narrow, well-defined energy (or wavelength) distribution is focused onto the sample. The narrow energy distribution around the energy of interest is typically achieved by monochromating the incident beam which is accomplished by many different ways depending on the instrument design. When the monochromatized incident beam of neutrons collides with the atoms in the sample, the strong nuclear interaction scatter the neutrons in various directions. The crucial information about the dynamics (or structure) in the sample can be obtained as this scattering phenomena changes energy distribution of the scattered neutrons with respect to the initial distribution. Typically, if the time scale of motions matches the time range of the instrument, then a strong interaction between neutrons and atoms of material under consideration is expected. On the other hand, if the motions are too slow, then most of the neutrons scatter elastically without much dynamic interaction with atoms. The dynamic range offered by an instrument defines how fast motions can be probed with respect to the instrumental resolution, which is the slowest possible measurement on an instrument. Typically, to match the time scales of atomic motions in material under consideration with the instrument, either temperature, pressure, or some other external variable is varied. There are two kinds of inelastic scattering that are typically observed in soft matter. The first is called inelastic scattering in which the shift in scattered peak from the incident energy indicates the energy of the excitation. This kind of scattering is typically observed in materials that have well-defined energy excitations, e.g., methyl group rotations in crystalline materials. Purely inelastic scattering is typically not observed in soft materials. The second type of scattering appears as broadening of the incident energy distribution over the elastic scattering and is typically referred to as QENS. This is the most relevant type of scattering that is observed in soft materials.

Neutrons possess a number of important properties that makes the neutron scattering technique so powerful in exploring motions particularly in soft matter physics. First, the wavelength of most facility produced neutrons range between 1 Å and 10 Å, which overlaps nicely with typical interatomic or intermolecular distances in soft organic materials. The length scale of the motions over which a motion is probed by a neutron depends on the wavelength of the neutron and is given by the scattering vector $Q = 4\pi\sin(\theta)/\lambda$. In the above expression, Q is the momentum transfer of neutron, θ is the scattering angle, and λ is the neutron wavelength. The momentum transfer Q is inversely related to the length scales probed by the neutrons. Accesses length scales by an instrument depend on a number of parameters; typically instruments probe scattering over a range of angles which provide Q range between $0.1 \text{ Å}^{-1} < Q < 3.0 \text{ Å}^{-1}$. In real space this will correspond to length scales approximately 2 Å–60 Å, well suited for characterizing

local atomic and molecular motions in soft materials. The second property of neutrons that makes them useful for measuring soft matter dynamics is their energies. If we calculate energies corresponding to the neutron wavelengths mentioned above, cold neutrons will have energies of the order of a few meVs. This energy is on the same order of magnitude as the activation energies for many of the solid state excitations, molecular relaxations, and dynamic processes that occur in soft materials. This simply means when a neutron gains or loses energy from a dynamic interaction with the sample, the change in the energy of the neutron is a significant fraction of the initial neutron energy and, therefore, easy to measure with certainty. In addition, due to their low energies (e.g., in comparison to X-rays), neutrons are typically nondestructive and sample is not altered or destroyed during or after the experiment which is very important particularly for biological samples.

The neutrons are either produced by nuclear fission (splitting of nucleus of heavy atoms) or spallation process (high-energy particles hit on heavy nucleus) and have high energies. The high-energy neutrons have to slow down to be used for QENS experiments because the energy of neutron should be comparable to the energy of diffusion process in the condensed materials. As we mentioned above, the energy of diffusion process in liquids is of the order of few meV. The cold neutron can be obtained by passing the high-energy neutrons through helium kept at 25 K (moderator), and outgoing neutrons will have an energy centered at 25 meV. The cold neutrons are nonrelativistic particles so the energy-momentum relationship is

$$E = \frac{p^2}{2m_n} \tag{14.1}$$

where p is the momentum and m_n is the neutron mass. Using de Broglie and Plank's equation $p = \hbar k$ and $k = 2\pi/\lambda$, the wavelength of a thermal neutron can be written as

$$\lambda = \frac{\hbar}{\sqrt{2\pi m_n E}} \tag{14.2}$$

For $E = k_B T = 300$ K, $\lambda = 1.8$ Å. As we can see, the thermal energy of the neutrons is comparable with the energy of vibrational and diffusional energy in condensed materials, and the wavelength is comparable with the interatomic distance in condensed materials.

Every element in the periodic table has a unique value of coherent and incoherent cross section. These values are available on the NIST neutron scattering center webpage [9]. The intensity of scattered neutron in a neutron scattering experiment depends on the coherent and incoherent scattering cross section and determines which one will dominate the signal. For example, water contains one oxygen and two hydrogen atoms. The coherent cross section of oxygen is 4.23 b and incoherent cross section is nearly zero. For hydrogen, the coherent cross section is 1.75 b, but the incoherent cross section is 80.2 b. The macroscopic incoherent scattering cross section of 1 mol of water will heavily dominate the overall scattering cross section.

Fig. 14.1 A representation of total (coherent + incoherent) and incoherent scattering cross sections in a number of materials occurring in soft matter physics. As one can see hydrogen's incoherent scattering cross section dominates heavily
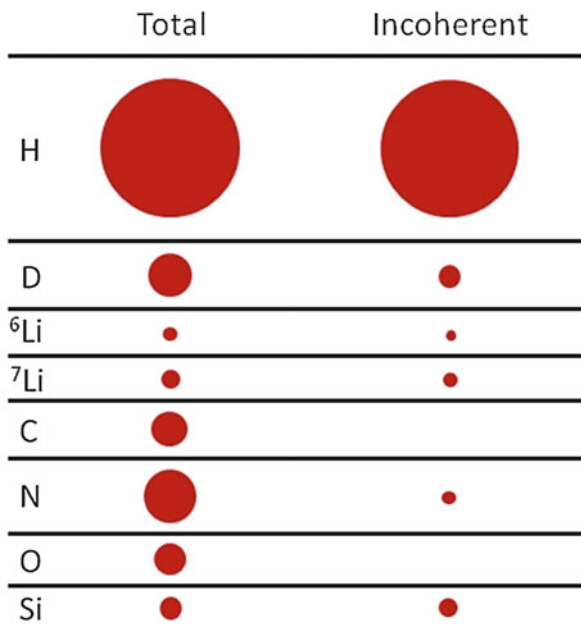
So in a neutron scattering experiment with water, the scattered intensity will mainly be due to incoherent scattering of hydrogen atoms. The incoherent cross section of hydrogen atoms is about 20 times larger than either coherent or incoherent neutron scattering cross section of any other element in the periodic table. This is the final reason why neutrons are ideal for measuring the dynamics in soft matter. This is shown schematically in Fig. 14.1 where the area of the circle represents the magnitude of the scattering cross section [10]. As the hydrogen cross section is much higher than other elements, in a typical experiment, incoherent scattering from hydrogen will dominate the overall measured signal. This is very useful because H dynamics are often difficult to quantify with complimentary optical and X-ray scattering techniques that are often insensitive to the lighter elements. The usefulness of neutron scattering is further enhanced by the fact that the isotopic substitution from hydrogen (H) to deuterium (D) greatly reduces this large scattering cross section. By selectively replacing certain H with D, one can study the dynamics isolated to a certain molecular group or component in a multicomponent systems (e.g., binary liquids or polymer blends). In biomolecular systems, substitution also helps in measuring dynamics of host and matrix indirectly where complete deuteration of either is not possible or too expensive, e.g., in case of hydrated proteins.

The total measured intensity in a neutron scattering experiment is a summation of incoherent and coherent intensities from the sample. For coherent scattering events, there is a spatial correlation between the scatterings from different atoms of the same type. These spatial correlations allow us to determine the pair-pair

correlation function, i.e., the spatial correlations between the different atoms of same type as a function of time and space. These correlations are often related with structures or the dynamics of such structures. For incoherent scattering, single particle is considered as there is no correlation between pairs of atoms. This kind of scattering leads to what is known as self-correlation functions. In this correlation function, the probability of finding the particle in a position after time t (defined by the energy exchange) is calculated. From the energy and angular dependence of the incoherent scattering, one can determine the time and length scale of the self-motions in soft matter. As most soft materials are hydrocarbons, their incoherent scattering is very strong and dominates the measured signal. If the pair correlation function is desired, then typically isotopic substitution is performed and hydrogens are replaced with deuterium that reduces incoherent scattering and coherent scattering can be enhanced and measured. Quasi-elastic neutron scattering is one of the most direct methods to quantify the time and length scales of soft matter dynamics in general.

In a QENS experiment, the quantities of interest are changes in energy and momentum transfers during the scattering process. The momentum transfer is directly measured from the angle of the scattering. To calculate the energy change of neutrons in a scattering process, the time-of-flight of the neutron from the sample to the detectors could be measured. The time-of-flight will be shorter if the neutrons gain energy or longer if the neutrons lose energy during the scattering process. The energy change and momentum transfer can be expressed in the form of double differential scattering cross section:

$$\frac{d\sigma}{d\Omega d\omega} \propto \frac{k_f}{k_i} S(Q, \omega) \tag{14.3}$$

k_f and k_i are scattered and incident wave vectors, respectively, and σ is the scattering cross section, $d\Omega$ is the solid angle, and $d\omega$ is the energy change [6]. The function $S(Q, \omega)$ is called the *dynamic structure factor* and it contains information on the dynamic processes of the sample within the resolution of the instruments. The $S(Q, \omega)$ are analyzed to get the dynamic information of the sample in a QENS experiments. The information contained in $S(Q, \omega)$ is function of momentum transfer (Q) and energy change in Q and ω space. To understand and better visualize the information contained in S(Q,ω), it can be converted to real space and time. The Q is related to real space by $d = 2\pi/Q$, where d is in length scale and energy is related to time so we can double Fourier transform the function $S(Q, \omega)$ to convert it to real space and time:

$$I(Q, t) = \hbar \int_{-\infty}^{+\infty} S(Q, \omega) e^{i\omega t} \, d\omega \tag{14.4}$$

$I(Q, t)$ is called intermediate scattering function. Further Fourier transforming in space $G(r, t)$ is the space Fourier transformation of $I(Q, t)$

$$G(r,t) = \frac{1}{(2\pi)^3} \int_{-\infty}^{\infty} I(Q,t)e^{-iQ.r}dQ \qquad (14.5)$$

$G(r, t)$ is called van Hove correlation function. The scattering from a sample can be due to incoherent or coherent process. So the function $G(r, t)$ that can be written as sum of $G(r,t) = G_d(r,t) + G_s(r, t)$ is called self-correlation function and $G_d(r, t)$ is called pair correlation function. $Gs(r, t)$ is the probability of finding the same particle at one point at $t = 0$ and at a later time t at the distance r. $G_d(r, t)$ is the probability for finding two different particles of same type at a position $R_i(0)$ and $R_j(t)$ separated by a distance r and at a time interval t. Following information about dynamic process can be obtained from incoherent and coherent scattering process and summarize what we discussed above:

Incoherent scattering: no spatial coherence in scattered neutrons and a constant
   intensity at different angle
   • Information on single particle:
   – Elastic incoherent scattering (Debye-Waller factor) : elastic incoherent struc-
     ture factor geometry of diffusive motion
   – Inelastic: diffusive dynamics (continuous, jump, rotations, jump length, res-
     idence time, and diffusion coefficients)
Coherent scattering: spatial coherence and intensity is due to superposition of
   scattered waves
   • Gives information on spatial correlations and collective motion:
   – Elastic: Where are the atoms? What are the shapes of objects?
   – Inelastic: Excitation spectrum – e.g., phonons.
   – Coherent QENS: Collective diffusion, shape fluctuation, α-relaxation.

   Therefore, single particle dynamics can be studied in materials that have dom-
inant incoherent scattering cross section. As we know that the hydrogen atom is the
strongest incoherent neutron scattering element in the periodic table, QENS is the
best technique for studying the diffusive dynamics in hydrogenated materials like
polymers, colloids, and biomaterials.

5   Types of Motions in Condensed Materials

Apart from the vibrational motions, atom/molecules in liquids move randomly due
to microscopic density (thermal) fluctuations. The random motion is influenced by
the density of the liquid. In the low-density liquids, particles hit and move randomly
on Brownian dynamics. However, as the density increases, atoms form cages by its
neighboring atoms. In such liquids atoms initially rattle in the cage formed by its
neighboring atoms for a short time and move to the next cage. This process is called
jump diffusion [11]. In liquids with even higher density, a group of atoms can move

together in the same fashion or collectively and has been observed recently. One of the advantages of QENS is that Brownian and the jump-diffusion process can be distinguished from the scattering data, and jump length and residence time (time in which atom rattled in the cage before it move to the next cage) can be calculated.

The diffusion process in liquids is stochastic, and therefore, atoms/molecules move randomly in all possible directions, and the energy change in the diffusion process is continuously distributed from nearly zero to few μeV volts. Therefore, unlike inelastic neutron scattering process (phonons or magnetic scattering), we do not observe any additional peak in the $S(Q,\omega)$ along with the elastic peak. Instead quasi-elastic broadening shows up over elastic peak. The QENS broadening of the elastic peak depends on the Q values, and the shape of the broadening can be in different functional form. In a purely Brownian dynamics, one observes a Lorentzian broadening of quasi-elastic width. In glass-forming and highly viscous liquids, the quasi-elastic broadening is rather complicated and can be described by Fourier transformed stretched-exponential function. By analyzing the momentum transfer dependence of the width of quasi-elastic spectra, details about atomic/molecular dynamics and microscopic transport mechanism in the sample can be obtained.

6 Designing of QENS Experiments

Every QENS spectrometer has its time window in which the dynamic process in the sample can be measured. The time window is defined by the wavelength and dynamic range accessible in the spectrometer. The typical time window of a chopper spectrometer is 0.05–10 ps and that of backscattering spectrometer is 50–5000 ps. So there should be an idea of time scale on which the dynamic process might be present in our sample for choosing the appropriate spectrometer. Sample size also matters in the QENS experiments. This is due to multiple scattering processes. Multiple scattering refers to the interaction of neutron with more than one atom before leaving the sample. To avoid multiple scattering, the thickness of the sample is chosen in a way that 90 % of neutrons are transmitted through the sample. By considering macroscopic coherent, incoherent, and absorption cross sections of the sample, the transmission coefficient can be calculated. For example, water is a very commonly studied material with QENS and water contains oxygen and two hydrogen atoms.

The transmission, T, relates to thickness, t, as

$$T = \exp(-\Sigma t)$$

$\Sigma \rightarrow$ is the macroscopic cross section: $\Sigma = n\sigma$.
n is the number density (number of atoms in a unit volume) (atoms/cm^3).
$\sigma \rightarrow$ is the microscopic cross section (barns/atom) 10^{-24}cm^2.

$$n = \frac{1\,\text{gm}}{\text{cm}^3} \times \frac{1\,\text{mole}}{18\,\text{gm}} \times \frac{6.02 \times 10^{23}}{\text{mole}} = \frac{3.34 \times 10^{22}}{\text{cm}^3}$$

$$\sigma = 2 \times 80 \times 10^{-24}\,\text{cm}^2$$

$$\Sigma = \sigma n = \frac{5.34}{\text{cm}}$$

Sample thickness, $t = \frac{-\ln(0.9)}{5.34} = 0.2\,\text{mm}$.

So the thickness of water sample for 90 % scattering should be 0.2 mm.

7 Instrumentation

7.1 Choosing the Right Instrument

The dynamic processes and relaxations that occur in soft matter span a broad range of time and length scales. To optimize instrument characteristics and functionality, generally, different instruments are designed to cover different ranges of time and length scales. A classic diagram showing time and energy against length scales is shown in Fig. 14.2 [10]. The three neutron scattering techniques that have been used extensively for soft materials include neutron spin echo spectroscopy (NSE) [12], backscattering spectroscopy (BS) [13], and time-of-flight (TOF) spectroscopy [14]. The main difference among the three techniques is the time and length scale probed by these instruments. The NSE is sensitive to the slowest motions. It is most sensitive to dynamic processes on a time scale of 100 ns to 0.05 ns, placing it in the micro- to nanosecond range. As larger objects tend to move slower, NSE is also sensitive to the longer range motions, and length scales on the order of 0.1–25 nm are covered. At these times and length scales, NSE can be used to monitor diffusive motions of membranes, polymer chains, or large scale collective motions that span across tens to hundreds of atoms. The BS spectrometers are sensitive to slightly faster and shorter range motions, e.g., time range of 5 ns to 0.01 ns and the length scales of about 3 Å to about 3 nm. In soft materials, these often include side group motions, methyl rotations, or crank shaft motions of chain segments and diffusion of simple liquids. The TOF spectroscopy is sensitive to the fastest dynamics of the three instruments, that is, to dynamics on the order of picoseconds and faster and over comparable length scales as in the BS instrument. At these time scales, the dynamical processes probed in TOF experiments are typically atomic or molecular vibrations and diffusion of liquids at higher temperatures. The TOF is used heavily to probe vibrational and high-frequency relaxation processes of the hydrogenous molecular groups in the sample.

QENS experiments require access to a neutron scattering facility as production of neutrons requires a reactor or spallation source. While there are only a handful of these in most major countries, access is often encouraged, and most users find the facilities open to the scientific and research communities in general. In the United
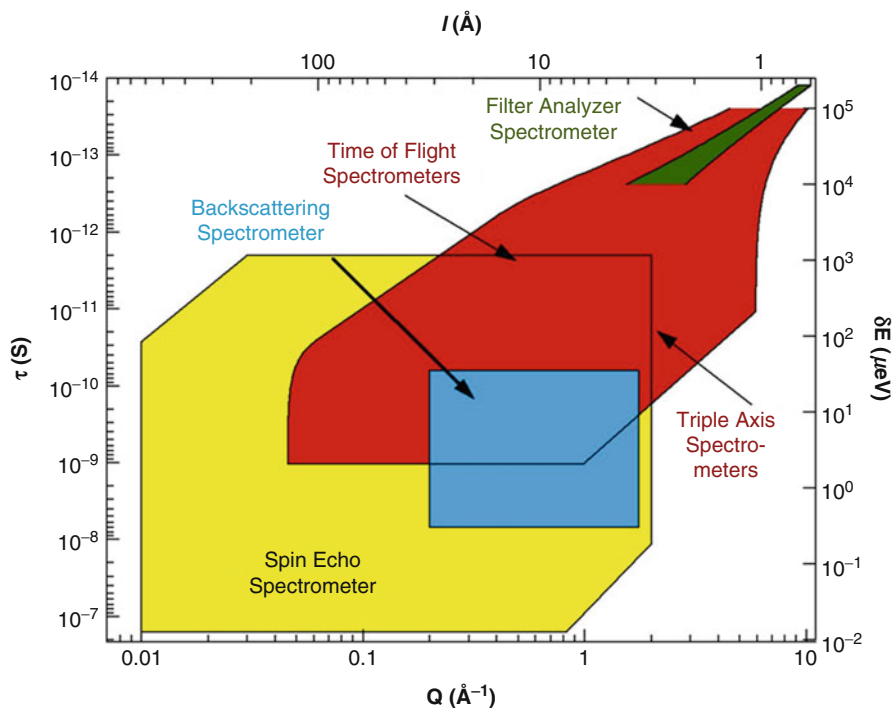
Fig. 14.2 A classic map showing time and length scales probed by different instruments for quasi-elastic neutron scattering. As can be seen NSE probes slowest and longer length scales, while TOF probes relatively faster and shorter length-scale motions [10]. For more details, check www.ncnr.nist.gov

States, two major neutron facilities are NCNR [10] and Spallation Neutron Source (SNS) [15]. In Europe, major facilities are Institut Laue-Langevin (ILL) [16] at Grenoble and Laboratoire Leon Brillouin (LLB) Saclay [17] at France, FRM II [18] in Munich, Germany, and European Spallation Source (ESS) at Lund [19], Sweden. All these facilities offer a number of NSE, BS and TOF spectrometers, which are typically used to explore the motions in soft materials and under confinement. Below we describe details about instrumentation.

7.2 Neutron Spin Echo Spectrometer

The neutron spin echo technique exploits neutron's spin and magnetic moment in a magnetic field. Polarized neutrons travel through two symmetric magnetic fields before and after the sample. At the sample a π spin flip occurs by a flipper. If the scattering process is strictly elastic, the Larmor precession angles in the two fields are equal and opposite, so that full polarization is recovered, irrespective of the initial neutron energy distribution [12]. Quasi-elastic scattering with the sample
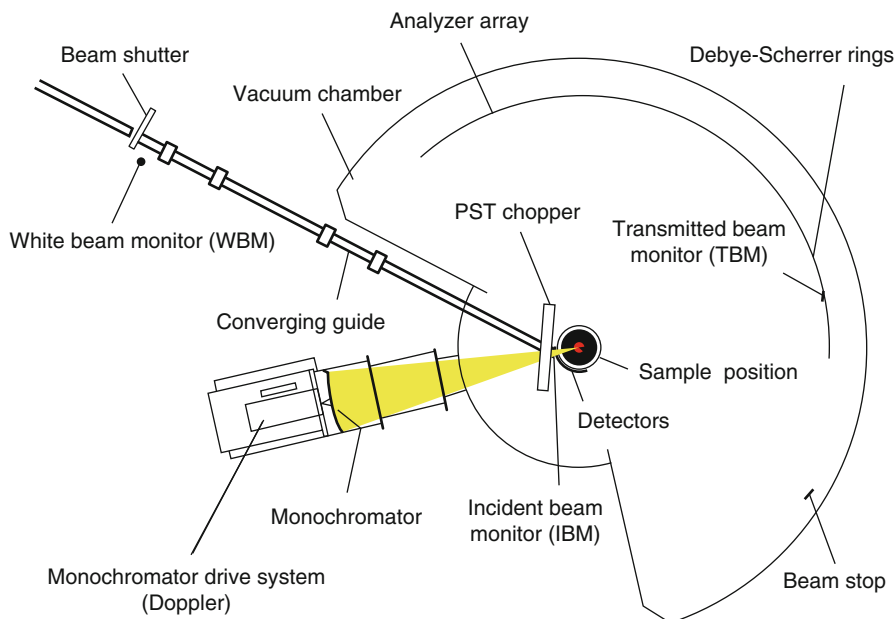
Fig. 14.3 A schematic representation of the NIST high-flux backscattering spectrometer [10, 13]. Typical BS spectrometers follow the same layout [20]

leads to a change in the neutron energy, resulting in a decrease in the polarization. With the manipulation of the neutron spin, NSE spectrometer directly measures the intermediate function S(Q,t) by scanning the magnetic fields in the coils and measuring the polarization. Measuring the scattering function directly in the time domain is a major advantage as modeling of dynamics is much easier in time domain in comparison to frequency domain where typically Fourier transformation is needed to convert the data to time domain (see below for more details). NSE typically is optimized to measure coherent scattering, and therefore, most studies on NSE deal with measurements of pair correlation functions in systems such as polymers, glass-forming liquids, and membranes. However, incoherent scattering can also be resolved by relatively longer counting times and can be directly compared to incoherent scattering measured on BS and TOF.

7.3 Backscattering Spectrometer

The BS spectrometer is an inverse geometry spectrometer where the final energy of neutrons is fixed. The details of the high-flux backscattering spectrometer (HFBS) installed at NIST are described in Fig. 14.3 [13]. A beam of neutrons travels through the converging guide and is reflected off of a phase space transformation chopper (PST), toward a monochromator.

The role of PST chopper is to increase flux at the desired wavelength (6.27 Å for Si(111) crystals) and deflect the enhanced beam toward the monochromator. The monochromator selects only the desired wavelength neutrons and focuses them to sample position. This is made possible by rotating PST by 180° in the meantime and allowing neutrons to pass through an open section. When the neutrons hit the sample, they scatter at different angles into the Debye-Scherrer ring of analyzers (made of the same material as monochromator). These analyzers reflect only those neutrons with a wavelength of 6.27 Å back toward a bank of ^{3}He detectors that resides just behind and slightly above the sample position. As the neutron optics for HFBS spectrometer is designed for 6.27 Å neutrons, only elastically scattered neutrons reach the detectors when the monochromator is static. This mode of the instrument is generally used to probe phase transitions and also to access overall mobility in samples and is popularly known as "fixed window scan" or "elastic scans." To access more details about the dynamics, one can oscillate the monochromator back and forth relative to the incident neutron beam. This Doppler shifts the reflected neutrons with a band of incident energies around energy corresponding to 6.27 Å. If the frequency and stroke of the Doppler drive oscillation are known, it is possible to calculate the broadened energy distribution of the Doppler-shifted, initially monochromatic neutron beam. However, only those Doppler-shifted neutrons that change back to their original incident 6.27 Å wavelength after scattering are reflected off of the analyzers and into the detectors. From this it is possible to determine the energy distribution of the scattered neutrons.

The energy resolution offered by HFBS is about 0.85 μeV FWHM, which means motions faster than 205 MHz can be explored by the HFBS spectrometer; slower motions appear as static and show up as elastic line. The maximum energy window defined by Doppler frequency is ± 36 μeV. All scattering events outside of the energy window, associated with fast relaxation processes, appear as background under the scattering spectrum. The other two major backscattering spectrometers that employ the concept of PST chopper are located at ILL [20], France, and FRM II [21], Munich, Germany. These are reactor-based BS spectrometers like HFBS at NIST. The energy resolution is somewhat similar for BS spectrometer at ILL, while the one at FRM II has slightly better resolution at 0.65 μeV.

Another backscattering spectrometer has been installed at the spallation neutron source at Oak Ridge. BASIS [22] is the first spallation source-based backscattering spectrometer that utilizes silicon crystals. It features a long primary path flight path and S(111) crystals just like HFBS with a near backscattering angle of 88°. The instrumental resolution has been controlled by introducing the elastic deformation of the crystals similar to reactor-based backscattering spectrometers. BASIS offers slightly broader resolution when compared with reactor-based BS spectrometers (3.5 μeV) but also offers much broader accessible dynamic range of ±100 μeV which can be extended to ±200 μeV under some conditions. The BASIS instrument is an excellent addition to cover the dynamic range gap that occurs when a typical BS spectrometer such as HFBS and a typical time-of-flight spectrometer such as DCS at NIST are employed.

7.4 Time-of-Flight Spectrometer

The TOF spectrometer is based on the concept of measuring the flight time of neutron. It operates on the principle that when scattered neutrons gain energy, they speed up, while neutrons slow down when they lose energy, and by measuring this accurately energy distribution can be established. A schematic in Fig. 14.4 depicts how a typical TOF spectrometer operates (taken from DCS spectrometer at NIST). The neutron beam enters a filter that only allows neutrons of a well-defined wavelength range to pass through. This filtered beam of neutrons then goes into a "chopper" that periodically releases pulses of neutrons onto the sample. The distance from the chopper to the sample and then from the sample to the detectors is accurately known. Since the energy or the speed of the incident beam of neutrons is known (defined by the chopper system), it is straightforward to predict how long it should take a given pulse of neutrons to leave the chopper, scatter from the sample elastically, and then reach the detector. If this time interval has changed, then neutrons have exchanged their energies with the sample. As Fig. 14.4 shows, there are a number of detectors equidistant from the sample, spread out in a semicircle which allows the dynamics to be probed over a large Q range. Typically, by varying the incident neutron wavelength, desired resolution can be chosen which typically falls in the range of 20–600 μeV (full width at half maximum). Though the Q range in most TOF spectrometers depend on the wavelength of the neutron, most TOF spectrometers offer Q range comparable to BS for soft matter studies.
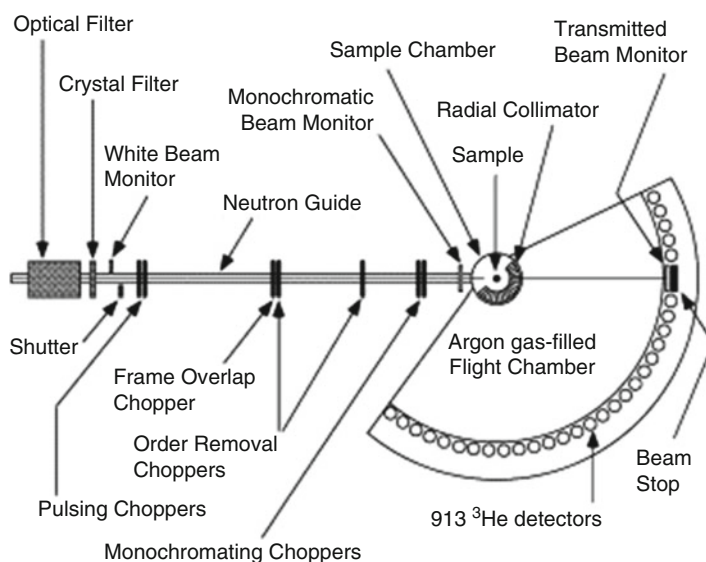
Fig. 14.4 A schematic representation of disk chopper spectrometer (Reprinted with permission from [14])

8   Understanding QENS Data

The fixed window scan (FWS) or the elastic scans are easiest to analyze and interpret as simply all scattered neutrons are counted as a function of an external parameter, e.g., temperature or pressure. A first-order phase transition shows up like a step in elastic intensity. If a relatively smeared change in elastic intensity is observed, this typically means that neutrons are interacting strongly with the sample, and therefore dynamics is well suited for BS time scales in that, e.g., temperature range. In order to understand the details about molecular motions under investigation, it is necessary to model the Q and T dependence of the observed QENS data. As we mentioned above, Q and ω dependence of the scattered neutrons contain all the spatial and temporal characteristics information of the dynamics that fall within the energy and Q resolution of the spectrometer. Most QENS measurements in soft materials focus on the incoherent neutron scattering given that the incoherent cross section dominates the scattering for hydrogenous materials and, therefore, provide self-correlation function of the hydrogens. This measured dynamic structure factor $S(Q,\omega)$ or $S(Q,t)$ must be normalized properly (discussed below) before being modeled suitably. The process of choosing an appropriate model for the motion is beyond the scope of this chapter. However, there are several textbooks dedicated to this subject; see, e.g., Refs. [6] and [23]. In the following we present a few simple models which are typically used to characterize simple motions in polymers and simple liquids.

8.1   Reduction of QENS Data

Following procedures are normally applied to get $S(Q,\omega)$ of the sample which are corrected for instrument factors and container scattering.

(a) *Monitor* normalization: For certain QENS experiments, the absolute values of intensity from different samples may need to be compared. As the neutron flux either from a reactor or spallation source varies with time, incoming neutron flux has to be normalized for such studies. This is done by measuring total count of neutrons before hinting the sample. A beam monitor is placed in front of the sample to count the total flux of incoming neutrons that hit the samples, and the total counts of the monitor are normalized with the detector counts.

(b) *Vanadium normalization (detector efficiency correction):* The efficiency of detectors may be different, and correcting the detector efficiently is done by normalizing the scattered data from pure vanadium having geometry similar to the sample. The reason for choosing the vanadium is that it is purely an incoherent scatterer, and scattered intensity is roughly independent of angle of scattering.

(c) *Self-absorption correction and background*: As the neutrons pass through samples, it may get absorbed by the sample and container. In addition, sample containers can scatter neutrons as well. These factors need to be taken into

account for deducing $S(Q,\omega)$. Following equation is generally used to correct for absorption and container scattering to get the absolute scattering from the sample [24]:

$$I_s(s) = I_{c+s}(s)\frac{1}{A_{s,sc}(s)} - I_c(s)\frac{A_{c,sc}(s)}{A_{s,sc}(s)A_{c,c}(s)} \qquad (14.6)$$

$I_s(s)$ = intensity from the sample

$I_c(s)$ = intensity from the container

$I_{c+s}(s)$ = intensity from the sample and container

$A_{s,sc}(s)$ = absorption coefficient for scattering in the sample and absorption in both samples and container

$A_{c,sc}(s)$ = absorption coefficient for scattering of container and absorption of both sample and container

$A_{c,c}(s)$ = absorption coefficient for scattering and self-absorption in container

(d) *Multiplication by detailed balance factor*: In atomic/molecular materials, particularly at low temperatures, the probability of finding atoms in the lowest-energy state is higher than in the high-energy state. Hence, when neutrons interact with nucleus, the probability of losing energy in the scattering process is higher than the probability of gaining energy. Therefore, the quasi-elastic broadening will not be symmetrical with respect to zero energy transfer. To account for this, the $S(Q,\omega)$ is multiplied by the Boltzmann factor:

$$S(Q,\omega) = \exp\left(\frac{\hbar\omega}{2k_BT}\right)S(-Q, -\omega) \qquad (14.7)$$

k_B is the Boltzmann constant and T is the temperature.

(e) *Multiple scattering corrections:* This is the case where the sample cannot be made thin enough and multiple scattering become dominant. In such cases the Q dependence of the relaxation time found to deviate for small Q values. There are few computer programs available for multiple scattering corrections [25].

8.2 QENS Data Analysis

A soft matter system, in general, exhibits a broad spectrum of relaxation processes whose characteristic times range from picoseconds to seconds. This makes the modeling slightly more challenging unlike molecular crystals where a well-defined model can be used to extract parameters that characterize a particular dynamic mode. The QENS data fitting and analysis often require trial and error since satisfying results need to achieve an acceptable mathematical fitting as well as make *physical* sense. The general Eq. 14.8 to model the QENS data can be read as [6]

$$S(Q, \omega) = DWF\{A(Q)\delta(\omega) + [1 - A(Q)]S_{QE}(Q, \omega)\} + BKG \qquad (14.8)$$

where DWF is the Debye-Waller factor, A(Q) is the elastic incoherent structure factor (EISF), $\delta(\omega)$ is the Dirac delta function at zero frequency, $S_{QE}(Q,\omega)$ is the quasi-elastic scattering model function, and BKG is the background. In the above equation, DWF takes into account all faster vibrational processes. For diffusive or diffusive-like processes, EISF approaches zero, which makes the data analysis simpler. For non-diffusive motions, EISF provides crucial information about the geometry of the motion. The Dirac delta function accounts for any processes that are slower than instrumental resolution, and typically flat background accounts for any processes that are faster than that can be accessed by instrument dynamic (or time) window. As the QENS measured data is resolution broadened, the above equation should be convoluted with instrumental resolution before it can be fitted to the measured experimental data. The first commonly used approach is to treat the QE signal, $S_{QE}(Q,\omega)$, by a single Lorentzian function[6, 23]. As Fourier transform of a Lorentzian function is a simple exponential function in the time domain, a Lorentzian function can be interpreted as a purely exponential relaxation process with a single relaxation time τ. In a liquid, atoms or molecules diffuse away in space with time due to relatively small molecular size. This shows up in the measured intermediate scattering function as it decays exponentially with relaxation time τ. This relaxation time depends on the diffusion constants and can be given by $\tau(Q) = D^{-1}Q^{-2}$ where D is the diffusion constant. In molecular liquids, individual molecules go through both rotational and translational motions. This means while the center of mass translates in space, these molecules also orient and reorient about their center of mass. Typically, it is assumed that these two motions are statistically uncorrelated and can be expressed separately. In the frequency domain, this scenario translates to a sum of two Lorentzians. As translational motion is strongly dependent on spatial access, typically there is a strong Q dependence of relaxation time or full width at half maximum (FWHM) that is typically accessed in frequency domain. In frequency domain, such a Q dependence can be fitted to jump-diffusion model as

$$FWHM = \frac{DQ^2}{1 + DQ^2\tau_0} \qquad (14.9)$$

where τ_0 is residence time. The local character of rotational motion typically produces Q-independent time scales or FWHM. As we discussed above, NSE directly measures the intermediate scattering function, S(Q,t), and therefore, data reduction is much simpler as no convolution with the instrumental resolution is needed and it simply can be divided. The above modeling generally works for simple liquids. However, for polymer segmental motion, a single Lorentzian (or two Lorentzians) is, often, not enough, and, usually, a stretched-exponential function or Kohlrausch-Williams-Watts (KWW) function [26] fits the data well. The KWW function, in time domain, is given below:

$$S(Q,t) \approx \exp\left\{-(t/\tau)^{\beta}\right\} \qquad (14.10)$$

In the above equation, τ is the characteristic relaxation time and β $(0<\beta<1)$ is the stretched-exponential shape parameter defining the non-exponential behavior of the relaxation. The KWW function has been very successful in describing the dynamics of amorphous liquids and polymer segmental motions in literature. The KWW model can be thought of as a distribution of relaxation times and has also been interpreted in heterogeneous and homogeneous scenarios of the molecular dynamics [27] where the dynamics is believed to be non-exponential inherently. However, fitting the QENS data to KWW is not straightforward and it requires caution when used. The KWW function has no exact functional form other than $\beta = 0.5$ [28] in frequency domain, and, therefore, Fourier transform of the experimental data is needed. This often leads to large errors due to limited time range available on neutron spectrometers. This problem can often be eliminated by combining different instruments and increasing the time range for measurements. In addition, shape parameter and relaxation time are strongly coupled, and the correlation matrix has to be examined carefully before analyzing the results. For polymer systems, generally, shape parameter β is found to be Q independent and very weakly dependent on temperature although some exceptions exist [29]. This makes the fitting procedure relatively easier as one can fix the shape parameter to average values and determine the relaxation times with better accuracy.

Typically, elastic intensity is measured as a function of temperature. The measured elastic intensities can be used to calculate mean square displacement (MSD) through Gaussian approximation. Harmonic oscillators are exactly described by a Gaussian function according to which the spatial distribution of the particles at long time is Gaussian and takes the form

$$I(Q,T)/I_0(Q) = \exp\left\{-Q^2 <u^2(T)> /3\right\} \qquad (14.11)$$

In the above equation, $I_0(Q)$ is the purely elastic intensity and can usually be measured on a sample at low temperatures where no dynamics is expected on the time scale of backscattering instrument. With this assumption, a plot of $\ln(I/I_0)$ versus Q^2 is linear, and the slope provides the value of the mean square displacement, $<u^2>$ at a given temperature. Although most atomic motions in soft condensed matter are admittedly anharmonic, this approximation has been useful for characterizing the dynamics of polymers and other glass formers.

9 Review of Recent Studies

In recent years QENS has been used for studying relaxation process in various materials, which includes ionic liquid, organic liquids, water, proton-conducting materials, metallic glass-forming melts, biomaterials, polymers, and various materials in nano- or mesoporous confined states. There are about 40–50 research

articles based on QENS experiments being published in every year since 1995. Among several fields of research explored by QENS in recent years, in this chapter we would like to discuss following important research result from QENS studies: dynamics in glass-forming alloy melts, dynamics of water in confinement, polymer under confinement, dynamics of uniquely synthesized nanoparticles, hydrogen-bonded liquids in vycor, solution under confinement, dynamics of gas in nanopores, and energy storage applications.

9.1   Dynamics of Glass-Forming Alloy Melts

The glass transition is a reversible transition. When a liquid is cooled below its melting temperature, it solidifies in the amorphous state. This phenomenon is generally called as glass transition. Irrespective of the nature of interatomic bonds or intermolecular bonds, in general, all liquids can be vitrified on fast cooling. According to the temperature dependence of viscosity the liquids, glass-forming materials are generally classified into two groups: strong and fragile [30]. The strong liquids show an Arrhenius dependence of viscosity but the viscosity of fragile liquids increases fourfold to fivefold in a short interval of temperature close to the calorimetric glass-transition temperature [31]. The reason for the huge increase in viscosity in a short interval is not yet understood [32]. Most of the recent QENS work on the glass transition was to understand the relaxation dynamics in the abovementioned temperature regime. Since metallic liquids spontaneously crystallize below the melting temperature, studying the dynamics below the melting temperature in the conventional way (using crucible) is not possible. To study the relaxation dynamics in the metallic supercooled liquids, electromagnetic and electrostatic levitation techniques have been used to overcome the crystallization problem [33, 34]. In these QENS studies, the experimental results were mainly compared with the theoretical predictions of dynamics in glass-forming liquids [35–37].

Theoretically, mode-coupling theory (MCT) has been very successful in explaining the dynamics of fragile glass-forming liquids. The theory predicted that the incoherent intermediate scattering function (ISF) decay in two steps [38]. The intermediate scattering function can be obtained from QENS experiments. This results in many QENS experiments with metallic glass-forming liquids that studied the shape of ISF and its momentum transfer dependence. The most important prediction of MCT was the existence of dynamic transition in the glass-forming liquids. The MCT predicted that at a critical temperature (Tc) the atomic or molecular transport mechanism changes from non-Arrhenius to Arrhenius temperature dependence, and the Tc depends on the density or packing fraction of the liquids.

Prof. Andreas Meyer was the first one to carry out a detailed study on the dynamics of dense metallic glass-forming liquids. He has investigated the atomic relaxation process in Zr- and Pd-based alloy melts [35, 36]. The relaxation processes in the abovementioned alloy melts were found to be in excellent agreements

Fig. 14.5 Intermediate
scattering function of liquid
$Pd_{40}Ni_{40}P_{20}$ measured close
to the melting temperature.
The decay of ISF is a two-step
process. The *solid* and *dotted
lines* are the fits with
Eqs. 14.12 and 14.15,
respectively
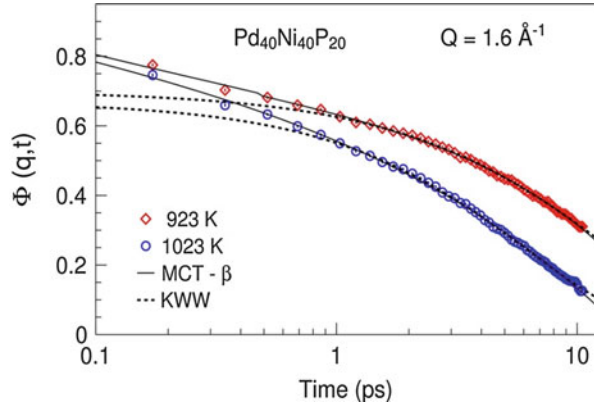
with MCT predictions. The self-correlation functions (S(Q,t) or I(Q,t)) of the alloy
melts measured above the melting temperature show two-step relaxation process,
and ISF holds the time-temperature superposition principle of MCT. The first step
in the decay of ISF is due to the cage rattling of atoms before the long-range
diffusion process and is called the β-relaxation process. The second step in the
decay of ISF is the long-range atomic transport process. The MCT has predicted
that the decay of first step in ISF due to the β-relaxation process should follow the
functional form (see Fig. 14.5):

$$I(Q,t) = f_Q + h_Q g_\lambda(t/t_\sigma) \tag{14.12}$$

where f_Q is the Debye-Waller factor and h_Q amplitude of β-relaxation process. The
scaling function $g_\lambda(t/t_\sigma)$ is defined by ISF shape parameter λ. The QENS data from
Zr- and Pd-based melts found to follow the above equation and results from the
fitting of Eq. 14.12 provided the crossover time t_σ and h_Q, which are temperature-
dependent parameter. Error bars throughout the text represent one standard devia-
tion unless defined otherwise. The MCT predicted that close to Tc the temperature
dependence of t_σ and h_Q with the scaling function,

$$t_\sigma \propto (T - T_c)^{1/2a} \text{ and } h_Q \propto (T - T_c)^{1/2} \tag{14.13}$$

From the temperature dependence of the t_σ and h_Q (Eq. 14.13), the critical temper-
ature (Tc) of the system was found out. The Tc calculated using the above equations
found to be about 1.2–1.3 times the calorimetric glass-transition temperature (Tg).
By tracer diffusion technique, Ratzke et al. have measured the diffusion coefficient
of Co atoms in the Pd-P-based alloy, and it shows a clear change in the diffusion
process from an Arrhenius process to non-Arrhenius process at a critical tempera-
ture of 1.2–1.3Tg, thus confirming the Tc obtained from the β-relaxation process
that was observed by the QENS experiments [4].

According to MCT the T_c can also be derived from the α-relaxation process and
the relaxation time of the α-process is controlled by packing fraction of the liquid.

The metallic liquids can be approximated by closed packed hard spheres, and the packing fraction can be calculated from the following equation: $\phi = \pi n r^3 / 6$, where n is the number density and r is the radius of the sphere (atom). The critical packing fraction ϕ_c is related to relaxation time as follows [39]:

$$\langle \tau_\alpha \rangle^{-1/\gamma} \propto [\varphi - \varphi_c] \tag{14.14}$$

where ϕ and $\langle \tau_\alpha \rangle$ are the packing fraction mean relaxation time of the alpha process, respectively. The critical packing fraction in hard-sphere liquids was calculated by the MCT and found to be 0.547. In a recent study of highly fragile metallic liquids, $Ni_{59.5}Nb_{40.5}$ and $Ni_{60}Nb_{34.8}Sn_{5.2}$, the critical packing fraction of 0.545 ± 0.002 was derived from the QENS data, showing excellent agreements with the MCT predictions [39]. A similar value for the critical packing fraction was obtained from the QENS data of $Ni_{80}P_{20}$, $Pd_{40}Ni_{40}P_{20}$ and $Pd_{43}Ni_{10}Cu_{20}P_{20}$ melts [40] (Fig. 14.6).

Study of glass-forming ability of metallic melts also been carried out using QENS technique recently. The glass-forming ability of system means how large in diameters can an alloy melt be cast into its fully amorphous state. Experimentally, it was observed that certain glass-forming alloys increases its glass-forming ability (GFA) by the minor addition of other elements. For example, $Ce_{70}Cu_{20}Al_{10}$ alloy is a glass-forming alloy, and it can be cast into its fully amorphous state only up to 2 mm in diameter. Only one atomic percentage addition of Nb increases the casting thickness by 10 mm in diameter. A QENS study of $Ce_{70}Cu_{20}Al_{10}$ and $Ce_{69}Cu_{20}Al_{10}Nb_1$ melts indicated shows that the Nb addition changes the dynamics of $Ce_{70}Cu_{20}Al_{10}$ melt; the intermediate scattering function is more stretched and the diffusion slows down with Nb addition [41]. The results indicate a strong correlation between melt dynamics and GFA of the metallic liquids.

Fig. 14.6 The relaxation times of Ni atoms in $Pd_{40}Ni_{40}P_{20}$ measured at different Q values rescaled with γ (2.7) plotted as a function of packing fraction (Reprinted with permission from [40] Copyright, European physical society)
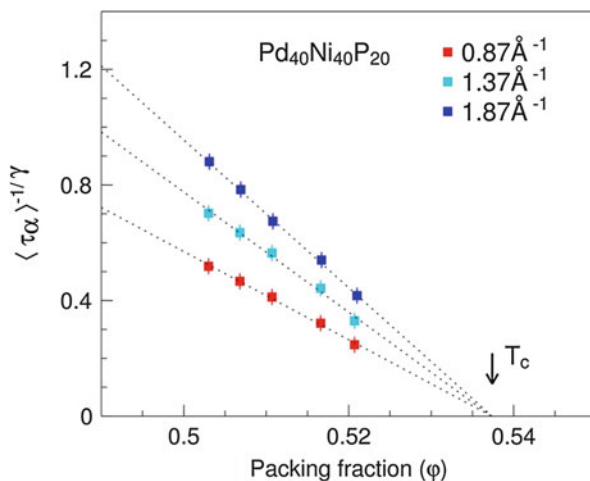
9.2   Dynamics of Water Under Confinement

9.2.1   Early Work Overview

It will be an understatement to say that water is the most important material on our planet. What makes water such a unique liquid is the fact that the physical properties of water are very different than a typical liquid. Water has been known to exhibit anomalous behavior in transport as well as thermodynamic properties, particularly below melting temperature [42]. For example, it has been reported that a number of thermodynamic functions and associated relaxation times seem to diverge around 228 K. These anomalies sparked a lot of interest; however, due to the unique water behavior at lower temperatures, no success has been achieved in making measurements down at supercooled temperatures. This is due to the so-called no man's land region where nucleation of crystals dominates and water freezes to hexagonal ice at around 235 K [43]. There have been a number of attempts to sneak into no man's land, e.g., by applying pressure, vitrification on cold substrate, and so on, but all attempts have had limited success. This is where confinement by nanopores offers a unique opportunity. It has been found that water can be supercooled below homogeneous nucleation temperature of 235 K under confinement. This temperature seems to decrease and completely disappear depending on the confining geometry. Before we discuss recent findings, it is important to discuss earlier work on water dynamics.

The dynamics of water evolved slowly over the years, starting more than 30 years ago. In earlier days, water was studied using incoherent QENS, coherent inelastic neutron scattering, X-ray scattering, as well as molecular dynamics simulations. First incoherent scattering measurements were reported by Chen et al. [44] who in their pioneering work used jump-diffusion model to explain water dynamics. In their original work, Teixeira et al. [45] showed the existence of collective, propagating high-frequency sound-like excitations. This collective mode appeared as shoulder on both sides of elastic peak. Bellissent-Funel et al. studied [46] incoherent scattering from water under confinement with vycor. The water molecules close to the hydrophilic surface performed very local rotational jumps whose diffusion rates were similar to bulk water. However, these water molecules had to wait longer before they jump to adjacent available site. In continuation work [47], dynamics data could be analyzed using a non-exponential KWW function, and no elastic contribution was needed. This piece of work established clearly that there was no "further" slower dynamics of water that exists and also that water dynamics is "non-exponential" contrary to popular belief as earlier data was fitted with a Lorentzian function that represent a simple exponential in time domain. The origin of non-exponential relaxation of water was attributed to diffusion of water that was strongly coupled and affected by the local structure of the neighboring shell or cage effects as described by MCT. Bellissent-Funel et al. [48] measured heavy water in the pores of a vycor glass to study the effect of confinement on the collective dynamics of water. They used an improved neutron spin echo spectrometer at two supercooled temperatures. The normalized scattering functions could be fitted well to KWW function. With these measurements, authors were clearly able to establish

presence of an α-relaxation in water. Using appropriate modeling, the authors were able to show that indeed water dynamics in supercooled regime can be described well in the general framework of the mode-coupling theory, and hence water behaves like a typical glass-forming liquid.

9.2.2 Recent Work Overview

Studies of water confined in vycor pores were limited due to a broad distribution of pore sizes. In addition, average pore size was about 50 Å which was not enough to completely supercool water and therefore explore water dynamics in deep supercooled regime. This problem was somewhat resolved by using a new mesoporous silica as confining material [49]. The advantage with these pores was that they had much narrower distribution as well as average pore size was much reduced to 22–25 Å. In this work, Faraone et al. measured water dynamics using a TOF spectrometer above freezing point of water and used relaxing cage model (RCM) for data analysis [50, 51]. As RCM has since been used extensively for water dynamics, we will explain main features of this model. In this model, the translational dynamics of water is expressed as the product of a short time harmonic motion and a long time delay. The rationale behind this approach is that at short times water molecule is still trapped inside the cage of the neighbors and the translation of molecule is harmonic. At longer times eventually water molecule breaks this cage and diffuses away. This process obviously involves the structural relaxation of cage and cannot be described by simple exponential or Lorentzian process in frequency domain. In this scenario, the relaxing cage model has the following form:

$$F_T(Q,T) = F_T^s(Q,T)\exp\left[-\left(\frac{t}{\tau}\right)^\beta\right] \tag{14.15}$$

The above equation is very similar to standard KWW function described above. However, the main difference comes from the fact that there is a well-defined meaning of each term. In the above equation, first term describes the rattling motion of the molecule inside the cage of its neighbors that can be described using a simple Gaussian term. The long term or the relaxation term is characterized by a structural relaxation time τ. Molecular dynamics (MD) simulations and experiments have shown that relaxation term follows a power law in Q of the form $\tau \sim Q^{-\gamma}$. If the exponent γ is 2, this would simply mean simple diffusion in space. MD results [52] at that time seemed to show that exponent value of 2 is achieved when Q approaches zero or essentially in hydrodynamic limit and seems to show a plateau around 1 for $Q \sim 1$ Å^{-1}. Authors were able to show that dynamics of water inside silica pores is heterogeneous, and they were able to show that a fraction of the water molecules was much slower than the water molecules in the inner parts of the pores. These molecules increase in number as temperature is lowered. A shape parameter of 0.75 was found to be reasonable which clearly indicate non-exponential character of water dynamics. Interestingly, due to confinement effects, dimensionality of water diffusion was found to be affected. It was found that the power exponent in Q

dependence slowly increased with temperature and was found to be lower than 2 at all temperatures.

Faraone et al. [53] reported for the first time the presence of fragile-to-strong crossover (FSC) in the water dynamics confined in MCM. The novel synthesis of even a smaller pore (18 Å and 14 Å) size of silica was the most crucial part as they were able to supercool water until about 200 K. Data was analyzed in terms of relaxing cage model and it was found that there was a clear evidence of abrupt change of relaxation time behavior at temperatures close to 225 K. At lower temperatures, an Arrhenius-like behavior was observed which turned sharply into super-Arrhenius behavior at crossover temperature. In terms of Angell's plot [54], these would correspond to strong and fragile behavior, respectively. This work was followed by a more detailed work, and the pressure effects on the dynamics of confined water were explored [55]. It was found that the FSC temperature depends on the pressure. The transition temperature decreases steadily with increasing pressure until it intersects the homogeneous nucleation temperature line of bulk water at pressure 1600 bar. Above this pressure, it is no longer possible to discern the characteristic features of the FSC. These measurements related fragile behavior at higher temperatures to high-density liquid, while the strong behavior was related with low-density liquid. In this interpretation, cusp-like behavior in relaxation plot was obtained when crossing the so-called Widom line in the one phase region. These measurements showed that 1600 bar is critical pressure above which two-phase liquid coexist, and therefore by changing temperature, only proportions of two phases change and thus cusp-like behavior will not be obtained. These results point to the presence of a second critical point in the water phase diagram (see Fig. 14.7). These results naturally sparked a lot of interest from researchers around the world and criticism as well [56]. The presence of crossover is inevitable as has been shown in water dynamics in a variety of systems which we discuss below.

Chu et al. [57] studied water dynamics in hydrophobic double-wall-carbon nanotubes (DWNT). The idea of these measurements was to see the effect of hydrophobicity as MCM-41 used earlier was strongly hydrophilic in nature. The FSC was detected at much lower temperature of 190 K. Faraone and coworkers [58] were able to synthesize a modified MCM that was hydrophobic in nature. The idea was to ensure the presence of the FSC under the same media but with different phobicity. These measurements, however, revealed the absence of FSC in the water dynamics down to 210 K. This, however, could be due to the lowering of the transition temperature as hydrophobic nature of the confining media seems to strongly decrease the crossover temperature. These measurements, however, provide a much clearer picture of water dynamics as this study used three different instruments covering a wider range of time scales. The picture that arose is that the water dynamics in hydrophobic MCM-41 is strongly heterogeneous as the dynamics show a broad distribution of relaxation times while retaining the Fickian diffusion. These results indicate that the chemical interactions between the wall and the water molecules play a very important role in driving the water dynamics in these materials. By comparing results with hydrophilic MCM-41, it was concluded
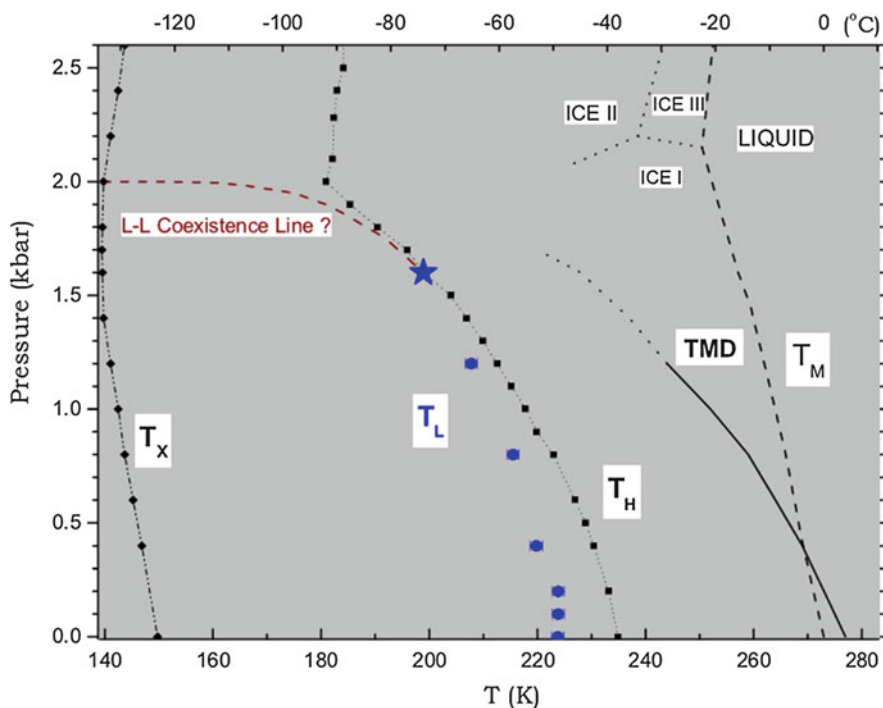
Fig. 14.7 The pressure dependence of fragile-to-strong crossover temperature is shown in the water pressure temperature phase diagram (Reprinted with permission from [55]. Copyright (2005) American Physical Society)

that around room temperature, the dynamics of water does not seem to be affected by the character of the surface whether hydrophilic or hydrophobic. However, on cooling down, water confined in hydrophilic walls experience a much more notice-able slowing down compared to hydrophobic MCM-41. These findings can be related to more extensive disruption of hydrogen bond formation in hydrophobic confinement.

How accurately FSC can really be determined has always been a question. We were able to determine the crossover temperature without artifact of the data analysis by using a different approach [59]. The determination of crossover tem-perature in above studies was performed on the basis of a change in the T dependence of relaxation time which could be subjective. In this study, we mea-sured water dynamics in a new hydrophobic material called CMK-1. We used the model-independent determination of the crossover temperature by calculating the derivative of the translational relaxation time in its Arrhenius plot. The peak position on the curve represents the temperature region where maximum slope is observed in the traditional Arrhenius plot (See Fig. 14.8). One finding of this work was that crossover temperature determined using this approach was about 20 K higher than the traditional approach. However, the trends were found to be the
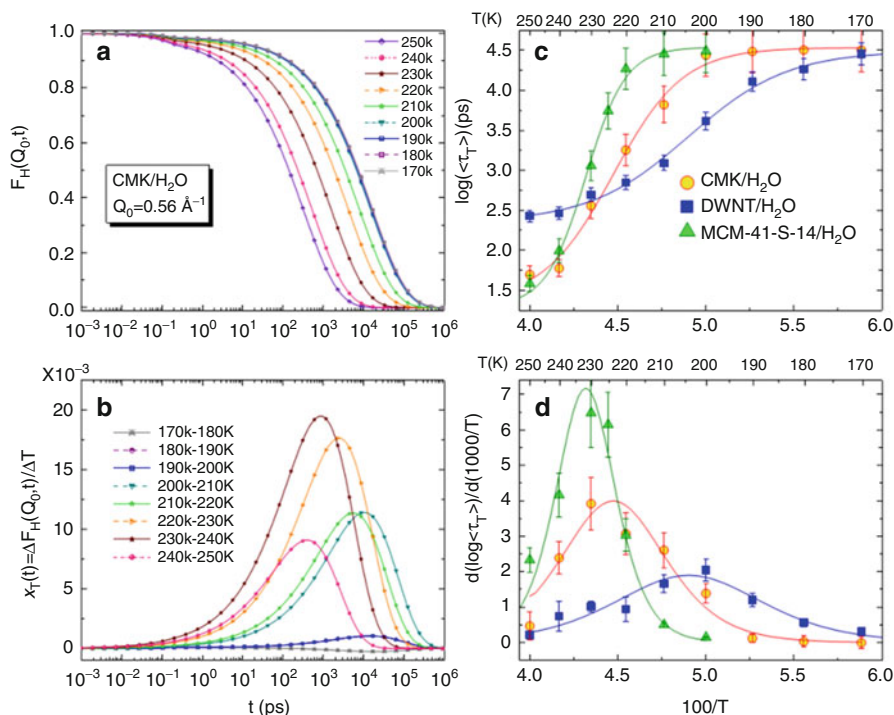
Fig. 14.8 (**a**) Intermediate scattering function (ISF) extracted from the QENS measurements for water confined in CMK-1. (**b**) Dynamic response function calculated from the ISF. (**c**) Time scales of water in different systems. (**d**) Derivative of relaxation time to extract crossover temperature (Reprinted with permission from [59]. Copyright (2010) American Physical Society)

same, e.g., hydrophilic MCM-41 has the highest and DWNT had the lowest. Surprisingly, CMK-1 showed a crossover that appears in between the two. These results showed that as far as chemical interactions of water and CMK-1 are concerned, CMK-1 is not truly hydrophobic as DWNT. This also opened up a case for the dimensionality – CMK-1 has 1 3D hydrophobic confinement, while the DWNT is 1D. These measurements eliminated some uncertainty about determination of FSC temperature.

In an attempt to understand the origin of FSC, Mamontov and coworkers studied water dynamics in surface water at low hydration levels on rutile [60]. They found that the FSC strongly depends on hydration level. In fact, FSC completely disappears when the hydration level goes below monolayer coverage of the mobile water! They attributed the crossover to water exchange between layers which obviously cannot start until the water coverage exceeds one monolayer. This work was further extended by Chu et al. [61] who discovered a qualitative change in elastic scattering due to surface freezing-melting transition. The motions that were localized at lower temperatures become delocalized at higher temperatures.

Mallamace and coworkers [62] studied three different types of water system, namely, water confined in nanotubes, water in the first hydration layer of protein, and water in a mixture with methanol. In these systems, water does not freeze and particularly in the last one is not geometrically confined. The viscosity data were analyzed using a power law approach in super-Arrhenius regime which defined the crossover temperature and the breakdown of the Stokes-Einstein relation (SER) and was compared with QENS data. The crossover temperature marks the boundary between two types of viscous behavior and marks the beginning of the decoupling of the self-diffusion coefficient from the viscosity. They found that SER violation occurred in all three systems at the same crossover temperature, i.e., 225 K. These results clearly show that these crossovers are independent of the dimensionality of the system under consideration and thus are due to the characteristic of water only. This has been supported by the computer simulations [63] where an onset of dynamic heterogeneity is shown to occur near this temperature. This study also supports the argument that crossover in water dynamics is not due to the confinement effects and suggest FSC may be an inherent part of water dynamics.

In continuation, to understand dynamics and transport properties of interfacial water, Faraone et al. [64] made measurements on the dynamics of water confined in voids between the well-defined and densely packed nanocages. The materials used in this study belong to a class of polyoxometalates. The cluster of $MO_{72}Fe_{30}$ exhibits a nanometer-sized cavity and 20 pores equivalent to 20 $MO_3Fe_3O_6$ rings. The diameter of the nanocapsule is 25 Å. About 150 discreet water molecules are present, 25 inside the cavity and the rest in the voids between the clusters while interacting with the surface via hydrogen bonds. Water dynamics in nanocapsule is found to be strongly heterogeneous, and it was attributed to different local environments experienced by water molecules. Interestingly, a fast process that had a mean square displacement of about 0.3 Å was observed. This was attributed to the center of mass rattling inside the harmonic potential generated by water molecules bonding with their neighbors and substrate. The diffusive dynamics obtained at slower time scales seem to be thermally activated and triggered by the breaking of the hydrogen bonds between the crystal water molecule and surface water ligand terminal O atoms of the nanocages. If compared with bulk water, this dynamics is strongly slowed down and the interaction of water molecules plays a key role during the assembly process. We later studied water dynamics in molybdenum-oxide Keplerate-type nanocages as well [65]. The dynamics of water molecules confined within the cage follows the Volino and Dianoux model [66] that describes scattering for a confined system in a spherical potential well with an in-cage diffusion coefficient. Somewhat similar cages have been produced using porous coordinate metal complexes, e.g., copper rubeanate. The shape of these cages is almost rectangular and size is about 0.7 nm. Water is absorbed in these cages and provides high proton conductivity for various applications. A series of papers have been published to discuss the mechanism of the transitions observed in these materials and also the conductivity mechanism has been offered based on QENS measurements. Please see Yamamuro's work for more details [67].

9.3 Polymers Under Confinement

Dynamics of polymers under high degree of confinement and on filler particles is very interesting for theoretical physics as well as for application purpose as confinement tend to alter a number of their important properties including their modulus. For example, previous work on polymers (PMMA, TMPC) containing C60 nanoparticles suggest that local segmental motions are suppressed due to the presence of nanoparticles [68]. Interestingly, confinement-induced increased mobility when PMPS is mixed with silicate sheets. This behavior has been attributed to the intimate mixing of PMPS chains with the surfactant on the silica sheets [69]. In this scenario, chain motion is coupled to the relatively mobile surfactant in confined spaces. Akcora et al. measured [70] PMMA-grafted nanoparticles using neutron scattering and rheology. They unambiguously showed that phase separation of polymer-grafted nanoparticles from matrix homopolymer is a universal property of grafted particle system. On the other hand, elastic scattering showed clearly that this macroscopic phase separation does not influence the local matrix chain dynamics.

We studied confinement effects on the segmental dynamics of 1,4 polybutadiene (PBD) in the presence of a high concentration of carbon black as filling particles [71]. The carbon black comprised of 17 nm particles fused into aggregates having a mean diameter of 54 nm. The interesting aspect of this particular carbon-fused particle is that it has reactive double bonds at the particle surface that serves as binding sites for polymer chains. One of the problems associated with studies in material under confinement is that some of the material fills the region in between particles and, therefore, behaves like bulk. Typically subtraction of signal from this bulk-like material is not easy and poses a number of challenges. Here we used cyclohexane to remove unattached polymer chains so all polymer chains are on the surface and bound to carbon black (CB) surface.

For the accurate determination of shape parameter, we measured dynamic mechanical loss modulus in almost seven orders of magnitude in frequency. We found a $\beta = 0.41$ for the neat PBD while modulus of PBD/CB obviously broadened and an approximate $\beta = 0.38$ fitted the data well although some deviations at lower frequencies remain. This is consistent with common notion that polymer spectra get broadened by the addition of nanoparticles. These same values were used for QENS data and fitted the data well. The Q dependence is shown in Fig. 14.9. As one can see for Q values lower than 0.9 $\mathring{A}^{-1}$, Gaussian approximation holds very well. At shorter length scales, Q dependence becomes weaker and is about 2 as expected from non-Gaussian behavior. For more details of this Gaussian-non-Gaussian crossover, please see Ref. [72]. Nanocomposites also show similar changes in Q dependence as can be seen, although this change occurs at smaller Q values. As for the shape parameter, we back calculated values of shape parameters that would give us the expected behavior in low and high Q range for the nanocomposite (inset Fig. 14.9b). It is clear that for larger Q values, all polymer segments are constraints by particles and the distribution of relaxation times is much narrower than at larger length scales.
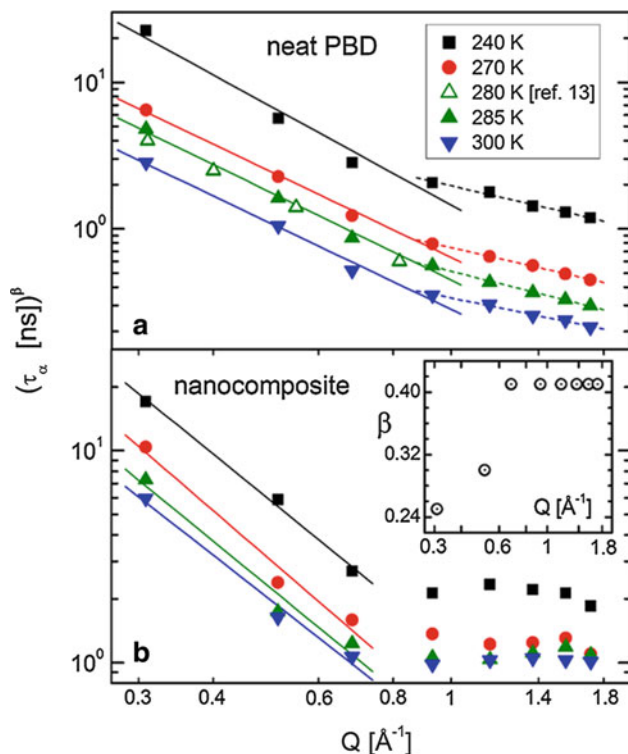
Fig. 14.9 Relaxation times extracted from QENS for neat polybutadiene and polybutadiene with carbon black. Inset shows expected values of shape parameter to fulfill Gaussianity (Reprinted with permission from [71]. Copyright (2013), American Chemical Society)

The neat PBD shows a sharp upturn in the MSD measured by backscattering in the range of 180–200 K [73]. Traditionally, this has been known as dynamic transition as this onsets the conformational relaxation. Though their T-dependences are similar, values of MSD for PBD/CB sample is much less specially at higher temperatures. This shows clearly that mobility of the polymer chains is heavily suppressed by interaction with carbon black. Interestingly, below dynamic transition both systems show very similar T dependence. This indirectly shows motions occurring in the lower temperature side are not affected as strongly by confinement. We analyzed QENS data in a rather different way to resolve multiple dynamic modes over a wide temperature range. We employed two Lorentzians, and the idea was to have one fast and one slow Lorentzians which in principle will cover nearby mobilities as well and therefore not too far off from the traditional KWW approach that we have used above. The data were analyzed assuming an immobile fraction, a slow mobile fraction, and a fast process weighted by their respective factions which are determined by data fitting. Figure 14.10 shows fraction of the different components plotted against the inverse of
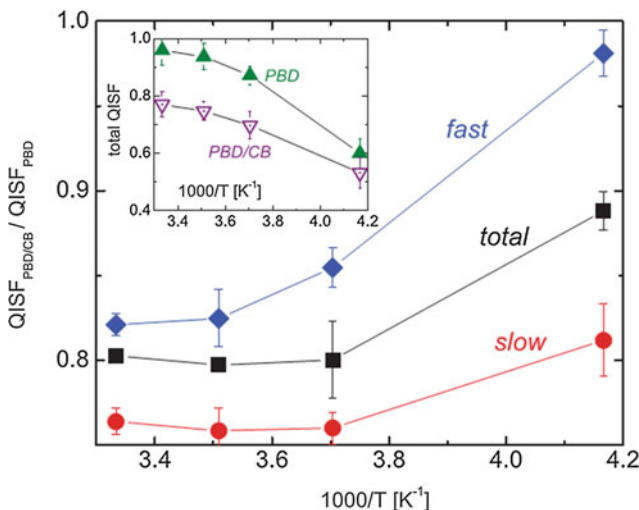
Fig. 14.10 Quasi-elastic fraction for different components for PBD/CB normalized to values for neat component plotted against inverse of temperature. As can be seen fraction reaches unity for fast component at lower temperatures (Reprinted with permission from [73]. Copyright (2013) AIP Publishing LLC)

temperature. These fractions are for PBD/CB sample that are normalized to neat PB values to check influence of confinement on chain mobility. These ratios show directly local immobilization of PB chains in the nanocomposites. It is interesting to note that the fast process has the highest ratio and approaches unity at low temperatures. This clearly indicates that fast process is less affected and shows less restrictions due to CB than that of the slow mode.

A great deal of information can also be had via diffusion constant and residence time (Eq. 14.9) determined for the slow mode. What is interesting is that slow modes show different temperature dependence for neat and CB sample. In addition, they seem to separate at lower temperatures, while there is not that much of a difference at higher temperatures. These results clearly show that at lower temperatures higher restrictions are observed on the dynamics of PBD due to CB. In addition, we found that wait time at the same temperature increased almost 80 % when going from neat to CB sample although average jump length increased only by a small fraction. These results indicate that "transient locking" where atoms are reversibly adsorbed to carbon surface manifests slow dynamics.

Boson peak has been known in amorphous systems for several decades now and general consensus is that they represent the excess density of vibrational states. Their origin is proposed to be due to the transverse vibrational modes associated with defective soft structure in the disordered state [74]. We observed Boson peak in both samples at all temperatures below T_g (Fig. 14.11). In agreement with HFBS results, the ratio of DCS QISF integrated in the energy range of 0.6 meV–20 meV of the bound to neat PBD increases as temperature decreases. Interestingly, at 60 K,
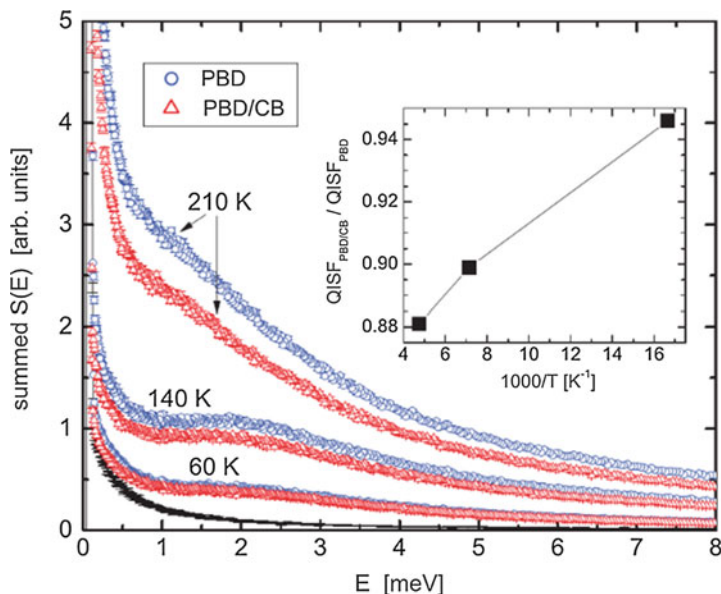
Fig. 14.11 Dynamic structure factor measured at DCS spectrometer for neat PBD and PBD/CB samples. Boson peaks can be seen around 2 meV. *Inset* shows normalized QISF as discussed in the text (Reprinted with permission from [73]. Copyright (2013) AIP Publishing LLC)

the number of mobile sites is identical for neat and nanocomposite. This shows that fast process and collective vibrations are essentially equivalent for both systems. These results also help understanding an earlier study [75] where it was reported that the mobility of polyisoprene defined by the breadth of the peak in the density of states at 25 meV increased by 1 meV below T_g in CB nanocomposites. However, a larger intensity of density of states was found for the neat polymer suggesting that the bound polymer has fewer mobile groups. Since the reinforcing mechanism for carbon black involves hydrogen atoms from the polymer interacting at the surface of the particle, interference from rapid reorientation of the methyl groups on the polyisoprene chain may lead to less constraint on the dynamics. This explains the qualitative difference between the effects of carbon black on polyisoprene in comparison to present results for PBD.

9.4   Dynamics of Uniquely Synthesized Nanoparticles

In recent years somewhat unique nanoparticles have been synthesized that have their own functionality and therefore show their own dynamics. These modified nanoparticles have found usage in industries as well as in applications we use on a daily basis. In this subsection we discuss some of these systems and their dynamics.

Fig. 14.12 Each silicon atom is bonded to one-and-a-half oxygen and to a hydrocarbon by a condensation reaction leading to bonded (RSiO1,5)n units (R = organic group and n = 6, 8, 10, 12)
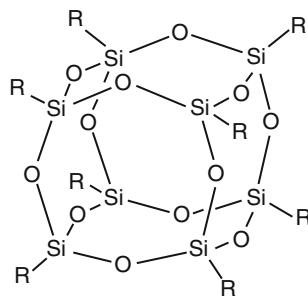
Fig. 14.13 MSD calculated using Gaussian approximation for M-POSS against temperature (Reprinted with permission from [77]. Copyright (2014) American Chemical Society)
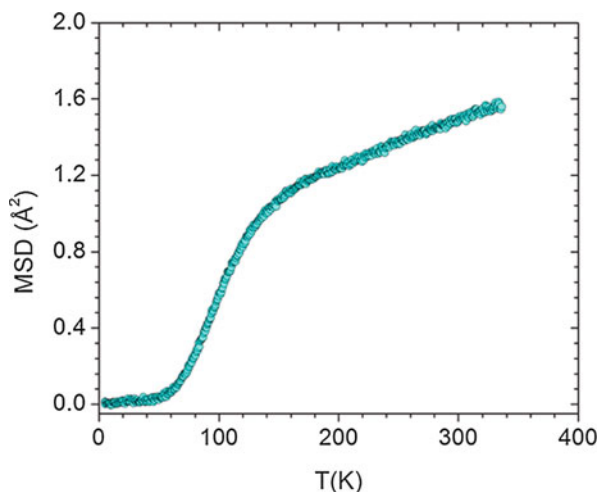
Polyhedral oligomeric silsesquioxanes (POSS) are a class of condensed three-dimensional oligomeric organosilica compounds with cage frameworks having different degrees of symmetry [76]. The POSS molecules can be considered as the smallest silica nanoparticles, and they have thus been incorporated in many polymers to form nanocomposites. Depending upon the attached ligand (Fig. 14.12), POSS can be achieved in crystalline, amorphous, or even liquid state at room temperature. In a recent study, we studied thoroughly structure and dynamics of M-POSS, one of the simplest in its family where all ligands are simple methyl groups [77]. The structure of this POSS was studied using X-ray scattering [78].

M-POSS was measured on backscattering in elastic mode and MSD was calculated result of which is shown in Fig. 14.13. From the crystallography, there are two distinct sets of methyl groups in the crystal which could have slightly different MSD, and therefore, results should be looked at keeping this in mind. As can be seen in Fig. 14.13 below 60 K, the MSD shows very weak T dependence and increases very gently. This gentle increase is due to the Debye-Waller factor of the

Fig. 14.14 The EISF values are plotted against Q at different temperatures. Note almost no temperature dependence in the entire temperature range (Reprinted with permission from [77]. Copyright (2014) American Chemical Society)
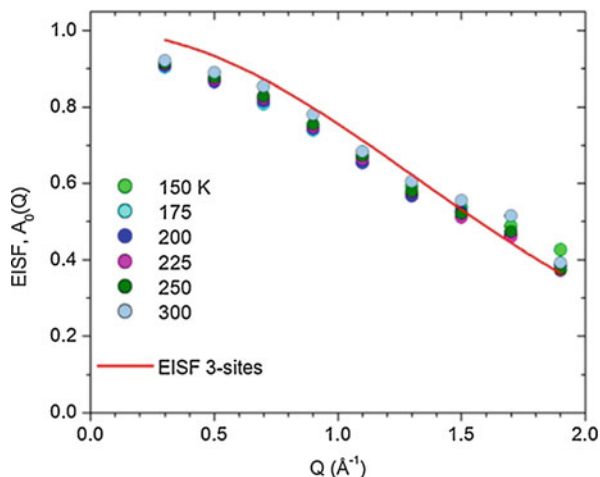
methyl groups as expected from harmonic vibrations. At around 60 K, methyl group rotations enter into ns time scale and exhibit a strong increase with increasing temperature. Another interesting change occurs at around 150 K where methyl group rotations are very rapid and go out of the instrument time window and a gentle linear T-behavior is observed. This linear behavior above 150 K also shows that other than methyl group rotations, no other dynamics enter into ns time scale.

QENS was measured at BASIS in the temperature range of 100 K–350 K. The data were fitted to a delta function and a Lorentzian function that takes care of broadening from the methyl groups. The symmetrical methyl groups rotate around their C_3 axes and can be modeled with a 3-site jump model [6, 23] where the hydrogen atoms for each methyl group are located on 3 sites equally spaced on a circle. The EISF for this model is given by

$$A(Q) = \frac{1}{3}[1 + 2j_0(Qd)] \tag{14.16}$$

where d is the jump distance separating the hydrogen atoms undergoing the rotational diffusion and j_0 is the spherical Bessel function of order zero. As can be seen, data can be fitted reasonably well (Fig. 14.14) with the above equation with a d value of 1.58 Å which is in good agreement with neutron diffraction data which yields an average value of 1.62 Å between H atoms. Although model fits the data reasonably well, some systematic deviations can be seen especially at lower Q values. These deviations are classic signature of multiple scattering in the system. As Q goes to zero, complete elastic intensity should be recovered and EISF should go to zero. Naively speaking, the amount of deviations from zero can give an idea of multiple scattering which does not look strong in our case.

Though EISF does not show any temperature dependence, FWHM show strong temperature dependence and can be used to calculate activation energy of the associated process. A plot of FWHM as a function of the inverse of temperature

yields a linear plot indicating Arrhenius behavior. The resulting activation energy for the methyl group rotations around the C_3 axes is 5.12 KJ/mol. This plot also provides attempt frequency which is calculated to be around 0.744 meV. The calculated activation energy for methyl group rotations and the typical attempt frequency in other methyl systems are somewhat different than calculated here. The discrepancy in activation energy could be due to contribution from the rotational tunneling of methyl groups. On the other hand, relatively lower attempt frequency indicates some coupling between the methyl groups. This has been supported by the fact that neutron diffraction measurements show relatively close proximity of the methyl groups of adjacent POSS molecule in the crystal lattice (C-C distance of about 3.7–4.3 Å). Recently, we studied in detail three more POSS systems where ligands were more complex. In particular, we studied octaisobutyl-POSS, octatrimethylsiloxy-POSS, and octadimethylsilane-POSS. These materials showed a number of phase transitions as well as more complex dynamics of methyl group. For more details see [79].

Proton exchange membranes for fuel cell have been good candidate to replace existing energy materials due to their appeal as clean source of energy for numerous applications. Typically PEMs are based on Nafion which relies heavily on water for conductivity as low water content Nafion films cannot provide enough conductivity for applications. In a recent work, we synthesized highly dense sulfonic acid functionalized mesoporous electrolytes that exhibit high proton conductivity under dry conditions [80]. For this purpose, tetramethoxysilane and 3-mercaptopropyltrimethoxysilane (MPTMS) were used. In order to achieve various loadings of sulfonic acid sites, an evaporation-induced self-assembly templating process was adopted. We prepared 3 samples for quasi-elastic measurements using 10 , 30, and 50 mol% of MPTMS which we call MP10-p, MP30-p, and MP50-p, respectively. XRD pattern and TEM images show that MP10-p and MP30-p have 2d-hexagonal structure, while MP50-p had wormhole structure. Pore diameters for all were found to be between 2 nm and 3 nm. Sulfonic acid group concentration depends on the p number; the higher the p number, the higher the sulfonic acid group density is. In order to isolate signal from the sulfonic acid group only, bromine-functionalized samples were prepared as well where sulfonic acid group was replaced with bromide (Br-MS).

As can be seen in Fig. 14.15a, Br-MS sample does not show any broadening over resolution at room temperature which shows that motions of propyl chains of the organic sulfonic acid and the silanol groups of the pore surface are not detectable on backscattering spectrometer. However, MP10-p, MP30-p, and MP50-p all show strong quasi-elastic broadening at 300 K over resolution (Fig. 14.15b). In addition, it can be seen that MP50-p showed stronger broadening when compared with MP10-p which is expected as hydrogen atoms density is higher in MP50-p sample.

These direct comparisons clearly show additional broadening results from the sulfonic acid sites only. Figure 14.15c compares spectra at 300 K and 370 K which clearly shows faster motions as temperature is increased indicating the process is thermally activated. The broadening over the elastic line can be fitted well with a delta and a Lorentzian function. The Q dependence of the FWHM for Lorentzian
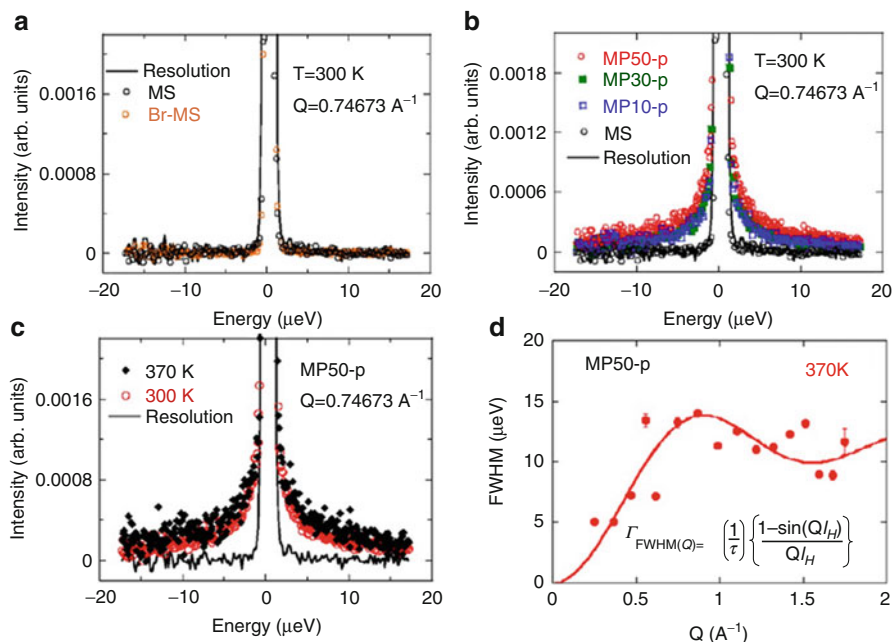
Fig. 14.15 (**a**) QENS spectra for Br-MS against resolution, (**b**) QENS spectra at 300 K for all materials, (**c**) temperature effects at QENS spectra for MP50-p, (**d**) extracted FWHM fitted to jump-diffusion model for MP50-p sample (Reprinted with permission from [80]. Copyright (2014) American Chemical Society)

function is shown in Fig. 14.15d which can be fitted well with jump-diffusion model. These results clearly show that proton in sulfonic acid can diffuse even without the presence of water. We believe the mechanism of proton diffusion is likely to be similar to what is observed typically in superprotonic conductors [81]. Average jump length obtained by the fitting is 4.3 Å which is consistent with distance to the nearest neighboring sulfonic acid site (~4 Å). We believe in these materials that the continuity of hydrogen bond is maintained by high density of sulfonic acid group. The available proton seems to conduct via proton self-diffusion within the hydrogen bond network formed by sulfonic groups. In this picture, distances of proton transport can be elongated by increasing the number of neighbors in the vicinity of sulfonic acid. Therefore, for higher proton conductivities under dry conditions, a high concentration of hydrogen bonds is necessary which in turn requires highly dense sulfonic acid sites.

Similar to the modified MCM above, 1,3diphenylpropane (DPP) was covalently tethered via a silyl-aryl-ether linkage in the mesopores of MCM-41 [82]. The geometric effect of pore radius was investigated with samples having pores in the range of 1.6 nm to 3.0 nm in diameter. The data was analyzed in terms of a model that accounted for the restricted diffusion where each hydrogen atom along the molecule diffuses in a sphere whose radius depends on the distance of the

individual hydrogen atom from the molecule's tethered point. Interestingly, smaller pore diameters and higher DPP surface coverage tend to provide larger length-scale diffusive motions. In both of these situations, molecules are forced to be away from the MCM-41 surface and into the interior of the pores where there is more volume available to diffuse away. The rate of diffusion increases in large pores as the surface coverage of DPP molecule is increased. This is more likely due to less-crowded pore interior resulting in faster motion.

9.5   Hydrogen-Bonded Liquids in Vycor

As we mentioned above, for simple liquids, general consensus is that there is a surface or interfacial layer of molecules tightly bound to the walls, while the remaining space is filled with bulk-like liquid. The connection between the surface wetting and observed dynamics has been investigated for over a decade. The dielectric relaxation of three glass formers with one (salol), two (pentylene glycol), and three hydroxyl groups (glycerol) showed that the thickness of the interfacial layer grows with increasing surface wetting and thickens as the temperature is reduced [83]. In another study of hydrogen-bonded materials, even more complex picture emerged where three layers were proposed [84]. From these studies and the results on water dynamics discussed above, it is clear that dynamics of glass-forming liquids in confinement is strongly heterogeneous. We measured three structurally similar glasses under vycor for this purpose – 2-propanol (PNOL), propylene glycol (PG), and glycerol which have one, two, and three hydroxyl groups, respectively [85].

The elastic intensity falls off more rapidly in confined samples than bulk. What is very interesting to see is the change in the way intensity drops off even at lower temperature. In case of glycerol, elastic intensity drops off faster in bulk before a sharper change in slope at 260 K occurs. The upturn at 260 K is related to the glass transition, and therefore, a change in T dependence below 260 K shows local and secondary relaxations that are affected by confinement effects. On the other hand, elastic intensity from PNOL shows clear freezing on cooling in the form of a liquid-to-solid phase transition. Interestingly, this drop is not observed in confined sample indicating confinement effects eliminated crystallization completely in PNOL. PG shows rather standard behavior of elastic intensity as it shows similar behavior for both bulk and confined until a sharp change in T dependence takes place at around 200 K.

As discussed above, MSD can be calculated from the elastic intensities in the Gaussian approximation using Eq. 14.11. In principle, the Gaussian approximation term is the first term in Taylor expansion, which can be terminated after Q^2 term for harmonic solid as non-Gaussianity is absent. However, if non-Gaussian contributions kick in, then the more general expansion can be written as [86]
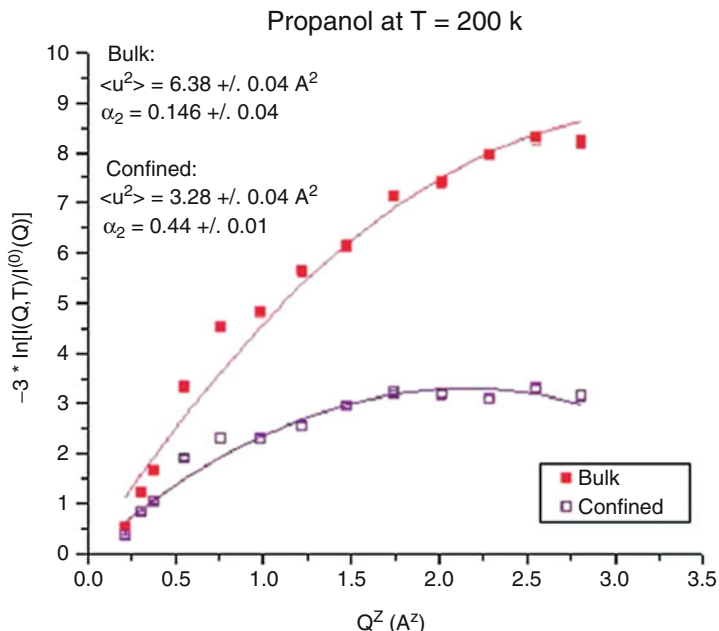
Fig. 14.16 MSD calculated assuming Eq. 14.17. As can be seen data fits nicely in the entire temperature range (Reprinted with permission from [85]. Copyright (2011) AIP Publishing LLC)

$$A(Q,T) = \exp\left[-\frac{Q^2 < u^2 >}{3} + \frac{\alpha_2}{2!}\left(\frac{Q^2 < u^2 >}{3}\right)^2 + \ldots\ldots\ldots\ldots\right] \quad (14.17)$$

In the above equation, α_2 represents the non-Gaussian contribution. The non-Gaussianity can be better understood by MD simulations [27]. As can be seen in the above equation, as Q increases second term starts to contribute significantly. There is a way around it though – one can always restrict Q range to lower side and avoid contributions from higher order terms. We used the above approach and also calculated MSD using only the lower Q range. The data fits very well to this approach and is shown in Fig. 14.16. However, the MSD values calculated for both bulk and confined propanol were within error bars. For propanol, α_2 parameter was found to be 0.14 for bulk, while it increased to 0.44 for confined sample at 200 K. Though higher non-Gaussianity is consistent with literature, the interpretation of parameter α_2 is still not so clear, and a detailed comparison with MD simulations is required. For more details on this, please see Ref. [87].

We also analyzed the MSD data of confined samples to see if a direct correlation with bulk MSD can be made. We tried to scale the confined data to recover bulk MSD above the glass transition which shows up as a sharp upturn in MSD. Interestingly, MSD data of PNOL and PG can be scaled with bulk by using factors

of 2.1 and 1.4, respectively. However, no factor can reproduce the data for bulk glycerol from confined glycerol data. This scaling points in the direction where stronger wetting seems to lead to higher mobility or less hindrance of the molecules. On the other hand, if we assume that the slow interfacial layer is too slow to be detected on backscattering spectrometer, then it is possible that bulk-like material at the center of the pores contribute to this MSD, while the slow interfacial layer contributes very little in the temperature range investigated here.

As briefly mentioned above, Q and T dependence of KWW shape parameter have been discussed for bulk polymers and simple liquids, but for confined liquids hardly any data exists. This is a very important aspect of the dynamics of confined liquids as Q dependence of shape parameter can be related to heterogeneity in these glasses. The relaxation function can be given as superposition of exponentials with some distribution of relaxation times as

$$\varnothing(t) = \int_0^\infty \rho(t) e^{-\frac{t}{\tau}} d\tau \qquad (14.18)$$

Therefore, the distribution ρ of relaxation time is strongly related with observed shape parameter β. As β decreases, the distribution broadened. In this sense, shape parameter can be considered as a direct measure of heterogeneity in the glass. However, there is a debate about the real origin of the non-exponential behavior in polymers, and it has also been suggested that non-exponential character of the relaxation does not need to be related to distribution and it could be inherent to the dynamics [27]. For the following discussion, we assume non-exponential behavior arises due to a distribution of relaxation times.

We plot shape parameters for representative propylene glycol in Fig. 14.17. As can be seen no temperature or Q dependence is observed for bulk PG, while it decreases monotonically as Q is increased in confined liquid. If we take shape parameter as a measure of heterogeneity, these measurements suggest that heterogeneity increases strongly at smaller length scales. According to Swenson et al. [88], this can be rationalized in terms of different averaging. Essentially, on smaller length scales more localized modes average out, while at larger length scales more global-like motions average or dominate the relaxation. As for the T-effects, for confined liquids, surprisingly as the temperature is increased, shape parameter decreased rather strongly. This opposite behavior in confined liquids can only be rationalized assuming as the liquid cools, the more mobile and faster liquid in the pore slows down becoming more like solid while the interfacial layer wetting the pore walls. This picture will increase overall heterogeneity as temperature is increased and therefore shape parameter will decrease.

As we mentioned above, shape parameter and relaxation time are strongly coupled and therefore a comparison of temperature dependence of relaxation time in a given system is rather difficult if shape parameters show temperature dependence as well. This can be resolved if an average relaxation time is calculated as follows:
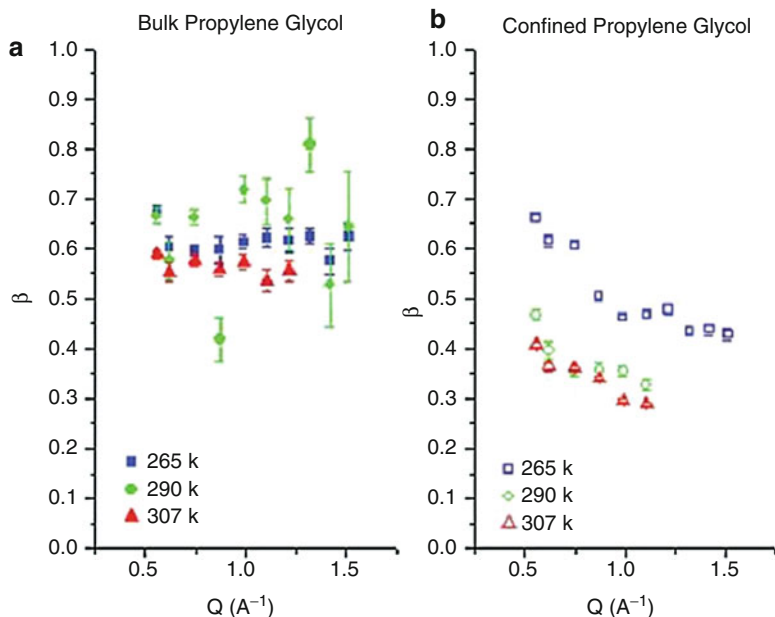
Fig. 14.17 Q dependence of shape parameter shown for (**a**) bulk PG and (**b**) confined PG (Reprinted with permission from [85]. Copyright (2011) AIP Publishing LLC)

$$< \tau >= \int_0^\infty \exp\left[-\left(\frac{t}{\tau}\right)^\beta\right] dt = \frac{\tau}{\beta}\Gamma\left(\frac{1}{\beta}\right) \qquad (14.19)$$

The Q dependence follow a power law $\tau(Q) \propto Q^{-\gamma}$ behavior at all temperatures for both bulk and confined liquids. For example, for PG at T = 307, 290 K, and 265 K, the exponent γ takes the values of 1.99, 1.65, and 1.68, respectively, while for confined PG, the exponent takes the values of 0.82 and 0.79 at the same temperatures. As can be seen, relatively much weaker Q dependence is observed for confined PG. This behavior is repeated for other two glass formers as well.

Although these results point out a number of features of confined dynamics, still a clear relationship between the surface wetting strength and effect on relaxation is not observed. If we compare absolute values, we find that the measured shift in relaxation times at a given temperature of PG is higher than glycerol. A very naïve interpretation of this shift is that relaxation is less affected when the liquid-matrix interaction is stronger, opposing the general consensus that stronger surface wetting leads to slower dynamics. An alternative interpretation is that motions occurring within the interfacial layers are too slow to be detected by instrument, and the observed relaxation is actually coming from the molecules that are near the core. Therefore, the data can be interpreted in a two mutually conflicting ways depending on whether the instrument probes the behavior of all the samples or only the liquid

core. These results press on the need for detail theoretical and simulation need in order to resolve these ambiguities from the data interpretation.

9.6   Solutions Under Confinement

Unlike neat liquids, only a few dynamical and structural studies have been reported on binary liquids in nanopores. These include the following mixtures: water/methanol, acetone/water, and isobutyric acid/water [89–92], only the last one being by neutron scattering. As there is scarcity of works on the binary liquids under confinement, we decided to discuss this study in detail. From the existing literature, it appears that the hydrophilic/hydrophobic character of each molecule and their abilities to form hydrogen bonding with the silanol groups of the wall can lead to a local demixing at the liquid/solid interface. To investigate these, Lerbret et al. studied glucose water solutions in bulk and under confinement [92]. Two confined solutions, i.e., 1 m and 3 m along with bulk 3 m solution, were measured using QENS. As QENS is very sensitive to hydrogen, care was taken to avoid hydrogen exchange between hydrogenated sugar and deuterated water. The five exchangeable hydrogens of glucose molecule were allowed to exchange with deuterium by mixing sugar with D_2O. Mixture was then dried and mixed again with D_2O. This is a neat trick that works in a number of situations where exchangeable hydrogens need to be exchanged with deuterium before the experiment. These authors looked at the cooperativity between glucose and water through elastic scattering by developing a mode for elastic intensities. They analyzed elastic scattering in terms of a sigmoidal function (more details can be found in Ref. [92]) superimposed on a sloping background. This way authors were able to characterize amplitude A, temperature T_0, and steepness of the transition B. The following form was used:

$$f(T) = A\left(1 - \frac{1}{1 + e^{-B\left(T - T^0\right)}}\right) + (C - DT) \tag{14.20}$$

In this scenario, when B is close to zero, the transition can be considered gradual and represent lower cooperativity, while higher values of B represent higher cooperativity, i.e., ability to crystallize. This should not be confused with cooperativity that is discussed when dealing with supercooled state of glass formers, origin of which is entirely different. The elastic scattering from three samples is shown in Fig. 14.18. This model fits the data rather well and the fitted values of B are equal to 1.67, 0.11, and 0.14 for the bulk, 1 m (mol/l), and 3 m confined solutions, respectively. Clearly the confinement leads to a significant decrease of the B parameter, showing the sugar/water solutions show a tendency for crystallization in the bulk and for supercooling under confinement. In addition, the presence
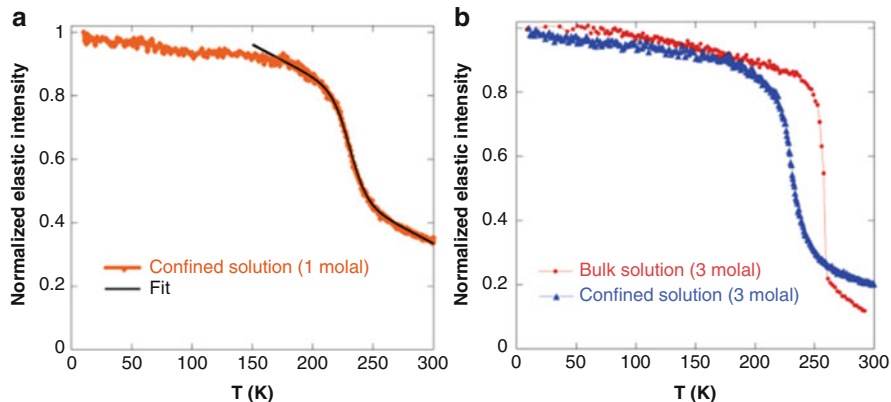
Fig. 14.18 Normalized elastic intensities plotted against temperature for bulk and confined solutions. Fits to Eq. 14.20 are shown as well (Reprinted with permission from [92]. Copyright (2011) American Chemical Society)

of sugar molecules in water leads to a decrease of cooperativity as shown by the lower B values in the 3 m bulk solutions than the value of bulk D2O.

Interestingly, QENS measurements on backscattering and time of flight showed no quasi-elastic broadening for the 3 m confined solution indicating relaxation times of sugar molecules in such a small environment are slower than 5 ns consistent with the scenario of strong localization of glucose molecules at the pore surface. On the other hand, data for confined 1 m solution clearly showed quasi-elastic broadening. This can be modeled by a combination of a delta function, a Lorentzian and a flat background. The FWHM of Lorentzian broadening follows jump-diffusion (Eq. 14.9)-like behavior. Due to strong confinement effects, diffusion coefficients of sugar can be measured below the melting temperature of bulk 1 m solution which is 275 K. The diffusion coefficient for glucose solutions confined in MCM-41 (3.2 nm) is about 30 % lower than that obtained for a confinement of 18 nm in literature [93]. As diffusion coefficients at 18 nm are very close to bulk values, this slowing down can be attributed to the formation of numerous additional hydrogen bonds between the solute molecules and the surface silanol groups present inside mesopores. These results are consistent with, e.g., water dynamics under confinement where water molecules form hydrogen bonding with confining media via silanol groups. These results have been supported by MD simulations where it is shown that MSD of glucose in the surface region is about an order of magnitude lower than that of glucose in the core region. This significant slowing down points to a high concentration of glucose in the vicinity of pore surface. These results show that the effects of nanoscale confinement on the behavior of hydrogen-bonded binary liquids not only depend on topological constraints from the pore but also on the relative affinities of both molecules for the pore wall that may lead to local demixing.

9.7 Effect of Nanoparticles on Conductivity

Polymer electrolytes are promising materials for electrochemical device applications particularly for rechargeable batteries and fuel cells. The area of polymer electrolyte has gone through various developmental stages from dry solid polymer electrolyte (SPE) to plasticized, gel, rubbery electrolytes to nanocomposite polymer electrolytes. In this development, neutron scattering has provided a tremendous amount of information about the role of polymer segmental dynamics in actual conduction and its mechanism. One of the major concerns that remains is the lower conductivities exhibited by these SPEs for real-world application. Accordingly SPEs have been modified in many ways to improve conductivity. One such modification is to improve the conductivity using nanoparticle fillers. Macrometer-sized ceramic fillers were used for a long time, but actual increase in conductivity was observed only when the size of the particle approached nanometer scale. The use of various fillers have substantially increased conductivity but still remains lower than that is required for practical purpose. Before we go into the details of how nanoparticles affect the conductivity in SPEs, it is important to understand how conductivity mechanism actually occurs in these materials. As far as the mechanism of conduction is concerned in SPEs, the common consensus is that Li ions move through the polymer host by breaking and reforming with ether oxygens, and somehow this transport mechanism is facilitated by segmental motions of polymer. In order to understand the role of nanoparticles, Fullerton et al. measured a number of lithiated polyethylene oxide samples with ether oxygen to lithium ratios ranging from 14:1 to 8:1 and Al_2O_3 nanoparticle concentrations ranging from 5 wt% to 25 wt% [94]. Small-angle neutron scattering data showed that nanoparticles are aggregated to a similar extent in all fillings so we can discard the effects of aggregates that are generally prevalent in SPE. Interestingly, nanoparticles improve conductivities at all temperatures but only at eutectic composition of 10:1. The QENS measurements showed no change in polymer segmental mobility indicating that nanoparticles actually do not improve conductivity at least by increasing polymer mobility as often believed. A rotational process was observed in both filled and unfilled samples which is consistent with the rotation of $(PEO)_6:LiClO_4$ which forms channel-like structure which is more conductive. Interestingly, this rotation becomes more restricted in the presence of nanoparticles at an ether oxygen to lithium ratio of 8:1. These results suggest that ether oxygen in $(PEO)_6:LiClO_4$ nuclei and the $(PEO)_6:LiClO_4$ fluctuations interact directly with the acidic sites on the nanoparticle surface at this concentration. As restriction of rotation does not seem to affect conductivity, it is hard to really pinpoint from these results how nanoparticles actually increase observed conductivity. Ganpatibhola et al. [95] studied the influence of nanofiller surface chemistry and ion content on the ability of nanoparticles to improve conductivity. The two types of nanoparticles used in this study are acidic α-Al_2O_3 and neutral γ-Al_2O_3. The acidic filler is found to be more effective at increasing conductivity at the non-eutectic compositions, whereas

the results were similar at eutectic concentrations. It appears that the eutectic concentrations maximize the influence of nanofillers, and therefore, surface chemistry effects are not dominant. In addition, rotation of $(PEO)_6$:$LiClO_4$ fragments is distinct at the eutectic composition with more restricted rotations that persists to higher temperatures than the other compositions. The restricted rotations of $(PEO)_6$:$LiClO_4$ remnants in nanocomposites compared to neat SPEs suggest that the nanoparticle surface stabilizes $(PEO)_6$:$LiClO_4$ remnants which due to their conductive nature help in achieving higher conductivities. Authors, however, did not find any signs of the presence of alternating layers of PEO and $(PEO)_6$/$LiClO_4$.

9.8   Methane Recovery from Coalbeds

In recent years lots of efforts have been done to recover methane from unminable coalbeds. Methane is a clean burning gas and it has high energy per unit mass. Methane is mainly adsorbed inside the coalbed which is about 2 km deep where mining the coal is not economical. Getting out of the adsorbed methane from the deep coalbeds is technically very challenging. However, a new technique has been tried to tap the methane from deep coalbed by pumping carbon dioxide (CO_2) gas. Since the adsorption rate for CO_2 on the coal surface is approximately twice that of methane, it can potentially displace methane that remains sequestrated in the pores of coal seams. To optimize the process of methane extraction from the coalbed, knowledge of methane diffusivity under various temperature and pressure is necessary.

Y. B. Melnichenkov and coworkers have reported the QENS studies on the diffusivity of methane under CO_2 and nitrogen (N_2) pressures [96]. They used carbon aerogel with 40 Å pore size to confine the methane and other gases. The surface chemistry of carbon aerogel and coal is very similar. Natural coal cannot be used in such experiments because it contains different sized pores, ranging from macro- to nanopores. The experiments were done by keeping 0.965 MPa of methane in carbon aerogel and applying extra CO_2 and N_2 pressure. Since the methane molecule contains four hydrogen atoms and oxygen or nitrogen does not have an incoherent neutron cross section, the experiments only provide the information on the diffusive motion of methane (See Fig. 14.19).

It was observed that, and clear from the figure 14.19, methane diffuses faster with CO_2 pressure, while the diffusivity of methane did not change with N_2 pressure. This experiment clearly indicates that CO_2 displace the adsorbed methane from the surface of the carbon aerogel. They also reported pressure dependence of diffusivity of methane alone and observed that the diffusivity of methane increases up to a pressure of 3 MPa, but further increasing the pressure decreases the methane diffusivity [97] (see Fig. 14.20). These results indicate that CO_2 is one of the best gases for displacing the adsorbed methane from unminable coals and about 3 MPa is the optimum pressure for such recovery process.
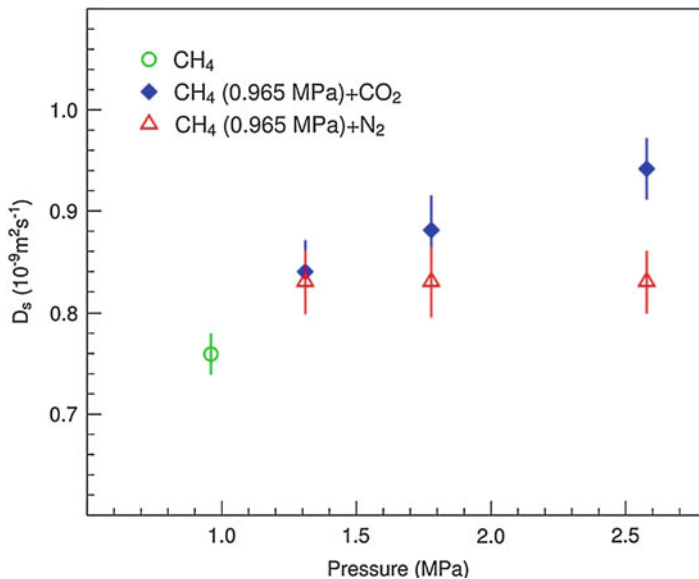
Fig. 14.19 The self-diffusivity of methane in nano-porous carbon aerogel as a function of applied CO_2 (*filled diamond*) and N_2 (*open triangle*) pressure. The data point at 0.965 MPa shows the diffusivity of pure CH_4 (Reprinted with permission from [96])

9.9   Energy Storage Applications

The demand of the energy increases day by day and fossil fuels will run out in coming years. The efficient utilization of electrical energy generated from solar, wind, and other intermittent sources require significant improvements in the energy storage capacity of electric energy storage devices like batteries and EDLCs. In many applications where rapid charge-discharge is required, batteries alone are insufficient to meet the necessary needs; for example, electric vehicles require a coupling of supercapacitors with batteries or fuel cells to deliver the high power needed during acceleration [98].

Electric double-layer capacitors (EDLCs) also known as supercapacitors offer a solution to the problem of fast charge-discharge rates [99]. The EDLS can charge and discharge electricity from a few minutes down to the millisecond range. Compared to common dielectric capacitors, EDLCs have much higher charge storage density and power. The capacitance of room temperature ionic liquid (RTIL)-based double-layer capacitors has been found to increase while confining the RTILs in the nano-porous electrode interfaces [100]. RTILs show the widest currently known stable voltage windows and they are nonvolatile and nonflammable; in contrast to other widely used electrolytes. The increase in capacitance shows oscillatory behavior with pore size of carbon electrode materials. Until now there is no clear understanding of the reason for the oscillatory behavior and how the dynamics of RTILs in the pores influence the capacitance.
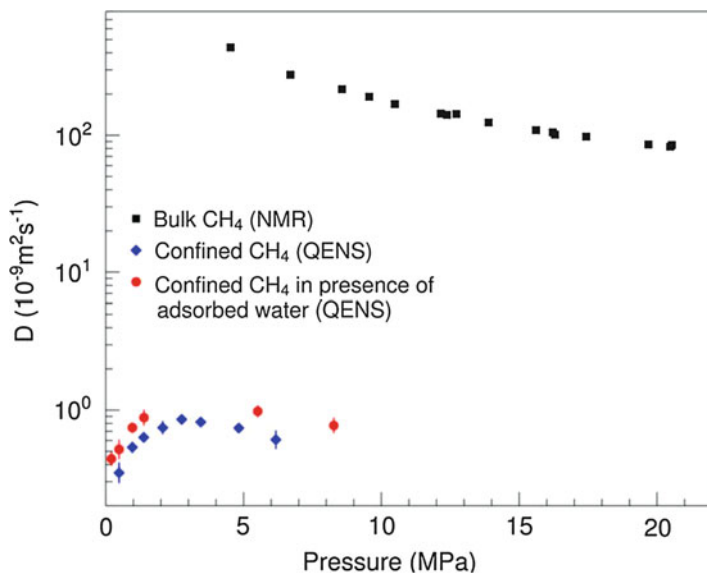
Fig. 14.20 The self-diffusivity of methane in nano-porous carbon aerogel at ambient temperature is a function of applied pressure. The *solid circles* are the data measured from carbon aerogel pores containing adsorbed water from atmospheric exposure, and the *solid diamonds* represent the diffusivities in dried aerogel. For comparison with bulk methane, diffusivity measured by NMR at ambient temperature is also shown (*solid squares*) (Reprinted with permission from [97])

It is known that confining fluid in nano- or mesopores is often associated with unusual structural and dynamical phenomena. For example, water can be supercooled much below its melting temperature and diffusion of water molecules is predicted to be faster than in their bulk state [101]. There have been several reported QENS studies on RTILs confined in the mesoporous carbon materials to understand dynamic and the relation with charge storage mechanism in supercapacitors. In recent QENS studies on [BMIM] [Tf2N] and [H2NC (demo) 2] [BETI] RTILs using a neutron backscattering spectrometer, two relaxation processes were observed in a time scale of 10–1000 ps. One of the relaxation processes is the in-cage rattling motion and the other is the long-range diffusion process. These RTILs were also examined for their relaxation behavior in the confined states (see Fig. 14.21).

It was observed that the long-range diffusion process is faster at low temperature (290 K), and on heating the same reaches a similar value as that obtained in the bulk liquids. The in-cage diffusion process, on the other hand, behaves differently in these RTILs [102]. In the [BMIM][Tf2N], the in-cage motion is comparatively faster than that of in the bulk at low temperature, and at high temperature it reaches the bulk value (see Fig. 14.22). But we made a surprising observation that the in-cage motion slows down on increasing with the temperature [103]. All the above mentioned studies were done when the RTILs were confined in the ordered
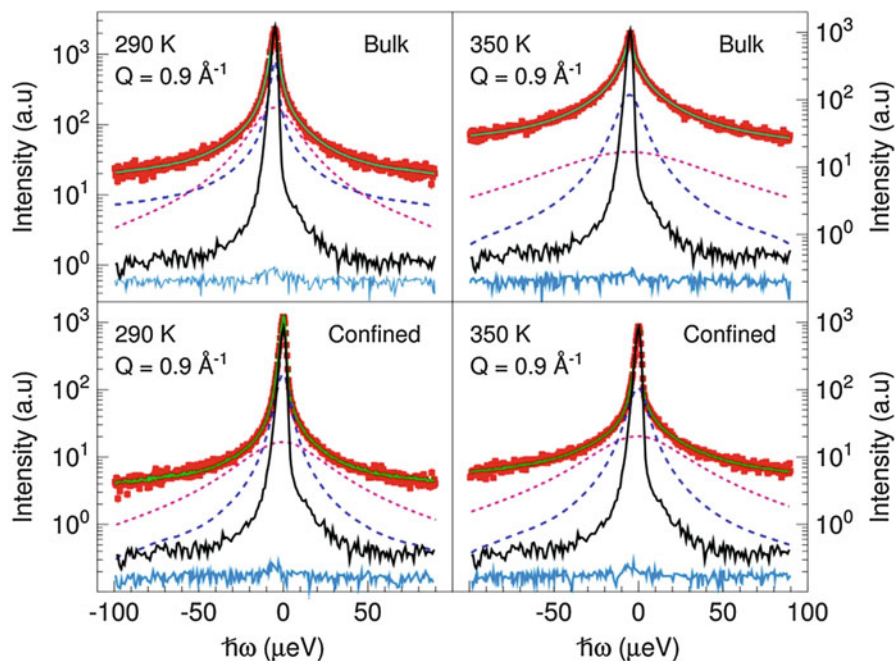
Fig. 14.21 Quasi-elastic spectra of BMIM-Tf2N in the bulk and confined in the mesoporous carbon materials (*solid squares*) and solid spectra are the resolution function. The *dotted* and *dashed lines* are quasi-elastic components of fast and slow components

Fig. 14.22 The self-diffusion coefficients of BMIM cations in the bulk and confined in mesoporous carbon materials plotted as a function of the inverse of temperature (Reprinted with permission from [102]. Copyright, European physical society)
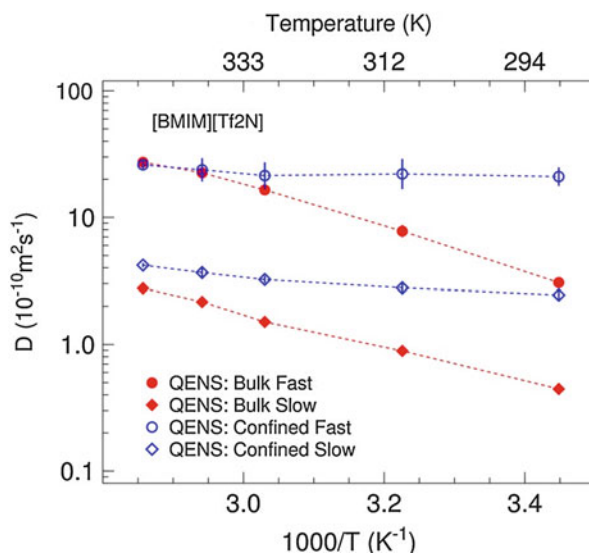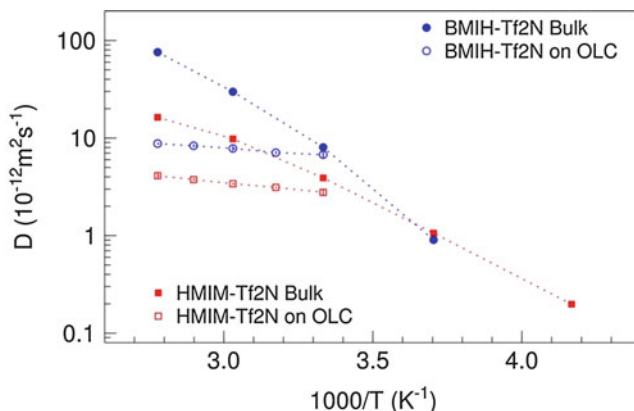
Fig. 14.23 The self-diffusivity of cations of BMIH-Tf2N and HMIM-Tf2N in the bulk and on the onion-like carbon surface plotted as a function of the inverse of temperature

mesoporous carbon materials with a pore size of 8.8 nm. A detailed understanding on the influence of diffusive dynamics on charge-discharge process in super-capacitors and diffusive dynamics of RTILs under the application of cyclic potential needs to be studied. There are no such studies reported so far.

Onion-like carbon (OLC) is an allotrope of carbon with large surface area. Because of large surface area, it is one of the best electrode materials for EDLCs. We have studied the dynamics of three different RTILs with varying molecular size of cations; EMIM-Tf2N, HMIM-Tf2N, and BMIH-Tf2N on the ILC surfaces. The anions in the ionic liquids are the same, Tf2N. Tf2N is an aprotic molecule and not sensitive to neutron. In the bulk states, the diffusivity of cations in these liquids show molecular size dependence; the smaller molecules diffuse faster and bigger cations diffuse slower. However, on the OLC surface, the diffusivities of the RTILs did not show the size dependence.

The diffusivity of biggest BMIH molecules was faster than that of HMIM (see Fig. 14.6). However, the smallest molecule, EMIM, still diffuses faster than the other two cations (HMIM and BMIH) on the OLC surface (see Fig. 14.23). The rate performance of the super-capacitors made with the same OLC and RTILs found to be dependent on the molecular size of the RTILs. The EMIM-Tf2N-containing super-capacitor gives a best rate performance compared to other two RTILs [103].

J. P. Embs and collaborators reported the dynamics of pyridinium-based ionic liquids (1-butylpyridinium bis(trifluoromethylsulfonyl)imide [BuPy][Tf2N] and 1-dodecylpyridinium bis(trifluoromethylsulfonyl)imide [C12Py][Tf2N]) with different alkyl chain length. Similar to the previous observation in BMIM-Tf2N, the pyridinium-based ionic liquids also show two diffusive motions in different time scales, and the slower of these motions can be described by a jump-diffusion model. The faster motion is the in-cage localized dynamics, which is found to be more complex. The chain and the ring of the cations contribute to the localized process and resulted in two different values of diffusion coefficients or relaxation times [104].

10   Conclusions and Future Perspective

We have shown that neutron scattering in particular quasi-elastic neutron scattering is a very powerful tool to investigate dynamics of a variety of materials under confinement. The unique access to length scale via momentum transfer makes QENS a very powerful technique as the nature and origin of motions can be probed more effectively; in particular self-motions can be probed in a unique way. Neutron scattering provides unique information about the geometry of the motion under consideration. The topic of dynamics under confinement has progressed a great deal because of the ability of neutron scattering to probe dynamics at different length scales for complete characterization. In this chapter we have reviewed and discussed a variety of materials under confinement, particularly from the soft matter field. The material that has benefitted the most by the geometrical confinement under nanopores is "water." As hydrogen bonding is broken, water is not able to crystallize, and successful measurements have been made in the so-called no man's land. It appears that water behavior is somewhat typical of a glass former in that region and typical properties of amorphous systems, e.g., polymers and small molecule glass formers are observed. However, unlike dynamics in these materials, dynamics of water clearly show fragile-to-strong crossover through the temperature dependence of relaxation times or FWHM. This has been observed not only in water under geometrical confinement but even in biomolecules where water is confined in hydration shell. The presence of FSC and its pressure dependence has provided the concept of a 2nd critical point and a Widom line has been drawn in the P-T phase diagram. There remain a number of unanswered questions that hopefully will be dealt in the near future. For example, the presence of low-density water and high-density water requires more detailed investigation of these water phases. The dynamics of water in nanocages has brought up the extreme heterogeneous dynamics of water, which seems to be related with the different environment experienced by water molecules. These studies show clearly that precaution must be taken when attributing spectrum broadness to distribution of time scales. This is further complicated as measurement of the slowest processes in confined systems depends on instrument's resolution. The NSE typically can resolve processes up to 20 ns and in some cases up to 100 ns. As studies seem to hint that a layer of simple liquids closest to the pore might be slower than what available instruments can resolve, pushing instrumentation to be able to resolve even slower process seems to be the most important point. This seems to have been taken seriously by scientific community, and NSE spectrometers that can resolve up to 200 ns are in sight, and instruments with resolution to be able to resolve up to 1000 ns are being proposed.

Neutron scattering has been used extensively to study polymer segmental motions under confinement. General consensus seems to be that overall polymer mobility under confinement is decreased. However, there seem to be cases where local segmental dynamics is affected by confinement, and in some cases, hardly any change on local dynamics is observed. In particular, the fast processes seem to remain unaffected by confinement effects. Nanoparticles have also been found very effective to increase conductivity in SPE. Using NS, a somewhat hindered rotation

of $(PEO)_6$:$LiClO_4$ has been characterized. The role of nanoparticles seems to be to act as a surface stabilizer which in turn provides a path for continuation and increased conduction in SPE. As nanoparticles are invisible to neutrons, conclusions about the role of nanoparticles have to be made rather indirectly. On the bright side, new materials are emerging that can be used as nanoparticles and exhibit their own dynamics. For example POSS seems to be very popular due to their use as polymer nanocomposites. We hope to learn the role of intrinsic dynamics of nanoparticles on the observed dynamics of guest molecules by employing such materials. This can particularly be interesting in identifying the role of nanoparticle in improving conductivity in SPE discussed above.

References

1. Risi CLS, Figueiredo Neto M, Akpinar E, Santos MBL (2013) Dynamic light scattering and viscosity measurements in a ternary and quaternary discotic lyotropic nematic liquid crystal: tuning the backflow with salt. Phys Rev E 88:022506
2. Shpyrko OG (2014) X-ray photon correlation spectroscopy. J Synchrotron Radiat 21:1057
3. Chmelik C, Kärger J (2010) In situ study on molecular diffusion phenomena in nanoporous catalytic solids. Chem Soc Rev 39:4864
4. Zöllmer V, Rätzke K, Faupel F, Meyer A (2003) Diffusion in a metallic melt at the critical temperature of mode coupling theory. Phys Rev Lett 90:195502
5. Sangoro JR, Kremer F (2012) Charge transport and glassy dynamics in ionic liquids. Acc Chem Res 45:525
6. Bée M (1988) Quasielastic neutron scattering principles and applications in solid state chemistry, biology and materials science. Adam Hilger, Bristol, England
7. Singwi KS, Sjolander A (1960) Diffusive motions in water and cold neutron scattering. Phys Rev B 119:3
8. Desmedt A, Soetens JC, Prager M, Russina M, Ollivier J (2011) Dynamics of methyl iodide clathrate hydrate, investigated by MD simulations and QENS experiments. J Phys Chem C 115:12689
9. http://www.ncnr.nist.gov/resources/n-lengths/
10. http://www.ncnr.nist.gov
11. Hamilton MA, Barnes AC, Howells WS, Fischer HE (2001) Ag+dynamics in the superionic and liquid phases of Ag2Se and Ag2Te by coherent quasi-elastic neutron scattering. J Phys Condens Matter 13:2425–2436
12. Mezei F (ed) (1980) Neutron spin echo, vol 128, Lecture notes in physics. Springer, Berlin
13. Meyer A, Dimeo RM, Gehring PM, Neumann DA (2003) The high-flux backscattering spectrometer at the NIST center for neutron research. Rev Sci Inst 74:275
14. Copley JRD, Cook JC (2003) The disk chopper spectrometer at NIST: a new instrument for quasi-elastic neutron scattering studies. Chem Phys 292:477
15. http://neutrons.ornl.gov/facilities/SNS/
16. http://www.ill.eu/
17. http://www-llb.cea.fr/en/
18. http://www.frm2.tum.de/en/index.html
19. http://europeanspallationsource.se/
20. https://www.ill.eu/instruments-support/instrumentsgroups/instruments/in16b/description/instrument-layout/
21. http://www.mlz-garching.de/spheres
22. http://neutrons.ornl.gov/basis/

23. Springer T (1972) Quasi-elastic neutron scattering for the investigation of diffusive motions in solids and liquids. Springer, Berlin/New York
24. Paalman HH, Pings CJ (1962) Numerical evaluation of x-ray absorption factors for cylindrical samples and numerical evaluation of x-ray absorption factors for cylindrical samples and annular sample cells. J Appl Phys 33:2635
25. Mancinelli R (2012) Multiple neutron scattering corrections, some general equations to do fast evaluations. J Phys: Conf Ser 340:012033
26. Kohlrausch R (1857) Theorie des elektrischen Rückstandes in der Leidner Flasche. Annalen der Physik und Chemie (Poggendorff) 91:179
27. Arbe A, Colmenero J, Alvarez F, Monkenbusch M, Richter D, Farago B, Frick B (2002) Non-Gaussian nature of the alpha-relaxation of glass-forming polyisoprene. Phys Rev Lett 89:245701
28. Rajagopal AK, Ngai KL (1991) In: Ngai KL, Wright GB (eds) Relaxations in complex systems. North Holland, Amsterdam
29. Tyagi M, Alegria A, Colmenero J (2005) Heterogeneous dynamics of poly(vinyl acetate) far above Tg: a combined study by dielectric spectroscopy and quasi-elastic neutron scattering. J Chem Phys 122:244909
30. Angell CA (2002) Liquid fragility and the glass transition in water and aqueous solutions. Chem Rev 102:2627–2650
31. Casalini R, Roland C (2004) Viscosity at the dynamic crossover in o-Terphenyl and Salol under high pressure. Phys Rev Lett 92:245702
32. Debenedetti PG, Stillinger FH (2001) Supercooled liquids and the glass transition. Nature 410:259
33. Holland-Moritz D, Stüber S, Hartmann H, Unruh T, Hansen T, Meyer A (2009) Structure and dynamics of liquid Ni36Zr64 studied by neutron scattering. Phys Rev B 79:064204
34. Kordel T, Holland-Moritz D, Yang F, Peters J, Unruh T, Hansen T, Meyer A (2011) Neutron scattering experiments on liquid droplets using electrostatic levitation. Phys Rev B 83:104205
35. Meyer A, Busch R, Schober H (1999) Time-temperature superposition of structural relaxation in a viscous metallic liquid. Phys Rev Lett 83:5027
36. Meyer A, Wuttke J, Petry W, Randl O, Schober H (1998) Slow motion in a metallic liquid. Phys Rev Lett 80:4454
37. Gotze W, Sjogren L (1992) Relaxation processes in supercooled liquids. Rep Prog Phys 55:241
38. Foffi G, Gotze W, Sciortino F, Tartaglis P, Voigtmann T (2004) α-relaxation process in binary hard-sphere mixture. Phys Rev B 69:011505
39. Chathoth SM, Damaschke B, Koza MM, Samwer K (2008) Dynamics singularity in multicomponent glass-forming metallic liquids. Phys Rev Lett 101:037801
40. Chathoth SM (2011) Microscopic glass-transition in Ni based metallic-glass forming melts. Europhys Lett 95:26001
41. Chathoth SM, Damaschke B, Embs JP, Samwer K (2009) Giant changes in atomic dynamics on microalloying metallic melt. Appl Phys Lett 95:191907
42. Speedy RJ, Angell CA (1976) Isothermal compressibility of supercooled water and evidence for a thermodynamic singularity at −45°C. J Chem Phys 65:851
43. Mishima O, Stanley HE (1998) The relationship between liquid, supercooled and glassy water. Nature 396:329–335
44. Chen SH, Teixeira J, Nicklow R (1982) Incoherent quasi-elastic neutron scattering from water in supercooled regime. Phys Rev A 26:3477
45. Teixeira J, Bellissent-Funel MC, Chen SH, Dorner B (1985) Observation of new short-wavelength collective excitations in heavy water by coherent inelastic neutron scattering. Phys Rev Lett 54:2681–2683
46. Bellissent-Funel M-C, Chen SH, Zanotti J-M (1995) Single-particle dynamics of water molecules in confined space. Phys Rev E 51:4558

47. Zanotti J-M, Bellissent-Funel M-C, Chen S-H (1999) Relaxational dynamics of supercooled water in porous glass. Phys Rev E 59:3084
48. Bellissent-Funel MC, Longeville S, Zanotti JM, Chen SH (2000) Experimental observation of the α-relaxation in supercooled water. Phys Rev Lett 85:3644
49. Faraone A, Liu L, Mou C-Y, Shih P-C, Copley JRD, Chen S-H (2003) Translational and rotational dynamics of water in mesoporous silica materials: MCM-41-S and MCM-48-S. J Chem Phys 119:3963
50. Chen S-H, Leao C, Sciortino F, Gallo P, Tartaglia P (1999) Model for single particle dynamics in supercooled water. Phys Rev E 59:6708
51. Liu L, Faraone A, Chen S-H (2002) Model for the rotational contribution to quasi-elastic scattering spectra from supercooled water. Phys Rev E 65:041506
52. Sciortino F, Gallo P, Chen S–H, Tartaglia P (1996) Supercooled water and kinetic glass transition. Phys Rev E 54:6331
53. Faraone A, Liu L, Mou C-Y, Yen C-W, Chen S-H (2004) Fragile-to-strong liquid transition in deeply supercooled confined water. JCP 121:10843
54. Angell CA (1995) Formation of glasses from liquids and biopolymers. Science 267:1924–1935
55. Liu L, Chen S-H, Faraone A, Yen C-W, Mou C-Y (2005) Pressure dependence of fragile-to-strong transition and a possible second critical point in supercooled confined water. Phys Rev Lett 95:117802
56. Doster W, Busch S, Gaspar AM, Appavou M-S, Wuttke J, Scheer H (2010) Dynamical transition of protein-hydration water. Phys Rev Lett 104:098101
57. Chu X-Q, Kolesnikov AI, Moravsky AP, Garcia-Sakai V, Chen S-H (2007) Observation of a dynamic crossover in water confined in double-wall carbon nanotubes. Phys Rev E 76:021505
58. Faraone A, Liu K-H, Mou C-Y, Zhang Y, Chen S-H (2009) Single particle dynamics of water confined in a hydrophobically modified MCM-41-S nanoporous matrix. J Chem Phys 130:134512
59. Chu X-Q, Liu K-H, Tyagi M, Mou C-Y, Chen S-H (2010) Low-temperature dynamics of water confined in a hydrophobic mesoporous material. Phys Rev E 82:020501
60. Mamontov E, Vlcek L, Wesolowski DJ, Cummings PT, Rosenqvist J, Wang W, Cole DR, Anovitz LM, Gasparovic G (2009) Suppression of the dynamic transition in surface water at low hydration levels: a study of water on rutile. Phys Rev E 79:051504
61. Chu X-Q, Ehlers G, Mamontov E, Podlesnyak A, Wang W, Wesolowski DJ (2011) Diffusion processes in water on oxide surfaces: quasielastic neutron scattering study of hydration water in rutile nanopowder. Phys Rev E 84:031505
62. Mallamace F, Branca C, Corsaro C, Leone N, Spooren J, Stanley HE, Chen S-H (2010) Dynamical crossover and breakdown of the Stokes-Einstein relation in confined water and in methanol-diluted bulk water. J Phys Chem B 114:1870–1878
63. Garrahan JP, Chandler D (2002) Geometrical explanation and scaling of dynamical heterogeneities in glass forming systems. Phys Rev Lett 89:035704
64. Faraone A, Fratini E, Todea AM, Krebs B, Muller A, Baglioni P (2009) Dynamics of water in voids between well-defined and densely packed spherical nanocages acting as polyprotic inorganic acids. J Phys Chem C 113:8635–8644
65. Faraone A, Fratini E, Garai S, Müller A, Tyagi M, Jenkins T, Mamontov E, Paul RL, Copley JRD, Baglioni P (2014) Incoherent quasielastic neutron scattering study of the relaxation dynamics in molybdenum-oxide keplerate-type nanocages. J Phys Chem C 118:13300–13312
66. Volino F, Dianoux AJ (1980) Neutron scattering law for diffusion in a potential of spherical symmetry: general formalism and application to diffusion inside a sphere. Mol Phys 41:271–279
67. Yamada T, Yonamine R, Yamada T, Kitagawa H, Tyagi M, Nagao M, Yamamuro O (2011) Quasi-elastic neutron scattering studies on dynamics of water confined in nanoporous copper rubeanate hydrates. J Phys Chem B 115:13563–13569

68. Kropka JM, Sakai VG, Green PF (2008) Local polymer dynamics in polymer-C60 mixtures. Nano Lett 8:1061–1065
69. Chrissopoulou K, Anastasiadis SH, Giannelis EP, Frick B (2007) Quasielastic neutron scattering of poly(methyl phenyl siloxane) in the bulk and under severe confinement. J Chem Phys 127:144910
70. Akcora P, Kumar SK, García Sakai V, Li Y, Benicewicz BC, Schadler LS (2010) Segmental dynamics in PMMA-grafted nanoparticle composites. Macromolecules 43:8275–8281
71. Roh JH, Tyagi M, Hogan TE, Roland CM (2013) Space-dependent dynamics in 1,4-polybutadiene nanocomposite. Macromolecules 46:6667–6669
72. Colmenero J, Alvarez F, Arbe A (2002) Self-motion and the alpha-relaxation in a simulated glass forming polymer: crossover from Gaussian to non-Gaussian dynamic behavior. Phys Rev E 65:041804
73. Roh JH, Tyagi M, Hogan TE, Roland CM (2013) Effect of binding to carbon black on the dynamics of 1,4-polybutadiene. J Chem Phys 139:134905
74. Shintani H, Tanaka H (2008) Universal link between the boson peak and transverse phonons in glass. Nat Mater 7:870–877
75. Nakatani AI, Ivkov R, Papanek P, Yang H, Gerspacher M (2000) Inelastic neutron scattering from filled elastomers. Rubber Chem Technol 73:847–863
76. Cordes DB, Lickiss PD, Rataboul F (2010) Recent developments in chemistry of cubic polyhedral Silsesquioxanes. Chem Rev 110:2081–2173
77. Jalarvo N, Gourdon O, Ehlers G, Tyagi M, Kumar SK, Dobbs KD, Smalley RJ, Guise WE, Ramirez-Cuesta A, Wildgruber C, Crawford MK (2014) Structure and dynamics of octamethyl-POSS nanoparticles. J Phys Chem C 118:5579–5592
78. Handke B, Jastrzebski W, Kowalewska W (2008) Structural studies of crystalline octamethylsilsesquioxane. J Mol Struct 887:159–164
79. Jalarvo N, Tyagi M, Crawford M (2015) Quasielastic neutron scattering study of POSS ligand dynamics. EPJ Web J 83:02007
80. Fujita S, Kamazawa K, Yamamoto S, Tyagi M, Araki T, Sugiyama J, Hasegawa N, Kawasumi M (2013) Proton conductivity under dry conditions for mesoporous silica with highly dense sulfonic acid groups. J Phys Chem C 117:8727–8736
81. Kamazawa K, Harada M, Araki T, Matsuo Y, Tyagi M, Sugiyama J (2014) Interrelationship between number of mobile protons, diffusion coefficient, and AC conductivity in superprotonic conductors, CsHSO4 and Rb3H(SeO4)2. J Phys Soc Jpm 83:074604
82. Kintzel EJ, Kidder MK, Buchanan AC, Britt PF, Mamontov E, Zamponi M, Herwig KW (2012) Dynamics of 1,3-diphenylpropane tethered to the interior pore surface of MCM-41. J Phys Chem C 116:923–932
83. Arndt M, Stannarius R, Gorbatschow W, Kremer F (1996) Dielectric investigations of the dynamic glass transition in nanopores. Phys Rev E 54:5377
84. Gorbatschow W, Arndt M, Stannarius R, Kremer F (1996) Dynamics of H-bonded liquids confined to nanopores. Europhys Lett 35(9):719
85. Prisk TR, Tyagi M, Sokol PE (2011) Dynamics of small-molecule glass formers confined in nanopores. J Chem Phys 134:114506
86. Zorn R (2007) Multiple scattering corrections of neutron scattering elastic scans. Nucl Instrum Methods Phys Res A 572:874–881
87. Zhang Y, Tyagi M, Mamontov E, Chen SH (2012) Quasi-elastic neutron scattering studies of the slow dynamics of supercooled and glassy aspirin. J Phys Condens Matter 24:064112
88. Swenson J, Bergman R, Longeville S (2001) A neutron spin echo study of confined water. J Chem Phys 115:11299
89. Aoyama N, Yoshihara T, Furukawa S-I, Nitta T, Takahashi H, Nakano M (2007) Molecular simulation study on adsorption of methanol/water mixtures in mesoporous silicas modified pore silylation. Fluid Phase Equilib 257:212

90. Furukawa S-I, Nishiumi T, Aoyama N, Nitta T, Nakano MJ (2005) A molecular simulation study on adsorption of acetone/water in mesoporous silicas modified by pore surface silylation. Chem Eng Jpn 38:999
91. Hellweg T, Schemmel S, Rother G, Bruulet A, Eckerlebe H, Findenegg GH (2003) De-mixing dynamics of binary liquid system in a controlled pore glass. Eur Phys J E 12:1
92. Lerbret A, Lelong G, Mason PE, Saboungi M-L, Brady JW (2011) Molecular dynamics and neutron scattering study of glucose solutions confined in MCM-41. J Phys Chem B 115:910–918
93. Lelong G, Price DL, Brady JW, Saboungi M–L (2007) Dynamics of trehalose molecules in confined solutions. J Chem Phys 127:65102
94. Fullerton-Shirey SK, Maranas JK (2010) Structure and mobility of PEO/LiClO4 solid polymer electrolytes filled with Al2O3 nanoparticles. J Phys Chem C 114:9196–9206
95. Ganapatibhotla LVNR, Maranas JK (2014) Interplay of surface chemistry and ion content in nanoparticle-filled solid polymer electrolytes. Macromolecules 47:3625–3634
96. Chathoth SM, He L, Mamontov E, Melnichenko YB (2012) Effect of carbon dioxide and nitrogen on the diffusivity of methane confined in nano-porous carbon aerogel. Microporous Mesoporous Mater 148:101–106
97. Chathoth SM, Mamontov E, Melnichenko YB, Zamponi M (2010) Diffusion and adsorption of methane confined in nano-porous carbon aerogel: a combined quasi-elastic and small-angle neutron scattering study. Microporous Mesoporous Mater 132:148–153
98. Faggioli E, Rena P, Danel V, Andrieu X, Mallant R, Kahlen H (1999) Supercapacitors for the energy management of electric vehicles. J Power Sources 84:261–269
99. Pandolfo AG, Hollenkamp AF (2006) Carbon properties and their role in supercapacitors. J Power Sources 157:11–27
100. Chmiola J, Largeot C, Taberna P-L, Simon P, Gogotsi Y (2010) Monolithic carbide-derived carbon films for micro-supercapacitors. Science 328:480–483
101. Verkerk P (2001) Dynamics in liquids. J Phys Condens Matter 13:7775–7799
102. Chathoth SM, Mamontov E, Dai S, Wang X, Fulvio PF, Wesolowski DJ (2012) Fast diffusion in a room temperature ionic liquid confined in mesoporous carbon. Europhys Lett 97:66004
103. Van Aken KL, McDonough JK, Li S, Feng G, Chathoth SM, Mamontov E, Fulvio PF, Cummings PT, Dai S, Gogotsi Y (2014) Effect of cation on diffusion coefficient of ionic liquids at onion-like carbon electrodes. J Phys Condens Matter 26:284104
104. Embs JP, Tatsiana B, Elena R, Verlaine F (2013) QENS study of diffusive and localized cation motions of pyridinium-based ionic liquids. J Phys Soc Jpn 82:1–6

Index